XL INTERNATIONAL SCIENTIFIC CONFERENCE ON INFORMATION, COMMUNICATION AND ENERGY SYSTEMS AND TECHNOLOGIES

ICEST 2005

Proceedings of Papers

Niš, 2005

ICEST 2005 - XL INTERNATIONAL SCIENTIFIC CONFERENCE ON INFORMATION, COMMUNICATION AND ENERGY SYSTEMS AND TECHNOLOGIES, Serbia and Montenegro, Niš, June 29 – July 1, 2005

Proceedings of Papers

Editor: Prof. Dr. Bratislav D. Milovanović

Technical Editor: Mr. Zoran Ž. Stanković

Published by: Faculty of Electronic Engineering, Niš, Serbia and Montenegro

Printed by: UNIGRAF, Niš, Serbia and Montenegro

Number of copies printed: 300

Printing of this edition has been financially supported by Serbian Ministry of Science and Environment Protection

ISBN: 86-85195-25-X

Dear Colleagues,

Welcome to the XL International Scientific Conference on Information, Communication and Energy Systems and Technologies - ICEST 2005. The conference is going to be held from June 29th until July 1st , 2005, at the Faculty of Electronic Engineering, University of Niš, Serbia and Montenegro. The Conference is, for the third time, jointly organized by the Faculty of Electronic Engineering, Niš, Serbia and Montenegro, the Faculty of Communications and Communication Technologies, Sofia, Bulgaria, and by the Faculty of Technical Sciences, Bitola, Macedonia. This is the second time that this big Balkan event takes place in Niš. Moreover, we have an honor to host all the participants at this jubilee Conference.

As to the earlier ICEST Conferences, many authors from institutions all over the Europe submitted their papers. This year, 184 papers have been accepted for oral or poster presentation. The Conference will also include a presentation of Yugoslav, Bulgarian and Macedonian IEEE section activitiy presentations of the latest journal issues: Facta Universitatis, Microwave Review and JISA INFO as well as several commercial presentations.

I hope that all participants will take opportunities not only to exchange their knowledge, experiences and ideas but also to make contacts and establish further collaboration. A social program, rich in events, will provide more relaxing atmosphere for meeting the colleagues.

I wish you successful presentations and pleasant stay in Niš!

On the behalf of the Technical Program Committee,

Prof. Dr Bratislav Milovanović,
Conference Chairman

XL INTERNATIONAL SCIENTIFIC CONFERENCE ON INFORMATION, COMMUNICATION AND ENERGY SYSTEMS AND TECHNOLOGIES

Serbia and Montenegro, Niš, June 29 – July 1, 2005

ICEST 2005

organized by

Faculty of Electronic Engineering,
Niš, Serbia and Montenegro

Faculty of Communications and Communication Technologies, Sofia, Bulgaria

Faculty of Technical Sciences,
Bitola, Macedonia

under auspices of

- **Serbian Academy of Science and Arts**
- **Serbian Ministry of Science and Environment Protection**
- **Serbian Ministry of Capital Investment**

in cooperation with:

- **Academy of Engineering Sciences of Serbia and Montenegro**
- **Yugoslavia IEEE Section**
- **National IEEE Communication Chapter and Society for Telecommunication**
- **National IEEE MTT Chapter and Society for MTT**
- **Society for ETRAN**

with support of many sponsors.

TECHNICAL PROGRAM COMMITTEE

Chairman:

B. Milovanović University of Niš, Serbia and Montenegro

Vice Chairmen:

D. Dimitrov, Technical University of Sofia, Bulgaria

C. Mitrovski, Univ. “St.Kliment Ohridski”- Bitola, Macedonia

Members:

E. Altimirski, Technical University of Sofia, Bulgaria
D. Antić, University of Niš, Serbia and Montenegro
R. Arnaudov, Technical University of Sofia, Bulgaria
M. Bogdanov, Univ. "Sv. Kiril i Metodij", Skopje, Macedonia
Z. Bojković, Univ. of Belgrade, Serbia and Montenegro
V. Ceselkovska, Univ. “St.Kliment Ohridski”- Bitola, Macedonia
B. Dimitrijević, University of Niš, Serbia and Montenegro
N. Dodov, Technical University of Sofia, Bulgaria
E. Ferdinandov, Technical University of Sofia, Bulgaria
Lj. Gavrilovska, Univ. "Sv. Kiril i Metodij", Skopje, Macedonia
M. Gusev, Univ. "Sv. Kiril i Metodij", Skopje, Macedonia
H. Hristov, Technical University of Sofia, Bulgaria
M. Janković, Comm. of Yug. PTT, Serbia and Montenegro
M. Kamilovski, Univ. "Sv. Kiril i Metodij", Skopje, Macedonia
M. Kostov, Univ. “St.Kliment Ohridski”- Bitola, Macedonia
B. Kovačević, Univ. of Belgrade, Serbia and Montenegro
R. Kunchev, Technical University of Sofia, Bulgaria
V. Manevska, Univ. “St.Kliment Ohridski”- Bitola, Macedonia
M. Milosavljević, Univ. of Belgrade, Serbia and Montenegro
G. Milovanović, University of Niš, Serbia and Montenegro
V. Milutinović, Univ. of Belgrade, Serbia and Montenegro
M. Momchedgikov, Technical University of Sofia, Bulgaria
D. Najdenov, Univ. “St.Kliment Ohridski”- Bitola, Macedonia
Lj. Panovski, Univ. "Sv. Kiril i Metodij", Skopje, Macedonia
Z. Petrović, Univ. of Belgrade, Serbia and Montenegro
R. Pranchov, Technical University of Sofia, Bulgaria
I. Prudius, Nat. Univ. “Lvivska Polytechnika”, Ukraine
V. Pulkov, Technical University of Sofia, Bulgaria
B. Reljin, Univ. of Belgrade, Serbia and Montenegro
B. Radenković, Univ. of Belgrade, Serbia and Montenegro
M. Radevska, Univ. “St.Kliment Ohridski”- Bitola, Macednia
M. Stanković, University of Niš, Serbia and Montenegro
N. Stojadinović, University of Niš, Serbia and Montenegro
G. Stojanov, Technical University of Sofia, Bulgaria
M. Stojčev, University of Niš, Serbia and Montenegro
D. Tasić, University of Niš, Serbia and Montenegro
Lj. Trpezanovski, Univ. “St.Kliment Ohridski”- Bitola, Macedonia

CONFERENCE ORGANIZING COMMITTEE

Chairman:

D. Antić, University of Niš, Serbia and Montenegro

Members:

J. Čivljak, University of Niš, Serbia and Montenegro
K. Dimitrov, Technical University of Sofia, Bulgaria
D. Janković, University of Niš, Serbia and Montenegro
V. Jović, University of Niš, Serbia and Montenegro
L. Lubih, Technical University of Sofia, Bulgaria
B. Milovanović, University of Niš, Serbia and Montenegro
P. Mitrevski, Univ. "St.Kliment Ohridski"-Bitola, Macedonia
Z. Perić, University of Niš, Serbia and Montenegro
Z. Stanković, University of Niš Serbia and Montenegro
B. Stefanovski, Univ. "St.Kliment Ohridski"-Bitola, Macedonia
D. Tasić, University of Niš, Serbia and Montenegro

TECHNICAL SUPPORT

A. Atanasković, University of Niš, Serbia and Montenegro
J. Joković, University of Niš, Serbia and Montenegro
A. Jovanović, University of Niš, Serbia and Montenegro
Z. Marinković, University of Niš, Serbia and Montenegro
M. Ranđelović, University of Niš, Serbia and Montenegro
T. Ranđelović, University of Niš, Serbia and Montenegro
M. Stojanović, University of Niš, Serbia and Montenegro
A. Stošić, University of Niš, Serbia and Montenegro

CONFERENCE SECRETARIAT

General Secretary:

Z. Stanković, University of Niš, Serbia and Montenegro

Members:

J. Ranđelović, University of Niš, Serbia and Montenegro
M. Milijić, University of Niš, Serbia and Montenegro

Faculty of Electronic Engineering
Aleksandra Medvedeva 14, 18 000 Niš, Serbia and Montenegro
phone: +381 18 [529 205, 529 303, 529 105]
fax: +381 18 588 399
e-mail: icest@elfak.ni.ac.yu

CONFERENCE INTERNET SITE

http://www.icest.medianis.net

LIST OF ICEST 2005 REVIEWERS

Prof. Dr. Kiril Anguelov
Technical University of Sofia, Bulgaria

Prof. Dr. Dragan Antić
University of Niš, Serbia and Montenegro

Prof. Dr. Rumen Arnaudov
Technical University of Sofia, Bulgaria

Mr. Aleksandar Atanasković
University of Niš, Serbia and Montenegro

Prof. Dr. Božidar Dimitrijević
University of Niš, Serbia and Montenegro

Prof. Dr. Peter Dineff
Technical University of Sofia, Bulgaria

Prof Dr. Goran Djordjević
University of Niš, Serbia and Montenegro

Mr. Goran T. Djordjević
University of Niš, Serbia and Montenegro

Doc. Dr. Nebojša Dončov
University of Niš, Serbia and Montenegro

Prof. Dr. Dragan Drača
University of Niš, Serbia and Montenegro

Prof. Dr. Dušan Drajić
University of Belgrade, Serbia and Montenegro

Mr. Predrag Eferica
University of Niš, Serbia and Montenegro

Prof. Dr. Elissaveta Gadjeva
Technical University of Sofia, Bulgaria

Prof. Dr. Miodrag Gmitrović
University of Niš, Serbia and Montenegro

Prof. Dr. Nataša Gospić
University of Belgrade, Serbia and Montenegro

Prof. Dr. Miruljub Grozdanović
University of Niš, Serbia and Montenegro

Prof. Dr. Vassil Guliashki
Institute of Information Technologies, Sofia, Bulgaria

Prof. Dr. Hristo Hinov
Technical University of Sofia, Bulgaria

Prof. Dr. Iliycho Iliev
Technical University of Sofia, Bulgaria

Mr. Predrag Ivaniš
University of Niš, Serbia and Montenegro

Prof. Dr. Rosen Ivanov
Technical University of Gabrovo, Bulgaria

Prof. Dr. Toni Janevski
University "Sv. Kiril I Metodije", Macedonia

Prof. Dr. Dragan Janković
University of Niš, Serbia and Montenegro

Prof. Dr. Milun Jevtić
University of Niš, Serbia and Montenegro

Mr. Jugoslav Joković
University of Niš, Serbia and Montenegro

Doc. Dr. Nataša Maleš-Ilić
University of Niš, Serbia and Montenegro

Doc. Dr. Dragan Mančić
University of Niš, Serbia and Montenegro

Mr. Zlatica Marinković
University of Niš, Serbia and Montenegro

Prof. Dr. Vera Marković
University of Niš, Serbia and Montenegro

Prof. Dr. Georgy Mihov
Technical University of Sofia, Bulgaria

Prof. Dr. Mikho Mikhov
Technical University of Sofia, Bulgaria

Prof. Dr. Ivan Milentijević
University of Niš, Serbia and Montenegro

Mr. Dejan Milić
University of Niš, Serbia and Montenegro

Prof. Dr. Dragiša Milovanović
University of Niš, Serbia and Montenegro

Dr. Zlatoljub Milosavljević
Filtroniclk, Finland

Doc. Dr. Danijela Milović
University of Niš, Serbia and Montenegro

Prof. Dr. Cvetko Mitrovski
Univ. "St.Kliment Ohridski"- Bitola, Macedonia

Prof. Dr. Milica Naumović
University of Niš, Serbia and Montenegro

TABLE OF CONTENTS

PLENARY SESSION

ORAL SESSIONS

CODING TECHNICS

POWER SYSTEMS AND DISTRIBUTION SYSTEMS

ELECTRONIC COMPONENTS, SYSTEMS AND TECHNOLOGY I

MICROWAVE ELECTRONICS

ELECTRICAL MACHINES

ELECTRONIC COMPONENTS, SYSTEMS AND TECHNOLOGY II

APPLIED ELECTROMAGNETICS

INDUSTRIAL ELECTRONICS

SIGNAL PROCESSING

TELECOMMUNICATION NETWORKS

IMAGE PROCESSING

ANTENNAS

MEASUREMENT SYSTEMS

WIRELESS COMMUNICATION

COMPUTER SYSTEMS AND APPLICATIONS

CONTROL SYSTEMS I

TELECOMMUNICATION SYSTEMS

INTERNET TECHNOLOGY AND APPLICATIONS

CONTROL SYSTEMS II

POSTER SESSIONS

PO1 – TELECOMMUNICATION SYSTEMS AND TECHNOLOGY

PO2 - SIGNAL PROCESSING AND NEURAL NETWORK

PO3 - COMPUTER SYSTEM AND INTERNET TECHNOLOGY

PO4 - ELECTRONICS

PO5 - EDUCATION QUALITY AND REMOTE ECOLOGICAL MONITORING

Session PL:

PLENARY SESSION

Comparing Semantic Web and Data Mining

Veljko Milutinovic[1],

Abstract - **The fields of semantic web and datamining are currently emerging and creating lots of scientific and commercial interest. The two fields are typically analyzed in isolation from each other. This paper represents an effort to treat them as two different approaches to the same final goal, and to treat them comparatively. In addition, it explains the essential issues of the two approaches, and gives some predictions about the future development trends.**

I. INTRODUCTION

A major goal of both datamining and semantic web is efficient retrieval of knowledge from large databases (single or distributed) or the Internet. In this context, the knowledge is treated through a synergistic interaction of information (data) and their relationships (links within a typical relational database or links on the web). Synergistic interaction implies also the cases in which the meaning of data differs from the cases when data is represented in isolation, to the cases when data is linked with other data, which is a special challenge for research efforts aimed at efficient knowledge retrieval.

If datamining and semantic web are compared from the point of view of how they facilitate retrieval of knowledge, a major difference is in the placement of complexity. In the case of datamining, complexity is (conditionally speaking) placed at run time and retrieval time. In the case of semantic web, complexity is (conditionally speaking) placed at compile time and design time.

In the case of datamining, data and knowledge are represented with simple mechanisms (typically based on HTML) and typically without metadata (data about data). Consequently, relatively complex algorithms have to be used, which means that complexity is migrated to the retrieval request time. In return, there is no complexity at system design time – one uses well developed algorithms and their standard implementations.

In the case of semantic web, data and knowledge are represented with complex mechanisms (typically based on XML), and with plenty of metadata (sometimes, a byte of data – a name – may be accompanied with a megabyte of data – descriptive information related to that name). Consequently, relatively simple algorithms can be used for data retrieval, which means that complexity placed at the data retrieval time is minimal. However, large and sometimes relatively sophisticated metadata have to be created at system design time – one has to invest large efforts into the metadata design, preprocessing, postprocessing, and general maintenance.

[1]Veljko Milutinovic, Fellow of the IEEE School of Electrical Engineering, University of Belgrade, Serbia

Major knowledge retrieval algorithms used with datamining are neural networks, decision trees, rule induction, memory based reasoning, and many others. Consequently, the stress in the datamining review part of this paper is on algorithms.

Major metadata design, processing, and maintenance tools used in semantic web are XML, RDF, and ontology languages. The ongoing research concentrates on issues like logic, proof, and trust. Consequently, the stress in the semantic web review part of this paper is on tools.

The rest of this paper is divided into three parts: an overview of datamining, an overview of semantic web, and conclusions that include trend predictions. With this final issue in mind (trend predictions), the two overview parts stress the point to be elaborated in the trends prediction part.

II. DATAMINING

This section contains a condensed overview. A detailed overview can be found in [1], which is a tutorial. That tutorial can be found on the web site of the author, and was presented many times at conferences, in house for industry, or as a university course, worldwide. Primarily, the issues are stressed which represent either the important bottlenecks of the approach or the potential solutions for the general problem of recognition of semantics in cases when data may change its meaning from one context to the other.

There are three major differences between datamining and database engineering: (a) Uncovering the hidden knowledge, (b) Treating the huge n-p complete search space, and (c) Implementing a multidimensional interface to the user.

With databases, one can do only the data retrievals conceptualized at the database design time. If a query is placed which is planed at the database design time, the database will deliver the requested information. However, if a query is made which is not predefined, the database will deliver a question mark! On the other hand, a datamine is supposed to be able to deliver answers even in such cases. This means that a major difference is in layers of intelligence that have to be placed on the top of a database, to create a datamine.

Next, traditional databases are typically much smaller compared to datamines, especially if datamining is done in the context of the entire Internet. This extra-large size means that linear search algorithms (sometimes used in the database environments) are absolutely useless in datamining environments.

Finally, the retrieved knowledge (in the case of datamine search) has to be presented to the user in a way which is easy to comprehend, especially in situations when the

meaning is dependent on the context. This requires complex graphical interfaces. On the other hand, in the case of database search, information is comprehensible even if presented in the form of tables or histograms or similar.

One possible definition of datamining implies that it represents automated extraction of predictive information from memory (large databases or the Internet), or communication lines (cell phones or data channels in general). With this in mind, the rest of this section concentrates on datamining problem types, algorithms, models, as well as some available software.

One can talk about a number of different problem types in datamining (data description and summarization, segmentation, classification, concept description, prediction, and dependency analysis), but in real systems, most of the time, one can recognize a combination of several problem types. This is important to know, because some of the algorithms (to be elaborated later) work better for one problem types, while other algorithms work better for other problem types. Consequently, if we have a combination of problem types, we have to use a combination of algorithms. As it will be seen later, especially in the case of less complex and less expensive tools, one tool supports one type of algorithm. So, treating a problem with various algorithms typically implies the usage of several tools.

One widely used class of algorithms is neural networks. These algorithms are especially useful if the nature of the problem is not well defined, and it is difficult to determine an exact explicitly defined algorithm for problem treatment. The approach uses an analogy with biological neurons and utilizes the so called artificial neurons.

Another widely used algorithm is decision trees. This algorithm is especially useful if all decision making parameters and conditions are well defined, and precise processing rules can be created. The approach uses if-then-else and case structures, to define all relevant rules.

Still another widely used algorithm is rule induction. This algorithm is used in situations when various opinion creators/leaders have different opinions, and it is not possible to set precise rules. Instead, a statistical set of rules is created, and it is allowed that various rules of the set contradict with each other. The approach uses rule definitions with specifications of confidence levels and weights.

The memory based reasoning approach is used much more widely than in datamining alone; it is used also in court practices, etc. This algorithm is used in situations when we have to reduce the problem size, in order to be able to apply more sophisticated algorithms only to a subset of cases that can not be resolved with memory based reasoning. The approach uses the concept of history size and majority logic.

Other algorithms of interest include logistic regression, discriminant analysis, generalized adaptive models, genetic algorithms, simulated annealing algorithms, etc. For research results of the author, in the domains of these algorithms, the interested reader is directed to the web site of the author [3].

The major datamining model (framework for the application of above mentioned algorithms) is the CRISP model which tries to decompose each problem into six different stages, and to apply the relevant algorithms to each stage separately (divide and conquer).

A comparison of 14 different tools is given in [1]. Each tool supports a different algorithm, and their cost (at the time of our research) spans the range of three orders of magnitude, which is a clear indication of the fact that the field is still in its development stages.

An important research issue in this emerging field is how to combine different algorithms, models, and tools, for maximal performance, especially in cases when the meaning of the required knowledge depends on the context.

III. SEMANTIC WEB

This section contains a condensed overview. A detailed overview can be found in [2], which is a tutorial. That tutorial can be found on the web site of the author, and was presented many times at conferences, in house for industry, or as a university course, worldwide. Primarily, the issues are stressed which represent either the important bottlenecks or the potential solutions for the general problem of recognition of semantics in cases when information changes the meaning from one context to the other.

The central elements of web today are the information portals responsible for indexing, referencing, and maintenance of data collections. The elements added by semantic web are metadata (S+), and they enable the information portals to be able to do a number of newly added sophisticated functions like interpretation, negotiation, planning, decision making, ratings, trust services, and many other ones. So, semantic web is an extension of the current web that enables computers to be more helpful to the real needs of their users.

The introduction of semantic enables the implementation of a number of qualitatively new concepts and applications on the web, like context awareness (linking based on the meaning of information elements, rather than on the predefined URLs), filtering (visited pages can be rated, which can later on be used for generation of automatic recommendations), annotations (one can add comments to the information on the web, which can be shared by future visitors of the same or related pages), privatization (one can create his/her own database of information from the web).

A layered model of semantic web implies 7 layers. The tower of semantic web is build on foundations consisting of metadata and URIs (Universal Resource Identifiers). The concept of URI is more general than the concept of URL. One URL refers to a specific web page, while one URI may refer to a finer granularity (subset of a web page, or even a single word on a web page). Consequently, semantic coverage can be made more sophisticated!

The major three development strategies of semantic web are: evolution support (building new techniques on the top of the existing ones), minimalist design (making large progress through small steps), and inference (based on the

predicate logic). Such a strategy is enabled by the existence of the concept of the called XML stack.

New vocabularies can be defined with RDF. As indicated before, with RDF one can combine simple metadata (atomic metadata) into more sophisticated metadata (molecular metadata). In this way, one enables that the semantic level of metadata is on the same level as the semantic level of typical user queries. This capability of RDF is enabled with the mechanism called reification. Another mechanism of importance is collections; it enables semantically related knowledge to be grouped, for easier handling.

Ontology is a specification of a conceptualization. Conceptualization is an abstract (simplified) view of the world that we wish to represent for some purpose. In other words, if we need to know only about one aspect of a problem, then all non-related knowledge has to be eliminated; however, without any negative impact on the semantics.

The most popular ontology languages are DAML+OIL or OWL. The OWL Lite is a subset of OWL. In these systems, the body of the ontology consists of classes, properties, and instances. The major component of an ontology is a taxonomy (class hierarchy). The major ontology related problem today is how to treat semantic ambiguities.

IV. Conclusion

This paper gives a comparative overview of datamining and semantic web, and underlines the urgent need for research leading to better concepts and tools for treatment of semantic ambiguities! For a more detailed treatment of these subjects, an interested reader is referred to the references of this paper, or to the proceedings of IPSI conferences [4].

References

In addition to the references listed here, an interested reader can consult also 7 different books, coauthored/coedited by the author of this paper, at his web site. Information form these books was also used in preparing this paper. A common characteristic of these 7 books is that for all of them, a Nobel Laureate wrote a foreword (7 different persons). They are related to IPSI conferences [4].

[1] Jovanovic, N., et al, 'Tutorial on Datamining,' galeb.etf.bg.ac.yu/vm/, May 2004.

[2] Vujovic, I., et al,'Tutorial on Semantic Web,' galeb.etf.bg.ac.yu/vm/, June 2004.

[3] Milutinovic, V., 'Web Site,' galeb.etf.bg.ac.yu/vm/, July 2005.

[4] 'IPSI Conferences Web Site' www.internetconferences.net, August 2005.

Session CD:

CODING TECHNIQUES

Turbo Coding Performances in Small Signal to Noise Ratio Environment

Ioana M. Bercă[1], Simona Halunga-Fratu[1], Octavian Fratu[1]

Abstract - **This paper investigates several aspects of interleaver design as well as encoder and decoder structure and algorithms in small signal to noise ratio environment. Several interleaver structures are investigated, namely block, helical, hybrid, even-odd and random and compared with respect to overall system BER results. SOVA and MAP decoder algorithms are used with different interleaver lengths. Extended simulations have been made to evaluate the BER performances of different structures and the results are presented in section 5.**

Keywords - **turbocodes, interleaver, decoder algorithm, BER.**

I. INTRODUCTION

Turbo coding respresents one of the most efficient technique of channel coding. It leads to higher data transmission rates and it improves the quality of the communication service. Turbocodes can work real close to Shannon limit capacity overcoming any other technique of channel coding known so far. The strong capacity of correction shown by the turbocodes was recognized and accepted for almost every type of channel.

Interleavers play a very important role in achieving good performances with these structures. Interleaving is the process of rearranging the ordering of the data sequence in a one-to-one deterministic format. The reverse process is deinterleaving which restores the received sequence to its original order. Interleaving is also a practical technique to enhance the error correcting capability of coding.

In this article we are analyzing the performances of turbocodes using several types of interleavers (such as odd-even interleaver, hybrid interleaver, random interleaver and block interleaver) and two algorithms: MAP and SOVA.

II. TURBO CODING AND ITERATIVE DECODING

A turbo Encoder is formed by a parallel concatenation of two recursive systematic convolutional (RCS) encoders separated by a random interleaver:

The encoder structure is called parallel concatenation because the two encoders operate on the same set of input bits rather than one encoding the output of the other. Thus turbo codes are also referred to as parallel concatenated convolutional codes.

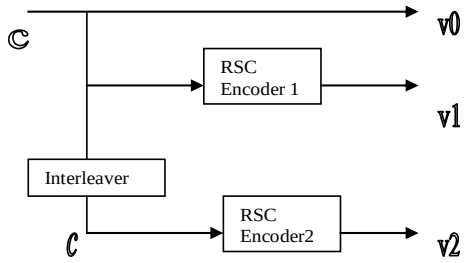

Fig.1. Encoder architecture

The interleaver in turbo coding is a pseudo-random block scrambler defined by a permutation of N elements with no repetitions. The roles of the interlevears are to generate a long block code from small memory convolutional codes; it decorrelates the inputs to the two decoders so that an iterative suboptimum decoding algorithm based on information exchange between the two component decoders can be applied.

The iterative decoder structure consists of two component decoders, serially concatenated via an interleaver, identical to the one used in the encoder, as shown in figure 2. The first decoder uses the received information bits r_0 and the parity bits generated by the first encoder r_1 in order to produce a soft output, which is interleaved and used to improve the estimate of the apriori probabilities for the second decoder. The other two inputs of the second decoder are the interleaved information sequence $\tilde{r}_0$ and the received parity sequence produced by the second encoder. This decoder produces a soft output also, that is de-interleaved and used by the first decoder to improve its apriori probabilities.

[1] "Politehnica" University of Bucharest, Splaiul Independenței 313, 77206 Bucharest 6, ROMANIA, bodita_79@yahoo.com , shalunga@elcom.pub.ro, ofratu@elcom.pub.ro

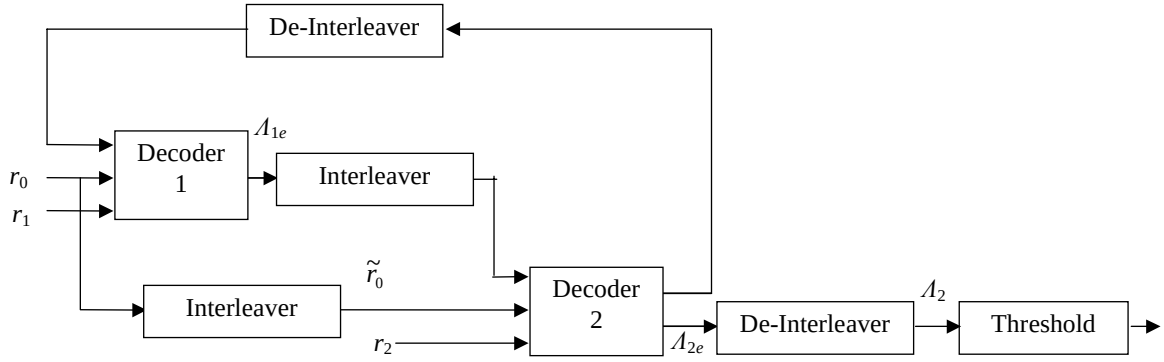

Fig.2. Iterative Decoder Architecture

The two decoders use the received sequences $r' = [\ldots\ t_{t,0},\ r_{t,1},\ t_{t+1,0},\ r_{t+1,1},\ \ldots]$ and $r'' = [\ldots\ \tilde{t}_{t,0},\ r_{t,2},\ \tilde{t}_{t+1,0},\ r_{t+1,2},\ \ldots]$ in order to compute the log-likelihood ratio for the overall code trellis

$$\Lambda(c_t) = \log\left[\frac{P(c_t = 1 \mid r', r'')}{P(c_t = 0 \mid r', r'')}\right] = \log\left[\frac{\sum_{t,c_t=1} P(r' \mid c)P(r'' \mid c)P(c)}{\sum_{t,c_t=0} P(r' \mid c)P(r'' \mid c)P(c)}\right] \quad (1)$$

for all the paths in the code trellis, and makes the decision

$$c_t = \begin{cases} 1\ ; & \Lambda(c_t) \geq 0 \\ 0\ ; & \Lambda(c_t) < 0 \end{cases} \quad (2)$$

The log-likelihood ratio from (2) can be determined using MAP, log-MAP, Max-Log-MAP and SOVA algorithms ([5], [6]).

III. Various Interleavers

One of the most significant part of a turbo-code is the designing of the interleaver. Their size, structure and algorithm considerably affect both performances and complexity of the code. For low Signal-to-Noise Ratios (SNR's) the performances are determined mainly by the size of the interleaver, while for large SNR's the structure design becomes the key factor.

A.. The Even-Odd Interleaver is a block interleaver structure. It maps the odd indexed bits on even-indexed positions and vice-versa. It is mathematically described by

$$[\pi(i) + i] \bmod 2 = 0, \quad (\forall) i \in A \quad (3)$$

This structure is used to break long error patterns that are not uniformly distributed within the sequence.

B. The Hybrid Interleaver is based on the same structure as the even-odd interleaver but the input sequence is randomly mixed before the interleaver operation. So if the input sequence is

$$c = (c_1, c_2, c_3, c_4, c_5, c_6, c_7, c_8, c_9)` \quad (4)$$

and the randomly mixed sequence is

$$\tilde{c} = (c_2, c_5, c_8, c_3, c_7, c_6, c_9, c_1, c_4) \quad (5)$$

Then, the interleaved sequence will be

$$\tilde{c} = (c_2, c_5, c_8, c_6, c_7, c_3, c_9, c_1, c_4) \quad (6)$$

The performances achieved with this kind of interleaver are high for a lower SNR.

C. The Random Interleaver uses *N* input bits written and read in a random way.

IV. 4. SOVA and MAP: Iterative Decoding Methods

The purpose of this article is to analyze the performances of turbo codes using several types of interleavers (such as odd-even interleaver, hybrid interleaver, random interleaver and block interleaver) and two algorithms: MAP and SOVA. We'll present next the methods used.

A.. MAP Algorithm is based on the minimization of the error probability criteria. The decoder generates optimal estimates like symbol a posteriori probabilities. For each transmitted symbol it generates a hard estimate and a soft output presented in the form of an a posteriori probability based on the received sequence *r*. A log-likelihood ratio is estimated like

$$\Lambda(c_t) = \log \frac{P_r\{c_t = 1 \mid r\}}{P_r\{c_t = 0 \mid r\}} \quad (7)$$

for $1 \leq t \leq \tau$, where τ is the length of the received sequence. This ratio is compared to a threshold leading to the hard estimate c_t:

$$c_t = \begin{cases} 1, & \Lambda(c_t) \geq 0 \\ 0 & \Lambda(c_t) < 0 \end{cases} \quad (8)$$

$\Lambda(c_t)$ is the soft information associated to the hard estimate c_t. This log-likelihood ratio can be used for the next step of the decoding process.

C. SOVA Algorithm is based on the same principle but it presents the advantage that it can be used on any input sequence (the MAP algorithm can be applied only to a sequence length limited). It estimates the soft information for each binary transmitted symbol based on the log-likelihood ratio $\Lambda(c_t)$ defined by

$$\Lambda(c_t) = \log \frac{P_r\{c_t = 1 \mid r_1^{\tau}\}}{P_r\{c_t = 0 \mid r_1^{\tau}\}} \tag{9}$$

where r_1^{τ} is the received sequence and $P_r(c_t=i|r_1^{\tau})$, i = 0,1 is the a posteriori probability of the transmitted symbol. This ratio is compared to a threshold leading to the hard estimate c_t

$$c_t = \begin{cases} 1, & \Lambda(c_t) \geq 0 \\ 0, & \Lambda(c_t) < 0 \end{cases} \tag{10}$$

SOVA is implemented by a bidirectional and recursive method which implies the positive and negative recursive methods. For reducing the complexity of the decoding algorithm the negative recursivity and the soft decision can be achieved simultaneous.

V. SIMULATION RESULTS AND CONCLUSIONS

In this paper we investigated the BER performances of block, helical, hybrid, even-odd and random interleavers with MAP and SOVA decoders, interleaver lengths 200 and 400 and different encoders polynomials, for small *Eb*/*N*0. The simulation results are presented in figures 3-7.

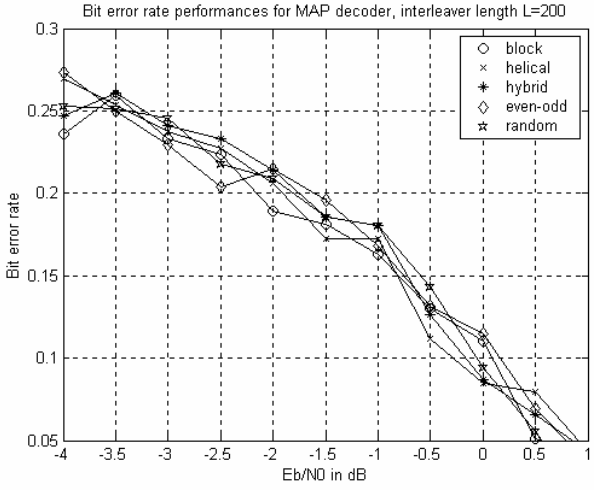

Fig. 3. BER performances for MAP decoder, L=200

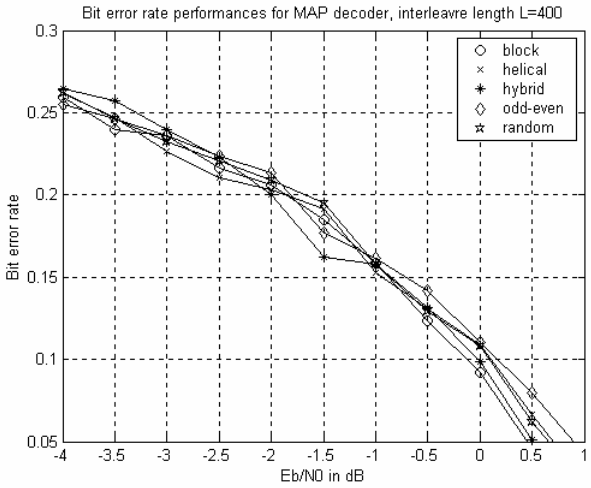

Fig. 4. BER performances for MAP decoder, L=400

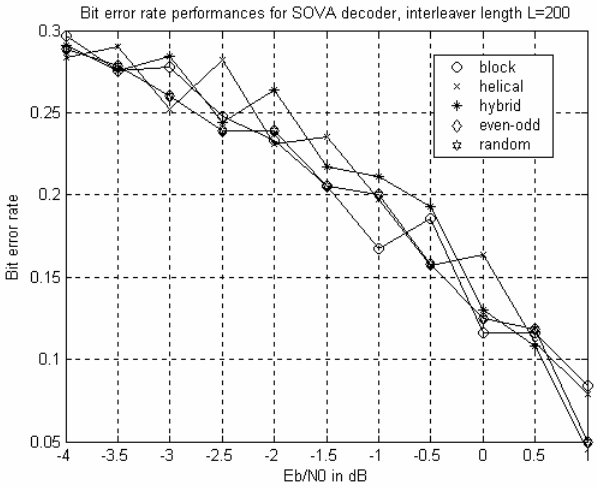

Fig. 5. BER performances for SOVA decoder, L=200

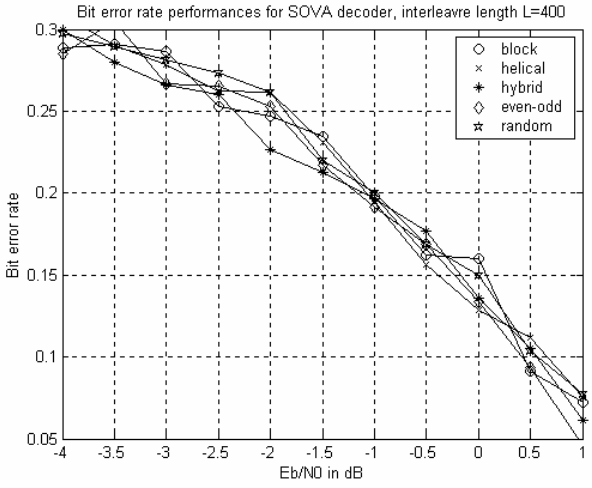

Fig. 6. BER performances for SOVA decoder, L=400

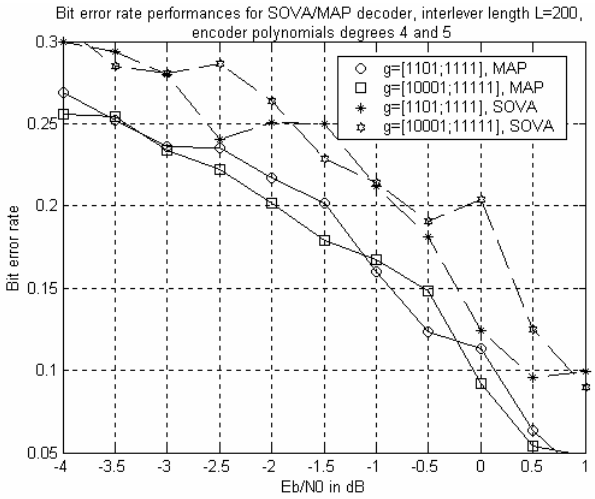

Fig.7- BER performances for SOVA/MAP decoder, interleaver length L=200 encoder polynomials degrees 4 and 5

This is a continuation of the work developed in [10]. From the results obtained several conclusions can be highlighted:

- the performances of the studied interleavers are very close to one another, differences being less than 0.05 in BER; the hybrid/random interleaver achieves still the best performances but the difference is no longer significant;
- the increase in the length interleaver brings a small improvement in BER but the difference is also very small (between 0.01 and 0.03), and it doesn't justify the implementation effort;
- the MAP performances are better than the SOVA ones, as shown in [6] with about 0.05 BER units. However the MAP decoder is much more complex than the SOVA one and the improvement still doesn't justify the effort;
- The memory encoder/decoder polynomials degree increase leads to better BER performances less than 0.7 units. This increase is more significant for the SOVA decoder. We consider that this increase does not justifies the exponential increase of the decoder complexity.

From those results we can conclude that if we have a system that operates at low *Eb*/*N*0 the best choice is to use the simplest structure possible (block interleaver, small framelengh, small degree polynomials, SOVA decoder).

REFERENCES

[1] C. E. Shannon "A mathematical Theory of Communications", *Bell Syst. Techn. Journal* Vol. 27, pp. 379-423 (part I) & 623-656 (part II), Oct 1948.

[2] C. Berrou, A. Glavieux and P. Thitimajshima, "Near Shannon limit error-correcting coding and decoding: turbocodes" *ICC-1993*, Geneva, Switzerlend, pp. 1064-1070.

[3] J. J. Ramsey, "Realization of Optimum Interleavers", *IEEE Trans. on Info. Theory*, Vol.16, No.3, May 1970, pp. 338-345

[4] G. D. Forney, Jr., "Burst Correcting Codes for Bursty Channels", *IEEE Trans. Comm*., Vol. 19, No. 5, Oct 1971, pp. 772-781.

[5] P. Robertson, E. Villebrun, P. Hocher, "A comparison of Optimal and Sub-Optimal MAP Decoding Algorithms Operation in the Log-Domain", *Proc. ICC'95*, Seattle, June 1995

[6] B Vuctic, "*Iterative Decoding Algorithms*", PIMRC'97, Sept 1997, Finland, pp. 99-120.

[7] Simona Halunga, Octavian Fratu, Dragos Paun, Ioana Berca, "Turbocodes Bit Error Rate Performances with Different Correlator Structures", *ELECTRONICS ET'2003, the 12th International Scientific and Applied Science Conference*, September 24-26, 2003, Sozopol Bulgaria, p. 106.

[8] A. Bărbulescu, S. S. Pietrobon : *"Interleaver design for turbo codes"*, 1994

[9] B. Vucetic, J. Yuan *: "Turbo Codes – Principles and Applications"*, Kluwer Academic Publishers 2001

[10] Simona Halunga, Octavian Fratu "New Interleaver Design Algorithms with Enhanced B.E.R. Performances", *Buletinul Stiintific al Universitatii "Politehnica" din Timisoara*, Tomul 49 (63), Fascicola 2, 2004, pag. 19

Self-Shrinking p-adic Cryptographic Generator

Zhaneta N. Tasheva [1], Borislav Y. Bedzhev [2], Borislav P. Stoyanov [3]

Abstract – **A new cryptographic pseudo random number generator (*PRNG*), called Self–Shrinking *p*–adic Generator (*SSPG*), is proposed in this paper. The *SSPG* sequence is evaluated and its balancing is proved. The results of statistical analysis of *SSPG* sequence are given. They show that the sequence generated by a *SSPG* is uniform, scalable, uncompressible, consistent, unpredictable and has large period. This gives the reason to consider the *SSPG* as suitable for a particular software cryptographic application in stream ciphers.**

Keywords – **Cryptography, stream cipher, PRNG.**

I. INTRODUCTION

The stream ciphers are an important tool for protecting information in digital form and for providing security services. The performance quality of the hardware and software stream ciphers depends on their crypto resistance, velocity and effectiveness. Mostly the crypto resistance of a stream cipher is connected with it ability to generate Pseudo Random Sequence with enormous period, uniform distribution of *d*-tuples for a large range of *d* and with good usually lattice structure in high dimensions.

In order to achieve high performance velocity and cost-effective software implementation, the Pseudo Random Number Generator (*PRNG*) architecture must be simple on the one hand and on the other must be combine with some nonlinear functions fast and cheap elements, like as Linear Feedback Shift Registers (*LFSRs*) and Feedback with Carry Shift Registers (*FCSRs*). Recently, some theorists [6], [8], [10] have used this new approach of stream cipher design and have proposed a few new architectures named Shrinking Generator [1] and Self–Shrinking Generator [5]. They are promising candidates for high-speed encryption applications due to their simplicity and provable properties. With regard, main goal of our paper is to suggest a novel Self–Shrinking Generator, utilizing *FCSRs*.

The paper is organized as follows. First, the basic theory of the self–shrinking generator is recalled. Second a new *PRNG* architecture, called Self–Shrinking p–adic Generator (*SSPG*) is presented. After then, some properties and statistical analysis of the *SSPG* sequence are given. Finally, the possible application areas of the *SSPG* are discussed.

[1]Zhaneta N. Tasheva is an Assistant Prof. Eng. PhD. in the Faculty of Artillery and Air Defence, National Military University, Shoumen, 1st Karel Shkorpil Str., Shoumen 9710, Bulgaria, E-mail: tashevi86@yahoo.com

[2]Borislav Y. Bedzhev is an Assoc. Prof. Eng. DSc. in the Faculty of Artillery and Air Defence, National Military University, Shoumen, 1st Karel Shkorpil Str., Shoumen 9710, Bulgaria, E-mail: bedzhev@mail.pv-ma.bg

[3]Borislav P. Stoyanov is an Assistant Prof. Mag. PhD. Student in the Shoumen University, Faculty of Computer Informatics, Shoumen, Bulgaria, E-mail: bpstoyanov@abv.bg

II. SELF-SHRINKING GENERATOR

Both the Shrinking Generator and Self-Shrinking Generator use the *LFSRs* and have a simple structure. Despite of this fact no successful cryptanalytic attack for both generators has been published so far.

The self-shrinking generator uses only one *LFSR* whose output sequence is shrunken under the control of the *LFSR* itself [5]. The self-shrinking can be applied to any binary sequences. In this process the original sequence $a=(a_0, a_1, a_2, \ldots)$ is considered as a sequence of pairs of bits. If a pair (a_{2i}, a_{2i+1}) equals the value $(1,0)$ or $(1,1)$, it is taken to produce the pseudo random bit 0 or 1, respectively. On the other hand, if the pair is equal to $(0,0)$ or $(0,1)$, it will be discarded, which means that it will not contribute an output bit to the new sequence $s=(s_0, s_1, s_2, \ldots)$.

Below some properties of self-shrunken maximum length *LFSR*-sequence will be recalled. The proofs of given theorems can be found in [5].

Theorem 1: The period *P* of a self-shrunken maximum length *LFSR*-sequence produced by an *LFSR* of length *N* satisfies:

$$P \geq 2^{\lfloor N/2 \rfloor}. \tag{1}$$

Theorem 2: The linear complexity *L* of a self-shrunken maximum length *LFSR*-sequence produced by an *LFSR* of length *N* satisfies:

$$L > 2^{\lfloor N/2 \rfloor - 1}. \tag{2}$$

The experimental results, shown by Willi Meier and Othmar Stafelbach [5], reveal that the linear complexity does not exceed the value $2^{N-1} - N + 2$.

At the end of this section, it ought to emphasize that the simple algebraic structure of the original *LFSR*-sequence has been destroyed during the self-shrinking due to the reasons:

- randomness of the positions, where the *LFSR*-sequence is shrunken;
- the *LFSR* is controlled by itself.

III. SELF-SHRINKING P-ADIC GENERATOR

In this section the basic architecture of a new Self-Shrinking *p*-adic Generator (*SSPG*) and some its properties will be presented.

A. The SSPG Architecture

The *SSPG* architecture (Fig. 1.) uses a *p*-adic *FCSR* [3] instead of a *LFSR* in contrast with the classic self-shrinking generator. This allows the generator to produce a number from 0 to *p*–1 in one step ($a_i = [0, 1, \ldots, p-1]$). The self-shrinking *p*-adic generator selects a portion of the output *p*-adic *FCSR* sequence controlling the *p*-adic *FCSR* itself by means of the following algorithm.

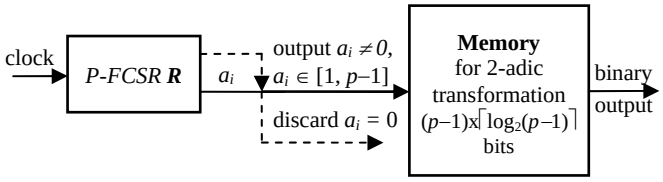

Fig. 1. Self-Shrinking *p*-adic Generator

Definition 1: The algorithm of the Self-Shrinking *p*-adic Generator (Fig. 1) consists of the following steps:

1. The *p*-adic *FCSR R* is clocked with clock sequence with period τ_0.

2. If the *p*-adic *FCSR* output number is not equal to 0 ($a_i \neq 0$), the output number forms a part of the *p*-adic *SSPG* sequence. Otherwise, if the output number of the *p*-adic *FCSR* is equal to 0 ($a_i = 0$), the *p*-adic output number of *SSPG* is discarded.

3. The shrunken *p*-adic *SSPG* output sequence is transformed in a usual binary sequence presenting every *p*-adic number with $\lceil \log_2 (p-1) \rceil$ binary digits, where $\lceil x \rceil$ is the smallest integer that is greater than or equal to real *x*. After that, every binary output number ***i***, ranging from **1** to ***p*–1**, is replaced with the binary number:

$$i - 1 + \frac{2^{\lceil \log_2 (p-1) \rceil} - (p-1)}{2}. \qquad (3)$$

TABLE I
BINARY PREZENTATION OF P-ADIC SSPG OUTPUT

***p*-adic number**	**Binary presentation of *p*-adic number**				
	***p* = 3**	***p* = 5**	***p* = 7**	***p* = 11**	***p* = 13**
1	0	00	001	0011	0010
2	1	01	010	0100	0011
3	–	10	011	0101	0100
4	–	11	100	0110	0101
5	–	–	101	0111	0110
6	–	–	110	1000	0111
7	–	–	–	1001	1000
8	–	–	–	1010	1001
9	–	–	–	1011	1010
10	–	–	–	1100	1011
11	–	–	–	–	1100
12	–	–	–	–	1101

The binary presentations of *p*-adic shrunken *SSPG* output numbers are shown with various prime *p* from 3 to 13 in Table I.

The proposed *SSPG* uses the generalization of 2-adic *FCSRs* [2], [3], [4] with stage contents and feedback coefficients in Z/(*p*) where *p* is a prime number, not necessarily 2.

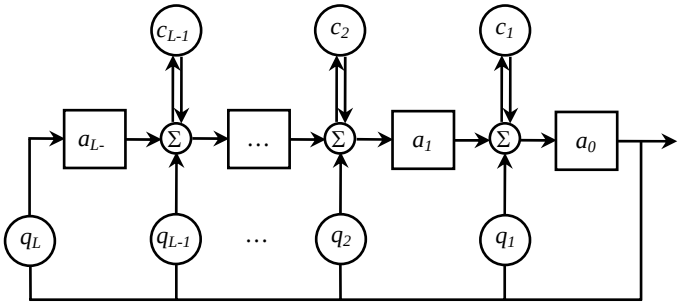

Fig. 2. Galois FCSR

Definition 2: A *p-adic feedback with carry shift register* (*FCSR*) with Galois architecture of length *L* (Fig. 2.) consists of *L stages* (or *delay element*s) numbered *0, 1, …, L-1*, each capable to store one *p*-adic (0, 1, …, *p*-1) number and having one input and one output; and a clock which controls the movement of data. During each clock cycle the following operations are performed:

1. The content of stage 0 is output and forms part of the *output sequenc*e;

2. The sum modulo *p* after stage *i*, depicted as "∑" on Fig. 2, passes to stage *i - 1* for each i, $1 \le i \le L-1$;

3. The output of the last stage 0 is introduced into each of the tapped cells simultaneously, where it is added fully (with carry) to the contents of the preceding stages. The $q_1, q_2, \ldots, q_L$ are the *feedback multipliers* and the cells denoted with $c_1, c_2, \ldots, c_{L-1}$ are the *memory* (or "*carry*") bits. If

$$q = -1 + q_1 p + q_2 p^2 + \ldots + q_L p^L \qquad (4)$$

is the base *p* expansion of a positive integer:

$$q \equiv -1 \pmod{p}, \qquad (5)$$

then *q* is a connection integer for a *FCSR* with feedback coefficients $q_1, q_2, \ldots, q_L$ in Z/(*p*).

With each clock cycle, the integer sums:

$$\sigma_j = a_{j+} a_0 q_j + c_j \qquad (6)$$

is accumulated.

At the next clock cycle this sum modulo *p*

$$a'_{j-1} = \sigma_n \pmod{p} \qquad (7)$$

passes on to the next stage in the register, and the new memory values are:

$$c'_j = \sigma_n \ (\text{div } p) . \qquad (8)$$

The nonlinearity of the proposed *SSPG* follows from the fact that it is unknown at which positions the *FCSR*-sequence is shrunken. As a result the linear algebraic structure of the original *FCSR*-sequence is destroyed. The software *SSPG* implementation is very fast because the pseudorandom generator produces $\lceil \log_2 (p-1) \rceil$ binary digits in every step.

B. The SSPG properties

In this subsection the period of *SSPG* sequences generated by maximum length *p*-adic *FCSR* will be established and it will be proved that the *SSPG* sequence is balanced.

Theorem 3: The period of the self-shrunken *p*-adic generator realized by maximum length *p*-adic *FCSR* of length *L* and connection integer *q* is:

$$T_{SSPG} = T^* . \lceil \log_2 (p-1) \rceil , \qquad (9)$$

where *T** is the quantity of output *p*-adic *FCSR* nonzero numbers.

Proof: Let $\boldsymbol{a} = (a_0, a_1, a_2, \ldots)$ be the output sequence of trivial *p*–adic *FCSR* (Fig. 2) of length *L* and connection integer *q* (Eq. (4)). By definition $\boldsymbol{a}$ is a maximum length sequence. Consequently, its period is *T*, where *T* is the multiplicative order of *p* modulo *q* (i.e. T is the smallest integer with property $p^T \equiv 1 (\text{mod } q)$) [10]. The self-shrunken *p*-adic sequence is periodic also, because every *SSPG* is a digital automat with limited quantity of possible inner states. Hence after appearing of all *T** nonzero elements of the original *FCSR* sequence, the output shrunken *p*-adic sequence will be repeated again. During the step 3 of *SSPG* algorithm every *p*-adic element of self-shrunken sequence is transformed into exactly $\lceil \log_2 (p-1) \rceil$ binary digits. Consequently the period of self-shrunken *SSPG* sequence is $T^* . \lceil \log_2 (p-1) \rceil$.

Theorem 4: The self-shrunken output *SSPG* sequence generated by maximum length *p*-adic *FCSR* of length *L* and connection integer *q* is a balanced sequence.

Proof: As is it known [2], [3], within the period of a *p*-adic *FCSR* sequence each of *p*–adic numbers from 0 to $p-1$ appears with approximately equal probability, i.e. every *p*–adic number, ranging from 1 to $p-1$, appears in the self-shrunken *p*–adic sequence approximately N_p times:

$$N_P \approx \left\lceil \frac{T}{p} \right\rceil . \qquad (10)$$

The *SSPG* algorithm utilizes a binary transformation of *p*–adic *FCSR* output elements during the step 3, which provides balanced distribution of binary digits 0 and 1. In order to prove this fact two cases will be considered.

Fist case: If the prime *p* can be present as $2^n + 1$, i.e. the odd number $p-1$ is a power of 2, then the output *p*–adic numbers from 1 to $p-1$ will be transformed into all binary numbers from 0 to $2^n - 1$ (may not be in a successive order). It is apparent that every permutation of the binary numbers from 0 to $2^n - 1$ is balanced, i.e. the number of 0s and 1s is exactly equal to $n.2^{n-1}$. This fact can be illustrated by means of Table I where:

- for $p = 3 = 2^1 + 1$ the number of 0s and 1s is equal to 1;
- for $p = 5 = 2^2 + 1$ the number of 0s and 1s is exactly $4 = 2.2^1$.

Consequently, if the prime *p* can be present in the form $p = 2^n + 1$, the numbers of 0s and 1s in the self-shrunken output *SSPG* sequence are balanced and equal to:

$$N_{0S} \approx N_{1S} \approx \left\lceil \frac{T}{2^n + 1} \right\rceil 2^{n-1} . n . \qquad (11)$$

Second case: If the odd number $p-1$ is smaller than $2^{\lceil \log2 (p-1) \rceil}$:

$$p - 1 < 2^{\lceil \log2 (p-1) \rceil} , \qquad (12)$$

then the smallest and the biggest $\frac{2^{\lceil \log_2 (p-1) \rceil} - (p-1)}{2}$ binary numbers in the range $0 \div 2^{\lceil \log2 (p-1) \rceil}$ -1 of all possible binary numbers are rejected during the step 3. Hence the quantity of 1s and 0s is balanced also and equal to $\frac{\lceil \log_2 (p-1) \rceil . (p-1)}{2}$. This fact can be illustrated by means of Table I where:

- for $p = 7 = 2^3 - 1$ the number of 0s and 1s is equal to $9 = 3.3 = 3.(7-1)/2$;
- for $p = 11 = 2^4 - 5$ the number of 0s and 1s is equal to $20 = 4.5 = 4.(11-1)/2$;
- for $p = 13$ the number of 1s and 0s is $24 = 4.6$.

Consequently, if the prime *p* satisfies the inequality:

$$p < 2^{\lceil \log2 (p-1) \rceil} + 1 \qquad (13)$$

the numbers of 0s and 1s in the self-shrunken output *SSPG* sequence are balanced and equal to:

$$N_{0S} \approx N_{1S} \approx \frac{1}{2} \left\lceil \frac{T}{2^n + 1} \right\rceil \lceil \log_2 (p-1) \rceil (p-1) . \qquad (14)$$

The transformation in step 3 (see Eq. (3)) eliminates the possibility of appearance the sequences of $2\lceil \log2 (p-1) \rceil$ consecutive 1s and $2\lceil \log2 (p-1) \rceil$ consecutive 0s also.

IV. Statistical Experimental Results

The randomness of binary sequences generated by *SSPG* was investigated by so-named "NIST suite", proposed by National Institute of Standards and Technology (USA). The NIST suite [7] includes sixteen tests. The tests examines on a variety of different types of non-randomness that could exist in a sequence. These tests are: frequency (monobit), frequency within a block, runs, longest-run-of-ones in a block, binary matrix rank, discrete Fourier transform (spectral), non-

overlapping template matching (consists of 148 subtests), overlapping template matching, Maurer's "Universal statistical", Lempel-Ziv compression, linear complexity, serial (consists of 2 subtests), approximate entropy, cumulative sums (consists of 2 subtests), random excursions (consists of 8 subtests), random excursions variant (consists of 18 subtests).

The testing process consists of the following steps [7], [9]:

1. State the null hypothesis. Assume that the binary sequence is random.

2. Compute a sequence test statistic. Testing is carried out at the bit level.

3. Compute the *p*–value, $p-\text{value} \in [0,1]$.

4. Compare the *p*–value to error probability α. Fix α, where $\alpha \in (0.0001, 0.01]$. *Success* is declared whenever $p-\text{value} \geq \alpha$; otherwise, *failure* is declared.

The 1 000 sequences of length 1 000 000 bits, generated by *SSPG* with $p = 5$, are tested. The seed of *SSPG* are changed in every 1 000 bits by modifying the connection taps, initial state and initial memory state of a *5*–adic *FCSR*. The results from all NIST statistical tests are given in Table II.

TABLE II
THE RESULTS FROM 5–ADIC SSPG STATISTICAL TESTS

Statistical Tests	**Results**
Frequency (monobit)	Pass
Frequency within a block	Pass
Cumulative sums	Pass
	Pass
Runs	Pass
Longest-run-of-ones in a block	Pass
Binary matrix rank	Pass
Discrete Fourier transform (spectral)	Pass
Non-overlapping template matching	Pass
Overlapping template matching	142 Subtests Pass 6 Subtests Failure
Maurer's "Universal statistical"	Pass
Approximate entropy	Pass
Random excursions	All 8 Subtests Pass
Random excursions variant	All 18 Subtests Pass
Serial	Pass
	Pass
Lempel-Ziv compression	Pass
Linear complexity	Pass

As one can see from Table II, most of the NIST statistical tests are passed. Only 6 subtests of non-overlapping template test are failed. It was observed that the distributions of *p*–values of sequences, passed the statistical tests, aren't distributed uniformly, i.e. the numbers of *p*–values that lie within each unity sub-interval aren't equal.

V. CONCLUSION

In this paper the architecture of new self-shrinking *p*–adic generator is suggested. A few important properties of *SSPG* sequences generated by maximum length *p*-adic *FCSR* are established. The results from statistical analysis show that the sequence generated by *SSPG* is uniform, scalable, uncompressible, unpredictable and has large period. This gives the reason to consider the *SSPG* as a fast software pseudorandom generator and it can be useful as a part of modern stream ciphers.

ACKNOWLEDGEMENT

We will be glad to thanks everyone who helps us to make some strong cryptanalysis of self-shrinking *p*–adic generator.

REFERENCES

[1] D. Coppersmith, H. Krawczyk, Y. Mansour, "The Shrinking Generator", *Proceedings of Crypto 93*, Springer-Verlag, pp. 22-39, 1994.

[2] A. Klapper, M. Goresky, "2-adic Shift Register. Fast Software Encryption", *Second International Workshop*, (Lecture Notes in Computer Science, vol. 950, Springer Verlag, N. Y.,) pp. 174–178, 1994.

[3] A. Klapper, M. Goresky, "Feedback Shift Registers, 2-adic Span, and Combiners With Memory.", *Journal of Cryptology*, Volume 10, Number 2, 1997, pp. 111-147, http://www.math.ias.edu/~goresky/pdf/2adic.jour.pdf

[4] A. Klapper, J. Xu, "Algebraic Feedback Shift Registers" *Elsevier Preprint*, 2003.

[5] W. Meier, O. Staffelbach, "The Self-Shrinking Generator" *Proceedings of Advances in Cryptology*, *EuroCrypt '94*, Springer-Verlag, pp. 205-214, 1998.

[6] P. van Oorshot, A. Menezes, S. Vanstone, "*Handbook of Applied Cryptography"*, CRC Press, 1997.

[7] A. Rukhin, J. Soto, J. Nechvatal, M. Smid, E. Barker, S. Leigh, M. Levenson, M. Vangel, D. Banks, A. Heckert, J. Dray, S. Vo, "A Statistical Test Suite for Random and Pseudo-Random Number Generators for Cryptographic Application", *NIST Special Publication 800-22* (with revision May 15, 2001) http://csrc.nist.gov/rng/.

[8] B. Schneier, "*Applied Cryptography"*, John Wiley & Sons, New York, 1996.

[9] J. Soto, "Statistical Testing of Random Number Generators", *NIST Special Publication*, http://csrc.nist.gov/rng/.

[10] Zh. N. Tasheva, B. Y. Bedzhev, V. A. Mutkov, "An Shrinking Data Encryption Algorithm with *p*-adic Feedback with Carry Shift Register", *Conference Proceedings of XII International Symposium of Theoretical Electrical Engineering ISTET 03*, Warsaw, Poland, 6-9 July, 2003., vol. II, pp. 397–400.

Bennett's Integral for Uniform Polar Quantization

Zoran H. Peric[1], Jelena R. Nikolić[2], Danijela R. Aleksić[3]

Abstract - **In this paper the analysis of Bennett's integral is given for uniform polar quantization for two-dimensional memoryless Gaussian sources with respect to granular distortion D_g , i.e. the mean-square error (MSE). The goal of this paper is finding simple equation for distortion solving Bennett's integral for uniform polar quantization and circular symmetric sources (iid Gaussian source).**

Keywords – **Bennett's integral, uniform polar quantization, normalized moment of inertia**

I. INTRODUCTION

The most important results in polar quantization was given by Swaszek and Ku who derived the asymptotically Unrestricted Polar Quantization (UPQ) [1]. Using asymptotic uniform polar analysis for calculating optimal numbers of magnitude levels and the numbers of reconstruction points for two-dimensional quantizers is done in [1, 2]. In [3] was given the analysis of vector quantization in order to determine the optimal maximal amplitude. In papers [4] and [5] were given analyses for asymptotic uniform polar quantization and asymptotic nonuniform polar quantization, respectively. Optimisatons was done with respect to granular distortion D_g , i.e. the mean-square error (MSE). In this paper Bennett's integral has been considered and succesful attempt has been made in order to extend it to the polar quantizer. Considerable attention has been focused on finding simple approximate formula for distortion that shows influence of key characteristics.

II. UNIFORM POLAR QUANTIZATION

For this analysis we use uniform polar quantizer with L madnitude levels and M_i phase reconstruction levels at the magnitude reconstruction levels m_i , $1 \le i \le L$. First we portion the magnitude range $[0, r_{L+1}]$ into magnitude rings with $L+1$ decision levels $\boldsymbol{r}=(r_1,\ldots,r_{L+1})$ ordered in turn such that $0=r_1<r_2<\ldots<r_L<r_{L+1}=r_{max}$. The magnitude reconstruction levels $\boldsymbol{m}=(m_1,\ldots,m_L)$ obviously satisfy succession $0<m_1<m_2<\ldots<m_L$. Let we assume that the total number of reconstruction points N is large enough. In that case magnitude decision levels and reconstruction levels are given in turn:

$$r_i = (i-1)\Delta, \qquad 1 \le i \le L+1 \tag{1}$$

$$m_i = (i-1/2)\Delta, \qquad 1 \le i \le L\ . \tag{2}$$

Let we consider distortion D as a function of the vector $P=(P_i)_{1\le i\le L}$ whose elements are values of phase quantization levels at the each magnitude levels. Said in other words, each concentric ring in quantization pattern is allowed to have a different number of partitions in the phase quantizer (P_i) for r in the i-th magnitude ring. Assuming that the representation points are centered in their respective cells, magnitude decision levels and reconstruction levels can be given as in Eqs. (1) and (2). Let we make a partition of each magnitude ring into M_i phase subpartitions. By denoting adjacent phase decision levels with $\phi_{i,j}$ and $\phi_{i,j+1}$, and the j-th phase reconstruction levels as $\psi_{i,j}$ for the i-th magnitude ring, $1\le j\le M_i$, following dependence is valid:

$$\phi_{i,j} = (j-1)\frac{2\pi}{P_i}. \tag{3}$$

Total distortion D may be written as the sum of granular and overload distortions, $D=D_g+D_o$. The granular distortion D_g can be given by:

$$D_g = \sum_{i=1}^{L}\sum_{j=1}^{P_i}\int_{\phi_{i,j}}^{\phi_{i,j+1}}\int_{r_i}^{r_{i+1}}[r^2+m_i^2-2rm_i\cos(\phi-\psi_{i,j})]\frac{f(r)}{2\pi}dr d\phi\ . \tag{4}$$

For this analysis we assume that the input is from a continuously valued circularly source with unit variance rectangular coordinate marginals and bivariate density function:

$$f(x,y) = p(\sqrt{x^2+y^2}). \tag{5}$$

Transforming to polar coordinates, the phase is uniformly distributed on $[0,2\pi)$ and the magnitude is distributed on $[0,\infty)$ with density function $f(r)=2\pi rp(r)$. The magnitude and phase are independent random variables. The transformed probability density function for the Gaussian source is:

$$f(r,\phi) = \frac{1}{2\pi\sigma^2}re^{-\frac{r^2}{2\sigma^2}} = \frac{f(r)}{2\pi} \tag{6}$$

[1]Zoran H. Perić is with the Faculty of Electronic Engineering, University of Nis, Beogradska 14, 18000 Nis, Serbia
E-mail: peric@elfak.ni.ac.yu
[2]Jelena R. Nikolić is with the Faculty of Electronic Engineering, University of Nis, Beogradska 14, 18000 Nis, Serbia
E-mail: njelena@elfak.ni.ac.yu
[3]Danijela R. Aleksić is with Telekom Serbia, Mobile Devision, 18000 Nis, SerbiaE-mail: danijelaal@telekom.yu

without lossing generality we assume that variance is σ^2=1. Suppose that a polar quantizer has many cells which are small and the source density is smooth. In that case granular distortion D_g of one cell is given by:

$$D_{i,j} = \frac{1}{2}\int_{R_{i,j}} \left[r^2 + m_i^2 - 2rm_i\cos\left(\phi - \psi_{i,j}\right)\right]\frac{f(r)}{2\pi}drd\phi \quad (7)$$

$$D_{i,j} = \frac{1}{2}\frac{f(m_i)}{2\pi}\int_{R_{i,j}} \left[r^2 + m_i^2 - 2rm_i\cos\left(\phi - \psi_{i,j}\right)\right]drd\phi\,. \quad (8)$$

The total granular distortion for polar quantization was found in [4]:

$$D_g^{pol} = \sum_{i=1}^{L}\sum_{j=1}^{P_i} D_{i,j} = \sum_{i=1}^{L} P_i D_{i,j} \quad (9)$$

$$D_g^{pol} = \sum_{i=1}^{L}\frac{\Delta}{12}\left(\frac{\Delta^2}{2} + \frac{2m_i^2\pi^2}{P_i^2}\right)f(m_i). \quad (10)$$

III. BENNETT'S INTEGRAL

A two-dimensional *N*-point scalar quantizer is characterized by a partition $S=\{S_1,S_2,...,S_N\}$ of two-dimensional Euclidean space R^2 into *N* quantization cells and code book, noticed as $C=\{y_1,y_2,...,y_N\}$ is consisting of *N* quantization points in two-dimensional Euclidean space R^2. A two-dimensional source vector $\boldsymbol{x}=\{x_1,x_2\}$ is quantized into one of the y_i's according to the quantization rule $Q(x)=y_i$ if $x \in S_i$. Encoding rate for two-dimensional quantizer, is $log_2N/2$. When applied to a random vector $\boldsymbol{x}=\{x_1,x_2\}$ with probability density $p(\boldsymbol{x})$, quantizer's distorsion can be given by:

$$D(S,C) = \frac{1}{2}\int \|\mathrm{x} - Q(\mathrm{x})\|^2 p(\mathrm{x})d\mathrm{x} \quad (11)$$

$$D(S,C) = \frac{1}{2}\sum_{i=1}^{N}\int_{S_i} \|\mathrm{x} - \mathrm{y}_i\|^2 p(\mathrm{x})d\mathrm{x} \quad (12)$$

where $\|\boldsymbol{x}\text{-}\boldsymbol{y_i}\|$ denotes Euclidean distance such that:

$$\|\mathrm{x} - \mathrm{y}_\mathrm{i}\| = \left(\sum_{j=1}^{2}\left(x_j - y_{ij}\right)^2\right)^{1/2} \quad (13)$$

and $p(\boldsymbol{x})$ is the two-dimensional density of $\boldsymbol{x}$.

Bennett showed that the mean-squared error of a scalar quantizer (k = 1), with meny small cells (N large) and with each y_i in the center of its cell may be accurately approximated as:

$$D(S,C) \cong \frac{1}{12N^2}\int \frac{1}{\lambda(x)^2}p(x)dx \quad (14)$$

where, $\lambda(x)$ is a function, called point density, and $\lambda(x)\Delta$ is the fraction of quantization points in a small interval of width Δ surrounding x. The integral without limits denotes an integral over the entire space. The right-hand side of previous equation is known as Bennett's integral. Althought originally derived for companders (quantizers consisting of a compressor, uniform quantizer, and expander) with λ equal to the derivative of the compressor function can be recognized by other quantizers, and is applied more generally. Bennett's integral shows how the distortion depends on the key characteristics of the quantizer, namely, the number of points N and a point density λ. Its utility is exemplified by the fact that one may use it to show that the best quantizers have:

$$\lambda(x) \cong \frac{p(x)^{\frac{1}{3}}}{\int p(x)^{\frac{1}{3}}dx}\,. \quad (15)$$

In following analysis we extend Bennett's integral to polar quantizer. We suppose that distortion for polar quantization may be approximated as:

$$D(S,C) = \sum_{i=1}^{L}\sum_{j=1}^{P_i} p\left(m_i,\psi_{i,j}\right)NM(i)vol^2\left(S_{i,j}\right) \quad (16)$$

where $vol(S_{i,j})$ denotes the volume of the cell S_i and $NM(i)$ denotes the normalized moment of inertia of the cell S_i about the point y_i with respect to the distorsion and can be expressed in turn:

$$vol\left(S_{i,j}\right) = rdrd\varphi = \frac{\left(r_{i+1}^2 - r_i^2\right)\pi}{P_i} = \frac{2m_i\Delta_r\pi}{P_i} \quad (17)$$

$$NM(i) = \frac{1}{12}\left(\frac{P_i\Delta_r}{4m_i\pi} + \frac{m_i\pi}{\Delta_r P_i}\right) \approx \frac{1}{12}\left(\frac{p(r)\Delta_r}{4r\pi} + \frac{r\pi}{\Delta_r p(r)}\right) = m(r,\varphi)\,. \quad (18)$$

The width of rings, noticed with Δ_r, in case of resticted uniform polar quantization is $\Delta_r = r_{max}/L$. Finally point density is found as:

$$\lambda(m_i,\psi_{i,j}) = \frac{1}{Nvol(S_{i,j})} \approx \frac{1}{N}\frac{p(r)L}{r_{\max}r2\pi} = \lambda(r,\varphi)\,. \quad (19)$$

After this approximation, D becomes:

$$D(S,C) = \int_0^{r_{\max}}\int_0^{2\pi} p_r(r,\varphi)\frac{m(r,\varphi)}{\lambda(r,\varphi)}rdrd\varphi$$

$$= \int_0^{r_{\max}} re^{-\frac{r^2}{2}} \left(\frac{1}{24}\frac{r_{\max}^2}{L^2} + \frac{\pi r}{\Delta(p(r))^2}\right)dr . \qquad (20)$$

By using the method of Lagrange multipliers with restriction for the total number of the reconstruction points N we obtained optimal point density $p(r)$ as:

$$p(r) = \frac{Nr_{\max}}{3\left(1 - e^{-r_{\max}^2/6}\right)} re^{-\frac{r^2}{6}} . \qquad (21)$$

Let distortion can be determinated as: $D(S,C) = I_1 + I_2$ where are:

$$I_1 = \int_0^{r_{\max}} \frac{r_{\max}^2}{24L^2} re^{-\frac{r^2}{2}} dr =$$

$$= \frac{1}{24}\left(\frac{r_{\max}}{L}\right)^2 \left(1 - e^{-\frac{r_{\max}^2}{2}}\right) \approx \frac{1}{24}\left(\frac{r_{\max}}{L}\right)^2 \qquad (22)$$

$$I_2 = \int_0^{r_{\max}} \frac{\pi^2}{6(p(r))^2} r^3 e^{-\frac{r^2}{2}} dr =$$

$$= \frac{1}{2}\left[\frac{3\pi\left(1 - e^{-\frac{r_{\max}^2}{6}}\right)L}{Nr_{\max}}\right]^2 \left(1 - e^{-\frac{r_{\max}^2}{6}}\right). \qquad (23)$$

Finally we find distortion as a solution of Bennett's integral for uniform polar quantizer as:

$$D^{\dim}(S,C) = \frac{1}{24}\left(\frac{r_{\max}}{L}\right)^2 + \frac{1}{2}\left[\frac{3\pi\left(1 - e^{-\frac{r_{\max}^2}{6}}\right)L}{Nr_{\max}}\right]\left(1 - e^{-\frac{r_{\max}^2}{6}}\right) \qquad (24)$$

The optimal number of levels is:

$$L = \frac{r_{\max}}{\sqrt[4]{108\left(1 - e^{-r_{\max}^2/6}\right)^3}} \sqrt{\frac{N}{\pi}} \qquad (25)$$

and we find distortion as:

The width of rings, noticed with Δ_r, in case of resticted uniform polar quantization is $\Delta_r = r_{max}/L$. Finally point density is found as:

$$\lambda(m_i, \psi_{i,j}) = \frac{1}{Nvol(S_{i,j})} \approx \frac{1}{N}\frac{p(r)L}{r_{\max} r 2\pi} = \lambda(r,\varphi). \qquad (19)$$

After this approximation, D becomes:

$$D(S,C) = \int_0^{r_{\max}} \int_0^{2\pi} p_r(r,\varphi)\frac{m(r,\varphi)}{\lambda(r,\varphi)} r dr d\varphi$$

$$= \int_0^{r_{\max}} re^{-\frac{r^2}{2}} \left(\frac{1}{24}\frac{r_{\max}^2}{L^2} + \frac{\pi r}{\Delta(p(r))^2}\right)dr . \qquad (20)$$

By using the method of Lagrange multipliers with restriction for the total number of the reconstruction points N we obtained optimal point density $p(r)$ as:

$$p(r) = \frac{Nr_{\max}}{3\left(1 - e^{-r_{\max}^2/6}\right)} re^{-\frac{r^2}{6}} . \qquad (21)$$

Let distortion can be determinated as: $D(S,C) = I_1 + I_2$ where are:

$$I_1 = \int_0^{r_{\max}} \frac{r_{\max}^2}{24L^2} re^{-\frac{r^2}{2}} dr =$$

$$= \frac{1}{24}\left(\frac{r_{\max}}{L}\right)^2 \left(1 - e^{-\frac{r_{\max}^2}{2}}\right) \approx \frac{1}{24}\left(\frac{r_{\max}}{L}\right)^2 \qquad (22)$$

$$I_2 = \int_0^{r_{\max}} \frac{\pi^2}{6(p(r))^2} r^3 e^{-\frac{r^2}{2}} dr =$$

$$= \frac{1}{2}\left[\frac{3\pi\left(1 - e^{-\frac{r_{\max}^2}{6}}\right)L}{Nr_{\max}}\right]^2 \left(1 - e^{-\frac{r_{\max}^2}{6}}\right). \qquad (23)$$

Finally we find distortion as a solution of Bennett's integral for uniform polar quantizer as:

$$D^{\dim}(S,C) = \frac{1}{24}\left(\frac{r_{\max}}{L}\right)^2 + \frac{1}{2}\left[\frac{3\pi\left(1 - e^{-\frac{r_{\max}^2}{6}}\right)L}{Nr_{\max}}\right]\left(1 - e^{-\frac{r_{\max}^2}{6}}\right) \qquad (24)$$

The optimal number of levels is:

$$L = \frac{r_{\max}}{\sqrt[4]{108\left(1-e^{-r_{\max}^2/6}\right)^3}}\sqrt{\frac{N}{\pi}} \quad (25)$$

and we find distortion as:

$$D^{\dim} = \frac{1}{2}\frac{\pi\sqrt{3}}{N}\left(1-e^{-\frac{r_{\max}^2}{6}}\right)^{\frac{3}{2}}. \quad (26)$$

Optimal point density is $p(r)=2Nr/(r_{max}L)$ in case of $\lambda(r,\varphi)=const$, and optimal number of magnitude levels is $L=\sqrt{N/\pi}$. Hence, distortion can be found as:

$$D_{gconst}^{\dim} = \frac{r_{\max}^2\pi}{12N}. \quad (27)$$

Table I gives parallel comparison of distortions $D_{gconst}^{\dim}$ and $D_g^{\dim}$ when number of quantization cells are N=256, N=4096 and N=65536.

TABLE I

COMPARED RESULTS FOR $D_{gconst}^{\dim}$ AND $D_g^{\dim}$ FOR A DIFFERENT BIT RATES (R) AND NUMBER OF RECONSTRUCTION POINTS (N)

R	N	$D_{gconst}^{\dim}$	$D_g^{\dim}$
4	256	0.0106	0.00637
6	4096	0.00106	0.00026
8	65536	0.000093	0.00000856

IV. CONCLUSION

The analysis of Bennett's integral is given for uniform polar quantization for two-dimensional memoryless Gaussian sources. This paper gives simple and complete analysis for constructing an optimal uniform polar quantizer for sources with optimal point density. We have calculated granular distortion and have found gain obtained by using optimal point density. The goal of tis paper is solving quantization problems for uniform polar quantizers by finding minimal distortion and optimal point density.

REFERENCES

[1] P. F. Swaszek, T. W. Ku, "Asymptotic Performance of Unrestricted Polar Quantizer", *IEEE Transactions on Information Theory*, vol.32, pp. 330-333, 1986.

[2] R. M. Gray and D. L. Neuhoff, "Quantization", *IEEE Transactions on Information Theory*, vol.44, no.6, pp. 2325-2384, October 1998.

[3] S. Na D. L. Neuhoff, "Bennett's Integral for Vector Quantizers," *IEEE Transaction on Information Theory*, vol.41, pp. 886-900, July 1995.

[4] Z. H. Perić, M. Č. Stefanović, "Asymptotic Analysis of Optimal Uniform Polar Quantization", *International Journal of Electronics and Communications*, vol.56, pp. 345-347, 2002.

[5] D. Aleksić "Asymptotic Analysis of Nonuniform Polar Quantiyation", Telfor, 2003.

Image Compression Based On Inverse Difference Pyramid with BPNN

Noha A. Hikal[1], Roumen K. Kountchev

Abstract - **In this paper a new developed algorithm for lossless compression of still grayscale images based on Back Propagation learning Neural Networks in correspondence with the method of Inverse Difference Pyramid (IDP) decomposition is presented. This algorithm is well suited to be used in Progressive Image Transmission (PIT). Advantage of the method is the adaptation of the neural network in accordance with the image contents, the minimization of the total number of pyramid levels and the increasing of the restored image quality.**

Keywords - **Inverse Difference Pyramidal Decomposition, Back Propagation Neural Networks, Image Coding**

I. INTRODUCTION

Image compression is an important tool to store and transmit visual information used for several applications. Compression of an image refers to a process in which the amount of data used to represent an image is reduced to meet a bit rate requirement (below or at most equal the maximum available bit rate), while the quality of the reconstructed image satisfies a requirement for a certain application and the complexity of the computation involved is affordable for the application. Progressive Image Transmission (PIT) [1] concept is of particular importance in browsing large image files. Progressive transmission of an image permits the initial reconstruction of an approximation followed by a gradual improvement of quality in image reconstruction. A coarse copy of the image is sent first to give the receiver an early impression of image contents then subsequent transmission provides image detail of progressively finer resolution. The observer may terminate transmission of an image as soon as its contents are recognized. In order to send image data progressively, the data should be organized hierarchically in the order of importance, from the global characteristics of an image to the local details. There are two types of data structures for progressive transmission depending upon the encoding method employed [2]:

- transform based image encoding,
- spatial encoding.

In a transform based encoding the image is first divided into a set of contiguous non-overlapping blocks, and then each block is transformed into a set of transform coefficients, (e.g, Discrete Cosine Transform (DCT) [3], the coefficients are then quantized before initiating its transmission. On the other hand, the spatial approach, like pyramidal encoding, generates a sequence of images with different resolution (corresponding with the pyramid levels), the image is successively reduced in spatial resolution and size by sub-sampling or averaging. The images are restored using the data from all pyramid levels, which is arranged, interpolated and summed.

II. PYRAMIDAL REPRESENTATION - STATE OF ART

The first pyramidal data structure is the Gaussian - Laplacian pyramid [4]. Gaussian Pyramid (GP) can be viewed as a set of low pass filtered copies of the original image. Laplacian Pyramid (LP) is a sequence of error images, each is a difference between two successive levels of Gaussian pyramid. Various pyramid data structures for progressive image transmission have been proposed like [5]: Mean Pyramid (MP), Reduced Sum Pyramid (RSP), and Reduced Difference Pyramid (RDP). For further refinement of the Laplacian pyramid was developed the Least Squared Laplacian Pyramid (LSLP) [6]. The corresponding LSLP is generated by adding an extra filter with auxiliary coefficients sequence after the down sampling process, this filter works on minimizing the energy of the Laplacian coefficients. Reduced Laplacian Pyramid (RLP) [7] is designed by discarding the reduction filter and adopting a halfband interpolator. In [8] a contrast pyramid coding technique, which differs in the way of computing the difference image was discussed. Instead of using the difference image to represent the information difference between two successive levels, a coding scheme consists of the generation of the contrast image with a simple nonlinear algorithm and a simple compandor model is used. The efficiency of contrast pyramid method comes from coding the contrast image. Centered pyramid [9] differ from other pyramids methods in that each coarser level node is suited exactly in the center of its finer level predecessors, which offers an accurate way of up projection and makes it helpful in contour, multi-scale detection and object recognition. Hierarchy Embedded Differential Image (HEDI) [10] is a technique similar to RDP but expanded and generalized to improve the speed for compressing and decompressing processes. Many pyramidal decomposition techniques showed improvements over Joint Photographers Experts Group (JPEG). The Inverse Pyramidal Decomposition with multiple Discrete Cosine Transform (IDP/DCT) was presented in [11]. The IDP decomposition differs in the way of obtaining pyramid levels, the word "inverse" refers to compute the pyramid levels from bottom (level zero) to the top. The novelty lies in the modeling performed at each pyramid level, which relies on the DCT of the input subimage. This new pyramid can be compared to subband DCT [12] to notice that the IPD/DCT offers better performances in terms of compression ratio with a fixed PSNR for each pyramid

[1]Noha A. Hikal is with Mansoura University, Communications Engineering Dept, Egypt,E-mail: eng_noha_hikal@yahoo.com

[2]Roumen K. Kountchev is with FCTT, Radiocom. Dept., Technical University of Sofia, Bul. Kl. Ohridsky 8, Sofia, Bulgaria, E-mail: rkountch@tu-sofia.bg

level. Coding and decoding processes are simple and flexible. Therefore, it is well adapted to the needs of users, and it is relatively simple for real time processing. Since the pyramid top now consists of the low frequency coefficients of the DCT, this makes it in correspondence with the requirement for PIT. As it is known, the DCT is image independent, which provides more simplicity than other methods (Fourier transform. KLT, etc). The number of coefficients necessary to ensure high quality of the restored image using DCT is relatively high. The NN's are interesting alternatives to this classical approach for image processing and compression techniques due to their quality image reproduction, lower matrices computational effort, and adaptation. In addition to the NN's structure features are such as their massively parallel structure, high degree of interconnections, capability of learning and self-organizing, which allow them to solve several problems in processing image data.

In this work, a new technique for building Inverse Difference Pyramidal (IDP) Decomposition for image compression based on merging IDP and Back Propagation learning rule NN's (BPNN) [13] is considered. This technique combines the advantages of both methods IDP and NN's, the adaptation and learning capabilities of NN's could improve the performance of IDP, decrease the number of pyramid levels, increase the quality of the reconstructed image, maximize PSNR and minimize MSE.

III. IDP-BPNN Image Compression Algorithm

A. IDP-BPNN Coding

Lossless coding of image data in accordance with IDP-BPNN procedure is performed in the following steps:

Step 1: The whole image B(i,j) of size $2^N x 2^N$ is divided in blocks each of them of size (*m* x *m)* pixels.

Step 2: For each block, a three layer NN (input layer, hidden layer, and output layer) is built. The large input layer consisting of (m^2) neurons feeds the small hidden layer consisting of (*m*) neurons, which then feeds the large output layer consisting of *(*m^2) neurons. This structure is referred to as a "bottleneck" type networks ($m^2/m/m^2$), shown in Fig. 1.

Step 3: Using row scanning, pixels of each block are arranged as a vector of length *(*m^2); these (m^2) components are considered the input vector of the three-layer NN.

Step 4: The Back propagation learning algorithm is used as an adaptive approximation algorithm, providing the most suitable *(m)* hidden weights values that approximate the (m^2) input vector with minimum mean squared error. This form of number of pixels reduction for each block is considered a spatial reduction form, which serves the PIT. The training of the NN proceeds as follows: for example, a 256x256 pixels training image is used to learn the bottleneck type network to create the required identity map. Training input–output pairs are produced from the training image by using blocks of size 8x8 pixels of the image itself. Once training is complete, image compression is demonstrated in the recall phase. The total number of *(m)* hidden weights from all blocks forms the coefficients of the first pyramid level (p=0).

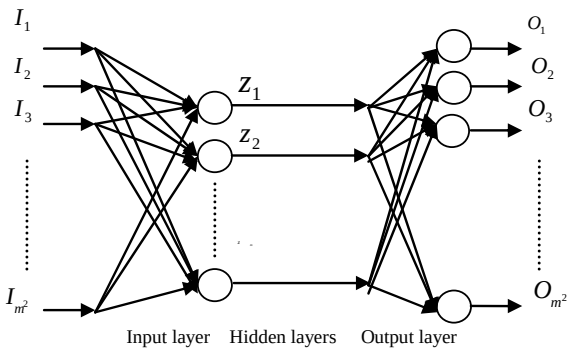

Fig. 1. Bottleneck type Neural Network

Step 5: The coefficients obtained are encoded using Run Length Encoding (RLE) [14] and transmitted.

Step 6: At the transmitter side, the reconstructed blocks will be recovered from these coefficients (after decoding process) in reverse arrangement using one layer BPNN *(m/* m^2) for each block, Fig.2. The difference is calculated pixel by pixel between the original image and the reconstructed blocks, which approximate the image results and in result is defined a difference image of the same size as the original one ($2^N x 2^N$).

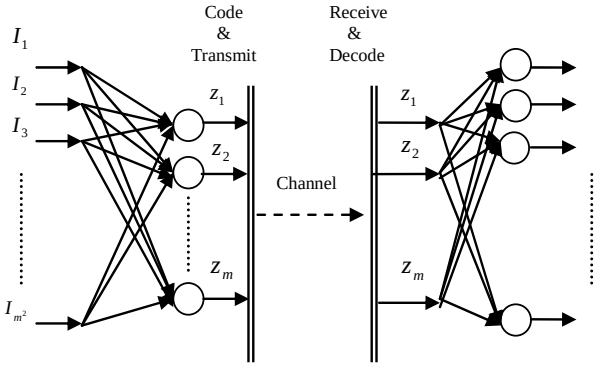

Fig.2. Compression/Decompression scheme for one block of size *mxm* using trained Bottleneck type Neural Network

Step 7: For the obtained differences image $E_0(i,j)$, each block is divided again into four sub-blocks with size (*m/2*x*m/2),* and again for each sub-block, a three layer NN is built of type ($(m/2)^2/m/2/(m/2)^2$).

Step 8: Following the same procedure, after training NN provides output sub-blocks of size (*m/2*x*m/2),* approximating the input sub-block. The total number of *m/2* hidden weights from all sub-blocks forms the coefficients of the second pyramid level (p=1), which will be encoded and transmitted later.

Step 9: At the transmitter side, the coefficients of the second pyramid level are used to generate a reconstructed version of the difference image $E_0(i,j)$. Pixel by pixel difference is obtained between $E_0(i,j)$ and its reconstructed version $E_0'(i,j)$. A new difference $E_1(i,j)$ is obtained, which must be divided into 4 sub-blocks again, each of size (*m/4*x*m/4),* and a new three layer NN is build in similar way as preceding ones. The total number of *m/4* hidden neurons for all sub-blocks form the coefficients of the third pyramid level (p=2), which will be encoded and transmitted later. The process continues with the

same manner till having a high quality reconstructed image. True image restoration is ensured when the hidden layer weight values are encoded and added in the transmitted data as well. It can be noticed that the obtained compressed coefficients (the values of the hidden weights) for each pyramid level contain a number of similar values. Thus, scanning these coefficients and apply Run-Length Encoding (RLE) algorithm on the scanned data could achieve further compression.

B. IDP-BPNN Decoding

The decoding of the lossless compressed image data in accordance with the general BPNN-IDP procedure is performed in following the steps.

Step 1: For each level p, Run Length Decoding process will be done to get the hidden weights values.

Step 2: The reconstructed blocks of the image are calculated using the corresponding reconstruction BPNN's arrangement for each level as the one's used at the transmitter side.

Step 3: The elements $B'(i,j)$ of the restored image from all levels are calculated in accumulation way

$$B'(i,j)=\sum_{p=0}^{P-1}\tilde{B}(i,j) \qquad (1)$$

for i, j = 0, 1, . ., 2^n-1 and $\tilde{B}(i,j)$ is the reconstructed image from each level p using BPNN's at the receiver side. Fig.3 illustrates the procedure of using IDP-BPNN at the transmitter and at the receiver. Fig.4 shows a general block diagram of IDP-BPNN decomposition and reconstruction.

C. Coding of color images

The coding of color images (written in format 4:4:4), based on the described algorithm, can be done by applying the algorithm on the matrix of every primary color component: R, G, B. In order to obtain higher compression ratio, the R, G, B components of every pixel (i,j) are transformed in Y, Cr, Cb [14] and the 4:4:4 format was converted into 4:2:0. Each one of the components Y, Cr, Cb is processed, applying the already described general BPNN-IDP coding algorithm to get a new matrices $\hat{Y}$, $\hat{Cr}$, $\hat{Cb}$ for each level, which approximate the original ones.

The decoding of the compressed color images is performed applying the BPNN-IDP decoding algorithm on the components $\hat{Y}$, $\hat{Cr}$, $\hat{Cb}$.

IV. Performance Evaluation of BPNN-IDP

To evaluate the performance of the proposed BPNN-IDP algorithm, the commonly known measures will be used which are:

- The Peak Signal to Noise Ratio (PSNR) obtained for the reconstructed image at each level p of the pyramid as:

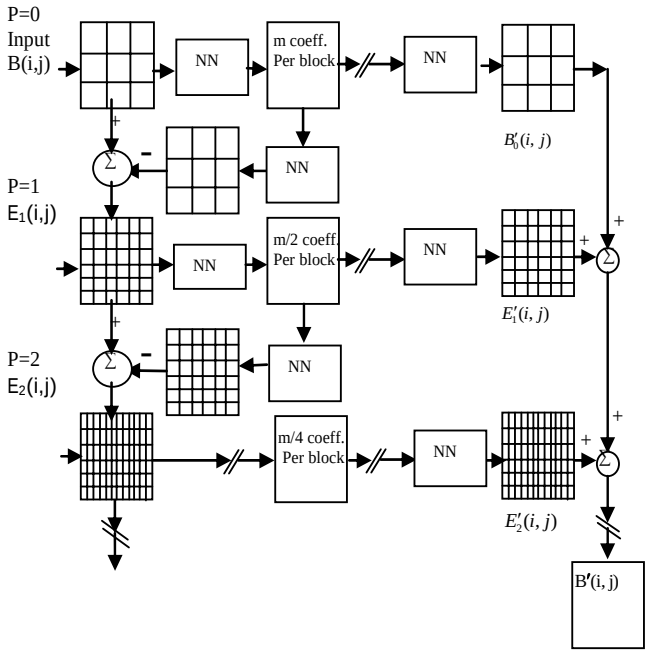

Fig.3. Block diagram of the 3-level IDP-BPNN decomposition and reconstruction

$$PSNR(p)=10\log_{10}\frac{B_{max}^2}{\bar{\varepsilon}^2(p)},dB \qquad (2)$$

Where $\bar{\varepsilon}^2(p)$ is the mean squared error (MSE) at level *p* and it is computed as:

$$\bar{\varepsilon}^2(p)=4^{-n}\sum_{i=0}^{2^n-1}\sum_{j=0}^{2^n-1}[B(i,j)-\hat{B}_p(i,j)]^2 \qquad (3)$$

- The amount of image compression (measured in bits-per-pixel): it was computed as the ratio of the total number of bits transmitted to the total number of pixels in the original image.

IV. Simulation Results

Simulations have been performed on the original bitmap images ”pepper” with size 512x512 pixels and “bird” with size 256x256 pixels. The investigation was done only for lossless compression (i.e, without quantization). Results in terms of PSNR, compression ratio, and number of levels are shown in Table 1. Figs.5 and 6 illustrate the quality results obtained on "pepper" and "bird" images with successive pyramid levels. Results obtained with other test image are very similar to the examined ones.

V. Conclusion

The goal of this study was to develop a new algorithm based on the inverse difference pyramidal decomposition. The novelty lies in modeling each pyramid level using BPNN. This new algorithm can be compared to the most similar pyramids proposed in articles concerning pyramidal decompositions. It can be underlined that, compared to IDP-

DCT decomposition, IDP-BPNN using the gradient descent rule which aims to minimize the mean squared error between the original and the reconstructed image in iterative way reduces the number of levels, required to reconstruct the image at the receiver side. The coding and decoding of the hidden weights values are relatively simple. The training process is time consuming, but the compression ratio and the quality of the reconstructed image are considerable. The future method development will be aimed at the adopting of efficient algorithms for speeding up the NN learning and at the compression ratio increasing with quantization of the hidden-layer coefficients.

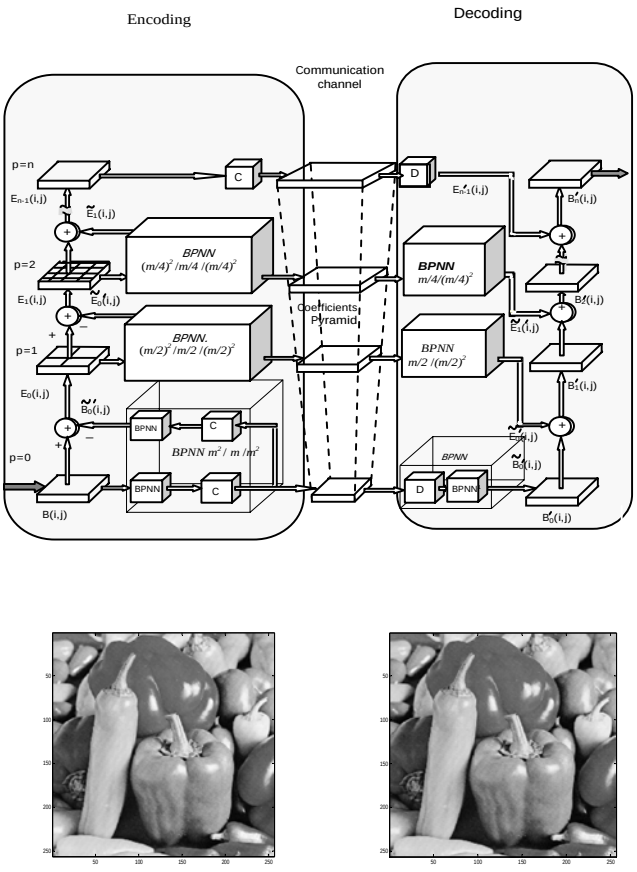

Fig.5. Quality results obtained for the original “bird” image with two-level pyramid

TABLE I. MODELING results for IDP-DCT [11] COMPARED WITH BPNN-IDP, ORIGINAL IMAGE "Pepper"

COMPARISON CRITERIA	IDP-DCT	IDP-BPNN
Level numbers	2	2
Transformation	DCT	BP learning
Subimage size p=0	8x8	16x16
Number of coefficients	4 per block	Square root [block Size] per block
PSNR at last level	31.06 dB	60.13 dB
bpp at last level	0.52	0.125

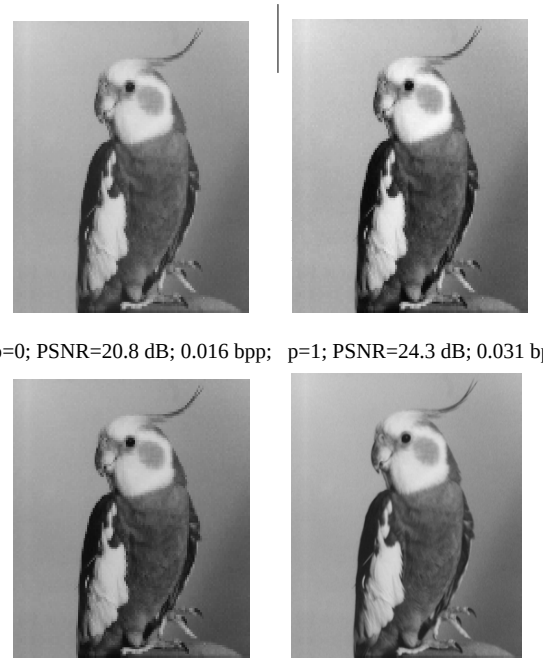

p=0; PSNR=20.8 dB; 0.016 bpp; p=1; PSNR=24.3 dB; 0.031 bpp

p=2; PSNR=26 dB; 0.125 bpp; p=3; PSNR=27.7 dB; 0.25 bpp

Fig.6. Quality results obtained with the original image “bird” for four-level pyramid

REFERENCES

[1] K. Tzou, "Progressive Image Transmission: A review and comparison of techniques" *Opt. Eng., Vol 26, pp. 581-589 July 1987.*

[2] A. Poularikas. "The Transforms and Applications Handbook". CRC Press 2000.

[3] K. Rao, P. Yip. " The Transform and Data Compression Handbook". CRC Press 2000.

[4] P. Burt. "The Laplacian Pyramid as a Compact Image Code". IEEE Trans. Commun., Vol 31, No. 4, April 1983.

[5] M. Goldberg. "Comparative Performance of Pyramid Data Structures for Progressive Image Transmission" IEEE Trans .Commun. Vol. 39, No.4, April 1991.

[6] M. M. Unser. "An Improved Least Square Laplacian Pyramid for Image Compression" IEEE Signal Processing, 27, pp. 187-203, 1992.

[7] B. Aiazzi, et al. "A Reduced Laplacian Pyramid for Lossless and Progressive Image Communication". IEEE Trans. Commun. Vol. 44, No.1 , 1996.

[8] Tian Hu Yu. "Novel Contrast Pyramid Coding of Images". Proceedings of the 1995, ICIP.

[9] P. Brigger et al. "Centered Pyramids" IEEE Trans - Image Processing, Vol-8 No-9, Sep. 1999.

[10] W. Kim, et al. "Hierarchy Embedded Differential Image for Progressive Transmission using Lossless Compression" IEEE Trans. Circints and Systems for Video Technology. Vol. 5, No.1, Feb. 1995.

[11] R. Kountchev, et al. "Inverse Pyramidal Decomposition with Multiple DCT". Signal Processing. Image Communication, 17 2002, pp. 201-218.

[12] Y. Wu, et al. "Low Bit Rate Subband DCT Image Compression" IEEE Trans. Consumer Election. 43 (2) May. 1997, pp. 134-140.

[13] Y. H. Hu, J. N. Hwang "Handbook of Neural Networks and Signal Processing”, CRC Press 2002.

[14] D. Salomon, "Data Compression: The complete reference" 3rd Ed., Springer-Verlag, New York, 2004.

Threshold Cryptosystems in Asynchronous Networks

Aleksandra Sešić[1], Veljko Malbaša[2]

Abstract–**Threshold cryptography makes it possible to design cryptographic systems in which some operations require the collaboration of several users. As a result, security of the system is increased. This paper aims at guiding readers into this interesting field under the asynchronous message-passing model of distributed computing.**

Keywords–**Threshold cryptosystem, verifiable secret sharing, proactive security, asynchronous system model.**

I. INTRODUCTION

Distributed cryptography, introduced in 1987, is a variant of traditional cryptography intended for distributed services. Several distributed cryptosystems have been proposed until now. Most of them have a threshold structure, which means that both the sets of corrupted servers that must be tolerated by the system and the sets that are qualified to perform some action are determined by their cardinality. Due to this fact, distributed cryptography is called also in general *threshold cryptography*. The surveys of threshold cryptography can be found in [1,2].

Threshold cryptosystem is a public key cryptosystem in which the secret key is shared among the set of users. Only some qualified subsets of users will be able to perform the operation related to the secret key (decrypting or signing). In this way, security of the system is increased, because the loss or theft of several shares of the secret key does not necessarily break the system's security.

We are especially interested in protocols that require no interaction or synchronization among the servers, and as such can be efficiently run on an *asynchronous communications network* where messages are delivered with arbitrary delay and in which the speeds of the nodes can get out of synchronism to an arbitrary extent. It is the weakest model (i.e., methods for this model work in other models, too) and the most realistic for distributed computing in today's large scale wide-area networks such as the Internet.

II. THRESHOLD CRYPTOSYSTEMS

A *threshold public-key cryptosystem* [3] looks similar to an ordinary public-key cryptosystem with distributed decryption. Given a ciphertext resulting from encrypting some message and more than $t+1$ valid decryption shares for that ciphertext, in a system which tolerates up to t faults, it is easy for a client to recover the message; this property is called *robustness*.

This means that corrupted players should not be able to prevent uncorrupted servers from decrypting ciphertexts, i.e., that the decryption service is available even if the adversary can send bad decryption shares. The key to robustness is validity checking, based on a public key system, where one can ignore all incorrect decryption shares without exhaustive searching to find out who sent the wrong decryption share. Notice that the message can be recovered *without revealing* the secret decryption key.

The scheme must also be secure against *chosen ciphertext attacks* [4] in order to be useful for all conceivable applications. This type of attack is one in which a cryptanalyst attempts to determine the *key* from knowledge of plaintext that corresponds to ciphertext selected (i.e., chosen) by the analyst. This type of attack is generally most applicable to public-key cryptosystems, for once the (private) key is known, all subsequent messages from the same source can be deciphered. For the threshold case, security means that the adversary cannot obtain any meaningful information from a ciphertext unless she has obtained a corresponding decryption share from at least one honest party.

In a *threshold signature scheme*, each server holds a share of the secret signing key and may generate shares of signatures on individual messages upon request. A *signing* algorithm takes as inputs a message, the public key and the secret key share. It outputs a signature share on the submitted message. The validity of a signature share can be verified for each server by a *share verification* algorithm. It takes as inputs a message, a signature share on that message from a server S_i along with the public key and local verification key of S_i. A *share combining* algorithm takes as input a message and $t+1$ valid signature shares on that message, along with public keys and the verification keys and outputs a valid digital signature on that message *without knowing* the actual secret signing key. This key speaks for the service but is never materialized at individual servers comprising the service. The signature can later be verified using the single, publicly known signature verification key. Notice that in particular, the threshold approach rules out the naïve solution based on traditional secret sharing, where the secret key is shared in a group but reconstructed by a single player each time when a signature is to be produced. Such a protocol would contradict the requirement that no t (or less) players can ever produce a new valid signature.

The two basic security requirements are *non-forgeability* and *robustness*.

Non-forgeability property means that t or less corrupted servers will not be able to forge signatures, i.e., to provide a valid signature on a message for which no honest party generated a signature share.

Robust threshold signature scheme can withstand the participation of dishonest signers during the signature computation operation. This is a mechanism that succeeds in constructing a valid signature even if the partial signatures

[1] Aleksandra Sešić is with Nopal, 21400 Bačka Palanka, Serbia and Montenegro, Email: asesic@nopal.co.yu

[2] Veljko Malbaša is with the School of Engineering, University of Novi Sad, 21000 Novi Sad, Serbia and Montenegro, Email: malbasa@uns.ns.ac.yu

contributed by some of the signers are incorrect. Due to robustness, corrupted servers will not be able to prevent the uncorrupted servers from computing correct signatures, i.e., it is infeasible for a computational bounded adversary to produce *t+1* valid signature shares that cannot be combined to a valid signature.

Threshold-cryptographic protocols ensure security as long as at most *t* of servers are broken into. They enhance the security against break-in attacks in many scenarios. However, threshold cryptography is also limited. Given sufficient amount of time, an attacker can break into servers one by one, thus eventually compromise the security of the system. This danger is particularly eminent in systems that must remain secure for long periods of time (such as certification authorities) or where secure recovery may be difficult (such as with secure communication).

Proactive security is a mechanism for protecting against such long-term attacks. Proactive cryptosystems operate in phases. They can tolerate the corruption of up to *t* different servers in every phase [5]. That is, first distribute the cryptographic capabilities among several servers. Next, have the servers periodically engage in a *refreshment protocol* that proactively reboots all servers at the beginning of every phase and subsequently refreshes the secret key shares. Knowledge of the shares from the previous phases becomes useless to attack the system in the future. This protocol will allow the servers to automatically recover from possible, undetected break-ins, and in particular will provide the servers with new shares of the sensitive data while keeping the sensitive data unmodified.

Share refreshing is a distributed protocol and in all proactive cryptosystems it relies on verifiable secret sharing. Verifiable secret sharing is a fundamental primitive in distributed cryptography [6] that has found its application in threshold cryptosystems. A verifiable secret sharing protocol allows each shareholder to verify that the share is consistent with other shares in case the dealer of shares might be faulty.

III. Cryptography versus Distributed Computing

The field of multi-party cryptographic protocols is where cryptography and distributing computing meet [7]. However, this field is considered as a part of cryptography, which is the consequence of the dominant role of cryptographic notions and techniques in the current research of cryptographic protocols. Most of the cryptographic research is concerned with two-party computations where typically an asynchronous message passing model is assumed (almost always implicitly). For multi-party cryptographic protocols a synchronous model consisting of either point-to-point channels or a single broadcast channel is used most frequently. Results for asynchronous communication and arbitrary networks of point-to-point channels were presented in [8,9,10].

IV. Related Work

A major complication for adopting threshold cryptography to asynchronous distributed systems is that many early protocols are not robust and that rely heavily on synchronous broadcast channels.

Shoup and Gennaro [4] present the first *robust threshold cryptosystem* that is also non-interactive, and as such integrates well into asynchronous communication model. Moreover, it is the first practical threshold cryptosystem that is provably secure against chosen ciphertext attack in the random oracle model. In the random oracle model cryptographic hash functions are replaced by a random oracle. This model was used informally by Fiat and Shamir [11] and later was rigorously formalized and more fully exploited in Bellare and Rogaway [12]. In the random oracle model the proof of security is viewed as "strong evidence" that the scheme is actually secure in the "real world". Authors presented and analyzed two schemes, which are based on the hardness of the Diffie-Hellman problem.

The *threshold RSA signature* scheme of Shoup [13] is unforgeable and robust in the random oracle model, assuming the RSA problem is hard. Signature share generation and verification is completely non-interactive.

First implementations of threshold signatures in asynchronous networks without random oracles are RSA signature schemes by Gennaro, Halevi and Rabin [14] and by Cramer and Shoup [15], which are based on strong RSA assumption.

The first practical *verifiable secret sharing* protocol for asynchronous networks together with a *proactive refresh protocol* is proposed by Cachin et al. [16]. The authors propose a model of *asynchronous proactive network* that extends an asynchronous network by an abstract timer that is accessible to every server. The timer defines the phase of a server locally. They assume that the adversary corrupts up to *t* different servers who are in the same local phase. Uncorrupted servers who are in the same local phase use private authenticated channels for communication. Message delay in such a channel must be no longer than the local phase lasts. Otherwise the message is lost. A proactive cryptosystem refreshes the shares of the secret key at the beginning of every phase. The liveness of the cryptosystem is based on the assumption that the adversary delays messages of the refresh protocol for no longer than the phase lasts. Otherwise the secret key may become inaccessible. This assumption seems reasonable because a phase typically lasts much longer than the maximal delay of a message in the real-world network. The *proactive refresh protocol* relies on a discrete logarithm-based verifiable secret sharing that is similar to Pedersen's scheme [17]. The servers exchange two asynchronous rounds of messages to reach *agreement* on the success of the sharing. Agreement is achieved by using a randomized asynchronous multi-valued Byzantine agreement primitive [18]. Cachin et al. [16] left open the question of how proactive secure message transmission could be implemented.

A protocol for proactive secure message transmission over an asynchronous network is presented in [19]. The authors specify proactive secure message transmission in terms of an idealized service that has simple deterministic semantics and hides cryptographic objects from its interfaces. Additionally, a real implementation is proposed and proved to be at least as secure as the ideal service. The solution relies on a hardware

assumption, i.e., a secure co-processor that cannot be corrupted by the adversary.

The first purely asynchronous group key exchange protocol that tolerates a minority of servers to crash is presented in [20]. A group of servers communicate over an asynchronous network to establish a common session key such that anyone outside the group that can only observe the network traffic cannot learn this key. Such a key can later be used to achieve multicast message confidentiality or data integrity. The protocol consists of the following two stages. In the first stage, the group members exchange keying information using two communication rounds. In the second stage, they execute consensus protocol to select the contributions from the first stage where the session key is computed. The protocol may use randomized asynchronous consensus in the fully asynchronous model or a consensus protocol in the asynchronous model augmented with a failure detector. It is shown that any group exchange protocol among n servers that tolerates $t>0$ servers to crash can only provide forward secrecy if the adversary occupies less than $n-2t$ servers and the presented protocol achieves this bound.

CODEX (COrnell Data Exchange)[21] is a distributed service for storage and dissemination of secret keys that uses an approach to building distributed services that are both fault-tolerant and attack tolerant. This approach includes asynchronous model of execution, which makes the system resistant to denial of service attacks. Byzantine quorum systems are used for storing the state, ensuring consistency among the servers, and proactive secret sharing with threshold cryptography implement confidentiality and authentication of service responses.

The storage and transmission of data files in distributed systems gives rise to significant security and reliability problems. Information dispersal algorithms store files by distributing them among a set of servers in a storage efficient way. The authors in [22] introduce the problem of verifiable information dispersal in an asynchronous network, where up to one third of servers as well as an arbitrary number of clients might have Byzantine faults. Consistency of the stored information is ensured by verifiability. The secrecy of the stored data is guaranteed with respect to an adversary that may mount adaptive attacks.

V. Future Research

The authors in [23] describe some research subjects that are important in the future development of distributed cryptography. For instance, there exist many situations in which general structures instead of threshold structures are required. Moreover, it is necessary to find new public key cryptosystems for non-threshold structures. The design of distributed cryptosystems with non-threshold access structure is closely related to the problem of performing multiparty computation on general access structures. The main question is how to find efficient linear secret sharing schemes with the multiplicative property and very little is known about that.

VI. Conclusion

We have presented main results in the field of threshold cryptography under the asynchronous model of distributed computing. We started with fundamental definitions, then pointed out the meeting place of cryptography and distributed computing, and finally presented several solutions with concluding remarks concerning future research.

References

[1] Y. Desmedt, "Threshold cryptography," *European Trans. on Telecommunicatons*, 5(4), pp. 449-457, July-August 1994, (Invited paper).

[2] Y. Desmedt, "Some Recent Research Aspects of Threshold Cryptography," *In Eiji Okamoto, George Davida, and Mashiro Mambo, editors, Information Security, The 1st International Workshop, ISW'97,* Tatsunokuchi, Ishikawa Japan, September 17-19, 1997.

[3] Y. Desmedt and Y. Frankel, "Threshold cryptosystems," *In G. Brassard, editor, Proc. CRYPTO 89*, pages 307-315. *Springer-Verlag, 1990, Lecture Notes in Computer Science No. 435.*

[4] V. Shoup and R. Gennaro, "Securing threshold cryptosystem against chosen ciphertext attack," *Proc. EURO-CRYPT '98, LNCS 1403*, 1998.

[5] R. Canneti, R. Gennaro, A.Herzberg, and D. Naor, "Proactive security: Long-term protection against break-ins," *RSA Laboratories' CryptoBytes, vol. 3, no.1,* 1997.

[6] B. Chor, S. Goldwasser, S. Micali, and B. Awerbuch, "Verifiable secret sharing and achieving simultaneity in the presence of faults," *Proc. 26th IEEE Symp. on Found. of Computer Science*, pages 383-395, 1985.

[7] O. Goldreich, "Cryptography and Cryptographic Protocols," *Distributed Computing*, v.16, n.2-3, p.177-199, September 2003.

[8] M. Ben-Or, R. Canetti and O. Goldreich, "Asynchronous Secure Computation," *25th ACM Symposium on the Theory of Computing*, pages 52-61, 1993.

[9] M. Ben-Or, B. Kelmer and T. Rabin, "Asynchronous Secure Computations with Optimal Resilience," *13th ACM Symposium on Principles of Distributed Computing*, pages 183-192, 1994.

[10] D. Dolev, C. Dwork, O. Waarts, and M. Yung, "Perfectly secure message transmission," *Journal of the ACM*, Vol. 40(1), pages 17-47, 1993.

[11] A. Fiat and A. Shamir, "How to prove yourself: practical solutions to identification and signature problems", *Advances in Cryptology-Crypto '86,* Springer LNCS 263, pages 186-194, 1987.

[12] M. Bellare and P. Rogaway, "Random oracles are practical: a paradigm for designing efficient protocols", *First ACM Conference on Computer and Communications Security*, pages 62-73,1993.

[13] V. Shoup, "Practical threshold signatures," *Proc. EURO-CRYPT 2000, LNCS 1087*, pp.207-220, 2000.

[14] R. Gennaro, S. Halevi, and T. Rabin, "Secure hash-and-sign signatures without the random oracle," *Proc. EUROCRYPT '99,* pp. 123-139, Springer, 1999.

[15] R. Cramer and V. Shoup, "Signature schemes based on the strong RSA problem," *ACM Transactions on Information and System Security*, vol. 3, no. 3, pp. 161-185, 2000.

[16] C. Cashin, K. Kursawe, A. Lysyanskaya, and R. Strobl, "Asynchronous Verifiable Secret Sharing and Proactive Cryptosystems," *Proc. 9th ACM Conference on Computer and Communications Security (CCS)*, pages 88-97, 2002.

[17] T. P. Pedersen, "Non-interactive and information-theoretic secure verifiable secret sharing," *In J. Feigenbaum, editor, CRYPTO '91, volume 576 of LNCS*, pages 129-140, Springer, 1992.

[18] C. Cashin, K. Kursawe, F. Petzold, and V. Shoup, "Secure and efficient asynchronous broadcast protocols," *Advances in Cryptology-Crypto 2001, 2001*.

[19] M. Backes, C. Cashin, and R. Strobl, "Proactive Secure Message Transmission in Asynchronous Networks," *Proc. 22nd ACM Symposium on Principles of Distributed Computing (PODC 2003)*, pages 223-232, July 2003.

[20] C. Cashin, and R. Strobl "Asynchronous Group Key Exchange with Failures," *Proc. 23rd ACM Symposium on Principles of Distributed Computing (PODC 2004)*, pages 357-366, July 2004.

[21] M. A. March, F. B. Schneider, "CODEX: A Robust and Secure Secret Distribution System," *IEEE Transactions on Dependable and Secure Computing*, January-March 2004 (Vol.1, No.1) pp. 34-47.

[22] C. Cashin, S. Tessaro, "Asynchronous Verifiable Information Dispersal," *Research Report RZ 3569, IBM Research*, December 2004.

[23] Research Group on Mathematics Applied to Cryptography, "Some trends for future research in distributed cryptography," *Stork Cryptography Workshop: Towards a Roadmap for Future Research*, November 26-27, 2002.

A Method for Synthesis of Generalized Barker Codes

Borislav Y. Bedzhev[1], Zhaneta N. Tasheva[2] and Borislav P. Stoyanov[3]

Abstract - **Signals, which auto-correlation function (*ACF*) has as small as possible side lobes, are preferred in communication applications. From historical point of view, the Barker codes are the first class of signals with this property. Due to their positive features the Barker codes have been studied intensively since their introduction in 1953. Despite of the taken efforts, there a lot of open problems exist still. With regard our paper suggests a method for synthesis of so-named six-phase or sextic generalized Barker codes (*SGBC*). Some aspects of practical applying of the suggested method are discussed. An unknown till now *SGBC* of length *n* = 18 is presented also.**

Keywords- **Communication system signaling, sextic generalized Barker codes.**

I. INTRODUCTION

The communications are in very rapid progress today. As a result, a lot of radio, television and local area wireless services are working together at every place and at very time. This situation leads to undesirable interferences of different signals and decreases the performance quality of the communication services. As known, the most effective method for precluding of multiple access interferences (*MAI*) is the usage of signals, which auto-correlation function (*ACF*) has as small as possible side lobes. It is necessary to emphasize that radio signals with this property are very important for some particular applications such as radars, time-synchronous networks and radio navigation (including global positioning) systems.

From historical point of view, the so-named Barker sequences or codes are the first class of signals with above type of *ACF* [1], [2]. As known, the Barker codes are radio signals, which are generated only by means of phase modulation. More specifically, an arbitrary complex phase modulated signal consists of *n* elementary pulses (waveforms) with duration τ which complex envelopes are:

$$\xi(j-1) = U_j \exp(i.\theta_j);\ j = 0,1,...n-1, \qquad (1)$$

where U_j and θ_j are the amplitude and the phase of j-th elementary pulse respectively. In this case the autocorrelation properties of a phase manipulated (*PM*) signal can be comprehensibly described by means of the aperiodic *ACF* of the sequence $\{\xi(j)\}_{j=0}^{n-1} = \xi(0), \xi(1),...\xi(j),...\xi(n-1)$, evaluated only in time-points $k\tau$:

$$R_{\xi\xi}(k) = \begin{cases} \sum_{j=0}^{n-1-|k|} \xi(j).\xi^*(j+|k|), & -(n-1) \le k \le 0, \\ \sum_{j=0}^{n-1-k} \xi^*(j).\xi(j+k), & 0 \le k \le (n-1). \end{cases} \qquad (2)$$

Here symbol "*" means "complex conjugation.

By definition, the Barker codes are the *PM* signals with the property:

$$|R(k)| \le 1,\ \ k \ne 0\,. \qquad (3)$$

Here the subscripts of *R* are omitted and this notation will be used for convenience henceforth.

In order to obtain maximal energy effectiveness of the transmitter and to simplify the complex processes in the communication devices the following limitations are imposed in the practice very often:

$$U_j = U_0 = const,\ \theta_j \in \{[(2\pi.l)/m];\ l = 0 \div m-1\}. \qquad (4)$$

The *PM* signals, satisfying (3), are named "*uniform*" and in the rest part of this paper our attention shall be focused on this type of *PM* signals.

Due to their positive features the Barker codes have been studied intensively since their invention in 1953 [3], [4], [5], [6], [7], [8], [9], [10]. Despite of the taken efforts, there a lot of open problems exist still [9]. For instance, originally the Barker codes were introduced as binary manipulated signals (i.e. $m = 2$ in (4)) but it has been found that they do not exist if *n* is an odd integer greater than 13 and may not exist if *n* is an even integer greater than 4. The later conjecture is not proved still (see [9], [10]).

With regard to the all above cited, our paper aims to suggest a method for synthesis of so-named six-phase or sextic generalized Barker codes (i.e. in (4)) [6], [9].

The paper is organized as follows. First, the basics properties of sextic generalized Barker codes (SGBC) are recalled. After then, a method for synthesis of SGBC is described. Some aspects of practical applying of the suggested method are discussed also. Finally, an unknown till now SGBC of length is presented.

[1]Borislav Y. Bedzhev is with the Faculty of Artillery, Air Defense and Communication Information System, National Military University, 1 Karel Shkorpil Str., 9713 Shoumen, Bulgaria, E-mail: bedzhev@mail.pv-ma.bg

[2]Zhaneta N. Tasheva is with the Faculty of Artillery, Air Defense and Communication Information System, National Military University, 1 Karel Shkorpil Str., 9713 Shoumen, Bulgaria, E-mail: tashevi86@yahoo.com

[3]Borislav P. Stoyanov is with the Faculty of Mathematics, Informatics and Economics, Shumen University, 1 Universitetska Str., 9700 Shoumen, Bulgaria, E-mail: bpstoyanov@abv.bg

II. BASICS OF SEXTIC GENERALIZED BARKER CODES

In this section of our report we shall prove some necessary conditions which must satisfy the aperiodic *ACF* of an arbitrary *SGBC*. They will be used in order to reduce the possible variants in the process of *SGBC* synthesis.

At the beginning we shall recall that our attention will be focused on the *SGBC* [6], [9]. This means that $m = 6$ in (4) and according to Eq. (1) the complex envelopes $\xi(j-1),\ j = 0,1,...n-1,$ of the elementary pulses (waveforms) with duration τ, forming a *SGBC*, belong to the set $\{\pm U_0,\ \pm \omega U_0,\ \pm \omega^2 U_0\}$. Here $\{\pm 1,\ \pm \omega,\ \pm \omega^2\}$ are the sixth roots of unity:

$$e^{\frac{2\pi}{6}i} = \frac{1}{2} + i\frac{\sqrt{3}}{2} = -\omega^2; e^{\frac{2\pi}{6}2i} = -\frac{1}{2} + i\frac{\sqrt{3}}{2} = \omega; e^{\frac{2\pi}{6}3i} = -1;$$
$$e^{\frac{2\pi}{6}4i} = -\frac{1}{2} - i\frac{\sqrt{3}}{2} = \omega^2; e^{\frac{2\pi}{6}5i} = \frac{1}{2} - i\frac{\sqrt{3}}{2} = -\omega; e^{\frac{2\pi}{6}6i} = 1. \quad (5)$$

Without losing of generality, it can be assumed $U_0 = 1[V]$ in Eq. (5). Now the following Proposition 1 will be stated.

Proposition 1: The side lobes of the aperiodic *ACF* of a *SGBC* can take only the values:

$$R(k) = 0, \quad \pm 1, \quad \pm \omega, \quad \pm \omega^2;\ k \neq 0. \quad (6)$$

Proof: As known, the complex numbers $\{\pm 1, \pm \omega, \pm \omega^2\}$ form a multiplicative group denoted as *C(6)* often. From this fact one can observe that the sum $R(k) = \sum_{j=0}^{n-1-k} \xi(j)\xi^*(j+k)$ comprises *n-1-k* terms, which belong to the set $\{\pm 1, \pm \omega, \pm \omega^2\}$. Hence:

$$R(k) = \alpha + \beta\omega + \gamma\omega^2, \quad (7)$$

where α, β и γ are integers. From Eq. (7) the magnitude of a *SGBC ACF* side lobe can be presented in the form:

$$|R(k)|^2 = (\alpha + \beta.\omega + \gamma.\omega^2)(\alpha + \beta.\omega + \gamma.\omega^2)^* =$$
$$= (\alpha + \beta.\omega + \gamma.\omega^2)(\alpha + \beta.\omega^2 + \gamma.\omega), \quad (8)$$

because $\omega^* = \omega^2$ и $(\omega^2)^* = \omega$ (see Eq. (5)). After opening of parentheses in Eq. (8), the result is:

$$|R(k)|^2 = \alpha^2 + \beta^2 + \gamma^2 + (\alpha.\gamma + \alpha.\beta + \gamma.\beta).\omega +$$
$$+ (\alpha.\beta + \beta.\gamma + \alpha.\gamma).\omega^2 = \alpha^2 + \beta^2 + \gamma^2 - \alpha\beta - \alpha\gamma - \beta\gamma. \quad (9)$$

Here it is taking into account that $1 + \omega + \omega^2 = 0$, $\omega^3 = 1$ and consequently:

$$(\alpha.\gamma + \alpha.\beta + \gamma.\beta).\omega + (\alpha.\beta + \beta.\gamma + \alpha.\gamma).\omega^2 =$$
$$(\alpha\beta + \beta\gamma + \alpha\gamma)(\omega + \omega^2) = -(\alpha\beta + \beta\gamma + \alpha\gamma). \quad (10)$$

Now the Eq. (9) can be presented in the form:

$$|R(k)|^2 = \frac{1}{2}\left[2\alpha^2 + 2\beta^2 + 2\gamma^2 - 2\alpha\beta - 2\alpha\gamma - 2\beta\gamma\right] =$$
$$= \frac{1}{2}\left[(\alpha^2 - 2\alpha\beta + \beta^2) + (\alpha^2 - 2\alpha\gamma + \gamma^2) + (\beta^2 - 2\beta\gamma + \gamma^2)\right] =$$
$$= \frac{1}{2}\left[(\alpha - \beta)^2 + (\alpha - \gamma)^2 + (\beta - \gamma)^2\right]. \quad (11)$$

After substituting with Eq. (11) in (3) one can obtain:

$$\frac{1}{2}\left[(\alpha - \beta)^2 + (\alpha - \gamma)^2 + (\beta - \gamma)^2\right] \leq 1, \quad (12)$$

and hence:

$$(\alpha - \beta)^2 + (\alpha - \gamma)^2 + (\beta - \gamma)^2 \leq 2. \quad (13)$$

It is straightforward that possible solutions of Eq. (13) are:

1) $\alpha = \beta = \gamma$;
2) $\beta = \gamma;\quad \alpha = \beta \pm 1 = \gamma \pm 1$;
3) $\alpha = \beta;\quad \gamma = \alpha \pm 1 = \beta \pm 1$;
4) $\alpha = \gamma;\quad \beta = \alpha \pm 1 = \gamma \pm 1$.

(14)

From Eqs. (14) it is apparent that the side lobes of the aperiodic *ACF* of a *SGBC* can take only the values:

1) $R(k) = \alpha + \alpha.\omega + \alpha.\omega^2 = \alpha(1 + \omega + \omega^2) = 0$;
2) $R(k) = (\beta \pm 1) + \beta.\omega + \beta.\omega^2 = \beta(1 + \omega + \omega^2) \pm 1 = \pm 1$;
3) $R(k) = \alpha + \alpha.\omega + (\alpha \pm 1).\omega^2 = \alpha(1 + \omega + \omega^2) \pm \omega^2 = \pm\omega^2$
4) $R(k) = \alpha + (\alpha \pm 1).\omega + \alpha.\omega^2 = \alpha(1 + \omega + \omega^2) \pm \omega = \pm\omega$. (15)

The Eqs. (15) complete the proof of Proposition 1.

III. METHOD FOR SYNTHESIS OF SEXTIC GENERALIZED BARKER CODES

All present available methods for signal synthesis seem to contain an element of trial and error [3], [4], [5], [6], [7], [8], [9], [10]. Consequently, the above proved Proposition 1 allows a significant reducing of computational complexity of programs, which are used for *SGBC* synthesis. This will be explained in more details in this section of our paper.

Our method for synthesis of *SGBC* comprises approximately $\lceil \log_2 n \rceil$ successive steps.

First step begins with the following polynomial presentation of the *ACF* of an arbitrary *PM* signal:

$$P(x) = F(x).F^*(x^{-1}) =$$
$$= R(-(n-1)).x^{-(n-1)} + R(-(n-2)).x^{-(n-2)} + ... + R(0) + ... +$$
$$+ R(n-2).x^{n-2} + R(n-1).x^{n-1} = \sum_{k=-(n-1)}^{n-1} R(k).x^k \ . \qquad (16)$$

Here:

$$F(x) = \xi(n-1).x^{(n-1)} + ... + \xi(1).x + \xi(0) \qquad (17)$$

is the polynomial, corresponding to the sequence $\{\xi(j)\}_{j=0}^{n-1}$ of complex envelopes of elementary pulses (see Eq. (1)), $R(k)$ are the *ACF* lobes, determined by Eq. (2), and $F^*(x^{-1})$ is the so - named reciprocal polynomial:

$$F^*(x^{-1}) = \xi^*(n-1).x^{-(n-1)} +$$
$$+ \xi^*(n-2).x^{-(n-2)} + ... + \xi^*(1).x^{-1} + \xi(0) \ . \qquad (18)$$

The main idea of our method for synthesis of SGBC is the computational complexity to be reduced by factoring of the polynomial $P(x)$**.** In order to realize this idea the Eq. (16) is examined $\mod(x-1)$, $\mod(x+1)$, $\mod(x-\omega)$ and $\mod(x+\omega)$ during the first step of our method. For instance:

$$P(x) = F(x).F^*(x^{-1}) \mod(x-1), \qquad (19)$$

is equivalent to the substitution $x = 1$ in Eq. (16). After this substitution and taking into account Eqs. (7) and (11), it is apparent that:

$$\sum_{k=-(n-1)}^{n-1} R(k) = \left[\sum_{k=0}^{n-1} \xi(k)\right]\left[\sum_{k=0}^{n-1} \xi^*(k)\right] =$$
$$= \left(\alpha_0 + \beta_0.\omega + \gamma_0.\omega^2\right)\left(\alpha_0^* + \beta_0^*.\omega^{-1} + \gamma_0^*.\omega^{-2}\right) =$$
$$= \left(\alpha_0 + \beta_0.\omega + \gamma_0.\omega^2\right)\left(\alpha_0^* + \beta_0^*.\omega^2 + \gamma_0^*.\omega\right) =$$
$$= \left(\alpha_0 + \beta_0.\omega + \gamma_0.\omega^2\right)\left(\alpha_0 + \beta_0.\omega + \gamma_0.\omega^2\right)^* =$$
$$= \frac{1}{2}\left[(\alpha_0 - \beta_0)^2 + (\alpha_0 - \gamma_0)^2 + (\beta_0 - \gamma_0)^2\right] \qquad (20)$$

Here α_0, β_0 и γ_0 are integers and consequently, the Eq. (20) proves the following Proposition 2.

Proposition 2: The double sum of the *ACF* lobes of a *SGBC* must be a sum of three exact quadrates.

In this way one can find that:

$$\sum_{k=-(n-1)}^{n-1} R(k)(-1)^k = \frac{1}{2}\left[(\alpha_1 - \beta_1)^2 + (\alpha_1 - \gamma_1)^2 + (\beta_1 - \gamma_1)^2\right], \qquad (21)$$

$$\sum_{k=-(n-1)}^{n-1} R(k)\omega^k = \frac{1}{2}\left[(\alpha_2 - \beta_2)^2 + (\alpha_2 - \gamma_2)^2 + (\beta_2 - \gamma_2)^2\right], \qquad (22)$$

$$\sum_{k=-(n-1)}^{n-1} R(k)(-\omega)^k =$$
$$= \frac{1}{2}\left[(\alpha_3 - \beta_3)^2 + (\alpha_3 - \gamma_3)^2 + (\beta_3 - \gamma_3)^2\right]. \qquad (23)$$

The number of all possible *ACF* of a *SGBC* is:

$$L(n) = (n-1)^7 \qquad (24),$$

because $R(-k) = R^*(k)$, $R(0) = n$ accordingly to (2) and due to Proposition 1. It ought to emphasize that Eqs. (6), (20)-(23) contain necessary conditions, which allow reducing the number $L(n)$ of possible *ACF* significantly. First step of our methods for *SGBC* synthesis ends with forming of a massive, containing the *ACF*, which have passed all sieves in Eq. (6), (20)-(23).

At the second step of our method every polynomial $P(x) = F(x).F^*(x^{-1})$ (see Eq. (16)), corresponding to a possible *ACF* found in the first step, is examined $\mod(x^3 - 1)$. It is utilized that:

$$x^3 - 1 = (x-1)(x-\omega)(x-\omega^2), \qquad (25)$$
$$F(x).F^*(x^{-1}) \mod(x^3 - 1) =$$
$$= \left[\sum_{k=0}^{\left\lceil\frac{n-1}{3}\right\rceil} \xi(3k) + \sum_{k=0}^{\left\lceil\frac{n-1}{3}\right\rceil} \xi(3k+1)x + \sum_{k=0}^{\left\lceil\frac{n-1}{3}\right\rceil} \xi(3k+2)x^2\right] \times$$
$$\times \left[\sum_{k=0}^{\left\lceil\frac{n-1}{3}\right\rceil} \xi^*(3k) + \sum_{k=0}^{\left\lceil\frac{n-1}{3}\right\rceil} \xi^*(3k+1)x^{-1} + \sum_{k=0}^{\left\lceil\frac{n-1}{3}\right\rceil} \xi^*(3k+2)x^{-2}\right] =$$
$$= \sum_{k=-\left\lceil\frac{n-1}{3}\right\rceil}^{\left\lceil\frac{n-1}{3}\right\rceil} R(3k) + \sum_{k=0}^{\left\lceil\frac{n-1}{3}\right\rceil} \left[R(-3k-1) + R(3k+1)\right].x +$$
$$+ \sum_{k=0}^{\left\lceil\frac{n-1}{3}\right\rceil} \left[R(-3k-1) + R(3k+2)\right].x^2 \mod(x^3 - 1). \qquad (26)$$

The second step of our method can be explained as follows. At the beginning, the possible *ACF* are taken successively from the massive, formed at the end of the first step. After that, the system of following equations:

$$\left[\sum_{k=0}^{n-1} \xi(k)\right]\left[\sum_{k=0}^{n-1} \xi^*(k)\right] = \sum_{k=-(n-1)}^{n-1} R(k)$$
$$\left[\sum_{k=0}^{n-1} \xi(k)\omega^k\right]\left[\sum_{k=0}^{n-1} \xi^*(k)\omega^{-k}\right] = \sum_{k=-(n-1)}^{n-1} R(k)\omega^k$$

$$\left[\sum_{k=0}^{n-1}\xi(k)(-\omega)^k\right]\left[\sum_{k=0}^{n-1}\xi^*(k)(-\omega)^{-k}\right]=\sum_{k=-(n-1)}^{n-1}R(k)(-\omega)^k \quad (27)$$

is solved, which allows the finding of the three partial sums $\sum_{k=0}^{\left\lceil\frac{n-1}{3}\right\rceil}\xi(3k)$, $\sum_{k=0}^{\left\lceil\frac{n-1}{3}\right\rceil}\xi(3k+1)$, $\sum_{k=0}^{\left\lceil\frac{n-1}{3}\right\rceil}\xi(3k+2)$ in the left side of Eq. (26).

The Eq. (16) is examined $\bmod(x^6-1)$ analogously during the third steps of our method. This allows finding the partial sums $\sum_{k=0}^{\left\lceil\frac{n-1}{6}\right\rceil}\xi(6k)$, $\sum_{k=0}^{\left\lceil\frac{n-1}{6}\right\rceil}\xi(6k+1)$, … $\sum_{k=0}^{\left\lceil\frac{n-1}{6}\right\rceil}\xi(6k+5)$.

In this way using approximately $\lceil\log_2 n\rceil$ steps all sequence $\{\xi(j)\}_{j=0}^{n-1}$ of complex envelopes of elementary pulses, forming a *SGBC*, is found.

IV. Conclusion

The above described method for synthesis of *SGBC* was realized as a computer program. With it the interval of code-lengths $14\le n\le 25$ was examined. It was found the following *SGBS*'s:

$$\xi(14)=+1,-\omega^2,-1,\omega^2,\omega^2,-1,\omega^2,\omega,\omega^2,-\omega^2,-\omega,\omega^2,\omega,+1; \quad (28)$$

$$\xi(15)=+1,-\omega^2,\omega,\omega^2,-\omega,\omega^2,\omega^2,\omega^2,\omega,\omega^2,$$
$$-\omega^2,-\omega,\omega^2,\omega,+1; \quad (29)$$

$$\xi(18)=+1,+1,\omega^2,-\omega,\omega,\omega,+1,-\omega^2,-\omega^2,\omega,$$
$$\omega,-\omega,-1,+1,-\omega^2,-\omega,\omega,+1. \quad (30)$$

The first two *SGBC* of length $n=14,\ 15$ respectively, are mentioned, but not shown in the literature [9]. The later one (see Eq. (30)) is unknown till now [3], [4], [5], [6], [7], [8], [9], [10].

At the end it ought to be mentioned that:

- the method for synthesis of *SGBC*, suggested in our paper, has good computational effectiveness;
- this method could be used successfully for finding of other signals, valuable for present communications.

Acknowledgement

Authors would to thank Professor Nikola Dodov, whose observations made the drafting of the paper the best possible.

References

[1] R. H. Barker, "Group synchronizing of binary digital systems", in *Communication theory*, pp. 273 – 287, London, 1953.

[2] R. J. Turyn, J. Storer, "On binary sequences", *Proc. of American Mathematical Society*, vol 12, pp. 394-399, 1961.

[3] S. W. Golomb, G. A. Scholtz, "Generalized Barker sequences", *IEEE Trans. on Information theory*, vol. IT -11, no. 4, pp. 533-537, 1965

[4] R. J. Turyn "Four phase Barker codes", *IEEE Trans. on Information theory*, vol. IT -20, no. 3, pp. 366-371, 1974.

[5] N. Zhang, S. W. Golomb "Uniqueness of the generalized Barker sequence of length 6", *IEEE Trans. on Information theory*, vol. IT -36, no. 5., pp. 1167-1170, 1990.

[6] N. Zhang, S. W. Golomb "Sixty-phase generalized Barker sequences", *IEEE Trans. on Information theory*, vol. IT -35, no. 4., pp. 911-912, 1989.

[7] N. Zhang, S. W. Golomb "A limit theorem for n-phase Barker sequences", *IEEE Trans. on Information theory*, vol. IT -36, no. 4, pp. 863 – 867, 1990.

[8] N. Zhang, S. W. Golomb "On n-phase Barker sequences", *IEEE Trans. on Information theory*, vol. IT -40, no. 4, pp. 1251-1253, 1994.

[9] N. Zhang, S. W. Golomb "7200-phase generalized Barker sequences", *IEEE Trans. on Information theory*, vol. IT -42, no. 4, pp. 1236-1238, 1996.

[10] N. Zhang, S. W. Golomb "Recent results on polyphase sequences", *IEEE Trans. on Information theory*, vol. IT -44, no. 2, pp. 817-824, 1998.

Telecommunication System with Two Kinds of Pseudo Random Sequences for Spectrum Expansion

Georgi D.Nenov, Galina P.Cherneva

Abstract – **The paper presents a method and the structure diagram of a telecommunication system where the input information spectrum expands by switching a number of pseudo random sequences. Switching is controlled by another similar sequence, the symbols of which last much longer. The system provides a high degree of protection against non-allowed access.**

Keywords – **Pseudo random sequences, spectrum expansion, protection against non-allowed access.**

I. INTRODUCTION

The protection of information is of substantial importance in different fields of modern society. It is necessary in regard to the concept of market where different economic interests oppose each other. The information protection is connected with the security of institutions and individuals.

There are different methods and means to protect information against non-allowed access. Most generally, they are based on using software and hardware resources.

The paper presents a method and a structure diagram of the telecommunication channel protection by scrambling and descrambling on two levels. On the first level this process directly concerns the primary signal, which is a carrier of information in digital kind. The second level has controlling functions in regard to the random sequences. They change in time according to a given dependency defined by a code combination.

It is known that there is a system of signal transmitting through scrambler and descrambler, which synchronize themselves each other [1]. The use of different code sequences is done by the keys K1,….Kn (Fig.1). They define the feedback in generators of random sequences, NLS (Noise like Signals).

The signal Si,, which is the information carrier, is supplied to the scrambler input. Let it consist of the lines given in Table 1. The summation by module 2 with a random sequence Ss is done in the summation device 1. The output signal Sout is obtained and it istransmitted along the line or is modulated to be transmitted along the radio line.

The dependency

$$S_{out} = S_i \oplus S_s \qquad (1)$$

where the symbol $\oplus$ means summation by module 2 ($\sum$ mod 2), is valid for Sout.

Authors are with the Higher School of Transport, Geo Milev Str.158, 1584 Sofia, Bulgaria

becomes narrower in the receiver with the same kind of sequence Ss, which is synchronized as the initial signals S1, S2,…, Sn in the scrambler and the discrambler are equal, i.e. the initial conditions are S1= S2=…=Sn=1.

The fifth line in Table 1 is corresponding to output signal in the receiver S'i. If differs from Si due to noises and distortions caused with transmitting.

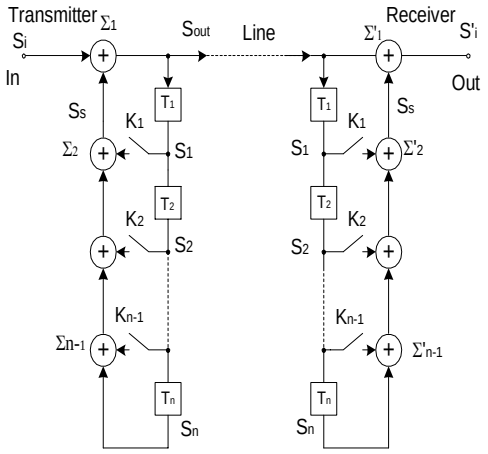

Fig.1

TABLE I
PAGE LAYOUT DESCRIPTION

1	S_i	1 1 1 1	0 0 0 0	1 1 1 1
2	S_s	1 0 1 0	1 0 1 0	0 1 1 0
3	S_{out}	0 1 0 1	1 0 1 0	1 0 0 1
4	S_s	1 0 1 0	1 0 1 0	0 1 1 0
5	S'_i	1 1 1 1	0 0 0 0	1 1 1 1
1	S_i	1 1 1 1	0 0 0 0	
2	S_s	0 1 1 1	0 1 0 1	
3	S_{out}	1 0 0 0	0 1 0 1	
4	S_s	0 1 1 1	0 1 0 1	
5	S'_i	1 1 1 1	0 0 0 0	

The summation according to module 2 of the signal along the line Sout (in that case it is an input signal for the receiver) and the elements of the sequence Ss created in the descramble is done in the summation device, i.e.

$$S'_i = S_{out} \oplus S_s \qquad (2)$$

The example shown in Table 1 is valid for a digital information signal, the symbols of which "1" and "0" are presented for clarity with a duration four times longer than the symbols of the random sequence and respectively, the same times longer than the delay T in the elements of displacing registers. The diagrams of Si and Ss from t = 0 to t = 9T are given in Fig. 2.

The protection of information against the non-allowed access is as more reliable as the pseudo-sequence Ss is longer,

because it takes longer to discover it. Another disadvantage is the complex character of generators.

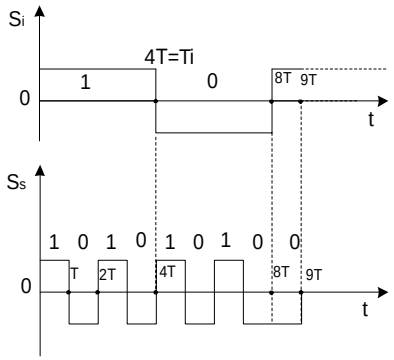

Fig.2

To improve the protectiveness, it is proposed to change the set of random sequences, which are created by switching of keys K1,…, Kn in the generators (Fig.1).

The choice of the given sequence from the set is made by a preliminary determination of correspondents.

The paper proposes to do the key control and the control on the sequences respectively using random sequence. The structure diagram of the system is given in Fig.3. The scrambler and descrambler of control are connected to the information component of the system. The interfaces are not shown to make the examination sampler. The same is made in regard to the synchronization of the two components.

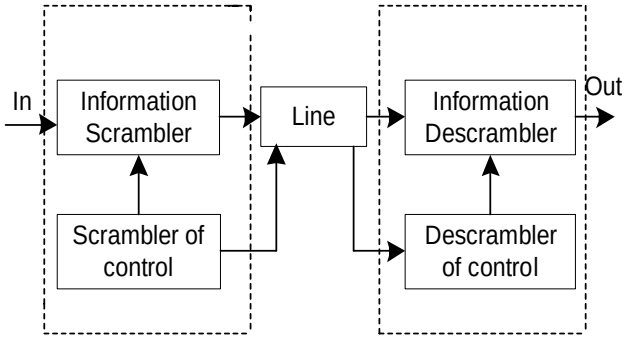

Fig.3

The initial protection of the system is provided by the information scrambler and its corresponding descrambler. Their structure is of the kind given in Fig. 1.

The controlling component contains scrambler and descrambler, the sequences of which do not need to be of full length, but symbols (elements) in them have to be of a duration many times longer than the time of switching. It means that they will change the sequences in the information component in intervals of sufficient length. It is necessary for the duration of a symbol or a code combination of the "controlling" sequence to be multiple number of times longer than the duration of a information" sequence

The prerequisites outlined can be reduced to the following quantity dependencies necessary for designing.

1. The duration T of a symbol of the random sequence Ss depends on the information transmitting and the channel flow capacity.

2. With examining the processes in real time, the duration of one symbol of the information sequence Si, i.e. Ti is of primary importance. As it is shown in Fig. 2, the condition Ti>>T should have been kept. It is quite indefinite and is kept with a ratio of Ti/T from several times to several orders, which can conditionally be expressed by the sign of multiplication (x) in the following way:

$$\frac{T_i}{T} = \times 1 \div 10^m; (m = \times 1) \qquad (3)$$

3. The other obligatory relation is between the length of the information random sequence Ss, which serves to expand the signal spectrum (carrying vibration) and the duration of the random sequence with a control function Sc. With using simple generators, they are respectively:

$$M_i = 2^i - 1 \text{ and } M_c = 2^c - 1 \qquad (4)$$

For this and other types of generators it is necessary to keep a requirement similar to (3),i.e

$$\frac{M_c}{M_i} >> 10^m; (m = \times 1) \qquad (5)$$

The satisfaction of the conditions (3) and (5) ensures system normal functioning.

The big values of *m* in (3) are favourable against the distortions of impulses in line Si. The effect towards the protection against the non-allowed access depending on *m* in (5) is reverse.

The method proposed is characterized with the following advantages in relation to the already-known methods of protection against the non-allowed access with information transmitting in the expanded spectrum systems.

1. The secret feature (protection) is ensured by two levels of random sequences, which extremely increases the degree of entropy. Hence it reduces the probability of access.

2. The main system components are well known and tested in practice.

3. There is no need of sequences with big length and using generators of more complicated structure.

The disadvantage of the system is the necessity of elements for coordinating and

synchronizing the information and control components of the system.

The method can be applied to the modern telecommunication systems of expanded spectrum with high requirements related to the protection of information against non-allowed access.

REFERENCES

[1] P. Watson, K. C. Gupta, "EM-ANN Models for Microstrip Vias and Interconnects", *IEEE Trans., Microwave Theory Tech.*,vol. 44, no. 12, pp. 2395-2503, 1996.

[2] Stallings W., *Wireless Commu-nications and Networking*, Prentice-Hall, 2002.

[3] Goiser Alois M.J., *Handbuch der Spread Spectrum Technik*, Wien – New York,1998

[4] Skler, B., *Digital Connection*, M., Williams, 2003 (in Russian)

[5] *Noise-Like signals in thesystems of transmitting infor-mation*, edited by. V.B. Pestryakov, M., Soviet Radio, 1973 (in Russian)

Session PS:

POWER SYSTEMS AND DISTRIBUTION SYSTEMS

Evaluation of Transmission Reliability Margin in Automatic Transmission Capacity Calculation

Dragan P.Popović[1]

Abstract: **The paper deals with an approach to the evaluation of Transmission Reliability Margin (TRM) in automatic cross-border transmission capacity assessment of electric power interconnections. It is based on advanced methodology for steady-state security analyses. The practical application of developed approach is made on example of transmission capacity calculation in condition of Second UCTE synchronous zone.**

Keywords - **Cross-border, Transmission Capacity, Automatic Mode, Transmission Reliability Margin, Open Electricity Market**

I. INTRODUCTION

An important issue in modern EPS's (Electric Power Systems) is to provide the necessary level of operational security. In recent years, the increased practical interest to this issue has been shown, and corresponding new challenges appeared, mainly due to increased loading of EPS's, combined with a process of liberalization in electric power market and restructuring of the power utilities. Open access power systems need accurate transmission capacities evaluation to guarantee secure operation for all transactions.

Also, the processes above mentioned are very important and topical for all countries in Southeast Europe, as well as for Serbia and Montenegro and its power industry, according to the following facts:

- *Reconnection the Second UCTE synchronous zone with the main part of the UCTE grid*

The Second UCTE synchronous zone was disconnected from the main UCTE grid since 1992, due to war consequences in former SFR Yugoslavia. Since then, there are only periodical island operations between the parts of these zones. The present Second UCTE synchronous zone is consisted of the networks of Albania (AL), Bosnia-Herzegovina (eastern part, RS), Bulgaria (BG), FYR Macedonia (MK), Greece (GR), Romania (RO), Serbia and Montenegro (SCG).The reconnection of the Second zone with the main UCTE grid is successfully made in 10 October 2004.

- *Establishment of Regional Electricity Market*

According to the Memorandum of Understanding [1], all the countries from South-east European region agreed upon the constitution of a competitive Regional Electricity Market (REM) in Southeast Europe. The proposed time period for creation of regional electricity market is last up to year 2006.

The basic objective of this paper is to present an approach to the evaluation of Transmission Reliability Margin (TRM) in automatic cross-border transmission capacity assessment (NTC-Net Transfer Capacity) of interconnections. It is based on advanced methodology for NTC calculation, using all its favourable properties, respecting the latest definitions [2], criterions, standards and practice [3] of European Transmission System Operators (ETSO). The relevant theoretical and practical aspects of this advanced methodology are given in [4, 5, 6, and 7].

The most complex and delicate part of NTC calculation is the evaluation of TRM, which is a security margin that copes with uncertainties on the computed TTC (Total Transfer Capacity) values [2, 3, and 8].

Those uncertainties may arise from: unintended deviation of physical flows due to the load-frequency control, emergency exchange caused by the unexpected unbalanced situations (big injection losses) in real time and inaccuracies in data and calculation models and/or method. This comprehensive set of possible uncertainties explains the existence of many different approaches for the solving of this problem in practice [8, 9, and 10].

The value of TRM can only be estimated, because it should consider all uncertainties of system operation. The value of TRM in majority of EPS is estimated, according the statistical analysis of past data (per instant, statistical study of individual tie line "errors", calculation of standard deviation of tie-line power e.t.c).

Next, in practice, the part of TRM, which corresponds to the inaccuracies in data and calculation models and/or method isn't bigger than 5% of computed TTC value. Also, in practice of ETSO, a reasonable value of TRM usually could be found by assuming an unpredictable power flow mismatch on each interconnecting lines (e.g. 100 MW), multiplied with the square root of its number ($\sqrt{l}$), i.e. TRM [MW] = $100\sqrt{l}$.

This paper deals with the possible way to the evaluation of TRM, respecting the facts that the above mentioned methodology for NTC calculation strictly evaluates the transmission effects of primary frequency and load-frequency controls, i.e. the significant "part" of TRM are included (except the part that takes into accounts the uncertainties on system conditions and the precision data in load-flow models).

This approach is based on two types of NTC calculation. First, the calculation of NTC is make for elements (lines and transformers) outage type of disturbances, and second, for generators outage type of disturbances. According to the automatic mode of NTC calculation, this approach enables very fast and efficient calculation of TTC, for those two types of disturbances. After that, it is possible to make a good estimation for TRM.

The first practical experiences in the application of this approach have been gained on an example of the synchronous

[1] Dragan P. Popović is with Nikola Tesla Institute, Koste Glavinića 8a, 11000 Belgrade, Serbia and Montenegro E-mail: dpopovic@ieent.org

parallel operation of the EPSs in the Second UCTE synchronous zone.

II. Methodological Aspects of Automatic Cross-Border Transmission Capacity Evaluation

This advanced methodology for automatic cross-border transmission capacity assessment is consisted in the following relevant parts, which differ to the usual approaches:

- Two procedures for initialisation of steady-state security analyses, i.e. the procedure for solving the initial load-flow problems, which precede these analyses [5];
- These procedures are fully consistent with the specially developed method for the following steady-state security analyses [4, 5]. Such characteristic of these procedures enables the unification of corresponding computer program, autonomy and uniformity of steady-state security analysis, as well as their successive realization, which have practical importance;
- The limits of generator reactive power are not constant, a priori defined quantities, but rather corresponding functions of relevant generator parameters and state variables [4]. Also, during the NTC calculation, the generator voltage reference is to be changed according to the corresponding change of generator active power;
- Procedure for fast contingency selection, which is based on results from the single iteration of specially developed fast decoupled load-flow solution method, in which the power system frequency is relevant variable [6];
- Procedure for forming the unified external network equivalents, with adaptive buffer system selection, consistently respecting the effects of primary voltage and frequency control of neighbouring power systems [11];
- Simple method for the accurate assessment of dynamic variation of power system frequency, during the operation of its primary control, as well as the quasi-stationary value of its frequency [12];
- Generalized injected models of transformer, which enables a simple presentation of both energy transformers with or without angle regulation as well as static phase shifting transformers (so-called series FACTS power flow controllers [13];
- Generalized model of generator participation in NTC calculation, which enables the selection of the most convenient ones regarding the real operational practice in new condition of liberalized electricity market [14]. The generation increase/decrease has to be performed proportionally, according to actual spinning reserve.
- Forming the practical and realistic security indices for selection of potentially critical disturbances, according to the real power performances and to the control and protection devices characteristics [6];
- For potentially critical contingency, the continuation of iterative procedure for solving the load-flow problem is performed (full contingency analysis), based on specially developed fast-decoupled method [4].
- The proposed methodology strictly evaluates the transmission effects of primary frequency and load-frequency controls, i.e. the significant "part" of TRM are included (except the part that takes into accounts the uncertainties on system conditions and the precision data in load-flow models).
- This method enables successive solution of the load-flow problem for a set of characteristic post-dynamic quasi-stationary states: states resulting from primary voltage and frequency control, states after the action of automatic secondary control of frequency and tie-line power and states after corresponding possible dispatch activities, if necessary (corrective control) [4].

III. Concept of Automatic Cross-Border Transmission Capacity Evaluation

Fig. 1 [7] presents the global concept of the proposed methodology (computer program STATIC developed in Nikola Tesla Institute) for automatic cross-border transfer capability calculation, using flow diagrams of the basic functions.

This methodology uses a unified data base (block 1), as a segment of the complex database necessary for the operational planning of EPS. For this purpose the UCTE data exchange format is used [15].

If the first option of application is selected (identification and verification of initial steady-state, with bad data processing), only load-flow solution in initial (base) steady-state is performed (block 2).

In the case of second option, after calculation the initial load-flow, the security assessment for this state is made (block 3). This assessment is made respecting the N-1 criterion (per example: outage of single lines 400, 220 and 110 kV, transformers 400/220 kV, 400/110 kV and generators) and N-2 criterion, in case of double circuit.

After the inauguration of initial steady-state that satisfied the security constraints, the automatic cross-border transmission capacity assessment is made. In order to determine the cross-border transmission limit between two neighbouring countries or zones, cross-border exchanges are gradually increased while maintaining the loads in the whole system unchanged until security limits are reached.

Starting from the common base case exchanges, the additional exchange is performed through an increase of generation on the exporting side and an equivalent decrease of generation on the importing side in automatic mode (in step of e.g. 50 MW). This generation shift is to be made stepwise until a network constraint is violated. The security assessment is also made respecting the N-1 security criterion (and N-2, in case of double circuit).

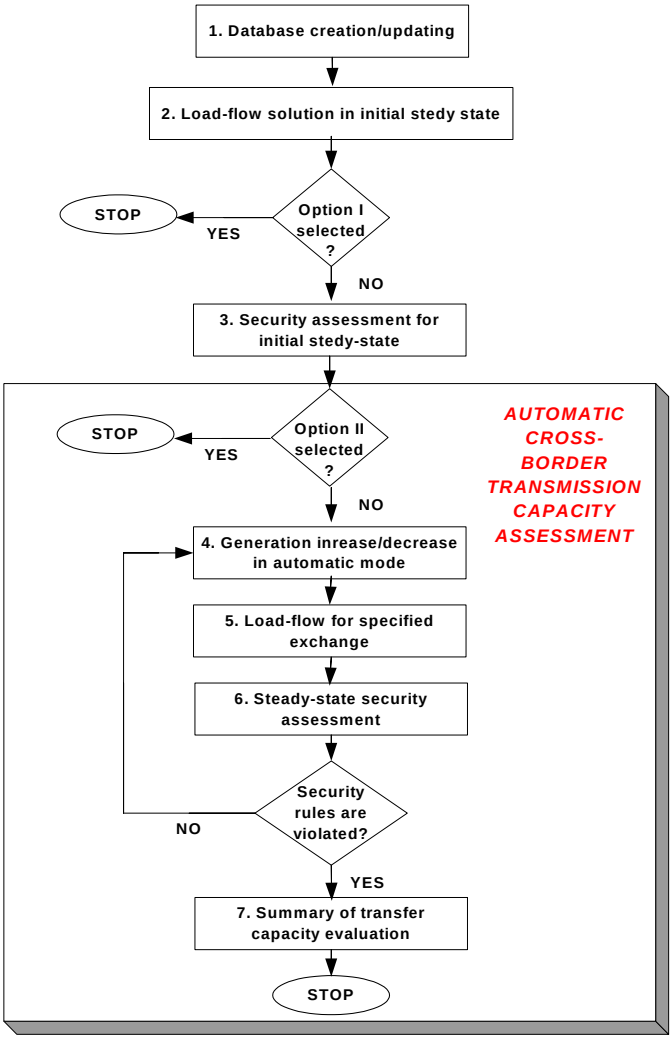

Fig. 1. Flow diagram of automatic cross-border transmission capacity assessment

The procedures, marked in following blocks 4 (generator increase/decrease in automatic mode, proportional to the actual spinning reserve), 5 (load-flow solution for specified exchange in step of 50 MW) and 6 (steady-state security assessment) are stopped, when predefined security rules are violated.

Finally, block 7 gives the summary of transfer capability evaluation. The output results are: TTC, TRM, NTC, Notified Transmission Flow (NTF) and Total Transfer Flow (TTF).

IV. Practical Application

The first practical experiences in the application of the developed approach to the evaluation of TRM have been gained on an example of the present state of the Second UCTE synchronous zone. Fig. 2 [7] shows the block diagram of examined interconnection with the active and reactive power flows (MW/Mvar) over the interconnecting lines in two cases: 1) without any exchange programs between the EPS's (except the exchange between Serbia and Montenegro and part of Republic Spike) and 2) when Romania exports 300 MW to Serbia and Montenegro (values given in parentheses).

Thus, in the first case, the BCE (Base Case Exchange) between the EPS's in interconnection considered (except the above mentioned exchange between SCG and RS) does not exist (”zero” exchange program). In these conditions, the physical power flows on interconnecting lines presented are so-called parallel (or ring) flows, i.e. the physical flow NTF (Notified Transmission Flow) only consists of parallel flows. In this state and also during the security assessment, the relevant network constraints (voltage and current limits) are not violated.

In second case (RO exports 300 MW to SCG), the power flow on interconnecting line Đerdap (SCG) – P. De Fier (RO) changes the direction, and this physical flow of 9 MW (now, in direction RO→ SCG) is in reality the NTF (which is now, in amount of along parallel power flows, results from above mentioned exchange 300 MW). Also, in this state the predefined security rules are satisfied.

This state of interconnection considered (with $BCE^{RO \rightarrow SCG}$ = 300 MW and $NTF^{RO \rightarrow SCG}$ = 9 MW) has been the starting point for automatic cross-border transmission capacity calculation, according the flow diagrams (blocks 4, 5, 6 and 7), given in Fig. 1. From many results that were obtained, the case of power exchanges between Romania (exports) and Serbia and Montenegro (imports) has been chosen as a good illustration.

For outage element type of disturbances (all elements, which are loaded more then 40% of own thermal limit are included), the procedure for automatic cross-border transmission capacity assessment is stopped when the total exchange RO → SCG was 750 MW. In this case, the critical outage was the outage of transformer 400/231 kV, 400 MVA in P. De Fier in Romania, and the critical element was the line 220 kV Paroseni-Baro Mare (RO), with 8% violation of thermal limit.

Thus, the Total Transfer Capacity $TTC^{RO \rightarrow SCG}$ in case considered was 700 MW. This quantity is 50 MW lower then above mentioned 750 MW, i.e. in case of exchange of 700 MW the security rules are still satisfied. Also, the quantity of ΔEmax was 400 MW (extra increase/decrease of generator's active power over the base case in automatic mode, which is ensured still the safe operation) and the Total Transfer Flow $TTF^{RO \rightarrow SCG}$ was 249 MW.

If above mentioned very simple practice (according to the relation TRM [MW] = $100\sqrt{I}$.) is applied in case considered (existence of the single interconnecting line between EPS's RO and SCG - line 400 kV P. De Fier (RO) – Đerdap (SCG)), the value of $TRM^{RO \rightarrow SCG}$ would be 100 MW, and the corresponding value of $NTC^{RO \rightarrow SCG}$ would be 600 MW.

However, the value of TRM shoud be respected the effects of primary frequency and load-frequency controls, as well as the effects of emergency exchange caused by the unexpected unbalanced situations (big injection losses, e.g. outage of big generators). In case of including this type of disturbances, in considered example of NTC calculation between EPS's RO i SCG, the automatic NTC calculation is stoped for total exchange of 550 MW. In this case, the critical outage was the outage of two generators in TPP Braila (RO) (injection loss of 310 MW and 200 Mvar). The consequences of this outage are

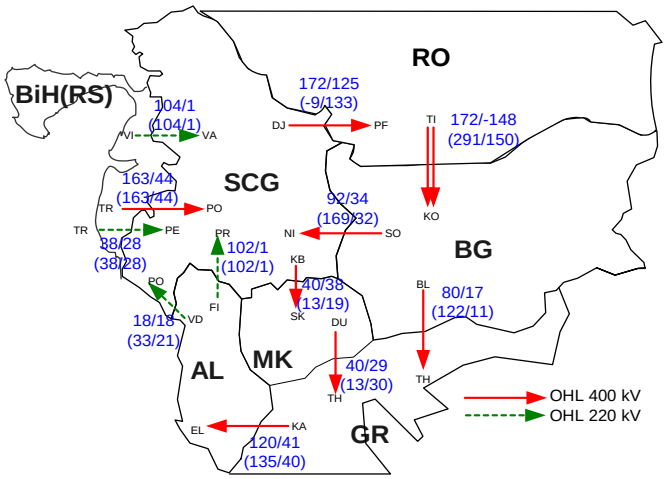

Fig. 2. Active and reactive powers on interconnecting lines of Second UCTE synchronous zone

the violation of voltage limit in several nodes, in part of EPS RO, near to this TPP.

Thus, in this practical example, the value of NTC $^{RO\rightarrow SCG}$ shoud be calculate in following maner:

$NTC^{RO\rightarrow SCG}=BCE^{RO\rightarrow SCG}+\Delta Emaxl^{RO\rightarrow SCG}-[(\Delta Emaxl^{RO\rightarrow SCG}-\Delta Emaxg^{RO\rightarrow SCG})+TRMo^{RO\rightarrow SCG}]=$

$=300+400-[(400-200)+35]=465$ MW

where:

$\Delta Emaxl^{RO\rightarrow SCG}$ – maximum value of extra increase/decrease of generator's active power over the base case, during the automatic NTC calculation, which is ensured still the safe operation, for outage element type of disturbances;

$\Delta Emaxg^{RO\rightarrow SCG}$ – maximum value of extra increase/decrease of generator's active power over the base case, during the automatic NTC calculation, which is ensured still the safe operation, for outage generator type of disturbances;

$TRMo^{RO\rightarrow SCG}$ – estimated part of total TRM, which corresponds to the inaccuracies in data and calculation models and/or method (usually, isn't bigger than 5% of computed TTC value).

In practical sense, in this example, $TRM^{RO\rightarrow SCG}=\Delta Emaxl^{RO\rightarrow SCG}-\Delta Emaxg^{RO\rightarrow SCG}+TRMo^{RO\rightarrow SCG}=235$ MW, because this value "covers" all outages of relevant generators up to the total exchange program RO → SCG 500(300+200) MW, and consequently, the realistic value of NTC $^{RO\rightarrow SCG}$ will be 465 MW.

However, it should be noted that is only one of possible approach, among many others, in contex of attempt to find a more accurate evaulation of TRM. Its is based on calculation of above mentioned values ΔEmaxl and ΔEmaxg, during automatic cross-border transmission capacity assessment.

Naturaly, the problem of more accurate evaluation of TRM needs the further research in thic topic. One possible direction, among other, is necessity of norming the amount of total emergency exchange, caused by the unexpected unbalanced situations (big injection losses, e.g. outage of big generators).

V. Conclusion

A possible way to the evaluation of TRM in automatic cross-border transmission capacity assessment of electric power interconnections has been presented It is based on advanced methodology for NTC calculation, using all its favourable properties, respecting the latest definitions, criterions, standards and practice of European Transmission System Operators. The possibilities of approach presented were demonstrated on example of existing electric power interconnection in Balkans.

Acknowledgement

The work in this paper was partially funded by the Ministry of Science, Technology and Development of Republic of Serbia, project No. ETR 242 .

References

[1] "Memorandum of Understanding on Regional Electricity Market in South East Europe and its integration into Internal Electricity Market", Athens, 2002.

[2] "Definitions of Transfer Capacities in Liberalized Electricity Markets", Final Report, ETSO, April, 2001.

[3] "Procedures for Cross-Border Transmission Capacity Assessments", ETSO, October, 2001.

[4] D.P.Popović, "An Efficient Methodology for Steady-State Security Assessment of Power Systems", International Journal of Electrical Power and Energy Systems, Vol. 10, No. 2, pp. 110-116, April 1988.

[5] D.P.Popović, Đ.M.Dobrijević, "An Improved Methodology for Security Assessment of Power Systems in Conditions of a Deregulated Environment", International Symposium-Bulk Power System Dynamics and Control V, Onomichi, Japan, Paper No 10, August 26-31, 2001.

[6] D.P.Popović, Đ.M.Dobrijević, N.A.Mijušković and D.J.Vlaisavljević, "An Advanced Methodology for Steady-State Security Assessment of Power Systems", European Transactions of Electrical Power Engineering, Vol. 11, No. 4, pp. 227-234, 2001.

[7] D.P.Popović, Đ.M..Dobrijević, S.V.Mijailović and Z.Z. Vujasinović, "Automatic Cross-Border Transmission Capacity Assessment in the Open Electricity Market Environment", 24 Session CIGRE, Paris, paper C2-209, 29 August- 3 September 2004.

[8] "A note on Transmission Reliability Margin evaluation", ETSO, February 2000.

[9] "Analysis of Electricity Network Capacities and Identification of Congestion", IAEW and CONSENTEC, Final Report, Aachen, December 2001.

[10] Dobson et al., "Electric Power Transfer Capability: Concepts, Applications, Sensitivity and Uncertainty'" University of Wisconsin, Madison WI USA, July 11, 2001.

[11] Đ.M.Dobrijević., D.P.Popović., N.A.Mijušković and D.J.Vlaisavljević, "A Unified External Network Equivalent in Steady-State Security Assessment of Balkan Interconnection", Black Sea EL-NET Regional Meeting, Suceava, Romania, paper No. I. 2. 2, 10-14. June 2001.

[12] D.P.Popović, S.V.Mijailović, "Fast Evaluation of Dynamic Changes of the Electric Power Systems Frequency during Primary Control", International Journal of Electric Power and Energy Systems, Vol. 19, No. 8, pp 525-532, November 1997.

[13] D.P.Popović, "Generalized model of transformer and load-flow" (in Serbian), journal "Elektroprivreda", No. 1, pp. 3-14., 2003.

[14] D.P.Popović, "Generalized model of generator participation in transmission capacity assessments of electric power interconnection" (in Serbian), journal "Elektroprivreda", No. 3, pp. 3-12, 2003.

[15] "UCTE data exchange format for load flows and three phase short circuit studies" (UCTE-DEF), Version 01, 2003.

An Approach for Calculation of Distribution Energy Losses Using Clustering Technique

Dragan S. Tasić[1] and Miodrag S. Stojanović [2]

Abstract – **This paper presents a method for calculation of annual distribution (electrical energy) losses based on clustering technique. Annual energy losses can be found calculating power losses for each hour during the year. However, this require large number of calculations (8760 i.e. 8784 for leap year). Clustering technique can be utilized to reduce the number of load flow calculations. In order to show applicability of clustering technique, annual simulation of distribution network has been made at the first. Power losses are calculated for each hour of the simulation. After that, number of clusters needed to obtain satisfying results is found.**

Keywords – **Distribution losses, Clustering technique, Estimation, Load category.**

I. INTRODUCTION

Power and energy losses are inevitable consequence of energy transmission and distribution from generation to consumer points. The total losses sometimes make ten or more percents of delivered energy. Therefore, it is important to have right estimate of losses, as well as to find ways for their reduction. Basic items of mentioned problems are: dispense technical and non-technical losses, determine structure of losses (distribution of losses throughout the network elements), locate critical elements from aspect of losses, and select optimal methods for losses reduction. The importance of technical losses becomes even higher for distribution utilities in deregulated environment since the non-technical losses will become out of concern (retail companies will take care of them).

Energy losses determination is more complex problem than determination of power losses, for which only conditions of the system at the specific moment are necessary. Namely, for determining energy losses in some network element, within specified time interval, it is necessary to know the curent curve of the element. Since this is very detailed work even in the case of only a few elements, it is usually simplified so that the load curve is divided into segments during which the load can be considered as constant. Calculation of energy losses, in this case, is reduced to a certain number of power losses calculations. Of course, this approach is correct only in the case when the load curve is not much variable. In other way, the approximation of load curve with small number of segments leads to great errors and, of course, bed final results.

In this paper clustering technique is applied to select characteristic states, based on which we can determine distribution energy losses with the satisfying accuracy. Using this technique, selection of characteristic states is made quite objectively. Presented method does not require to much of knowledge about a distribution network that has being analyzed, which enables its application even in the cases of sudden changes in circumference and structure of consumption as well as in configuration of network.

[1]Dragan S. Tasić is with the Faculty of Electronic Engineering, University of Niš, Aleksandra Medvedeva 14, 18000 Niš, Yugoslavia, E-mail: dtasic@elfak.ni.ac.yu

[2]Miodrag S. Stojanović is with the Faculty of Electronic Engineering, University of Niš, Aleksandra Medvedeva 14, 18000 Niš, Yugoslavia, E-mail: miodrag@elfak.ni.ac.yu

II. SIMULATION OF LOAD CURVES

Knowledge of load curves for each particular element is needed for exact calculation of distribution energy losses. That is not possible, because of measurements are made only at some locations in the network. Therefore, it is imposed problem to estimate load curves of network elements based on the available data. This paper only discusses application of clustering technique to annual distribution losses calculation problem. Therefore, load curves of network elements are simulated without considering estimation aspects. Two simulation methods, with quite different load curves, are applied in order to point out general applicability of the clustering technique.

The first simulation method requires knowledge of the following data for each element:

- annual peak loading (winter maximum $S_{\max}^{W}$),
- annual minimal loading (summer minimum $S_{\min}^{S}$),
- minimal daily loading of the day when annual peak loading appears ($S_{\min}^{W}$),
- maximal daily loading of the day when annual minimal loading appears ($S_{\max}^{S}$),
- hour when annual peak loading appears ($T_{\max}^{W}$),
- hour when maximal daily loading appears on the day of annual minimal loading ($T_{\max}^{S}$).

The hours when daily peaks on the days of annual minimum and maximum appear are considered in order to comprehend different load types, i.e. non simultaneous of daily peak loadings for load nodes.

It is supposed maximal and minimal daily loadings are changed during the year following the cosine functions. Beside this, it is supposed that annual peak demand appear on the January 1. Maximal and minimal daily loadings of node *k* on the day *i* are:

$$S^{i}_{\max k}=S^{\mathrm{W}}_{\max k}-(S^{\mathrm{W}}_{\max k}-S^{\mathrm{S}}_{\max k})\cos(2\pi\frac{i}{n_d}) \ , \quad (1)$$

$$S^{i}_{\min k}=S^{\mathrm{W}}_{\min k}-(S^{\mathrm{W}}_{\min k}-S^{\mathrm{S}}_{\min k})\cos(2\pi\frac{i}{n_d}) \ . \quad (2)$$

where n_d is number of days (365 or 366 for a leap year).

The hour of the day *i* when daily peak loading appears is:

$$T^{i}_{\max k}=T^{\mathrm{W}}_{\max k}-(T^{\mathrm{W}}_{\max k}-T^{\mathrm{S}}_{\max k})\cos(2\pi\frac{i}{n_d}) \ . \quad (3)$$

When maximal and minimal powers as well as hour of daily peak are determined for day *i*, we can calculate power for each hour of day *i*. Power of load node *k* for hour *j* of day *i* is:

$$S^{i,j}_{k}=S^{i}_{\min k}+(S^{i}_{\max k}-S^{i}_{\min k})\cos(2\pi\frac{j-T^{i}_{\max k}}{24}) \ . \quad (4)$$

A form of supposed annual loading curve for the node *i* is shown on the Fig. 1.

The second simulation method starts from the assumption that each load node can put into one of load categories. Hourly load patterns for different load categories (Fig. 2) are known as well as annual peak loading of each load node. Beside that, it is known variation of maximal and minimal relative daily loading during the year (Fig. 3).

Maximal and minimal loading of load node *k* for day *i* are:

$$S^{i}_{\max k}=S^{\mathrm{W}}_{\max k}\cdot p_{\max}(i) \ , \quad (5)$$

$$S^{i}_{\min k}=S^{\mathrm{W}}_{\min k}\cdot p_{\min}(i) \ . \quad (6)$$

When powers $S^{i}_{\max k}$ and $S^{i}_{\min k}$ are determined, we can calculate power of load node *k* for *j*-th hour of *i*-th day considering curves on Fig 3:

$$S^{i,j}_{k}=S^{i}_{\min k}+(S^{i}_{\max k}-S^{i}_{\min k})\,p^{d}(j) \ . \quad (7)$$

III. CLUSTERING TECHNIQUE

Clustering is one of the methods for analyzing and processing large and not well-known amount of data. This is the method of classifying the data set into subsets, clusters, based on a defined similarity measure [1, 2]. On this way, a set of characteristic states that describe analyzed problem can be generated.

The main characteristic of the cluster is its center. The center of cluster or centroid is an average of all examples that belong to this cluster. In other words, it is representative of all examples that belong to the cluster.

In many cases, there is no clear criterion under which "real" number of clusters can be determined. That is the reason for experimenting with different number of clusters in order to determine what way of clustering is appropriate for specific application.

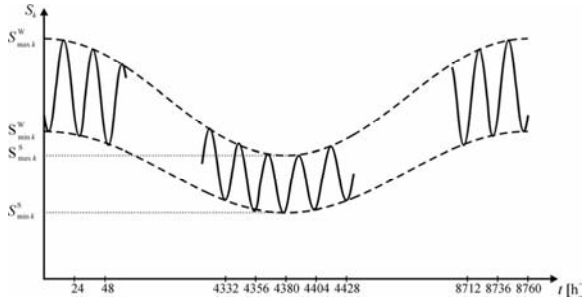

Fig.1. Cosine form of annual load curve

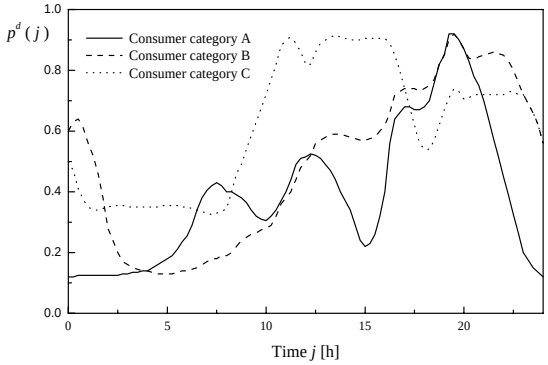

Fig.2. Hourly load patterns for different consumer categories

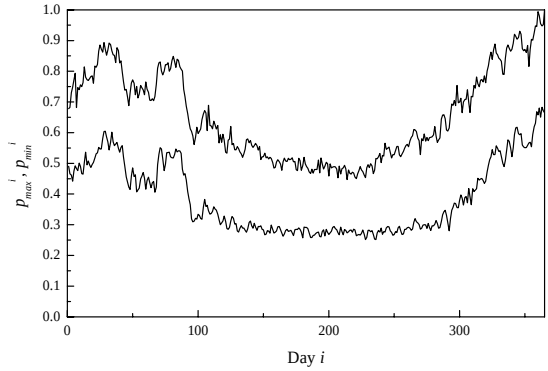

Fig.3. Variation of maximal and minimal daily loading during the year

In process of preparing data for clustering, there is a need for normalization of data. This is done because in many cases the task of classifying data which represent different kinds of variables is faced (for example powers, voltages, currents,..). Normalization enables computation of the classifying centers that are completely independent of the physical units of variables (V, A,…). With this procedure value range of every attribute is brought to the range 0÷1. Therefore, normalized maximal value of every attribute will be 1, and normalized minimal value 0. It should be noticed that normalization at the same time mean increasing the influence of variables witch change in a narrow range. Otherwise, it should be pointed out that the normalization is not necessary in cases where analyzed problem is one-dimensional.

There are a large number of algorithms for solving the clustering problem. Most of them are based on methods of "joining", "cutting" and "rearranging". These methods are used in popular algorithms: clustering through minimum graph tree, algorithm of maximum cross-section and reclassification based on the nearest average.

In this paper clustering is made on the complete state vector that includes active and reactive powers of all load nodes and root node voltage for every hour during the year. Therefore, dimension of the state vector is:

$$DVS = 2 \cdot N_{\ln} + 1 \ , \tag{8}$$

where $N_{\ln}$ is number of load nodes.

Firstly, the normalization of attributes using the general relations has been done:

$$x_{ji} = \frac{X_{ji} - X_{j\min}}{X_{j\max} - X_{j\min}} \ , \tag{9}$$

where $X_{j\max}$ is maximum and $X_{j\min}$ minimum of *j*-th attribute by all examples.

Then the clustering of data on subset of hours is done. As a similarity measure (degree of association) Euclidian distances has been utilized. In general case for two vectors *X* and *Y* of dimension *N* Euclidian distance is determined by the relations:

$$ED(XY) = \left[\frac{1}{N} \sum_{i=1}^{N} (X_i - Y_i)^2 \right]^{1/2} \ . \tag{10}$$

The clustering is done in the way that distance between the center of the each cluster and every example that belongs to that cluster, is smaller than a priory defined boundary Euclidian distance ε_k. The process of clustering begins with the first considered example that is set to be the center of first cluster. Then, by the determined order, the classifying of second example is done. If the Euclidian distance is smaller then the boundary one, it is put in the first cluster, otherwise it forms the second cluster. In the case when second example is put in the first cluster, a new center of that cluster should be recalculated. Then, the distance between the third example and the center of the first and second cluster, if it exists, is calculated. This example is put in the nearest cluster, i.e. in the cluster from which center has the smallest distance, under condition that the distance is smaller then specified boundary Euclidian distance. If that is not the case, it forms a new cluster. The procedure is carried out until all the examples are classified. According to this, it is clear that the number of cluster depends on the boundary value of Euclidian distance, and is not known at the beginning of clustering process.

Since complete state vector is considered, attributes of the example which represents the center of cluster are, of course, active and reactive powers of load nodes, as well as the voltage of root node. The center of cluster is determined by general equation:

$$b_{jk} = \frac{\sum_{i=1}^{r_k} x_{ji}}{r_k} \ , \tag{11}$$

where b_{jk} is *j*-th attribute of center of *k*-th cluster, and r_k number of examples that belong to *k*-th cluster.

After finished clustering process, a detailed calculation of characteristic states of network is made by procedure presented in [3]. As the result of calculations are obtained node voltages, power flows and power losses for each network element, as well as the total power losses. It is considered that loads are constant during the set of hours that belong to the cluster. Because of that, annual energy losses can be calculated as sum of power losses of cluster centers multiplied by the number of hours that belong to that cluster.

IV. TEST EXAMPLE

The presented procedure is used for determining annual energy losses of the test network shown in Fig. 4. The data about lines are given in [4], while data about maximal and minimal node powers as well as rated powers of distribution transformers are shown on Table I. This table also shows the time when appear winter and summer peak loading for each load node. Load nodes are classified into three consumer categories marked generally as A, B and C category (for example residence, commerce and industry).

TABLE I
MAXIMUM POWERS AND PARTICIPATION OF CUSTOMER CATEGORIES

	$P^W_{\max}$ [MW]	$P^W_{\min}$ [MW]	$P^S_{\max}$ [MW]	$P^S_{\min}$ [MW]	$Q^W_{\max}$ [MVAr]	$Q^W_{\min}$ [MVAr]	$Q^S_{\max}$ [MVAr]	$Q^S_{\min}$ [MVAr]	$t^W_{\max}$ [h]	$t^S_{\max}$ [h]	category	S_n [MVA]
1	0.30	0.24	0.18	0.06	0.18	0.10	0.096	0.0240	14	17	A	0.25
2	0.27	0.15	0.15	0.12	0.12	0.024	0.06	0.03	15	19	A	0.25
3	0.36	0.24	0.30	0.12	0.24	0.18	0.18	0.06	12	18	A	0.4
4	0.18	0.12	0.12	0.06	0.09	0.06	0.075	0.03	16	20	B	0.25
5	0.18	0.12	0.15	0.06	0.06	0.03	0.045	0.015	14	12	B	0.25
6	0.60	0.30	0.48	0.21	0.30	0.18	0.21	0.09	15	16	A	0.4
7	0.60	0.39	0.36	0.15	0.30	0.24	0.24	0.06	16	19	A	0.4
8	0.18	0.12	0.12	0.06	0.06	0.03	0.045	0.015	13	19	A	0.25
9	0.18	0.12	0.12	0.06	0.06	0.03	0.045	0.021	14	19	C	0.25
10	0.135	0.075	0.075	0.045	0.09	0.03	0.06	0.03	15	18	A	0.25
11	0.18	0.12	0.12	0.06	0.105	0.075	0.075	0.045	15	15	A	0.25
12	0.18	0.12	0.12	0.06	0.105	0.045	0.075	0.045	11	20	B	0.25
13	0.36	0.24	0.24	0.12	0.24	0.18	0.21	0.06	10	18	B	0.4
14	0.18	0.12	0.12	0.06	0.03	0.018	0.021	0.009	12	16	A	0.25
15	0.18	0.12	0.12	0.06	0.06	0.03	0.045	0.021	13	15	C	-
16	0.18	0.12	0.12	0.06	0.06	0.03	0.045	0.021	14	17	A	0.25
17	0.27	0.21	0.18	0.09	0.12	0.06	0.06	0.052	15	17	A	0.25
18	0.27	0.18	0.18	0.09	0.12	0.06	0.09	0.052	15	19	A	0.25
19	0.27	0.18	0.12	0.09	0.12	0.06	0.09	0.036	13	19	B	0.25
20	0.27	0.18	0.18	0.09	0.12	0.06	0.09	0.036	16	19	C	-
21	0.27	0.18	0.18	0.09	0.12	0.06	0.09	0.03	12	18	A	0.4
22	0.27	0.21	0.18	0.06	0.15	0.12	0.09	0.03	13	15	A	0.4
23	0.84	0.60	0.56	0.30	0.40	0.30	0.30	0.15	14	16	A	0.63
24	0.84	0.60	0.56	0.27	0.40	0.22	0.30	0.15	12	17	A	0.63
25	0.18	0.12	0.12	0.03	0.075	0.045	0.045	0.015	13	17	A	0.25
26	0.18	0.12	0.12	0.06	0.075	0.045	0.045	0.018	13	17	A	0.25
27	0.18	0.12	0.12	0.03	0.075	0.03	0.03	0.021	13	18	A	0.25
28	0.36	0.24	0.24	0.12	0.15	0.12	0.15	0.036	14	18	A	0.4
29	0.60	0.24	0.42	0.18	0.18	0.12	0.12	0.03	15	18	B	0.4
30	0.45	0.39	0.30	0.15	0.21	0.15	0.15	0.06	16	17	A	0.4
31	0.63	0.33	0.33	0.15	0.30	0.21	0.21	0.06	14	18	B	0.63
32	0.18	0.12	0.12	0.06	0.12	0.03	0.12	0.03	15	20	A	0.25

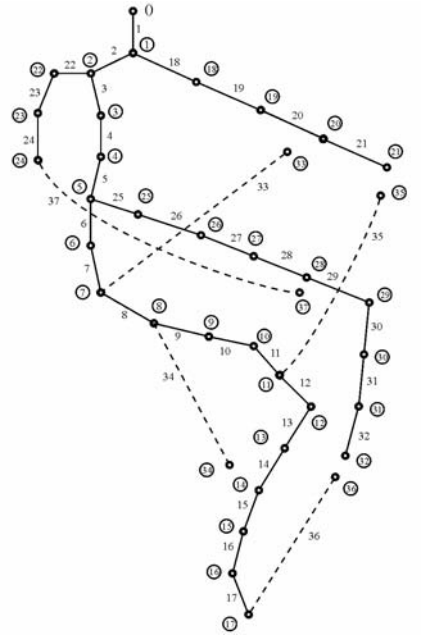

Fig.4. Test network with 32 nodes

TABLE II
RESULTS OF THE FIRST SIMULATION METHOD

number of clusters	ΔW_{a_p} [MWh]	Δ%	ΔW_{a_q} [MVArh]	$\Delta W_{a_p}^{L}$ [MWh]	$\Delta W_{a_q}^{L}$ [MVArh]	$\Delta W_{a_p}^{T_{Fe}}$ [MWh]	$\Delta W_{a_p}^{T_{Cu}}$ [MWh]	$\Delta W_{a_q}^{T_{Cu}}$ [MVArh]
1	4585.3	10.8	4716.4	3706.4	2465.2	195.64	683.27	2251.2
2	4896.7	3.49	5044.8	3972.3	2643.6	195.5	728.88	2401.2
3	4997.4	1.5	5151.5	4058	2701	195.45	743.91	2450.5
5	5037.5	0.71	5194.2	4092.2	2723.9	195.43	749.90	2470.2
10	5042.4	0.61	5205.1	4094.1	2725.2	195.43	752.88	2479.9
20	5057.6	0.32	5223.6	4106.1	2733.3	195.42	756.05	2490.2
25	5060.5	0.26	5227.4	4108.3	2734.8	195.42	756.79	2492.6
30	5064.7	0.175	5232.3	4111.8	2737.1	195.42	757.55	2495.2
50	5067.9	0.115	5236	4114.2	2738.8	195.42	758.18	2497.2
100	5070	0.07	5238.6	4116	2740	195.42	758.63	2498.7
8760	5073.6		5243	4118.9	2741.9	195.41	759.37	2501.1

TABLE III
RESULTS OF THE SECOND SIMULATION METHOD

number of clusters	ΔW_{a_p} [MWh]	Δ%	ΔW_{a_q} [MVArh]	$\Delta W_{a_p}^{L}$ [MWh]	$\Delta W_{a_q}^{L}$ [MVArh]	$\Delta W_{a_p}^{T_{Fe}}$ [MWh]	$\Delta W_{a_p}^{T_{Cu}}$ [MWh]	$\Delta W_{a_q}^{T_{Cu}}$ [MVArh]
1	2582.9	10.83	2546.9	2014.1	1341.7	202.57	366.21	1205.2
2	2800.5	3.32	2777.3	2199.4	1465.6	202.47	398.59	1311.7
3	2849.8	1.62	2832.5	2243.2	1494.3	202.45	406.93	1333.6
5	2864.6	1.11	2845	2254.2	1502.2	202.44	408.05	1342.8
10	2873.5	0.8	2854.5	2261.7	1507.3	202.44	409.39	1347.2
20	2886.3	0.36	2870.4	2271.7	1514.1	202.43	412.16	1356.3
25	2889.3	0.26	2874.3	2274	1515.6	202.43	412.87	1358.7
30	2890.1	0.23	2875.3	2274.7	1516.1	202.43	413.03	1359.2
50	2891.1	0.20	2876.2	2275.5	1516.7	202.43	413.25	1359.5
100	2894.5	0.08	2880.7	2278.1	1518.4	202.43	413.95	1362.2
8760	2896.8		2883.4	2279.9	1519.7	202.43	414.41	1363.7

Results of calculation are shown on Table II and Table III. The second and the fourth columns of tables show total active and reactive losses, the fifth and the sixth columns line losses, while columns 7, 8 and 9 show transformer losses. The third column of tables shows errors in percents for total active losses calculated using clustering technique. Exact values of loses are obtained summing power losses for each hour during the year. This corresponds to calculation with 8760 clusters. Differences between energy losses for the first and the second simulation method are obviously result of using the quite different load curves. In other hand, the errors made for same number of clusters is approximate for both simulation methods. This shows that presented method is very robust.

Results given in Table II and Table III also show rather decreasing of error with increasing number of clusters. For the case of three clusters error is less then 2%, and for five clusters error is less then 1%. This error is quite acceptable. Computing time increases with increasing the number of clusters. Therefore authors suggest 5-10 clusters for distribution losses calculation. The range is suggested because of increasing of computing time is not continual. Thus the problem maybe solved quicker with 6 than with 8 clusters. The reason for this lies in the methodology of boundary distance determination for chosen number of clusters.

V. CONCLUSION

The method for distribution losses calculation using clustering technique is presented in this paper. Presented method enables the total energy losses determination as well as determination energy losses for each network element (structural losses analysis). Simulations that have been made by the authors show that satisfying results can be obtained with a quite small number of clusters. Considering the fact that smaller number of clusters requires less of computing time, it is pointed out here that for the need of determining electrical energy losses in distribution network is enough to use up to 10 clusters.

REFERENCES

[1] N. Arsenijević, N. Rajaković, D. Muškatirović, "Proračun gubitaka energije na godišnjem vremenskom horizontu u prenosnoj mreži elektroenergetskog sistema EPS-a", JUKO-CIGRE, Herceg Novi, 16-20. septembar 2001., R 38-04 i R 38-05.

[2] ***, Analiza gubitaka električne energije u prenosnoj mreži EPS-a i iniciranje mera za njihovo sniženje, Studija urađena za EPS, Beograd, 2000.

[3] D. Shirmohammadi, H. W. Hong, A. Semlyen, G. X. Luo, "A Compensation-Based Power Flow Method for Weakly Meshed Distribution and Transmission Networks", IEEE Trans. on Power Systems, Vol. 3., No. 2, May 1988, pp. 753-762.

[4] S. K. Goswami, S. K. Basu, "A New Algorithm for the Reconfiguration of Distribution Feeders for Loss Minimization", IEEE Trans. on Power Delivery, Vol. 7., No. 3, July 1992, pp. 1484-1491.

[5] Hang-Ching Kuo, Yuan-Yih Hsu, "Distribution System Load Estimation and Service Restoration Using a Fuzzy Set Approach", IEEE Trans. on Power Delivery, Vol. 8, No. 4, October 1993.

Loss Factor in Distributive Area of Utility "Elektrodistribucija" Nis

Dobrivoje P. Stojanovic[1], Lidija M. Korunovic[2], Miroslav O. Veselinovic[3], Sladjan Lj. Jovanovic[4], Andrija Lj. Vukasinovic[5]

Abstract – **In this paper new coefficients in loss factor equations which are used for calculation of variable energy losses in distribution networks are proposed. These coefficients are found on the base of statistic elaboration of annual load diagram database in distributive area of utility "Elektrodistribucija" Nis. Coefficient values are established in the equations of polynomial and exponential form. The equations with proposed coefficients have been tested at many consumption diagrams, when average error is established less than one percentage and maximal error does not exceed 2,36%. At the same time, it is found that standard formulae from the literature make a mistake in the calculation of energy losses in the range from 5% to nearly 20%.**

Keywords – **Energy losses, Loss factor, Load factor, Distribution networks.**

I. INTRODUCTION

In a process of power transmission and distribution, power and energy losses appear unavoidably in all network elements from the sources to the consumers, in all voltage levels. They depend on many factors, mostly on network condition and on network operation mode. One part of energy losses is a consequence of constructive features of electrical devices and whole network and they can not be avoided by any measure, while the other part depends on operation mode of distribution network. Both parts can be considered as technical losses of electrical energy. According to the way of appearance, technical losses are divided on:

- dependable on voltage or constant losses and
- dependable on load or variable losses.

[1]Dobrivije P. Stojanovic is with the Faculty of Electronic Engineering, A. Medvedeva 14, 18000 Nis, Serbia and Montenegro, E-mail: dstojanovic@elfak.ni.ac.yu

[2]Lidija M. Korunovic is with the Faculty of Electronic Engineering, A. Medvedeva 14, 18000 Nis, Serbia and Montenegro, E-mail: lidijak@elfak.ni.ac.yu

[3]Miroslav O. Veselinovic is with the Faculty of Electronic Engineering, A. Medvedeva 14, 18000 Nis, Serbia and Montenegro, E-mail: miroslav@elfak.ni.ac.yu

[4]Sladjan Lj. Jovanovic is with Power Distribution Company "Elektrodistribucija" Nis, dr Z. Djindjica 46, 18000 Nis, Serbia and Montenegro,
E-mail: sladjan@edn.co.yu

[5]Andrija Lj. Vukasinovic is with Power Distribution Company "Elektrodistribucija" Nis, dr Z. Djindjica 46, 18000 Nis, Serbia and Montenegro, E-mail: andrija@elfak.ni.ac.yu

Constant energy losses are mostly consequence of voltage, and they exist in no-loaded network. They appear as iron losses of power and measuring transformers, as dielectric losses in cables and capacitors and the losses due to corona and leakage currents through shunt admittance of overhead lines. Beginning from the fact that network voltage is kept in relatively narrow limits, it can be considered that voltage dependable power losses are approximately constant. It enables simple determination of energy losses in any period of time.

Variable energy losses appear, duo to current flow, in all network element in a path of power transmission and distribution from the source to the consumption place. These losses are proportional to the second power of total current and they are the most expressed in lines and power transformers. A task of almost all methods for energy losses calculation is to find variable energy losses in the network as more realisic and complete as it possible, with the aim to discover the locations where the biggest unjustified losses appear and where are bottlenecks in transmission and distribution. After that, the measures for loss reduction are undertaken and to bring the network as closer as it possible to techno-economical state of optimality from the point of view of energy losses.

In utilities, energy losses are calculated as a difference between available and sold electrical energy and these are so called account losses. The losses obtained on that way are significantly bigger than aforementioned technical losses, because they include nontechnical, so called commercial, losses. Commercial losses appear due to unregistered consumption (thefts, unauthorised network connections, selfconsumption of utilities). The losses due to allowed tolerance in set up of measuring devices also belong to this group. Besides, commercial losses appear due to impossibility of simultaneous reading of all measuring devices.

Great number of papers, in the world [1,2] and in our country [3,4,5,6,7,8] are dedicated to the problem of energy losses calculation. They give empirical formulae for evaluation of losses or discussions about their accuracy and domain of application. All proposed formulae for calculation (evaluation) of losses became as result of statistic elaboration of available data about consumption diagrams for particular country or region. Existence of many formulae says that none of them is absolutely accurate, and can not be unreservedly applied to any network. Fundamental intention is to find connection between energy losses and maximum power losses in the same period of time. In that way, power losses calculation only for one, maximum, operation condition enables to find energy losses with sufficient accuracy.

Formulae give equivalent duration of maximum losses (τ) or of loss factor (ϑ) in analytical form. There is unique connection between these two quantities.

This paper only concerns to technical loss subgroup which is a function of loads (variable losses). Variable losses can be well evaluated in power system parts as distributive systems and radial transmission subsystems are, because of one direction of power flow and easy finding of load diagram characteristics. Formulae for energy loss calculation, used in our country, originate from the first half of twentieth century and in the middle of this century they are slightly modified. Taking into account specificity of our network, researches in [3]s proposed the methodology for calculation of losses in transmission networks and established formulae for loss calculation in some regions in former Yugoslavia. Some loss studies has been done, but they mostly relate to transmission lines.

Beginning from the fact that in the meantime it came to significant consumption overdistribution between voltage levels and to consumption structure change, authors of this paper consider that it is a deadline to research consumption diagrams and to propose new formulae for energy loss calculation. In this purpose, appropriate (ten years) database about consumption diagrams for distributive area of utility "Elektrodistribucija" Nis is used. Namely, from the year 1993., load data in the points of electrical energy purchasing, obtaining from ARES measuring device, are systematically recorded and processed. By elaboration of these data, load factors are identified and loss factors are found for all substations where utility "Elektrodistribucija" Nis is buying electrical energy for consumer supply at it's territory. Loss factor is expressed as second degree polynomial and in the shape of exponential function. Polynomial coefficients and the exponent are found for all months in the year, winter and summer season and for whole year. At the end, average values of coefficients are given for five years period. It is shown, consumption characteristics at complete distributive area of utility "Elektrodistribucija" Nis are almost the same, and there is small dispersion of calculation results. Based on found coefficient values in the formulae for loss factor, the accuracy of most frequently used formulae is tested.

Calculations show that existing formulae for loss energy evaluation, in some cases, give result with not tolerable error of 10%, and sometimes near to 20%. It leads to conclusion that it is indispensably to discover accurate coefficient values in formulae used for loss evaluation in the utilities of Elektoprivreda Srbije.

II. Loss Calculation Methodology

Active energy losses in a line of resistance R , at variable load $I(t)$, in a period of time T , can be calculated as:

$$\Delta W = 3R\int_0^T I^2(t)dt \,. \tag{1}$$

If a load was constant in whole interval T , i.e. if $I(t) = I_m = const$, corresponding energy losses would be:

$$\Delta W = 3RI_m^2 T \,. \tag{2}$$

The ratio between real losses which arise from time variable current $I(t)$ and the losses which originate from constant maximum current I_m is called *loss factor*.

$$\vartheta = \frac{\Delta W}{\Delta W_m} = \frac{3R\int_0^T I^2(t)dt}{3RI_m^2 T} \,. \tag{3}$$

If it was assumed that voltage and power factor stood constant, then loss factor could be expressed by means of active power as a parameter:

$$\vartheta = \frac{\Delta W}{\Delta W_m} = \frac{\int_0^T P^2(t)dt}{P_m^2 T} \,. \tag{4}$$

Beginning from the fact that in most cases maximum (peak) power data are available, energy losses in a period of T hours, in accordance with Eqs. (1) and (2), will be:

$$\Delta W = 3RI_m^2 T\vartheta \,, \tag{5}$$

or

$$\Delta W = R\frac{P_m^2}{U_n^2 \cos^2\varphi} T\vartheta \,. \tag{6}$$

Important characteristic of load diagram is load factor defined as the ratio between total transmitted (taken over) energy and energy which could be transmitted at maximum load during the same observed time:

$$m = \frac{W}{P_m T} = \frac{\int_0^T P(t)dt}{P_m T} = \frac{P_{av}}{P_m} \,, \tag{7}$$

where P_{av} is average load power in a period T **.**

Load factor value can be easy found from available data about transmitted energy W and maximum power P_m, for example from Eq. (7), because at energy purchasing locations the measuring devices for energy and peak power registration are regularly installed. Therefore, many researchers searched the connection between loss factor and load factor. There are many analytical expressions in literature which give connection between them. These expressions are derived so that load duration curve is firstly normalised and then appropriate symbolic curve is found by fitting. It is shown [6] that loss factor has values in the range from m^2 to m.

In authors opnion, most simple and for practice most acceptable function of loss factor is this one proposed by Buller and C.A. Woodrow in [1]:

$$\vartheta = mx + (1-x)m^2 \,. \tag{8}$$

Problem of energy loss evaluation is to find a coefficient x for typical load diagrams at examined territory or in the whole utility. Based on available database on load diagram it is easy

to calculate load factor and loss factor and then coefficient x from Eq. (8), as:

$$x = \frac{\vartheta - m^2}{m - m^2}. \quad (9)$$

Using normalised values of load diagrams in one year period, load factor is calculated according to Eq. (10) and loss factor according to Eq. (11):

$$m = \frac{1}{8760}\sum_{i=1}^{8760} P_i\ , \quad (10)$$

$$\vartheta = \frac{1}{8760}\sum_{i=1}^{8760} P_i^2\ . \quad (11)$$

If load diagram was expressed through appropriate fitted curve, *f(P)*, load factor could be calculated using Eq. (12)

$$m = \frac{1}{8760}\int_0^{8760} f(P)dt\ . \quad (12)$$

In similar way, loss factor is calculated

$$\vartheta = \frac{1}{8760}\int_0^{8760} f(P_i^2)dt\ . \quad (13)$$

Sometimes loss factor is given in dependence on load factor as an exponential function (14)

$$\vartheta = m^k\ . \quad (14)$$

Exponent k would be simply calculated, if the values for θ and m were previously found, as

$$k = \frac{\ln \vartheta}{\ln m}\ . \quad (15)$$

III. Calculation Results and Its Analysis

Since June 1993., thanking to the installation of registration device ARES, the power in nine points, where utility "Elektrodistribucija" Nis is buying electrical energy, has been attended continuously. Appropriate database has been created so it enables elaboration of load diagrams on this territory. Data elaboration results about consumption in period from the year 2001. to 2004. are shown in this paper for following three transformer substations called:

- NIS 1 110/35 kV,
- NIS 2 400/220/110 kV,
- NIS 3 110/35 kV.

In substations NIS1 and NIS 3 power and energy measuring is performed at 35kV level and in substation NIS 2 at level 110kV. These substations supply biggest part of the area of utility "Elektrodistribucija" Nis, which encircles Nis town and its wider surroundings, except the area of town Aleksinac.

The data from ARES are recorded every 15 minutes, so total data number per measuring location is 4x24x365=35040 for ordinary and 4x24x366=35136 for leap-year. These data are elaborated per years, per seasons (summer and winter) and monthly.

Load factor and loss factor are calculated in concordance with Eqs. (10) and (11), real number of points are taken into account (N=35040 for ordinary and N=35136 for leap-year):

$$m = \frac{1}{N}\sum_{i=1}^{N} P_i\ , \quad (16)$$

and

$$\vartheta = \frac{1}{N}\sum_{i=1}^{N} P_i^2\ . \quad (17)$$

Inside this investigation, 70 sets of annual data, for nine measuring locations, are elaborated for five to ten years in dependence of available data. There were mostly nine annual data which represented consumers supplied from Nis 2 substation. The oldest data were from the year 1993. and the newest ones from 2004.

Calculation results for 12 data sets are shown in Table I. Annual load factor is changing in narrow limits from the least value 0.367634 to 0.54892, and average value is 0.490312. Annual loss factor of considered load diagrams varies from the minimum value of 0.16762 to the maximum of 0.33629, and its average value is 0.278565.

Constant coefficient x in Eq. (8), for load factor, is obtained from Eq. (9) as the result of putting average values of loss factor and load factor. Thus, it is obtained $x = 0.1533585$, and loss factor from Eq. (8) becomes

$$\vartheta_1 = 0{,}1533585m + 0{,}846641m^2\ . \quad (18)$$

Equation (17) can be written in exponential form with exponent $k = 1.792457$,

$$\vartheta_2 = m^{1{,}792457}\ . \quad (19)$$

Exponent k is calculated from Eq. (14).

Proposed formulae for loss factor calculation, Eqs. (18) and (19), are tested for all considered cases. At the same time, two following empirical formulae, which are most frequently used for annual loss calculation, are checked:

$$\vartheta_3 = 0{,}17m + 0{,}83m^2 \quad (20)$$

and

$$\vartheta_4 = (0{,}124 + 0{,}876m)^2\ . \quad (21)$$

Original form of Eq. (21) shows equivalent time of annual losses

$$\tau = \left(0{,}124 + \frac{T_m}{10000}\right)^2 8760\ , \quad (22)$$

where T_m denotes duration of maximum load.

Percentage errors of proposed Eqs. (18) and (19) and of Eqs. (20) and (21) from literature are cited in Table I. Proposed Eqs. (18) and (19) for loss factor calculation give the least errors; middle errors are 0.89% for polynomial Eq. (18) and 0.84% for exponential Eq. (19). Maximum errors are 1.9% and 1.924% , respectively. Equation (20) gives the result

with average error of 2,21% and maximum error of 4.426%, while Eq. (21) makes average error of 10.987% and maximum of 18.69%. It is interesting to mention that Eq. (18) and (19) have positive and negative errors in the range from the least to the biggest load factor. On the other side, the errors of Eqs. (20) and (21) are always positive and they are greater at lower load factors. Equation (21) errors are the biggest and almost three times bigger than the errors obtained by application of Eq. (20). It is reasonable, because Eq. (21) is proposed on the base of experimental measurements which were performed in the middle of the last century in Russia.

TABLE I
CHARACTERISTIC VALUES OF CONSUMPTION DIAGRAMS AND PERCENTAGE ERRORS OF PARTICULAR EQUATIONS

No. of discrete loads	Peak load	Load factor	Loss factor	Constant coefficient	Percent error using			
N	P_m [kW]	m	ϑ	x	Eq. 18	Eq. 19	Eq. 20	Eq. 21
35040	63252	0.520681	0.310252	0.15684151	-0.280180	0.058158	2.208326	8.471571
35040	127260	0.443068	0.232846	0.14806668	0.560802	-0.173770	4.173554	12.63867
35040	126192	0.367634	0.167621	0.13965222	1.900971	-0.757440	6.656013	18.69531
35040	64260	0.532025	0.316568	0.13462187	1.473599	1.924369	5.945658	9.980669
35040	117740	0.473874	0.258564	0.13640214	1.634998	1.407878	6.157528	12.40679
35040	103224	0.455617	0.242965	0.14263649	1.094554	0.579951	5.131308	12.63147
35040	65688	0.540334	0.326927	0.14078078	0.955556	1.474740	4.829255	9.139415
35040	115080	0.508480	0.295632	0.14836303	0.422318	0.636887	3.721507	9.679870
35040	103048	0.484358	0.271983	0.14966779	0.338909	0.261172	3.620840	10.53274
35136	65604	0.548920	0.336290	0.14125523	0.891151	1.477254	4.691965	8.789828
35136	113680	0.504228	0.291163	0.14767906	0.487617	0.655036	3.865479	9.911186
35136	96712	0.504528	0.293966	0.15768292	-0.367730	-0.198380	2.113956	8.964340
Maximum	127260	0.548920	0.336290	0.15768292	1.900971	1.924369	2.113.956	18.69531
Minimum	63252	0.367634	0.167621	0.13462187	0.277667	0.003372	4.426282	8.471571
Average	96811.67	0.490312	0.2787314	0.14530414	0.867366	0.800419	2.208326	10.986820

IV. CONCLUSION

This paper shows results of load diagram researches during the last ten years in the area of utility "Elektrodistribucija" Nis, which supplies near 150.000 consumers. Based on statistic data elaboration, new coefficient values in equations for loss factor calculation are proposed. Equations with new coefficients give significantly better results in wide range of loss factors then equations from literature. These equations can be used in the networks where current is proportional to the power, that is a case in distribution systems and radial transmission networks.

Although these coefficients are found for consumption area of utility "Elektrodistribucija" Nis, they are recommended for the other areas, because load characteristics in almost all utilities of "Elektroprivreda Srbije" are the same.

Present computer abilities and available database enable that exposed methodology for loss factor calculation can be used for finding equations corresponding to load characteristics on particular territory.

Further researches should be oriented to load diagrams classification according to the type of settlements and consumer structure.

REFERENCES

[1] F. H. Buller and C. A. Woodrow, "Load Factor-Equivalent Hour Values Compared", *Electrical World*, July 14, 1928.

[2] M. W. Gustafson and I. S. Baylor, "The Equivalent Hours Loss Factor Revisited", *IEEE 88 WM* 166-1.

[3] J. Topic at all., *Methodology for Electrical Energy Loss Determination in Transmission Networks*, Institute for Electrical Power Industry Zagreb, Zagreb, 1982. (in Serbian)

[4] D. Stojanovic, *Problems of Electrical Power and Energy Losses in Middle and Low-voltage Distribution Network in Urosevac*, Faculty of Electrical Engineering Pristina, Pristina, 1989. (in Serbian)

[5] D. Stojanovic, P. Grkovic, D. Savovic, "PDM – Software Package for Middle-voltage Distribution Networks Calculation", *Elektroprivreda*, no. 3, pp. 65-72, 1997. (in Serbian)

[6] T. Gonen, *Electric Power Distribution System Engineering*, McGraw-Hill Book Company, New York, 1986.

[7] M. Kostic, "Accuracy and Selection of Formula for Calculation of Losses in Power Networks", *Elektroprivreda*, no. 1, pp 65 – 75, 2000. (in Serbian)

[8] D. Tasic, M. Stojanovic, "Analysis of Equations Application on Electrical Energy Losses Assessment", *Elektroprivreda*, no. 2, pp. 27 – 38, 2002. (in Serbian)

Asymmetrical Load-Flow Solution by Fast Decoupled Method in Sequence Domain

Ljupco D. Trpezanovski[1], Vladimir C. Strezoski[2] and Metodija B. Atanasovski[3]

Abstract – **In this paper a very fast method for asymmetrical load-flow solution in sequence domain is presented. The proposed method is based on the standard Fast Decoupled method for symmetrical load-flow solution applied on the positive- sequence circuit, enhanced with two systems of linear equations which represent negative- and zero-sequence circuits. Few recently published procedures are used to establish this method in sequence domain. The real power system is analyzed by proposed method and the results are compared with results obtained by standard Fast decoupled method in phase domain.**

Keywords – **Asymmetrical load-flow, sequence domain, Fast Decoupled method.**

I. INTRODUCTION

Two very important studies for the power systems are load-flow and faulted states analysis. The steady state symmetrical load-flow studies (SLF) are performed in the more efficient and comfortable sequence domain instead of in the phase domain. Symmetrical states are good approximations of usual states of three-phase power systems. But actually, because of the presence of long unbalanced (untransposed) lines, asymmetrical or single-phase loads (as induction furnaces and traction motors etc.), asymmetrical states in power systems are occurred. These states cause: negative-sequence currents at generator terminals rise heating in their rotors; malfunctions of protective relays; zero-sequence currents increase greatly the effect of inductive coupling between parallel transmission lines; higher power system loss, etc.

For more precise analysis of three-phase power system asymmetrical states, the asymmetrical load-flow (ALF) analysis is required. ALF calculations are also required to study the effects of various phase arrangements of transmission lines, single pole switchings, etc.

The solution of ALF problem was successfully performed using methods in phase domain (Newton-Raphson and Fast decoupled procedures) [1-3]. But unfortunately, there are mutual couplings between phases and 6x6 node-admittance matrices which describe the generators, transformers and lines are not sparse. This fact implies increasing of both: memory for problem storage and CPU time for problem solution in the phase domain. Therefore, there was a question: are the methods in sequence domain more efficient against the methods in phase domain?
Long time the sequence domain was avoided in the ALF methods because of: presence of phase shifts of the three-phase transformers (ideal transformers with complex turns ratios in their sequence circuits); mutually couplings among sequence circuits for unbalanced lines and asymmetrical phase loads which cannot be specified in the sequence domain. Recently published procedures as: new scaling concept [4], unbalanced line decoupled model in sequence domain [5], [6], enhanced bus classification and synthesizing procedure [7], [11] and asymmetrical phase loads model specified in the sequence domain [6], [10] enabled to establish a few new methods for ALF calculations in sequence domain. The Reduced admittance matrix method [8] and fast method [9] in sequence domain are more efficient than any method in phase domain.

[1]Ljupco D. Trpezanovski and [3]Metodija B. Atanasovski are with the Faculty of Technical Sciences, University St. Kliment Ohridski, I. L. Ribar bb, 7000 Bitola, Macedonia, E-mail: ljupco.trpezanovski@uklo.edu.mk

[2]Vladimir C. Strezoski is with the Faculty of Engineering, University of Novi Sad, Fruskogorska 11, 21000 Novi Sad, Serbia and Montenegro, E-mail: vstr@uns.ns.ac.yu

II. NEW APPROACH FOR POWER SYSTEM ELEMENTS MODELING

The most important step of the ALF methods establishing in sequence domain is power system elements modeling. These models should have such properties that the entire power system can be modeled with three decoupled positive-, negative- and zero-sequence circuits.

The synchronous generator is balanced element of the power system. In the sequence domain it can be presented with three decoupled sequence circuits. Each sequence circuit is represented with corresponding impedance ($\underline{z}_G^d$ for positive-, $\underline{z}_G^i$ for negative- and $\underline{z}_G^o$ for zero-sequence). If the generator is grounded the $\underline{z}_{nG}$ represents the generator grounding impedance. With the sequence admittances obtained from the sequence impedances, the 6x6 node-admittance matrix representing the synchronous generator in the sequence domain is formed [10].

Balanced transmission overhead lines can be presented with three lumped-π decoupled sequence circuits. Each circuit consists series admittance between line ends and two equal shunt admittances at the line ends. Consequently, 6x6 node-admittance matrix for the line model will be sparse. If the unbalanced lines are considered in sequence domain there are inductive and capacitive couplings among positive-, negative- and zero-sequence circuits. These couplings are expressed by mutually non-zero admittances in the 6x6 node-admittance matrix for the line model which is not sparse. In this case the line model cannot be presented with lumped-π decoupled sequence circuits. But decoupling procedure explained in [5], enables to express the couplings by compensation current sources instead of mutually admittances. The current controlled sources in series and shunt branches of each sequence lumped-π circuit include the coupling influences from the other sequences. Now, the unbalanced line model can be presented with three decoupled sequence lumped-π circuits, with sparse 6x6 node-admittance matrix.

Another problem to establish new methods for ALF calculation in sequence domain was transformer model. The three-phase transformer with complex turn ratio can be treated as a balanced element and its model can be presented with the three decoupled sequence circuits. But the problem of complex turn ratio still exists because ideal transformers with complex turns ratios disturb the symmetry and the simplicity of deriving power system node-admittance matrices in the sequence domain. Transferring the values from the absolute to the relative value domain by the standard PU system doesn't solve the problem of phase shifting. Application of the "New scaling concept" definitely eliminates these problems. The result of scaling the absolute in relative values with this concept is transformer model represented with three decoupled sequence circuits in which only the transformer (and grounding) impedances exist. The phase shifts are eliminated from the sequence circuits and transformer 6x6 node-admittance matrix is simple and sparse [10], [11].

The load model in phase domain is given by specified load active and reactive powers for each phase. If the complex voltages from the load buses *k* are on disposal, the injected complex currents for each phase can be calculated. With known complex currents in phase domain and inverse transformation matrix [11], injected complex currents in node *k* in any sequence circuit can be obtained very easy. From the sequence complex voltages and currents, the sequence complex powers can be calculated. Thus, the load model in sequence domain can be presented through injected complex currents or injected complex powers in node *k* of any sequence circuit. The widely explanation of power system elements modeling in sequence domain can be find in [10].

Consequently, all necessary conditions for all (balanced and unbalanced) power system elements representation with decoupled sequence circuits are achieved. Thus, the entire power system can be modeled with three decoupled positive-, negative- and zero-sequence circuits.

III. NEW BUS CLASSIFICATION AND SYNTHESIZING PROCEDURE

The classifications of buses applied in all ALF methods in phase or sequence domain for example as proposed in [1-3], [5], [6] were taken directly from classical SLF problem statements. They consist of three types of buses: "load busbars", "generator busbars" and a "slack (or swing) busbar; or: "PQ bus", "PV bus" and "θV (slack) bus". Their definitions were generalized for the purpose of the ALF problem statement. But these definitions are not performed in a full accordance with the nature of the ALF problem, because they do not enable a correct treatment of Q limits enforcement at PV buses.

In the new classification there are $P_\Sigma V$ type buses in which the value of three-phase injected active power (P_Σ) and the control law of the automatic voltage regulator (AVR) are specified. The θV bus (slack bus) is a bus in which the angle of a voltage and the control law of the generator AVR are specified. To provide a correct treatment of reactive power limits enforcement at the generators (at $P_\Sigma V$ buses), a new type of buses called $P_\Sigma Q_\Sigma$ are introduced. In this type of buses values of the three-phase injected active and reactive powers (sums of phase powers P_Σ and Q_Σ) are specified. All three types of buses mentioned above are suppressed in the high voltage buses of their corresponding step-up transformers. The last PQ type of buses is a standard type of buses in which values of three pairs of phase injected active and reactive powers are specified. More detailed explanation for the different types of buses is given in [7], [9].

The general representation of the sequence circuits for a generator and its step-up transformer are shown on Fig. 1. The bus presented in this figure denoted as *g*, can be of θV, $P_\Sigma V$ or $P_\Sigma Q_\Sigma$ type.

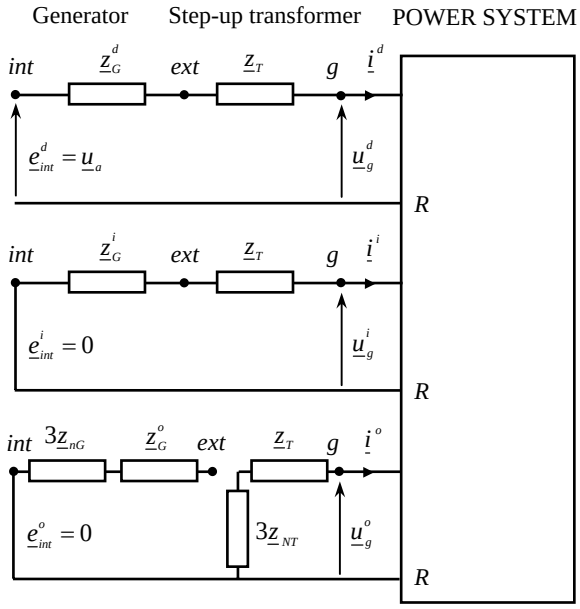

Fig. 1. Scaled sequence circuits of synchronous generator and step-up transformer.

Usually, in practice the voltage control and the active power control are associated with the high voltage transformer bus *g*. The generator internal bus voltage, as well as the voltage drops on the generator and transformer impedances are not of interest simultaneously with values of other power system quantities. Thus, the equivalent impedance in the positive- sequence circuit can be omitted and equivalent impedances in the negative- and zero-sequence circuits can be suppressed in the transmission network as it is shown on the Fig. 2. The procedure which enable to exclude the external and internal generator buses and associate the bus properties to the high voltage buses in their corresponding step-up transformers is called synthesizing procedure. Also suppression of the negative- and zero-sequence impedances in the power system is part of this procedure. This suppression enables zero-valued injected currents and powers in the corresponding negative and zero-sequence nodes *g*. Therefore, the injected currents and powers are different from zero only at the positive-sequence node.

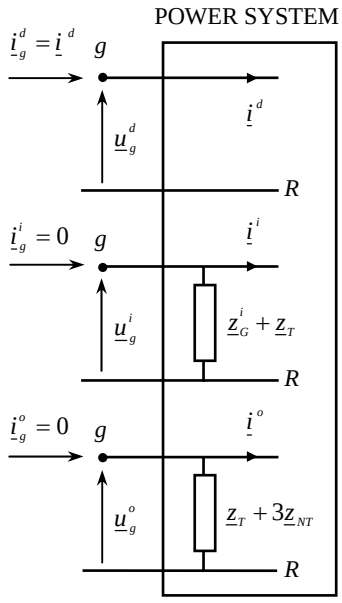

Fig. 2. Sequence circuits of a generator and its step-up transformer represented after synthesizing procedure.

Now, the issue of shortage of four equations corresponding to each $P_{\Sigma}V$, θV and $P_{\Sigma}Q_{\Sigma}$ bus in the sequence domain can be solved [7]. One more benefit of the synthesizing procedure is power system buses reduction. Thus, the power system with N_G generators and total number of buses n can be treated as a system with $r = n - 2N_G$ buses or $3r$ nodes.

IV. Fast Decoupled Method Definition

Taking into account all above mentioned procedures, entire power system can be presented with positive-, negative- and zero-sequence scaled, decoupled and node-reduced circuits. In accordance with these facts, the system of three linear nodal-voltage equations represents the base ALF model in sequence domain:

$$\mathbf{Y}^{d}_{r\times r}\mathbf{U}^{d}_{r} = \mathbf{I}^{d}_{rc}, \tag{1}$$

$$\mathbf{Y}^{i}_{r\times r}\mathbf{U}^{i}_{r} = \mathbf{I}^{i}_{rc}, \tag{2}$$

$$\mathbf{Y}^{o}_{r\times r}\mathbf{U}^{o}_{r} = \mathbf{I}^{o}_{rc}, \tag{3}$$

where $\mathbf{Y}^{d}_{r\times r}$, $\mathbf{Y}^{i}_{r\times r}$, $\mathbf{Y}^{o}_{r\times r}$ are node-admittance; $\mathbf{U}^{d}_{r}$, $\mathbf{U}^{i}_{r}$ and $\mathbf{U}^{o}_{r}$ are node-voltage matrices for positive-, negative- and zero-sequence decoupled circuits respectively. The matrices of node injected complex currents, corrected by compensation currents (as result of circuits decoupling) are denoted as $\mathbf{I}^{d}_{rc}$, $\mathbf{I}^{i}_{rc}$ and $\mathbf{I}^{o}_{rc}$. At first Eq. (1) can be conjugate and than multiply from the left by a diagonal matrix containing the complex positive-sequence voltages. As the result of this procedure, a new nonlinear system of equations representing the power system positive-sequence is obtained:

$$\mathbf{U}^{d}_{r,dij}\left(\mathbf{Y}^{d}_{r\times r}\right)^{*}\left(\mathbf{U}^{d}_{r}\right)^{*} = \mathbf{S}^{d}_{rc}. \tag{4}$$

In Eq. (4), matrix $\mathbf{S}^{d}_{rc}$ represents complex, compensated injected powers in the positive sequence circuit nodes [11].

Applying the Taylor's procedure, the nonlinear system of equations given by matrix Eq. (4), can be transformed in the new linear system of equations. This new system is consisted of equations for differences between the injected specified and calculated powers $-\Delta\mathbf{S}^{d}_{kor}$ in the power system positive-sequence circuit nodes, represented by the Jacobian $\mathbf{J}^{d}$ (for this sequence circuit) and unknown differences of voltage magnitudes and angles given by the matrix $\Delta\mathbf{X}^{d}$:

$$\mathbf{J}^{d}\Delta\mathbf{X}^{d} = \Delta\mathbf{S}^{d}_{kor}. \tag{5}$$

or in the well known form with sub-matrices:

$$\begin{bmatrix}\mathbf{H}^{d} & \mathbf{N}^{d}\\ \mathbf{M}^{d} & \mathbf{L}^{d}\end{bmatrix}\begin{bmatrix}\Delta\theta^{d}\\ \Delta\mathbf{U}^{d}/\mathbf{U}^{d}\end{bmatrix} = \begin{bmatrix}\Delta\mathbf{P}^{d}_{kor}\\ \Delta\mathbf{Q}^{d}_{kor}\end{bmatrix}. \tag{6}$$

Actually, the matrix Eq. (6) has the same form as the equations which represents the symmetrical Newton-Raphson load-flow model [12]. The elements of the sub-matrices $\mathbf{H}^{d}$, $\mathbf{N}^{d}$, $\mathbf{M}^{d}$ and $\mathbf{L}^{d}$ in iteration h, can be calculated as:

$$H^{d(h)}_{ki} = \left.\frac{\partial P_k}{\partial\theta_i}\right|^{d(h)} = U^{d(h)}_{k}U^{d(h)}_{i}\left(G^{d}_{ki}\sin\theta^{d(h)}_{ki} - B^{d}_{ki}\cos\theta^{d(h)}_{ki}\right), \tag{7}$$

$$N^{d(h)}_{ki} = U^{d(h)}_{i}\left.\frac{\partial P_k}{\partial U_i}\right|^{d(h)} = U^{d(h)}_{k}U^{d(h)}_{i}\left(G^{d}_{ki}\cos\theta^{d(h)}_{ki} + B^{d}_{ki}\sin\theta^{d(h)}_{ki}\right), \tag{8}$$

$$M^{d(h)}_{ki} = \left.\frac{\partial Q_k}{\partial\theta_i}\right|^{d(h)} = -U^{d(h)}_{k}U^{d(h)}_{i}\left(G^{d}_{ki}\cos\theta^{d(h)}_{ki} + B^{d}_{ki}\sin\theta^{d(h)}_{ki}\right), \tag{9}$$

$$L^{d(h)}_{ki} = U^{d(h)}_{i}\left.\frac{\partial Q_k}{\partial U_i}\right|^{d(h)} = U^{d(h)}_{k}U^{d(h)}_{i}\left(G^{d}_{ki}\sin\theta^{d(h)}_{ki} - B^{d}_{ki}\cos\theta^{d(h)}_{ki}\right), \tag{10}$$

$$H^{d(h)}_{kk} = \left.\frac{\partial P_k}{\partial\theta_k}\right|^{d(h)} = -Q^{d(h)}_{k} - B^{d}_{kk}\left(U^{d(h)}_{k}\right)^{2}, \tag{11}$$

$$N^{d(h)}_{kk} = U^{d(h)}_{k}\left.\frac{\partial P_k}{\partial U_k}\right|^{d(h)} = P^{d(h)}_{k} + G^{d}_{kk}\left(U^{d(h)}_{k}\right)^{2}, \tag{12}$$

$$M^{d(h)}_{kk} = \left.\frac{\partial Q_k}{\partial\theta_k}\right|^{d(h)} = P^{d(h)}_{k} - G^{d}_{kk}\left(U^{d(h)}_{k}\right)^{2}, \tag{13}$$

$$L^{d(h)}_{kk} = U^{d(h)}_{k}\left.\frac{\partial Q_k}{\partial U_k}\right|^{d(h)} = Q^{d(h)}_{k} - B^{d}_{kk}\left(U^{d(h)}_{k}\right)^{2}. \tag{15}$$

Because in the power systems X/R>>1 and differences between angles $\theta^{d(h)}_{ki} = \theta^{d(h)}_{k} - \theta^{d(h)}_{i}$ are very rare greater than 10^0, the next approximations can be taken into account:

$$G^{d}_{ki} << B^{d}_{ki};\ \cos(\theta^{d(h)}_{k} - \theta^{d(h)}_{i}) \approx 1;\ \sin(\theta^{d(h)}_{k} - \theta^{d(h)}_{i}) << 1. \tag{16}$$

These approximations applied in Eqs. (7) to (15), give zero-valued sub-matrices:

$$\mathbf{N}^{d} \approx \mathbf{0} \text{ and } \mathbf{M}^{d} \approx \mathbf{0}. \tag{17}$$

Taking into account the above explanations, and Eqs. (2), (3), (6) and (17) the new developed Fast Decoupled method for ALF solution in sequence domain is defined as:

$$\mathbf{H}^{d} \cdot \mathbf{\Delta\theta}^{d} = \Delta\mathbf{P}^{d}_{kor}, \tag{18}$$

$$\mathbf{L}^{d} \cdot \mathbf{\Delta U}^{d} / \mathbf{U}^{d} = \Delta\mathbf{Q}^{d}_{kor}, \tag{19}$$

$$\mathbf{Y}^{i}_{r\times r}\mathbf{U}^{i}_{r} = \mathbf{I}^{i}_{rc}, \tag{20}$$

$$\mathbf{Y}^{o}_{r\times r}\mathbf{U}^{o}_{r} = \mathbf{I}^{o}_{rc}. \tag{21}$$

With the proposed method, the problem of ALF solution is considered as solution of SLF problem with standard Fast decoupled procedure (Eqs. (18) and (19)) [13] and solution of two supplementary systems of linear equations representatives of negative- and zero-sequence power system circuits Eqs. (20) and (21) respectively.

V. METHOD VERIFICATION

The Fast decoupled method is tested on the entire power system of the Republic of Macedonia consisting of 63 buses of 400, 220 and 110 kV voltage level, 53 lines, 5 interconecting transformers and 9 equivalent generators with step-up transformers. Eight states (variants) are considered. Each of the variants is solved with Fast decoupled three-phase load-flow method in phase domain (FD ALF-abc) [2] and proposed method in sequence domain (FD ALF-dio). The first state V1 is symmetrical. All other seven states are more or less asymmetrical. For the purpose to eliminate the influence of the computer type, the results are given in relative units. The base case is V1 solved with proposed Fast decoupled method in sequence domain. The results of total number of iterations and relative CPU time for each variant solution are given in Table I.

TABLE I.

RESULTS OF THE CALCULATIONS.

Number of iterations/CPU relative time								
M \ V	**V1**	**V2**	**V3**	**V4**	**V5**	**V6**	**V7**	**V8**
FD ALF-abc	7/ 8,2	7/ 8,2	57/ 11,54	9/ 8,34	8/ 8,24	10/ 8,36	7/ 8,16	7/ 8,25
FD ALF-dio	9/ 1,0	9/ 1,0	19/ 1,39	8/ 1,05	8/ 1,03	8/ 1,09	9/ 1,04	8/ 1,01
abc-r.time / dio-r.time	8,2	8,2	8,3	7,9	8,0	7,7	7,8	8,2

* **M**- method; **V**- variant.

From the results of the Table I it is obvious that proposed Fast decoupled method for ALF in sequence domain is very efficient, robust and much more faster than standard method for ALF in phase domain. Because the power system node-admittance matrix in sequence domain is sparse, the memory storage required for the proposed method is significantly smaller then the Fast decoupled method for ALF in phase domain.

VI. CONCLUSION

Recently published procedures as: enhanced bus classification, sequence circuits decoupling, new scaling concept, synthesizing procedure and approximations which are justified for the power systems enable new approach for ALF problem solution. In this paper the efficient very fast method based on the standard Fast decoupled method is established. The efficiency is achieved in memory requirements and CPU time for calculations. The form of the decoupled positive-sequence part of the presented ALF model is reduced to the form of the classical SLF problem. Thus, the standard SLF Fast decoupled procedure [13] is applied inside the ALF solution procedure. The negative- and zero-sequence parts of the presented ALF model are represented by two systems of linear equations and solved by Gauss's method.

REFERENCES

[1] R.G.Wasley, M.A.Shlash, "Newton-Raphson algorithm for 3-phase load flow", PROC. IEE, Vol. 121, No. 7, pp. 630-638, July 1974.

[2] J.Arrillaga, B.J.Harker, "Fast-decoupled three-phase load flow", PROC. IEE, Vol. 125, No. 8, pp. 734-740, August 1978.

[3] J.Arrillaga, C.P.Arnold, B.J.Harker, *Computer Modelling of Electrical Power Systems*, John Wiley & Sons Ltd, 1983.

[4] V.C.Strezoski, "New scaling concept in power system analysis", IEE Proc.-Gener. Transm. Distrib., Vol. 143, No. 5, pp. 399-406, 1996.

[5] X.-P.Zhang, H.Chen, "Asymmetrical three-phase load-flow study based on symmetrical component theory", IEE Proc.-Gener. Transm. Distrib., Vol. 141, No. 3, pp. 248-252, 1994.

[6] X.-P.Zhang, "Fast Three Phase Load Flow Methods", IEEE Trans. on PS, Vol. 11, No. 3, pp. 1547-1554, August 1996.

[7] V.Strezoski, Lj.Trpezanovski, "Three–phase asymmetrical load–flow", International Journal of Electrical Power and Energy Systems, Vol. 22, No. 7, pp. 511-520, October 2000.

[8] Lj.Trpezanovski, V.Strezoski, "Reduced Admittance Matrix Method for Asymmetrical Load-Flow in Sequence Domain", XXXVIII International Scientific Conference Information, Communication and Energy Systems and Technologies, Proceedings, pp. 446-462, Sofia, Bulgaria, 2003.

[9] Lj.Trpezanovski, V.Strezoski, M.Atanasovski "Fast Method for Asymmetrical Load-Flow Solution in Sequence Domain", XXXIX International Scientific Conference on Information, Communication and Energy Systems and Technologies, Proceedings, Vol. 1, pp. 31-34, Bitola, Macedonia, 2004.

[10] Lj.Trpezanovski, V.Strezoski, "Power System Elements Modeling in Sequence Domain", XXXVII International Scientific Conference on Information, Communication and Energy Systems and Technologies, Proceedings, Vol. 2, pp. 459-462, Nis, Yugoslavia, 2002.

[11] Lj.Trpezanovski, *Asymmetrical Load Flow Calculation in Power Systems*, PhD thesis (in Serbian), University of Novi Sad, Faculty of Technical sciences, Novi Sad, July 2000.

[12] W.F.Tinney, C.E.Hart, "Power Flow Solution by Newton's Method", IEEE Trans. on PAS, Vol. PAS-86, No. 11, pp. 1449-1460, November 1967.

[13] B.Stott, O.Alsac, "Fast decoupled load flow", IEEE Trans. on PAS-93(3), pp. 859-869, 1974.

Impact of Transient Stability of Dispersed Generation on Relay Time Settings of Distribution Feeders

Metodija B. Atanasovski[1]

Abstract – **Increased presence of dispersed generation (DG) has significant technical impact on radial or weakly meshed distribution network on which it is connected. Distribution management system functions like power flow calculations, fault analysis, relay settings, state estimation, network reconfiguration, etc. are significantly affected by the DG. This paper reports an investigation to determine the impact of transient stability of small hydro DG unit on the relay time settings of distribution network feeders emanated from the substation to which DG is connected. Results from a case study are presented and discussed.**

Keywords – **DG, transient stability, critical clearing time, relay time setting, NEPLAN, distribution network.**

I. INTRODUCTION

Increased presence of DG has significant technical impact on radial or weakly meshed distribution network on which it is connected. Since the distribution network with DG is not passive, all issues about planning, construction, maintaining and operation of the distribution network become very interesting and need re-investigation. Actually, overall model of the distribution network should be renewed. Distribution management system functions like power flow calculations, fault analysis, relay setting, state estimation, network reconfiguration, etc. are significantly affected by the DG. It means that the distribution management system functions should be re-considered in order to respect the presence of DG in the distribution network [1,2].

From the perspective of the electrical interface that will be interconnected to the power system, there are generally two types of DG resources that can be connected [3]:

1. Electronically interfaced generators
2. Rotating machine interfaced generators

Electronic interfaces are inverter-based units and rotating machine interfaced DG are synchronous or induction generator based machines.

The main idea of this paper is to determine the impact of transient stability of DG on the relay time settings of distribution network feeders emanated from the substation to which DG is connected. Detailed investigation of this problem has already been done in [5], for two types of DG resources: CHP schemes with gas turbine synchronous generator and wind farms with induction generator. DG transient stability studies are similar to large scale power system transient stability studies, except that DG capacity is normally very small relative to the bulk system and has no significant influence on its frequency or stability. This paper is also focused (as [5]) on the investigation of the ability of rotating synchronous generator (SG) of small DG hydro unit to remain synchronized and determining its critical clearing time (CCT), when feeder disturbance occurred on the distribution network. For that purpose a case study with small hydro DG unit connected to distribution network is simulated using NEPLAN [4] power system software package, Results from a case study are presented and discussed.

[1]Metodija B. Atanasovski is with the Faculty of Technical Sciences, I.L.Ribar bb, 7000 Bitola, Macedonia, E-mail: metodija.atanasovski@uklo.edu.mk

II. CRITICAL CLEARING TIME OF SYNCHRONOUS GENERATOR VS. DISTRIBUTION FEEDER RELAY TIME SETTING

The concept of stability is well defined for the case of synchronous machines. During normal operating conditions a synchronous generator connected on a distribution network run at synchronous speed with a rotor angle δ_0 corresponding to an electrical output power P_e and mechanical input power P_m. When a fault occurs on the network, P_e suddenly reduces due to a sudden change in network voltage. This leads to the acceleration of SG to account for the difference between input/output powers, according to the well known swing equation [5,6]:

$$\frac{d^2\delta}{dt^2} = \frac{\omega_s}{2H}\left(P_m - P_e\right) \tag{1}$$

where

ω_s angular frequency
t time
H inertia constant of the rotating mass.

When the fault is cleared at time t_c which corresponds to a rotor angle δ_c, the power demand by the network re-establishes and generator find itself generating power greater than P_e due to a new rotor angle. Assuming that the input mechanical power remains unchanged the extra power is supplied from the kinetic energy of the rotating mass. However due to the moment of inertia the rotor angle continues to increase , but because the input power is less than the output power the generator begins to decelerate passing its synchronous speed. The oscillation of the speed (and rotor angle) continues for a while, but eventually they settle to a new steady-state condition and the system is considered stable. Otherwise, δ continues to increase further and generator losses synchronism with the network and is considered unstable. There is a maximum rotor angle below which synchronous generator can retain a stable operation. This position is known as critical clearing angle. The

corresponding maximum critical time is known as critical clearing time [6].

In distribution networks, for short circuit protection, overcurrent relays are usually used. Overcurrent protection has two setting dimensions: current and time. This settings are performed on the basis of two types of calculations [7]: 1)steady-state (power flow or state estimation is used) and 2) short circuit. In order to achieve one of the basic principles of protection design, removal of a fault with minimum tripping of equipment or disruption supply, proper coordination (time setting) of protective devices should be done. This however may lead the operation time of protective devices near the substation HV/MV of a distribution network, to be as high as 1-1,5 seconds.

When DG is connected into a distribution network on the substation HV/MV, the operating time of protective devices installed on load feeders may exceed the critical clearing time required to maintain the stability of DG.

III. MODELLING THE CASE STUDY NETWORK WITH NEPLAN

The case study network considered in this paper is shown in Fig. 1. It consists of a distribution network with DG hydro u with 3,2 MVA synchronous generator. Synchronous generator with NEPLAN is simulated with fully detailed subtransient model using typical data for time and reactance constants for hydrogenerators [6]. The machine reactances and inertia are normally per unitized on the machines voltage and MVA base. With NEPLAN control circuits function blocks, prime mover (governor and turbine) is simulated, using nonlinear turbine model [6] assuming inelastic water column and also speed governor is modeled for account of gate position and rate limits. The hydraulic turbine governors have a very slow response from the viewpoint of transient stability, but their effects can be more significant in studies of small isolated systems. For simulation of excitation system simplified IEEE AC4A excitation system model is used [6]. Generator is integrated into the distribution network at 20 kV voltage level through 2x1,6 MVA 0,4/20 kV/kV step-up transformers and 20 kV distribution line 1. 110 kV grid is represented by infinite model with voltage source behind its Thevenin's equivalent impedance. The fault level of the 110 grid is assumed 5000 MVA. HV/MV substation is represented by three windings transformer 110/20/10 kV/kV/kV and 31,5/31,5/10,5 MVA/MVA/MVA. The load is connected to the substation through distribution line 2 and 20/0,4 kV/kV transformers. Load characteristic is represented with constant impedance model. Both lines 1 and 2 are simulated with π-equivalent circuit with impedance of $(0{,}413 + j0{,}36)\Omega/km$. All transformers are modeled in a same way as in short circuit calculations.

IV. SIMULATION AND RESULTS

Simulation is performed for a three-phase fault on line 2 at location F (see Fig. 1.), which is on 20% of the length of line

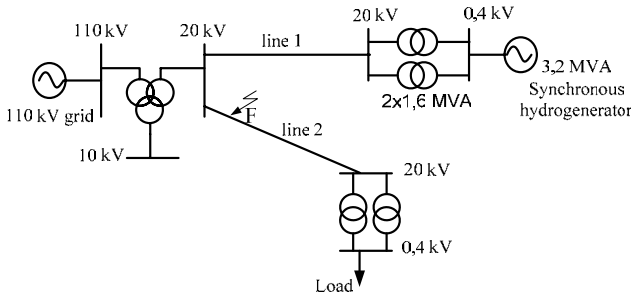

Fig.1. Schematic diagram of the case study network

2 from the substation HV/MV. Results for fault duration of 200 ms are shown on Fig. 2. The corresponding generator rotor angle position is shown on Fig. 2(a). This figure shows that rotor angle assumes a stable position following few oscillations after the removal of the fault. It can be seen from Fig 2(b) that generator terminal voltage magnitude has dropped to a value 30% of its nominal voltage, but after isolation of the fault the voltage retained its normal operation level. The corresponding variation of generator stator current is shown on Fig 2(c).

After several simulations for different durations of three-phase fault at location F, it was found that the critical clearing time of the SG is 340 ms. Fig. 3(a) and 3(b) show the variation of generator rotor angle and its terminal voltage, following a three-phase fault at location F with a duration of 350 ms. It can be seen from Fig. (3a) that the rotor angle continues to grow and the generator continues to accelerate until it loses its synchronism with the network.

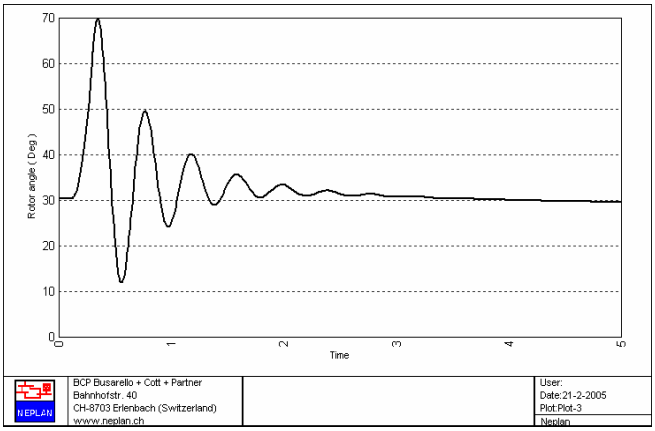

(a)

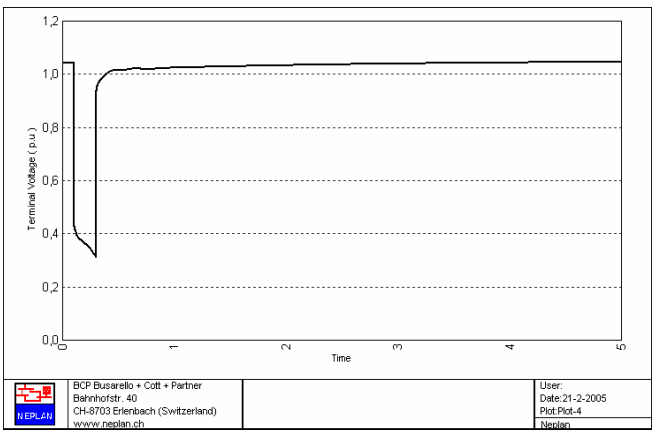

(b)

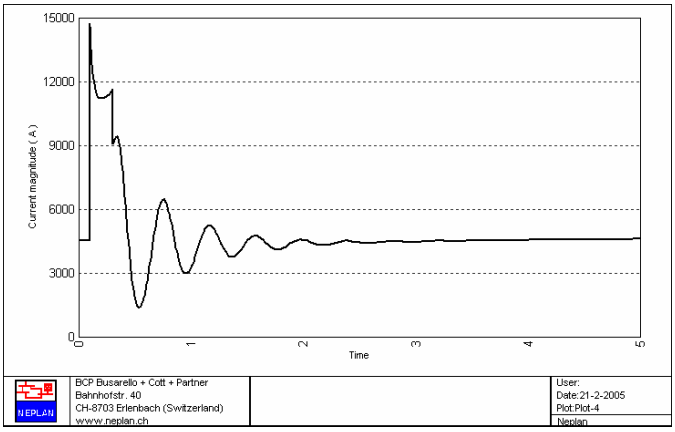

(c)

Fig.2. (a) Variation of rotor angle of SG following a three-phase 200 ms duration fault on the network. (b) Variation terminal voltage of SG following a three-phase 200 ms duration fault on the network. (c) Variation of generator stator current following a three-phase 200 ms duration fault on the network.

V. CONCLUSION

NEPLAN software package, has been successfully used in this paper to simulate distribution system with small DG hydro unit with synchronous generator. The simulation is then used to investigate the impact of transient stability of DG hydro unit with synchronous generator on the relay time settings on the distribution network feeders. For the case study under consideration, it has been found that the maximum clearing time of a three-phase fault at the beginning of a load feeder is 340 ms. The results confirm the conclusions in [5] that immaterial of the type of the dispersed generator used and network under consideration, the maximum clearing time can be much lower than the expected operating time of protective relay usually applied for distribution feeders. It is, therefore, important that protection coordination should be carefully done when integration of DG into a distribution network is considered.

REFERENCES

[1] Rade M. Ciric, Antonio Padilha, Iara Fernanda Ehrenberg Dossi Denis, Luis F. Ochoa, “Integration of the Dispersed Generators in Distribution Management System”, 2003 IEEE Bologna Power Tech Conference, June 23th-26th.

[2] Final Report WG 37-23, “Impact of Increasing Contribution of Dispersed Generation on the Power System”, *CIGRE Study Committee no 37*, September 1998.

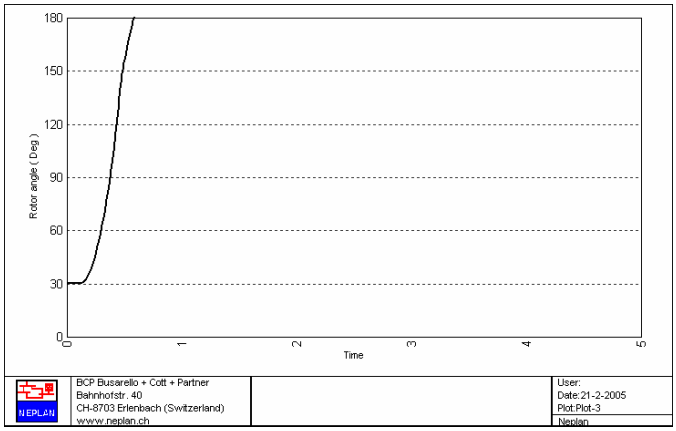

(a)

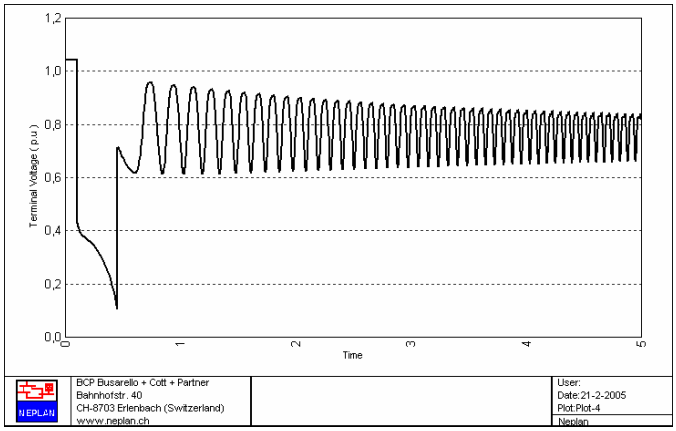

(b)

Fig. 3. (a) Variation of rotor angle of SG following a three-phase 350 ms duration fault on the network. (b) Variation terminal voltage of SG following a three-phase 350 ms duration fault on the network.

[3] Philip P. Barker, Bradley K. Johnson, “Power System Modeling Requirements for Rotating Machine Interfaced Distributed Resources” IEEE Working Group on Distributed Resources Modeling and Analysis, 2002

[4] NEPLAN User’s Guide V5, BCP Bussarelo+Cott +Partner, www.neplan.ch.

[5] Salman K. Salman, Ibrahim M. Rida, “Investigating the Impact of Embedded Generation on Relay Settings of Utilities Electrical Feeders”, IEEE Transactions on Power Delivery, Vol. 16, No. 2, April 2001.

[6] P. Kundur, “Power System Stability and Control”, EPRI Power System Engineering Series, McGraw-Hill, Inc., 1993

[7] Dragan Popovic, Dusko Bekut, Valentina Treskanica, “Specijalizovani DMS algoritmi”, DMS Group, Novi Sad 2004.

Possibilities for Remote Reading of Electric Power System Parameters

Peter I. Yakimov[1], Stefan J. Ovcharov[2], Nikolay T. Tuliev[3] and Angel T. Stanchev[4]

Abstract – **The paper presents the investigation of some possibilities for remote reading of electric power system parameters. The purpose is to transmit data for the values of the measured parameters from different points of the electric power system to a central point. There are described possibilities using radio communication, industrial network and Ethernet communication.**

The presented results will be used in further investigation of more complex systems for electric power management.

Keywords – **Measuring transducer, Communications, Interface, Industrial networks, Ethernet**

I. INTRODUCTION

The electric power system might be divided to the following parts – manufacturing, distribution and consumption. The stability and correct function of the entire system depends on the right operation and interconnection between all components of the system – power plants, power lines, sub-stations, transformers, circuit breakers, loads and etc. The correct control of the system requests a large amount of information for the parameters in different points. There are in use transducers (fig. 1), which measure the values of the main parameters of the three phase electric power system – voltage, current, frequency, active power, reactive power, power factor, active energy and reactive energy [1].

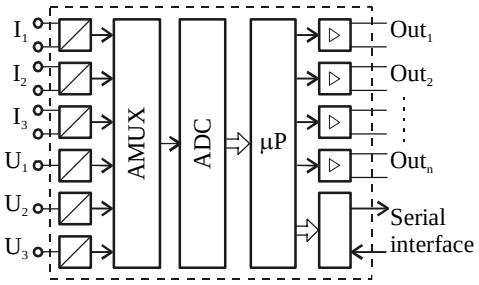

Fig. 1. Block diagram of an universal transducer

Most of the transducers have two types of interface: analog and digital. The output quantities of the analog outputs can be load independent direct current or direct voltage signals. The range of the current outputs may be different - -5mA÷+5mA, 0mA÷20mA or 4mA÷20mA. Usually the range of the voltage outputs is 0÷10V.

The digital interface is usually serial in order to minimize the number of the wires. The standard is mainly RS485, RS232 or LON. There are custom defined interfaces also.

II. DATA TRANSMISSION USING THE DIFFERENT INTERFACES

The transducers may have several analog outputs and they have to be electrically insulated (fig. 1). In some transducers every output is driven by previously determined input variable but in another one there is a possibility for programming which measured variable will control a given output. There must be a response between the ranges of the input variable and the output quantity. The resolution in output signal generating must not be less than in measuring in order for true transmission of the input value. The receiver must have the same resolution. So, the receiver's parameters limit the accuracy. Another disadvantage of the analog interface are the lack of correspondence between the number of the outputs and the number of the measured and calculated by the transducer variables, and the number of connecting wires.

The digital interface uses only two or three wires but presents the possibility to transmit the values of all parameters of the electric power system and contrary to the analog interface the transfer can be bidirectional. This allows a smart transducer to be programmed and checked by external computer. The disadvantage of analog signal synthesis with high resolution does not exist because the transferred data is digital. This transfer has higher noise immunity than the analog. The digital interface is suitable for transmitting the values of the energy. It is very difficult to read the values of the energy using analog output because of the continuous integration of the power, which leads to permanent increasing of the output quantity and fast reaching the upper limit of the output range. The high rate of data transfer enables transmission of large amount of information. The data transmitted by the transducer includes the values of phase voltages (U_1, U_2, U_3), phase currents (I_1, I_2, I_3), active power (P), reactive power (Q), frequency (f), active and reactive energy in four quadrants (ENAPL, ENAMI, ENRPL, ENRMI), phase angles (φU_1, φU_2, φU_3, φI_1, φI_2, φI_3), ratios of the voltage and current measuring transformers (K_U, K_I).

[1]Peter I. Yakimov is with the Faculty of Electronic Engineering and Technologies, Dept. of Electronics, Technical University - Sofia, 1000 Sofia, Bulgaria, E-mail: pij@tu-sofia.bg

[2]Stefan J. Ovcharov is with the Faculty of Electronic Engineering and Technologies, Dept. of Electronics, Technical University - Sofia, 1000 Sofia, Bulgaria, E-mail: sjo@tu-sofia.bg

[3]Nikolay T. Tuliev is with the Faculty of Electronic Engineering and Technologies, Dept. of Electronics, Technical University - Sofia, 1000 Sofia, Bulgaria, E-mail: ntt@tu-sofia.bg

[4]Angel T. Stanchev is with the Faculty of Electronic Engineering and Technologies, Dept. of Electronics, Technical University - Sofia, 1000 Sofia, Bulgaria, E-mail: astanchev@tu-sofia.bg

The quantities and the number of bytes for each of them are presented in Table I.

TABLE I

TRANSMIT DATA DESCRIPTION

Quantity	Number of bytes
Phase voltage - U_1	2
Phase voltage – U_2	2
Phase voltage – U_3	2
Phase current - I_1	2
Phase current – I_2	2
Phase current – I_3	2
Active power - P	2
Reactive power - Q	2
Frequency - f	2
Positive active energy - ENAPL	4
Negative active energy - ENAMI	4
Positive reactive energy - ENRPL	4
Negative reactive energy - ENRMI	4
Phase angle - φU_1	2
Phase angle - φU_2	2
Phase angle - φU_3	2
Phase angle - φI_1	2
Phase angle - φI_2	2
Phase angle - φI_3	2
Voltage transformer ratio - K_U	2
Current transformer ratio – K_I	2

At a given point of the electric power system – power plant, sub-station, there are usually a big number of transducers. It is useful to be included in a computer network. The digital interface makes it possible.

The network can be developed using the well known configurations – star, ring, bus etc. In order to minimize the connections bus topology is suitable.

III. APPLICATIONS OF REMOTE READING OF ELECTRIC POWER SYSTEM PARAMETERS

In the Development Laboratory for Semiconductor Circuit Engineering (http://www.tu-sofia.bg/r&ds/PS/home.htm) at Technical University of Sofia have been designed universal transducers for use in the electric power system. They have two-wire instrumental serial interface, which enables development of industrial network (fig. 2) [2]. It is configured using bus topology. In order to connect a standard unit – PC or operator's station to the developed network there must be an adapter to translate the logic levels of the industrial interface in accordance with a standard interface, for example RS232.

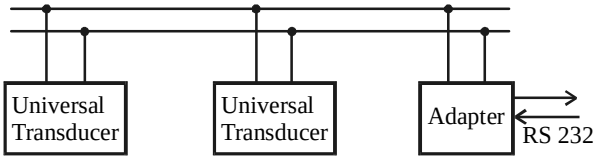

Fig. 2. Universal transducers in an industrial network

The two-wire instrumental serial interface operates reliably when the length is up to 100 m.

When the distance to the central point is longer there is a need to use another approach of communication.

The data might be transferred using telephone line. This requests telephone modems. The telephone modem allows connecting the industrial network to LAN. Disadvantage is the low rate of data transfer limited by the telephone line. Better results will be obtained using ISDN line.

A possible solution is the radio communication [3]. In this case the adapter must have radio modem (fig. 3).

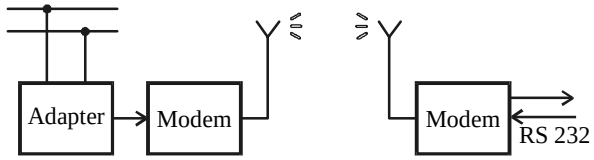

Fig. 3. Radio communication data transfer

This approach is suitable when the network of transducers is developed in area, which is not connected to the telephone network. The solution is useful when the data is collected using mobile hand-held devices. Disadvantage is the need of independent radio frequency. Better results will be obtained using GSM, but the area must be covered by GSM operator.

If the region is covered by local area network possible approach is to connect the industrial network using Ethernet module [4]. The adapter must conform the two-wire instrumental serial interface to Ethernet controller (fig. 4).

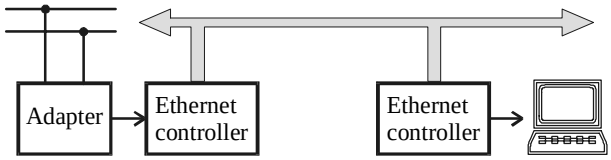

Fig. 4. Data transfer through Ethernet

This approach ensures data transfer rate up to 10Mbits/s.

IV. CONCLUSIONS

The efficient electric power management requires transfer of large amounts of information for the parameters of the system. This forces introduction of new approaches for distance communication. A perspective solution is development of industrial networks connected via Ethernet.

REFERENCES

[1] www.gmc – instruments. com

[2] Ovcharov St., P. Yakimov, Instrumental interface for industrial network development, "Electrotechnics and electronics", Sofia, Bulgaria, in press (in Bulgarian)

[3] Ovcharov St., P. Yakimov, C. Lukarsky, N. Nikolov, K. Gornishky, A. Dimitrov, System for distance reading of electricity meters, Proceedings of 10th Scientific Symposium "Metrology'2000", September 14-17, 2000, Sozopol, Bulgaria, pp. 104-107 (in Bulgarian)

[4] Ovcharov St., N. Tuliev, A. Stanchev, Adapter module for Ethernet Network Communication over TCP/IP, Proceedings of the 13th International Scientific and Applied Science Conference "Electronics ET'2004", September 22-24, 2003, Sozopol, Bulgaria, book 2, pp. 60-65

An Approach to the Investigation and Assessment of the Electric Field Non-Uniformity

Peter Dineff[1], Raina Tzeneva[2]

Abstract – **The experimental-and-theoretical approach to studying the effect of the field geometrical structure, which acts through its transition from uniform field to non-uniform one as a result of varying the ratio of the active anode and cathode areas, upon the anodic aluminum dissolution in solutions of sodium chloride is presented in a finished form, said ratio being assumed to be a measure for the non-conformity with Faraday laws. Two non-uniformity factors of the electric field are used: α – the "length" geometrical factor, and β – the "surface" geometrical factor. The general factor is determined by the product of the two factors: $G = \alpha\beta$. The distribution of the current density in the experimentally investigated cases of anodic dissolution is visualized by appropriate mathematical modeling of the electric field.**

Keywords – **Anode dissolution, electric field geometry or topology, electrolysis, general non-uniformity factor, length geometrical factor, non-uniformity, surface geometrical factor.**

I. INTRODUCTION

The scientific literature does not indicate any generally accepted mechanism of aluminum anodic dissolution in electric field of various degree of non-uniformity which could be not only of theoretical importance, but also of great practical value for applying effectively the aluminum as anode material in electrocoagulation, electroflotation, electro-M process, etc. [1, 2].

The objective of the present theoretical and experimental investigations is to study the effect of the electric field non-uniformity on the galvanostatic anodic dissolution of technically pure aluminum in a comparatively wide range of variation of the quantity of electricity and the degree of non-uniformity.

Electric field parameters characterizing the change in the geometrical (topological) field structure and helping the comparison of the non-uniformity degrees of different electric fields, e. g. the degree of field non-uniformity β, the electrode polarity, and the relative length of the average currant tube α, have been defined [1, 2].

II. THEORETICAL INVESTIGATION

There are two ways to change the electric field of conductivity structure:

$ varying the ratio between the electrode – anode and cathode, active areas S_a and S_c, or changing the degree of non-uniformity $\beta \geq 1$ ($\beta = 1$ for uniform electric field) [1]:

$$\beta = S_g^o \, S_g^{-1} = S \, S_g^{-1} = S \left(S_a \, S_c\right)^{-1/2} , \quad (1)$$

where S is anode S_a^o and cathode S_c^o active area for uniform electric field: $S = S_g^o = S_a^o = S_c^o = \left(S_a^o \, S_c^o\right)^{1/2}$, and S_g^o - the geometrical mean of anode and cathode areas; $S_g = \left(S_a \, S_c\right)^{1/2}$ - the geometrical mean of anode and cathode areas for non-uniform electric field, S_a and S_c - the anode and cathode active areas; electrodes polarity may be straight (*SP*) - $S = S_a$ or reverse (*RP*) – $S = S_c$;

$ varying the apparent relative length of the average current tube $\alpha \geq 1$ ($\alpha = 1$ for uniform electric field):

$$\alpha = l \, d^{-1} , \quad (2)$$

where d is the distance between the two electrodes or the minimum possible length of the current vector tube: $l = d$ and $\alpha = 1$ for uniform electric field.

For a non-uniform electric field of conductivity the electric resistance R_{NU} of electrolysis cells may be expressed by the resistance R_U for a uniform field:

$$R_{NU} = \rho l S_g^{-1} = \rho \alpha d S^{-1} = \rho d S^{-1} \alpha\beta = R_U \alpha\beta \quad (3)$$

$$G = R_{NU} \, R_U^{-1} = \alpha \, \beta , \quad (4)$$

where G is the general degree of non-uniformity.

The degree of non-uniformity β can be an independent factor of the electrolysis which is modified by varying the ratio between areas S_a and S_c, and the polarity of electrodes: *SP* - $S = S_a$ or *RP* - $S = S_c$, while keeping $S_g = const$.

The apparent length α follows the changes of the voltage U across the electrolysis cell in a galvanostatic regime, $I = const$, of anodic dissolution of aluminum:

$$I = U \left(\rho \, \lambda \, \alpha \, \beta\right)^{-1} = U \left(\rho \, \lambda \, G\right)^{-1} = const ; \quad (5)$$

$$U \, \alpha^{-1} = const \;\; (\rho = const, \lambda = const, \beta = const ; \quad (6)$$

[1]Peter Dineff is with the Department of Electric Apparatuses, Faculty of Electric Engineering, Technical University of Sofia, Blvd. Kliment Ohridski 8, 1000 Sofia, Bulgaria, E-mail: dineff_pd@abv.bg

[2]Raina T. Tzeneva is with the Department of Electric Apparatuses, Faculty of Electric Engineering, Blvd. Kliment Ohridski 8, 1000 Sofia, Bulgaria, E-mail: tzeneva@tu-sofia.bg.

where $\lambda = d\, S_g^{-1}$ is the geometric factor of the electric resistance of electrolysis cell.

For the same time of electrolysis t_e the quantity of electricity Q transferred through the solution remains constant, too, or $Q = I\, t_e = const$, in the galvanostatic regime of electrolysis.

In the galvanostatic regime of electrolysis the basic relationships representing the influence of non-uniformity upon anodic dissolution of aluminum may be presented in the following way:

$$M_a = \eta_a\, M_F = \frac{A\,\eta_a}{F\,z}\,\frac{t_e}{\rho}\,\frac{U}{\lambda\,\alpha\,\beta} = m_a\,\frac{t_e}{\rho}\,\frac{U}{\lambda\,G}; \quad (7)$$

$$w = \frac{W}{M_a} = \frac{Q\,U}{M_a} = \frac{F\,z}{A\,\eta_a}\,\frac{\rho}{t_e}\,\lambda\,\alpha\,\beta\,Q\;; \quad (8)$$

$$w = \frac{l}{m_a}\,\frac{\rho}{t_e}\,\lambda G Q; \quad (9)$$

$$R = \rho\;\lambda\;\alpha\;\beta = \rho\;\lambda\;G\;; \quad (10)$$

$$N_e = \frac{z}{\eta_a}, \quad (11)$$

where M_a is the mass of anode dissolved aluminum, g; η_a - the current efficiency; F = 96 487 is Faraday's number representing the quantity of electrons, C/mol; z = 3 – the normal oxidation level of aluminum; A – the atom weigh of aluminum, g/mol; w - the specific energy consumption per unit of dissolved aluminum mass, (W.s)/g; W – the energy consumption, W.s; R – the resistance of the electrolysis cell, Ω; N_e - the effective oxidation level.

III. General Formulation of Investigations

The dissolution of plane-parallel electrodes made of aluminum 99.5 with main additions: 0.26 Fe, 0.14 Si, 0.10 Cu, and 0.001 Mg (mf%), has been studied [4, 5].

The electrolysis has been performed under galvanostatic conditions of direct current at room temperature (20 ^{0}C) in a 0.052 M solution of chemically pure sodium chloride (NaCl) in distilled water. The volume of the electrolysis cell is 1 dm^3. The electrolysis time t_e is t_e = 900 s (15 min).

The quantity of electricity Q has been varied at five levels: 144, 432, 720, 1008, and 1440 C. The electrodes active area S is S = 16 cm^2, and the current has been determined as 0.16, 0.48, 0.80, 1.12, and 1.60 A, respectively.

The distance between the electrodes remains unchanged: d = 15 mm. The geometrical structure of the electric field has been changed at three levels of the non-uniformity degree β, namely β = 1, $\sqrt{2}$, and 2. The electrodes under test are made with the following dimensions: (40 x 40 x 10) mm, (40 x 20 x 10) mm, and (20 x 20 x 10) mm, respectively. The back and side walls of electrodes are electrically insulated by a coating of epoxy resin defining precisely the size of the active electrodes' area.

The mass of dissolved aluminum M_a has been determined gravimetrically, after appropriate washing and drying, in five parallel experiments [4, 5].

Additional investigations have been carried out with the task of modelling and visualizing with the aid of modern software products the **3-D** spatial distribution of the current density of $\vec{J}$ and the geometrical structure change for various values of the non-uniformity degree β. The electric field $\vec{J}$ in the electrolysis cell has been modeled spatially by using the method of boundary elements.

Pictures of the distribution of current density $\vec{J}$ for the three experimentally investigated cases of non-uniformity are shown in Figs. 1, 2, and 3.

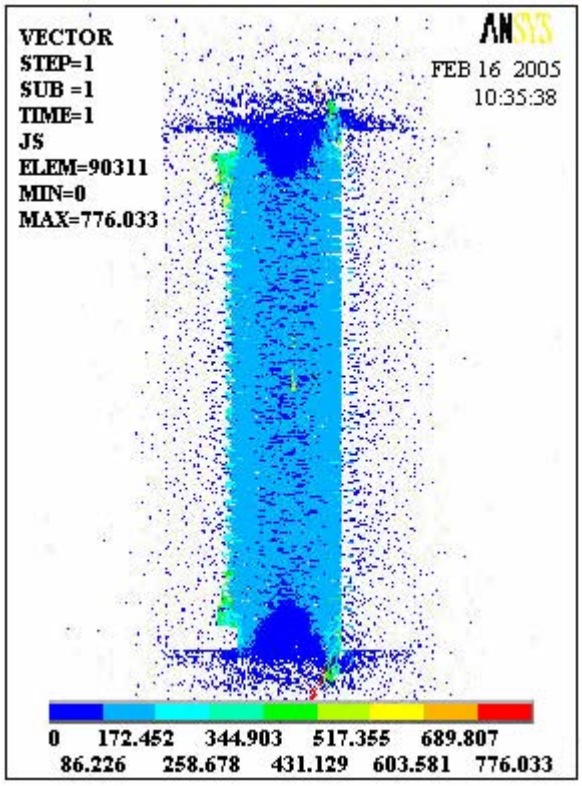

Fig. 1. Sectional view of the geometrical structure of the electric field of an electrolysis cell, which is represented by the distribution of the vectors of current density $\vec{J}$ for plane-parallel configuration of two identical aluminum electrodes of active area S = 16 cm^2 (β = 1) and distance d = 15 mm between them. The electrodes are electrically insulated over the back wall as well as over all side ones. The geometrical mean of the current density is $\vec{J}_g$ = 625 A/m^2.

The presented **3-D** visualization of the electric field corresponds most exactly to the real structure of the electric field created. The **2-D** distributions presented in [4] are a rather rough approximation as the electric insulation of the surrounding walls as well as the back one of the electrodes creates a very characteristic structure of the electric field that cannot be modeled by products for 2-D analysis as *Quickfield* or *FEMM*.

In the **3-D** modeling the edge effect is expressed by suction of the field inward between the electrodes, Figs. 1, 2, and 3, while the **2-D** plane-parallel mathematical models show the edge effect by outward swelling. In the plane-parallel **2-D** model it is impossible to insulate electrically the two surrounding walls of electrode, which are situated in parallel to the plane of modeling.

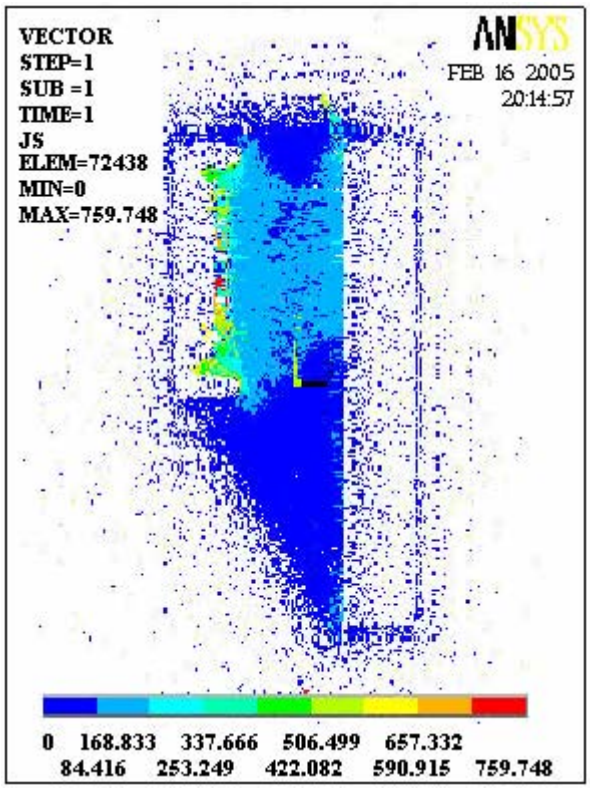

Fig. 2. Sectional view of the geometrical structure of the electric field of an electrolysis cell, which is represented by the distribution of the vectors of current density $\vec{J}$ plane-parallel configuration of two aluminum electrodes of active areas S = 8 cm^2 and 16 cm^2, respectively, ($\beta = \sqrt{2}$) and distance d = 15 mm between them.

IV. Results and Discussion

The mass of aluminum dissolved at the anode, M_a, has been determined experimentally, and then all the remaining characteristics of the anodic dissolution are calculated in accordance with equation 10-14.

All calculations are performed for specific electric resistance of the electrically conductive media ρ = 1.352 Ωm and geometrical factor of the resistance, λ = 9.375 m^{-1}.

The regression relationships obtained show a relatively weak dependence of the current efficiency η_a upon the quantity of electricity Q,:

$$\eta_a = 121.60 + \frac{542.92}{Q}, \; r = 0.9986 \qquad (12)$$

The current efficiency η_a decreases with increasing the quantity of electricity Q in the interval studied $Q \in [144 - 1440]C$, changing relatively weakly: from 1.25 to 1.22, or within the range of 2.5 %. The current efficiency is higher than one, which indicates the presence of a process going in parallel to the Faraday anodic dissolution, namely corrosion of aluminum [3, 4].

The effective oxidation level N_e may be also represented by the regression equation obtained – equation 12, and equation 11, $Q \in [144 - 1440]C$:

$$N_e = \frac{Q}{40.53\,Q + 180.97}, \; r = 0.9986 . \qquad (13)$$

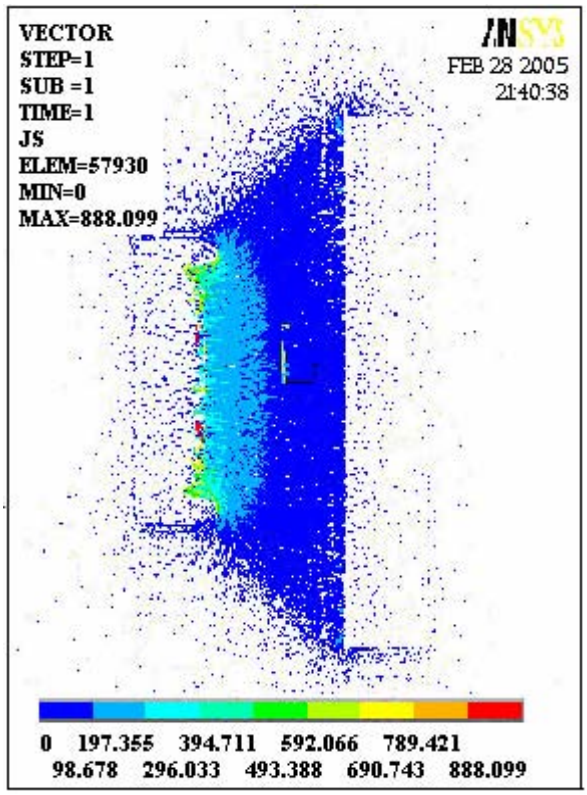

Fig. 3. Sectional view of the geometrical structure of the electric field of an electrolysis cell, represented by the distribution of the vectors of current density $\vec{J}$, for plane-parallel configuration of two aluminum electrodes of active areas S = 4 cm^2 and 16 cm^2 ($\beta = 2$) and distance d = 15 mm between them.

The experimentally determined effective oxidation level N_e is lower than the normal oxidation level of aluminum $z = 3$, and changes within a comparatively narrow range from 2.39 to 2.46.

According to the known hypothesis for the stepwise mechanism of the anodic oxidation of aluminum at varying the effective oxidation level in the region $2 < N_e < 3$, two of the oxidation stages are realized inevitably with the participation of the anode (in accordance with Faraday), while about 50 % of the aluminum ions taking part in the third act of oxidation do not get into contact with the anode.

The influence of the general degree of non-uniformity G or of the geometric factor of electrolysis cell $\lambda\alpha\beta$ on the mass of anodically dissolved aluminum M_a for straight (*SP*) and reverse (*RP*) polarities of the electrodes is shown graphically in Fig. 4.

The observed relative shortening of the average current tube may be explained with the tightening action exerted by the proper magnetic field of the current.

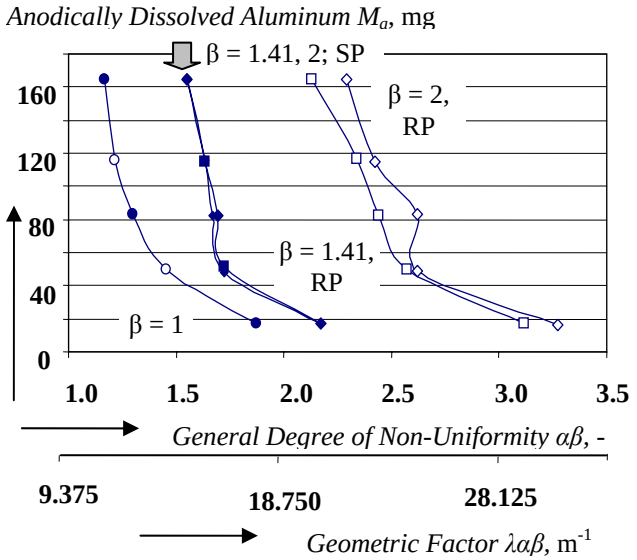

Fig. 4. Dependence of the mass of anodically dissolved aluminum M_a on the general degree of non-uniformity $G = \alpha\beta$, the general geometric factor $\lambda\alpha\beta$, and the degree of non-uniformity β at straight and reverse polarity of electrodes.

Analogous considerations are made for the specific energy consumption w, which is the quantity of electric energy used in anodic dissolution and corrosion, Fig. 5.

In all cases examined increasing the anodic dissolution rate, $M_a\ (t_e = 900\ s)$ becomes the cause of a fast increase in the electric energy consumption.

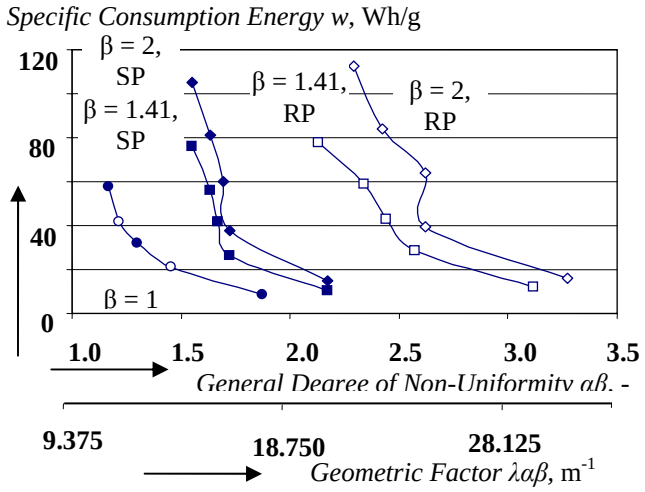

Fig. 5. Dependence of the specific energy consumption w on the general degree of non-uniformity G = $\alpha\beta$, the degree of non-uniformity β, and the general geometrical factor $\lambda\alpha\beta$ at straight and reverse polarity of electrodes.

The present investigation permits making an addition to the increase in the electric energy consumption at a higher degree of non-uniformity of the field, already established by us in [4]. The more non-uniform electric field leads to a more essential increase in the electric energy consumption at higher rates of anodic dissolution of aluminum.

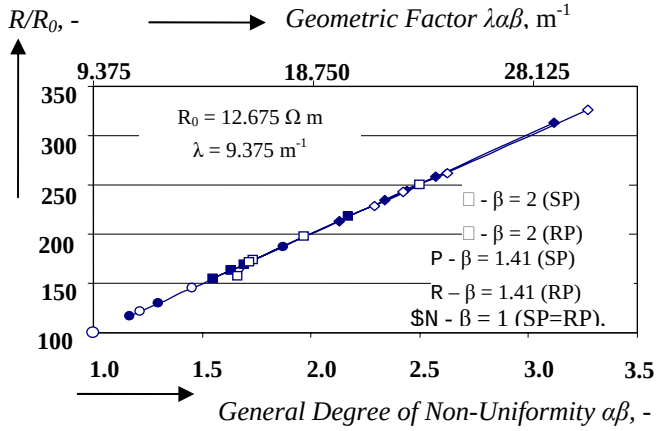

Fig. 6. Dependence of the relative electric resistance R/R_0 (R_0 = 12.675 Ωm) on the general degree of non-uniformity $G = \alpha\beta$, the degree of non-uniformity β, and the general geometric factor $\lambda\alpha\beta$ at straight and reverse polarity of electrodes.

The relative change in resistance R / R_o depends linearly on the change in the general degree of non-uniformity $G = \alpha\beta$, Fig. 6.

The assumed hypothesis of linearity of the electrically conductive medium is confirmed, because $R_0 = \rho\,\lambda$ should remain of constant value for the change in the general non-homogeneity of the electric field, G, in order to be manifested the linear relationship observed in Fig. 6.

Irrespective of the polarity of the electrode system – straight or reverse, all operating points are located on the straight line for a change in the quantity of electricity within the range $Q \in [144 - 1440\ ]C$.

V. Conclusion

Changing the non-uniformity degree β exerts much weaker influence on the rate of anodic dissolution and on the specific consumption of electric energy than the increase in the quantity of electricity transferred through the electrolyte. The high rates of anodic dissolution and corrosion define the considerably increased consumption of electric energy in this case, which is practically independent of the non-uniformity of the electric field. The non-uniformity of the electric field contributes essentially to increasing the electric energy consumption at high rates of anodic dissolution.

The high rates of anodic dissolution and corrosion and the high values of the electric current, respectively, define the observed relative shortening of the elementary vector current tubes. An explanation of this fact may be connected with the influence of its own magnetic field that „tightens" the region of conductivity, or with the so called pinch-effect.

References

[1] P. Dineff, E. Sabeva, *Indian Journal of Chemical Technology*, Vol. 11, July, pp. 486-494, 2004.

[2] P. Dineff, E. Sabeva and I. Dobrevsky, *Corrosion Science*, Vol. 36, No 4, pp. 717-732, 1994.

Session ELI:

ELECTRONIC COMPONENTS, SYSTEMS AND TECHNOLOGY I

Linear Current Starved Delay Element

Goran S. Jovanović[1] and Mile K. Stojčev[2]

Abstract – **In this paper the instructions for preparing camera ready paper for the Conference ICEST 2005 are given. The recommended, but not limited text processor is Microsoft Word 97/2000/XP/2003. The global instructions for preparing paper with any text processor are given, too. For the LATEX users using the IEEEtran.sty is recommendable and it can be obtained from the IEEE web page http://www.ieee.org.**

Keywords – **Camera-ready paper, Proceedings of papers, ICEST 2005.**

I. INTRODUCTION

Variable delay elements are inverter–based circuits used for fine, precise, and accurate pulse delay control in a high-speed digital integrated circuits. In order to achieve wide phase shift variable delay elements are realized as a chain of inverters. The chain of inverters is called delay line. In complex VLSI ICs, delay lines are constituents of DLLs (Delay Locked Loops) [1], TDCs (Time-to-Digital Converters) [4], VCOs (Voltage Controlled Oscillators) [5], Pulse-Width Control Loops (PWCLs) [3], etc.

In VLSI ICs, the DLL is routinely employed in order to obtain correct synchronization and elimination of clock skew among different digital blocks [1], such as CPU and SDRAM interface, etc. In addition, DLL is used for on-chip clock generation [1], and vernier delay patterns implemented in time-to-digital converter [4]. VCO for PLL application is realized when voltage controlled delay elements are connected in a ring [5]. Duty cycle converter (DCC) is another application, based on delay element that can independently adjust the delay of a rising/falling clock's edge [3]. In general, systems with feedback loop, which regulate pulse-width using delay elements, are referred as Pulse-Width Control Loop (PWCL). In all above–mentioned applications, variable delay elements are crucial building blocks, critical from aspect of design, since they determine precise and accurate pulse time reference.

This paper is organized as follows. Section 2 deals with an overview of existing types of voltage controlled delay elements. The modified bias circuit, with reciprocal current regulation, is described in Section 3. Hardware structure of the delay line and simulation results are considered in Section 4. Finally, Section 5 gives a conclusion.

[1]Goran S. Jovanović is with the Faculty of Electronic Engineering, Beogradska 14, 18000 Niš, Serbia and Montenegro, E–mail: joga@elfak.ni.ac.yu

[2] Mile K. Stojčev is with the Faculty of Electronic Engineering, Beogradska 14, 18000 Niš, Serbia and Montenegro, E–mail: stojcev@elfak.ni.ac.yu

II. CLASSIFICATION OF DELAY LINE ELEMENTS

Variable delay line elements can be classified as digital- or voltage-controlled.

Digitally controlled delay line elements are realized as series of delay elements of variable length [7]. The number of elements in a chain determines the amount of the delay. Delay elements provide fixed and quantized time delays. These kinds of delay line elements are suitable for coarse-grain delay variation in a wide range of regulation.

Voltage controlled delay line elements, alternatively called analog voltage controlled delay line elements, are suitable for fine-grain delay variation. They are efficient in applications where small, accurate, and precise amount of delay is necessary to achieve. Usually, these types of delay lines are realized using shunt capacitor [2] or current starved delay elements [1].

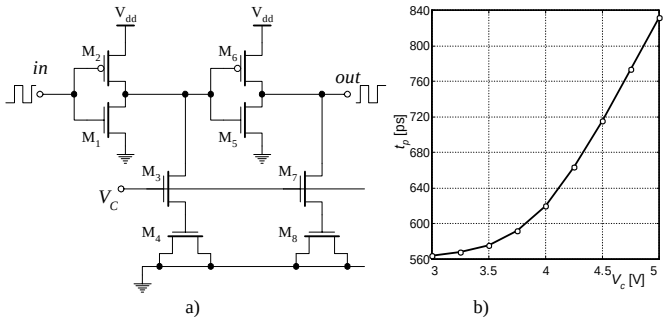

Fig.1. Shunt capacitor delay element a) scheme and b) typical characteristic delay in term of control voltage

Shunt capacitor delay element (see Fig. 1 a) is capacitive loaded inverter. In this case, the transistor (M_3 or M_7) acts as a linear resistor and defines the charging/discharging current of a load capacitor (transistor M_4 or M_8). Indirectly it changes the delay of output pulses. This type of delay element has the following disadvantages: a) the output capacitor occupies large silicon area; b) the amount of a delay and the active range of voltage regulation are small [2].

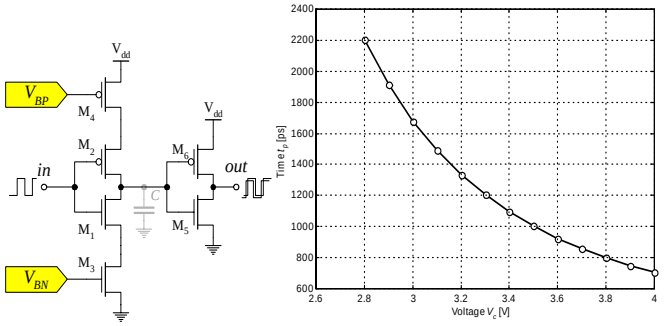

Fig. 2. Current starved delay element a) scheme and b) typical characteristic delay in term of control voltage

Current starved delay elements are implemented using current inverters (transistors M_4 and M_3 in Fig. 2 a). By controlling the charging/discharging current of the output parasitic capacitor C, we can regulate the propagation delay of this element [1].

A. Delay: Analytical model

Time delay in analog voltage controlled delay elements are defined by the following formula [6]:

$$t_{delay} = \frac{C}{I_{cp}} V_{sw} \tag{1}$$

where: C is load output capacitance, I_{cp} corresponds to charging/discharging current of C, and V_{sw} is a clock buffer (inverter) swing voltage.

According to Eq. (1), linear delay variation, t_{delay}, is possible to achieve if either C or V_{sw} varies linearly. Let now analyze both cases:

a) **Capacitor, *C***: load capacitor can take one of the following two forms: parasitic or integrated. The parasitic capacitor depends of technological parameters (length of wiring, layout, etc.) and for a given hardware structure has constant value. Integrated capacitors can be realized as fixed and variable. MOS capacitor is usually realized with fixed value. Its value is defined by technological parameters and silicon area. Variable capacitor is realized as inversely polarized PN junction and its value dominantly depends of the inverse voltage. Its capacitance in function of inverse voltage is nonlinear. Time delay regulation, defined by Eq. (1), can be realized only with variable capacitor, by changing its inverse control voltage, V_{ctrl}, but the transfer function, $t_{delay}=F(V_{ctrl})$, will be nonlinear. We do not propose this solution.

b) **Swing voltage, V_{SW}**: it is an input voltage level at which the state at the output of the clock buffer (inverter) changes. In standard inverter's realization $V_{SW} = V_{dd}/2$, and cannot be variable. If we replace the inverter with comparator, as is described in [6], then it is possible to achieve linear regulation of the swing voltage, i.e. linear delay regulation. Critical design block of this solution [6], from aspect of high-speed operation, is a comparator. This solution meets our design goal but only for low frequency operation.

III. BIAS CIRCUIT WITH RECIPROCAL CURRENT REGULATION

The bias circuit is building block of a delay element. It determines the magnitude of current I_{cp}, defined be Eq. (1). At its input the bias circuit is driven by a single ended control voltage, V_{ctrl}, while at the outputs it generates symmetrical bias voltages, V_{BP} and V_{BN} (see Fig. 3). Directly, V_{BP} and V_{BN} provide DC operating conditions for inverter's current transistors, M_2 and M_3, while indirectly they determine the charging/discharging current, I_{cp}, of a parasitic inverter's load capacitor C_{load}.

In standard realizations [2], we have that $I_{cp}=k\cdot V_{ctrl}$, where the term k is a constant determined by a bias circuit structure. Analyzing Eq. (1), under condition that $I_{cp}=k\cdot V_{ctrl}$ is valid, we conclude that $t_{delay}=f(V_{ctrl})$ is a non-linear function. Our motivation now is to modify the structure of a standard bias circuit described in [2] in such a way that the transfer function $t_{delay}=F(V_{ctrl})$ is linear.

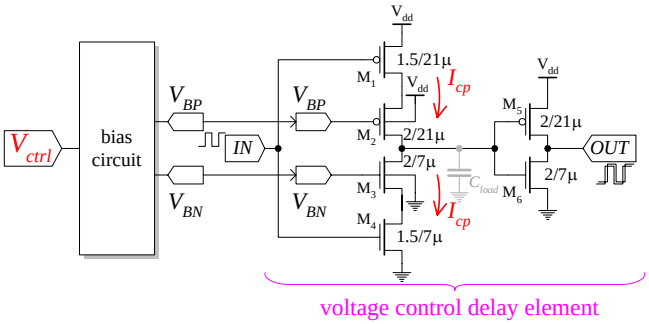

Fig. 3. Voltage control element and bias circuits

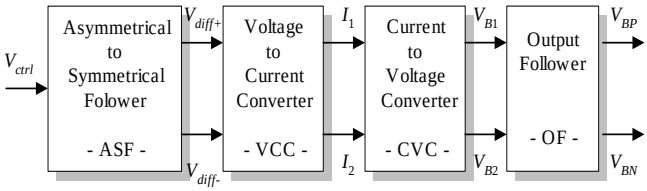

Fig. 4. Block scheme of bias circuit

Our proposal related to novel design of the bias circuit, at block schematic level, is sketched in Fig. 4. As can be seen from Fig. 4. the bias circuit is composed of four serially connected blocks. The first block in a chain, Asymmetrical-to-Symmetrical-Follower (ASF), converts the single ended control voltage V_{ctrl} into differential form represented by two output signals V_{diff+} and V_{diff-}, respectively. The second block, Voltage-to-Current-Converter (VCC), linearly converts the symmetrical input voltages, $+V_{diff}$ and $-V_{diff}$, into symmetrical outputs currents I_1 an I_2, respectively. The third block, Current-to-Voltage-Converter (CVC), converts the currents I_1 and I_2 into voltages V_{B1} and V_{B2}. The conversion process is non-linear and is based on the square route MOSFET transfer function [8]. Finally, the last block in a chain called Output-Follower (OF) converts the asymmetrical input voltage V_{B1} into two voltages V_{BP} and V_{BN}. These output voltages are used for polarization of the delay element stage (see Fig. 3).

Structures of blocks VCC, CVC and OF, at transistor level, are pictured in Fig. 5. Transistors M_{B1} (M_{B2}), M_{B3} (M_{B4}) and M_{B5} (M_{B6}) are constituents of VCC and form a band-gap current source I_0' (I_0")=12.5µA. Transistors M_{D1} and M_{D2} are parts of the VCC's differential input stage. Output currents I_1 and I_2, are defined by the following relations

$$I_1 = I_0^{'} + \frac{V_{diff}}{R} \quad \text{and} \quad I_2 = I_0^{''} - \frac{V_{diff}}{R} \tag{2}$$

where R is a resistor connected between sources of transistors M_{D1} and M_{D2}, and $V_{diff} = V_{diff+} - V_{diff-}$. According to Eq. (2), we conclude that a linear dependence exists between the input voltage V_{diff} and output currents I_1 and I_2, respectively.

Transistors M_{A1} and M_{A2} are parts of CVC, and act as active load resistors. The CVC's output voltages V_{B1} and V_{B2} are defined as

$$V_{B1} = \sqrt{\frac{I_1}{k_n}} + V_{tn} \quad \text{and} \quad V_{B2} = \sqrt{\frac{I_2}{k_n}} + V_{tn} \tag{3}$$

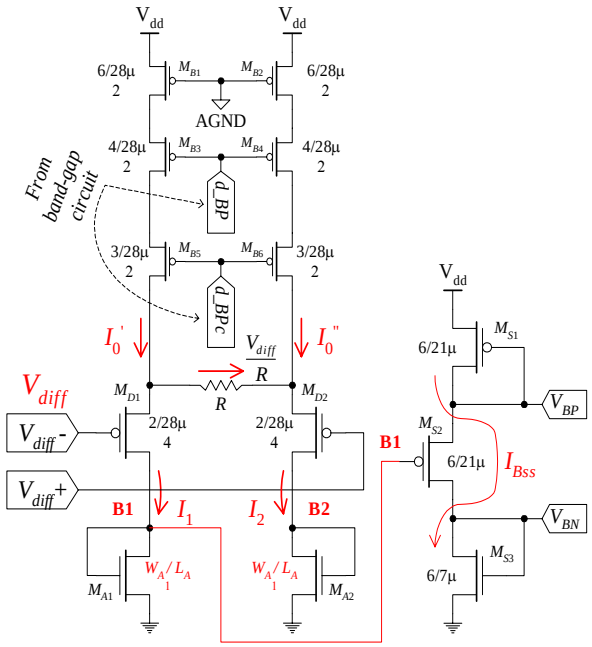

Fig. 5. Scheme of a bias circuit

The voltage V_{B1} drives the stage OF. At the outputs of OF two voltages, V_{BP} and V_{BN}, that are used for polarization of current starved delay elements, are generated.

The current I_{Bss} through transistors M_{s1}, M_{s2} and M_{s3}, see Fig. 5, is defined by the following formulas

$$I_{Bss} = k_p\left(V_{dd} - V_{BP} - V_{tp}\right)^2 \tag{4}$$

$$I_{Bss} = k_p\left(V_{BP} - V_{B1} - V_{tp}\right)^2 \tag{5}$$

from Eq. (4) we obtain

$$V_{BP} = V_{dd} - V_{tp} - \sqrt{\frac{I_{Bss}}{k_p}} \tag{6}$$

after substituting Eqs. (6) into (5) on obtain

$$I_{cp} = k_p\left(V_{dd} - 2V_{tp} - \sqrt{\frac{I_{cp}}{k_p}} - V_{B1}\right)^2 \tag{7}$$

where I_{Bss} is equal to I_{cp} since the composition of bias stage OF and a delay element forms two pairs of current mirrors (transistors M_{s1} (M_{s3}) and M_2 (M_3)) sketched in Fig. 5. By rearranging Eq. (7) we obtain

$$I_{cp} = \frac{k_p}{4}\left(V_{dd} - 2V_{tp} - V_{B1}\right)^2 \tag{8}$$

Finally, if we substitute V_{B1} from Eq. (3) we have

$$I_{cp} = \frac{k_p}{4}\left(V_{dd} - 2V_{tp} - V_{tn} - \sqrt{\frac{I_1}{k_n}}\right)^2 \tag{9}$$

Eq. (9) can be represented in the following form

$$I_{cp} = A + B\cdot\sqrt{I_1} + C\cdot I_1 \tag{10}$$

where constants A, B and C are equal to

$$A = \frac{k_p}{4}\left(V_{dd} - 2V_{tp} - V_{tn}\right)^2,\quad B = -\frac{k_p}{4}\frac{2\left(V_{dd} - 2V_{tp} - V_{tn}\right)}{\sqrt{k_n}},\quad C = \frac{1}{4}\cdot\frac{k_p}{k_n}.$$

Let note that Eq. (10) approximates a reciprocal relation between the current I_{cp} and control voltage V_{diff}.

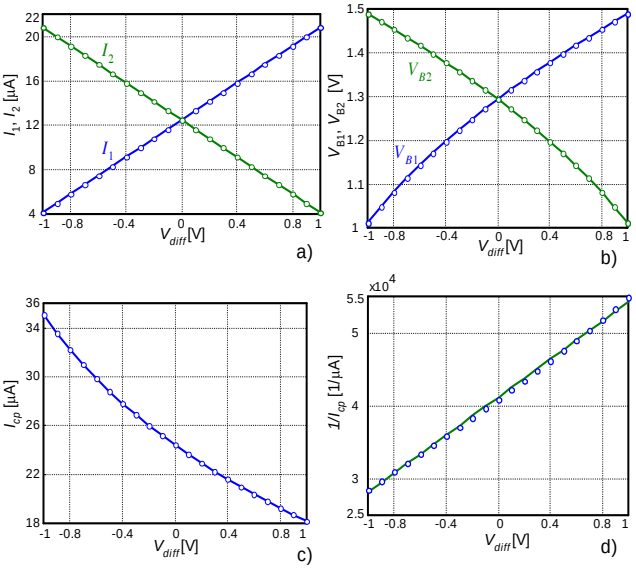

Fig. 6. Dependencies among output currents and input voltages of a bias circuit given in Fig. 5. according to the analytical model

In order to test the derived the analytical model, we will use the following technological and operating parameters for 1.2 µm CMOS technology:

C_{ox}=1.41e-3 F/m^2; μ_p=195E-4 m^2/V*s; μ_n=555E-4 m^2/V*s; k_n=0.5*78.255 µA/V^2; k_p=0.5*27.495 µA/V^2; V_{tn}=0.6259V; V_{tp}=1.14V; I_0=12.5µA; R=120kΩ; V_{dd}=5V;

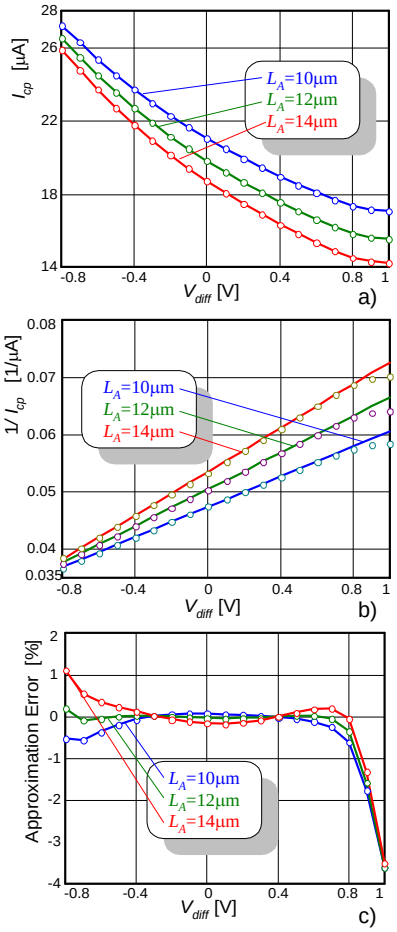

Fig. 7. HSpice simulation of biacircuits

By using the proposed analytical model, dependencies of currents (I_1, I_2 and I_{cp}) and voltages (V_{B1} and V_{B2}) in a bias circuit are calculated by a program Matlab in four steps (see Fig 6. According to Fig. 6 c) and d) we can conclude that the approximation is possible within a range I_{cp_max}:I_{cp_min} =36μA:18μA=2:1.

The design of bias circuit is verified using HSpice simulation. During simulation are used models of level 47 that correspond to 1.2μm double-metal double-poly CMOS technology. As simulation's parameter the channel length, L_A, of NMOS transistors, M_{A1} and M_{A2}, was used. Let note that M_{A1} and M_{A2} represent active loads for the CVC block. Active load NMOS transistors channel length L_A, of transitors M_{A1} and M_{A2}, defines the parameter $k_n=(\mu_n C_{ox}/2)*(W_A/L_A)$ in Eq. (10). During simulations, three different L_A values that correspond to 10, 12 and 14 μm, for supply voltage V_{dd}=5V and temperature T=27°C as constants, were used. The obtained simulation results are presented in Fig. 7.

As a conclusion, HSpice simulation of a bias circuit confirms that between the delay elements charge current I_{cp} and the control voltage V_{diff} a reciprocal relation exists. Relative approximation error is less then 1%, when the control voltage is in a range of ±0.8V.

IV. Current Starved Delay Line with Linear Delay Regulation

Our proposal concerning realization of the delay line consists of four delay element stages (see Fig. 8). As can be seen from Fig. 8, each stage is composed of voltage controlled delay element, VCDE$_i$, and an output buffer, OB$_i$, i = 1,..,4. VCDEs are of standard current starved delay elements sketched in Fig. 4, while OBs are realized with two large inverters connected in cascode. According to Fig. 8, the bias circuit is constituent of the delay line.

HSpice simulations results that relate to the delay line are presented in Fig 10. Models of level 47, for 1.2μm CMOS technology, during simulation, were used.

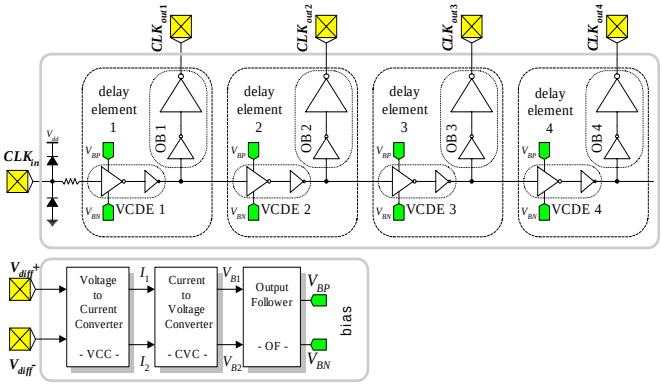

Fig. 8. Four stage delay line block scheme

During simulation, dimensions of bias circuit's active load transistors were selected to be W_A/L_A=14μm/14μm, the supply voltage was V_{dd}=5V and temperature T=27°C. Simulation results concerning delay line characteristics, for both leading and trailing clock edges, in term of control voltage, are pictured in Fig. 9 a). The appropriate absolute value of non-linearity error, in function of the control voltage, is given in Fig. 9 b). The delay line is operative within the frequency range from 20 to 33MHz. According to the obtained results, (see Fig. 9 b) we see that the linearity error is less then 500ps when the control voltage varies in the range of ±0.8V.

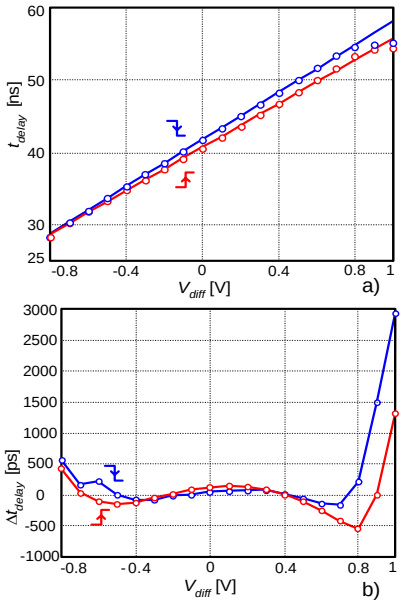

Fig. 9. HSpice simulation of time delay t_{delay} in term of control voltage V_{diff}

V. Conclusion

In this paper, we describe an implementation of a linear voltage controlled delay line. The delay line is constituent of the DLL circuit. HSpice simulation results points to the fact that for 1.2μm CMOS technology high delay linearity (< 500 ps) within the full range of regulation (from 30 to 60 ns) is achieved.

References

[1] Y.Moon, et al., "An All-Analog Multiphase Delay-Locked Loop Using a Replica Delay Line for Wide-Range Operation and Low-Jitter Performance", *IEEE JSSC*, vol.35, No. 3, pp. 377-384, March 2000.

[2] M. Maymandi-Nejad, M. Sachdev, "A digitally Programmable Delay Element: Design and Analysis", *IEEE Trans. on VLSI Systems*, vol. 11, No. 5, October 2003.

[3] M. Fenghao, C. Svensson, "Pulsewidth Control Loop in High-Speed CMOS Clock Buffers", *IEEE JSSC*, vol. 35, No. 2, pp. 134-141, February 2000.

[4] P. Dudeck et al., "A high–resolution CMOS time–to–digital converter utilizing a vernier delay line", *IEEE JSSC*, vol. 35, No. 2, pp. 240–246, February 2000.

[5] J. Chiang and K. Chen, "The Design of an All-Digital Phase-Locked Loop with Small DCO Hardware and Fast Phase Lock", *IEEE Trans. on CAS–II*, vol. 46, No. 7, pp. 945-950, July 1999.

[6] G. Jovanović, M. Stojčev, "Voltage Controlled Delay Line for Digital Signal", *Facta Universitatis, Series: Electronics and Energetic*, vol. 16. No. 2, pp. 215-232, August 2003.

[7] A. Hatakeyama, et al., "A 256-Mb SDRAM Using a Register-Controlled Digital DLL", IEEE JSSC, vol. 32, No. 11, 1997.

[8] K. Bult, H.Wallinga, "A Class of Analog CMOS Circuits Based on the Square-Law Characteristic of an MOS Transistor in Saturation", IEEE JSSC, vol. 22, No.3, pp. 357-365, June 1987

Study of a Galvanomagnetic Digital-to-Analogue Converter

Anatolii T. Aleksandrov[1], Nikola D. Draganov[2]

Abstract - **The paper studies a galvanomagnetic digital-to-analogue converter, built around specialized ICs LM2917 and MLX1881. A schematic circuit diagram has been developed. The paper presents the conversion characteristics obtained by experiment and determines the optimal range of input variable conversion. It also studies the influence of the adjusting elements (resistor and capacitor) and the supply voltage upon the power consumption and the frequency range.**

Keywords – **galvanomagnetic sensors, magneto-sensitive integrated circuits, control, regulator, digital-to-analogue converter**

I. INTRODUCTION

The measurement of electric and non-electric quantities is a major task of modern electronic systems, the solution of which allows their adaptation to the control environment. Therefore it is necessary to develop new devices and to improve the existing ones designed for conversion and processing of the quantities measured with a greater accuracy, sensitivity and variation range. They find application in electronics, automation, electrical appliances, chemistry, medicine, etc., where the measurement and control of environment parameters is of utmost importance for the device operation or for correct analysis [5].

There are various devices available for magnetic field sensing. Most of them are based on a Hall element. The development of microelectronics has enabled the development of integrated circuits with built-in Hall elements, allowing not only detecting, but also processing of the signal [1, 2, 3, 4, 6].

The aim of the work presented in the paper is the synthesis of a galvanomagnetic digital-to-analogue converter, allowing detection of a pulse-varying magnetic field.

II. PRESENTATION

A galvanomagnetic digital-to-analogue converter has been developed, based on specialized integrated circuits MLX1881 and LM2917, whose flow chart is presented in Fig. 1. It consists of a magneto-sensitive integrated circuit (MSIC), frequency-to-voltage converter unit, a supply unit and a tuning unit

[1] Anatolii T. Aleksandrov is with the Technical University, 4 H. Dimitar str. 5300 Gabrovo, Bulgaria, E-mail: alex@tugab.bg

[2] Nikola D. Draganov is with the Technical University, 4 H. Dimitar str. 5300 Gabrovo, Bulgaria, E-mail: nikola_draganov@mail.bg

The magneto-sensitive integrated circuit MLX1881 manufactured by *Melexis* exhibits stable conversion characteristics and high sensitivity. The MSIC output is a digital signal having frequency proportional to the magnetic field frequency.

The frequency-to-voltage converter is of the LM2917 type of *National Semiconductor*, enabling a common indicating instrument to be connected at its output.

The tuning unit consists of elements (capacitors C_1, C_2 and resistor R_4) accomplishing a change in the conversion characteristics and the sensitivity of the frequency-to-voltage converter.

The schematic circuit diagram of the galvanomagnetic digital-to-analogue converter is presented in Fig. 6.

The circuit operation consists in conversion of the magnetic pulses sent to the MSIC into a voltage level proportional to the pulse variation frequency.

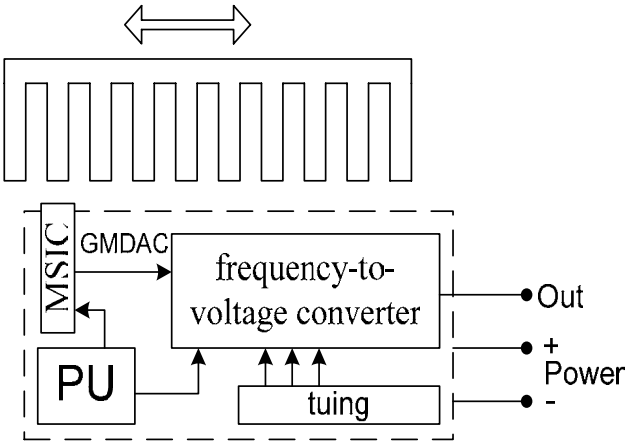

Fig. 1 Flow chart of a galvanomagnetic digital-to-analogue converter

A pulse series is generated when supply voltage is fed to the MSIC output and when there are magnetic pulses of certain frequency there. The frequency of the pulse series is completely identical with the frequency of the magnetic pulses. The signal from the MSIC output is entered at the frequency-to-voltage converter input, built around integrated circuit LM2917, and is converted from pulse into analogue voltage signal. The converter operation mode is regulated by means of tuning capacitors C_1, C_2 and resistor R_4.

With view to choosing an optimal operation mode, experimental tests have been carried out, which show the way the output voltage U_0 changes with the value of resistance R4 and the capacitance of capacitors C_1 and C_2. Fig. 2 shows the dependence of output voltage U_0 on the capacitance of capacitor C_2 $U_0=\varphi(C_2)$ when resistor R_4 = 100kΩ, capacitor C_1 = 1μF and supply voltage U_{DD} = 12V, while Fig. 3 shows

the transfer characteristics $U_0 = \varphi(f)$ depending on the value of resistance R_4.

The analysis of the results obtained shows:

- as the value of capacitor C_2 rises, the range within which the output voltage varies for the same frequency range widens, and therefore the sensitivity of the galvanomagnetic converter increases;
- when the resistance value rises to 250kΩ, a rise in the conversion transconductance and dynamics is observed.

The way in which U_0 varies is due to the attenuator functions of resistor R_4 resistance and capacitor C_1 capacitance in the frequency-to-voltage converter. These functions determine the dynamics of the entire converter. As can be seen in Fig. 4, the optimal value of this resistance is 100kΩ, since it covers the entire frequency range of the converter.

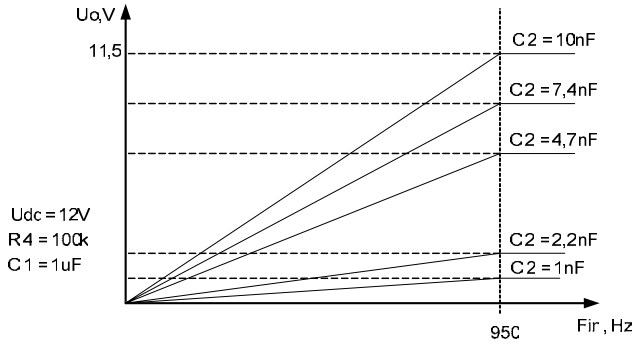

Fig. 2 Influence of the capacitor C_2 value on the change in the transient response

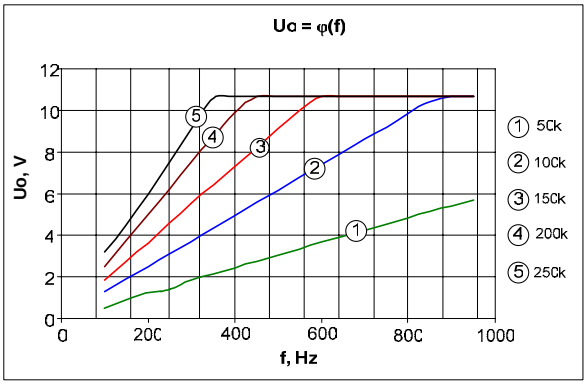

Fig. 3 Family of transfer characteristics showing the influence of R4 on the converter dynamics

The influence of the capacitor C_1 value on the value of the output voltage U_0 is analogous. When its value is raised, a rise in the circuit dynamics is observed. The maximum value of capacitor C_1 is 1μF.

The values of the tuning elements C_1, C_2 and R_4 are determined entirely subject to the converter range obtained by experiment, presented graphically in Fig. 4.

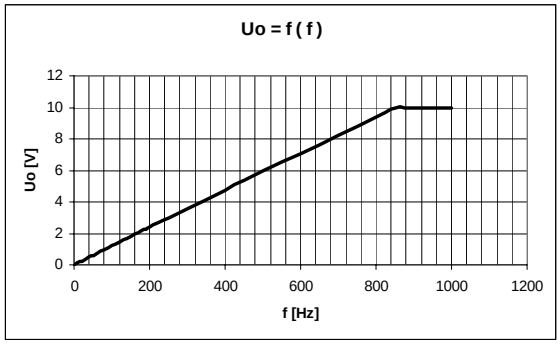

Fig. 4 Transfer characteristic of the converter determining the frequency range

III. CONCLUSION

1. A galvanomagnetic converter has been developed based on a magneto-sensitive integrated circuit MLX1881 manufactured by *Melexis* and an integrated frequency-to-voltage converter LM2917 manufactured by *National Semiconductor*. A flow chart and a schematic circuit diagram have been developed and experimental transient responses are shown, giving idea about the conversion range of the input variable.

2. A good sensitivity and stability of the transfer characteristic (Fig. 4) is achieved by means of the tuning elements, as well as capability of adequate response in case of abrupt changes in the input value.

3. By using an integrated frequency-to-voltage converter, a relatively low power consumption of the device can be achieved (Fig. 5).

4. The proposed device can be applied in speed monitoring and control systems of rotating or linear-displacement mechanisms, namely in devices for monitoring and automatic regulation of electric motor rotation frequency, for various applications in the automobile industry, etc.

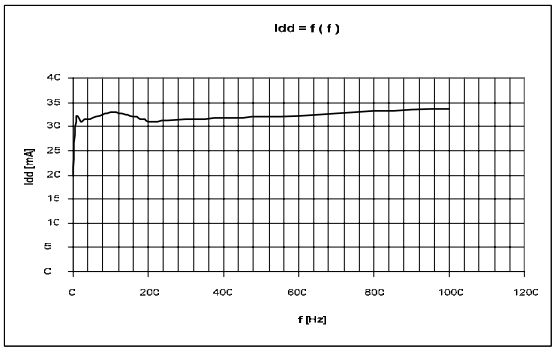

Fig. 5 Power consumption of the device with different values of the input variable

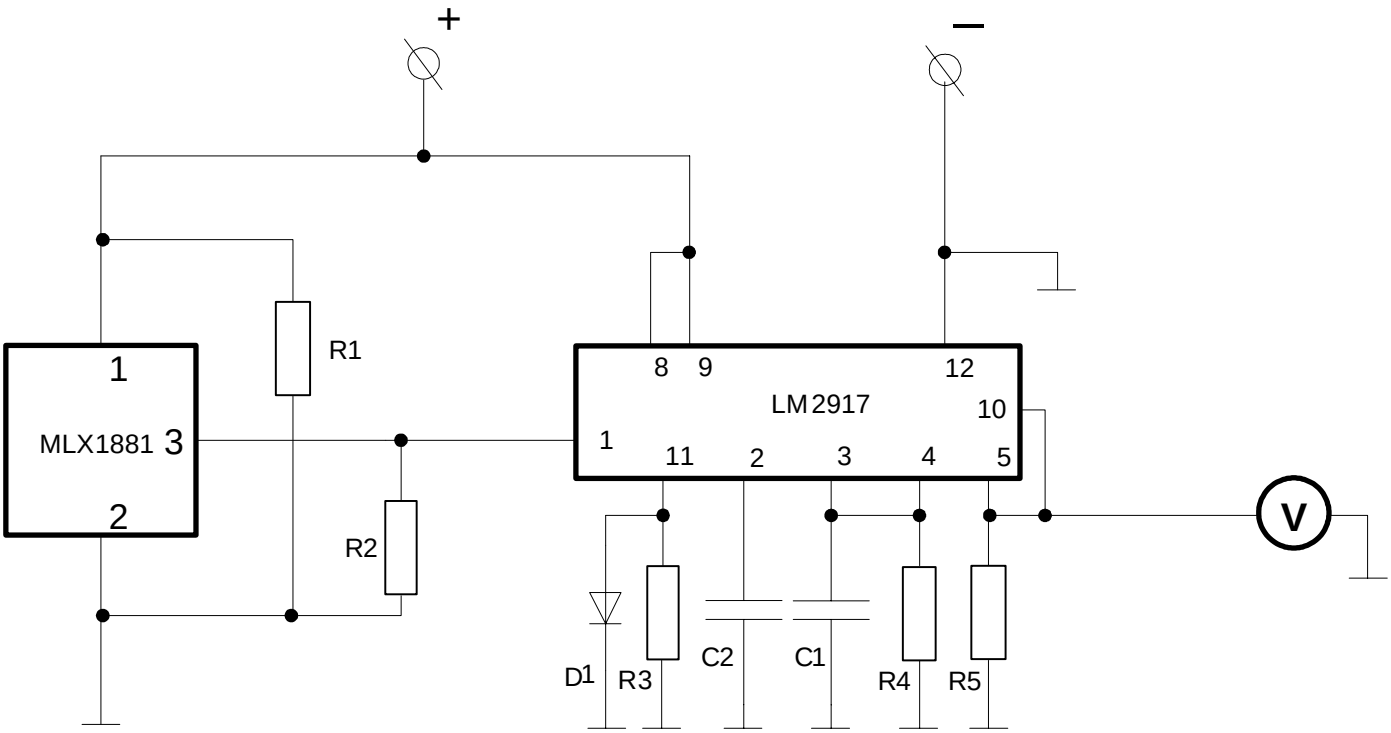

Fig. 6 Schematic circuit diagram of a galvanomagnetic digital-to-analogue converter

IV. REFERENCES

[1] Alexandrov A. T., I. S. Simeonov, “Galvanomagnetic Device for Electric Current Measurement”, Journal of the Technical University of Gabrovo, vol. XXIV/00 (in Bulgarian).

[2] [2] Nikolov D., “Application of Sensors for Magnetic Field in Measurement of Linear and Angular Displacement”, Avtomatika i Informatika Journal, issue 4, 1998 (in Bulgarian)

[3] Rumenin Ch., “Multisensors for Magnetic Field and Temperature in Contactless Wattmeters”, Avtomatika i Informatika Journal, issue 5, 1998 (in Bulgarian).

[4] Takov T., “Semiconductor Sensors”, Tehnika, Sofia, 1986 (in Bulgarian).

[5] Göpel W., J. Hesse, J. N. Zemel, SENSORS, A Comprehensive Survey Vol.1, “Fundamentals and General Aspects”, VCH, Weinheim, 1989.

[6] Göpel W., J. Hesse, J. N. Zemel, SENSORS, A Comprehensive Survey Vol.5, “Magnetic Sensors”, VCH, Weinheim, 1989.

Galvanomagnetic Regulator of Induction Motor Rotation Frequency

Anatolii T. Aleksandrov[1], Nikola D. Draganov[2]

Abstract – **Galvanomagnetic ICs exhibit stable conversion characteristics, high sensitivity and have small dimensions and a low price. On the basis of their advantages, a regulator of induction motor rotation frequency with a galvanomagnetic analogue-to-digital converter has been developed, built around specialized ICs LM2917 and MLX1881. The system provides for both rotation frequency regulation and process monitoring. The paper presents the synthesized flow chart and schematic diagram of the regulator. It studies its operation algorithm and manifests its conversion characteristics.**

Keywords - **galvanomagnetic sensors, magneto-sensitive integrated circuits, control, regulator, digital-to-analogue converter**

I. Introduction

Modern electronic and automatic systems in the area of electronics, chemistry, medicine, food industry normally have an induction motor as its major component and its rotation frequency needs to be regulated. This stems from the necessity for providing the optimal speed for the manufacturing processes.

There are various methods and devices available for rotation frequency regulation. They are differentiated by several basic criteria, the most important of them being the type of the process control system – open (without feedback) or closed-loop (with a feedback). The devices available for rotation frequency regulation also differ in the elements providing the feedback – direct (when the rotation frequency is monitored) and indirect (when the current in the stator winding is monitored), as well as in the way of regulation [1, 3, 4].

Over the last few years the development of microelectronics has brought about the introduction of galvanomagnetic sensors in many areas of electronics, automatics, electric drives. Magneto-sensitive integrated circuits (MSICs) have been developed, based on a Hall sensor, which are characterized by low price, high sensitivity and linear conversion characteristics [3, 5, 6, 7, 8].

The aim of the work presented in the paper is the synthesis and study of a galvanomagnetic device, allowing the regulation of induction motor rotation frequency.

[1] Anatolii T. Aleksandrov is with the Technical University, 4 H. Dimitar str. 5300 Gabrovo, Bulgaria, E-mail: alex@tugab.bg

[2] Nikola D. Draganov is with the Technical University, 4 H. Dimitar str. 5300 Gabrovo, Bulgaria, E-mail: nikola_draganov@mail.bg

II. Presentation

A regulator of induction motor rotation frequency has been synthesized, built around a galvanomagnetic analogue-to-digital converter based on specialized ICs LM2917 and MLX1881. The flow chart of the device is presented in Fig. 1. It consists of a galvanomagnetic digital-to-analogue converter (GMDAC), a control unit (CU), a supply unit (power supply) and an induction motor (IM).

The GMDAC has been synthesized on the basis of a magnetosensitive integrated circuit MLX1881 manufactured by Melexis and an integrated frequency-to-voltage converter LM2917 manufactured by National Semiconductor [2]. This unit makes it possible to monitor and convert the rotation frequency of the induction motor rotor, proportional to the change in output voltage. The GMDAC entirely replaces the devices that have been used so far for monitoring of rotor rotation frequency, including tachogenerators, rotary incremental encoders, etc.

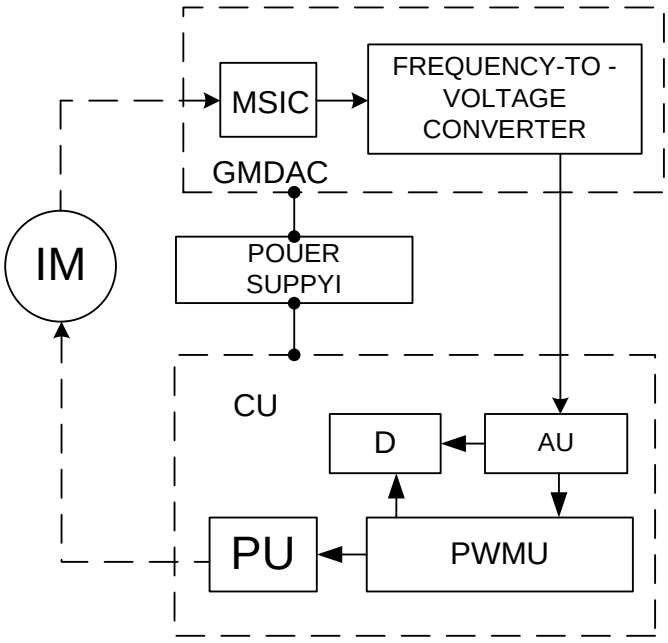

Fig. 1. Flow chart of a galvanomagnetic regulator of induction motor rotation frequency

The rotation frequency monitoring in the GMDAC is performed by a magneto-sensitive IC, which is mounted in the IM stator. This IC has been developed using MOS technology and is able to sense magnetic fields with minimum intensity $B_{min}=5mT$. This allows it to be built in electric motors having different powers. As a result of the rotor rotation, the MSIC generates a pulse series with

frequency proportional to the rotor rotation frequency. Using the frequency-to-voltage converter, the pulse series from the MSIC is converted into proportionally varying voltage. The stable and linear conversion characteristics of MSIC MLX1881 and of the integrated converter LM2917 make it possible to precisely monitor and convert the induction motor rotation frequency.

The parameters characterizing the GMDAC, obtained after the latter has been studied [2], are as follows: maximum reading frequency f_{max}=850*Hz* , maximum output voltage at frequency f=850*Hz* and supply voltage U_{DD}=12*V* – U_{DD}=12*V*, current consumption at f=850*Hz* and U_{DD}=12*V* – I_{DD}=0,5*A*

The control unit consists of an assigning unit (AU), display (D), pulse-width modulation unit (PWMU) and power unit (PU).

The control unit establishes the way the system is controlled. Depending on that, the type of circuit solutions of the AU and PU is determined. In this case control through pulse-width modulation of the control signal is established, which ensures smooth characteristics and easy implementation.

The schematic diagram of the galvanomagnetic regulator of induction motor rotation frequency is presented in Fig. 4, and its operation principle is illustrated by means of the time charts in Fig. 2.

When the device is switched on, the electric motor starts to unwind up to a certain predefined speed. As a result of unwinding the IM rotor, the MSIC (IC 1) starts generating the pulse series ($U_{P1}=\varphi(t)$, (Fig. 2a), whose frequency is proportional to the rotor rotation frequency. The generated pulse series starts at the input of the integrated frequency-to-voltage converter (IC 2), which converts it to a voltage level. By means of the potentiometer-type voltage divider (R4, R5) and the trimmer potentiometer PR3, the voltage level is entered at the non-inverting input of the comparator IC 3.1. An assigning voltage level from the potentiometer-type voltage divider (R7, R8) and potentiometer PR6 is entered at the other input of the same comparator.

When the signal from the GMDAC (U_{P2}, Fig. 3b) becomes greater than the assigned one (U_{P3}, Fig. 3b), a high level (U_{P4}, Fig. 3c) is established at the comparator output IC 3.1. This high level is entered at the non-inverting input of the comparator IC 3.2. A signal (U_{P5}) from the saw-tooth voltage generator is entered at the other input of the same comparator, the generator consisting of an integrated circuit IC 3.3, resistors R9, R19, R11 and capacitor C2. The amplitude of the linearly varying voltage is 5*V*, and its frequency is 50 *Hz*.

As a result of the dynamic comparison of the levels – the assigned one and the one measured, a pulse series ($U_{P6}=\varphi(t)$) is obtained at the comparator output IC 3.2 (point p6, Fig. 4), with a variable mark-to-space ratio depending on the current value of the signal from the GMDAC, whose magnitude is proportional to the rotation frequency of the IM shaft.

The width-modulated signal controls a triac optocoupler IC4, which has a built-in null detector. Thanks to this feature, the optocoupler not only performs a galvanic sweep of the circuit, but also allows commutation of the switching element only when the supply mains voltage passes through zero.

The induction motor IM is connected in the power circuit of the triac switch S1. Its smooth control depends entirely on the frequency of the saw-tooth generator voltage.

Thus, whenever the motor rotation frequency decreases, mark-to-space ratio of the control pulses (U_{P6}, Fig. 2d) will increase, and consequently, the IM rotation frequency will increase to the level defined by the assigned voltage (U_{P3}, Fig. 2b).

The proposed device for regulation of IM rotation frequency makes it possible to measure and assign the rotation frequency. The display unit is built around a specialized integrated circuit ICL7107. It allows the control of a 3.5-digit LED display VD1. Depending on the position of switch K1, the measurement unit is positioned either in measurement mode (position 1) or in assignment mode (position 2) of the IM shaft rotation frequency. In assignment mode the signal is taken from the sliding switch of the assigning potentiometer PR6, while in measurement mode it is taken from the sliding switch of the trimmer potentiometer PR3. The modes can also be switched automatically with a minimum rotation of the potentiometer axis PR6.

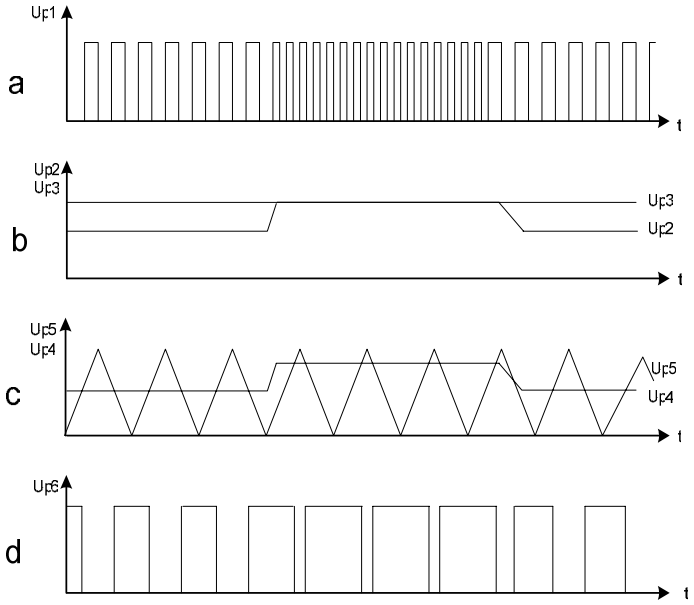

Fig. 2. Time charts illustrating the operation of the galvanomagnetic regulator of induction motor rotation frequency.

In order to prove the efficiency of the proposed galvanomagnetic regulator, experimental tests have been conducted with an IM, type BA 9/2, ~220V/50Hz (manufactured by "Al. Atanasov" Company, Etropole).

The following results have been obtained:

1. The galvanomagnetic device proposed allows: precise regulation of the induction motor rotation frequency within the range from 694 min^{-1} to 1838 min^{-1} with accuracy ±5% with only one magnetosensitive IC; smooth regulation by means of pulse-width modulation; monitoring of the controlled and assigned parameter (rotation frequency).

2. The functional characteristics of the proposed regulator depend mainly on the action of the GMDAC, whose conversion characteristics in optimum operation (*R2*=100*k*Ω,

C1=1*μF* **[2]**) mode are presented in Fig. 3. Their analysis shows:

-The dependence U_{P2}=φ(f) (Fig. 3a), characterizing the change in voltage at the GMDAC output (U_{P2}) upon the frequency (*f*) of the input voltage is linear up to 850 *Hz*, the output voltage varying 0*V* up to 10.2 *V*. Above 850 *Hz* the change in the rotation frequency of the IM shaft does not affect the magnitude of the output voltage and it remains equal to 10*V*. The transconductance in the operation interval is S = 85 *Hz/V*.

-The value of the current consumed I_{DD} remains relatively constant, and as the frequency changes *f* = 10 ÷ 1000 *Hz*, I_{DD} is within the range 31 ÷ 35 *mA* (Fig. 3b). This is an indicator for the operation of the synthesized frequency regulator in a stationary mode.

-The characteristics presented in Fig. 3c U_{P2}=φ(U_{DD}), illustrating the change in voltage at the GMDAC output depending on the supply voltage when the input signal has a frequency *f* = 100*Hz*; 250*Hz*; 500*Hz*; 750*Hz*; 900*Hz*, show that the sensitivity of the regulation device rises with the rise in frequency.

The experimental results obtained show that the synthesized frequency regulator operates steadily in the frequency range *f* = 10 ÷ 850*Hz*, and its sensitivity rises with the rise in frequency.

III. CONCLUSIONS

1. A galvanomagnetic device has been developed for regulation of induction motor rotation frequency, built around a magneto-sensitive integrated circuit MLX1881 manufactured by Melexis and an integrated frequency-to-voltage converter LM2917 manufactured by National Semiconductor. The flow chart and the schematic diagram of the regulator have been developed. Time charts are presented, which describe its operation.

2. An optimal operation interval has been established for the synthesized galvanomagnetic regulator: supply voltage U_{DD}=12*V*, regulation range from 694 min^{-1} to 1838 min^{-1} with accuracy ±5%, current consumption I_{DD}=0,8*A*. It has been determined on the basis of the tests conducted of the conversion characteristics of the galvanomagnetic analogue-to-digital converter, on which the functional characteristics of the regulator are mainly dependent.

3. The proposed galvanomagnetic device for regulation of induction motor rotation frequency is easy to adjust and manufacture, it exhibits small interference from the mains, due to the use of a Zero Cross optocoupler, has low cost and provides good operation. It also exhibits good sensitivity and is capable of adequate response to very fast or very slow rises or falls in the input quantity.

4. The proposed galvanomagnetic regulator of induction motor rotation frequency provides a further concrete application of digital magneto-sensitive integrated circuits.

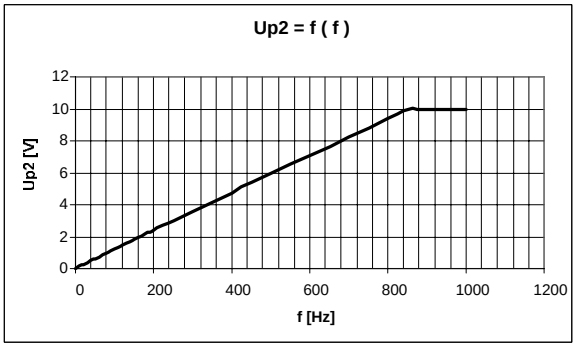

a

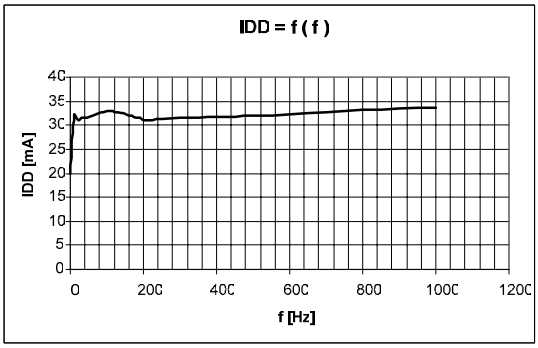

b

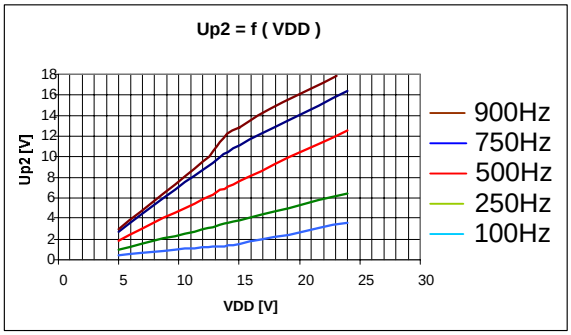

c

Fig. 3. Conversion characteristics of the galvanomagnetic digital-to-analogue converter

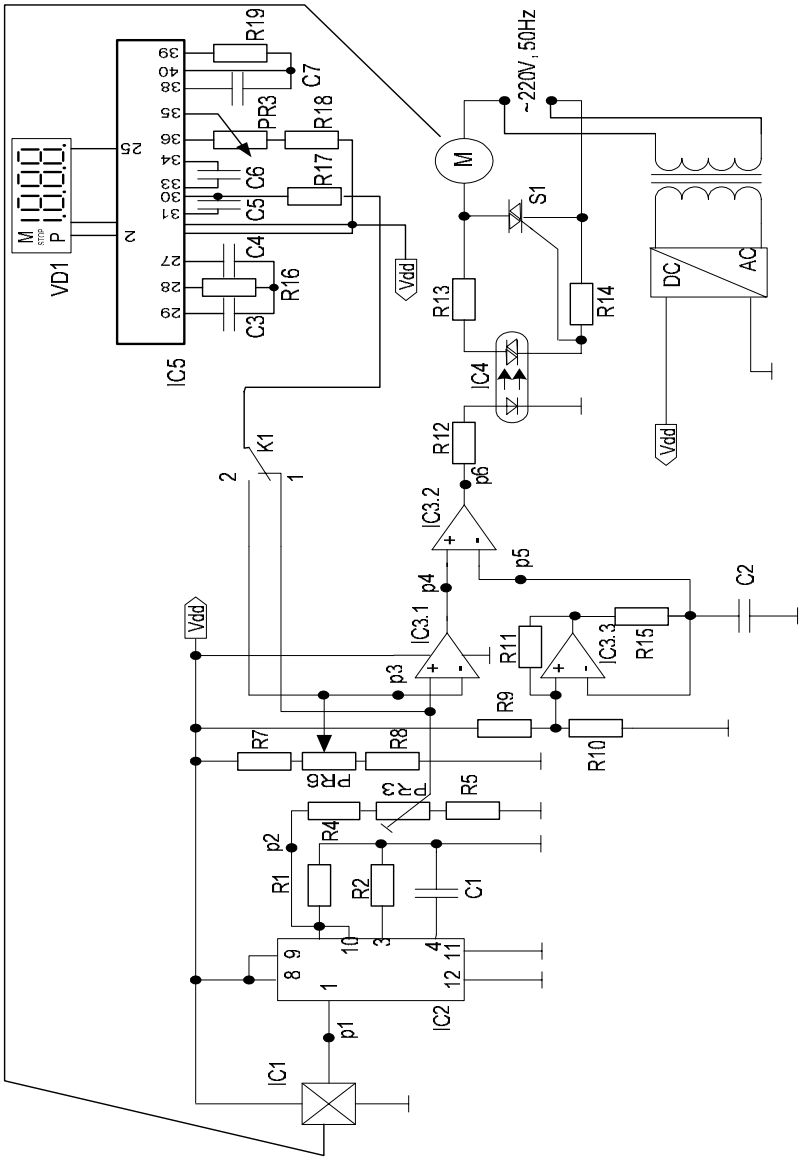

Fig. 4. Schematic diagram of a galvanomagnetic regulator of induction motor rotation frequency

REFERENCES

[1] Aleksandrov A. T., I. S. Simeonov, „Galvanomagnetic device for measuring of electric current", Bulletin of Technical university of Gabrovo, Vol. XXIV/00.

[2] Aleksandrov A., N.Draganov, "Investigation of galvanomagnetic digital-to-analog converter", ICEST 2005.

[3] Georgiev P., "Electronics regulatort of electric-leading ", "Vasil Aprilov", Gabrovo 1999.

[4] Radev R., "Control theory", Classical Methods, Part 1, "ALMA MATER International", Gabrovo 1999.

[5] Rumenin Ch., „Multisensors for magnetic field and temperature in non-contact wattmeter", magazine „Avtomatika I informatika", number 5, 1998.

[6] Takov T., „Semi-conductors sensors ", „Technics", Sofia, 1986.

[7] Göpel W., J. Hesse, J. N. Zemel, SENSORS, A Comprehensive Survey Vol. 1, "Fundamentals and General Aspects", VCH, Weinheim, 1989.

[8] Göpel W., J. Hesse, J. N. Zemel, SENSORS, A Comprehensive Survey Vol. 5, "Magnetic Sensors", VCH, Weinheim, 1989.

Analysis and Design of Voltage Controlled LC Amplifiers using Current-Feedback Amplifiers

Ivailo M. Pandiev[1]

Abstract - **This paper discusses the development of a specific type of voltage controlled LC amplifier using a current-feedback amplifier (CFA). The center frequency of the proposed selective amplifier is controlled by applying a voltage to the parallel resonator with varactor capacitive branch. The main advantage of this new configuration is the insignificant influence of the load over the parameters of the amplifier. Some recommendations for designing this kind of analogue circuit are given based on simulation results and symbol analysis of the transfer function. To confirm the validity of the design procedure, simulation results are compared with measurements of the electrical parameters in a practical LC amplifier, where is found good agreement between simulations and measurements.**

Keywords – **LC amplifier, Current-Feedback Amplifier (CFA), Frequency control, Varactor tuning, PSpice simulations.**

I. INTRODUCTION

The voltage controlled LC amplifiers (LC-tuned amplifiers) and LC oscillators (VCOs) are essential building blocks of contemporary communication systems [2]-[4]. Simultaneously the new CFA are gaining popularity as alternative building blocks for analogue signal processing because of offering advantages over the conventional op amps. The main advantages are wide bandwidth which is relatively independent of the closed-loop gain, very high slew rate and simplicity of realization of various functions with the least possible number of external passive components.

The symbolic representation of CFA based on the second-generation current conveyor (CCII) is shown in Fig. 1. The

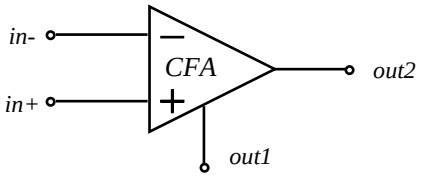

Fig. 1. The CFA symbol

main difference between the CFA and the CCII is the unity gain voltage buffering of the *out1* compensation terminal of the CCII to obtain the *out2* output terminal of the CFA [5]. The output terminal of the CFA is low impedance (voltage source) and the compensation terminal is high impedance (current source). This high impedance in the terminal *out1* allows connect a parallel resonator (LC tank) with varactor capacitive branch. In [8] is proposed LC amplifier using CFA with compensation terminal and LC tank. This circuit simple can be converted into LC-tuned amplifier by replacing the capacitor in the resonator with series back-to-back connection of two varactors. This paper presents a new LC-tunrd amplifier using CFA with compensation terminal and resonator consists of inductor and series connection of varactors. The proposed analogue circuit has the following advantages over the single transistor LC amplifier: (1) the insignificant influence of the load over the parameters of the LC tank; (2) ability for independent fine tuning of voltage gain, Q factor, and center frequency; (3) high input and low output resistance.

II. CIRCUIT DESCRIPTION

The proposed circuit of the voltage controlled LC amplifier is shown in Fig. 2. It is based on a CFA with compensation terminal and with negative voltage feedback, implemented with the resistors R_1 and R_2. This configuration achieves higher input impedance compared to the inverting amplifier. The capacitor C_1 made the voltage feedback frequency-dependence. A parallel LC tank was connected to the additional op amp compensation terminal (*out1* in Fig. 2), where the input resistance is very high. The LC tank consists

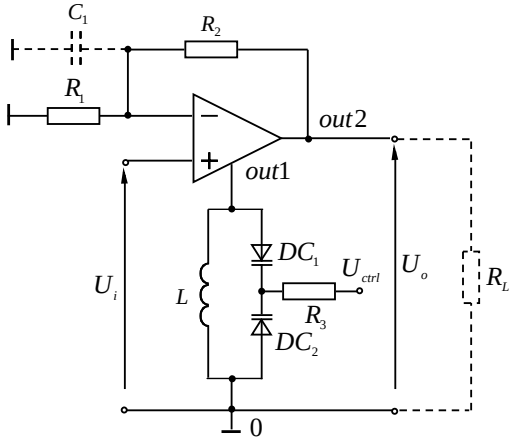

Fig. 2. LC-tuned amplifier using CFA with correction terminal

of inductor L and series back-to-back connection of two varactors (DC_1 and DC_2). This connection allows lower capacitance at high dc control voltages (U_{ctrl}) compared to maintaining the tuning ratio of a single varactor. The back-to-back varactor connection also helps reduce distortion and effect of mounting capacitances.

The analysis of the proposed LC amplifier was performed using nodal voltage method and the equivalent circuit shown in Fig. 3. In the equivalent circuit CFA is substituted with

[1]Ivailo M. Pandiev is with the Faculty of Electronics from Technical University of Sofia, Kliment Ohridski 8, 1000 Sofia, Bulgaria. E-mail: ipandiev@tu-sofia.bg

linear macromodel which represent the small-signal behavior of the real devices [9]. This model includes the following elements: ideal input and output buffer (voltage follower); controlled current source (I_{in}); resistance of the inverting input (R_{in}); active and reactive components (R_t and C_t) of the transmission resistance z_t ; output resistance (R_o). The inductor L of the resonator can be presented with serial-parallel equivalent circuit, as shown in Fig. 3. The active resistance r_L of the inductor determines the losses, and C_a is the parasitic capacitance of the pins. The varactors are substituted with the parallel equivalent circuits as shown in

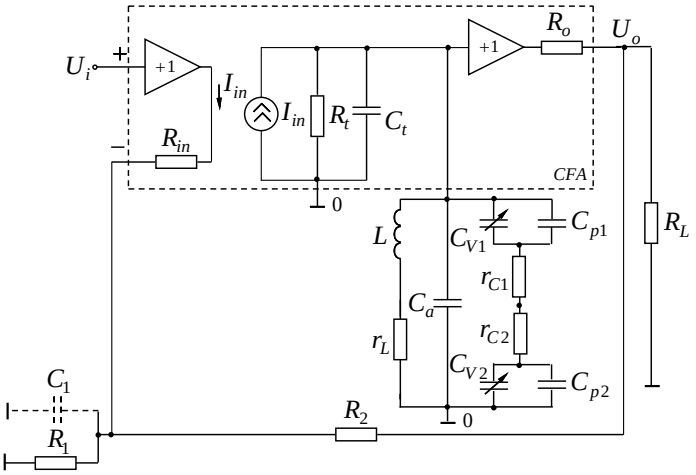

Fig. 3. Equivalent circuit of the LC-tuned amplifier using CFA with correction terminal.

Fig. 3, where $C_{v(1,2)}$ is a varactor capacitance, $r_{c(1,2)}$ is a series resistance determines the losses and $C_{p(1,2)}$ is a mounting capacitance between pins. According to the SPICE model, varactor capacitance $C_{v(1,2)}$ is a function of the applied reverse dc voltage (U_{ctrl}) and can be expressed as follows:

$$C_v = \frac{C_{JO}}{\left(1+\frac{U_{ctrl}}{U_J}\right)^m} + C_p , \qquad (1)$$

where C_{JO} is a zero-bias junction capacitance, U_J – junction potential, and m – grading coefficient (0,5 by default).

The Y-matrix of the circuit with load R_L was composed using the well-known formulas introduced in [1], and after the transformations is obtained the following expression for the transfer function:

$$\dot{A}_U = \frac{1+\frac{R_2}{R_1}+j\omega C_1 R_2}{\left[1+\frac{R_2}{R_{re}}\left(1+\frac{R_{in}}{R_1}+\frac{R_{in}}{R_2}\right)\left(1+\frac{R_o}{R_L}\right)\right]\left[1+jQ_e\left(\frac{\omega}{\omega_o}-\frac{\omega_o}{\omega}\right)\right]}, \qquad (2)$$

where equivalent quality factor of the amplifier is

$$Q_e = \frac{R_2\left(1+\frac{R_{in}}{R_1}+\frac{R_{in}}{R_2}\right)\left(1+\frac{R_o}{R_L}\right)}{\rho\left[1+\frac{R_2}{R_{re}}\left(1+\frac{R_{in}}{R_1}+\frac{R_{in}}{R_2}\right)\left(1+\frac{R_o}{R_L}\right)\right]}, \qquad (3)$$

characteristic resistance of the LC tank is

$$\rho = \sqrt{L/C_e} , \qquad (4)$$

equivalent resonance resistance of the LC tank is

$$R_{re} = R_{rL} \,||\, R_{rC} \,||\, R_3 \,||\, R_t \qquad (5)$$

($R_{rL} = \rho^2 / r_L$, $R_{rC} = \rho^2 / r_{C_e}$, $r_{C_e} = r_{C_1} + r_{C_2}$),

center (resonance) frequency is

$$\omega_o = 1/\sqrt{LC_e} , \qquad (6)$$

and equivalent capacitance is

$$C_e = C_{V_e} + C_t + C_a + C_M , \qquad (7)$$

where $C_{V_e} = C_{V1} \,||\, C_{V2}$ is equivalent varactor capacitance, and C_M is the mounting capacitance.

According to Eq. (2) for the center frequency $\omega = \omega_o$, the voltage gain is maximum, e.g.

$$\left|\dot{A}_U(\omega_o)\right| = A_U = \frac{\sqrt{\left(1+\frac{R_2}{R_1}\right)^2 + (\omega_o C_1 R_2)^2}}{1+\frac{R_2}{R_{re}}\left(1+\frac{R_{in}}{R_1}+\frac{R_{in}}{R_2}\right)\left(1+\frac{R_o}{R_L}\right)} . \qquad (8)$$

For the frequencies near to the resonance, e.g. $\omega \approx \omega_o$, the pass band $B_{0,7}$ of the amplifier can be calculated by:

$$B_{0,7} = f_o / Q_e . \qquad (9)$$

III. LC Amplifier Design Procedure

The design method of voltage controlled LC amplifier suggested in this paper is based on the above analytical formulas as well as of the design methodology presented in [3]. The circuit elements are calculated using pre-defined: range of frequencies in which the LC amplifier should be tuned ($f_{o_{min}}$, $f_{o_{max}}$), voltage gains ($A_{U_{min}}$, $A_{U_{max}}$) at those frequencies, and *instantaneous* bandwidth range ($B_{0,7_{min}}$, $B_{0,7_{max}}$) the amplifier has within the tuning range or quality factors ($Q_{e_{\min}}$, $Q_{e_{\max}}$).

The design procedure for the LC amplifier shown in Fig. 2, is based on the following sequence:

A. Center frequency, Q factor and voltage gain

The amplifier's average center frequency, Q factor, and voltage gain is given by

$$f_{o_{av}} = \sqrt{f_{o_{min}} . f_{o_{max}}} , \qquad (10)$$

$$B_{0,7_{av}} = \sqrt{B_{0,7_{min}} . B_{0,7_{max}}} , \qquad (11)$$

$$Q_{e_{av}} \geq f_{o_{av}} / B_{0,7_{av}} , \qquad (12)$$

$$A_{U_{av}} = \sqrt{A_{U_{min}} . A_{U_{max}}} . \qquad (13)$$

B. Current feedback amplifier

The CFA is selected according to the following conditions:

- Presence of an additional correction terminal of the IC with high impedance;
- Unity gain frequency $BW > (1{,}2 \div 2) f_{o_{\max}}$;
- High transfer resistance, so that for selected LC elements to accomplish the condition $R_t >> R_{rL} \,||\, R_{rC} \,||\, R_3$.

C. Inductor L

The inductance of the inductor for the LC tank is selected. The following empirical values for the inductance can be recommended according to the center frequency:

- $L \geq 100\mu H$ for $f_{o_{av}}$ within $100kHz \div 1MHz$;
- $L = 10\mu H \div 100\mu H$ for $f_{o_{av}}$ within $1 \div 10MHz$;
- $L \leq 10\mu H$ for $f_{o_{av}} \geq 10MHz$.

The inductor with quality factor Q_L larger than the amplifier equivalent quality factor $Q_{e_{av}}$ (Eq. (12)) is selected. The values of the elements forming the inductor serial-parallel equivalent circuit (r_L, L and C_a), shown on Fig. 3, are determined empirically.

D. Varactors

The tuning device has to provide a variable capacitance within a range:

$$C_{Ve_{min}} = \frac{1}{(2\pi f_{o_{max}})^2 L} - (C_t + C_a + C_M), \tag{14a}$$

$$C_{Ve_{max}} = \frac{1}{(2\pi f_{o_{min}})^2 L} - (C_t + C_a + C_M), \tag{14b}$$

where C_M is the mounting capacitance (usually between 2 and 10pF). According to equations (14a) and (14b), the smallest capacitance tunes the highest tunable frequency, $f_{o_{max}}$, and the largest capacitance the lowest one, $f_{o_{min}}$. The varactor with $(C_{d_{\min}} / 2) \leq C_{Ve_{\min}}$ and $C_{d_{\max}} / 2 \geq C_{Ve_{\max}}$ is selected, where [$C_{d_{min}}$, $C_{d_{max}}$] is the capacitance range of the tuning element. The average value of the varactor capacitance can be calculated by

$$C_{Ve_{av}} = \frac{1}{(2\pi f_{o_{av}})^2 L} - (C_t + C_a + C_M). \tag{14c}$$

E. Equivalent resistance R_{re} and tuning terminal resistance R_3

$$\rho_{av} = \sqrt{\frac{L}{C_t + C_{Ve_{av}} + C_a + C_M}}, \tag{15}$$

$$R_{rL} = \rho_{av}^2 / r_L, \tag{16a}$$

$$R_{rC} = \rho_{av}^2 / r_{C_e}, \tag{16b}$$

where $r_{C_e} = r_{C_1} + r_{C_2}$.

$$R'_{re} = R_{rL} \,||\, R_{rC} \,||\, R_t, \tag{17a}$$

$$R_3 \geq (3 \div 5) R'_{re}, \tag{17b}$$

$$R_{re} = R_{rL} \,||\, R_{rC} \,||\, R_3 \,||\, R_t. \tag{17c}$$

F. Feedback resistors R_1 and R_2

$$R_1 = (\rho_{av} Q_{e_{av}} - R_{in} A_{U_{av}}) / A_{U_{av}}, \tag{18a}$$

$$R_2 = \frac{\rho_{av} Q_{e_{av}}}{\left(1 - \frac{\rho_{av} Q_{e_{av}}}{R_{re}}\right)\left(1 + \frac{R_{in}}{R_1}\right)}. \tag{18b}$$

The calculated values for the resistors R_1 and R_2 according to equations (18a) and (18b) have to be consistent with the values obtained by
$R_1 \geq R_{in}$, and $R_2 \leq 1/\left[2\pi f_{o_{\max}} C_t (1 + R_{in} / R_1)(1 + R_o / R_L)\right]$ [9].

G. Capacitance C_1

In the cases where it is necessary to obtain greater voltage gain for a given quality factor, and feedback resistors, a capacitance C_1 is connected in parallel to the R_1. The capacitance C_1 can be calculated by

$$C_1 = \frac{\sqrt{A_{U_{av}}^2 \left[1 + \frac{R_2}{R_{re}}\left(1 + \frac{R_{in}}{R_1} + \frac{R_{in}}{R_2}\right)\right]^2 - \left(1 + \frac{R_2}{R_1}\right)^2}}{\omega_{o_{av}} R_2}. \tag{19}$$

IV. LC Amplifier Design Example

In this section a specific design of a voltage controlled LC amplifier will be performed following the previously described technique. The initial design requirements and specifications are given in Table I.

TABLE I
DESIGN SPECIFICATIONS

$f_{o_{min}}$	3MHz
$f_{o_{max}}$	12MHz
$A_{U_{av}}$	20 ($f_{o_{av}} = 6MHz$, $R_L = 500\Omega$)
$Q_{e_{\max}}$	12
$Q_{e_{\min}}$	8

The systematic design approach provided in Section III is next applied. First, from equations (10), (11), (12) and (13) the design center frequency $f_{o_{av}}$, voltage gain $A_{U_{av}}$ at this frequency, and *instantaneous* bandwidth range $B_{0,7_{av}}$ is determined. The circuit was implemented using AD844A [6]

with the following electrical parameters: $BW = 60MHz$, $R_t = 3M\Omega$, $C_t = 4{,}5pF$, $R_{in} = 50\Omega$ and $R_o = 15\Omega$. For the LC tank is selected inductor $L = 10\mu H$ ($Q_L \approx 200$). The values of the elements forming the inductor serial-parallel equivalent circuit are: $r_L = 1{,}97\Omega$, $L = 9{,}83\mu H$ and $C_a = 890\,fF$.

Next, making use of (14a), (14b), and (14c) the capacitances are: $C_{Ve_{min}} = 17{,}6\,pF$, $C_{Ve_{max}} = 282\,pF$, and $C_{Ve_{av}} = 70{,}4\,pF$. Once the previous parameters are determined a tuning varactor BB112 [7] is placed in the resonant tank circuit for frequency tuning. The parameters $R_3 = 200k\Omega$, $R_1 = 500\Omega$ and $R_2 = 2{,}2k\Omega$ is calculated using (17c), (18a) and (18b). Finally the parameter $C_1 = 220\,pF$ is obtained using equation (19). The design parameter values and their variation range obtained through the design technique are shown in Table II with the parameters of the LC-tank for the smallest and the highest tunable frequency.

TABLE II
LC-TUNED AMPLIFIER DESIGN PARAMETERS

f_o	6MHz, $3\text{MHz} \le f_o \le 12\text{MHz}$
A_U	21.4, $9.1 \le A_U \le 42$ ($R_L = 500\Omega$)
Q_e	8.65, $8.94 \le Q_e \le 11.23$
ρ	376Ω, $188\ \Omega \le \rho \le 753.7\ \Omega$
Q_{LC}	76, $38 \le Q_{LC} \le 152$
R_{re}	28.5kΩ, $11.8\text{k}\Omega \le R_{re} \le 114\text{k}\Omega$

The practical LC-tuned amplifier is simulated making use of the op amp macromodel AD844A/AD from standard PSpice library. The AD844A/AD is fourth level of complexity model, providing maximum accuracy of the modeled electrical parameters. The results of the simulations and measurements of the amplifier are given in Fig. 4 for different control voltages. As can be seen it meets the initial requirements given in Table I and the error is smaller than 5%. The total harmonic distortion of the output signal U_o is less than 4% ($U_{im} = 100mV$, $f_o = 6MHz$, and $R_L = 500\Omega$). Table III resumes the performance of the LC-tuned amplifier shown in

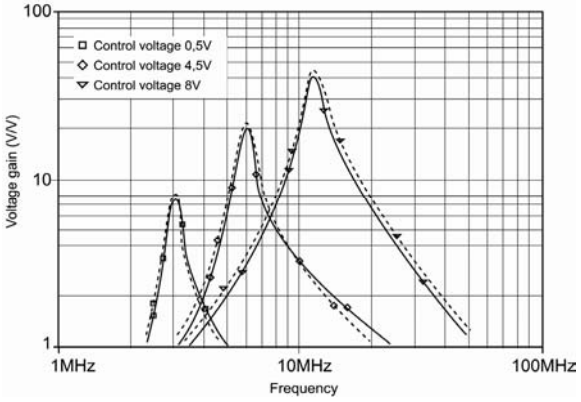

Fig. 4. Voltage gain versus frequency for various control voltages: simulations and measurements (dashed line).

TABLE III
LC-TUNED AMPLIFIER MEASURED RESPONSE

$f_{o_{min}}$	3MHz
$f_{o_{max}}$	12MHz
$A_{U_{av}}$	20.1 ($f_{o_{av}} = 6MHz$, $R_L = 500\Omega$)
$Q_{e_{max}}$	12.29
$Q_{e_{min}}$	9.06

VI. CONCLUSIONS

A voltage controlled LC amplifier using CFA with additional compensation terminal has been presented. The center frequency of the proposed circuit can be changed by applying a dc control voltage to the parallel resonator with varactor capacitive branch. A systematic procedure to design this type of analogue circuit based on symbol analysis of the transfer function has been presented. Validity of the design procedure have been tested by comparing simulations with measurements of the electrical parameters in a practical LC amplifiers, where is found that simulation and measurement results are in good agreement.

REFERENCES

[1] J. Vlach, K. Singhal, *Computer Methods for Circuit Analysis and Design*, Van Nostrand Reinhold, 1994.

[2] U. Tietze, Ch. Shenk, *Halbleiter-Schaltungstechnik*, Springer-Verlag, 1994.

[3] G. Penelva, G. Risueno, and J. Alonso, "A Simple Method to Design Wideband Electronically Tunable Combline Filters," *IEEE Trans. on Microwave Theory and Techniques*, vol. 50, pp. 172-177, January 2002.

[4] Application note – APN1013, "A Differential VCO Design for GSM Handset Applications," *Alpha Industries*, 2004.

[5] Mucha, I., "Approaching Low Power with Current Op Amps," *European Conference on Circuit Theory & Design*, Brno, 1995, pp. 529-532.

[6] AD844 60MHz 2000V/μs Monolithic Op Amp – Data sheet, *Norwood, Mass., Analog Devices*, 2003.

[7] BB112 AM variable capacitance diode – Data sheet, *Philips Semiconductors*, 1996.

[8] I. Pandiev, "Analysis and design of LC amplifiers using current-feedback amplifiers", *Proceedings of the Technical University of Sofia*, vol. 53, 2004, pp. 47-55.

[9] W. Jung, *Op Amp Applications*, Norwood, Mass., Analog Devices, 2002.

A Behavior Macromodel of Closed-Loop Sample-and-Hold Amplifier with Active Integrator

Ivailo M. Pandiev[1]

Abstract – **In this paper is proposed a behavior SPICE macromodel of Sample-and-Hold Amplifiers (SHAs) using closed-loop architecture. The circuit model is developed applying basic macromodeling technique: simplification and build-up. Computer models of linear dependent and independent voltage and current sources in the equivalent circuit are incorporated. The macromodel topologies comprise of three stages: input transconductance amplifier, low-leakage switch and output active integrator with hold capacitor. The model proposed here represents the full functional and logical behavior of the real devices. It reflects the two modes of operation (sample mode and hold mode) and the two transition between the modes (sample-to-hold and hold-to-sample) and the corresponding parameters: offset voltage and current, input resistance and capacitance, CMRR, acquisition time, slew rate, droop rate, etc. To confirm the validity of the SHA model, simulation results are compared with the data sheet parameters of the IC, where is found good agreement between simulations and performance of the actual devices.**

Keywords – **Sample-and-Hold, Behavior Modeling, Circuit simulations, SPICE, Verification.**

I. INTRODUCTION

The sample-and-hold function is one which is basic to the data acquisition and data distribution systems. Since the most leading companies of such type of analog circuits usually do not publish corresponding computer library models it is useful to have on one's disposed a macromodel of a concrete selected IC for preliminary analyses in the design process.

The SPICE simulator is actually the standard ECAD tool for the IC design. It contains intrinsic models for the most of the IC devices that give a good accuracy for the purely electrical simulations within the device safe operating area.

There are exits four methods to improve the accuracy of the SPICE models: the structural macromodeling, the C code modeling, AHDL modeling and Analog Behavior Macromodeling (ABM) [5]. In [2] a VHDL-AMS SHA macromodel is presented, which reflect the basic functionality and model some of the second-order effects of the real ICs. The drawbacks are the leak of portability to the SPICE like simulators. In [3] a structural macromodel of closed-loop sample-and-hold circuit is presented. This model allows one to simulate arbitrary user circuits with respect to the behavior in both the time and frequency domains including error parameters and the temperature dependence of several parameters. The main disadvantage of the structural macromodeling is the complexity of the equivalent circuit and the difficulty of obtaining all model parameters. This method is mainly used modeling the parasitic elements of an IC device.

The last generation of SPICE simulators has introduced a new and powerful modeling technique ABM that contains in building a sub-circuit description of the device, using linear and nonlinear voltage and current sources to implement the device's internal static and dynamic equations. The main advantages of the ABM method are the portability to all SPICE simulators and also the user's access to the macromodel's internal equations and variables.

In this paper is presented a behavior macromodel of closed-loop SHA, which can adequately represent the main electrical performances of the real ICs. Since the most manufactures of the SHAs usually do not publish information for the internal structure it is useful to develop equivalent circuit with behavior models from standard ABM SPICE compatible library. As well to keep the universality of the proposed macromodel some of the specific effects and elements of the actual ICs, which have not essential influence over the functionality (for example temperature dependence of the parameters, noise, internal feedback resistors, etc) are not presented in the equivalent circuit.

II. MACROMODEL DEVELOPMENT

The macromodel of a SHA is developed using the analog bloc modeling method introduced in [2]. This method is based on a Top-Down analysis approach and applying simplification and build-up macromodeling technique.

An interesting model structure is a closed-loop sample-and-hold amplifier with active integrator, as shown in Fig. 1 [1]. This architecture with a suitable choice of parameters and elements accurately represents a broad class of IC SHAs.

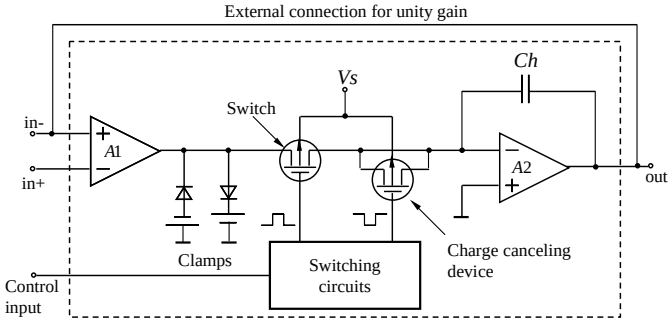

Fig. 1. Closed-loop Sample-and-Hold architecture.

The sample-and-hold ideal behavior macromodel is so defined using ideal internal elements and provides an ideal sample-hold behavior. In developing SHA model the transconductance amplifier A1 and output op amp A2 are

[1]Ivailo M. Pandiev is with the Faculty of Electronics from Technical University of Sofia, Kliment Ohridski 8, 1000 Sofia, Bulgaria, E-mail: ipandiev@tu-sofia.bg

replaced with ideal voltage controlled sources. For convenience, the transconductance of the amplifier A1 is selected to be less than unity and the value of A2 is chosen to be greater than unity. The analog FET switch and clamp diodes are replaced with ideal voltage controlled switches. The input and output waveforms of the ideal model predicted by OrCAD PSpice are shown in Fig. 2.

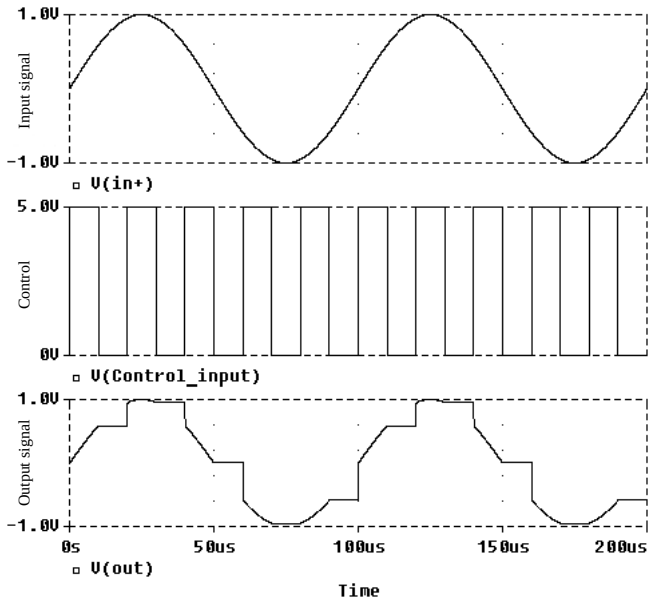

Fig. 2. Sample-and-Hold (S/H) Waveforms Showing the Input Sampled (Top), the S/H Control (Middle), and the S/H Output (Bottom)

However, ideal model not present several second-order effects, such as acquisition time, slew rate, feedthrough, etc. In response of these needs is developed improved macromodel with additional internal components. The equivalent circuit of this model is shown in Fig. 3, where the different elements are presented as hierarchical blocs.

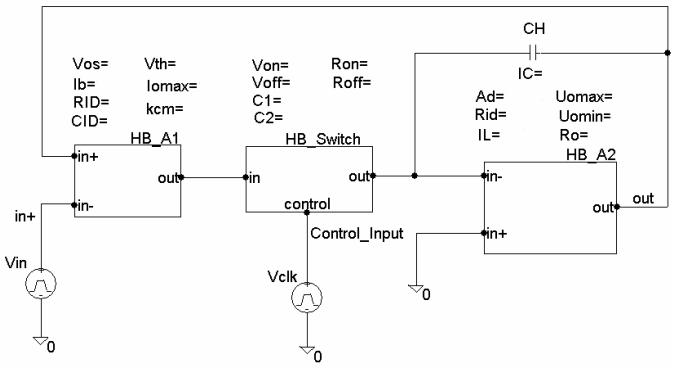

Fig. 3. Circuit diagram of the SHA macromodel.

The circuit of Fig. 3 is subdivided into tree stages: input stage – HB_A1, switch drive circuit (second stage) – HB_Switch, and output stage (third stage) – HB_A2. *The input stage*, shown in Fig. 4a consists of linear voltage controlled current source G1, passive elements and additional dependent and independent sources. This stage provides the necessary linear and nonlinear differential mode (DM) and common-mode (CM) input characteristics. The DM transconductance gain is provided by the elements consisting of maximum output current I_{omax} and threshold voltage *Uth* defined in the TABLE parameter of G1. The differential voltage gain is

$$A_{G1} = \frac{Io\,max}{Uth} \approx \frac{CH}{t_s(\varepsilon)} ln\left(\frac{1}{\varepsilon}\right), \quad (1)$$

where *CH* is the hold capacitance, $t_s(\varepsilon)$ is the settling (acquisition) time and ε is the error when settling occurs (for example 0,01 or 0,1 percent from the output voltage) [7].

The CM gain is produced by the elements *Gcm1*, *Gcm2*, *Ecm* and *Rcm*. Empirically, a value of *Rcm* is chosen equal to 1kΩ. The current sources *Gcm1* and *Gcm2* are chosen linear one-port generators having the following equations:

$$I_{G_{cm1}} = k_{cm} U(in+,0), \quad (2a)$$

$$I_{G_{cm2}} = k_{cm} U(in-,0), \quad (2b)$$

where $U(in+,0) = U(in-,0) = U_{cm}$ is the input common-mode voltage. The current thus generated $I_{G_{cm1}}$ and $I_{G_{cm2}}$, will flow through the resistor R_{cm}, towards the internal ground. In such a way the voltage $U(2,0) = (I_{G_{cm1}} + I_{G_{cm2}}) R_{cm} = 2k_{cm} U_{cm}$ will

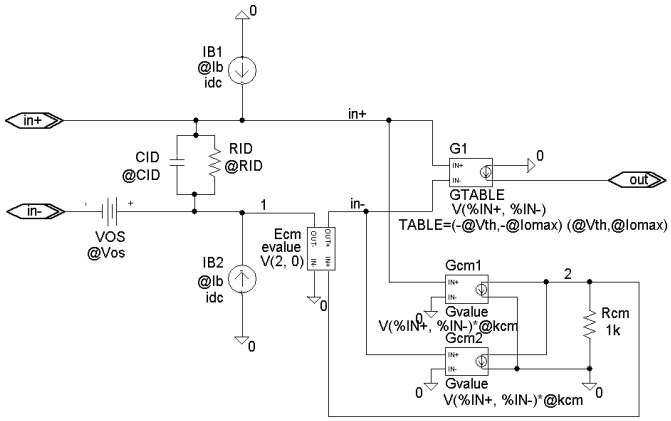

Fig. 4a. Equivalent circuit of the input stage (HB_A1).

depend upon the amplitude of the common-mode input voltage. The voltages generated at node 2 are used for forming the equation of input voltage-controlled voltage source E_{cm} as follows:

$$U_{E_{cm}} = k_{1,E_{cm}} U(2,0). \quad (3)$$

For convenience, the coefficient $k_{1,E_{cm}}$ of the polynomial source E_{cm} is selected equal to unity. Then the output current of the stage, predicted by the input common-mode voltage is

$$I_{out} = 2A_{G1} U_{Ecm} = 2A_{G1} k_{cm} R_{cm} U_{cm}. \quad (4)$$

The CM gain can be found with the following equation:

$$A_{cm} = \frac{I_{out}}{U_{cm}} = 2A_{G1} k_{cm} R_{cm}. \quad (5)$$

The CM rejection ratio (*CMRR*) is the ratio of the DM gain and CM gain [7], i.e.

$$CMRR = \frac{A_{G1}}{A_{cm}} = \frac{1}{2k_{cm} R_{cm}}. \quad (6)$$

The elements *RID* and *CID* produces the input resistance and capacitance. Offset voltage is modeled with the

combination of an ideal voltage source VOS and an initial condition voltage (*IC*) of the hold capacitor, while input bias/offset currents are modeled by properly setting the currents on the input sources *IB1* and *IB2*. The slew rate of the proposed macromodel is determined by the charging of the holding capacitor CH with the output current of source G1. The slew rate is given by

$$SR = Iomax/CH\ , \tag{7}$$

where *SR* is the slew rate of the SHA model in the sample mode. According to Eq. (1) the maximum output current of G1 is

$$Iomax = A_{G1}Uth\ . \tag{8}$$

Substituting into (7) gives

$$SR = \left(A_{G1}Uth\right)/CH\ . \tag{9}$$

The second stage (Fig. 4b) uses a two ideal voltage controlled switches S1 and S2 and several passive elements. In the sample mode S1 is closed and S2 is open, current source G1 provides charging current to the holding capacitor *CH*. When the S1 is open and S2 is closed, the circuit is in the hold mode

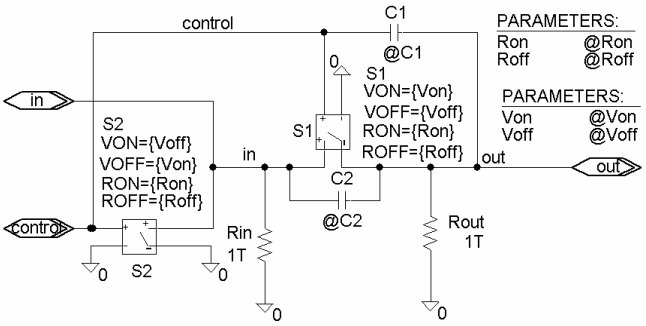

Fig. 4b. Equivalent circuit of the second stage (HB_Switch).

with the capacitor holding the value of the input voltage which was present at the instant the S1 was opened. Sample-and-hold offset is modeled with the capacitor C1, and the capacitor C2 produces the frequency dependence of the feedthrough attenuation ratio [4]. In the transition from sample mode to hold mode, the turn-off of the sampling switch S1 results in charge injection effects into C1 that introduce a sample-to-hold offset (jump) error ΔU_{SH}, which is dependent on the total clock voltage variation ΔU_C according to

$$\Delta U_{SH} = \Delta U_C.\left(C1/CH\right). \tag{10}$$

During the hold mode (S1 is turn off) there also is some penetration of the input ac signals through the capacitor *C*2. The feedthrough attenuation ratio (*FA*) of the macromodel can be calculated with

$$FA \approx 20\,lg\left(CH/C2\right). \tag{11}$$

The resistance in a sample and hold mode of the switch circuit are modeled with parameters *Ron* and *Roff*. The parameters *Von* and *Voff* provide the threshold voltages during the transitions between the modes of operations. The parameters *Ron*, *Roff*, *Von* and *Voff* of the switches S1 and S2 are defined in the equivalent circuit with additional elements 'param' (Special.lib). *The output stage* (Fig. 4c) provides the proper output resistance, operating voltage range of the SHA, etc. Droop rate is the rate at which the output voltage is changing due to the leakage from the hold capacitor. In the proposed macromodel the droop rate is presented with the combination of the I_{iB}^{+}, I_{iB}^{-} and *Rid*. The rate of voltage change is

$$DroopRate = I_L / CH\ . \tag{12}$$

The parameters U_{omax} and U_{omin} of the voltage source *Eo* produce the desired maximum voltage excursion. The output voltage range at higher frequencies is limited by the slew rate. The maximum output voltage range is given by

$$Uomax = \left|Uomin\right| = SR/\left(2\pi f\right), \tag{13}$$

where f is the power bandwidth. The input and output resistance of the stage is modeled with resistors R_{id} and R_o.

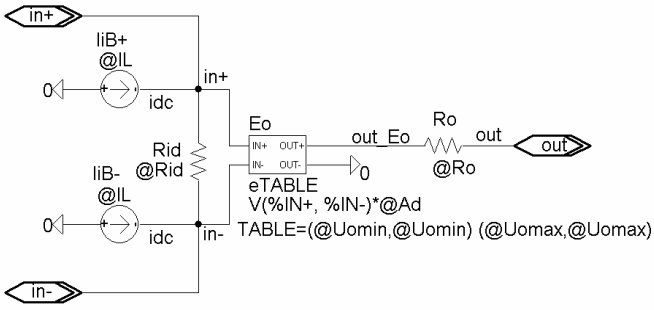

Fig. 4c. Equivalent circuit of the output stage (HB_A2).

III. Design Procedure

The design method of the SHA macromodel suggested in this section can be split into two basic steps. The first step consists of the model parameters selection using typical values of the IC data sheet.

TABLE I
DESIGN EQUATIONS FOR THE SHA MACROMODEL

$CH = C_h$	$V_{off} = V_{off-LowVoltage}$
$A_{G1} = \frac{CH}{t_s(\varepsilon)} ln\left(\frac{1}{\varepsilon}\right)$	$Ron = 1\Omega\ ,\ Roff = 1.10^{12}\,\Omega$
$U_{th} = \frac{CH}{A_{G1}} SR$	$C1 = CH\,\frac{\Delta U_{SH}}{\Delta U_C}$
$I_{omax} = SR.CH$	$C2 = 10^3 (CH/10^{\frac{FA}{20}})$
$k_{cm} = 1/(2R_{cm}CMRR)$	$A_d = A_{d-OpAmp}$
$VOS = IC(CH) =$ $= V_{OS\_OffsetVoltage}$	$R_{id} = R_{id-OpAmp}$
$I_b = I_{iB}$	$I_L = CH.(DroopRate)$
$RID = R_{id}$	$U_{omax} = U_{out}^{+}$
$CID = C_{id}$	$U_{omin} = U_{out}^{-}$
$V_{on} = V_{on-HighVoltage}$	$R_o = R_{o-dc}$

Expressions are developed to relate the performance of the SHA and the macromodel to the parameters and elements of

the macromodel. A summery of all design equations is presented in Table I. The determination of the element values of the macromodel proceeds from the input, transfer, and output characteristics of the SHA.

The second step of the proposed design method is macromodel verification and validation. The purpose of verification is to guarantee the correct behavior of each element or group of elements in the model. Verification is effectively a '*micro*' check of the model. During the verification process each element is tested in turn to ensure that, 1) they behave in the manner intended by the model code and, 2) that their behavior is representative in the real world. A valid model is both accurate and able to meet the objectives of the simulation project for witch it is being used. The purpose of validation is to guarantee the correct degree of accuracy by checking that the overall behavior of the model is representative in the real world. Model validation can be seen as a '*macro*' check of the simulation. During the validation it is particularly important to compare the performance of the model against the real system. For the goals of validation it is necessary to collect data that represents the average behavior of the real device [4].

IV. THE AD585 MACROMODEL

In this section, a numerical example is used to illustrate the development of the parameters of the SHA macromodel. For the example, the electrical characteristics and parameters of the AD585 closed-loop SHA are used [6]. The AD585 is a complete monolithic sample-and-hold circuit consisting of transconductance input amplifier in series with low leakage analog switch and JFET input integrating amplifier (Fig. 1). In fact AD585 is typical representative of the closed-loop topology using the most contemporary SHAs implementation.

The development procedure follows the sequence of expressions of Table I. The final results are presented in Table II.

TABLE II
MACROMODEL PARAMETERS

$CH = 100\,pF$	$V_{on} = 2V$
$A_{G1} = 307\mu S$	$V_{off} = 0{,}8V$
$U_{th} = 3{,}257V$	$C1 = 60\,fF$
$I_{omax} = 1mA$	$C2 = 7{,}5\,pF$
$k_{cm} = 50nS$	$A_d = 200.10^3$
$R_{cm} = 1k\Omega$	$R_{id} = 1T\Omega$
$VOS = IC(CH) = 5mV$	$I_L = 100\,pA$
$I_b = 2nA$	$U_{omax} = 10{,}8V$
$RID = 1T\Omega$	$U_{omin} = 10{,}8V$
$CID = 10\,pF$	$R_o = 1k\Omega$

Validation checks have been performed on the SHA macromodel developed through simulation modeling of the four modes of operation of the real device. In Table III is given comparison between macromodel parameters and data sheet parameters. Notice that the average error is not higher than 3%, which guarantee the correct degree of accuracy.

TABLE III
SHA PERFORMANCE CHARACTERISTICS

Parameter	Conditions	AD585 Macromodel	AD585 Data Sheet
Sample/Hold mode parameters			
Acquisition time	10V Step to 0,01%	3,19μs	3μs
Droop Rate	A=+1	1,001V/s	1V/s
Sample-to-Hold Offset	A=+1	2,93mV	3mV
Feedthrough	$20V_{p-p}$, 10kHz	0,51mV	0,5mV
Transfer parameters			
Open-Loop Gain	$20V_{p-p}$, A=+1	200,000	200,000
Common-Mode Rejection	V_{cm}=10V	80dB	80dB
Full Power Bandwidth	V_o=$20V_{p-p}$	159kHz	160kHz
Slew Rate	V_o=$20V_{p-p}$	9,84V/μs	10V/μs
Operating Voltage Range	-	10,8V	10,8V
Analog input parameters			
Offset voltage	-	5mV	5mV
Bias Current	-	2nA	2nA
Input Capacitance	f=1MHz	10pF	10pF
Input Resistance	V_o=$20V_{p-p}$	10TΩ	10TΩ
Digital input parameters			
Logic Low Voltage	-	0,8V	0,8V
Logic High Voltage	-	2V	2V

VI. CONCLUSIONS

In this paper, a behavior SPICE macromodel of a closed-loop SHAs has been presented. The proposed model accurately predicts the circuit behavior for nonlinear dc, ac, and large-signal transient responses. The macromodel is implemented as a hierarchical blocks and the structure of their netlist confirm to the standard SPICE format.

REFERENCES

[1] K. R. Stafford, P. R. Blanchard, "A Complete Monolithic Sample/Hold Amplifier," *IEEE J. Solid-State Circuits*, vol. 9, pp. 381-387, Dec. 1974.

[2] M. Cousineau, D. Stadarovski, M. Lescure, "Analog Circuit Modelling Method – Sample-and-Hold Development," *MIXDES 2003*, Poland, June 2003.

[3] U. Jörges, G. Jummel, G. Müller, M. Reinhold, "A Macromodel of Sample-and-Hold Circuits," *International J. of Circuit Theory and Applications*, vol. 25, pp. 483-502, Dec. 1998.

[4] E. D. Shoikova, I. M. Pandiev, "Commercial Sample/ Track-and-Hold Amplifier Macromodel Development," *ET'2003*, book 3, pp. 84-90, Bulgaria, September 2003.

[5] D. Andreu, D. Stepan, S. Josse, "Introduction to Behavioural Modelling and PLL Behavioural Modelling," *Newsletter www.spice-club.com*, 09/2001.

[6] AD585 High Speed, Precision SHA – Data sheet, *Norwood, Mass., Analog Devices*, 2003.

[7] K. Laker, W. Sansen, "*Design of Analog Integrated Circuits and Systems*," McGraw-Hill, 1994.

Statistical Optimization of Frequency Converter for Radiocommunication System

Galia I. Marinova[1], Dimitar I. Dimitrov[2]

Abstract - **The paper presents a specific methodology for a statistical optimization of a frequency converter in radiocommunication systems. The study is performed in the environment ORCAD/PSPICE 9.2. and IESD. Optimization steps and results from circuit simulations are presented. In order to implement the circuit for different channel conversions a parametric range for a set of sensible parameters is determined nominally and statistically.**

Keywords - **statistical optimization; frequency converter;**

I. Introduction

The paper continues the research on the development of specific methodologies for statistical optimization of different types of circuits for radiocommunication applications, presented in previous papers [2,3,6]. These papers develop the methodology for statistical optimization with IESD simulator described in [4,5] and improves existing methods as for example [9].

A specific methodology for statistical optimization of a frequency converter for radiocommunication system is proposed. The frequency converter permits to transmit TV signal from channels IV and V through S-channels for cable TV or to exploit TV retranslators of VHF range (I and II TV channels) on areas with cut relief where UHF signals are transmitted with big losses.

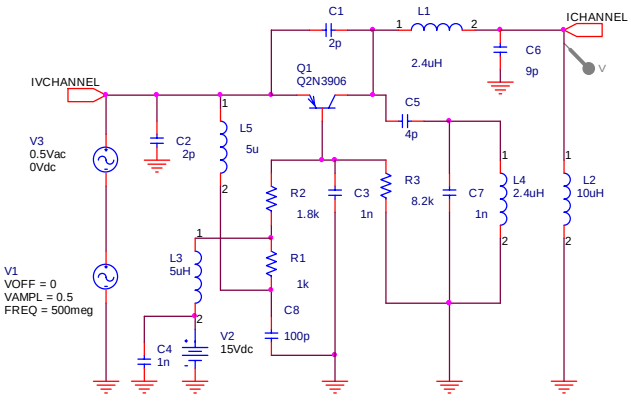

Figure 1. Frequency converter from 500MHz to 50MHz

[1]Galia I. Marinova is with the Faculty of Communications and Communications Technologies, Technical University-Sofia, Kliment Ohridski 8, 1000 Sofia, Bulgaria, e-mail: gim@tu-sofia.bg

[2] Dimitar I. Dimitrov is with the Faculty of Communications and Communications Technologies, TUS, Kliment Ohridski 8, 1000 Sofia, Bulgaria, e-mail: ddim@tu-sofia.bg

Figure 1 presents the circuit of a frequency converter from [1] which permits the conversion from UHF range (TV channel IV - 500MHz) in VHF range (TV channel I - 50MHz). A table is given in the paper for the necessary variations of a set of circuit element values in order to cover the different conversion options.

II. Steps of the Specific Methodology for Optimization of the Frequency Converter

The specific methodology for the statistical optimization of the frequency converter has the following steps:

- Specification and constraints definition;
- Nominal analysis and estimation for the conversion between two TV channels;
- Statistical analysis of the frequency converter in ORCAD/Pspice 9.2 and IESD;
- Definition of the Goal function for statistical optimization;
- Statistical optimization of the frequency converter through optimal tolerancing;
- Implementation of the frequency converter for different channel conversions.

The specific methodology steps are described in details..

III. Description of the Specific Methodology Steps for the Statistical Optimization of the Frequency Converter

A. *Specification and constraints definition*

The specification of the frequency converter is to convert the channels IV and V into channels I, II and S-channels [see 8]:

f (Vout, f(Vin)=500MHz) ∈{50MHz;175.25MHz; 182.25MHz; 189.25MHz; 196.25MHz; 203.25MHz; 217.25MHz; 224.25MHz}

f (Vout, f(Vin)=800MHz) ∈ {80MHz;175.25MHz; 182.25MHz; 189.25MHz; 196.25MHz; 203.25MHz; 217.25MHz; 224.25MHz},

where Vin and Vout are the input and output voltages of the frequency converter and f is frequency.

The constraints for the frequency converter are defined from the standards of Bulgarian telecommunications Company from [7]:

f(Vout)±5%, THD(Vout)<20%, SNR(f(Vout))>40dB,

where THD is the coefficient of total harmonic distortion when a sinusoidal signal is applied to the input and SNR is the signal to noise ratio.

B. Nominal analysis and estimation of the frequency converter

Figure 2 presents the results for the output voltage and the SNR from simulation of the frequency converter from figure 1 in frequency area with AC and NOISE analysis in ORCAD/PSPICE. The value for SNR in the output is:

SNR (50MHz)=109dB.

Figure 3 presents the results from the simulation in Time area for the input and output voltages of the frequency converter. The input voltage is sinusoidal with 500MHz frequency. The output voltage is sinusoidal with 50MHz frequency. A Fourier analysis is performed in order to estimate the total harmonic distortion of the output signal. The value of the THD is: THD(Vout) = 4.54%.

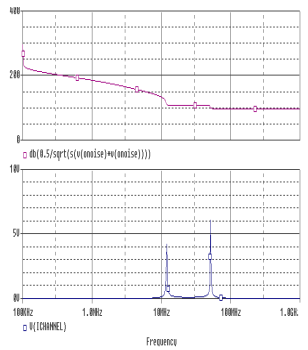

Figure 2. Gain and SNR from AC simulation in ORCAD/PSPICE

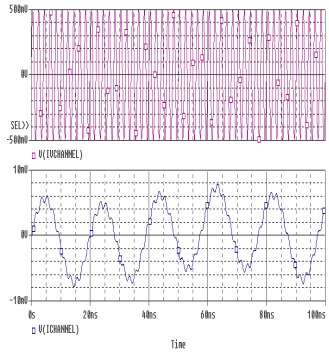

Figure 3.Input and output voltage converting 500MHz to 50MHz from Time area simulation in ORCAD/PSPICE

C. Statistical analysis of the frequency converter

The statistical analysis of the frequency converter is performed in ORCAD 9.2 and IESD simulators. The tolerances of all R,C,L elements in the circuit from figure 1 are 10%. Figure 4 presents the results for the output voltage of the frequency converter from Monte Carlo simulation with 100 runs in time domain. The histogram of output voltage period is built by the PSPICE option PERFORMANCE ANALYSIS, defined as:

XatNthY(V(ICHANNEL),0,2)

Figure 5 presents the results for the output voltage and the SNR of the frequency converter from a Monte Carlo simulation with 100 runs in frequency domain (AC sweep). A histogram is determined for the SNR value at the output for 50MHz. A Fourier analysis is performet at any MC run and the values of the THD coefficients are detrmined at any run. Statistical processing is performed with the simulator IESD for the circuit parameters determined from the 100 MC runs. Figure 6a presents the histograms of the THD coefficient and of the frequency values for the output voltage. Figure 6b presents the correlation between the THD and the frequency of the output voltage in the frequency converter. The value of the linear correlation coefficient r is:

R(THD(Vout), f(Vout))=0.9195

There is a strong linear correlation between the output voltage frequency and the output voltage total harmonic distortion in the frequency converter from figure 1.

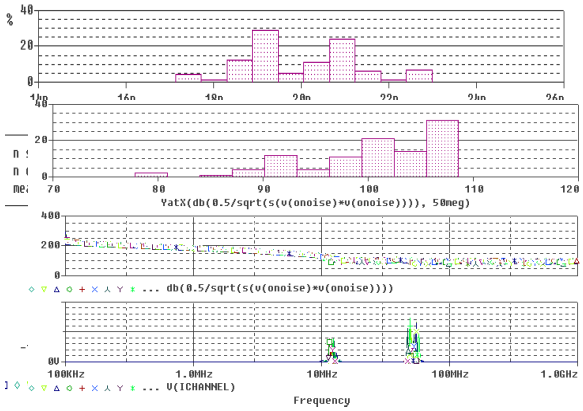

Figure 4. Statistical simulation in time area for the outcome voltage with 10% tolerances for all R,L,C elements

Histogram for the period of the outcome voltage

Figure 5. Statistical simulation with AC sweep for the outcome voltage and the SNR. Histogram of the SNR(50MHz)

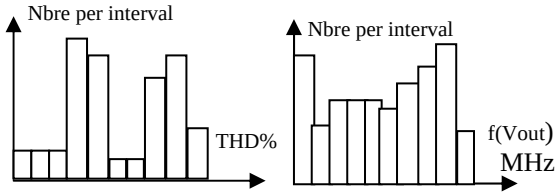

Figure 6a. Histograms of the output voltage frequency and total harmonic distortion built in the IESD simulator

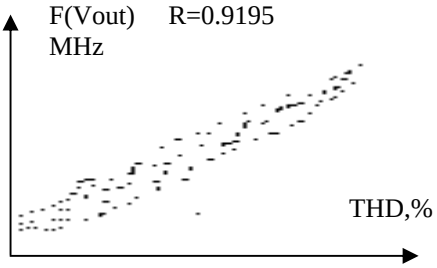

Figure 6b. Statistical correlation between the outcome voltage frequency and the total harmonic distortion estimated from IESD simulator

D. Definition of the Goal function for statistical optimization

Taking in consideration the results from the statistical analysis of the frequency converter described in previous paragraph, the statistical optimization task is defined as follows:

- The objective is to perform optimal tolerancing for the circuit from figure 1 with 100% Yield following the constraints defined in point A.
- Tolerancing is performed for the R,L,C elements.

The goal function for statistical optimization of the frequency converter is to determine the maximal tolerance values for all R,L,C elements in the circuit which guarantee

100% Yield (0% Fail) following the constraints for the output voltage: frequency f(Vout)=50MHz±5%, total harmonic distortion TDH(Vout)<20% and signal to noise ratio SNR<40dB. The goal function is formulated as follows:

Max tol{Ci, i=1,8, Lj, j=1,5; Rk, k=1,3}, f(Vout,f(Vin)=500MHz)=50MHz±5%, THD(Vout)<20%, SNR(Vout)>40dB}, Yield=100%, Fail=0%

E. Statistical optimization of the frequency converter

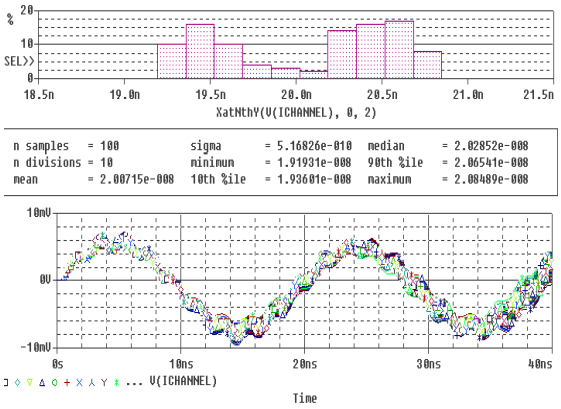

Figure7. Statistical simulation in time area for the outcome voltage of the statistically optimized frequency converter. Histogram for the period of the outcome voltage

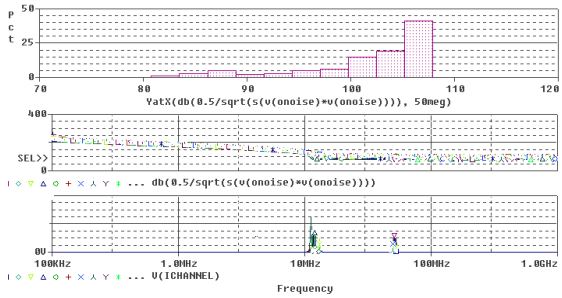

Figure 8. Statistical simulation with AC sweep for the outcome voltage and the SNR of the statistically optimized frequency converter. Histogram of the SNR(50MHz)

The statistical optimization which consists in optimal tolerancing is realized in IESD and ORCAD 9.2 environment. The initial values for the tolerances of all R,L,C elements in the circuit are 10%. Monte Carlo simulations in time and frequency areas are realized with 100 runs each. The values for the parameters f(Vout) - frequency of the output voltage, T(Vout) - period of the output voltage, k=f(Vout)/f(Vin) - frequency conversion coefficient, SNR (Vout,50MHz) - signal to noise ratio at 50MHz are extracted at any run. The Yield and Fail values are determined from the constraints from point A. The reason for the 30% fail is the output voltage frequency variation.

The circuit's elements which influence mostly the output voltage frequency are determined from the worst results between the 100 Monte Carlo runs and they are: C5, C6,C7,L1,R1. At the second step the tolerances of these elements are decreased: Tol(C5, C6,C7,L1,R1)=5%. Fail decreases to 10%. The last step brings Tol(C5, C6,C7,L1,R1)=2% and then 100% yield and 0% fail are obtained. Data for the optimal tolerancing steps are presented in Table 1.

Figures 7 and 8 present the results from the Monte Carlo simulation of the frequency converter after the optimal tolerancing in time and frequency areas. Histograms of the output voltage period and SNR(Vout,50MHz) are built for the statistically optimized circuit.

TABLE 1. OPTIMAL TOLERANCING STEPS FOR THE FREQUENCY CONVERTER

Element name and nominal value	Step 1	Step2	Step 3
C1, 1nF	10%	10%	10%
C2, 2pF	10%	10%	10%
C3, 1nF	10%	10%	10%
C4, 1nF	10%	10%	10%
C5, 4pF	10%	5%	2%
C6, 9pF	10%	5%	2%
C7, 1nF	10%	5%	2%
C8,100pF	10%	10%	10%
L1,2.4μH	10%	5%	2%
L2, 10μH	10%	10%	10%
L3, 5μH	10%	10%	10%
L4, 2.4μH	10%	5%	2%
L5, 5μH	10%	10%	10%
R1, 1k	10%	5%	2%
R2, 1.8k	10%	10%	10%
R3, 8.2k	10%	10%	10%
Fout	43-58MHz (50±7)MHz 50MHz±35%	46.9-52.9MHz (50±3)MHz 50MHz±6%	48.3-51.8MHz (50±1.8)MHz 50MHz±3.6%
Tout	17.3-23ns 20ns±35%	18.9ns-21.3ns 20ns±12%	19.3-20.7ns 20ns±3.5%
K= Fin/Fout	8.6-11.6 10±15%	9.34-10.66 10± 6%	9.65-10.35 10± 3.5%
Total Harmonic Distortion	0.%-19.3%	0.44%-19.4%	2.47% - 16.4%
SNR (50MHz)	79-109dB	80-109dB	82-108dB
Yield Fail	70% 30%	90% 10%	100% 0%

F. Implementation of the frequency converter for different channel conversions

The frequency converter from figure 1 is tuned to convert 500MHz input signal into 50MHz output signal. In order to perform the conversions between different channels as defined in the specification from point A, the circuit parameters the influence the output frequency, given the input frequency are determined and they are: L1,L4,C5 and C6.

Table 2a presents how the initial values for L1,L2,C5 and C6 can be modified in order to perform a conversion from channel V (800MHz) at the input to channel II (80MHz) at the output. Two ways are possible: modifications of L1 and L4 values or modifications of C5 and C5 values. The second option is more suitable for realization of the frequency converter as an integrated circuit. Then C5 and C6 can be realized as varicaps.

Table 2b presents how the initial values for L1, L4, C5 and C6 can be modified in order to perform the conversions from channels IV and V to S-channels for cable TV. The output frequency is most sensitive forward L1. For this purpose the value of L1 is modified for any conversion case. For some neighbor S-channels the values obtained for L1 are very close to each other, so 1% tolerance is determined for L1.
An additional optimization for this set of conversions could be performed in order to avoid mistakes in the channel conversions.

IV channel →I channel 500MHz →50MHz 2ns →20ns	V channel→ II channel 800MHz →80MHz 1.25ns→12.5ns
L1=2.4μH **L4=2.4μH** **C5=4pF** **C6=9pF**	Varying L1, L4
	L1=0.85uH L4=0.85uH **C5=4pF C6=9p**
	Varying C5, C6
	L1=2.4μH L4=2.4μH C5=2.8pF C6=2.1pF

TABLE 2A

TABLE 2B

V channel → S-channels	C5=1p, 1% C6=1p, 1% L4=1μH, 1% Varying L1	IV channel→ S-channels	C5=1p, 1% C6=1p, 1% L4=1μH, 1% Varying L1
800MHz → 175.25MHz 1.25ns → 5.7ns	L1=1.2μH, 1%	500MHz→ 175.25MHz 2ns → 5.7ns	L1=1.25μH, 1%
800MHz → 182.25MHz 1.25ns → 5.5ns	L1=1μH, 1%	500MHz→ 82.25MHz 2ns → 5.5ns	L1=1.2μH, 1%
800MHz → 189.25MHz 1.25ns → 5.3ns	L1=0.87μH, 1%	500MHz→ 189.25MHz 2ns → 5.3ns	L1=1.1μH, 1%
800MHz → 196.25MHz 1.25ns → 5.1ns	L1=0.83μH, 1%	500MHz→ 196.25MHz 2ns → 5.1ns	L1=0.93μH, 1%
800MHz → 203.25MHz 1.25ns → 4.9ns	L1=0.82μH, 1%	500MHz→ 203.25MHz 2ns → 4.9ns	L1=0.82μH, 1%
800MHz → 217.25MHz 1.25ns → 4.6ns	L1=0.77μH, 1%	500MHz→ 217.25MHz 2ns → 4.6ns	L1=0.62μH, 1%
800MHz → 224.25MHz 1.25ns → 4.5ns	L1=0.71μH, 1%	500MHz →224.25MHz 2ns → 4.5ns	L1=0.58μH, 1%

IV. CONCLUSION

The paper presents a specific methodology for statistical design of a frequency converter circuit. A strong linear statistical correlation between the THD and the output signal frequency were determined through the statistical estimations of the circuit behavior. The optimal design is determined for a set of channel conversions between IV and V channels to I, II and S-channels (for cable TV). The optimal design is oriented to realization of the frequency converter as an integrated circuit. An additional statistical optimization is planned in order to avoid mistaking the conversion to neighbor S-channels.

ACKNOWLEDGEMENT

The authors acknowledge the National Science Fund for the financial support under grant I-1203/02.

REFERENCES

[1] D. Dimitrov, J.Benbasat, A.Mindov, "Frequency converter for UHF range in TV sets", "Radio, Televizia, elektronika", №3, 1977

[2] G. Marinova, D. Dimitrov, "Statistical analysis and optimization of voltage regulator circuit using IESD and ORCAD environment", *Proceedings of XXXVIII International Scientific Conference on Information, Communication and Energy Systems and Technologies ICEST'2003,* Sofia, Bulgaria, 2003, pp. 478-482.

[3] G. Marinova, D. Dimitrov, "Statistical optimization of filters in radiocommunication systems with IESD simulator", *Proceedings of XXXIX International Scientific Conference on Information, Communication and Energy Systems and Technologies ICEST'2004,Bitola*, Macedonia, 2004, pp. 639-649.

[4] G. Marinova , "Statistical design simulator for electronic design – IESD", *The European Design and Test Conference, Users Forum*, Paris, March 11-14, 1996, pp. 297

[5] G. Marinova, "Statistical optimization of electronic circuits in the simulator IESD", Proceedings of "Prilojenie na matematikata v tehnikata", Sofia, 1992, pp. 144-148, (in bulgarian)

[6] G. Marinova, "Statistical optimization of TV modules in IESD", TELSIKS'2003, Serbia and Montenegro, October 1-3 2003, pp.143-146

[7] Ts. Vassileva, St. Popov, "Bulgarian Telecommunications Company methodology for estimation of the technical performances of the radio and TV equipment and systems and the quality of the transmitted and emitted signals ", Sofia, 1999 (in bulgarian)

[8] D. Makedonski, K. Konov, "Satellite and cable TV, Part II, Cable TV", DIOS, Sofia, Bulgaria, 2002 (in bulgarian)

[9] Zhang J. C., Styblinski M. A., "Yield and variability optimization of integrated circuits", Klewer Academic Publisher 1999

New PSPICE Modeling and Simulation Method for Multiple Mode Oscillation for ECAM

D. N. Vizireanu[1], I. Pirnog[2], R. M. Udrea[3]

Abstract - **This paper presents new methods of simulating the algebraic functions as well as the solving of non-linear differential equations using PSPICE, one of the most well known circuit analysis program. A new negative resistance oscillator model was used for the single and multiple mode LCR networks of ECAM. The results obtained by numerical integration of the differential equations using a new PSPICE method are compared with the analytic approximations.**

Keywords - **PSPICE, nonlinear circuits, ECAM.**

I. INTRODUCTION

This paper presents new methods of simulating the algebraic functions as well as the solving of non-linear differential equations using PSPICE.

In this paper we present the following aspects: integrated circuits simulation, PSPICE sub circuits achievement for simulating algebraic functions and solving non-linear differential equations.

A new negative resistance oscillator model was proposed by Walker and Connelly [1], [2]. In this paper an analytic approximation to the periodic solutions for LCR networks of Emitter Coupled Astabil Multivibrator (ECAM) is obtained.

These predictions are compared with the results obtained by numerical integration of the differential equations using a new PSPICE method.

II. PSPICE ALGEBRAIC FUNCTIONS SIMULATION

The circuit from Fig. 1 is used for showing the way that PSPICE works in simulating algebraic functions.

And we will also use the equations:

$$E_3 = E_2 \ , \ V_4 = \ln V_i , \tag{1}$$

We make the presumption that the voltage commanded source E_4 is:

$$E_4 = 10^{12}\left(E_3 - E_2\right), \tag{2}$$

[1]Dragos Nicolae Vizireanu is with the Faculty of Electronics, Telecommunications and Information Technology of "Politehnica" University, Iuliu Maniu 1-3, 7000 Bucharest, Romania, E-mail: nae@comm.pub.ro.

[2]Ionut Pirnog is with the Faculty of Electronics, Telecommunications and Information Technology of "Politehnica" University, Iuliu Maniu 1-3, 7000 Bucharest, Romania, E-mail: ionut@comm.pub.ro.

[3]Radu Mihnea Udrea is with the Faculty of Electronics, Telecommunications and Information Technology of "Politehnica" University, Iuliu Maniu 1-3, 7000 Bucharest, Romania, E-mail: mihnea@comm.pub.ro.

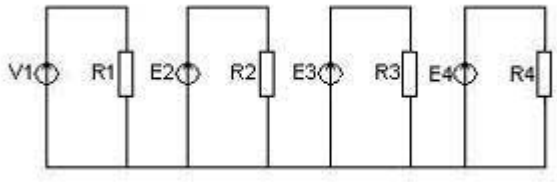

Fig. 1. Function generation sub circuit.

then:
$$E_3 - E_2 = \frac{E_4}{10^{12}} \tag{3}$$

Also, if we consider that E_2 and E_3 are much bigger than $E_4/10^{12}$, we obtain:

$$E_3 = E_2 . \tag{4}$$

Using PSPICE there can be generated a set of algebraic functions using the circuit from Fig. 1 and Eq. (5). This idea is based on the following presumptions:

a) E_2 and E_3 have a polynomial dependence for V_i and E_4;

b) $E_4 = F\left(V_i\right)$;

c) it is possible that an equilibrium is obtained in the conditions of Eq. (6).

Example, if the output voltage E_4 must be:

$$V_4 = \ln V_i \text{, or } V_i = e^{V_4} \tag{5}$$

where V_i is the input voltage, if we impose:

$$E_3 = V_i , \tag{6}$$

then, in the conditions of Eq. (5), we obtain:

$$V_i = e^{V_4} \text{, or } V_4 = \ln V_i \tag{7}$$

Using the same method there can be generated also other algebraic functions that can be represented as a polynomial decomposition.

Integration simulation is based on the dependence between the voltage and the current of a capacitor.

The circuit that corresponds to this function is represented in Fig. 2. R_4 is used in parallel with the capacitor to allow achieving of static points at the start of the PSPICE algorithm. Its value must be as big as possible in order to have no influence in the function of the circuit.

The loading current of the capacitor simulated by the current source F_4, commanded by the voltage source V_i (where: $R_3 = 10k\Omega$) is:

$$F_4 = \frac{V_i}{R_3} \tag{8}$$

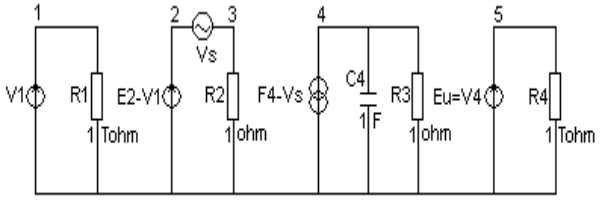

Fig. 2. The integration subcircuit.

The V_4 voltage can be written:

$$V_4 = \frac{1}{C_4}\int F_4 dt \ . \tag{9}$$

If $E_5 = V_4$ and $C_4 = 100\mu F$, Eq. (8) becomes:

$$V_5 = \int V_i dt \ . \tag{10}$$

With the help of the C_4 capacitor we can control the initial conditions for integration.

III. Solving the Nonlinear Differential Equations for the Emitter-Coupled Astable Multivibrator (ECAM)

In the scientific literature there are a multitude of algorithms for solving the nonlinear differential equations. An approach needs two aspects:
a good knowledge of the mathematical algorithm, for choosing the most appropriate algorithm to use;
the knowledge of a programming language for the implementation of the algorithm.

The purpose of this paragraph is to present a new method, simple and fast, to solve the nonlinear differential equations using PSPICE.

A. Single-Mode E.C.A.M.

In [1], [2] Walker and Connelly proposed a new negative resistance oscillator model for a class of current, negative resistance oscillators.

The equivalent circuit is presented in Fig. 3.

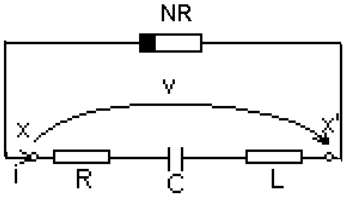

Fig. 3. The single-mode ECAM

The model [1] between x and x' is:

$$v = -a\cdot i + \frac{b}{2}\ln\left(\frac{1-c\cdot i}{1+c\cdot i}\right) \tag{11}$$

where:

$$a = 2RC \ , \ b = 2V_R \ , \ c = \frac{1}{L} \tag{12}$$

The nonlinear differential equation for the single-mode oscillator circuit in Fig. 3 is:

$$0 = \frac{d^2 i}{dt^2} + \frac{R-a}{L}\left(1 + \frac{bc}{R-a}\cdot\frac{1}{1-c^2 i^2}\right)\frac{di}{dt} + \frac{i}{LC} \tag{13}$$

With the notation,

$$\omega^2 = \frac{1}{LC} \ , \ \beta = \frac{bc}{a-R} \ , \ \varepsilon = \frac{a-R}{\sqrt{\frac{L}{C}}} \tag{14}$$

and the changing of variables:

$$i \to \frac{X}{C} \ , \ t \to \frac{t}{\omega} \tag{15}$$

the Eq. (13) becomes:

$$\frac{d^2 x}{dt^2} - \varepsilon\left(1 - \frac{\beta}{1-x^2}\right)\frac{dx}{dt} + x = 0 \tag{16}$$

The Eq. (16) can be written:

$$\frac{d^2 x}{dt^2} = E_a + E_b + E_c \ , \ E_a = -x^2\frac{d^2 x}{dt^2} \tag{17}$$

$$E_b = \varepsilon\left(1-\beta-x^2\right)\frac{dx}{dt} \ , \ E_c = x\left(1-x^2\right) \tag{18}$$

B. N-Mode E.C.A.M.

The equivalent circuit is presented in Fig. 4.

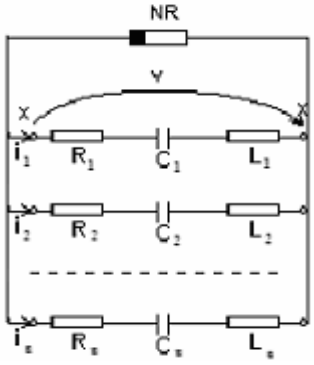

Fig. 4. The n-mode ECAM

The differential equations for the n-mode ECAM circuit were derived [2]:

$$\frac{d^2 i_j}{dt^2} - \frac{a-R_j}{L_j}\left[\frac{di_j}{dt} + \frac{a}{a-R_j}\sum_{\substack{k=1\\k\neq j}}^{n}\frac{di_k}{dt} + \right.$$

$$\left. + \frac{bc}{R_j - a}\frac{\sum_{\substack{k=1\\k\neq j}}^{n}\frac{di_k}{dt}}{1-c^2\left(\sum_{k=1}^{n} i_k\right)^2} + \frac{i_j}{L_j c_j}\right] = 0 \tag{19}$$

$$j = \overline{1,n}$$

with the conditions: $-1 < c\left(\sum_{j=1}^{n} i_j\right) < 1$.

The transformation of variables:

$$i_j \to \frac{x_j}{C_j};\ j=\overline{1,n}\ ,\ x_j=\frac{a-R_j}{L_j};\ j=\overline{1,n} \tag{20}$$

$$\text{and } \omega_1^2=\frac{1}{L_1C_1};\ \omega_2^2=\frac{1}{L_2C_2},\ \beta_j=\frac{bc}{a-R_j};\ j=\overline{1,n}, \tag{21}$$

$$\tau_j=\frac{a}{a-R_j};\ j=\overline{1,n}, \tag{22}$$

allows us to obtain the dimensionless forms:

$$\frac{d^2x_j}{dt^2}-\pi_j\left[1-\beta_j\frac{1}{1-\left(\sum_{k=1}^{n}x_k\right)^2}\right]\frac{dx_j}{dt}+$$

$$+\omega_j^2x_j-\pi_j\left[\tau_j-\frac{\beta_j}{1-\left(\sum_{k=1}^{n}x_k\right)^2}\right]\sum_{\substack{k=1\\k\neq j}}^{n}\frac{dx_k}{dt}=0 \tag{23}$$

$$j=\overline{1,n}$$

We investigate these equations with a new computational method using PSPICE and to determine an analytical approximation for periodic solutions.

The interest for these equations is based on the fact that they represent a model of equations that describe a new class of nonlinear differential equations. Enforcing quasi-linear with:

$$\pi_1 << \omega_1,\ \pi_2 << \omega_2,...,\pi_n << \omega_n \tag{24}$$

permits approximate solutions for Eq. (23):

$$\begin{aligned} &x_1=\alpha_1(t)\sin(\theta_1),\quad x_2=\alpha_2(t)\sin(\theta_2)\\ &x_j=\alpha_j(t)\sin(\theta_j),\quad j=\overline{1,n}\end{aligned} \tag{25}$$

with:

$$\begin{aligned} &\theta_1=\omega_1t+\Phi_1(t),\quad \theta_2=\omega_2t+\Phi_2(t),\\ &\theta_j=\omega_jt+\Phi_j(t),\quad j=\overline{1,n}\end{aligned}\ . \tag{26}$$

The method of equivalent linearization [4] will permit construction of the time derivatives of (23). Applying the linearization method to (23) with (24) assumed gives:

$$\frac{d\alpha_1}{dt}=\frac{\alpha_1x_1}{2}\left[1-\frac{2\beta_1}{c^2\alpha_1^2}\left(1-\sqrt{1-c^2\alpha_1^2-\sum_{\substack{k=1\\k\neq j}}^{n}\frac{c^2\alpha_k^2}{2}}\right)\right] \tag{27}$$

$$\frac{d\alpha_j}{dt}=\frac{\alpha_jx_j}{2}\left[1-\frac{2\beta_j}{c^2\alpha_j^2}\left(1-\sqrt{1-c^2\alpha_2^2-\sum_{\substack{k=1\\k\neq j}}^{n}\frac{c^2\alpha^2}{2}}\right)\right] \tag{28}$$

With: $$\frac{d\Phi_1}{dt}=0,\frac{d\Phi_2}{dt}=0,....,\frac{d\Phi_n}{dt}=0 \tag{29}$$

The steady-state amplitudes of oscillation may be obtained by equating Eqs. (27) and (28) to zero.

We can have analytic approximation to the periodic solutions. These predictions are compared with the results obtained by PSPICE numerical integration of the differential equations.

C. Example: Double-Mode E.C.A.M.

The equivalent circuit is presented in Fig. 5.

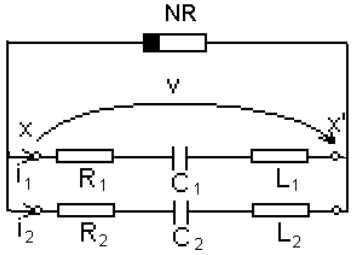

Fig. 5. The double-mode ECAM

Applying the analytical method from the multiple mode ECAM for the double mode ECAM we obtain :

$$\frac{d\alpha_1}{dt}=\frac{\alpha_1x_1}{2}\left[1-\frac{2\beta_1}{c^2\alpha_1^2}\left(1-\sqrt{1-c^2\alpha_1^2-\frac{c^2\alpha_2^2}{2}}\right)\right] \tag{30}$$

$$\frac{d\alpha_2}{dt}=\frac{\alpha_2x_2}{2}\left[1-\frac{2\beta_2}{c^2\alpha_2^2}\left(1-\sqrt{1-c^2\alpha_2^2-\frac{c^2\alpha_1^2}{2}}\right)\right] \tag{31}$$

Using the following definitions:

$$Y_1=C_2\alpha_1^2>0,Y_2=C_1\alpha_2^2>0, \tag{32}$$

we can rewrite Eqs. (30) and (31):

$$\frac{Y_1^2}{4\beta_1^2}+\left(1-\frac{1}{\beta_1}\right)+\frac{Y_2}{2}=0 \tag{33}$$

$$\frac{Y_2^2}{4\beta_2^2}+\left(1-\frac{1}{\beta_2}\right)+\frac{Y_1}{2}=0\,. \tag{34}$$

We have the conditions:

$$0<\beta_1<1;\ 0<\beta_2<1 \tag{35}$$

The next step is the comparison of the analytical approximations for the periodic solutions and the results obtained by PSPICE numerical integration of the differential equations.

IV. The Pspice Method to Solve Nonlinear Equations for E.C.A.M.

PSPICE has become the standard computer program for most electrical simulation.

Higher-level abstraction and hierarchy can be modeled using controlled sources and subcircuits blocks. The nonlinear function applies only to the time domain. PSPICE supports the polynomial sources.

A functional model for single mode is presented in Fig. 6 and for double mode in Fig. 7.

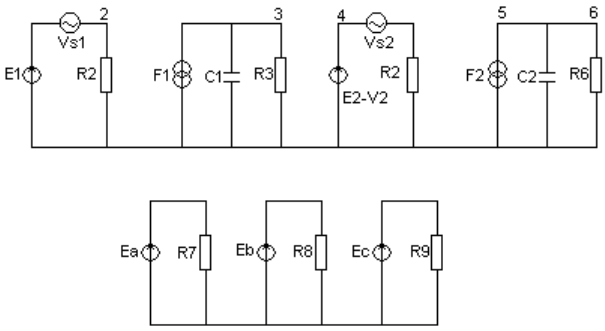

Fig. 6. PSPICE equivalent scheme for single mode nonlinear differential equation

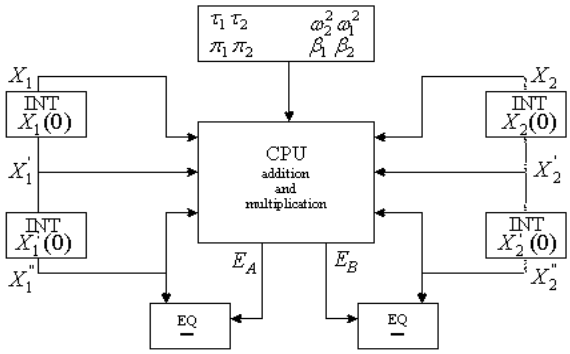

Fig. 7. PSPICE blocks (double mode)

Addition and multiplication (CPU block in Fig. 7) can be achieved with polynomial voltage-controlled current source (VCCS):

EA 3 0 *POLY* (2) 1 0 2 0 0 1 $*V(3)=V(1)+V(2)$

EB 4 0 *POLY* (2) 1 0 2 0 0 0 0 0 1 $*V(3)=V(1)+V(2)$

where $V(1), V(2), V(3), V(4)$ are voltages at nodes 1, 2, 3 and 4, in reference to ground (node 0).

The integrator (INT blocks in Fig. 7):

$$V_c(t)=\frac{1}{C}\int i_c(t)dt+v_\infty \tag{36}$$

is used in PSPICE to model the capacitor. If

$$i_c(t)=\frac{V_i}{R} \tag{37}$$

with $R=10k\Omega$ and $C=100\mu F$:

$$V_c(t)=\int V_i dt+v_\infty . \tag{38}$$

If we have (EQ blocks in Fig. 7):

$$E_3-E_2=\frac{E_4}{10^{12}} \tag{39}$$

and:

$$E_{2,3}<<E_4, E_4=10^{12}(E_3-E_2) \tag{40}$$

giving:

$$E_3=E_2 \tag{41}$$

The PSPICE program has 4 block levels.

INPUT DATA block: using controlled sources we have eight parameters:

$\pi_1, \tau_1, \omega_1, \beta_1, \pi_2, \tau_2, \omega_2, \beta_2$.

INT blocks: compute the integrator blocks, here are the initial conditions.

CPU block: here we have multiplication, addition and return E_{c1} and E_{c11} .

EQ blocks: close the loops, with relations $X_1=E_{c1}$ and $X_2=E_{c11}$.

The dimensionless forms for the PSPICE simulation are:

$$x_1''=E_{c1}$$

$$E_{c1}=x_1''(x_1+x_2)^2+\pi_1\left[1-\beta_1-(x_1+x_2)^2\right]x_1'- \\ -\omega_1^2x_1+\pi_1\left[\tau_1-\beta_1-\tau_1(x_1+x_2)^2\right]x_2' \tag{42}$$

$$x_2''=E_{c11}$$

$$E_{c11}=x_2''(x_1+x_2)^2+\pi_2\left[1-\beta_2-(x_1+x_2)^2\right]x_2'- \\ -\omega_2^2x_2+\pi_2\left[\tau_2-\beta_2-\tau_2(x_1+x_2)^2\right]x_1' \tag{43}$$

V. Results of Numerical Integration

Using the PSPICE program we compare the theoretical results with the result of numerical computation.

Over 200 runs with several initial conditions prove that we can have a stable oscillation for double and multiple-mode ECAM. The general prediction error is 10 %.

VI. Conclusions

In this paper were introduced a new and improved PSPICE method for simulating linear and nonlinear equations.

An analytic approximation to the periodic solutions for the single and double-mode LCR networks of E.C.A.M. is obtained.

A PSPICE method has been proposed to solve the nonlinear differential equations.

Over 200 sets of initial conditions and parameters prove that the obtained results were in a good agreement with theoretical predictions.

References

[1] S. S. Walker, J. A. Connelly, "A new negative resistance oscillator model", Circuits, Systems and Signal Processing 2, pp. 213-238, 1983

[2] "Investigation of the mathematical properties of a new negative resistance oscillator model", Circuits, Systems and Signal Processing 2, pp. 187-205, 1992

[3] ***, PSPICE, Microsim Corporation, Irvine, SUA, 1992

[4] N. Minorsky, "Introduction to Non-Linear Mechanics", J.W.Edwards, Ann Arbor, Michigan, 1947.

[5] "Nonlinear ordinary differential equations", G. P. Flessas, P. G. L. Leach, 2005.

Session ME:

MICROWAVE ELECTRONICS

An Automated Procedure for MESFETs / HEMTs Noise Modeling Against Temperature

Zlatica Marinković, Olivera Pronić, Jovana Ranđelović, Vera Marković

Abstract - **An automated procedure for accurate noise parameter prediction of microwave MESFETs / HEMTs against temperature is proposed in this paper. An improved modification of the Pospieszalski's noise model is used. The temperature dependences of the noise model elements are modelled using an artificial neural network. After training of the network and its assignment to the transistor noise model, noise parameters can be easily obtained for each temperature from the operating range without need for measured data. In that way, it is necessary to acquire the measured data and extract the elements only for a certain number of temperatures used for the network training. Furthermore, once developed model remains the same for all operating temperatures and therefore does not require additional optimizations and changes as the temperature changes.**

Keywords - **neural network, MESFET, HEMT, noise modelling**.

I. INTRODUCTION

Accurate small-signal and noise models of low noise microwave transistors (MESFETs and HEMTs) are very important for the computer-aided design of active circuits used in modern wireless systems. Hence, extensive work has been carried out in the field of signal and noise modeling of these devices. Since their physical models are too complex and require many input technological parameters, the empirical noise models are more often used, [1]-[3]. During the last decade, two-parameter Pospieszalski`s noise model [3] turns out to be the most suitable one for implementation into the standard commercial circuit simulators This model generally shows good agreement with measured data, but some deviations can still be observed, since the correlation between two noise sources is completely ignored in this model. However, it has been found that the inaccuracy caused by this approximation is not negligible at higher frequencies. In [4], the correlation between the noise sources is taken into account by defining the third equivalent noise temperature, called the correlation temperature.

Further, transistor signal and noise characteristics are temperature and bias dependant, but most of the existing transistor noise models including the Pospieszalski's one, are valid only for specific temperature and bias point. Authors of this paper have proposed the procedure for accurate prediction of noise parameters of microwave MESFETs / HEMTs for various device ambient temperatures, [5]. A drawback of this model is that it is necessary to extract the elements of the model for each further temperature point. It is basically an optimisation process that can be time-consuming. Furthermore, the measured signal and noise data for each new temperature point are requested for the extraction, which could take much efforts and time, since the measurements, especially of the noise parameters, require complex equipment and procedures.

A new approach to overcoming these problems using artificial neural networks to model temperature dependences of model elements and parameters is proposed here. The artificial neural networks have been chosen as a modeling tool since they have the ability to learn from the presented data, and therefore they are especially interesting for problems not fully mathematically described. It should be noted that they fit non-linear dependencies better than polynomials. There are many papers referring results of applications of the neural networks in the microwave area, [6]-[10].

Development of the proposed model and its implementation in standard microwave simulators are described in the paper. An example of modeling the specific device is provided as well.

II. IMPROVED TRANSISTOR NOISE MODEL

The schematic of GaAs FET package model equivalent circuit including noise sources is shown in Fig.1. The intrinsic circuit, which is common for most of the transistor models, denoted by a dashed line, is embedded in a network representing device parasitics.

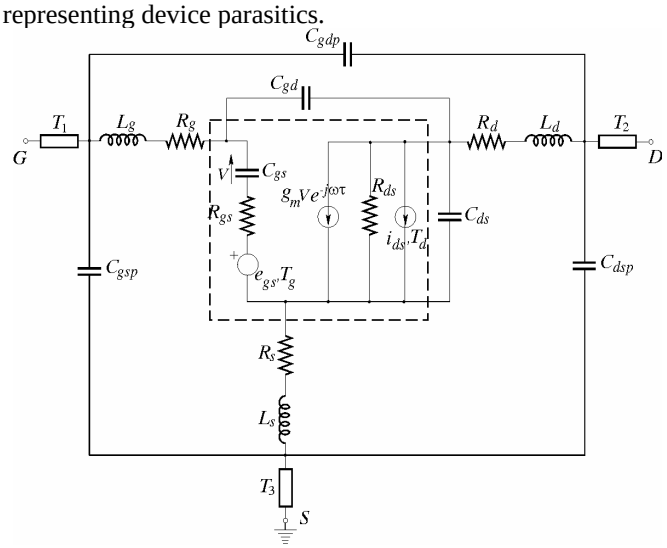

Fig.1. MESFET / HEMT package equivalent circuit including noise sources

The Pospieszalski's noise model, [3], is based on simple expressions for noise parameters of MESFET / HEMT intrinsic circuit as the functions of the equivalent circuit

Authors are with the Faculty of Electronic Engineering, Aleksandra Medvedeva 14, 18 000 Niš, Serbia and Montenegro
e-mail: [zlatica,oljap, jovanar, vera]@elfak.ni.ac.yu

parameters (ECP): transistor intrinsic circuit elements and equivalent gate and drain temperatures. However, the transistor noise parameters (minimum noise figure F_{min}, optimal source reflection coefficient Γ_{opt} and normalized noise resistance $r_n = R_n/50$) calculated in this way do not perfectly match measured noise parameters. The Pospieszalski's noise model accuracy could be improved in a way authors proposed earlier in [5]. In order to minimize deviations that exist between measured and modelled noise parameters, a correction procedure based on incorporation of frequency-dependent error correction functions into the noise equations is applied. Actually, the ratio of the experimental and simulated transistor noise parameter values is calculated for each of four noise parameters over the entire frequency range. Then, curve-fitting procedure is applied on these sets of data, in order to obtain suitable frequency dependences. In this way, corresponding mathematical functions are determined for all four noise parameters (F_{min}, $Mag(\Gamma_{opt})$, $Ang(\Gamma_{opt})$ and r_n). The obtained functions represent error correction functions for improving the Pospieszalski's noise model. Namely, each intrinsic circuit noise parameter obtained by approach proposed in [3] is multiplied by corresponding error correction function and by using that new set of equations, more accurate prediction of noise parameters is achieved.

III. Artificial Neural Network for the ECP Extraction

According to the above described approach, for each new temperature from the operating range it is necessary to repeat ECP extraction procedure. Since it implies complex acquiring of measured data and an optimisation as well, in order to increase efficiency of the considered method, artificial neural networks are proposed to be applied for the extraction of ECP in the whole operating range of temperatures.

A standard MLP (*Multilayer Perceptron Network*) is suitable to be used for overcoming this problem. It consists of neurons grouped into layers (an input layer, an output layer, as well as several hidden layers), [6]. Each neuron from one layer is connected to all neurons from the next layer, but there are no connections among neurons in the same layer. Each neuron is characterized by an activation function and each connection between neurons is characterized by a weight. The MLP network is a *feed forward* structure, meaning that input signals are presented to the neurons in the input layer and fed through the network to the output layer neurons. Responses of the output neurons yield the output data vector.

The neural network „learns" relationship among sets of input-output data (training set) by adjusting neural network parameters (connection weights and biases of activation functions) in order to minimize difference between the desired values and neural network obtained values. During this training process, at the beginning input vectors are presented to the input neurons and output vectors are computed. Further, partial derivatives of the difference between the desired values and neural network obtained values are calculated for each sample from the training set and used for updating the weights and biases of the neurons.

The training process proceeds until errors are lower than prescribed values or until maximum number of epochs (epoch is the whole training set processing) is reached. The most common training algorithms are based on *backpropagation* algorithm, [6]. Once trained, the network provides fast response for all vectors from the input space without any additional change of its structure or its parameters. Furthermore, it provides correct response for the input values completely different from training ones, i.e. it has a generalization capability.

For the purpose of the ECP determination versus temperature an MLP neural network with one hidden layer is proposed (Fig.2). It has one neuron in the input layer corresponding to the ambient temperature (*T*), while the number of the neurons in the output layer corresponds to the number of temperature dependent ECP (let this number be denoted as *N*). Neurons from the input and output layers have linear activation functions and hidden neurons have sigmoid activation functions $F(u) = 1/(1+e^{-u})$. Therefore, values of the ECP can be obtained according to the following matrix equation

$$\mathbf{ECP} = \mathbf{W_2} * F(\mathbf{W_1} * T + \mathbf{B_1}) + \mathbf{B_2} \qquad (1)$$

where $\mathbf{W}_1$ and $\mathbf{W}_2$ are weight matrices between the input and the hidden layer and between the hidden and the output layer, respectively, and $\mathbf{B}_1$ and $\mathbf{B}_2$ are bias matrices for the hidden and the output layer, respectively.

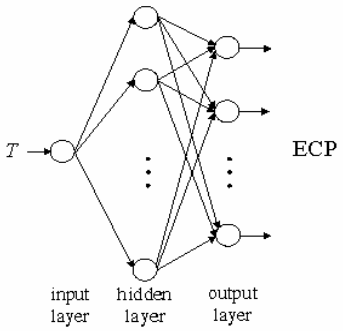

Fig.2. MLP neural network for ECP determination

The network is trained using extracted ECP values for certain number of operating temperatures. After the training is done, ECP for any temperature from the operating temperature range are determined by simple finding neural network response.

IV. Model Implementation in a Circuit Simulator

The neural network developed in the proposed way is assigned to the improved transistor noise model described in the Section 2. The network assignment, i.e. its implementation in a standard microwave simulator such as ADS, [11] can be done as the following. At first, a set of expressions corresponding to the trained neural network is generated

according to its structure and values of its parameters. This can be automated within the training software environment. Further, these expressions are put in a VAR (Variables and Equations) block within the schematic of the improved transistor model in the microwave simulator. The VAR block outputs are values of the ECP and they are assigned to the corresponding elements and parameters of the model and used for the further device noise simulation for any temperature and frequency from the operating range. The principle of the proposed noise parameters' determination is presented in Fig. 3.

In this way a new user-defined library element representing the considered device is created. Since the model has the temperature as an input it can be used for noise parameters' determination in the whole temperature range without changes in its structure and avoiding need for measured data acquiring and optimisation procedures.

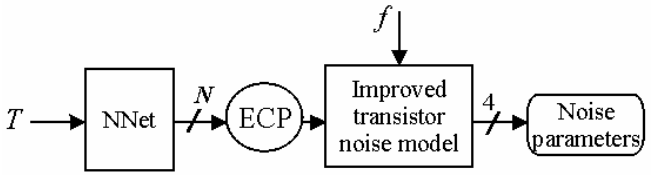

Fig.3. Determination of the transistor noise parameters

V. NUMERICAL RESULTS

The proposed method has been applied to a packaged microwave HEMT, type NE20283, from NEC. Measured values of S and noise parameters over the temperature range from –40°C to 60°C (20°C step) have been used for the development of the model. These data have been obtained earlier at the University of Palermo, Italy [12].

First, the ECP of Pospieszalski's transistor noise model have been extracted from the available measured data, and the noise parameters are simulated. Further, for the temperature T=60°C, the appropriate error correction functions for the noise parameters have been determined. As it has been shown in [5], the most suitable form of the error correction function is a polynomial form. It has been also shown that the proposed model with once determined error correction functions enables efficient noise modelling of the same transistor for various temperatures.

In order to increase the efficiency of the considered improved noise model, an MLP neural network is trained to predict ECP dependences on the temperature. According to Section 3 and as it has been referred in [13], this network has one input neuron, five hidden neurons and 20 output neurons. Nineteen of the output neurons correspond to 19 small-signal circuit elements and the last one to the equivalent drain temperature. The equivalent gate temperature is assumed to be equal to ambient temperature, [3]. The ECP extracted from the measured values of noise parameters have been used as the training data.

In Fig 4 there are examples of the temperature dependence prediction of the complex transconductance magnitude g_m and time delay τ using this neural network.

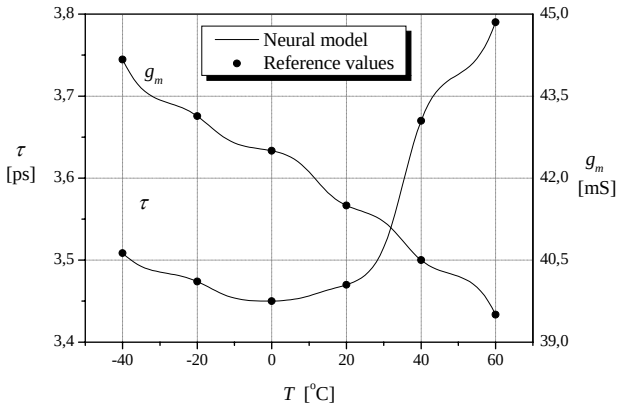

Fig. 4. Prediction of the transistor model elements: g_m and τ

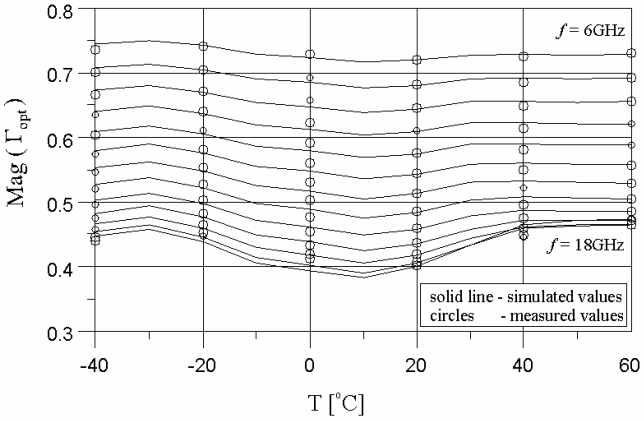

Fig.5. The magnitude of optimum reflection coefficient

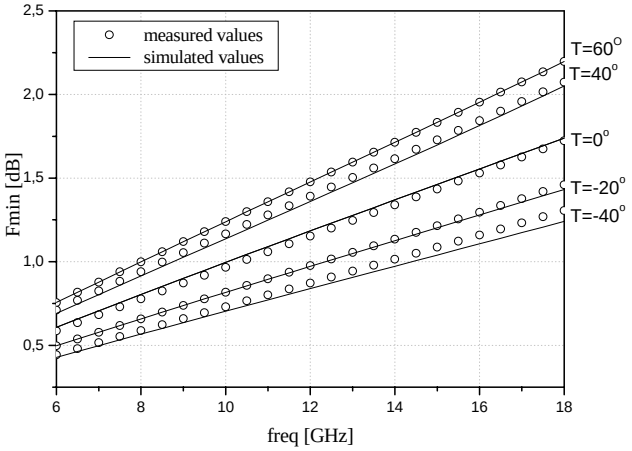

Fig.6. Minimum noise figure

In Figs. 5, 6 and 7 there are some results for the noise parameters obtained by the model shown in Fig.1 whose ECP are extracted using the neural network. The model accuracy improvement according to the procedure proposed in [5] is included too. The magnitude of optimum reflection coefficient versus temperature in the frequency range (6 - 18) GHz is shown in Fig 5. Frequency dependences of the minimum noise figure and the normalized equivalent noise resistance are shown in Figs. 6 and 7, respectively. Circles denote the measured values are solid lines values simulated from the

proposed model. It can be observed that the simulated values match well the measured values.

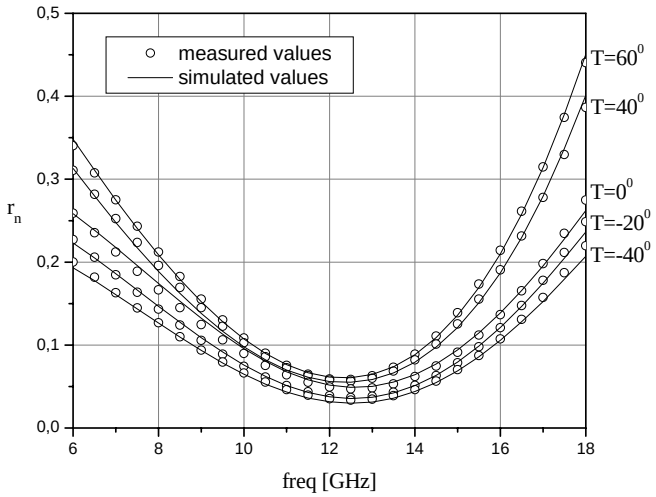

Fig.7. Equivalent noise resistance

VI. CONCLUSION

An efficient procedure for incorporating temperature dependence into the noise models of microwave MESFETs / HEMTs is proposed in this paper. It is started from an earlier proposed accurate transistor noise model. As the temperature dependence is not incorporated directly in the model, for each operating temperature it is necessary to extract model elements and parameters (ECP) from the measured scattering and noise parameters. The extraction can be time consuming and the measurements require complex equipment and procedures. This problem is overcome by using an artificial neural network for modelling of temperature dependences of the ECP. The network is trained using the extracted ECP values for a certain number of operating temperatures. Once this network is trained its structure remains unchanged.

After the network assignment to the earlier proposed improved transistor noise model, a new user-defined library element representing the considered device in a standard circuit simulator is created and can be used for further noise analysis of the circuits that contain the device. Besides incorporating the temperature dependence in the model, this method provides results that agree well with measured characteristics.

ACKNOWLEDGEMENTS

This work has been supported by the Ministry of Science and Environmental Protection of Republic of Serbia under the project No. 101351.

Authors would like to thank to Prof. Alina Cademmi, University of Messina, for providing the measured data used for this work.

REFERENCES

[1] M. S. Gupta, O.Pitzalis, S.E.Rosenbaum, P.T.Greiling, "Microwave Noise Characterization of GaAs MESFETs: Evaluation by On-Wafer Low-Frequency Output Noise Current Measurement", IEEE Trans. Microwave Theory Tech., vol. MTT-35, pp. 1208-1218, December 1987.

[2] H. Fukui, "Design of Microwave GaAs MESFET's for Broadband Low-Noise Amplifiers", IEEE Trans. Microwave Theory Tech., vol. MTT-27, pp. 643-650, July 1979.

[3] M. W. Pospiezalski, "Modeling of noise parameters of MESFET and MODFET and their frequency and temperature dependence" IEEE Trans. Microwave Theory Tech., vol. MMT-37, pp.1340-1350, Sept. 1989.

[4] V. Marković, B. Milovanović, N. Maleš-Ilić, "MESFET Noise Model Based on Three Equivalent Temperatures", Proceedings of 27th European Microwave Conference, Jerusalem, Israel, 1997, pp. 966-971.

[5] O. Pronić, G. Mitić, J. Ranđelović, V. Marković: "New procedure for accurate noise modelling of microwave FETs versus temperature", Electronics Letters, Vol.40, No.24, pp.1551-1553, 2004.

[6] Q. J. Zhang, K. C. Gupta, Neural Networks for RF and Microwave Design, Artech House, 2000

[7] P. M. Watson, K. C. Gupta, "Design and optimizacion of CWP circuits using EM-ANN models for CPW components", IEEE Trans., Microwave Theory Tech.,vol. 45, no. 12 pp. 2515-2523, 1997

[8] G. L. Creech, B. J. Paul C. D. Lesniak, T. J. Jenkins, and M. C. Calcatera, "Artifical neural networks for fast and accurate EM-CAD of microwave circuits", IEEE Trans., Microwave Theory Tech., vol. 45, no. 5 pp. 794-802, 1997

[9] M. Vai, S. Prasad, Neural networks in microwave circuit design – beyond black box models, Int. J. RF and Microwave Computer-Aided Eng., Special issue on Applications of Artificial Neural networks to RF and Microwave Design, 1999, pp. 187-197.

[10] V.Marković, Z.Marinković, "HEMT Noise Neural Model Based on Bias Conditions", The Int. Journal for Computation and Mathematics in Electrical and Electronic Engineering - COMPEL, Vol. 23 No.2, 2004, pp.426-435

[11] Advanced Desing System-version 1.5, Agilent Eesof EDA, 2000.

[12] A. Caddemi, A. Di Paola, M, Sannino, "Microwave noise parameters of HEMTs vs. temperature by a simplified measurement procedure", Proceedings of EDMO96 Conference, Weetwood Hall, Leeds, 1996, pp. 153-157.

[13] Z. Marinković, V. Marković, B. Milovanović, "Implementation of Temperature Dependence in Small-Signal Models of Microwave Transistors Including Noise", 24th Conference on Microelectronics MIEL 2004, Niš, Serbia and Montenegro, 2004, pp. 355-358.

Small-Signal Models of Heterojuction Bipolar Transistors Based on Neural Networks

Vera Marković, Aleksandar Stošić

Abstract: **Heterojunction bipolar transistors are considered to be a promising technology in microwave wireless communications. A convenient approach for small-signal modeling of heterojunction bipolar transistors based on neural networks is presented in this paper. Developed neural models enable an efficient prediction of device S parameters over the whole frequency range and over the broad ranges of operating conditions. Testing on the input data not used in the training procedure shows good accuracy of the model.**

Keywords - **Heterojunction bipolar transistors, small-signal models, neural networks**

I. Introduction

Heterojunction Bipolar Transistors (HBT) have become very promising devices for different applications at the microwave and millimeter-wave frequencies [1], [2]. For example, HBT's are used for power amplifiers as well as for low noise amplifiers in mobile communication systems. This device tecnology is considered as very convenient for RF front-end circuits in next-generation wireless communications.

Important condition for any successful design work is the availability of efficient and accurate device models. During the last decade a tremendous work has been done for developing physical and empirical HBT models [3],[4]. Despite this fact, we still do not have an unified, accurate model standard for HBTs. The main reason is that the device physics is very complicated and the range of operating conditions is broad. The existing models based primarily on the physical background are inconvenient because of too many coefficients that are difficult to extract. The other models are mostly based on the traditional optimisation techniques or on the direct extraction of the equivalent circuit elements.

Last years, from the the aspect of efficiency, accuracy and simplicity, neural network approach has been considered to be a good solution for microwave device modeling [5]. As highly nonlinear structures, neural networks are able to model nonlinear relations between two different data sets. Once trained, the neural model provides fast response for different input vectors that in principle can cover the whole operating range. A very important property of neural networks is generalisation capability [6], which provides sufficiently accurate response for different input vectors not included in the training set, without additional computational efforts or new measurements.

Neural network approach has recently been proposed for modeling of microwave transistors for both small-signal and large-signal applications, but there are still not too many published results in this field. Most of them are related to the standard microwave FETs (MESFETs and HEMTs). The authors' results related to the development of small-signal and noise neural models of MESFETs and HEMTs have been presented in [7]-[9]. On the other hand there are only a few published results in the area of HBT modeling by using the neural network approach [10].

In this paper, the development of neural models for AlGaAs/GaAs HBTs is presented. The attention is paid to small-signal HBT applications. The neural models enable an efficient prediction of transistor's S parameters over the wide frequency and bias condition ranges.

II. Advantages of the HBT's for Wireless Communication Applications

The heterojunction bipolar transistors are composed of two different semiconductor materials with different band gap widths [11]. $Al_xGa_{1-x}As/GaAs$ npn structure is used very often and its application has matured to commercial level. A heavily doped n+ GaAs layer is grown first for the collector contact, followed by a lightly doped n GaAs layer for the collector. A heavily doped p+ GaAs layer is used for the base. Again, a wide-band-gap AlGaAs layer is grown for the emitter. Heavily doped n+ GaAs layer is grown to facilitate the fabrication of low-resistance ohmic contacts.

High injection efficiency is obtained in HBTs by using a material with a larger energy band gap for the emitter than that used for the base material. The large energy band-gap emitter blocks injection of holes from the base. Therefore, the doping concentration in the base and emitter can be adjusted over a wide range with little effect on injection efficiency. Thereby, HBT can provide good current gain simultaneously keeping lower base resistance and parasitic capacitance than conventional bipolar transistors. Due to this advantages, HBT provide a cutoff frequency f_T over 100 GHz. Hence, in comparison with Si bipolar junction transistors (BJTs), HBTs show better performance in terms of emitter injection efficiency, base resistance, base-emitter capacitance, and cutoff frequency. They also offer good linearity, low phase noise and high power-added efficiency. Due to good linearity properties in operational rating, HBT could be used in RF amplifiers for mobile communication.

In comparison with field effect transistors, HBT processing requires less demanding lithography, therefore, HBTs can cost

Vera Marković and Aleksandar Stošić are with the Faculty of Electronic Engineering, A. Medvedeva 14, 18000 Niš, Serbia & Montenegro, E-mails: vera@elfak.ni.ac.yu, stosha@elfak.ni.ac.yu

less to fabricate and can provide improved lithographic yield. This technology can also provide higher breakdown voltages and easier broad-band impedance matching.

III. Modeling of the HBT S Parameters Using Neural Networks

The HBT data that can be found in the manufacturer's data sheets are mostly limited to a number of discrete frequency points and, in the best cases, at a few bias conditions. On the other hand, reliable and accurate models of HBTs for whole frequency operating range and for wide bias condition ranges are required for the optimisation and design of microwave active circuits based on HBT technology. In this paper, neural network models are presented that can predict magnitudes and angles of all four S parameters of HBTs for any frequency and bias condition point within the transistor's operating range. For this purpose, a MLP (Multi-Layer Perceptron) network structure [6] has been used. The network has four layers: one input layer, two hidden layer, and one output layer. The number of neurons in the input and output layers is determined by the chosen number of input and output parameters. In this case, there are three neurons in the input layer that correspond to the DC bias V_c, DC base current I_b, and frequency *f*, and eight neurons in the output layer that correspond to the magnitudes and angles of the scattering parameters.

Neural network has been trained using a back-propagation algorithm [6]. A training set could be obtained by measurements, or from the simulation by using some other, often very complex model that requires much efforts and time. It is very important that the whole operating range of the device is adequately covered by the training set data. In this research a training set is generated by using the experimental data.

In principle, there are two approaches for the selection of number of neurons in hidden layers. The first approach is to perform the training procedure with a fixed number of neurons that is chosen in advance. The second one is to train several neural networks with different number of neurons in the hidden layers and select the best neural network comparing all models. In this research we have used the second approach.

In order to compare models' accuracy, average test error (ATE [%]), worst-case error (WCE [%]), and the *Pearson Product-Moment* correlation coefficient (r) between the referred and the modeled data have been calculated. The correlation coefficient indicates how well the modeled values match the referent values, i.e. a value near 1 indicates an excellent predictive ability. It is important to note that the test procedure has been done not only for the data from the training set, but also for the data that are not used in the training process, with the aim to check the generalization capability of developed neural networks.

IV. Modeling Results

In this research we have modeled six different AlGaAs HBT's, within 0.05÷40 GHz frequency range. The data for training sets that we used in modeling procedure had been obtained by collaboration with a microwave laboratory at Northeastern University, Boston, USA, where HBT S-parameter measurements were performed.

With the aim to illustrate the effectiveness and accuracy of neural modeling procedure, the results for a HBT device marked as HBT40020-002-8 are presented here. The total number of S parameters data used in training and test procedure for the selected HBT transistor was 5880. The data refers to the frequency range (0.05÷40) GHz. The frequency range was divided into four subranges as follows: first subrange (0.05÷0.5) GHz with 0.05 GHz step, second subrange (0.5÷1) GHz with 0.1 GHz step, third subrange (1÷10) with 1 GHz step, and fourth subrange (10÷40) GHz with 2 GHz step. Therefore, operating frequency range was covered with 35 discrete frequency points. S parameters were measured for different combination DC collector bias and base current in the whole frequency range. DC collector bias had the fallowing values: 1V, 3V, 4V, and DC base current had the fallowing values [μA]: 22, 39, 61 107, 195, 401 and 791. Therefore, the measurements were performed at 735 operating points and eight S parameter data (magnitudes and angles) correspond to each point: Mag(S_{11}), Ang(S_{11}), Mag(S_{12}), Ang(S_{12}), Mag(S_{21}), Ang(S_{21}), Mag(S_{22}) i Ang(S_{22}). Training set was obtained by extracting 595 data points from the measurement data. Therefore the training set contained 4760 S-parameters data. In order to check the generalization capability of neural network, a test set is generated from the rest of data points containing 1120 S-parameters data.

With the aim to avoid the errors caused by a rapid change of some S parameters angle characteristics between the values -180° and +180°, a conversion of the angle range from (-180÷180)° to the range (0÷360)° was performed.

Several neural networks with different number of hidden neurons were trained using the same training set. Number of hidden neurons varied between 9 and 16 neurons. The number of training epoch each network was limited on maximum 180. Time needed for training process on a Pentium 4 with processor declared on 2500+ and 512MB RAM was two hour and 15 minutes. However, once trained, the network provides fast response for different input vectors.

In order to improve the accuracy of neural models, multiplied training of the same network was performed. Namely, every new training process on the same neural network generates different errors. The reason for that is random setting of initial values of neural networks' weights and bias for each new training process. Therefore, in this research triple training process on each neural network has been performed with the aim to achieve better accuracy of the model. These models have then been applied to get the scattering parameter values for various bias values different from the ones used for training. The simulated results were compared with experimentally obtained data. On the basis of that, a model marked as 2M4_16_15 has been selected as the best model. The number 2 denotes second successive selected neural network training. The number 4 shows that the neural network has four layers. Numbers 16 and 15 denote the number of neurons in the first and second hidden layer, respectively.

As an illustration of selected model's accuracy, the scatter plots (correlation coefficient characteristics) for Mag(S) and

Angle(S) are shown in Fig. 1, where the outputs of the neural model are given on the Y axis and the experimental data are given on the X axis. It is important to note that the inputs in the neural model used for this calculation do not belong to the training set. It can be seen that simulated values match the measured data with a great accuracy forming linear correlation characteristics.

Fig. 2 shows the magnitudes and angles of all four *S* parameters versus frequency, obtained by using the chosen neural model, at four different bias points that have not been included in the training set:

(1) $V_c = 1V$, $I_b = 107\mu A$; (2) $V_c = 3V$, $I_b = 39\mu A$;

(3) $V_c = 3V$, $I_b = 195\mu A$; (4) $V_c = 4V$, $I_b = 107\mu A$.

For the comparison purpose, the corresponding experimental data are shown in the same figure. It can be seen that there is an excellent agreement of our model with the measured values. That shows that the developed neural model has a good generalisation ability.

V. CONCLUSION

The obtained results show that the neural network approach can be used as an efficient tool for small-signal modeling of HBT transistors. HBT neural models enable accurate prediction of magnitudes and angles of S parameters over the whole frequency range and over the broad ranges of operating conditions. In principle, some additional effects like the temperature could also be involved by including new neurons into the input layer and and by using appropriate training sets.

In comparison with other modeling approaches that could be applied for novel active devices used in modern communication systems, neural network approach has advantages from the aspect of simplicity, efficiency and accuracy. An insight into the physical operating mechanism is not necessary since a black-box approch is used. Neural network models provide simple and reliable prediction of device characteristics and can be easily implemented within the standard microwave circuit simulators.

REFERENCES

[1] N.L.Wang, "Transistor Technologies for RFICs in Wireless Applications", *Microwave Journal*, pp. 98-110, February, 1998.

[2] P.F.Chen et al., "Application of GaInP/GaAs DHBTs to Power Amplifiers for Wireless Communications", *IEEE Trans. Microwave Theory Tech*., vol. MTT-47, pp. 1433-1437, August 1999.

[3] R.Plana, L.Escotte, "Noise Properties of Microwave Heterojunction Bipolar Transistors", *MIEL'97 Proceedings*, pp. 215-222, Yugoslavia, 1997.

[4] A.Garlapati, S.Prasad, "Large Signal Characterization of Heterojunction Bipolar Transistors", *Proceedings of MICROCOLL'99*, pp. 181-189, Hungary, 1999.

[5] Q. J. Zhang, K. C. Gupta, *Neural Networks for RF and Microwave Design*, Artech House, 2000.

[6] S. Haykin, *Neural networks*, New York, IEEE, 1994.

[7] V.Marković, Z.Marinković, B.Milovanović, "New Neural Models of Microwave Transistor Noise Parameters Based on Bias Conditions", *Proc. of the Conference on Microelectronics MIEL'02*, Nis, Yugoslavia, pp. 405-408, 2002.

[8] V. Marković, Z. Marinković, "Signal and Noise Neural Models of pHEMTs", *6th Seminar on Neural Network Applications in Electrical Engineering, NEUREL-2002*, pp. 185-190, Yugoslavia, 2002.

[9] Z.Marinković, V.Marković, A.Caddemi, B.Milovanović, "Microwave Transistor Noise Models Including Temperature Dependence", *Proceedings of 6th International Conference TELSIKS 2003*, pp. 561-564, Niš, Serbia and Montenegro, 2003.

[10] K. Munshi, P. Vempada, S. Prasad, E. Sonmez, H. Schumacher, "Small signal and large signal modeling of HBT's using neural networks" *Proceedings of the 6th International Conference on Telecommunications in Modern Satellite, Cable and Broadcasting Services, TELSIKS 2003*, Vol 2, pp: 565- 568, Iss., 1-3 Oct. 2003.

[11] Anssi Hovinen, *Process Development and Device Modeling of Gallium Arsenide Heterojunction Bipolar Transistors*, doctoral dissertation, Helsinki University of Technology, http://www.hut.fi, 2001.

ACKNOWLEDGEMENTS

Authors would like to thank Prof. Sheila Prasad, Northeastern University, Boston, USA, for providing the experimental data used in this work.

This work has been supported by the Ministry of Science, Technologies and Development of Republic of Serbia under the project No. 1351.

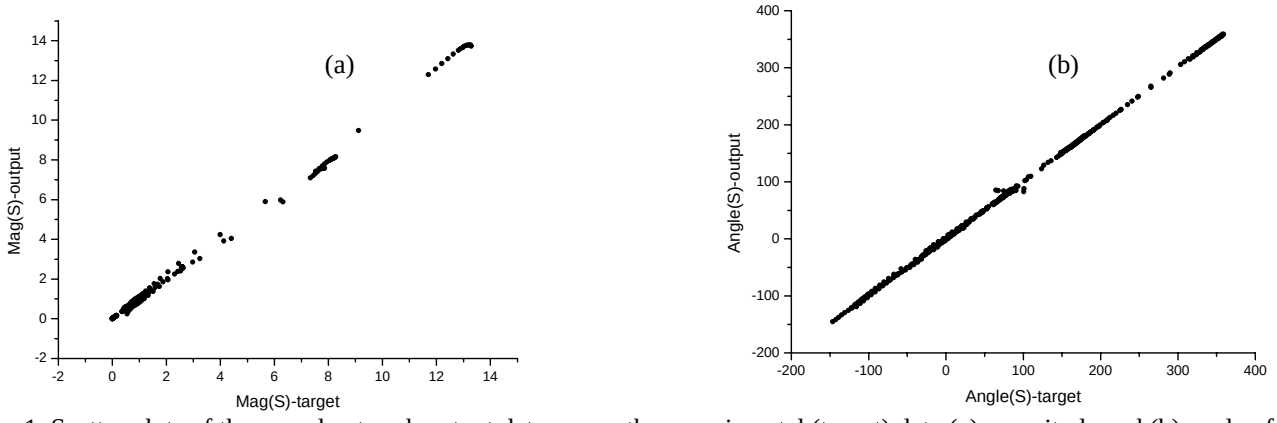

Figure 1. Scatter plots of the neural network output data versus the experimental (target) data:(a) magnitude and (b) angle of *S* parameters

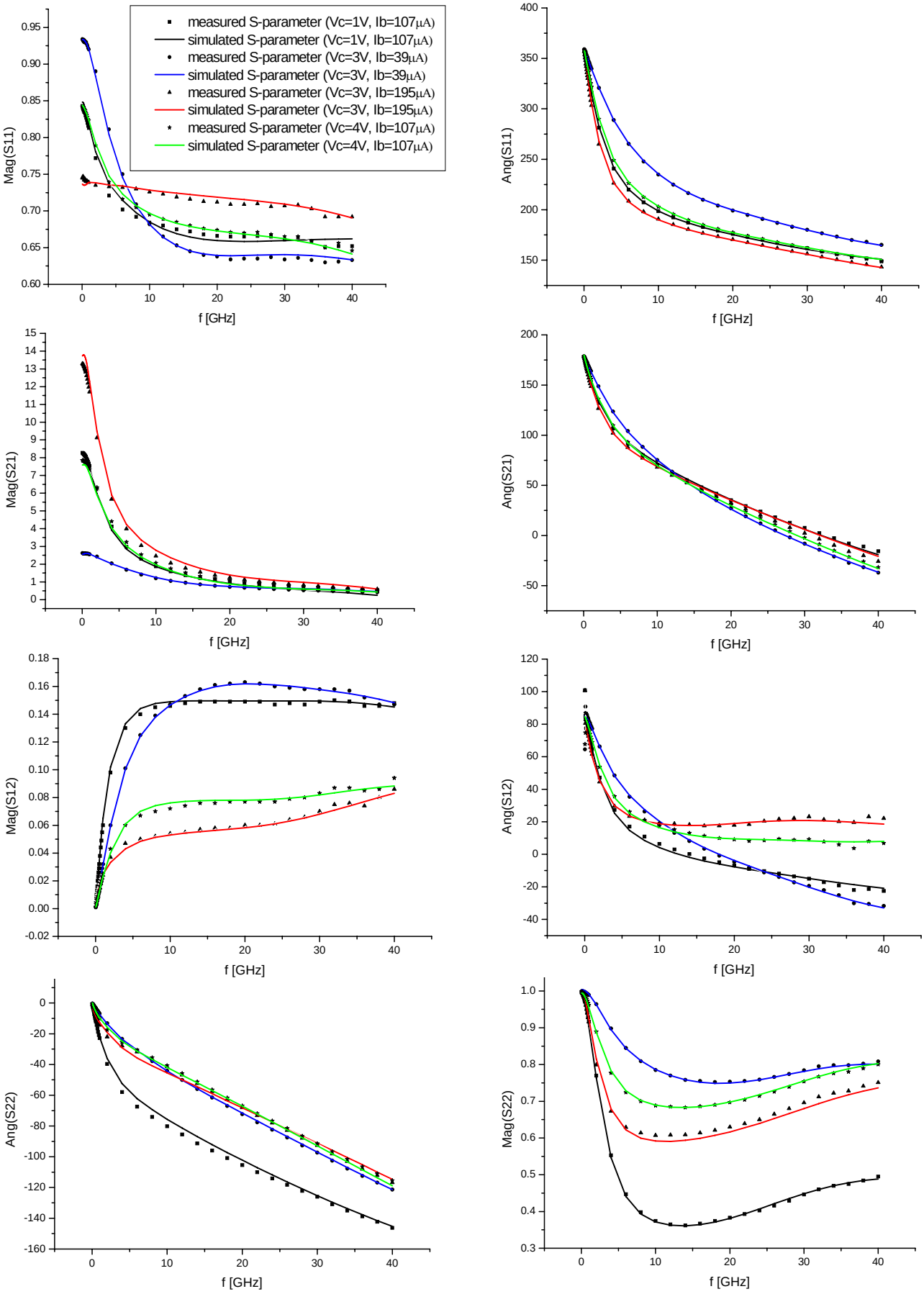

Figure 2. Results for *S* parameter characteristics obtaine by the neural model, compared to the experimental data

New Linearization Technique for Third- and Fifth-Order Intermodulation Products in Multichannel Amplifiers

Jovana Ranđelović, Natasa Maleš-Ilić, Bratislav Milovanović

Abstract — **New linearization technique that reduces the third and fifth-order intermodulation products is proposed in this paper. It introduces two independent sources in the linearization circuit from which one produces the second harmonics (IM2) and the other generates both the second harmonics and fourth-order nonlinearities of the fundamental signals (IM2+IM4). The reduction of the third- and fifth- order intermodulation products has been achieved by applying a new approach for a wide range of the fundamental signals' power going close to 1dB compression point. Also, proposed linearization technique enables that the phases of the injected signals do not need to be set on the optimal values and can fluctuate within appropriate range.**

Keywords – **Third- and fifth- order intermodulation products, linearization technique**

I. INTRODUCTION

The third-order intermodulation products are the major concern in microwave amplifiers in base stations of wireless communications systems. Besides the IM3 products, the fifth-order intermodulation products (IM5), that are the results of microwave amplifier nonlinearity as well, should be considered. The effects of fundamental signals' second-order nonlinear products, IM2, to the IM3 products in multichannel microwave amplifiers have been investigated and applied so far [1-4]. The IM2 term relates to the second harmonics at frequencies $2\omega_i$ and products at frequencies that are the sum of pairs of the fundamental signal frequencies, $\omega_i+\omega_j$. The linearization technique with the injection of IM2 signals decreases IM3 power levels without affecting the power levels of the fundamental signals but the reduction of the fifth-order intermodulation cannot be accomplished using this technique.

The linearization method described in [5] has opportunity to lower both the IM3 and IM5 products. It uses the IM2 signals and the fourth-order nonlinear signals of the fundamental ones (IM4), which are brought into the amplifier through the two different paths. However, the linearization circuit of the amplifier is far more complex than in the case when only the IM2 signals are led into the amplifier.

The linearization of the third- and fifth-order intermodulation products proposed in this paper exploits the IM2 signals in one injection path and the IM2 together with the IM4 signals (IM2+IM4) in the other. These signals are generated independently at the outputs of two nonlinear components at which inputs are the fundamental signals. Thus, this approach simplifies the linearization circuit of the microwave amplifier in comparison with the linearization technique proposed in [5].

Nataša Maleš-Ilić, Jovana Ranđelović, Bratislav Milovanović are with the Faculty of Electronic Engineering, Aleksandra Medvedeva 14,18000 Nis, Serbia and Montenegro,
E-mails: {jovanar, natasam, bata@elfak.ni.ac.yu)

II. ANALYSIS

The nonlinear transfer characteristic of the active component, MESFET, can be represented by a five term Taylor's series by introducing higher order nonlinearities up to fifth-order. The relation between the input voltage and output current is expressed as follows if transconductance is considered as a dominant nonlinearity.

$$i_{out}(t) = g_{m_1} v_{in}(t) + g_{m_2} v_{in}^2(t) + g_{m_3} v_{in}^3(t) + g_{m_4} v_{in}^4(t) + g_{m_5} v_{in}^5(t) \quad (1)$$

Two sinusoidal fundamental signals at the frequencies ω_i (i=1,2) with amplitudes V_{ω_i}, and phases φ_{ω_i}, are driven into the amplifier together with their second harmonics (IM2 signals) at the frequencies $2\omega_i$, with amplitudes $V_{2\omega_i}$, and phases $\varphi_{2\omega_i}$ which are put into the amplifier through one path. The IM2 and IM4 signals at frequencies $2\omega_i$, and $3\omega_i$-ω_j, $i\neq j$ $\in$(1,2), respectively, are injected through the other path. The amplitudes and phases of IM2 signals from the second path are $V'_{2\omega_i}$, and $\varphi'_{2\omega_i}$, whereas the IM4 signals' amplitudes and phases are $V_{\omega_{3i-j}}$, and $\varphi_{\omega_{3i-j}}$. Therefore, the input voltage can be written as:

$$v_{in} = \sum_{i=1}^{2} V_{\omega_i}\cos(\omega_i t) + \sum_{i=1}^{2} V_{2\omega_i}\cos(2\omega_i t + \varphi_{2\omega_i}) + \sum_{i=1}^{2} V'_{2\omega_i}\cos(2\omega_i t + \varphi'_{2\omega_i}) + \sum_{\substack{i=1 \\ i\neq j}}^{2}\sum_{\substack{j=1 \\ j\neq i}}^{2} V_{\omega_{3i-j}}\cos(3\omega_i t - \omega_j t + \varphi_{\omega_{3i-j}}) \quad (2)$$

Substituting Eq. (2) into Eq. (1) all IM3 and IM5 products can be calculated. The output current of the IM3 products at frequencies $2\omega_i$-ω_j ($i\neq j$=1,2) are expressed by Eq. (3) including nonlinear mixing products that are the results of square, g_{m2}, and cubic, g_{m3}, terms in the amplifier transfer characteristic. The first term in Eq. (3) relates to the

interaction between fundamental signals. The second term is dominant in reduction of the original IM3 product (the first term) by adjusting the appropriate IM2 signal in case when the linearization is performed by injection of only the IM2 signals. The influence of the injected IM2 signals to the IM3 product has been considered in [1-4].

$$
\begin{aligned}
I_{out(2\omega_i-\omega_j)} &= \frac{3}{4}V_{\omega_i}^2 V_{\omega_j} g_{m3}\cos\left(2\omega_i t-\omega_j t\right)\\
&\quad + V_{\omega_j} V_{2\omega_i} g_{m2}\cos\left(2\omega_i t-\omega_j t+\varphi_{2\omega_i}\right)\\
&\quad + V_{\omega_j} V'_{2\omega_i}\, g_{m2}\cos\left(2\omega_i t-\omega_j t+\varphi'_{2\omega_i}\right)\\
&\quad + V_{\omega_{3i-j}} V_{\omega_i} g_{m2}\cos\left(2\omega_i t-\omega_j t+\varphi_{\omega_{3i-j}}\right)\\
&\quad + \frac{3}{2}V_{2\omega_i} V_{2\omega_j} V_{\omega_j} g_{m3}\cos\left(2\omega_i t-\omega_j t+\varphi_{2\omega_i}-\varphi_{2\omega_j}\right)\\
&\quad + \frac{3}{2}V'_{2\omega_i} V'_{2\omega_j} V_{\omega_j} g_{m3}\cos\left(2\omega_i t-\omega_j t+\varphi'_{2\omega_i}-\varphi'_{2\omega_j}\right)\\
&\quad + \frac{3}{2}V_{2\omega_i} V'_{2\omega_j} V_{\omega_j} g_{m3}\cos\left(2\omega_i t-\omega_j t+\varphi_{2\omega_i}-\varphi'_{2\omega_j}\right)\\
&\quad + \frac{3}{2}V'_{2\omega_i} V_{2\omega_j} V_{\omega_j} g_{m3}\cos\left(2\omega_i t-\omega_j t+\varphi'_{2\omega_i}-\varphi_{2\omega_j}\right)\\
&\quad + \frac{3}{2}V_{\omega_{3i-j}} V_{2\omega_i} V_{\omega_i} g_{m3}\cos\left(2\omega_i t-\omega_j t+\varphi_{\omega_{3i-j}}-\varphi_{2\omega_i}\right)\\
&\quad + \frac{3}{2}V_{\omega_{3i-j}} V'_{2\omega_i} V_{\omega_i} g_{m3}\cos\left(2\omega_i t-\omega_j t+\varphi_{\omega_{3i-j}}-\varphi'_{2\omega_i}\right) \quad (3)
\end{aligned}
$$

The third term is the consequence of the injection of IM2 signals from IM2+IM4 source and square nonlinearity. The fourth term is the result of interaction between fundamental and appropriate IM4 signal. The linearization approach proposed in this paper suggests that the g_{m2} mixing products (second, third and fourth terms in Eq. (3)) be combined to cancel the original IM3 products. Additionally, there are terms at IM3 frequencies that are the results of the cubic nonlinearity in the amplifier characteristic. These products are generated by mixing the fundamental signal and two IM2 signals as well as the fundamental, IM2 and IM4 signals. The IM2 and IM4 signals can originate from the same source (fifth, sixth and tenth terms) or from the independent sources (seventh, eightieth and ninth terms).

In Eq. (4) the first term expressing the output current of the IM5 products at frequencies $3\omega_i$-$2\omega_j$ is formed due to the existence of fundamental signals and amplifier nonlinearity of the fifth-order. The second term is the mixing product between the fundamental signal and the injected IM4 signal at frequency $3\omega_i$-ω_j. Therefore, by adjusting the amplitude and phase of the appropriate IM4 signal the original IM5 product (the first term) can be reduced. The IM5 products are also expressed in terms of g_{m3} mixing terms made by reaction between the two IM2 signals and fundamental one.

All mixing terms which stand by g_{m3} in Eqs. (3) and (4) can be neglected for lower power of the fundamental signals, up to approximately 10 dB back off from 1-dB compression point. In the case of higher power of the input signals those terms affect the power of IM3 and IM5 products depending on the phases of the injected IM2 and IM2+IM4 signals. Accordingly, if the IM2 signals injected through two different paths have opposite phases (or that they differ in phases for more than 90°) the seventh term in Eq. (3) will decrease the fifth term, the eightieth term will reduce the sixth term and the last two will influence each other. It is obvious from Eq. (4) that the g_{m3} mixing terms behave exactly the same.

$$
\begin{aligned}
&I_{out(3\omega_i-2\omega_j)} =\\
&\frac{5}{8}V_{\omega_i}^3 V_{\omega_j}^2 g_{m5}\cos\left(3\omega_i t-2\omega_j t\right)\\
&+ V_{\omega_j} V_{\omega_{3i-j}} g_{m2}\cos\left(3\omega_i t-2\omega_j t+\varphi_{\omega_{3i-j}}\right)\\
&+ \frac{3}{2}V_{2\omega_i} V_{2\omega_j} V_{\omega_i} g_{m3}\cos\left(3\omega_i t-2\omega_j t+\varphi_{2\omega_i}-\varphi_{2\omega_j}\right)\\
&+ \frac{3}{2}V_{2\omega_i} V'_{2\omega_j} V_{\omega_i} g_{m3}\cos\left(3\omega_i t-2\omega_j t+\varphi_{2\omega_i}-\varphi'_{2\omega_j}\right)\\
&+ \frac{3}{2}V'_{2\omega_i} V_{2\omega_j} V_{\omega_i} g_{m3}\cos\left(3\omega_i t-2\omega_j t+\varphi'_{2\omega_i}-\varphi_{2\omega_j}\right)\\
&+ \frac{3}{2}V'_{2\omega_i} V'_{2\omega_j} V_{\omega_i} g_{m3}\cos\left(3\omega_i t-2\omega_j t+\varphi'_{2\omega_i}-\varphi'_{2\omega_j}\right) \quad (4)
\end{aligned}
$$

III. Amplifier Design

The amplifier with the additional circuitry for the injection and adjustment of IM2 as well as IM2+IM4 signals is represented in Fig. 1. The broadband single-stage amplifier designed as described in [3] has been used for the nonlinear amplifier denoted as Amp.

The fundamental signals are led to the inputs of two components with high-order and low–order non-linear characteristics. Therefore, in the point denoted as P1, Fig.1, both IM2 and IM4 signals are generated with high power and IM2>IM4, while at the point P2, the IM2 signals have sufficient power levels, and IM4 can be neglected. The IM2 and IM2+IM4 signals obtained at points P2 and P1, respectively, are adjusted in amplitudes and phases through two separated paths. They are combined with the fundamental signals at the amplifier input (P3). The phase shifters, variable attenuators, power combiners/splitters, bandpass filters are additional components included in the injection paths of the IM2 and IM2+IM4 signals.

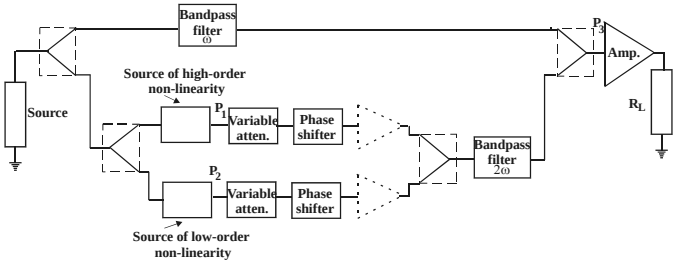

Fig 1. Amplifier with the circuit for linearization

The design of the amplifier with the linearization circuit has been carried out by the program named Advance Design System (ADS). In simulation the ideal elements from the library of this software have been used for the linearization circuit's components. For the components denoted as nonlinear sources with low and high-order nonlinearity, the

amplifier designed and supplied with different biases has been used in simulation.

IV. Simulated Results

The designed amplifier with the additional circuit for the linearization has been tested for three sinusoidal fundamental signals at frequencies 2.5 GHz, 2.51 GHz and 2.522 GHz for two signals' power levels, –6 dBm and -1 dBm that is 5 dB below 1-dB compression point. The results for IM3 products (the first and second kind) at frequencies 2.478 GHz and 2.488 GHz, as well as IM5 products at frequencies 2.456 GHz, 2.466 GHz 2.468 GHz are shown in Table I. Column (d) shows the results obtained by the linearization approach presented in this paper when the IM2 and IM2+IM4 signals are adjusted on optimal amplitudes and phases. The achieved results are compared with the IM power levels without applying linearization technique (col. a), after linearization with the injection of only IM2 signals (col. b), and after linearization attained by using IM2 and IM4 signals, [5], (col. c).

Various results are gained for different input power levels and kinds of IM3 and IM5 signals. For example, all IM3 products at frequencies $2\omega_i$-ω_j (the first kind) and ω_i+ω_j-ω_k (the second kind) $i \neq j \neq k \in (1,2,3)$ are approximately reduced by 32 dB for input power level –6 dBm. The reduction rate is descending with the higher input power, so that the IM3 products of the first and second kinds are reduced by approximately 11 dB at -1 dBm input power. If the results referring to all IM5 products are concerned then the improvements are 10 dB for –6 dBm up to 3 dB for -1 dBm input power for ($3\omega_i$-$2\omega_j$) kind of the IM5 products. The IM5 products at frequencies ($2\omega_i$+ω_j-$2\omega_k$) are lowered by 11 dB for both power levels, while the IM5 products at frequencies ($3\omega_i$-ω_j-ω_k) are decreased by 13 dB for -6 dBm and by 2 dB for -1 dBm.

It follows from the simulated results that considerably greater reduction of IM5 power levels are obtained by the injection of IM2 and IM2+IM4 signals than in the linearization with the IM2 signals only. Also, it is clear that at the input power level -1 dBm the reduction of IM3 products is negligible by applying merely the IM2 signals' injection. In contrast to this, all IM3 products are suppressed by 11 dB by using the linearization technique suggested in this paper. The results relating to the IM3 products is better in the proposed technique than in the case when the IM2 signals are put into amplifier through one path and IM4 signals are injected through the other path. Additionally, the linearization circuit of the latter linearization approach contains four components (variable attenuator, phase shifter, power splitter and combiner) more than in the circuit shown in Fig.1 that suits the linearization technique proposed in this paper.

Additionally, the linearization approach presented in this paper allows that the IM2 signals from one injection path can have the phases from the range of 80^0 while the phase of IM2+IM4 signals in the other injection path can vary in the range of $\Delta=20^0$ as displayed in Fig. 2 for the input power level -6 dBm. The output spectra containing the fundamental signals, IM3 and IM5 products before (dashed lines) and after the linearization (solid lines) for -20° deviation from the optimal phase in the injection path of the IM2 signals are shown in Fig.3.

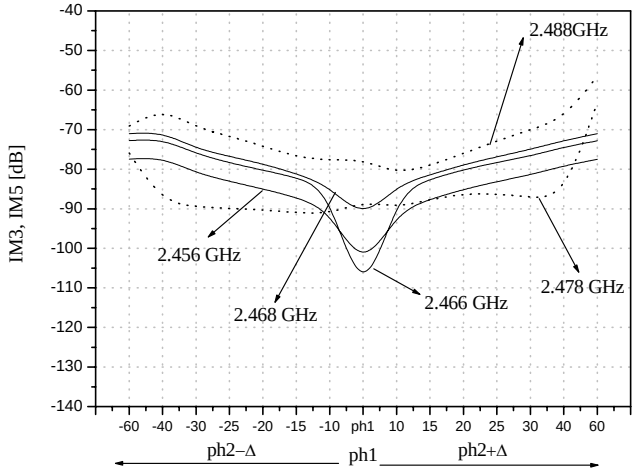

Fig 2. IM3 and IM5 products after linearization for various phases of IM2 and IM2+IM4 signals in case of -6 dBm input power

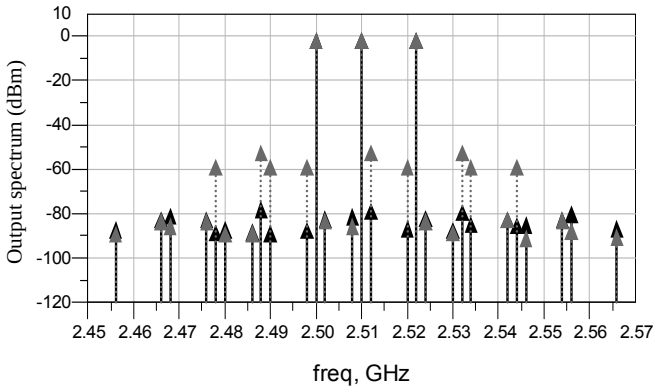

Fig 3. Output spectrum for -6 dBm input power of fundamental signals; before (dashed line) and after linearization (solid line) for -20^0 deviation from the optimal phase.

When the output power is -1 dBm, the fluctuation of the IM2 signals' phases in one injection path is limited to the range of 30° while the same parameter should stay within Δ'=15° range in the other injection path as illustrated in Fig. 4. Fig. 5 shows the output spectrum for -15^0 variation from the optimal phase in the injection path of IM2 signals.

Viewing the results one can notice nearly the same power of the IM3 products in case when phases in two injection paths take values from appropriate range as achieved for the optimal case. The IM5 products become worse for a few decibels than they had been before linearization for -6 dBm input power. In the case of -1 dBm input power the IM5 products are lowered, with the exception at 2.456 GHz frequency, in comparison with the state before linearization. The rate of reduction is slightly less than in the optimal case and depends on the frequencies. All the more remarkable is that the IM5 products in the considered power range of the input signals are kept either lower than the reduced IM3 products or nearly equal to them.

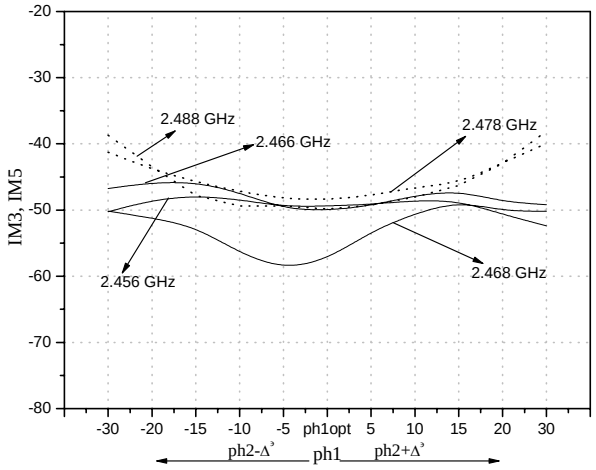

Fig. 4. IM3 and IM5 products after linearization for various phases of IM2 and IM2+IM4 signals in case of -1 dBm input power

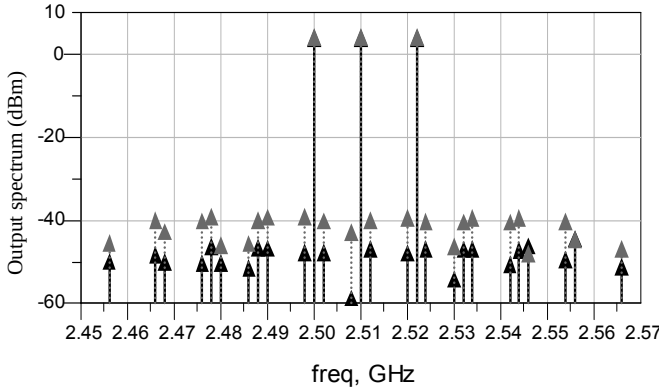

Fig 5. Output spectrum for -1 dBm input power of fundamental signals; before (dashed line) and after linearization (solid line) for $+15^0$ deviation from the optimal phase.

V. CONCLUSION

The linearization approach proposed in this paper uses the IM2 signals generated at the output of a low-order nonlinear component and IM2 +IM4 signals appearing as the output of a high-order nonlinear component. Those signals are adjusted and led to the amplifier input through the two separated paths. The proposed technique gives good results in reduction of the IM3 and IM5 products for lower power of the fundamental signals of up to 10 dB back off from 1-dB compression point. Also, satisfactory decrease of the IM3 power levels can be achieved for the higher power of fundamental signals near 1-dB compression point. Those results are nearly the same as in the case when the IM2 signals are driven through one path, while only the IM4 signals are injected through the other path, but considerably better than in the linearization with only the IM2 signals. Quite the most important fact is that the linearization circuit is not as complex as in the linearization with the IM2 and IM4 signals. On the top of that, the phases in two different injection paths are not constrained on optimal values and can fluctuate within appropriate range.

REFERENCES

[1] D. Jing, W. S. Chan, S. M. LI, C. W. Li, "New linearization method using interstage second harmonic enhancement", IEEE Microwave and Guided Wave Letters, Vol. 8, pp. 402-404, 1998.

[2] C. S. Aitchison, M. Mbabele, M. R. Moazzam, Dj. Budimir, and F. Ali, "Improvement of third order intermodulation products of RF and microwave amplifiers by injection", IEEE MTT Transactions on Microwave Theory and Techniques, Vol.49, pp.1148-1154, June 2001.

[3] N. Maleš-Ilić, B. Milovanović, Đ. Budimir, "Amplifiers with improved IMD performance for multi-channel wireless systems", Proc. Int. Conf. European Microwave Conference, September 2002, Milan, Italy.

[4] N. Maleš-Ilić, B. Milovanović, Đ. Budimir, "Improvement in "Second Harmonics" Linearization Technique for Multichannel Amplifiers", *Microwave and Optical Technology Letters*, Vol.38, No. 2, pp. 150-153, July 2003.

[5] N. Maleš-Ilić, Đ. Budimir, B. Milovanović: "Linearization Technique for Reducing Third- and Fifth-Order Intermodulation Distortion Products in Multichannel Amplifiers" Proc. of International Conference EUMC 03, Munich, Germany, October, 2003.

TABLE I: THE POWER LEVELS OF IM3 AND IM5 PRODUCTS WITHOUT APPLYING LINEARIZATION (COL. A)), WITH THE INJECTION OF IM2 SIGNALS (COL. B)), WITH THE INJECTION OF IM2 AND IM4 SIGNALS (COL. C)), AND WITH THE INJECTION OF IM2 AND IM2+IM4 SIGNALS (COL. D))

	2.456 $3\omega_i-2\omega_j$				2.466 $2\omega_i+\omega_j-2\omega_k$				2.468 $3\omega_i-\omega_j-\omega_k$				2.478 $2\omega_i-\omega_j$				2.488 $\omega_i+\omega_j-\omega_k$			
Pwr. [dBm]	a)	b)	c)	d)	a)	b)	c)	d)	a)	b)	c)	d)	a)	b)	c)	d)	a)	b)	c)	d)
-6	-87	-91	-110	-102	-81	-84	-100	-93	-83	-87	-91	-102	-57	-85	-83	-89	-50	-81	-81	-82
-1	-44	-44	-48	-49	-39	-39	-49	-50	-41	-43	-53	-58	-38	-40	-47	-48	-39	-41	-44	-50

Amplitude Modulation of the Class E Power Amplifier

Iliya N. Nemigenchev[1], Iliya V. Nedelchev[2]

Abstract **In this paper is presented a highly effective radio-frequency power amplifier class E. The linear dependence of the amplitude output voltage from the supply voltage gives opportunity for its usage at the radio transmitters of AM signals. Here are presented the analytical dependences of the amplifier's parameters when working in carrier modes and AM signals. The amplitude frequency, static modulation, dynamic modulation and frequency modulation characteristics of the amplifier with output peak power P_{pk}=116 W and working frequency f_s = 3.5 MHz are presented.**

Keywords – **Amplitude Modulation, High Efficiency RF Power Amplifier, Class E .**

I. Introduction

RF power amplifiers, class E occur determining for the energetic, and technical-economical parameters of the radio transmitters. The best way for increasing the efficiency of the power amplifier is the usage of the switch working mode, due to which under certain conditions is achieved a maximum efficiency and the output power in the load.

The resonant amplifiers class E, working in the switch mode absolutely satisfy these requirements as they work at efficiency above 96%.

It has got a linear dependence of the output voltage from the voltage of the drain, as the angle of conduction and the form of the output voltage do not depend on the change of the supply voltage. This leads to linear modulation characteristics, as the distortion of the modulation envelope can easily be done under 1%.

II. Theoretical Analisis

A. Carrier mode

The basic circuit of power amplifiers class E working in carrier mode is shown on fig. 1. MOSFET transistor is used which turns periodically with the carrier frequency. The optimal effective work of the amplifiers class E is obtained when the voltage on the transistor V_{DS} and its declination (dV_{DS}/dt) are zero [1], [2], [5], [7], when transistor turns on. The maximum power is obtained when duty cycle is 50 % [1], [6].

[1]Iliya N. Nemigenchev is with the Technical University Dep KTT, H.Dimitar4,5300Gabrovo, Bulgaria,E-mail: nemig@tugab.bg

[2]Iliya V. Nedelchev is with the Technical University Dep. KTT, H. Dimitar 4, 5300 Gabrovo, Bulgaria,E-mail: lined@tugab.bg

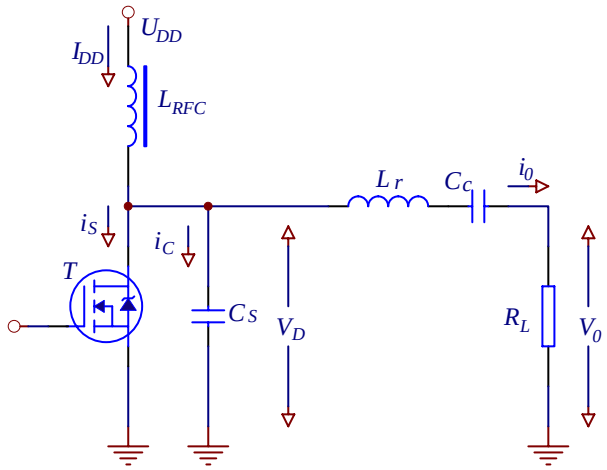

Fig. 1. A basic circuit of power amplifiers class E

For analysis and design of amplifier in optimal mode is done the equivalent circuit on fig. 2. For duty cycle 50 % should be satisfied the following ratios: [1], [2], [6]. For analysis L_r is divided to L_c and ΔL. ΔL is obtained from the equation

$$\Delta L = \frac{\pi(\pi^2 - 4)R_L}{16\omega_c} \approx 1.1525\frac{R_L}{\omega_c} \quad (1)$$

The following equations are used to obtain:

- the inductance

$$L_c = \frac{(Q - 1.152)R_L}{\omega_c} \quad (2)$$

- the capacitances

$$C_c = \frac{1}{L\omega_c^2} \quad (3)$$

and

$$C_s = \frac{8}{\pi(\pi^2 + 4)\omega_0 R_L} \approx \frac{0.1836}{\omega_c R_L} \quad (4)$$

- the resonant frequencies

$$\omega_r = \frac{1}{\sqrt{C_c L_r}} = \frac{1}{\sqrt{C_c(L_c + \Delta L)}} \quad (5)$$

and the quality factor

$$Q_r = \frac{\omega_r L_r}{R_L} = \frac{1}{\omega_r C R_L} \quad (6)$$

Resultant resonant circuit has lower resonant frequency ω_r from the frequency of the carrier ω_c, which is determined by the value of the qualitative Q_r. This leads to non-linear distortions of AM output voltage on R_L, because the upper and lower side bands of the modulated oscillation are transmitted through the load resonant circuit with different amplitude and

delay. This occurs especially at the amplification of SSB signals.

In order to eliminate the influence of the inductance L_{RFC} on the distortion AM signal should satisfy the condition [4]

$$L_{RFC\min} = \left(\frac{\pi^2}{4} + 1\right)\frac{R_L}{f_c} \approx 3.5\frac{R_L}{f_c} \quad (7)$$

B. AM at amplifier class E

On the compiled equivalent scheme for the aims of the analysis the switching transistor is modeled as a switch in series with a static drain-to-source on-resistance (Fig. 2). The amplitude of the output voltage is proportional to the voltage on the drain V_D [1], [2], [4]

$$V_{0m} = \frac{4}{\sqrt{\pi^2 + 4}}\left(V_{DD} - V_{R_{ON}}\right) \approx 1.074\left(V_{DD} - V_{R_{ON}}\right) \quad (8)$$

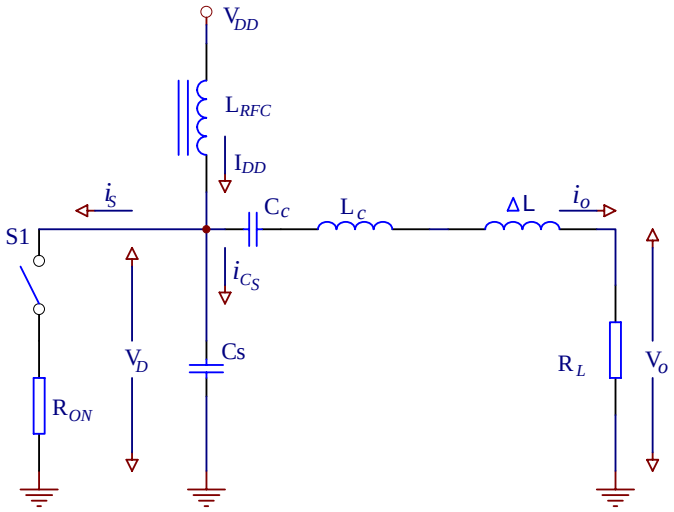

Fig. 2. Equivalent circuit of amplifier class E

Amplitude modulation with a good linearity could be obtained when the voltage on turn-on transistor depends on the current through the drain; the controlling signal at high frequencies passing through the capacitance C_{GD} does not exert influence when the modulating signal is of a little value and the output capacity of the transistor C_{DS} is not with significant value in respect of C_S .

The analysis of the amplitude modulation at amplifier class E is done on the basis of the equivalent circuit shown on Fig. 2 under the following assumptions:

-the static modulation characteristic $V_{0m}=f(V_{DD})$ is linear and is described by the expression (8);

-the distortions caused by the inductance L_{RFC} are zero, condition (8);

-the amplifier works in optimal, condition from (1) to (4).

At the analysis will be used harmonious modulating oscillation

$$v_m(t) = V_m \cos\omega_m t \quad (9)$$

From AM signal obtained at the output of the amplifier only the fundamental component transmits to the load (carrier, lower and upper side bands) while other components are suppressed by resonant circuit.

$$v_{D1}(t) = V_{D1}(1 + m\cos\omega_m t)\cos\omega_c t =$$
$$= V_{D1}\left[\cos\omega_c t + \frac{m}{2}\cos(\omega_c - \omega_m)t + \frac{m}{2}\cos(\omega_c + \omega_m)t\right] \quad (10)$$

The voltage transfer function from the drain to R_L is

$$\overline{K} = Ke^{j\varphi} = \frac{1}{1 + j\left(\frac{\omega L_r}{R_L} - \frac{1}{\omega C_c R_L}\right)} = \frac{1}{1 + jQ_r\left(\frac{\omega}{\omega_r} - \frac{\omega_r}{\omega}\right)} =$$
$$= \frac{1}{1 + jQ_r\left(\frac{\omega_c}{\omega_r}\cdot\frac{\omega}{\omega_c} - \frac{\omega_r}{\omega_c}\cdot\frac{\omega_c}{\omega}\right)} \quad (11)$$

where Q_r is determined by expression (4). From (1) and (4) we can write down

$$\frac{\omega_c}{\omega_r} = \frac{\frac{\pi(\pi^2 - 4)}{16} + \sqrt{4Q_r^2 + \left[\frac{\pi(\pi^2 - 4)}{16}\right]^2}}{2Q_r} \quad (12)$$

From (10), we obtain modules and arguments of voltage of the transfer function at the carrier frequency ω_c, lower sideband (ω_c - ω_m) and upper sideband (ω_c + ω_m).

$$K_c = K(\omega_c) = \frac{1}{\sqrt{1 + \left[\frac{\pi}{16}(\pi^2 - 4)\right]^2}} \approx 0.665 \quad (13)$$

$$\varphi_c = \varphi(\omega_c) = -\arctan\left[\frac{\pi}{16}(\pi^2 - 4)\right] \approx 49.05^0 \quad (14)$$

$$K_l = K(\omega_c - \omega_m) =$$
$$= \frac{1}{\sqrt{1 + \left\{Q_r\left[\frac{\omega_c}{\omega_r}\left(1 - \frac{\omega_m}{\omega_c}\right) - \frac{1}{\frac{\omega_c}{\omega_r}\left(1 - \frac{\omega_m}{\omega_c}\right)}\right]\right\}^2}} \quad (15)$$

$$\varphi_l = \varphi(\omega_c - \omega_m) =$$
$$= -\arctan\left\{Q_r\left[\frac{\omega_c}{\omega_r}\left(1 - \frac{\omega_m}{\omega_c}\right) - \frac{1}{\frac{\omega_c}{\omega_r}\left(1 - \frac{\omega_m}{\omega_c}\right)}\right]\right\} \quad (16)$$

$$K_u = K(\omega_c + \omega_m) = \\ = \frac{1}{\sqrt{1+\left\{Q_r\left[\frac{\omega_c}{\omega_r}\left(1+\frac{\omega_m}{\omega_c}\right)+\frac{1}{\frac{\omega_c}{\omega_r}\left(1+\frac{\omega_m}{\omega_c}\right)}\right]\right\}^2}} \quad (17)$$

$$\varphi_u = \varphi(\omega_c + \omega_m) = \\ = -\arctan\left\{Q_r\left[\frac{\omega_c}{\omega_r}\left(1+\frac{\omega_m}{\omega_c}\right)-\frac{1}{\frac{\omega_c}{\omega_r}\left(1+\frac{\omega_m}{\omega_c}\right)}\right]\right\} \quad (18)$$

From expressions (10) and (13) to (18) we fix AM output tension

$$v_0(t) = V_{D1}\{K_c\cos(\omega_c t+\varphi_c)+ \\ +\frac{m}{2}K_l\cos[(\omega_c-\omega_m)t+\varphi_l]+ \\ +\frac{m}{2}K_u\cos[(\omega_c+\omega_m)t+\varphi_u]\} \quad (19)$$

The output voltage could be written as

$$v_0(t) = V_0(t)\cos[\omega_c t+\phi(t)] \quad (20)$$

The amplitude V_0 *(t)* and the initial ϕ(t) of the output voltage change due the course of time. Essential is the change of the amplitude

$$V_0(t) = V_{D1}\left\{\left[K_c\cos\varphi_c+\frac{m}{2}K_l\cos(\omega_m t-\varphi_l)+\right.\right. \\ \left.+\frac{m}{2}K_u\cos(\omega_m t+\varphi_u)\right]^2+ \\ +\left[K_c\cos\varphi_c-\frac{m}{2}K_l\sin(\omega_m t-\varphi_l)+\right. \\ \left.\left.+\frac{m}{2}K_u\sin(\omega_m t+\varphi_u)\right]^2\right\}^{1/2} \quad (21)$$

As a result of this that the amplifier works at higher frequency than resonant for C_c –L_r resonant circuit upper sideband is transmitted suppressed with less amplitude and larger phase. The two sidebands components are transmitted from the drain to R_L with different magnitudes and different delays. This causes harmonic distortion of the envelope of the AM output voltage [4]. In addition, the fundamental component of the envelope decreases with f_m .

III. RESULTS

On the basis of above formulated material was designed power amplifier class E with the following parameters f_c*=3.5 MHz,* L_{RFCmin}*=50 μH, Lc =20.12 μH, Cc=100 pF, ΔL=2.62 μH,* C_s*=167 pF,* R_L*=50 Ω ,Q=10,* V_{dc}*=50 V,* V_m*=50 V,* P_{pk}*=115 W,* P_{out}*=25 W* and MOSFET transistor IRFBC40.

A computer simulation is executed on the power amplifier. We examined its work in carrier mode. On Fig. 3 are shown the waveforms of the control voltage, the voltage at the output of the amplifier, the waveform of the current through radio frequency choke, the waveform voltage on the load. Results show the work of the amplifier at optimal mode.

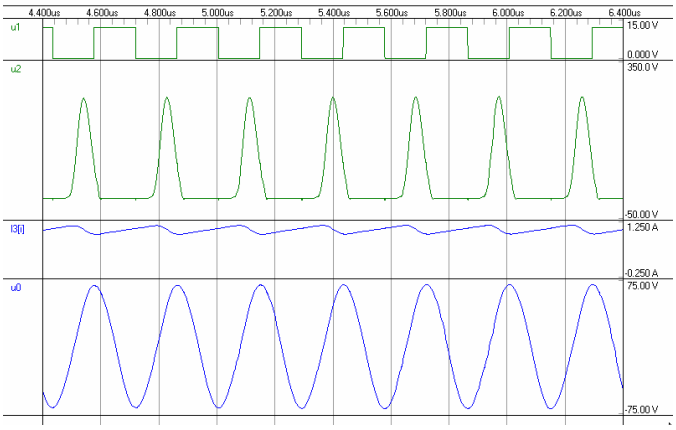

Fig. 3. Waveform of the voltages at amplifier class E

Here is shown the static modulation characteristic of the amplifier which presents the dependence of the output voltage from drain voltage $V_{0m}=f(V_D)$. The dependence is comparatively linear and it is a precondition for a linear amplitude modulation.

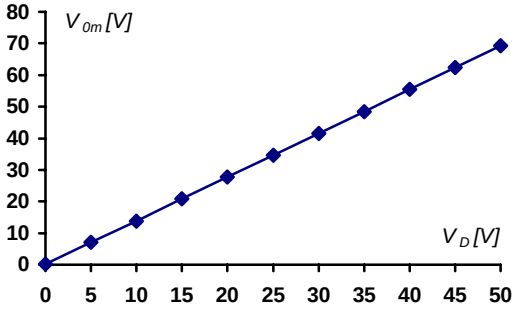

Fig. 4. Dependence $V_{0m}=f(V_D)$.

In RF range the modulating signals AM are with frequency band not wider than 4,5 kHz. That is why measured frequency modulation characteristic $m=f(f_m)$ is done in such frequency range. Modulation index *m* changes with not more than 1,2 % in the whole frequency range which for office connections and broadcasting completely satisfy the requirements.

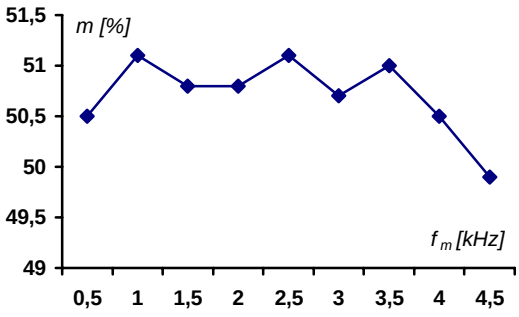

Fig. 5. Dependence $m=f(f_m)$

The dependence of modulation index from modulation voltage $m=f(V_m)$ is the dynamic modulation characteristic shown on Fig.6. The characteristic is linear, which is a factor for reduction of the distortion of the form of envelope at AM.

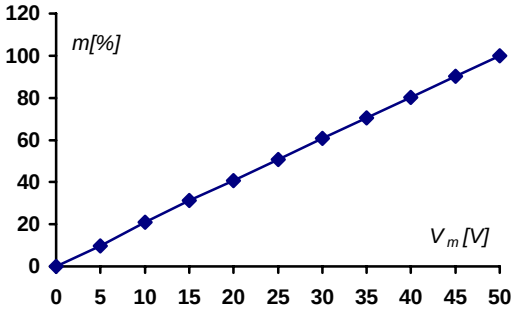

Fig. 6. Dependence $m=f(V_m)$

The work of power amplifier class E in a mode of amplitude modulation with $m=100$ % is shown on Fig. 7. The waveform of the voltage on the drain V_D and on the load V_0 shows that there are not distortions.

Results show that amplifier can be used successfully for constructing of radio transmitters for AM and CW.

IV. Conclusion

The precise analysis of resonant amplifier class E shows that it works very well with AM signals. The non-linear distortions of envelope of AM output are a result of the following reasons: transistor; output load circuit; radio frequency choke.

The non-linear distortions caused by transistor are very low in view of the fact that the conduction angle and the form of the output voltage are not change by variations of the supply voltage. The serial resonant circuit in the load circuit should be detuned by the carrier frequency to obtain optimum-efficiency operation of the amplifier. The distortions increases with the relation of modulation and carrier frequency f_m/f_c, the depth of the modulation m and the qualitative factor of the load circuit Q_r and they can reach mote than 10 %.

The non-linear distortions could be reduced under 1 % if f_c/f_m >50 and Q_r >15. Radio frequency choke should be chosen by compromise between the distortions and the optimal work of the amplifier. Too high inductance of the radio frequency choke reduces the depth of modulation m, while too low one disturbs the effective performance. The simulation shows that the process of amplitude modulation in amplifier class E is very good.

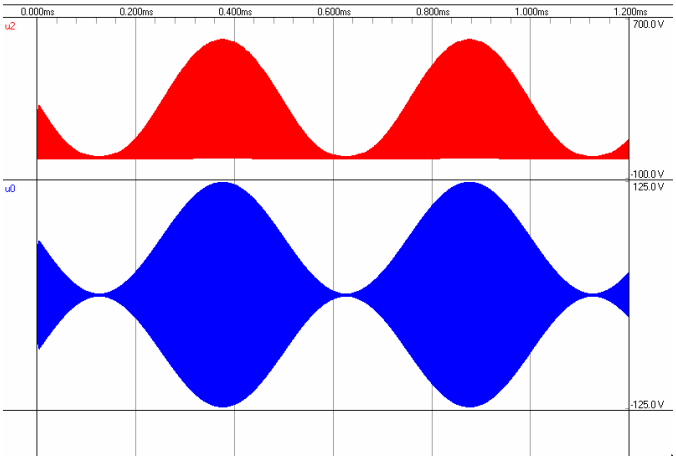

Fig. 7.The waveform of V_D and V_0.

References

[1] F. Raab, “Idealized Operation of the Class E Tuned Power Amplifier”, *IEEE Transactions on Circuits and Systems*, vol. Cas. 24, no 12, pp 725-735, December 1977.

[2] H. Krauss, F. Raab, “Solid State Radio Engineering. New York, *Jon Wiley & Sons, Ins.*, 1980.

[3] J. Ebert, M. Kazimierczuk, “Class E High-Efficiency Tuned Power Oscillator”, *IEEE Journal of Solid-State Circuits*, vol. Sc.-16 no. 2, pp. 62-65, April 1981.

[4] M. Kazimierczuk, “Collector Amplitude Modulation of the Class E Tuned Power Amplifier”, *IEEE Traansactions on Circuits and Systems*, vol. Cas-31, no. 6, pp. 543-549, June 1984.

[5] N. Sokal, A. Sokal, " Class E-A New Class of High-Efficiency Tuned Single-Ended Switching Power Amplifiers", IEEE Journal of Solid-State Circuits, vol. Sc.-10 no. 3, pp.168-176, June 1975.

[6] N. Sokal, “Class E RF Power Amplifiers”, QEX, Jan/Feb 2001, pp. 9-20.

[7] S. Cripps, “RF Power Amplifiers for Wireless Communications”, *Artech House, Boston London*, 1999

Amplifier Noise Model with Thevenin Input Source

Pesha D. Petrova[1]

Abstract – **An amplifier noise model is described. The equivalent noise input voltage is derived for the case where the source is represented by a Thevenin source. The correlation between noise sources is taken into consideration. The effect of both series and shunt impedance at the input on the equivalent noise is analyzed. Amplifier noise simulations are performed. MATLAB simulation results are presented.**

Keywords – **amplifier noise model, Thevenin source, series impedance, shunt admittance, MATLAB simulation**

I. INTRODUCTION

Noise behavior is an important characteristic of electronic circuits, including analog amplifiers, as it usually determines the fundamental limit of the performance of circuits.

The significance of the noise performance of each analog circuit is the limitation it places as the smallest input signals the circuit can handle before the noise degrades the quality of the output signal. For this reason, the noise performance is usually expressed in terms of equivalent input noise signal, which gives the same output noise as the circuit under consideration. This fact allows replacing the real noisy network by noiseless network and equivalent input noise signal [1], [2]. This approach of noise modeling can be successfully applied to the analog amplifiers.

A general noise model of an amplifier can be obtained by representing all internal noise sources to the input. In order for the reflected sources to be independent of the source impedance, two noise sources are required – a series voltage source and a shunt current source [3]. Both Thevenin's and Norton's theorems may be used to develop noise models for amplifiers. The equivalent noise input voltage and current can be determined if the source is represented by a Thevenin or by a Norton equivalent.

In many cases the correlation between the noise sources is neglected. In fact, the noise generators are always correlated and the correlation causes the addition input noise voltage or input noise current. In other words, the correlation between noises sources effects on the circuit equivalent input noise. Therefore, for precision noise analysis of the amplifiers, it is always necessary to take into consideration the effect of the correlation coefficient that can vary between -1 and 1. This is very important prerequisite to develop more effective and accurate amplifier noise models.

[1]Pesha D. Petrova is with the Department of Communication Techniques and Technologis, Technical University of Gabrovo, 4, H. Dimitar Str., 5300 Gabrovo, Bulgaria, E-mail: daneva@tugab.bg

II. AMPLIFIER NOISE MODEL WITH THEVENIN SOURCE

The amplifier noise model with a Thevenin noise input source is shown in Fig.1. In this model V_S is the source voltage, $Z_S = R_S + jX_S$ is the source impedance, V_{tS} is the thermal noise voltage generated by the source, and V_n, I_n are the noise sources representing the noise generated by the amplifier.

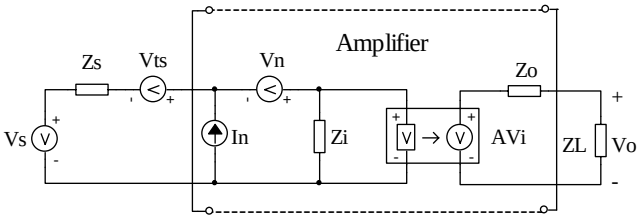

Fig.1. Vn – In amplifier model with Thevenin source.

The amplifier output voltage is given by

$$V_O = \frac{AZ_i}{Z_S + Z_i}\frac{Z_L}{Z_O + Z_L}[V_S + (V_{tS} + V_n + I_n Z_S)] \quad (1)$$

where A is the voltage gain, Z_i is the input impedance, Z_O is the output impedance, and Z_L is the load impedance. The equivalent noise input voltage V_{ni} can be considered as the voltage in series with V_S that generates the same noise voltage at the output as all noise sources in the circuit [3]. It consists of the terms in parenthesis in Eq. (1) and is given by

$$V_{ni} = V_{tS} + V_n + I_n Z_S \quad (2)$$

In fact, this is the noise across Z_i considering Z_i being an open circuit, i.e. it is the Thevenin input voltage. From the Eq. (2) it follows that V_{ni} can be calculated independently of the amplifier.

The mean-square value of V_{ni} is solved for as follows

$$v_{ni}^2 = \overline{(V_{tS} + V_n + I_n Z_S)(V_{tS}^* + V_n^* + I_n^* Z_S^*)} = 4kT\,\mathrm{Re}(Z_S)\Delta f + v_n^2 + 2v_n i_n\,\mathrm{Re}(cZ_S^*) + i_n^2 |Z_S|^2 \quad (3)$$

where k is the Boltzman's constant, T is the temperature in Kelvin's, Δf is the bandwidth in Hertz, and $c = c_r + jc_i$ is the correlation coefficient between V_n and I_n and it is assume that V_{tS} is independent of both V_n and I_n.

If Z_i is considered to be a short circuit, the short-circuit or Norton input current is given by

$$I_{i(sc)} = \frac{1}{Z_S}\left[V_S + \left(V_{tS} + V_n + I_n Z_S\right)\right] \qquad (4)$$

It is obvious that the term in parenthesis of Eq. (4) is V_{ni} given by Eq. (2) and it follows that V_{ni} can be solved for by either calculating the open-circuit input voltage or the short-circuit input current.

A. Effect of a Series Impedance at the Input

Fig.2 presents the input circuit of an amplifier with impedance Z_1 added in series with a Thevenin source.

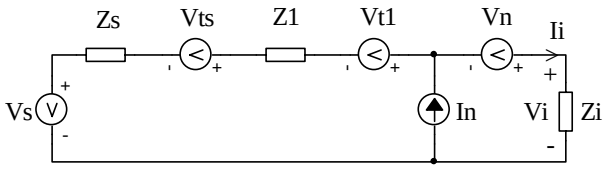

Fig.2. Amplifier input circuit with Thevenin source and series impedance added at input.

The noise source V_{t1} models the thermal noise generated by Z_1. The equivalent noise voltage in series with the source can be solved for by first solving for the open-circuit or Thevenin input voltage, i.e. the input voltage considering Z_i being an open circuit. The Thevenin input voltage in this instance can be expressed as

$$V_{i(oc)} = V_S + V_{ni} \qquad (5)$$

where V_{ni} is the equivalent noise voltage in series with the source. It can be represented as

$$\begin{aligned} V_{ni} &= V_{tS} + V_{t1} + V_n + I_n\left(Z_S + Z_1\right) = \\ &= V_{tS} + V_{nS} + I_{nS} Z_S \end{aligned} \qquad (6)$$

where V_{nS} and I_{nS} are the new values of V_n and I_n on the source side of Z_1. It follows from this equation that

$$V_{nS} = V_{t1} + V_n + I_n Z_1 \qquad (7)$$

$$I_{nS} = I_n \qquad (8)$$

It can be concluded that the addition of series impedance at the input of an amplifier changes the V_n noise but does not change the I_n noise. If Z_1 is lossless, it generates no noise itself so that V_{t1} = 0. The mean-square values and the correlation coefficient for V_{nS} and I_{nS} are obtained as

$$v_{ns}^2 = 4kT\,\mathrm{Re}\left(Z_1\right)\Delta f + v_n^2 + 2v_n i_n\,\mathrm{Re}\left(cZ_1^*\right) + i_n^2\left|Z_1\right|^2 \qquad (9)$$

$$i_{nS}^2 = i_n^2 \qquad (10)$$

$$c_s = \frac{c v_n i_n + i_n^2 Z_1}{v_{ns} i_{ns}} \qquad (11)$$

The mean-square equivalent noise input voltage, therefore, is

$$\begin{aligned} v_{ni}^2 &= 4kT\,\mathrm{Re}\left(Z_S + Z_1\right)\Delta f + v_n^2 + \\ &+ 2v_n i_n\,\mathrm{Re}\left[c\left(Z_S^* + Z_1^*\right)\right] + i_n^2\left|Z_S + Z_1\right|^2 \end{aligned} \qquad (12)$$

It can be seen from this expression that Z_1 = 0, i.e. Z_1 a short circuit, has no effect on the noise. Hence, series impedance should have a magnitude much less than the magnitude of the source impedance if it is not to increase the noise.

B. Effect of a Shunt Admittance at the Input

Fig. 3 illustrates the input circuit of an amplifier with admittance Y_2 added in parallel with the source.

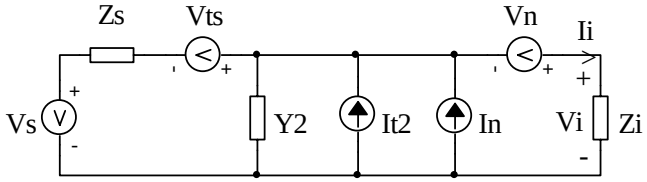

Fig.3. Amplifier input circuit with Thevenin source and shunt admittance added at input.

The noise source I_{t2} models the thermal noise generated by Y_2. As is shown above, the equivalent noise voltage in series with the source can be solved for by first solving for the short - circuit or Norton input current, i.e. the input current corresponding Z_i to be a short circuit. The input current for this case is

$$\begin{aligned} I_{i(sc)} &= \frac{V_S + V_{tS}}{Z_S} + V_n\left(\frac{1}{Z_S} + Y_2\right) \\ &+ I_{t2} + I_n = \frac{1}{Z_S}\left(V_S + V_{ni}\right) \end{aligned} \qquad (13)$$

where V_{ni} is the equivalent noise voltage in series with the source and

$$V_{ni} = V_{tS} + V_n(1 + Z_S Y_2) + (I_{t2} + I_n)Z = \\ = V_{tS} + V_{nS} + I_{nS} Z_{SS} \quad (14)$$

V_{nS} and I_{nS} are the new values of V_n and I_n on the source side of Y_2. It follows from this equation that

$$V_{nS} = V_n \quad (15)$$

$$I_{nS} = I_{t2} + V_n Y_2 + I_n \quad (16)$$

It follows that the addition of shunt admittance at the input of an amplifier changes the I_n noise but does not change V_n noise. If Y_2 is lossless, it generates no noise itself so that I_{t2} = 0. The mean-square values and the correlation coefficient for V_{nS} and I_{nS} may be expressed as

$$v_{ns}^2 = v_n^2 \quad (17)$$

$$i_{ns}^2 = 4kT\,\mathrm{Re}(Y_2)\Delta f + v_n^2 |Y_2|^2 + 2v_n i_n \,\mathrm{Re}(cY_2) + i_n^2 \quad (18)$$

$$c_s = \frac{c v_n i_n + v_n^2 Y_2^*}{v_{ns} i_{ns}} \quad (19)$$

The mean-square equivalent noise input voltage is given by

$$v_{ni}^2 = 4kT\,\mathrm{Re}\left(Z_S + |Z_S|^2 Y_2\right)\Delta f + v_n^2 |1 + Z_S Y_2|^2 + \\ + 2v_n i_n \,\mathrm{Re}\left[c(1 + Z_S Y_2) Z_S^*\right] + i_n^2 |Z_S|^2 \quad (20)$$

It can be seen from this expression that Y_2 = 0, i.e. Y_2 an open circuit, has no effect on the noise. It can be concluded that shunt impedance should have a magnitude much greater than the magnitude of the source impedance if it is not to increase the noise.

III. Simulation Results

Analogue networks usually consist of series and parallel components at the input to the amplifier. One method of analyzing the effect of these components on the amplifier noise is by transforming the noise sources from the amplifier input back to the source by use the above relations. To demonstrate this approach the input circuit of an amplifier, shown in Fig. 4, is analyzed.

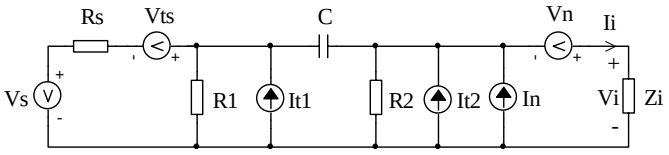

Fig.4. Amplifier input circuit.

Let v_{na}, i_{na} and c_a be the new values to the left of R_2. They are given by

$$v_{na} = v_n \quad (21)$$

$$i_{na} = \left[\frac{4kT\Delta f}{R_2} + \frac{v_n^2}{R_2^2} + 2v_n i_n \,\mathrm{Re}\left(\frac{c}{R_2}\right) + i_n^2\right]^{1/2} \quad (22)$$

$$c_a = \frac{c v_n i_n + \dfrac{v_n^2}{R_2}}{v_{na} i_{na}} \quad (23)$$

The new values v_{nb}, i_{nb}, and c_b to the left of a capacitor C are described by expressions

$$v_{nb} = \left[v_{na}^2 + 2v_{na} i_{na} \,\mathrm{Re}\left(c_a Z_C^*\right) + i_{na}^2 |Z_C|^2\right]^{1/2} \quad (24)$$

$$i_{nb} = i_{na} \quad (25)$$

$$c_b = \frac{c_a v_{na} i_{na} + i_{na}^2 Z_C}{v_{nb} i_{nb}} \quad (26)$$

Let v_{nc}, i_{nc} and c_c be the new values to the left of R_2. They are given by

$$v_{nc} = v_{nb} \quad (27)$$

$$i_{nc} = \left[\frac{4kT\Delta f}{R_1} + \frac{v_{nb}^2}{R_1^2} + 2v_n i_n \,\mathrm{Re}\left(\frac{c_b}{R_1}\right) + i_{nb}^2\right]^{1/2} \quad (28)$$

$$c_c = \frac{c_b v_{nb} i_{nb} + \dfrac{v_n^2}{R_1}}{v_{nc} i_{nc}} \quad (29)$$

The equivalent noise voltage in series with the source is

$$v_{ni} = \left[4kTR_S\Delta f + v_{nc}^2 + 2v_{nc} i_{nc} \,\mathrm{Re}(cR_S) + i_{nc}^2 R_S^2\right]^{1/2} \quad (30)$$

To investigate the relations between the amplifier noise and its input component parameters Matlab simulations with $v_n = 2nV,\ i_n = 1.5pA,\ c = 0.2 + 0.1,\ \Delta f = 1Hz$ have been performed.

In Fig. 5 the effect of the resistance R_2 on the noise current to the left of R_2 for two temperature values is presented. It can be concluded from these results that the increase of parallel impedance R_2 reduces the noise current to the left of R_2, i.e. the noise current on the source side of R_2 is inversely proportional to the parallel impedance.

Fig. 6 shows the simulated noise voltage to the left of the capacitor C versus frequency for capacitance varying from 6.3nF to 15nF. It is obvious that the noise voltage is greater at lower frequencies that at higher frequencies. Furthermore, the capacitance increase, i.e. the series impedance decrease reduces the noise voltage.

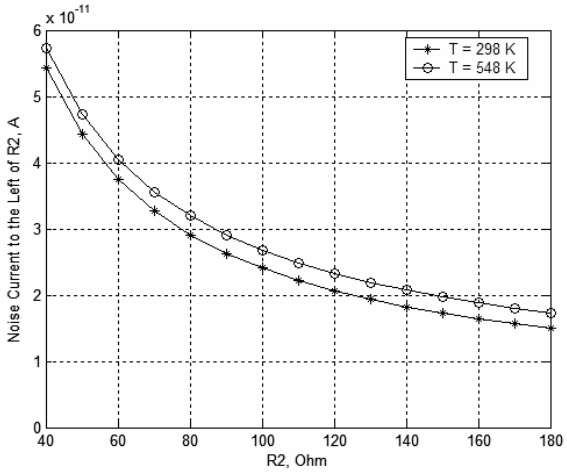

Fig.5. Noise current to the left of parallel resistor R_2 versus R_2 for two temperature values.

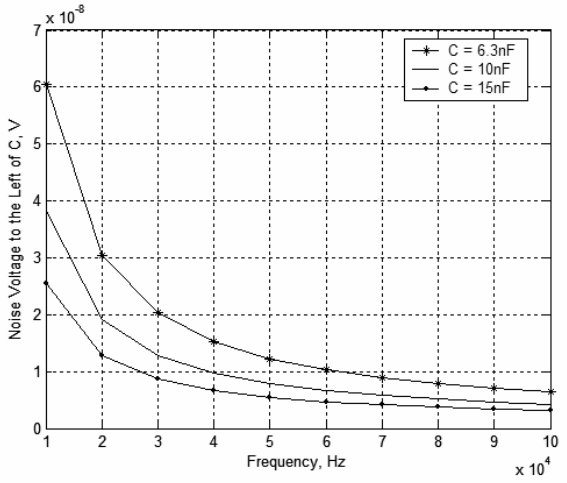

Fig.6. Noise voltage frequency response to the left of series capacitor C for capacitance varying from 6.3nF to 15nF.

In Fig. 7 is presented the noise current contributed by the parallel resistor R_1 for three temperature values. It can be seen the noise current changes in the same manner as the noise current in Fig. 5, but the temperature effect is larger.

Fig.8 demonstrates the simulated equivalent noise voltage in series with the source varying both, source resistance R_S and temperature value T. It can be said that the equivalent input noise voltage variation for this case is nearly linear, while it reduces nonlinear with R_1, R_2, and C increase.

The results in Fig.8 are obtained with f=100kHz, C=10nF, R_1=1kΩ, R_2=100Ω.

The expressions for equivalent input noise voltage due to the series and parallel components presented here constitute a compact and consistent set of equations, very useful for design purposes. The results show that the decrease in noise voltage can be obtained at the expense of either reduced series impedance or a reduced parallel admittance. The simulation results can be used to choose the suitable input amplifier component values that provide a minimum noise.

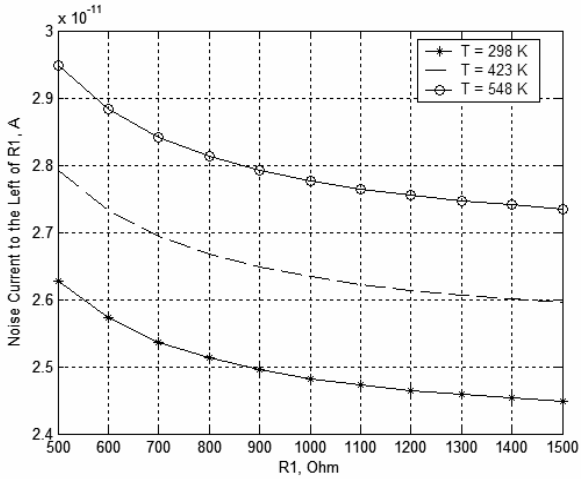

Fig.7. Noise current to the left of parallel resistor R_1 versus R_1 for three temperature values.

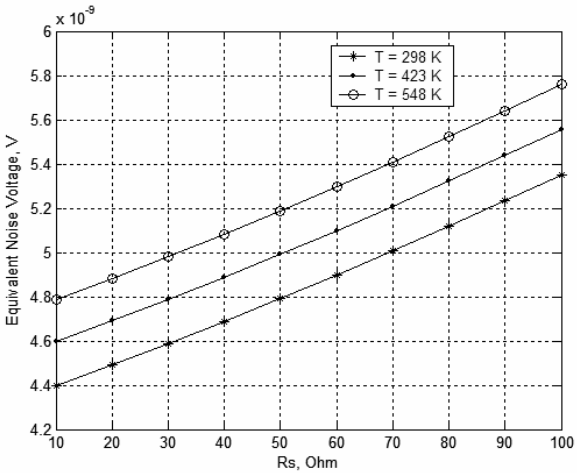

Fig.8. Dependency of equivalent input noise voltage on source resistance for three temperature values.

IV. CONCLUSION

An approach for amplifier noise modeling and analysis is developed. Noise simulation results support an availability of the approach proposed. The results allow a wide range of designers to analyze accurately and in a simple manner the effect of series and parallel input amplifier components on the equivalent input noise in series with the source and to minimize the noise.

REFERENCES

[1] AC Analysis and Noise Analysis for Analog Circuits, University of California, Berkeley, 2003.

[2] Herry W. Ott, Noise Reduction Techniques in Electronic Systems, Edition 2, ISBN: 0471850683, 1991.

[3] Jieh-Tsorng Wu, Noise Analysis and Modeling, National Chiao-Tung University, 2001.

Low Sensitivity Cascaded Quadruplet Microwave Filters

Marin Nedelchev[1], Ilia Iliev[2]

Abstract: **The paper presents a modification of the chained filtering function for low sensitivity cascaded quadruplet microwave filters. The new filtering function uses generalized Chebyshev polynomials as a seed function. It is estimated and compared the responses' sensitivity of modified chained filter and conventional Chebyshev filter. It is proven that the attenuation of the chained filters is 6dB less than the Chebyshev filter.**

Keywords: **Microwave filter, chained filtering function, low sensitivity, coupling matrix.**

I. INTRODUCTION

The synthesis and design of cross-coupled microwave filters is a subject of intense research efforts due to their importance in modern wireless communication systems. Most of them are from the Chebyshev family and have symmetrical responses. This filter class is equiripple in the passband and realize pairs of prescribed transmission zeros (TZs).

A major topology of symmetrical response microwave filters is the cascaded quadruplet (CQ) topology. The coupled resonators are arranged in quadruplets and the coupling and routing diagrams for 4-, 6- and 8-order filter are shown on fig.1. CQ filters may realize $N/2$ prescribed finite TZs. Each quartet may be identified with the production of a TZ pair. If the cross coupling is negative a pair of attenuation poles will be created. If it is positive a real axis pole pair will result with group delay self equalization.

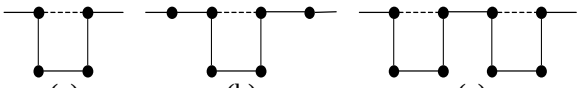

Fig.1 Coupling and routing diagrams for CQ filters of (a) 4-, (b) 6-, (c) 8- order filter

The calculation of the generalized Chebyshev polynomials for the filter synthesis is described in [1]. The matrix rotations order for reduction of the folded coupling matrix to a matrix corresponding to the CQ topology is outlined in [2]. In [3] is studied the sensitivity of different microwave filter topologies to the variation of the coupling coefficients.

[1]Marin Veselinov Nedelchev – PhD student in Dept. of Radiotechnic in Faculty of Communications and Communication Technologies in TU –Sofia E-mail mnedelchev@abv.bg
[2]Ilia Georgiev Iliev – Assoc. Professor in Dept. of Radiotechnic in Faculty of Communications and Communication Technologies in TU –Sofia E-mail: igiliev@tu-sofia.bg

The filter's sensitivity depends on the frequency separation between the return-loss zeros. The wider is the frequency separation between the return-loss zeros, the lower is the sensitivity of the filter to the manufacturing errors. The increasing of the filter order leads to decreasing the frequency separation and consequently the filter sensitivity grows up

A solution of the problem with the sensitivity of microwave filters to the variation of the coupling coefficients is a proper grouping of the return-loss zeros. The result of the grouping is the reduction of the filter sensitivity. The idea of return-loss zeros grouping is exploited in [4]. However the using of generalized Chebyshev polynomials as a seed function leads to filters with multiple TZs. This approach constraints the microwave filter synthesis. The increasing of the filter order leads to growing up multiplicity of the TZs instead of increasing the number of realizable TZs.

This paper proposes modified chained filtering function for low sensitivity microwave filters with CQ topology. It is estimated the filter responses sensitivity to the coupling coefficient variation and the tuning accuracy of the coupled resonators. Chebyshev and modified chained filtering function filters are synthesized and it is estimated their sensitivity to verify the presented theory.

II. MODIFIED CHAINED FILTERING FUNCTION

The reflection and transmission coefficients of a lossless filter, comprised of *N* resonators, are presented as a ratio of polynomials. Generally, these polynomials are of *N-th* order.

$$S_{11}(s)=\frac{F_N(s)}{E_N(s)}\ ,\ S_{21}(s)=\frac{P_N(s)}{\varepsilon E_N(s)} \tag{1}$$

where

$$\varepsilon=\frac{1}{\sqrt{10^{RL/10}-1}}\cdot\left.\frac{P_N(s)}{F_N(s)}\right|_{s=j} \tag{2}$$

RL is the maximum return loss.

For a passive lossless circuit is valid the energy saving law: $S_{11}^2+S_{21}^2=1$. Consequently:

$$\left|S_{21}(s)\right|^2=\frac{1}{1+\varepsilon^2\Phi_N^2(s)} \tag{3}$$

where $\Phi_N=\dfrac{F_N(s)}{P_N(s)}$ is the filtering function.

The Chebyshev approximation uses as a filtering function the generalized Chebyshev polynomials, expressed as [1]:

$$C_N(\omega)=\cosh\left[\sum_{k=1}^{N}a\cosh(x_k)\right] \tag{4}$$

where $x_k = \dfrac{\omega - 1/\omega_k}{1 - \omega/\omega_k}$ and ω_k are the prescribed transmission zeros.

The filtering function for CQ filters of even order and pairs of symmetrical finite TZs is introduced as:

$$\Phi_{2N}(s) = C_N(s)C_N^*(s) = \frac{F_N(s)F_N^*(s)}{P_N(s)P_N^*(s)} \tag{5}$$

where $s = j\omega$, and $C_N^*(s)$ is the generalized Chebyshev polynomial $C_N(s)$ with complex conjugate coefficients (4).

The filter realizability is ensured by the fact that each function in the product is realizable.

It is necessary to sort the TZs in ascending order with alternatively changing signs when computing $C_N(s)$. For example if the prescribed TZs of the filter are ±1.8, ±2.5 and two zeros in the infinity, they should be sort in the following way: 1.8, -2.5, ∞. The polynomial $C_N(s)$ is synthesized as described in [1].

It is important to ensure that the transfer and reflection vectors are orthogonal in order to satisfy the unitary conditions for the scattering matrix [5]. It follows that the phase difference between the S_{21} vector and the average of the phases of S_{11} and S_{22} must be an odd multiple of $\pi/2$ rad.

The filter synthesis proceeds with computing the coupling matrix for a given filter topology from the proposed filtering function.

The reduction of the sensitivity for the modified chained filtering function filter leads to decreasing the filter attenuation in the stopband. Using the approximation:

$$C_N(\omega) \approx 2^{N-1}\omega^N \tag{6}$$

which is valid for large ω and for N-even, it is easily derived that attenuation of the modified filter is *6 dB* less than the Chebyshev filter with the same maximum level of return loss.

This fact must be taken into account when synthesizing a filter, in order to ensure the necessary attenuation in the stopband.

With the proposed modification of the chained filtering function filters, the zeros of the reflection coefficient groups in pairs and the frequency separation between them increases. The frequency separation of two zeros in a group depends on the position of the TZs. The further from the cut off frequency are the TZs, the smaller is the frequency separation in the group. When all prescribed TZs approach infinity, the two frequencies in the group theoretically coincide. In practice, the zeros in the group are very close, because of the inaccurate tuning of the resonators and the manufacturing errors.

III. MODIFIED CHAINED FILTERING FUNCTION FILTERS SENSITIVITY

The transmission and reflection coefficients for a lossless *N-th* order filter depend only on the coupling matrix [6]:

$$S_{21} = -2j[A]^{-1}_{n+2,1} \text{ and } S_{11} = 1 + 2j[A]^{-1}_{11} \tag{7}$$

The matrix $[A]$ is related to the coupling matrix $[M]$ by the relation $[A] = -j[R] + \omega[W] + [M]$. Here $[R]$ is a $(n+2)\times(n+2)$ matrix, whose only non-zero entries are $R_{11} = R_{n+2,n+2} = 1$. $[W]$ is similar to the $(n+2)\times(n+2)$ identity matrix, except that $W_{11} = W_{n+2,n+2} = 0$. $[M]$ is the $(n+2)\times(n+2)$ symmetric coupling matrix.

To analyze the filter sensitivity to the variation of the coupling coefficients, it is necessary to know the partial derivatives of S_{21} and S_{11} with respect to the entries in the coupling matrix. They are derived in [6]:

$$\frac{\partial S_{11}}{\partial M_{pq}} = -4jP_{pq}[A]^{-1}_{p1}[A]^{-1}_{q1} \quad \text{for } p \neq q \tag{8a}$$

$$\frac{\partial S_{11}}{\partial M_{pp}} = -2jP_{pp}[A]^{-1}_{p1}[A]^{-1}_{p1} \tag{8b}$$

$$\frac{\partial S_{21}}{\partial M_{pq}} = 2jP_{pq}\left([A]^{-1}_{(n+2),p}[A]^{-1}_{q1} + [A]^{-1}_{(n+2),q}[A]^{-1}_{p1}\right) \quad \text{for } p \neq q \tag{8c}$$

$$\frac{\partial S_{21}}{\partial M_{pp}} = 2jP_{pp}[A]^{-1}_{n+2,p}[A]^{-1}_{p1} \tag{8d}$$

Since the reflection and transmission coefficients involve the magnitude of the scattering parameters, the following expression is used to determine the partial derivative of the magnitude of a complex quantity Z in terms of the gradient of Z [3]:

$\dfrac{\partial|Z|}{\partial x} = \mathrm{Re}\left[\dfrac{|Z|}{Z}\dfrac{\partial Z}{\partial x}\right]$, where $\mathrm{Re}[.]$ means the real part of a complex number.

The impact of the variation of each coupling coefficient on the transmission and reflection coefficients is estimated by the formulas (8). In [3] are introduced the sensitivity estimates of S_{11} and S_{21} simplify the analysis:

$$K_1 = \sum_{i,j}\left|\frac{\partial|S_{11}|}{\partial M_{ij}}\right| \text{ and } K_2 = \sum_{i,j}\left|\frac{\partial|S_{21}|}{\partial M_{ij}}\right| \tag{9}.$$

The sums (9) run over all entries of the coupling matrix. These estimates form the worst case, when all effects from the errors sum and lead to the maximum degradation in the filter responses. The parameters K_1 and K_2 are functions of the normalized frequency and it may be analyzed the frequency dependence of the filter sensitivity to the coupling coefficient variation.

The CQ filters are synchronously tuned and all diagonal elements in the coupling matrixes are zeros. The terms (8b) and (8d), corresponding to M_{ii} should be included in the

sums (9), because the shifts in the resonant frequency alter the filters' responses. All sensitivities corresponding to the other zero entries in the coupling matrix are neglected. The cross correlation between two coupling coefficients is assumed to be zero.

IV. RESULTS

4-th and 8-th order CQ filters with Chebyshev and modified chained filtering functions are synthesized to investigate their sensitivity. Using the procedures outlined above, it is computed the coupling matrixes for both type filters and the sensitivity estimates. The chained function cross-coupled filters have lower attenuation in the stopband than the cross-coupled Chebyshev filters.

A .4-th order filter with a symmetrical pair of TZs placed on $\omega_{z1} = 2.7$ *and* $\omega_{z2} = -2.7$

Both filters have maximum return loss value of $-20dB$. Following the synthesis procedure outlined in [5], the coupling coefficients for Chebyshev filter are derived as: $M_{S1} = M_{4L}$=1.0289, $M_{12} = M_{34}$=0.8922, $M_{23} = 0.7345$, $M_{41} = -0.0866$. Using the modified chained filtering function and following the same synthesis procedure, the coupling coefficients are: $M_{S1} = M_{4L}$=1.1696, $M_{12} = M_{34}$=1.0483, $M_{23} = 0.8095$, M_{41} = -0.1341.

The frequency responses of the filters are shown on fig.2. It is clearly seen from fig.2a, that the modified chained filtering polynomials leads to return loss zeros grouping. As closer to the cutoff frequency are the prescribed TZs, as further are the two RL zeros are within the group. Generally the frequency separation between the RL zeros groups is wider then the Chebyshev filter, which is obvious when comparing fig.2a and fig.2b. The maximum value of the return loss of the modified chained function filter is smaller than the prescribed value of $-20dB$, because of the RL zeros grouping. The attenuation in the stopband of the modified filter is $6dB$ smaller than the Chebyshev filter.

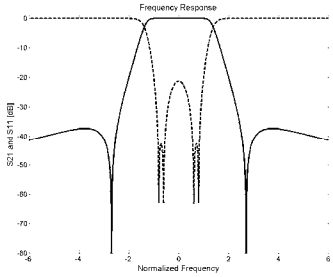

(a)

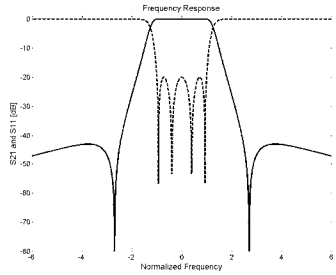

(b)

Fig.2. Reflection (dashed line) and transmission (solid line) coefficients versus normalized frequency for (a) Modified chained function filter and (b) Chebyshev filter

The sensitivity estimates, derived in accordance to formulas (9), are shown on fig.3.

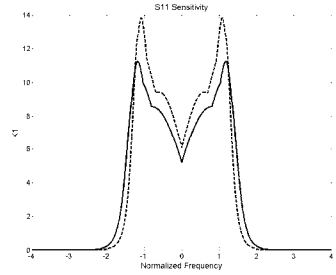

(a)

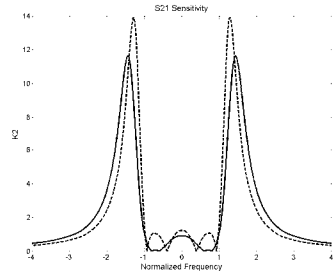

(b)

Fig.3 Variation of: (a) K_1 and (b) K_2 against the normalized frequency for Modified chained function filter (solid line) and Chebyshev filter (dashed line)

The improvement in the S_{11} sensitivity of the modified chained function filter is about 13% and for S_{21} with 10%, comparing to the Chebyshev filter. Out of the passband, the sensitivity of the Chebyshev filter responses is smaller than the modified chained filter.

B.8-th order filter with two symmetrical pair of TZs placed on $\omega_{z1,2} = \pm 1.39$ *and* $\omega_{z3,4} = \pm 3.22$

Two filters with maximum return loss value of $-20dB$ are synthesized, following the synthesis procedure outlined in [5], using the Chebyshev and modified chained filtering functions. The coupling coefficients for the Chebyshev filter are: $M_{S1} = M_{8L}$=0.9873, M_{12}=0.8159, $M_{23} = 0.6044$, $M_{34} = 0.5437$, $M_{45} = 0.5348$, $M_{56} = 0.5048$, $M_{67} = 0.7202$, $M_{78} = 0.7904$, M_{41} = -0.0268, M_{58} = -0.2041. The coupling

coefficients for the modified chained filter are found as: $M_{S1} = M_{8L}$=1.1011, M_{12}=0.9200, $M_{23} = 0.6415$, $M_{34} = 0.5668$, $M_{45} = 0.5367$, $M_{56} = 0.5043$, $M_{67} = 0.7762$, $M_{78} = 0.8830$, M_{41} = -0.0337, M_{58} = -0.2606. The frequency responses for both filters are shown on fig.4.

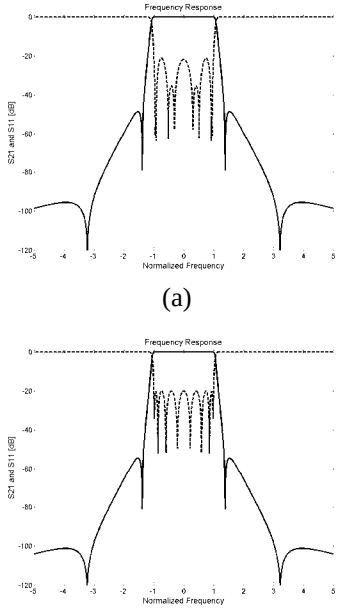

Fig.4. Reflection (dashed line) and transmission (solid line) coefficients versus normalized frequency for (a) Modified chained function filter and (b) Chebyshev filter

As it is seen from fig.4a, the RL zeros are gathered in four groups, each of two zeros. The frequency separation between them is comparatively wider than the Chebyshev filter, shown on fig.4b. The frequency separation between the zeros in the group depends on the position of the prescribed finite pairs of TZs. Further is the pair from the cutoff frequency, the closer are the RL zeros in the group. For high order filters, very closely placed pairs of TZs to the passband may vanish the effect of grouping the RL zeros. The sensitivity of that kind of filter is comparative to the corresponding Chebyshev filter.

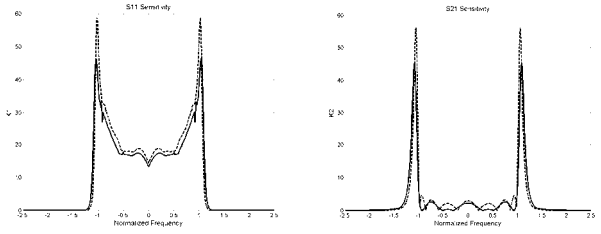

(a) (b)

Fig.5 Variation of: (a) K_1 and (b) K_2 against the normalized frequency for Modified chained function filter (solid line) and Chebyshev filter (dashed line)

Although the maximum return loss is set to $-20dB$, for the modified chained function filter this value is a bit smaller.

It is obvious from fig.5, that the sensitivity of the S_{11} and S_{21} for the modified chained function filter is lower than the Chebyshev filter. In the passband the improvement in the return loss and insertion loss estimates is respectively 10% and 13%. In the stopband the sensitivity of the Chebyshev filter is better than the modified filter.

V. CONCLUSION

The paper proposes a modification of the chained filtering function using generalized Chebyshev polynomials and grouping return loss zeros in order to increase the frequency separation between the groups. The result is improvement in the filter sensitivity to manufacturing errors and frequency shifts in the resonant frequencies. The filter's sensitivity to coupling coefficient variation is analyzed by means of sensitivity estimates. It is compared the Chebyshev filter and modified chained function filter sensitivity. It is seen from the analysis that in the passband the improvement of the sensitivity of the return loss is about 13% and for the insertion loss is about 12%. The Chebyshev filter sensitivity estimates have lower values in the stopband.

It is proven that the modified chained function filter' attenuation in the stopband is $6dB$ less than the Chebyshev filter. To ensure the necessary attenuation in the stopband it must increase the filter order. The coupling coefficients of the modified filter are 10% bigger than the Chebyshev filter coefficients.

The proposed method for approximation is applicable for millimeter wave filters, where the manufacturing errors are crucial, and for high sensitivity filter topologies.

REFERENCES

[1] Cameron, R.J., General Coupling Matrix Synthesis Methods for Chebyshev Filtering Functions, IEEE Trans. On MTT, April 1999, pp.433-442

[2] Cameron, Rhodes, J.D., Asymmetric Realization for Dual-Mode Bandpass Filters, IEEE Trans on MTT 1981 Jan., pp.51-58

[3] Amari, S., Rosenberg, U. On the Sensitivity of Coupled Resonator Filters without Some Direct Couplings, IEEE Trans on MTT June. 2003, pp.1767-1773

[4] M. Guglielmi and G. Connor. Chained Function Filters. 1997 Microwave and Guided Wave Letters, Dec. 1997 pp. 390-392.

[5] Cameron, R., Advanced Coupling Matrix Synthesis Techniques for Microwave Filters, IEEE Trans on MTT-50, Jan.2003, pp.1-10

[6] Amari, S. Sensitivity Analys of Coupled Resonator Filters, IEEE Trans. On Circuits and Systems, Oct. 2000 pp.1017-1022

Active Splitter

Peter St. Apostolov[1], Dimitar I. Dimitrov[2]

Abstract - **A four-pole VHF and UHF band active splitter is described below. Its transmission gain is almost one. The broadband matching of the splitter is made by an imitation of transmission line whit impedance 75 Ω. The input capacitance of the MOS transistors is used. All the values of the band are calculated. An electrical circuit scheme and measurement results are given.**

Keywords - **Active splitter, broadband matching, active circuit element, active element, cut-off frequency, VHF and UHF band, return loss, WSVR, LC filter, MOS-transistors.**

I. INTRODUCTION

As the cable television is coming into its own and in connection with building of closed TV nets it is necessary to connect more than one TV set to the signal source. The most widely distributed splitters are the passive ones. These passive devices represent two or more pole broadband transformers. There also are splitters that use resistive division with good matching but they bring some losses. Depending on the scheme a four pole resistive divider brings fading between 8 and 12 dB.

II. SYNTHESIS IMPLEMENTATION

The given scheme is a four pole active splitter. Every pole has transmission loss near one. A broadband matching method is applied. A low pass LC filter is used. Its characteristic impedance is 75 Ω and it is shown on Fig 1.

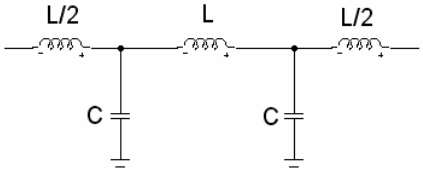

Fig. 1

Instead of the capacitors C the internal capacitances of the four MOS transistors are connected (two transistor BF998 are connected in parallel). Using [4] their internal capacitance is 2,1pF. The inductance and the cut-off frequency f_c of this filter is calculated using [2]:

$$L = z_0^2 C = 75^2.2.2,1.10^{-12} = 23,625.10^{-9}\,[\mathrm{H}], \quad (1)$$

$$f_c = \frac{1}{\pi\sqrt{LC}} = \frac{1}{\pi\sqrt{23,625.10^{-9}.4,2.10^{-12}}} = 1010,6.10^6\,. \quad (2)$$

Obviously the pass band is long enough to cover the TV envelopment. The scheme is given on Fig. 2

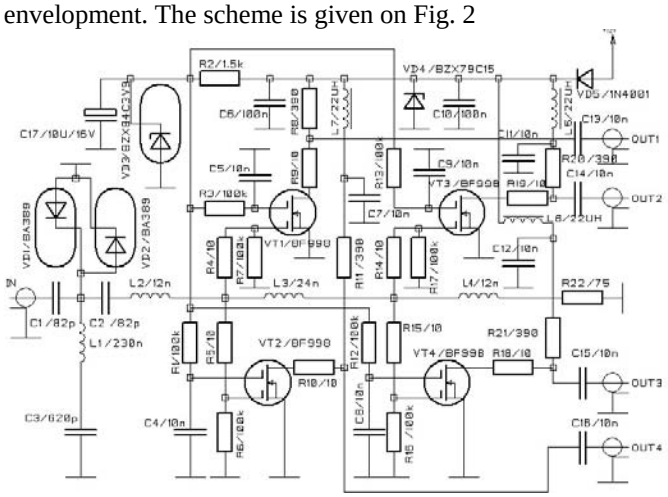

Fig. 2

In the lead-in an inverse Hausdorff high-pass filter with 75Ω impedance is connected. Its cut-off frequency is 30 MHz. It has maximal-flat characteristics in the pass band and a minimum attenuation in stop band 27[dB]. The inverse Hausdorff filters have better linearity of the phase-frequency response in comparison with the elliptic and inverse Chebyshev's filters [3]. The PIN diodes VD1 and VD2 protect the splitter from atmospheric over voltage. The transistors VT1÷VT4 are aperiodic broadband amplifiers with gain about one. The zener diode VD3 ensure fore voltage 3,9V supplied to the second gates of the transistors. The resistors connected in series with the first gates and drains of the transistors protect the amplifiers against self-oscilation.

Having in mind the newly introduced elements, the equivalent scheme of the filter is shown on Fig. 3.

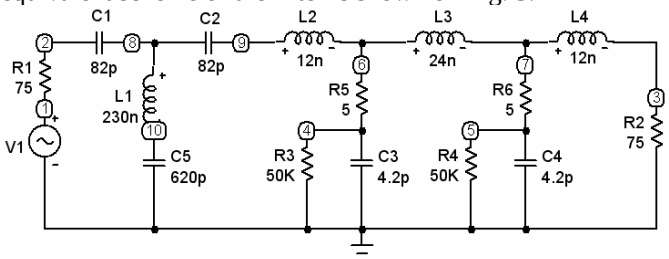

Fig. 3

The inductances L_1, L_2, L_3 and L_4 are calculated using [1]. For $\frac{D}{b} \le 1$:

[1]Peter St. Apostolov, Ms. Sc., Assoc. Fellow, IST-Sofia,
E-mail: p_apostolov@abv.bg
[2]Dimitar I. Dimitrtov, is with the faculty of communications tehnologies TU – Sofia, Kl. Ohridski 8, 1000, Sofia, Bulgaria
E-mail:ddim@tu-sofia.bg

$$L = \frac{\pi^2 D^2 w^2}{b}\left[1 - \frac{4}{3\pi}\left(\frac{D}{b}\right)^2 + \frac{1}{8}\left(\frac{D}{b}\right)^2 - \frac{1}{64}\left(\frac{D}{b}\right)^4\right].10^{-7}. \quad (3)$$

For $\frac{D}{b} > 1$:

$$L = \pi D w^2 \left\{2\left[1 + \frac{1}{8}\left(\frac{b}{D}\right)^2 - \frac{1}{64}\left(\frac{b}{D}\right)^4\right]\ln\left(\frac{4D}{b}\right) - \right.$$
$$\left. - \left[1 - \frac{1}{64}\left(\frac{b}{D}\right)^2 - \frac{1}{48}\left(\frac{b}{D}\right)^4\right]\right\}.10^{-7}, \quad (4)$$

where D is the average diameter of the coil, b is the length and w is the number of the windings. If the diameter of the isolated wire is 0,35mm the next values are calculated:

L_1 – ten dense windings over solid body with diameter 3mm – inductance 225,5 nH.

L_2, L_4 – two dense windings over solid body with diameter 2mm – inductance 12,57 nH.

L_3 – three dense windings over solid body with diameter 2mm – inductance 23,28 nH.

Fig. 4 shows a computer simulation of magnitude response in node 3 of the equivalent scheme on Fig. 3. There you can see that the frequency band of the active splitter is 30MHz÷809MHz.

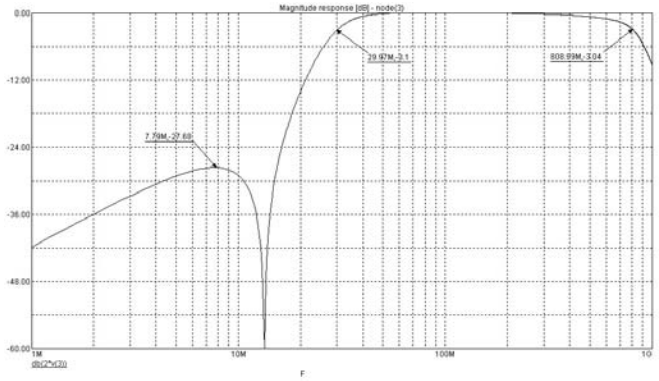

Fig. 4

Fig. 5 shows a computer simulation of magnitude response in node 4 of the equivalent scheme on Fig. 3.

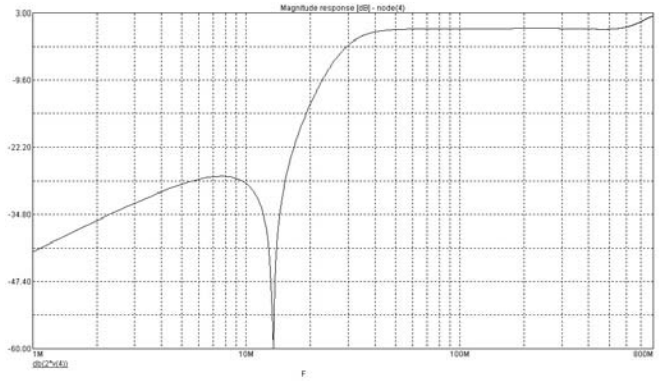

Fig. 5

On Fig. 6 is shown the measured magnitude response of the active splitter on output 1 (OUT1) in its practical realization.

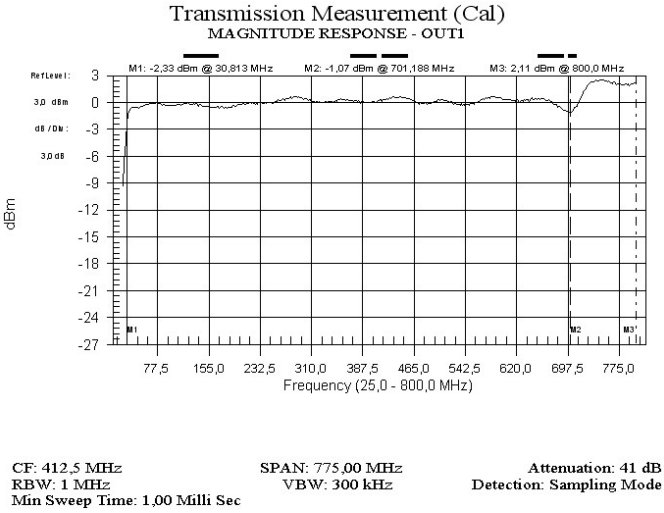

Fig. 6

Fig. 7 shows a computer simulation of magnitude response in node 5 of the equivalent scheme.

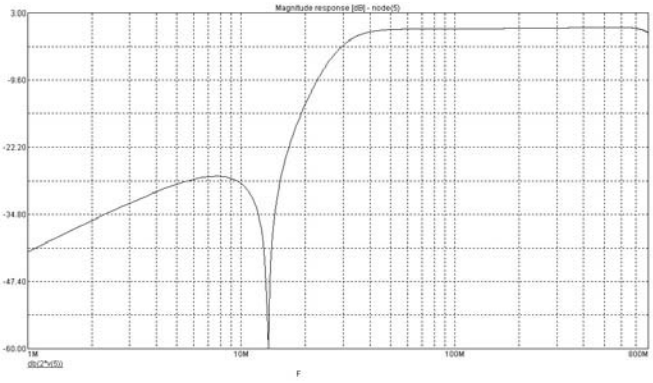

Fig. 7

On Fig. 8 is shown the measured magnitude response of the active splitter on output 2 (OUT2) in its practical realization.

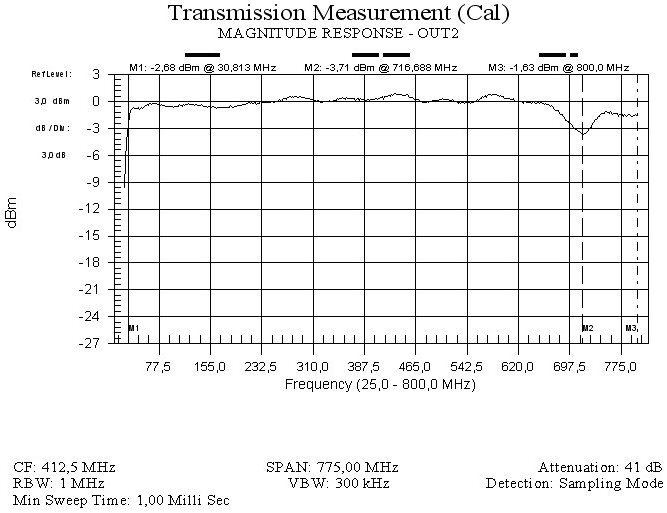

Fig. 8

On Fig. 9 is shown the measured input return loss a in [dB].

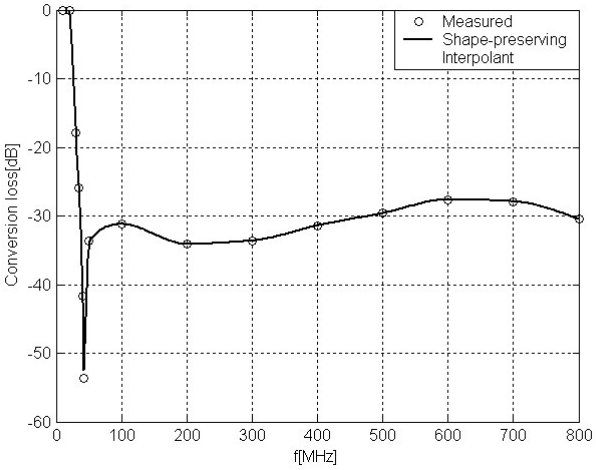

Fig. 9

WSVR is calculated from [2]:

$$|r| = 10^{-0,05a}; \tag{5}$$

$$\text{WSVR} = \frac{1+|r|}{1-|r|}. \tag{6}$$

On Fig. 10 is shown the active splitter's input WSVR.

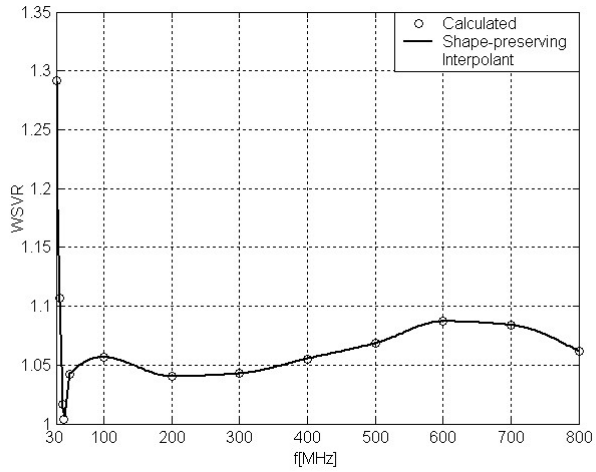

Fig. 10

The values of WSVR are less than 1,3, where in band 36-800MHz they are less than 1,09.

The consumption of the active splitter is about 55 mA (12V-DC), the signal isolation between two arbitrary outputs is more than 36dB.

III. CONCLUSION

– An electrical scheme is built of an active splitter using MOS transistors.

– Through the realization of the electrical scheme the formulas (1), (2), (3) and (4) give the necessary accuracy.

– The illustrated computer simulation of the electrical scheme in the examination frequency band covers the measured parameters of the practical realization.

– The MOS transistor active splitter is realized and successfully realized in many objects in Republic of Bulgaria.

REFERENCES

[1] Savov, G., Constructing and technology of the radio electronic apparatuses –Sofia, Technica, 1970

[2] Lendi, R., D. Davis, A. Albrecht – Radio engineer's guide – Moscow – Electrical Publishing House 1967

[3] Apostolov P. S. "Hausdorff LC Filters", - *ICEST 2004 Conference Proceedings*, pp.59-62, Bitola, Macedonia, 2004.

[4] Philips Semiconductor Concise Catalogue 1995, pp. 4-53

Fibre Based Microwave Absorbers for Radio Communication Technique

R.I. Shtarkova[1], N.T. Dishovsky[2]

Abstract – **A technology for treating of coco-nut fibres with absorbing compounds based on styrene butadiene latex and absorption active fillers was developed. Lightweight broadband microwave absorbers, intended for elimination undesired signals in radio- and television technique were obtained.**

Keywords - **Microwave absorber, Absorbing compound**

I. INTRODUCTION

The development of new improved and more effective microwave absorbing materials in the last years is determined by the growth of the fields of their potential applications [1-3]. These materials have to meet the following main requirements :

- Minimal reflection and maximal absorption of the electromagnetic waves
- Wide exploitation frequency range
- High strength and firmness
- Minimal dimensions and weight
- Ability to work in wide range of mechanical and temperature conditions
- Reliability and durability
- Reproduction of all exploitation parameters [4,5].

The aim of the paper is to present a technology and latex based compounds developed for production of fibre based microwave absorbers, intended for elimination undesired signals in radio- and television technique (especially high quality parabolic antennas).

The main tasks, that we had to solve to achieve optimal parameters of the absorbers and to meet the requirements mentioned above were:

1. To select a suitable fibres and elastomer in a latex form
2. To select absorption active fillers
3. To develop a latex based absorbing compounds with sufficient stability, so that it could be used for fibre treating
4. To develop a technology for coating the fibres with the absorbing compounds

[1]R.I. Shtarkova is with Technical University, 8 Kl. Ohridsky blvd, 1000 Sofia, E-mail: rchtarko@tu-sofia.bg
[2]N.T. Dishovsky is with University of Chemical Technology and Metallurgy, 8 Kl. Ohridsky blvd, 1756 Sofia, E-mail: dishov@uctm.edu

II. SAMPLE PREPARATION

Coco-nut fibres was used as a basic materials because of their low cost and low weight. Styrene butadiene latex (Baystal S 30R, product of Bayer: styrene content – 59%, emulsifier system-anionic, solid content - 50%, density - 1,03 $g.cm^{-3}$, viscosity according to Brookfield, temperature 25^0 C – 41 mPa.s, pH 4) was selected as polymer matrix, because it gives articles with better resistance to climatic aging, excellent compatibility with different kind of fillers and also good dielectric properties. Graphite and furnace carbon black were used as absorbing fillers. The filler's concentration ranged from 5 to 40 mass parts in relation to the solid content of the latex. As a dispersing agent was used an aqueous solution of sodium salt of the condensation product of naphtalene-β-sulphonic acid and formaldehyde (Tamol NN 9104, product of BASF). Aromatic polyglycol ether (Emulwin W, product of Bayer) was used as emulsifier and stabilizer to protect the latex from mechanical and chemical influences.

On the basis of a lot of experiments the following absorbing compound was develop for treating of coco-nut fibres (mass parts to latex solid content):

1. Styrene butadiene latex– solid content – 36,0
2. Sulphur – 6,0
3. Aromatic polyglycol ether - 1,0
4. Sodium salt of the condensation product of naphtalene-β-sulphonic acid and formaldehyde (Tamol NN 9104) – 2,0
5. Zinc oxide – 10,0
6. Kaolin – 29,0
7. N,N-diethyl-benzothiazyl sulphenamide (Wobesit AZ) –10,0
8. Graphite, furnace carbon black – 11- 14

The filler was first converted to dispersions. To the absorption active filler was added an optimum amount of dispersing agent (5% aqueous solution of Tamol NN 9104) and the mixture was homogenized After that the latex with the requisite ingredients were slowly added in portions with constant stirring. As a result the absorbing latex compound was obtained. The technology of fibrous absorbing materials obtaining consist of: treating and coating the previously prepared coco-nut fibres with latex based absorbing compound, afterwards drying the coco-nut matting and vulcanization.

Two technological variants were used for coating the fibres with absorbing compound. By the first one a fibrous plane with the needed thickness was immersed in a tank filled with absorbing compound. After good moistening the plane was

drained off, dried and at the end was vulcanized. Two fibrous planes with density equal to the half of the needed one were used by the second variant. Both planes were sprinkled even bilateral, then were stuck in a press, dried and vulcanized.
Our preference to the second variant was determined not only by the better quality of the absorbing coating, but also by its higher economy. By this variant could be precisely dosed the quantity of the absorbing compound, needed for the sample preparation.

The numerous experiments showed that these variants for coating the fibres with absorbing compound did not provide absorbing materials with enough reproducible parameters and were not sufficiently technological, having in mind the future industrial production. The better the fibres were steeped with the absorbing suspension in the depth, the more constant the electrical parameters of the material were. That was why the use of the centrifugal principle was necessary. Due to the centrifugal forces, it became possible the penetration of the absorbing latex compound through the fibrous planes and steep even of the fibres.

By this method the obtaining of absorbing fibrous planes, having strictly defined mass, through controlling of the centrifuging time offered not difficult.

Final technological stage of absorbing materials production is the vulcanization, which is completed in autoclaves and with a regimes follows:

- time of reaching temperature of 120^0 C – 10 min
- time of vulcanization – 25 min
- time of cooling by air – 15 min

III. Sample Testing

For measuring of the attenuation coefficient of the absorbing material it was used experimental equipment the most close to the conditions in which is expected to be used the absorbing material (AM). In real conditions the AM is placed on a metal ring, which encircles the aperture of the parabolic reflector of the antenna, high-quality production. An electromagnetic wave is transmitted from the antenna with a definite radiation pattern. In that way the wave reaches to the metal ring, faced with AM, under angle α. That angle is determined by the angle of the first side lobe from the radiation pattern and in this case, it is approximately 11 degrees. Next step is to make experimental equipment, shown on Figure 1.

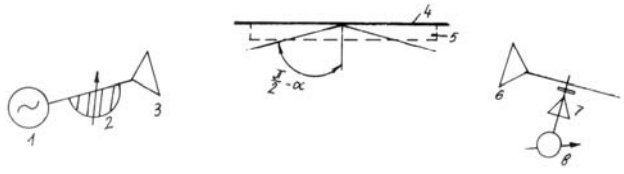

Fig. 1. Experimental equipment for measurements of the attenuation coefficient

The power from high frequency (HF) generator 1 passes through variable attenuator 2 and reaches transmitting antenna 3. In the far-field region of antenna 3 is placed a metal screen under an angle ($\pi/2$ - α) rad. On the other side of screen 4 under the same angle is fixed receiving antenna 6 with detector 7 and indicator 8. If antenna 3 transmits to the screen 4, receiving antenna 6 will receive definite power P_1 that is given on indicator 8. In case of putting AM 5 on screen 4, antenna 6 will receive power P_2 (antenna 3 transmits constant power). In order to measure the attenuation coefficient in AM it is necessary to reduce the transmitted power in the first case (without AM on the screen) with variable attenuator 2 so that the indicator has to show the same power value measured in second case with AM on the screen. The difference in the indications of the attenuator gives the value of attenuation coefficient.

IV. Results and Discussion

The results of attenuation coefficient measuring for two different frequencies – 2 and 3 GHz, are shown on fig. 2. For comparison are given the values for a similar existing absorbing material, produced by other company [6].

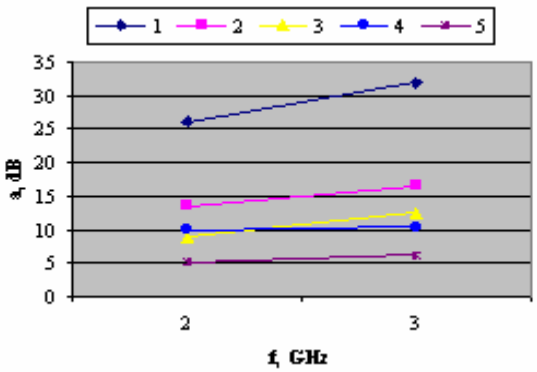

Fig. 2 Attenuation coefficient frequency dependence (samples 1and 4 – absorbing filler carbon black, first and second variant; samples 2 and 3 – absorbing filler graphite, first and second variant; sample 5 – material, produced by other company).

It is evident, that the best results for attenuation coefficient are obtained when using the first technological variant and carbon black as absorption active filler, but the mass of each fibrous plane is increased. By increasing the frequency aattenuation coefficient grows up and has significantly higher values for those absorbers than for the existing material.

Due to the requirements for absorbing material properties reproduction and a low mass of the absorbers a new series of experiments were carried out. In them was used graphite as absorption active filler. For a more constant deposition of the absorbing compound on the fibres was used the principle of centrifuging.

In Table 1 the results of the attenuation coefficient of five different samples are given

TABLE I
ATTENUATION COEFFICIENT, dB

Frequency range, GHz	S 1	S 2	S 3	S 4	S 5
1,7 – 2,1	6	5,5	5	7	5
5,6 – 6,1	14	15	12	13	11
5,9 – 6,4	16	15	12	13	11
7,4 –7,7	15	15	14	14	13
7,9 – 8,5	16,5	15,5	16,5	20	12

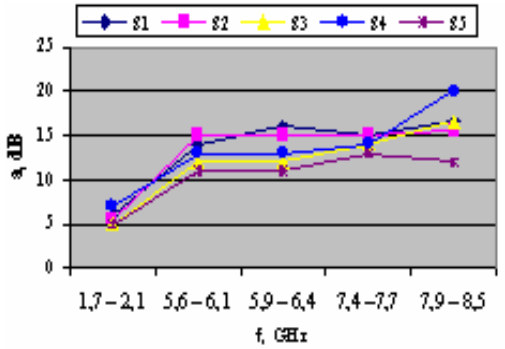

Fig.3. Attenuation coefficient frequency dependence for five samples

For the same five samples on Fig. 3 it can be seen the attenuation coefficient frequency dependence. In a common case, the attenuation coefficient grows up with the increasing of the frequency.

Fibrous absorbing planes position toward the transmitter of the parabolic antenna discounts the possibility of a perpendicular fall of electromagnetic energy on their surfaces. This can lead to an eventual returning of a part of the energy (reflection). This fact and the absorbing mechanism of electromagnetic energy in this kind of materials (mainly diffusion, because of their specific structure and uneven surface), explain why we do not have to measure the reflection coefficient. In the beginning of our experiments, we measured the coefficient of a standing wave on an initial plane (before the deposition of absorbing compound). The corresponding value was 1.1-1.3 for a frequency of 8-8.5 GHz. It showed an almost ideal matching on the border surface free space – fibrous material and an absence of electromagnetic energy reflection.

The absorbing material was put to a climatic test – resistance to cold and heat on standard methods. It was evaluated that AM had the same parameters from minus 55^0 C to plus 55^0 C.

In order to get information for the reliability of the absorbing material it was tested in an extreme conditions – repeating cycles with a sudden change of temperature (minus 40^0 C – plus 70^0 C). On the next parameters' check, it was proved that the parameters suited the requirements.

V. CONCLUSION

A technology and styrene butadiene latex based compound for obtaining of fibre broadband microwave absorbers are developed. The absorbers obtained may be used to reduce the side lobes in the radiation pattern of the parabolic antennas high-quality production, used for radio-relay lines, for equipment of anechoic chambers used in the measuring microwave antennas techniques, etc.

The mass of a fibrous absorbing plane (dimensions 1000x600x30 mm) is not greater than 1.450 kg, absorption coefficient is not less than 5 dB in the range 1,7 – 5,6 GHz and not less than 10 dB in the range 5,6 – 8,5 GHz.

Fibre based microwave absorbers keep its parameters in the temperature range from minus 55^0 C to plus 55^0 C.

REFERENCES

[1] P. Annadurai, A. K. Mallick, D. K. Tripathy, "Studies on microwave shielding materials based on ferrite- and carbon black-filled EPDM rubber in the X-band frequency", *J. Appl. Polym. Sci*., no. 83, pp.145-150, 2002.

[2] S. Sindhu, M. R. Anantharaman, B. P. Thampi, K. A. Malini, P. Kurian, "Evaluation of a.c. conductivity of rubber ferrite composites from dielectric measurements", *Bull. Mater. Sci*., vol. 25, no. 7, pp. 599-607, 2002

[3] N. E. Kazantseva, A. T. Ponomarenko, V. G. Shevchenko, C. Klason, "Magnetically Textured Composite Materials as Elements of Electromagnetic Wave Absorbers", *Taylor & Francis*, vol. 20, no. 6, pp. 453-466, 2000

[4] V. Murthy, S. Sundaram, B. Vishwanathan, *Microwave Materials*,Narosa Publishing House, 1994

[5] U. Kovneristi, I. Lazareva, A. Ravaev, *Materiali, pogloshtaushtie SVCH-izluchenia*,Moskva, Nauka, 1982 (in Russian)

[6] Emerson & Cuming Microwave Products Catalog – www.eccosorb.com

Session EM:

ELECTRICAL MACHINES

Method for Determination of Mechanical Life of Electric Machines

Totjo Iliev*

Abstract: **This paper presents a method for determination of residual life of electric machines. The method is based on the cumulation of data base by means of microprocessor system and its consequent processing through relevant mathematical facility.It also allows to be hooked up to computer networks.**

I. INTRODUCTION

With the higher specification requirements in terms of machine structure and performance , the methods for control and diagnostics which employ both nondestructive and operation-without –interference techniques, are gaining greater importance. Trouble free operation of the machine under investigation is indicative of the capacity of the electric machine to sustain its serviceability during its operating time which is measured in work hours. Diagnostics in this case aims at foreseeing possible breakages which will help eliminate consequent breakdowns and ensuing cost of repair. Electric machines diagnostics is automatically carried out over various time intervals which depend on the individual machine features and relevant estimation of results. The aim here is to obtain information about the physical condition of the machine by using its electrotecnical parameters.

Control over bearings would be of no use if the machine failed. Accordingly, disturbances are not to be merely accepted, but the underlying reason should be eliminated.

II. EXPLANATION

Fig. 1 shows the suggested device by means of which information is obtained concerning electric current fluctuations during machine operation as well as its harmonious content (see Fig.2)

This information is obtained by means of electric current pliers with standart interface coupled with a microcomputer. Database is extended by including information about the change in rotation frequency and temperature (see Fig. 3) during operation. This is achieved by employing a special device built with a single chip microprocessor which is connected to the microcomputer through interface RS 232.

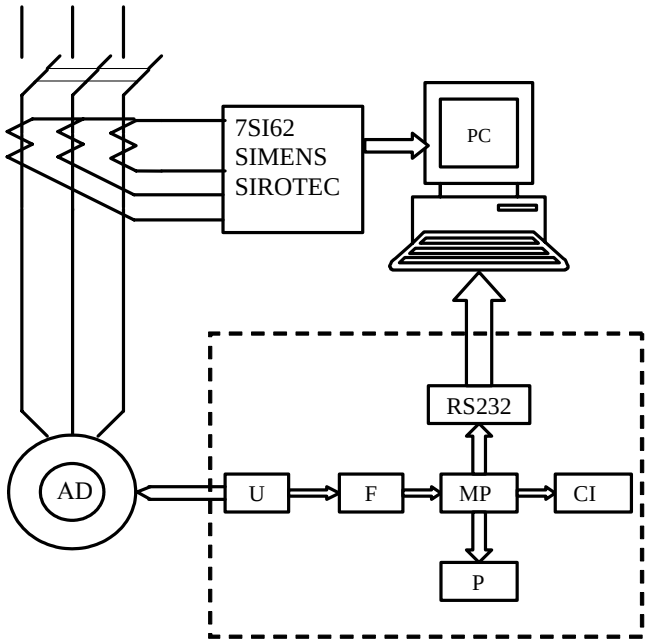

Fig. 1

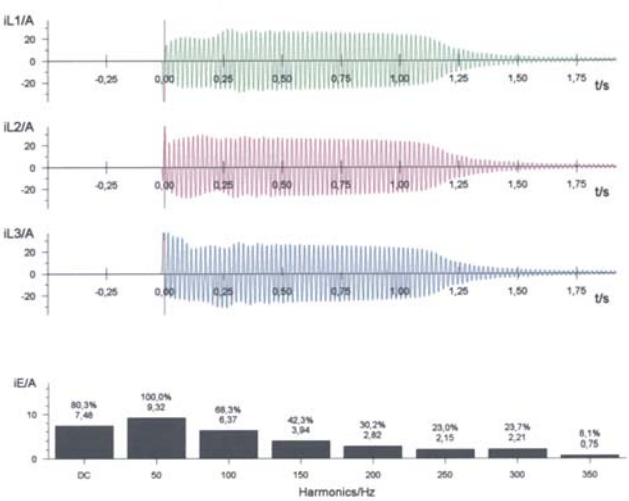

Fig.2

* Technical University of Gabrovo, Bulgaria
E-mail: tiliev@mail.bg

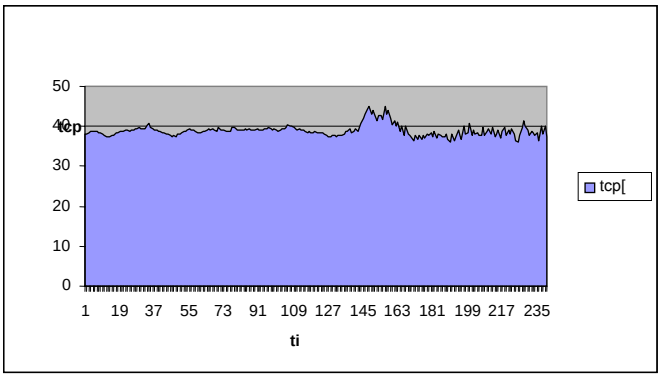

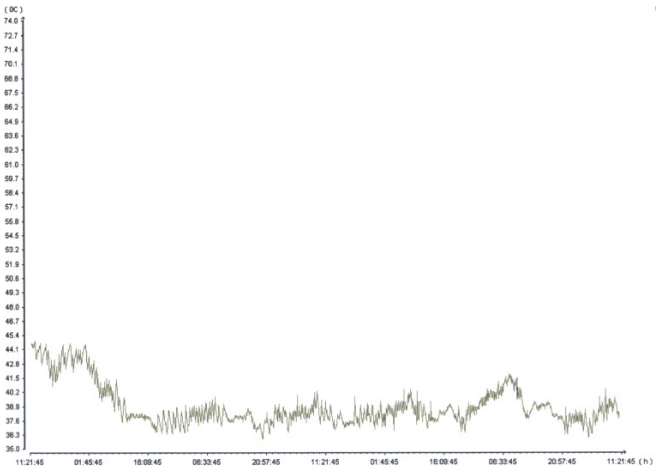

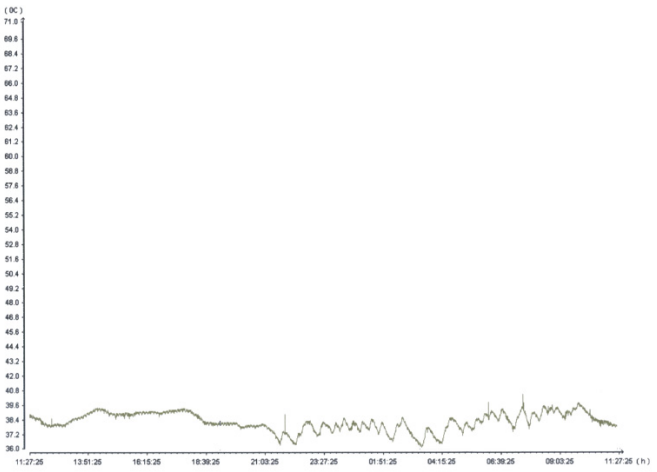

Fig. 3

Input entries of values include technical parameters quoted in the machine catalogue such as diameter and length of shaft, air gap, height etc and, also, rated power, rated frequency of rotation, rated current and rated moment. Fig.4 shows the variation in the effective value of current recorded over a definite period of time. All investigations were carried out on electric motor featuring the following parameters:

P_H = 7,5 kW;
n = 2880 min^{-1};
U_H = 380/660 V;
f = 50 Hz;

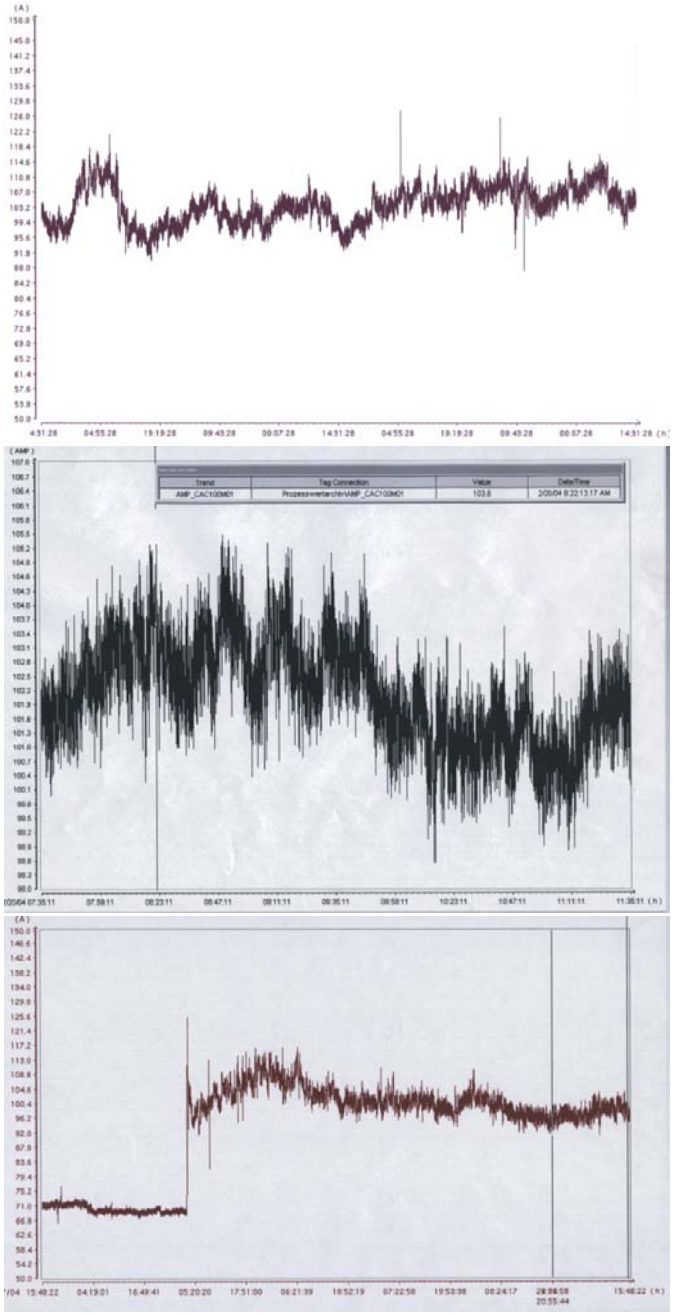

Fig.4

I_H = 14,7 A;
cosφ = 0,89.

The electric motor is supplied through a frequency converter to ensure smooth switch -on and off, however, the nonsinusoidal character of the current causes overheating of insulation. Fig. 2b presents the harmonic analysis of the current whereas Fig.5 shows the readings related to to the residual service life of the electric motor.

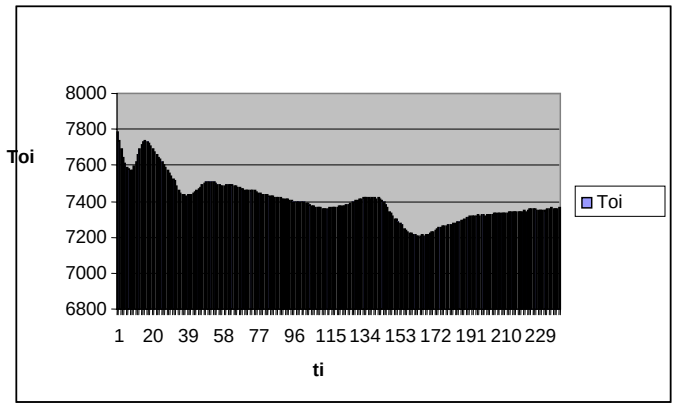

Fig.5

III. CONCLUSION

Proper determination of service life of any electro-technical unit appears to be a very important feature of its existing rate of operation.All technical procedures conducted in connection with machine maintenance would ensure longer operation time and fewer overhauls. This method of control of bearings does not affect machine operation , allows to build up data arrays without interrupting its work and requires no special attending.Feasible inclusion in a network of a number of investigated units enables minimal attending staff to carry out unbiased and precise predictions of possible failures in them. A USB cable could be used to transfer the information to a central computer which controls a certain type of manufacture thus considerably reducing maintenance and wear and tear cost.

REFERENCES

[1] Bozhilov G., Ivanov D., Determination of thermal durability of insulation in electric machines and transformers, 1998 Sofia
[2] Sokolov E., Reliability of Electric Machines. 1990 Sofia
[3] Bolotin V. Service life of machines and structures 1998 Moscow
[4] International Standard ISO 10816 – 2 , 96
[5] 5 http:// vibration.narod .ru

Experimental Investigations of Overvoltages on High-Voltage Motors Insulations in Industrial Plants

Petar Vukelja[1], Radomir Naumov[2], Jovan Mrvić[3], Dejan Hrvić[4]

Abstract - **The results of experimental investigations of overvoltages appearing on the insulation of 6 kV motors in industrial plants are presented in the paper. The investigatons of overvoltages were carried out at switching-in and switching-out of motors and at earth-fault appearance in six industrial plants. Switchings-in and switchings-out of motors were carried out by means of minimum oil circuit-breakers. On the basis of the analysis of investigation results, the measures which should be undertaken in order to reduce stresses on stator windings insulation of high-voltage motors are suggested.**

Keywords: - **Insulation, Overvoltage, Motor, Industry**

I. INTRODUCTION

The most spread electric-power networks in industrial plants are 6 kV voltage networks. These are cable networks having isolated neutral point. They are supplied from 35 kV or 110 kV networks, through 35kV/6kV or 110kV/6kV transformers. On the end of cable lines, a few tens up to a few hundreds of meters long, high-voltage voltage motors and 6kV/0.4kV tranformers are connected. Switchings-in and switchings-out are carried out through switching devices at the beginning of cable lines. These are most frequently minimum oil circuit-breakers. Overvoltage phenomena in these networks are frequent. They are most frequently due to switching devices operation, and than to earth fault and short-circuit. Overvoltages stress, and can endanger the insulation of 6 kV network and therefore the stator winding insulation of 6 kV motors, as well.

In this paper the results of experimental investigations of overvoltages on stator windings of high-voltage motors in six industrial networks are presented. The overvoltages were investigated at switching-in and switching-out 6 kV motors and at the establishment and interruption of earth fault. The overvoltages were recorded by means of digital oscilloscopes, with using capacitive voltage dividers which truly transfer the phenomena of the order from 1 MHz to several Hz.

[1] Dr Petar Vukelja, Electrical Engineering Institute "Nikola Tesla", Koste Glavinića 8a, 11000 Beograd, Srbija i Crna Gora,
E-mail: pvuk@ieent.org
[2] Radomir Naumov, Electrical Engineering Institute "Nikola Tesla", Koste Glavinića 8a, 11000 Beograd, Srbija i Crna Gora,
E-mail: rnaum@ieent.org
[3] Jovan Mrvić, Electrical Engineering Institute "Nikola Tesla", Koste Glavinića 8a, 11000 Beograd, Srbija i Crna Gora,
E-mail: jmrvic@ieent.org
[4] Dejan Hrvić, Electrical Engineering Institute "Nikola Tesla", Koste Glavinića 8a, 11000 Beograd, Srbija i Crna Gora,
E-mail: dehrvic@ieent.org

II. OVERVOLTAGES AT EARTH FAULT APPEARANCE

An earth fault in the network with isolated neutral point has no influence to the operation of high-voltage motors. In the majority of industrial networks, an earth fault is only signalized and just after determination of its location is cleared, taking into care not to interrupt technological processes being in course. Investigations of overvoltages at the establishment and interruption of earth fault were carried out in all six 6 kV networks [4,6,8].

The earth fault have been established by switching-in one of the cable lines in the network on which one of phase conductors was previously connected to the earthing. Over 40 cycles of earth fault switching-in and switching-out were carried out in the networks of industrial plants.

Intermittent earth-fault is performed in three networks of industrial plants. It was established and interrupted, by means of isolated stick with an earthed metal part fixed on the top, by its approaching to, and removing from one of the 6 kV phase conductors. During performing intermittent earth fault, several tens and even hundreds of earth fault establishments and interruptions occurred.

The overvoltages appearing at earth fault establishment defined in relative units (p.u.) in relation to the peak value of phase-to-phase voltage in stable regime immediately before earth fault occurrence, have not surpassed 2.6 p.u.. At intermittent earth-fault the highest measured overvoltage was 3.3 p.u.. Their frequencies and steepnesses also are not high. At earth fault establishment, the frequency of their oscillation moves up to a few kHz. With earth fault interruption, overvoltage appeared most frequently on the phase which have had the earth fault, but not above 1.8 p.u.. For one of the motors, the transient voltages on two phases, that is, on the stator-winding insulation, at earth-fault appearance in the third phase, are shown in Fig. 1.

In three networks the earth fault interruption gave rise to the appearance of the second subharmonic ferroresonance with overvoltages to earth up to 2.3 p.u. [4,6]. Phase-to-phase voltages to which high-voltage motors are connected, in the course of ferroresonance stay unchanged and they operate normally. However, phase-to-earth voltages are significantly higher than normal. Besides basic harmonic (50 Hz) they contain much expressed second subharmonic (25 Hz) and somewhat less expressed harmonic having frequency of several Hz.

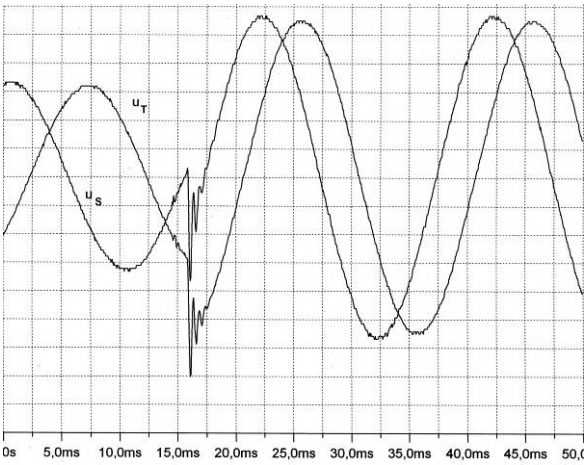

Fig. 1. Transient phase-to-earth voltages u_S and u_T on the stator-winding insulation of the 6kV, 600kW motor, at earth-fault appearance on the R-phase.

III. SWITHCINGS-IN AND SWITCHINGS-OUT OF HIGH-VOLTAGE MOTORS

The investigations of overvoltages on the insulation of high-voltage motors at their switching-in and switching-out are carried out in four networks of industrial plants on all together 13 motors having power from 170 kW to 2 MW [5,6,7]. These are induction motors with cage rotor. The motors were switched in and out by means of domestic and foreign minimum oil circuit-breakers. Switchings-out were performed during motor normal operation and during acceleration. Switchings-out in acceleration, that is switchings-out immediately after motor switching-in, are not rare appearance. Most frequently they occur when all technological conditions for starting the facility driven by the motor are not fulfilled, or the over-current protection of the motor is not properly adjusted. The transient phase-to-phase voltages at motor switching-in and switching-out were recorded in all three phases.

The transient voltage process at switching-in lasts for a few ms. The frequency of oscillations usually do not surpass a few kHz. The highest overvoltage measured during 93 switchings-in of motor, that is, in the sample of 93x3=279 elements amounts 2 p.u., and mean overvoltage value in the sample is 1.2 p.u.. For one of the motors, the transient voltages on two phases, that is, on the stator-winding insulation, at motor starting-up are shown in Fig. 2.

The transient process during motor switching-out in normal operation in every one of phases lasts shortly – 1 to 2 ms. Damped oscillations appear, having frequency up to a few Hz. After this transient process, the phase-to-phase voltages decrease gradually with frequency, which also decreases. The highest overvoltage measured at 46 switchings-out during motor normal operation, that is, in the sample of 46x3=138 elements, is 2.4 p.u., and the mean overvoltage value in the sample is 1.2 p.u.. For one of the motors, the transient voltages on two phases, that is, on the stator-winding insulation, at motor switching-out during normal operation, are shown in Fig. 3.

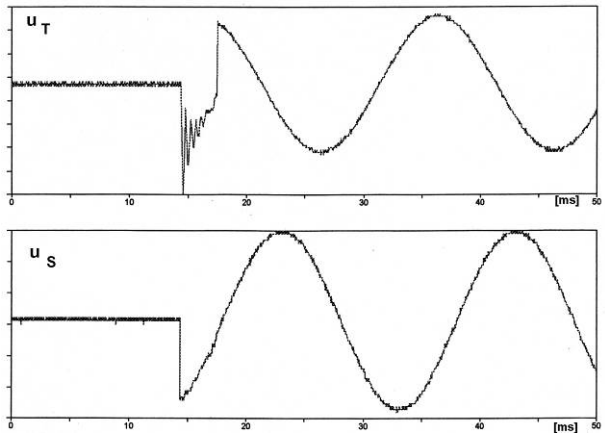

Fig. 2. Transient phase-to-earth voltages u_T and u_S on the stator-winding insulation of the 6kV, 630kW motor, at its starting-up.

The transient process at switching-out of the motor in acceleration on every one of phases lasts shortly, 1-2 ms with damped, high oscillations, having frequency a few kHz. After transient process, phase-to-phase voltages fall to zero value. The highest overvoltage measured during 49 switchings-out of the motor in acceleration, that is, in the sample of 49x3=147 elements, is 4.65 p.u., and the mean value of overvoltage in the sample is 2.2 p.u..

In figure 4, for one of the motors, the transient voltage process is shown on two phases of the stator winding insulation, at motor switching-out during acceleration.

IV. TEST AND WITHSTAND VOLTAGES OF STATOR WINDINGS INSULATION OF HIGH-VOLTAGE MOTORS

In the IEC 60034-15 Standard, the test voltage of stator winding insulation to earth of motors is power frequency, short-duration voltage:

$$U_i=(2U_n+1)\ \text{kV}$$

and lightning impulse voltage:

$$U_a=(4U_n+5)\ \text{kV}$$

(U_n – motor rated voltage in kV).

For motors having rated voltage U_n=6 kV, the peak value of power-frequency test voltage is $13\sqrt{2}$ kV, and in relative units, in relation to the peak value of phase-to-earth voltage ($6\sqrt{2}/\sqrt{3}$) kV of the 6 kV network, it amounts 3.8 p.u.; the test value of lightning impulse voltage expressed in the same way, in relative units, amounts 5.9 p.u..

In the Technical recommendation TP 32 of the Power Industry of Serbia [1] the power-frequency test voltage of the motor stator winding is the same as in IEC 600034-15 Standard.

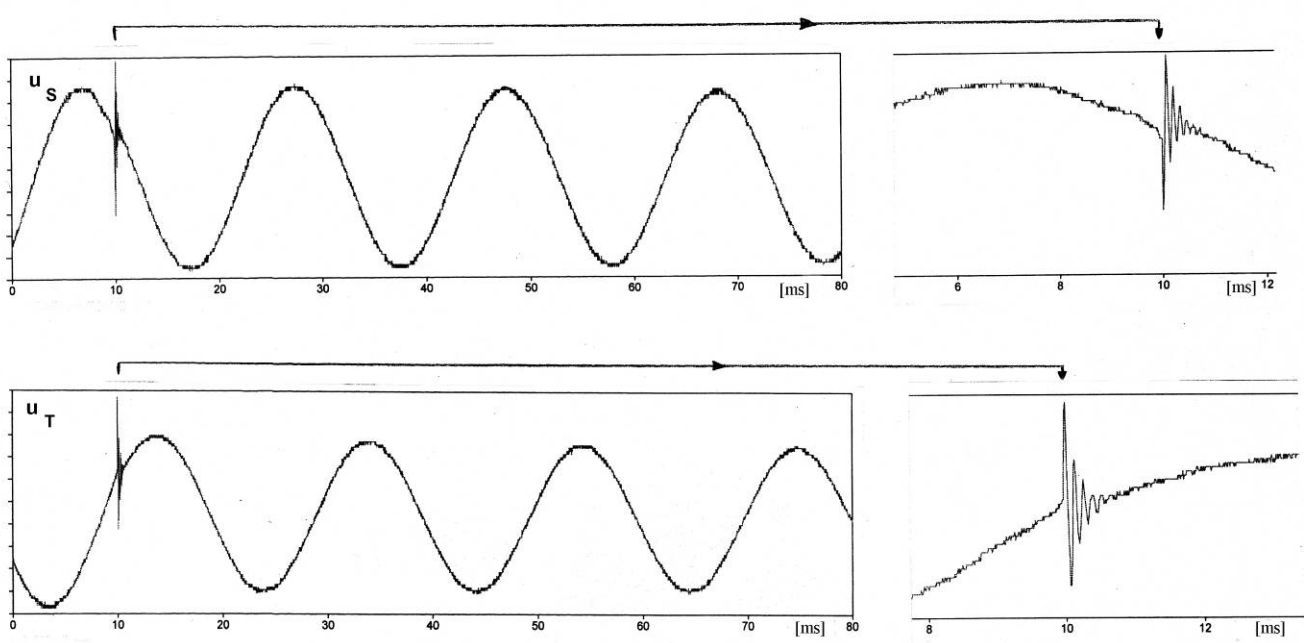

Fig. 3. Transient phase-to-earth voltages u_S and u_T on the stator-winding insulation of the 6kV, 630kW motor, at its switching-out during normal operation.

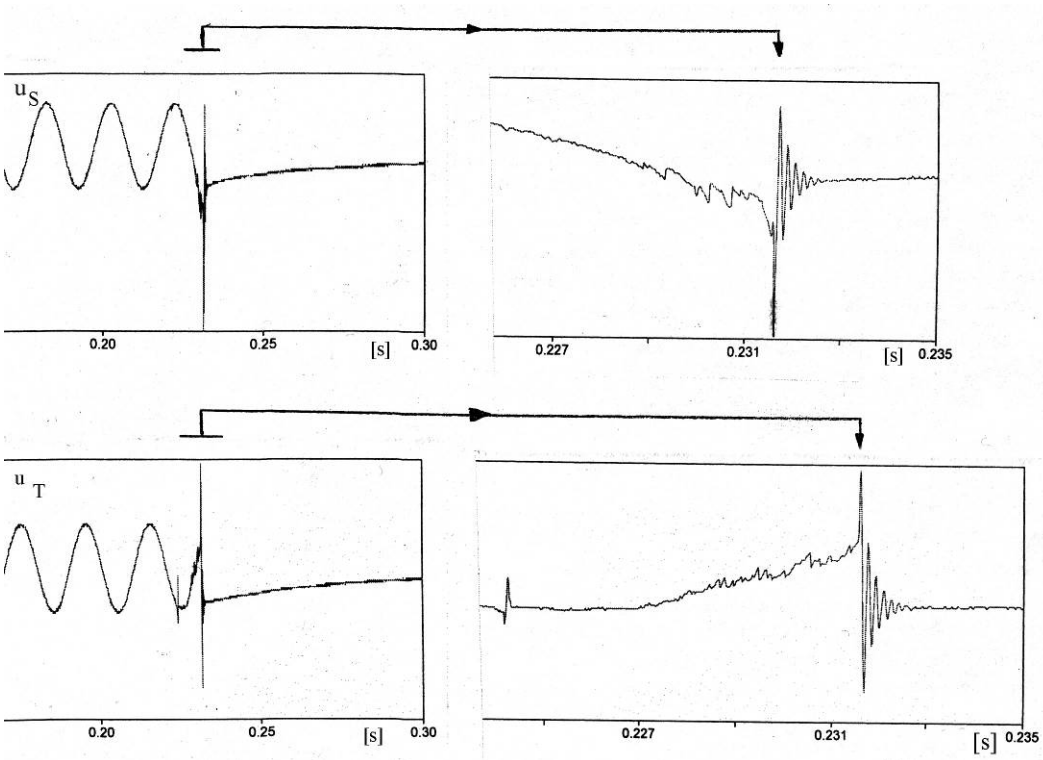

Fig. 4. Transient phase-to-phase voltages u_S and u_T on the stator winding insulation of the 6kV, 500kW motor at its switching-out during acceleration.

The impulse withstand voltage to earth of the motor stator winding according to the draft of the IEEE Working group [2] (insulation aging during exploitation is taken into consideration) is:

$$U_p=1{,}25\sqrt{2}\,(2U_n+1)\ \text{kV}$$

(U_n - motor rated voltage in kV).

Expressed in relative units, for motors having rated voltage U_n=6 kV it amounts 4.7 p.u.. It is also the lowest margin for

the insulation withstand voltage given by the Working group 13.02. CIGRE [3].

V. ANALYSIS OF INVESTIGATION RESULTS

Experimental investigations on 6 kV industrial networks have shown that overvoltages, appearing on the stator winding insulation of high-voltage motors at earth fault occurrence and switching operations of minimum oil circuit-breakers, have frequencies up to several kHz. As such, they can be classified to overvoltages with slow rise-time. According to [2], the withstand voltage of the stator winding insulation for such overvoltages should be at least 4.7 p.u.. By analysis of overvoltages determined by experimental investigations, it is observed that, overvoltages, appearing at switching-out the motor during acceleration, have the values which are close to withstand voltage values. The reason for such high overvoltages is current cutting, in the course of oil circuit-breaker opening operation, before passing through its natural zero value. This phenomenon is particularly expressed at older types of minimum oil circuit-breakers. Minimum oil circuit-breakers of more contemporary production, at switching-out, cut the current at lower values, and consequently, the overvoltages are lower. The overvoltages appearing at switching-out the motor during acceleration, considerably stress the stator winding insulation and their appearance should be limited or restrained. All remaining overvoltages, which appear at earth fault occurrence and at switching-in and switching-out of motors in normal operation, are not that high as to require the measures for their limitation. It only shall be provided that in the 6 kV network do not appear ferroresonant oscillations which may last for hours, if not eliminated by changes occurring in the network (switching-in or switching-out of some cable line with motor or 6 kV/0.4 kV transformer, earth-fault etc.).

VI. CONCLUSIONS

On the basis of the results analysis of investigations of overvoltages on the stator winding insulation of high-voltage motors in the 6 kW networks of industrial plants, the conclusion can be drawn that some of them are significantly stressed and even endangered. In order to reduce dielectric stresses of stator windings insulation of high-voltage motors it is necessary to undertake the following:

a) Prevent the motor switching-in by means of certain restrains, if all conditions for putting into operation of facilities driven by them are not met.
b) Overcurrent protections of motors shall be set in such a way that strong currents appearing during motor acceleration do not activate them.
c) If the measure under /a/ cannot be realized, and switchings-out of the motor in acceleration occur, it is necessary to protect the stator windings insulation to earth by surge arresters. They can be mounted at the entrance of the motor cable line and even better, if feasible, at motor terminals.
d) Prevent the appearance of ferroresonance by introducing the resistor of about 20 ohms resistance at the ends of the broken delta secondary windings of the voltage transformers set in the measurement cell.
e) Determine as soon as possible the earth-fault spot, when it appears. Eliminate it as soon as possible, taking care not to produce damage in the production procedure.
f) Avoid switchings-in and switchings-out of circuit-breakers of cable lines with high-voltage motor, except switching-out that one on which an earth fault occurred. By such operations of circuit-breakers, excessively higher overvoltages can appear than those registered by investigations.

REFERENCES

[1] Technical recommendation TP32 “Insulation systems of rotating machines” ZEP Beograd 1982.

[2] IEEE Working Group of progress, report-Impulse voltage strength of AC rotating machines, IEEE Transactions on Power Apparatus and Systems, Vol. PAS-100, No.18, August 1981.

[3] Working Group 13.02 of Study Committee 13 - Interruption of small inductive currents: Chapter 3, Part B, Electra 1984, No.95.

[4] P.Vukelja, R.Naumov, M.Vučinić, P.Budišin: “Experimental investigatons of overvoltages in neutral isolated networks”, IEEE PROCEEDINGS–C, Vol. 140, No.5, september 1993.

[5] P.Vukelja, R.Naumov, M.Vučinić, P. Budišin: “Experimental investigations of high-voltage motor switching surges IEEE Proc.-Gener. Transm. Distrib., Vol. 142, No.3, May 1995.

[6] P.Vukelja, M.Vučinić, J.Mrvić, D.Radulović: “Overvoltages in an Industrial Substation 10 kV and 6 kV Networks”, 4th international Power Systems Conference, Timisoara, Romania, 8-9 November, 2001, pp.372-2-378.

[7] P.Vukelja, J.Mrvić, D.Hrvić, N.Simić: “Overvoltages and currents at switching-in and switching-out high-voltage motors in the 6 kV network of Sartid”. Institute “Nikola Tesla” collection of papers, book 16, Belgrade 2004, pp.79-90.

[8] P.Vukelja, J.Mrvić, D.Hrvić, M. Šupić, M.Petrović: “Overvoltages and currents at the appearance of earth fault in 6 kV networks of Sartid” Institute “Nikola Tesla” collection of papers, book 16, Belgrade 2004, pp.69-78.

Prophylactic Monitoring of Impedanca of Turbogenerator's Rotor Winding at Unit 3 of TPP Bitola

Natasa D. Mojsoska[1]

Abstract: **In this paper is elaborated prophylactic monitoring of impedance of turbogenerator's rotor winding at unit 3 of TPP Bitola. It is explained the measuring principle. The results are given from last 8 years, they are anylized, diagrams are made and the conclusion is given for the meaning of prophylactical monitoring of impedance. I must mention that the impedance of rotor winding performed only one of the important parametars relevant for objective estimation for condition of insulating system of the generator.**

Keywords: **generator, insulating system, prophylactic monitoring, impedance**

I. INTRODUCTION

Statistical research shows that insulating system is the weakest point of turbogenerator. Therefore nessesity for better care for this part of genetator.

This paper is only a part of whole project which consist of prophylactic monitoring of insulating system of large turbogenerators. During every annual repair mesuring are made at advanced determinating program with basic purpose for diagnosting condition of insulating system. That increase efficiency and reliability during exploatation. Basic characteristics and parameters for determineting state of insulation are: impedances, inductances, electrical insulating rezistance R_{iz}, koeficient of absorption K_a and factor of dielectric power loses wich depends of voltage $tg\delta = f(U)$, intensity of partial discharge, current in insulating system, dieletric strenght e.t.c.

One of these parametars is impedance of rotor winding that is the main issue at this work. All results and analyses are conserned to turbogenerator at unit 3 of TPP Bitola.

According to prophylactical research of impedance of rotor's winding at period of 1997 till 2004 sistematization is made, comparison of results and grafical diagrams are given. Also is estemed behavier of impedance at past eight years.

II. MEASURING OF IMPEDANCE OF ROTOR'S WINDING OF TURBOGENERATOR

Rotor's impedance is one of the basik values which are examinated during the annual repair for following of insulating systems condition.

Current - voltage method is used for measuring in two cases:

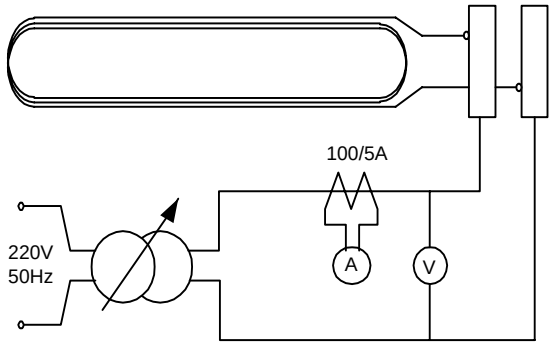

Fig.1 Survey of the measuring of rotor's impedance

1. while rotor is moving
2. while rotor doesn't move

At first case impedance is measured in dependense of number of rounding of turbogenerator Z=f(n) and at second case impedance is depending of voltage Z=f(U).

Measuring is performed according to Fig.1

Next instruments and equipment are used:

- current transformer	accuracy class 0.2	tupe TK-20
- ammeter	accuracy class 0.2	tupe E 514
- voltmeter	accuracy class 0.2	tupe E 515
- switch	50A	tupe AP 50
- megeohmmeter	M 4100/3	500V

As a source of alternating current is used autotransformer.

During turning off the generator primary and secundary current are measured by ammeter and the voltage too. So we calculated the impedance by Eq. 1

$$Z=U/I \quad [\Omega] \quad (1)$$

Method is the same for turning on the work where have enlargement of speed of rotation within $500min^{-1}$.

Measuring of characteristics Z=f(n) while rotor is moving is made two times during the retair. Once when rotor is turning off and the second time when the turbogenerator is turning on with increasing the speed of rotation within $500min^{-1}$.

III. RESULTS OF MEASURING OF ROTOR'S IMPEDANCE OF TURBOGENERATOR

The prophylactic monitoring of impedance in this paper is made since 1997 till 2004year. Rezults are sistematized by years and are given in Tables I and II. Table I is conserned to measuring of impedance during turning off the turbogenerator and Table II during turning on.

[1] Natasa D. Mojsoska is with the Faculty of Technical Sciences, I.L.Ribar bb. 7000 Bitola, Macedonia E-mail: natmojso@freemail.com.mk

TABLE I

RESULTS OBTAINED FROM OBSERVATION OF IMPEDANCE OF ROTOR'S WINDING DURING TURNING OFF THE TURBOGENERATOR

n [min^{-1}] / year	3000	2500	2000	1500	1000	500
1997	3.500	3.500	3.505	3.527	3.561	3.692
1998	3.516	3.603	3.633	3.580	3.636	3.695
1999	3.516	3.603	3.633	3.580	3.636	3.695
2000	3.867	3.953	3.953	3.953	3.973	4.192
2001	3.389	3.517	3.541	3.547	3.610	3.798
2002	-	3.714	3.714	3.714	3.763	3.887
2003	3.544	3.544	3.607	3.607	3.673	3.923
2004	3.525	3.525	3.508	3.538	3.552	3.679
Z_{sr} [Ω]	3.568	3.620	3.637	3.631	3.676	3.820

TABLE II

RESULTS OBTAINED FROM OBSERVATION OF IMPEDANCE OF ROTOR'S WINDING DURING TURNING ON THE TURBOGENERATOR

n [min^{-1}] / year	500	1000	1500	2000	2500	3000
1997	3.894	3.745	3.712	3.699	3.706	3.706
1998	3.994	3.850	3.775	3.768	3.754	3.741
1999	3.994	3.850	3.775	3.768	3.754	3.741
2000	2.825	2.860	2.860	2.895	2.900	2.940
2001	3.960	3.960	3.870	3.850	3.790	3.790
2002	4.090	3.980	3.980	3.970	3.860	3.850
2003	-	-	-	-	-	-
2004	-	-	-	-	-	-
Z_{sr} [Ω]	3.739	3.708	3.662	3.658	3.627	3.628

Measuring are made when increasing and discreasing the speed of rotation for 500 min^{-1}.

The Table II shows that in 2003 and 2004 yaer characteristics Z=f(n) when turbogenerator is tirning on are not taken. So that years are not calculated in the diagrams.

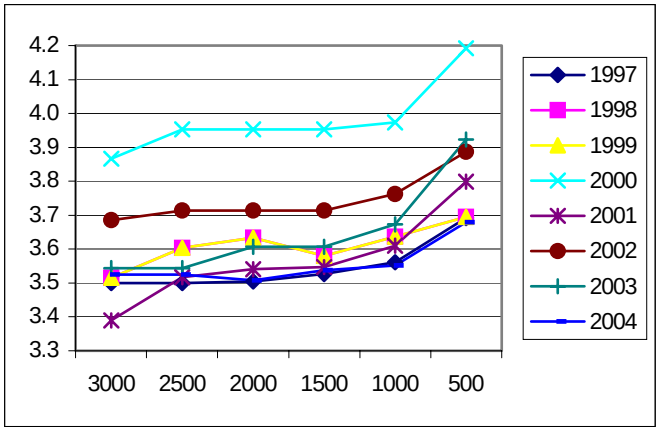

Fig.2 Dependance of impedance from speed of rotation Z=f(n) during turning off the turbogenerator

On the base of these Tables are created following diagrams, whereby is presented dependance of rotor impedance of speed of rotation for each yaer continualy, fig.2 and fig.3.

Characteristics Z=(n) should not have sudden leaps. That will indicate that there is some mistake in measuring or winding, that is nessesery further ezamination to remove it.

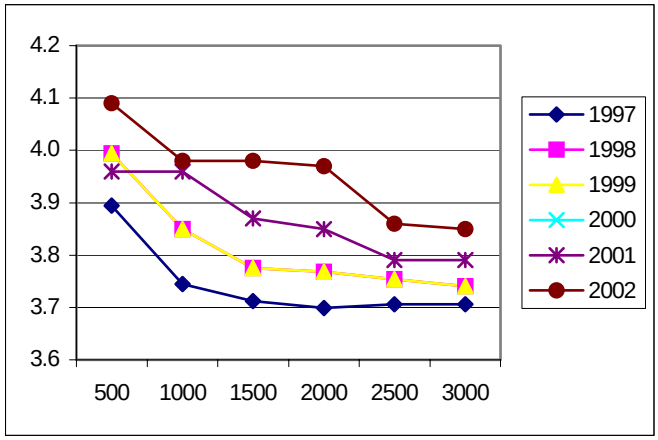

Fig.3 Dependance of impedance from speed of rotation Z=f(n) during turning on the turbogenerator

IV. ANALYSES OF RESULTS OF IMPEDANCE OF ROTOR'S WINDING AT UNIT 3 OF TPP BITOLA

In experimental part of this paper work is measured impedance of rotor's winding of sinchronous turbogenerator at unit 3 of TPP Bitola with special view to results of past eight years. Their sistematization is given in Tables I and II and are created the diagrams according that tables.

With purpose for better view and analyse of measuring, an average value of impedance is calculated for characteristic Z=(n) in both cases. Then in dependence of speed of rotation is created diagram with trend of direction (linear), given on Figs.4 and 5. with that a comparison is made for all following years.

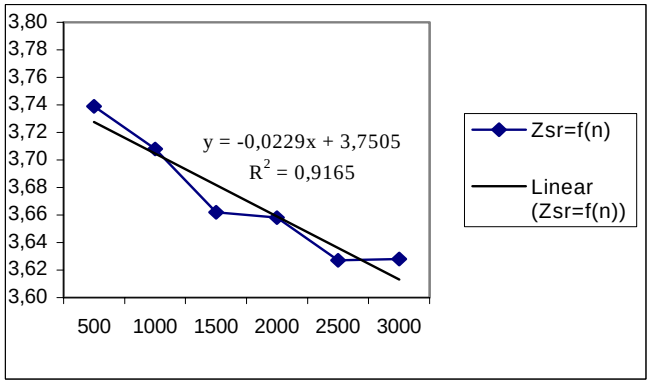

Fig. 4 Trend of direction of Z=(n) during turning on the turbogenerator

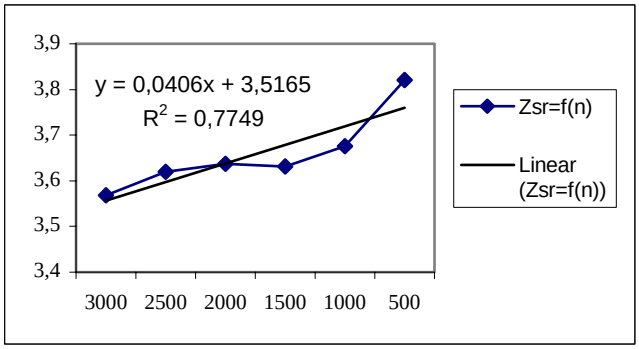

Fig. 5 Trend of direction of Z=(n) during turning off the turbogenerator

From previous diagrams can be noticed that in all past years impedance value of rotor winding is moving in the frame that is allowed and that is no sudden leaps. Also there are no big diferences from the trend direction.

From analyse and comparison of mesured and calculated values we can accepte that this way of prophylactical following is usefull for investigation and observation of insulation system.

V. CONCLUSION

In this paper widely is presented a method of exzamination of insulating system of large sinchronous turbogenerators. A detailed veiw is given for observation for
impedance of rotor's winding and prophylastic monitoring of it.

As it refers in introduction there are two cases of measuring: while rotor is moving characteristics Z=f(n) ang when it stops characteristics Z=f (U). But I can notice that the second type of measuring Z=f (U) is not done from 1997 till now or that informations were not available to me. What is the reason for that I can not tell, maybe timing for repair doesn't allow or the research team thought that is not nessesery.

This year 2005 repair is not predicted for unit 3 of TPP. That means that none of relavent parametars from nessesery examinations will be measured.

It is proposed for doing constantly repairs every year, to complete the documentation and making comparison of rezults from the previous years. The purpose is complete review of behaviour of insulating system and faster predicting of potentially critical condition of any of relevant parametars which defined the system.

REFERENCES

[1] D. Hristovski - ″ Research of electrical machines ″ , ETF ZONIK kompjuteri - Skopje 1996.

[2] Elaborates, annual reports and protocols from annual year and capital repairs of turbogenerators at unit 3 of TPP Bitola

[3] T. Paspalovski. - " Examinationof large turbogenerators in capital repair" CIGRE Conference Proceedings, pp. 39-46.

[4] N. Mojsoska - "Teoretic and prophylactic research of effiency in exploatation of sinchronous turbogenerator at unit 3 of TPP Bitola" master thesis, ETF Skopje 2001.

Calculation of Leakage Flux in Stator and Rotor Windings and Reactances of Solid Salient Poles Synchronous Motor by Finite Element

Mirka Popnikolova Radevska[1]

Abstract – **In this paper is presented a methodology for numerical determination and complex analysis of a Solid Salient Poles Synchronous Motor (SSPSM), product of MAWDSLEY with rated data: 3.52 kW, 240 V, exitation current I_f =5.5 A, and 1500 r. p. m. Programe package FEM 3D, for calculation in magnetostatic case is applied in order leakage fluxes in active parts of stator and rotor windings and the part of the winding overhangs to be calculated. Leakage fluxes are determined from the value of magnetic vector potential A. For that purpose a cross section on each local coordinate systems for five layer of the active length and the rotor und stator overhangs are presentation.**

Keywords – **Solid Salient Poles Synchronous Motor, programme package FEM-3D, Calculation of leakage flux, Motor reactances.**

I. INTRODUCTION

FEM 3D is proven numerical tool for analyzing electromagnetic phenomena in electrical machines and devices. This method enables to enter "inside the machine" and to evaluate exactly magnetic quantities such as air gap flux or leakage flux in any part (layer) of the motor. Using numerical calculation performed by FEM. 3D, they can be calculated more precisely which improves overall accuracy of motor reactances. Mathematical model is generated by dividing motor domain per z-axis in five layers and is presentation in Fig.1.

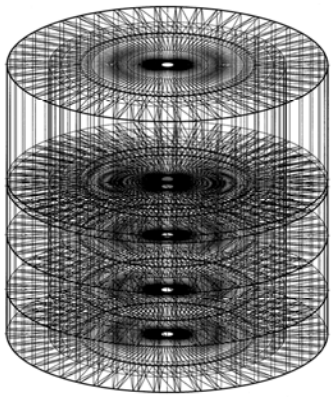

Fig. 1. 3 D view of the mesh.

[1]Mirka Popnikolova Radevska is with Technical Faculty, Ivo Lola Ribar b.b., 7000 Bitola, Macedonia, E-mail: mirkare@mt.net.mk

In first layer are placed active parts of stator and rotor winding while winding overhangs are placed in second, third and fourth axial layer. Each layer is divided into sub-domains wit local coordinate system. FEM 3D automatically generates mesh of finite elements and calculated the values **A** in each node of the 3D mesh.

The cross section of first layer and currents density is presentation in Fig. 2.

Fig. 2. Cross section of first axial layer with current densities.

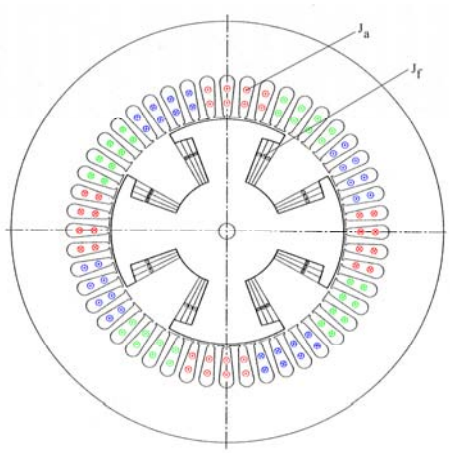

A part of cross section of second and third axial layer and currents density is presentation in Fig. 3.

Fig. 3. A part of cross section of second and third axial layer and currents density.

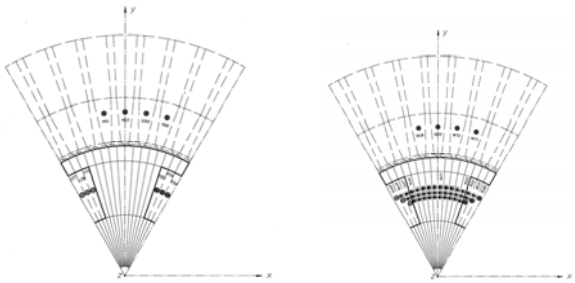

II. CALCULATION OF LEAKAGE FLUXES IN STATOR AND ROTOR WINDINGS

Computation of leakage fluxes of stator winding is made in active parts of stator winding and the parts of the windings placed in channel or second, third and fourth axial layer of mathematical model Fig. 1. and Fig. 2 and Fig. 3. Leakage flux in active part of the motor windings is determined from the value of magnetic vector potential **A**. Leakage flux is

calculated when current is in direction z-axis, and normal vector of magnetic induction **B** which creates leakage flux is in the direction of x-axes. The Leakage flux in active part of motor winding, when the excitation current $I_f = 0$, and rated stator current I_{an} in phase A is calculated according to Eq.1 :

$$\Delta\Psi_{Iki} = l_s \frac{N_k}{4} \frac{\Delta A_i}{\Delta y} \qquad (1)$$

I-denotes first axial layer, *k*-channel leakage, *i*-number of channel, Δy -radial channel length, N_k -number of conductors. Total leakage flux in first axial layer or in active part of stator winding per poles is read out from the output file POT. DAT of FEM 3D and its value is:

$$\sum \Delta\Psi_{Iki} = \sum_{i=481}^{482} \Delta\Psi_{Iki} + \sum_{i=527}^{528} \Delta\Psi_{Iki} \qquad (2)$$

$$\sum \Delta\Psi_{Iki} = 0.004034 \text{ Vs}$$

Calculation of leakage flux in second and third layer of stator winding represents the leakage flux in winding overhangs. Method of calculation is identical as in the first layer. Now local coordinate system is placed in sub-domains which approximately represent winding overhangs. In Eq. 1, only lengths of stator winding overhangs in second and third layer are replaced and following results are gained respectively:

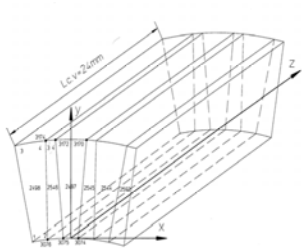

Fig. 4. Local coordinate system in winding overhangs of stator winding, where is:

$$\sum \Psi_{IIki} = 7.676 \times 10^{-5} \text{ Vs}$$

$$\sum \Psi_{IIIki} = 3.449 \times 10^{-2} \text{ Vs}$$

Leakage flux in fourth axial layer is determined from Eq. $\mathbf{B} = rot\mathbf{A}$. Now, local coordinate system is placed as it is shown on Fig. 4.

l_{SIVcv} – axial length of fourth layer, $b_k = 55.9$mm- channel width, $t_I = 99.7$mm- pitch channel-tooth, b_z – width of stator tooth, N_k – number of conductors per channel.

A. Leakage flux per **k** –ort

1. For y=const, $ls_{c.v.}$=24mm

According to Eq.1., leakage flux in overhangs over channels has value:

$$\sum \Psi_{IVay} = 0.236 \text{ Vs}$$

2. For x=const. following the same Eq. calculated value of leakage flux is:

$$\sum \Psi_{IVax} = 0.222 \cdot 10^{-3} \text{ Vs}$$

Total leakage flux in stator winding per **k** ort is calculated froom root square of $\sum \Psi_{IVay}$ and $\sum \Psi_{IVax}$ and its value is:

$$\sum \Psi_{IVa} = 0.324 \cdot 10^{-3} \text{ Vs.}$$

B. Leakage flux per **i** ort

1. For $y = const$, $\Delta x = b_k$

$$\sum \Delta\Psi_{bky} = 0.00596 \text{ Vs}$$

2. For $y = const.$, $\Delta x = b_z$

$$\sum \Delta\Psi_{IVbzy} == 0.00399 \text{ Vs}$$

Total Leakage flux in winding overhangs for $y = const.$ per **i** ort is calculated as:

$$\sum \Delta\Psi_{IVby} = \Delta\Psi_{IVbky} + \Delta\Psi_{IVbzy} = 0.0096 \text{ Vs}$$

Total Leakage flux in winding overhangs $z = const.$ per **i** ort is:

$$\sum \Delta\Psi_{IVb} 0.0102 \text{ Vs}$$

Total Leakage flux in stator winding overhangs per pair of poles is found from:

$$\sum \Delta\Psi_{IV\,c.v.} = 2 \cdot \sum \Delta\Psi_{IV\,a} + \sum \Delta\Psi_{IV\,b}$$

Computation of leakage fluxes of rotor winding is made in active parts of rotor winding and the parts of the windings placed in channel or second, and third axial layer of mathematical model Fig. 1. and Fig. 2 and Fig. 3. It is assumed that rated current flows trough rotor winding $I_f = I_{fn} = 5.5\text{A}$, and the current in the stator winding is $I_a = 0$. Local coordinate system is placed it is shown in Fig. 5. and Fig. 6. Normal vector of **B** is in direction of x-axis. Leakage flux is also in the direction x-axis. Calculation is made according to Eq. 1. Value of leakage flux per pair poles is:

$$\sum \Delta\Psi_{If} = \sum_{i=103}^{105} \Delta\Psi_{Ifi} + \sum_{i=186}^{188} \Delta\Psi_{Ifi} \qquad (3)$$

$$2\sum \Delta\Psi_{If} = 0.0143 \text{ Vs}$$

Leakage flux in second and third layer is calculated regarding sub-domains which define winding overhangs of rotor winding in second layer Fig. 5.

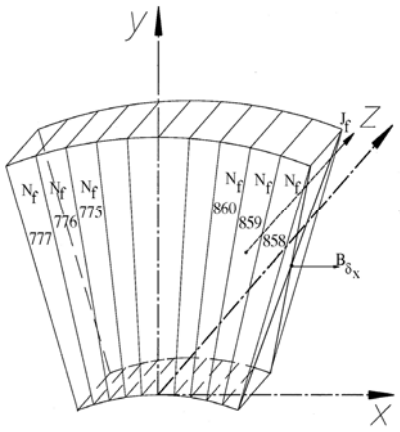

Fig. 5. Local coordinate system in second axial layer of rotor winding overhangs.

Values of **A** in each node of this sub-domain are calculated. Sum of all leakage fluxes in second layer is:

$$\sum \Delta\Psi_{IIf} = \sum_{i=775}^{777} \Delta\Psi_{IIfi} + \sum_{i=858}^{860} \Delta\Psi_{IIfi} \qquad (4)$$

$$\sum \Delta\Psi_{IIf} = 0.01456 \text{ Vs}$$

Leakage flux in third layer is calculated:

$$\sum \Delta\Psi_{IIIfc.v.} = \frac{N_f}{4} \cdot l_{III} \left(\sum_{i=1441}^{1446} \Delta\Psi_{IIIi} + \sum_{i=1533}^{1536} \Delta\Psi_{IIIi} \right) \qquad (5)$$

And its value per pair of poles is:

$$2 \cdot \sum \Delta\Psi_{IIIfc.v.} 0.02442 \text{ Vs}$$

III. Calculation of leakage reactances in stator and rotor windings

In above sections is explained method of calculation of leakage fluxes in active parts as well as in winding overhangs. Leakage fluxes close around the winding itself. These fluxes determined leakage reactances of the SSPSM.

Leakage reactance to be calculated value of leakage flux which closes around winding active part must be know.

Leakage reactance in first axial layer is calculated using the total leakage flux. There the inductance is calculated:

$$L_{Ik} = \frac{\sum \Delta\Psi_{ki}}{I_{an}} = 0.00446 \text{ H}, \quad I_{fn} = 0 \text{ A} \qquad (6)$$

$$X_{Ik} = \omega \cdot L_{Ik} = 1.4005\ \Omega$$

Leakage reactances in second, third and fourth axial layer of stator winding are:

$$X_{IIk} = \omega \cdot L_{IIk} 0.0241\ \Omega$$

$$X_{IIIk} = \omega \cdot L_{IIIk} 0.108\ \Omega$$

$$X_{IVc.v.} = 0.656\ \Omega$$

Totalleakage reactance of stator winding is calculated as sum of reactances in all four layers:

$$X_{\sigma a} = X_{Ik} + X_{IIk} + X_{IIIk} + X_{IVc.v.} \qquad (7)$$

Considering the value of leakage flux in active part of rotor winding, inductance and reactance in this part of winding are calculated:

$$L_{If} = \frac{\sum \Delta\Psi_{If}}{I_{fn}} = 0.0026 \text{ H}, \quad I_{an} = 0 \text{ A} \qquad (8)$$

$$X_{If} = \omega \cdot L_{If} = 0.816\ \Omega$$

Leakage reactance in second and third layer are:

$$X_{IIf} = 0.831\ \Omega$$

$$X_{IIIc.v.} = 0.697\ \Omega$$

Total leakage reactance in rotor winding is:

$$X_{\sigma f} = X_{If} + X_{IIf} + X_{IIIc.v.} = 0.0491 \text{ p.u.} \qquad (9)$$

IV. Conclusion

Using contenporary numerical method for magnetic field calculation FEM. 3D leakage fluxes in SSPSM are calculated. Futher flux distribution in motor air-gap is also calculated. These values enabels us to calculate motor equivalent inductance per d and q axises, motor self inductances as well as leakage reactances in stator and rotor windings. Value of calculated leakage reactance of stator

winding $X^*_{\sigma a} = 0.0431$ p.u. is compared with value gained from analytic calculation $X^*_{\sigma a} = 0.0694$ p.u. Compared result show reasonable agreement. Knowing that analytical calculation of inductances is always with cetain approximations, this proves FEM as accurate numerical method for motor parametar calculation.

REFERENCES

[1] M. Popnikolova Radevska: “Contribution for Computation the parameters and characteristics analysing of the SSPSM”, Dissertation, Skopje, 1996, Macedonia.

[2] M. Popnikolova Radevska, M. Cundev, L. Petkovska: "Electromagnetic Field Analyses and Computatio of Electromagnetic Characteristics of Solid Salient Poles Synchronous Motor", *ICEM’98 Conference Proceedings*, pp.707-709, Istanbul, Turkey, 1998.

[3] M. Popnikolova Radevska, V. Sarac, M. Cundev, L. Petkovska: “Computation of Solid Salient Poles Synchronous Motor parameters by 3D Finite Element Mrthod ”, EPNC Symposium on Electromagnetic Phenomena in Nonlinear Circuits, p.p. 111-114,Belgium,Leuven,1998

Influence of the Non-symmetrical Three-Phase Loads on the Transformer and Supply Grid

George T. Todorov [1], Georgi I. Ganev [2]

Abstract - **The paper discusses the operation of the distribution transformer with non-symmetrical load connected. The transformer operates with an isolated neutral wire of the star-connected secondary winding. The influence of the load variation on the voltage of the supply grid is analysed and analytical expressions for the additional core loss are given. Experiments confirm the influence of the load non-symmetry on the losses, power factor and reactive power of the transformer.**

Keywords - **transformer, non-symmetrical load, losses.**

I. INTRODUCTION

Different modes of operation of the three-phase power transformers with symmetrical and non-symmetrical load are discussed in a number of books [1,4,5,6,7]. Short circuit on the secondary (low voltage) winding is usually presented as a typical non-symmetrical mode. It is assumed also that the grid supplies the transformer with a sinusoidal waveform symmetrical three-phase voltage. This is correct for the high-power network transformers while for the distribution transformers 20/0,4 kV non-symmetry of the supply voltage may occur in certain load. Strong requirements to the electric power quality are defined in the European and national standards [2,9], including to the symmetry of the three-phase voltage. According to [9] the RMS value of the negative sequence voltage must not exceed 2% (and 3% only for some regions).

Normally the LV grid operates with an earth-connected neutral but in recent years it is of frequent occurrence the transformer to operate with a neutral wire isolated for a certain period of time. The aim of the present paper is to analyse the operation of the three-phase distribution transformer with an isolated neutral wire connected to non-symmetrical three-phase load.

II. SUPPLY VOLTAGE NON-SYMMETRY

Core type (three-leg) distribution transformer with D/y connection is under consideration. The neutral wire of the star-connected secondary winding is isolated. Three-phase resistive load is connected to the secondary winding at steady state.

[1]George T. Todorov is with the Technical University of Sofia, Faculty of Electrical Engineering, 8, Kliment Ohridski St., bl.12, 1000, Sofia, Bulgaria, E-mail: gtto@tu-sofia.bg

[2]Georgi I. Ganev is with the Technical University of Sofia, branch Plovdiv, 25, Tzanko Dustabanov St., 4000, Plovdiv, Bulgaria, E-mail: geoganev@yahoo.com

According to the reasons the non-symmetry of the primary voltage could be:

- So called "transverse" non-symmetry in the supply grid (MV line)

It occurs at transient phase to earth or phase to phase short-circuit in the MV line. This transient short-circuit causes drops in the sinusoidal waveform of the supply voltage. It is possible in MV grids with a neutral wire connected to the earth via Peterson's coil and could lead to fleeting non-symmetry in the three-phase voltage. This kind of non-symmetry is of short duration, happens accidentally and is not under consideration in the present paper.

- Non-symmetry caused by the non-symmetrical load connected

The equivalent circuit in Fig.1 shows the investigated distribution transformer connected to the symmetrical three-phase voltage supply E_A, E_B, E_C via symmetrical line with an impedance Z_1.

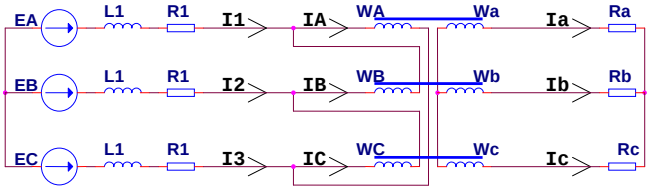

Fig.1 Equivalent circuit

Three-phase resistive load is connected to the secondary winding of the transformer. As the neutral is isolated

$$\dot{I}_a + \dot{I}_b + \dot{I}_c = 0.$$

At the symmetrical load the currents $\dot{I}_a, \dot{I}_b$ and $\dot{I}_c$ are equal with a lag of 120° (Fig. 2a). Each phase current lags behind the corresponding phase voltage to a small angle.

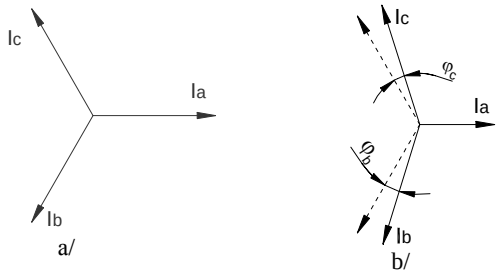

Fig 2. Phasor diagram of the transformer's secondary currents at symmetrical (a) and non-symmetrical (b) load

Assume that we reduce the load of phase *A* keeping constant the load of phases *B* and *C*. As seen in Fig. 2b this will change the lag between the currents - $\dot{I}_b$ will go at φ_b ahead and $\dot{I}_c$ - at φ_c behind the corresponding vectors at symmetrical load.

In this case I_b will lead the voltage U_b and I_c will increase the lag behind U_c despite of the resistive load.

If we keep constant the load of phase *A* (R_a=*const*) and reduce the load of phases *B* and *C* the lag between the currents will change in opposite direction – the current I_b will lag behind the voltage U_b and I_c will lead the voltage U_c. At a constant total load of the transformer (*Pr=const*) the result of this changed current's lag is an increase in the current values and the transformer losses.

The non-symmetry of the load currents causes lag change of the currents in the primary winding of the transformer also and change of the reactive power consumption. Under considered example the transformer's consumption will be different for the three phases – mainly resistive power for phase *A*, resistive-capacitive power for phase *B* and resistive-inductive power for phase *C*. The reactive power components increase proportional to the load current's non-symmetry.

Although the transformer is connected to the symmetrical three-phase voltage E_A, E_B, E_C, the load's non-symmetry affects on the transformer's supply voltage. Due to the different values and lag of the currents in the transformer's primary winding, the voltage drops in the line impedance Z_1 are different and the voltage on the transformer's terminals forms non-symmetrical system (Fig. 3).

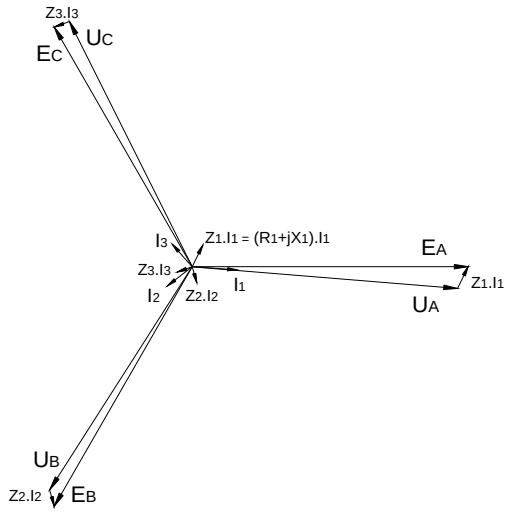

Fig. 3. Phasor diagram of the transformer's supply voltage

III. INFLUENCE OF THE VOLTAGE NON-SYMMETRY ON THE TRANSFORMER'S LOSSES

The operation of the transformer with non-symmetrical supply voltage is analysed in [3]. Using the symmetric component method (Fortescue transformation) it is shown that the transformer's core loss depends on the coefficient of the voltage non-symmetry ε_U:

$$\frac{P_{a,\varepsilon}}{P_a} = 1 + \frac{\varepsilon_U}{2 + 1{,}5\, l_a / l_b} + \varepsilon_U^2 , \qquad (1)$$

where ε_U - coefficient of the voltage non-symmetry

$\varepsilon_U = U_2 / U_1$

U_1 - positive sequence component voltage;

U_2 - negative sequence component voltage;

l_a, l_b – leg and yoke length.

The zero sequence voltage produces zero sequence magnetic flux in the transformer's legs, which causes additional core loss in the legs

$$\frac{P_{a,\alpha}}{P_a} = \frac{2\alpha^2}{1 + 0{,}75.l_a / l_b}\left(\frac{1-\lambda}{2+\lambda}\right)^2 , \qquad (2)$$

where α – unbalance coefficient $\alpha = U_o / U_1$;

λ - coefficient equal to

$\lambda = \Lambda_{\mu,2} / \Lambda_{\mu,1} = (3l_a + 2l_b)/2l_b$;

$\Lambda_{\mu,1}$, $\Lambda_{\mu,2}$ are the magnetic permeability coefficients of the end legs and middle leg of the transformer respectively.

The loss in the transformer's tank and accessories due to the zero sequence magnetic flux is equal to:

$$\frac{P_{k,\alpha}}{P_k} = \left(1 + 4.\alpha.\frac{1-\lambda}{2+\lambda}\right)^2 \qquad (3)$$

For the distribution transformers manufactured by Elprom-Trafo CH AG, Kjustendil, Bulgaria, widely used in Bulgarian energy power system, the above equations can be written as follows:

$$\begin{aligned} P_{a,\varepsilon}/P_a &= 1 + 0{,}354.\varepsilon_U + \varepsilon_U^2 \\ P_{a,\alpha}/P_a &= 0{,}425.\alpha^2 \\ P_{k,\alpha}/P_k &= (1 - 2{,}2.\alpha)^2 \end{aligned} \qquad (4)$$

IV. EXPERIMENTAL RESULTS

Series of experiments are made to verify the theoretical analysis of the load non-symmetry influence. Three-phase transformer TT16002 with ratings as follows is used: S_r=1200VA, P_{sc}=68W, P_0=21,6W, winding's connection D/y, isolated Y-center of the secondary winding. Power quality analyzers MI2192 (manufactored by METREL - Slovenia) and CA8332 (manufactored by Chouven Arnoux - France) are used to carry out the measurements. Three-phase resistive load is connected to the secondary winding of the transformer. All experiments start form symmetric load and next we vary one of the currents in large range – from 0,9.I_r to 0,2.I_r. Three series of experiments are carried out - at 0,9I_r; 0,67I_r and 0,33I_r, compared to the symmetrical load.

The phasor diagrams in Fig. 4 show the currents measured in the transformer's primary winding at variation of the load non-symmetry. At a symmetrical load (Fig. 4a) the lag between currents is equal to 120°. Diagrams in the next three figures (Figs. 4b,c,d) show the change of the primary current's lag, caused by the reduction of the load current I_c. Although the load is resistive, it's non-symmetry increases the current's lag proportionally to the non-symmetry increase.

The change of the lag of the currents in the MV line (φ_A, φ_B, φ_C) and the load currents (φ_a, φ_b, φ_c) versus the coefficient of the current non-symmetry ε is shown in Fig. 5. As it is seen in the figure due to the load non-symmetry the lag is bigger in the primary currents.

The reactive power consumption depends on the non-symmetry also. Measurements are carried out for 3 values of

the load current and the results are shown in Fig. 6. The reactive power of each phase is shown in relation to one third of the transformer's magnetizing power at symmetrical load. Fig. 6a shows the reactive power variation when the currents $I_a = I_b \approx 0{,}9I_r$ and the current I_c vary from $0{,}9.I_r$ to $0{,}2.I_r$. When the load current is lower than the rated one - $I_a = I_b \approx 0{,}67I_r$ (Fig. 6b) and $I_a = I_b \approx 0{,}33I_r$ (Fig. 6c), and the current I_c vary from $0{,}9.I_r$ to $0{,}2.I_r$ the reactive power depends on the relation between the currents. For example the reactive power of phase B is inductive at $I_a, I_b < I_c$ and capacitive at $I_a, I_b > I_c$.

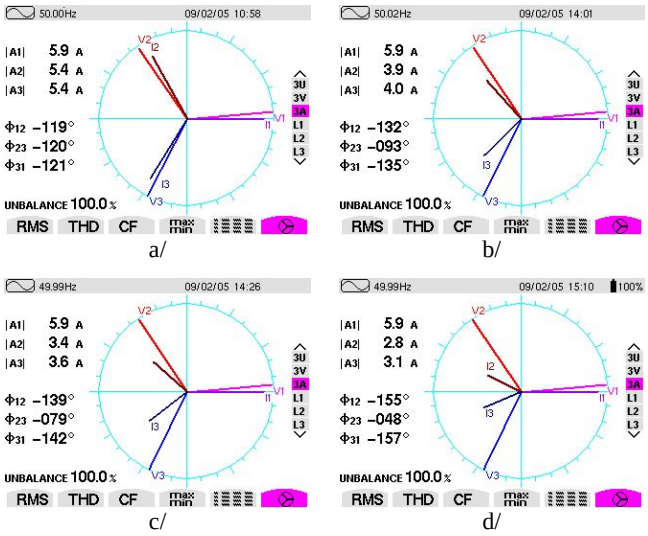

Fig. 4. Phasor diagrams of of the primary winding currents and voltages at 4 values of the load

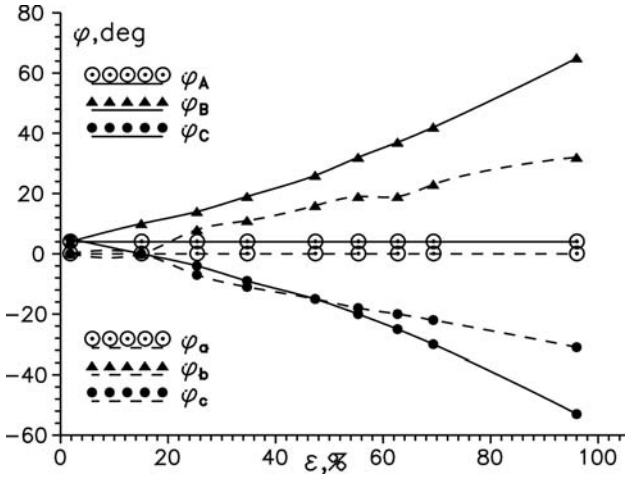

Fig. 5. Change of the lag of the primary winding currents and the load currents

The coefficient of the voltage non-symmetry increases with the increase of the load current non-symmetry (Fig. 7). The value of this coefficient is calculated as follows:

$$\varepsilon_U = \varepsilon_{U,nonsym} - \varepsilon_{U,sym} \quad (5)$$

Due to the non-symmetry of the resistive load the relative magnetizing power slightly increases (Fig. 8) and the power factor significantly decreases (Fig. 9). The reason is the increase of the reactive components of the currents and of the total input power of the transformer. An increase of the transformer loss was found also (Fig.10).

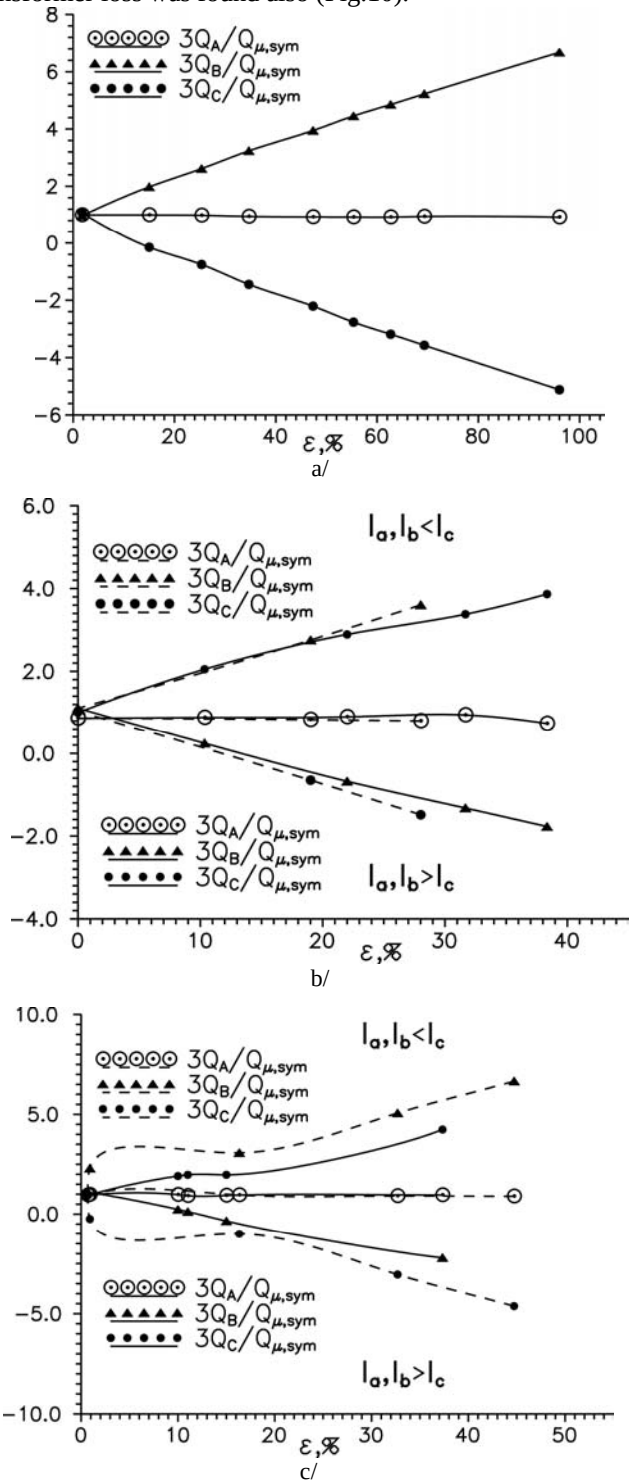

Fig. 6. The relative reactive power versus the coefficient of the current non-symmetry

V. CONCLUSION

1. The non-symmetrical load connected to the secondary winding with an isolated neutral causes change in the phase currents lag. It depends on the values and the proportion between the currents.

2. The non-symmetry of the load currents causes also lag change of the currents in the primary winding and non-symmetry of the transformer's supply voltage.

3. Due to the non-symmetry the power factor decreases and an increase in the losses and the reactive power occurred even though the load is resistive.

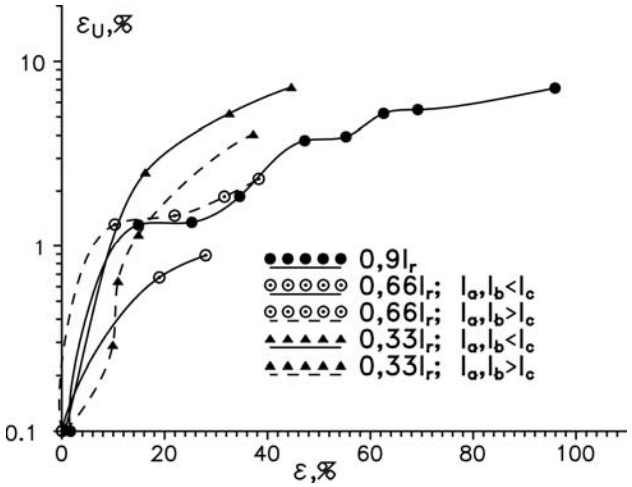

Fig. 7. Coefficient of the voltage non-symmetry versus coefficient of the current non-symmetry

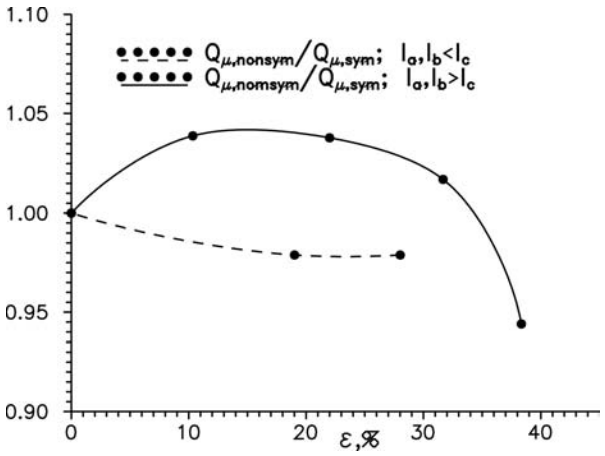

Fig. 8. Relative magnetizing power at load current 2/3 of the rated

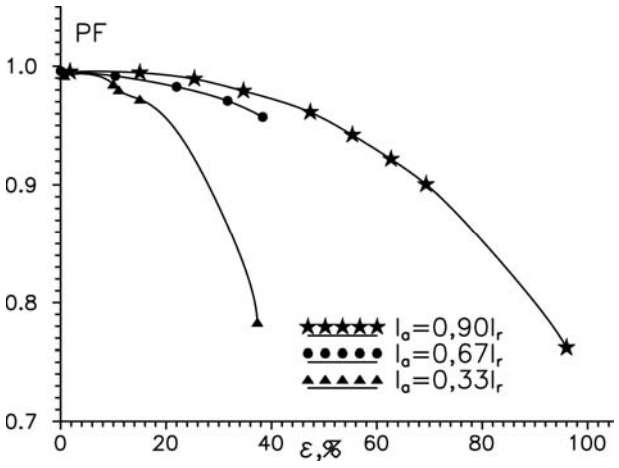

Fig. 9. Power factor versus current non-symmetry coefficient

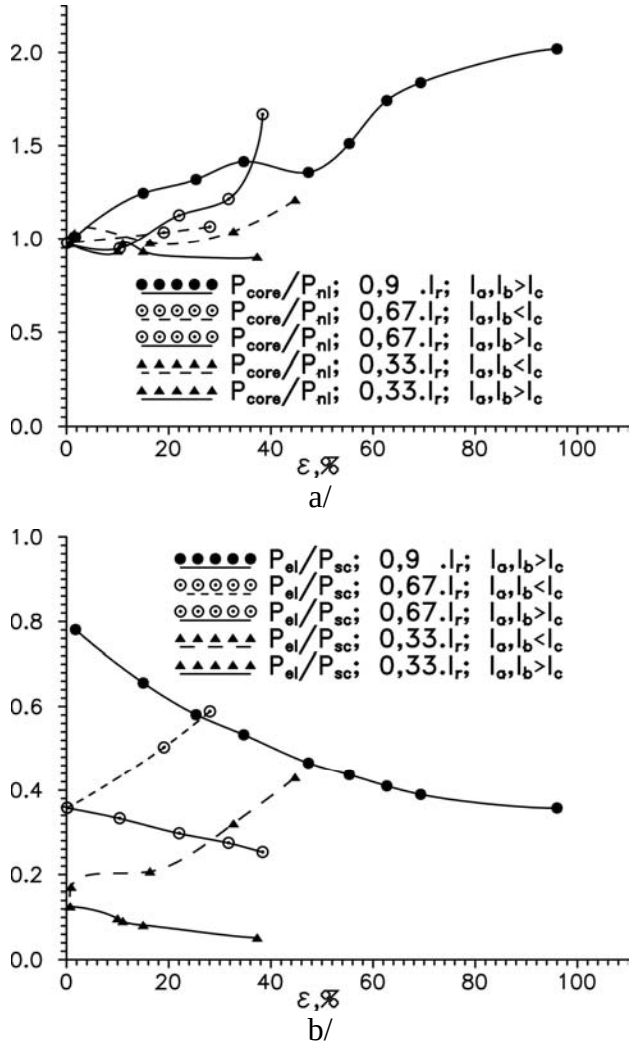

Fig. 10. Transformer losses versus current non-symmetry coefficient

REFERENCES

[1] Ангелов, Димитров. Електрически машини, София, 1976.

[2] БДС 10694-80, Електрическа енергия. Норми за показателите за качество на електрическата енергия при приемниците.

[3] Ганев Г., Г.Тодоров, Р.Янков. Изследване на влиянието на несиметрията на захранващото напрежение върху загубите в трифазен трансформатор, Съюз на учените в България, Пловдив, 2004, 74-79.

[4] Иванов-Смоленский А.В., Электрические машины, Москва, 1980.

[5] Петров Г.Н. Электрические машины. ч.I, Москва, 1974

[6] Попов Ив. Електрически машини, ч.II, София,1960.

[7] Сергеенков Б.Н.,В.М.Киселев, Н.А.Акимова. Электрические машины - трансформаторы, Москва, 1989.

[8] Сидеров С., Н.Матанов, Б.Бойчев, В.Георгиев. Алгоритъм за оценка на основните показатели на електромагнитна съвместимост в електроснабдителни системи с микропроцесорен анализатор, Годишник на МГУ"Св.Иван Рилски", св.III. София, 2003, стр.175-179.

[9] BS EN 50160, Voltage Characteristics of Electricity Supplied by Public Distribution Systems

Multiparameter Control of a Cross-Flow Turbine

Stanimir Y. Yordanov[1], Krasimir H. Ormanzhiev[2]

Abstract: **In this paper a general structure of a computer-implemented, object-oriented software system is describe. The system uses the intelligence mechanisms and is intended for the control of technical objects that function both in predictable and random environments. The object for studying is automatic system is made of a turbo the pump, a complex pressure pipeline, cross-flow turbine and electric generator. The results of experiment have been presented in graphical curves.**

Keywords: **Real-Time problems; RTS System Kernel functions; centrifugal turbo-pump; pressure penstock; cross-flow turbine**

I. INTRODUCTION

The study of dynamical processes in pressure turbo-system at parallel work of the hydraulic turbo-alternator fed by means of a common pressure penstock is of great significance during design and optimization of the operation of such equipments as water-power stations, pumping stations, etc. [1, 2, 4].

During system adjustment unestablished (dynamical) processes originate [3, 5, 6]. The maximum pressure rise in the pressure penstock has to be limited by consideration for the strength dimensioning of the penstock as well from the point of view of the quality of turbine adjustment

The requirements towards governors of the water turbines are quite various as well as they are conditioned by the special features and variety of their modes of exploiting, i.e.:

- work in energy-system with high power;
- work in isolated energy-district;
- work of idle stroke;
- work at unloading with switching off the generator from energy-system.

At the up-to-date energy-system, the automatic governors must possess not only high qualitative parameters in connection with supporting the values of revolotions of the turbines but in the best way to react on all governing influences.

II. DESCRIPTION OF THE DEVELOPED STAND

The stand scheme for experimental study of pressure turbo-system is shown in Fig.1. It consists of the following elements: 1 – reservoir; 2 - vacuum gauge; 3 - entrifugal pump; 4- electrical motor; 5, 8, 14, 17, 18, 20, 22 – sensor for low pressure**;** 7, 9, 10, 12, 13, 30, 40 - valve door; 24 - cross-flow turbine;15- ADC/DAC; 16 – personal computer; 19 - valve door and electrical motor; 20 - block for generator loading; 28 - three-phase synchronous generator; 33 - electrical motor; 36,37-sensor for high pressure**;** 38-hydrostation; 39 - suction valve; 34, 35 - suction valve;41-sensor for position of the input valve; 32 - auxiliary centrifugal pump; 31 – contact manometer;29–tachogenerator; 42- hydrocilinder; 25 control panel for power;26 – block for loading of the synchronous generator; 27 - driving belt; Depending on the situation of valve doors 11 and 12, scheme with long or short pressure penstock can be realized. In the two cases, parallel working hydraulic turbo-alternator is imitated by passing the working fluid from the pressure penstock through the valve door 18.

A scheme with short pressure penstock is realized at open valve door 12 and close one 11.

The supplied flow from centrifugal pump joins in the short pressure penstock (with diameter d=200 mm) as one part passes through the water turbine but the other one – through the valve door 18.

A scheme with long pressure penstock is realized at close valve door 12 and open one 11. The penstock sector between 11 and 13 valve doors is made of polyvinyl chloride (PVC) with diameter d=100 m and length *l*=48 m.

The disturbances in the system can be supplied in consequence of the alteration of the valve door 18 situation or by the variation of the adjusting blade situation of turbine. The alteration of electric load only influence on the revolutions of the turbine and generator but not on the pressure and flow in the pressure penstock. This is due to the fact that the water turbine is active and a governor, which is used to compensate the variation of the revolutions by means of rotating the input blade, is missing. For realizing the control, apparatus-programme system, which is composed of primary transducer, programmable controller, personal computer (PC) and software for controlling, is developed.

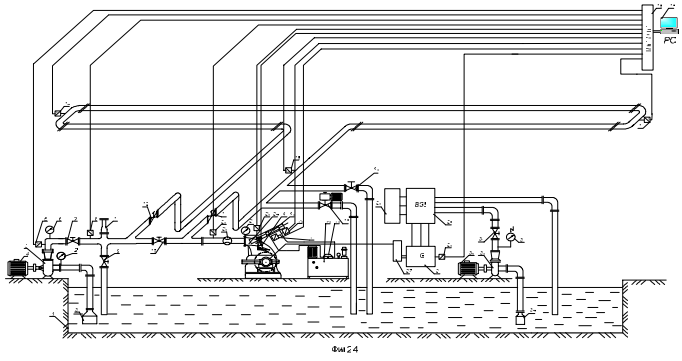

Fig. 1: Scheme of the stand

For accomplishing the observation, three sensors are used as follows: two ones for pressure of a type *PS3310* and one for revolutions of a type *PIVTM6*. By means of the sensors for pressure, the flow pressure is observed at the beginning of the penstock immediately after the pump and the flow pressure at the beginning of the water turbine (Fig.1). By means of the tachogenerators the turbine revolutions are kept up with. The signals, received from sensors by means

[1]Stanimir Y.Yordanov Technical University of Gabrovo, 4 H.Dimitar str. Gabrovo 5300,Bulgaria e-mail:sjjordanov@tugab.bg
[2]Krasimir H.Ormanzhiev Technical University of Gabrovo, 4 H. Dimitar str. Gabrovo 5300, Bulgaria e-mail: orman@tugab.bg

of the controller *ADDA-12*, are transformed in digital signal as well as they are supplied to PC for processing. After analysing the received information control signals are elaborated. The controller support observation simultaneously on 16 analogue and it has ones analogue output. The signal transformation is performed by means of 12 bit analogue-to-digital converter for the eight channels as well of 12 bit analogue-to-digital converter for the remaining 16 inputs. The input signals are in the range of 0-5V for the sensors of a type *PS3310* as well of 0-10V for the sensors of a type *PIVTM6*.

The measurement accuracy depends on many factors as follows:

- the transformation accuracy for 8 bit analogue-to-digital converter is 0.01953125V, which is equivalent to the pressure in the order of 1.953125.103 Pa or for the revolutions of the water turbine – 6.06 min-1; the transformation accuracy for 12 bit analogue-to-digital converter is 0.0012220703125V, which is equivalent to the pressure in the order of 1.2.102 Pa or for the revolutions of the water turbine – 0.36 min-1;
- errors caused by disturbances along the trace. These disturbances depend on the line length, the length and type of the cable for connection between the sensors and controller. The availability of strong electromagnetic fields in the close proximity to the line for connection exerts an influence on the accuracy.

For example, the signal received by the sensor for pressure on the penstock input is highly become noisy because of the sensor nearness to the engine driving the water pump. The signal by tachogenerator is influenced by the electromagnetic field made by the generator.

For diminishing the effect of the parasite noises and for improving the measurement accuracy, 12 bit analogue inputs are used as the signals before entering in them, passes through low-frequency filters for the disturbance compensation. The scanning cycle is determined by the following factors:

- time for signal transformation by analogue-to-digital converter (26μs per one input);
- time for data processing by the controller;
- time for analyzing the i/o commands supplied to the controller by PC;
- time for data transmission between controller and PC.
- time for information processing by PC, etc.

For compensating the effect of the parasite signals and for improving the response time it is worked in the following directions:

- designing of controllers for signal transformation by the sensors which will be placed in maximum proximity to the transducer. Thus, the disturbances along the connection between controllers and sensors will be eliminated; the time for signal transformation will be reduced because of parallel execution of the operations under transformation.
- variation of the interface for connection between controllers and PC.

III. Structure of a Software System

The control of the system is based on the object oriented system “Cunami” (fig. 2). Cunami is a system of hight precision class, developed for control of technological processes and active quality monitoring. This system is developed for Window NT. His module structure is well appropriate for treatment of a large class of problems.

The plant control is fulfiled by control module with an multiparameter control law. After analising of all processes and all perturbations in the system the following variables were included in the control law:

- generator speed;
- position of the blade on the input of the water turbine;
- pressure on the input of the water turbine;
- pressure on position 18.

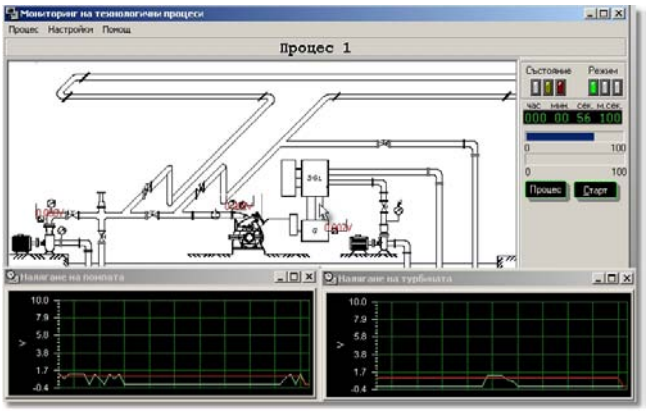

Fig.2. Control module

At this stage the electrical parameters of the generator are not included in the control law. However they will be included later. The structural scheme of the controller is shown on Fig. 3

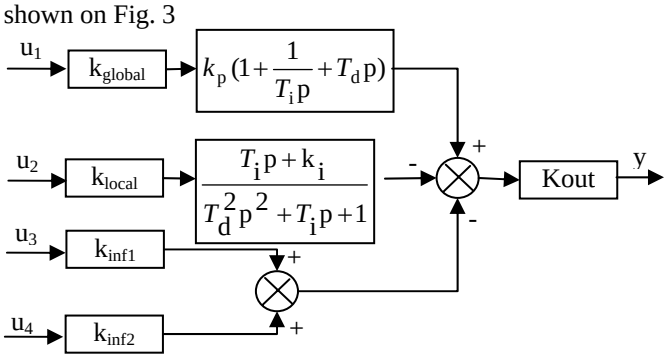

Fig.3. Structure of the controller

The controller is realized according to the following recurrent equation:

$$u(k) = k_p \left\{ \begin{array}{l} e(k) + \frac{T_0}{T_i} \sum_{i=1}^{k} e(i) + \frac{T_0}{T_i} [e(k) + \\ + 3e(k-1) - 3e(k-2) - e(k-3)] \end{array} \right\} \quad (1)$$

In real life conditions a hight level of noise is observed. Our analysis shows that this noise is in relatively restricted frequency band. However for decreasing of his influence software sensors are realized in real time according to the following transfer functions:

$$W(z^{-1}) = \frac{b_0 + b_1 z^{-1}}{1 + a_1 z^{-1}} \text{ and } W(z^{-1}) = \frac{b_0 + b_1 z^{-1}}{a_1 + a_1 z^{-1} + a_2 z^{-2}} \quad (2)$$

As a result the noise level has been reduced in an admissible range for stable functionning of the control

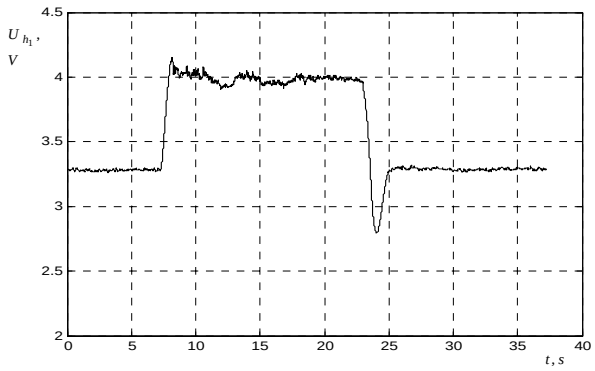

Fig.4a. Pressure of output the pump

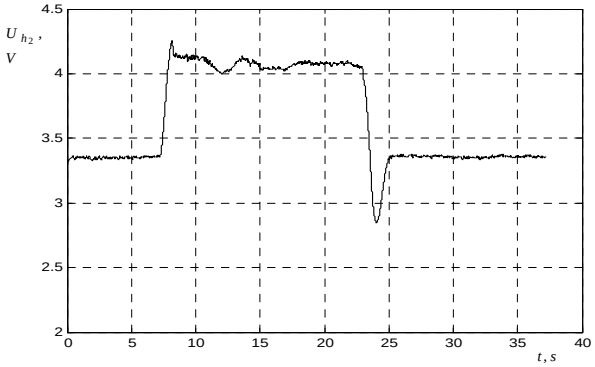

Fig.4b. Pressure of input the turbine

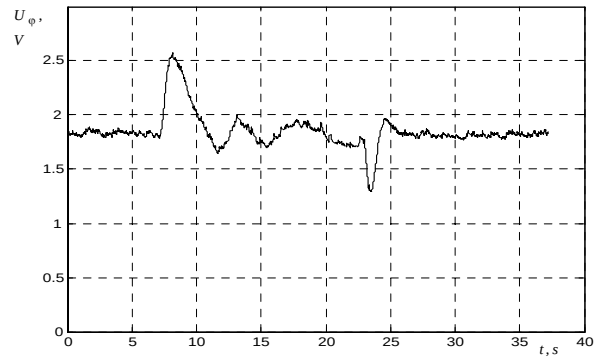

Fig.4c. Turnover of the generator

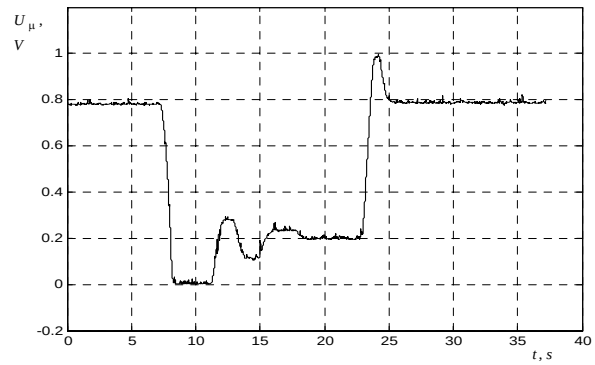

Fig.4d. Position in blade of the water turbine

Fig. 4. Automated control system with short pressure pipeline transient behaviour in the case of step change of the cargo instant

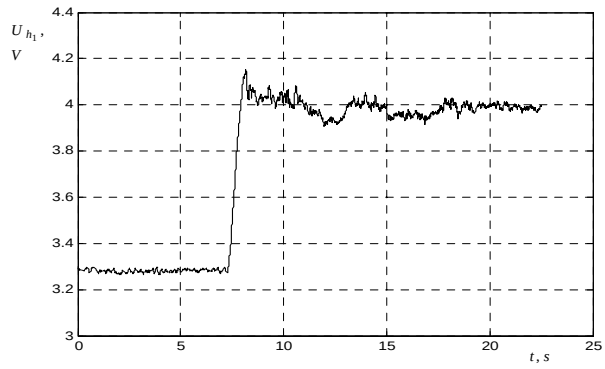

Fig. 5a. Pressure of output the pump

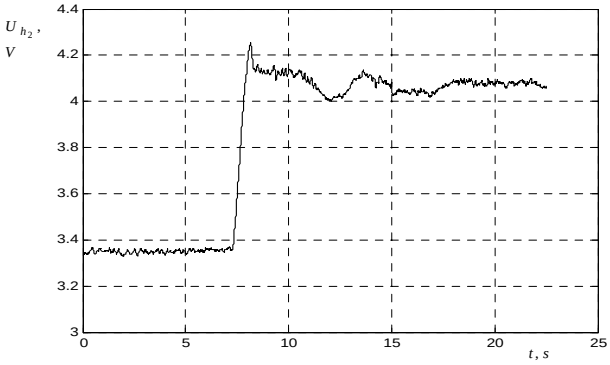

Fig.5b Pressure of input the turbine

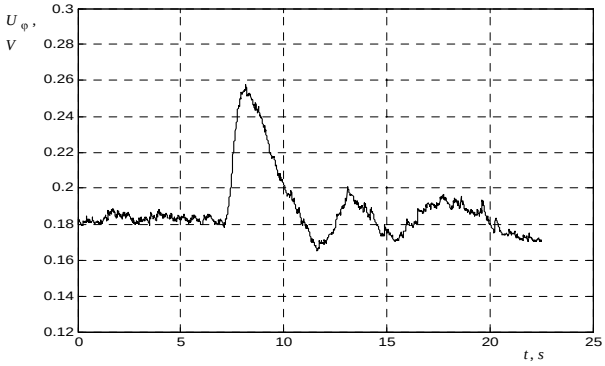

Fig.5c Turnover of the generator

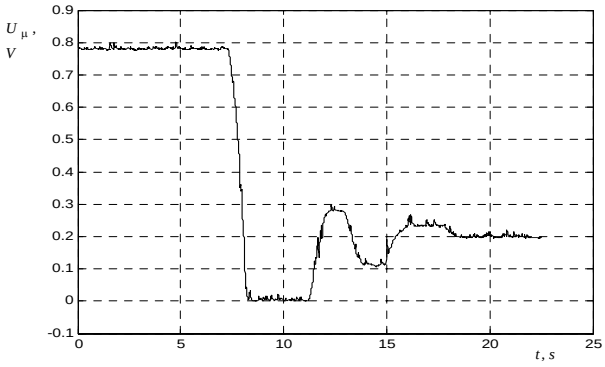

Fig.5d Position in blade of the water turbine

Fig.5. Processes in the system at unloading of the generator

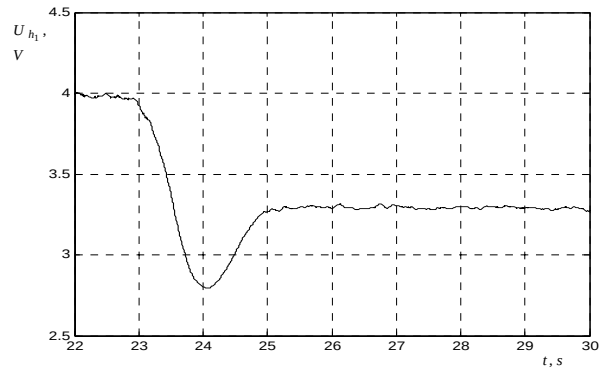

Fig.6a. Pressure of output the pump

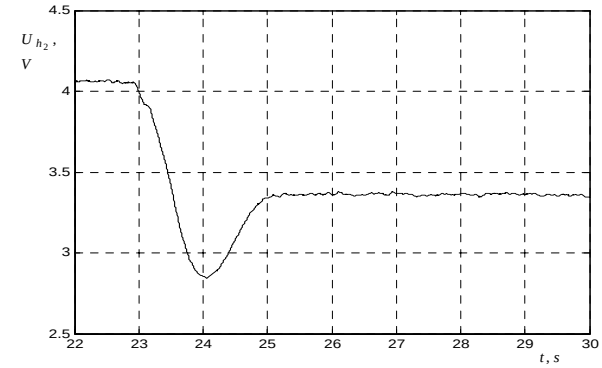

Fig.6b. Pressure of input the turbine

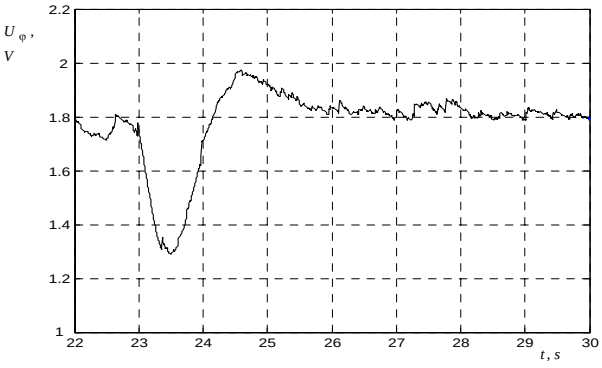

Fig.6c Turnover of the generator

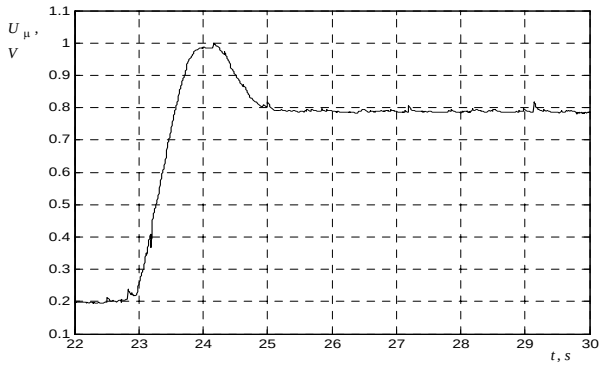

Fig.6d. Position in blade of the water turbine

Fig.6. Processes in the system at 17% loading of the generator

Some investigations with PD and multiparameter controllers have been performed. The results obtained show that with the multiparameter controller the reaction time of the system has been decreased with about 5 % due to the predicted action of the additional feed backs. Some results concerning the dynamical behaviour of the system are shown on Fig. 4,5 and 6.

The water turbine as a control plant is with a big time constant – so the transient processes in the case of load changes of the generator are about 15 s. The pressure pipeline has an indecent influence on the dynamical behaviour of the system due to of the possible of hydraulic-hit. The regulation is strongly influenced by perturbations occuaring in the connection from sensors to controller

IV. CONCLUSION

The developed automated system provides a possibility for studying in real time the dynamical processes flowing in the following pressure system: turbopump-pressure penstock-water turbine. The system is equipped with the required measuring and registrating apparatus. For decreasing of the reaction time structure or/and parameters optimization of the system is needed with an appropriated quality criterion including all sensors information.

V REFERENCES

[1] S. Mansoor, D. Jones, D. Bradley, F. Aris, and G. Jones, Hardware-In-The-Loop Simulation of a Pumped Storage Hydro Station", Proceeding of the IASTED International Conference PES2000, Marbella, Spain, 2000, pp. 571 – 577.

[2] T.Viersma, Analisis, Synthesis and Design of Hydraulic Servosystem and Pipelines, Elsevier, 1980.

[3] P. Ivanov, Dynamics of Automated Hydro- and Pneumo-system, Gabrovo, 1984 (in Bulgarian)

[4] H. Weber, F. Prillwitz, M. Hladky and H. Asal, Development of Reality Oriented Models of Power Plants and Power Systems for Restoration Studies, IFAC Symposium on Power Plants & Power Systems Control Brussels, Belgium, 2000.

[5] H. Weber, Investigation of the dynamic Behaviour of a High Pressure Hydro Power Plant in the Swiss Alps during the Transition from interconnected to isolated Operation, 12th Power System Computation Conference, Dresden, 1996, pp 1049 – 1054.

[6] Yordanov S., T. Todorov, System for quality control and monitoring of the main variables of electrothechnical systems, Int. Conf. ET2000 –Sozopol (in Bulgarian)

[7] Yordanov S. The Real-Time Expert Control Systems International Conference on Computer Systems and Technologies - *CompSysTech'2002*

[8] K. Ormandzhiev and P. Ivanov, Control Optimization of Parallel Working Water Turbines Fed by Means of Common Pressure Pipeline, HEFAT, Victoria Falls, 2003.

[9] Ormandzhiev K., P.Ivanov, Optimal control of active water turbine Pelton type, 2nd International Conference "Research and development in mechanical industry" RaDMI 2002, Vrniachka Bania, Yugoslavia, September 02 – 04 2002, pp. 1001 - 1006

Start up Current in Direct Torque Controlled Induction Motor Drives

Vojkan Kostic[1], Nebojsa Mitrovic[2], Milutin Petronijevic[3], Milan Bebic[4]

***Abstract* – In this paper DTC method is analysed with aspect of start up stator current. It is observe that start up stator current reach significant value. It can destroy switch powers of the inverter. A control method to limit start up stator current amplitude is presented. Simulations results are carried out for the comparison of a start up classical DTC scheme without current limitation and with hereby. Presented simulations results verify the effectiveness of the proposed stator current limitation strategy.**

***Keywords* – Induction Motor, Direct Torque Control, Start up Stator Current Limitation.**

I. INTRODUCTION

DTC schemes to become an alternative for the classic variable speed AC drives. A fast dynamic can be achieved by calculating the instantaneous torque and flux. Using switching table not only simplifies the control system, but also decreases computing time. With a three phase voltage source inverter, there are six non-zero voltage vectors and two zero voltage vectors which can be applied to the machine terminals. Integrating emf using measuring current and voltage vectors or DC link voltage can estimate the stator flux. The torque can be calculated using *qd* components of the estimated flux and measured currents [1-5].

Besides its advantages in application, the conventional DTC system has its drawback. First, its switching frequency varies according to the motor speed and the hysteresis bands of torque and flux. Second, large torque ripple is generated especially in a low speed region. Third, in DTC the stator current contains much more harmonics than that fed with sinusoidal voltage. Fourth, possible problems during start up.

One of problems during start up is short magnetizing transient with significant value of stator current. It can destroy switch powers of the inverter. Consequently, a current limit control is required [6,7].

[1]Vojkan Kostic is with the Faculty of Electronic Engineering, Aleksandra Medvedeva 14, 18000 Nis, Serbia and Montenegro, E-mail: vkostic@elfak.ni.ac.yu

[2]Nebojsa Mitrovic is with the Faculty of Electronic Engineering, Aleksandra Medvedeva 14, 18000 Nis, Serbia and Montenegro, E-mail: nesa@elfak.ni.ac.yu

[3]Milutin Petronijevic is with the Faculty of Electronic Engineering, Aleksandra Medvedeva 14, 18000 Nis, Serbia and Montenegro,
E-mail: milutin@elfak.ni.ac.yu

[4]Milan Bebic is with the Faculty of Electrical Engineering, Bulevar Revolucije 73, 11000 Belgrade, Serbia and Montenegro, E-mail: bebic@etf.bg.ac.yu

After a description of DTC theory and transient current problems in start up, a control method to limit stator current amplitude is presented. Simulations results are carried out for the comparison of a start up classical DTC scheme without current limitation and with hereby. Presented simulations results verify the effectiveness of the proposed stator current limitation strategy.

II. PRINCIPLES OF DIRECT TORQUE CONTROL

The implementation of the DTC scheme requires flux linkages and torque computations and generation of switching states through a feedback control of the torque and flux directly without inner current loops.

The stator *q* and *d* axis flux linkages are:

$$\lambda_{qs} = \int (V_{qs} - R_s i_{qs})dt \tag{1}$$

$$\lambda_{ds} = \int (V_{ds} - R_s i_{ds})dt \tag{2}$$

where R_s is stator resistance and V_{qs}, V_{ds}, i_{qs}, i_{ds} are voltage and current *qd* components.

Consider the inverter shown in Fig. 1. The terminal voltage V_a, with respect to negative of the *dc* supply, is determined by a set of switches, S_a, consisting switching device T_1 and T_2 as shown in Table I. The switching of S_b and S_c sets for line *b* and *c* can be similarly derived. The total number of switching states possible with S_a, S_b, and S_c is eight and they are shown in Fig. 2. The stator *qd* voltages for each state are given by:

$$V_{qs} = V_{as} \tag{3}$$

$$V_{ds} = \frac{1}{\sqrt{3}}(V_{cs} - \mathrm{V_{bs}}) = \frac{1}{\sqrt{3}} V_{cb} \tag{4}$$

The limited states of the inverter create discrete movement of the stator voltage phasor $\mathrm{V_s}$, consisting of the resultant of V_{qs} and V_{ds}.

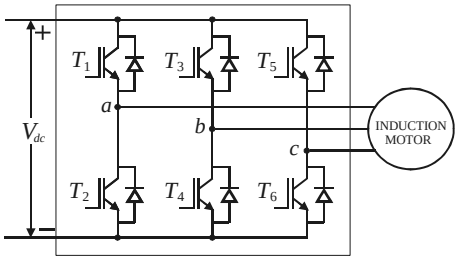

Fig. 1. Power circuit configuration of induction motor drive

TABLE I
SWITCHING STATE OF INVERTER PHASE LEG *a*

T_1	T_2	S_a	V_a
On	Off	1	V_{dc}
Off	On	0	0

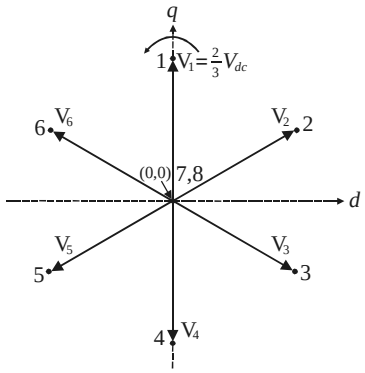

Fig. 2. Inverter output voltages

A uniform rotating stator flux is desirable, and it occupies one of the sectors at any time, Fig. 3 (for classical DTC). The stator flux phasor has a magnitude of λ_s with instantaneous position θ_{fs}.

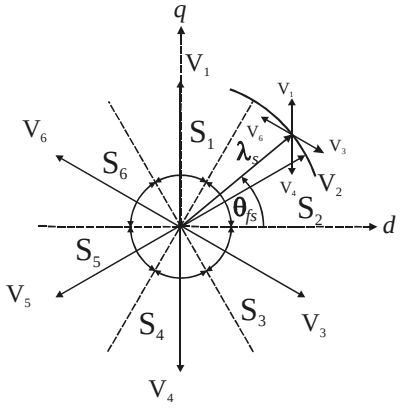

Fig. 3. Division of sectors for stator flux identification

If the stator flux phasor is in sector 2, Fig. 3, the left influencing voltage phasor has to be either V_6 or V_1. As seen from phasor diagram, in case switching voltage phasor V_1, the flux phasor increases in magnitude. In case of phasor V_6, it decreases. This implies that the closer voltage phasor set increase the flux and the farther voltage phasor set decreases the flux and both of them change (rise) the flux phasor in position. Similarly for all other sectors, the switching logic can be developed. A flux error (λ_s^*-λ_s) thus determines which voltage phasor has to be called, and this flux vector is converted to a digital signal S_λ with hysteresis controller with hysteresis band of $\delta\lambda_s$. The switching logic to realize S_λ is given in Table II.

TABLE II
SWITCHING LOGIC FOR FLUX ERROR

State	S_λ
λ_s^* - λ_s > $\delta\lambda_s$ / 2	1
λ_s^* - λ_s < - $\delta\lambda_s$ / 2	0

Torque control is exercised by comparison of the command torque to the torque measured from the stator flux linkages and stator currents as:

$$T_e = \frac{3}{2}\frac{P}{2}(i_{qs}\lambda_{ds} - i_{ds}\lambda_{qs}) \tag{5}$$

where P is pole number.

Torque error is processed through hysteresis controller to produce digital outputs, S_T as shown in Table III. Interpretation of S_T is as follows: when it is 1 amount to increasing the voltage phasor, 0 means to keep it at zero, -1 requires retarding the voltage phasor.

TABLE III
SWITCHING LOGIC FOR TORQUE ERROR

State	S_T
T_e^* - T_e > δT_e / 2	1
-δT_e / 2 ≤ T_e^* - T_e ≤ δT_e / 2	0
T_e^* - T_e < -δT_e / 2	-1

Combining the flux error output S_λ, the torque error output S_T, and the sextant of the flux phasor S_θ, a switching table can be realized to obtain the switching states of the inverter. The sectors of the stator flux space vector are denoted from S_1 to S_6. Stator flux modulus error after the hysteresis block can take just two values. Torque error after the hysteresis block can take three different values. The zero voltage vectors V_7 and V_8 are selected when the torque error is within the given hysteresis limits, and must remain unchanged. Finally, the classical DTC look up table is shown in Table IV.

TABLE IV
SWITCHING STATES FOR CLASSICAL DTC

S_λ	S_T	S_1	S_2	S_3	S_4	S_5	S_6
1	1	V_6	V_1	V_2	V_3	V_4	V_5
1	0	V_8	V_7	V_8	V_7	V_8	V_7
1	-1	V_2	V_3	V_4	V_5	V_6	V_1
0	1	V_5	V_6	V_1	V_2	V_3	V_4
0	0	V_7	V_8	V_7	V_8	V_7	V_8
0	-1	V_3	V_4	V_5	V_6	V_1	V_2

III. START UP CURRENT LIMITATION METHOD

Stator current amplitude is determined by equation:

$$i_s = \sqrt{i_{ds}^{\ 2} + i_{qs}^{\ 2}} \tag{6}$$

where:

$$i_{qs} = \frac{L_r}{L_s L_r - M^2}\left(\lambda_{qs} - \frac{M}{L_r}\lambda_{qr}\right) \tag{7}$$

$$i_{ds} = \frac{L_r}{L_s L_r - M^2}\left(\lambda_{ds} - \frac{M}{L_r}\lambda_{dr}\right) \tag{8}$$

and L_s, L_r, M stator self-inductance, rotor self-inductance, mutual inductance, respectively.

Before start up of no magnetized induction machine, stator and rotor fluxes' *qd* components are equal to zero. When start up, flux and torque have be increase and, in accordance with

DTC principles, inverter generate appropriate voltages. It provokes a fast variation of stator flux and much slower variation of rotor flux. It follow, in accordance with (6) to (8) can be expect a fast variation of stator current amplitude.

In other words, during start up of no magnetized induction machine, due to a fast stator flux and torque transient, occur short transient with stator current significant value. It can destroy switch powers of the inverter. Consequently, a current limit control is required.

A strategy of solving current limitation problem is to add magnetizing machine with a zero torque control in applying a delay on the torque reference application. During the magnetizing phase, a same non zero voltage is applied until the stator flux amplitude reaches its reference, λ_s*. This magnetizing method doesn't respect DTC principles since stator flux control is chosen as against torque progression witch reduce torque control performance.

An example is given in Fig 4, with applied a non-zero voltage vector V_1 (magnetizing phase 1). There is no tangential variation of the stator flux vector, the stator pulsation and torque are null. However, stator flux amplitude progress very quickly in the machine and provokes a fast variation of stator current amplitude. To control current variation a zero voltage vector is applied when the amplitude of the stator current reaches its limit value, $i_{s\lim}$ (magnetizing phase 2). The current control is carried out by a simple hysteresis controller whose a bandwidth is $\Delta i_{s\lim}$. When stator flux reaches its reference value, magnetization is over and begins DTC control.

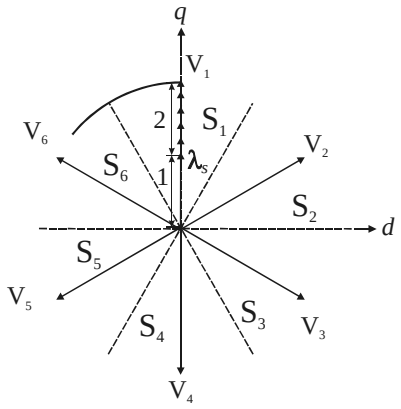

Fig. 4. Start up strategy with stator flux control

IV. Simulation Results

Simulations have been carried out for the comparison of a start up classical DTC scheme without magnetizing phase and with hereby. The simulations were conducted using Matlab/Simulink simulation package. Simulation model is discretized with 2 μs. The system is run under nominal load torque and with nominal rotor speed. Control system sampling frequency and switching frequency is 10 kHz. The motor's parameter is listed in Table V. Stator current limit is set to 15 A and stator current controller bandwidth is set to 5 % of current limit.

Fig. 5 and 6 shows stator flux, effective value of stator current, electromagnetic torque and rotor speed in start up of induction machine without magnetizing phase. It can be noted that torque response is fast, but stator current start up value reach significant value (about 600% of rated value). It can destroy switch powers of the inverter if is larger of inverter switch maximal current. Fig. 9a and 9b shows stator flux locus in this case.

TABLE V
Induction Motor Parameters

Rated power	2.2 kW
Rated line to line voltage	380 V
Pole pairs	1
Rated torque	8.61 Nm
Rated stator flux	0.936 Vs
Rated stator current	5.26 A
R_s	2.615 Ω
R_r	2.3957 Ω
L_s	0.282 H
L_r	0.282 H
M	0.2717 H
Load inertia	0.0184 kgm^2

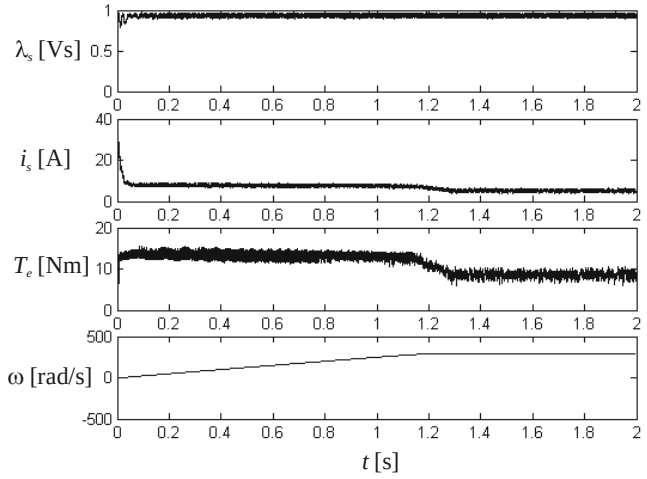

Fig. 5. Start up of induction machine without magnetizing phase

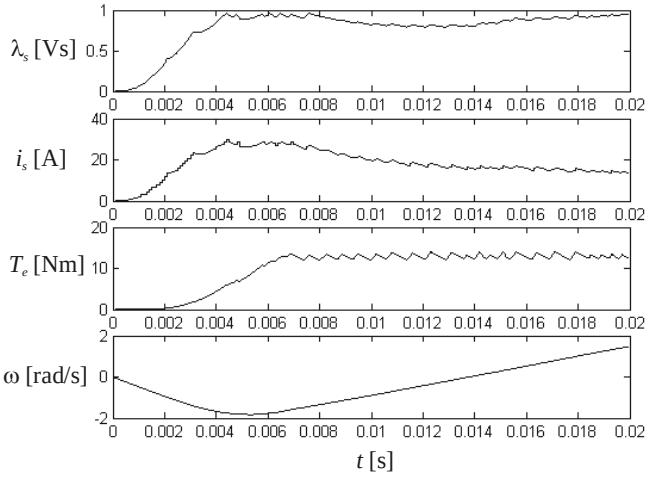

Fig. 6. Start up of induction machine without magnetizing phase (first 0.02 seconds)

Fig. 7 and 8 shows stator flux, effective value of stator current, electromagnetic torque and rotor speed in start up of induction machine with magnetizing phase. It can be noted that torque response is delayed and slower than in foregoing case, but stator current start up value is limited. Fig. 9c and 9d shows stator flux locus in this case. It can be noted that similarity of stator flux of Fig. 9d and Fig. 4 that was expected.

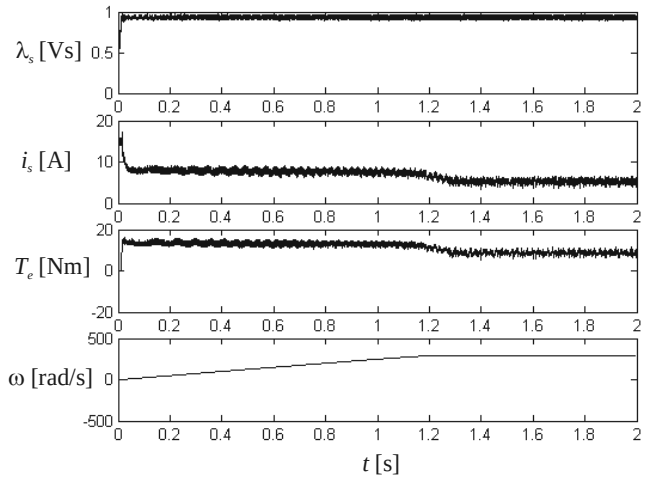

Fig. 7. Start up of induction machine with magnetizing phase

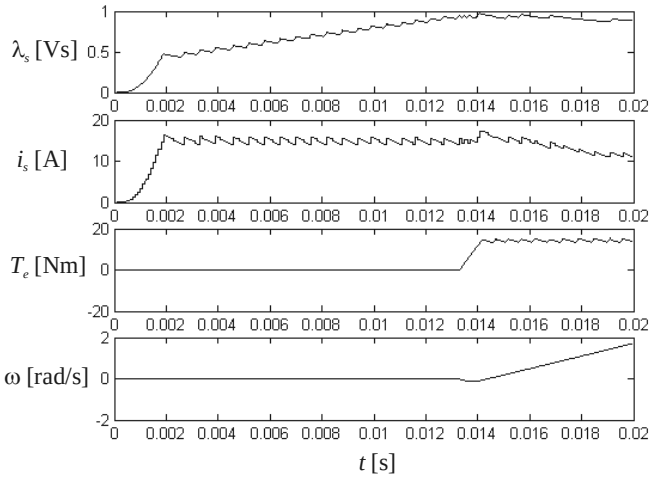

Fig. 8. Start up of induction machine with magnetizing phase (first 0.02 seconds)

V. CONCLUSION

In this paper, a current limitation strategy is presented to limit stator current amplitude in start up of an induction machine controlled by DTC method. This current limitation strategy is simple and easy to practical implementation in DTC algorithm. Simulation results show that the proposed strategy limits start up current. In that manner switch powers of the inverter are secure.

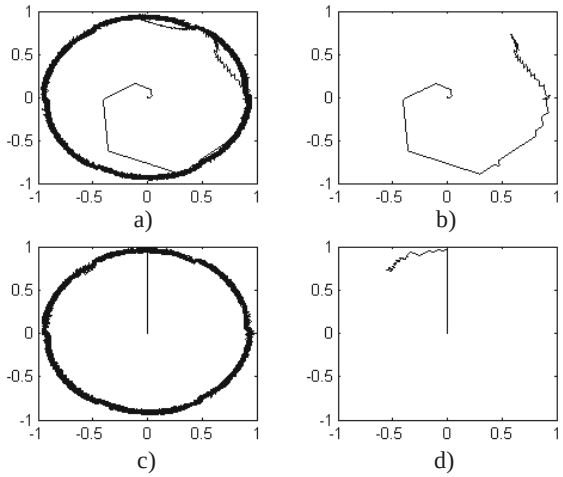

Fig. 9. Flux locus in start up of induction machine
a) without magnetizing phase
b) without magnetizing phase (first 0.02 seconds)
c) with magnetizing phase
d) with magnetizing phase (first 0.02 seconds)

REFERENCES

[1] I. Takahashi, T. Noguchi, "A new quick-response and high-efficiency control strategy of an induction motor," IEEE Transactions on Industry Applications, vol. 22, No. 5, pp. 820-827, 1986.

[2] T. G. Habatler, F. Profumo, M. Pastorelli, L. Tolbert, "Direct Torque Control of Induction Machines using Space Vector Modulation", IEEE Transactions on Industry Applications, vol. 28, No. 5, pp. 1045-1053, Sept/Oct 1992.

[3] Vojkan Kostić, Nebojša Mitrović, Milutin Petronijević, Borislav Jeftenić, "DIREKTNO UPRAVLJANJE MOMENTOM ASINHRONE MAŠINE", 12th INTERNATIONAL SYMPOSIUM on POWER ELECTRONICS - Ee 2003 (XII Međunarodni simpozijum Energetska elektronika – Ee 2003), NOVI SAD, SERBIA & MONTENEGRO, November 5th - 7th, 2003, Paper No. T2-1.5, pp. 1-4.

[4] Nebojsa Mitrovic, Vojkan Kostic, Milutin Petronijevic and Borislav Jeftenic, "Comparison by Simulation of Torque Control Schemes for Electric Drive Application", ICEST 2003, 16-18 October 2003, Sofia, Bulgaria, Proceedings of Papers, pp. 417-420.

[5] Nebojsa Mitrovic, Vojkan Kostic, Milutin Petronijevic and Borislav Jeftenic, "Simulation of Direct Torque Control Schemes for Electric Drive Application, Part I", SCIENTIFIC BULLETIN of "POLITEHNICA" University of Timisoara, Transactions on AUTOMATIC CONTROL and COMPUTER SCIENCE, Vol. 49(63), No. 1, 2004, ISSN 1224-600X, Timisoara, pp. 83-86.

[6] Y. A. Chapuis, D. Roye, "Direct Torque Control and Current Limitation Method in Start up of an Induction Machine", Power Electronics and Variable Speed Drives, IEE Conference, London, UK, September 21-23, 1998, pp. 451-455.

[7] Y. A. Chapuis, T. Kosaka and N. Matsui, "Performance Improvement in Start up Condition for DSP-Based Direct Torque Control of an Induction Machine", International Power Electronic Conference, IPEC'00, Tokyo, Japan, April 2000, vol. 3, pp. 1189-1194.

Computer Simulation of Voltage Sag Effects on Adjustable Speed Drives

Milutin P. Petronijević[1], Borislav I. Jeftenić[2], Nebojša N. Mitrović[3], Vojkan Z. Kostić[4]

Abstract – **In this paper was presented a possibility of computer usage for voltage sag effects on electrical drives with frequency converters. First of all it was given guidelines for making appropriate system simulation model, where especially were stressed how to estimate the most important parameters for modeling. Complete model was made in MATLAB, and than we turn attention to speed and torque deviation in modern speed controlled drives. It is also presented the influence of the adequate control algorithm in drive behavior.**

Keywords – **Voltage Sag, Adjustable Speed Drives, Speed Deviation, Power Quality.**

I. INTRODUCTION

The aim of the paper is to introduce the possibility of valid voltage sag (dip) influence simulation on modern adjustable speed drive (ASD) in which case, main parameters to obtain realistic results are pronounced. Computer simulation of ASD, because of the complexity and analog/discrete nature, needs long computing term. On the other side, experimental researches ([1]) of ASD voltage sags sensitivity request very expensive and sophisticated equipments: voltage sag generators, programmable load and high performance data acquisition system with current, voltage, speed and torque sensors. Meanwhile it should be emphasized the fact that it is necessary to accomplish great number of tests, some of which can lead to equipment under test destruction. The installed power rising in equipment results significantly influence in facility price and testing time extending.

The advantage of computer simulation is a chance for virtual equipment testing in wide range of power with no extra cost. Simultaneously it is posed a question of accurate modeling and results validity having in mind disadvantage of particular converter data. Based on authors' practical experience it will be presented recommendation for a good simulation model of the system: voltage sag generator – frequency converter – induction motor.

The following lines will explain this paper organization. The Second section shows, based on previous paper, concrete voltage sag effects on adjustable speed drives. The Third section especially points out mechanical irregularity in drive operation as drop in speed and torque/speed pulsation during voltage sags. It was made analysis in FOC and DTC drives, where in Fourth section was presented some simulation results for mentioned phenomena. In last section parameters where listed which must be known for right converter behavior modeling in voltage sag conditions.

[1]Milutin P. Petronijević is with the Faculty of Electronic Engineering, Beogradska 14, 18000 Nis, Serbia & Montenegro, E-mail: milutin@elfak.ni.ac.yu

[2]Borislav I. Jeftenić is with the Faculty of Electrical Engineering, Kralja Aleksandra 73, 11000 Belgrade, Serbia & Montenegro, E-mail: jeftenic@etf.bg.ac.yu

[3]Nebojša N. Mitrović is with the Faculty of Electronic Engineering, Beogradska 14, 18000 Nis, Serbia & Montenegro, E-mail: nesa@elfak.ni.ac.yu

[4]Vojkan Z. Kostić is with the Faculty of Electronic Engineering, Beogradska 14, 18000 Nis, Serbia & Montenegro, E-mail: vkostic@elfak.ni.ac.yu

II. VOLTAGE SAG EFFECTS

Voltage sag problems referring to induction motor drives with frequency converters can be classified in to four categories according to the point of appearance:

(i) input side lapse;
(ii) DC link under-voltage;
(iii) inverter side over-current, and
(iv) induction motor operation disarrangement.

In some sensitive devices, for example adjustable speed drives, it is important to consider the possibility of phase angle jump influences. In [2] voltage sags ranged in 7 types based on sagged phase number and phase angle difference which is shown in Fig.1. Phase angle jump can appear as a result of fault transferring over transformer (for example for transformer winding connection Yd, Dy and Yz) and/or changing *X*/*R* ratio of power supply. It should be also known that phase angle jump limited by concrete power supply line parameters and the fact that the phase angle difference between phase and line-line voltages are 30 degrees. Theoretical maximum phase angle jump value is 90 degrees, but the most probable value in real power system is 30^o ([3]).

Input unit at industry standardized frequency converter is usually full bridge diode rectifier. Transient voltage sags or steady-state voltage unbalance conditions in the three-phase input line voltages can cause the rectifier stage to transition into single-phase rectifier operation. Unbalanced voltage sag can cause high current asymmetry with values far over nominal ones. In [2] was discussed the influence of input and DC link inductance on input current RMS values where taken out the circumstances of converter trip.

If the DC link capacitor discharges its energy and the DC link voltage reaches the minimum allowed value (V_{DCmin}) under-voltage protection will be activated. This minimum level can be adjusted in the range from 65-70% up to 85-90% of rated DC link voltage. DC voltage drop under minimum level can lead to the appearance of the high inrush input current when the power-up again. Minimum DC bus voltage depends on maximum diode bridge current, i.e. DC bus charging circuit limitation. In [5] was identified that voltage sag type and depth, value of DC link capacitor and output load

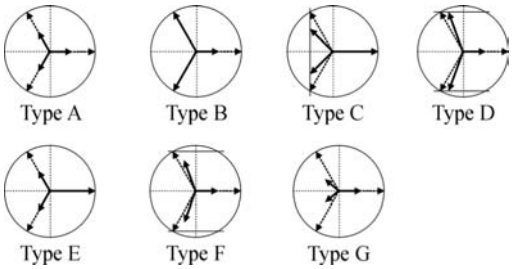

Fig. 1. Voltage sag types

significantly affect on voltage sag tolerance curve.

At output converter terminals Pulse Width Modulation (PWM) voltage was delivered according to the given control rules. Nowadays, three basic control principles are used in frequency converters: V/f, Field Oriented Control (FOC), and Direct Torque Control (DTC) with their own sub-variants. Control principle effect is diverse and noticed in distinction in various voltage sag sensitivity curves ([6]), drop in speed differences ([7]), and speed deviation features during unbalanced voltage sags.

Some processes with multi-motor ASD (for example dried section of the paper machine with speed synchronized drives and load sharing) cannot tolerate the loss of accurate speed or torque control, even for a few seconds due to damage the final product or halt of the process. Beside this, torque pulsation leads to aside effects for example: noise increasing, vibration or mechanical resonance exciting. In this work analytic relation and simulation results for speed deviation were emphasized.

III. Voltage Sag Speed Deviation

Limits as consequences of PWM converter maximum output current (I_{max}) and maximum output voltage (U_{max}) can be represented in relation to the appropriate stator quantity through the following equations:

$$i_{qs}^2 + i_{ds}^2 \le I_{\max}^2 \text{, and} \tag{1}$$

$$u_{qs}^2 + u_{ds}^2 \le U_{\max}^2 \tag{2}$$

where particular variables and their numerical values are given in Table I. Maximum output current is determined by maximum continuous current of inverter semiconductor switches or induction motor rated current, i.e. maximum allowable thermal capacity of the converter or induction motor.

The maximum stator voltage depends on the available DC-link voltage V_{DC} and pulse-width modulation (PWM) strategy. In this paper, PWM strategy based on voltage space vector (SVPWM) is used, and then the output phase voltage on converter terminals, neglecting voltage drop on switches, is:

$$u(t) = (V_{DC}/2) \cdot m \cdot \sin(\omega t + \varphi). \tag{3}$$

Maximum possible modulation index in linear modulation range is 2/√3. In practice, industrial frequency converters have different over-modulation methods, so in simulation model it has to be taken into consideration. If over-modulation is used it can be supposed that output voltage reconstruct input one in complete.

TABLE I
List of Symbols and Nominal Values

R_s	Stator resistance, 7.845 Ω
R_r	Rotor resistance, 7.187 Ω
L_{ls}, L_{lr}	Stator and Rotor Leakage Inductance, 31mH
L_m	Magnetising Inductance, 0.815 H
u_{sd}, u_{sq}	Direct and Quadrature axis Stator Voltages
i_{sd}, i_{sq}	Direct and Quadrature Stator Currents
i_{rd}, i_{rq}	Direct and Quadrature Rotor Currents
P	No. Pole Pairs, 1
P_n	Nominal Motor Power, 2200W
U_n	Supply network rated line-line voltage rms value, 380V
ω_n	Nominal rotor angular speed, 297 rad/s
σ	Total leakage coefficient, 0.049
T_r	Rotor time constant, 0.174s
m	Modulation index

Induction motor electromagnetic torque, based on two-phase mathematical model ([8]), can be calculated using the following formula:

$$T_e = \frac{3}{2} P \frac{L_m}{L_r} (i_{qs}\lambda_{dr} - i_{ds}\lambda_{qr}). \tag{3}$$

Aligning the reference frame *d*-axis with rotor flux linkage phasor, will gain:

$$\lambda_{qr} = 0, \lambda_{dr} = \lambda_r. \tag{4}$$

In steady state, all quantity differences will be zero, and can be counted that $i_{dr} = 0$, and:

$$T_e = c_1 i_{ds} i_{qs} \tag{5}$$

where $c_1 = \frac{3}{2} P \frac{L_m^2}{L_r}$.

Equation (2) in steady state and voltage limit condition, having in mind the relationship (4); can be written as ([7]):

$$A i_{ds}^2 + C i_{qs}^2 + B i_{ds} i_{qs} \le U_{\max}^2 \tag{6}$$

where:

$$A = R_s^2 + \omega_s^2 L_s^2;\ B = 2R_s\omega_s \frac{L_m^2}{L_r};\ \text{and}\ C = R_s^2 + \omega_s^2 \sigma^2 L_s^2.$$

In the above equations ω_s represents synchronous reference frame speed.

To achieve RFO control for set speed value, angular frequency of the stator variables should be:

$$\omega_s = \omega + \frac{R_r}{L_r} \frac{L_m}{\lambda_{dr}} i_{qs}, \tag{7}$$

where ω represents rotor angular speed. **It should be mentioned that in case the condition (4) introduction is not**

predicted the drive control method, so simplified Eqs. (5) and (7) are with generalized meaning.

Considering that RFO control is ideal one (actual values follow the commanded ones completely) and for induction motor parameters done in Table I, value of rotor flux reference value λ_r is setting at the value which corresponding to the motor breakdown torque and slip values which result in maximum torque per ampere value. Appropriate value *d*-axis reference current (further named as "breakdown value") is given as:

$$i_{ds}^{*} = \lambda_r / L_m \tag{8}$$

The maximum torque under current limit based on Eq. (5) will be:

$$T_{e\_Imax}^{(RFO)} = c_1 \, i_{ds}^{*} \sqrt{I_{\max}^2 - i_{ds}^{*2}} \, . \tag{9}$$

Replacing Eqs. (7) and (8) in Eq. (6), finding out $i_{qs}(\omega, U_{\max}, i_{ds}^{*})$ and final changing in Eq. (5) we achieve torque-speed characteristics for RFO controlled drives under voltage limit (i.e. RFO controlled drive maximum torque under voltage limit):

$$T_{e\_Umax}^{(RFO)} = c_1 \, i_{ds}^{*} i_{qs}(\omega, U_{\max}, i_{ds}^{*}) \, . \tag{10}$$

Solving Eq. (10) numerically, curves corresponding to maximum torque achieved respecting voltage limit existing. In Fig. 2 were shown curves of motor maximum torque calculated according to Eqs. (9) and (10), where it should be especially have in mind the fact that *d*-axis reference current changing (curves B and C) significantly influence on maximum available torque under RFO control. This fact can be used for voltage sag consequence overcoming as shown in details in [7].

Accepting that the DTC is ideal and that stator flux magnitude λ_s^{*} remains constant and equal to the proposed one, in synchronous reference frame can be added the following one:

$$\sqrt{(\lambda_{ds})^2 + (\lambda_{qs})^2} = \lambda_s^{*} \, . \tag{11}$$

Solving the last equation for motoring regime operation and having in mind motor flux equation leads to:

$$i_{ds} = \sqrt{(\lambda_s^{*})^2 - \sigma^2 \cdot L_s^2 \cdot i_{qs}^2} \, / L_s \, . \tag{12}$$

Substitution (12) into (5) gives the torque in DTC drive:

$$T_e = \frac{c_1}{L_s} i_{qs} \sqrt{(\lambda_s^{*})^2 - \sigma^2 \cdot L_s^2 \cdot i_{qs}^2} \, . \tag{13}$$

The maximum value of (13) is:

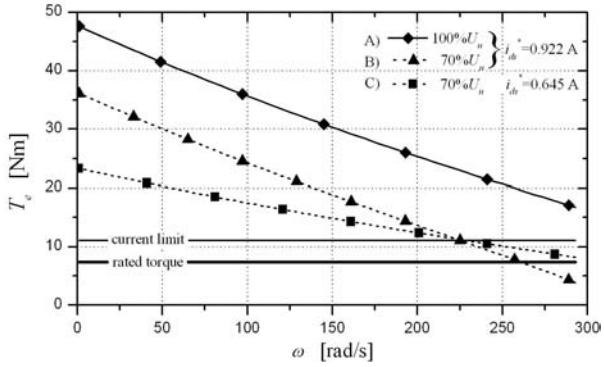

Fig. 2. Maximum torque under voltage and current limit

$$T_{e\max}^{(DTC)} = \frac{c_1}{2} \frac{(\lambda_s^{*})^2}{\sigma L_s^2} \, . \tag{14}$$

Maximum torque value, if the stator current magnitude is constrained by the maximum power converter output current I_{max}, can be found by combining (12), (1) and (5), which leads us to:

$$T_{e\_Imax}^{(DTC)} = \frac{c_1 [(L_s^2 I_{\max}^2 - \lambda_s^2)(\lambda_s^2 - \sigma^2 L_s^2 I_{\max}^2)]^{1/2}}{(1-\sigma^2) L_s^2} \, . \tag{15}$$

Considering Eq. (13) under circumstances from Eqs. (6) and (7), the maximum torque values under voltage limit can be found which are presented in Fig. 3 (curve A). In the same figure was shown reference stator flux λ_s^{*} selection influence on maximum torque as well (curves B and C).

On the basis of the previous discussion can be concluded that for ASDs voltage sag behavior analysis is necessary to know kind of motor control (RFO or DTC), control parameters (i_{ds}* or λ_s^{*}) and concrete converter limits as well as maximum output current I_{max} and voltage U_{max}.

In [9] was presented input voltage unbalance influence on undesired torque and speed ripple. Especially it is valuable the detail that undesirable low frequency torque component exist in single line to ground faults (SLGFs) on input converter side, which is also the most common fault in power supply network. In the case of V/Hz control induction motor torque can be found as:

$$T_e = T_{e0} + T_{e2} \cos(2\omega_i t + \phi_2) + T_{e4} \cos(4\omega_i t + \phi_4) \tag{16}$$

where subscripts "2" and "4" mean 2nd and 4th magnitude torque components and their appropriate phase angle. Electromagnetic torque mean value is designated as T_{e0} and in steady state regime it is equal to load torque. In next Section we present simulation results which turn attention to torque pulsation difference according to the control method applied.

IV. Simulation Results

Great number of simulation results connecting to drop in speed and control algorithm influence can be discovered in [7], when drop in speed minimization is specially stressed. Because of the limited space, we will only present the results

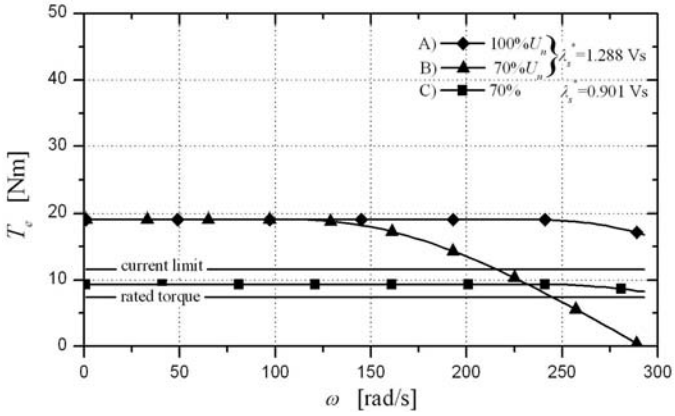

Fig. 3. Maximum torque under voltage and current limit in rated voltage and voltage sag cases

in speed deviation through control method influence. For motor data in Table I and for RFO and DTC control algorithm in Fig. 4 were shown instantaneous torque values and their harmonic spectra in SLGF on converter input terminal (voltage sag type B). It is clearly noticeable that in case of DTC control has no undesirable torque harmonics as in case RFO control

From the point of view of power converter designer, DC link capacitor value is determined by maximum voltage ripple allowed for given output load. DC link capacitor value in practice can be in wide range ([3]) and its influence on torque harmonics components magnitude is shown in Fig. 5. It warns us that for accurate torque deviation modeling under voltage sag condition is necessary to know actual DC bus capacitor value.

V. CONCLUSION

Based on results in previous papers and this work as well we will recommend the following guidelines for modeling of voltage sag effects on ASDs:

- firstly, voltage sag generator model has to enable all seven voltage sag type simulations including phase asymmetry existence, point of sag initiation and phase angle jump.
- diode model effect in input rectifier bridge is minor.
- the knowing of DC bus inductance value and eventually input side inductance as well is important for input current

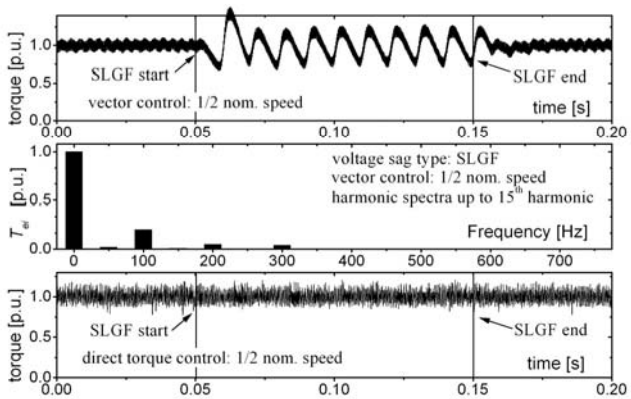

Fig. 4. Motor torque deviation under RFO and DTC control and their harmonic spectra (industrial drive with C=85μF/kW)

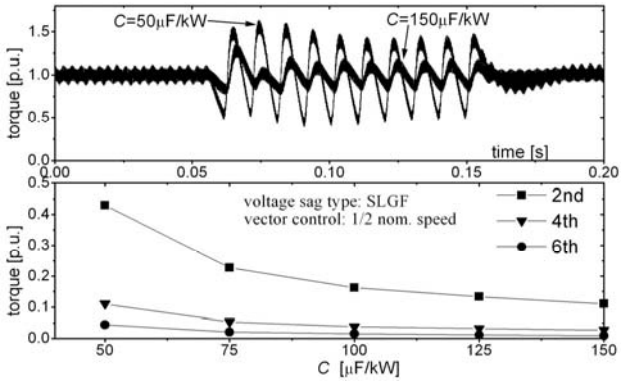

Fig. 5. DC bus capacitor value influence on torque harmonics

asymmetry calculation.

- DC link capacitance value has significant influence on its discharge time and torque and speed ripple as well as presented in this work.
- semiconductor switch model influence is minor.
- PWM switching strategy model (modulation scheme) is very important for induction motor behavior modeling.
- induction motor model must be included dynamic effects (*dq*-model) and type and value of mechanical load.

REFERENCES

[1] K. Stockman, F. D'hulster, K. Verhaege, J. Desmet, R. Belmans, "Voltage dip immunity test set-up for induction motor drives," *Proceedings of the 11th International Symposium on Power Electronics Ee2001*, pp. 303-307, Novi Sad, Yugoslavia, 2001.

[2] M. H. J. Bollen, *Understanding power quality problems: Voltage sags and interruption*s, IEEE Press series on Power Engineering, New York, 2000.

[3] S. Djokić, "Generalised Methodology for the Assesment of Voltage Sag Performance Indices ans Equipement Sensitivity," PhD Thesis, UMIST, UK, 2004. [Online] Available: http://www.umist.ac.uk/departments/mcee/research/Publications/Djokic_PQ_Thesis.pdf

[4] J.L. J. L. Duran-Gomez, P. N. Enjeti, and B. O. Woo, "Effect of Voltage Sags on Adjustable-Speed Drives: A Critical Evaluation and an Approach to Improve Performance", *IEEE Trans., Ind. Applicat.*, vol. 35, no. 6, pp. 1440-1449, 1999.

[5] M. H. J. Bollen, and L. D. Zhang, "Analysis of Voltage Tolerance of AC Adjustable-Speed Drives for Three-Phase Balanced and Unbalanced Sags", *IEEE Trans., Ind. Applicat.*, vol. 36, no. 3, pp. 904-910, 2000.

[6] M. Petronijevic, V. Kostic, N. Mitrovic, and B. Jeftenic, "Modern PWM drives voltage sags sensitivity", ICEST 2004, Proceedings of Papers, pp. 663-666 June 16-19, 2004, Bitola, Macedonia

[7] M. Petronijevic, B. Jeftenić, N. Mitrovic, and V. Kostić, "Voltage Sag Drop in Speed Minimization in Modern Adjustable Speed Drives", *IEEE Symposium ISIE05 (accepted for publication)*, Dubrovnik, Croatia, 2005.

[8] P. Vas, Sensorless vector and direct torque control, Oxford University Press, 1998.

[9] K. Lee, T. M. Jahns, W. E. Merkopec, and T. A. Lipo, "Closed-Form Analysis of Adjustable Speed Drive Performance Under Input Voltage Unbalance and Sag Conditions", *PECS'04*, Aachen, Germany, 2004.

The Slip Impact on Electromagnetic Shaft (EMSh) : A law or a Particular Case

Fellag.S.A[1], A. Boukadoum[2]

Abstract-**The electrical drive, exploitational and economical, characteristics improving can be achieved by increasing the synchronizing torque that allow the maintain of speed synchronization between motors in their deferent operating regimes, at deferent degree of load carrying. In this paper we study the possibilities of synchronizing torque increasing in electromagnetic shaft system. The results and impact of slip changing ways , calculation that is carried upon 2.8 kW induction machines, have been presented and discussed.**

I. INTRODUCTION

For several multiple motor drives that need speed synchronisation between their motors and, where mechanical connection between them is not preferred or possible, electrical(Esh) and electromagnetic(EMSh) shafts can be used [1,2]. Such systems are capable to deliver enough good as driving as well as synchronising (ST) torques. The laters are a determinant factor to bring motors to tough speed concordance. In this paper we will provide a study of EMSh that use induction rheostat (IR) between motors, in order to show possible ways of increasing synchronising torque.

II. EQUIVALENT EMSH SCHEME :

In fig. A is shown the electrical scheme of EMSh. The equivalent scheme is shown in fig.1 as in [1,2]. Here: r1, x1-active resistance an reactance of stator windings; r2', x2'-active resistance and reactance of rotor windings; rd1,r'd2-additional resistance in stator and rotor circuits consequently; rμ,xμ- resistance and reactance of motor magnetic circuit; r0', x0'-resistance and reactance of IR windings; r'_m, x'_m-resistance and reactance of IR magnetic circuit .

All rotor's circuit parameters are referred to stator.
On the basis of EMSh equivalent circuit we will develop torque formulae that allow the system to be investigated.

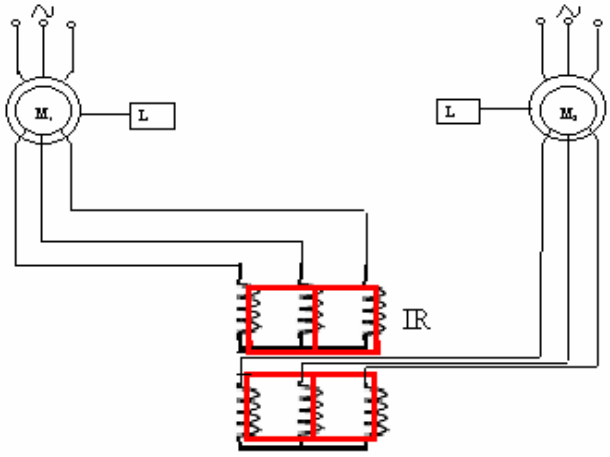

Fig.1 EMSh electrical scheme

Ta

king $x_k = x_1 + x_2$, and with $\dot{U}_1$, $\dot{U}_2$ -voltage vectors of first and second motors, from the scheme we can write:

$$\dot{U}_1 = \dot{I}_{21}\left[r_1 + \frac{r_2}{s} + \frac{r_0}{s} + \frac{r_m}{\sqrt{s}} + j\left(x_k + x_0 + \frac{x_m}{\sqrt{s}}\right)\right] + \dot{I}_{22}\left[\frac{r_m}{\sqrt{s}} + j\frac{x_m}{\sqrt{s}}\right] \quad \ldots\ldots\ldots(1)$$

$$\dot{U}_2 = \dot{I}_{22}\left[r_1 + \frac{r_2}{s} + \frac{r_0}{s} + \frac{r_m}{\sqrt{s}} + j\left(x_K + x_0 + \frac{x_m}{\sqrt{s}}\right)\right] + \dot{I}_{21}\left[\frac{r_m}{\sqrt{s}} + j\frac{x_m}{\sqrt{s}}\right] \quad \ldots\ldots\ldots(2)$$

[1]Fellag.S.A is with the Université Technologique de Tizi Ouzou- Département d'Electrotechnique- Algérie
E-mail:felags@yahoo.fr

A. Boukadoum is with the Université de Skikda -Département de Génie Electrique , E-mail:boukadoum2003@yahoo.fr

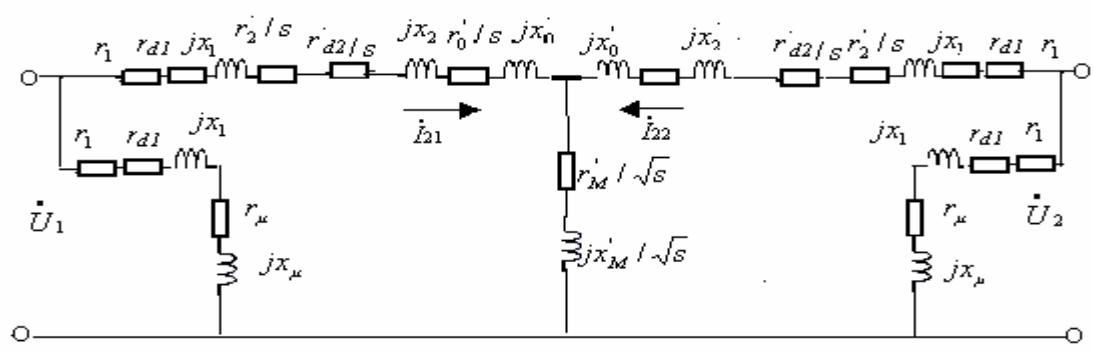

Fig 1.Equivalent scheme of EMSh

After some conversion rotor current vectors can be written as:

$$I_{21}=\frac{1}{2}\left[\frac{U_1+U_2}{Z+2Z_m}+\frac{U_1-U_2}{Z}\right] \text{……..(3)}$$

$$I_{22}=\frac{1}{2}\left[\frac{U_1+U_2}{Z+2Z}+\frac{U_2-U_1}{Z}\right] \text{……(4)}$$

With :

$$Z=\left|n+r_{d1}+\frac{r_2}{s}+\frac{r_{d2}}{s}+\frac{r_0}{s}+j\left(x_K+x_0\right)\right|$$

$$Z_m=\frac{r_m}{\sqrt{s}}+j\frac{x_m}{\sqrt{s}}$$

In the case when both motors carry the same load we have $\dot{U}_1=\dot{U}_2=U$, where U is a source voltage. But in case of deferent load this would yield an angle (α) between their rotors .If this rotors' deference position will be represented by the deference between vector voltages $\dot{U}_1$, $\dot{U}_2$, then we can write:

for the first motor : $\dot{U}_1=U\,.\,e^{-j\alpha}$ ……..(5);

for the second : $\dot{U}_2=,U\,.\,e^{j\alpha}$ ……..(6);

Torque of induction motor generally for one phase in synchronizing watts can be given as:

$$M=\frac{U}{2}\left(\dot{I}+\overset{*}{I}\right)-\left(\left|I\right|^2R_S\right) \text{……..(7)}$$

where R_S is resistance in stator circuit.

With U -phase voltage;

$\dot{I}$ -rotor current vector; $\overset{*}{I}$ -its conjugate

As it is seen it is composed from two parts ,the second one represent losses in stator circuits . If we ignore those loses the torque for multiphase consideration would gain more simply expression [2,4] :

$$M=\frac{U_f mp}{2\omega_0}\left(\dot{I}+\overset{*}{I}\right) \text{.....(8)}$$

With U_f -phase voltage; m-number of phase; p-number of pair pole; ω_0 speed of stator magnetic field.

$\dot{I}$ -rotor current vector; $\overset{*}{I}$ -its conjugate.

Applying 1-6 and 8, we can write the formulae of EMSh torque as :

$$M_{1,2}=\frac{U_f mp}{2\omega_0}\left\{\frac{\left(n+r_{d1}+\frac{r_2}{s}+\frac{r_{d2}}{s}+\frac{r_0}{s}\right)\left(1-\cos\alpha\right)}{\left(n+r_{d1}+\frac{r_2}{s}+\frac{r_{d2}}{s}+\frac{r_0}{s}\right)^2+\left(x_k+x_0\right)^2}+\right.$$

$$\left.\frac{\left(n+r_{d1}+\frac{r_2}{s}+\frac{r_{d2}}{s}+\frac{r_0}{s}+\frac{2r_m}{\sqrt{s}}\right)\left(1+\cos\alpha\right)}{\left(n+r_{d1}+\frac{r_2}{s}+\frac{r_{d2}}{s}+\frac{r_0}{s}+\frac{2r_m}{\sqrt{s}}\right)^2+\left(x_k+x_0+\frac{2x_m}{\sqrt{s}}\right)^2}\pm\right.$$

$$\left.I\sin\alpha\left[\frac{x_k+x_0}{\left(n+r_{d1}+\frac{r_2}{s}+\frac{r_{d2}}{s}+\frac{r_0}{s}\right)^2+\left(x_k+x_0\right)^2}-\right.\right.$$

$$\left.\frac{\left(x_k+x_0+\frac{2x_m}{\sqrt{s}}\right)}{\left(r_1+r_{d1}+\frac{r_2}{s}+\frac{r_{d2}}{s}+\frac{r_0}{s}+\frac{2r_m}{\sqrt{s}}\right)^2+\left(x_k+x_0+\frac{2x_m}{\sqrt{s}}\right)^2}\right]\cdot\Bigg\}$$

Here: (+)-Represent torque of 1st motor; (-)-the second ;
Representing all parameters through xk torque finaly will have the following form:

$$M_{\bullet 1,2}=\frac{M_{1,2}}{M_m}=\Bigg\{\frac{\left(k_{S1}+k_{d1}+\frac{k_{r2}}{s}+\frac{k_{d2}}{s}+\frac{k_1}{s}\right)(1-\cos\alpha)}{\left(k_{S1}+k_{d1}+\frac{k_{r2}}{s}+\frac{k_{d2}}{s}+\frac{k_1}{s}\right)^2+(1+q_1)^2}+\frac{\left(k_{S1}+k_{d1}+\frac{k_{r2}}{s}+\frac{k_{d2}}{s}+\frac{k_1}{s}+\frac{2k_2}{\sqrt{s}}\right)(1+\cos\alpha)}{\left(k_{S1}+k_{d1}+\frac{k_{r2}}{s}+\frac{k_{d2}}{s}+\frac{k_1}{s}+\frac{2k_2}{\sqrt{s}}\right)^2+\left(1+q_1+\frac{2q_2}{\sqrt{s}}\right)^2}\pm$$
$$\sin\alpha\left[\frac{1+q_1}{\left(k_{S1}+k_{d1}+\frac{k_{r2}}{s}+\frac{k_{d2}}{s}+\frac{k_1}{s}\right)^2+(1+q_1)^2}-\frac{1+q_1+\frac{2q_2}{\sqrt{s}}}{\left(k_{S1}+k_{d1}+\frac{k_{r2}}{s}+\frac{k_{d2}}{s}+\frac{k_1}{s}+\frac{2k_2}{\sqrt{s}}\right)^2+\left(1+q_1+\frac{2q_2}{\sqrt{s}}\right)^2}\right]\Bigg\}$$

$M_m=U_f^2 mp/2\omega_0 x_k$ -critic torque of shorted rotor induction machine $Kr_2=r_2/x_k$;*Kd1=rd1/*x_k; *Kd2=rd2/*x_k $k_1=r_0/x_k$;q1= x_0/x_k ; $k_2=r_m/x_k$;q2= x_m/x_k .

For calculation deferent IR parameters can obtained from the practical notion, that IR power factor is about .7-.8 and the parameters of IR windings(*xo,ro*) are very low before r_m: (0.1 - 0.2) r_m. Taking that in account all IR parameters will be expressed in function of k2 :
q2=tgφ.K2; k1≈q1=(.1-.2) [1].

To draw graphs for simplicity was chosen two identical motors with the same parameters.

The calculation were performed with parameters of motors type AK/51/4 with Pn=2.8kw and
n_0= 1500min-1.

III. GRAPHS' ANALISIS AND COMMENTARY :

Fig.2 shows angular characteristics drawn with deferent slip values . As it is seen with slip increasing the synchronizing capacity of system will increase.
The slip increasing in EMSh is possible by several ways. In our paper we will investigate three of them: 1) by regulating additional rheostat from stator circuits;2)by regulating additional rheostat from rotor circuits ;3) by changing IR parameters.

Let's to declare at first that the 1st and the 2sd ways can have a forward–easy access to their regulation .The third is not.

To compare the behavior of EMSh system with each way, we have first drawn mechanical characteristics -in case when motors carry the same load (α=0)-figures 2, 3,and 4- for the first, second, and third ways consequently. Characteristics show that all these approaches can provide a fair working characteristics for system in symmetric load regime.
Fig.2 reflect the characteristics of stator rheostat regulating .

As it is seen these characteristics is similar to those of individual induction machine having a constant resistance in rotor circuit and regulating resistance from stator circuit.
The fig3 and fig4 characteristics are similar to those of individual induction machine when regulating rheostat from rotor circuits.
Characteristics of fig.4 are obtained changing all IR parameters in function of its active resistance .
All these characteristics may meet the needs of load with ,for example, constant character . All these ways have one in common : the slip increasing as their parameters increase.

The behaviour of each way in case of asymmetric load carrying (α =90) can be shown plotting synchronizing ST torques in function of slip. The ST in EMSh (the part of torque with sin(α))as its predecessors , can be given as[1,2,3]:

$$M_S=\left(\frac{1+q_1}{\left(k_{s1}+k_{a1}+\frac{k_{s2}}{s}+\frac{k_{a2}}{s}+\frac{k_1}{s}\right)^2+(1+q_1)^2}-\frac{1+q_1+\frac{2q_2}{\sqrt{s}}}{\left(k_{s1}+k_{a1}+\frac{k_{s2}}{s}+\frac{k_{a2}}{s}+\frac{k_1}{s}+\frac{2k_2}{\sqrt{s}}\right)^2+\left(1+q_1+\frac{2q_2}{\sqrt{s}}\right)^2}\right)\sin\alpha \quad ...(11)$$

the graphs ,for each way consequently, are presented in fig.5,6 and 7. As it shows characteristics : only IR parameters changing can improve the ST torques.
As we drew the characteristics the losses in stator circuits has been ignored . This would not influence the 2nd and 3rd ways in case of medium-high power machines . For the 1st approach this can not be said . This why the characteristics of 1st way are only qualitative and are enough to evaluate

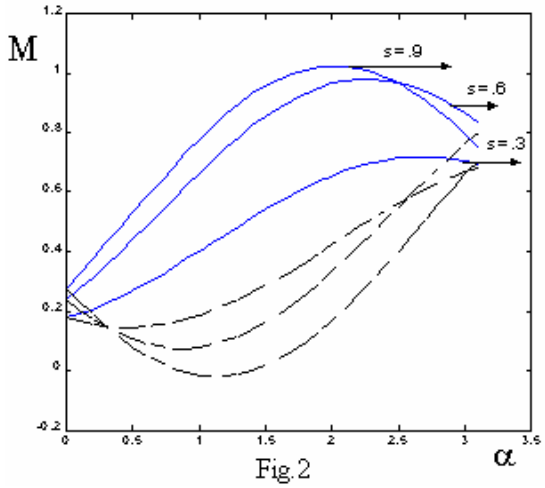

Fig.2

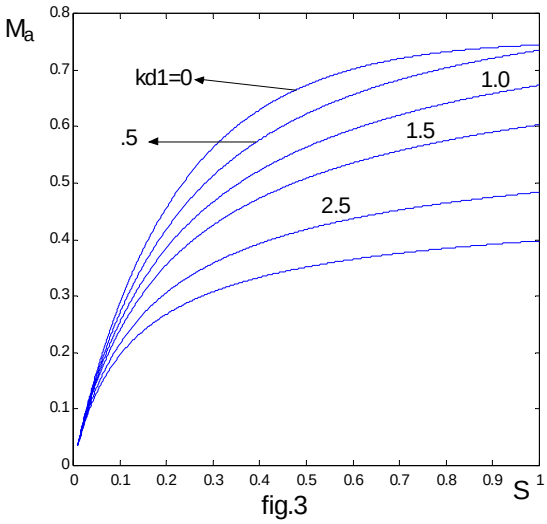

fig.3

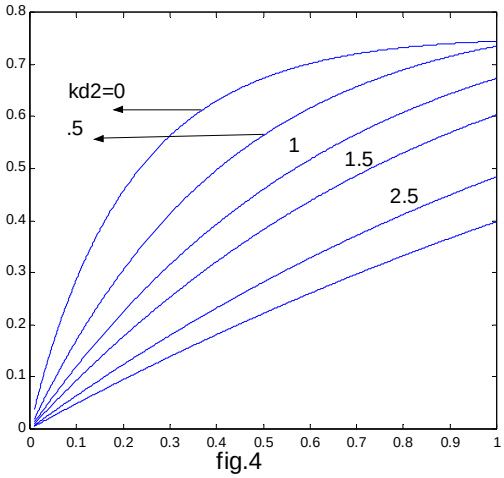

fig.4

this approach . The real characteristics of this way ,as it is easy to judge viewing (7) , will be more curvy and the ST torque yet by far worse . The real stator parameters considering may be in accommodate manner got, as in induction machines , using diagram circle method. Both the circle diagram and the analytical developing of (7) did not stand as aim in this paper .

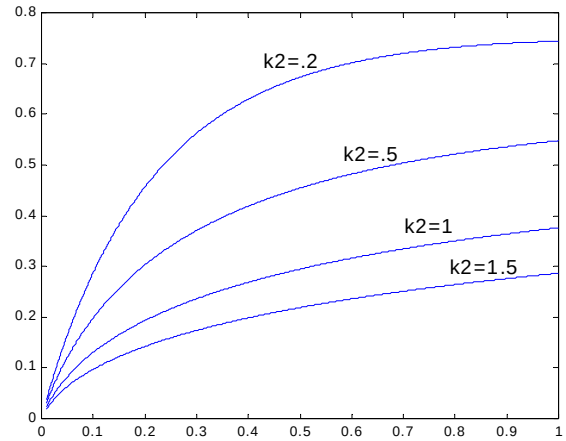

fig.5

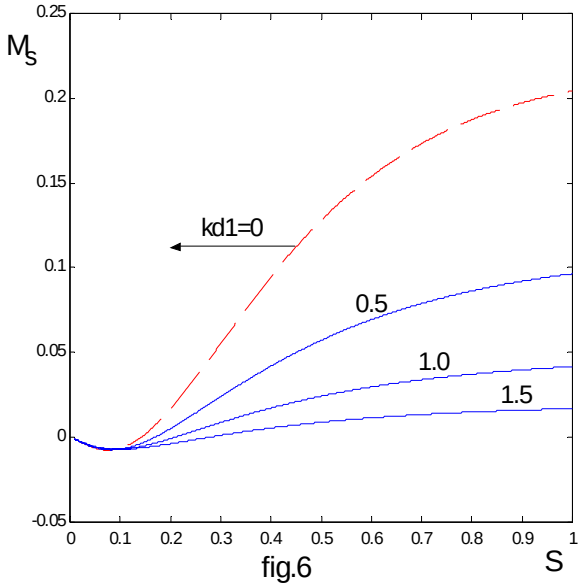

fig.6

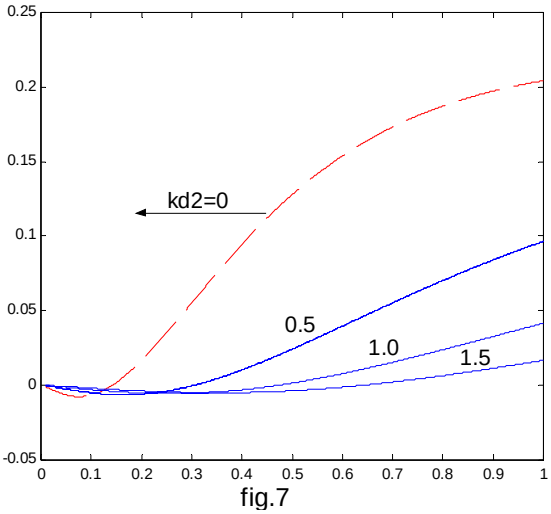

fig.7

In the end it is to mention that the influence of slip in Esh (electrical shaft) has been reported in many earlier works. Sometimes had been used the rotation of ESh anti-field to increase slip and therefore the ST torques .Had been used ,either , its increasing by regulating the common resistance [3,4]. The works in case of additional rheostat in rotor and

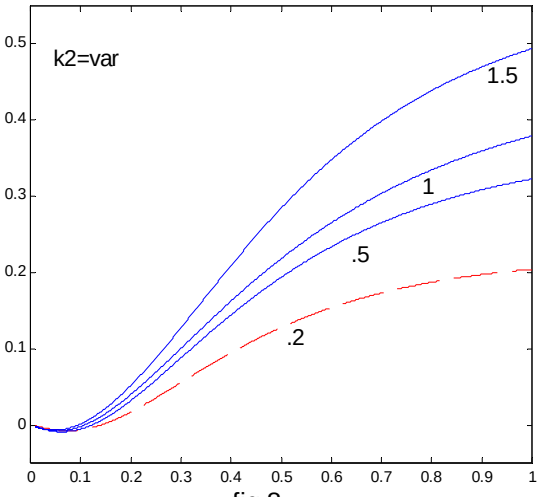

fig.8

stator circuits for EMSh system (and also it would be said for ESh), and also their presentation as ways for slip changing is for the first time.

IV. Conclusion

The study have shown that the slip increasing though do not affect EMSh system in symmetric load carrying by the several presented ways the ST torques can only be improved acting on induction rheostat parameters. Regardless that because of the forward–easy regulation access, the remain ways can be recommended for EMSh speed regulation in symmetric regimes.

References :

[1] N.M. Usmankhodjaev. P.I.Belokovski, B.C. Usmanov "A.C.1396234CCP.Mnogodvigateni lectroprivodperemenova toka" / / bul.izobret.1988 n°:18.

[2] N.MUsmankhodjaev,S.Fellag. Mnogodvigatelni "Electroprivod s electro-electromagnitnoi svyazi asynxronix mashin dla konveirov bolshoi protyajenosti" Uzbekski journal 'problimi energetiki I informatiki'1998. n° 01.

[3] F.Ungruh. G. Jordan. Cictemi "Coglasovanova vracheni asinxronix elektrodvigateli". Energia. 1971. pp 48-51; pp139-141.(translation from deutch language)

[4] "The quality study of EMSh with deferent approaches of changing IR parameters" Isef'03.slovinia.maribor.

Session ELII:

ELECTRONIC COMPONENTS, SYSTEMS AND TECHNOLOGY II

Methods and Means for Charging and Control of Accumulating Batteries for Mobile Phones

Stoyan S. Gishin[1], Dimitar I. Dimitrov[2], Sava Savov[3]

Abstract - **In the report are examined contemporary methods for optimal charging and testing of hermetic accumulating batteries. These batteries are used as a charging module of contemporary mobile communication devices (for example GSM devices). Direct application of the above-described methods is charging and control of the supplying module such as nickel-metal hybrid hermetic accumulating batteries. The examinations for charging and testing are based on the process of management and control of the sources of impulse current. The continuance of the positive current impulses is automatically regulated by microprocessor system. It controls the dynamic situation of the electrical-chemical system. Impulse current' sources are programmable. They are used to maintain the computer control and process management. Methods and means (apparatuses) are realized as laboratory models in order to be used for education of students from the Communication technique and technology faculty, Computer systems and management, Electronic technique and technology, where students study electro-chemical current sources, which is a part of the University curricula for the above-mentioned faculties.**

I. INTRODUCTION

In the past years electrochemical current sources (ECHCS) found a great practical application in telecommunications, mobile phones, video cameras and etc.The basic requirement for ECHCS is to be hermetically-sealed, which allows the usage in different geometric position. The hermetic accumulators were created thanks to the following technical and technological solutions:

a. jelly-formed electrolyte from sulphur acid;

b. lead alloys are used without any content of for cast (mould) of positive and negative current-conducting bars for accumulators.

c. methods were developed for the charging of the accumulators, without gas-emissions with microprocessor control and process management.

d. optimal ratio between active mass and effective additions, leading to the minimum gas-emissions through the charge with the speed of the self-discharge

e. constructions are developed of the accumulators and batteries, excluding emission of steam and drops of electrolyte through re-combination of ions.

Practically through the production of hermetic lead accumulators the great appliance is found in the lead-calcium alloy, containing 0,1-0,2 % calcium and minimum quantity of added tin.

I. Leading company in production of capsulated, hermetic starter accumulators is EXIDE – USA, that sells its production through out the world, incl. in Bulgaria through CENTRA – EXIDE EUROPE Company. The basic advantages of these accumulators are that they have more than 20 % higher start current compared to accumulators with the same nominal capacity, but produced from other accumulator's companies.

The hermetic accumulating batteries that are wide spread in mobile GSM apparatuses are lead, nickel-metal hydride, li-ion and etc.

During the conducting of experimental researches and tests is used the hypothetic scheme shown on Fig. 1

Typical for the scheme for realization of the impulse current with computer control and process management is that it allows the usage of currents with different shapes, shown on Fig. 2 and Fig. 3.

Theoretical calculations and practical researches show that in the beginning and in the end of the charging of the CHECHCS resistance of the electro-chemical system is the biggest and respectfully the electrochemical processes are the most often met. This shows that electrolysis processes for separation and respectfully fulfillment of CHECHCS with oxygen and hydrogen are the most common in the beginning and in the end of the electrochemical processes during charging.

Considerable improvement of electrical and exploitation characteristics of chemical current sources, as well as economy of electro energy are obtained through usage of basic electro technological processes of DC current with periodically changing polarity. The continuity of the positive current impulses is bigger that the continuity of the negative current impulses, that are constant during the processe

[1]Stoyan S. Gishin. Associate Professor of Electrical technology Department of El. Apparatuses Fac. Electrical Technique, Technical University of Sofia, Bulgaria, e-mail: mytreo@mail.bg

[2]Dimitar I. Dimitrov is with the Faculty of Communications and Communications Technologies, Technical University of Sofia, Bulgaria, 8 Kliment Ohridski Str., 1000 Sofia, Bulgaria, e-mail: ddim@tu-sofia.bg

[3]Sava Dimitrov Savov, Associate Prof. Physics, Physics Faculty, "St. Kliment Ohridski" Sofia University, Sofia, Bulgaria

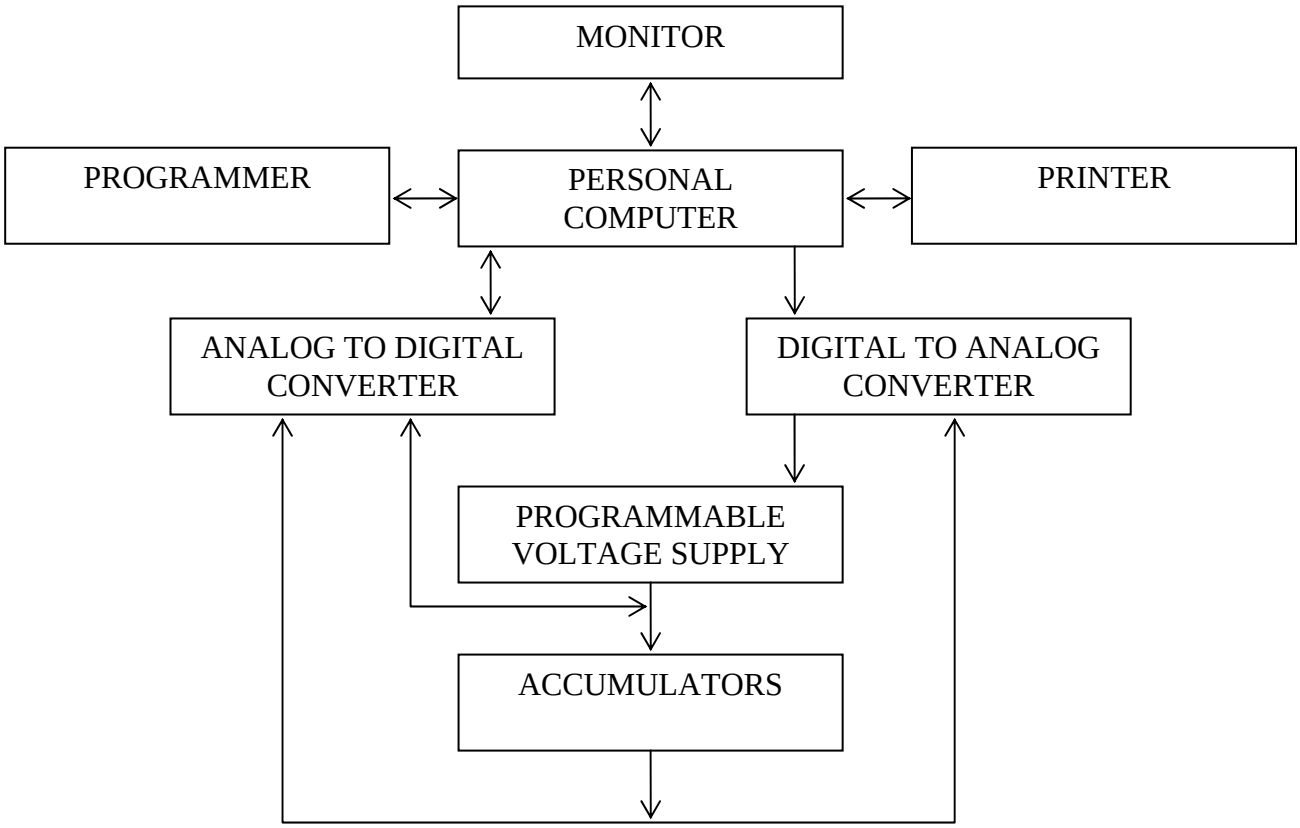
MONITOR
PROGRAMMER
PERSONAL COMPUTER
PRINTER
ANALOG TO DIGITAL CONVERTER
DIGITAL TO ANALOG CONVERTER
PROGRAMMABLE VOLTAGE SUPPLY
ACCUMULATORS

Fig. 1.

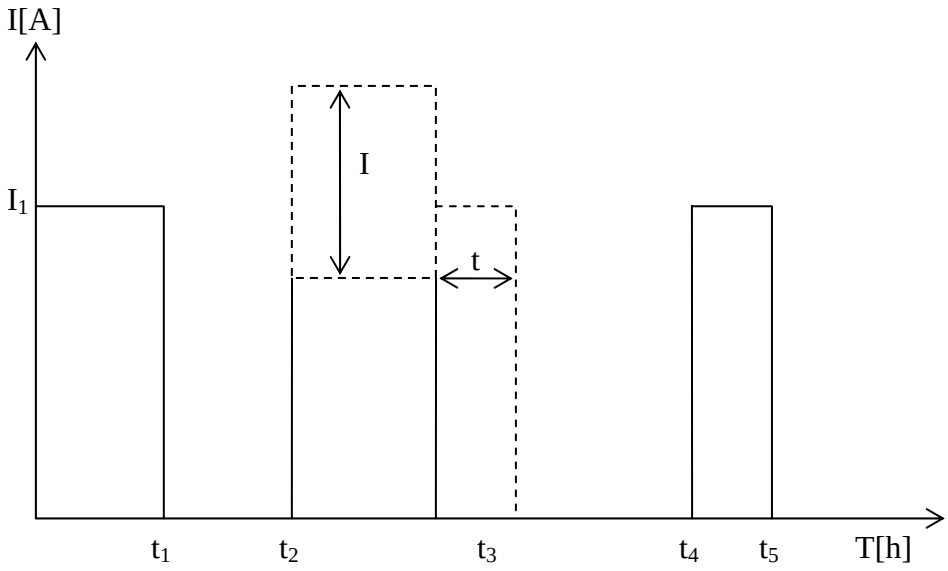
I[A]
I
I1
t
t1
t2
t3
t4
t5
T[h]

Fig. 2.

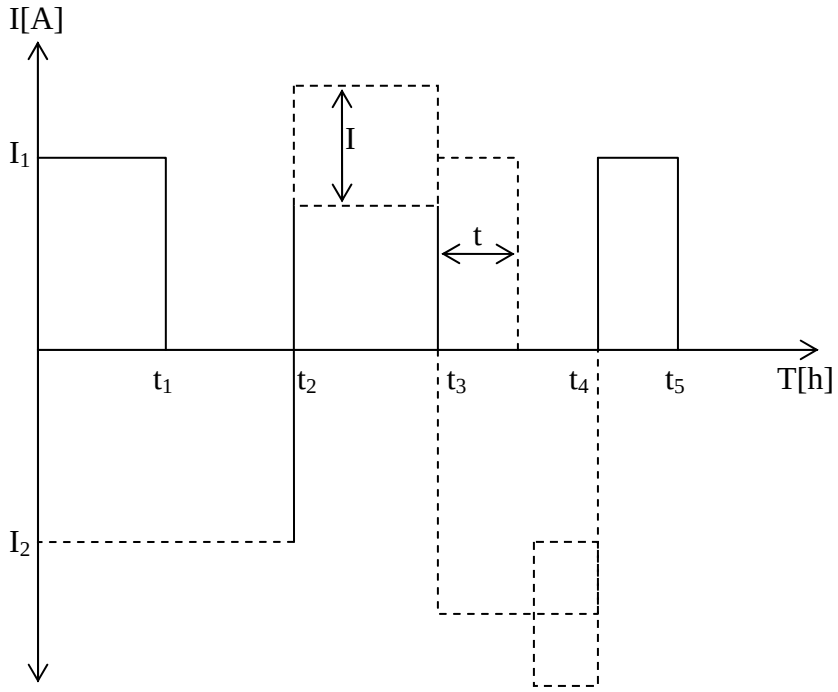

Fig. 3.

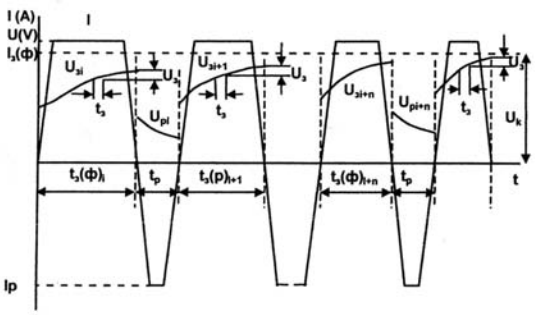

Fig. 4.

In the Sofia Technical University is developed a method for block electro forming and charging of accumulators and batteries with usage of impulse current. The main point of this method, which is registered as a patent, consist in the fact that the continuity of the positive current impulses is calculated automatically, as with microprocessor system is followed the dynamic situation of the electrochemical system – Fig. 4.

Following the dynamic situation of the accumulator is a process that consists of periodical (10-30 sec.) measurement of the change in the electric voltage ΔU and when this growth is less that preliminary given value is changes the polarity of the charged current impulse and discharged impulse is passed to the accumulators.

Some of the GSM devices producers recommend to discharge fully the used accumulating batteries and after that to charge them for a definite time. We consider that this is not right for the ECHCS from the exploitation point of view.

In accumulating batteries for mobile GSM devices it is correct to maintain full charging of the accumulating batteries that would lead to the reduction of the conducting of the prejudicial electrochemical processes. All this leads to reduction of the flow of the out of side processes and respectively the gas emission that fills the accumulating batteries and thus increasing the inner resistance of the accumulating batteries. The internal ohm resistance is increasing considerably and when the accumulating batteries are deeply discharged. There is considerable growth in the internal resistance of the hermetic batteries in the end of the charge and especially during recharging. In the end of the charge of the batteries if they are not switched off, irrespectfully of the fact that the market and used charging devices reduce the value of the current, the temperature of the electrochemical system is rising. This temperature growth automatically changes the internal ohm resistance of the batteries, which allows changing the dynamic state of the electrochemical system and the current value doesn't decrease. This leads to the continuation of the charging process in not-optimal state of the electrochemical system and thus reducing the exploitation life of the batteries.

According to the conducted experimental and theoretical researches two main conclusions can be derived:

1. Not to allow deep discharge and recharge of the batteries, that leads to the reduction of their exploitation life.
2. It is preferable to regularly optimally fully charge the batteries that would increase their exploitation life.

REFERENCE

1. Gishin S., Accumulators. Technical University. Sofia, 2003.
2. Gishin S., Patent USA No: 421664.
3. Gishin S. and co., Manual for laboratory practice of Electro-chemical technologies. Technical University. Sofia, 2005.

Temperature Influence on the Parameters and Characteristics of the Optoelectronic Elements. Circuits for Temperature Compensation

Ivan S. Kolev[1], Tsanko V. Karadzhov[2] Elena N. Petkova[3]

Abstract – **The temperature influence on the parameters and characteristics of the light sources LEDs, photodetectors, photodiodes – avalanche and PIN, phototransistors, and optocouplers – photodiode and phototransistor optocouplers are considered. Expressions for the influence of the temperature on the parameters of the optoelectronic elements are given. Temperature compensation for circuits with optoelectronic elements is proposed**

Keywords–**Optoelectronic Element, Temperature Compensation, LED, Photodetector, PIN Photodiode.**

I. LIGHT SOURCES

Forward voltage of LEDs decreases when temperature increases. It is

$$U_F(T°) = U_F(20°C) - TKU_F.\Delta T \quad (1)$$

Temperature coefficient of U_F, $TKU_F \approx -1.5$ *mV/°C*

The current-voltage characteristic of a LED is expressed as follows:

$$I_F = I_R\left(e^{\frac{U_F}{m.\varphi_T}} - 1\right) \quad (2)$$

When taking the logarithm of expression (2)

$$U_F = \frac{m.K.T}{q}\ln\left(1+\frac{I_F}{I_R}\right) \quad (3)$$

where: $\frac{KT}{q}$ - temperature potential, $\frac{KT}{q}$=25 mV by (25°C);

I_R – LED's reverse current;
T – temperature, °C;
K – Boltzmann's constant;
q – electron charge.

[1]Ivan S. Kolev. Department of Electronics, Technical University – Gabrovo, Street "Hadji Dimiter" No. 4, 5300 Gabrovo, Bulgaria, phone: +359 66 801064.

[1]Tsanko V. Karadzhov. Department of Electronics, Technical University – Gabrovo, Street "Hadji Dimiter" No. 4, 5300 Gabrovo, Bulgaria, phone: +359 66 801064, e-mail: karadjov_st@abv.bg

[3]Elena N. Petkova. Department of Electronics, Technical University – Gabrovo, Street "Hadji Dimiter" No. 4, 5300 Gabrovo, Bulgaria, phone: +359 66 801064.

The dependence of U_F on temperature is shown in fig.1. The shift of LED's volt-ampere characteristic caused by temperature is shown in fig.2.

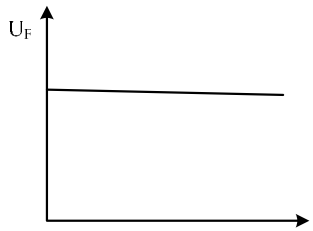

Fig. 1

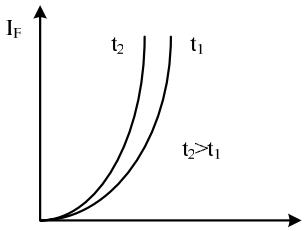

Fig. 2

The radiation of LED as a result of temperature has a negative temperature coefficient

$$I_V(\Phi_V) = (-0.55 \div -1)\%/°K$$

$$I_{V,t°} = I_{V\,20°C} - TKI_V.\Delta T$$

The example value of the decrease of radiation power caused by temperature is 100 μW/°C.

The relative change of the LED's radiation as a result of temperature is shown in fig.3.

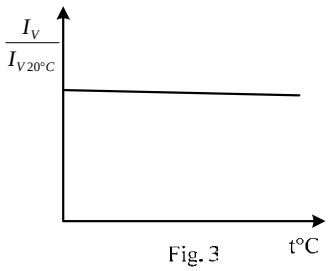

Fig. 3

The length of the LED's wave – λ and the width of the forbidden band E_g are related by the expression:

$$\lambda, \mu m = \frac{1.24}{E_g(eV)} \quad (4)$$

The higher the temperature, the smaller the width of the forbidden band, and the longer the LED's wave. The temperature coefficient $TK\lambda_P \approx +0.3$ nm/°K.

The shift of the LED's radiation spectrum towards greater lengths of the wave when temperature increases are shown in fig.4.

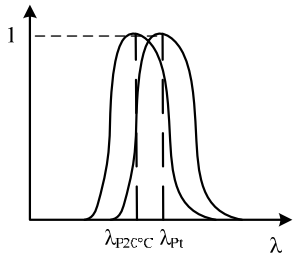

Fig. 4

II. PHOTODETECTORS

A. PIN photodiodes

With photodiodes the dark current I_D mainly depends on temperature and TKI_D is positive – fig. 5.

$$I_{D,t^\circ} = I_{D20^\circ C}.e^{\frac{kT}{q}} \quad (5)$$

This can be explained with the concentration of the non-basic current carriers P_0

$$P_0 \sim e^{\frac{-Eg}{KT}} \quad (6)$$

Figure 5 is described by expression (5)

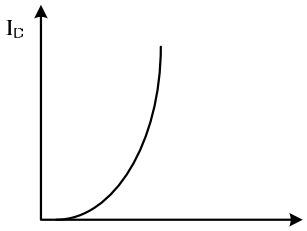

Fig. 5

The photodiode's photocurrent has a positive temperature coefficient and it slightly increases when temperature increases – fig. 6.

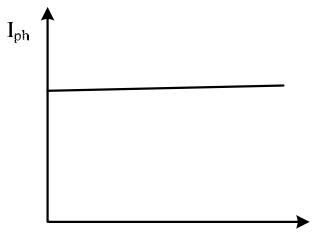

Fig. 6

The current through the photodiode is determined by the expression:

$$I = I_S\left(e^{\frac{U}{m\varphi_T}} - 1\right) - I_{Ph} \quad (7)$$

To reduce the influence of the temperature on the photodiode, the photodiode has to be cooled or photodiodes with a wide forbidden band (photodetectors for ultraviolet or violet ranges) have to be used. With them the dark current has a value of pA.

A. Photogalvanic Mode of Photodiodes

The Ph.E.M.F. generated from the photoelement is:

$$E_{ph} = \frac{KT}{q}\ln\frac{I_{phsh} - I_{RL}}{I_D} \quad (8)$$

where: I_{RL} – load current;
I_{phsh}

if $I_{RL} \approx 0$

$$E_{ph} \approx \frac{KT}{q}.\frac{I_{ph}}{I_D} \quad (9)$$

The photocurrent of a short circuit has a positive temperature coefficient, for example 0.2 %/K.

The Ph.E.M.F. of the photoelement has a negative temperature coefficient.

B. Avalanche Photodiodes

The reverse voltage of an avalanche photodiode has a positive temperature coefficient $TKU_R \sim +0.3$ V/°K

The coefficient of the avalanche multiplication M has a negative temperature coefficient – fig.7.

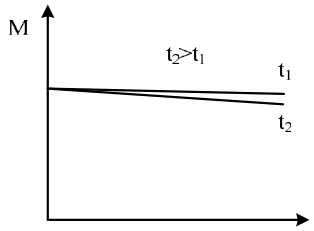

Fig. 7

C. Phototransistors

The photocurrent of the phototransistor is:

$$I_{ph} = h_{21E}.I_{phPD} + I_D \quad (10)$$

The dependences of I_D and I_{ph} on the temperature are shown respectively in fig.5 and fig.6.

Expression (10) shows that the photocurrent of the phototransistor increases when temperature increases.

III. OPTOCOUPLERS

A. Photodiode Optocouplers

The current transmission ratio CTR of the photodiode optocouplers has a negative temperature coefficient

$$CTR_{t°C} = CTR_{20°C} - TKCTR.\Delta T \quad (11)$$

B. Phototransistor Optocouplers

With phototransistor optocouplers there is a particular temperature interval where a temperature compensation of the CTR coefficient takes place in the optocoupler. The radiation power of an IRED has a negative temperature coefficient whereas the photocurrent and the dark current have a positive one – fig.8.

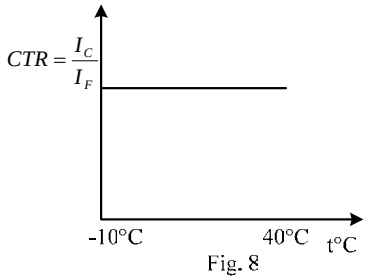

Fig. 8

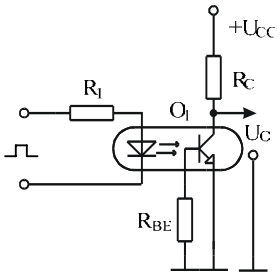

Fig. 9

To obtain good temperature stability of the phototransistor and a maximal signal/noise ratio, a resistor R_{BE} is connected between the base and the emitter of the phototransistor – fig.9.

$$R_{BE} = \frac{KT/q}{4I_D}\left(\frac{h_{21E}-1}{h_{21E}+1} + \sqrt{h_{21E}}\right) \quad (12)$$

For example, when $\varphi_T = KT/q = 25.10^{-3}$V, $h_{21E}=100$, $I_D = 100.10^{-9}$A, R_{BE}~686kΩ, R_{BE}=680kΩ is chosen. At 25°C, the voltage of the collector when the phototransistor is turned off is:

$$U_{CEH} = U_{CC} - I_D R_C = U_{CC} - \Delta U_{RC} \quad (13)$$

When U_{CC}=5V, R_C=1kΩ, $I_D = 100.10^{-9}$A, ΔU_{RC}=0.1mV, $U_{CEH} \approx U_{CC}$

The temperature resistances of the LED and the phototransistor of the CNY17 optocoupler are:

LED – R_{th}=750 K/W, Phototransistor – R_{th}=500 K/W

The change of the preliminary characteristic of the phototransistor optocoupler caused by temperature is shown in fig.10.

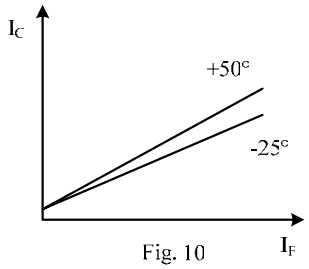

Fig. 10

The voltage between the phototransistor collector and emitter in a saturation mode is:

$$U_{CEsat} = R_{CEsat}\left(I_{ph} + I_D\right) \quad (14)$$

R_{CEsat} – resistance between the phototransistor collector and emitter in an ON state (100÷200) Ω.

I_{ph} and I_D increase when temperature increases. Therefore, U_{CEsat} also increases when temperature increases – fig.11.

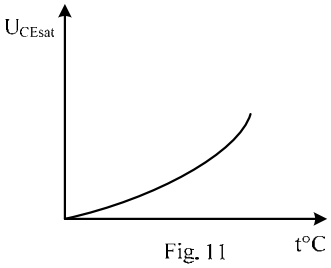

Fig. 11

$$U_{CEsat} \equiv \varphi_T = \frac{KT}{q} \equiv T \quad (15)$$

To obtain a good temperature stability of the optocoupler phototransistor, the base is fixed by a negative potential – fig.12.

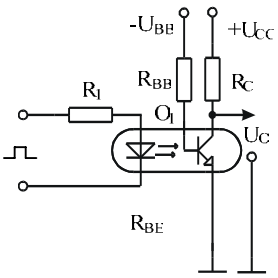

Fig. 12

The following can be written for the collector current:

$$I_C = h_{21E}.I_B^+ \quad (16)$$

$$I_C = CTR.I_F \quad (17)$$

The following is obtained from (16) and (17):

$$I_B^+ = \frac{CTR.I_F}{h_{21E}} \quad (18)$$

$$I_F = \frac{U_I - U_F}{R} \quad (19)$$

$$I_B^+ = CTR\frac{U_I - U_F}{R.h_{21E}} \quad (20)$$

When the phototransistor is set ON by the source current, U_{BB} is:

$$I_B^- = \frac{U_{BB} - U_{BE}}{R_{BB}} \quad (21)$$

IV. Circuits for Temperature Compensation

A. Photogalvanic Mode of Photodiodes

In order for the voltage across the load R_L to be constant when temperature changes and the photodiode operates in a photogalvanic mode, the circuit in fig.13 is used. Within it the thermistor R_T has a negative temperature coefficient.

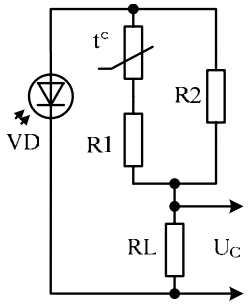

Fig. 13

B. Photodiode Operation Mode of Photodiodes. Differential Circuit

VD2 is non-operating. It is used for temperature compensation – fig.14.

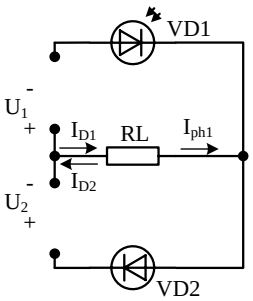

Fig. 14

The current across the load R_L is:

$$I = I_{ph1} + I_{D1} - I_{D2} \approx I_{ph1} \quad (22)$$

$$I_{D1} = I_{D2}$$

C. Bridge Circuit

R_L>>R. The current I is determined by the expression (22) $I \approx I_{ph1}$

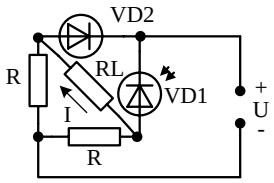

Fig. 15

D. Circuit for Temperature Compensation of Phototransistor Optocouplers

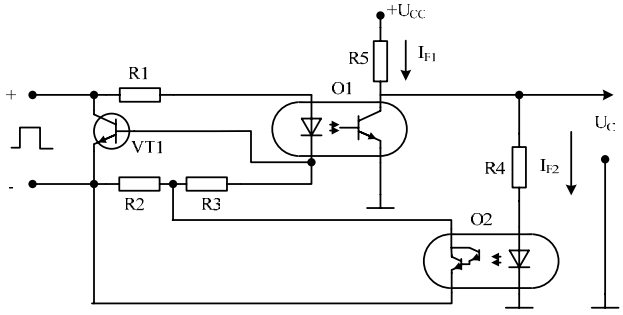

Fig. 16

R_4>R_C

The transistor VT1 is a current regulator. The 02 optocoupler is in a circuit of an optic negative feedback. The current across the optocoupler LED is:

$$I_F \approx \frac{U_{BE}}{R_3 + R_2 \,||\, R_{CEO2}(I_{F2})} \quad (23)$$

V. Conclusion

The aim of study of temperature influence at parameters and characteristics of optoelectronic elements is to develop new circuits. Using these circuits will improve functional capabilities of optoelectronic devices.

References

[1] Ivanov, V. I., Aksenov, A. I. and A. M. Ushin. Semiconductor Optoelectronic devices. Book. Moskva., Energyatom's, publishing, 1988.

[2] Kolev, I. S. Optoelectronics. Gabrovo, Technical University, University Publication. "V. Aprilov", 2004.

[3] Kolev, I. S. Infrared optoelectronics. Gabrovo, Technical University, University Publication. "V. Aprilov", 2004.

[4] Kolev, I. S. and T. S. Todorov. Optoisolators and application. S., Technics, 1988.

[5] Siemens. Si-Foto-Detektoren und IR-Lumineszenz-dioden. Data Book, 1996.

[6] Siemens. Opto-Halbleiter. Datenbuch, 1998/99

Improved Design Centering In a Reduced Search Space for Electronic Circuits Optimization

Galia I. Marinova[1], Vassil G. Guliashki[2]

Abstract - **The paper presents an improved version of DCSDR method for efficient design centering for electronic circuits. The choice of simplex vertex for current reflection is more precise. A new step is added for the case when the last iteration was unsuccessful but there are element values, which are not reflected towards the corresponding best value in the simplex, i. e. there are available unexplored search directions. Thus designs which initial values are close to the optimal can also be treated. An extended investigation on different circuits is performed.**[+]

Keywords - **Statistical design methodology, Design centering, Discrete optimization**

I. INTRODUCTION

The design centering objective is to find out the optimal values for the parameters of circuit elements in order to obtain maximal yield. The optimal tolerancing goal is to obtain the optimal tolerance values for the parameters of the circuit elements in order to avoid fail by reducing tolerances where necessary and in order to reduce cost by increasing tolerances where it is possible. Statistical design methodology is based on nominal design and includes design centering and optimal tolerancing. Theory for design centering and optimal tolerancing can be found in [7]. Implementations of design centering are presented in [2, 4]. In design centering a Monte Carlo analysis is performed (by means of IESD statistical simulator [3]) to estimate the yield during the optimization procedure.

The design centering problem can be defined as:

$$\textbf{Min} \qquad F = \sum_{i=1}^{m} \delta_i \tag{1}$$

$$\textbf{subject to:} \quad \delta_i = \begin{cases} 1 \text{ if } J(x) \notin [Lb, Ub]; \\ 0 \text{ if } J(x) \in [Lb, Ub]; \end{cases} \tag{2}$$

$$l_j \le x_j \le u_j; \quad j = 1,\ldots,n; \tag{3}$$

$$x \in Z_+^n, \tag{4}$$

where $J(x)$ is the output signal of the circuit under consideration, Lb and Ub are the bounds (lower and upper) of $J(x)$, x_j, $j = 1,\ldots,n$; are the parameters of the elements, which values have to be optimized, and which accept discrete values only. Z_+^n is the set of nonnegative integral n-dimensional vectors, l_j and u_j are bounds of x_j, such that $(u_j–l_j)/(2u_j).100 = tol_j$ determines the tolerance of x_j. Here m is a positive integer number equal to the number performed Monte Carlo simulations by means of statistical simulator IESD (see [3]) on the circuit under consideration. The optimal solution of **(1-4)** is F=0.

The optimal tolerancing problem can be defined as:

$$\textbf{Max} \quad F_T = (\min_{j=1,\ldots,n} tol_j) \tag{5}$$

$$\textbf{subject to:} \quad \sum_{i=1}^{m} \delta_i = 0 \tag{6}$$

$$\delta_i = \begin{cases} 1 \text{ if } J(x) \notin [Lb, Ub]; \\ 0 \text{ if } J(x) \in [Lb, Ub]; \end{cases} \tag{7}$$

$$u_j = x_j + x_j \,.\, tol_j / 100 \tag{8}$$

$$l_j = x_j - x_j \,.\, tol_j / 100 \tag{9}$$

$$l_j \le x_j \le u_j; \quad j = 1,\ldots,n; \tag{10}$$

$$tol_j \in T; \quad T = \{1, 2, 5, 10, 15\} \tag{11}$$

$$x \in Z^n, \tag{12}$$

where the variables tol_j are the tolerances of parameters x_j, $j=1,\ldots,n;$ and x_j, $j=1,\ldots,n;$ Lb, Ub, are beforehand known constant integers.

II. THE DESIGN CENTERING METHOD IN A REDUCED SEARCH SPACE DCSDR

The problem (1)-(4) is a combinatorial one (see constraints (4)) and belongs to the class of NP-hard optimization problems. For this reason the statistical optimization methods solving this problem could be very time consuming. Usually the complete enumeration of the permitted range options is large. A heuristic has been proposed in order to limit the trials number (see [2]). At each step best and worst performance randomly generated circuits are used to define the values and the tolerances at the next step. This approach is effective, but also could be rather inefficient when the number of circuit elements n is large and great number of parameter variations must be investigated. To improve the efficiency a direct search method for fast design centering (FDC) was proposed in [4]. It is based on the Nelder and Mead's method [6], known as the most efficient among the direct search methods. FDC method is modified correspondingly for the discrete search space. The drawback of FDC method is that the number of simplex vertices is (n+1), that is greater than the number of circuit elements n, and for large n great number of Monte Carlo simulations should be performed.

[1]Galia I. Marinova is with the Technical University of Sofia, Faculty of Telecommunications, Sofia -1000, Bul. "Kliment Ohridski", N°8, Bulgaria, E-mail: gim@tu-sofia.bg ;

[2]Vassil G. Guliashki is with the Institute of Information Technologies, Sofia-1113, "Acad. G. Bonchev" Str., Bl. 29A, Bulgaria, E-mail: vgoul@iinf.bas.bg ;

Performing design centering it turns out that very often the circuit output $J(x)$ depends stronger on the variation of some "sensitive" circuit elements than on the variation of the left over elements. This feature of the problem (1)-(4) makes it possible to use reduced search space, optimizing only the "sensitive" elements. Based on this idea a design centering method with space dimension reduction (DCSDR) solving the problem (1)-(4) was proposed in [5]. In this way the search process is enhanced considerably. The search step in DCSDR method is calculated like that one in FDC method. To keep the constraints (4) the step components are rounded off to integer values. In contrast to the FDC method, which uses simplex with (n+1) vertices, where n is the number of circuit elements, the simplex in DCSDR method has (k+1) vertices, where k is the number of "sensitive" circuit elements. Another way used to make the search procedure in DCSDR faster than that one in FDC is to perform Monte Carlo analysis not in each simplex vertex like the FDC method, but only at the initial step and at the end of each DCSDR optimization iteration.

Other specific feature of DCSDR method is that the initial simplex is constructed not as trivial regular simplex (see [6]), but in different way. Let $J(x)$ be the output signal function of the circuit and Jd be the desired value of the output signal. To evaluate the steps quality during the DCSDR iteration the measure of deviation from the desired value is used: $D(x) = |J(x)-Jd|$. Let among the vector variations obtained after the initial Monte Carlo analysis x^B be the vector, for which $D(x^B)$ has minimal value and let x^W be the vector, for which $D(x^W)$ is maximal. The vectors x^{Mi}, i = 1, …, n; are constructed, where $x^{Mi}_j = \{ x^B_j$ if $i \neq j$; x^W_j if $i = j\}$. As starting simplex vertices are chosen vector x^B and k vectors among x^{Mi}, i = 1, …, k; for which the deviation of $J(x)$ is relative great, i. e. the k vectors corresponding to variations of "sensitive" elements. It is expected, that the optimization by reflection the worst simplex vertex through the weight center of the left over simplex vertices with objective - minimizing $D(x)$ will move the simplex to a search space region, where its weight center would improve the F value.

The steps of the method are presented as follows:

Step 0. Give the starting value of:

- iterations limit *itlim*, where *itlim* > 0,
- the vector of elements parameters $x^{(0)}$,
- l_j and u_j for each parameter x_j , j = 1, …, n;
  The tolerance value $tol_j = 100.(u_j - l_j)/(2.u_j)$;
- the lower and the upper bound for the output signal Lb and Ub. The desired output signal value is usually $Jd=(Lb+Ub)/2$.

Set the iteration counter *icount* = 0.

Step 1. Perform a Monte Carlo analysis in $x^{(icount)}=x^{(0)}$. Let $D(x)$ has obtained its minimal and maximal value correspondingly in vectors x^B and x^W during the analysis. In case $F(x^{(icount)})=0$, go to *Step* 13. Otherwise go to *Step* 2.

Step 2. Use x^B and x^W to construct the vectors x^{Mi}: $x^{Mi}_j = \{ x^B_j$ if $i \neq j$; x^W_j if $i = j\}$, i = 1, …, n.

Step 3. Calculate the rate of influence on the output signal value for the change of each x_i, i = 1, …, n; : $\sigma_i = |[(J(x^{Mi}) - J(x^B))/(J(x^W) - J(x^B)]/[(x^W_i - x^B_i)/x^B_i]|$. Create an index set I from indices i, for which $\sigma_i > \theta$, where $\theta \in (0, 1)$ and could be different for different circuits. Usually θ = 0,03. Let there are k such indices in I, where $k \leq n$.

Iteration:

Step 4. Fix the values of all elements, which indices $i \notin I$. Construct a nonregular simplex in the reduced k-dimensional space, determined by the left over elements. The simplex has k+1 vertices. One of them is x^B and the others are x^{Mi}, $i \in I$.

Step 5. Find among the k+1 simplex vertices the vector $x^{(j)}$, for which $D(x^{(j)}) = \max D(x^{(i)})$, i = 1, ..., k+1;

Step 6. Find the weight center of the k left over simplex vertices:

$$\boldsymbol{x_c} = \frac{1}{k}\sum_{i=1}^{k} \boldsymbol{x}^{(i)} \qquad (13)$$

Step 7. Construct the vector:

$$\boldsymbol{x = x^{(j)} + \lambda(x_c - x^{(j)}),} \qquad (14)$$

where λ = 2; (In case the last found vector x at *Step* 7 is again that one with max $D(x)$ start *Step* 7 with λ = 1.5;) Round off each component x_j to the closest feasible discrete value (see (**4**)), so that the constructed vector $x \in Z^n_+$. In case $D(x) < D(x^{(j)}$, replace $x^{(j)}$ by x and go to *Step* 5, otherwise change λ (simplex contraction): λ=1.5 and construct a new vector x using (**14**). Round off each x_j to the closest feasible discrete value. In case $D(x) < D(x^{(j)}$, replace $x^{(j)}$ by x and go to *Step* 5, otherwise change λ (simplex contraction): λ=1.25 and construct a new vector x using (**14**). Round off each x_j to the closest feasible discrete value. In case $D(x) < D(x^{(j)}$, replace $x^{(j)}$ by x. Go to *Step* 8.

Step 8. Find the weight center of all simplex vertices:

$$\boldsymbol{x_t} = \frac{1}{k+1}\sum_{i=1}^{k+1} \boldsymbol{x}^{(i)} \qquad (15)$$

Step 9. Set *icount*=*icount*+1. Set $x^{(icount)} = x_t$. Perform a Monte Carlo simulation in $x^{(icount)}$. In case $F(x^{(icount)})=0$, go to *Step* 13.

End of the Iteration

Step 10. In case the last iteration was unsuccessful, i. e. $F(x_t)$ has greater value than the last found $F(x)$, and if there are components $i \in I$, for which x_i has not being reflected towards the corresponding component x^B_i during the iteration, then construct a vector $p = \Sigma(x^{(icount-1)} - x^{Mi})$. Let among the simplex vertices $x^{(j)}$ be the vector, for which $D(x^{(j)}) = \max D(x^{(i)})$, i=1,..., k+1;

Construct the vector:

$$\boldsymbol{x = x^{(j)} + p} \qquad (16)$$

and perform a Monte Carlo analysis in it.

Step 11. If *icount* = *itlim* go to *Step* 13.

Step 12. Let $D(x)$ has obtained its minimal and maximal value correspondingly in vectors x^B and x^W during the simulation. Construct the vectors x^{Mi}: $x^{Mi}_j = \{x^B_j$ if $i \neq j$; x^W_j if $i = j\}$, $i = 1, \ldots, n$. Go to *Step* 4.

Step 13. End of the search process.

To complete the statistical optimization technology, the design centering should be followed by an optimal tolerancing search procedure.

III. Illustrative Examples

A. Design centering of voltage regulator circuit

The voltage regulator circuit from [4, 5] is used to illustrate the performance of DCSDR method (see Fig. 1). The parameters that can be optimized are the resistors R_1, R_2, …, R_6 and the capacitor C_1. Two applications of the voltage regulator circuit are studied: one for 24 V stabilized output voltage and another one for 15 V stabilized output voltage.

- The output voltage of the circuit should be constant 24 ± 0.5 V and the desired value *Jd* = 24.00 V. This case was studied in [4, 5]. The objective here is to minimize *F* (see (**1**)) until *F*=0. The Monte Carlo analysis is performed with 100 randomly generated circuits with given tolerances.

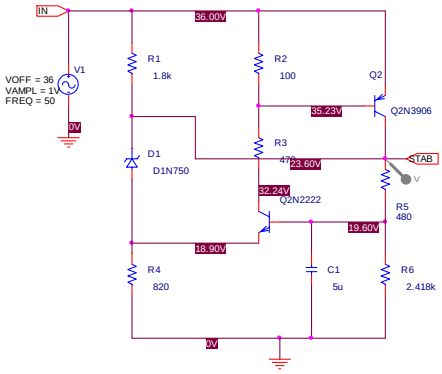

Fig. 1. Voltage regulator circuit

After a Monte Carlo analysis with 1% tolerance for all R, C elements the circuit output $J(x)$ did not violate the *Lb* and *Ub* bounds in all the 100 cases. When 2% tolerance of elements values was chosen, 3 from 100 randomly generated circuits had an output voltage above 24.5 V, i. e. *F*=3, when *m*=100, tol_j = 2%, j = 1,…,7;. The results obtained after one DCSDR iteration are as follows: R_1 = 1810Ω, R_2=100Ω, R_3=472Ω, R_4=820Ω, R_5=476Ω, R_6=2451Ω and C_1=5μF. The optimal tolerances found for the corresponding circuit elements are: 15%, 15%, 15%, 10%, 2%, 2%, 15%.

- The circuit from Fig. 1 was tested here subject to another output voltage constraints: The output voltage should be constant 15 ± 0.15 V and the desired value *Jd* = 15.00 V. In this case the constraints are stronger than in the first one. The tolerances are accepted to be 1% for all circuit elements. At the initial solution 2 from 100 randomly generated circuits had an output voltage above 15.15 V, i. e. *F*=2, when *m*=100, tol_j = 1%, j = 1,…,7;. The elements which have influence on the circuit output value are R_2, R_4, R_5 and R_6. At *Step* 3 are calculated: σ_2 = 1.68, σ_4 = 3.04, σ_5 = 39.76, σ_6 = 39.23. As sensitive are accepted the elements R_5 and R_6. The reduced dimension of the search space is 2. The results obtained after the first DCSDR iteration are presented in Table 1.

Higher tolerance values for the found solution x_t lead to fail.

TABLE 1

Solution	*F*	R1 [Ω]	R2 [Ω]	R3 [Ω]	R4 [Ω]	R5 [Ω]	R6 [Ω]	C1 [μF]
$x^{(0)}$	2	1800	100	470	820	449	1356	5
x^B		1800	100	470	820	455	1355	5
x^W		1798	100	472	824	452	1363	5
$x^{(1)}\lambda$=2		1800	100	470	820	461	1372	5
$x^{(2)}\lambda$=1.5		1800	100	470	820	460	1359	5
x_t	0	1800	100	470	820	459	1362	5

B. Design centering of pulse controlled voltage regulator

A pulse controlled voltage regulator from [1] is used as second experimental circuit. It is presented on Fig. 2

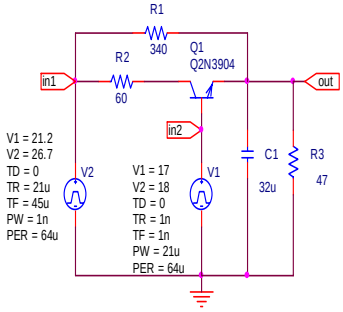

Fig. 2. Pulse controlled voltage regulator

The parameters that can be optimized are the resistors R_1, R_2, R_3 and the capacitor C_1. The output voltage of the circuit should be constant 15 ± 0.15 V and the desired value *Jd* = 15.00 V. The tolerances are accepted to be 10% for all circuit elements. At the initial solution 53 from 100 randomly generated circuits violated the constraint on the output voltage value, so *F* = 53. At *Step* 3 are calculated: σ_1 = 0.57, σ_2 = 1.81, σ_3 = 3.7, σ_4 = 0.027. As sensitive are accepted the elements R_2 and R_3. The reduced dimension of the search space is 2. The first DCSDR iteration was unsuccessful. The method from [5] would stop the optimization without finding a better solution. A look at the output voltage histogram from Fig. 3 (upper one) could explain this drawback. The histogram of the stabilized output voltage value for the initial design is close to Gaussian distribution and means, which is 14.987 V, is very close to the desired value of 15 V. To overcome the mentioned drawback the new *Step* 10 is added to DCSDR method. The design centering continues following the improved method. The fail is reduced for the optimal circuit values from 53% to 33%. The histogram for the stabilized output voltage for the optimized circuit is presented on Fig. 3 (the lower one). The means in this case is 15.027 V.

The distribution in the optimized design is similar to the initial one, but slowly shifted to the right and thus follows better the constraints. The optimized element values will be a better start point for a future optimal tolerancing and will permit 100% yield (0% fail - F=0) with lower tolerance reduction, than in the initial case. The results for the optimization steps are presented in Table 2.

TABLE 2

Solution	F	R1 [Ω]	R2 [Ω]	R3 [Ω]	C1 [μF]
$x^{(0)}$	53	340	60	47	32
x^{B}		341	60	47	32
x^{W}		340	57	37	34
$x^{(1)}$ λ=2		340	57	57	32
$x^{(2)}$ λ=1.5		340	59	45	32
$x^{(3)}$ λ=2		340	58	49	32
x_t	59	340	58	48	32
x	33	340	61	49	32

The histograms of the circuit before and after design centering from Fig. 2 are presented on Fig. 3.

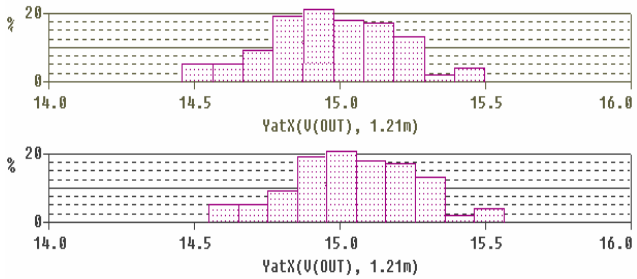

Fig. 3. Histograms for the output voltage of pulse controlled voltage regulator before and after design centering

IV. Conclusion

The paper presents the improved version of DCSDR method for design centering using search space with reduced dimension. Comparing the efficiency of FDC method [4] and of DCSDR method [5], the last method is more efficient because it performs (*itlim*+1) Monte Carlo analyses and *itlim*.(*k*+1) evaluations of $J(x)$. The FDC method performs [(*n*+1) + *itlim*] Monte Carlo analyses. For the test experiments here one Monte Carlo analysis generates 100 random circuits, i. e. 100 evaluations of $J(x)$ are calculated. Usually $n > k$ and the iteration limit *itlim* is a small positive integer. The improved DCSDR method performs one more Monte Carlo analysis if Step 10 is used at the end of calculations, but this method is able to solve design centering tasks when the initial design values are close to the optimal ones. This case was unapproachable by the method from [5]. The new method was tested on three different circuit designs, which confirmed its advantages compared to the former version.

Acknowledgement

This research is partly supported by The National Science Fund, MON, Bulgaria, Project I-1203/2002

References

[1] G. I. Marinova, D. I. Dimitrov "Statistical estimation of multiple realizations in radiocommunication modules synthesis", proposed for ICEST'2005, June 29 - July 1, Nis, Serbia and Montenegro, 2005.

[2] G. I. Marinova, D. I. Dimitrov "Statistical analysis and optimization of voltage regulator circuit using IESD and ORCAD environment", ICEST'2003, October 16-18, Sofia, Bulgaria, 2003, pp. 478-482.

[3] G. Marinova "Statistical design simulator for electronic design – IESD", *The European Design and Test Conference*, *Users Forum*, Paris, March 11-14, 1996, pp. 297.

[4] G. Marinova, V. Guliashki, "Fast design centering method for electronic circuits", Proceedings of 6th International Conference on Telecommunications in Modern Satellite, Cable and Broadcasting Services TELSIKS'2003, Nis, Serbia and Montenegro, 2003, pp. 701-704.

[5] G. Marinova, V. Guliashki, D. Dimitrov, "A design centering method with space dimension reduction", Proceedings of ELEKTRONIKA'2004 Conference, Sofia, Bulgaria, 21-22. 05. 2004, pp. 134-139.

[6] G. V. Reklaitis, Ravindran A., Ragsdell K. M. „*Engineering Optimization. Methods and Applications*", John Wiley and Sons, 1983.

[7] Zhang J. C. and M. A. Styblinski, "*Yield and variability optimization of integrated circuits*", Klewer Academic Publishers, 1995.

Graphical Application Development Environment for Analog Microcontrollers

George T. Nikolov[1], Marin B. Marinov[2], Boyanka M. Nikolova[3]

Abstract – **Analog microcontrollers' development is one of the fastest growing segments of engineering, and will continue to be for the foreseeable future as consumers demand smarter cars, appliances, intelligent sensors, and so on. The evolution of these commercial technologies will propel virtual instrumentation into being more applicable to a growing number of applications. In present paper the approach of integrating these advanced technologies in one environment is proposed.**

Keywords – **Analog Microcontrollers, Embedded Systems, Virtual Instrumentation, Graphical ADE, LabVIEW.**

I. INTRODUCTION

The analog microcontrollers combine precision analog functions, such as high resolution ADCs, DACs, voltage and current references, with an industry-standard microcontroller and embedded flash memory. With theirs mixed-signal IC architecture, they delivers on the needs of today's sensor and measurement systems designers. Using their functionality it is possible to significantly increase the performance and dramatically cut the development time of data acquisition systems.

The base building blocks of typical analog microcontroller (Analog Devices ΣΔ MicroConverter ADuC834Products) are shown in fig.1.

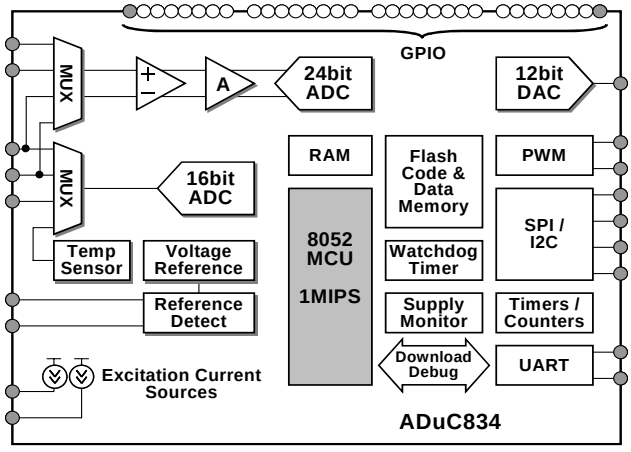

Figure 1 The building blocks of analog microcontroller

[1]George T. Nikolov - Faculty of Electronics, Technical University of Sofia, 8 "Kliment Ohridski" Bld., Sofia, Bulgaria, E-mail: gnikolov@tu-sofia.bg
[2]Marin B. Marinov - Faculty of Electronics, Technical University of Sofia, E-mail: mbm@tu-sofia.bg
[3]Boyanka M. Nikolova - Faculty of Communications, Technical University of Sofia, E-mail: bnikol@tu-sofia.bg

As can be considered by reconfigurations and reprogramming of these blocks the developer can compose a multitude of measurement configurations.

One of the features of the more of the analog microcontroller's product is the ability of the device to download code to its on-chip program memory [1]. This in-circuit code download feature is usually conducted over the device serial port. Serial download capability allows developers to re-program the part while it is soldered directly onto the target system avoiding the need for an external device programmer. Serial download also opens up the possibility of system upgrades in the field. This means that users can upgrade system firmware in the field without having to swap out the device.

The great disadvantage of such system firmware upgrading is the necessity of low-level programming. Although there is library of ANCI-C functions, currently targeted at the Keil environment [2], the lack of integrated software framework for microcontrollers is obviously. This framework must decrease the complexities of integrating multiple measurement devices into a single system by providing standard interfaces to all I/O devices, and must provide development tools to rapidly configure, build, deploy, maintain, and modify high-performance measurement and control solutions.

In last few yeas Application Development Environments (ADEs) play a critical role in a measurement and automation software framework. With these tools, the system developers design and integrate the system that takes measurements, controls processes, implements calibration and linearization routines, displays information to the end user or connects with other applications. In addition it is imperative that the ADE provide high-level, intuitive development paradigms so that a wide variety of users can rapidly build measurement and control systems. Obviously, the ADEs used to develop such measurement solutions should provide an easy-to-use design model, compiled performance, and application-level programming flexibility for a complete range of applications.

For maximum development productivity, the ADE should include comprehensive statistical and numerical analysis functions, as well as high-performance signal processing and control algorithms common in measurement applications including functions such logic control, noise reduction, spectral measurements, digital filtering, signal detection, numerical integration and differentiation, curve fitting, fractional-octave analysis, and order analysis.

It is well known that National Instruments LabVIEW is one of an industry-leading ADE for designing test, measurement and control systems [5]. It provides an easy-to-use application development environment designed specifically for the needs of engineers and scientists. LabVIEW offers powerful features

that make is easy to connect to a wide variety of hardware and other software.

One of the most powerful features that LabVIEW offers is its graphical programming environment. With LabVIEW, it is easy to design custom virtual instruments by creating a graphical user interface on the computer screen through which the user can:

- Operate the instrumentation program;
- Control selected hardware;
- Manipulate and analyze acquired data;
- Display and publish results.

In addition the benefits offered by Lab VIEW and concerning concretely the analog microcontrollers are:

- Visualize the microcontroller's configuration;
- Ability of fast reconfiguration for acquires various measurement data;
- Easy to implement calibration and linearization techniques.

Although LabVIEW provides the tools required for most applications, LabVIEW also is an open development environment. This mean that the developers can easy upgrade or create new applications without discontinue the working programs.

The underlying idea promoted in this presentation is to create measurement system based on analog microcontroller in such way that the hardware only to converts the incoming signals into digital signals that is sent to the computer. The microcontroller device does not compute or calculates the final measurement. That task is left to the software that resides in the computer. The same devices can perform a multitude of measurements by simply changing the software application that is reading the data. So in addition to controlling, measuring and displaying the data the user application for an ADE based microcontroller system also play the role of the firmware that would exist inside in special purpose measurement system.

The principal approach to integrate the Analog Devices family of precision analog microcontrollers in LabVIEW ADE is described in next section.

II. Including Analog Microcontrollers in LabVIEW

As with LabVIEW, engineers interface with real-world signals, analyze data for meaningful information, and share results and applications, than the environment can be observed as be composed of three base parts. The first one is for data acquisition, second for data manipulation and analyzing, and the last one for data presentation and publishing. Following this division the developed ADE for analog microcontrollers just like is divided in three parts:

- Downloader consisting of number of programs and functions that controls data acquisition;
- Library consisting of created and build-in Virtual Instruments (VI) and subVI for data manipulation and
- Number of top level VI for data representation.

As has been mentioned the serial download capability of ADuC family microcontrollers allows users to re-program the device while it is assembled onto the target system. The core of presented graphical ADE is so called downloader created in LabVIEW. The downloader consists of number of Virtual Instruments (VIs) witch hierarchy is shown in fig.2. The brief description of each VI purpose follows:

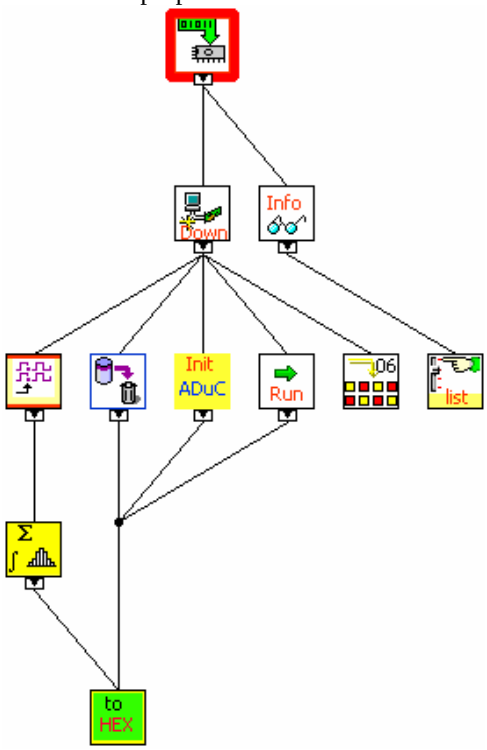

Figure 2 The downloader's hierarchy

ADuC_Program Select.vi This is a subVI that shows the files in Intel HEX format available in library (folder HEX Application). The folder HEX Application has been done specially for developers to keep the created downloadable programs (in HEX format), their descriptions (in txt format), and configuration of MicroConverter for each program (in jpg format).

ADuC_Downloader.vi By this subVI the user can select the appropriate program in Intel HEX format ant download it in the processor embedded in ADuC3xx family Analog Microcontrollers (8052 core).

ADuC_Create Application List.vi The subVI reads the application directory. Any HEX and TEX file which are contained in the directory (HEX Application) are listed. If the files are available and are successfully opened the Title of the files window is read and placed in a list which will be used to create a selection list.

ADuC_Initialise.vi The subVI send the data package via Serial VI to interrogate the ADuC3xx connected in serial port. It performs a VISA's Serial Port Write and Serial Port Read. If the communication is realized the ADuC must return the interrogation data <name> and version of embedded downloader.

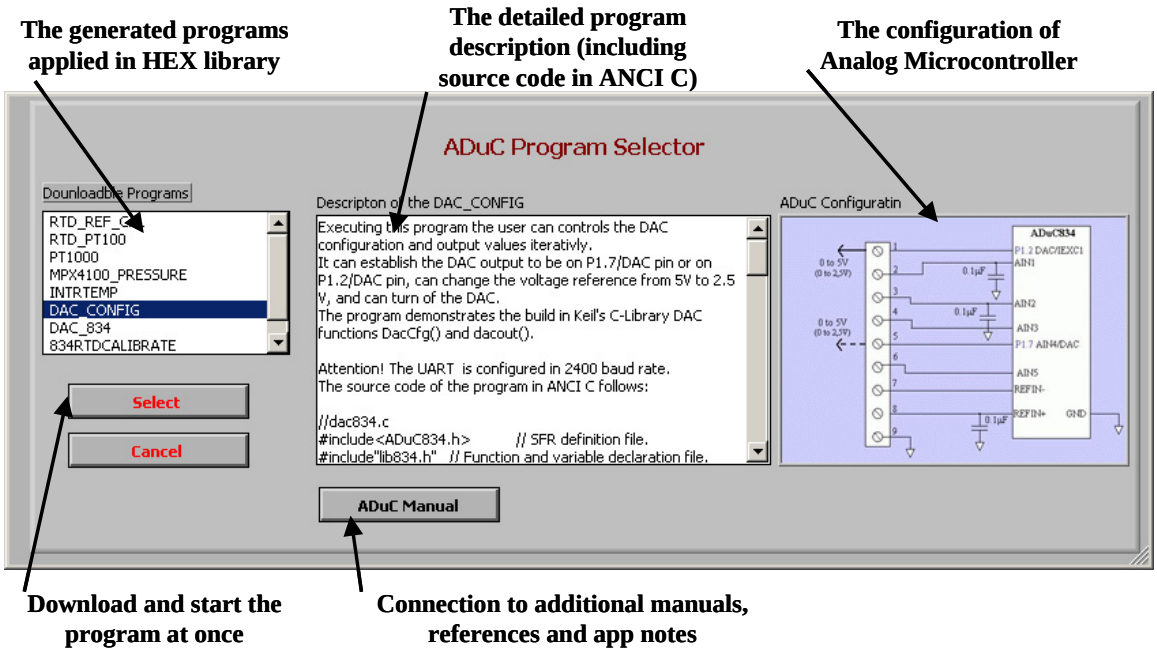

Figure 3 The initial user interface

ADuC_Erase_Memory.vi The subVI erases memory before downloading a program.

ADuC_Download.vi This subVI is the core of downloader. It gets the HEX data and sent it to ADuC3xx program memory.

ADuC_Run_ACK.vi This subVI performs diagnostic function. It is used to read ACK when the HEX program running successfully.

ADuC_Run.vi The subVI starts the program execution.

ADuC_Convert to Hex String.vi This VI Converts download Data packets from decimal string to hexadesimal string.

ADuC_Check Sum.vi This subVI check sum for Intel HEX format and append check sum value to HEX string.

An example demonstrating the benefits of graphical ADE is shown in figure 3. The initial user interface that appears when the user executes the graphical downloader consists from three main dialog windows.

The available programs in folder HEX Application are listed in left upper corner of the user interface. It is necessary to note that only HEX files that have appended description files with same name would be appeared in the list.

In the center of the user interface the detailed description of programs is positioned. This description includes the base functionality of program, the serial poll baud rate, and if is possible the source code in ANCI C.

The image suggesting the user how to make external connections for properly operation of measurement system is located in the right part of the user interface. This removes the necessity of weary searching the information in additional documentations for pin names, connector numbers, types, ets.

When the user choose the appropriate program he has opportunity to interrogate, erase memory, download and run the program at once by simple pushing the button “Select”. All mentioned activities are left invisible for the developer.

In order to add new application in the folder HEX Applications the developer must fulfill the following steps:

- Create or acquire the program code in standard Intel HEX format.
- Wright or take some available documentation describing the program’s functionality and characteristic.
- Save the documentation in plain text format.
- Draw the configuration of analog microcontroller and save the schematics in JPEG format.

The developer must keep in mind that for propriety recognition the names of these three files must be equal.

The second part of suggested ADE consists of various VIs and subVIs for data manipulation. Some of these VIs are buid-in LabVIEW libraries of functions and some for their particularity are created additionally.

LabVIEW has more than four hundred build-in function designing specifically for extracting useful information from set of acquired data. Examples include mathematics, frequency analyses, peak detection, curve fitting, statistics, and many more. It is obvious that developer after acquiring data from analog microcontroller as decimal (or hexadecimal) digits has a great number of opportunities to scale data as necessity. He can be involve calibration coefficients, make linearization by polynomial curve fitting, establish optimization procedures, etc.

The third piece of the introduced graphical environment is

presentation, which encompasses data visualization, user interface design, web-publishing, report generation and data management. Because LabVIEW was designed specifically for engineers and scientists, the user can take advantage of measurement-specific interface design tools.

III. Putting the Environment into Practice

Executing graphical ADE for analog microcontrollers a number of application was created and stored in library. To accomplish experiments as acquisition hardware is used the Analog Devices MicroConvertor ADuC834 (fig.1). This analog microcontroller is a complete smart transducer front end, integrating two high resolution sigma-delta ADCs (24 and 16 bits), an 8-bit MCU, and program/data Flash/EE memory on a single chip.

To illustrate the benefits of created environment some of typical examples would be applied in this section.

In Fig. 4 the graphical user interface for atmospheric pressure measurement is shown.

The measurement system is made up by simply connecting the pressure sensor MPX4100A to primary ADC inputs of microcontroller. The Motorola's MPX4100A series piezo-resistive transducer is a monolithic, signal conditioned, silicon pressure sensor [4]. This sensor provides an accurate, high-level analog output signal that is proportional to applied pressure. The ratiometric function of both the A/D converter and the pressure sensor device makes all voltage variations from the power supply rejected by the system.

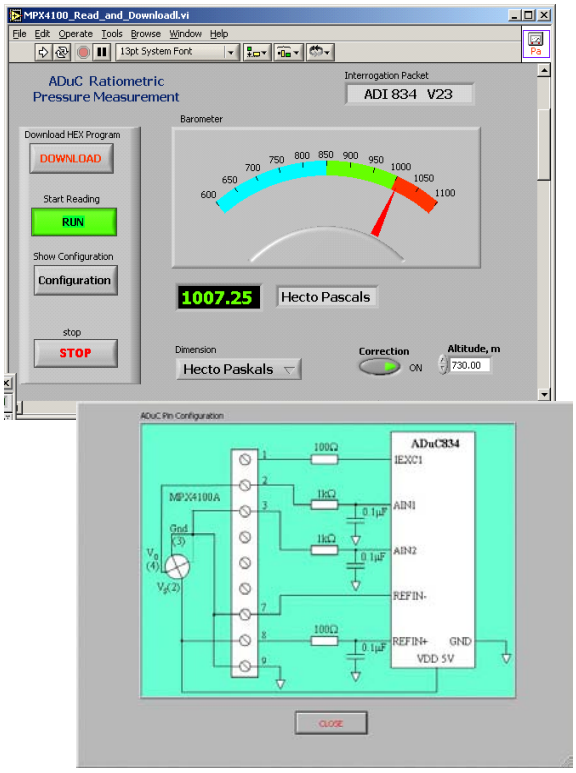

Figure 4 Atmospheric Pressure Measurement

Figure 5 shows graphical user interface for a typical analog measurement application of the ADuC834, namely an interface to an RTD (Resistive Temperature Device). The arrangement is commonly referred to as a 4 - wire RTD configuration [3]. Here, the on-chip excitation current sources are enabled to excite the sensor. The excitation current flows directly through the RTD generating a voltage across the RTD proportional to its resistance. This differential voltage is routed directly to the positive and negative inputs of the primary ADC. The same current that excited the RTD also flows through a series resistance R_{REF} generating a ratiometric voltage reference.

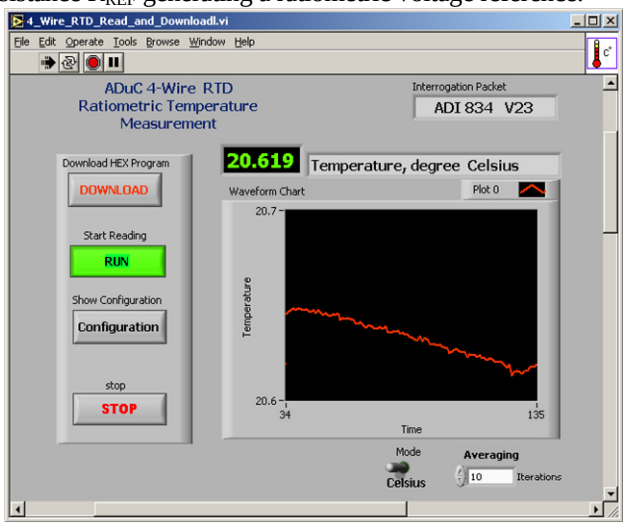

Figure 5 RTD Temperature measurement

As can be seen in the figures the user interface is designed to keep some similarity regardless of which type of physical phenomena is measured – pressure, temperature or any other.

In the left part of interface are positioned the controlling buttons. Button "Download" is used to download and start program. "Run" serves data acquisition and properly manipulation for desired result representation. The "Configuration" button pushes additional window with system configuration (fig.4). "Stop" breaks the program executing.

IV. Conclusion

In order to integrate the embedded systems or particularly analog microcontrollers and virtual instrumentation in one software framework, the appropriate graphical application development environment is created. For experimental work the Analog Devices MicroConvertor ADuC834 and National Instruments LabVIEW are maintained. With insignificant modifications, the presented approach can be used also for other similarly products. Since the author's conception is based in open architecture it is possible to include continuously new programs for various applications.

References

[1] Analog Devices, "Understanding the Serial Download Protocol" Technical Note - uC004, Ver 2.1 Sept 2001.

[2] Analog Devices, "Using the ADuC834 C-library", Technical Note - uC008, Ver 0.1 Dec 2001

[3] King G., Fukushima T." RTD Interfacing and Linearization Using an ADuC8xx MicroConverter", AD, AN709, 2004.

[4] Freescale Semiconductor "Sensor Device Data Book", DL200/D, Rev. 5 2003.

[5] National Instruments, "Measurement and Automation Catalog", 2005

Comparative Analysis of Image Threshold Algorithms for VHDL Real Time Applications

Nikolay Nenov[1], Todor Djamiykov[2], Volker Zerbe[3], Dimitar Alexiev[4]

Abstract – **This paper presents comparative analysis of various threshold methods. After the analysis, the right algorithm is selected. This algorithm is appropriate for real-time applications and implementation in FPGA. It is used in an optoelectronic system for calculation of laser spot position. This system uses CMOS image sensor, which brings additional restrictions to choose a proper algorithm.**

Keywords - **Grayscale Thresholding, FPGA, Real-time Applications, CMOS image sensor.**

I. INTRODUCTION

Optoelectronic systems are widely used in industry. The goal of the described comparative analysis is to choose the proper threshold algorithm. This algorithm will be used in optoelectronic system for laser spot position measurement. The basic application of this system is: Measurement of decentre of lens and the bend of rails. The block diagram of this system is shown if Figure 1.

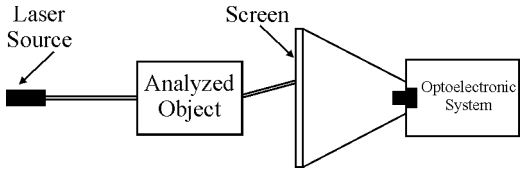

Fig.1 Block diagram of the optoelectronic system

Laser beam is used for determination of etalon direction. The beam is passed though the object and the measured parameter provokes deflection of the beam proportional to the measured value. The laser beam is projected at the transparence diffuse screen of the system and it is viewed like light spot. On the other side of this screen there is a camera of the optoelectronic system, which scans the screen with its CMOS image sensor. The output from the CMOS image sensor is processed by FPGA.

The Grayscale Image Threshold algorithm is the first step of series of calculations in the optoelectronic system for measurement of laser spot position. For the proper determination of its coordinates the spot must be separated from the background.

[1]Nikolay Nenov is with the Technical University of Sofia - Bulgaria, Faculty of Electronic Engineering and Technology
[2]Todor Djamiykov is with the Technical University of Sofia - Bulgaria, Faculty of Electronic Engineering and Technology
[3]Volker Zerbe is with the Technical University of Ilmenau - Germany, Faculty of Electronic Engineering and Technology
[4]Dimitar Alexiev is with the Technical University of Sofia - Bulgaria, Faculty of Electronic Engineering and Technology

After that the system makes calculations with all pixels belonging to the object, in order to calculate centre of mass (COM). The COM coordinates are coordinates of laser spot. The Decision of this task is connected with specific problems.

II. PROBLEM STATEMENT

In image processing applications the gray level values assigned to an object are different from gray level values of the background [1]. The pixel which belongs to the laser spot has grater intensity than background. The output of a threshold process is a binary image which is obtained by assigning pixels with values less than the threshold with zero and the remaining pixels with ones.

Let us consider that image $\boldsymbol{\varepsilon}$ is a digital image from the CMOS sensor, with M rows and N columns and L gray levels for each pixel. The pixel with coordinates (i,j) is denoted by $\boldsymbol{\varepsilon}(i,j)$. The threshold level T, is a value in the range $T \in (0,L-1)$. Let b(i,j) is a binary image and each pixel from b corresponds to the pixel from $\boldsymbol{\varepsilon}$ [1]. The threshold process is defined by Equation (1):

$$b(i,j) = \begin{cases} 0, \varepsilon(i,j) < T \\ 1, \varepsilon(i,j) \geq T \end{cases} \quad (1)$$

For the proper calculation of the coordinates of the object, an important factor is the precise definition of T.

The ideal laser spot is a circle with Gaussian distribution of energy. There are various effects which deform the laser spot. The photons from the laser beam have great value of intensity and they can saturate some pixels in the CMOS sensor. Because of internal effects in laser source and optical distortion, the spot may not be a circle and don't have Gaussian distribution of energy. The angle, in which laser beam gets the screen, also distorts the spot. Calculation of the centre of mass (COM) uses coordinates and the intensity of each pixel belongs to the object. For this reason the result of the threshold process is not a binary image – see Equation (2).

$$g(i,j) = \begin{cases} 0, \varepsilon(i,j) < T \\ \varepsilon(i,j), \varepsilon(i,j) \geq T \end{cases} \quad (2)$$

Used CMOS image sensor has VGA resolution. The laser spot is consisting of 100 to 500 pixels. This is less than 0.2% of the entire image. The laser spot is quite little and this makes the task for its separation hard. Figure 2 shows a real

image from the laser beam over a screen of the optoelectronic system.

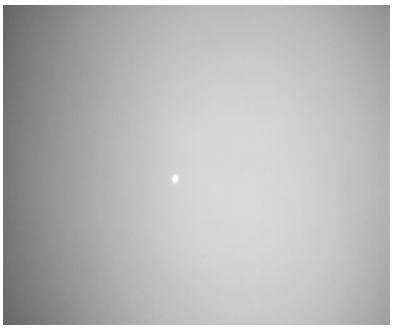

Fig. 2 Image of the laser spot over the screen of the system

III. Algorithm Survey

Because of the mentioned special features of the laser beam not all of the threshold algorithms can be used. The choice of right threshold algorithm has to be made according to the following criteria:

1. Possibility to work in real time – simple and fast algorithm, simple optoelectronic system, minimal delays, ability for work without memory. Used algorithm has to be fast and simple.
2. Possibility for work with CMOS image sensor – The information is obtained from the sensor pixel by pixel and row by row. Algorithm doesn't have to use neighbor pixels, because this requires additional memory.
3. Possibility for implementation in programmable logic device (PLD) – PLD can execute only simple mathematical operations like addition, subtraction and multiplication. The other operations require additional algorithms. With simple algorithms it is possible to perform division and calculate square root [2]. PLD's also work easy with integer numbers. Using integer numbers doesn't have to decrease the precision of used algorithm.
4. Possibility for finding small objects – separation of the image to small regions can make algorithm to find more than one object, because of local artifacts in the image. The used algorithm can not use local methods.

In the literature the threshold techniques are categorized into six groups as follows [4]:

- Histogram shape based methods. The histogram of the image is viewed as a mixture of two Gaussian distributions associated to the object and background classes: Sezan, Carlotto, Tsai, Olivo. Figure 3 is a histogram of the spot from Figure 2. It is clearly seen that the histogram has a lot of picks, due to noises and differences in illumination of the screen. MathCAD simulation shows that the pixels from the spot have level more than 230. Because small size of the spot, it do not provoke pick in the histogram. The methods based on the histogram are not applicable to solve the problem, because they do not correspond to criterion 4.

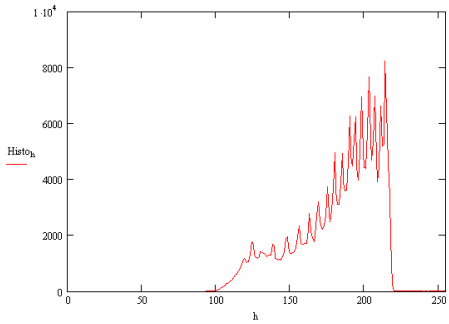

Fig. 3 Image of laser spot and its histogram

- Clustering based methods. The pixels are clustered in two classes as either background or foreground. Some of these methods are iterative: Riddler, Yanni and Otsu. They are slow methods. Some of them use complicate for realization functions like *log* or *exp*, which are hard for implementation in FPGA: Jawahar, Kittler and Lloud. These methods do not correspond to criteria 1 and 3.
- Entropy based methods. They use the difference in entropy between the foreground and background regions: Kapur, Brink, Yen and Shanbag. All of them require complicate calculations, which are difficult for implementation in programmable logic devices – criterion 3.
- Object attribute based methods. They find a measure of similarity between the grey level and the binarized images: Tsai, Hertz, and Leung. All of these methods also use complicated functions which are hard to implement in FPGA – see criterion 3.
- Spatial methods. They use higher-order probability distribution and/or correlation between pixels: Pal, Abutalep and Cheng. These methods also use hard to implement in FPGA mathematical functions and do not correspond to criterion 3.
- Local methods. They calculate the threshold value at each pixel based on the local image characteristics: Niblack, Sauvola, Bernsen, and Yasuda. These are statistic methods, making calculations over small regions from the image. They are fast methods, but not corresponding to criterion 4.

The results from the survey are shown in Table 1.

Table 1 Compare between groups of threshold algorithms

	Criterion			
Groups of Algorithms	1	2	3	4
Histogram based	✓	✓	✓	X
Clusters based	x	✓	x	✓
Entropy based	✓	✓	x	✓
Object Attribute	x	✓	x	✓
Spatial based	✓	x	x	✓
Local	✓	✓	✓	x

The table shows, that no one of these groups of threshold algorithms satisfies all criteria.

The local method of Niblack calculates threshold level using mean value and standard deviation from regions with size 15x15 pixels. In [1] it is described a global threshold algorithm of Hamadani. This method is similar to Niblack's method. The modified method of Hamadani is used in optoelectronic system.

IV. ALGORITHM DESCRIPTION

The method of Hamadani is statistic method [1]. It uses mean value m and standard deviation σ of the entire frame. The threshold level is linear combination of m and σ – Equation (3).

$$T = k_1 m + k_2 \sigma \quad (3)$$

The weights k_1 and k_2 are pre-selected, based on image type in order to optimize performance. For a given image $\varepsilon \in R^x$. The mean value is given by Equation (4):

$$m = \frac{1}{M.N} \sum_{i=1}^{M} \sum_{j=1}^{N} \varepsilon(i, j) \quad (4)$$

M and N are numbers of rows and columns in the image. Standard deviation is given by Equation (5):

$$\sigma = \sqrt{\frac{1}{M.N} \sum_{i=1}^{M} \sum_{j=1}^{N} (\varepsilon(i, j) - m)^2} \quad (5)$$

Chosen algorithm is simulated in MathCAD using various values for k_1 and k_2. Tests with 20 images of laser spots are performed. Figure 4 shows the results for image from Figure 2.

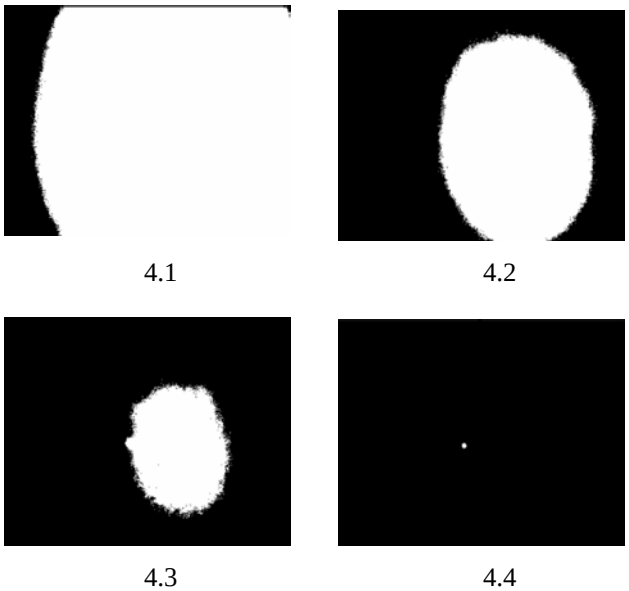

4.1 4.2

4.3 4.4

Fig. 4 Image after thresholding

Table 2 shows threshold levels for various values for k_1 and k_2 and calculated threshold level T.

Table 2 Values for k_1, k_2 and calculated threshold level T

	Coefficients		
Image	**k_1**	**k_2**	**T**
4.1	0,5	2	147
4.2	1	0,5	196
4.3	1	1	210
4.4	1	2	237

The simulation shows that the best values for k_1 and k_2 are $k_1 = 1$ and $k_2 = 2$.

V. ALGORITHM IMPLEMENTATION

The basic applications of the optoelectronic system are measurement of decentre of lens and measurement of bending of rails.

A. Measurement decentre of lens

To measure the decentre of lens, laser beam passes through geometric axis of lens and it is projected at the screen of the optoelectronic system. When the lens routing around its geometric axis, the decentre drives to deviation of the laser spot over the screen. The deviation of the laser spot is proportional to the decentre of the lens. For good measurement it is needed a big number of images for one turn of lens. Used CMOS image sensor provides 30 frames per second (33.3 ms for one frame) and optoelectronic system must calculate coordinates of the laser spot for each frame. For adaptation to the changes in illumination, the threshold level is calculated in each frame. For this reason the algorithm of Hamadani is modified. The measurement is made during two consecutive frames in which spot can move, but the mean value and the standard deviation are constants in practice.

During the first frame the mean value is calculated. In the second frame the standard deviation is calculated and at the end of the second frame the threshold level is calculated. The threshold level is used in the next (third) frame. In the second frame simultaneously with the standard deviation, the next mean value is calculated. The threshold level is calculated continuously. The algorithm is shown in Figure 5.

B. Measurement of bending of rails

For the measurement of the bending of rails, the laser source is located at the end of the rail. The laser beam gets into the screen of a measurement system. Optoelectronic system moves along the rail and makes photos at a definite distance. Each bend provokes radial moving of the system.

This is detected by the measurement system like deviation of the laser spot. The photos are not continuous and two following images can be quite different. The threshold level is calculated using one frame and this is made at each frame. The time between two following frames must be minimum 33.3 ms. In this case external SRAM memory is used. The algorithm is shown in Figure 6.

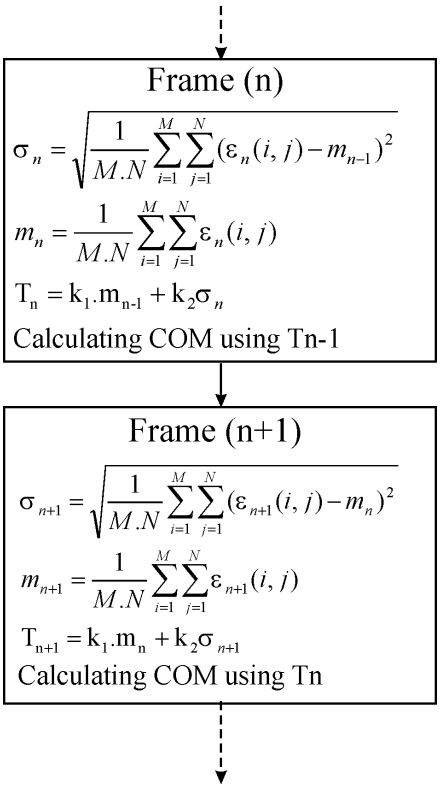

Fig. 5 Algorithm for decentre of lens measurement

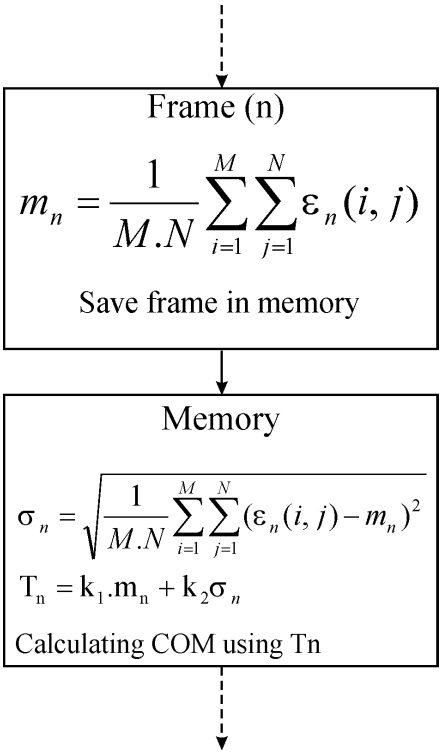

Fig. 6 Algorithm for definition the bend of rails

VI. CONCLUSION

In the paper it is made a comparison between various threshold algorithms according to offered criteria. After that the right algorithm for real-time applications is chosen. This algorithm was simulated in MathCAD. Figure 4 shows its ability to find small objects. It is implemented in FPGA like a part of complex optoelectronic system. Modified algorithms for work in real time are proposed. They are written in VHDL.

VII. REFERENCES

[1] Ritter, G. X. Computer Vision Algorithms in Image Algebra, New York, CRC Press, 2001.
[2] Roth, Ch. H. Digital System Design using VHDL, International Thomson Publishing, 1998.
[3] Parker, J. R. Algorithms for Image Processing and Computer Vision, New York, John Wiley & Sons Inc, 1997.
[4] Sezgin M. Survey over image thresholding techniques and quantitative performance evaluation, Journal of Electronic Imaging 13 (1), pp. 146 – 165 (January 2004).

Statistical Estimation of Multiple Realizations in Analog Synthesis

Galia I. Marinova[1], Dimitar I. Dimitrov[2]

Abstract - **The paper presents a method for statistical estimation of multiple realizations in analog circuit synthesis. The case study of a frequency converter with different power supply realizations is presented as an implementation of the method for combinatorial optimization of a design with multisolution synthesis in radiocommunications. The statistical estimation permits also to exanimate the influence between the different stages in a module.**

Keywords: **- statistical optimization, radiocommunications modules, analog circuit synthesis, switch mode power supply, frequency converter**

I. Introduction

The paper presents a method for statistical estimation of multiple realizations of analog circuits. The method develops the statistical optimization methodology with the simulators IESD and ORCAD/PSpice 9.2 from [4] and it is based on the theory for statistical optimization of a design in case of multiple synthesis solutions, presented in [5]. More theoretical aspects for statistical optimization are presented in [7]. The method permits to compare different synthesis solutions for a circuit, with given specifications and constraints, through the statistical estimation for each solution. It permits also to estimate statistically the mutual influences between the different stages integrated in a module. A case study is proposed for different power supply solutions of a frequency converter for radiocommunications. Two synthesis solutions are studied for the 15VDC power supply of the frequency converter - realization of the output voltage stabilization with a voltage regulator (VR) circuit and another realization with a switch mode power supply (SMPS) circuit. The voltage regulator and the switch mode power supply are studied and optimized nominally and statistically. The frequency converter is first studied with an ideal power supply of 15Vdc and then it is integrated with the VR and SMPS circuits. A goal function is defined for the determination of the optimal solution for the synthesis of the frequency converter module with a power supply circuit. The different synthesis solutions are simulated and estimated statistically and the optimal design solution is determined. The mutual influences between the frequency converter and the two power supply circuits are estimated and some conclusions are draft for their performances.

[1]Galia I. Marinova is with the Faculty of Communications and Communications Technologies, TUS, Kliment Ohridski 8, 1000 Sofia, Bulgaria, e-mail: gim@tu-sofia.bg

[2] Dimitar I. Dimitrov is with the Faculty of Communications and Communications Technologies, TUS, Bulgaria, e-mail: ddim@tu-sofia.bg

II. Multisolution Synthesis of a Module for Radiocommunications

Multiple synthesis solutions for the power supply of a frequency converter module are studied. It is an implementation of the method proposed, in radiocommunications.

A. Multisolution synthesis of a frequency converter realized with different power supply circuits

Figure 1 presents the frequency converter (FC) from [3] and three synthesis solutions: figure 1a, whit an ideal 15Vdc voltage power supply; figure 1b, where the stabilized voltage comes from a voltage regulator circuit; figure 1c, where the stabilized voltage comes from a switch mode power supply.

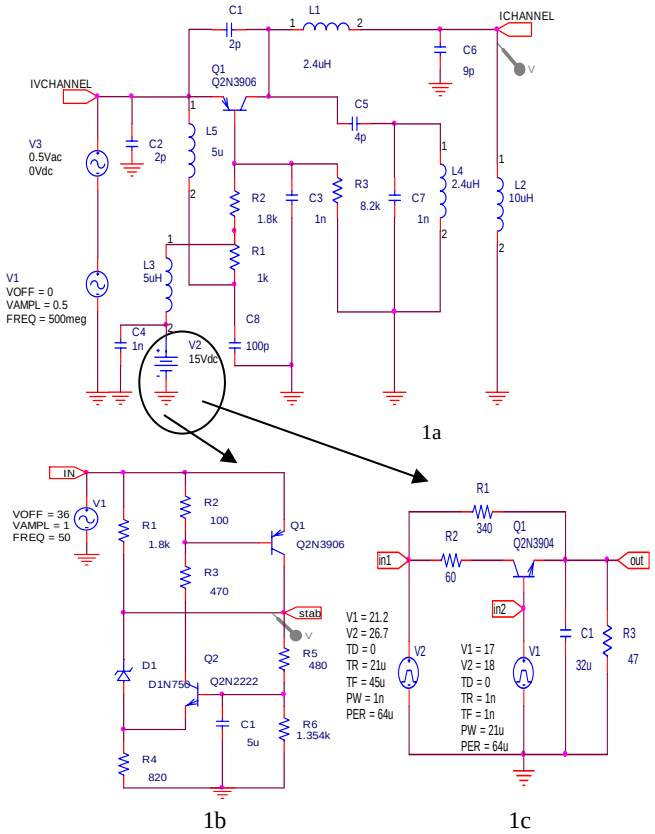

Figure 1. Multisolution synthesis of a frequency converter with different power supplies a)frequency converter with ideal power supply of 15dc b) voltage regulator circuit c) switch mode power supply circuit

The circuits from figures 1a,1b and 1c are studied nominally and statistically. The statistical optimization of FC is studied in [3].

B. Nominal and statistical estimations of the power supply circuits

The specification of the power supply circuit is to provide a 15V stabilized output voltage with less than 1% pulsation. The constraints on the DC voltage statistical variations are defined for each circuit.

- **Voltage regulator circuit**

The voltage regulator (VR) circuit from figure 1b is studied and optimized nominally and statistically in [2]. There the circuit is specified for 24V stabilized voltage. In order to integrate VR with the frequency converter module, the stabilized voltage is specified to 15V and the design is parameterized through a new value for R6=1.354kΩ. The input and output voltages obtained from nominal simulation with ORCAD/PSpice 9.2 in time area for the VR are presented on Figure 2a. Figure 3a presents the 100 Monte Carlo simulation runs in Time area for the stabilized voltage, of the VR with the optimal tolerance values defined from [2]. The VR elements have the following parameters:

VR={1.8kΩ,15%; R2=100Ω,15%;R3=470Ω,15%;
R4=820Ω,10%; R5=480Ω,1%; R6=1.354k Ω,1%;
C1=5μF,15%}

- **Switch mode power supply**

The circuit of the switch mode power supply is presented on figure 1c. It is studied analytically in [1].

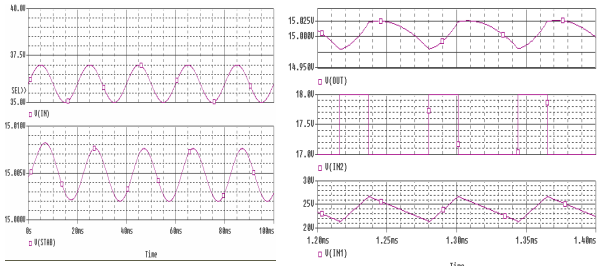

2a 2b

Figure 2. Nominal response in time domain a) input and output stabilized voltages of the voltage regulator b) iput pulses and output stabilized voltages of the switch mode power supply

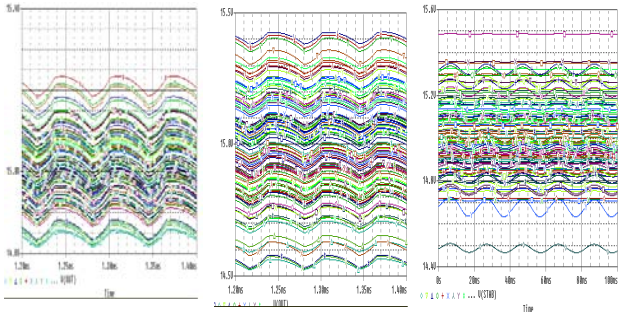

Figure 3. Statistical simulation of the voltage regulator and the switch mode power supply a) stabilized voltage of the voltage regulator b) stabilized voltage of the initial design of the SMPS c) stabilized voltage of the statistically optimized SMPS design

The nominal design from [1] was for 195V stabilized voltage and it is modified for 15V stabilized voltage through the parameter definition of the pulse voltages V1 and V2, which control the stabilized voltage value. Figure 2b presents the nominal response in time domain for the input pulses and the output stabilized voltage for the SMPS.
The goal function for optimal tolerancing of the SMPS circuit is to obtain the maximal tolerance values that guarantee 100% yield following the circuit constraints for VDC=15V±1%, and for output voltage pulsation amplitude inferior than 0.15V. As for all runs the pulsation is inferior than 0.15V, the goal function takes in consideration only the constraints on the output voltage. The goal function is defined as follows:

Max tol(R1,R2,R3,C1)
[V1pulse(21.2V, 26.7V,0.21μs,45μs, 1ns, 64μs),
V2pulse(17V, 18V,0,1ns, 1ns, 64μs),
Vdc=15V±0.15V, VMpulsatios<0.15V]

The statistical design steps for the optimal tolerancing of the SMPS are presented in table 2.

TABLE 1. OPTIMAL TOLERANCING STEPS FOR THE SMPS CIRCUIT

SMPS elements	Step1	Step2	Step3
R1	15%	5%	5%
R2	15%	15%	15%
C1	15%	15%	15%
R3	15%	5%	2%
Stabilized voltage Vdc	14.56-15.42V	14.79-15.27V	14.852-15.15V
Yield Fail	60% 40%	85% 15%	100% 0%

The optimal design of the SMPS circuit is determined as:

SMPS={R1=340Ω,5%; R2=60Ω,15%; R3=47Ω,2%,
C1=32μF,15%}

Figure 2b presents the statistical simulation results in time area for the output voltage of the initial SMPS circuit from step 1 in Table 1. Figure 2c presents the output voltage for the statistically optimized SMPS circuit from step 3 in Table1.

III. STATISTICAL ESTIMATION OF THE MULTIPLE REALIZATIONS OF THE FREQUENCY CONVERTER MODULE WITH DIFFERENT POWER SUPPLIES

A goal function is defined for the statistical optimization of the synthesized modules integrating FC with a power supply. The different synthesized solutions are analyzed nominally and statistically and then they are estimated statistically. The influence of the FC circuit on the power supply circuits is determined.

A. Goal function for combinatorial optimization of the frequency converter module with different power supplies

The constraints for the frequency converter parameters are defined from the telecommunication standards in [6]. The three circuit realizations are:

C1=C(FC,Vdc=15V) - FC with ideal 15VDC power supply
C2=C(FC,Vdc(VR)) - FC with VR
C3=C(FC,Vdc(SMPS)) - FC with SMPS

The results from the Monte Carlo simulations in time and frequency area, for each realization, are defined as follows:

MC(C1)={T±ΔT(C1),F±ΔF(C1),SNR(50MHz) ±ΔSNR(C1), THD±ΔTHD(C1)}
MC(C2)={T±ΔT(C2),F±ΔF(C2),SNR(50MHz) ±ΔSNR(C2), THD±ΔTHD(C2)}
MC(C3)={T±ΔT(C3),F±ΔF(C3),SNR(50MHz) ±ΔSNR(C3), THD±ΔTHD(C3)}

The yield and the fail, for each circuit realization, are defined as:
m-number of MC runs for a circuit

$$Yield(C)=Yield(MC(C),m)=\frac{\sum_{k=1}^{m} Yk \cdot 100\%}{m},$$

$$Fail(C)=100\%-Yield(C)$$

k=1,m
Tk∈20ns±5% (Fk∈50MHz±5%)
& THDk<20%
&SNRk(50MHz)>40dB
=> Yk=1
Tk∉20ns±5% (Fk∈ 50MHz±5%)
& THDk>20%
&SNRk(50MHz)<40dB
=> Yk=1

The goal function for the optimal circuit design from the multiple synthesis solutions is defined as follows:

Copt = C1, Yield(ci)=100%(Fail=0%),
Min(T(Ci)-20ns) & Min ΔT(Ci),
[Min(F(Ci)-50MHz) & Min ΔF(Ci)]
& Min THD(Ci) & MinTHD_H(Ci)
& Max SNR(Ci) & MaxSNR_L(Ci)

where THD_H(Ci) is the higher value for the THD coefficient for all the Monte Carlo runs of the circuit Ci
MaxSNR_L(Ci) is the lower value for the SNR for all the Monte Carlo runs of the circuit Ci.

As the goal function includes several criteria it could occur different circuit realizations to be optimal for different criteria. In order to define the optimal solution, a priority of the different criteria in the goal function should be defined.

B. Statistical simulation of the multiple realizations of the frequency converter module

Figure 4a presents the realization of the frequency converter module with a voltage regulator and figure 4b presents the realization of the FC with a switch mode power supply circuit.

Figure 5a and 5b present the results from the Monte Carlo simulations in time and AC area for the stabilized voltage, the output voltage and the SNR, of the circuits C2 and C3.

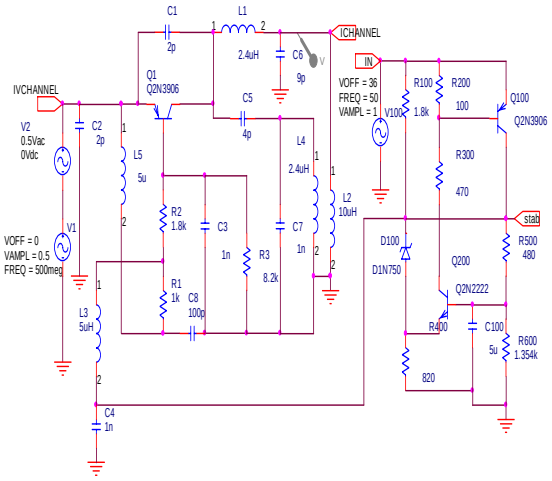

Figure 4a. Frequency converter with voltage regulator

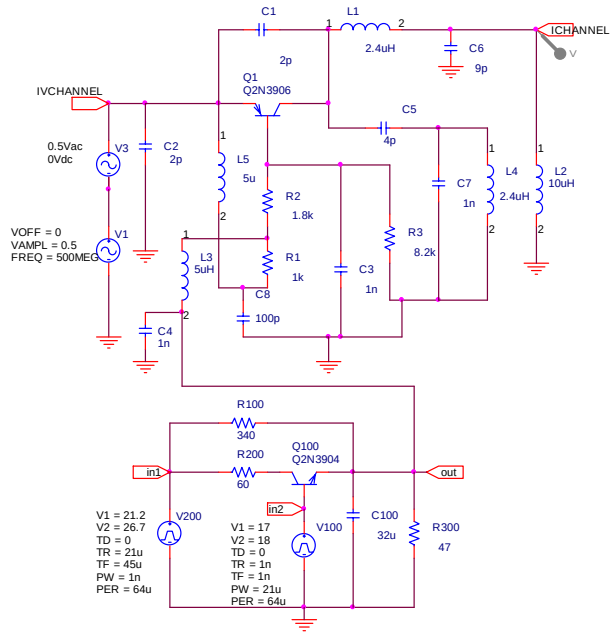

Figure 4b. Frequency converter with switch mode power supply

Table 2 presents the estimations of the different synthesis solutions for the frequency converter module. These estimations will serve the application of the criteria from the goal function.

Table 2 permits to determine the influence of the statistical variations of the power supply circuits on the FC behavior, and to define the influence of the statistical variations of the FC on the different power supplies. It permits also to compare the different power supply realizations with the case of ideal 15VDC power supply of the FC.

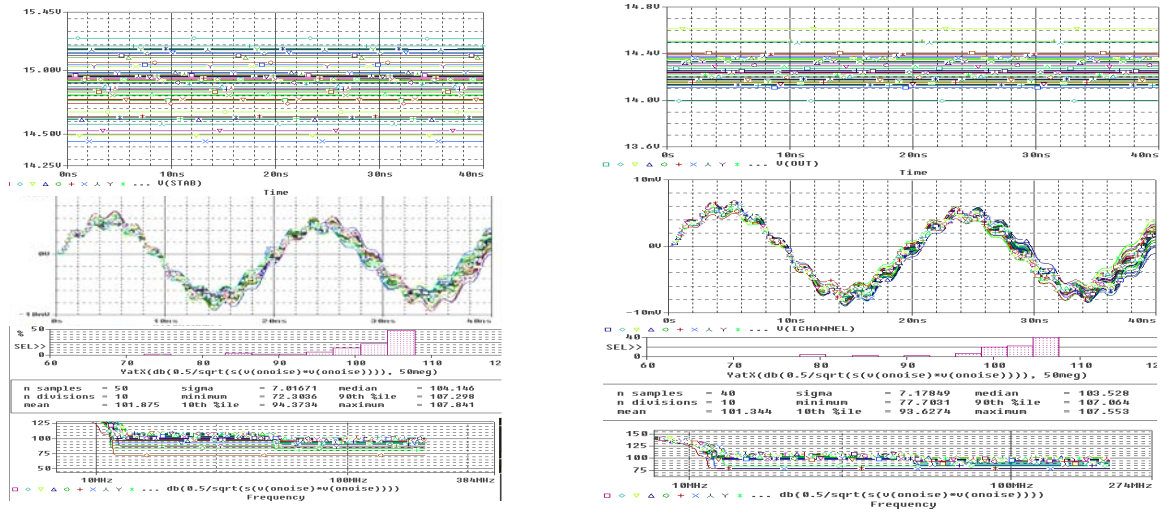

5a 5b

Figure 5. Results from Monte Carlo simulations in time and AC area for the stabilized voltage, the output volatge and the signal to noise ratio a) for the FC and VR b) for the FC and SMPS

TABLE 2. NOMINAL AND STATISTICAL ESTIMATIONS OF THE DIFFERENT SYNTHESIS SOLUTIONS FOR THE FREQUENCY CONVERTER MODULE

Multiple realizations of the FC module with different power supplies / **Nominal and statistical simulation of the different synthesis solutions for the FC module**	**C1(FC,15Vdc)**	**C2(FC,Vdc(VR))**	**C3(FC, Vdc(SMPS))**
	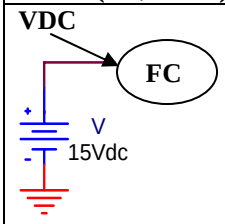	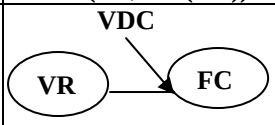	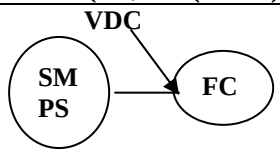
Nominal design of the frequency converter	Vdc=15V T=20ns F=50MHz THD=4.54% SNR(50MHz)=109dB	Nominal design of the voltage regulator	Nominal design of the switch controlled power supply
		Vdc=14.961V T=20.222ns F=49.45MHz TDH=10.45% SNR=106.489dB	Vdc = 14.274V T= 20.453ns F=48.9MHz TDH=9% SNR=86dB
		Optimal design of the voltage regulator	Optimal design of the switch controlled power supply
		Vdc =14-15.34V T=19.61-20.70-21.05ns F=48.3-51MHz TDH=6.4-12.16% SNR=105.77-106.343dB	Vdc = 14.127-14.651V T=20.2-20.57ns F=48.61-49.5 TDH=8.6-11% SNR=106.4-106.7dB
Optimal design of the frequency converter obtained by optimal tolerancing	Vdc=15V T=19.3-20.7ns F=48.3-51.84MHz THD=2.47-16.4% SNR=82-108dB	Nominal design of the voltage regulator	Nominal design of the voltage regulator
		Vdc = 14.96-14.962V	Vdc =14.2702-14.2784V
		Optimal design of the voltage regulator	Optimal design of the switch controlled power supply
		Vdc = 14-15.24V T=19.14-20.77ns F=48.14-52.25MHz TDH=4.91-16.78% SNR=72.3-107.8dB	Vdc = 13.99-14.65V T=19.24-20.9ns F=47.85-51.97MHz TDH=0.344-12.61% SNR=77.7-107.55dB

The comparison between the results in Table 2 for the realizations of the FC module with VR and with SMPS circuits and the results for the FC module with an ideal 15V dc power supply, show that both synthesis solutions are slightly different from the ideal case and they don't deteriorate considerably the FC module performance. The results for the nominal designs of the FC (with 0% tolerances) and the statistically optimized VR and SMPS circuits (with optimal tolerances) show the impact of the power supply variations on the FC module parameters. The variations of the power supply value influence considerably the FC parameters.

C. Statistical estimation of the influence the frequency converter has on the different power supply circuits

The influence of the FC on the stabilized voltage pulsation of the VR and of the SMPS circuits is estimated. The nominal and statistical simulation with ORCAD/PSpice 9.2 of the FC with SMPS shows that there are not pulsation from the FC induced to the stabilized SMPS voltage. But the simulations of the FC with the VR circuit show that the FC induces pulsation into the stabilized voltage. The results from the nominal simulations in time area for the stabilized voltage of the FC with VR circuit, which are presented on figure 6a show that the pulsation induced from the FC to the stabilized voltage is:

Vstab(pulsation)= {-14.892V,+0.047V}
ΔVstab(pulsation)= {-0.108V,+0.047V}
freq(Vstab(pulsation))=38MHz

The stabilized output voltage with the pulsation induced from the FC covers still the constraints for the VR circuit: Vstab=15V±0.15V.

Figures 6b and 6c present the results from statistical simulation of the pulsation induced in the stabilized voltage from the FC. The response on figure 6b is from a simulation of a nominal VR circuit (with 0% tolerances) and statistically optimized FC (with optimal tolerances). The response from figure 6c is from a simulation of the statistically optimized FC and the statistically optimized VR (both with optimal tolerances). In both cases the constraints are not broken and the yield remains 100%. These data allow to conclude that the SMPS circuit is less sensible to influences from the FC than the VR circuit is. Tables 3a and 3b present data for the variations of the stabilized voltage values for the VR and for the SMPS circuits in nominal designs and in designs where they are integrated with the FC circuit.

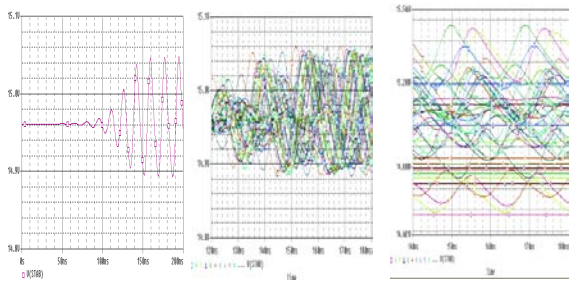

Figure 6. Pulsation of the stabilized voltage in the voltage regulator induced by the frequency converter a) nominal design FC+VR b) nominal design of the VR and optimal tolerances of the FC c) design with optimal tolerances of the FC and VR

TABLE 3A. ESTIMATIONS FOR THE VR

Voltage regulator -VR	Stabilized voltage Vdc
VR, nominal design	15V
VR, optimal tolerances	14.7-15.4V
VR nominal design FC nominal design	14.961V
VR, nominal design FC, optimal tolerances	14.96-14.962V
VR, optimal tolerances FC, optimal tolerances	14-15.24V

TABLE 3B. ESTIMATIONS FOR THE SMPS

SMPS	Stabilized voltage Vdc
SMPS, nominal design	15V
SMPS, optimal tolerances	14.85-15.15V
SMPS, nominal design FC, nominal design	14.274V
SMPS, nominal design FC, optimal tolerances	14.2702-14.2784V
SMPS, optimal tolerances FC, optimal tolerances	13.99-14.65V

The examination of these data shows that the stabilized voltage value of the SMPS circuit is less sensible to element tolerances than the stabilized voltage value of the VR circuit is. But the value of the stabilized voltage of the SMPS falls down with 720mV when it is integrated with the FC circuit. In that case the value of the stabilized voltage in VR decreases with 39mV.

IV. OPTIMAL SOLUTION FOR THE FREQUENCY CONVERTER MODULE

The two module realizations C2 and C3 are estimated following the definition of the goal function from point IIIA and results are given in table 4.

TABLE 4. ESTIMATION OF THE GOAL FUNCTION CRITERIA FOR THE TWO REALIZATIONS

Realization parameter	C2	C3	Criteria application	Optimal circuit
T-20ns	0.222ns	0.453ns	(T-20ns)(C2)< (T-20ns)(C3)	C2
ΔT	1.09ns	1.66ns	ΔT(C2)< ΔT(C3)	C2
F-50Hz	0.55MHz	1.1MHz	(F-50MHz)(C2)< (F-50MHz)(C3)	C2
ΔF	4.11MHz	4.12MHz	ΔF(C2)< ΔF(C3)	C2
THD	10.45%	9%	THD(C3)< THD(C2)	C3
THD_H	16.7%	12.61%	THD_H (C3)< THD_H(C2)	C3
SNR	106.48dB	86dB	SNR(C2)> SNR(C3)	C2
SNR_L	72.3dB	77.7dB	SNR_L (C2)< SNR_L (C3)	C3
Yield Fail	100% 0%	100% 0%	Yield(C2)= Yield(C3) Fail=(C2)= Fail(C1)	C2,C3

A general conclusion is that both solutions are suitable for FC converter module realizations Anyway depending of the priority criteria definition in the goal function an optimal solution for the frequency module with a 15V dc power supply is determined as follows:

- If the priority in the optimization criteria is given to the constraints on the period and frequency and the SNR of the output voltage, the optimal solution is the one realized with the FC and the VR:
  Copt(T(F),SNR)=C2
- If the priority in the optimization criteria is given to the THD or to the SNR_L, then the optimal solution is the one realized with the FC and the SMPS:
  Copt(THD, SNR_L)=C3.

V. CONCLUSION

The method for statistical estimation of multiple synthesis solutions, proposed in this paper was implemented for a radiocommunications example consisting in the optimal synthesis of a frequency converter module with a power supply. Two different power supply solutions (one with a voltage regulator circuit and another with a switch mode power supply circuit) were estimated and then compared following the criteria from a goal function. The optimal solution was determined depending on priorities of the criteria in the goal function. Besides this the influences between the FC,VR and SMPS circuits were studied and it was proven that the FC induces pulsation in the VR and it doesn't induce pulsation in the SMPS circuit. Although the SMPS circuit proves to be less sensitive than the VR circuit, the optimal realization of the FC module estimated on the higher priority of the constraints, on the output voltage frequency, is the module realized with the VR circuit.

The study described in this paper proves the large possibilities for implementation of the statistical estimates in optimal synthesis of analog circuits and more precisely for radiocommunication modules. Additional case studies in radiocommunications would enlarge the optimal synthesis know-how in this area.

ACKNOWLEDGEMENT

The authors acknowledge the National Science Fund for the financial support under grant I-1203/02.

REFERENCES

[1] D. Dimitrov, "Analytical expressions for calculation of pulse voltage regulator with resistor regulation", *Elektronika i elektrotehnika*, Vol. 2, 1990, pp.9-12

[2] G. Marinova, D. Dimitrov, "Statistical analysis and optimization of voltage regulator circuit using IESD and ORCAD environment", *Proceedings of XXXVIII International Scientific Conference on Information, Communication and Energy Systems and Technologies ICEST'2003*, Sofia, Bulgaria, 2003, pp. 478-482.

[3] G. Marinova, D. Dimitrov, "Statistical optimization of frequency converter for radiocommunication system", submitted to ICEST'2005, Nis, Serbia and Montenegro, 2005

[4] G. Marinova , "Statistical design simulator for electronic design – IESD", *The European Design and Test Conference, Users Forum*, Paris, March 11-14, 1996, pp. 297

[5] G. Marinova, "Statistical optimization of electronic circuits in the simulator IESD", *Proceedings of "Prilojenie na matematikata v tehnikata"*, Sofia, 1992, pp. 144-148, (in Bulgarian)

[6] Ts. Vassileva, St. Popov, "Bulgarian Telecommunications Company methodology for estimation of the technical performances of the radio and TV equipment and systems and the quality of the transmitted and emitted signals ", Sofia, 1999

[7] Zhang J. C., Styblinski M. A., "Yield and variability optimization of integrated circuits", Klewer Academic Publisher 1999

Session AE:

APPLIED ELECTROMAGNETIC

Introduction of Heaviside Criterion Fulfillment Factor for Transmission Line Analysis

Bratislav Milovanović[1], Aleksandar Marinčić[2], Nebojša Dončov[1]

Abstract –**In this paper, Heaviside criterion for TEM transmission line, that provides wave propagation along a line without dispersion, is presented. Through an introduction of Heaviside criterion fulfillment factor, an influence of per-unit length inductance increase on the transmission line behaviour is discussed. Limit values of characteristic propagation functions are derived and an analysis of their behaviour in the frequency domain for different values of proposed factor is done.**

Keywords – **transmission line, Heaviside criterion, fulfillment factor**

I. INTRODUCTION

The effect of loss on a transmission line causes attenuation and dispersion of a propagating wave. With dispersion, different frequencies in a signal spectrum propagate with different velocities and lead to distortion of any non-sinusoidal wave form. Both the attenuation and distortion resulting from loss in transmission lines were responsible for the delay in the development of long distance telephone communication of speech in the early days of the telephone. In 1893, Heaviside developed the transmission line theory based on Maxwell's equations [1], which made preconditions for a telephone transmission of human voice over a long distance. Until that time, the transmission line was described by a diffusion equation, which in circuit term, involves a distributed series resistor and paralell capacitor network.

Taking proper account of the inductance, Heaviside noticed that the effects of attenuation and distortion both decreased as inductance is increased. Analysing the frequency dependence of propagation constant, he derived the relation between the primary per-unit length parameters of transmission line (so-called Heaviside criterion) from the condition of minimum losses. When this criterion is fulfilled, both attenuation constant and velocity of propagation are independent of frequency. Transmission line with such primary parameters has an infinitive bandwidth assuming that only TEM wave propagates. In that case, an output signal is of the same waveform as an input signal; it is only attenuated and delayed in regard to the input signal.

As telecommunication lines generally have a small per-unit length inductance ($LG << RC$), Serbian scientist Mihajlo Pupin suggested that, in order to increase inductance, telephone lines should be loaded in series with discrete coils placed at regular intervals along a line [2,3]. In 1900, he experimentally verified the proposed approach in his laboratory at Columbia University in USA. This method, today well-known as Pupin loading, is still used in local and trunk telephone lines. At frequencies for which wavelength λ is a significantly greater than the spacing a of the loading coils ($\lambda >> \pi a$ [4]), pupinized line is behaved as an equivalent line obtained as if L were increased continuously along the line.

This paper represents a continuation of novel research work, presented in references [5,6], established with the main goal to enlighten the scientific achievements of Mihajlo Pupin. In this paper, an influence of per-unit length inductance increase on transmission line characteristics is presented. For that purpose, a new parameter - Heaviside criterion fulfillment factor is introduced. Also, the limit values of characteristic functions determining propagation along the line, for two end frequencies, $\omega \to 0$ and $\omega \to \infty$ are derived. Their behaviour in the frequency domain for different values of suggested factor is analysed and the appropriate conclusions are given.

II. PARAMETERS OF LOSSY TRANSMISSION LINE

Propagation constant of a lossy TEM transmission line can be expressed as [4]:

$$\gamma(\omega) = \alpha(\omega) + j\beta(\omega) = \sqrt{(R + j\omega L)(G + j\omega C)} \qquad (1)$$

where: α is an attenuation constant in Np/m or dB/m, β is a phase constant in rad/m, R, L, G and C are primary per-unit length resistance, inductance, conductance and capacitance of transmission line, respectively and ω is a radial frequency in rad/s. Solving a system of two equations, obtained by equating the real and imaginary parts of left and right side of Eq.(1), for unknown α and β, leads to:

$$\alpha^2(\omega) = \frac{RG - \omega^2 LC}{2} + \sqrt{\left(\frac{\omega^2 LC - RG}{2}\right)^2 + \left(\frac{\omega(LG + RC)}{2}\right)^2} \qquad (2)$$

$$\beta^2(\omega) = \frac{\omega^2 LC - RG}{2} + \sqrt{\left(\frac{\omega^2 LC + RG}{2}\right)^2 + \left(\frac{\omega(LG - RC)}{2}\right)^2} \qquad (3)$$

How attenuation constant depends on frequency, different components in signal spectrum will be differently attenuated. This effect, known as amplitude distortion, is combated with the use of band-pass filters, which split the signal into various frequency bands at the output end. For each band different application factor A is used so that product $\alpha(\omega)A(\omega)$ is constant at all frequencies.

Characteristic impedance of lossy TEM transmission line is a complex quantity as well and it can be calculated as:

[1]Bratislav Milovanović and Nebojša Dončov are with the Faculty of Electronic Engineering, Aleksandra Medvedeva 14, 18000 Niš, Serbia and Montenegro, E-mail: [bata,doncov]@elfak.ni.ac.yu

[2]Aleksandar Marinčić, SANU member, is with the Faculty of Electrical Engineering, Bulevar Kralja Aleksandra 73, 11000 Beograd, Serbia and Montenegro, E-mail: emarinci@etf.bg.ac.yu

$$Z_c(\omega)=|Z_c(\omega)|e^{j\varphi_c(\omega)}=\sqrt{(R+j\omega L)/(G+j\omega C)} \quad (4)$$

In telecommunications, a modulated signal is regularly propagated along the line, occupying a considerable frequency band. Two quantities can be used to define its velocity of propagation: the phase velocity, v_p, as a velocity of propagation for the carrier and the group velocity, v_g, as a velocity of propagation for the envelope of modulated signal or velocity with which energy is propagated along the line:

$$v_p(\omega)=\frac{\omega}{\beta(\omega)}, v_g(\omega)=\frac{d\omega}{d\beta(\omega)} \quad (5)$$

In reality, function $\beta(\omega)$ is not a straight line so that v_p and v_g are generally different from each other. Also, they vary with frequency. Since the group velocity represents velocity of propagation of the various components in the modulated signal frequency spectrum, the time taken for the components to be propagated along a line of given length will not be the same. Then, it would be impossible to reconstruct the spectrum of transmitted signal at output which leads to the so-called signal phase distortion. Such an effect, known as dispersion, is a great problem in telecommunications and it can be overcome by inserting expensive variable delay lines in each frequency band. For a unit length line, the phase and group delay are related to the phase and group velocity as:

$$\tau_p(\omega)=\frac{1}{v_p(\omega)}=\frac{\beta(\omega)}{\omega}, \tau_g(\omega)=\frac{1}{v_g(\omega)}=\frac{d\beta(\omega)}{d\omega} \quad (6)$$

Of possible interest for an analysis are values of previously defined parameters for $\omega\to0$ and $\omega\to\infty$. To determine them, we start from the product of phase and group delay:

$$\tau_p(\omega)\tau_g(\omega)=\frac{\beta(\omega)}{\omega}\frac{d\beta(\omega)}{d\omega}=\frac{1}{2\omega}\frac{d\beta(\omega)^2}{d\omega}=\tau_{pg}(\omega) \quad (7)$$

Finding the derivation of Eq.(3) per ω, it can be obtained:

$$\tau_{pg}(\omega)=\frac{1}{4}\left(2LC+\frac{2\omega^2L^2C^2+L^2C^2+R^2C^2}{\sqrt{(R^2+\omega^2L^2)(G^2+\omega^2C^2)}}\right) \quad (8)$$

Using L'Hopital's rule and the previous equation, the value of phase delay for $\omega\to0$ is:

$$\tau_p(\omega)|_{\omega\to0}=\sqrt{\frac{d\beta^2/d\omega}{d\omega^2/\omega}}_{|\omega\to0}=\sqrt{\tau_{pg}(\omega)|_{\omega\to0}} \quad (9)$$

$$\tau_p(\omega)_{\omega\to0}=\frac{(LG+RC)/2}{\sqrt{RG}}=\sqrt{LC}\frac{(LG+RC)/2}{\sqrt{RGLC}} \quad (10)$$

Applying $\omega\to0$ on Eq.(7) and using Eq.(9) it can be shown that the values of phase delay and group delay are equal for $\omega\to0$:

$$\tau_g(\omega)_{\omega\to0}=\frac{(LG+RC)/2}{\sqrt{RG}}=\sqrt{LC}\frac{(LG+RC)/2}{\sqrt{RGLC}} \quad (11)$$

Similarly, the values of phase and group delay for $\omega\to\infty$, can be found as:

$$\tau_p(\omega)|_{\omega\to\infty}=\tau_g(\omega)|_{\omega\to\infty}=\sqrt{LC} \quad (12)$$

The values of phase constant and characteristic impedance for these two end frequencies are easily obtained from Eqs.(3) and (4), respectively, and they are:

$$\beta(\omega)=\begin{cases}0, & \omega\to0\\ \infty, & \omega\to\infty\end{cases}, Z_c(\omega)=\begin{cases}\sqrt{R/G}, & \omega\to0\\ \sqrt{L/C}, & \omega\to\infty\end{cases} \quad (13)$$

To determine the limit values of attenuation, the following relation between attenuation and phase constant is used:

$$\alpha(\omega)=\frac{\omega(LG+RC)}{2\beta(\omega)}=\frac{(LG+RC)/2}{\beta(\omega)/\omega} \quad (14)$$

Having in mind that denominator in last equation represents phase delay whose values for two end frequencies are already determined by Eqs.(10) and (12), the values for attenuation constant for $\omega\to0$ and $\omega\to\infty$ are:

$$\alpha(\omega)=\begin{cases}\sqrt{RG}, & \omega\to0\\ \sqrt{RG}\dfrac{(LG+RC)/2}{\sqrt{RGLC}}, & \omega\to\infty\end{cases} \quad (15)$$

III. HEAVISIDE CRITERION

The condition of minimum losses is obtaned from $d\alpha^2/dL=0$ which, using Eq.(2), can be expressed as [4]:

$$\sqrt{\left(\frac{G^2+\omega^2C^2}{R^2+\omega^2L^2}\right)}\omega^2L-\omega^2C=0 \quad (16)$$

From the last equation, the well-known Heaviside criterion is yielded: $LG=RC$. When this relation is fulfilled, attenuation along a line and its characteristic impedance are independent of the frequency while a phase characteristic linearly depends on frequency. Eqs.(2), (3) and (4) are simplified:

$$\alpha(\omega)=\sqrt{RG} \quad (17)$$

$$\beta(\omega)=\omega\sqrt{LC} \quad (18)$$

$$Z_c(\omega)=\sqrt{R/G} \quad (19)$$

The transmission line with such primary per-unit length parameters, satisfying Heaviside criterion, imposes an equal phase and group delay for all components in signal spectrum which means that any signal will be propagated along the line without distortion:

$$\tau_p(\omega)=\tau_g(\omega)=\sqrt{LC} \quad (20)$$

IV. HEAVISIDE CRITERION FULFILLMENT FACTOR

For the transmission line with primary per-unit length parameters R, L, G and C, the required inductance for fuffillment factor of Heaviside criterion is obtaned as:

$$L_H=\frac{RC}{G} \quad (21)$$

We note the ration of per-unit length inductance of the line and required Heaviside's per-unit length inductance as $l=L/L_H$.

The values of characteristic propagation functions for two end frequencies $\omega\to 0$ and $\omega\to\infty$ as a function of factor l as well as their values for l=1 are given in Table 1.

Propagation functions	$\omega\to 0$	$\omega\to\infty$	*Heaviside* condition (l=1)
$\beta(\omega)$	0	∞	$\beta_H = \omega\sqrt{L_H C}$
$\alpha(\omega)/\alpha_H$	1	$\frac{(l+1)/2}{\sqrt{l}}$	$\alpha_H = \sqrt{RG}$
$\lvert Z_c(\omega)\rvert / Z_{cH}$	1	$\sqrt{l}$	$Z_{cH} = \sqrt{R/G}$
$\tau_p(\omega)/\tau_{pH}$	$(l+1)/2$	$\sqrt{l}$	$\tau_{pH} = \sqrt{L_H C}$
$\tau_g(\omega)/\tau_{gH}$	$(l+1)/2$	$\sqrt{l}$	$\tau_{gH} = \sqrt{L_H C}$

Table 1 *Values of characteristic propagation functions for $\omega\to 0$, $\omega\to\infty$ and Heaviside criterion*

In order to graphically illustrate the areas of changes of characteristic propagation functions with frequency, new functions have been introduced and shown in Fig.1:

$$f_a(l)=\frac{l+1}{2},\ f_g(l)=\sqrt{l},\ f_k(l)=\frac{f_a(l)}{f_g(l)}=f_k(1/l) \quad (22)$$

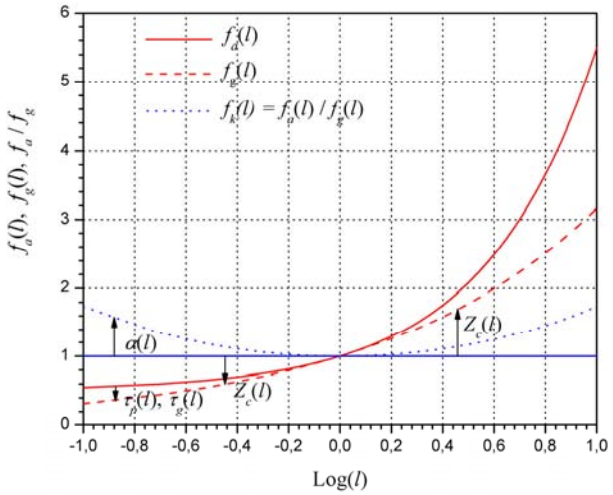

Fig.1 *Areas of changes of characteristic propagation functions with frequency versus factor l*

The lines used in telecommunications have a small per-unit length inductance and as a result, factor l is, in reality, always smaller than 1 (even with inserted Pupin coils) but for the purpose of theoretical analysis, the values of l bigger than 1 are taken into account as well. From the Fig.1 it can be noticed that the increase of factor l narrows the area of possible changes of attenuation and characteristic impedance as well as phase and group delay with frequency. This behaviour is valid until l equal to 1 and then there is a reversed proces with the further increase of l. In addition, around l=1, the changes of these parameters with frequency can be neglected. From the Table 1 and Fig.1 the following relations which identify the areas of changes of attenuation constant, characteristic impedance, phase and group delay with factor l are:

$$1 \le \alpha(\omega)/\alpha_H \le f_k(l) \quad (23)$$

$$\begin{aligned} f_g(l) \le \lvert Z_c(\omega)\rvert / Z_{cH} \le 1,\ l \le 1 \\ 1 \le \lvert Z_c(\omega)\rvert / Z_{cH} \le f_g(l),\ l \ge 1 \end{aligned} \quad (24)$$

$$f_a(l) \ge \tau_{p(g)}(\omega)/\tau_{p(g)H} \ge f_g(l) \quad (24)$$

Dependance of attenuation constant, characteristic impedance, phase and group delay, normalized with their value at fulfilled Heaviside criterion, as well as the value of phase constant for different values of factor l are shown in Figs.2,3,4,5 and 6, respectively. The considered frequency range is up to 4 KHz because it is suitable to the baseband telephone signal transmission. Besides, at these relatively low frequencies, the variation of primary per-unit length parameters with frequency can be neglected. Primary parameters used for calculation are those used for La Manche channel cable [5]: R=14.2 Ω/mile, C=138 nF/mile and G=24 μS/mile. Inductance required for fulfillment of Heaviside criterion is obtained from Eq.(21) as L_H=0.08165 H/mile. The value of factor l is changed by increasing per-unit length inductance of line.

From the Fig.2 it can be seen that normalized attenuation curves, independantly from factor l, start from 1 or α_H, and then monotonically increase approaching asymptotically, with frequency increase, to the lines determined with function $f_k(l)$. This behaviour is the same for factor l and $1/l$, because $f_k(l)=f_k(1/l)$, (curve $\alpha(l)$ is symmetrical in regard to l=1, see Fig.1).

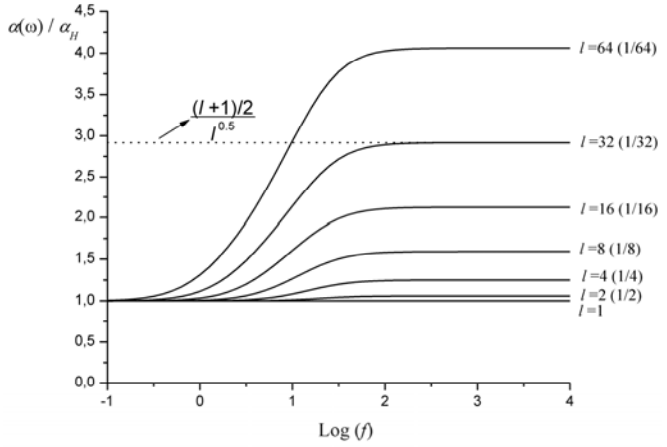

Fig.2 *Normalized function $\alpha(\omega)$ for different values of factor l*

Characteristic impedance curves show a different behaviour for factor l and $1/l$ (Fig.3). In both cases, these curves start from 1 or Z_{cH} , and with frequency, they are approaching asymptotically to the lines $f_g(l)$. However, in the first region (l<1), curves of characteristic impedance monotonically decrease, while in the second region (l>1) monotonically increase.

Curves of phase and group delay (Fig.4 and 5), for given l, start from the points defined by function $f_a(l)$ and, with frequency increase, they are approaching to the lines whose location is determined by function $f_g(l)$. In the frequency range up to 100 Hz, the changes of phase and group delay with

frequency are the most significant. For l>1 delays are greater than the values corresponding to Heaviside criterion, $\tau_{pH} = \tau_{gH}$, given in Table 1, and for l<1 inserted delays are smaller. In addition, for the same value of factor l, phase delay and group delay start from the same point and finish at the same point.

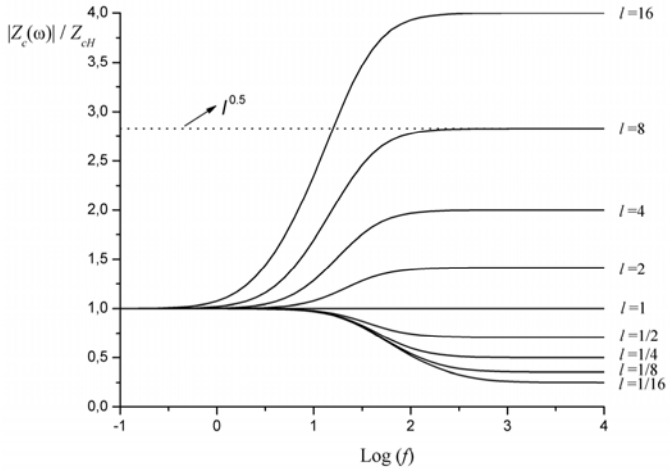

Fig.3 *Normalized function $Z_c(\omega)$ for different values of factor l*

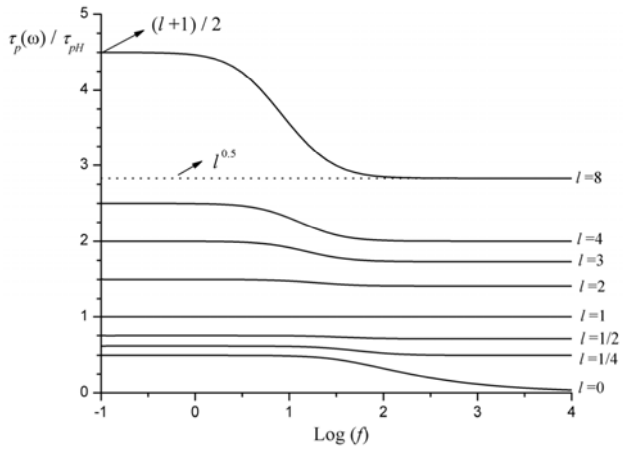

Fig.4 *Normalized function $\tau_p(\omega)$ for different values of factor l*

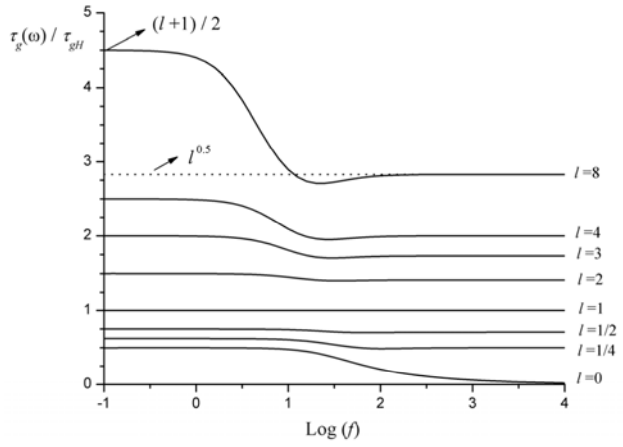

Fig.5 *Normalized function $\tau_g(\omega)$ for different values of factor l*

In Fig.6 the values of phase constant, calculated by using Eq.(3), are shown for different values of factor l. It can be noticed that the curve representing dependance of phase constant with frequency is linearized with increase of l. For l=1 the value of phase constant corresponds to its value at fulfilled Heaviside criterion, β_H, given in Table 1. In that case, signal is propagated along the line without dispersion while phase velocity and group velocity are equal at all frequencies.

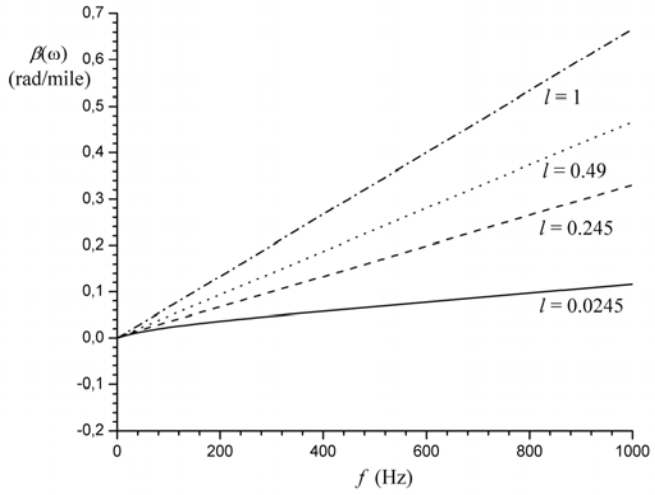

Fig.6 *Function $\beta(\omega)$ for different values of factor l*

V. CONCLUSION

In this paper, a behavior of characteristic functions, defininig propagation along a lossy TEM transmision line, as a function of per-unit length inductance increase is analysed. For an analysis purpose, a new parameter - Heaviside criterion fulfillment factor is introduced. Limit values of considered functions are expressed through the proposed factor. Presented results allow for, for an example, an estimation for how much per-unit length inductance should be increased (by inserting Pupin coils) to keep changes of attenuation, phase and group delay in acceptable limits from the signal propagation dispersion point of view. Future research will be based on a full wave matrix analysis of pupinized transmission line as a function of number of equally inserted discrete coils per wavelength corresponding to the maximum frequency of interest.

REFERENCES

[1] L. Cohen, *Heaviside's Electrical Circuit Theory*, McGraw Hill Book Co., London, 1928.

[2] M. Pupin, *Art of Reducing Attenuation of Electrical Waves and Apparatus Therefore*, patent No. 652 230, June 19, 1900, application filed December 14, 1899.

[3] P. Miljanić, *Theory of Periodical Electric Currents Propagation*, Edition of Serbian Academy of Sciences and Arts, Beograd, 2004, in Serbian.

[4] P.F. Combes, *Microwave Transmission for Telecommunications*, John Wiley & Sons, 1991.

[5] A. Marinčić, R. Biljić, "Heaviside Criterion and Cable Bandwidth", *XII Telecommunications Simposium TELFOR 2004*, Beograd, 23-25 November 2004, in Serbian.

[6] A. Marinčić, "Analysis of Transmission Line with Periodical Inductance Loading", *Microwave Review*, Vol.10. No.2, 2004, pp.43-48.

Transmission Properties of Gradient Index Metamaterial Slabs

Milan Maksimović[1], Zoran Jakšić[2], Nils Dalarsson[3]

Abstract – **We analyzed electromagnetic wave propagation through an interface between conventional dielectric and double-negative ("left-handed") metamaterial where the interface may be graded to an arbitrary degree. We investigated slab structures with linear, exponential and tangent hyperbolic spatial dependence of refractive index. To this purpose we utilized numerical procedure based on the modified transfer matrix method to calculate transmission. The obtained results may be of interest in designing optimized gradient index lenses applicable in ranges from microwave to optical, as well as in improvement of antireflection coatings.**

Keywords – **electromagnetic metamaterials, double negative materials, left-handed metamaterials, LHM, gradient index**

I. Introduction

A new paradigm in the area of electromagnetic materials is the left-handed metamaterials (LHM), also known as double negative (DNG) metamaterials [1]. These are artificial composites structured at subwavelength level which furnish a negative value of refractive index in a certain wavelength range. The direction of the Pointing vector in an LHM is opposite to that of the wavevector, i.e. the vectors of the electric and magnetic field and the wavevector form a left-oriented set, contrary to conventional materials ("right-handed" – RHM).

Typically a unit cell of an LHM consists of an element furnishing negative magnetic permeability (e.g. split-ring resonator) and an element furnishing negative dielectric permittivity (e.g. thin-wire inductive structures). Important works on this topic include Pendry's [2]-[5], while the first theoretical predictions were published in [6] and the first experimental confirmations were presented in [7].

The LHM structures offer a host of unique properties [1], and thus appear convenient for various applications not attainable with conventional materials. Different practical solutions have already been proposed, e.g. high-gain, electrically small antennas for the microwave [8], subwavelength resonant structures (resonant cavities much thinner than their operating wavelength) [9], superlenses or perfect lenses (lenses for subwavelength imaging of both far-field and evanescent near-field components of electromagnetic field which are not diffraction limited) [5], magnetic materials at THz and even optical frequencies [10], novel transmission lines [11], etc.

Continuously graded index structures offer a number of advantages over conventional elements with homogeneous and/or step index profile since they offer an additional degree of freedom in the design of the desired characteristics. Gradient index elements in conventional dielectrics have been analyzed and designed as early as in 1962 [12].

Electromagnetic metamaterials with refractive index continuously varying in space combine favorable properties of both the graded profiles and the LHM and thus promise increased practical usability in various applications, lensing and filtering being just a few of them. Thus these have been extensively studied – e.g. [1], [5], [13]-[16]. Ramakrishna described a spherical perfect lens composed of media with permittivity and permeability graded as ~1/r [15]. Smith et al [16] proposed the use of metamaterial lenses instead of conventional positive index ones for the coupling with radiative elements in high-gain antenna applications because of the reduced geometrical aberration profile in comparison to the conventional ones. Sang et al. analyzed the use of graded particles composites in the design of negative refractive index response [13]. Experimental studies of graded index LHM have been reported in e.g. [16].

In RHM, the approach to the calculation of reflection and transmission was published in [12] for the case of graded antireflection coatings. Approximate analytical solutions for electric field were done using the WKB approximation of the Helmholtz equation for some special gradient index profiles (e.g. linear or exponential dependences) [17]. As far as the authors are informed, no calculations of graded metamaterial structures were published until now.

In this work we analyze electromagnetic behavior of graded refractive index interfaces between RHM and LHM slabs using a modified transfer matrix technique (TMM). We analyze different realistic geometries including linear, exponential and tangent hyperbolic.

II. Gradient Index Profiles

Fig. 1 shows a 1D structure consisting of a RHM/LHM/RHM sandwich where the refractive index between the RHM and LHM slabs is continually graded. We considered linear, exponential and tangent hyperbolic dependences in the graded zone.

[1]Milan Maksimović is with the IHTM – Institute of Microelectronic Technologies and Single Crystals, Njegoševa 12, 11000 Belgrade, Serbia and Montenegro, E-mail: maksa@nanosys.ihtm.bg.ac.yu

[2]Zoran Jakšić is with the IHTM – Institute of Microelectronic Technologies and Single Crystals, Njegoševa 12, 11000 Belgrade, Serbia and Montenegro, E-mail: jaksa@nanosys.ihtm.bg.ac.yu

[3]Nils Dalarsson is with the Royal Institute of Technology, Stockholm, Sweden, E-mail: Nils.Dalarsson@telia.com

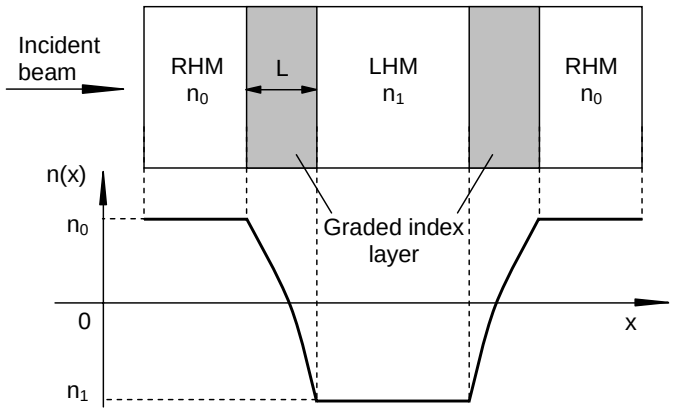

Fig. 1. Top: Structure consisting of a left-handed metamaterial slab (n_1) between two slabs of conventional lossy dielectric (n_0), where RHM-LHM interfaces are graded. Bottom: position dependence of the real part of refractive index

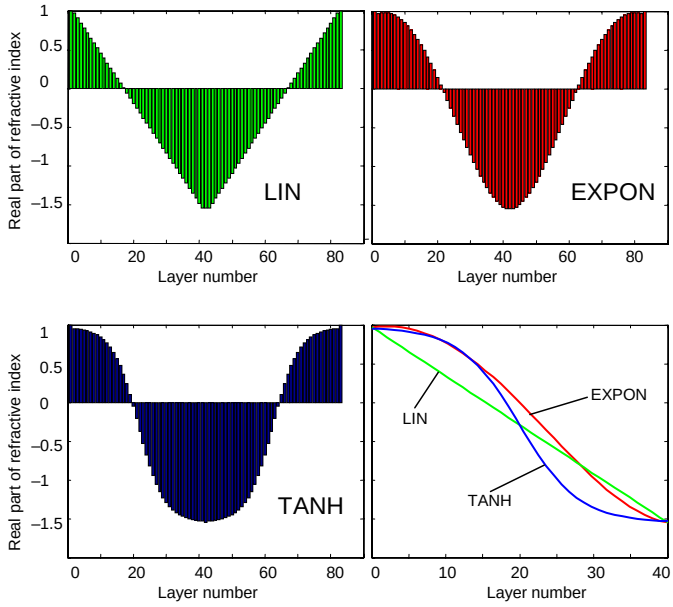

Fig. 2. The linear, exponential and tangent hyperbolic profiles used in transmittance calculation. Upper row and bottom left show the division used for gradient approximation

The position dependence of the real part of the refractive index for the linear gradient has the form

$$n(x) = n_0 + (n_1 - n_0)\frac{x}{L}, \tag{1}$$

in the exponential case it becomes

$$n(x) = n_0 \exp\left[\frac{x}{L}\ln\left(\frac{n_1}{n_0}\right)\right], \tag{2}$$

while the tangent hyperbolic dependence is

$$n(x) = \frac{n_0 + n_1}{2} - \frac{n_0 - n_1}{2}\tanh\frac{x}{L}. \tag{3}$$

The dependences (1)-(3) are shown in Fig. 2.

III. Calculation Results and Analysis

We assumed that the beam is incident from and exiting to the same medium, which is vacuum or air, with purely real and positive refractive index equal to 1. We assumed that the index profile grading started from vacuum refractive index 1 to a negative index value of –1.5. We considered lossy medium in which the imaginary part of the refractive index was 0.001. Similar to a number of references (e.g. [9]), we disregarded dispersion effects. Approximation of the small losses and dispersionless metamaterial is common practice in literature, as far as one is solely interested in effects arising from negative value of refractive index. It is true that the majority of contemporary experimental results show that negative values of refractive index appear with a relatively large dispersion and in very narrow bandwidths. However, there are also known experimental results that lead to conclusion of possibility of obtaining larger frequency bandwidth for LHM behavior [1], [11].

The calculation was done by the transfer matrix method according to the procedure outlined in [17]. To this purpose we divided the calculation region into N=80 layers with a constant value of refractive index throughout each layer. The refractive index in the layers was determined using eqs. (1)-(3) as the value in the midline of each layer. For comparison, we also calculated the electromagnetic transmission through an abrupt interface in which refractive index changed from +1 to –1.5.

First we calculated transmission for different graded profiles for the case when subdivision strata had a quarter-wavelength thickness, $4\, n_i\, L_i = \lambda_0$. We chose this condition to obtain "well behaved" and periodic transmission spectra convenient for comparison with known results. The results (Figs. 3, 4) show that the graded multilayers have somewhat lower transmission compared to that of the abrupt interface. The result is similar to the situation with conventional positive-index materials.

Another result is that exponential and linear profiles furnish practically an identical spectral transmission. A similar result is obtained for the case when constant geometrical thickness strata are taken instead of those with constant optical quarter-wave thickness (Fig. 5). The absolute values of transmission were also similar for both of these situations. Of the calculated structures, tangent hyperbolic offered the lowest values of transmission. This particular behavior of transmission spectra can be easily understood when compared with known results for ordinary postitve index graded multilayer in this configuration.

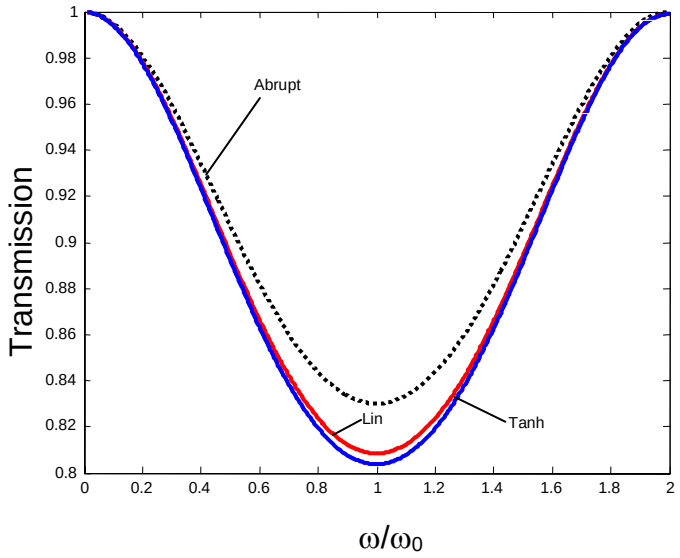

Fig. 3. Transmission of different multilayer structures with graded refractive index, quarter-wavelength thickness of subdivision strata

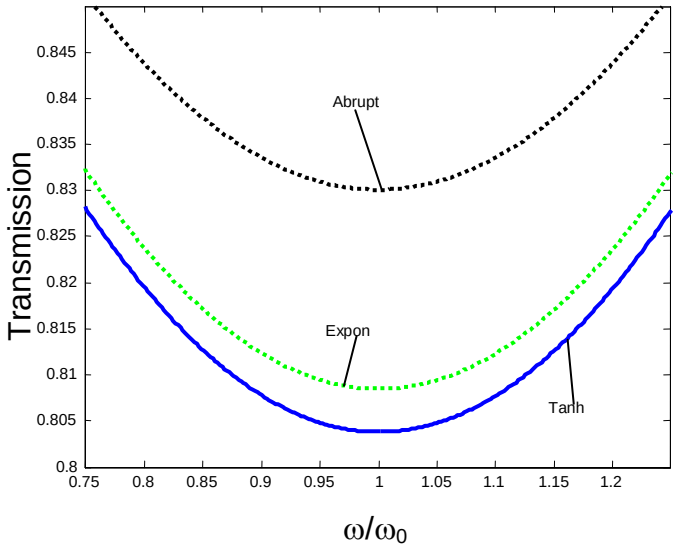

Fig. 4. Transmission of different multilayer structures with graded refractive index, quarter-wavelength thickness of subdivision strata

A more pronounced difference between diverse grading profiles can be obtained by proper choice of LHM parameters, but our intention was only to analyze graded structure transmissions as opposed to abrupt change of refractive index.

An overall conclusion is that the behavior of the spectral transmission of graded LHM interfaces is similar to the one in the case of conventional materials with positive refractive index.

It can be seen from Fig.6 that the transmission spectra for Tanh profile keep the minimal transmittance at about the same value for different optical thicknesses, but introduce oscillatory pattern in the transmission spectra as we change the normalization wavelength. It is interesting that the differences are more noticeable at higher frequencies.

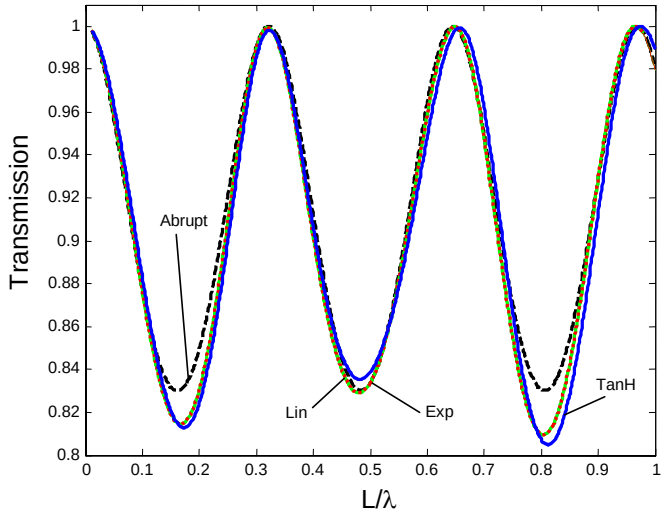

Fig. 5. Transmission of different multilayer structures with graded refractive index, constant geometrical thickness of subdivision strata

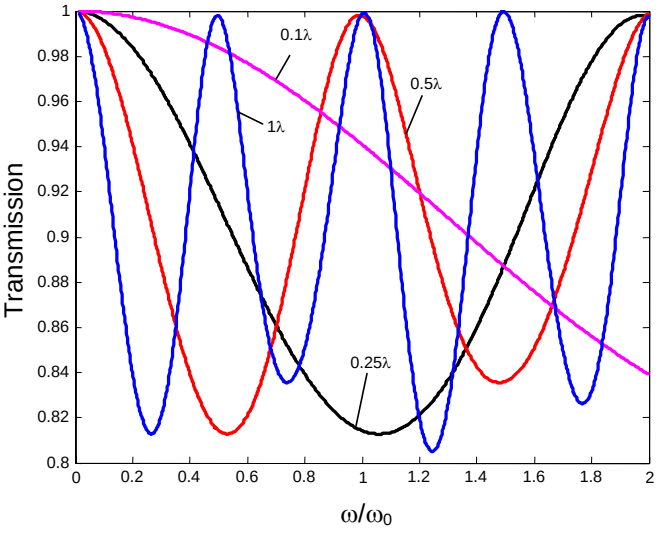

Fig. 6. Transmission of Tanh profile for different values of the graded region thickness. Each homogeneous layer has the same optical thickness, defined as $n_iL_i=\lambda_0N$, where N=0.1, 0.25, 0.5, and 1.0.

Another interesting case for consideration is shown in Fig. 7 where we chose the graded layer to be only a small portion of the slab's fixed thickness. We chose again a Tanh profile for gradient index. We assumed that the slab thickness was quarter-wavelength and that the sum of all optical thicknesses of the strata in the graded region was $\lambda_0/4$, but that the number of layers varied. Thus the optical thickness of each layer was $n_iL_i=\lambda_0/4N$.

The transmission curve in Fig. 7 reveals information of the influence that graded interfaces have on transmission when this interface region has a much smaller optical thickness than the optical thickness of the whole slab. The difference from the case of the abrupt change of refractive index becomes less prominent with the refinement of the subdivision. This is expected behavior and in agreement with [13], [16] .

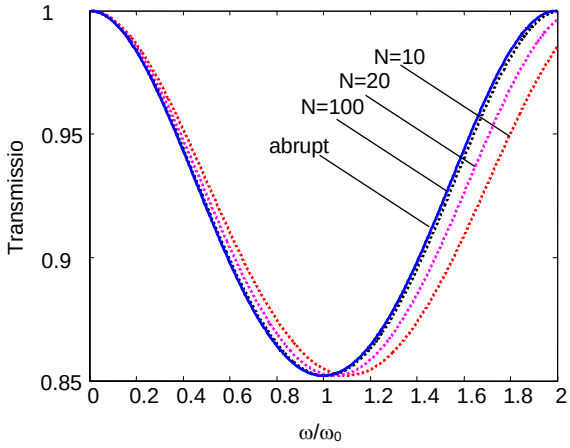

Fig. 7. Transmission of Tanh profile for different number of the equidivision for graded region . Each homogeneous layer has the same optical thickness. Central part of structure has quarter-wavelength optical thickness

IV. Conclusion

We considered electromagnetic wave propagation through slabs containing left-handed metamaterials with graded refractive index. Linear, exponential, hyperbolic and tangent hyperbolic dependences were analyzed by the transfer matrix method. The calculations were done for lossy media, while the dispersion was neglected.

The behavior of negative-index graded profiles is similar to the one of positive index material. Bearing in mind that at the same time negative index materials offer a significantly wider bandwidth in passband filtering structures than positive index materials, this points out to the possibility to utilize LHM structures instead of the conventional ones to obtain enhanced functionality. With this in mind, the gradient index metamaterial use may be anticipated in a wide range of applications, e.g. as an alternative to conventional gradient-index (GRIN) lenses and similar passive elements for electromagnetic beam shaping and directing, for high-efficiency antireflection structures, etc. Such use may be combined with the applications where magnetic response is required in the terahertz range.

Acknowledgment

This work was partially funded by the Serbian Ministry of Science and Environmental Protection within the framework of the project 6151.

References

[1] S. A. Ramakrishna, "Physics of negative refractive index materials", *Rep. Prog. Phys.* 68, pp. 449–521, 2005

[2] J. B. Pendry, A J Holdenz, D. J. Robbinsz and W. J. Stewartz, "Low Frequency Plasmons in Thin Wire Structures", *J. Phys.: Condens. Matter* 10:4785-4788, 1998

[3] J. B. Pendry, A. J. Holden, D. J. Robbins, and W. J. Stewart, "Magnetism from conductors and enhanced nonlinear phenomena", *IEEE Trans. on Microwave Theory and Tech.*, 47 (1999) 2075.

[4] J. B. Pendry, "Negative Refraction Makes a Perfect Lens", *Phys. Rev. Lett.*, 85:3966-3969, 2000

[5] J. B. Pendry, D. R. Smith, "Reversing Light: Negative Refraction", *Physics Today*, 57:37-44, 2004.

[6] V.G. Veselago, "The electrodynamics of substances with simultaneously negative values of epsilon and mu", *Sov. Phys. Uspekhi*, 10:509-514, 1968.

[7] Smith, D. R., W. J. Padilla, D. C. Vier, D. C. Nemal-Nasser, S. Schultz, "Composite medium with simultaneously negative permeability and permittivity", *Phys. Rev. Lett.*, Vol. 84, pp. 4184-4187, 2000

[8] R. W. Ziolkowski, A. D. Kipple, "Application of Double Negative Materials to Increase the Power Radiated by Electrically Small Antennas", *IEEE Trans. Ant.Propag.*, Vol. 51, No. 10, pp. 2626-2640, 2003

[9] N. Engheta, "An Idea for Thin Subwavelength Cavity Resonators Using Metamaterials With Negative Permittivity and Permeability", *IEEE Ant. Wireless Propag. Lett*, Vol. 1, No. 1, pp. 10-13, 2002

[10] J. B. Pendry, A. J. Holden, D. J. Robbins, and W. J. Stewart, "Magnetism from conductors and enhanced nonlinear phenomena", *IEEE Trans. on Microwave Theory Tech.*, 47 (1999) 2075

[11] A. J. Viitanen, S. A. Tretyakov, "Metawaveguides formed by arrays of small resonant particles over a ground plane", *J. Opt. A: Pure Appl. Opt.* 7, pp. S133–S140, 2005

[12] Peter H. Berning, "Use of Equivalent films in the design of infrared multilayer antireflection coatings", *J. Opt. Soc. Am.*, Vol. 52(4), pp. 431-436, 1962

[13] Zh.-F. Sang, Zh.-Y. Li, "Effective negative refractive index of graded granular composites with metallic magnetic particles", *Phys. Lett. A*, Vol. 334, pp. 422–428, 2005

[14] J.B.Pendry, S.A. Ramakrishna, "Focusing light using negative refraction", *J. Phys.: Cond. Matt.*, Vol. 15 (37) , pp. 6345-6364, 2003

[15] S.A. Ramakrishna, J.B.Pendry, "Spherical perfect lens: Solutions of Maxwell's equations for spherical geometry", *Phys. Rev. B*, vol. 69 (11), pp. 1151151-1151157, 2004

[16] D.R. Smith, J.J. Mock, A.F. Starr, D. Schurig, "A gradient index metamaterial, preprint", http://arxiv.org/, physics/0407063, 2004

[17] P. Yeh, *Optical Waves in layered Media*, John Wiley & Sons, 1988

Composite Left-Handed/ Right-Handed TLM (Transmission Line Metamaterials) with Quasi-Periodically Ordered Unit Cells

Milan Maksimović[1], Zoran Jakšić[2]

Abstract – **In this paper we consider quasi-periodic 1D structures composed from positive- and negative ("left-handed") refractive index material layers. Our consideration is based on the recently proposed approach to the implementation of left-handed metamaterial structures using L-C loaded transmission lines. We present transmission spectra analysis of Fibonacci-type ordered left-handed/right-handed composite.**

Keywords – **Electromagnetic Metamaterials, Double Negative Materials, Left-Handed Metamaterials, LHM, Transmission Line metamaterials, Backward Waves, Quasi-Periodicity, Fibonacci**

I. INTRODUCTION

A left-handed metamaterial (LHM) may be defined as an artificial medium which supports propagation of backward-traveling electromagnetic waves – those with anti-parallel phase and group velocity [1]. In other words, the direction of the Pointing vector in such material is opposite to that of the wavevector, i.e. $\vec{E}, \vec{H}, \vec{k}$ in an LHM form a left-oriented triplet, contrary to the conventional materials which thus may be dubbed "right-handed materials" – RHM.

The geometric features of an LHM have subwavelength dimensions and thus at the operating frequency such materials can be described by the effective medium approach. In a left-handed medium its effective magnetic permeability and dielectric permittivity are simultaneously negative, with a consequence that its refractive index is also negative (in order to preserve causality) [2]. The seminal papers on LHM include those Veselago's and Pendry's [3], [4], [5].

The left-handed structures possess many unique properties. Snell's law is reversed in them, as well as the Doppler shift and Cerenkov radiation [1]. The main applications utilizing LHM include the so-called superlenses [6] which enable imaging of both far-field and evanescent near-field components of electromagnetic field. Another one are subwavelength resonant cavities [7] (i.e. resonant cavities with dimensions much smaller than the operating wavelength). Different practical solutions stemmed from this, e.g. high-gain, electrically small antennas for the microwave [8], materials possessing magnetic properties at THz frequencies, different microwave transmission lines [9], directional couplers, resonators, filters, antireflection structures and many more [10]. In this very dynamic field new applications appear virtually every day. According to the *Science* journal, left-handed metamaterials were among the top ten scientific breakthroughs of the year in 2003 [11].

The first practical structures acting as left-handed materials included thin metallic wires [4] for creation of effective media with negative dielectric permittivity, and split ring resonators (SRR) for negative magnetic permeability [5]. These elements ('particles') are arranged in a unit cell, which is the smallest element of an LHM and whose multiplication furnishes the macroscopic or mesoscopic left-handed medium. Experiments confirming the functionality of such structures started with [12].

Left-handed media containing thin wire and SRR elements are necessarily resonant. Due to their resonant nature, negative values of refractive index are available only in a very narrow range of wavelengths. In addition to that, these media are always lossy.

An alternative approach to LHM was proposed in June 2002 in [13] and [14] and later published in [15], [16]. It utilizes the well-known duality between filters and distributed networks to produce left-handed materials based on transmission lines – the so-called transmission line metamaterials (TLM). There is a direct analogy between the voltage/current in a transmission line and the components of the electric and magnetic fields. Besides offering larger bandwidths and much smaller losses, the unit cells of TLM can be equipped with lumped circuit elements, allowing an additional degree of freedom in design. Additionally, [15] proposed the fabrication of dynamically tunable TLM by using lumped varactors instead of capacitors. TLM are especially suitable for RF and microwave devices.

A more practical application of TLM is LHM/RHM combination. A name coined for it was CRLH (composite Right/Left Handed) materials [17]. Such transmission lines behave as LHM at low frequencies and as RHM at high frequencies.

Filtering applications of LHM almost naturally bring to mind their combination with quasiperiodic structures which enable different practical applications with unique properties [18]. In spite of that, no papers appeared until today which deal with quasiperiodic transmission line metamaterials.

This paper analyses quasiperiodic CRLH transmission line structures. The parameters of the structures were analyzed by

[1]Milan Maksimović is with the IHTM – Institute of Microelectronic Technologies and Single Crystals, Njegoševa 12, 11000 Belgrade, Serbia and Montenegro, E-mail: maksa@nanosys.ihtm.bg.ac.yu
[2]Zoran Jakšić is with the IHTM – Institute of Microelectronic Technologies and Single Crystals, Njegoševa 12, 11000 Belgrade, Serbia and Montenegro, E-mail: jaksa@nanosys.ihtm.bg.ac.yu

the transfer matrix method. Fibonacci-sequence scheme was chosen to study transmission and reflection properties for waves propagating along structure based on TL metamaterial.

II. THEORY

In an ideal case, conventional (RHM) materials are equivalent to a distributed L-C network with series inductance and parallel capacitance. A transmission-line based LHM is then obviously equivalent to a dual distributed network with series capacitance and shunt inductance. This is a high-pass filter structure and supporting backward wave propagation. In this paper we use concept of CRLH composite right-handed/left-handed transmission line metamaterial, as described in [17]. This choice is justified within framework of realizable structures that are already experimentally produced [15]. A unit cell of a realistic TLM structure includes parasitic series inductance and shunt capacitance (Fig. 1 a).

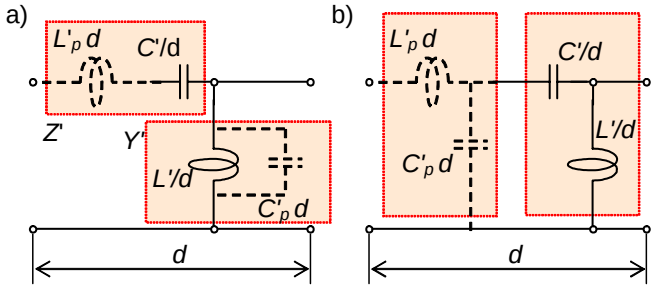

Fig. 1. a) An equivalent circuit for a unit cell with a length d of lossless transmission line CRLH metamaterial with corresponding per unit length parameters (primed). Index "p" denotes the parasitic inductance and capacitance (dashed lines). b) the same equivalent circuit for the balanced case.

The per-unit length impedance Z' and admittance Y' for the 1D unit cell in Fig. 1 are given as

$$Z'(\omega) = j\left[\omega L'_p - \frac{1}{\omega C'}\right],\quad Z'(\omega) = j\left[\omega C'_p - \frac{1}{\omega L'}\right] \qquad (1)$$

where 'prime' stands for 'per unit length'. The complex propagation constant γ is defined as $\gamma = \alpha + j\beta = (Z'Y')^{1/2}$.

Here β denotes the real propagation constant (attenuation constant). Phase velocity is $v_p = \omega/\beta$. If $L'_p C' = L' C'_p$, we have the so-called balanced case. In this case the equivalent circuit for the unit cell presented in Fig. 1b is valid.

The propagation along the line is described by the well-known telegrapher's equation (e.g. [15]). The dispersion of the attenuation constant β for the balanced case is described by

$$\beta(\omega) = \omega\sqrt{L'_p C'_p} - \frac{1}{\omega\sqrt{L'C'}} \qquad (2)$$

Since the propagation constant of a material is defined as $\beta = \omega(\mu\varepsilon)^{1/2}$, the refractive index of a TLM is given by

$$n = c / v_p = c\beta / \omega \qquad (3)$$

From (2) and (3) it can be seen that at low frequencies the TLM refractive index is negative, and at high frequencies it is positive (Fig. 2). This means that below a certain frequency a CRLH transmission line behaves as a left-handed material and at higher frequencies it is conventional RH medium. The transition between the two regions occurs at n=0. This characteristic frequency is $\omega_0 = [LC]^{-1/2}$. Although β is zero at ω_0, which corresponds to an infinite guided wavelength ($\lambda_g = 2\pi / |\beta|$), wave propagation still occurs since in this case γ is always purely imaginary.

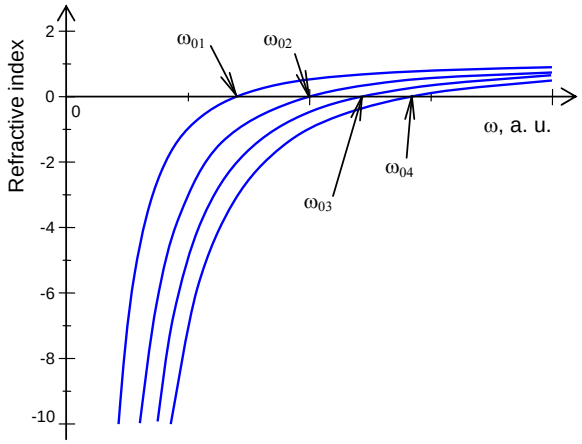

Fig. 2. Refractive index dependence on frequency for a balanced CRLH metamaterial.

A quasi-periodic structure often met in literature is the Fibonacci lattice, which belongs to substitution lattice sequences [18]. The transmission and reflection of these structures were widely studied in conjunction with electromagnetic spectral properties of quasi-crystals, superlattices, optical and microwave multilayers.

We give a general description of Fibonacci sequence and then map abstract objects to their concrete instances in transmission line metamaterial realization scheme. We proceed further by applying Fibonacci sequence scheme in order to study transmission and reflection properties for waves propagating along structure based on TL metamaterial.

A substitution lattice can be defined as a combination of physical settings with the corresponding rules of change. A physical setting is mapped on strings of formal symbols belonging to a predefined finite set. The initiator is a string of symbols from a finite set, called alphabet, from which the process starts. The rules of change are mapped on the rewriting rules for symbols in words, starting from the initiator, which are applied on each symbol in a word. The system evolution is described through a finite sequence of symbols.

We start with an alphabet $\Xi = \{A, B\}$, and denote Ξ^* as the set of all finitely long words that can be written in this alphabet. The rewriting rule is denoted by ξ and represents mapping from Ξ to Ξ^* by specifying action that ξ has on each letter of any word in transforming it to its image letter. The Fibonacci sequence can be described with rewriting rules $A \rightarrow \xi(A)=AB$, $B \rightarrow \xi(B)=A$. In instancing those sequences to the electromagnetic multilayer structures we define two refractive indices (n_A, n_B) and geometrical lengths (d_A, d_B) that

correspond to (*A*) and (*B*). The number of elements increases according to the Fibonacci number, $F_n=F_{n-1}+F_{n-2}$ ($F_0=F_1=1$), and the ratio between the number of different elements *A* and *B* is equal to the golden mean number $\left(1+\sqrt{5}\right)/2$. Fibonacci generations are *B*, *A*, *AB*, *ABA*, *ABAAB*, etc.

Further we define that the constitutive layers have an equal optical thickness which is that of a quarter-wavelength slab $n_Ad_A=n_Bd_B=\lambda_0/4$. Our structure consist from layers with refractive index n_A and vacuum (or air) layers $n_B=1$. The incident and the output region are also air.

III. Results and Discussion

We calculated the spectral properties of CLRH transmission line metamaterials using the transfer matrix technique (TMM) (e.g. [19]). To be able to compare the spectral transmission of quasi-periodic (Fibonacci) transmission lines for the case of conventional (A: RHM; B: RHM) to those of the "left-handed" (A: LHM; B: RHM) structures, we assumed that the refractive index n_A was constant in the frequency range under consideration. Since TLM have much wider bandwidth than the SRR-based LHM, this assumption is valid (although the same assumption is often applied for all structures, including those SRR-based – e.g. [7]; for an in-depth consideration see [1]). Fig. 3 shows the comparison of 12th generation Fibonacci sequences between $n_A=1.5$ and $n_A=-1.5$.

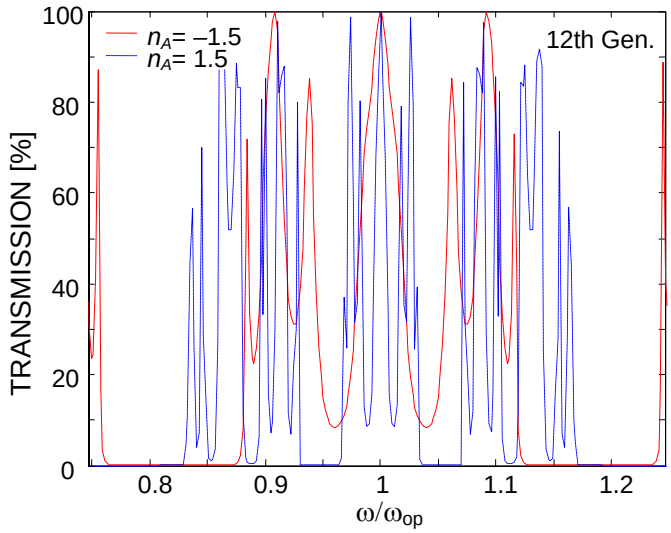

Fig. 3. Comparison of transmission spectra of 1D transmission lines with 12th generation Fibonacci-sequence layers. Solid: material A is left-handed, $n_A=-1.5$. Dashed: material A is right-handed, $n_A=1.5$. In both cases B is conventional, $n_B=1$.

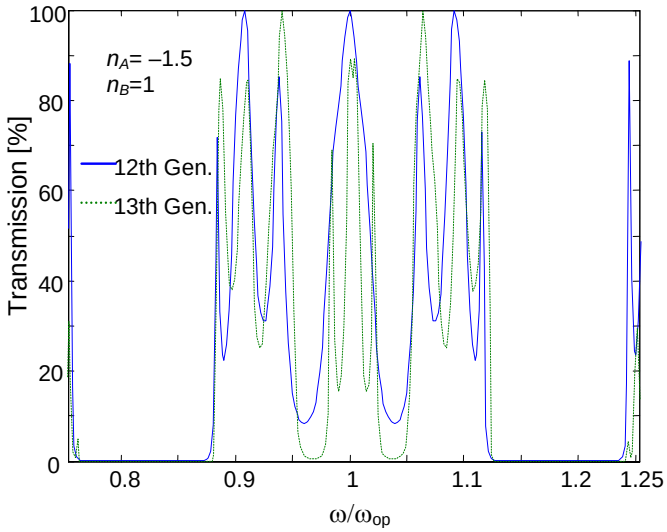

Fig. 4. Spectral transmission of 1D CLRH transmission line metamaterial with Fibonacci-sequence layers. Solid: 12th generation, dashed: 13th generation. Material A is left-handed, $n_A=-1.5$, B is conventional, $n_B=1$.

It can be seen that for the CLRH situation the spectra are wider and without sharp oscillations characteristic for the RHM. However, the mode localization property and self-similarity of the spectral images are fully retained. The comparison of two successive generations (Fig. 4) shows that the sequential splitting of the localized modes also exists, the same as in the RHM-RHM case.

Further we include the refractive index dispersion defined by a realistic set of transmission line metamaterial parameters [17]. For $L_p=L=1$ nH, $C_p=C=1$ pF and a characteristic length scale of $d=1$ mm, we obtain a refractive index in the form $n(\omega)=9.5(1-\omega_0^2/\omega^2)$ where $\omega_0=31$ GHz. The operating frequency $\omega_{op}=28.8$ GHz. The refractive index dispersion is shown in Fig. 5.

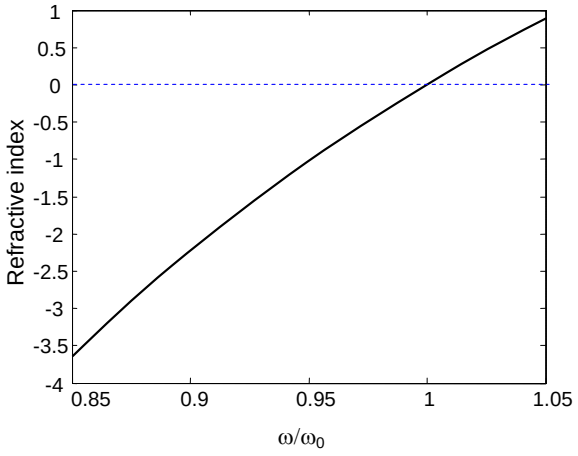

Fig. 5. Refractive index dispersion for LHM part of the CLRH transmission line for $L_p=L=1$ nH, $C_p=C=1$ pF, $d=1$ mm.

Fig. 6 shows the calculated spectral transmission of the TLM using the realistic transmission line negative refractive index dispersion.

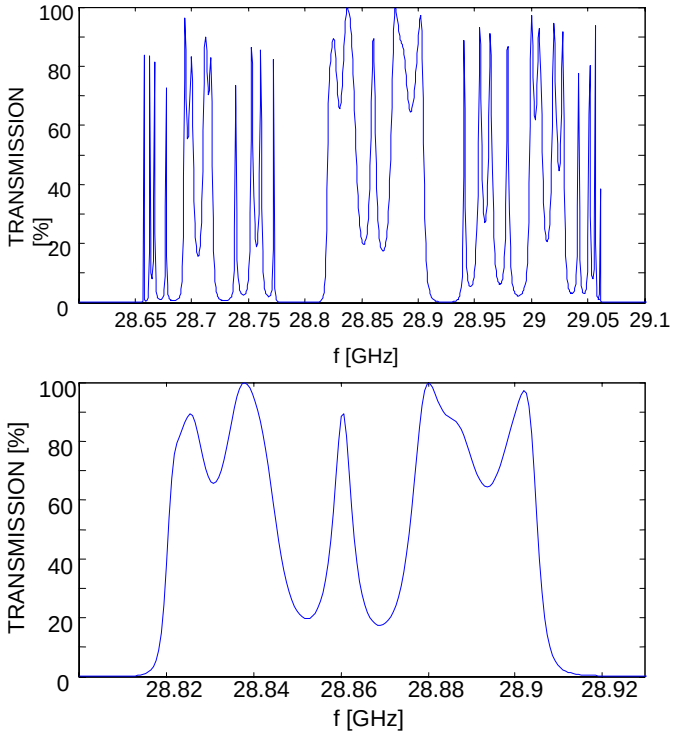

Fig. 6. Top: spectral transmission of 13th generation Fibonacci-sequence CLRH transmission line metamaterial for negative refractive index dispersion shown in Fig. 5. Bottom: the same dependence for a narrower frequency range 28.80–28.93 GHz.

Spectral self-similarity and mode localization can still be seen in Fig. 6, confirming the applicability of the proposed scheme for filtering applications.

IV. Conclusion

We considered electromagnetic wave propagation through quasi-periodically ordered transmission lines containing left-handed metamaterials. The quasi-periodicity was in the form of Fibonacci series. Our calculations were performed using the transfer matrix approach.

All the basic properties characterizing spectral properties of quasi-periodic structures in conventional materials are retained, i.e. the self-similarity property, sequential splitting when increasing generation and the appearance of narrow and high multiple peaks. Left-handed metamaterials addition to the transmission lines act by smoothing the peaks, while at the same time retaining all the mentioned benefits of quasi-periodic geometry. In addition to that, transmission lines containing negative index materials offer wider bandwidths and a number of other unique properties. We conclude that it may be expected that the combination of transmission line metamaterials and quasiperiodic structure could show enhanced functionality in filtering and other applications.

Acknowledgment

This work was partially funded by the Serbian Ministry of Science and Environmental Protection.

References

[1] S. A. Ramakrishna, "Physics of negative refractive index materials", *Rep. Prog. Phys.* 68, pp. 449–521, 2005

[2] R. W. Ziolkowski, E, Heyman, Wave propagation in media having negative permittivity and permeability, *Phys. Rev. E*, 64, 056625.1-15, 2001

[3] V.G. Veselago, "The electrodynamics of substances with simultaneously negative values of epsilon and mu", *Sov. Phys. Uspekhi*, 10:509-514, 1968.

[4] J. B. Pendry, A J Holdenz, D. J. Robbinsz and W. J. Stewartz, "Low Frequency Plasmons in Thin Wire Structures", *J. Phys.: Condens. Matter* 10:4785-4788, 1998

[5] J. B. Pendry, A. J. Holden, D. J. Robbins, and W. J. Stewart, "Magnetism from conductors and enhanced nonlinear phenomena", *IEEE Trans. on Microwave Theory and Tech*., 47 (1999) 2075.

[6] J. B. Pendry, "Negative Refraction Makes a Perfect Lens", *Phys. Rev. Lett*., 85:3966-3969, 2000

[7] N. Engheta, "An Idea for Thin Subwavelength Cavity Resonators Using Metamaterials With Negative Permittivity and Permeability", *IEEE Ant. Wireless Propag. Lett*, Vol. 1, No. 1, pp. 10-13, 2002

[8] R. W. Ziolkowski, A. D. Kipple, "Application of Double Negative Materials to Increase the Power Radiated by Electrically Small Antennas", *IEEE Trans. Ant.Propag*., Vol. 51, No. 10, pp. 2626-2640, 2003

[9] A. J. Viitanen, S. A. Tretyakov, "Metawaveguides formed by arrays of small resonant particles over a ground plane", *J. Opt. A: Pure Appl. Opt*. 7, pp. S133–S140, 2005

[10] T. Itoh, "Prospects for metamaterials", *Electronics Lett*., 40, 16, pp. 972-973, 2004.

[11] "Breakthrough of the year: The runners-up," *Science*, 302, 5653, pp. 2039–2045, 2003.

[12] Smith, D. R., W. J. Padilla, D. C. Vier, D. C. Nemal-Nasser, S. Schultz, "Composite medium with simultaneously negative permeability and permittivity", *Phys. Rev. Lett*., Vol. 84, pp. 4184-4187, 2000

[13] C. Caloz, H. Okabe, T. Iwai, T. Itoh, "Transmission line approach of left-handed (LH) materials," in Proc. USNC/URSI National Radio Science Meeting, San Antonio, TX, June 2002, vol. 1, p. 39.

[14] A. K. Iyer, G. V. Eleftheriades, "Negative refractive index metamaterials supporting 2-D waves," in *IEEE MTT-S Int. Microwave Symp. Dig.*, vol. 2, Seattle, WA, June 2–7, 2002, pp. 1067–1070.

[15] L. Liu, C. Caloz, C. Chang, T. Itoh, "Forward coupling phenomenon between artificial left-handed transmission lines," *J. Appl. Phys*., 92, 9 , pp. 5560-5565, 2002.

[16] G. V. Eleftheriades, A. K. Iyer, " Planar Negative Refractive Index Media Using Periodically *L–C* Loaded Transmission Lines", *IEEE Trans. Microw. Theory Techniques*, 50, 12, pp. 2702-2712, 2002

[17] A. Lai, C. Caloz, T. Itoh, "Composite Right/Left-Handed Transmission Line Metamaterials", *IEEE Microwave Magaz.* pp. 34-50, 2004.

[18] E. L. Albuquerque, M. G. Cottamb, "Theory of elementary excitations in quasiperiodic structures", *Physics Reports* 376, pp. 225–337, 2003

[19] M. N. O. Sadiku, *Numerical Techniques in Electromagnetics*, CRC Press 2001

Overlapping Domain Decomposition for Coupled Magnetic and Thermal Fields

Daniela Cârstea[1], Ion Cârstea[2], Alexandru Cârstea[3]

Abstract – **The work presents a domain decomposition approach for coupled magnetic and thermal fields at low frequency applications in electromagnetic devices. The analysis domain for the two fields is divided into overlapping subdomains where the decomposition pattern is imposed by physical considerations. In this way a substantial reduction of the computing resources is obtained. As target example we consider the electric furnace based on the induction-heating phenomenon. The model is an axisymmetric field both for magnetic field and the thermal field. The mathematical model for magnetic field is based on time-harmonic Maxwell equations in vector magnetic potential formulation for axisymmetric fields. The model for the heat transfer is the heat conduction equation. A numerical model based on the finite element method is developed.**

Keywords – **Coupled fields; domain decomposition; finite element method; numerical simulation; induction heating**.

I. INTRODUCTION

An electric engineering problem can be formally divided into electric and magnetic sub problems, with disjoint or overlapping subdomains. In each subproblem we can use different mathematical models with interface conditions on the common pseudo boundaries between electric and magnetic subdomains. In other words we must choose between two options:

- An artificial subdivision which is the general principle of the domain decomposition
- A natural division imposed by the problem particularities

An artificial subdivision of the whole field domain does not change the solution of the field problem but a natural subdivision can lead to a better convergence. The pseudo boundary surface may be selected to follow some natural surfaces, such as the material interface.

The pseudo boundary conditions are treated in terms of the mathematical models developed in each subdomain. For example in the electromagnetic problems we can use different potential formulations (scalar and/or vector potentials).

The differences appear at the pseudo boundary. In principle the treatment of the pseudo boundary condition is the same but in vector potential formulations we have a vector quantity. Let us consider the magnetic field problem in the induction heating for the target example. Let us suppose that the domain is divided into 2 disjoint subdomains Ω_1 and Ω_2 with the common pseudo boundary S_B. The natural interface condition for this problem is:

$$\upsilon_1(\bar{n}\times\bar{B})\big|_1 = \upsilon_2(\bar{n}\times\bar{B})\big|_2$$

The subscripts 1 and 2 refer to the two regions that the pseudo boundary separates and the normal direction on the interface surface is assumed to point from subdomain 1 into subdomain 2. Physically, the interface condition means that the tangential magnetic flux density has a discontinuity if the permeability differs in the two media:

$$\frac{\left|\overline{B_t}\right|_1}{\left|\overline{B_t}\right|_2} = \frac{\mu_1}{\mu_2}$$

where the subscript "t" indicates the part of the vector B which lies in the tangential plane at the interface surface. If the permeability is a scalar, the direction of the tangential vector is the same on both sides of the interface.

The natural boundary condition at an exterior boundary S of the whole domain can be considered for zero-reluctivity space as:

$$\overline{B_t} = 0$$

These boundary conditions are natural and therefore, they need not be explicitly imposed on any approximate solution.

If we consider the A-formulation and FEM for a 2D domain Ω with the boundary Γ, the Galerkin's method leads to the following equation for steady-state magnetic field:

$$\int_{\Omega^e} \nu(\nabla A\cdot\nabla N - J\cdot N)d\Omega - \oint_{\Gamma}\upsilon N.\frac{\partial A}{\partial n}d\Gamma = 0$$

with A the unknown vector potential and N the weighting vector function.

At a boundary point between two subdomains, A and ∂A/∂n are supposed unknown in each subdomain. The FEM gives an equation for each subdomain so that two equations are necessary to have a complete system. At the interface between two magnetic media those conditions are the continuity of the vector potential A and of the tangential magnetic field H_t = $\nu.\partial$A/∂n.

In this work we limit the discussion to the through heating by induction. The process is critically dependent on the uniformity of the temperature in the workpiece so that a

[1] High School Group of Railways. Str. Brâncusi, nr. 9. Craiova, Romania. E-mail: danacrst@yahoo.com
[2] University of Craiova, Faculty of Automation, Computers and Electronics. Blv. Decebal, nr.5. Craiova, Romania. E-mail:incrst@yahoo.com
[3] University of Craiova, Faculty of Automation, Computers and Electronics. Blv. Decebal, nr.5. Craiova, Romania. E-mail:ncarstea@hotmail.com

computer-aided design of the induction devices is a major requirement of the design [4].

II. MATHEMATICAL MODELS FOR COUPLED FIELDS IN INDUCTION HEATING

Induction heating is a convenient method for bulk-heating metals to a prescribed temperature. In our target example we consider a long iron cylindrical workpiece immersed in the field of a cylindrical coil (solenoid) supplied with alternating current. In figure 1 an axial section in the device is shown. The coil (3) is formed by rectangular bars and is surrounded by the air (2). The coil is normally water-cooled and has refractory lines.

The problem of induction heating in this example is an axisymmetric problem. Some standard assumptions are considered that lead to a 2D-scalar problem:

- The device has a rotational symmetry
- Current density J has only the azimuthal component in the θ-direction
- Materials have isotropic physical properties
- The source is a coil with wires of rectangular cross-section

This application can be modelled using mathematical models for axisymmetric fields because both magnetic field and thermal field have geometrical and physical symmetry. In other words we can use the differential models in cylindrical coordinates for axisymmetric fields.

The mathematical model for the electromagnetic field using A-formulation is a 2D-scalar model in (r-z) plane [1]:

$$\frac{\sigma}{r}\frac{\partial(rA)}{\partial t} - \nabla\left[\frac{\upsilon}{r}\nabla(rA)\right] = J_S \qquad (1)$$

or for the harmonic-time case:

$$\frac{\partial}{\partial r}\left[\frac{\upsilon}{r}\frac{\partial(rA)}{\partial r}\right] + \frac{\partial}{\partial z}\left[\frac{\upsilon}{r}\frac{\partial(rA)}{\partial z}\right] - j\sigma\omega\frac{\upsilon}{r}(rA) = -J_S \qquad (2)$$

Equation (1) represents the electromagnetic field description, with σ – the electric conductivity, ν – the magnetic reluctivity and J_s - the excitation current density. It is solved with specified initial and boundary conditions that depend on the problem.

The heat transfer problem in homogeneous orthotropic material is described in terms of the temperature T ([1],[2]):

$$\frac{\partial}{\partial t}[(c\gamma)(T).T] + \nabla[-k\ \ (T).\nabla\ \ T] = \rho(T).J^2(A) \quad (3)$$

The significances of the quantities are: T(r,z,t) is temperature in the point with co-ordinates (r, z) at the time t; k is the tensor of thermal conductivities; γ is the specific mass; c is the specific heating and J is the global current density. The current density J includes both the driving and skin effect. The term J can be computed as

$$J = \nabla \times H$$

In the inner and outer thermal insulating layers of the coil the driving term is missing.

The boundary conditions are convective and radiation conditions, that is:

$$-k\frac{\partial T}{\partial n} = h(T - T_\infty) \qquad (4)$$

$$-k\frac{\partial T}{\partial n} = \alpha_r(T^4 - T_\infty^4) \qquad (5)$$

where h and α_r are the transfer coefficients at the boundaries.

The model is non-linear because the specific heat c and the thermal conductivity k are dependent on the temperature. The coupling between the magnetic and thermal fields is represented through both the heat sources in (3) and the dependency on the temperature of the electromagnetic properties from (1).

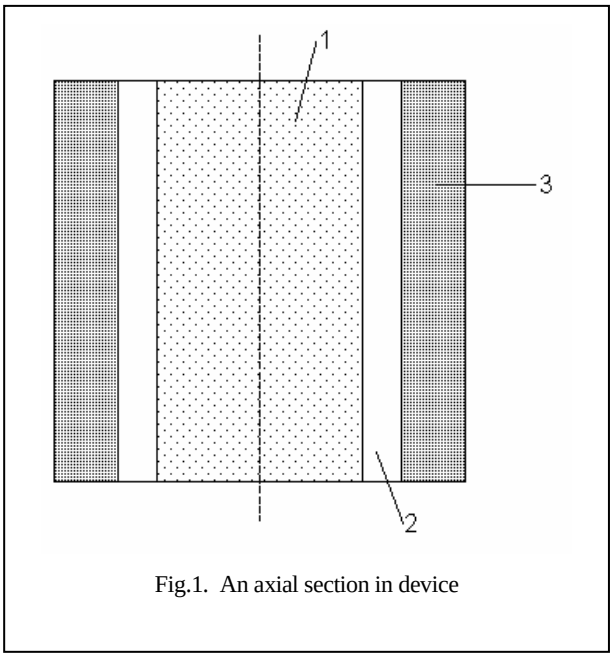

Fig.1. An axial section in device

Conventional coils are constructed from hollow copper pipe and are water-cooled to remove the heat generated in the conductors. An alternative approach is to use litz-wire in the construction of the coil, thereby ensuring that the losses in the coil are reduced. Nearly all through-heating coils use thermal insulation between the coil and the workpiece. This protects the winding and its insulation from the radiant heat and acts as a muffle around the workpiece. The coil conductors are characterised by the lack of eddy currents in a simplified model.

III. A NUMERICAL MODEL BASED ON THE OVERLAPPING DOMAIN DECOMPOSITION

The domain decomposition can be used only for magnetic field computation [3], or it can be used in coupled model by a strategy that we present in this section. The analysis domain plotted in the figure 1 can be decomposed in two subdomains that are not disjoint. The physical considerations are followed in this decomposition. For many eddy-current problems the magnetic flux penetration into a conductor without internal

sources of the magnetic field is confined mainly to surface layer. This is the skin effect. The skin depth δ depends on the material properties μ, ω and σ so that for the small depths all of the effects of the magnetic field is confined to a surface layer [4].

In steady-state low-frequency eddy current problems in magnetic materials, the mathematical model is the diffusion equation (1). The skin effect can be exploited in two directions:

- To reduce the space domain in analysis with a fine mesh close to conductor surfaces
- To reduce the material volume since a significant proportion of the conductor is virtually unused

The penetration depth is given by the formula [4]:

$$\delta = \sqrt{\frac{2}{\omega\sigma\mu}} \qquad (6)$$

In other words for problems with the skin depth very small all the effect of the field is confined to a surface layer. Designer engineers use the formula (6) considering the permeability and the conductivity as constants. In reality the two physical parameters change during heating. The changes in the value of δ affect the loss in the material and depend on the process (conduction or induction). For example, if the conductivity decreases by x, the depth increases by √x, that is the current penetrates deeper into the metal. If the magnetic material heats, its resistivity (the inverse of the conductivity) rises but its relative permeability remains substantially constant up to the Curie point. In this point it drops suddenly to unit.

For low frequency applications the field depth is large. For an industrial frequency we can compute the depth in workpiece and limit the magnetic field analysis at this depth. In the thermal field analysis we reduce the field domain at the workpiece. The two domains are overlapping on a surface defined by the penetration depth of the magnetic field in workpiece. For a range of the frequencies and the temperatures we can compute the range of the depth penetration. In order to cover the whole domain of frequencies we select the maximum value of the depth. The depth penetration depends on the material properties so that the boundary of the field in conductor can change in time.

In the figure 1 the field domain in a finite element model is plotted with the horizontal axis Oz and vertical axis Or. For the thermal field we use a Neumann boundary condition, combining a given boundary heat flux with convection and radiation:

$$-k\left.\frac{\partial T}{\partial n}\right|_{\Gamma} = q_n + h(T - T_\infty) + \alpha(T^4 - T_\infty^4)$$

with T_∞ - the surrounding medium temperature, q_n the heat flux and n the outward unit normal on the boundary.

IV. NUMERICAL RESULTS

Figure 1 shows a long cylindrical workpiece excited by a close-coupled axial coil. The problem is an axisymmetric heating device. The coil is assimilated with a massive conductor. In the numerical model we can consider or ignore the eddy currents in the coil. If we ignore the eddy-currents in the coil the electric conductivity is equal to zero and the domain for thermal field is reduced to the workpiece volume.

The geometry and the physical properties are defined as in the tables I, II and III.

TABLE I
Coil conductor's properties

Relative permeability	1
Conductivity	$6.3\ 10^7$ S/m
Thermal conductivity	140 W/K.m
Specific density	380 J/Kg.K
Metal density	8700 Kg/m^3

TABLE II
Workpiece's properties

Relative permeability	500
Conductivity	$1\ 10^7$ S/m
Thermal conductivity	100 W/K.m
Specific density	200 J/Kg.K
Material density	7800 Kg/m^3

TABLE III
Air's properties

Relative permeability	1
Conductivity	0 S/m
Thermal conductivity	0.01 W/K.m

The depth penetration for a low frequency was 4 mm. The amplitude of the current in the coil is 40 000 A.

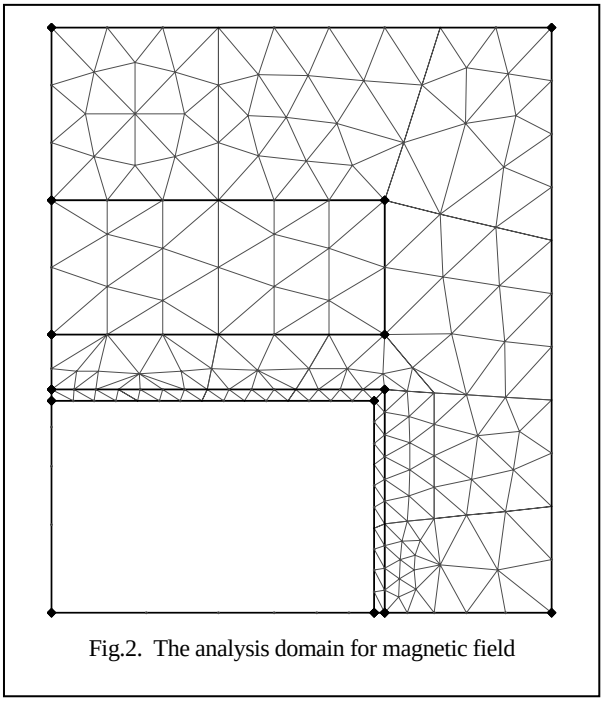

Fig.2. The analysis domain for magnetic field

In the figures 3-5 the results of the numerical simulation are plotted using QuickField [5]. The finite element method was used for the numerical modelling both magnetic field and thermal field. In fig. 3 the temperature of the workpiece surface is plotted. Starting with the initial temperature 40 ^{0}C,

the variations of the temperature in two points are plotted in the figure 5.

In fig. 4 the final distribution of the temperature on the axis of the workpiece in the center direction is plotted.

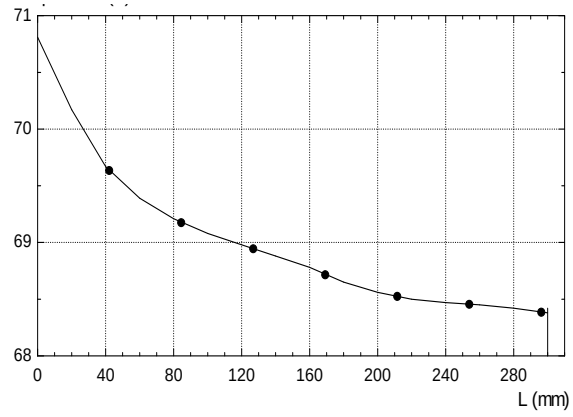

Fig.3. The final temperature on the external surface of the workpiece

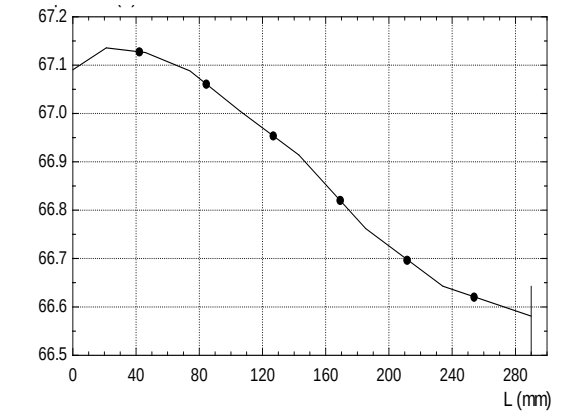

Fig.4. The final temperature on the axis of the workpiece

Some relevant aspects must be considered in the design of the CAD software for coupled magneto-thermal problems:

- The thermal source term in the heat equation can be defined by the time-mean of the ohmic power loss. The motivation is simple: the time constant of the magnetic phenomenon is small compared to the diffusion time of the heat transfer.
- A cascade solution may be more efficient than a fully coupled model. In some applications there is a strict coupling between magnetic and thermal equation at each time instant, but in many situations we can split the analysis of the magnetic field by the analysis of the thermal field.
- It can be used a predefined temperature profile of a material for updating the magnetic field at specified temperatures. For example, at Curie temperature the material properties change dramatically. After this critical point the magnetic field equation must be updated.
- The analysis domain can be divided in more subdomains with different solvers for the coupled problems.

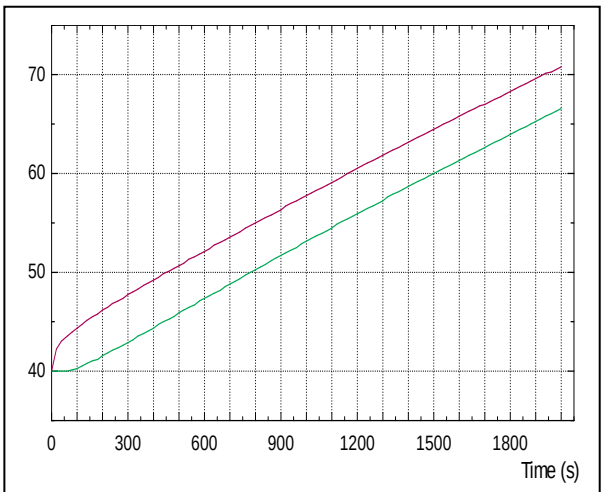

Fig.5. The temperatures in the center and in the corner of the workpiece (the above curve)

V. CONCLUSIONS

In this paper we presented a numerical model for the induction heating of cylinders in large furnaces. The model was based on the simplifying assumptions but we did not ignore the non-linear effect of the temperature distribution. The radiation effect and convection were considered on the workpiece surface.

REFERENCES

[1] Cârstea, D. "CAD tools for magneto-thermal and electric-thermal coupled fields". *Research Report in a CNR-NATO Grant*. University of Trento. Italy, 2004.

[2] Cârstea, D., Cârstea, I. *CAD in electrical engineering.* Editor: Sitech, Craiova. 2000.

[3] Alonso, A., Valli, A. "A domain decomposition approach for heterogeneous time harmonic Maxwell equations". In: *Computer methods in applied mechanics and engineering*, 143 (1997), pg. 97-112.

[4] Davies, E.J. *Conduction and Induction Heating.* IEE Power Engineering Series 11, Peter Peregrinus Ltd. London, U.K. 1990.

[5] *** QuickField program Version 5.2. User's guide. Tera Analysis.

A Simplified Model for Coupled Magnetic and Thermal Fields in High Frequency Applications

Daniela Cârstea[1], Ion Cârstea[2], Alexandru Cârstea[3]

Abstract – **The work presents a simplified model for coupled magnetic and thermal fields in solid conductors in the context of the finite element method.**

Our target example is the induction heating at high frequency where the depth penetration of the magnetic field in a conductor workpiece is very small. This fact is exploited in the sense of reduction of the analysis domain and computational effort. In a numerical model based on finite element method (FEM) this effect can be exploited by the use of a special boundary condition, known as the surface impedance condition. In this way we don't waste run-time of a program based on FEM.

The mathematical model for magnetic field is based on Maxwell equations in vector magnetic potential formulation for axisymmetric fields. The model for the heat transfer is the heat conduction equation. A numerical model based on the finite element method is developed.

Keywords – **Coupled fields; finite element method; numerical simulation; induction heating**.

I. INTRODUCTION

Induction heating is used extensively in the metal industry. It is an illustrative engineering example for the thermal conductivity problem in which the heat is generated by ohmic losses from eddy currents induced in conducting materials, such as metals.

Induction heating is a convenient method for bulk-heating metals to a set temperature. It replaces furnaces, which tend to be large and which have the disadvantage of long start-up and shutdown times, so that their effectiveness is low. The induction heater is relatively small in size and is immediately available for use. It is clean and relatively efficient.

The special feature of induction heating is that the heat is produced in the material by currents flowing in it. In induction heating, the heat is generated by the passage of currents through the material but they are induced from a separate source.

Whatever the configuration, induction heating always involves a varying magnetic field. An induction-heating device can be assimilated to a transformer. The metal to be heated becomes the secondary circuit of a transformer. In a simplified model, the primary coil it always constructed of copper, since it is important to keep losses to a minimum so that the heating is done to maximum efficiency.

From the general theory, the induced currents will effectively flow in about a skin depth δ – depending on frequency of the source current and the two properties of the material - resistivity and relative permeability.

In this section we present some algorithmic skeletons for numerical simulation of the induction heating in metal cylinders using linear and non-linear models. The example is a model for the induction-heating furnace without iron core.

In the electromagnetic problems the field domain consists of more regions that differ by the electric properties. Thus, in induction heating the analysis domain consists in the following region:

- A conducting region where the eddy currents are induced
- A conducting region with externally imposed currents and the magnetic permeability of the free space
- A non-conducting region with low permeability magnetic materials without any kind of currents

In each region we can use different potential formulations and the coupling of the three regions is ensured by the interface conditions: the continuity of $H \times n$ and $B.n$.

The choice of the potential formulation in each region is a difficult task and depends on the problem particularities. In several cases the problem characteristics and the computation accuracy required allow a decoupling and a cascade solution. If this approach is not possible an approach which is frequently applied is to solve each equation separately and to recouple them in some way.

II. MATHEMATICAL MODELS FOR COUPLED FIELDS IN INDUCTION HEATING

Many areas of electrical engineering require the solution of problem in which the electromagnetic field equations are coupled to other partial differential equations, such as those describing thermal, fluid flow or stress behaviour. These phenomena are described by equations that are coupled. The coupling between the two fields – electromagnetic and thermal - is a natural phenomenon and only in a simplified approach the field analysis can be treated as independent problem.

In several cases, it is possible a decoupling and a cascade solution of the coupled equations. One approach is to solve each field equation separately, recouping then the set in some way.

Another attractive and efficient approach of solving coupled differential equations is to consider the set as a single system. In this way a single linear algebraic system for the whole set of differential equations is obtained after

[1]Daniela Cârstea is with the High School Group of Railways. Str. Brâncusi, nr. 9. Craiova, Romania. E-mail: danacrst@yahoo.com

[2]Ion Cârstea is with the University of Craiova, Faculty of Automation, Computers and Electronics. Blv. Decebal, nr.5. Craiova, Romania. E-mail:incrst@yahoo.com

[3]Alexandru Cârstea is with the University of Craiova, Faculty of Automation, Computers and Electronics. Blv. Decebal, nr.5. Craiova, Romania. E-mail:ncarstea@hotmail.com

discretization, and is solved to a single step. If one or more equations are non-linear, non-linear iterations of the whole system are required.

Generally, in the mathematical and numerical simulation of transient induction heating problems, it is necessary to solve two systems of equations: one for the electromagnetic field and the other for the thermal field. These systems are strongly coupled and non-linear, since the thermal sources represent the electromagnetic field effects and the magnetic and thermal properties of the material change with the temperature. This inherent coupling of the two mathematical models leads to an increase in the numerical model dimensions due to the vectorial nature of the electromagnetic quantities.

The mathematical models of the coupled fields are:

- the transient heat conduction equation with boundary conditions of convective and radiation type
- Maxwell equations in potential formulations (especially in multi-potential formulations)

The constructive particularities of the electromagnetic device must be accounted for in a numerical model in order to develop efficient computer program. For example, the main particularities of the induction heating are:

- The thermal time constants are bigger than the electric time constants.
- The heat source is the power dissipated by the eddy currents so that the accuracy of the computation of the eddy current density influences the problem accuracy
- The workpieces are generally composed by only a single material so that it is not necessary to include discontinuities in the electric conductivity
- The variations of the electromagnetic properties (permeability, electric conductivity) are continuous.

The particularities of the problem can be exploited in some directions although a unified approach is a desirable requirement for an expert system in the area of coupled problems. The following directions can be exploited in our target example:

- The electromagnetic computation can be done as a sequence of sinusoidal electrical steady-state
- The most important electromagnetic field parameter from the viewpoint of the thermal field is the current density so that the computation accuracy of this quantity is very important
- The lack of discontinuities in electric conductivity allows the use of magnetic vector potential formulation
- The computation accuracy of J depends of the simulation method. For example, if J is derived by a "*rot*" operation as J= rot H, the accuracy of J is not the same accuracy as H. If the density is directly computer as J=-jωσA, then the accuracy of J is the same accuracy as A.

The mathematical model for the heat transfer is the heat conduction equation:

$$(c\gamma)\frac{\partial T}{\partial t} = \nabla(k\nabla T) + q \qquad (1)$$

$$T(x,0) = f(x) \quad x \in \Omega \qquad (2)$$

$$-k\frac{\partial T}{\partial n} = g(x,t) \quad x \in \Gamma, \quad t \succ 0 \qquad (3)$$

The significances of the quantities are: T(r,z,t) is temperature in the point with co-ordinates (r, z) at the time t; k is the tensor of thermal conductivities; q is the heat source (the ohmic losses due to the eddy-currents); g is a known function that leads to convection, Neuman or radiation condition.

The electromagnetic field model is Maxwell's equation in formulation with the magnetic vector potential A:

$$\nabla \times (\nu\nabla \times \bar{A}) = \bar{J} \qquad (4)$$

with J – the total current density:

$$\bar{J} = -\sigma(\frac{\partial \bar{A}}{\partial t} + \nabla V) \qquad (5)$$

Induced losses are:

$$P = \frac{1}{2\sigma}\int_S |\bar{J}|^2 dS$$

For the magnetic field there are two basic types of boundary conditions on the boundary Γ of the space domain Ω (Dirichlet and Neumann conditions):

$$\bar{A}(x,y,t)\Big|_\Gamma = \overline{A_D}(x,y,t)$$

$$\upsilon\frac{\partial \bar{A}}{\partial n}\Big|_\Gamma = \bar{H}\times\bar{n} = \overline{H_n}(x,y,t)$$

where the subscript n has the significance of the normal component of the field variable.

In harmonic time applications, with V a scalar electric potential, the electric the current density is:

$$\overline{J^*} = -j\sigma\omega\overline{A^*} - \sigma\nabla V^*$$

and the field model becomes:

$$\nabla \times (\nu\nabla \times \overline{A^*}) + j\sigma\omega\overline{A^*} + \sigma\nabla V^* = 0 \qquad (6)$$

where the superscript * denotes the complex value.

III. A SIMPLIFIED NUMERICAL MODEL

The computation of the eddy current distribution in a conductor using 3D model is a difficult and computationally expensive problem. To reduce the computation complexity the concept of the surface impedance is used. This approach is appropriate in those applications where the skin depth of the eddy currents induced is small compared with the thickness of the conductor. The idea of this approach is simple: the conductor is replaced by an appropriate boundary condition.

For many practical eddy current problems as the induction heating devices the magnetic flux penetration is confined to surface layers. Thus, a sinusoidal magnetic field with the amplitude B_m at the conductor surface and parallel to the surface has an exponential decay in the conductor:

$$B = B_m.\exp(\frac{-x(1+i)}{\delta})$$

In a point on surface of the conductor, the surface impedance is defined by the components of the electric and magnetic fields:

$$Z_t = \frac{E_t}{H_s}$$

where subscripts t and s denote the tangential direction for the two fields. The tangential magnetic field, H_s, is due to excitation.

If the skin depth δ is small, it is not economic to do a discretization of the solid conductor. This idea is exploited in many numerical models by considering a special boundary condition known as the surface impedance condition. In an A-formulation for two-dimensional magnetic problems the boundary is:

$$\frac{\partial A}{\partial n} = -\frac{(1+i)}{\delta \mu_r} A = -\beta A$$

This condition in a finite element model leads to the evaluation of a term as:

$$\int_\Gamma N_i \frac{\partial A}{\partial n} d\Gamma = -\beta (\int_\Gamma N_i N_j d\Gamma) A_i$$

In the modelling of the induction heating we can use this concept by decomposition of the whole domain into two subdomains.

As target example we consider a long cylindrical workpiece excited by a close-coupled axial coil (figure 1). The problem is an axisymmetric heating device. The coil is assimilated with a massive conductor. A quarter of the whole domain is considered.

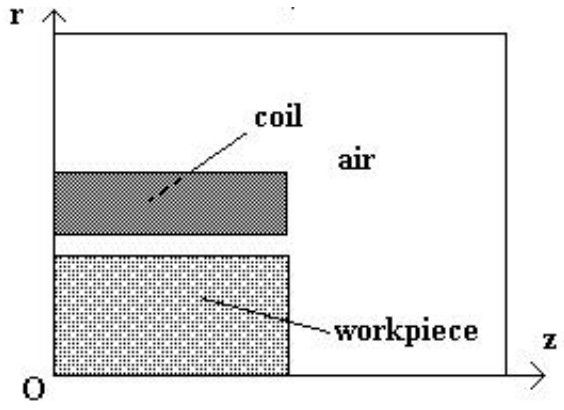

Fig.1. The whole analysis domain

The main advantages of the use of the surface impedance are:

- Reduction of the size of the problem domain
- Reduction of the solution time for the numerical model

Practically, the whole domain of the problem can be decomposed into 2 subdomains:

- A subdomain Ω_1 contains current source (the coil) and the air
- A subdomain Ω_2 consists in the workpiece (a metal cylinder) and source-free

The solid conductor may be modelled using the Poynting vector that replaces the solid conductor. In the figure 2 the analysis domain is plotted.

Numerical algorithms were developed using this concept. The first stage of any algorithm involves the evaluation of the

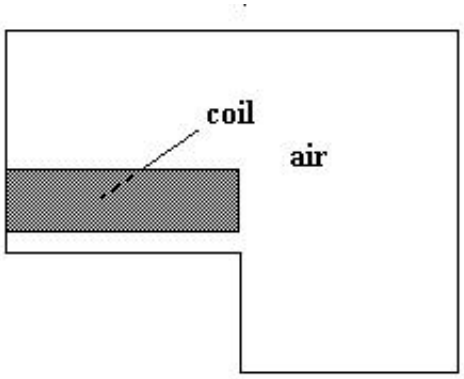

Fig.2. The reduced analysis domain

ohmic losses developed in the conducting part.

Concerning the target example, a *simplified algorithmic skeleton* consists in the decomposition of the whole domain in two disjoint subdomains Ω_1 and Ω_2 with the following properties:

- A subdomain Ω_1 for electromagnetic field analysis that does not include the workpiece (replaced by the surface impedance);
- A subdomain Ω_2 for the thermal field that include the workpiece with the heat generated by the electromagnetic field on the workpiece surface.

The algorithm consists into 2 stages:

- Computation of the electromagnetic field in the subdomain 1 by replacing the subdomain 2 with a surface term
- Computation of the thermal field consisting of the solid conductor only but having a common boundary with the first subdomain.

The boundary condition for the thermal on the common boundary is derived from the electromagnetic solution. In this algorithm we consider that the heat penetrates the workpiece by the outer surface. This assumption is valid at high frequency or for the cases where the dept penetration of the magnetic field is very small. We can use Poynting vector to get real and reactive components of power, that is:

$$\overline{S} = \overline{P} + j\overline{R} = \overline{E} \times \overline{H}^*$$

with H^* the conjugate complex of H.

The power in workpiece is given by $P \times S$, with S the surface area, and P the real part of the Poynting vector. This value is used in the computation of the boundary condition for the analysis domain.

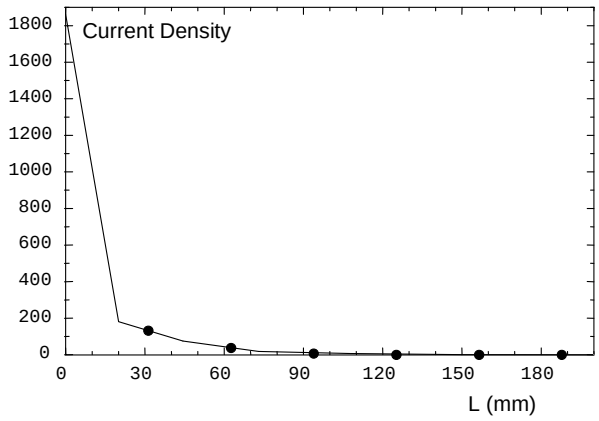

Fig.3. The current density in the workpiece

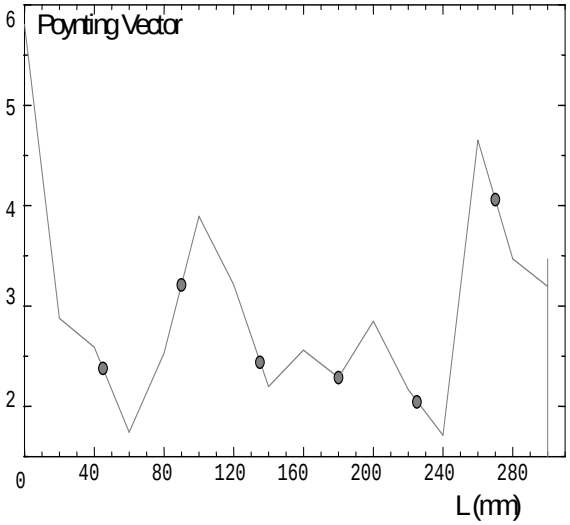

Fig.4. Values of Poynting vector at workpiece surface

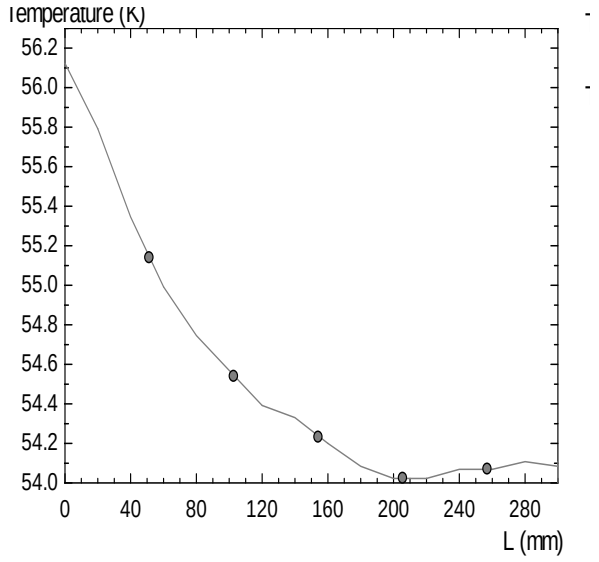

Fig.5. Final temperature on the external surface (tf=500s)

IV. NUMERICAL RESULTS

The numerical models were obtained by the finite element method for axisymmetric fields. For numerical simulation we used the program Quickfield [4]. In our target example we considered a workpiece of the metal with the conductivity 1.10^7 [S/m]. The frequency was 1 MHz. The copper coil has the conductivity of $6.3\ 10^7$ [S/m]. We made more simulations for a frequency range from 1 KHz to 1 MHz. The Figure 3 shows the current density [A/mm^2] in the workpiece along the centerline (the axis Or). The depth of penetration is small and can vary with the temperature.

RMS power flow through the external axial surface of the workpiece (Poynting vector flow) is computed with the formula:

$$P = \int (\bar{S}.\bar{n})ds$$

The variation of the vector Poynting to the workpiece surface is plotted in the figure 4 and can be used for heating computation in the workpiece.

At a frequency of 1000 Hz the final temperature is shown in the figure 5 for a time interval equal to 500 s.

V. CONCLUSIONS

In this paper we presented a simplified model for the numerical simulation of the induction heating of cylinders in large furnaces. The model was based on the concept of the surface impedance with direct impact on the computing resources. At high frequency the penetration depth of the magnetic field in a metal is very small so that we can eliminate the workpiece domain in the magnetic field computation. The model is based on the simplifying assumption that all the heat entered at the surface. This assumption is valid if the frequency is very high for the depth of heating to be small compared with the radius of the workpiece. The finite depth of penetration changes the temperature in the workpiece considerably.

REFERENCES

[1] Cârstea, D. "CAD tools for magneto-thermal and electric-thermal coupled fields". *Research Report in a CNR-NATO Grant*. University of Trento. Italy, 2004.

[2] Cârstea, D., Cârstea, I. *CAD in electrical engineering.* Editor: Sitech, Craiova. 2000.

[3] Davies, E.J. *Conduction and Induction Heating.* IEE Power Engineering Series 11, Peter Peregrinus Ltd. London, U.K. 1990.

[4] *** QuickField program Version 5.2. User's guide, 2004. Tera Analysis.

Boundary Conditions for Device Simulation in Mixed Area

Ilya T. Tanchev[1] , Ventceslav D. Draganov[2]

Abstract - **This paper extends the capabilities of device simulation by studying, characterizing, and improving the boundary conditions around the physical device simulation so that advance radio frequency (RF), and high speed components can be accurately modeled. The many small variation of parameters take effect on functions and his approximation. This work proposes directions of solution parameter of analyst simulation in specific boundary. Paper presented by way of example calculation of parameter for MOSFET element and graphical staff.**

Keywords - **device simulation, model, mix area, boundary condition.**

I. INTRODUCTION

By each iteration of process simulation needed information the value of current and value of electrical tension. For each small variation in form $\nu = \Delta V e^{-j\omega t}$ needed linearization of current $i = \Delta V e^{-j\omega t}$ and his calculation. With this operation used thoroughly law of Kirchoff.. In this current is;

$$i = Y\nu = \left(\frac{dI}{dV}\Delta V + j\omega \frac{dQ}{dV}\Delta V \right) e^{-j\omega t} \qquad (1.0)$$

and ratio of real current and real tension to current ant tension calculated be done; $dI/dV = \Delta I_R / \Delta V$,
tool responded and for $dQ/dV = \Delta I_I / (\omega \Delta V)$.

II. IN PARTICULAR OF METHOD

Algorithm for description change and analyst function of calculation value of simulation is presented in many work [6], [8], [2] and ICECT; ICEST forum. In publication show interest the algorithm of frequency dependence element. This operation is non desirable by trivial simulator. Problem is interesting from point of frequency. As a eliminated the frequency $\omega \to 0,$ signal and small variation of signal have decrypted in;

$$\begin{bmatrix} J-D \\ D \quad J \end{bmatrix} \begin{bmatrix} X_R \\ X_I \end{bmatrix} = \begin{bmatrix} B \\ 0 \end{bmatrix}, \ldots \qquad (1.1)$$

Were J is matrix of Jacoby from elements. X_R and X_I is reality and imaginary component. Important parameters presented be; $\Delta\psi$, Δn and Δp. [2]. with *B* be reflected boundary conditions, and *D* - frequency. That expressed with matrix. [6], [7];

$$D = \omega \begin{bmatrix} 0 & 0 & 0 \\ 0 & j\dfrac{\partial G_n}{\partial n} & 0 \\ 0 & 0 & j\dfrac{\partial G_p}{\partial p} \end{bmatrix} = \omega K , \qquad (1.2)$$

where: frequency characteristic is presented in non-linear vector *G*. If divide reality and imaginary part to writhed;

$$JX_R - DX_I = B, \ ; \ DX_R + JX_I = 0, \qquad (1.3)$$

Reality component possibility presented in;

$$X_R = J^{-1}(B + \omega K X_I), \quad X_I = -J^{-1}(\omega K X_R),$$

If frequency ($\omega \to 0,$) to component $\omega K X_I$ is ignore and for X_R possibility;

$$X_R = \lim\left(J^{-1}(B + \omega K X_I)\right) = J^{-1}B, \qquad (1.4)$$

, analog in appearance;

$$X_I = -J^{-1}(\omega K X_R) = \omega \tilde{X}_I , \qquad (1.5)$$

Where X_I and $\tilde{X}_I$ is depended frequency parameters models. For each iterations ΔI calculated parameters from X_R and X_I is Ψ, n and p. Therefore ΔI possibility calculated whit two components – reality and imaginary;

$$\Delta I = F(X_R) + j\omega F(\tilde{X}_I), \qquad (1.6)$$

[1]Ilya T. Tanchev is with the Technical University of Varna, - department of Electronic – Varna, Studentska Str. №1, Bulgaria, E-mail: itta@ms3.tu-varna.acad.bg
[2]Ventceslav D. Draganov is with the Technical University of Varna, - department of Electronic – Varna, Studentska Str. №1, Bulgaria,

Function $F(X)$ literalized about X_R и X_I et courant value have two component – reality and imaginary;

$$\frac{dI}{dV}=\frac{F(X_R)}{\Delta V},\ \frac{dQ}{dV}=\frac{\omega F(\tilde{X}_I)}{\omega\Delta V}=\frac{F(\tilde{X}_I)}{\Delta V}, \qquad (1.7)$$

In this method (method Newton) form calculations of iterations be observe following priority; (especially if formula accepted frequency component). That is very often by approach characteristic specific communication devices.

- Calculation of two component increment time from work, but give possibility of put coefficients in matrix et achievement got approach.
- Give way possibility of ignore some frequency approach who are non desirables in integrated area from simulation.
- Make easier transfer the parameters between models. Give possibility some parameters to by ignored and other approach.
- Algorithm to by some more effective from case where ΔV = 1.0V.

III. EXPOSITION

A. Determination of currant in model

Flow currant consists in two components – reality and imaginary. Calculation of reality component based of parameters; $\Delta I_n, \Delta I_p, \Delta I_i$, founded constant currant resolution from;

$$I_n = A(qD_n\Delta n - q\mu_n n\Delta\Psi), \qquad (1.8)$$

$$I_p = A(-qD_p\Delta p - q\mu_p p\Delta\Psi), \qquad (1.9)$$

Currant owing of small change calculated in reality functions;

$$\Delta I_n = \Delta\Psi\frac{\partial I_n}{\partial\Psi}+\Delta n\frac{\partial I_n}{\partial n}, \qquad (2.0)$$

were currants consisting in two component. Real part ΔI are received by parameters $\Delta\Psi, n$ and Δp and evaluate resolution whit *Xr,* and imaginary – whit *Xi.* To value are calculated form specific case and method of connection in mixed area.

B. Very small variation in mix area;

For approach very small variations currant signals and fix lap in model electron device need have real value. Connection input / output pin models need transfer very small currant variation for very small time period. Expression is;

$$I_\Delta = \varepsilon\frac{\partial E}{\partial t}=\varepsilon\frac{\partial}{\partial t}(-\Delta\Psi), \qquad (2.1)$$

Approach small change currant signal possibility whit high precision if in model provide for restrict value and have algorithm of processing. Very import part of modeling is fact of reaction approach characteristic et method of calculation of this model function at small variation without existence noise. . In define this problem need read variation in form; $\Delta Ve^{-j\omega t}$ at algorithm of linearization of ratio *I/V* with $e^{-j\omega t}$. Neglect component $e^{-j\omega t}$ insert inaccuracy by connect characteristic and transfer parameters. This process reiterates and fault of iteration multiply. This cause of correct read very small variation of currant and correct integer in system equation needed value Ψ, in each point in model;

$$\Psi = \Psi_{k(dc)} + \Delta\Psi_k e^{-j(\omega t-\Phi_k)}, \qquad (2.2)$$

Supported (1.3) and [2], [7] for each small variation currant in each pin of model possibility writhed;

$$I_{kl(\Delta)} = \varepsilon\frac{\partial}{\partial t}\left(\frac{\partial\Psi}{\partial x}\right)=-A_{kl}\frac{\partial}{\partial t}\left(\frac{\Psi_k-\Psi_l}{\Delta L_{kl}}\right), \qquad (2.3)$$

Used method Popov-Sendov (numerical method) can be able currant;

$$I_{kl(\Delta)}=-A_{kl}\frac{\partial}{\partial t}\left(\frac{-j\omega(X_{Rk}-X_{Rl})+\omega(X_{Ik}-X_{Il})}{\Delta L_{kl}}\right)e^{-j\omega t}, \qquad (2.4)$$

This non originally (physically) change but this is solution in very high accuracy. With at this are choices coefficient and variation. Some other priority is performance currant in addition sum in case included boundary parameter in concrete point calculation. Received sum is linear and if lay operator *H* for reality and imaginarily parts possibility give *In* and *Ip* used (2.4) This expression have two part et reality part included boundary coefficient;

$$\mathrm{Re}(\Delta I_d)=\varepsilon H\left(\frac{\omega A_{kl}(X_{Ik}-X_{Il})}{\Delta L_{kl}}\right), \qquad (2.5)$$

If accept $\omega\to 0$, then ω^2 incline toward 0. This process is height and a minimal variation is insignificant com reality part. In some case boundary conditions is important and these variation need included in volt-ampere characteristic. Transfer these boundary in equation in next model scheme is condition of correct simulation. For imaginary part are;

$$I_m(\Delta I_d)=\varepsilon\omega H\left(\frac{A_{kl}(X_{Rk}-X_{Rl})}{\Delta L_{kl}}\right), \qquad (2.6)$$

In this way problem of approach in $\omega\to 0$, none presented.

C. Transient annalists frequents element in mix area

Calculation and including small variation in transient annalist allow moment t_0 and simulation time t_s for very small period Δt. Decision in $t_s = t_0 + \Delta t$ is normally. In this way, each iteration calculates currant and tension for dish time moment. Way used method constantly currant annalist calculated step by step at changes is reality of part of time period $t_0 + \Delta t$. This demonstrate whit matrix Jacobin for calculate *Xr* and *Xi* in model whit parameter Ψ, n and p.

Calculation currant is analog in (2.5) and (2.6). Small variations of value are finding in (2.0).

IV. Work Problem

Change small variation currant by annalist**.**

Small change signals and functions in time make calculation difficult. This fact hampers but small currant and tension is blend with signals noise. In transient analysis important is time function. This is idealizing function and approach of frequency elements is difficult. When this elements are work in mix area and change value of parameters whit functions, resolve is some more. In this case should deduce work whit this equation should reflect this small variation. At the same time equation are satisfy demand of work in mix area. On this basis are construct interface for transferring parameters in mix area.

If time of simulation is; t_s to $t + \Delta t$, is period of annalist. Change in function variation is;

$$\Psi_k(t_0) = \Psi_{k(t_0)}, \tag{2.7}$$

Used (**2.1**), to possible define change from Ψ, for each time step;

$$I_{dk} = \varepsilon \frac{\partial}{\partial t}\left(-\frac{\partial}{\partial x}(\Psi)\right) = -\varepsilon A_{kl}\frac{\partial}{\partial t}\left(\frac{\Psi_k - \Psi_l}{\Delta L_{kl}}\right), \tag{2.8}$$

if this formula develop in full reach value from currant;

$$= I_{do(kl)} - \varepsilon A_{kl}\left(\frac{(X_{Rk} - X_{Rl}) + j(X_{Ik} - X_{Il})}{\Delta t \Delta L_{kl}}\right), \tag{2.9}$$

Observably on have two components for analysis – one as classic algorithm and other for transient analysis whit on algorithm as frequency parameters. If frequency parameter is not necessary et. $\omega \to 0,$ to her possibility ignore. In other case read really and imaginary parts;

$$\mathrm{Re}(\Delta I_d) = -\varepsilon H\left(\frac{A_{kl}(X_{Rk} - X_{Rl})}{\Delta t \Delta L_{kl}}\right), \tag{3.0}$$

$$\mathrm{Im}(\Delta I_d) = -\varepsilon H\left(\frac{X_{Ik} - X_{Il}}{\Delta t \Delta L_{kl}}\right) = -\varepsilon\omega H\left(\frac{\tilde{X}_{Ik} - \tilde{X}_{Rl}}{\Delta t \Delta L_{kl}}\right), \tag{3.1}$$

Calculation reality component depend on frequency impossibility. For concrete case decision at imaginary component needed. Verification this thesis based simulators used algorithms in (1.0), or crested new models toward existing. Many work of this problem view created concrete algorithm for specific case. Generally cases they used specific interfaces in products; SYNOPSYS, CADENCE or simulators Philips. Shown formulas are able used for created new interface or perfecting exist module. For control calculation used laboratory result [3], [4], work whit this result simulator IBM FIELDAY and Device PISCES [3], [4], and interface created in this case; [1], [6].

V. Experimental Investigations

Annalist for check mix approach.

Annalist make for *dI/dV* by *DC* annalist from MOSFET element, when frequency is zero and two experiment by frequency various at 0,1 to 100Hz. Result from premier two case is laboratory and viewed in test bulletin [3], [2], [8]. Also to element created calculation from formulas in paragraph; 1.0 and 2.0, as from received results builder graphical function and compare whit laboratory test.

Basic parameters used whit MOSFET transistor is;

- *5V tension;*
- *Switching time from 0 to 5V – 100ps;*
- *work time* t_s *= 50ps;*
- *Calculations step* $\Delta t = 5\,ps$ *;*
- *Tension of gait from 2.0V to 3.0V by step 0.01V;*

Calculated dI/dV and $\Delta I/\Delta V$ and his derivative. Manifest small signals and his relationship variations. Also calculations cost dI_i/dV_1, dI_i/dV_2, give possibilities investigate connection drain whit for opposite element (input primitive model).

VI. Inference

Specific parameters of MOSFET element are included in (3.0), (3.1), and calculate. At fig. 1.0 and fig. 2.0 view that deference his received whit experimental measure value and calculated value is five percent not more. In this sum of percents not included error of calculations (value grow round) and calculations of value outside range.

In this case result, address one self accepted accuracy is goodish, by approach of classic models or simulators [5], [3].

When ignore frequencies variations elements $\omega \to 0,$ to this propose is about 1%.

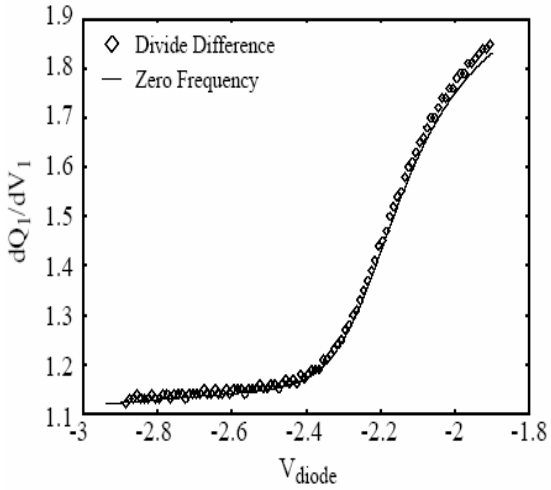

Fig. 1. Test results

VII. CONCLUSION

Offered method included two components at calculations currant in models simulations. This is component of reality parts, and component of imaginary parts.

- View similar / equal approach in currant whit small variation.
- Give possibilities of calculated small change variations. If this not needed give point of ignore.
- In approach add frequency dependence whit imaginary component.
- Result is five percent of two parts, and many one per reality component.

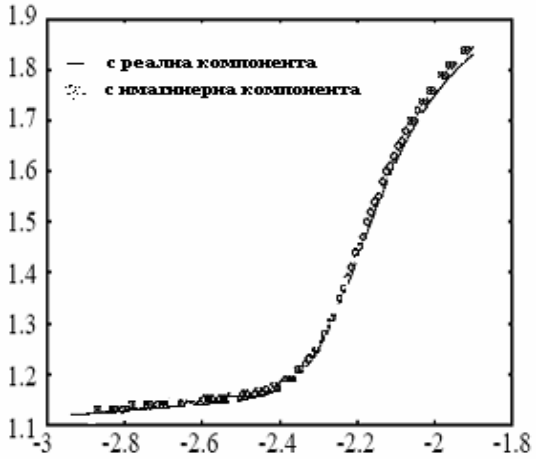

Fig. 2. Calculated result approach

REFERENCE

[1] Il. T. Tanchev**.,** "Transfer The Parameter Between Elements Model in AC-DC Design Area for Simulation", *13' International Scientific and Applied Science Conference, ELECTRONICS – ET'2004*, P1.28, pp. 136, Sozopol, Sept. 22-24,

[2] S. Laux. "Techniques for Small Signal Analysis of Semiconductor Devices." IEEETransactions on Electronic Devices. Vol. ED-32, No. 10, pp. 2028-2037, Oct. 1986.

[3] S. Furry, J. Johnson, G. Fiorenza, and R. Logan. Fielday II User's Manual.Ver. 7.5.0. IBM Microelectronics, 1995.

[4] J. Johnson, S. Furry, and D. Cole. Fielday II Theoretical Manual. Ver. 7.1.0. IBM, Microelectronics, 1995.

[5] B. Johnson, T. Quarles, A, Newton, D. Peterson, and A. Sangiovanni-Vincentelli. SPICE Version 3f User's Manual. The Regents of the University of California.,Berkeley, 1992.

[6] И. Танчев, Л. Райковска, В. Драганов "Оптимизиране на алгоритми за симулация на аналогови елементи в интегрирана среда", Международна конф. на НТС – СЕЕС ЕЛЕКТРОНИКА-2004, стр. 146-151, София, 21-22 май 2004г. ISBN 954-90209-3-2

[7] Сендов Б., В. Попов, "Числени методи" I и II част Наука Изкуство, София, 1976 година

[8] F. Rotella, Z. Yu, R. Dutton. "Mixed-Mode Device/Circuit Simulator." Part III:Pisces 2ET with Applications Documentation. Board of Trustees of Leland, Stanford University. Stanford, CA. Dec. 1994

Computer Simulation of Space Interference of Low Frequency Electromagnetic Signals in the Human Body

Dimitar C. Dimitrov[1], Galina P. Peykova[2]

Abstract-**Low frequency interference devices have a wide range of application in medicine for successful treatment for rheumatism, skin diseases, liver diseases, muscular pain relief, contusions, sprains, chronic diseases. The main target of the article is to present a method of detailed description of low frequency electromagnetic signals in the human body.**

Keywords: **Space intereferece, Low frequency electromagnetic signals, Human body**

I. Introduction

In this example a low frequency interference device consists of two electrode couples (electrodes in each couple are parallel each other with rectangular shape). They make electromagnetic signals, whose vectors depend on time. The result of operating at the same time signals is a time - dependent signal ($\vec{E}(t)$). Its magnitude and direction change.

The voltage of the first electrode couple has constant low frequency f_1=4000Hz and for the second electrode couple it is variable: f_2=4000 ÷ 4100Hz, changing linearly. As a result two different angular frequencies are available ω1,ω2. And the result vector will certainly pass through quasi-resonant frequency of a fixed group of human muscles. The voltage at the end of electrode couples is constant and there are not side effects of inductance. The signal should reach deeply into the space of human body. Formulae below meet this requirements:

$$\vec{E}_1 = \left|\vec{E}_1\right| \times \cos(\omega_1 \times t) \quad (1)$$

$$\vec{E}_2 = \left|\vec{E}_2\right| \times \cos(\omega_2 \times t) \quad (2)$$

II. Mathematical Analysis

Tension is a fundamental characteristic to every electromagnetic field. Its absolute value can be estimated, using the principle of Coulomb.

The tension magnitude in a fixed point can be found by placing there a positive charged particle Q and observing the force between two charged particles.

$$\vec{E} = \frac{\vec{F}}{Q} \Rightarrow E = \frac{q}{4 \times \pi \times \varepsilon \times r^2} \quad (4)$$

The principle of Coulomb is operative only for particle suppliers of energy. If each electrode from the first couple is a particle supplier of energy, the tension in the fixed point will be defined as:

$$E_1 = \frac{q}{4 \times \pi \times \varepsilon \times r_1^2} + \frac{q}{4 \times \pi \times \varepsilon \times (d_1 - r_1)^2} \quad (5)$$

r_1 and $(d_1 - r_1)$ are the distances between the fixed point and each "charged particle" of energy.

There are lots of charged particles on the surface of each electrode:

$$E_1 = \int_0^{\varphi_1}\int_{r_a}^{r_b} \frac{q_1}{4 \times \pi \times \varepsilon \times r_1^2} \times dr d\varphi + \int_0^{\varphi_2}\int_{r_a}^{r_b} \frac{q_1}{4 \times \pi \times \varepsilon \times r_1^2} \times dr d\varphi + \int_0^{\sigma_1}\int_{r_c}^{r_d} \frac{q_1}{4 \times \pi \times \varepsilon \times \left(\frac{d_1}{\cos(\delta)} - r\right)^2} \times d\left(\frac{d_1}{\cos(\delta)} - r\right) d\sigma + \int_0^{\sigma_2}\int_{r_c}^{r_d} \frac{q_1}{4 \times \pi \times \varepsilon \times \left(\frac{d_1}{\cos(\delta)} - r\right)^2} \times d\left(\frac{d_1}{\cos(\delta)} - r\right) d\sigma \quad (6)$$

The fixed point is T. The perpendicular lines from point T to the first and second electrodes from first couple are denoted respectively by TT_1 and TT_2. $T_1T_2 = d_1$, $TT_1 = r_1$, $TT_2 = d_1 - r_1$. There is a surface **α** through line d_1. **α** is perpendicular to both electrodes and its intersection with electrodes is parallel (respectively perpendicular) to electrode's boundaries (fig.3). $\alpha \cap Q_1Q_2Q_3Q_4 = AB$ ($AB \parallel Q_1Q_2, Q_3Q_4$; $AB \perp Q_1Q_4, Q_2Q_3$).

$\alpha \cap Q_5Q_6Q_7Q_8 = CD$

[1]PhD. Dimitar. C. Dimitrov Assoc. Prof. is with The Faculty of Communications and Communications Technologies, Technical University of Sofia, Email: dcd@tu-sofia.bg

[2]Galina P. Peykova is with Faculty of Computer Systems and Control, Technical University of Sofia, Email: galina_peykova@abv.bg

$(CD \parallel Q_5Q_6, Q_7Q_8; CD \perp Q_5Q_8, Q_6Q_7)$.

$TA = r_a$, $TB = r_b$, $TC = r_c$, $TD = r_d$.

Inside Integral Expression: Inside integral covers charged particles, situated in segments AB and CD. The result of integrating formula 5 is:

$$E_1 = \int_{r_a}^{r_b} \frac{q_1}{4\times\pi\times\varepsilon\times r^2}\times dr + \int_{r_c}^{r_d} \frac{q_1}{4\times\pi\times\varepsilon\times\left(\frac{d_1}{\cos(\delta)}-r\right)^2}\times d\left(\frac{d_1}{\cos(\delta)}-r\right)$$

$$= -\left(\frac{q_1}{4\times\pi\times\varepsilon}\right)\Bigg|_{r_a}^{r_b} - \left(\frac{q_1}{4\times\pi\times\varepsilon\times\left(\frac{d_1}{\cos(\delta)}-r\right)}\right)\Bigg|_{r_c}^{r_d}$$

$$= \left(\frac{q_1}{4\times\pi\times\varepsilon}\right)\times\left(\frac{1}{r_a}-\frac{1}{r_b}+\frac{1}{r_c}-\frac{1}{r_d}\right) \quad (7)$$

The plane surface of **α** leads to the following conclusions:

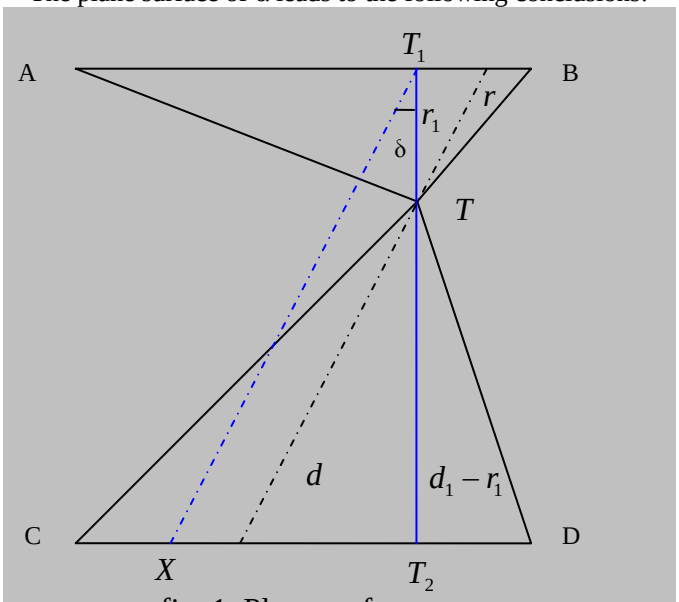

fig. 1. Plane surface α

r_1 starts at TA and ends at TB, and $(d_1 - r_1)$ starts at TD and ends at TC. If r_1 coincides with r, then $(d_1 - r_1)$ coincides with d. From triangle T_1T_2X :

$$\cos(\delta) = \frac{d_1}{d+r} \Rightarrow d = \frac{d_1}{\cos(\delta)} - r \quad (8)$$

d is the integration variable for the second integral from formula 7.

Outside Integral Expression:

The second integral takes all the charged particles on the surfaces of the electrodes under consideration. (formula 6.). It is the result of moving of AB and CD over the surface of electrodes at angles φ1, φ2, σ1, σ2.

$\angle ATQ_1 = \angle BTQ_2 = \varphi_1$, $\angle ATQ_4 = \angle BTQ_3 = \varphi_2$, $\angle CTQ_5 = \angle DTQ_6 = \sigma_1$, $\angle CTQ_8 = \angle DTQ_7 = \sigma_2$

After integrating formula 7.:

$$E_1 = \left(\frac{q}{4\times\pi\times\varepsilon}\right)\times\int_0^{\varphi_1}\left(\frac{1}{r_a}-\frac{1}{r_b}\right)\times d\varphi + \left(\frac{q}{4\times\pi\times\varepsilon}\right)\times\int_0^{\varphi_2}\left(\frac{1}{r_a}-\frac{1}{r_b}\right)\times d\varphi + \left(\frac{q}{4\times\pi\times\varepsilon}\right)\times\int_0^{\sigma_1}\left(\frac{1}{r_c}-\frac{1}{r_d}\right)\times d\sigma + \left(\frac{q}{4\times\pi\times\varepsilon}\right)\times\int_0^{\sigma_2}\left(\frac{1}{r_c}-\frac{1}{r_d}\right)\times d\sigma \quad (9)$$

The rectangular triangles Q_1AT and Q_4AT have right angle at apex A. The rectangular triangles Q_2BT and Q_3BT have right angles at apex B. The rectangular triangles Q_5CT and Q_8CT have right angles at apex C. The rectangular triangles Q_6DT and Q_7DT have right angles at apex D. Therefore:

$$\cos(\delta_i) = \frac{r_l}{r_l'} \Rightarrow r_l = r_l' \times \cos(\delta_i)$$

$$\cos(\delta_i) = \frac{r_l}{r_l''} \Rightarrow r_l = r_l'' \times \cos(\delta_i)$$

$$where: \delta = \varphi, \sigma; i = 1,2; l = a, b, c, d \quad (10)$$

$r_a' = TQ_1$ $r_b' = TQ_2$ $r_c' = TQ_6$ $r_d' = TQ_5$

$r_a'' = TQ_4$ $r_b'' = TQ_3$ $r_c'' = TQ_8$ $r_d'' = TQ_7$

The result from formulas 9. and 10. is formula 11.:

$$E_1 = \left(\frac{q}{4\times\pi\times\varepsilon}\right)\times\int_0^{\varphi_1}\left(\frac{1}{r_a^{'}\times\cos(\varphi)}-\frac{1}{r_b^{'}\times\cos(\varphi)}\right)\times d\varphi$$
$$+\left(\frac{q}{4\times\pi\times\varepsilon}\right)\times\int_0^{\varphi_2}\left(\frac{1}{r_a^{''}\times\cos(\varphi)}-\frac{1}{r_b^{''}\times\cos(\varphi)}\right)\times d\varphi$$
$$+\left(\frac{q}{4\times\pi\times\varepsilon}\right)\times\int_0^{\sigma_1}\left(\frac{1}{r_c^{'}\times\cos(\sigma)}-\frac{1}{r_d^{'}\times\cos(\sigma)}\right)\times d\sigma$$
$$+\left(\frac{q}{4\times\pi\times\varepsilon}\right)\times\int_0^{\sigma_2}\left(\frac{1}{r_c^{''}\times\cos(\sigma)}-\frac{1}{r_d^{''}\times\cos(\sigma)}\right)\times d\sigma \tag{11}$$

Revised formula is:

$$E_1 = \left(\frac{q}{4\times\pi\times\varepsilon}\right)\times\left(\frac{r_b^{'}-r_a^{'}}{r_a^{'}\times r_b^{'}}\right)\times\int_0^{\varphi_1}\frac{d\varphi}{\cos(\varphi)}$$
$$+\left(\frac{q}{4\times\pi\times\varepsilon}\right)\times\left(\frac{r_b^{''}-r_a^{''}}{r_a^{''}\times r_b^{''}}\right)\times\int_0^{\varphi_2}\frac{d\varphi}{\cos(\varphi)}$$
$$+\left(\frac{q}{4\times\pi\times\varepsilon}\right)\times\left(\frac{r_d^{'}-r_c^{'}}{r_d^{'}\times r_c^{'}}\right)\times\int_0^{\sigma_1}\frac{d\sigma}{\cos(\sigma)}$$
$$+\left(\frac{q}{4\times\pi\times\varepsilon}\right)\times\left(\frac{r_d^{''}-r_c^{''}}{r_d^{''}\times r_c^{''}}\right)\times\int_0^{\sigma_2}\frac{d\sigma}{\cos(\sigma)} \tag{12}$$

The solution of the integral is:

$$\int_0^{\varphi_1}\frac{d\varphi}{\cos(\varphi)} = -\ln\left|tg\left(\frac{\left(\frac{\pi}{2}-\varphi_1\right)}{2}\right)\right| \tag{13}$$

To compute the value of E_1 it is necessary to find $r_i, r_i^{'}, r_i^{''}, \quad i=a,b,c,d;$ and angles $\varphi_1,\varphi_2,\sigma_1,\sigma_2$. The method is:

- Finding the equation of line TT_1. For that it is necessary to find the equations of the plains of electrodes by figuring out the determinant below:

$$\begin{vmatrix} x & y & z & 1\\ x_1 & y_1 & z_1 & 1\\ x_2 & y_2 & z_2 & 1\\ x_3 & y_3 & z_3 & 1 \end{vmatrix} = 0 \tag{14}$$

The plane's equation is:

$$A\times x + B\times y + C\times z + D = 0 \tag{15}$$

The normal vector of plains $Q_1Q_2Q_3Q_4$ and $Q_5Q_6Q_7Q_8$ coincides with the directional vector of TT_1: $T_1T_2 \perp Q_1Q_2Q_3Q_4$.

Point T is situated on TT_1. Point T has space coordinates T($t_1,\ t_2,\ t_3$). Therefore the normal vector of plains $Q_1Q_2Q_3Q_4$ and $Q_5Q_6Q_7Q_8$, called vector ($\vec{N}$), is: $\vec{N}(A,\ B,\ C)$.

T_1T_2 equation is:

$$T_1T_2 \equiv \frac{x-t_1}{A} = \frac{y-t_2}{B} = \frac{z-t_3}{C} \tag{16}$$

- Finding x,y and z coordinates of point $T_1(t_1^{'},\ t_2^{'},\ t_3^{'})$. For that purpose it is requiring to be solved the system of equations:

$$\begin{cases} \dfrac{t_1^{'}-t_1}{A} = \dfrac{t_2^{'}-t_2}{B} = \dfrac{t_3^{'}-t_3}{C} \\ A\times t_1^{'} + B\times t_2^{'} + C\times t_3^{'} + D = 0 \end{cases}$$

- Finding the equation of line AB.

$AB \parallel Q_1Q_2$. They both have the same directional vector. The equation of Q_1Q_2 is:

$$Q_1Q_2 \equiv \frac{x-x_1}{x_2-x_1} = \frac{y-y_1}{y_2-y_1} = \frac{z-z_1}{z_2-z_1} \tag{17}$$

And the directional vector has co-ordinates ((x_2-x_1), (y_2-y_1), (z_2-z_1)).Therefore the equation of Q_1Q_2 is:

$$AB \equiv \frac{a_1-t_1^{'}}{x_2-x_1} = \frac{a_2-t_2^{'}}{y_2-y_1} = \frac{a_3-t_3^{'}}{z_2-z_1} \tag{18}$$

where $A(a_1,\ a_2,\ a_3)$.

- Finding the co-ordinates of point A.

Q_1Q_4's equation is:

$$Q_1Q_4 \equiv \frac{x-x_1}{x_4-x_1} = \frac{y-y_1}{y_4-y_1} = \frac{z-z_1}{z_4-z_1} \tag{19}$$

Solving the system of equations:

$$\left|\begin{array}{l}\dfrac{a_1-t_1^{'}}{x_2-x_1}=\dfrac{a_2-t_2^{'}}{y_2-y_1}=\dfrac{a_3-t_3^{'}}{z_2-z_1}\\[2ex]\dfrac{a_1-x_1}{x_4-x_1}=\dfrac{a_2-y_1}{y_4-y_1}=\dfrac{a_3-z_1}{z_4-z_1}\end{array}\right.$$

The required coordinates are: $A(a_1,\ a_2,\ a_3)$.

Finding the coordinates of points B($b_1,\ b_2,\ b_3$), $C(c_1,\ c_2,\ c_3), D(d_1,\ d_2,\ d_3)$ is in the same manner. The necessary distances are:

$$TA=\sqrt{(a_1-t_1)^2+(a_2-t_2)^2+(a_3-t_3)^2}$$
$$TB=\sqrt{(b_1-t_1)^2+(b_2-t_2)^2+(b_3-t_3)^2}$$
$$TC=\sqrt{(c_1-t_1)^2+(c_2-t_2)^2+(c_3-t_3)^2}$$
$$TD=\sqrt{(d_1-t_1)^2+(d_2-t_2)^2+(d_3-t_3)^2}$$
$$TQ_i=\sqrt{(x_i-t_1)^2+(y_i-t_2)^2+(z_i-t_3)^2},$$
$$where: i=1\div 8$$

Angles $\varphi_1,\varphi_2,\sigma_1,\sigma_2$ comes from formulas 10. The tension E_1 in the fixed point T comes from formula 12. Finding tension E_2 is analogous to finding tension E_1.

Calculating charged particle on the surfaces of the electrodes: There is a solid body. Its volume is V, surface S, volume charges q. A definition says:

$$div\vec{D}=\rho,$$

(20)

The result after integrating of it is:

$$\iiint\limits_{(V)}\left(div\vec{D}\right)\times dV=\iiint\limits_{(V)}\rho\times dV=q$$

(21)

In a result of Maksuel's postulate:

$$\iiint\limits_{(V)}\rho\times dV=\oiint\limits_{(S)}\vec{D}\times d\vec{S}=q$$

(22)

and material characteristic:

$$\vec{D}=\varepsilon\times\vec{E}$$

(23)

is Gauss's law:

$$\oiint\limits_{(S)}\vec{E}\times d\vec{S}=\frac{q}{\varepsilon}$$

(24)

Putting it into practice for electrodes of the low frequency interference device, it assumes the following structure:

$$\oiint\limits_{(Se)}\vec{E}\times d\vec{S}=\iint\limits_{(Se)}E\times dS$$
$$=E\times\iint dS=E\times Se=\frac{q}{\varepsilon}$$

(25)

The charge on the surface of the electrodes is:

$$q=E\times\varepsilon\times Se=\frac{U}{d}\times\varepsilon\times Se,$$

(26)

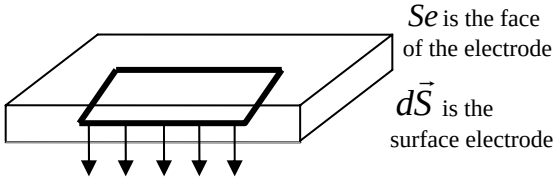

fig. 2. Charged particles on electrodes

There is tension only at the down side of the electrode. $E=\frac{U}{d}$, U-voltage at the end of each electrode couple, d - distance between electrodes. The charges on the surfaces of the couples are q_1 and q_2.

Finding The Vectors of The Tension: Using formulas 1. and 2. Total vector is : $\vec{E}=\vec{E}_1+\vec{E}_2$

It is a sum of space coordinates of $\vec{E}_1$ and $\vec{E}_2$.

$$E_i=E_{1i}+E_{2i}\quad i=x,y,z$$

(27)

III. Conclusion

1. A mathematical analysis of space-temporal configuration of low-frequency currents in the case of interference in the human body is given in the paper.
2. The presented mathematical description can be a base for computer simulation of space-temporal configuration of low-frequency currents in the case of interference in the human body is given in the paper.
3. An optimization of apparatus for intereferent currents in the process of design can be obtained using the above mentioned computer simulation

References

[1] S. P. Papazov, S.L. Farhi, "Theoretical Electrical Engineering", part 3, 1994.
[2] SIEMENS Medical Engineering Group, "Units for Physical Therapy And Diagnosis".
[3] D. Dimitrov, "Communication systems in medicine", Technical University, Sofia, 2005.
[4] "Higher Mathematics – lectures and exercises", Technical University, Sofia.
[5] "Electrical Engineering - lectures and exercises" , Technical University, Sofia.

Session IE:

INDUSTRIAL ELECTRONICS

The Circuits of Resonant Inverters with Limited Voltage across the Commutating Inductors

Nikola P. Gradinarov[1], Dimitar D. Arnaudov[2], Nikolay L. Hinov[3]

Abstract – **The paper presents a review of resonant inverters circuits with limited voltage across the commutating inductors. In the paper are shown the priority, which it has over the classical resonant inverters. Some of the circuits can work in both regimes – with natural commutation and with forced commutation (current source inverter).**

Keywords – **limited voltage across the commutating inductors, resonant inverters, current source inverter, improved output characteristics.**

I. INTRODUCTION

For the resonant inverters (RI) with limited voltage across the commutating inductors (LVCI), there is no matter if they operate in natural or forced commutation mode, a lot of performances working with non-constant load can be reached as they possess better characteristics. Usually these loads are typical for various technologies as: induction heating, melting, hardening, switching power supplies, electronic ballast for fluorescent lamps etc**.**

II. THE REVIEW OF VOLTAGE LIMITED CIRCUITS

The one of the circuits that improves resonant inverters output characteristics is shown on figure 1. In these circuits there is additional device that limits voltage across the commutating inductors [1]. This is the half-bridge resonant inverter with divided power supply. To the classical circuit there are added additional devices C_F, L_F, VD1 and VD2, witch improve the resonant inverters output characteristics. When the value of the coefficient of hesitation k [2] is $1<k<1.5$, the diodes VD1 and VD2 have not conditions for turning-on. In this case the circuit from figure 1 works as classical resonant inverters (CRI). If at the technology process by any reasons the voltages across the devices increases (increment of the voltage across the commutating inductor Lk1 over 0,5Ud), that the diodes VD_1 and VD_2 are turned-on and limits the voltage across the commutating inductors to the 0,5Ud level. The level 0,5Ud is the voltage level to which the capacitors C_F are charged. At these conditions the voltage across the switching devices are not higher than 1,5Ud. The limitation of the voltage level can be regulated by dividing the commutating inductors Lk in two parts and connecting a part of Lk in series with load Z and commutating capacitor Ck. This circuit (fig.1) has a "harder" output characteristic.

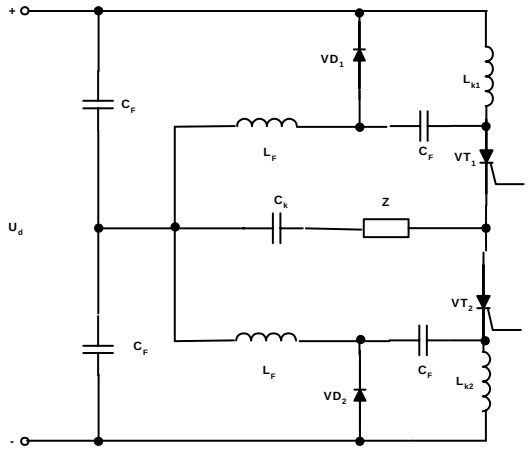

Figure 1. - Half-bridge resonant inverter

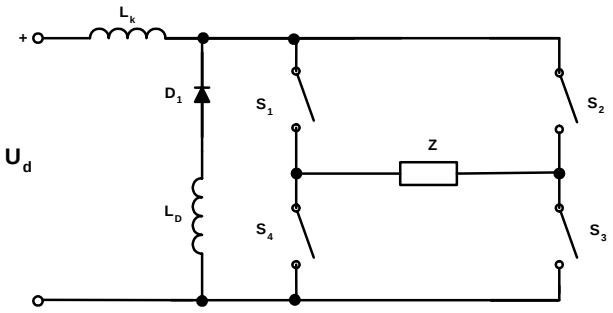

Figure 2. Full-bridge inverter

The priority of this circuit is that it keeps the voltage across the switches at significant load changes without complicate the converters driving, regulation and protection system. The disadvantage of this RI is the increased the number of devices and installed power.

The method of the VLCI [3,4] is characterized with the fact that for a part of the semi period of output current, the power circuit configuration changes by including the group (or groups) witch contain from diode and inductor. In some cases the inductors can be in absence. By including the additional inductance the level of limit could be changed. As result of

[1]Prof. DrSc Nikola P. Gradinarov - Faculty of Electronic Engineering and Technology at Technical University – Sofia, Kliment Ohridski Str. 8, 1000 Sofia, Bulgaria E-mail: n_gradinarov@tu-sofia.bg;

[2]PhD Dimitar D. Arnaudov - Higher College of Telecommunication and Posts - Sofia, Acad. St.Mladenov Str.1, Student's city, 1700 Sofia, Bulgaria, E-mail: d_arnaudov@yahoo.com;

[3]Nikolaj L. Hinov - Faculty of Electronic Engineering and Technology at Technical University – Sofia, Kliment Ohridski Str. 8, 1000 Sofia, Bulgaria E-mail: hinov@tu-sofia.bg;

this the current that flows through the load consists of two currents. The first current is due to the storage energy from the equivalent commutating capacitors, and the second is due to the power supply. The first current can be resonant or non-periodical. They flow to the moment when the difference between them becomes zero. After that, only the current due to the power supply flows. The priority of this method is that it can be used for RI and CSI.

The fundamental circuit, realizing this method (VLCI) is shown on figure 2. For the power switches all types power switching devices can be used. The AC circuit Z (parallel resonant load circuit), must work at frequency above resonant load frequency. In this case we obtained the serial resonant circuit, in which the capacitors are obtained by the displacement of complex load.

The principle of operation follows:

When the switches S1 and S3 are turned-on, thought the load Z flow two currents – the first current is due to the storage energy from the equivalent commutating capacitors and flows through circuit S_1 - Z - S_3 - L_D - D_1 - S_1, and the second is due to the power supply and flows through the circuit (+)U_d - L_k - S_1- Z - S_3-(-)U_d.

They flow to the moment when the difference between them became zero. After that, only the current due to the power supply flows. When the switches S2 and S4 are turned-on, the principle of the operation is the same as when the switches S1 and S3 were turned-on. The improvement of the output characteristics is due to the fact that the energy stored in the equivalent commutating capacitor is returned to the load.

The waveforms given at figure 4 show the principle of operation of RI with VLCI from fig.2. At fig.3 the waveforms when the circuit from fig.2 works as CSI are shown.

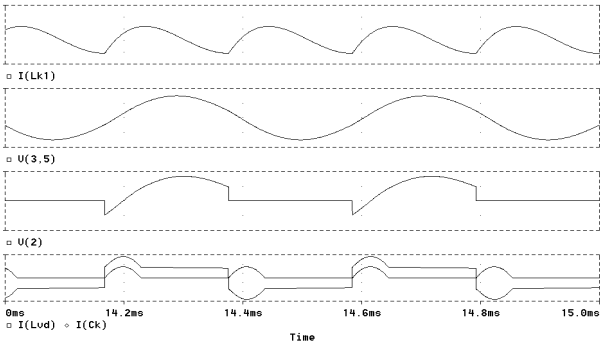

Figure 3. Waveforms for CSI with VLCI

Fig.3 shows the waveforms of: (I_{Lk1})-input current, (V(3,5))-output voltage across the load, (V(2))- voltage across the switch, (I_{Ck})- current though the load and (I(L_{Vd}))- current though the additional devices VD_1 and L_D. The waveforms make it obvious that the additional circuit decreases the value of di/dt and switching loses.

Figure 4 shows the waveforms, when circuit from fig.2 operates as CSI with LVCI where: (I_{Lk1})- input current, (V(4,6))- output voltage across the load, (V(2))- voltage across the switch, (I_{Ck})- current though the load and (I(d_1)) - current though the additional devices VD_1 and L_D.

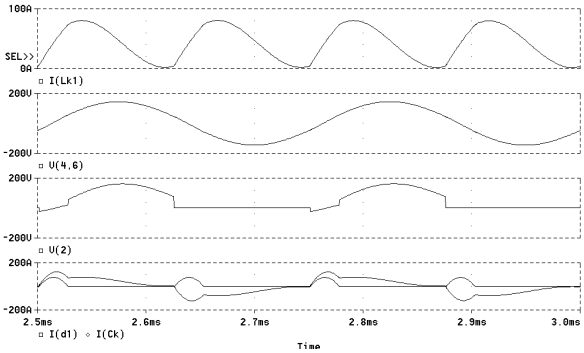

Figure 4. Waveforms for RI with VLCI

The biggest advantage of this method is the possibility of the power circuit to tune the regime at significant load changes or failure situations. The stabilizing effect follows: if by any reasons the energy stored to the commutating capacitors increases than energy at established mode, then for a longer part of the period of the driving frequency the energy will be returned to the load. This decreases the current from the DC power supply (DCPS). On the other hand when the energy stored to the commutating capacitors is decreased, then less energy is returned to the load and this increases the current from the DCPS.

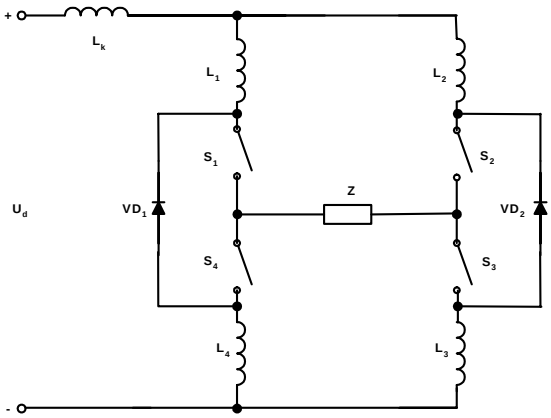

Figure 5. CSI with VLCI and common diode

When using the method of VLCI for a higher output power, it's necessary to use a few limiting diodes in parallel. To avoid the devices, which are necessary to equalize the currents through them, the circuits shown on figure 5 and figure 6 are offered [5].

The inductors $L_1 \div L_4$ are connected in series with the switches and they protect from di/dt. The principle of operation is the same as described above. The protection inductors are to equalize the currents through the limited diodes. Because of the fact, that the limiting diodes VD_1 and VD_2 are on only one time per period of the output frequency, they are in two times lower loaded compared to the main circuit (fig.2).

The circuit shown at fig.6 can be named CSI with reverse diodes. At the classical resonant inverters with reverse diodes, which are dependent of regime of work (above or under the load's resonant frequency), the device that are in on-state can be two diodes, two switches or reverse diode and switch.

For a difference from the classical resonant inverters with reverse diodes, in this circuit (with VLCI) two switches and two diodes are conducting simultaneously.

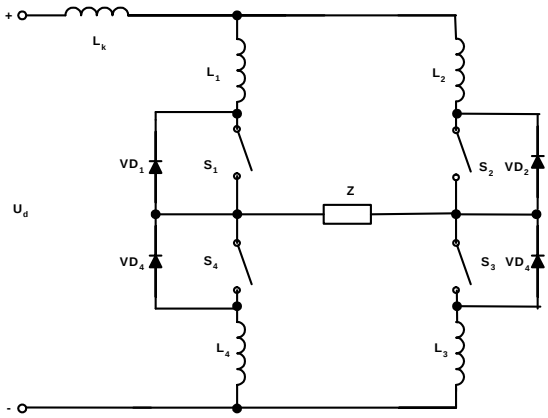

Figure 6. CSI with VLCI and individual diode

The principle of operation for a CSI with RD follows:

When the switches S_1 and S_3 are turned-on, then through the load Z three currents begin to flow – the first is caused by DCPS (+)U_d - L_k - L_1 - S_1 - Z - S_3- L_3- (-)U_d, and the other two are caused by the stored energy in the equivalent commutating capacitors and they flow through the circuit - S_1 - Z - VD_2 - L_2 - L_1 - S_1 and S_3 - L_4 - VD_4- Z - L_3 - S_3. When the another two switches S_2 and S_4, are conducting the processes are the same as when working S_1 and S_3.

In this circuit the diodes are four times lower loaded as comparison with the circuit shown at fig.2.

After this review of the circuits with VLCI, it can be resumed that they have lot of advantages in comparison with the other methods for improving the output characteristics. The advantages of this circuit are: - that it keeps the voltage across the switches constant at significant load changes without complication of the converters driving circuits, regulation and protection system; - lack of regime in which there is a reverse energy to the DCPS; - decreases the switching losses; allow to the circuit to tune the regime of work. The improvement of the output characteristics does not worsen the energy efficiency.

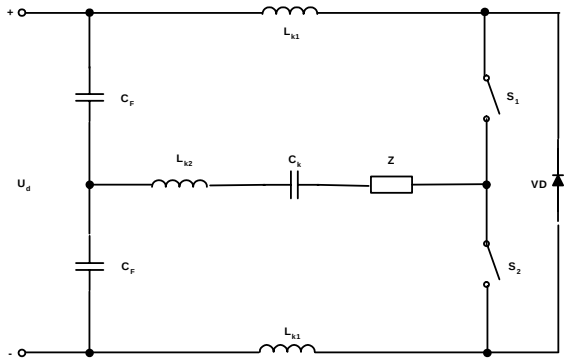

Figure 7. Half-bridge RI with VLCI

An improved half-bridge circuit is shown at fig.7. It has better characteristics due to the fact that a part or the whole of the resonant inductor is outside of the bridge at the DC network. Additional reverse diode, common to both devices is added. It works under the load's resonant frequency.

The waveforms at figure 10 show established mode behavior of the circuit. These diagrams are derived from computer simulation. The voltage across the power switches can be changed by varying the coefficient β, which shows the ratio between the part of the resonant inductor, which is outside the bridge and the full inductor. When the whole inductor is outside the bridge the voltage across the power switches is at its possible minimum and depends on the Q-factor of the resonant circuit. When β is decreased the device becomes similar to the classical RI without RD.

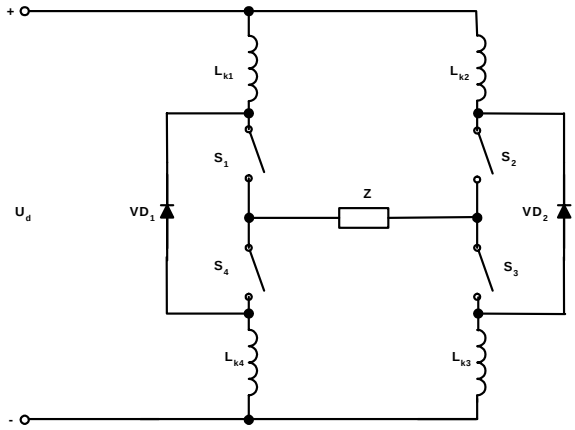

Figure 8. Full-bridge RI with VLCI

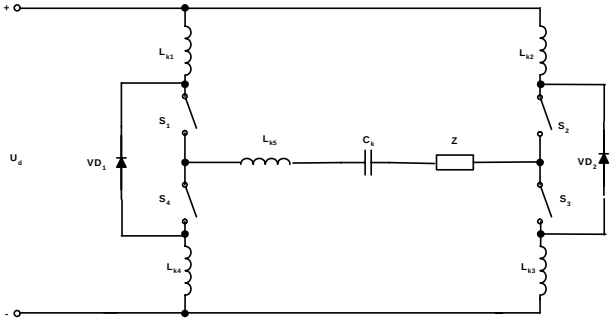

Figure 9. Full-bridge RI with VLCI

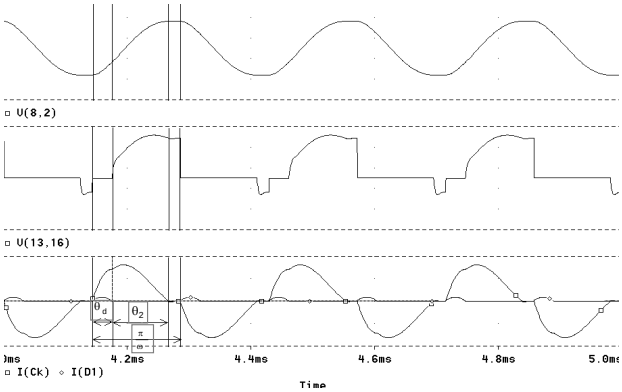

Figure 10. Waveforms for full-bridge RI with VLCI

The circuit shown on fig.8 is the full-bridge RI with VLCI. Its principle of operation is similar to the half-bridge's: When the switches S_1 and S_3 are turned-on, through the load Z three currents flow – the first is caused from +Ud-Lk1-S1-Z-S3-

Lk3- -Ud, the second is caused by the stored energy in the equivalent commutating capacitors and flows by circuit Z-S3-D2-Lk2-Lk1-S1-Z and respectively the third Z-S3-Lk3-Lk4-D1-S1-Z. The currents that flow in the secondary circuits cause faster discharging of the equivalent commutating capacitor and therefore decrease the current from DCPS.

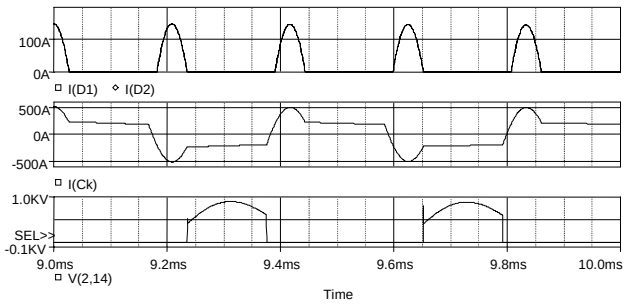

Figure 11. Waveforms of full-bridge CSI with VLCI from fig.5

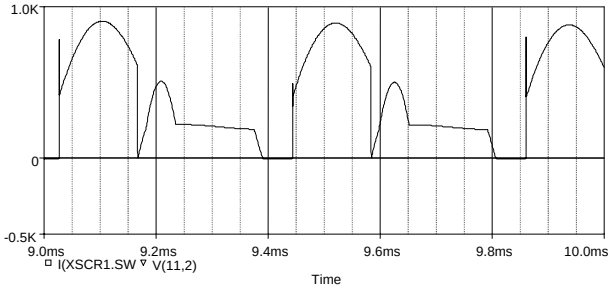

Figure 12. Waveforms of full-bridge CSI with VLCI from fig.5

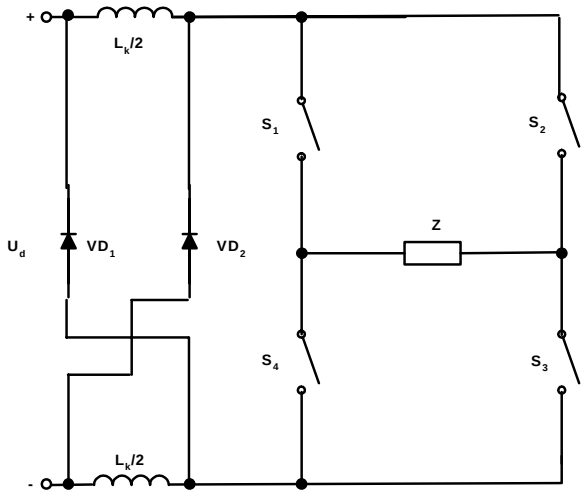

Figure 13. Full-bridge RI with VLCI

Another circuit of inverter with VLCI is shown at figure 13. The principle of operation is not different than the inverters described above. The difference in this inverter is that the commutating inductors are divided in two equal parts (this is the circuit for high power current source inverters). When the diodes are conducting the equivalent commutating inductors is Ld=Lk/4. The better output characteristics of CSI are due to the fact that the diodes limit the voltages across the input inductor Lk. Using the results from the analyses for CSI working with complex load [6] we obtained equations for the inductor's voltage. When S1 and S3 (or S2 and S4) are turned on, the voltages across the inductor Lk/2 is: $U_{Lk}=k_I.Ud$ where, k_I – coefficient of hesitation of CSI, which corresponds to the coefficient k [7] at classical RI. From the operating principle it can be seen that the diodes will not conduct when $k_I<1$. The voltage limitation will occur when $k_I>1$. The other advantage of these inverters is the additional devices that ensure the limitation of the inductor over voltages are not necessary.

The limitation to various voltage levels can be obtained if the voltage is limited only at part of the commutating inductors Lk. This circuit (fig.10) can be used successfully not only for CSI but can be used for inverters with natural commutation.

If the resonant inductor is divided in tree equal parts and the third part (L=Lk/3) is connected in load diagonal, the limitation will occur when k>1,5 (the limiting diodes will turn on). Therefore in normal mode the effect of the additional group is insignificant. At certain conditions it can be used only for protection circuit when an accident situation occurs.

III. CONCLUSION

This method can be used successfully not only for CSI but can be used for inverters with natural commutation. The better output characteristics of inverters with VLCI are due to the fact that the diodes limit the voltage across the inductors. This is an effective method of protection from over voltages and over currents.

REFERENCES

[1] Patent USSR №877755, kl. H 02M 7/51 1981.

[2] Nachev N., G. U. Maleev, "Power electronics", Technica, Sofia, 1979.

[3] Gradinarov N. P., N. L. Hinov, "Resonant inverters with improved output characteristics", *ELECTRONIKA'98 Conference Proceedings*, pp.223-229, Botevgrad, Bulgaria, 1998.

[4] Gradinarov N., Hinov L., "Resonant inverters with improved output characteristics", Patent BG№63445 B1 H 02 M 7/00, 1999, Bulgaria.

[5] Gradinarov N., Hinov L., "Methods and circuits for resonant inverters output characteristics improving", Patent BG№ 62112 , B1 H 02 M 7/00, 1996, Bulgaria.

[6] Hinov N. L., N. P. Gradinarov, "Analysis of an autonomy resonant inverters with forsed commutation", Proceedings of the sixth international scientific and applied science conference "ELECTRONICS '97" 24-27 September 1997., Sozopol, Bulgaria, pp.61-67.

[7] Gradinarov N. P., "Research elaboration and development of resonant inverters with technical application" Doctorate Thesis. Technical University –Sofia, 2002.

[8] Vakovski D., "Computer designing of resonant inverters with forced commutation", National conference with international participants, Conference *Proceedings* "ELECTRONIKA'2002", pp.213-220, DNT, 17-18 Oct. 2002, Bulgaria, Sofia.

Typical of the Inverters Transitive Processes

Hristo P. Hinov[1]

Abstract – **The free oscillations method has been applied to the series inverter. The equations have been canonized and the inverter parameters have been reduced to two. The inverter functions have been stylized. The whole operation process is described only by the function of the first half-period, modified by the current start point. The dependence between the sequential start points has been derived. A recurrent dependence has been applied for the formulation of the stationary mode. The mode accumulations are presented in a power series. The development of the transient process is presented depending on the inverter parameters and frequency. The operations have been summarized for both elementary and complex inverters. Author's conclusions: The free oscillations method is applicable for the mathematical interpretation of the inverter. The first half-period, starting from zero initial conditions, is multiplied and functionally presents all subsequent half-periods in the operation process of the inverter. The start point is the result of the completed half-periods and determines the mode level (voltage and current) of the current half-period. The position of the start point depends on the relationship between the natural frequency and the timer frequency. The transient process is represented by a fractal (broken line), whose diminishing segments are at equal angles. The broken line tends to the start point of the stationary mode.**

Key words – **inverter, free oscillation**.

I. INTRODUCTION

The functional presentation of electromagnetic processes taking place in inverters is traditionally influenced by the concept of forced oscillations [1], [2], [3]. The references analyze the inverter reaction under the influence of the square pulses from the commutated supply voltage.

The present article develops the alternative approach, according to which the inverter is treated as a freely oscillating system within each half-period. The periodic commutations in the inverter keep activating the temporary solutions to the differential equations, which is the mathematical interpretation of free oscillations.

The aim is to study the transient process and formulate the inverter stationary mode.

Inverters are sources of high-frequency energy and consist of controllable electronic switches and an oscillatory system (resonant circuits). The switches are usually transistors connected in parallel to diodes, which form a four-arm bridge. The transistors are controlled by a timer determining the generated frequency. The timer closes the switches along one bridge diagonal and opens the switches along the other action diagonal at intervals T_t /2 – called half-periods /HP/. The of the switches causes free oscillations. The free oscillations energy is realized in a separate part of the same oscillatory system.

[1]Prof. Hristo P. Hinov is with the Faculty of Electronic Engineering, Technical University of Gabrovo, H. Dimitar Str.4, 5300 Gabrovo, Bulgaria,
E-mail: hino@abv.bg.

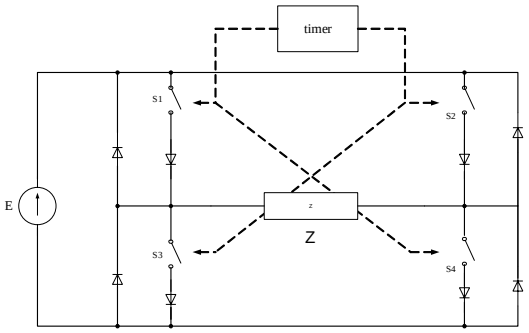

Fig.1. Object Circuit

Fig.1 presents the object circuit. The oscillatory system Z is determined by the number and type of the characteristic equation roots.

If Z is characterized by the only (real) root, then the inverter is determined as "elementary".

The popular series inverter has a pair of complex conjugate roots, but the analysis presented also refers to other configurations of Z, in which a complex pair of roots dominates.

The complex inverters, with a lot of root Z, can be presented as a combination of the preceding types or their processes can be interpreted by means of multidimensional matrix operators.

II. ELECTROMAGNETIC PROCESS IN A SERIES INVERTER

The series inverter is suitable for demonstrating the base processes in inverters. Its two-terminal network Z consists of a capacitor, inductance and resistor, connected in series.

A. Equations and parameters

The differential equation of the series inverter is:

$$L(dI/dt) + RI + (1/C)\int Idt = E$$

The roots of the characteristic equation determine:

- $\omega = [(LC)^{-1} - (R/2L)^2]^{0.5}$ – natural frequency,
- $\varepsilon = (R/2L)/\omega \approx 1/2Q$ – atténuation. $(Q=(L/C)^{0.5}/R)$

A priority of the method applied is the substitution of a current angle called "phase" for the current time: $\theta = \omega t$.

The angle-phase symbolizes the current time in the inverter in the same way as the clock presents time by means of an angle (thirty degrees signify an hour).

The phase is a limited argument: $0 \le \theta \le \theta_s$. The maximum phase, called cycle: $\theta_s = \pi (T_t / T_0)$, is proportional to the timer period T_t, related to the natural period $T_0=2\pi/\omega$. The cycle θ_s is the angular route traveled by the "inverter clock hand" Eq. 1, for the timer interval Tt/2.

The four circuit parameters (C, L, R and period T_t) have been reduced to the two dimensionless quantities – attenuation ε and cycle θ_s. These are the degrees of freedom or the inverter coordinates. They are combined in the complex parameter:

$$\dot{p} = (-\varepsilon + j)\theta_s \qquad (1)$$

The solutions to the differential equation are presented in dimensionless quantities:

- Capacitor voltage $u(\theta) = -1 + u_s \exp(-\varepsilon\theta) \cos\theta$,
  Where: u = U/E, us random starting voltage.
- Current across inductance $i(\theta) = i_s \exp(-\varepsilon\theta) \sin\theta$,
  Where: $i = I (L/C)^{0.5}/E$, i_s random starting current.

B. Dynamics of the primary phase vector

The last two quantities are presented jointly by a complex function, the real part of which is voltage, and the imaginary part is the current [4], [5]:

$$F_1(\theta) = - 1 + \exp((-\varepsilon+j)\,\theta) \qquad (2)$$

This is a rotating vector in a complex plane. It is primary because it describes the inverter start from zero initial conditions: $u_s=0$, $i_s=0$. It describes a spiral with center (-1, 0), traveling the angular route θ_s, and completes its half-period development in the final point

$$F_1 = - 1 + \exp(\dot{p}).$$

The timer replaces the conduction switches of the bridge in the final point, causing the so-called commutation in the inverter. The commutation changes the source direction, which is manifested by changing the signs in the last equality.

The second half-period does not start from the zero, but from the inverse F_1:

$$S_2 = 1 - \dot{q} \qquad (3)$$

Where the complex number $\dot{q} = \exp(\dot{p}) = \exp((-\varepsilon+j)\,\theta_s)$, is the completed development of the exponential function in Eq. 2.

The described development and final of the first half-period deserve special attention, because each subsequent half-period reproduces them at a higher mode and energy level.

C. General form of the phase vector

The second half-period is presented by a phase vector (PV) similar to Eq. 2 but starting from a point, which is the result of the first half-period action:

$$F_2(\theta) = - 1 + (1+S_2)\exp((-\varepsilon+j)\,\theta).$$

The general form of the phase vector is the generalization of the last equality, which is valid for a half-period of an arbitrarily high number:

$$F_n(\theta) = - 1 + (1+S_n)\exp((-\varepsilon+j)\,\theta) \qquad (4)$$

The PV (Eq. 4) can be presented in the form: $F_n(\theta) = F_1(\theta) + S_n \exp((-\varepsilon+j)\,\theta)$

The phase vector of a random half-period in the operation process of the series inverter is determined by the primary PV ΦB – Eq. 2 and by the start point /SP/ S_n, formed by the preceding half-period.

Fixing the argument in Eq. 4 at its limit $\theta = \theta_s$ and performing the commutation inversion, the SP of the next half-period is obtained.

The law of the start point's reproduction is:

$$S_{(n+1)} = 1 - (1+S_n)\,\dot{q} \qquad (5)$$

Both the PV and point (Eq. 5) can be presented as the sum of the primary SP S_1 and the preceding one S_n, reduced by the complex $\dot{q}$: $S_{(n+1)} = S_1 + S_n\,\dot{q}$.

D. Direct definition of the stationary mode

Although the stationary mode of the inverter is a product of the preceding process, its direct determination is also possible, applying important recurrent dependences and properties.

For example, if the mode reproduction principle is applied in stationary mode, then each half-period will repeat the preceding one. To achieve such reproducibility it is sufficient to equalize two subsequent SP: $S_{(n+1)}=S_{(n)} = S$. The substitution is applied in Eq. 5, which determines the stationary mode of the series inverter by means of the start point definition:

$$\dot{S} = \frac{1-\dot{q}}{1+\dot{q}} \qquad (6)$$

If the substitutions applied in Eq. 3 are used, the hyperbolic form of the stationary mode will be obtained:

$$\dot{S} = th(-\dot{p}/2) \qquad (7)$$

E. Accumulations in the transient process

The different half-periods of the inverter operation are determined by there start points S_n. It is the varying parameter in Eq. 4, which characterizes the inverter transient process. Starting from $S_1 = 0$ and applying Eq. 5, the following start points are obtained:

$$S_2 = 1 - \dot{q};$$
$$S_3 = 1 - 2\dot{q} + \dot{q}^2;$$
$$S_4 = 1 - 2\dot{q} + 2\dot{q}^2 - \dot{q}^3;$$

The following power series is obtained for a half-period number of arbitrary magnitude:

$$S_n = 1-2\dot{q}+2\dot{q}^2-2\dot{q}^3+\ldots+2(-\dot{q})^{(n-2)}+(-\dot{q})^{(n-1)} \qquad (8)$$

The signs in Eq. 8 are alternative, and the coefficients are pairs, except the first and the last term. For each elapsed half-period the end of the series is complemented by a term of a higher power. The coefficient of the last-but-one term is also complemented. These are the mode accumulations, which are a result of the preceding half-periods.

The series is complemented to an exact geometric progression and allows the application of a limit transition when $n\to\infty$, which is a second proof of the stationary mode law Eq. 6 and respectively – Eq. 7.

The development of Eq. 8 through the sequential half-periods provides a good vision for course of the transient process. It is expedient to reformulate Eq. 5, so as to emphasize the accumulation at the end of the series: $S_{(n+1)} = S_{(n)} + (1-\dot{q})(-\dot{q})^{(n-1)}$.

With each subsequent half-period two terms are added to Eq. 8, which complement the higher powers of the polynomial or series.

F. Characteristics of the accumulation

The alternative signs in the polynomial – Eq. 8 are a result of the commutation inversion described; however, prior to it another transfer has been performed – functional transfer. It is expressed in the completed development of the exponential function in Eq. 4 or the complex number $\dot{q} = \exp((-\varepsilon+j)\theta_s)$. It is not accidental that the inverter cycle is $\theta_s = \pi \pm \alpha$ [5] [6], which leads to an encoded minus of $\dot{q}$:

$$-\dot{q}_{(\alpha)} = \exp(-\varepsilon(\pi\pm\alpha)+j(\pm\alpha)) = r_{(\alpha)} \qquad (9)$$

The imaginary part of Eq. 9, or the angular route, has a reduced argument at the expense of the derived minus. The polynomial Eq. 8 is restructured in:

$$S_n = 1+2r+2r^2+2r^3+\ldots+2r^{(n-2)}+r^{(n-1)} \qquad (10)$$

The imaginary sign alternativeness is eliminated and the power series has the form of a normal geometric progression.

The complex character of Eq. 10 facilitates the visualization of the transient process – Fig. 2. The figure presents two open polygons, which form a broken line – fractal. The fractal sides decrease and are directed to a definite point – the limit. Each side is deviated from the preceding one at an angle of 30^0, added in the case of the upper fractal and subtracted for the lower one (declination $\pm\alpha$). The angles are the start points of the first ten half-periods, starting from $S_1=0$, $S_2=1+r$ etc. according to Eq. 10.

The two fractals express the transient processes in two inverters having equal attenuation (Q-factor = 3). One of the examples is characterized by a half-period angle $\theta_s = \pi+\alpha = 210^0$ – long cycle. The other inverter operates with a short cycle $\theta_s = \pi-\alpha = 150^0$. Equal declination is chosen for the two examples $\pm\alpha=30^0$.

The different cycles of the two examples are obtained from the same inverter, but at with different frequency modes. In the first example the "long cycle", timer dictates a frequency that is less than the natural frequency, $T_t > T_0 = 2\pi/\omega$. In the second - short cycle – the other way round, $T_t < T_0$, as a result of which frequency greater than the natural frequency is generated.

The complex number (Eq. 9) in the long-cycle inverter has a positive imaginary part and their power sum (Eq. 10) is in the first quadrant. Due to an analogous reason the start point of the short-cycle inverter is in the fourth quadrant. This difference leads to significant commutation and recuperation differences, which are the object of other articles [5] [6].

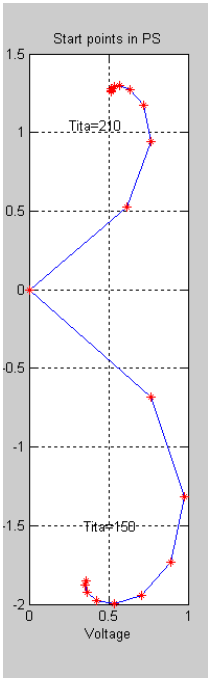

Fig.2 Start points

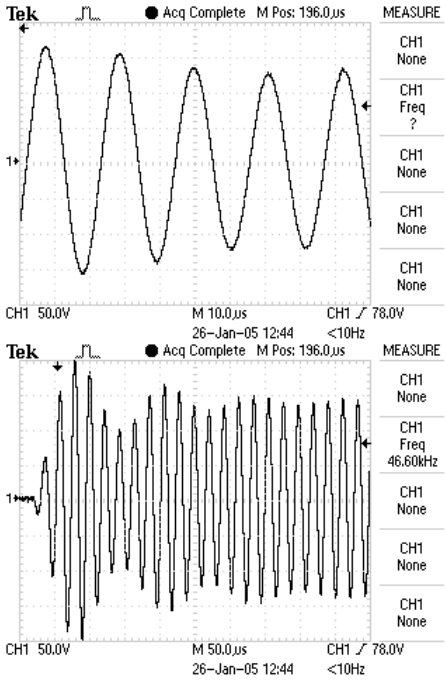

Fig.3 Transient process

The line segments (corresponding to voltages and currents) in the short-cycle inverter ($\theta_s=150^0$) are greater, because it has shorter time for realization (absorption) of the energy and it increases the accumulations in the reactive elements.

Fig.3 demonstrates the shell of the transient process typical for inverters with low attenuation. The stationary mode is reached when the fractal is circumferentially moved closer to the limit point, the so-called alternative convergence of Eq. 10.

G. Electromagnetic process in an aperiodic inverter

Inverters, whose oscillatory systems are characterized by one real root only, have just one reactive element and develop an aperiodic process.

Their phase vector is determined by a real quantity Eq. 1 $p=-\varepsilon\theta_s$. The power series (Eq. 8) of the transient process and its limit (Eq. 6) have the same form, but are real-scalar. They can be presented as a separated case of their complex analogues.

H. Electromagnetic process in a complex inverter

The inverter, whose oscillatory system is characterized by several roots, develops a complex oscillatory process. The free oscillations are a sum of the elementary oscillations that determine their roots. The operations described must be interpreted by matrix operators.

III. CONCLUSIONS

- The free oscillations method is applicable for the mathematical interpretation of the inverter. Its application allows the formulation of the stationary mode and the power of the inverter [4], [5], [6].
- The first half-period, starting from zero initial conditions, is multiplied and functionally determines all subsequent half-periods in the inverter operation process.
- The start point is the result of the completed half-periods and determines the mode level (voltage and current) of the current half-period.
- The position of the start point depends on the relationship between the natural frequency and the timer frequency.
- The transient process is represented by a fractila (broken line), whose diminishing segments are at equal angles. The fractila tends to the start point of the stationary mode.

REFERENCES

[1] B.D.Bedford, R.G.Hoft, Principles of Inverter Circuits. J.Willey & Sons, New York, 1964, chapt.3.

[2] V. A. Chvanov, Dynamics of Autonomous Inverters with Direct Commutation, Moscow, Energiya, 1978 (in Russian)

[3] M. H. Rashid, Power Electronics, Circuits, Devices and Applications. *Pearson Prentice-Hall International, Inc.,2004*, chapt. 8.

[4] H. P. Hinov, Accumulations in a Series Inverter, *Proceedings of the Technical University, XVII-1994*, pp. 158-164.

[5] H. P. Hinov, V. V. Rankovska, Analysis of an Asymmetric Inverter in Phase Space, *ICEST, 16-19 June 2004*, pp. 403-406, Bitola, Macedonia.

[6] H. P. Hinov, Short Cycle Inverter, (forthcoming).

Microprocessor Control of Inductive Cumulation Inverter

Hristo Z. Karailiev[1], Valentina V. Rankovska[2], Vladimir H. Karailiev[3]

Abstract – **To achieve an optimal operation mode of a class of inductive cumulation inverters in the low frequency range the control need to be done in real time. Automatic regulation of the cumulation time duration is necessary to maintain an optimal mode, as the load parameters change dynamically (the object temperature). A variant of a microprocessor control maintaining an optimal mode is presented in the paper. Structure variants for the various blocks and criteria for selecting proper circuits are defined.**

Keywords **– microprocessor control, inductive cumulation, real time operation, time estimating.**

I. Introduction

In many workings out dealing with inverter operation control, various circuits are suggested, using specialized integrated circuits working as PWM regulators. These circuits do not have the needed flexibility; they do not react to the inverter mode changes in real time.

In order to achieve an optimal control mode, it is necessary to gather data about the inverter operation modes from suitable sensors in strictly defined control points in every moment.

It is necessary to measure the values of the controlled parameters [1], [3], to estimate them and to generate such control signals for the cumulation time in order not to exceed the admissible voltages and currents for the elements building up the inverter.

The real load parameters Z_T (R_T, L_T) must be taken into consideration, having in mind, that with increasing the temperature of the processed part (material) in real time, these parameters change fulfilling a certain law [1], [2].

At low temperatures the active load component has low values tending to increase. The reactive component remains constant in a considerably wide temperature range. That is why the quality factor of the inverter at the beginning of the technological process has big values:

$$Q_e = \frac{\rho_e}{R_e} = \frac{\sqrt{\frac{L_e}{C}}}{R_e} \qquad (1)$$

which can result in considerable increasing the voltage amplitude across the inverter reactive components, respectively across the transistor implementing cumulation.

[1] Hristo Z. Karailiev is with the Technical University, 4 H. Dimitar str. 5300 Gabrovo, Bulgaria, E-mail: hkarailiev@gmail.com

[2] Valentina V. Rankovska is with the Technical University, 4 H. Dimitar str. 5300 Gabrovo, Bulgaria, E-mail: rankovska@tugab.bg

[3] Vladimir H. Karailiev is with the Technical University, 4 H. Dimitar str. 5300 Gabrovo, Bulgaria, E-mail: vkarailiev@gmail.com

The major aim in the report is to develop an architecture of an inductive cumulation inverter microprocessor control.

Major problems solved in the report:

- To estimate the maximum time values for measurement, conversion and generating the control signals;
- To suggest proper ideas for gathering information about the inverter operation modes and for generating a control signal for the cumulation time;
- To coordinate the transient inverter processes with the control device operation in real time;
- To develop the structure of the inductive cumulation inverter control microprocessor device.

II. Formulation of the Task for Inductive Cumulation Inverter Control in Real Time

The basic circuit of an inductive cumulation inverter is shown in Fig. 1.

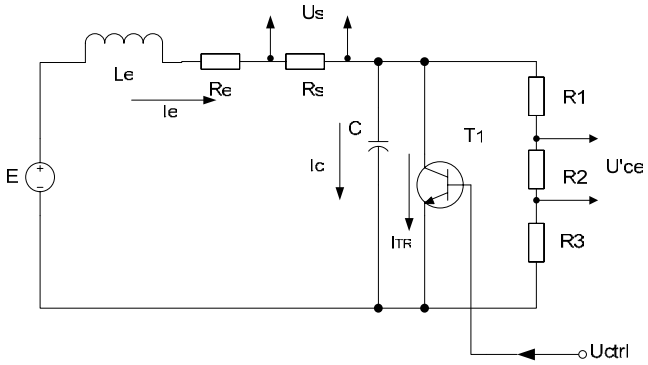

Fig. 1. Inductive cumulation inverter circuit

L_e equivalent inductance of the inverter resonant circuit (Eq. 2):

$$L_e = L_1 - L_{imp} \qquad (2)$$

R_e equivalent active resistance of he inverter resonant circuit (Eq. 3):

$$R_e = R_1 + R_{imp} \qquad (3)$$

R_s a resistor giving information about the value of the current in the primary circuit of the inverter;

C capacitance in the primary circuit;

T_1 transistor defining the energy cumulation in L_e;

U_{ctrl} control signal with duration τ , intended to switch on the transistor T_1;

U'_{ce} voltage, proportional on the voltage across the capacitor U_c.(Eq. 4):

$$U'_{ce} = U_c \frac{R_2}{R_1 + R_2 + R_3} \qquad (4)$$

The period of the inverter with cumulation is defined by two components (Eq. 5):

$$T = \tau + \tau_s \tag{5}$$

Where:

τ is the time for cumulation;

τ_s time for inverter free oscillations.

The illustration of the transient process in the inductive cumulation inverter operation is shown in Fig. 2.

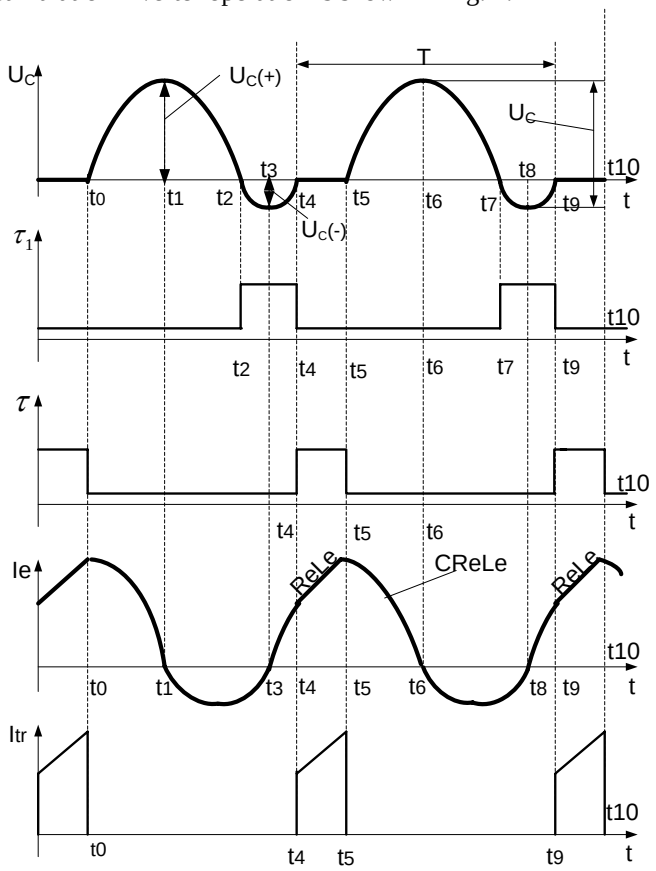

Fig. 2. Waveforms illustrating the typical moments of the transient process of the inverter

On the waveform for U_c the moment t_1 and t_6 from the transient process define the maximum voltage values, and the moment t_3 and t_8 define the minimum voltage values.

The inverter current trough the inductivity L_e and R_s for the above mentioned moments (t_1, t_3, t_6, t_8) becomes zero.

That is why the hardware defining of those moments has been made with zero current comparator, using the information from the resistor R_s.

It is necessary to start a fast ADC at those moments to define the value of the voltage across the capacitor (transistor) (Eq. 6):

$$U_c = U_{c(+)} + |U_{c(-)}| \tag{6}$$

Thereby it is necessary to estimate whether the condition (Eq. 7) is fulfilled:

$$U_c \le k(U_c)_{\partial on} \tag{7}$$

Where $0{,}9 \le k \le 0{,}95$ is a reliability coefficient;

$(U_c)_{\partial on}$ – the maximum admissible value of the voltage across the capacitor (transistor).

The moment t_4 and t_9 form the transient process set the beginning of the cumulation process (switching on the transistor) and the time constant of the circuit becomes *ReLe*. The hardware defining of those moments has been made by a zero voltage comparator basing on the information, got from the resistive divider *R1, R2, R3*.

The duration of the cumulation time τ has been determined automatically by software. The object function in the algorithm is emission of maximum power through the load without breaking the maximum admissible voltage and current values through the transistor.

The transistor current gains its maximum value at the end of the time intervals for the cumulation (the moment t_0, t_5, t_{10}).

As the current I_e through L_e and R_s and the current through the transistor I_{tr} during the cumulation time $(t_4 \div t_5), (t_9 \div t_{10})$ have got approximately one and the same value (Eq. 8):

$$I_e \approx I_{tr} \tag{8}$$

and after (t_0, t_5, t_{10}) free oscillations through L_e, R_s and C begin, we can get information about the maximum value of the current through the transistor by single measurement of the current I_e at that moment. Therefore at the moment t_0, t_5, t_{10} the microcontroller will generate a signal to stop the cumulation and to start the measurement of I_{tr} by the second channel of the ADC, using the information from R_s.

III. Architecture of a Microprocessor Device Controlling an Inductive Cumulation Inverter

The control signal generated by the PWM (OUT 2) of the microcontroller has been connected to the input of the block, shown in Fig. 3.

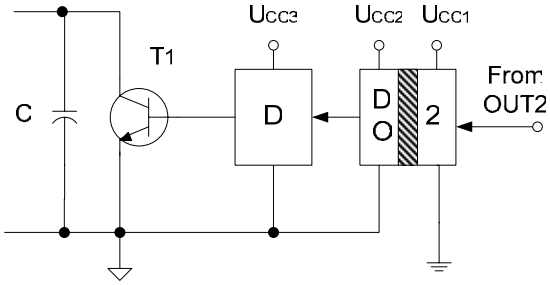

Fig. 3. Cumulation control signal block

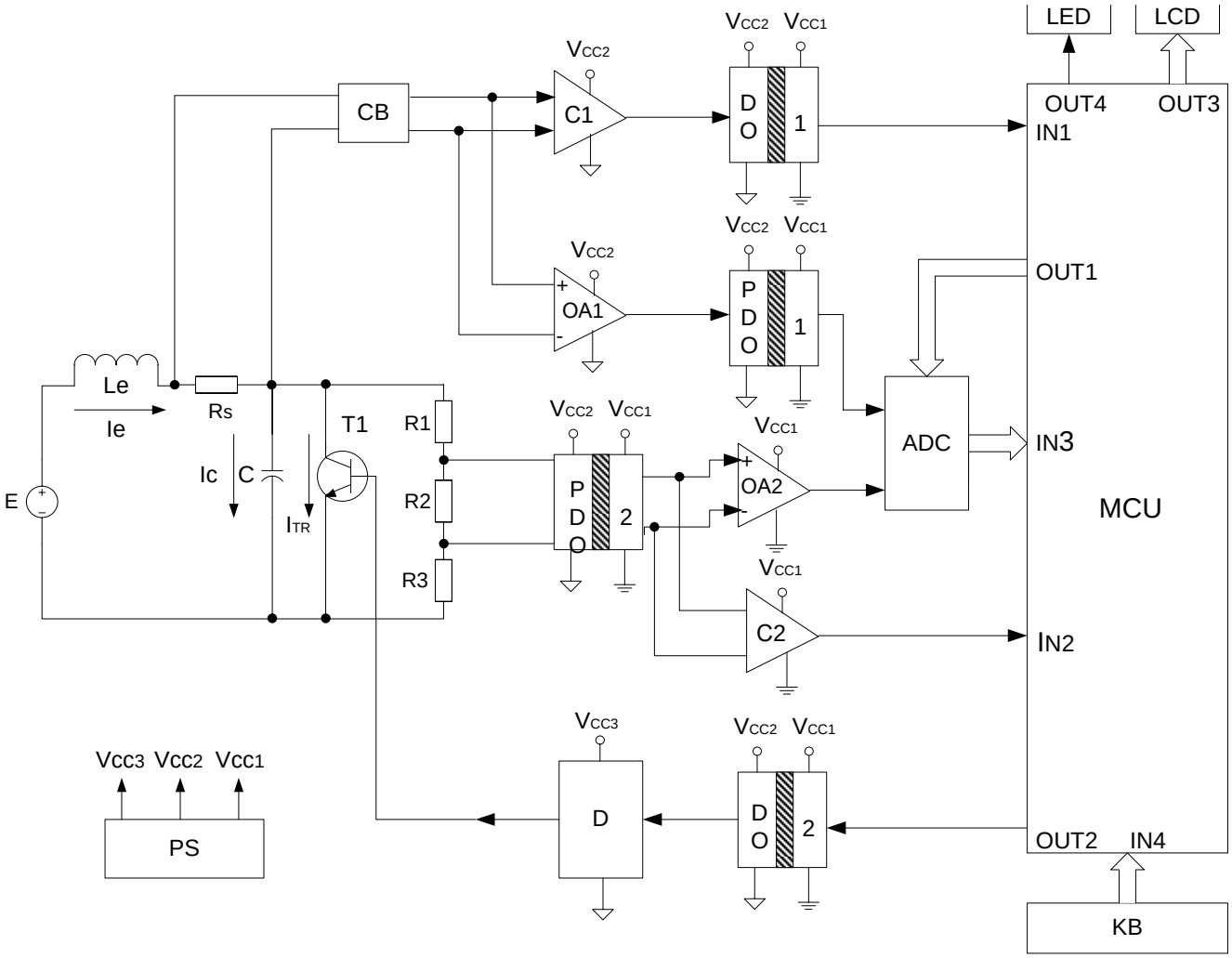

Fig. 4. MCU control device architecture of an inductive cumulation inverter

Using the results from the simulation in [1] for the transistor T_1 it is evident that $(U_{ce})_{\partial on} \le 1200\ V$ and the current through the transistor is $(I_{tr})_{max} \le 50\ A$. Hence BUP314 can be used.

As a driver, forming the signal for the transistor can be used the standard IC IR2113.

As a digital opto-coupler (*DO2*) making the galvanic isolation of the control signal, generated by the microcontroller, IC IL710 can be used.

The common time delay of the signal τ_{del1} can be calculated using the datasheets of the IC, used in Fig. 3, and the maximum time durations $(t_{on})_{max}$ and $(t_r)_{max}$.

The signal, formed at the moments t_1, t_3, t_6 and t_8 (Fig. 2), will generate an interrupt request on the input *IN1* of the microcontroller. The source of the signal is the voltage U_s across the resistor R_s (Eq. 9):

$$U_s = I_e \,.\, R_s \tag{9}$$

The time delay of that signal is due to the following blocks: Co-ordination Block (CB), Comparator 1(C1) and DO1, and its value is τ_{del2} (Fig. 4, Eq. 10):

$$\tau_{del2} = \tau_{CB} + \tau_{C1} + \tau_{DO1} \tag{10}$$

The digital values for the signal about the voltage U_{ce} across the transistor at the moment t_1 and t_3 will be received with delay τ_{del3} due to the blocks *PDO2*, Op-Amp 2 (*OA2*), *ADC* and the software delay for calculating the actual value (Eq. 11).

$$\tau_{del3} = \tau_{PDO2} + \tau_{OA2} + \tau_{ADC} + \tau_{sw} \tag{11}$$

That is why the voltage U_{ce} will be measured at the moments $t_1 + \Delta t$, $t_3 + \Delta t$, $t_6 + \Delta t$ and $t_8 + \Delta t$ instead of t_1, t_3, t_6 and t_8, where:

$$\Delta t = \tau_{del\ 2} + \tau_{del\ 3} \tag{12}$$

In order not to allow a flagrant measuring error it is necessary to select the elements, forming τ_{del2} and τ_{del3}, to be with proper parameters so that the Eq. 13 to be fulfilled.

$$\Delta t < \frac{1}{2}(t_4 - t_2) = \frac{1}{2}(t_9 - t_7) \tag{13}$$

The digital signal values of the current through the transistor I_{tr} at the moment t_0, t_5 and t_{10} will be formed with a delay τ_{del4} due to the blocks *CB*, *OA1*, *PDO1*, *ADC* and the program delay for calculating the actual value (Eq. 14):

$$\tau_{del4} = \tau_{CB} + \tau_{OA1} + \tau_{PDO1} + \tau_{ADC} + \tau_{SW} \quad (14)$$

So the current through the transistor I_{tr} will be measured in the moments $t_5 + \tau_{del4}, t_{10} + \tau_{del4}$ instead of t_5, t_{10}.

In order not to allow a big error when measuring the current through the transistor I_{tr} , it is necessary the elements forming τ_{del4} to be faster if it is possible.

The signal on the input *IN2* of the MCU will be late in relation to the moment t_2 and t_7 with τ_{del5}, due to the blocks *PDO2* and *C2*,

$$\tau_{del5} = \tau_{PDO2} + \tau_{C2} \quad (15)$$

so the actual moments are (Eqs. 16):

$$t_2' = t_2 + \tau_{del5}$$
$$t_7' = t_7 + \tau_{del5} \quad (16)$$

The inverter cumulation time $\tau = t_5 - t_4 = t_{10} - t_9$ is a function of the operation mode and will be discussed in another paper.

VIII. CONCLUSIONS

In this paper the following results are presented and systematized:

- An attempt is made to harmonize the transient processes in an inverter, operating in an inductive cumulation mode, with the operation of a control device working in real time;
- The maximum values of the times for measuring, conversion and generating control signals are estimated;
- An architecture of a microprocessor device controlling the operation of an inductive cumulation inverter is designed;
- Preconditions for making an algorithm of the inverter control process by regulating the cumulation time are found.

REFERENCES

[1] H. Hinov, H. Karailiev, V. Rankovska, “Inverter Model and Decomposition in the 3D Space”, ICEST 2005 Conference Proceedings, Nis, Serbia & Montenegro, 2005.

[2] H. Karailiev, V. Rankovska, G. Donev, “Two-channel Circuits for Generation of Control Signals with Programmable Duration and Frequency”, ICEST 2004 Conference Proceedings, pp.453-456. Bitola, Macedonia, 2004.

[3] T. Reimann, R. Krümmer, J. Petzoldt, “Ïnvestigation of the Current Balance and Power Loss Distribution of Parallel Connected IGBTs During Active Voltage Clamping”, PCIM 2000 Conference Proceedings, pp. 257-262, Nürnberg, Germany, 2000.

Inverter Model and Decomposition in the 3D Space

Hristo P. Hinov[1], Hristo Z. Karailiev[2], Valentina V. Rankovska[3]

Abstract - **The magnetic coupling inverter is a typical object of power electronic. The differential equations from the third order are canonicated. The residuum's law has been applied for the first time, towards such object like inverter and it has been decomposed to its components.**

Keywords **– inverter, phase model.**

I. INTRODUCTION

The generated energy transferring through magnetic coupling is an often met approach in power electronics. The magnetic coupling is in the base of induction heating, where the inductor and the heated metal work as a transformer, except as a transformer for galvanic isolation, or for load fitting.

The influence of the magnetic coupling at inverters is often ignored [1] with the hypothesis that it does not change the oscillating process. The mathematical interpretation shows increasing the order of the differential equations and processes, typical for the complex inverters.

The aim of the present analysis is a decomposition of the object and the processes in it to their components. The analytic methods, connected with the theorem for the residuum's has been applied, and a three-dimensional phase space model has been built up.

II. CIRCUIT, EQUATIONS, SOLUTIONS

The inverter with magnetic coupling (IM) – Fig. 1, has been met both independently and built in more complex structures. It consists of two magnetically coupled circles, primary and secondary.

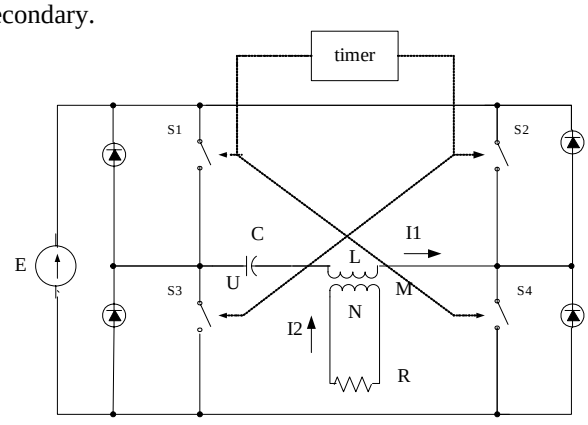

Fig. 1. Base circuit

The differential equations are the following:

$$\begin{aligned} C(dU/dt) &= I_1 \\ L(dI_1/dt) + U - M(dI_2/dt) &= E \\ M(dI_1/dt) &= N(dI_2/dt) + RI_2 \end{aligned} \quad (1)$$

where the capacitor voltage U and the currents I, H are functions of the time t. After dividing by the derivatives and applying the substitutions:

Dispersing $\Sigma^2 = 1 - k^2$, connected with the coefficient of magnetic coupling $k = M/(LN)^{0,5}$;

Phase argument $\theta = \Omega t$, where $\Omega = (CL)^{-0,5}$;

Fading decrement $\varepsilon = (R/N)/\Omega$;

Dimensionless voltage $u = U/E$;

Dimensionless currents $i_1 = (I_1/E)(L/C)^{0,5}$, $i_2 = (I_2/E)(N/C)^{0,5}$.

The argument θ is limited by the boundaries of the half-period $0 \le \theta \le \theta_s$. The boundary is $\theta_s = (T_t/T_0)$, it is proportional of the time period T_t, divided by its own period $T_0 = 2\pi/\varpi$. Then Eq. (1) assumes the following:

$$\begin{aligned} du/d\theta &= i_1 \\ \Sigma^2 di_1/d\theta &= -u - \varepsilon k i_2 + 1 \\ \Sigma^2 di_2/d\theta &= -ku - \varepsilon i_2 + k \end{aligned} \quad (2)$$

The characteristic equation is as follows:

$$\Sigma^2 p^3 + \varepsilon p^2 + p + \varepsilon = 0 \quad (3)$$

The roots of Eq. (3) are divided by their frequency ϖ, which means that it is accepted for a conditional unit: $(\varpi = 1)[(-\delta + j),(-\delta - j),(-\rho)]$. The real constants δ and ρ express the fading (reduction) for a unit of angle – radian.

According to the theorem for the residuum's the solution of Eq. (2) is a function of the roots of Eq. (3) and its general view is the following:

$$\begin{aligned} u(\theta) &= A_u \exp(-\delta\theta)\cos(\theta+\alpha) + B_u \exp(-\rho\theta) - 1 \\ i_1(\theta) &= A_{i1} \exp(-\delta\theta)\cos(\theta+\beta) + B_{i1} \exp(-\rho\theta) \\ i_2(\theta) &= A_{i2} \exp(-\delta\theta)\cos(\theta+\gamma) + B_{i2} \exp(-\rho\theta) \end{aligned} \quad (4)$$

The addends or the components can be grouped into two vectors:

$$a(\theta) = \mathrm{rot}(\theta) + \mathrm{ex}(\theta) - 1 \quad (5)$$

The first vector is rotating and it is called **rot**-vector. The other one represents the movement on a straight line and it is called **ex**-vector. They represent the two types of free oscillations (FO): sinusoidal and aperiodic, which exist in the inverter.

By the increasing of the argument the vectors reduce their modules and they get near to the point of the steady solution (-1, 0, 0). Although they develop in the 3D phase space (PS) each of the vectors is with lower order. **Ex**-vector is a segment

[1] Hristo P. Hinov is with the Technical University, 4 H. Dimitar str. 5300 Gabrovo, Bulgaria, E-mail: hino@abv.bg

[2] Hristo Z. Karailiev is with the Technical University, 4 H. Dimitar str. 5300 Gabrovo, Bulgaria, E-mail: hkarailiev@gmail.com

[3] Valentina V. Rankovska is with the Technical University, 4 H. Dimitar str. 5300 Gabrovo, Bulgaria, E-mail: rankovska@tugab.bg

in the space and it is one-dimensional, **rot**-vector is a two-dimensional.

The structure of Eqs. (4) and (5) presumes that its components develop independently from each other.

III. Phase Model

The phase model represents the regime parameters – currents and voltages, with their dynamics and interconnection. It is situated in the 3D PS, marked by a coordinate system (u, i_1, i_2). Eq. (4) describes a phase trajectory (PT) when increasing the argument θ. PT is a space line put round rotational body, given in Fig. 2.

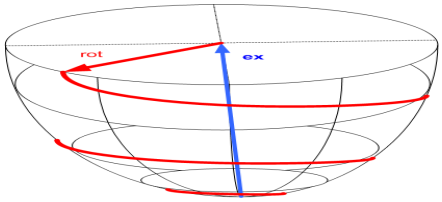

Fig. 2. Phase model

The body is flattened with less height corresponding to the **ex**-vector and with rounded vertex because of the bigger real root.

The vectors in the PS simultaneously express the regime (currents and voltages) and the energy which on the other hand is the main reason for the regime dynamics. The regime parameters (currents and voltages) are vectors and their belonging energy is a scalar. The quadrature of each vector in the PS defines a portion of energy [3].

Combining the regime and energy presentation defines the theorem for their mutual position:

If two vectors in the PS distribute the energy of a third vector – energy carrier, the two vectors are cathetuses of the energy-carrier. (6)

The three vectors make a right-angled triangle whose hypotenuse is the regime energy-carrier. Thus the quadrature of the hypotenuse, respectively the carried in energy, is distributed as the sum of the quadratures of the cathetuses.

The vectors (5) submit to the theorem (6), they are cathets and they divide the starting energy expressed by the hypotenuse – Figs. 2, 3 and 5.

If the inverter reaction is provoked in relation to its own aperiodic oscillation by substitution the current $i_2 = A\exp(-\rho\theta)$ and its derivative in Eq. (2), the coordinates of the **ex**-vector $\mathbf{ex}[1,-\rho,k/(\sum^2 \rho-\varepsilon)]$ are derived.

The **ex**-vector coordinates are defined only by the roots and the inverter circuit parameters. It defines an unchangeable straight line in the PS which is the "staunch" – the axis of the PM. It is extremely important that the **ex**-vector is a normal of the plane in which the **rot**-vector rotates.

IV. First Start

The first half period starts with the first activating of the switches S1 and S3 at zero starting conditions. The first half period has prevalent role as is in the development of the inverter, because on every next half period it reproduces itself on a higher energy level.

At the start the first equation of (4) is reduced to A+B=1. It expresses the distribution of the single x-axis segment between the two FO, presented by the vectors **rot**-vector and **ex**-vector. The single x-axis segment [(0, 0, 0)-(-1, 0, 0)] is the distance between the start point and the steady solution point of Eq. (4). It matches the voltage of the source E and it is the energy carrier which activates the free oscillations in the inverter.

There is a differential connection between the voltage *u* the primary current i_1, expressed by the first equation of Eqs. (1) and (2). This connection is applied in the second equation of (4) and for the start state of the ordinates it is derived: $\delta A - \rho B = 0$.

The two start equations are added in a system:

$$\begin{aligned} A+B&=1 \\ \delta A-\rho B&=0, \end{aligned} \qquad (4s)$$

from which the distributing constants of the voltage are defined:

$$A=\rho/(\delta+\rho);\ B=\delta/(\delta+\rho) \qquad (7)$$

These are the two vectors voltages or their x-axes in the PS, depending only on the roots. The second equation in Eq. (4s) is about the primary current i_1:

$$i_{rot}=i_{ex}=(\delta\rho)/(\delta+\rho) \qquad (8)$$

It has one and the same start value and different directions at the two free oscillations. These currents are balancing and their sum expresses the zero starting condition of the start.

The projection of the **ex**-vector and the **rot**-vector in the main plane $\mathbf{u0i_1}$ are shown in Fig. 3. The projections of the two vectors form an obtuse angle faced towards the single x-axis segment. The x-axis segment, as a base of the projection (obtuse) triangle, is divided by its height on the mentioned dividing segments A and B. The proportion of their lengths is the same as that of the inverter roots: $A/B=\rho/\delta$.

The currents (8) are the height of the projection (obtuse) triangle. If its height is lengthened to the average geometric number of the dividing segments: $h=(AB)^{0,5}$, it will define the whole start triangle of the PS:

$$h=(\delta\rho)^{0,5}/(\delta+\rho) \qquad (9)$$

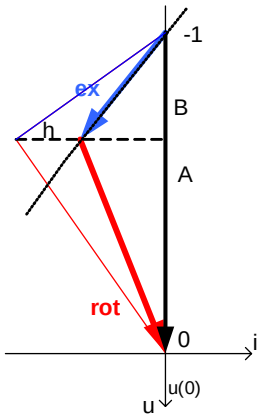

Fig. 3. Starting triangle

It is right-angled because it fulfils the condition of theorem (6) and it is in the main plane **u0i$_1$**, as it is shown in Fig. 3. The relation between the height of the start triangle and its projection is: $h/i=(\delta\rho)^{-0,5}$.

On the other hand the height of the start triangle in the PS is the vector sum of the two currents: $h^2=i_1^2+i_2^2$. The secondary current i_2 or the z-axis is:

$$i_2=(\delta\rho-(\delta\rho)^2)^{0,5}/(\delta+\rho)=i_1((1/\delta\rho)-1)^{0,5} \qquad (10)$$

The representing of the secondary current i_2 by the primary i_1 is possible in induction heating, where the secondary current develops in a massive and extremely heated part and it has no evident and accessible circuit for the ampere meters.

The dependence of the processes on the two currents vector sum: $h^2=i_1^2+i_2^2$ shows that the two currents influence on the FO as one resultant current. This leads to the conclusion that the separate free oscillations structure in their own elementary sub-spaces and that they are only included in the multi-dimensional PS.

The FO vectors in PS depend only on their roots:

$$\boldsymbol{ex}[\delta,-\delta\rho,-\delta\rho((1/\delta\rho)-1)^{0,5}]/(\delta+\rho) \qquad (11)$$
$$\boldsymbol{rot}[\rho,\delta\rho,\delta\rho((1/\delta\rho)-1)^{0,5}]/(\delta+\rho)$$

The vector coordinates x -axes (11) are influenced only by the distributing segments A and B. The rest of the coordinates are equal and balancing each other. They define the vectors in a way that except the regime values (voltage and currents) their adequate energy is also expressed.

The moduluses of (11) are the cathets of the single x-axis segment [(0,0,0),(-1,0,0)], which as a hypotenuse defines the start triangle:

$$|ex|=(\delta^2+\delta\rho)^{0,5}/(\delta+\rho)=(B)^{0,5}$$
$$|rot|=(\rho^2+\delta\rho)^{0,5}/(\delta+\rho)=(A)^{0,5} \qquad (12)$$

The moduluses (12) can be defined also by the distributing angle α - Fig.5, where:

$$tg\alpha=\delta/\rho;\quad |ex|=\sin\alpha;\quad |rot|=\cos\alpha \qquad (13)$$

An IM with a couplings coefficient k=0,6 and Q-factor=3 is taken as a numeric example, which roots are $\delta=0{,}08$ and $\rho=0{,}25$ [2]. The energy-carrier x-axis is divided between the **rot**-vector *A=0,76* and the **ex**-vector *B=0,24*. The dividing segments *A* and *B* express the distribution of the source voltage between the two inverter free oscillations. If *E=500 V*, then $A=\rho/(\delta+\rho)=25/33=76\%$ or 375 V activate the harmonic free oscillation, presented by the **rot**-vector, and the other 121 V activate the aperiodic free oscillation, presented in the PS by the **ex**-vector. It is just as if IM combines two autonomous inverters: serial inverter sourced with voltage E=379 V and aperiodic RC inverter, sourced with E=121 V. The primary current i_1 on the y-axis is 0,06, and the second i_2 on the z-axis is 0,42. The two currents in the two vectors are equal in length and with different signs:

ex [8,-2,-14]/(33) or [0.24,-0.06,-0.42];
rot [25,2,14]/(33) or [0.76,0.06, 0.42].

The divisor angle between **rot** and the x-axis in Eq. (13) is $\alpha=18°$; then the vector moduluses are: $|ex|=\sin\alpha=0{,}310$ and $|rot|=\cos\alpha=0.951$. The data is given in Table I.

TABLE I
VECTOR DATA

Distribution	**ex**	**rot**
Voltage %	24	76
Relative coordinates	8,-2,-14	25,2,14
Modulus %	31	95.1

V. RELATIVE COORDINATE SYSTEM

A relative coordinate system (RCS) is selected, where FT is in canonic position as is shown in Fig. 5. The new RCS has been got from the old base coordinate system (BCS) by a rotation. The rotation orientates the z-axis of the new RCS towards its matching with the directress of the **ex**-vector, given in Fig. 4, where the starts of the two coordinate systems become common.

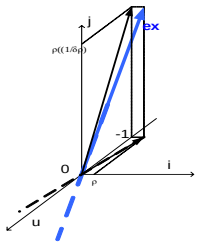

Fig. 4. **Ex**-vector in the PS

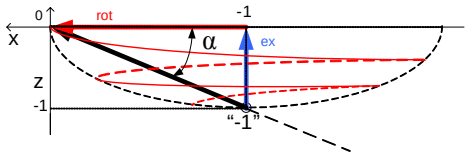

Fig. 5. Third main plane

The x-axis of the BCS is a half-line in the third projection plane (x0z) – Fig.5. The steady solution (-1) is on that half-line, where the center of the PT is, except the basic point (0,0,0). The cathets of the start triangle or the vectors of the FO are oriented towards the x-axis and the z-axis.

The vectors of the FO are connected by the energy-carrier – the hypotenuse, but they develop in their own independent spaces of the RCS. The **ex**-vector is only on the z-axis and the rest coordinate axes are for the **rot**-vector. It develops only in the first main plane **x0y.**

Magnifying scales $1/\cos\alpha$ for the x-axis and $1/\sin\alpha$ for the y-axis are introduced, so the steady point "-1" in BCS is reproduced also in "-1" on the x-axis and on the z-axis.

VI. DYNAMICS OF THE FIRST PHASE VECTOR

The development of the processes is expressed by the PV dynamics (Eq. 5), which was decomposed to the vectors of the two FO and it was structured in the RCS. It begins its development during the first half-period, starting from zero starting conditions. This "primary" development deserves special attention, because in every next half-period it reproduces itself on a higher level.

The aperiodic FO vector - $\boldsymbol{ex}\,\theta$, forms the z-axis in RCS:

$$z(\theta) = -1 + \exp(-\rho\theta) \tag{14}$$

The periodic FO vector, rotating $\boldsymbol{r}(\theta)$ (**rot**-vector), develops in the main plane **x0y** of the RCS. The vector $\boldsymbol{r}(\theta)$, decomposed by the x-axis and the y-axis vectors in a matrix, assumes the following:

$$\vec{r}(\theta) = \begin{bmatrix} r_x \\ r_y \end{bmatrix} = \begin{bmatrix} \exp(-\delta\theta)\cos\theta \\ \exp(-\delta\theta)\sin\theta \end{bmatrix} \tag{15}$$

The first main plane **x0y** is express as complex, where Eq. (15) assumes the complex view:

$$\dot{r}(\theta) = \exp((-\delta + j)\theta) \tag{16}$$

Eq. (5) changes, expressed as a matrix of coordinate vectors:

$$\vec{F}_1\begin{pmatrix} x \\ y \\ z \end{pmatrix} = -\begin{pmatrix} 1 \\ 0 \\ 1 \end{pmatrix} + \begin{bmatrix} \mathrm{Re}(\dot{r}(\theta)) \\ \mathrm{Im}(\dot{r}(\theta)) \\ z(\theta) \end{bmatrix} \tag{17}$$

The periodic vector complex equation (16) allows reducing Eq. (17):

$$\vec{F}_1(\dot{r}, z) = -\begin{pmatrix} 1 \\ 1 \end{pmatrix} + \begin{pmatrix} \dot{r}(\theta) \\ z(\theta) \end{pmatrix} \tag{18}$$

The x-axis and the y-axis are expressed by the real and the imaginary parts of the complex operator $\dot{r}(\theta)$ (Eq. 16), and the z-axis by the scalar $z(\theta)$ (Eq. 14).

The final point of Eq. (!8) is a combinations of the final points of Eqs. (16) and (14) at $\theta = \theta_s$:

$$F_1(\theta_s) = \begin{pmatrix} -1 + \dot{q} \\ -1 + q \end{pmatrix} \tag{19}$$

where the complex *q'=exp(p')* is the final value of Eq. (16) $p' = (-\delta + j)\theta_s$.

The real *q=exp(p)* is the final value of Eq. (14) $p = -\rho\theta_s$.

The start point (0,0,0) and the final point (19) define the PT segment, passed by the primary PV for the half-period interval $(T_t / 2 = \theta_s / \omega))$.

The primary PV dynamics finishes with so called commutation. The timer activates the inverse bridge switches at the final point and it initiates a source direction change, represented by a change of the signs in Eq. (19).

The second half-period starts at point:

$$S_2 = \begin{pmatrix} 1 - \dot{q} \\ 1 - q \end{pmatrix} \tag{20}$$

VII. Components of the IM (Sub invertors)

The upper operations have been made simultaneously, but they have been separated in two independent "containers".

The development of the periodic FO or **rot**-vector is exactly the serial inverter development [3], [4]. The aperiodic FO simultaneous development, represented by the **ex**-vector, is a one-dimensional elementary inverter development [5].

These are the two sub-inverters – Fig. 6, to which IM is decomposed. They develop synchronous, but independently from each other. Their common connection is only the injected energy at the commutation transition, which they distribute each other. The quadratic forms of this distribution have been proved.

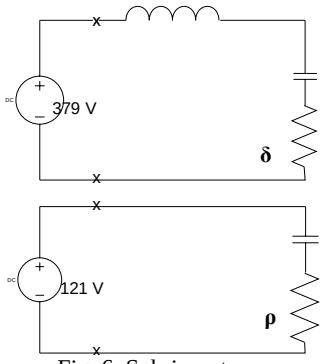

Fig. 6. Sub-inverters

The regime distribution of the source voltage has been demonstrated in the example and it has been shown in Fig. 7.

The serial sub-inverter has got a stationary mode, defined by the commutation point: S_s=2,085(26,5^0)=1,866+j0,93; scale M_a=0,5CE^2=0,144[J]; power P=14,42 kW at 10 kHz [4]. The aperiodic sub-inverter has got a stationary mode, defined by the point S_a=0,63/1,37=0,462, that assigns it power P=4,56 kW.

VIII. Conclusions

1. The theorem of the residuum's can be applied on the power inverters.
2. The complex inverters can be decomposed on components – sub-inverters from first and second order.
3. The inverter phase model is effective in the three-dimensional space too.
4. The free oscillation processes develop in independent relative sub-spaces embraced by the three-dimensional phase space.

References

[1] M. H. Rashid, "Power Electronics, Circuits, Devices and Applications", Pearson Prentice-Hall International, Inc., 2004.

[2] Х. П. Хинов, "Характеристично уравнение на инвертор с индуктивна връзка", *UNITECH'04 Conference Proceedings*, 1-222, Gabrovo, Bulgaria, 2004.

[3] H. P. Hinov, V. V. Rankovska, "Analysis of an Asymmetric Inverter in Phase Space", *ICEST 2004 Conference Proceedings*, pp. 403-406, Bitola, Macedonia, 2004.

[4] Х. П. Хинов, "Фазов анализ на симетричен инвертор". Известия на ТУ Габрово /под печат/.

[5] Ch. P. Chinow, "Geometrische Modellierung elektromagnetischer Prosesse in einfachen Wechselrichtern", 4-WK, pp. 19-21, Mittweida, DDR, 1976.

Investigation and Frequency Characteristics of the High Order Voltage – Fed RLC Inverter for Induction Heating

Michail H. Antchev[1] and Evgeniy I. Popov[2]

Abstract - **A voltage-fed RLC inverter with free - wheeling diodes for induction heating having a high order circuit is studied. The load is replaced by serially connected resistance and reactance. The inverter parameters are determined. The frequency controlling characteristics are obtained and confirmed. It is suggested to maintain resonance of the load.**

Keywords - **Voltage-fed inverter, RLC inverter, High-order circuit, Frequency characteristics, Resonance.**

I. INTRODUCTION

The voltage-fed RLC inverter with free - wheeling diodes (Fig. 1) applies widely for induction heating and melting due to the limited voltage across the power semiconductor devices even for large variations of the load. The circuit can operate either in oscillatory, critical or over damped mode depending on its parameters. In over damped, critical and oscillatory mode when the controlling frequency $\omega = 2\pi f$ is higher than the inherent resonant frequency ω_0 of the serial inverter circuit the inverter must be constructed with fully controllable devices (transistors or GTO thyristors) and free - wheeling diodes. Only in oscillatory mode when the inverter operates at a frequency lower than the inherent resonant frequency the power semiconductor devices (shown on the figure as switches) may be conventional thyristors making the power circuit cheaper. But thyristors require sufficient circuit turn-off time and have limitations concerning di/dt and dv/dt. The voltage-fed RLC inverter has not been analyzed in the practical case when the inverter circuit is of high order due to the influence of the load circuit [1,2]. The frequency characteristics of the main quantities of such an inverter when the controlling (output) frequency varies are also not known.

That's why this paper is aimed at performing an investigation of the high order power circuit of the voltage-fed RLC inverter with free – wheeling diodes for induction heating and melting and obtaining the frequency control characteristics of the main parameters. This will allow a method for control of the inverter operation to be suggested. Simulations and experiments should confirm the results.

II. ASSUMPTIONS

A bridge circuit is under study. Other configurations can be easily reduced to the bridge one. The power losses in the inverter are neglected. The commutation of the power semiconductor devices is instantaneous. The quality factor of the load circuit is sufficiently high that the voltage across the load has a close to the sine wave shape. The method of transitory values is applied.

[1]Michail H. Antchev is with the Faculty of Electronic Technique and Technologies, Technical University, Sofia – 1000, Bul. Kl. Ohridski 8, Bulgaria, email: antchev@tu-sofia.bg.

[2]Evgeniy I. Popov is with the Faculty of Electronic Technique and Technologies, Technical University, Sofia – 1000, Bul. Kl. Ohridski 8, Bulgaria, email: epopov@tu-sofia.bg.

III. REPRESENTATION OF THE LOAD CIRCUIT

A parallel equivalent circuit containing the frequency dependent active resistance R_l and inductance L_l represents the inductor heater:

$$R_l = R_{lr}\left(\frac{\omega}{\omega_{lr}}\right)^{n_1} \tag{1}$$

$$L_l = L_{lr}\left(\frac{\omega}{\omega_{lr}}\right)^{n_2-1} \tag{2}$$

where ω_{lr} is the resonant frequency of the load circuit R_l, L_l, C_l

$$\omega_{lr} = \frac{1}{\sqrt{C_l L_{lr}}} \tag{3}$$

R_{lr}, L_{lr} are the inductor parameters for the resonant frequency. The values of n_1 and n_2 are given in [3].

If the quality factor of the load circuit R_l, L_l, C_l at resonance

$$Q_r = R_{lr}\sqrt{\frac{C_l}{L_{lr}}} \tag{4}$$

is high enough the load voltage is almost sine wave and the load can be represented by a serial equivalent circuit containing the parameters R_{eq}, X_{eq} (Fig. 2).

$$\frac{R_{eq}}{R_{lr}} = \frac{\left(\frac{\omega}{\omega_{lr}}\right)^{n_1}}{1+Q_r^{\,2}\left(\frac{\omega}{\omega_{lr}}\right)^{(2n_1-n_2+1)}\left(\frac{\omega}{\omega_{lr}}-\frac{\omega_{lr}}{\omega}\right)^2} \tag{5}$$

$$\frac{X_{eq}}{R_{lr}} = \frac{Q_r\left(\frac{\omega}{\omega_{lr}}\right)^{\left(2n_1+\frac{1-n_2}{2}\right)}\left(\frac{\omega_{lr}}{\omega}-\frac{\omega}{\omega_{lr}}\right)}{1+Q_r^{\,2}\left(\frac{\omega}{\omega_{lr}}\right)^{(2n_1-n_2+1)}\left(\frac{\omega}{\omega_{lr}}-\frac{\omega_{lr}}{\omega}\right)^2} \tag{6}$$

Below the resonance of the load circuit the equivalent reactance X_{eq} is in fact a serial equivalent inductance L_{eq}. Therefore the serial inverter circuit consists of $R = R_{eq}$, $L = L_{eq} + L_S$, $C = C_S$. Above the resonance of the load the equivalent reactance X_{eq} is a serial equivalent capacitance C_{eq} and the serial inverter circuit consists of $R = R_{eq}$,

$L = L_S$, $C = \frac{C_{eq} C_S}{C_{eq} + C_S}$. Then the voltage across the inverter capacitor C is divided between the capacitors C_S and C_{eq} in accordance with the theory of electrical engineering [4].

$$\frac{L_{eq}}{L_{lr}} = \frac{Q_r^2 (\frac{\omega}{\omega_{lr}})^{(2n_1 + \frac{1-n_2}{2})} (\frac{\omega_{lr}^2}{\omega} - 1)}{1 + Q_r^2 (\frac{\omega}{\omega_{lr}})^{(2n_1 - n_2 + 1)} (\frac{\omega}{\omega_{lr}} - \frac{\omega_{lr}}{\omega})^2} \quad (7)$$

$$\frac{C_{eq}}{C_l} = \frac{1 + Q_r^2 (\frac{\omega}{\omega_{lr}})^{(2n_1 - n_2 + 1)} (\frac{\omega}{\omega_{lr}} - \frac{\omega_{lr}}{\omega})^2}{Q_r^2 (\frac{\omega}{\omega_{lr}})^{(2n_1 + \frac{1-n_2}{2})} (\frac{\omega^2}{\omega_{lr}^2} - 1)} \quad (8)$$

IV. MODE OF OPERATION

The mode of operation is determined from the diagram shown in Fig. 3 [5], where the load coefficient of the inverter is

$$B = \frac{\sqrt{1 + \omega^2 C^2 R_{eq}^2}}{\omega^2 LC} \quad (9)$$

and the load power factor of the inverter is

$$\cos\varphi = \frac{1}{\sqrt{1 + tg^2 \varphi}} = \frac{\omega C R_{eq}}{\sqrt{1 + \omega^2 C^2 R_{eq}^2}} \quad (10)$$

V. PARAMETERS OF THE INVERTER CIRCUIT

The fourth order inverter circuit is reduced to a second order RLC circuit. Its parameters are calculated as follows:

The damping coefficient is

$$\delta = \frac{R_{eq}}{2L} \quad (11)$$

The inherent frequency of the serial inverter circuit for:

- Oscillatory mode ($R_{eq} < 2\sqrt{L/C}$) is

$$\Omega = \omega_0 = \sqrt{\frac{1}{LC} - \delta^2} \quad (12)$$

- Over damped mode ($R_{eq} > 2\sqrt{L/C}$) is

$$\Omega = \sqrt{\delta^2 - \frac{1}{LC}} \quad (13)$$

- Critical mode ($R_{eq} = 2\sqrt{L/C}$) is

$$\Omega = \delta \quad (14)$$

The angle θ_2 ($\theta_2 > 0$) is

$$\theta_2 = \frac{\Omega}{\omega}\pi = \frac{\pi}{n} \quad (15)$$

The following functions and constants are introduced: $f_S(x)=sinx$, $f_C(x)=cosx$, c=+1 for oscillatory mode; $f_S(x)=shx$, $f_C(x)=chx$, c=-1 for over damped mode; $f_S(x)= x$, $f_C(x)=1=const$, c=0 for critical mode.

Then the a coefficient and the angle θ_1 ($\theta_1 > 0$) can be determined from

$$a = \frac{f_S(\theta_1) / f_C(\theta_1)}{1 - \frac{\delta}{\Omega} f_S(\theta_1) / f_C(\theta_1)} = \frac{f_S(\theta_2)}{e^{\frac{\delta}{\Omega}\theta_2} + f_C(\theta_2) - \frac{\delta}{\Omega} f_S(\theta_2)} \quad (16)$$

The generalized coefficient of hesitation is

$$K = \frac{1}{1 + \exp(-\frac{\delta}{\Omega}\theta)[(ca + \frac{\delta}{\Omega} + a\frac{\delta^2}{\Omega^2}) f_S(\theta_2) + f_C(\theta_2)]} \quad (17)$$

The peak and initial voltages across the inverter capacitor C are

$$V_{Cm} = [2(\frac{K}{K_1} - K) - 1]V_d \quad (18)$$

where K_1 is the value of K but for angle θ_1 instead of θ_2 .

$$V_0 = (2K - 1)V_d \quad (19)$$

The average value of the inverter input current is

$$I_d = \frac{V_d}{\Omega L} \cdot \frac{1}{\theta_2} \cdot \frac{2(2K-1)}{\frac{\delta^2}{\Omega^2} + c} \quad (20)$$

The average value of the inverter input current between 0 and θ_1 is

$$I_1 = abs[\frac{V_d}{\Omega L} \cdot \frac{1}{\theta_2} \cdot \frac{2(2K_1 - 1)}{\frac{\delta^2}{\Omega^2} + c} \cdot \frac{K}{K_1}] \quad (21)$$

The average value of the inverter input current between θ_1 and θ_2 is

$$I_2 = abs[\frac{V_d}{\Omega L} \cdot \frac{1}{\theta_2} \cdot \frac{2}{\frac{\delta^2}{\Omega^2} + c} \cdot (\frac{K}{K_1} - 1)] \quad (22)$$

I_1 and I_2 are used for calculation of the average currents through the power semiconductor devices.

Initial inverter current for a half-period

$$I_0 = 2aK \cdot \frac{V_d}{\Omega L} \quad (23)$$

For $\omega \le \omega_0$ the thyristor circuit turn-off time is

$$t_{q.c.} = \frac{(\theta_2 - \theta_1)[rad]}{\omega_0} \quad (24)$$

The transitory value of the inverter current for a half-period is expressed by

$$i(\theta) = \frac{V_d}{\Omega L} \cdot 2K \exp(-\frac{\delta}{\Omega}\theta)[(1 + a\frac{\delta}{\Omega}) f_S(\theta) - a f_C(\theta)] \quad (25)$$

where $\theta = \Omega t$, t is time.

The transitory value of the inverter capacitor voltage C for a half-period is

$$v_C(\theta) = V_d \{1 - 2K \exp(-\frac{\delta}{\Omega}\theta)[(ca + \frac{\delta}{\Omega} + a\frac{\delta^2}{\Omega^2}) f_S(\theta) + f_C(\theta)]\} \quad (26)$$

VI. LOAD VOLTAGE DETERMINATION

The RMS of voltage across the load circuit R_l, L_l, C_l can be determined from its harmonic components as follows

$$V_l = \sqrt{\sum_{m=1,3,5,...} V_{l(m)}^2} \tag{27}$$

Each harmonic component of the load voltage is expressed by

$$V_{l(m)} = \frac{V_d}{\omega_0 L} \cdot \frac{c_{(m)}}{\sqrt{2}} \cdot \sqrt{R_{eq(m)}^2 + X_{eq(m)}^2} \tag{28}$$

where $R_{eq(m)}$ and $X_{eq(m)}$ are calculated from Eqs. (5) and (6), exchanging $\frac{\omega}{\omega_{lr}}$ with $\frac{m\omega}{\omega_{lr}}$.

The normalized peak value of the m – harmonic component of the inverter current is

$$c_{(m)} = \sqrt{a_{(m)}^2 + b_{(m)}^2} \tag{29}$$

The expressions for $a_{(m)}$ and $b_{(m)}$ are rather complicated functions of m, ω/Ω and δ/Ω. They can be derived from Eq. (25) in accordance with [4]. These expressions are known to the authors but for the sake of brevity are not given here.

VII. FREQUENCY CHARACTERISTICS

A MATLAB program processes all the mathematical information describing the steady state operation of the inverter together with its load circuit in the allowed frequency range. The frequency characteristics of the inverter are obtained and graphically displayed in Fig. 4 for the particular case corresponding to a practically implemented inverter with the following data: V_d=500 V; L_S=0.3 mH; C_S=4 μF; R_{lr}=4 Ω, f_{lr}=4000 Hz, $\cos\varphi_{lr}$=0.24254, n_1=0, n_2=1, f=3000 – 4800 Hz. The first set of graphics shows: five times the average input current of the inverter $5I_d$ [A] (solid line), the load voltage V_l [V] (dotted line), five times the circuit turn-off time of the thyristors $5t_{q.c.}$ [μS] (dashed line). The second set of graphics shows: one fifth of the peak serial capacitor voltage $V_{CSm}/5$ [V] (solid line), twice the RMS value of the inverter current $2I_S$ [A] (dotted line), five times phase angle of the load circuit $5\varphi_{eq} = 5arctg(X_{eq}/R_{eq})$ [deg] (dashed line). The same MATLAB program can calculate frequency characteristics for different input data and modes of operation. These characteristics are original. Other parameters of the circuit can also be calculated and displayed. The calculation is more precise if the shape of the load voltage is closer to the sine-wave form. That is checked for each particular frequency.

Many conclusions about the inverter operation can be drawn from the frequency characteristics. In general the increase of the controlling frequency leads to increases of the input current (power), load voltage, peak serial capacitor voltage and RMS value of the inverter current, and to decreases of the circuit turn-off time of thyristors and phase angle of the load. But around the resonant frequency of the load the character of the most functions is opposite and the changes of the corresponding parameters are not so large. Therefore if the parameters of the load R_l, L_l vary during the induction heating process it is advisable to maintain a resonance of the load circuit R_l, L_l, C_l by exercising an influence on the inverter controlling frequency [6].

VIII. DIRECT SIMULATION OF THE STEADY STATE

The inverter steady state can be directly simulated by applying the method described in [7]. This method is experimentally confirmed. According to it the initial conditions of the circuit state variables for the steady state and continuous inverter current mode (most widely applied) can be calculated using a matrix exponential from:

$$[x(0+)] = ([Co] - \exp([A].T/2))^{-1}. \\ .([1] - \exp([A].T/2)).(-[A])^{-1}.[B].[V_d] \tag{30}$$

where $[A]$ and $[B]$ are the state matrixes of the circuit, $[V_d]$ is the vector of the supplying voltages (constant), $T/2 = 1/(2f)$ is the half-period, [1] is a unity matrix. $[Co]$ is a diagonal matrix of the same order as $[A]$, where the element Co_{ii}=-1 if it relates state variables in the beginning and in the end of the half period for the a.c. circuit of the inverter, and Co_{ii}=+1 if it relates state variables in the d.c. circuit of the inverter. For the exceptional discontinuous inverter current mode the calculation is more complicated but is also possible according to [7]. For the inverter under study the state variables vector is

$$[x] = \begin{bmatrix} u_{C_S} & i_{L_S} & u_{C_l} & i_{L_l} \end{bmatrix}^t \tag{31}$$

and the state matrixes are

$$[A] = \begin{bmatrix} 0 & 1/C_S & 0 & 0 \\ -1/L_S & 0 & -1/L_S & 0 \\ 0 & 1/C_l & -1/(R_l C_l) & -1/C_l \\ 0 & 0 & 1/L_l & 0 \end{bmatrix} \tag{32}$$

$$[B] = \begin{bmatrix} 0 & 1/L_S & 0 & 0 \end{bmatrix}^t \tag{33}$$

Co_{ii}=-1 for i=1;2;3;4.

After determining the initial conditions of the state variables for the steady state the state variables themselves are calculated as functions of time for one half-period from:

$$[x(t)] = \exp([A]t).[x(0+)] + \\ + ([1] - \exp([A]t)).(-[A]^{-1}).[B].[V_d] \tag{34}$$

Taking into account Eqs. (30) - (34) a MATLAB program is created for direct simulation of the steady state processes in the inverter under study. The results from the MATLAB programs for calculating the frequency characteristics and for simulation of the steady state mode are compared. The comparison shows that both results are in good agreement. That confirms the correctness of the analysis, the frequency characteristics and the program for their calculation. The detailed simulation results for the power inverter are graphically displayed (Fig. 5) for the steady state and f=4000 Hz. The first set of diagrams shows: five times the inverter current i_{CS} [A] (solid line) and twice the load voltage v_l [V] (dotted line). The second set of diagrams shows: the serial capacitor voltage v_{CS} [V], twice the voltage across the first

power electronic device v_{VS1} [V] (dashed line), twice the current through the load inductance i_{Ll} [A] (dotted line).

IX. A METHOD FOR CONTROL

As it was said when the load parameters R_l, L_l vary during the induction heating it is recommended to maintain resonance (φ_{eq}=0) of the load circuit R_l, L_l, C_l. This is done by following the phase angle between the load voltage and the inverter current, and influencing the controlling frequency. But the inverter current is distorted and has intervals of interruption in discontinuous inverter current mode. That is why it is advisable to follow the phase angle between the current through the load capacitor C_l – i_{Cl} and the voltage of the serial capacitor C_S - v_{CS}. For resonance these signals are in anti-phase but can be made to be in phase by proper connections of the windings of the measuring feedback transformers. The controlling system is fully described in [6].

X. CONCLUSION

An investigation of the high order power circuit of a voltage-fed RLC inverter with free – wheeling diodes for induction heating is performed. The original frequency control characteristics of the main parameters of the inverter circuit are calculated and graphically displayed. A MATLAB simulation program confirms the frequency characteristics. A method for control of the inverter operation is suggested.

REFERENCES

[1] N. P. Gradinarov, "Investigation, development and progress of autonomous resonant inverters for electro technology applications" *Dr. Sc. Thesis, Technical University* – Sofia, Bulgaria, 2002. (In Bulgarian).

[2] N. L. Hinov, "Power converters of electrical energy for industrial applications" *Ph. D. Thesis, Technical University* – Sofia, Bulgaria, 1998. (In Bulgarian).

[3] E. I. Berkovitch, G. V. Ivenskiy, Yu. S. Yoffe, A T. Matchak, V. V. Morgun, *Higher frequency thyristor converters for electro technology applications*, Leningrad, Energoatomizdat, 1983 (in Russian), pp. 8-13.

[4] G. I. Atabekov, *Fundamentals of circuit theory*, Moscow, Energy, 1969 (in Russian), pp.131-132, 100.

[5] E. I. Popov,. "A new unified approach towards the analysis of semiconductor RLC inverters" *Proceedings of the scientific conference with international participation "Electronics'98"*, 15-16.10.1998, Botevgrad, Bulgaria, pp.208-215.

[6] M. Hr. Antchev, "A system for frequency automatic control of a resonant inverter", *Scientific Journal "Electro-industry and device building"*, vol.XXIV-4, 1989, Sofia, Bulgaria, (In Bulg.), pp.20-23.

[7] E.I. Popov, "Direct determination of the steady-state mode in autonomous inverters", *Scientific Journal "Electrical Engineering and Electronics"*, Sofia, Bulgaria, (In Bulg.), (Under print).

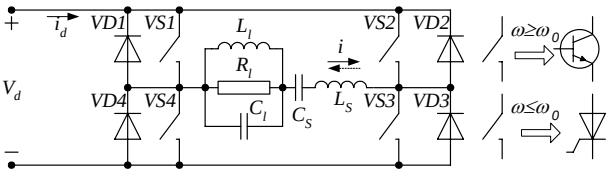

Fig. 1. Voltage – fed RLC inverter with free – wheeling diodes.

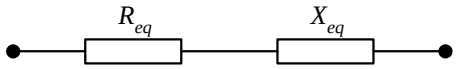

Fig. 2. Serial equivalent circuit of the load (L_l, R_l, C_l).

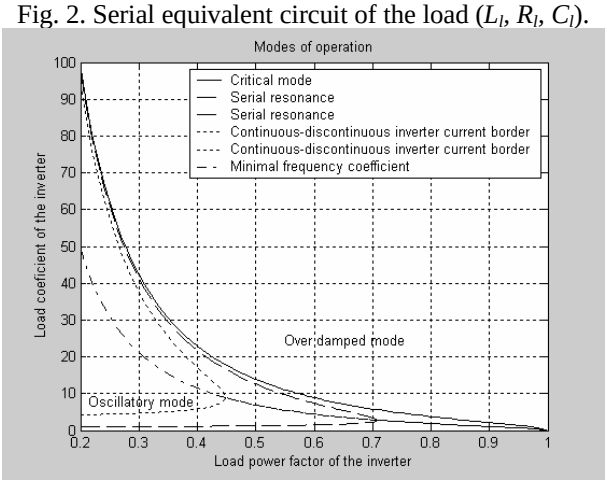

Fig. 3. The diagram of the inverter modes of operation.

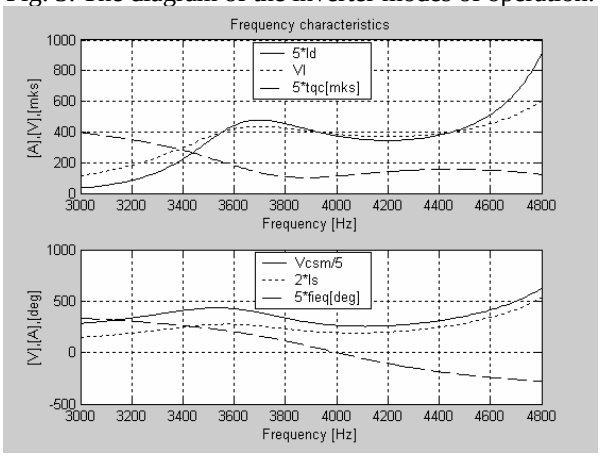

Fig. 4. Frequency characteristics of the inverter.

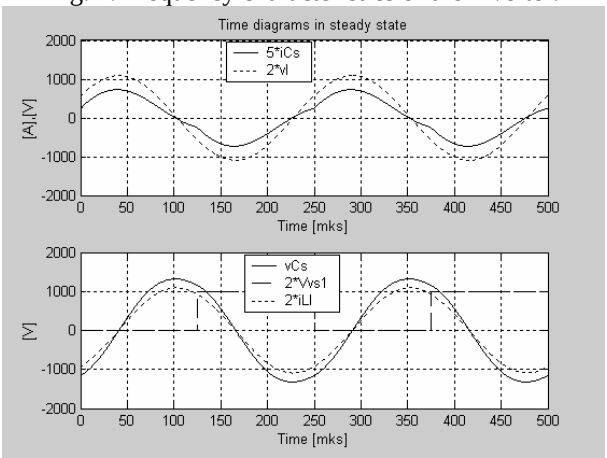

Fig.5. Detailed simulation results at f=4000 Hz.

Modeling and Investigation of an Inductive Cumulation Inverter

Hristo Z. Karailiev[1], Hristo P. Hinov[2], Valentina V. Rankovska[3]

Abstract – **A class of inverters for little and medium power, characterized with dynamic change of the load parameters, have been studied. A real time control is needed to maintain an optimal operation mode of inverters with inductive cumulation. An approach for inverter modeling and investigation by means of MATLAB, SIMULINK and PLECS is suggested in this paper. As a result of modeling the relation of the cumulation time and the load change having in mind the maximum admissible transistor current and the maximum admissible voltage between collector and the emitter is studied.**

Keywords – **inverter, induction heating, inductive cumulation, modeling, cumulation time.**

I. Introduction

In many practical cases using the inverters for little and medium power for hardening and metal melting etc. is needed. Varying the heating temperature in a definite range, the load parameters Z_T (R_T,L_T) change accordingly. The active and reactive load components change leads to a change of the free oscillations of the oscillating circuit.

The time for forced energy accumulation in the oscillating circuit inductivity has been added as a parameter at inductive cumulation inverters. There is a risk of oscillations failing if the cumulation time is defined too short, and if it is defined too long there is a risk to exceed the puncture voltage of the transistor and his current value.

The major aim of this report is modeling and investigation of an inductive cumulation inverter. The goal is to accumulate data needed as a base in designing a microprocessor control device.

Major problems solved in the report:

- To study a single-switch inverter operation modes at parameters varying at admissible limits;
- To study the admissible cumulation time limits at changing the real load consumption without exceeding the transistor puncture voltage $(U_{CE})_{don}$ and the maximum admissible current value $(I_{TP})_{don}$.

II. Formulation of the Task for Modeling and Investigation of an Inductive Cummulation Inverter

The base inverter circuit used for modeling and investigation is shown in Fig. 1.

The components of the circuit are the following:

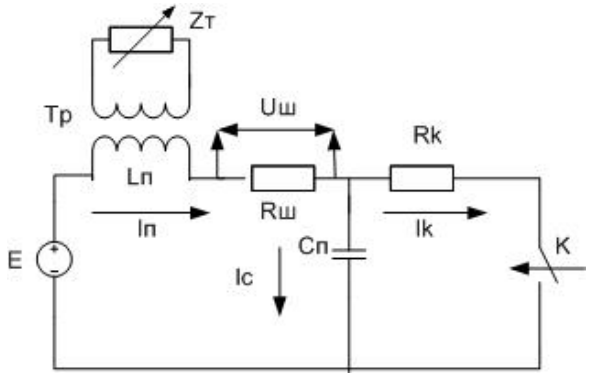

Fig. 1. Inductive cumulation inverter circuit

E	Direct voltage source
T_P	Linear transformer for galvanic isolation of the load Z_T from the source
Z_T	(R_T,L_T) – inductor parameters varying with temperature change
L_{II}	Transformer primary side inductivity
C_{II}	Capacitance in the serial oscillating circuit
R_{III}	Shunt resistor for monitoring the current value in the oscillating circuit
R_K	Switch K resistance when it is closed
K	Switch, when it is open it allows cumulating energy in L_{II}

The major analytical dependencies of the oscillation circuit free oscillations, when there is no load connected in the secondary side and no cumulation are given below:

$$\rho = \sqrt{\frac{L_{II}}{S_{II}}} \text{ - characteristic impedance} \quad (1)$$

$$Q = \frac{\rho}{P_{II}} \text{ - Q-factor of the circuit} \quad (2)$$

$$\delta = \frac{R}{2L} \text{ - oscillating circuit damping} \quad (3)$$

$$\varepsilon = \frac{\delta}{\omega} = \frac{1}{2Q} \text{ - phase oscillating circuit damping} \quad (4)$$

$$\omega = \sqrt{\frac{1}{L_{II}C_{II}} - \delta^2} = \sqrt{\frac{1}{L_{II}C_{II}} - (\frac{R_{II}}{2L_{II}})^2} \quad (5)$$

- own resonant frequency of the circuit

$$T = \frac{1}{f} = \frac{2\pi}{\omega} \text{ - own oscillations period} \quad (6)$$

When there is a cumulation, i.e. when the switch K is opened for time τ, the operation mode of the inverter and its major characteristics change. This fact can be used further to control the operation mode of the inverter. Then the period and the oscillation frequency will be as follows:

[1] Hristo Z. Karailiev is with the Technical University, 4 H. Dimitar str. 5300 Gabrovo, Bulgaria, E-mail: hkarailiev@gmail.com

[2] Hristo P. Hinov is with the Technical University, 4 H. Dimitar str. 5300 Gabrovo, Bulgaria, E-mail: hino@abv.bg

[3] Valentina V. Rankovska is with the Technical University, 4 H. Dimitar str. 5300 Gabrovo, Bulgaria, E-mail: rankovska@tugab.bg

$$T_K = T + \tau, \text{ or } f_K = \frac{1}{T+\tau} \quad (7)$$

On the other hand when increasing the temperature in the heated metal qualitative changes have been done in it. The active impedance value R_T increases and at the magnet distortion point μ_r becomes 1. These qualitative changes lead to increasing the equivalent impedance R_{PE} and L_{PE} at the primary side of the oscillating circuit.

$$R_{\Pi E}=R_{\Pi} + R_{BH} \quad (8)$$
$$L_{\Pi E}= L_{\Pi} - L_H$$

As a result the equivalent characteristic impedance ρ_e decreases and $R_{\Pi E}$ increases. This leads to decreasing the equivalent Q-factor Q_e, i.e.:

$$t^{\circ}C \rightarrow L_{\Pi E} \downarrow \rightarrow \rho_e \downarrow \rightarrow R_{\Pi E} \uparrow \rightarrow Q \downarrow \quad (9)$$

The following conclusions can be made as a result of the upper reasoning:

1. At the technological process the qualities of the heated metal and the equivalent parameters of the oscillating circuit have been changing and the generated oscillations in the inverter may fail at high temperatures.
2. It is necessary to gather information about the inverter operation mode continuously and to generate control signal with regulated duration for the switch *K* for optimal energy cumulation in the inductivity.
3. It is necessary to accumulate data about the time parameters of the oscillating circuit and together with cumulation time regulation it is necessary not to exceed the admissible values of the voltage $(U_{CE})_{\partial on}$ and the transistor current $(I_{TP})_{\partial on}$.

III. MODELING AND INVESTIGATION OF THE OPERATION MODES OF AN INDUCTIVE CUMULATION INVERTER

A base for the modeling is the results got about single-switch cumulation inverter at variable temperature from t_{min} to t_{max} [1]. From the results it can be seen, that R_T increases 3,5 times at t_{max} in relation to its value at $t_{min}= 20^{\circ}C$. The inductivity decreases 2,5 times at the magnet distortion point in relation to L_T at temperature $t_{min}= 20^{\circ}C$.

The modeling of the single-switch inductive cumulation inverter has been made based on upper conclusions. The program SIMULINK and the instrumentation toolbox PLECS have been used for that purpose [2], [3].

The model of the control circuit using the SIMULINK library is shown in Fig. 2. The electrical circuit of the inverter has been modeled using the PLECS library and it is shown in Fig. 3.

The block circuit for the modeling of the inverter control part has been built up using the blocks – multiplexer, multiplying block and scopes for monitoring the measured values. Considerable place has given to the Setting Cumulation Time Block (SCTB). It has been built up using the approach DDS (Data Direct Synthesis). The change step of the cumulation time duration has been set by setting the parameters of the *Delays* block. In our case a step 1.10^{-7} [s] has been selected, but if it is necessary it can be decreased.

The cumulation time duration has been set by the operator by the block *Constant 3* (Fig. 2) and it can vary from $\tau_{\min}$, at which damping oscillations occur, to $\tau_{\max}$.

The maximum value of $\tau_{\max}$ has been limited by two factors – the transistor (capacitor) puncture voltage and the maximum admissible transistor current value.

The voltage maximum value $(U_{CE})_{bb}$ is:

$$(U_{CE})_{bb}=U_{CEmax}(t_1)- U_{CEmin}(t_2) \quad (10)$$

where t_1 and t_2 are the moments at which U_{CE} has got maximum and minimum value accordingly. In order not to occur a puncture in the capacitor and the transistor the following condition should be fulfilled:

$$(U_{CE})_{bb} \le k(U_{CE})_{\partial on} \quad (11)$$

where $0{,}9 \le k \le 0{,}95$ is a sure coefficient.

The second factor liming $\tau_{\max}$ is the maximum admissible current value of the transistor, i.e. it is necessary to fulfill the condition:

$$I_{TP} \le k(I_{TP})_{\partial on} \quad (12)$$

The moment, at which the control signal for switching on the transistor is generated, is important. In order not to dissipate needless thermal power on the transistor it is advisable it's switching on to be made during the interval when $U_{CE} \le 0$. That's why it is necessary the transition moment to be fixed, when U_{CE} changes it's sign from (+) to (-). At modeling it have been done by the means of zero voltage comparator which input signal has been taken from the voltage U_{CE} by resistor divider *R5* and *R6* (Fig. 3).

At the moments t_1 and t_2 when the transistor voltage has maximum value U_{CEmax} and minimum value U_{CEmin} accordingly the oscillator circuit current value is zero. That's why it is advisable to use a zero current comparator receiving an input signal from the resistor $R_{Ш}$.

Having in mind Figs. 2 and 3, the change range of L_{Π} and R_{Π} when varying the temperature from $\tau_{\min}$ to $\tau_{\max}$ at previously defined primary values of the oscillator circuit parameters, information about the operation modes has been gathered (voltages, currents, power, time intervals). Simultaneously the cummulation time changes in advisable limits by SCTB. Three values have been taken for the source voltage: E, E+10%, E-10%. The simulation data results are shown in Table I. Some typical timing diagrams about voltages, currents and time intervals are shown in Figs. 4 and 5.

The relation between the inductor current (position 1) and the transistor voltage (position 2), the time interval τ_1 (position 3), and the cumulation time (position 4) are shown in Fig. 4. The voltage has maximum and minimum values accordingly at zero current values. That is why the maximum allowed values can be selected and controlled by means of a zero current comparator.

The relation between the primary inductor winding currents (position 1) and the transistor current (position 2) is shown in Fig. 5.

TABLE I
INVERTER SIMULATION DATA AT CHANGING L_T, R_T AND τ

E [V]	$R_T[\Omega]$	L_T [μH]	$\tau[\mu S]$	$\tau_1[\mu S]$	I_{TP}[A]	P_1[kW]	$U_{ce(+)}$[v]	$U_{ce(-)}$[v]	U_{ce}[v]	P_2[kW]	U_t[v]	I_T[A]
279	2	30	6,4	11.5	29.2	1.2	740	-103	843	0,8	207	42,5
310	2	30	6,4	11	32	1.3	833	-123	956	0,9	234	48,4
341	2	30	6,4	3.4	20	1.5	915	-135	1050	1	258	53,2
279	6,6	30	30	5.5	33	3.4	810	-40	850	2,7	395	52,1
279	6,6	30	80	8.7	38	6.5	910	-93	1003	5,8	455	61
310	6,6	30	25	3.5	34	3.8	860	-15	875	2,9	412	53,5
310	6,6	30	80	8.5	43.1	7.2	1010	-105	1115	6,5	507	68
341	6,6	30	30	5.7	40	6	1000	-47	1047	4,8	482	63,8
341	6,6	30	40	7.0	43.8	7	1050	-80	1130	6	525	69,7
279	6,6	12	35	3.5	31.1	3.8	800	-18	818	3,4	385	55,3
279	6,6	12	80	5.8	38.9	7.2	850	-47	897	5,8	418	60,5
310	6,6	12	35	3.2	39.9	4.5	890	-20	910	4	425	62,3
310	6,6	12	100	8.9	43.4	8	950	-55	1005	7,2	485	67,5
341	6,6	12	35	4.1	43.4	6.1	980	-25	1005	5,5	470	67,6
341	6,6	12	100	6.0	47.6	11.2	1045	-60	1105	9,7	535	74,3

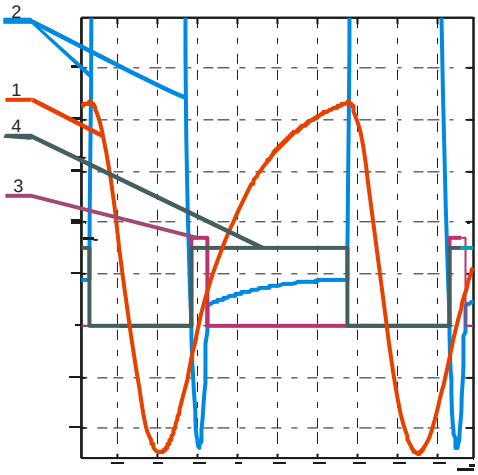

Fig. 4. Inductivity and transistor currents and voltages

Position 1 inductivity current
Position 2 transistor voltage
Position 3 time interval duration τ_1
Position 4 cumulation time duration τ

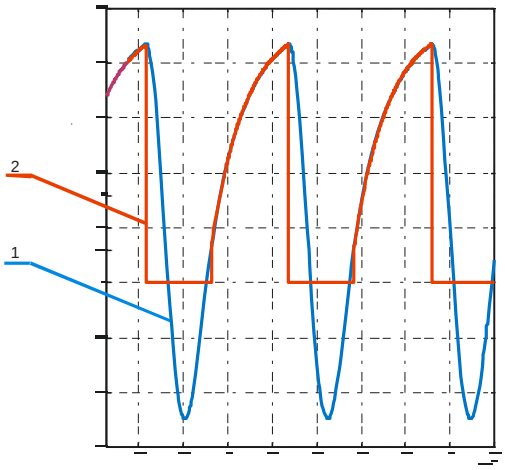

Fig 5. Inductivity and transistor currents

Position 1 inductivity current
Position 2 transistor current

VIII. CONCLUSIONS

The following conclusions can be made from the modeling of the single-switch inverter circuit at varying load parameters and from the results:

- The time interval τ_1, when the transistor voltage is negative, varies in the range of $\tau_{1\min}$ to $\tau_{1\max}$ and the negative amplitude Uc(-) must be measured and transformed into digital form.
- The cumulation time τ at zero initial values of R_T and L_T for the defined circuit has minimum value $\tau_{\min}$ and it must be changed with step $\leq 0{,}1\mu S$.
- The maximum value of the cumulation time is limited by the maximum allowed value U_{CE} of the transistor and the maximum allowed transistor current $(I_{TP})_{don}$. Therefore the voltages $U_{C(+)}$ and $U_{C(-)}$ and the current I_{TP} must be measured.
- The structure of the block SCTB in Simulink is suggested. It is based on the DDS approach. The block SCTB allows generating programmable delays with duration and step, defined by an operator.

REFERENCES

[1] Dr Ch. Hinow, Dr Georg Hinow, "Betrieb eines Wechselrichters mit inductiver Kummulation", Elektrische Bahnen., Heft 11/2004, 28.08.2004, pp.490-493

[2] "Simulink. Model-Based and System-Based Design. Using Simulink", The MathWorks, Inc., 2004, www.mathworks.com.

[3] "PLECS User Manual". Plexim GmbH, 2002-2004, www.plexim.com

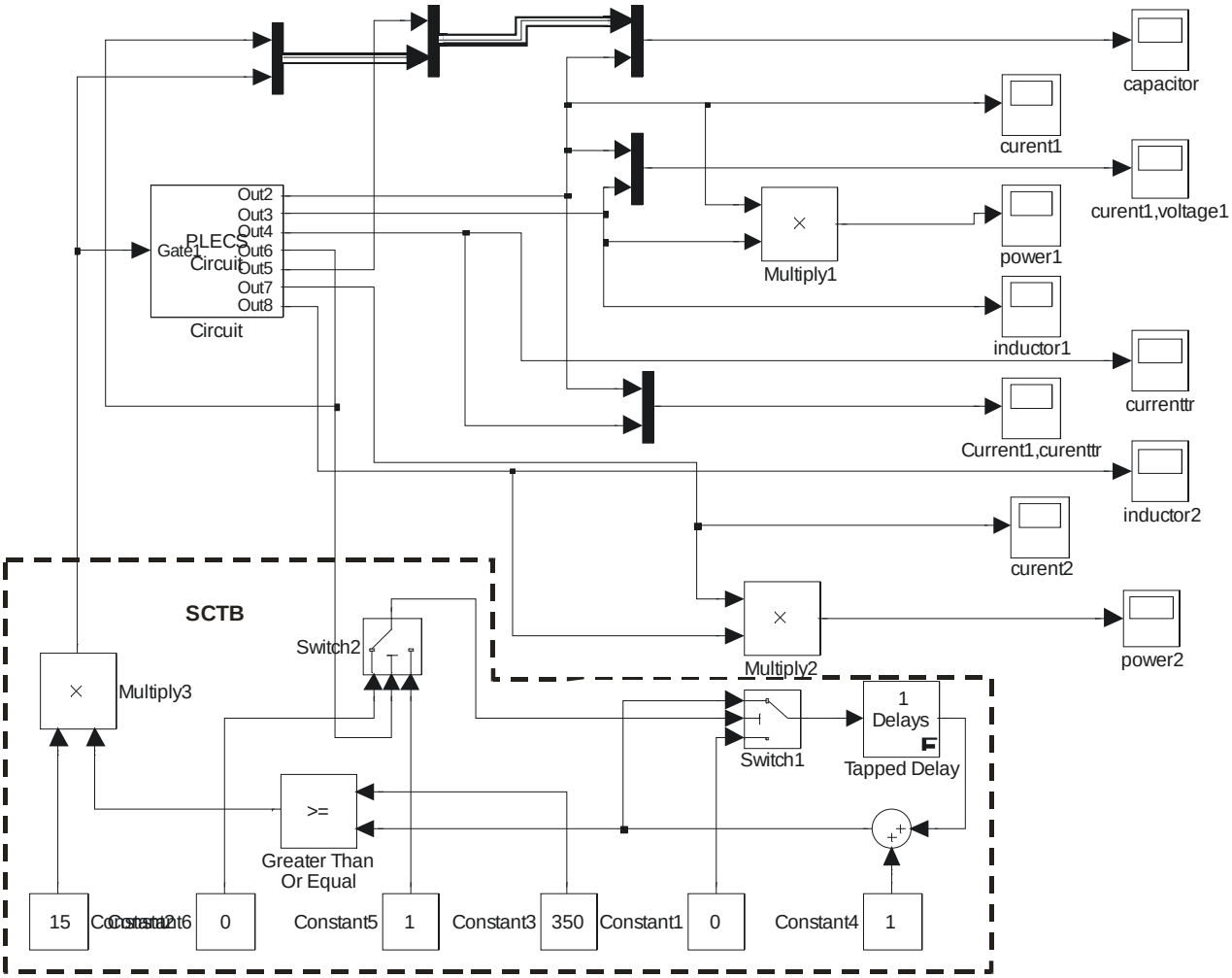

Fig. 2. Control part model of the inductive cumulation inverter

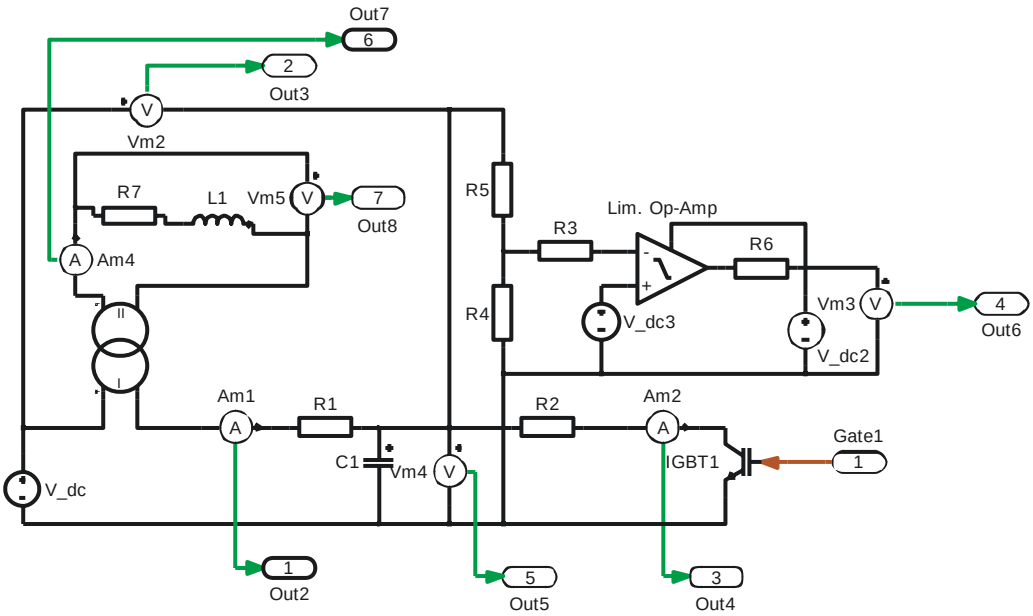

Fig. 3. Inductive cumulation inverter circuit

Design of resonant inverters using specialized software

Dimiter Vakovsky[1], Nikolaj Hinov[2], Nikola Gradinarov[2]

Abstract – **In this paper presents an integrated software system, which automates the sequence for designing and analysis of resonant inverters. The system includes linking between specialized mathematical software (MathCAD) and electronic simulation software (PSpice).**

Keywords – **MathCAD, PSpice, CAD, Automation in electronics.**

I. INTRODUCTION

The design of power electronic devices is related with significant expenses of time and materials. For optimization the design process different automated systems are created. One of the base tasks related to the development of the automated systems for computer aided design of power electronic devices is the creating of mathematical models for designing of electronic devices [4, 5, 6 ,8]. These models present the objects with a corresponding approximation depending on the actual needs.

An important requirement when creating these models is the possibility that the developed automated systems to be easily serviced and to have minimum hardware requirements. On the other hand these automated systems must allow creating of the necessary documentation for realization of the corresponding devices.

II. AUTOMATION OF THE DESIGN

A. Object and sequence of the design

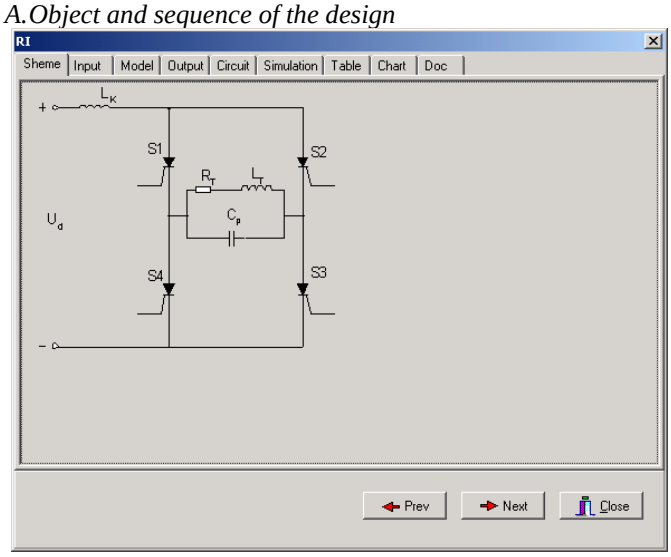

Fig. 1. Resonant inverters

Fig. 1 shows the schematic of the device, which is the objective of the automated design.

The sequence of designing of the resonant inverters has the following stages, which are realized in the presented software:

- Choice of the schematic
- Setting the input/output parameters of the device
- Choice of the components according to the mathematical model
- Visualization the values of the circuit components
- Creating the simulation model
- Simulating the electronic circuit
- Obtaining the results as graphics
- Analysis of the simulation results
- Creating the project documentation

B. Software architecture

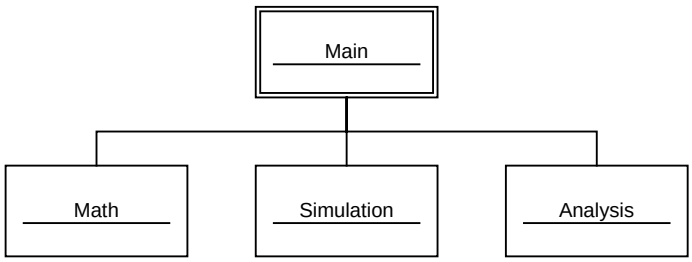

Fig. 2. Software architecture

Using the program environment Delphi develops the presented software system. The possibilities for component programming with linkage between the different software products under Windows are used. The system is built on several units, which are shown at fig. 2. The base unit (**Main**) integrates the rest of the units in the system. The unit **Math** realizes the mathematical model of the resonant inverter, obtained by the environment of the math MathCAD [11]. The unit has as an input the base input/output parameters of the circuit, and it outputs the values of the components of the resonant inverter circuit. The exchanged data is presented, according to the object-oriented model. After the calculations, the results are converted in order to be suitable for simulation of the device. The next component of the system is the simulation unit, which is called **Simulation**. The **Simulation** unit is realized in the environment of the PSpice simulation software. The PSpice program is part of the designing system OrCAD. The standard data format, incoming into the unit is the "CIR" file, and the standard output is "DAT" file, which contains values of the currents and the voltages of the examined circuit [12].

[1]Dimiter I. Vakovsky is with the Faculty of Applet Mathematics and Informatics, Kliment Ohridski 8, 1000 Sofia, Bulgaria, E-mail: vakovsky@tu-sofia.bg

[2]Nikolaj Hinov and Nikola Gradinarov are with the Faculty of Electronic Engineering, Kliment Ohridski 8, 1000 Sofia, Bulgaria, E-mail: hinov@tu-sofia.bg

C. Mathematical model

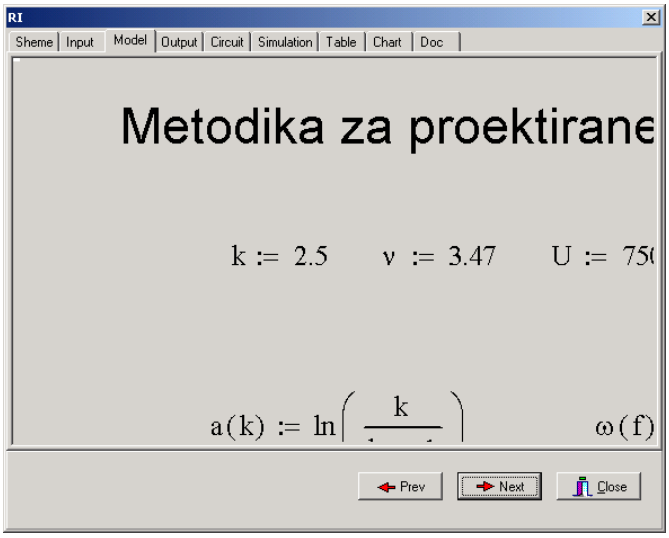

Fig. 3. Mathematical model

Fig. 3 shows the mathematical model of the designed device. In the presented paper mathematical models realized in the MathCAD environment are used [6, 8]. Depending on the needs of the engineer and the type of the modeled device, it could be chose a mathematical model, which has the corresponding features [7, 2, 10, 3, 9].

D. Simulation model

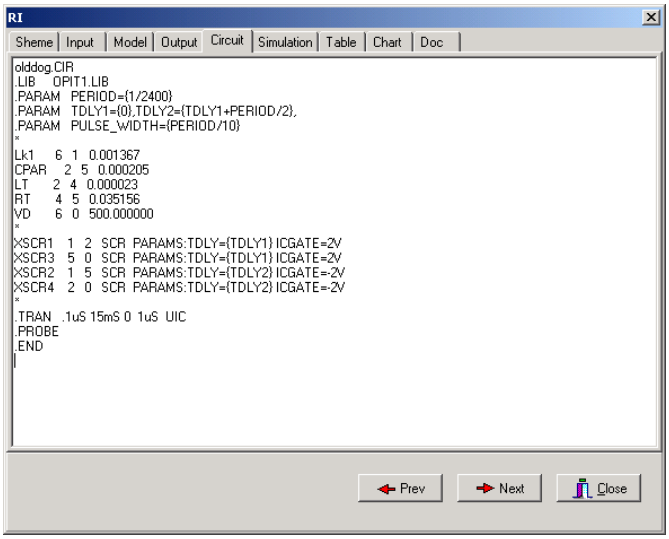

Fig. 4. Simulation (CIR) file

Fig. 4 presents the simulation model of the device. It is obtained, basing on the chosen circuit and the values of the components derived from the mathematical model.

E. Simulation

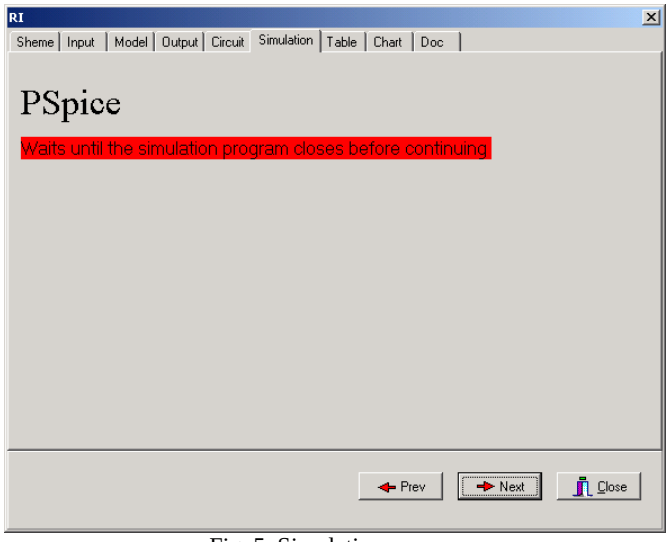

Fig. 5. Simulation process

Fig. 5 presents the user screen, which is shown through the simulation process and it shows to the user, that certain time is necessary to conclude.

F. Table result

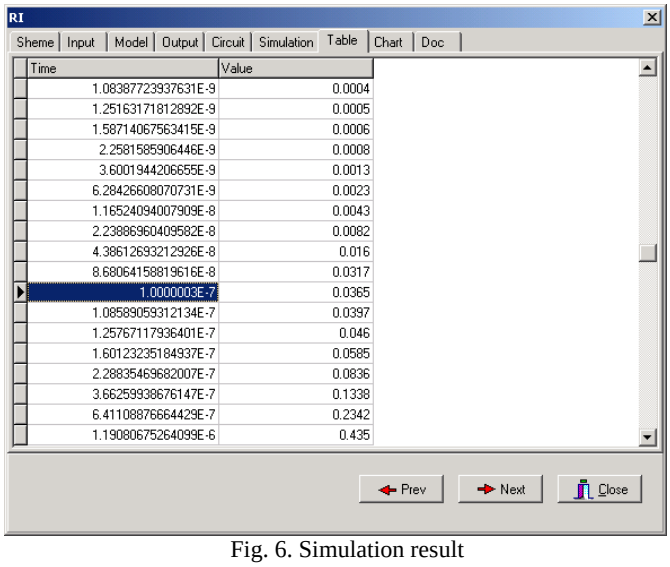

Fig. 6. Simulation result

Fig. 6 presents the simulation result in graphical way. In the first column is the time progress, and in the second there are the values of the input current.

III. EXAMPLE

G.Graphical result

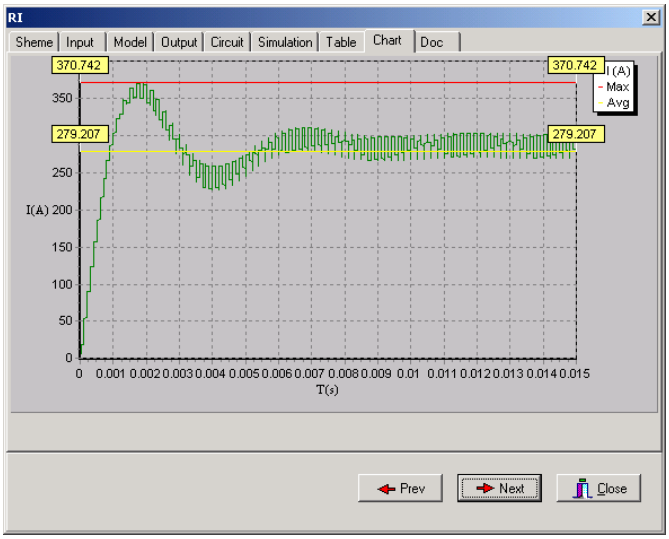

Fig. 7. Simulation result

Fig. 7 presents the simulation result for the moment values of the input current. The graph shows also the average and the maximum value of this current [8, 1].

H. Project documentation

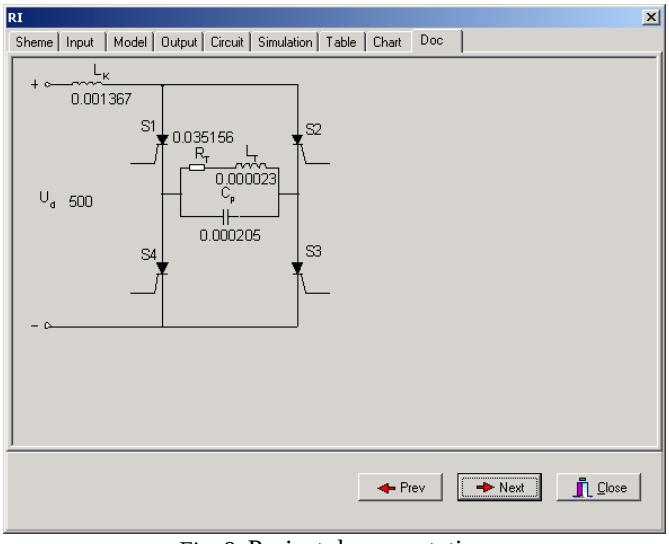

Fig. 8. Project documentation

Fig. 8 shows the last stage of the designing sequence – creating the project documentation.

I. Input Data

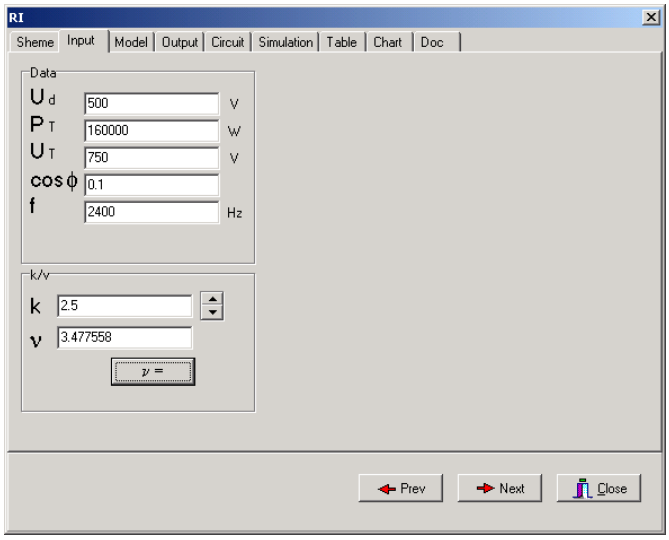

Fig. 9. Input data

Fig. 9 presents user dialog for the input data, which is necessary for the design.

J. Output data

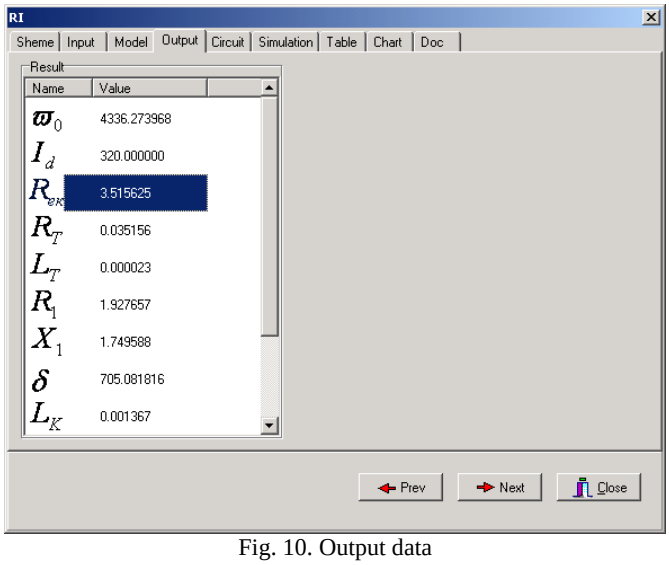

Fig. 10. Output data

Fig. 10 presents the result from the mathematical modeling, showing the values of the components of the chosen circuit and some other parameters of the designed device.

IV. CONCLUSION

In the presented automated system are embedded the phases for designing the power electronic devices, which are related to: choice of power circuit, electrical design, computer simulations of the operation of the examined circuit, comparison between the results of the simulation and the design and creating the project documentation.

The developed system allows designing of autonomous inverters at various input data and choice of optimum decision depending on the particular requirements. It also allows the learners to control the results after performing the tasks of designing the different types power electronic devices, which are applicable at the electrotechnologies.

REFERENCES

[1] Karov R. D., G. V. Dicheva, "Methods for design of parallel-serial current source inverter", Proceedings at national conference with international participation "ELECTRONIKA '2004", Sofia, 2004, p.p. 322-327.

[2] Karov R. D., "Theoretical generalization, dual correlation and schematic improvements of power inverter circuits and sections", Dissertation for Doctor of Sciences, Sofia, 2004.

[3] Ventzislav Valtchev, Alex Van den Bossche, Jan Melkebeek, Dimitre Yudov, 'Design Considerations and Loss Analysis of Zero Voltage Switching Boost Converter', IEE Proceedings – Electric Power Applications, Vol.148. No 1, January 2001, pp. 29-33. ISSN 1350-2352

[4] Hinov N. L., N. P. Gradinarov, "Analysis of an autonomy resonant inverters with forsed commutation", Proceedings of the sixth international scientific and applied science conference "ELECTRONICS '97" 24-27 September 1997., Sozopol, Bulgaria, pp.61-67.

[5] Hinov N. L., M. L. Bobcheva, N. P. Gradinarov, "A procedure for the design of series-parallel current-source inverter", Magazine ELEKTROTECHNICA & ELECTRONICA, vol.3-4, 2000, pp.15-19.

[6] Gradinarov N. P., "Research elaboration and development of resonant inverters with technical application" Doctorate Thesis. Technical University –Sofia, 2002.

[7] Todorov T. S., Madjarov N. D., Alexiev D., Ivanov P., "Autonomous inverters", Gabrovo, 1996.

[8] Gradinarov N.P., N.L. Hinov, D.D. Arnaudov, " Determination of value of commutating inductors for current-source inverter", Proceedings of the ninth international scientific and applied science conference "ELECTRONICS'2002" 20-23 September 2002, Sozopol, Bulgaria, pp.154-158.

[9] Arnaudov D. D., "Semiconductor converters of electrical energy with limiting voltage on the commutating devices", PhD Thesis, Technical University –Sofia, 2003.

[10] Arnaudov D. D., "Design of resonant converters with limiting voltage on the commutating capacitors", Proceedings of the National conference with international participation "ELECTRONICA'2002" 17-18 October 2002, Sofia, Bulgaria, pp.61-70.

[11] www.mathsoft.com

[12] www.orcad.com

Short Cycle Inverter

Hristo P. Hinov[1], Hristo Z. Karailiev[2], Valentina V. Rankovska[3]

Abstract - **The paper determines the dependence between inverter frequency and cycle. It formulates the stationary mode based on the symmetry at the bridge circuit. The phase model has been built and the inverter characteristics, recuperation and control have been proved. A relation has been formulated between the inverter mode and energy. A map has been drawn out, covering the mode and power of all short cycle inverters. The following conclusions have been drawn: The stationary mode in the case of bridge inverters can be formulated as an effect of functional symmetry; The transistor is only activated after the current in the diode on the same bridge arm has been reduced to zero; The diode is switched on when the transistor on the adjacent arm of the bridge is deactivated (switched off); The inverter is only controlled by the trailing edges of the gate pulses; The diodes of short cycle inverters perform a typical recuperative process; Soft commutation is practically impossible; The inverter power depends only on the voltage of the start commutation point.**

Keywords - **Inverter, Phase model.**

I. INTRODUCTION

The series inverter /SI/ is a source of high-frequency energy and a fundamental object of research in power electronics [1]. The inverter forms its operation cycle within the timer half-period $T_t/2$.The object of the present article is the SI which generates frequency higher than its own, as a result of which it develops a shortened operation cycle.

The aim is to formulate the stationary mode, which, in addition to voltages and currents, should cover the inverter power.

The phase analysis method is used for this purpose, and its basic postulates are applied to the SI [2]. The applications there refer to inverters which operate at a frequency lower than their own and develop a lengthened operation cycle ($\theta_S = \pi + \alpha$).

The present article is an expansion of [2] into a mode area, where the object has different properties.

A series bridge inverter with reverse diodes /SI/ is shown in Fig. 1. Normally the switches are transistors controlled by a timer, which determines the generated frequency. The timer closes the switches along one of the bridge diagonals and opens the switches along the other diagonal at intervals $T_t/2$ – half-periods that determine the generated frequency. This causes a periodical change in the direction of source E relative to the resonant CLR circuit and free oscillations, which are the object of the present article.

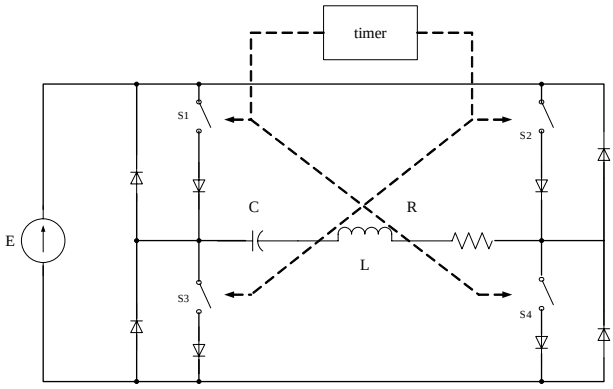

Fig.1. Series inverter circuit

II. EQUATION AND PARAMETERS

The differential equation of the inverter is:

$$L(dI/dt) + RI + (1/C)\int Idt = E$$

The roots of the characteristic equation determine:

- Natural frequency: $\omega = [(LC)^{-1} - (R/2L)2]0.5$
- Attenuation: $\varepsilon = (R/2L)/\omega = 1/2Q$

A priority of the method applied is the replacement of the current time by a current angle called "phase": $\theta = \omega t$.

Just like the clock represents time by means of an angle (thirty degrees mean an hour), in the same way the phase angle represents the current time in the inverter.

The phase is a limited argument: $0 \le \theta \le \theta_S$. The maximum phase, called cycle: $\theta_S = \pi (T_t/T_0)$, is proportional to the timer period T_t, relative to the own period $T_0=2\pi/\omega$. The cycle θ_S is the angular path traveled by the "inverter clock hand" over the timer interval $T_t/2$ or $\theta_S < \pi$, ($\theta_S = \pi - \alpha$).

The four circuit parameters (C, L, R and period T_t) have been reduced to just the two dimensionless quantities – attenuation ε and cycle θ_S. These are the degrees of freedom or inverter coordinates. They are combined in a single complex parameter:

$$p = (-\varepsilon + j)\,\theta_S \qquad (1)$$

The solutions to the differential equation are represented in dimensionless quantities:

- Capacitor voltage:

$$u(\theta) = -1 + u_S \exp(-\varepsilon\theta)\cos\theta$$

where: $u = U/E$, u_S arbitrary start voltage.

- Current across inductance:

$$i(\theta) = i_S \exp(-\varepsilon\theta)\sin\theta$$

where: $i = I(L/C)^{0.5}/E$, i_S arbitrary start current.

The two mode quantities are represented together by a single complex quantity, the real part of which is the voltage, and the imaginary one is the current [3].

[1] Hristo P. Hinov is with the Technical University of Gabrovo, Republic str.1, 5300 Gabrovo, Bulgaria. E-mail: hino@abv.bg
[2] Hristo Z Karailiev is with the Technical University of Gabrovo, Hadzi Dimitar str.4, 5300 Gabrovo, Bulgaria, E-mail: hkarailiev@gmail.com
[3] Valentina V. Rankovska is with the Technical University of Gabrovo, Hadzi Dimitar str.4, 5300 Gabrovo, Bulgaria E-mail: rankovska@tugab.bg

$$F(\theta) = - 1 + (1+ S_n) \exp((-\varepsilon+j)\ \theta) \qquad (2)$$

The start significations u_S and i_S correspond to a zero phase $\theta = 0$ and refer to a random number (n) of the half-period $F(0) = S_n$. The start complex point is

$$S_n = (u_S + j\ i_S)$$

Both the combination of voltage and current, and their equivalent complex form Eq. (2) define the phase vector /PV/. It reduces its module when the phase θ increases and tends to reach the "stable" point $u(\infty) = -1$, $i(\infty) = 0$.

When in the complex plane, the PV rotates and, although its hand gets shorter, it represents the "inverter clock". The peak of the PV describes a spiral, which starts from the starts point S_n and tends to the stable point (-1,j0).

The spiral segment in inverters has a cycle of about 180^0, $\theta_S = \pi \pm \alpha$, which, substituted in Eq. (2) determines the final point of the half-period:

$$F(\theta_S) = - 1 + (1+ S_n) \exp(p) \qquad (3)$$

When in the final point Eq. (3), the timer activates the inverse switches of the bridge and causes the so-called commutation in the inverter. The commutation causes a change in the direction of the source, which can be expressed by a change in the signs of Eq. (3), therefore the next half-period starts from the point:

$$S_{n+1} = 1 - (1+ S_n) \exp(p) \qquad (4)$$

III. Stationary Mode

In the stationary mode each of the following half-period reproduces the preceding one, which only requires the reproduction of the start point:

$$S_{n+1} = S_n = S$$

The reproduction principle applied in Eq. (4) determines the start commutation point describing the inverter stationary mode:

$$S = (1-\exp(p))/(1+\exp(p)) \qquad (5)$$

The point and the mode depend only on the two inverter coordinates, attenuation ε and phase θ_S. The start point can also be represented in a hyperbolic form:

$$S = \text{th}\ (-p/2) \qquad (6)$$

The interpretation of the general dependences under the condition of a short cycle $\theta_S = \pi - \alpha$ specifies (1):

$$p = -\exp(-\varepsilon(\pi - \alpha)) \exp(-j\ \alpha) \qquad (1.1)$$

The substitution of Eq. (1.1) in Eq. (5) or Eq. (6) determines the position of S, similar to p, in the fourth quadrant, in the case of negative voltage and negative current.

The start of the phase trajectory is related to the commutation in the inverter or the replacement of the bridge arms. The above-mentioned negative current before the start commutation point can only be the current of the inverse transistor, and immediately after the commutation the negative current can only be transferred into the reverse diode. Hence the commutation in a short cycle inverter is connected to the deactivation (switching off) of the transistor and the transfer of current in the diode of the bridge adjacent arm. The commutation is an effect of the trailing edge of the gate pulse.

The relationships proved above form a complete mathematical model of the inverter stationary mode.

IV. Phase Model

The geometric interpretation of the mathematical dependences is the phase model /PM/, which visualizes the dynamics and the relationships in the inverter.

The phase trajectory /PT/ of odd-numbered half-periods is described by the vector Eq. (2), which is centered on the abscissa in point -1. The vector starts in point S and, rotating counter-clockwise, completes the upper spiral segment in point –S.

The PT or the spiral of even-numbered half-periods is an inverse repetition of the preceding one: $F(\theta_S+\theta) = - F(\theta)$. The spiral of even-numbered half-periods intersects the first closed curve, broken in commutation, in points S and –S .

The commutation is reflected by the PM as a change in the vector center.

Fig. 2 presents an example referring to inverters with Q-factor = 2.5 and cycle $\theta_S = 2.5$ (143^0), which corresponds to frequency relation $T_t/T_0 = 0.8$.

The ordinate of the rotating vector represents the current and its function can be traced from the right-hand intersection point with the abscissa. The transistor current there is zero and increases in the first quadrant. After its maximum $i_m = 2.15$, with phase $\theta_{im} = 80^0$, the current is completed in point – S with coordinates: voltage $u_S = -1.65$ and current $i_S = 1.85$. The transistorized segment has a duration of $\theta_t = 110^0$. The transistor is switched off in commutation point – S and the current is taken over by the diode in the bridge inverse wing.

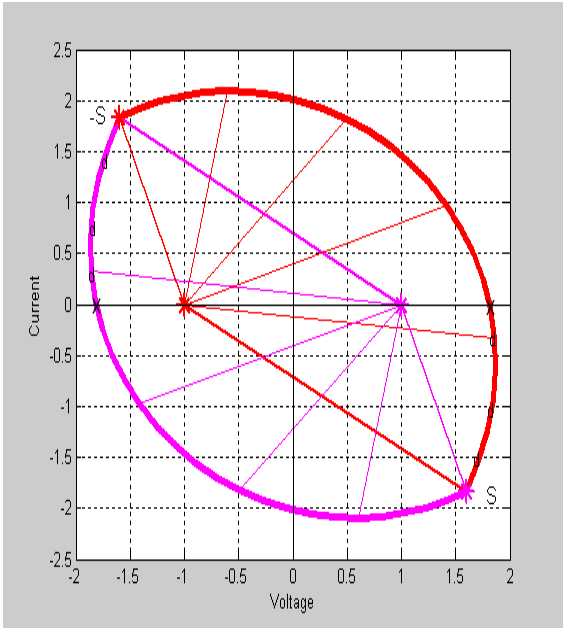

Fig.2. Phase model

The diode segment is positioned in the second quadrant and continues $\theta_d = 33^0$ ($\theta_S = \theta_t + \theta_d$). The diode segment θ_d is determined relative to the inverse center +1.

The inverse diode is switched off when the current is reduced to zero.

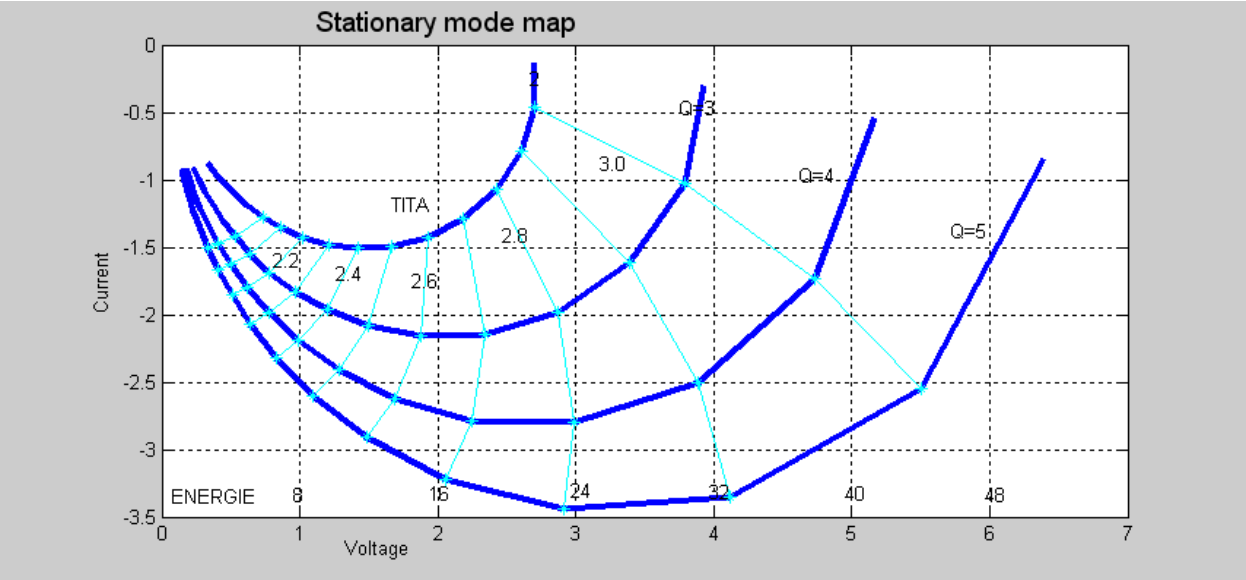

Fig.3 Stationary mode map

The diode segment reduces the current to zero, with a steep drop to the abscissa, accompanied by an insignificant rise in voltage. It can be concluded that the inverse diode performs recuperation, transferring the reactor energy mainly to the source, a process typical for the object.

The connection to the inverse transistor is performed when the current is zero and the development of the odd-numbered half-period repeats the processes described above.

This connection does not change the conductivity of the bridge arm; like in the case of a regular conductor the current has changed its direction.

The soft commutation of the transistor requires the leading edge of its gate pulse to be passed in advance to an arbitrary point in the previous diode interval. The exact choice of the moment of the gate leading edge is insignificant, because the voltage is zero and the transistor has to wait until the moment the diode is switched off. This gives ground for the following conclusions:

- The transistor is only activated after the current in the diode on the same bridge arm is reduced to zero.
- The diode is switched on when a transistor on the bridge adjacent arm is deactivated (switched off).
- Short cycle inverters are only controlled by the trailing edges of the gate pulses.
- The gate pulses must have greater duration than that of the transistor current.

The duration of the gate pulses is limited between the transistor interval and the cycle: $\theta_t < \theta_g < \theta_S$. Although the gate pulse can last as long as cycle θ_S, the stationary mode automatically shortens the transistor interval to θ_t, at the expense of the recuperation diode interval θ_d.

The rhomboid with vertexes in the start commutation points S, –S and in the centers (1,0), (-1,0), has the angles of the inverter cycle $\theta_S = \pi - \alpha$. More precisely, θ_S is the angle at the centers, while α is the angle at S. As the cycle θ_S increases, its complainer α decreases and the rhomboid tends to a position on the abscissa. This process is described in the following parts of the article.

V. Stationary Mode Map

The start point S on the spiral identifies the entire stationary mode. In addition to its function for constructing the PM, it illustrates the inverter power. S is the radius of circles, which are used to determine the maximum voltage, maximum current, and a number of other parameters.

The set formed by all start points is the mode map, which illustrates the properties of all inverters of this type – Fig. 3.

Inverters in power electronics have the typical significations: $2 \leq Q \leq 5$ (Q-factor = $(L/C)^{0.5}/R$) and cycle $1.5 \leq \theta_S \leq 3.1$, which, when applied to Eq. (5) or Eq. (6) determine the start point S.

The mode map is a net of two arc families. The lengthened arcs have a fixed Q-factor and are the frequency characteristics of the inverter. The approximation of cycle θ_S to π ($\alpha > 0$) increases the power in the second abscissa scale. It is essential to maintain the distance to this limit $\theta_S \neq \pi$ ($T_t < T_0$), otherwise there is a risk of short circuit across the transistors.The vertical arcs have a fixed cycle θ_S. These arcs are the inverter load characteristics, since the varying Q represents the changes in the load.

The mode amplitude is typical for both the great values of Q, and the great values of θ_S, where the timer frequency approaches the inverter natural frequency. The map can be used for design and optimization of the series inverter, as well as for other applications.

VI. Energy and Power

Power is a priority in power electronics, since the efficiency and productivity of various devices is based on it. Conventional methods reach the power required by means of time-consuming procedures connected with working out equations, solutions, stylization of the solutions, such as average or quadratic mean current, etc. These procedures are

additionally complicated with inverters due to their discrete-switch principle of operation.

For direct determination of the inverter power we use the quadratic relationship between mode levels and energy levels in the PM – Fig. 2. If the capacitor of an arbitrary inverter is charged up to the source voltage E, then its energy is:

$$Ma = 0.5CE^2 \quad [J] \qquad (7)$$

Then the abscissa unit - (1,0) in Fig.2, will present simultaneously the voltage E of the capacitor and the energy portion Eq. (7) in it.

The same is proved for the ordinate unit (0,1) of the PM, which presents the base portion of energy Eq. (7) simultaneously with the current.

The base portion of energy Eq. (7) is the energy scale of the inverter.

In addition to the mode significance (voltage and current) of its coordinates (u, i), any point of the PM, also presents the sum of their coordinates energies.

$$A = (u^2+i^2)*Ma \quad [J] \qquad (8)$$

The mode quadratures between the parentheses in Eq. (8) are the quadratures of the radius vector, which summarizes the remarkable relation between the mode and the energy:

Any vector in the PM represents energy that is proportional to its module quadratures.

The energy which is realized in resistance R of the inverter is illustrated by the difference between the modules of the start vector and the final vector. These vectors intersect in start point S – Fig.2. They are the equal sides of an isosceles triangle, the base of which is is the abscissa segment between spiral centers –1 and +1.

The quadratures of the difference in the sides is easy to determine using the coordinates of the start point S (u_S, i_S):

$$\mathbf{a}/2 = [(u_S+1)^2 + i_S^2] - [(u_S-1)^2 + i_S^2]$$

The equality shows the energy realized for a half-period. Although it presents a quadratures, its relatively simple transformation eliminates the coordinate quadratures. The energy for a full period is:

$$a = 8\ uS \qquad (9)$$

The active energy in the inverter depends only on the start point voltage. This allows the mode map in Fig. 3 to be supplemented with a second abscissa scale, along which the active energy can be reported directly.

The inverter power is the product of the multiplication of Eq. (9) by the scale Eq. (7) and by the frequency - $f = 1/T_t$:

$$P = f\ \mathbf{a}\ Ma \quad [W] \qquad (10)$$

VII. CONCLUSIONS

The stationary mode in bridge inverters can be formulated as an effect of the functional symmetry.

The transistor is only activated after the current in the diode on the same bridge arm is reduced to zero.

The diode is switched on when a transistor on the bridge adjacent arm is deactivated (switched off).

The inverter is only controlled by the trailing edges of the gate pulses.

The diodes perform a recuperative process.

Soft commutation is practically impossible.

The inverter power depends only on the voltage at the start point.

REFERENCES

[1] M. H. Rashid, “Power Electronics, Circuits, Devices and Applications”, Pearson Prentice-Hall International, Chapter 8, Inc., 2004.

[2] H. P. Hinov, “Analysis of a Series Inverter”, (forthcoming)

[3] H. P. Hinov, V. V. Rankovska, “Analysis of an Asymmetric Inverter in Phase Space”, *ICEST* 2004, *Conference Proceeding*, pp. 403-406, Bitola, Macedonia, 2004.

Session SP:

SIGNAL PROCESSING

Method and Example of Errors Evaluation During the Conversion of a Band Wide Signal

Petre Tzv. Petrov[1]

Abstract - **There is a possible solution of the classical problem for calculating the sampling frequency Fd when sampling analog signal with several components (a band wide signal). The example has five frequency components. For each frequency component Fs a sampling factor N=Fd/Fs and an amplitude error Emax is calculated.**

Keywords - **sampling frequency, errors, band wide signal**

I. INTRODUCTION

Sampling a band wade signal (BWS) is a common task in the signal processing electronic equipment. During this process a lot of parameters should be evaluated in order to have knowledge about the differences between the analog signal (AS) or the "analog original" and its digital representation (the "digital copy" or the approximation of the AS). Normally, as a result of this evaluation the following parameters should be calculated:

- Signal sampling factor (SSF) N=Fd/Fs where Fd is the sampling frequency and Fs is the maximal frequency of interest in the BWS. The SSF was discussed in [1,2]. Most frequently (but not always) the SSF N is greater or equal to 2 (N>=2).
- Calculating the minimum number of the converters bits (MNCB) n in order to neglect the converters error.
- Calculating the differences (e.g. amplitude errors, peak to peak amplitude errors, etc) between the AS and its digital approximation .

The purpose of this paper is to apply the method developed by the author in [1, 2, 3] and to give an example of amplitude errors evaluation during the sampling of a band wide signal (BWS) (AS build by several sinusoidal and cosinusoidal (SS and CS) components.

II. THE TASK

Definition: The simplest BWS which contains two line in its spectrum (one of them is the Direct Current (DC) component with amplitude B and the other is a SS with frequency Fs, amplitude Am and phase B), has four basic parameters (Am, Fs, φ, B) and could be defined with Eq. 1

$$A=Am*\sin(2*\pi*Fs+\varphi)+B \quad (1)$$

Assuming B=0 and φ=0 in (1) simplifies the Eq. (1) of AS but does not reduce the number of the parameter to reconstruct to two. It is just giving the value of zero to two of them. Consequently in order to reconstruct this AS in a simple way we are in need of sampling factor N>=4 [1, 3] or one sample per parameter to reconstruct.

It was proven in [3] that the maximum amplitude error Emax during sampling the SS A=Am*sin(2*π*Fs) is calculated with Eq. 2

$$Emax= (1- \sin(90- (180/N)) \quad (2)$$

where N=Fd/Fs is the SSF (in this case N>=2) and the number of the converter bits n should be infinity (n→∞).

In this paper we will examine an example of sampling a BWS with five spectrum components with different amplitudes. The signal is defined by Table 1. The phase relations are defined in one particular moment and could vary in time due to instability of the parameters of the sources and the circuits. The components of the AS could exists in any combinations (some or all of the components could disappear temporarily).

The task consist of calculating the SSF N, the sampling frequency Fd and the number of the converters bits n in order to satisfy the following conditions:

- Maximal amplitude error Eamax (assuming Eamax equal to resolution of the converter in amplitude) for every frequency component should be less than +-5%;
- Maximal amplitude error Eamax should be distributed between the amplitude error EN from the SSF N and error Eadc from the limited number of the converters bits n.
- We will chose an appropriate analog to digital converter (ADC) with the calculated number of bits n and conversion time Tc.

III. THE SOLUTION

The problem will be solved in several steps (common for most of the similar applications).

Step 1: Evaluation of the maximal signal amplitude Asmax and calculating the full scale voltage Vfs of the converter.

Since the phase of each of the signal components is unknown and could be variable the evaluation of the maximal signal amplitude (Asmax) and the maximal signal peak-to-peak amplitude (Asppmax) could be made accordingly to the worst case scenario principle "The maximal signal amplitude could be as high as the sum of the amplitudes of its components". In this case the sum of the amplitude of all

[1] Petre Tzvetanov Petrov is with "Microengineering"-Sofia, Bulgaria and expert-lecturer with OFPPT-Casablanca, Morocco. E-mails: ppetre@caramail.com and ptzvp@yahoo.fr.

components is Asmax<= 4.9V and Asppmax=2*Asmax<= 9.8V.

The full scale (FS) voltage of the converters Vfs should be higher or equal to Appmax. We are chousing Vfs approximately 10V because this is one of the industry standard voltage ranges. Also we could select and industry standard voltage reference source withVref=10.240V.

Vref, Vfs, the minimal (Vinmin) and maximal (Vinmax) input voltage of the converter should be appropriately selected in order not to have underflow or overflow of the input range. It is desirable that the maximum of the input signal to use at least the half of the input range of the ADC (to be higher that Vfs/2 and to activate all of the ADC bits. For this purpose the maximum amplitude and peak to peak amplitude of the AS should de exaluated. This could be done in a theoretical or in practical way or in both way. The minimal value of AS should be at least 10*LSB (LSB= Least Significant Bit) in order to maintain at least 10% relative accuracy. The "underflow" and the "overflow" should be avoided because there will be irreversible lost of information. In most of the cases selecting and industry standard input range is making easier the practical implementation.

In this example the sum of the amplitude of frequency components Amax is

Amax = A1+A2+A3+A4+A5=4.9V

We could admit that the maximal amplitude of the AS is not higher than 4.9V and the maximal peak-to-peak amplitude of the signal is not greater than 2*4.9V=9.8V. Vfs and the Vref of the ADC could be chosen at industry standard 10.240V. With Vref=10.240V, the minimal output voltage will be 0.0V and the maximal will depend of the number of the converter bits and should be higher than 9.8V calculated above or Vfs>9.8V. From the other side normally we are having Vfs =Vref-1*Vlsb, where Vlsb is the voltage step for one LSB.

TABLE I
AN EXAMPLE OF BAND WIDE SIGNAL WITH FIVE COMPONENTS

Input test signal				
# (I)	Compo-nent	Am= App/2	App	Fsi
1	DC	2.5V*	5V	0Hz*
2	SS	0.6V	1.2V	2.5Hz
3	CS	0.8V	1.6V	22Hz
4	SS	0.3V	0.6V	150Hz
5	CS	0.7V	1.4V	460Hz
Obtained results after the sampling (n=10 bit)				
# (I)	+-5%*Am	Number of LSB	Ni = Fd/Fs	Emax, [%]
1	+-125mV	+-12.5	∞	0.0
2	+-30mV	+-3	1840	0.000146
3	+-40mV	+-4	209.1	0.0113
4	+-15mV	+-1.5	30.7	0.523
5	+-35mV	+-3.5	10	4.83

Notes: (*) – conditional value; (#) the index is changing from 1 to 5 because the signal has five frequency components; SS/CS – sinusoidal/cosinusoidal signal; The results are for Fd=4600Hz, n=10 bit, LSB=10mV and Eadc=+-0.0488%.

Step 2:. Calculating the number of the converters bits

We have to estimate the effective resolution for each signal component and especially the case with the component with the smallest amplitude (component #4 in this case). The resolution for the component #4 or Resmin4 should be less than +-15mV (+-5% from 0.3V) or

Rezmin4=+-5%*Am4=+-3%*0.3V=+-15mV<=+-0.5*LSB

Now we could calculate the maximal value of one LSB.

If +-0.5*LSB<=+-15mV, then 1*LSB<=30mV

It is possible to calculate the minimal number of the equally spaced step in the transition characteristic of he converter Lvmin in order to have Rezmin4 equal to one level

Lvmin = Vfs/Rezmin4=10V/30mV=333.3 levels.

The minimal number of the ADC bits is

nmin=lg(Lvmin)=lg(333.3)= 8.38 bits

We could choose a 9-bit converter. But a good idea is to use a converter with from 1 to 4 bits more that the calculated value due to the additional sources of errors. With n=10 bits the levels are

Lv(n)=Lv(10)=2*exp(10)=1024 levels

This is satisfying our solution because

Lv(10)=1024 levels >Lvmin=333.3 levels

In case of 10-bit converter one LSB will correspond to 10mV because

Vlsb=Vref/2exp(n) = 10240mV/1024=10mV<30mV

The maximal input voltage for the ADC is

Vfs=Vref-1*LSB=10240mV-10mV=10230mV

The resolution of the ADC is

Res(n)=Res(10)=+-0.5*Vlsb=+-10mV/2=+-5mV

And correspond to the task because

Rezmin4<=+-15mV.

The error of the ideal 10-bit ADC Eadc is

Eadc(10)=(+-1/2)*Vlsb=+-(1/2)*100%/2exp(n)=

= +-(1/2)*100%/2exp(10)= +-0.0488%

It is important to note two results:

- Usually, the sampling error (SE) of the components with highest frequency depends mainly from the SSF N.
- Usually, the SE of the components with the lowest frequencies depends mainly on the number of the converters bits n.

As we could see from the Table I that for the components 1, 2 and 3 the error EN is less than Eadc, and for the components 4 and 5 EN is greater than Eadc.

Step 3: Calculating N=Fd/Fs and Fd

Accordingly to the theorem of Kotelnikov-Shannon-Whitaker the sampling frequency Fd should be chosen according to the Eq. 3

$$Fd=2*Fsmax= 2*Fs5=2*460Hz=920Hz \quad (3)$$

Here will apply a the approach discussed in [1, 2, 3]. We will calculate the SSF N=Fd/Fs for each frequency component. A special attention should be paid to the component with the highest frequency because it will be with the smallest SSF and with the highest possible amplitude error. In this example the component #5 with amplitude Am5=0.7V and with frequency

Fs5=460Hz has the maximal signal frequency. The amplitude resolution for this component is +-35mV or +-5%*Am.

The amplitude error of +-5% should be distributed between: 1/ The amplitude error AN5 due to the finite SSF N5=Fd/Fs5; 2/ The error of the converter Eadc (In the ideal case Eadc is the same for all frequency components).

We could apply the model of the maximal or root-mean-square (rms) error or any other appropriate model. The second is given with the formulae:

Ea5rms= sqr(EN5rms*EN5rms+Eadcrms*Eadcrms),

Where Ea5rms is the rms error for the component #5,

Eadcrms is the rms error for an ideal 10-bit ADC.

If we apply the model for the maximal error for he component #5 we will obtain.

EN5max=EN - Eadc=5%-0.0488%=4.95%.

Usually for he highest frequency component the difference between EN5rms and EN5max is small. Also, for the highest frequency components Eadc is smaller that EN. (The error of the finite number of bits n is lower then the amplitude error from the possible not sampling the SS/CS in its maximum which depend on the SSF N=Fd/Fs)

We are calculating the SSF for the component #5:

N5=180/(90-arcsin(1-EN5max))=

=180/(90-arcsin(1-0.0495))=9.94

We are accepting N5=10 and the sampling frequency Fd is

Fd=N5*Fs5=10*460Hz=4600Hz

The sampling period Td is

Td=1/Fd=1/4600Hz=217.39us

Now with sampling frequency Fd=4.6kHz we have the guarantee that with 10-bit ADC all components of the AS will be converted (transferred into digital codes) with amplitude error less than required Eamax=+-5%.

The Eq. 2 could be used in order to calculate the maximal possible amplitude error for each component for Fd=4600Hz. The results are given in Table 1 (EN1max=0.0, EN2max=0.000146%, EN3max=0.0113%, EN4max=0.523%, EN5max=4.83%).

It should be noted that the following equation n=lg(1/Emax), [bit] could be considered *as the quantity of information in amplitude* transferred from the AS to its digital "copy" (if Emax is considered equal to one step of the transfer characteristic of the conveter).

IV. SELECTING AN APPROPRIATE ADC

There are a lot of ADC with accuracy of 10 or more bits, with serial or parallel output interface and with conversion time Tc less than 200 us which are suitable candidates for that task. The solution will be tested on a 8-bit 6809 microprocessor and the ADCs with parallel interface were selected:

- 10-bits ADCs: AD571K (Tc=25us), AD573K (Tc<20us) and AD579 (Tc<1.8us).
- 12-bits ADCs: AD572 (Tc<25us), AD574AK(Tc<35us), AD674A(Tc=15us) and ADADC80 (Tc=25us).

Also, there are several micro-controllers with 10-bit internal ADC which could be used as an intelligent peripheral ADC to the testing system (e.g. PIC 18F876, 68HC12 etc.). The internal source of errors and code distribution of ADC should be evaluated before taking the final decision.

If we are using the 10-bit ADC with parallel outputs AD574AK (Tc<35us, LSB=10mV) without S/H we could sample AS with peak to peak amplitude App=10Vpp and frequency Fsmax(adc), calculated with the formula:

Fsmax(adc) = 0.5*LSB/(π*App*Tadc)=

=5mV/(π*35us*10Vpp)=4.5Hz.

If we choose ADC AD574AK together with SH AD585 we could sample AS with peak to peak amplitude up to 10Vpp and frequency up to 10 kHz. In most of the cases the AS at the ADC input should not change more than +-0.5*LSB (sometimes even less than that value) for the time of one conversion (in this case Tcmax=35us). From the practical point of view the ADC with internal SH are interesting, e.g.:

- 10-bit ADC AD7579/AD7580 with up to 50000 conversions/sec and "band wide" up to 25KHz;
- 12-bit AD678 with up to 200000 conversion/sec and "band wide" up to 500 KHz

We will chose the model AD571K (Tc=25us, n=10) because the its parameters are satisfying and the price is acceptable.

V. SELECTING A SAMPLE AND HOLD CIRCUIT

We should select an appropriate SH circuit in order to sample and hold the AS during the conversion time of the ADC. During the selection process the following should be taken into the consideration:

- The aperture time Tap(sh) of the SH should be low enough for the selected ADC (n=10 bits in this case), maximal signal frequency (Fsmax=460Hz) and sampling frequency Fd= 4.6KHz (Td=217.4us);
- The "sample time" Ts should be much lower than Td in order not increase the conversion time Tc of the ADC. For example with Td=217.4us we should select Ts<10 us in order to have accuracy less than +-0.5*LSB=+-0.0488%.

We will use SH model SHC298AM of Burr-Brown. It has 12-bit accuracy, band wide for large signal (+-10V) up to 16 kHz (with hold capacitor Ch=10nF), SR of the output voltage typically 2V/us, maximal aperture time Tapmax= 200ns and sample time with accuracy of 0.01% when the input voltage is changed with step 10V less than 10us. In order not to increase the conversion error of the ADC the signal of the SH input should not change during the conversion more than the value Ea(S/H) calculated below

Ea(S/H) <=+-0.5*LSB=+-0.0488%=+-5mV

The maximal frequency of the SS with peak to peak amplitude App=Vfs=10.230V, which could be processed with SH with aperture time error less than +-0.5*LSB is

Fsmax(S/H)=Ea(S/H)/π*Tapmax*App=

=5mV/(3.14*200ns*10.23V)=779Hz>460Hz

The frequency calculated above is higher than the maximal frequency component (Fs5=Fmax=460Hz) and consequently the choice of the SH is appropriate.

If the peak to peak amplitude is App=10V and the resolution of ADC is Eadc=+-5mV and the maximal signal

frequency is Fsmax=460Hz we could calculate the maximal allowed aperture time Tapmax for SH

$$Tapmax = Eadc/(\pi*App*Fsmax) = 5mV/(\pi*460Hz*10.23V) = 338ns.$$

The sample and hold factor (SHF) Nsh is defined with the Eq. 4 in [1]:

$$Nsh = Tapadc/Tapsh \quad (4)$$

Where Tapadc is the aperture time of the ADC (or the conversion time of the ADC) and Tapsh is the aperture time of SH. In fact the aperture time of SH (Tapsh) is replacing the aperture time of ADC (Tapadc).

In fact SH is useful only if Tapsh<<Tapadc. This is the reason of introducing the parameter "sample and hold factor" (SHF) given with the Eq. (4) which is measuring the effectiveness of the addition of the SH in front of ADC. Normally SHF Nsh>>1 and is guaranteeing then the band with of the ADC will be enlarged with the addition of SH and not reduced. More information about the ADC and SH could be found in [4, 5].

VI. The importance of the relative accuracy and the amplitude error

When the amplitude of the AS to be sampled is changing the number of bits activated is changing also. Lets us compare the cases of two samples from two different signals sampled with 10-bit ADC with codes from 0 to 1023:
Case 1: The samples are in the range from 0 to 10*LSB.
Case 2: The samples are in the range from 0 to 600*LSB.
In both cases the absolute rounding error is +-0.5*LSB or +-0.0488% (for n=10bit) from the full scale (FS). The relative rounding error is quite different in both cases. In the first case the relative error E1 is

$$E1 = 100\%*(+-0.5*LSB/10*LSB) = +-5\%$$

In the second case the relative error E2 is

$$E2 = 100\%*(+-0.5*LSB/600*LSB) = +-0.083\%$$

If the samples are processed digitally (for example in the same filter section) the results from the processing the second signal will be much more accurate.

In conclusion there is a need of formula guaranteeing the maximal amplitude error (the maximal difference between the amplitude value of the signal and the maximal sample) which in fact is guaranteeing that at least one sample per period will have at least the guaranteed amplitude. The Eq. (2) is guaranteeing the maximal amplitude error Eamx during the sampling a SS with amplitude A and the maximal value Amax of the samples after the ADC or Amax=A-Emax.

VII. Control of the solution

The AS coming from most the signal sources is band limited (Fsmax << ∞) and with limited peak-to- peak amplitude (Aspp<<∞). That means that it has a limited maximal slew rate (SRmax << ∞) and could de represented as a finite sum of SS and CS and a direct current (DC) component. These AS could be modeled successfully with a set of analog or digital sinusoidal generators.

The control of the solution is made with modeling the example given before with set of SS and CS signal generators and comparing the signal before ADC with signal after the reconstructing DAC. Moreover the samples are stored in the memory and sorted in order to find the maximal and minimal value and errors are searched. Five signal sources were used and a five input precision summing stage with TL071 or LF356 operational amplifier was used.

The amplitude, frequency, phase and a DC component of each signal component were evaluated and compared with the input signals. The test was made for any signal component and for any combination of them. When two or more signal components are added and processed the inter-modulation distortions (IMD) were discarded in order to simplify the task. The hardware is described in [2].

VIII. Conclusions

A method and example of errors evaluation during the sampling of a BWS was given. The SSF N=Fd/Fs, the sampling frequency Fd, the maximal amplitude error Emax, the number of the converters bits n and the SHF Nsh were calculated in order to satisfy previously done amplitude error for each signal component. Electronic components for a practical realization were selected.

The method is simple and effective and is applicable for any analog to digital conversion system. It is applicable to system with microprocessor, micro-controllers and a free running ADC+DAC system and is useful for testing analog channels including analog to digital conversion.

This example is an application of the method of evaluation of the amplitude errors during A to D conversion of single or multi-tone signal. It is important because due to he phase changes and/or instability of some frequency component could be lost or and adverse interference could be produced.

Work should de done in order to build much more representative and comprehensive models and equipment of the sampling and signal reconstruction process.

References

[1] Petrov P. Tzv., "Sampling factor and amplitude errors during the sinusoidal and cosinusoidal signal conversion", *ICEST-2004*, June 16-19, Bitola, Macedonia.

[2] Petrov P. Tzv., "Method and examples of calculating the sampling frequency when the maximum rate of change and amplitude of the signal are known", *ICEST-2004*, June 16-19, Bitola, Macedonia

[3] Petre Tzv. Petrov, "Method of calculating the sampling frequency in function of the maximal error of signal conversion". Telecom-2003, Varna, 9-11 October, 2003, Bulgaria.

[4] Analog Devices Inc., CD ROM 2004 Designer's Reference Manual, USA

[5] National Instruments, Analog/Interface Data Book, summer 1999 edition.

Influence of the Window Function to the Time-Frequency Characterization of Electrocardiogram

Sinisa S. Ilic[1], Vidosav Stojanovic[2], Aleksandar Zoric[3]

Abstract – **In this paper the study of influence of the window function to the Time – Frequency characterization of the ECG signal using STFT is presented. Our idea was to create real time STFT diagram of ECG signal in the existing PC based ECG device. In order to achieve STFT diagram with as many details as possible a lot of calculations in signal processing must be done. But, some calculations can take a time that is not enough for real time rendering of the STFT diagram. By proper selection of the window function and window length we can obtain good compromise for showing STFT diagram of ECG signal in real time.**

Keywords - **ECG, STFT diagram, window function, window length**

I. INTRODUCTION

The ECG signal represents an electrical stimulus to the heart muscles. Four chambers exist in the heart: Left and Right Atrium and Left and Right Ventricle. There are valves (Mitral and Tricuspid) between Atriums and Ventricles which enable the blood flow from Atriums to Ventricles. When the heart muscle contracts or beats (called systole) it pumps blood out of the heart. The heart contracts in two stages. In the first stage the Right and Left Atria contract at the same time, pumping blood to the Right and Left Ventricles. Then the Ventricles contract together to pump blood out of the heart. Then the heart muscle relaxes (called diastole) before the next heartbeat. This allows blood to fill up the heart again. Each step in the process described is stimulated by the electric signal generated in the Sinoatrial node which is located in the Right Atrium. Voltages which can be measured on the body skin are usually in the range ±1mV. Plotted changes of the voltages described create Electrocardiogram (ECG). Typical ECG signal, with denoted parts described above is shown in Figure 1.

P wave denotes the spread of electrical activity over the Atria and the beginning of its contraction, QRS complex denotes the spread of electrical activity over the ventricles and the beginning of its contraction and T wave denotes the recovery phase of the ventricles.

[1]Sinisa S. Ilic is with the Faculty of Technical Sciences, 28000 Kosovska Mitrovica, Serbia and Montenegro, E-mail: sinisasilic@yahoo.com

[2]Vidosav Stojanovic is with Faculty of Electronic Engineering, Aleksandra Medvedeva 14, 18000 Nis, Serbia and Montenegro, E-mail: vitko@factaee.elfak.ni.ac.yu

[3]Aleksandar C. Zoric is with the Faculty of Technical Sciences, 28000 Kosovska Mitrovica, Serbia and Montenegro, E-mail: aczoric@yahoo.com

It is obvious that changes in the electric stimulus result in the improper work of the heart. Doctors can find irregularity of the heart activity based on the waveform of the ECG signal in the time domain, but lot of information is also hidden in the frequency domain.

Our idea was to create "real time" computer ECG which would offer possibility to ECG specialist to monitor ECG signal in Time and Time – Frequency Domain. For some suspicious waveform of ECG signal in Time Domain, specialist could switch to Time – Frequency Domain monitoring in real time and look for spectral deviations. Of course, because of the refreshing rate of the ECG screen in the real time it is preferable to decrease sample rate and a number of samples in the window. So, the prime task was to select sample rate, window function and a number of samples in the window in order to render Time-Frequency diagram in real time, but also not to decrease quality of information consisted in the diagram.

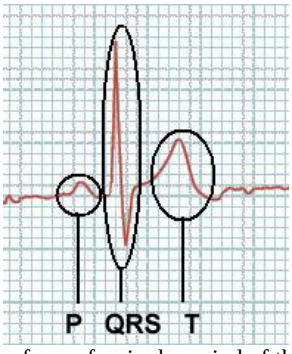

Fig. 1. Typical waveform of a single period of the electric stimulus of the heart

II. BACKGROUND OF THE TIME-FREQUENCY ANALYSIS

We can take several periods (cycles) of the ECG waveform and calculate its spectrum, in order to obtain amplitudes and phases of the spectral components. This information is enough to determine which spectral components take part in the signal, what is the amplitude ratio between them and what is the bandwidth of the signal. But, this is not enough to indicate how a signal's frequency contents evolve in time. This is very important for a range of heart diseases, i.e. deviation of the moments where some frequency components appear in relation to the beginning of the parts described (P, QRS, T) can show irregularity of the heart work.

There are several ways to obtain dynamic spectrum analysis over time. One of them, Short Time Fourier

Transform (STFT), uses functions that are concentrated in both time and frequency domains.

The short-time Fourier transform of a sequence x(n) is defined by

$$X_{STFT}(e^{j\theta}, n) = \sum_{m=-\infty}^{\infty} x(n-m)w(m)e^{-j\theta m} \quad (1)$$

where *w(m)* is suitable window sequence. Window function extracts finite-length portion of sequence *x(n)* such that spectral characteristic of the section extracted is approximately stationary over the window for practical purposes. The STFT is computed at the finite set of discrete values of θ. To be more precise, let the window be of length L defined in the range $0 \le m \le L-1$. We sample $X_{STFT}(e^{j\theta}, n)$ at the N equally spaced digital frequencies $\theta_k = 2\pi k/N$ with $N \ge L$ as indicated in following equation

$$X_{STFT}(k, n) = \sum_{m=-\infty}^{\infty} x(n-m)w(m)e^{-j2\pi km/N} \quad (2)$$

for $0 \le k \le N-1$. It follows from above equation, assuming $w(m) \neq 0$, that $X_{STFT}(k, n)$ is simple DFT of $x(n-m)w(m)$. Note that X_{STFT} is two-dimensional sequence and is periodic in k with a period N.

Finaly, the sampled STFT for a window defined in the region $0 \le m \le L-1$ is given by

$$X_{STFT}(k, lR) = \sum_{m=-\infty}^{\infty} x(lR-m)w(m)e^{-j2\pi km/N} \quad (3)$$

where *l* and *k* are integers such that $-\infty < l < \infty$ and $0 \le k \le N-1$.

Problem in STFT is that one cannot know what spectral components exist at what instances of times. What one can know are the time intervals in which certain band of frequencies exist, which is a resolution problem.

A simple way to characterize a signal simultaneously in time and in frequency is to consider its mean localizations and dispersions in each of these representations. This can be obtained [4], [6], [7] by considering $|x(t)|^2$ and $|X(\theta)|^2$ as probability distributions and looking at their mean values and standard deviations:

$$t_m = \frac{1}{E_x}\int_{-\infty}^{\infty} t|x(t)|^2 dt \quad (4)$$

$$\theta_m = \frac{1}{E_x}\int_{-\infty}^{\infty} \theta|X(\theta)|^2 d\theta \quad (5)$$

$$T^2 = \frac{4\pi}{E_x}\int_{-\infty}^{\infty} (t-t_m)^2|x(t)|^2 dt \quad (6)$$

$$B^2 = \frac{4\pi}{E_x}\int_{-\infty}^{\infty} (\theta-\theta_m)^2|X(\theta)|^2 d\theta \quad (7)$$

$$E_x = \int_{-\infty}^{\infty} |x(t)|^2 dt < \infty \quad (8)$$

where t_m is "time center of the signal", θ_m is "frequency center of the signal", T is temporal width of the signal and B is spectral width of the signal. The product $T \cdot B$ shows the uncertainty area and should be greater or equal to 1 (it is equal to 1 only for Gauss window). We used three window function in this paper: Gauss, Hamming and Blackman. Equations for these windows are following:

$$gw(k+1) = e^{-\frac{1}{2}\left(\alpha\frac{k-N/2}{N/2}\right)^2} \quad (9)$$

$$hw(k+1) = 0.54 - 0.46\cdot\cos\left(2\pi\frac{k}{N-1}\right) \quad (10)$$

$$bw(k+1) = 0.42 - 0.5\cos\left(2\pi\frac{k}{N-1}\right) + 0.08\cos\left(4\pi\frac{k}{N-1}\right) \quad (11)$$

where $0 \le k < N$, and N is window length.

III. Optimisation Of STFT Parameters

ECG waveforms are recorded using the virtual 12-leads ECG device [1] with sample rate of 2880 Hz. According to the [2] valuable frequency components are up to 100 Hz, but it is for the spectrum of the whole signal. Some valuable frequency components may appear in time-frequency analyses which are greater than 100Hz. We have built a function in Matlab software, which has 3 input parameters: rate of reducing the sampling frequency (decimation), window function and window length.

A. Influence of the Window length

The window length is very important in two ways. By increasing the window length, resolution in frequency axis is better – spectral components are closer one to each other. But the time resolution is then poor because the same signal pattern will be included in a number of overlapping windows. It will result in impossibility to find out when the pattern starts in time. By decreasing the window length, resolution in time axis is better, but resolution in a frequency axis is worst. It means that spectral components along the frequency axis represent amplitude not of the frequency which exists in signal, but rather of the wider range of frequencies. For sampling frequencies between 72 and 288 Hz after decimation, and number of the samples in the window of 32 and 64, we can obtain that spectral component in the diagram represents ranges between 1.125 and 9 Hz. Also, according to the parameters selected, widths of the windows are between 0.111s to 0.889s. If we

presume that basic frequency of the heart work (frequency of occurring PQRST components) is between 0.5s (120 bpm) to 2s (30 bpm), window width should be below 0.5s. It would ensure that window covers only or less than one single cycle of PQRST components.

B. Influence of the Window function

Each of the window functions has different influence on a signal it multiplies with. We have used Hamming, Gauss and Blackman window.

The criteria for selecting window function was spectrum of the functions and product T x B described above. Product T x B is calculated for discrete window functions and the values are: 0.996, 1.0041 and 1 for Hamming, Gauss and Blackman window functions respectively, but if there was no ECG signal.

In order to save calculations of an amplitudes of the window functions in time instants T, 2T, … nT which multiply appropriate samples in the time window of the ECG signal, it is enough to create 6 arrays: 3 arrays (for each window type) of 32 values (for 32 samples in window) and 3 arrays of 64 values.

C. Selection of the parameters

Our plan was to refresh the ECG signal in Time Domain with original sample rate, but for rendering the diagram in Time-Frequency Domain to select following parameters:

- Sample rate of 144 or 288 Hz,
- Hamming, Gauss, or Blackman Window,
- Number of the samples in the window: 32 or 64,
- Number of the samples between the overlapping windows: 4.

Sample rate of 144/288 Hz gives spectrum up to 72/144 Hz, which should be enough to show significant time-frequency components of ECG signal, and downsampling is then 10/20.

The relative sidelobe attenuation of the Hamming, Gauss and Blackman window functions are: -42.5dB, -312.5dB and 58.1dB respectively. Attenuation of the components in the Hamming window outside of the main lobe is around 42.5dB, which offer possibility to see higher frequency components in the diagram.

Product TxB is changing in time for the windowed ECG signal that can bee seen in the Figure 2. The maximum values of uncertainty are calculated by using Hamming and the minimum by using Gauss window function. But, as it can been seen later, decreasing of the product i.e. decreasing of the time-frequency uncertainty does not lead us to the better representation of time-frequency analysis of the signal.

The width of the window is 0.222s (for 32 samples) or 0.444s (for 64 samples) and between the overlapping windows is 0.027s which is enough to obtain time resolution for detailed monitoring of ECG signal.

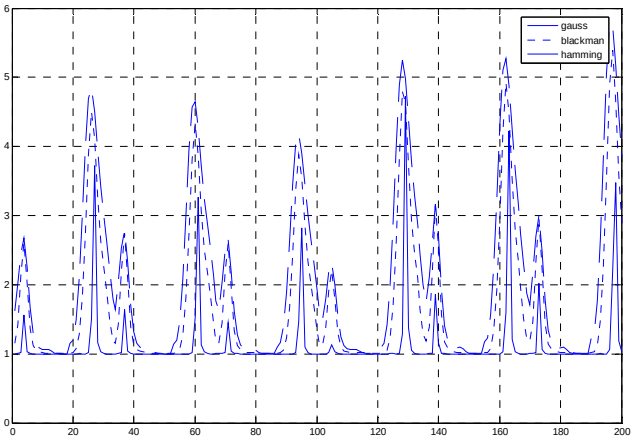

Fig. 2 – Product T x B for the windowed ECG signal

IV. EXAMPLES AND EXAMPLE

In the figures below, Time Domain waveform of 4th Cordial lead and it's 3D Frequency-Time diagrams are shown. Sample frequency (fs) is 144Hz, window length (w) is 0.44s and 0.22s, time resolution is $\Delta t = 0.0278$s, frequency resolution is $\Delta f = 2.25$Hz and 4.5Hz for number of the samples in the window of n=64 and n=32 samples. Figures 3 and 4 show diagrams using the Hamming and figures 5 and 6 using the Gauss windowing function with $\alpha = 10$.

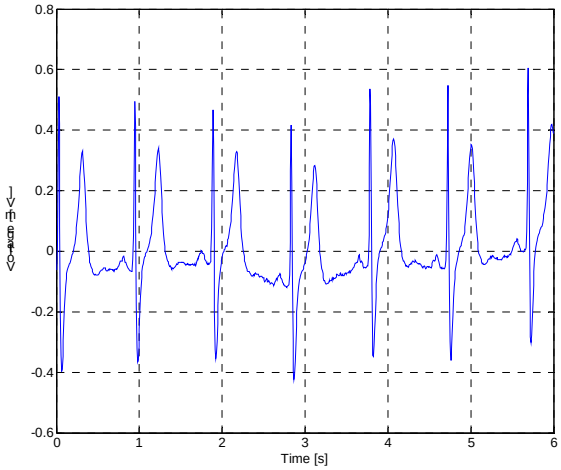

Fig. 3 – Time Domain waveform of the ECG signal has been analyzed

If we take a look on figures 4 and 5, we can see that better time resolution is obtained by using 32 samples in the window. Also, more details in higher frequencies can be seen in the diagrams which are obtained by using the Hamming window function.

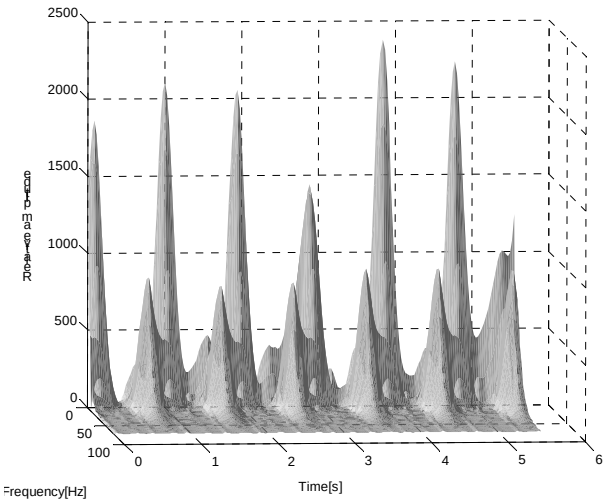

Figure 4 – 3D diagram using the Hamming window with w=0.44s, fs=144Hz, n=64 samples

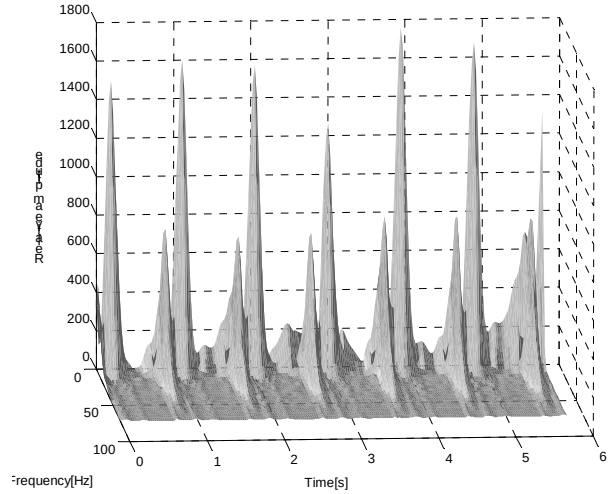

Fig. 5 – 3D diagram using the Hamming window with w=0.22s, fs=144Hz, n=32 samples

Considering processing time that computation of windowing function and FFT needs for 32 samples against 64 samples in the window, and quality of the diagrams presented for sample rate of 144Hz, we can say that selection of 32 samples in the window is good choice which guarantees satisfactory quality.

Also we can see that 3D spectrograms in figures 5 and 6 are similar although they represent processing using windows of different types and different number of samples in the window.

V. CONCLUSION

In this paper is presented study how window function impacts on the Time – Frequency characterization of the Semi – periodic biopotentials of the myocard by implementing the STFT. Although the initial idea was to select the window function that has the best resolution for the time-frequency diagram of the ECG signal according to minimization of the Heisenberg uncertainty principle, studies and examples showed that this is not the case for typical ECG signal.

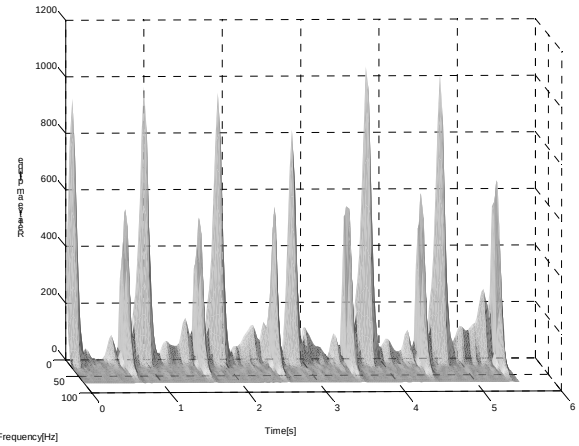

Fig. 6 – 3D diagram and the contour plot using the Gauss window with w=0.44s, fs=144Hz, n=64 samples

The aim of the study was to implement “real time” STFT analysis in the existing PC based Electrocardiogram software.

Results of comparing STFT of the real ECG signal of two types of window functions with different number of samples in the window show that better frequency resolution of STFT diagram is achieved by selection of the Hamming window function, while satisfactory time resolution is achieved by selection of 32 samples in the window.

Conclusion obtained represents good compromise of parameters selected in order to show STFT diagram in real time.

REFERENCES

[1] Zoric A., Djordjevic B., Martinovic D., Obradovic S. : “12-Leads Virtual ECG”, *International Scientific Conference UNITECH-02*, pp. 172-177, Gabrovo, Bulgaria, 2002.

[2] Zoric A., Djordjevic B., Martinovic D., Obradovic S. : “PC Software for Spectral Analysis of ECG Signals”, *International Scientific Conference UNITECH-03, Proceedings ISBN* 954-683-167-0, pp. I-202 – I-205, Gabrovo, Bulgaria, 2003.

[3] Shie Qian, Dapang Chen, “Joint Time – Frequency Analysis – Methods and Applications”, *Prentice Hall PTR*

[4] F Auger, P.Flandrin, P.Goncalves, O.Lemoine “Time – Frequency Toolbox for use with MATLAB – Tutorial” 1995-1996

[5] Dale Dubin, “Brza interpretacija EKG, kurs sa testiranjem”, *M.D. IGRO sportska knjiga Beograd*, Kultura, 1988.

[6] Notes on the Uncertainty principle, http://www-inst.eecs.berkeley.edu/~ee120/04fall/Fall04/Lectures/uncertaintyprinciple.pdf

[7] D.S. Taubman, “Signal Processing 2 – Time-Frequency Analysis”, *http://www.eet.unsw.edu.au/*

Comparison of Sound Absorption Coefficients Determined by Different Methods

Miroslava A. Milošević[1], Dejan G. Ćirić[1], Aleksandar M. Pantić[2]

Abstract –**One of the important acoustic properties of an absorbing material is the absorption coefficient. It can be measured using different methods. Some of them are classified as laboratory methods, while some others can be applied not only in laboratories, but also in other environments and in situ. The comparison of absorption coefficients obtained by four methods, impedance tube, reverberation room, intensity method, and reflection method are made in this paper. For that purpose, the absorbing material of the same type but different samples is used. The results obtained by the methods using diffuse sound field are similar, with some deviations specific for a particular method. The values of absorption coefficient for reflection method are closest to the values for impedance tube method since both methods are based on normal sound incidence.**

Keywords – **Sound absorption coefficient, impedance tube, reverberation room, intensity method, reflection method.**

I. INTRODUCTION

The absorption is a property of acoustic material that allows a reduction in the amount of reflected sound energy. The introduction of an absorbent on the surfaces of a room reduces the sound pressure level in the room since the part of sound energy striking the room's surfaces is absorbed. In that, the acoustic energy is usually transformed into heat energy. Absorption of a given material is frequency dependent and it is affected by the size, shape, location, and method of mounting [1, 2].

Sound absorbing materials have been extensively used in the field of noise control engineering and architectural acoustics in order to obtain the desired characteristics of the sound field. Today's growing focus on noise control issues and the sound quality as an important aspect of product design even increases their significance. Because of that, it is important to have the values of the parameters of absorbing materials used for acoustical treatments. One of the important acoustical parameters is the frequency characteristic of absorption coefficient. It describes the efficiency of the material or the surface to absorb the sound. It is defined as the ratio of the absorbed sound energy to the incident energy. The knowledge of absorption coefficient is very valuable for all tasks related to acoustical design of a room such as prediction of reverberation time, planning model experiments or computer simulation of the sound propagation in enclosures [1].

The characterisation of an absorbing material and determination of its absorption coefficient can be done using different measurement methods. They are divided on laboratory methods and methods that can be applied in situ. The former group contains wave tube method, reverberation room method, and intensity method [1,3,4] while the latter is based on reflection method [5,6]. The results of absorption coefficient obtained by the mentioned methods are compared here. The same type of absorbing material, rock-wool, but different samples was used. In addition, the measurements were performed by different institutions, different equipment and operators, and in a long time period with more than 15 years between the first and the last measurements.

II. MEASUREMENT OF SOUND ABSORPTION USING DIFFERENT METHODS

A. Measurement of absorption coefficient in impedance tube

The sound absorption coefficient, reflection factor as well as surface impedance of materials and objects can be determined by means of a device known as impedance or standing wave tube. The method is specified in corresponding standard [4]. For that purpose, only normal sound incidence is used and the standing wave pattern of a plane wave in the tube, which is generated by the superposition of an incident sinusoidal wave with the plane wave reflected from the test object, is evaluated.

In order to determine the absorption coefficient, it is sufficient to measure the maximum p_{max} and the minimum p_{min} values of the sound pressure, i.e. the pressures in the nodes and anti-nodes of the standing wave in the tube. Thus, the sample's sound absorption coefficient is:

$$\alpha = 1 - |R|^2 = 1 - \frac{(p_{\max} - p_{\min})^2}{(p_{\max} + p_{\min})^2}, \quad (1)$$

where R is the reflection factor.

The absorption coefficient is a function of frequency and measurement over the frequency range of interest is required. The simplicity, reliability, and accuracy of this traditional method have been proven in practice. However, the measurement procedure itself is relatively time-consuming. Because of that, several attempts have been made to replace

[1] Miroslava A. Milošević and Dejan G. Ćirić are with the Faculty of Electronic Engineering, Aleksandra Medvedeva 14, 18000 Niš, Serbia and Montenegro, E-mail: mmilosevic@elfak.ni.ac.yu and dciric@elfak.ni.ac.yu

[2] Aleksandar M. Pantić is with "Vunizol" A.D., Rock wool and concrete elements Factory, Belo Polje, 17530 Surdulica, Serbia and Montenegro, E-mail: apantic@ptt.yu, vunizol@ptt.yu

this procedure such as applications of impulse response measurements [1].

B. Measurement of absorption coefficient in reverberation room

Reverberation room is a room having a long reverberation time, specially designed to make the inside sound field as diffuse as possible. For that purpose, it is designed to minimize the sound absorption of all surfaces, which are typically smooth and rigid. [1, 2, 7]

The reverberation room method (on ideal conditions) is used for determination of the sound absorption coefficient for random sound incidence. The evaluation of the sound absorption coefficient in a reverberation room is based on a number of simplifications and approximate assumptions concerning the sound field and the size of the absorber [1]. Measurements are normally carried out in a certificated laboratory where a standardized reverberation room is used in accordance with the standard [7].

The results of the measurements depend on the size and form of the area of the test sample, but also on the degree of diffusion of sound waves in the room. The results are influenced by the location of the loudspeaker and microphone in the room too. It is recommended that the loudspeaker is placed in a corner, and that the microphone is moved or rotated during the measurement. It has been confirmed that testing of the same specimen of an absorbing material in different laboratories and using only the reverberation room method lead to considerable disagreement in the results [1]. This emphasizes the uncertainty related to the accuracy and reliability of the results obtained with this method.

C. Determination of absorption coefficient by intensity method

Starting from the definition of absorption coefficient and the characteristics of sound intensity as a vector quantity, the methodical procedure for the absorption coefficient measurement for random sound incidence in the regular parallelepiped rooms, which don't satisfy the necessary condition for the application of the reverberation room method, has been developed [3]. The measurement procedure is based on the relation between the absorption coefficient and sound intensity:

$$\alpha = \frac{4 I_\alpha \rho c}{p^2}, \tag{2}$$

where I_α is the intensity absorbed by the specimen and p is the sound pressure in the room where sound field is considered to be diffused.

The measurement procedure includes the sound intensity and the sound pressure measurements. Since the measurement precision can be influenced by the local changes of these quantities, the measurements are carried out in a number of points and the obtained values are averaged. The incident sound energy can be determined by sound pressure measurements in the middle part of the room, on the measurement surface divided into segments of the area ΔS_i, whereas the absorbed sound energy can be determined by mapping of the sound intensity right above the specimen on the measurement surface divided into segments of the area ΔS_j. The ratio of the absorbed sound energy to the incident sound energy defines the absorption coefficient:

$$\alpha = \sum_{j=1}^{m} I_j \Delta S_j \Big/ \sum_{i=1}^{n} \frac{p_i^2}{4\rho c} \Delta S_i, \tag{3}$$

where p_i is the sound pressure measured on the i-th segment, n is the number of the segments for sound pressure measurements, I_j is the sound intensity measured on the j-th segment and m is the number of the segments for intensity measurements [3].

If the values of the sound pressure and sound intensity are respectively expressed by the sound pressure level L_p and sound intensity level L_I obtained in measured bands, the sound absorption coefficient can be determined by the following equation [3]:

$$\alpha = 10^{\frac{L_I - (L_P - 6)}{10}}. \tag{4}$$

In this way, defined measurement procedure gives the frequency characteristic of the sound absorption coefficient.

III. MEASUREMENT OF ABSORPTION COEFFICIENT BY REFLECTION METHOD

A. Theory of the reflection method

Measurements of absorption coefficient in situ are based on a measure of the complex pressure reflection factor determined by means of acoustic signals impinging on and reflecting from the test specimen. Because of that, they are usually designated as reflection method. There have been several approaches how to apply this method such as scheme with pure tones in an anechoic room, techniques based on impulse response measurements using spark source, blank shots, correlation technique or even cepstral analysis [5].

The sound absorption coefficient can again be obtained using reflection factor R from Eq. 1. Since the reflection factor is a complex number, its measurement is equivalent to the measurement of specific surface impedance. However, the phase information is not used for determination of absorption coefficient. According to the definition of reflection factor, it is necessary to detect incident and reflected signals from the test surface. For that purpose, the same microphone can be used. There are two approaches related to the placement of the microphone. In the first one, the microphone is placed at some distance from the test surface, usually at half of the distance between the loudspeaker and the surface, Fig. 1a). Relevant impulses are given in Fig. 2a). In the second approach, the microphone is placed relatively close to the test surface [6], which is shown in Fig. 1b), and corresponding impulses are shown in Fig. 2b).

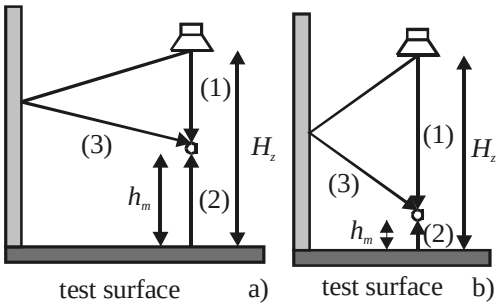

Fig. 1. Set-up for absorption coefficient measurements a) microphone at some distance from the test surface, b) microphone close to the test surface

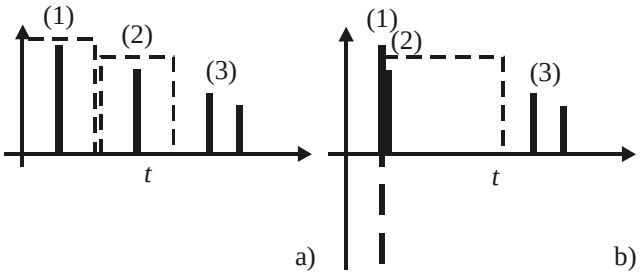

Fig. 2. Impulses obtained using the set-up from a) Fig. 1a) and b) Fig. 1b) where (1) represents the incident impulse, (2) the reflected impulse and (3) parasitic reflections

The basic difference between these approaches is related to time separation of the impulses. The first approach enables direct time separation and extraction of the incident impulse and reflected one assuming that the duration of the incident impulse is short enough, i.e. it decays to negligible values at the point where the reflected impulse starts. The impulses are extracted applying appropriate window function in time domain. It has been shown that the best results are obtained using the right-half Blackman-Harris window [5]. Opposite to the first approach, there is almost no time separation between the incident and reflected impulses in the second approach. Because of that, it is necessary to cancel incident impulse by subtraction assuming that it is exactly known [6]. In order to have the incident impulse for subtraction, it is measured in the pseudo-free-field condition where the loudspeaker-microphone arrangement is located remote from reflecting surfaces.

The spectrum of the sound reflected from the test surface P_r can be expressed as:

$$P_r = C_r R P_i e^{-2\pi i f \tau_r}, \quad (5)$$

where C_r is the correction factor ($C_r=(H_z-h_m)/(H_z+h_m)$), P_i is the spectrum of incident sound, and τ_r is the time delay due to the path difference [5]. The absorption coefficient can be now calculated as:

$$\alpha = 1 - \frac{1}{C_r^2}\frac{|P_r|^2}{|P_i|^2}. \quad (6)$$

B. Application of reflection method on developed measurement system

The described reflection method was applied on developed measurement system based on PC. The impulse responses were measured using maximum length sequence (MLS) technique. MLS of degree of 15 was used as an excitation signal. Both mentioned approaches shown in Fig. 1 were applied, but only the results obtained using the second one are presented here. The microphone was placed close to the test surface (approximately 10 cm from it), while the distance between the loudspeaker and microphone was somewhat more than 1 m. Since it was necessary to measure the pseudo-free-field incident impulse in addition to the measurement in front of the test specimen, the distance between the loudspeaker and microphone was kept constant in these measurements using a suspended construction.

Tested absorbing material was the rock-wool "Vunizol" L of density of 50 kg/m^3 manufactured in "Vunizol" A.D. The panels of dimensions 100×50×5 cm^3 were placed on the wall of one of the laboratories of Faculty of Electronic Engineering in Niš similar to the classroom. The total sample size was approximately 2.5×2 m^2.

After subtraction of incident impulse, the reflected impulse was separated from parasitic reflections applying the right-half Blackman-Harris window directly in time domain. This subtraction enabled usage of longer window and obtaining of higher resolution of the results. The window length and the resolution were only limited by parasitic reflections from other surfaces relatively close to the absorber.

IV. Analysis of Measured Results

This section compares the absorption coefficients of the same type of absorbing material mentioned before but different samples obtained by described four methods. In addition, the methods were applied by different institutions, by different operators and even with considerable time difference among the measurements. Thus, more than 15 years passed between the first measurements carried out by the reverberation room method and the last ones performed by the reflection method.

The results obtained by means of the impedance tube in the certified laboratory and given in the report [8] are used here as the reference (Fig. 3). The shape of presented curve is typical for the rock-wool absorbing material, with the values close to 100 % (or 1 in absolute units) above 1 kHz.

The frequency characteristics of absorption coefficient determined by the reverberation room and intensity method are plotted in Fig. 4 [3]. Since original data obtained by the reverberation room method according to the standard [7] have some values above 100 %, they are normalised to have maximum value of 100 %. The measurements by intensity method were carried out in two regular parallelepiped empty rooms of different volumes (8.8x6.2x3.8 m^3 and 7.6x5.2x3.8 m^3) and the results for both rooms are given here. Although there are some deviations between the presented results for two methods in the observed frequency range, they are rather similar.

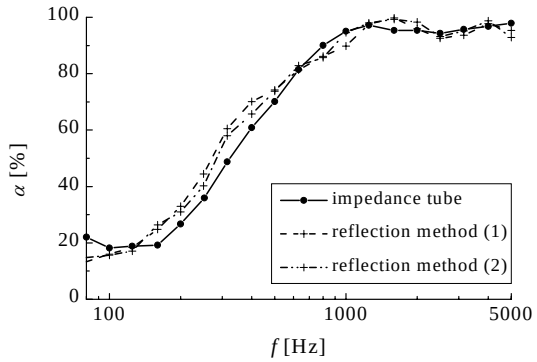

Fig. 3. The frequency characteristics of absorption coefficient of rock-wool determined by impedance tube and reflection method

The shape of the curve already seen for other methods exists for reflection method too, Fig. 3. The results from two measurements carried out by the described second approach of reflection method are shown in the figure, where the absorbing material was completely dismantled after the first one and placed again on the same wall. There is only a small deviation between the curves for these two measurements.

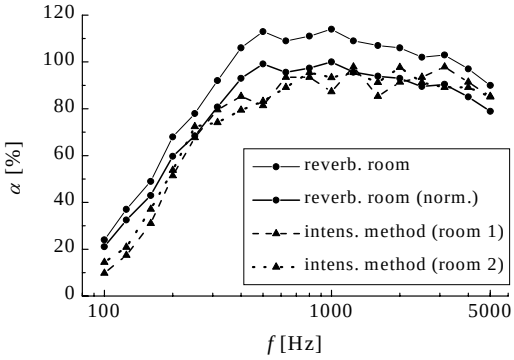

Fig. 4. The frequency characteristics of absorption coefficient of rock-wool determined by reverberation room and sound intensity method

The characteristics of absorption coefficient for all four used methods are approximately the same for frequencies above 1 kHz. However, at lower frequencies, characteristics are similar to each other for methods in which the measurements are performed in the diffuse sound field – the reverberation room method and intensity method. Also, similar characteristics at lower frequencies are obtained for methods in which the measurements are performed only for normal sound incidence – the impedance tube method and reflection method.

The statistical values of absorption coefficient calculated using both measured coefficient and law of energy density distribution in diffuse sound field as a function of incidence angle are not presented here. This calculation is not so important because the obtained values often deviate from the ones determined by the measurement in diffuse sound field. The reason could be inappropriate assumption of the mentioned dependence of sound energy distribution and incidence angle.

V. Conclusion

The results of absorption coefficients of the same absorbing material but different samples determined by different methods, different institutions, and operators, and even measured with the time distance of more than 15 years are compared here. The pattern common for the rock-wool absorbing material is seen in all the results. The values of the absorption coefficient are similar for corresponding sound field and incidence type.

The results obtained by reflection method are closest to the results obtained by impedance tube. Thus, although these two methods use specimens of completely different sizes and placed in a different way, the absorption coefficient in both of them is measured only for normal incidence.

In that way, it is shown that the reflection method, in principle, can give measurement results that are in a good agreement with impedance tube method. Thus, the advantages of this method such as characterisation of material in situ can be utilised.

References

[1] H. Kuttruff, *Room acoustics*, 3rd Edition, UK, E&FA Spon, 1991.

[2] L. L. Beranek, *Acoustics*, New York, McGraw Hill, 1977.

[3] M. Praščević, M. Milošević and D. Cvetković, "Determination of Absorption Characteristic of Materials on Basis of Sound Intensity Measurement", *Journal de Physique IV*, vol. 4, pp. 159-162, 1994.

[4] ISO 10534-1: *Acoustics - Determination of Sound Absorption Coefficient and Impedance in Impedance Tubes – Part 1: Method Using Standing Wave Ratio*, 1996.

[5] M. Garai, "Measurement of the Sound-Absorption Coefficient In Situ: The Reflection Method Using Periodic Pseudo-random Sequences of Maximum Length", *Applied Acoustics*, vol. 39, pp. 119-139, 1993.

[6] E. Mommertz, "Angle-Dependent In-situ Measurements of Reflection Coefficients Using a Subtraction Technique", *Applied Acoustics*, vol. 46, pp. 251-263, 1995.

[7] ISO 354: *Acoustics – Measurement of Sound Absorption Coefficient in Reverberation Room*, 1985.

[8] Institute for testing of materials (IMS): *Report 2791/96 – testing of rock-wool "Vunizol"*, Belgrade, 1996.

Active Inverse Hausdorff Filters

Peter St. Apostolov[1], Michael Bl. Momchedjikov[2]

Abstract - **This paper presents a method for synthesis of two kinds of active inverse filters with Hausdorff-type transfer characteristic. The filter frequency characteristics are determined and a comparison with Chebyshev inverse filters is given.**

Keywords - **Approximation, Polynomial, Synthesis, Active inverse filter, Hausdorff, Chebyshev, Frequency characteristic.**

I. INTRODUCTION

Hausdorff filters are implemented by "shifted" Delta-function approximation $\chi(x)$ with Hausdorff polynomial (Fig. 1):

$$P_n(x) = \varepsilon T_n\left(\frac{2x}{2-\alpha\varepsilon}\right) = \varepsilon T_n\left(\frac{x}{1-\alpha\varepsilon/2}\right), \quad (1)$$

where ε is the Hausdorff space, T_n is Chebyshev polynomial of first order and *n* degree, α is a parameter. The $\alpha\varepsilon$ product determines precision estimation of approximated "shifted" Delta-function in point 1 where it has first-order indeterminacy or infinite steepness.

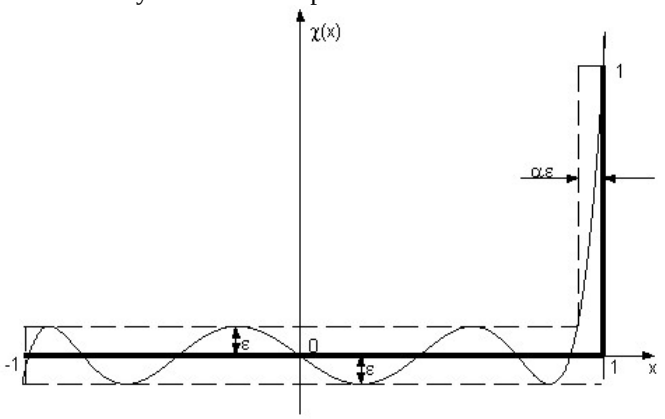

Fig. 1

The inverse Hausdorff filters are of two types: A type and B type [2]. They have characteristics similar to Chebyshev inverse filters. Magnitude responses of third-order Hausdorff inverse filters compared to Chebyshev inverse filter are shown on Fig. 2. The three characteristics have identical pass-bands. For infinite attenuation frequencies the following equations are valid:

$$f_A = f_C/(1-\alpha\varepsilon/2);\ f_B = f_C(1-\alpha\varepsilon/2). \quad (2)$$

[1]Peter St. Apostolov, Ms. Sc., Assoc. Fellow, IST-Sofia, E-mail: p_apostolov@abv.bg

[2]Michael Bl. Momchedjikov, Prof. D-r, Eng, TU – Sofia, FKTT, Radiocommunication; E-mail: momche_tu@abv.bg

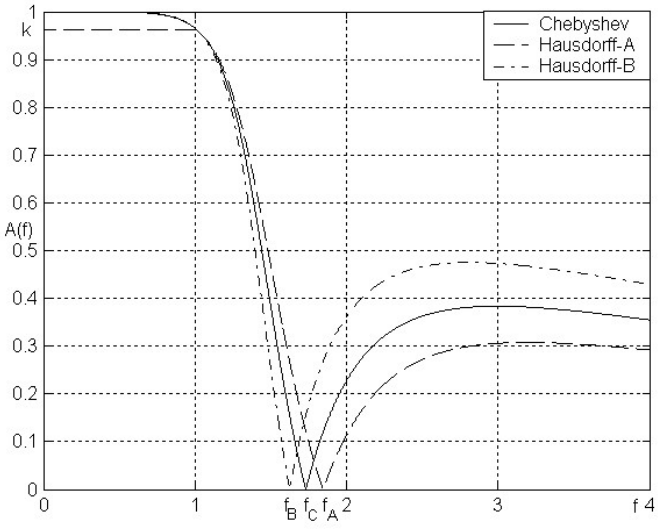

Fig. 2

II. SYNTHESIS IMPLEMENTATION

Let's take an example to illustrate the filter synthesis:
An active inverse Hausdorff filter is to be calculated - of A type, forth order $n=4$, cut-off frequency $f_c = 1\text{KHz}$; stop frequency $f_s = 2.135\text{kHz}$, limit frequency characteristic drop $DA = 2\text{dB}$, pass-band gain $A_0 = 1$, selective component values $R = 10\text{k}\Omega$ and $C = 10\text{nF}$. The filter will consist of two cascade two-order amplifier stages - Boctor circuit [3], [4].
The limit frequency characteristic drop is calculated:

$$k = \sqrt{10^{0.1DA} - 1} = 0.7648. \quad (3)$$

The attenuation of inverse Chebyshev filter of the same stop frequency's input data is defined [1]:

$$DS_{ch} = 10\log\left[k^2\text{ch}^2\left(n\text{Ach}\frac{f_s}{f_c}\right)\right] = 40\text{dB}. \quad (4)$$

From the established value the Hausdorff space and the product $\alpha\varepsilon$ could be found [2]:

$$\varepsilon = \frac{1}{\sqrt{10^{0.1DS_{ch}} - 1}} = 0.01; \quad (5)$$

$$\alpha\varepsilon = 2\frac{\text{ch}\left[\frac{1}{n}\text{Ach}\left(\frac{1}{\varepsilon}\right)\right] - 1}{\text{ch}\left[\frac{1}{n}\text{Ach}\left(\frac{1}{\varepsilon}\right)\right] + 1} = 0.6725. \quad (6)$$

The inverse Hausdorff filter stop-band minimal attenuation and equivalent ripple ε_1 is defined:

$$DSH_{\min} = 10\log\left\{k^2\mathrm{ch}^2\left[n\mathrm{Ach}\frac{f_s}{f_c\left(1-\alpha\varepsilon/2\right)}\right]+1\right\} = 55.4531\mathrm{dB} \quad (7)$$

$$\varepsilon_1 = \frac{1}{\sqrt{10^{0.1DSH_{\min}}-1}} = 0.0017\cdot \quad (8)$$

The active inverse Hausdorff filter stop frequency attenuation is equal to:

$$DSH = -10\log\frac{\varepsilon_1^2\mathrm{ch}^2\left(n\mathrm{Ach}\frac{1}{1\text{-}\alpha\varepsilon/2}\right)}{1+\varepsilon_1^2\mathrm{ch}^2\left(n\mathrm{Ach}\frac{1}{1\text{-}\alpha\varepsilon/2}\right)} = 27.8341\mathrm{dB}\cdot \quad (9)$$

The filter poles and zeros are defined:

$$\sigma_i = -\sin\left(\frac{2i-1}{n}\frac{\pi}{2}\right)\mathrm{sh}\left[\frac{1}{n}\mathrm{Ash}\left(\frac{1}{\varepsilon_1}\right)\right]; \quad (10)$$

$$\Omega_i = \cos\left(\frac{2i-1}{n}\frac{\pi}{2}\right)\mathrm{ch}\left[\frac{1}{n}\mathrm{Ash}\left(\frac{1}{\varepsilon_1}\right)\right]; \quad (11)$$

$$\omega_{Pi} = \frac{1}{\left(1-\frac{\alpha\varepsilon}{2}\right)\left(\sigma_i + j\Omega_i\right)} = \begin{pmatrix} -0.1216 - j0,3110 \\ -0,3186 - j0.1399 \\ -0,3186 + j0.1399 \\ -0.1216 + j0,3110 \end{pmatrix}; \quad (12)$$

$$\omega_{Zi} = \frac{j}{\left(1-\frac{\alpha\varepsilon}{2}\right)\cos\left(\frac{2i-1}{n}\frac{\pi}{2}\right)} = \begin{pmatrix} j1.0824 \\ -j1.0824 \\ j2.6131 \\ -j2.6131 \end{pmatrix}; i = 1,...,n\ . \quad (13)$$

The filter amplifier stages indexes are calculated [4]:

$$\Omega_{Pi} = \left|\omega_{Pi}\right| = \begin{pmatrix} 0,334 \\ 0,348 \end{pmatrix}; \quad (14)$$

$$\Omega_{Zi} = \left|\omega_{Zi}\right| = \begin{pmatrix} 1.0824 \\ 2.6131 \end{pmatrix},\ i = 1,...,\mathrm{int}\left(\frac{n+1}{2}\right)\cdot \quad (15)$$

The coefficient is defined:

$$k_f = \mathrm{ch}\frac{\mathrm{Ach}\sqrt{\frac{1}{10^{0.1DA}-1}}}{n} = 3.2166\cdot \quad (16)$$

Denominated pole-zero frequencies can be found from:

$$\omega_{Pi} = 2\pi f_c\Omega_{Pi}k_f = \begin{pmatrix} 21876 \\ 52813 \end{pmatrix}\mathrm{Hz}; \quad (17)$$

$$\omega_{Zi} = 2\pi f_c\Omega_{Zi}k_f = \begin{pmatrix} 21876 \\ 52813 \end{pmatrix}\mathrm{Hz}\cdot \quad (18)$$

Selective values 10kΩ and 1nF are assigned to R_{7i} and C_{8i} to define circuit minimal capacitance:

$$C_{1\min i} = \frac{C_{8i}A_0^2\left[Q_{Pi}^2\left(\omega_{Zi}^2-\omega_{Pi}^2\right)+\omega_{Pi}^2\right]^2}{\omega_{Zi}^2Q_{Pi}^2\left(A_0-1\right)+\omega_{Zi}^2\omega_{Pi}^2Q_{Pi}^2\left(A_0^2-A_0\right)+\omega_{Pi}^2A_0\left(\omega_Z^2-A_0\omega_{Pi}^2\right)} = \begin{pmatrix} 37.713 \\ 5.5399 \end{pmatrix}\mathrm{nF}. \quad (19)$$

Standard values are accepted:

$$C_{1i} = \begin{pmatrix} 47 \\ 10 \end{pmatrix}\mathrm{nF}\cdot \quad (20)$$

Discriminants are calculated:

$$D_i = C_{1i}^2\omega_{Zi}^4 - 4C_{1i}C_{8i}A_0^2\omega_{Pi}^2\left(\omega_{Pi}^2+Q_{Pi}^2\omega_{Zi}^2\right) = \begin{pmatrix} 497.7723 \\ 776.2355 \end{pmatrix}. \quad (21)$$

Then the remain circuit elements are determined:

$$R_{4i} = \frac{R_{7i}\left(\omega_{Zi}^2-A_0\omega_{Pi}^2\right)}{\omega_{Pi}^2A_0} = \begin{pmatrix} 95.048 \\ 553.98 \end{pmatrix}\mathrm{k\Omega}; \quad (22)$$

$$R_{2i} = \frac{C_{1i}\omega_{Zi}^2-\sqrt{D_i}}{2C_{1i}C_{8i}A_0Q_{Pi}\omega_{Pi}^3} = \begin{pmatrix} 4.5668 \\ 8.2311 \end{pmatrix}\mathrm{k\Omega}; \quad (23)$$

$$R_{3i} = \frac{1}{C_{1i}C_{8i}R_{2i}\omega_{Pi}^2} = \begin{pmatrix} 102.27 \\ 245.65 \end{pmatrix}\mathrm{k\Omega}; \quad (24)$$

$$R_{5i} = \frac{-Q_{Pi}R_{2i}}{Q_{Pi}+R_{2i}^2C_{1i}C_{8i}Q_{Pi}\omega_{Pi}^2-R_{2i}C_{1i}\omega_{Pi}} = \begin{pmatrix} 454.36 \\ 310.01 \end{pmatrix}\mathrm{k\Omega}; \quad (25)$$

$$R_{6i} = \frac{R_{7i}Q_{pi}}{C_{8i}\omega_{Pi}\left(R_{2i}R_{4i}C_{1i}Q_{Pi}\omega_{pi}-R_{7i}\right)} = \begin{pmatrix} 11.360 \\ 4.7029 \end{pmatrix}\mathrm{k\Omega}\cdot \quad (26)$$

The active inverse Hausdorff A-type filter electrical schematics is shown on Fig. 3

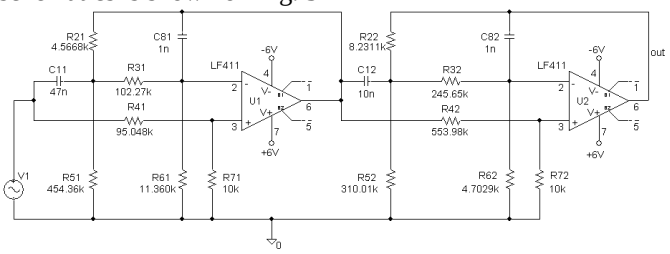

Fig. 3

The filter magnitude response is shown on Fig. 4. The marked values coincide with the values calculated in formulas (7) and (9).

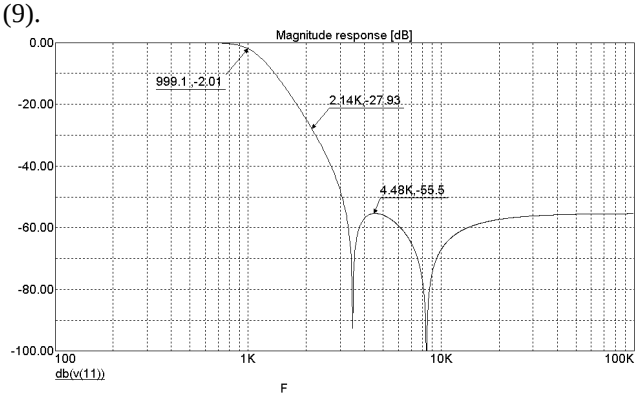

Fig. 4

An active inverse Hausdorff B-type filter [2] can be calculated using the described procedure. The changes are the following:

Formula (7) becomes:

$$DSH_{\min B} = 10\log\left\{k^2\mathrm{ch}^2\left[n\mathrm{Ach}\frac{f_s\left(1-\alpha\varepsilon/2\right)}{f_c}\right]+1\right\}. \quad (27)$$

Formula (9) becomes:

$$DSH_B = -10\log\frac{\varepsilon_1^2\mathrm{ch}^2\left[n\mathrm{Ach}\left(1\text{-}\alpha\varepsilon/2\right)\right]}{1+\varepsilon_1^2\mathrm{ch}^2\left[n\mathrm{Ach}\left(1\text{-}\alpha\varepsilon/2\right)\right]}. \quad (28)$$

Formula (12) becomes:

$$\omega_{Pi} = \frac{1-\frac{\alpha\varepsilon}{2}}{\sigma_i + j\Omega_i}. \quad (29)$$

Formula (13) becomes:

$$\omega_{Zi} = \frac{j\left(1-\frac{\alpha\varepsilon}{2}\right)}{\cos\left(\frac{2i-1}{n}\frac{\pi}{2}\right)}. \qquad (30)$$

An active inverse Hausdorff B-type filter electrical schematics with the same input data is shown on Fig. 5.

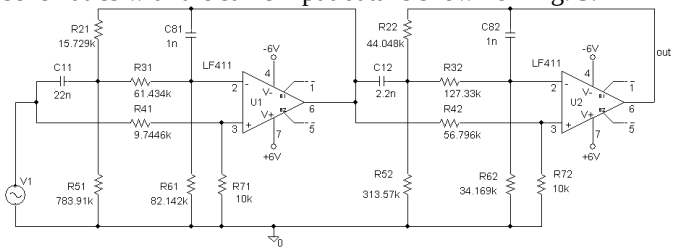

Fig. 5

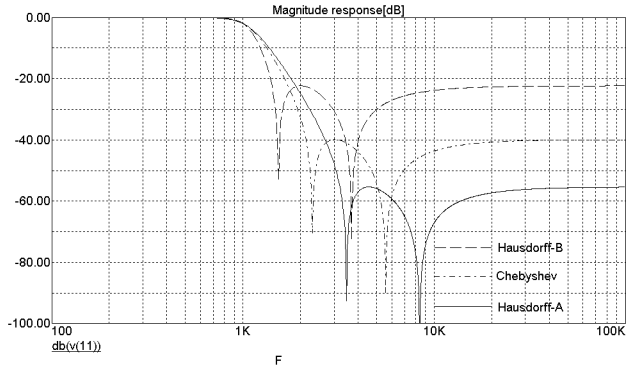

Fig. 6

Active inverse Hausdorff A and B - type frequency characteristics compared to the same input data Chebyshev filter frequency characteristics are shown on Fig. 6, 7 and 8.

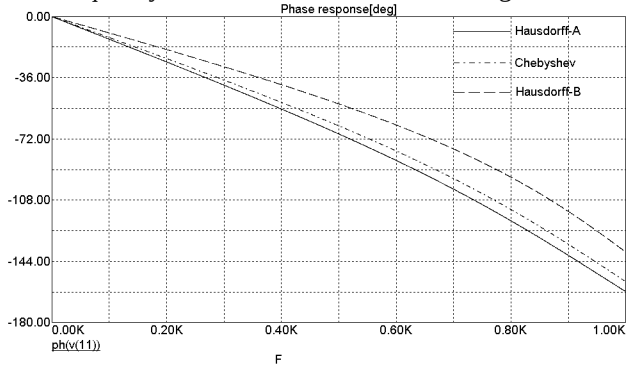

Fig. 7

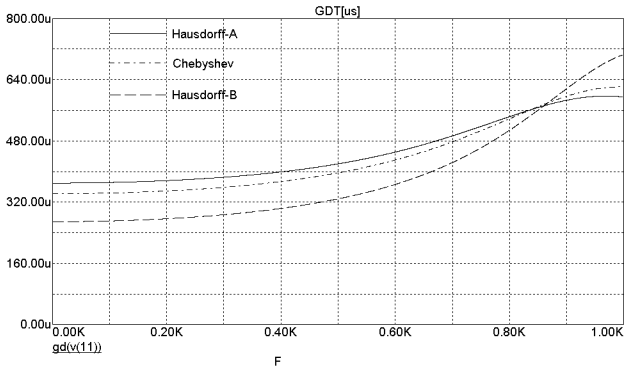

Fig. 8

III. CONCLUSION

On the figures we can see that the two types of inverse Hausdorff filters are complimentary of one another. Compared to Chebyshev's, the first type shortcomings are second type advantages. This leads to greater opportunities in filter design. The frequency characteristics specificity is defined from Hausdorff space with a parameter α. This means that the inverse Hausdorff filters are unique and without analogous using other type of approximation.

REFERENCE

[1] Стоянов, Г., И. Узунов, Л. Райковска и Р. Брадваров. Анализ, "Синтез и проектиране на електрически филтри с персонални компютри". С., Техника, 1991.

[2] Apostolov P. S. "Hausdorff LC Filters", - *ICEST 2004 Conference Proceedings*, pp.59-62, Bitola, Macedonia, 2004.

[3] Schaumann, R., M.E. van Valkenburg, "Design of Analog Filters", Oxford University Press 2001, ISBN 0-19-511877-4.

[4] "Inverse Tshebyschev Tiefpassfilter" - Download http://www.krucker.ch/DiverseDok/Papers.html

Low Sensitivity Design of IIR Filters Obtained as a Tapped Cascaded Interconnection of Identical Allpass Subfilters

Valentina I. Anzova[1], Kamelia S. Ivanova[2], Georgi K. Stoyanov[3]

Abstract – **In this paper an improved method of design of low sensitivity multiplierless IIR digital filter is proposed. First a tapped cascaded interconnection of identical allpass subfilters is designed and then first- and second-order allpass sections with minimized sensitivities are introduced, which is improving considerably the filter behavior in a limited wordlength environment. The method is verified experimentally.**

Keywords – **IIR digital filters, allpass filters, low sensitivity, multiplierless**

I. INTRODUCTION

The number of the structures for realization of recursive digital filters, developed in the last 40 years, appeared to be very high. Most of these structures, however, are having only a textbook value, because when realized in a limited wordlength environment, they behave badly and their magnitude characteristics can not meet even some simple specifications. One of the best known realizations is build as a parallel connection of allpass structures [1]. Even though having extremely low sensitivity in the passband (PB) this realization creates problems in the stopband (SB) and in order to keep the SB attenuation within given limits, it is necessary to work with very high wordlength. A very interesting way to solve this problem was developed in [2], where some additional tap coefficients have been introduced in the parallel structure and then it was decomposed to a cascade of identical substructures. Another way to improve the SB behavior of the parallel allpass structure was advanced in [3] and it was based on the sensitivity minimization of the allpass sections used.

The main aim of this paper is to apply this approach to the structure from [2]. And if it works, to investigate the possibilities to obtain a multiplierless realizations without using some complicated optimization procedures, in order to avoid the degradation of the shape of the filter magnitude, as it was done in [4].

II. DESIGN METHOD DESCRIPTION

In this section we shall introduce briefly the method of Saramaki and Renfors [2]. It starts with a tapped parallel allpass structure, as shown in Fig. 1a, where $A(z)$ and $B(z)$ are all pass filters, usually realized as cascades of first- and second-order allpass sections.

[1]Valentina I. Anzova is with the Faculty of Communications and Communications Technologies, Technical University, Kliment Ohridski 8, 1000 Sofia, Bulgaria, E-mail: via@tu-sofia.bg

[2]Kamelia S. Ivanova is with the Faculty of Communications and Communications Technologies, Technical University, Kliment Ohridski 8, 1000 Sofia, Bulgaria, E-mail: ksi@tu-sofia.bg

[3]Georgi K. Stoyanov is with the Faculty of Communications and Communications Technologies, Technical University, Kliment Ohridski 8, 1000 Sofia, Bulgaria, E-mail: gks@tu-sofia.bg

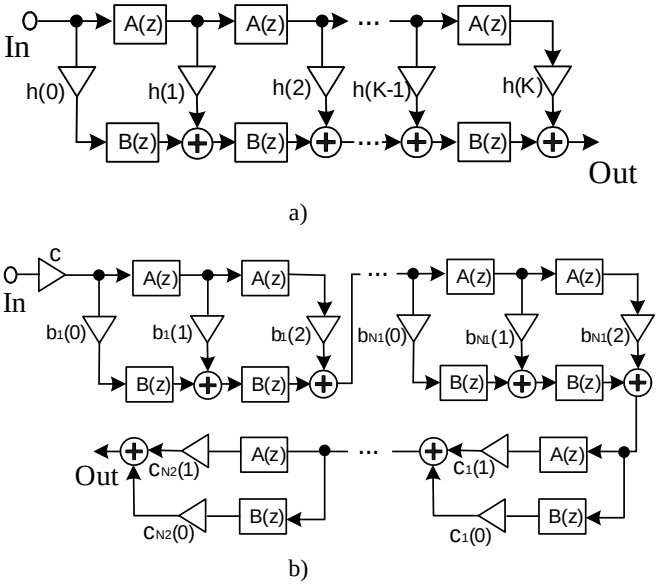

Fig. 1 Initial tapped cascaded interconnection of identical allpass subfilters structure (a); final structure (b)

The overall transfer function of this structure is [2]:

$$H(z) = \sum_{n=0}^{K} h(n)[A(z)]^n [B(z)]^{K-n} \tag{1}$$

The specifications for the overall filter are formulated as

$$\begin{aligned} 1-\delta_p \le |H(e^{j\omega})| \le 1+\delta_p \quad & for\ \omega \in X_p \\ |H(e^{j\omega})| \le \delta_s \quad & for\ \omega \in X_s, \end{aligned} \tag{2}$$

where the PB regions X_p and SB regions X_s may consist of several bands.

The design of the overall filter $H(z)$ can be separated into two parts – the design of a prototype nonlinear phase FIR filter $\tilde{H}(z)$, containing the additional tap coefficients $h(n)$ and the design of an elliptic filter $F(z)$, determining the two allpass sections.

$F(z)$ is an IIR filter implemented as a parallel connection of two allpass filters. The amplitude response of the elliptic filter

$$F(z) = \frac{1}{2}[A(z) + B(z)] \tag{3}$$

is given by

$$|F(e^{j\omega})| = |\cos\{[\varphi_B(\omega) - \varphi_A(\omega)]/2\}| \tag{4}$$

where $\varphi_B(\omega)$ and $\varphi_A(\omega)$ are the phase responses of the allpass filters $A(z)$ and $B(z)$.

The frequency response of the overall filter can be obtained from the frequency response of the prototype filter as it is described in [2]. The frequency transformation

$$\Omega = \varphi_B(\omega) - \varphi_A(\omega), \tag{5}$$

converts PB and SB performance of a prototype nonlinear phase FIR into that of overall filter:

$$\tilde{H}(e^{j\Omega}) = \sum_{n=0}^{K} h(n) e^{-jn\Omega}. \tag{6}$$

Both lowpass nonlinear phase FIR filter and allpass subfilters meet following specifications:

$$\begin{aligned} 1-\delta_p \le |\tilde{H}(e^{j\Omega})| \le 1+\delta_p \quad & for\ 0 \le \Omega \le \Omega_p \\ |\tilde{H}(e^{j\Omega})| \le \delta_s \quad & for\ \Omega_s \le \Omega \le \pi \end{aligned} \tag{7}$$

$$\begin{aligned} 1-\hat{\delta}_p \le |F(e^{j\omega})| \le 1 \quad & for\ \omega \in I_p \\ |F(e^{j\omega})| \le \hat{\delta}_s \quad & for\ \omega \in I_s, \end{aligned} \tag{8}$$

where

$$\hat{\delta}_p = 1-\cos(\Omega_p/2), \quad \hat{\delta}_s = \cos(\Omega_s/2). \tag{9}$$

The optimal allpass sections can be found by designing a minimum odd order lowpass elliptic filter which meets the requirements of Eq. (8). This filter is implemented as a sum of two allpass sections $A(z)$ and $B(z)$ whose orders differ by one. The Herrmann – Schüssler technique (see [2][5] for details) is used for designing the nonlinear phase FIR filter meeting Eq. (7).

III. Allpass Filter Structures

It is well known that digital filters realized as a parallel connection of two allpass structures have an extremely low passband sensitivity and low roundoff noise. But in order to have only real coefficients, the transfer function (3) must be only of odd-order, when it is lowpass or highpass. The allpass branches $A(z)$ and $B(z)$ are usually realized as a cascade connection of first and second order sections. In [2][5] these sections are realized using the well known wave lattice structures (Fig. 2a and Fig. 3a), often called Gray-Markel (GM)- sections [6]. The transfer functions of these sections are:

$$H_{GM1}(z) = \frac{b+z^{-1}}{1+bz^{-1}} \tag{10}$$

$$H_{GM2} = \frac{-a_1 - a_2(1-a_1)z^{-1} + z^{-2}}{1-a_2(1-a_1)z^{-1} - a_1 z^{-2}} \tag{11}$$

The GM-sections are really famous and posses indisputable merits, but our observations show that they behave badly when realizing poles near z=1. It was shown in [3] that much better for realization of such poles are the section ST1 [7] (Fig. 2b) and LS2 [3] (Fig. 3b). The transfer functions of these sections are given by:

$$H_{ST1}(z) = \frac{-(1-a)+z^{-1}}{1-(1-a)z^{-1}} \tag{12}$$

$$H_{LS2} = \frac{1-c_2+(-2+2c_1+c_2)z^{-1}+z^{-2}}{1+(-2+2c_1+c_2)z^{-1}+z^{-2}} \tag{13}$$

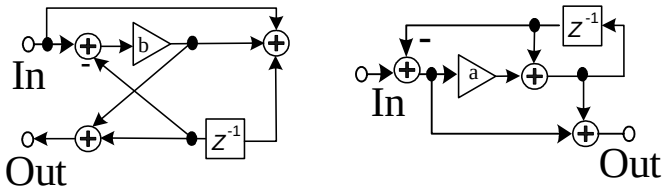

a) GM1 b) ST1

Fig. 2 First-order allpass sections

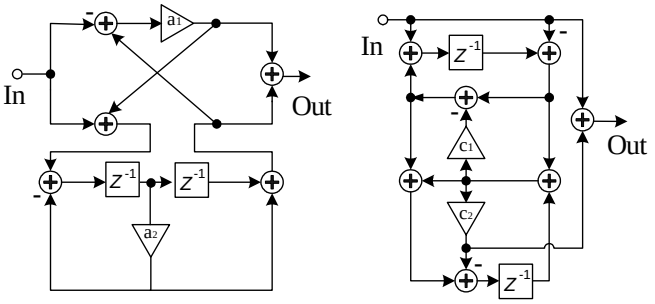

a) GM2 b) LS2

Fig. 3 Second-order allpass sections

We have investigated the sensitivities of the GM1, GM2, ST1 and LS2 for the transfer function coefficient values as given in Table II corresponding to poles very near z=1 (a narrow-band LP filter). The results for the worst-case sensitivities vs. frequency are given in Figs. 4 and 5. It is clearly seen that the low-sensitivity sections ST1 and LS2 are having many times lower sensitivities for all frequencies, but the difference is especially strong at the maximal points. It is expected that after using the low-sensitivity sections, it will be possible generally to shorten the filter coefficients wordlength and, in our case, to introduce handy multiplierless representations of these coefficients without causing some unacceptable degradation of the magnitude shape.

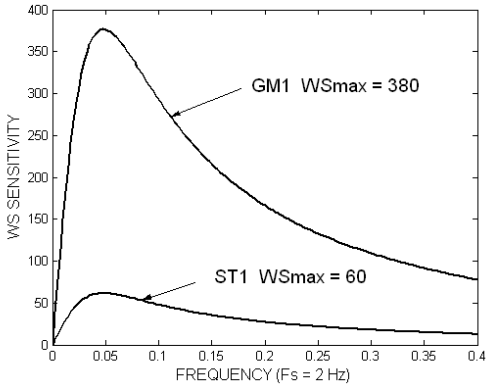

Fig. 4 Worst-case sensitivities of the first-order allpass sections with coefficients *a* and *b* as given in Table II

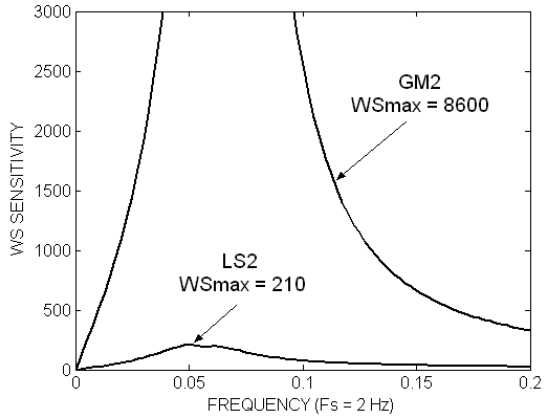

Fig. 5 Worst-case sensitivities of the second-order allpass sections with coefficients a_i and c_i as given in Table II

IV. Experiments and Comparisons

In this experiment a lowpass IIR filter with PB edge $\omega_p = 0.05\pi\ rad/s$ and SB edge $\omega_s = 0.12\pi\ rad/s$ is considered. The maximum ripple in PB is $\delta_p = 0.0009$ and in SB – $\delta_s = 0.000009$. For elliptic filter realized as a parallel connection of two allpass sections, the filter order 9 is estimated.

If the number of subfilters K in structure shown in Fig. 1 is 4, then the estimated order of an elliptic subfilter $F(z)$ is 3. Therefore, the order of $A(z)$ is two, and the order of $B(z)$ is one.

The magnitude of the prototype FIR filter obtained using the method described in [5], is shown in Fig. 6. The best extraripple prototype filter solution meeting the specifications in Eq. 7 has PB and SB frequencies $\Omega_p = 0.14\pi\ rad/s$ and $\Omega_s = 0.9835\pi\ rad/s$. In this case, the required ripples for the elliptic subfilter are $\hat{\delta}_p = 0.024$ and $\hat{\delta}_s = 0.0258$. The prototype filter transfer function $\tilde{H}(z)$ can be factored into one second order section and two first order sections (Fig. 1b). Table I presents received tap coefficients.

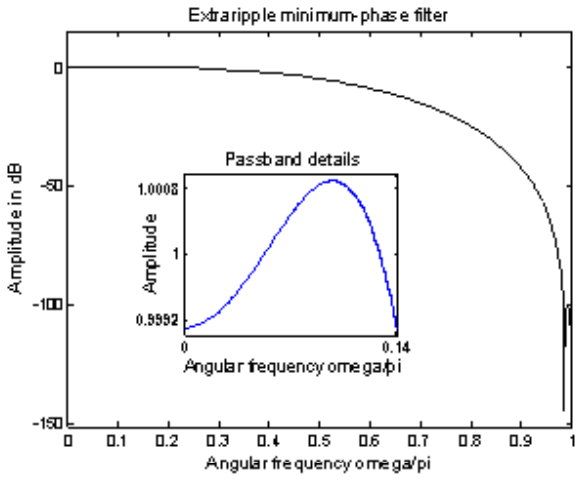

Fig. 6 The prototype FIR filter

TABLE I
QUANTIZED TAP COEFFICIENTS

First order sections		
	$c_k(0)$	$c_k(1)$
First section	$2^{-3}+2^{-4}+2^{-8}$	$2^{-3}+2^{-4}+2^{-8}$
Second section	1	$-2^{-2}-2^{-4}-2^{-5}-2^{-8}$

Second order sections			
	$b_k(0)$	$b_k(1)$	$b_k(2)$
First section	1	2^1-2^{-9}	1

In this paper, different low-sensitivity structures are used for implementation of elliptic subfilter $F(z)$. First, the low-sensitivity sections LS2 and ST1 are used for design of the allpass filters $A(z)$ and $B(z)$. Then, for comparison, the filters $A(z)$ and $B(z)$ are designed with GM-sections. Fig. 7 gives the amplitude responses of the elliptic subfilter $F(z)$ realized with LS2 and ST1 ($F_{LS}(z)$), and by wave lattice sections ($F_{GM}(z)$). Because of the extremely low sensitivities of the sections LS2 and ST1 to the multiplier coefficients variation, the elliptic subfilter $F_{LS}(z)$ realization magnitude does not differ from the ideal after the coefficients are quantized with 8 bits. Fig. 8 gives the optimal amplitude response of the overall filter and PB and SB details. It is clear from this figure that filter implemented with subfilters $F_{LS}(z)$ meets filter specification in Eq. 2 without general multipliers better than filter realized with subfilters $F_{GM}(z)$. All the coefficient values in Table II are representable as a sum of powers of two.

TABLE II
QUANTIZED COEFFICIENTS FOR ALLPASS SUBFILTERS

	Low sensitivity		Wave lattice
a	$2^{-3}+2^{-6}$	b	$2^0-2^{-3}-2^{-6}$
c_1	2^{-6}	a_1	$-2^0+2^{-3}-2^{-7}$
c_2	$2^{-3}-2^{-6}$	a_2	$2^0-2^{-5}+2^{-7}$

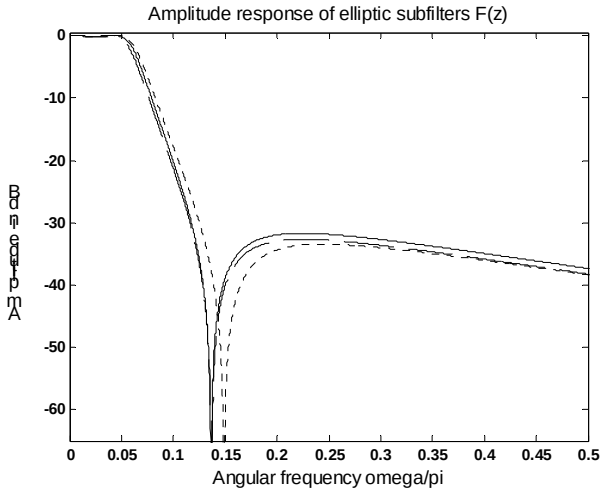

a)

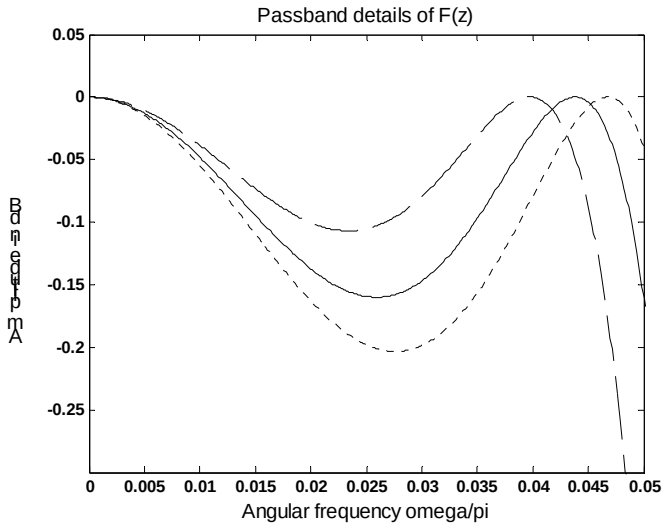

b)

Fig. 7 The amplitude response - solid line; $F_{LS}(z)$ - dashed line and and $F_{GM}(z)$ – dotted line a) overall filter $F(z)$ b) passband details

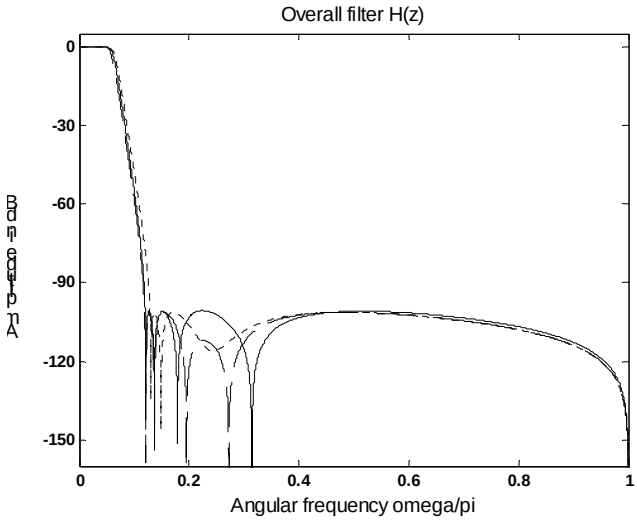

a)

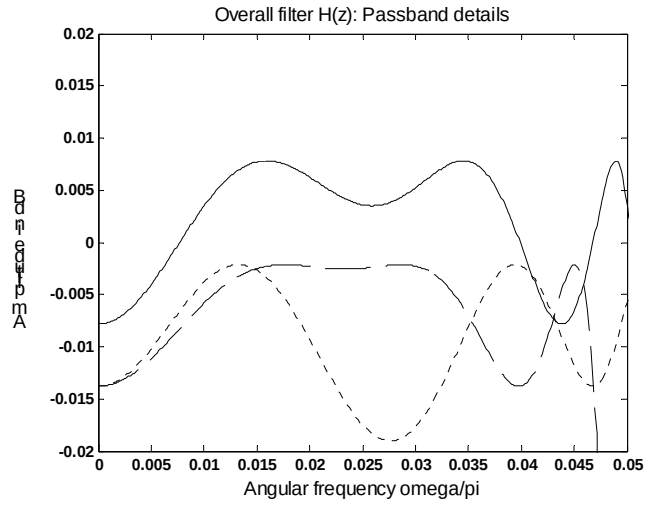

b)

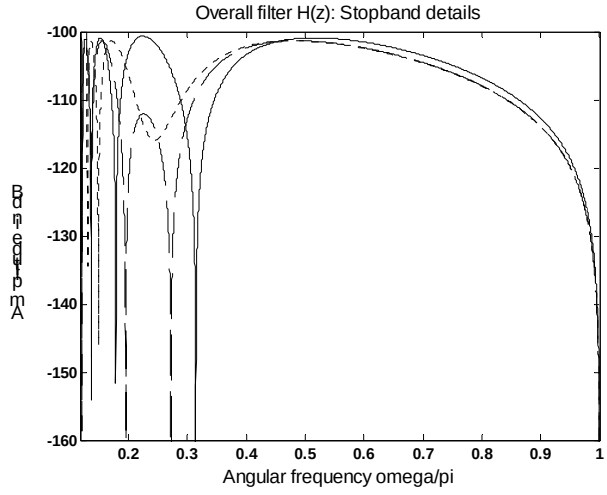

c)

Fig. 8 The amplitude response: a) the overall original IIR filter - solid line; quantized filter with $F_{LS}(z)$ subfilters - dashed line and quantized filter with $F_{GM}(z)$ subfilters – dotted line b). Passband details c). Stopband details

V. CONCLUSION

A substantial improvement of the method of Saramaki and Renfors for design of recursive digital filters was achieved in this paper by introduction of an additional step in the design procedure. It was shown that the sensitivity of the stopband attenuation can be considerably reduced if the allpass sections used in the subfilters are with minimized sensitivities for the stopband frequency range. As a result, it becomes possible to reduce the coefficient wordlength or to simplify the multiplierless representation of these coefficients without destroying the magnitude shape. Shorter coefficients means, on the other hand, lower power consumption, which is very important for portable telecommunication equipment realizations.

REFERENCES

[1] S. Mitra**,** Digital signal processing: a computer-base approach, Second Edition, McGraw-Hill, 2001.

[2] T. Saramäki and M. Renfors, "A novel approach for the design of IIR filters as a tapped cascaded interconnection of identical allpass subfilters", *in Proc. 1987 IEEE Int. Symp. Circuits Syst. (Philadelphia, PA)*, pp. 629–632, May 1987.

[3] G. Stoyanov and M. Kawamata, "Improved tuning accuracy design of parallel-allpass-structures-based variable digital filters", *Proc. ISCAS'98, Monterey, California*, Vol. 5, pp. V-379-V-382, May 1998.

[4] J. Kaakinen and T. Saramäki, Design of very low-sensitivity and low-noise recursive filters using a cascade of low-order lattice wave digital filters. *IEEE Trans. Circ. Syst.* –II, Vol. 46, No7, pp.906-913, July 1999.

[5] T.Saramäki, "Scripts on System level DSP Algorithms", *Internal Edition of Signal Processing Lab*, Tampere University of Technology, Tampere, Finland.

[6] R. Ansari, B. Liu, "A class of low-noise computationally efficient recursive digital filters with applications to sampling rate alterations", *IEEE Trans. Acoust., Speech, Signal Processing*, Vol. ASSP-33, pp. 90-97, Feb. 1985.

[7] G. Stoyanov and H. Clausert, A comparative study of first order digital all-pass structures, "*Frequenz*", vol. 48, No 9/10, Sept./Oct. 1994 pp. 221-226

A New Adaptive Complex Narrowband Fourth-Order IIR Filter Section

Zlatka Nikolova[1], Georgi Iliev[2], Georgi Stoyanov[3]

Abstract – **In this paper a very low sensitivity fourth-order complex band-pass filter section with independent tuning of the central frequency and the bandwidth is developed. Then, a band-stop adaptive filter structure is formed around this section, using LMS algorithm to adapt the central frequency. The developed filter circuit is providing a low computational complexity and a very fast convergence.**

Keywords – **complex digital filters, sensitivity, adaptive digital filters.**

I. INTRODUCTION

Adaptive notch filters are indispensable for many digital signal processing (DSP) applications to separate, enhance or track narrow-band and sinusoidal signals mixed with a broadband noise. If such signal consists of real and imaginary parts, a complex coefficients adaptive filter must be implemented.

The complex adaptive systems are subjects of study in a great number of publications. In [1] a new complex adaptive notch filter for parameter estimation of complex sinusoids and chirp signals mixed with wideband noise is proposed. A complex multirate filter-bank-based adaptive notch filter is developed to solve the co-existing problem of CDMA and TDMA systems [2]. Reference [3] investigates digital complex adaptive filter algorithms to cancel the radio frequency interference in VDSL system. In [4] cascaded realization of complex adaptive infinite impulse response (IIR) notch filters are discussed.

In all this works, like in many others, the attention is focused mainly on the adaptive algorithms, their efficiency and methods of improvement. But the adaptive complex circuits used and their properties couldn't be neglected as they influence significantly the quality of the adaptive process. These circuits are, however, merely mentioned in [1]– [4] and they tend, generally to be quite complicated.

In this paper we develop a fourth-order complex band-pass (BP) filter section with independent tuning of the central frequency and bandwidth (BW). The new complex variable filter conducts very well in finite word-length environment and demonstrates very low coefficient sensitivity without influence of both – variable and adaptive processes parameters.

The paper is organized as follows. The fourth-order variable complex digital filter is derived and investigated in section 2. Section 3 defines the system model for adaptive complex narrowband filtering. In section 4, simulation results for elimination/enhancement of narrow-band complex signals are presented and discussed. Finally, section 5 concludes the paper.

[1] Zlatka Nikolova is with the Dept. of Telecommunications, Technical University of Sofia, Bulgaria, e-mail: zvv@tu-sofia.bg
[2] Georgi Iliev is with the Dept. of Telecommunications, Technical University of Sofia, Bulgaria, e-mail: gli@tu-sofia.bg
[3] Georgi Stoyanov is with the Dept. of Telecommunications, Technical University of Sofia, Bulgaria, e-mail: gks@tu-sofia.bg

II. COMPLEX DIGITAL FILTER CIRCUIT DERIVATION

We shall try now to develop a fourth-order variable complex digital filter satisfying the following requirements. The filter must be of IIR type in order ensure higher selectivity with lower order transfer function. It should contain canonical number of multipliers and delays and it must be free of parasitic effects like delay-free loops. The last problem can be avoided after applying a proper design procedure, like the proposed in [5] new method of design of complex variable BP/BS filters with independently tuneable central frequency and BW. That method provides wider range of tuning of the BW and higher freedom of the central frequency tuning. The new filter should have low coefficient sensitivity in order to decrease the degradation of its magnitude characteristic after the coefficients are quantized. And we try to develop narrow-band variable BP filters because such filters are needed for most of the practical applications.

A proper real LP second-order circuit, such as to satisfy above-described requirements is the filter section shown in Fig. 1, good properties of which are certainly proved in [5], [6] after detailed investigations.

In order to make the LP filter BW-variable, we apply on $H(z)$ (2) the Constantinides LP to LP spectral transformation:

$$z^{-1} \rightarrow \frac{z^{-1}-\beta}{1-\beta z^{-1}}. \qquad (1)$$

Afterwards expand the coefficients functions of β into Taylor series taking the linear terms only in order to avoid delay-free loops, according to the well known procedure proposed in [7].

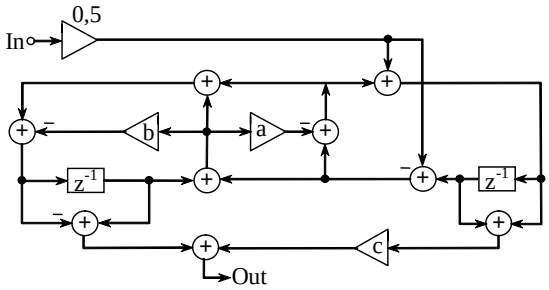

Fig.1 Real-coefficients second-order low-sensitivity LP filter section

The transfer function this section realizes is:

$$H(z)=\frac{(ac-b)-(a-2)}{2c}\,\frac{1+2\dfrac{(ac+b)+(a-2)}{(ac-b)-(a-2)}z^{-1}+z^{-2}}{1+(2a+b-2)z^{-1}+(1-b)z^{-2}}\,. \qquad (2)$$

Then we replace the multiplier coefficients a, b and c in the section (Fig. 1) by the composite multipliers ($\hat{a}$, $\hat{b}$ and $\hat{c}$) containing also β, after applying the LP to LP spectral transformation (1). Thereby, the transfer function $H_V(z)$ of the BW-variable LP filter is obtained. It is easy to show that $\hat{c}$ is independent of β, i.e. $\hat{c}=c$. Thus, we have two variable by β multipliers $\hat{a}=a+\beta.f$ and $\hat{b}=b+\beta.e$, where f and e are coefficients calculated by means of a and b as follows: $f=a(2a+b-4)$ and $e=b(2a+b-2)$. The structure of a composite multiplier is shown in Fig 2

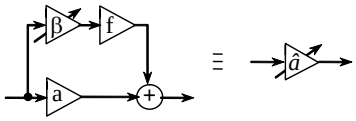

Fig.2 The composite multiplier obtained after Constantinides LP to LP spectral transformation and followed Taylor series truncation

The rotation transformation:

$$z=ze^{-j\theta} \text{ or } z^{-1}=z^{-1}(\cos\theta+j\sin\theta)\,, \qquad (3)$$

applied on $H_V(z)$ generates the BP complex coefficient transfer function $H_{CV}(z)$, which is variable with respect to both the BW and the central frequency. As complex function $H_{CV}(z)$ can be presented by two real coefficients fourth-order functions:

$$H_V(z)\xrightarrow{z=ze^{-j\theta}}H_{CV}(z)=H_R(z)+jH_I(z)\,, \qquad (4)$$

and realized by the complex structure in Fig.3.

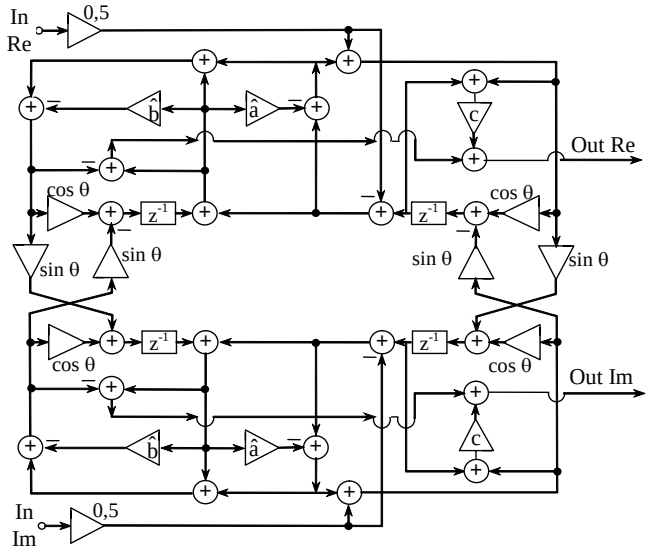

Fig.3 Complex-coefficient fourth-order low-sensitivity BP filter section

Having two inputs and two outputs (both couples real and imaginary), the structure is described by four real-coefficient BP transfer functions two by two equal with ±sign and related to $H_{CV}(z)$ as follows:

$$H_{RR}(z)=H_{II}(z)=H_R(z)=\frac{B_2-B_3}{2c}\,\frac{1+A\left(\dfrac{4B_3}{B_2-B_3}+B_1\right)z^{-1}+}{1+2A(B_1-2)z^{-1}+}\times$$
$$\times\frac{+\left[\dfrac{2(B_2+B_3)(B_1-2)}{B_2-B_3}+(1-B_4)(A^2-C^2)\right]z^{-2}+A\left(\dfrac{2B_4(B_2+B_3)}{B_2-B_3}+B_1-2\right)z^{-3}+B_4z^{-4}}{+\left[(B_1-2)^2+2B_4(A^2-C^2)\right]z^{-2}+2AB_4(B_1-2)z^{-3}+B_4^2z^{-4}} \qquad (5)$$

and

$$H_{RI}(z)=-H_{IR}(z)=H_I(z)=\frac{B_2-B_3}{2c}\cdot$$
$$\frac{C\left(\dfrac{4B_2}{B_2-B_3}-B_1\right)z^{-1}+2AC(1-B_4)z^{-2}+C\left[(B_1-2)-\dfrac{2B_4(B_2+B_3)}{B_2-B_3}\right]z^{-3}}{1+2A(B_1-2)z^{-1}+\left[(B_1-2)^2+2B_4(A^2-C^2)\right]z^{-2}+2AB_4(B_1-2)z^{-3}+B_4^2z^{-4}} \qquad (6)$$

where

$$B_1=2\hat{a}+\hat{b};\ B_2=\hat{a}c-\hat{b};\ B_3=\hat{a}-2;$$
$$B_4=1-\hat{b};\quad A=\cos\theta;\quad C=\sin\theta \qquad (7)$$

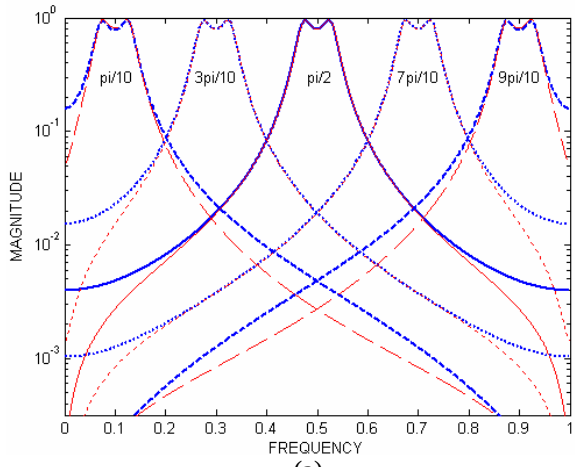

(a)

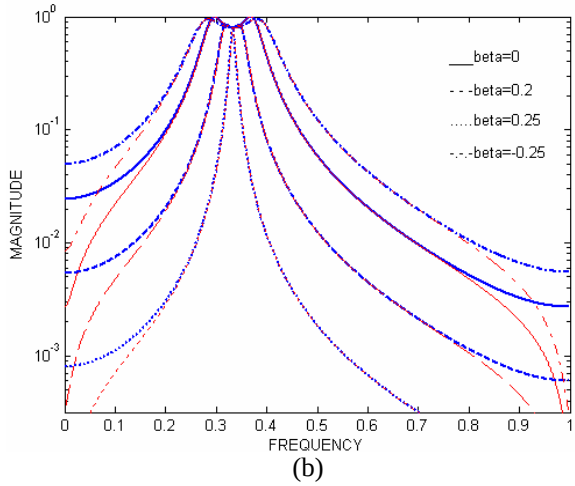

(b)

Fig.4 Magnitude responses of the variable complex BP fourth-order filter for (a) different values of θ; (b) different values β.

The BW of the obtained variable complex filter can be turned by changing of β, while the central frequency can be shifted by changing of θ.

In Fig.4a it is shown how the central frequency of the magnitude responses of $H_R(z)$ (5) (the bold lines) and $H_I(z)$ (6) is turned by trimming of θ, while β=0.13 is fixed. The tuning of the BW by changing β and fixed $\theta=\pi/3$ is without problems for rather wide range as it is shown in Fig.4b.

It is well known that all the properties (sensitivity including) of the real LP/HP prototype will be inherited by the complex BP/BS filter, obtained after the transformation (3) is applied. It was shown in [6] that both filters real and complex have very low coefficient sensitivity. The behavior of the complex section in a limited word-length environment is also investigated (Fig.5). Obviously the magnitude response isn't destroyed even for very short word-length.

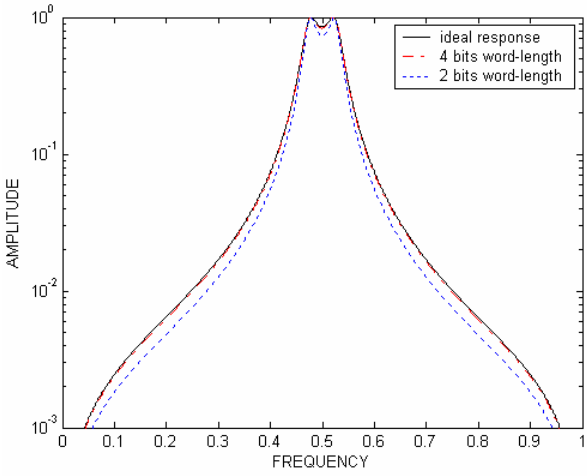

Fig.5 Magnitude responses of the variable complex BP fourth-order filter section for different word-length $(\theta=\pi/2;\beta=0.15)$.

III. Adaptive Complex Narrowband Filtering

In Fig. 6 the block-diagram of the new adaptive filter is shown. In the following we consider the input/output relations for corresponding BP/BS filters - equations (8)-(11).

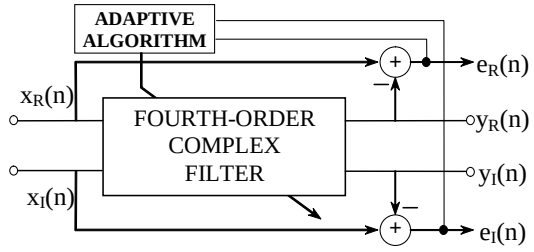

Fig. 6 Block-diagram of a versatile adaptive complex narrowband filter

For the BP filter we have the following real output:

$$y_R(n)=y_{R1}(n)+y_{R2}(n), \quad (8)$$

where $y_{R1}(n)$ is the part of the real output signal when the input signal is $x_R(n)$, while $y_{R2}(n)$ is obtained when $x_I(n)$ is the input signal. Similarly, for the imaginary output we get:

$$y_I(n)=y_{I1}(n)+y_{I2}(n). \quad (9)$$

For the band-stop filter we have - real output:

$$e_R(n)=x_R(n)-y_R(n), \quad (10)$$

and imaginary output

$$e_I(n)=x_I(n)-y_I(n). \quad (11)$$

The cost-function is the power of band-stop filter output signal:

$$[e(n)e^*(n)], \quad (12)$$

where

$$e(n)=e_R(n)+je_I(n). \quad (13)$$

We apply a Least Mean Squares (LMS) algorithm to update the filter coefficient responsible for the central frequency as follows:

$$\theta(n+1)=\theta(n)+\mu\mathrm{Re}[e(n)y'^*(n)], \quad (14)$$

μ is the step size controlling the speed of convergence, (*) denotes complex-conjugate, $y'(n)$ is the derivative of $y(n)=y_R(n)+jy_I(n)$ with respect to the coefficient subject of adaptation.

IV. Experiments

We test our filter for elimination/enhancement of narrowband complex signals. Input signal is a mixture of white noise and complex (analytic) sinusoidal signal.

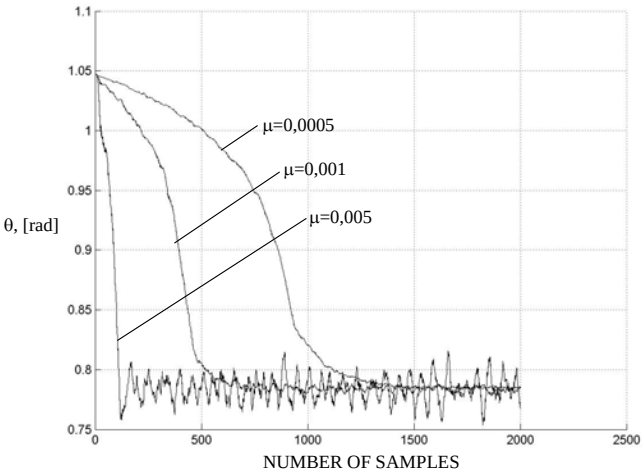

Fig. 7: Trajectories of filter coefficient θ for different step size μ

In Fig. 7 the learning curves for different values of step size μ are shown. It is seen that for μ>0.001 the convergence is so fast that it takes less than 100 iterations to adapt.

In Fig. 8 the results for different filter bandwidth are presented. It is obvious that the filter is behaving quite conventionally. It should be mentioned that if some other (non low-sensitivity) LP-prototype was used, the coefficient β could not take values larger than 0.06-0.1 without destroying the magnitude shape. Thus we can always obtain a faster convergence because of the wider BW.

Finally, in Fig. 9 we show the behaviour of our filter for quite a wide range of sinusoidal frequencies. It is seen that in all the cases our filter converges to the proper frequency value.

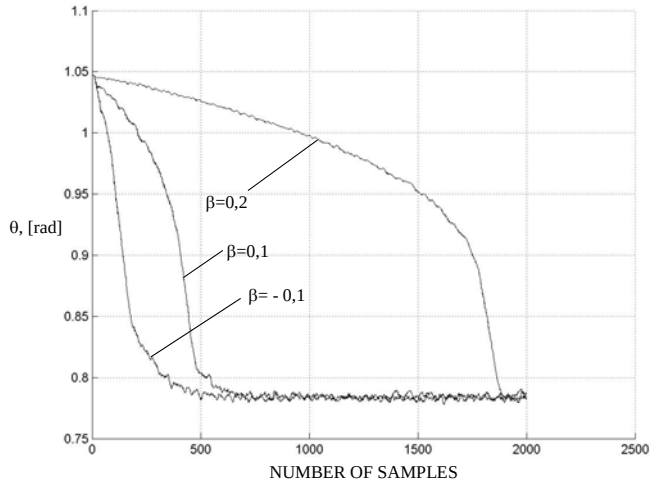

Fig. 8: Trajectories of filter coefficient θ for different BW

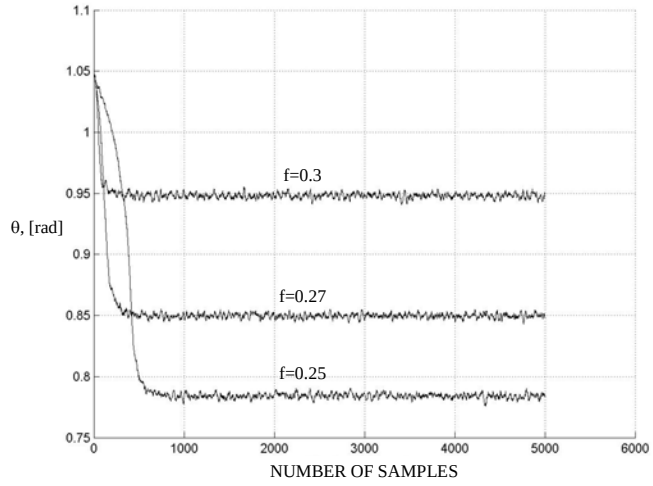

F ig. 9: Trajectories of filter coefficient θ for different central frequency

V. CONCLUSIONS

A very low-sensitivity variable complex fourth-order BP filter section with very precise and completely independent tuning of the BW and central frequency was designed in this work. The improved method of design permits the BW to be tuned in much wider frequency range compared to other well known methods and without any requirements to fix some of the cutoff frequencies. By changing the transformation factor θ , the cen - tral frequency is able to be tuned over the entire frequency band also adaptively by applying an LMS algorithm. The accuracy of tuning is very high and it is possible to use coefficients with shorter word-length decreasing thus the power consumptions for both, adaptive filtering and updating the coefficients.

The convergence of the adaptive algorithm for the developed variable complex filter is investigated experimentally and the efficiency of the adaptation is indisputable proved.

The main advantages of the proposed adaptive complex structure could be summarized as follows: very low coefficient sensitivity providing resistance against quantization effects, very high accuracy of tuning and adaptation – features very important for telecommunication applications. The structure is demonstrating a very fast convergence and has a low computational complexity.

REFERENCES

[1] Soo-Chang Pei and Chien-Cheng Tseng, “Complex adaptive IIR notch filter algorithm and its applications”. *IEEE Transactions on Circuits and Systems II: Analog and Digital Signal Processing*, vol. 41, No. 2, pp. 158-163, Feb. 1994.

[2] S. Hara, T. Matsuda, K. Ishikura and N. Morinaga, “Coexistence problem of TDMA and DS-CDMA systems-application of complex multirate filter bank”, *Global Telecommunications Conference, 1996. GLOBECOM '96. 'Communications: The Key to Global Prosperity*, vol. 2, pp. 1281–1285, 1996.

[3] Yaohui Liu, Timo I. Laakso, Paolo S.R. Diniz. ”Adaptive RFI Cancelation in VDSL Systems”, *ECCTD’01- European Conference on Circuit Theory and Design*, August 28-31, 2001, Espoo, Finland

[4] S. Nishimura and Hai-Yun Jiang, “Cascaded realization of complex adaptive IIR notch filters”, *Proc. of the 40th Midwest Symposium on Circuits and Systems*, vol.2, pp. 691–693, 1997.

[5] G. Stoyanov and Zl. Nikolova, “Improved Method of Design of Complex Coefficients Variable IIR Digital Filters”, *TELECOM’99*, Varna, Bulgaria, vol. 2, pp.40-46, Oct. 1999.

[6] G. Stoyanov, M. Kawamata, Zl. Valkova. “New first and second-order very low-sensitivity bandpass/ bandstop complex digital filter sections”. *Proc. IEEE 1997 Region 10th Annual Conf. "TENCON’97"*, Brisbane, Australia, vol. 1, pp. 61-64, Dec. 2-4, 1997

[7] S. Mitra, Y. Neuvo, H. Roivainen. ”Design of recursive digital filters with variable characteristics”. *Int. J. Circuits Theory Appl.*, vol.18, pp.107-119. 1990.

Convergence Analysis of an LMS Adaptive Low Sensitivity Biquadratic Digital Filter Section

Maria Nenova[1], Georgi Iliev[2], Georgi Stoyanov[3]

Abstract – **This paper presents a mean convergence analysis of a low sensitivity biquadratic filter section transformed into adaptive by using an LMS algorithm. The structure allows independent tuning of the central frequency and the bandwidth of the bandpass/bandstop realizations. The mean convergence analysis of the adaptation process is then presented. All results received for theoretical bounds are also verified experimentally.**

Keywords –**notch IIR structure, adaptive LMS algorithm, convergence analysis**

I. INTRODUCTION

Over the years, a variety of IIR structures for adaptive digital filters have been investigated and implemented [1], [2], [3]. Many of them are second-order sections [2], but they are not useful for a realization in the low frequency band, because of their high sensitivity. A biquadratic section (called BQ3) is investigated thoroughly in [4], [5] and in [4] BQ3 is improved so that the section is very efficient for applications in the low frequency band, resulting from its considerably low sensitivity of the poles near z=1. An important feature when designing second-order section is that they should employ a canonic number of multipliers (two in BQ3) in contrast to the structures investigated in [6]. This second-order section is also implemented here because it allows independent tuning of the central frequency and the bandwidth of bandbasss/bandstop realizations.

Initially, the adaptive algorithms were of Gauss-Newton's type or its simplifications [1], [6], [7]. Most of them include modifications of the gradient oriented algorithms as in [3]. Moreover in [7] it is shown that a significant number of those algorithms have a high computational complexity and slow convergence. In [8] a modification of the least-squares algorithm is proposed, avoiding matrix inversion and having very fast convergence.

In this paper the BQ3 section is first transformed into adaptive by incorporating an LMS adaptive algorithm. This algorithm is one of the widely used in the adaptive signal processing,because of its low computational complexity.

Then mean convergence analysis, similar to the one in Ref.[1] is performed.

[1]Maria V. Nenova is with the Faculty of Communications and Communications Technologies, Technical University, Kliment Ohridski 8, 1000 Sofia, Bulgaria, E-mail: mvn@tu-sofia.bg

[2]Georgi L. Iliev is with the Faculty of Communications and Communications Technologies, Technical University, Kliment Ohridski 8, 1000 Sofia, Bulgaria, E-mail: gli@tu-sofia.bg

[3]Georgi K. Stoyanov is with the Faculty of Communications and Communications Technologies, Technical University, Kliment Ohridski 8, 1000 Sofia, Bulgaria, E-mail: gks@tu-sofia.bg

Finally some experiments are conducted to verify the theoretical results.

II. DESIGN METHOD DESCRIPTION

The biquadratic section BQ3, given in Fig.1 was proposed in [4],[5], it is realizing (at different outputs) bandpass/bandstop transfer functions and it was shown that it has extremely low sensitivities for pole near z=1.

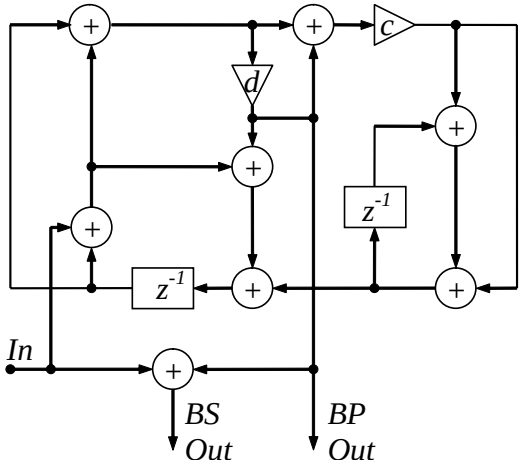

Fig. 1 Biquadratic section BQ3 with its BP and BS outputs

The transfer functions at the BP and BS output of the structure are [5]:

$$H_{BP}(z)=\frac{d(1-z^{-2})}{1+(-2+4c+2d-4cd)z^{-1}+(1-2d)z^{-2}}, \quad (1)$$

$$H_{BS}(z)=\frac{(1-d)[1-2(1-2c)z^{-1}+z^{-2}]}{1+(-2+4c+2d-4cd)z^{-1}+(1-2d)z^{-2}}. \quad (2)$$

Their bandwidth BW:

$$BW=\cos^{-1}\frac{1-2d}{1-2d+2d^{2}}, \quad (3)$$

is depending only on *d*, so it can be controlled and tuned independently.

The central frequency depends generally on the coefficients *c* and *d*, but once the BW is tuned and *d* – fixed, this frequency can easily be tuned by changing *c*.

When the BS output is used:

$$\theta_z=\cos^{-1}(1-2c) \quad (4)$$

III. LMS Adaptive Algorithm

Usually when a BS filter is used for adaptive tracking of a narrow band signal. The BW is fixed to some given value and thus only the center frequency becomes a subject of adaptation. It is seen from (4) that in BQ3 it could easily be performed by changing *c*. If the adaptation is done according to the Least Mean Squares algorithm, the updated value of *c* will be calculated as:

$$c(n+1) = c(n) - \mu e(n) g(n). \tag{5}$$

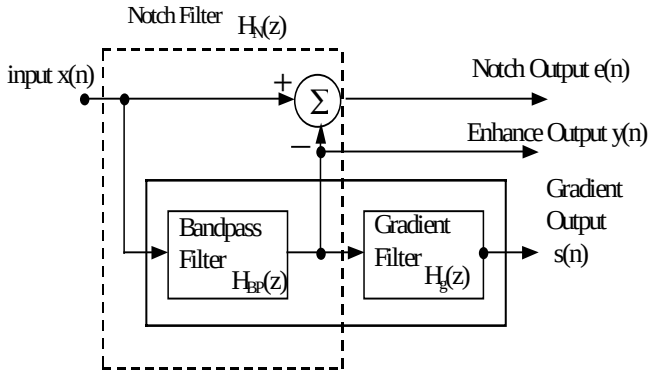

Fig.2 An adaptive IIR notch filter

The adaptive notch filter configuration and the whole structure are shown in Fig.2.

In equation (5) $g(n)$ is the gradient function of $e(n)$ with respect to the coefficient *c*. If $e(i)$ represents the error signal at the BS output on Fig.1 and $x(i)$ is the input signal, we can easily obtain from Eq.(2) the following difference equation:

$$\begin{aligned} e(i) = {} & (1-d)x(i) + (-2 + 4c(i) + 2d - 4dc(i))x(i-1) \\ & + (1-d)x(i-2) - (-2 + 4c(i) + 2d - 4dc(i)) \\ & e(i-1) - (1-2d)e(i-2). \end{aligned} \tag{6}$$

Hence the signal $g(n)$ in function of *c* is:

$$g(i) = \frac{\partial e(i)}{\partial c(i)} = 4(1-d)[x(i-1) - e(i-1)]. \tag{7}$$

IV. Mean Convergence

Let's assume that the input signal consists of an unknown sinusoid and a noise. The noise is white Gaussian with zero-mean

$$x(i) = A\cos(\omega_0 i + \theta) + v(i)\,, \tag{8}$$

where A represents the sinusoid amplitude, θ is the initial phase, ω_0 is the angular frequency and $v(i)$ is the noise. The frequency of the input sinusoid is estimated by searching the optimum coefficient *c* for which the adaptation error is minimal.

Investigations are based on the assumption of the local linearization [9] of the gradient function about the point where the function is stationary, the error surface is flat in areas far from the minimum and is steepest near the stationary point It gives us a possibility to constrain stability bounds for μ around the area of the optimal solution.

The signals $e(i)$ and $g(i)$can be expressed not only with a difference equations, but also as:

$$e(i) = \left|H_N(e^{j\omega_0})\right| A\cos(\omega_0 i + \theta + \varphi_N(\omega_0)) + v_1(i), \tag{9}$$

$$g(i) = \left|H_g(e^{j\omega_0})\right| A\cos(\omega_0 i + \theta + \varphi_g(\omega_0)) + v_2(i). \tag{10}$$

Here $H_g(e^{j\omega_0})$ is the gradient transfer function and $H_N(e^{j\omega_0})$ is the notch transfer function.

Because of the linearization about the stationary point it can be presumed that near this point the notch transfer function is a linear function of *c*. Therefore the gradient function is constant

$$H_{BP}(e^{j\omega_0}) = \frac{d(1-e^{-2j\omega_0})}{D(e^{j\omega_0})} \approx 1. \tag{11}$$

Hence the denominator $D(z)$ can be approximated to:

$$D(e^{j\omega_0}) \approx d(1-e^{-2j\omega_0}). \tag{12}$$

Substituting (11) and (12) into the expression for the bandpass transfer function and the gradient transfer functions result in:

$$\begin{aligned} H_{BS}(e^{j\omega_0}) &= \frac{4(1-d)e^{-j\omega_0}c^*}{D(e^{j\omega_0})} = \frac{4(1-d)e^{-j\omega_0}c^*}{d(1-e^{-2j\omega_0})} = \\ &= \frac{2(1-d)c^*}{d\sin\omega_0}, \end{aligned} \tag{13}$$

$$\begin{aligned} H_g(e^{j\omega_0}) &= \frac{4(1-d)e^{-j\omega_0}}{D(e^{j\omega_0})} = \frac{4(1-d)e^{-j\omega_0}}{d(1-e^{-2j\omega_0})} = \\ &= \frac{2(1-d)}{d\sin\omega_0}. \end{aligned} \tag{14}$$

For simplification we use the following notation for the common term of (13) and (14):

$$B = \frac{2(1-d)}{d\sin\omega_0}. \tag{15}$$

The exact value of the adaptive coefficient *c* is:

$$c = \delta + c^*, \tag{16}$$

where δ represents the deviation from the optimal solution c^*. For further simplification we introduce:

$$\gamma_i = \omega_0 i + \theta + \varphi(\omega_0). \tag{17}$$

into (9) and (10) and, having in mind (11) – (14)finally get:

$$e(i) \approx AB(c^* + \delta)\cos(\gamma_i) + v_1(i), \quad (18)$$

$$g(i) \approx AB\cos(\gamma_i) + v_2(i). \quad (19)$$

V. Mean Convergence Analysis

Using the expression for the adaptive algorithm in (5) and (16) $\delta(i) = c(i) - c^*$ we derive the update of the adaptive coefficient c :

$$\begin{aligned}\delta(i+1) \approx \delta(i) - \mu[&A^2B^2(c^* + \delta)\cos^2(\gamma_i) + \\ &ABc^*\cos(\gamma_i)v_2(i) + AB\cos(\gamma_i) \\ &v_1(i) + v_1(i)v_2(i)].\end{aligned} \quad (20)$$

In order to perform the mean analysis we introduce some additional, simplifications similar to those in [1]. The sinusoid phase θ is assumed to be uniformly distributed in [-π, π] and the white Gaussian noise has a variance σ^2_n. We have assumed that there is approximately no correlation between $cos(\gamma_i)$ and $v_1(i)$, as well as between $cos(\gamma_i)$ and $v_2(i)$. Consequently, the correlation between $cos(\gamma_i)$ and $\delta(i)$ and between $v_1(i)$ and $v_2(i)$ is zero, because they are uncorrelated.

Using this assumptions for the mathematical expectation of $\delta(i)$ the expression (20) becomes:

$$E[\delta(i+1)] \approx E[\delta(i)] - \mu E\begin{bmatrix} A^2B^2\delta(i)\cos^2\gamma_i + \\ + A^2B^2c^*\cos^2\gamma_i \end{bmatrix}. \quad (21)$$

If we neglect the term not containing $\delta(i)$ we finally get:

$$E[\delta(i+1)] \approx E[\delta(i)]\left(1 - \mu\frac{A^2B^2}{2}\right). \quad (22)$$

If the algorithm is to be stable it is required that :

$$\left|1 - \mu\frac{A^2B^2}{2}\right| < 1. \quad (23)$$

We have chosen a stricter criterion for μ than what is taken in[1], as seen from (21). Solving the expression (23) with respect to μ we will obtain:

$$0 < \mu < \frac{d^2\sin^2\omega_0}{A^2(1-d)^2} \equiv \mu_{\max}. \quad (24)$$

The step size depends on the sinusoid amplitude and on d which is responsible for the pole radius.

This expression shows how to control the upper bound of the step size μ and the dependence of μ on the sinusoid amplitude and the pole radius expressed by:

$$d = \frac{1-r^2}{2}. \quad (25)$$

VI. Simulation Results

The simulation are made for the signal-to-noise ratio SNR=20dB and SNR=10dB. For SNR=20dB, the amplitude of the input sinusoid is unity and the noise variance σ_n^2 is 0.1. The step size μ and coefficient d are varied in order to investigate the adaptation process for different values. Experiments are performed with f_s=8 kHz.

The adaptation process of the LMS algorithm in (5) to sinusoid with frequency 200Hz, for different bandwidths is illustrated in Fig. 3.

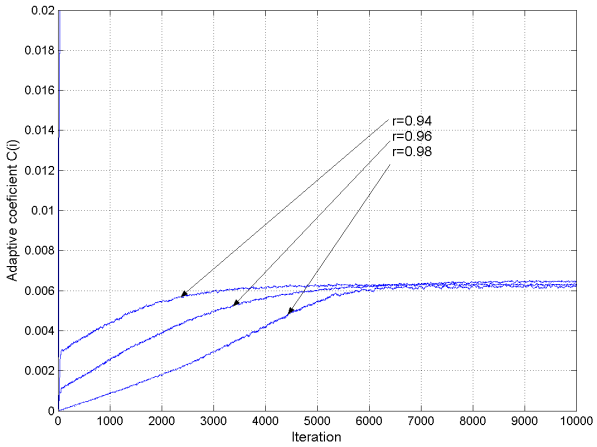

Fig. 3 Adaptation with different bandwidths for frequency of 200Hz

From the learning curves it can be concluded that the greater the pole radius/BW is, the faster the adaptation speed is.

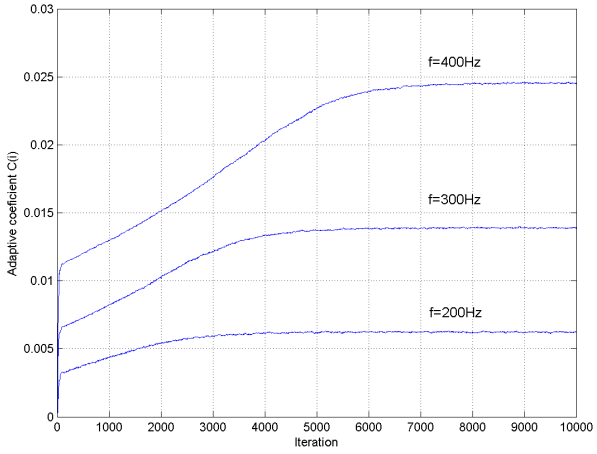

Fig.4 Investigation of tracking of different frequencies with SNR=10dB

It is seen that the best result is achieved for the lowest frequency, which is due to the implemented structure features.

The theoretical bounds for the step size μ for different pole radii are compared graphically with the experimental bounds for a sinusoidal signal with a frequency of 200Hz in Fig.5:

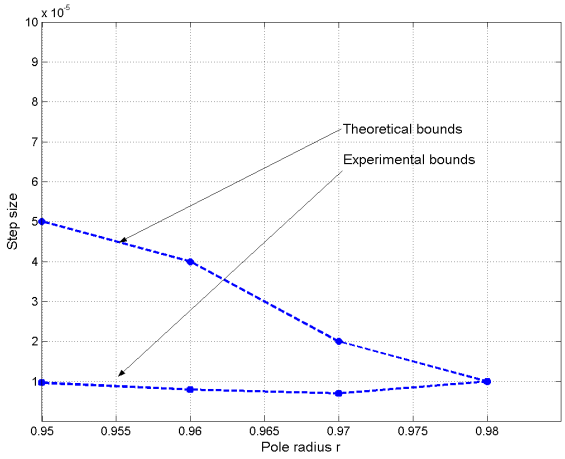

Fig.5 Theoretical and experimental stability bounds for f=200Hz

It is also seen that the experimentally obtained bound is staying constant for all values of r.

Fig.6 presents the analytical and theoretical bounds for μ for two different SNR's.

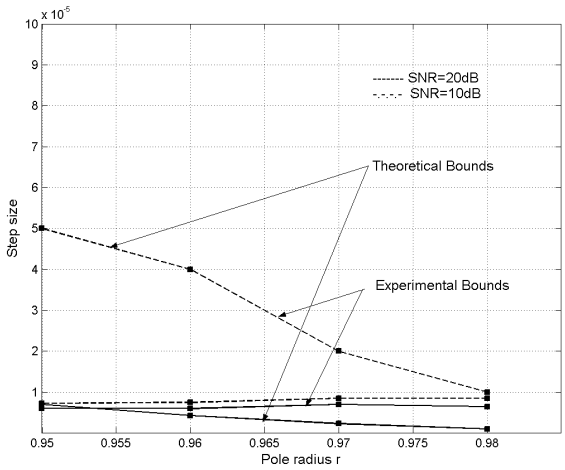

Fig.6 Investigation of theoretical and experimental bounds for different SNRs

We can conclude from this figure that the step sizes of μ are approximately equal for the two values of SNR.

VII. CONCLUSIONS

A new biquadratc filter section with independent tunning of the central frequency and the bandwidth was turned to adaptive with an LMS algorithm for adaptation of the central frequency.

Then the mean convergence of the notch filter so obtained was investigated and the bounds for the adaptation step size have been defined. A number of simplifications have been performed and the theoretical results for the step size bounds have been confirmed. A mean square convergence analysis still remains to be done.

REFERENCES

[1] M. Petraglia, J. Shynk, and S. Mitra, "Stability bounds and steady-state coefficient variance for a second-order adaptive IIR notch filter", *IEEE Trans. On Signal Processing*, Vol. 42, No. 7, pp. 1841-1845, July 1994

[2] Kwan, T. and K. Martin: "Adaptive detection and enhancement of multiple sinusoids using a cascade of IIR filters", *IEEE Trans. Circuits Syst.*, Vol. CAS-36, No. 7, pp. 937-947, July 1989.

[3] Soderstrand, M. et al., "Suppression of multiple narrow-band interference using real-time adaptive notch filters", *IEEE Trans. Circuits Syst.-II*, Vol. 44, No. 3, pp. 217-225, March 1997.

[4] Stoyanov G., "A comparative study of variable biquadratic digital filter sections sensitivities and tuning accuracy, Proc. Int. Conf. "*Telecom'2002*", Varna, Sv. Konstantin, pp. 674-681, Oct. 10-12, 2002.

[5] G. Stoyanov, G. and M. Kawamata, "Variable biquadratic digital filter section with simultaneous tuning of the pole and zero frequencies by a single parameter", *Proc. Interantional Symposium on Circuits And Systems'2003*, Bangkok, Thailand, vol. 3, pp. III-566–III-569, May 2003.

[6] Martin, K and M. T. Sun, "Adaptive filters suitable for real-time spectral analysis", *IEEE Trans. Circuits Syst*., Vol. CAS-33, No. 2, pp. 218-229, Feb. 1986.

[7] D.V.B.Rao and S. Y. Kung, "Adaptive notch filtering for retrieval sinusoidals in noise", *IEEE Trans. Acoust., Speech&Signal Process*, Vol.ASSP-32, pp.791-802, Aug. 1984

[8]. Matsuura, K., E. Watanabe and A. Nishihara, "Adaptive line enhancers on the basis of least-squares algorithm for a single sinusoid detection", *The Institute of Electronics, Information Communication Engineers (IEICE) Trans. Fundamentals*, Vol. E82-A, No. 8, pp. 1536-1543, Aug. 1999.

[9] J. R. Treichler, in *Adaptive Filters*, C. F. N. Cowen and P. M. Grant, Eds. Englewood Cliffs, NJ:Prentice-Hall, 1985, pp. 60-90.

Denoising Functional MRI: A Comparative Study of Different Temporal Techniques

Mohamed A. Mohamed[1], Fatma Abou-Chadi[1], and Bassem K.Ouda[2]

Abstract - **In this paper, we present a comparative study of different denoising techniques applied to functional magnetic resonance imaging (*fMRI*) sequences. The performance of these techniques was investigated using a simulated *fMRI* time series data with noise levels. The performance of these techniques was evaluated with respect to two quantitative measures; signal-to-noise ration (*SNR*), and shape preservation. As a result of the comparative study it has been found that denoising using Wavelet transform with reverse biorthogonal basis functions provides the best performance among all denoising techniques.**

Keywords - **Functional Magnetic Resonance Imaging (*fMRI*), Signal-to-Noise-Ratio (*SNR*), Hemodynamic Response Function (*HRF*), and Statistical Parametric Mapping (*SPM*)**

I. INTRODUCTION

Functional neuroimages often need preprocessing before being subjected to statistical analysis [1]. A common preprocessing step is denoising. In this paper we study different *fMRI* temporal denoising techniques. The performance of these techniques is compared with respect to (i) the improvement of the *SNR*, and (ii) the shape preservation of active region.

The remainder of this paper is organized as follows: Section-II presents an overview of *fMRI* imaging techniques; Section-III presents modeling of *fMRI* data, Section-IV a discussion of the performance evaluation criteria. Classification of different denoising techniques was presented in Section-V. Section-VI presents time domain denoising techniques. Section-VII provides transformed domain techniques. In Sections IIX and IX the results and conclusions were presented, respectively.

II. OVERVIEW OF FMRI

Functional neuro-imaging is a fast evolving area aimed at measuring brain activity during task performance [2]. *FMRI* is the most recently developed modality, which distinguishes itself from earlier methods (e.g. *PET*, *SPECT*, etc.) in that no exposure to ionizing radiation is evolved, better spatial and temporal resolution is achieved, and a relatively straightforward co-registration to anatomical MRIs acquired on the same machine can be attained.

[1]M.A. Mohamed and Fatma Abou-Chadi are with the Dept. of electronics and comm., Faculty of Engineering, Mansoura University, Egypt. E-mail: mazim12@yahoo.com and F-abochadi@ieee.org

[2]Bassem K.Ouda is with the Department of biomedical engineering and systems, Faculty of Engineering, Cairo University, Egypt. E-mail: bkouda@yahoo.com

The main problem associated with *fMRI* techniques is the poor signal-to-noise ratio (*SNR*), where the intensity of the detected *MRI* signal is mainly dependent on the applied static field, (e.g. the maximum signal change is 5% for $B_0 = 1.5T$). Therefore, a preprocessing step for noise reduction is necessary, in order to improve the *SNR*.

In general, *fMRI* time-courses can be modeled as the summation of the activation signal, physiologic and random noise components [3, 4]. Let us assume the observed signal $x(k)$, the activation signal $s(k)$, and the composite noise $n(k)$, representing all types of artifacts, then

$$x(k) = s(k) + n(k) \tag{1}$$

III. MODELING FMRI DATA

Simulating a set of *fMRI* time series representing the brain function under both resting and activated states would cover, in general, both temporal and spatial variations in time courses, in this work only temporal variations are considered [3, 4].

A. Modeling the HRF

HRF refers to the local changes in blood oxygenation as an effect of increased neuronal activity [4, 5]. The *HRF* to a sensory input is transient, delayed and dispersed in time. Fig.1 shows the simulated *HRF* of the from

$$s(k) = \left(1 - exp\left(-\frac{k}{T_1}\right)\right)^3 . exp\left(-\frac{k}{T_2}\right) \tag{2}$$

where T_1 and T_2 are constants that can be adjusted to obtain the desired shape, and k represents the sampling time (i.e. the number of samples within each epoch). In the described simulation $T_1 = 5.0$ and $T_2 = 7.5$.

B. Physiologic Noise

Physiologic noise is composed of respiration, a signal of high amplitude and long duration, and cardiac pulsation; a signal of low amplitude and short duration [3]. This noise type was simulated as a periodic signal consisting of two fundamental frequencies, $1\ Hz$ and $0.2\ Hz$, and the first three harmonics superimposed on a small dc as shown in Fig.2. The choice of these frequencies is based on a heart rate of $60\ beats/min$, and respiration rate of $12\ breaths/min$.

C. Random Noise

Random noise introduced to *fMRI* due to imaging system itself, subject motion, etc. Random noise was simulated using random number generator, shown in Fig.3.

D. Composite Noise

During the measurement of real *fMRI* signals all types of *MRI* artifacts simultaneously corrupt the measured signal. Therefore, the composite noise is the summation of scaled versions of all previously simulated artifacts [2]. Fig.4 shows a simulated *HRF* corrupted with composite noise.

IV. THE PERFORMANCE EVALUATION CRITERIA

The performance of all the denoising techniques was evaluated using two different quantitative measures. These measures are shortly described below.

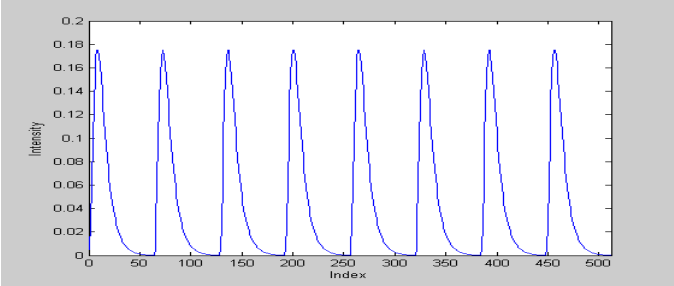

Fig.1 The simulated HRF for 8 epochs each has 64 samples.

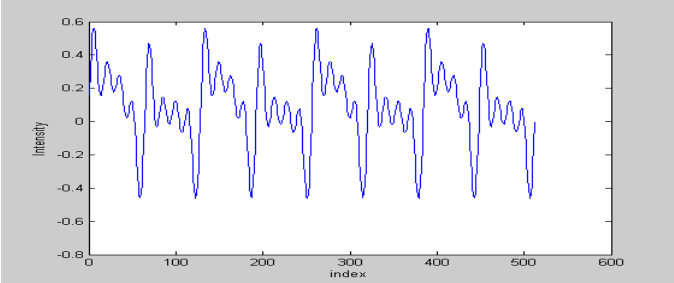

Fig.2 Simulated physiologic noise for 8 epochs each has 64 samples.

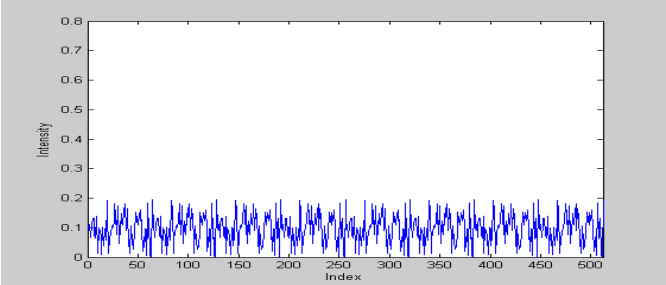

Fig.3 Simulated random noise for 8 epochs each has 64 samples.

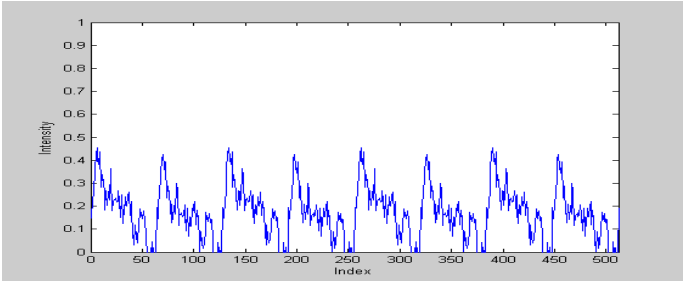

Fig.4 Simulated random noise for 8 epochs each has 64 samples.

A. Signal-to-Noise-Ratio (SNR)

SNR is an important quantitative measure for evaluating the performance of the applied technique. In which, *SNR* is computed and compared before and after denoising [1]. In this article the *SNR* is defined as

$$SNR = \left(\frac{Variance\ of\ \ Pure\ Information}{Variance\ of\ \ Additive\ Noise} \right) \tag{3}$$

B. Shape Preservation

This parameter may be estimated using the correlation coefficient (R) between the original x and output y signals [1, 6]:

$$R = \frac{\sum_i (x_i - \tilde{x})(y_i - \tilde{y})}{\sqrt{\sum_i (x_i - \tilde{x})^2 \sum_i (y_i - \tilde{y})^2}} \tag{4}$$

V. DENOISING TECHNIQUES

Denoising techniques can be classified into temporal and transformed techniques. Here, two temporal denoising techniques will be discussed; (i) linear, and (ii) nonlinear. On the other hand, in transformed domain (i) frequency domain, and (ii) wavelet domain techniques, will be discussed.

VI. TEMPORAL DENOISING TECHNIQUES

A. Linear Filters

Linear filters tend to destroy oscillations and other fine details, and perform poorly in the presence of signal dependent noise, physiologic noise [7, 8].

1. Mean Filters

The mean techniques is a simple, intuitive and easy to implement method of smoothing data, *i.e.* reducing the amount of intensity variation between one sample and its neighbors [7].

2. Gaussian Filters

The Gaussian smoothing operator is a convolutional operator, similar to the mean filter [7], but it uses different weights representing the shape of a Gaussian distribution

$$h(i) = \frac{1}{\sqrt{2\pi}\sigma} exp\left(-\frac{(i-m)^2}{2\sigma^2} \right) \quad (5)$$

where σ is the standard deviation, and *m* is the mean value.

3. Wiener Filter

Wiener filter is the solution of the linear minimum squared error problem of estimating a signal s, from a measured signal x using a filter, $h(k)$. It can be shown easily that the frequency response of the non-causal Wiener filter is

$$H(w) = \frac{P_s(w)}{P_s(w) + P_n(w)} \quad (6)$$

where $P_S(w)$ and $P_n(w)$ represent the power spectral density of the original signal and noise, respectively. Intuitively, the action of Eq.6 is to keep frequency bands where the signal power is much stronger that that of the noise and to severely attenuate frequencies where noise predominates. A natural extension of the Wiener filter is to allow it to be time-varying. In principle, this should only require substituting the signal and noise power spectral densities with their time-dependent counterparts [5].

4. Coherent Average

Coherent average (*CA*) assumes that a series of M equidistant and identical stimuli are applied to the system, and the following assumptions were satisfied [9]; (i) The response $s(k)$ will be complete before the next stimulus occurs, and invariant with time, (ii) The delay time between stimulus and the start of the response is constant, and (iii) The noise $n(k)$ has the properties; additive, uncorrelated with either the stimulus or the response, stationary. The *CA* signal $y(k)$ follows from

$$y(k) = \frac{1}{M} \sum_{i=0}^{M-1} x(k + iT) \quad (7)$$

5. Robust Weighted Average (RWA)

In case non-stationary artifacts, it is better to use an adaptive weighted average filter; called robust weighted average. *RWA* should have a set of properties given by Huber et al in [10]. Here, the main problem is the estimation of the noise power spectrum, in order to evaluate the adaptive weight. The weighted average is given by

$$y(k) = \tilde{x}(k) = \sum_{i=1}^{N} w_i x_i(k) \quad (8)$$

where w_i is the weight matrix.

B. Non-Linear Filters

In non-linear filters, noise is removed without any attempt to identify it [7, 8], where, the filters employ a low pass filter on groups of samples with the assumption that the noise occupies the high frequency spectrum.

1. Median Filters

Median filter often does a better job than the mean filter of preserving useful detail in the data. Like the mean filter, the median filter considers each sample in the data in turn and looks at its nearby neighbors to decide whether or not it is representative of its surroundings [8].

2. Weighted Median (WM) Filters

Weighted median filters can be defined in two distinct ways; however both definitions give exactly the same output [11]. *WM* filters are special case of weighted ordered statistic filters. There are two familiar weighted median techniques; positive integer weights and positive non-integer weights [11].

$$y(k) = med\left[\sum_{i=1}^{N} w_i x(k+i) \right] \quad (9)$$

VII. TRANSFORMED DOMAIN TECHNIQUES

A. Frequency Domain Techniques

In frequency smoothing methods the removal of noise is achieved by designing a frequency domain filter. These methods are time consuming and depend mainly on the filter characteristics [8].

1. Spectrum Subtraction (SS)

The spectral subtraction provides an estimate of the signal spectrum as the difference between the noisy spectrum and an estimate of the noise spectrum [12]. The corresponding power spectra would therefore related by

$$P_S(w) = P_X(w) - P_N(w) \quad (10)$$

where $P_{S(w)}$ and $P_X(w)$ are the power spectra of the original and measured pixel time-course, respectively. The power spectrum of the noise, $P_N(w)$, can be estimated from locations where the deterministic signal is absent. Here, the amplitude square of the Fourier transform is used as the periodgram estimate of the power spectrum. Spectrum

subtraction may result in negative estimated of the power spectrum, in which case they would have to be mapped to non-negative values, here mapped to zero. The estimate Fourier transform of the recovered signal, in terms of power and phase, is given by

$$Y(w) = \sqrt{P_s(w)}.e^{j\theta_X(w)} \quad (11)$$

Finally, the signal $y(k)$ can be obtained by taking the inverse *FFT* of the Fourier transform of Eq.11.

B. Wavelet Domain Filters

Wavelet bases are bases of nested function spaces, which can be used to analyze signals at multiple scales. Wavelet coefficients carry both time and frequency information, as the basis functions varies in position and scale. The wavelet transform efficiently converts a signal to its wavelet representations; in one level a signal x is splitted into an approximate part cx_1 and a detail part dx_1 [7, 8, and 13]. In multilevel decomposition, only the approximate part is further decomposed.

1. Thresholding Wavelet Coefficients

The wavelab package contains a number of schemes for the wavelet-based denoising [14], based on thresholding detail coefficients in the wavelet domain. There are two main thresholding techniques; (i) soft thresholding, and (ii) hard thresholding [15].

2. Wavelet Packet Transform

Wavelet packets *(WP)* are waveforms indexed by three naturally interpreted parameters: position, scale, and frequency [16] for a given orthogonal wavelet function, a library of bases called *wavelet packet bases* were generated. The decomposition parameters of a given dataset are chosen based on an entropy-based criterion. The main difference between wavelet transform and *WP* is that, in *WP* both approximate and detail coefficients are decomposed, instead of approximate coefficients in the case of wavelet transform.

3. Smoothing Wavelet Coefficients

Major interests of the recent papers on the noise reduction using wavelet transform are the determination of the wavelet transform and the choice of thresholding parameters [16]. Thresholding in wavelet domain is to smooth or to remove some coefficients of wavelet transform of the measured signal. Through the thresholding operation, the noise content of the signal is reduced effectively under the non-stationary environment. In this part, a *LPF* was used to smooth the wavelet transform coefficients instead of thresholding method.

VIII. RESULTS

The following set of tables and figures show the results of applying different denoising techniques in both time domain and transformed domain. Six levels of *SNR* were used. These are: 0.25, 0.50, 0.75, 1.0, 2.0, and 3.0. Some techniques require certain parameters, which are determined via trial and error approaches. Tables from 1 to 3 give the output *SNR*, while tables from 4 to 6 provide the values of *R* between noisy input and the filtered signal at each level of noise. It has been found that using a transformed technique based on wavelet transform of mother function reversed biorthogonal of order 2.8 and soft thresholding of balanced sparcity norm will give the best performance from the point of view of *SNR* and *R*.

IX. CONCLUSION

We have compared temporal smoothing and transformed denoising techniques for a simulated *fMRI* time-series. Summarizing all the presented results of the comparative study, it was found that the wavelet transform based on reversed biorthogonal of order 2.8 basis function and soft thresholding with balanced sparcity norm, provides the best denoising from the point of view of *SNR*, and correlation coefficient.

Table.1: Results of applying temporal filters

Filter Type	SNR_i					
	0.25	0.50	0.75	1.00	2.00	3.00
Mean	3.46	5.15	5.89	6.33	7.07	7.32
Med	2.84	4.00	5.05	5.98	8.74	10.66
Wiener	7.74	7.36	7.18	7.06	6.84	6.75
Gaus	6.65	6.65	6.65	6.65	6.65	9.23
C.A.	1.27	2.67	3.99	5.13	8.60	11.01
RWA.	4.68	4.83	4.99	5.29	6.18	6.94
S.S.	1.10	2.00	2.75	3.39	5.24	6.44

Table.2: Results of applying wavelet transform

Filter Type	SNR_i					
	0.25	0.50	0.75	1.00	2.00	3.00
DB.3	1.31	2.48	3.52	4.47	7.55	10.15
Sym.5	1.31	2.48	3.52	4.47	7.55	10.15
Mey.	1.36	2.66	3.93	5.15	9.68	13.74
Haar	1.33	2.36	3.19	3.92	6.41	8.62
Bior	1.33	2.63	3.91	5.16	10.02	14.60
Rbior	1.47	2.91	4.31	5.69	10.91	15.72
Coif.3	1.47	2.90	4.31	5.69	10.91	15.72

Table.3: Results of applying wavelet packet

Filter Type	SNR_i					
	0.25	0.50	0.75	1.00	2.00	3.00
DB.3	1.11	2.21	3.24	4.18	7.58	10.16
Sym.5	1.11	2. 21	3.24	4.18	7.58	10.16
Mey.	1.16	2.36	3.57	4.80	9.61	14.00
Haar	1.14	2.14	3.03	3.85	6.57	8.54
Bior	1.20	2.50	3.82	5.13	10.68	15.63
Rbior	1.11	2.30	3.46	4.72	9.88	14.99
Coif.3	1.21	2.40	3.58	4.74	8.70	11.69

Table.4: Correlation coefficients of temporal filters						
Filter Type	SNR_i					
	0.25	0.50	0.75	1.00	2.00	3.00
Mean	0.56	0.65	0.70	0.78	0.81	0.87
Median	0.60	0.67	0.73	0.79	0.86	0.91
Wiener	0.72	0.79	0.82	0.87	0.91	0.94
Gauss.	0.67	0.73	0.80	0.85	0.90	0.92
C.A.	0.70	0.73	0.81	0.87	0.90	0.91
R.W.M.	0.69	0.71	0.82	0.85	0.87	0.89
S.S.	0.67	0.70	0.76	0.80	0.84	0.88

Table.5: Correlation coefficients of wavelet transform						
Filter Type	SNR_i					
	0.25	0.50	0.75	1.00	2.00	3.00
DB.3	0.69	0.78	0.86	0.91	0.94	0.95
Sym.5	0.69	0.78	0.86	0.91	0.94	0.95
Meyer	0.71	0.81	0.85	0.88	0.93	0.96
Haar	0.64	0.74	0.78	0.82	0.88	0.91
Bior	0.71	0.81	0.86	0.88	0.94	0.95
Rbior	0.73	0.83	0.87	0.89	0.94	0.96
Coif.3	0.71	0.80	0.85	0.87	0.92	0.94

Table.6: Correlation coefficients of wavelet packet						
Filter Type	SNR_i					
	0.25	0.50	0.75	1.00	2.00	3.00
DB.3	0.69	0.80	0.85	0.88	0.94	0.96
Sym.5	0.66	0.77	0.82	0.85	0.91	0.93
Meyer	0.68	0.79	0.84	0.88	0.93	0.95
Haar	0.62	0.73	0.78	0.82	0.88	0.91
Bior	0.69	0.80	0.86	0.89	0.94	0.96
Rbior	0.67	0.79	0.84	0.87	0.94	0.96
Coif.3	0.68	0.79	0.84	0.87	0.94	0.96

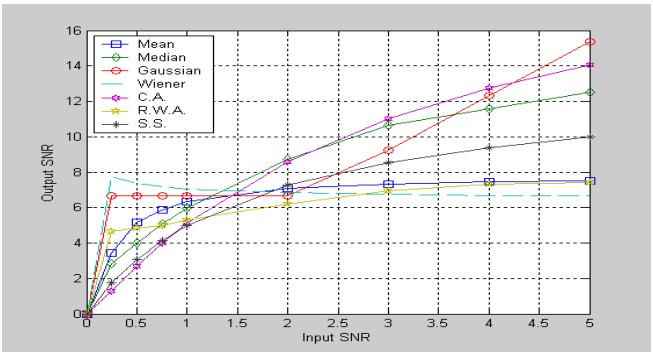

Fig.5 The results of SNR_o for temporal techniques.

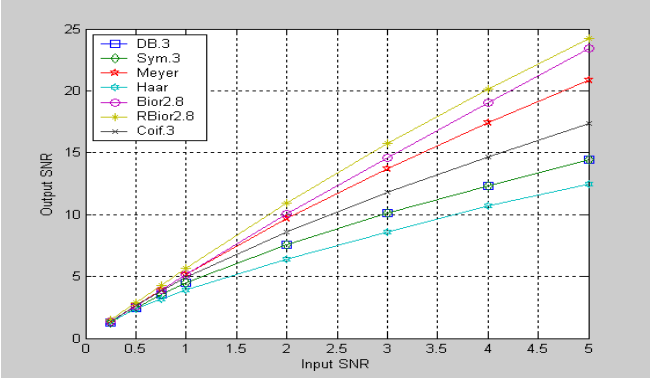

Fig.6 The results of SNR_o for wavelet transform.

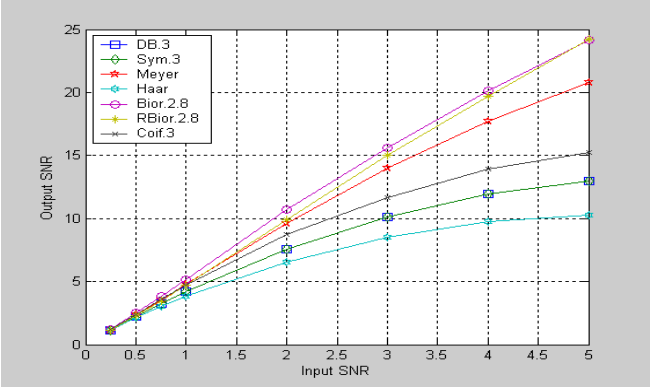

Fig.7 The results of SNR_o for wavelet packet.

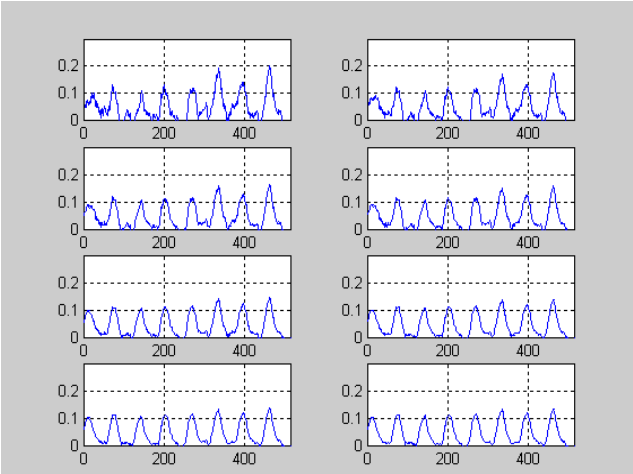
Fig.8 The output signal of robust weighted average.

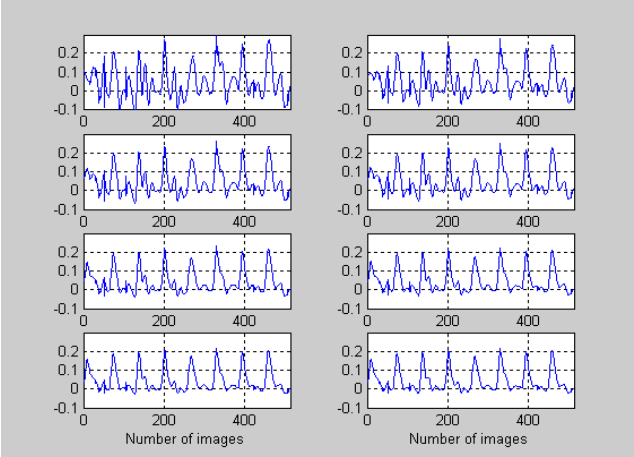

Fig.9 The output signal of wavelet transform based on reversed biorthogonal.

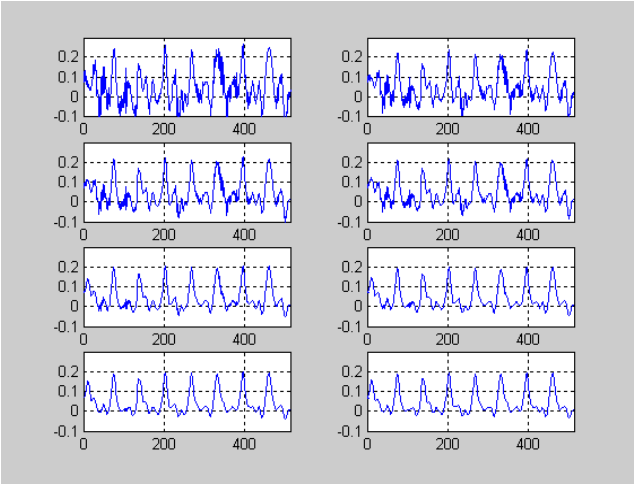

Fig.10 The output signal of wavelet packet based on reversed biorthogonal.

REFERENCES

[1] Wink A.M., and Roerdink J.B., “Denoising functional MR images: a comparison of wavelet denoising and Gaussian smoothing”, University of Groingen, the Netherlands, 2000.

[2] Friman O., "Adaptive Analysis of Functional MRI Data," PhD. Thesis, Department of Biomedical Engineering Linkopings University, September, 2003.

[3] Le T.H and Hu X., "Retrospective Estimation and Correction of Physiological Artifacts in fMRI by Direct Extraction of Physiological Activity from MR Data," MRM, Vol.35, pp. 290-298, 1996.

[4] Horn J.V., and Ellmore T.M., "Modeling the Hemodynamic Response Function in fMRI Using Linear Time Invariant Systems,", National Institute of Health, Bethesda, Maryland, USA, 2003.

[5] LaConte S., Ngan S., and Hu X., "Wavelet Transform-Based Wiener Filtering of Event-Related fMRI Data," MRM, Vol.44, pp.746-757, 2000.

[6] Friston K.J., Holmes A.P., Worsley K.J., Poline J.P., Frith C.D., and Frackowiak R.J., "Statistical Parametric Maps in Functional Imaging: A Linear Approach Model",

[7] Fisher R., Perkins S., Walker A., and Wolfart E., "Image Processing Learning Resources", 2004.

[8] Motwani m.C., Gadiya M.C, Motwani R.C., and Harris F.C., "Survey of Image Denoising Techniques", University of Nevada, Reno, Dept. of Comp. Sci & Engr., Reno., 2003.

[9] Rompelman, Ros; H. H., "Coherent Averaging Technique/; A Tutorial review," J. Biomed. Eng. Vol. 8, pp. 24- 29, January, 1986.

[10] Leski J.M, "Robust Weighted Average," IEEE Trans. on Biomed. Eng. Vol.49, No.8 August 2002.

[11] Harja O., Astola J., and Neuvo Y., "Analysis of the properties of median and weighted median filters using threshold logic and stack filter representation", IEEE Trans. of Signal Processing, Vol.39, No.2, pp.395-410, Feb. 1991.

[12] Ouda B., "Analysis and Processing Strategies for Functional Magnetic Resonance Imaging Data", PH.D. thesis, Faculty of Eng., Cairo Univesity, Egypt, 2002.

[13] Rao R.M. and Bopardikar A.S., "Wavelet Transforms: Introduction to Theory and Applications," Addison-Wesley Longman, 1998.

[14] Buckheit J.B., and Donoho D.L., 91995) Wavelab and Reproducible Research. Dept. Statist., Stanford University, Stanford, C.A.

[15] Unser M., "Splines: a perfect fit for medical imaging", IEEE Trans. On Signal Processing, pp.22- 38, November, 1999.

[16] Oktem R., Oktem L., and Egiazrian K., "A Wavelet Packet Transform Based Image Coding Algorithm", Taemepre University of Technology, Signal Processing Lab. Finland.

A Geometry based Approach for Identification of Image Objects

Mariana Ts. Stoeva[1], Violeta T. Bojikova[2], Vihren V. Stoev[3]

Abstract - **In this paper we present a new technique for identification of images from image collection that are similar by shape to the objects they contain. Our shape similarity retrieval model is based on histogram description of object shape that is independent on translation, scale, rotation and reflection transformations.**

Keywords **– image database, query processing, content based image retrieval, shape description**.

I. INTRODUCTION

The content based image information systems require a new visual approach for query specification, new indices for data assignation and new methods for similarity retrieval between the query and the target. These are more and more challenging tasks due to the extreme increase of the number and sizes of image archives.

In this paper we present a new technique for image retrieval from image collection that are similar by shape to the objects they contain. Our shape similarity retrieval model is based on histogram description of object shape that is independent on the translation, rotation and reflection transformations. This description forms a multi-dimensional index for the object shape with a relatively low dimension. The defined similarity distance reflects the understanding for shape similarity. We illustrate a similarity query processing architecture consistent with our model. The carried out experiments demonstrate the applicability and the efficiency degree of the proposed technique.

II. SHAPE DESCRIPTION

The following methods are used in the existing visual systems for shape description: boundary based geometrical methods; geometrical region based methods and region based transform methods, described in [4]. Most of the methods derive object shape description with no dependence on translation [2]. Just a few of the shape descriptions are invariant in case of rotation and scaling [1],]3].

The method, proposed in this paper describes object shape but this description does not depend on possible translation, scale and rotation of the object and has relatively low dimension.

The object of application interest is derived through segmentation by one of the existing methods from the assigned on pixel level image. We assume that a gray scale image of dimension m×m contains only one object $F:\Im m\times\Im m\rightarrow\Re$. The pixel based description of F is geometrically described by n contours of the object $F=(Cj, 0\leq j \leq n-1)$. The object contours C_0, C_1, …,C_n are obtained by a common algorithm. The contours C_j are joint multitudes of pixels assigned by their k-number of coordinates $C_j=((xji, yji), 1\leq i \leq k)$, where C_0 is the external k-dimension contour of the object and C_1, C_2..., C_{n-1} are possible internal contours. Fig. 1 illustrates the obtainment of histogram object shape description.

The transformation uses the centroid features of the image object extracted from object external contour C_0 according the equasion (1). The centoid (X_0, Y_0) keeps its relational spatial location with respect to the contour points regardless of translation, rotation and scaling transformation.

$$X_0 = \frac{1}{k}\sum_{i=1}^{k} x_{0i} \qquad Y_0 = \frac{1}{k}\sum_{i=1}^{k} y_{0i} \tag{1}$$

The coordinate system center is conventionally displaced to the point - centoid (X_0, Y_0). The external and the internal contours Decart coordinates are transformed. The transformation is presented by Eqs. (2) and (3).

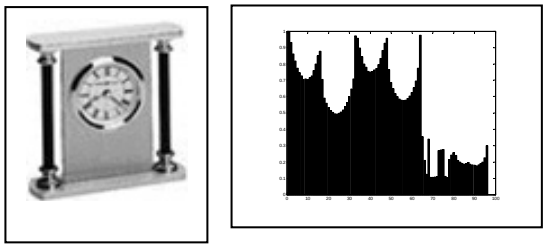

Fig.1: Segmented object and histogram shape description.

$$x'_{ji} = \frac{1}{r_{0\max}}(x_{ji}-x_0)\cos\alpha + \frac{1}{r_{0\max}}(y_{ji}-y_0)\sin\alpha$$

$$y'_{ji} = -\frac{1}{r_{0\max}}(x_{ji}-x_0)\sin\alpha + \frac{1}{r_{0\max}}(y_{ji}-y_0)\cos\alpha \tag{2}$$

[1]Mariana Stoeva Technical University Varna, Department of Computer Science ,Varna, Bulgaria, E-mail: mariana_stoeva@abv.bg

[2]Violeta Bojikova Technical University Varna, Department of Computer Science, Varna, Bulgaria,Email: vbojikova2000@yahoo.com

[3]Vihren Stoev International University, Bremen 28759,College Ring 7, Germany, Email:v.stoev@iu-bremen.de

Angle α is defined by the angle (polar coordinate) of the "start" point of the external contour. This "start" point is uniformly determined invariantly to rotation by using

$$r_{ji}=\begin{cases}+\sqrt{x_{ji}^{'2}+y_{ji}^{'2}}, & \text{за} y_{ji}^{'}>0 \text{ или } y_{ji}^{'}=0, x_{ji}^{'}>0\\ -\sqrt{x_{ji}^{'2}+y_{ji}^{'2}}, & \text{за} y_{ji}^{'}<0 \text{ или } y_{ji}^{'}=0, x_{ji}^{'}<0\end{cases}$$

$$\theta_{ji}=\begin{cases}\operatorname{arctg}\dfrac{y_{ji}^{'}}{x_{ji}^{'}}, & \text{за } x_{ji}^{'}\neq 0 \quad 0\le\theta_{ji}<\pi\\ \pi/2, & x_{ji}^{'}=0\end{cases} \qquad (3)$$

recursive selective function (4). For an ordered multitude V({v_i}, i=1,…,n) from a typical for the external contour of the object points is obtained the ordered multitude P({p_i}, i=1,…,n) from geometric measurements of the feature p for these points of V. These measurements are the radius-vectors of the points from the external contour, the angles and the areas of the segments they make with the centroid.

$$V_P=\rho(V,P)=\begin{cases}V, & ako \quad V=V_{\max}\\ \rho(V_{\max},\varphi_P(V_{\max})), & ako \quad V\neq V_{\max},\end{cases}$$

$$където: \qquad V_{\max}=\operatorname{Max}(V,P)=(\{v_i\}, p_i=p_{\max}) \qquad (4)$$

The maximal Euclidian distance from the centroid to the external contour points is determined $r_{0max} = \max|r_{0i}|$. Then a guiding for the outer contour pixel is determined. A first- rate criterion for guiding pixel assignation is its coordinate to satisfy the requirement $|r_{0i}| = r_{0max}$. In case of more than one pixel available, for which $|r_{0i}| = r_{0max}$, a more complicated criterion is utilized, accounting the number and coordinates of the points of the contour between the maximums. A rotation of the contour C_j around point (X_0,Y_0) with angle α comes after so that the specified as guiding pixel lies on the positive direction of the 0X axis after the rotation. This rotation aims the orientation of every one contour in one and the same way C_j=((rji, θji), $1\le i\le k$, $0\le\theta_{ji}<\pi$), $0\le j\le n-1$. From this way transformed contour coordinates the multidimensional index F=(($F_{\theta i}$), $1\le i\le l$), describing the object shape in type of histograms is obtained. The value of the histogram is formed by the intersection points of the contours with axes, passing through the coordinate system beginning and subtending an angle θ_i with the positive direction of the X axis. The angle θ ($0\le\theta_i<\pi$) varies from 0 up to π by uniform step $\Delta\theta = \pi/l$, where the overall number l of the axes may have a value 2^1, 2^2, 2^3,…, m. In order to describe all pixels $\Delta\theta \approx \pi/m$, for images with dimension m×m, the number l of the axes intersecting the contours is $l \approx m$.

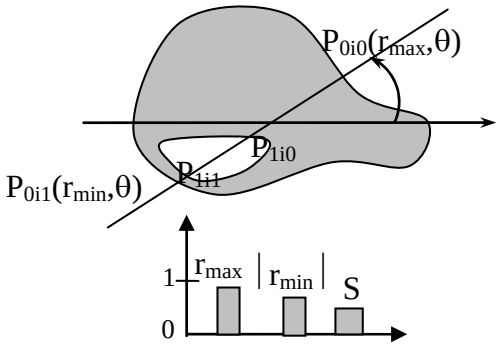

Fig.2. Illustration of the evaluation of 3 columns of histogram description.

The fact, that an arbitrary line intersects any contour C_j even number of times is used. Let the line passing through the beginning of the coordinate system and subtending with the X axis angle θ_i =const intersects the contour C_j in P_j points were P_j is an even number: $F\cap\theta_i=((r_{jis}), 1\le s\le P_j, P_j\ge 2)$. Eq. (5) presents three histograms obtained for one axis of intersection, where i is the consecutive number the axis θ_i=const ($\theta_i=\Delta\theta(i-1)$ $0\le\theta_i<\pi$) ($1\le i\le l$) and l is the number of axes.

$$F_{\theta i}(f_i,f_{l+i},f_{2l+i})=\begin{cases}f_i=C \quad \max_r((r_{0ip}), 0\le p\le p_{0n})\\ f_{l+i}=C \quad |\min_r((r_{0ip}), 0\le p\le p_{0n})|\\ f_{2l+i}=C\ \dfrac{1}{2}\sum_{i=0}^{n}\sum_{p=0}^{p_{jn}}(-1)^j(-1)^p r_{jip}\end{cases} \qquad (5)$$

Object shape description gets the mode $F(f_1,f_2,\ldots,f_n)$. It forms the multidimensional index for shape, stored in the databases. The multidimensional index for shape have dimension 3l. The maximal index dimension for image with dimension m×m is 3m, or, for image 512 ×512 the maximal dimension is 1536 D, that is a relatively low dimension for such an image.

III. SIMILARITY RETRIEVAL

Content based query processing imposes the definition of a similarity evaluation criterion, named retrieval value or similarity distance. Let the shape query is transformed into an image histogram description $Q(q_1,q_2,\ldots,q_n)$, and the image in the database has histogram description $F(f_1,f_2,\ldots,f_n)$, where q_i, f_i are histograms. The retrieval value between Q and F for the examined retrieval model is determined by Eqs. (6), where C is a constant of presentation and L is the description lenghth.

$$D(Q,F)=\frac{1}{C^2L}\min\left\{\begin{array}{l}\sum_{i=1}^{L}(q_i-f_i)^2\\ (q_1-f_1)^2+(q_{l/3+1}-f_{l/3+1})^2+(q_{2l/3+1}-f_{2l/3+1})^2+\\ \quad+\sum_{i=2}^{l/3}(q_{2l/3+2i-1}-f_{2l/3+2i-1})^2+(q_{l/3+i}-f_{l/3+2i})^2+(q_{2l/3+i}-f_{3l/3+2i})^2\end{array}\right. \quad (6)$$

The used quadratic functions are already approved as appropriate distance functions for similarity search. In the chosen by us similarity distance the first two components account the external contours similarity and the third component accounts the similarity of all the internal contours. In our understanding for similarity, consistent with the medical appliance, the similarity weight of the external contour is much higher than that of the internal contours similarity. The computation frame of the process of similarity calculation and an example of similarity between two objects are shown in Fig. 3. The distance between the shape descriptions of the two objects alarm clocks is shown too.

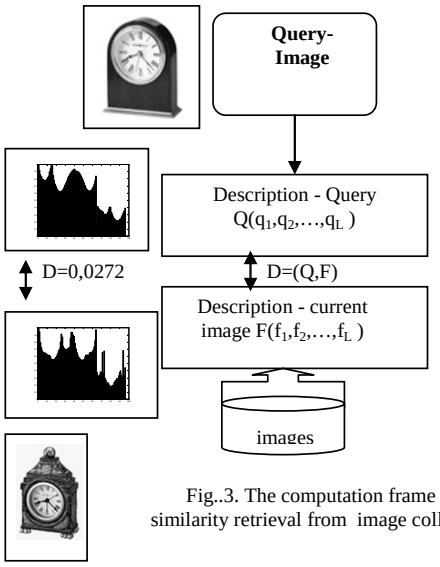

Fig..3. The computation frame of similarity retrieval from image collection

IV. Experimental Results

Our algorithms are implemented in MatlabR12 and C+ + and are evaluated on test database of 2000 images from a medical image collection. The images are transformed in order to get dimensions 256×256, and their index with dimension 3l = 384 for l = 128. The presented results illustrate the desired behavior of our similarity model with respect to the returned answers. The results demonstrate good filter selectivity and performance in the high-dimensional image space. As a sample query we chose the image of object - human arteriosclerosis coronary artery existing in DB. The collection includes also some modified by us images of the same object, transformed by translation or rotation and also images of the same transformed object but with different number of internal contours added. The experiments for robustness of the access confirmed the results invariance to arbitrary transformations. Fig.4 shows the results for an evaluated similarity for 4 objects from the experimental data. The experiments show good sensibility of the similarity distance to recognize big as well as small differences of objects shapes.

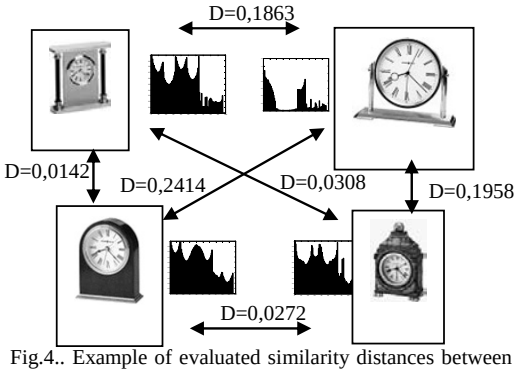

Fig.4.. Example of evaluated similarity distances between 4 objects shape descriptions.

V. Conclusions

In this paper we presented a geometrically based shape similarity model. This model is invariant with respect of the transformations translation, scaling, rotation and reflection and possesses invariability and stability. We illustrated the process of similarity calculation consistent with our model. The carried out experiments demonstrate the applicability and the efficiency degree of the proposed technique.

REFERENCES

[[1] M. Gr. Albanesi, L. Lombardi Wavelets for Shape Recognition in Image Retrieval: a Simple Case Studi Proc. Image and Video content based retrieval, 1998 pp.81-88

[2] M. Ankerst, H. Kriegel, t.Seidi, A Multistep Approch for Shape Similarity Search in Image DataBases, Proc. IEEE Trans. on Knowledge and Data Ingenering, vol. 10, no 6, 1998 pp. 996-1004

[3] S. Derrode, M. Daoudi, F. Ghorbel, Invariant content-based image retrieval using a complete set of Fourier–Mellin descriptors, IEEE International Conference on Multimedia Computing Systems, Vol. 2, 1999, pp. 877–881

[4] P. Stanchev “Object-Oriented Image”, Model Technology of object-Oriented Languages and Systems TOOLS Eastern Europe’99 Blagoevgrad, pp 98-109, 1999

Session TN:

TELECOMMUNICATION NETWORK

Optimal Solution for Routing and Wavelength Assignment Problem in Optical WDM Networks

Goran Marković[1], Vladanka Aćimović-Raspopović[2]

Abstract - **We consider the routing and wavelength assignment *(RWA)* problem in multi-hop optical WDM networks with static traffic demands. In the case of static traffic, the connection requests are given in advance, and the objective is typically to minimize the number of used wavelengths in a network. Since the number of available wavelengths per a fiber is limited by technological reasons, *RWA* problem solution is crucial for improvement of optical WDM network efficiency. In this paper, the routing and wavelength assignment is considered as the optimization problem based on integer linear programming resolving. We developed the software that gives the optimal solution of the RWA problem. The simulations of the RWA problem on a ring, mesh and fully connected network with six routing nodes are performed and the network performances are compared.**

Keywords – **optical WDM network, routing and wavelength assignment (RWA), optimal solution, integer programming**

I. INTRODUCTION

The ever increasing demands for higher transmission bandwidth require new design solutions for future telecommunication networks. Optical networks employing *Wavelength Division Multiplexing (WDM)* technique are believed to be the next generation networks that can meet the agile future requirements. Recent developments in *WDM* technology have led to a tremendous research interest in WDM-based optical network designing [2,3,4].

In *WDM* networks several optical signals using different wavelengths are carried over a single optical fiber. Thus the huge available capacity of an optical fiber can be used more efficiently. Each wavelength is a separate, signal-carrying communication channel called a lightpath. A *lightpath* is simply a high bandwidth circuit-switched communication channel, carrying data at up to several gigabits/second. It is set up by assigning a dedicated wavelength to it on each physical link on its path between the end nodes in a network.

WDM technique brings out new problems in coordination of wavelengths usage in network [1,4,5]. In particular, when it is needed to establish a connection between a node pair, a route must be found and a wavelength has to be assigned to carry the information. The problem is known as the *routing and wavelength assignment (RWA)*. Resolving the *RWA* problem has received a lot of attention in optical WDM networks researching. The current well-known routing approaches, such as fixed routing, fixed-alternate routing and adaptive routing are the basic routing strategies that are widely used for the resolving this problem.[1,6,7].

Ones the route has been chosen for a connection request (or a lightpath), the wavelengths have to be assigned to each lightpaths in such a manner that any two lighpaths traverse over the same physical link are assigned a different wavelength. If wavelength conversion cannot be performed at network nodes, the lightpaths must be established on the same wavelength over all physical links along the path between two end nodes. This is known as the wavelength continuity constraint. Different wavelength assignment approaches have been extensively researched in the literature [1-7]. The wavelength assignment algorithms can be broadly classified into most-used, least used, fixed order and random order depending on the order in which the wavelengths are searched.

In this paper the optimal solution for routing and wavelength assignment problem in multi-hop optical *WDM* network with static traffic demands and without the wavelength conversion possibility is considered.

With static traffic demands, the entire set of connection requests are known in advance and the routing and wavelength assignment problem is performed off-line. In such situation, the objective is to minimize the required network resources such as the number of wavelengths needed to set up a certain set of lightpaths or the number of fibers in network for a given physical topology. An alternative of minimizing the number of wavelengths is to maximize the number of connections that can be established (blocking minimization) for a given fixed number of available wavelengths.

An exact optimal solution for a given *RWA* problem can be obtained by solving the corresponding combinatorial *RWA* using the integer linear programming. Such an approach, especially when applied to large problem solving, may be computationally expensive. In spite of using sophisticated techniques such as branch-and-bound methods, the computation time may be an exponential function of the number of source-destination pairs and the network connectivity degree. However, for a practical network, an optimal solution for RWA problem could be obtained in reasonable time. The proposed approach could be applied for solving the RWA problem in different network topologies.

II. PROBLEM STATEMENT

Consider a given physical network that has *N* routing nodes connected in any topology. Two end nodes may require a

[1] Goran Marković is with the Faculty of Transport and Traffic Engineering, Vojvode Stepe 305, 11000 Belgrade, Serbia and Montenegro, e-mail:g.markovic@sf.bg.ac.yu

[2] Vladanka Aćimović-Raspopović is with the Faculty of Transport and Traffic Engineering, Vojvode Stepe 305, 11000 Belgrade, Serbia and Montenegro, e-mail: v.acimovic@sf.bg.ac.yu

number of connection requests between them and all of those requests are known *a priori*. We assume that the network resources, such as the available number of wavelengths per fiber links or the number of optical transmitters and receivers in optical nodes are also given. The objective of the RWA problem is to select the routes throughout the network for all required connections with the wavelengths assignment such that no two lightpaths using the same wavelength traverse through the same physical link. The objective is to minimize the number of required wavelengths in the network. This goal can be achieved using *integer linear programming (ILP) optimization.* A total number of lighpaths that are established over one physical link defines a congestion of a particular link.

Analytical formulation of the RWA *ILP* optimization problem is given as follows:

$$F = min \sum_{w=1}^{W} \lambda_w \tag{1}$$

where F is the objective function in terms of required number of wavelengths that has to be minimized. With W the maximum available number of wavelengths in the network that is assumed to be large enough to establish all the required connections is denoted. It is assumed that all the links in a network have the same value of W. Wavelength λ_w is the binary decision variable that has the value 1, if the wavelength w is used at any link in the network, otherwise $\lambda_w=0$.

Two constraints that have to be satisfied for the observed optimization problem can be formulated as follows:

$$\sum_{w=1}^{W} x_w^k = r_k, \forall k \in K = \{i,j\}, i,j \in \{1,2,...,N\}, i \neq j \tag{2}$$

$$\sum_{k} x_{w,l}^k \leq \lambda_w, \forall w \in W, l \in L \tag{3}$$

$$x_{w,l}^k \in \{0,1\}, \forall k \in K, w \in W$$
$$\lambda_w \in \{0,1\} \ \forall w \in W \tag{4}$$

where the used symbols have next notations:
W - total number of available wavelengths in network,
K- set of node pairs in network,
L - set of all physical links in network,
N - number of routing nodes in network,
r_k - the number of connections required between node pair k,
$x_{w,l}^k$ - binary decision variable that has the value 1, if the wavelength w is used at all links l along the path between node pair k, otherwise it has the value 0.

The constraint formulated by (2) is considered with traffic demand requirements. For all node pairs, $k \in K$, the number of required connections, r_k, between two end nodes has to be satisfied. With the constraint (3) we obtain that only one lightpath on particular wavelength w can pass over a link l. In other words, no two lightpaths using the same wavelength w can be established over one physical link l.

To resolve the described RWA optimization problem we developed the software that is based on binary integer programming. Its application gives the optimal solution of RWA problem for particular network topology. Input parameters of this software are the traffic demands matrix, the physical network topology and the maximal available number of wavelengths in the network. For resolving the routing problem, we assume that the fixed-alternate routing strategy is applied. In fixed-alternate routing, multiple fixed routes, that are computed off-line, are considered as the candidate paths for a connection that need to be established. In this approach, each node in the network forms its routing table that contains an ordered list of a number of fixed routes to each destination node. These routes could be, for example, the first shortest path, the second shortest path, etc. For all connection requests, optimization model try to find a route-wavelength pair, so that the total number of required wavelengths is minimized. All of the candidate paths and available wavelengths are considered simultaneously until the required set of connection requests is satisfied. We assume that the number of available wavelengths is large enough to establish all the required connection requests. Then the total number of wavelengths for all of the established lightpaths is determined as the objective function value.

III. NETWORK MODEL

We consider the optical WDM transport network with 6 routing nodes, interconnected by a single fiber links for each direction. Simulations of routing and wavelength assignment problem are performed for network topologies with various degree of connectivity, beginning with the simplest variant of a ring network, via a mesh to fully connected architecture. Figure 1 illustrates considered topologies in our simulation.

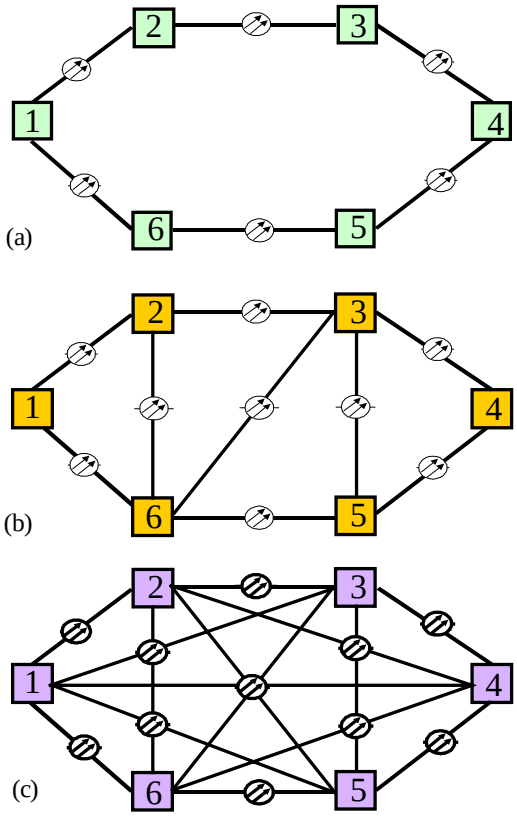

Fig. 1 Considered network topologies: a) ring, b) mesh, c) fully connected network

IV. Simulation Results

For the simulation purposes, we assumed that the traffic demand matrix R is given in the form of requests of required number of connections between end nodes with the randomlyy distributed values between 1 and 3. The matrix R is symmetric, which means that connection requests in both directions are the same. An example of a generated traffic matrix R, which is considered throughout the simulation, is given as:

$$R = \begin{bmatrix} - & 2 & 1 & 1 & 2 & 2 \\ 2 & - & 1 & 3 & 1 & 3 \\ 1 & 1 & - & 1 & 2 & 1 \\ 1 & 3 & 1 & - & 2 & 3 \\ 2 & 1 & 2 & 2 & - & 1 \\ 2 & 3 & 1 & 3 & 1 & - \end{bmatrix} \quad (5)$$

By running developed software for the ring network topology given in Fig. 1-a and for the traffic demands given by (5), we obtain the optimal solution for routing and wavelength assignment design, as given in Table I.

TABLE I
Optimal RWA solution for ring network topology

Node pair	Selected route(s)	Assigned wavelength(s)	Lightpath # (wavelengths)
1-2	1→2	λ_7, λ_8	8
1-3	1→2→3	λ_6	-
1-4	1→2→3→4	λ_2	-
1-5	1→6→5	λ_6, λ_7	-
1-6	1→6	λ_2, λ_8	8
2-3	2→3	λ_8	8
2-4	2→3→4	λ_3, λ_4, λ_5	-
2-5	2→3→4→5	λ_7	-
2-6	2→1→6	λ_3, λ_4, λ_5	-
3-4	3→4	λ_1	8
3-5	3→4→5	λ_6, λ_8	-
3-6	3→2→1→6	λ_1	-
4-5	4→5	λ_1, λ_5	8
4-6	4→5→6	λ_2, λ_3, λ_4	-
5-6	5→6	λ_1	6

We can see that each of the total offered 26 connection requests could be satisfied in this network by using the routes and wavelengths as it is shown in Table I. Note that in these network topology only two possible routes between each node pair exists and that it is required to use minimum of 8 different wavelengths in the network to satisfy all the connection requests. All the lighhtpaths are established over corresponding shortest path. The obtained results for used wavelengths on each physical link are given in the last column of Table I. We can see that for all links in the ring network, except for the link 5-6, minimum number of different wavelengths to satisfy all the connection requests is 8. Therefore, the link congestion is equal to 75% for the link 5-6 and 100% for other links in the network.

The results of simulation for routing and wavelength assignment optimization problem in mesh network topology, given by Figure 1-b are shown in Table II. We assumed the same traffic demand matrix, as it is given by equation (5). We assumed also that maximum 8 wavelengths are available over each link in the network.

From the obtained results, we can see that all connection requests can be also successfully satisfied, but in this case with less number of wavelengths over links compared to the previously analyzed ring network for the same traffic demands. For resolving the RWA problem in this network topology, we limited the possible routes between end nodes in network on those that contain maximum three hopes. Therefore, for the given network topology, it can be seen that each node pair has not the same number of candidate paths such that the assumed constraint is satisfied. Maximum number of possible paths between two nodes, for observed mesh network is 5 and this is only a case between nodes 2 and 5. For other node pairs the number of candidate paths that satisfy chosen hop constraint is either three or four. We sorted possible routes in routing table in increasing order of their hop number, such as the first shortest path(s), the second shortest path(s), etc. From the results given in the last column of Table 2, we can obtain the optimal (minimum) number of wavelengths over all links in the network such that all of the connection requests can be successfully satisfied.

TABLE II
Optimal RWA solution for mesh network topology

Node pair	Selected route(s)	Assigned wavelength(s)	Lightpath # (wavelengths)
1-2	1→2	λ_6,λ_7	4
1-3	1→2→3	λ_1	-
1-4	1→2→3→4	λ_8	-
1-5	1→6→5	λ_3, λ_4	-
1-6	1→6	λ_1, λ_2	2
2-3	2→3	λ_3	7
2-4	2→3→4	λ_5, λ_6, λ_7	-
2-5	2→3→5	λ_2	-
2-6	2→6	λ_1, λ_2, λ_3	3
3-4	3→4	λ_4	8
3-5	3→5	λ_1, λ_3	3
3-6	3→6	λ_4	4
4-5	4→5	λ_1, λ_2	2
4-6	4→3→6	λ_1, λ_2, λ_3	-
5-6	5→6	λ_1	3

For the fully connected network topology, we assumed maximum 2 available wavelengths over each link. For the routing problem we limited the candidate paths on those that contain maximum two hops. As the result, we have total of 5 candidate paths (1 direct and 4 two-link alternate paths) for each node pair. For this network topology, the optimization model gives a solution of the RWA problem that is shown in Table III. We can see that all of the connection requests can be satisfied with maximum 2 wavelengths over each fiber.

TABLE III
Optimal RWA solution for fully connected topology

Node pair	Selected route(s)	Assigned wavelength(s)	Lightpath # (wavelengths)
1-2	1→2	λ_1, λ_2	2
1-3	1→3	λ_1	2
1-4	1→4	λ_2	2
1-5	1→5	λ_1, λ_2	2
1-6	1→6 1→3→6	λ_2 λ_2	2
2-3	2→3	λ_2	2
2-4	2→4 2→3→4	λ_1, λ_2 λ_1	2
2-5	2→5	λ_1	2
2-6	2→6 2→5→6	λ_1, λ_2 λ_2	2
3-4	3→4	λ_2	2
3-5	3→5	λ_1, λ_2	2
3-6	3→6	λ_1	2
4-5	4→5	λ_1, λ_2	2
4-6	4→6 4→1→6	λ_1, λ_2 λ_1	2
5-6	5→6	λ_1	2

From the results obtained by performed simulations we can leave out the fact that the network connectivity greatly respond to the required number of wavelengths over physical links. The results presented in this paper show that in the case of great network connectivity such as in extremely considered example of fully connected network topology, the required optical resources or number of wavelengths could be significantly reduced. We developed the software that can simulate the routing and wavelength assignment problem in any optical WDM network topology. By using this software we can obtain the optimal results for the RWA problem in concrete network example and so minimize the required network resources for given traffic demand scenario.

We also performed a lot of simulations for the considered network topologies with various traffic demands that may represent the forecasted traffic in future period. By carrying out these simulations we obtained the results that are similar to those represented in this paper. The general conclusion is that the required number of wavelengths for given traffic demands is greatly dependent on degree of network connectivity and the applied route selection principle. Therefore, the software that is developed for simulation purposes is able to provide the best results for the complex optimisation RWA problem for any topology and for concrete values of traffic demands in particularly considered real optical communication network.

V. Conclusion

The optical WDM networks employing wavelength routing are considered as the most promising solution for future telecommunication infrastructure. The routing and wavelength assignment problem is one of the most significant problems in designing such networks. Efficiently resolved RWA problem can greatly improve the using of network resources. Therefore, the optimal resolving of RWA problem is crucial task. With this aim, we developed the software that simulates the routing and wavelength assignment problem, based on integer linear programming optimisation. The input parameters of our software are the traffic demand matrix in the form of the required number of connection requests and the concrete physical network topology. The software outputs are the routes and assigned wavelengths for established connections. The objective of applied optimisation model is to minimize the required number of wavelength in the given WDM network topology. We tested our model on different network topologies to illustrate how the network connectivity affects to the network resources utilisation. Developed software can be efficiently applied on any given network topology in the case of small network dimensions.

Acknowledgement

This paper is a result of researching project sponsored by the Ministry of Science and Environment Protection of Republic of Serbia.

References

[1] C. S. Ram Murthy, M.Gurusamy, *WDM Optical Networks - Concepts, Design and Algorithms*, Prentice Hall, 2002.

[2] B. Mukherjee, "WDM Optical Communication Networks: Progress and Challenges" *IEEE Journal on Selected Areas in Communications*, Vol.18, No.10, pp. 1810-1824. October 2000.

[3] A. Marinčić, V. Aćimović-Raspopović, »Evolution of WDM Optical Networks«, Facta Universitatis, Series: electronic and energetics, Vol.14, No. 2, August 2001.

[4] P. Kaminow et al., "A Wideband All-Optical WDM Network", IEEE J.Select. Areas Commun., vol.14, no.6, pp.780-799, June 1996.

[5] Rajiv Ramaswami, Kumar N. Sivarajan,"Design of Logical Topologies for Wavelength-Routed Optical Networks", *IEEE J. Select. Areas Commun.*, vol.14, no.6, pp.840-851, June 1996.

[6] R. Ramaswami, K.N. Sivarajan, "Routing and Wavelength Assignment in All-Optical Networks", *IEEE/ACM Transaction on Networking*, vol.3, no.5, pp.489-500, October 1995.

[7] V. Aćimović-Raspopović, G. Marković, „ Routing in Optical WDM Network", *Proc. of TELFOR Conference*, 2003, (original in Serbian), available at www.telfor.org.yu

Network Convergence of Voice and Data Technology Test for the Efficiency of Listening Quality Using VoDSL

Sarhan M. Musa[1]

Abstract -**This paper presents a baseline test for the listening quality (LQ) using voice over digital subscriber line (VoDSL) access technology by using voice/listening quality(V/LQ) transmission with voice compression while countinously downloading file. The design of an experimental VoDSL network architecture is presented. We identify the efficiency of the LQ based on the following digital subscriber line (DSL) service levels, 640K/640K, 1.5M/256K, and 3.0M/512K for each American National Standards Institute (ANSI) loops.**

Keywords **-Voice over Digital Subscriber Line (VoDSL), Digital Subscriber Line (DSL), Integrated Access Devices (IAD), Listening Quality (LQ).**

I. INTRODUCTION

The next generations of telecommunications providers around the globe are engaging in the rapid development of a new service that will combine both data communications and telephony. VoDSL has been developed with the rapid increase of the Internet and of the data traffic through network convergence of voice and data [1]. VoDSL service has the capability to provide the customers with converged voice and data, including local and long distance telephone service, plus high speed Internet access, on a single DSL copper line. The tests and the requirements demonstrated of VoDSL equipment for voice functionality and voice quality (VQ) in the DSL forum technical report are in [2]. We used on our test asymmetric digital subscriber lines (ADSL), because it provides a "life-line" capability, so that if the power fails, one telephone line will still work. It has a lower bandwidth upstream than downstream. It transmits high bit rate data in the down direction from the central office (CO) to the subscriber (downstream), with typical bit rates from 1.5 to 8 Mb/s, and lower bit rate data in the reverse (up) direction from the subscriber to the CO (upstream), with bit rates from 64 to 640 Kb/s [3]. ADSL is used for asymmetric services to residential and small office home office (SOHO) customers. This paper contains results that can be used in evaluating VoDSL solutions that offers multiple voice connections simultaneously with data onto the high speed digital line offered by ADSL line. The results are based on the V/LQ of VoDSL. In section 2, we present description of the network architecture for V/LQ test setup.
In section 3, we have a discussion on the subscriber loop plant noise. Section 4 is the result of the tests performed while section 5 is the conclusion.

[1]Sarhan M. Musa is with the Faculty of Engineering Technology, Prairie A&M University, Prairie View, TX 77446, USA, E-mail:sarhan_musa@pvamu.edu

II. DESCRIPTION OF THE NETWORK ARCHITECTURE

We used the V/LQ transmission with voice compression while continuously downloading file to verify the ability to support up to eight derived lines and the LQ on the integrated access devices (IADs) for VoDSL. The following DSL service levels were used 640K/640K, 1.5M/256K and 3.0M/512K for each ANSI loops. Figure 1 shows the fixed wireline networks test setup for the access evolution of broadband services using VoDSL technology for V/LQ transmission. We verified the V/LQ transmission with voice compression and the maximum number of line connections in compressed mode operation that can be supported without any problems based on figure 1.

The customers can have multiple IADs based on their needs. Each IAD has 4-8 telephone interfaces plus an Ethernet interface. We test one IAD based on VoDSL solutions. Eight telephones are connected to the IAD that resides in the customer premises through plain old telephone service (POTS). Data from the personal computer (PC) source running file transfer protocol (FTP) is provided to the IAD via the Ethernet. IAD interconnects the customer's premises equipment (CPE) and ADSL service and it converts POTS to Asynchronous transfer mode adaptation layer type 2 (AAL2). It uses the same virtual path identifier/virtual channel identifier (VPI/VCI) for voice and data. So these have to be mapped to unique values before transmission on the same pipe out of the digital subscriber line access multiplexer (DSLAM), for example, 0/39 to 0/209. All the Voice calls are digitized in the form of AAL2 cells and sent over the same permanent virtual circuit (PVC), for example, 0/38. AAL2 allows us to use the same VPI/VCI for multiple users. Users do not necessarily have to coexist in an asynchronous transfer mode (ATM) cell. Each cell can carry data from just one user. The data rides separate PVC (e.g. 0/39). Both these PVCs are transported over the ADSL copper connection to a DSLAM. The DSLAM aggregates all the PVCs onto a single connection, for example, a DS-3, and sends it to an ATM switch. The ATM switch separates the voice and data calls. The voice PVCs go to a voice gateway. The voice gateway converts the ATM traffic into time division multiplexing (TDM) analog traffic and interfaces to a Class 5 switch via GR-303 Interfaces. The voice calls go to public switched telephone network (PSTN) that connected to POTS, which carries the voice calls to the telephones. On the other hand, the data is sent to a router through digital signal-level 3 (DS-3) and to the Internet then to a PC running FTP through Ethernet.

We need to confirm the dial tone on all the ports of the IAD by connecting phones to the ports and taking them off hook at

the same time as well as individually and recording the number of phones that simultaneously have dial tone. We make calls from each port of the IAD to a phone connected to the PSTN, and we repeat the same from a PSTN phone to each port of the IAD. We enable voice compression and verify the number of phones having dial tone. These tests performance are based on the Asymmetric Digital Subscriber Line Wireline Simulator (ADSL WLS) which is located between the IAD (at customer) and DSLAM (at CO) is used to generate and receive the traffic between the customer and CO after assigning the following loops: ANSI Loop #7 with 24 DSL disturbers, ANSI Loop #9 with 24 DSL disturbers, and ANSI Loop #13 with 24 DSL disturbers. Figure 2 shows some examples of the copper loops impairments as made up of pairs from sections of several cables between the central office and the customer.

III. Subscriber Loop Plant

The connections of the telephones by the twisted pair of copper wires to the network can experience some form of noise. The noise arises from the thermal noise of the twisted pair itself, the noise generated internally by the receiving modem, and signals electromagnetically coupled into the phone line [4]. We will concentrate on crosstalk noise, that is, the undesired coupling of a signal from one communication channel to another, and it occurs when some of the transmissions signal energy leaks from the cable. There are two types of crosstalk: near-end crosstalk (NEXT) and far-end crosstalk (FEXT). NEXT is the result of a leaking from nearby transmitting source into a receiver through the coupling between pairs. FEXT is the noise detected by the receiver located at the far end of the cable from the transmitter (noise source). Figure 3 shows two types of DSL crosstalk. Where pairs j and i belong to the same distribution cable and operate in full duplex. NEXT and FEXT models are specified in appropriate DSL standards for the purpose of guiding simulation study.

Galli and Kerpez [5] studied the theoretical analysis methods of summing crosstalk mixed sources. According to [5] the received power spectral densities (PDSs) of NEXT and FEXT due to more than one crosstalk disturber for n interfering signals of the same kind become

$$N_{ext}[f,n] = S(f)X_N f^{1.5} n^{0.6} \quad (1)$$

$$F_{ext}[f,n,l] = S(f)X_F f^2 l\,|H(f)|^2\, n^{0.6} \quad (2)$$

where n is the number of interfering signals, f is the frequency, $S(f)$ is the PSD of the disturbing signal, l is the loop length , $H(f)$ is the transfer function of the loop, and X_N and X_F are constants determined by measurements. Now, when $n=1$, that is, one pair-to-pair crosstalk disturber, thus

$$N_{ext}[f] = S(f)X_N f^{1.5} \quad (3)$$

$$F_{ext}[f,l] = S(f)X_F f^2 l\,|H(f)|^2 \quad (4)$$

the starting point is expressed in the 1 % worst case for crosstalk. Crosstalk noise at high frequency can be a major limitation for providing high speed digital communications through the twisted pair loop plant. However, it can be ignored at voice frequency because it is very small. According to Werner [6] the signal-to-noise ratio (SNR) under NEXT can be expressed as

$$SNR_n \approx \frac{e^{-2d\zeta\sqrt{f}}}{\chi f^{1.5}} \quad (5)$$

where d is the loop distance in feet, ζ is constant equal to 9 x 10^{-7} for 2 gauge loop, χ is constant equal to 8.8 x 10^{-14} for the 49 disturber 1 % worst case NEXT model, and f is the frequency in Hz. The SNR under FEXT can be expressed as

$$SNR_f = \frac{1}{\psi f^2 d} \quad (6)$$

where ψ is constant equal to 8 x 10^{-20} for the 49 disturber 1% worst case FEXT model. The SNR bandwidth limited by a receiver background white noise (AWGN) can be expressed as

$$SNR_w = 1\times 10^{10} e^{-2d\zeta\sqrt{f}} \quad (7)$$

where assuming that a -40dbm/Hz transmitted power density level and a -14 dbm/Hz receiver background noise power density level.

IV. Results

We used analog phones for testing, and the V/LQ is done using a digital speech level analyzer (DSLA) from Malden Electronics. This generates phonetically balanced speech samples and assesses the Mean Opinion Score (MOS) value which is claimed to have very good correlation with actual subjective assessment. The scaling for listening quality based on five categories: 4 +x (Excellent), 3 +x (Good), 2 +x (Fair), 1+x (Poor), 0 or other (Unacceptable), where x is a decimal number. The following results in figures 4-12 were observed for the DSL service levels 640K/640K, 1.5M/256K, and 3.0M/512K for each ANSI loops mentioned previously: First, the LQ_s are excellent at both speeds for the customer and the variations are very small in range of 1% for each DSL level. However, if we need to be more concerned on the 1% range, it is clearly shown that the LQ for -10 dbm (excellent quality) is greater than -40dbm (good quality) for both DSL service levels. Second, the LQ is better for the customer when the perceptual analysis measurement systems (PAMS) from the CO to the customer than the verse Third, the highest LQ for the customer is 4.31 for ANSI loop #13 with 24 DSL disturbers at speeds 640k / 640k. The lowest LQ for the

customer is 4.27 for ANSI Loop #7 with 24 DSL disturbers at the same speed. But, the highest LQ for the customer is 4.27 for ANSI loop #9 and loop #13 with 24 DSL disturbers at speeds 1.5 KM/256K. The lowest LQ for the customer is 4.26 for ANSI Loop #7 with 24 DSL disturbers at 1.5M/ 256k. On the other hand, the highest LQ for the customer is 4.29 for ANSI loop #9 with 24 DSL disturbers at speed 3.0M / 512k. The lowest LQ for the customer is 4.26 for ANSI Loop #13 with 24 DSL disturbers at 3.0M / 512k.

V. CONCLUSION

It has been shown that the following DSL service levels 640K/640K,1.5M/256K and 3.0M/512K, for each American National Standards Institute (ANSI) loops have been used to provide better voice/listening quality for customers. From the previous figures 4-12, it is clearly shown that -40dbm has more attenuation (cable loss) than -10dbm, which made the last produce better LQ using VoDSL. The downstream band is greater than the upstream that can make the LQ better for customer who receives the call from the CO than verse. The listening qualities are in excellent service for customer and the variation is very small limited to 1% range for the DSL service levels 640K/640K, 1.5M/256k and 3.0M/512k for each ANSI loop.

REFERENCES

[1] R. Franz, "Optimal Migration towards Voice/Data Convergence," *ICCT 2000 contribution.*

[2] DSL Forum Technical Report TR-049, "*VoDSL Interoperability Test plan*," May 2002.

[3] Network and Customer Installation Interfaces-Asymmetric Digital Subscriber Line (ADSL) Metallic Interface, ANSI Standard T1.413, *1995*.

[4] J. Cioffi, P. Silverman, and T. Starr, "Digital subscriber lines," *Computer Networks 31, 283-311 (1999)*

[5] Stefano Galli and Kenneth J. Kerpez, "Methods of summing crosstalk from mixed sources-part I: theoretical analysis," *IEEE Transaction on Communications, Vol. 50, No. 3, march 2002.*

[6] J. J. Werner, "The HDSL environment," *IEEE Transaction selected areas in communications. 9 (6) (1991) 785-800.*

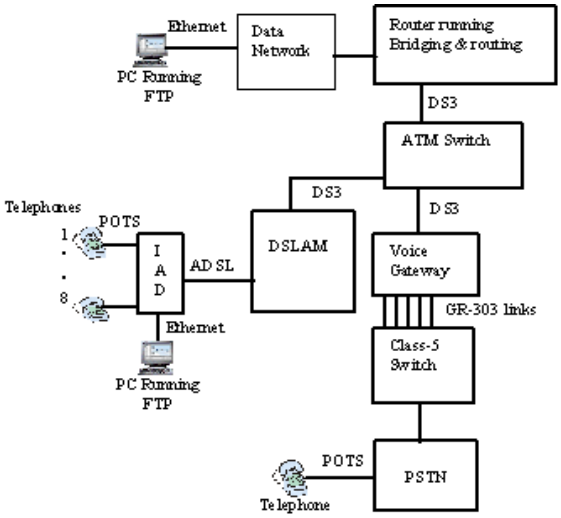

Fig. 1. Voice quality test transmission configuration

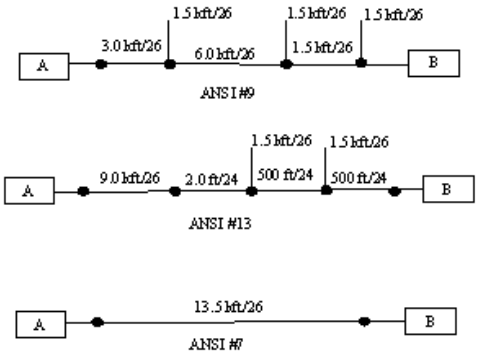

Fig. 2. Examples of ANSI loop descriptions

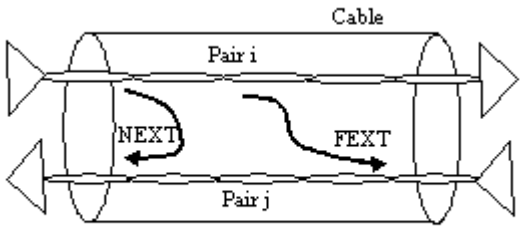

Fig. 3. NEXT and FEXT crosstalk

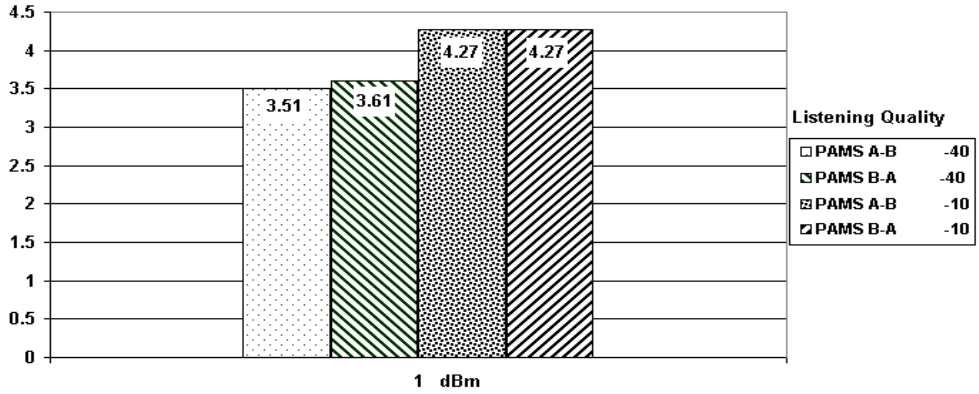

Fig. 4. DSL Service Level 640k / 640k for ANSI Loop #7 with 24 DSL disturbers

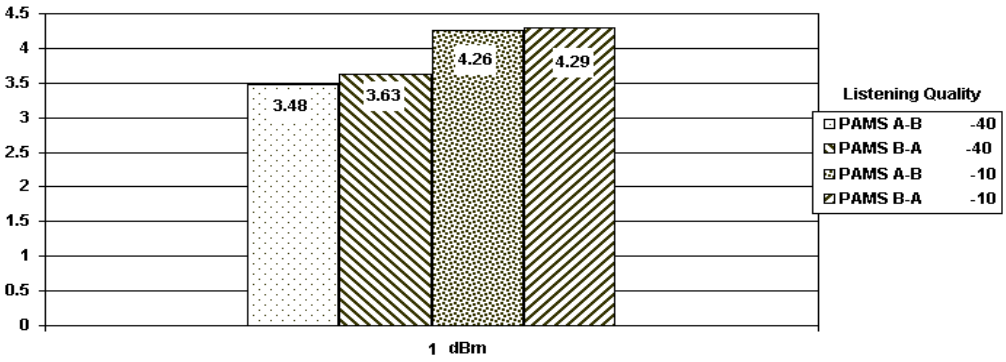

Fig. 5. DSL Service Level 640k / 640k for ANSI Loop #9 with 24 DSL disturbers

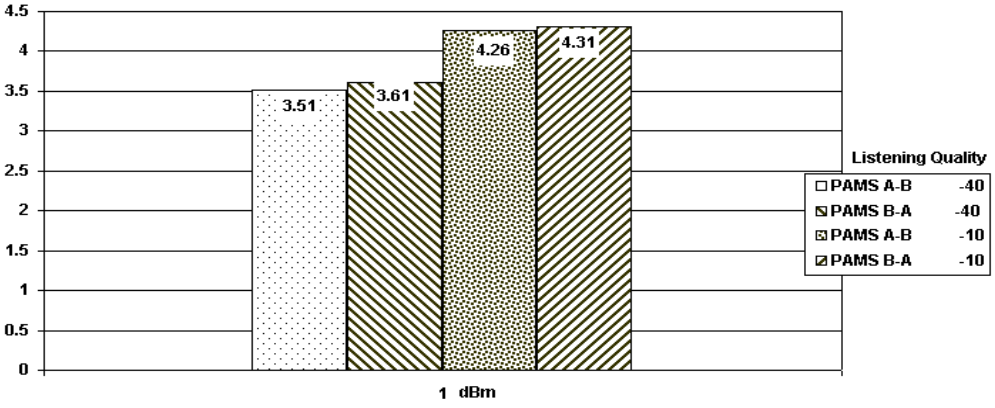

Fig. 6. DSL Service Level 640k / 640k for ANSI Loop #13 with 24 DSL disturbers

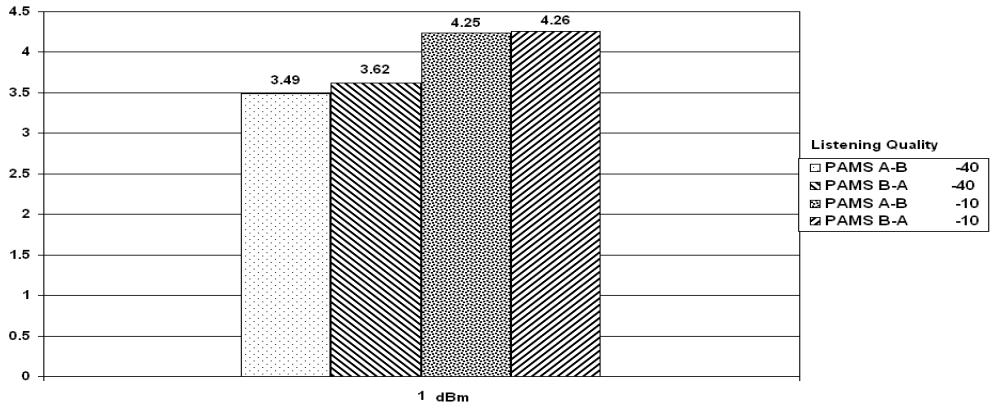

Fig. 7. DSL Service Level 1.5 KM/256K for ANSI Loop #7 with 24 DSL disturbers

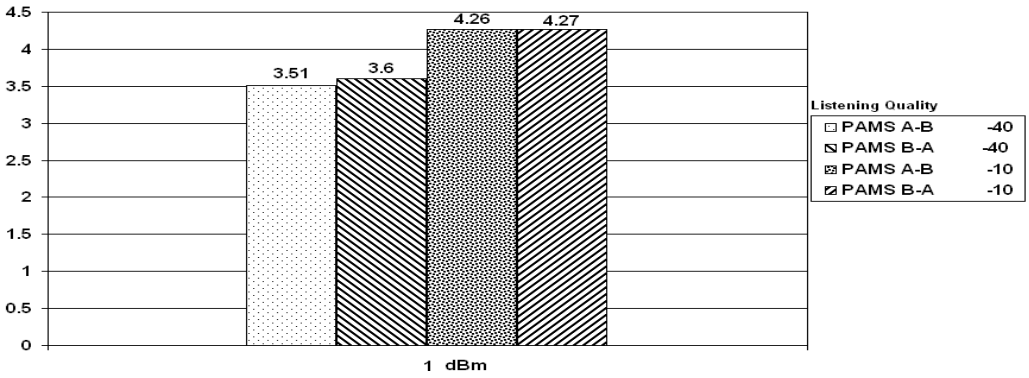

Fig. 8. DSL Service Level 1.5M / 256k for ANSI Loop #9 with 24 DSL disturbers

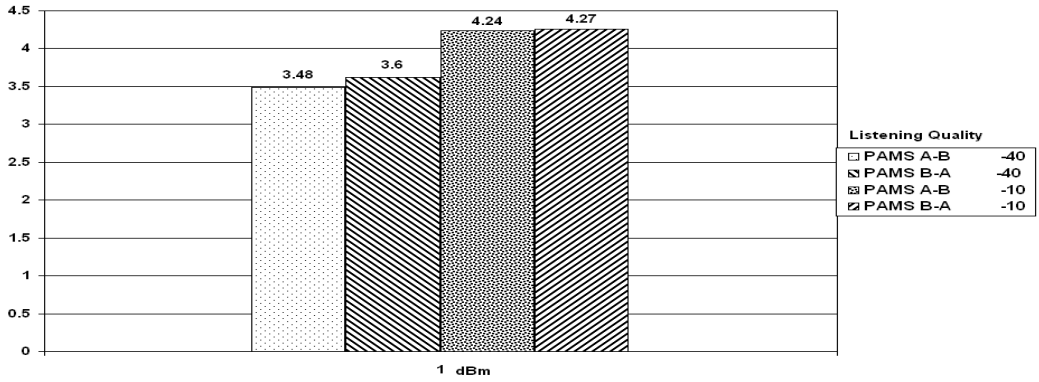

Fig. 9. DSL Service Level 1.5M / 256k for ANSI Loop #13 with 24 DSL disturbers

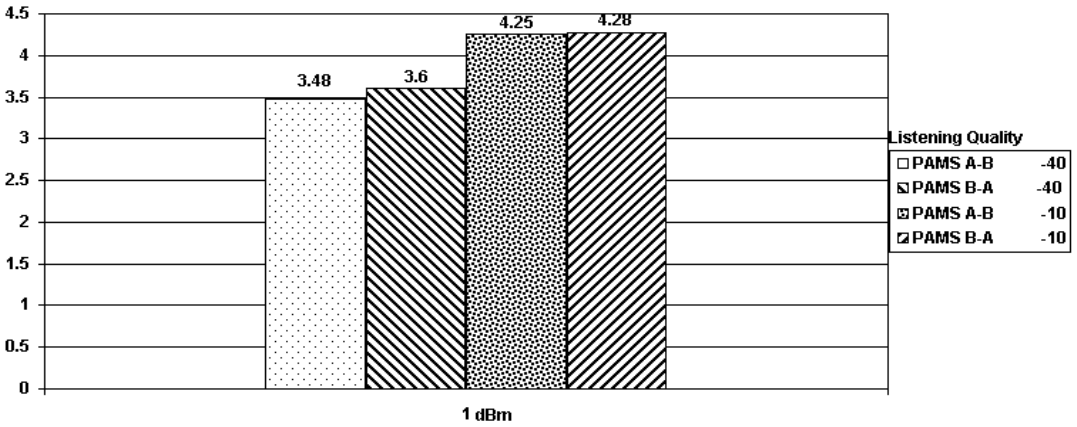

Fig. 10. DSL Service Level 3.0M / 512k for ANSI Loop #7 with 24 DSL disturbers

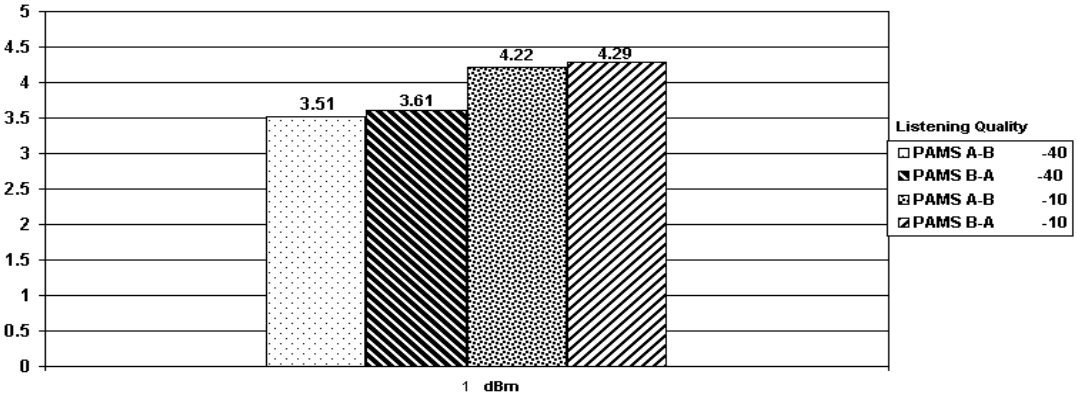

Fig. 11. DSL Service Level 3.0M / 512k for ANSI Loop #9 with 24 DSL disturbers

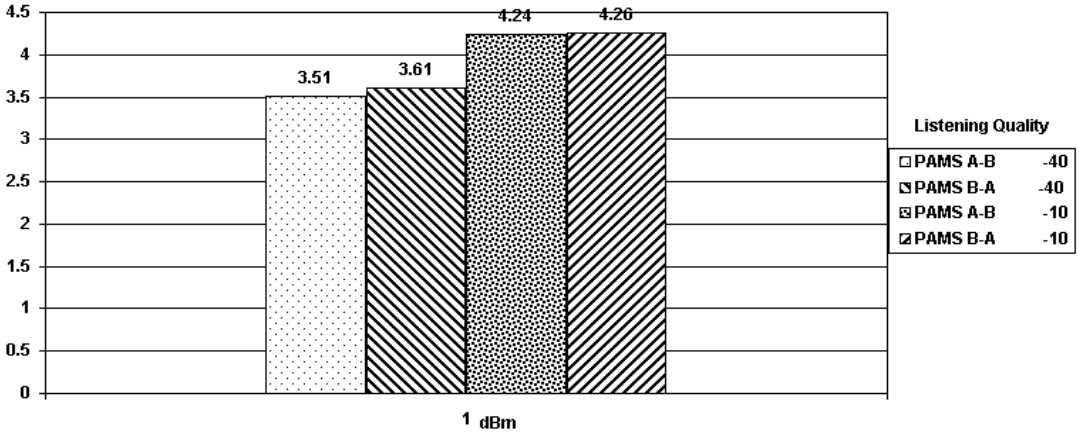

Fig. 12. DSL Service Level 3.0M / 512k for ANSI Loop #13 with 24 DSL disturbers

Implementation of Radio over Fibre Techniques for Low Cost Radio Access in Local Multipoint Distribution Systems

Milan Jankovic[1], Borislav Odadzic[1]

Abstract - **In this paper we focus on the Hybrid Fibre Radio (HFR) techniques for use within Local Multipoint Distribution Systems (LMDS). In section two we introduce the concept and reasons for considering HFR in LMDS, whereas section three is dedicated to one of the main advantages; the possibility for centralised dynamic frequency allocation. Section four describes the most relevant optical modulation techniques. This leads to the selection of the most appropriate solutions for this application.**

Keywords – **Hybrid Fibre Radio, Local Multipoint Distribution System,, Optical BB modulation, Analogue RF modulation Dynamic frequency allocation**.

I. INTRODUCTION

The integration of wireless and optical networks is a potential solution for increasing capacity and mobility as well as decreasing costs in the backbone of access network. By using Hybrid Fibre Radio (HFR), the capacity of optical networks can be combined with the flexibility and mobility of wireless access networks. The concept HFR means to transport information over optical fibre by modulating the light with the radio signal. This modulation can be done directly with the radio signal or at an intermediate frequency. HFR is a relatively new concept when considering the transmission of analogue RF waves over fibre. The practical deployment of such systems will depend on the technological development of electro-optical devices capable of modulating light waves with RF signals. Such an architecture can give several advantages:

- Reduced complexity at the antenna site. This can be achieved because modulation/demodulation, up/down-converting, multiplexing, etc. can be performed at a central office serving several antenna sites.
- Radio carriers can be allocated dynamically to the different antenna sites. In this way, more efficient use of the radio resources can be made since each carrier can be allocated to the cell where it is mostly needed.

At the same time, Local Multipoint Distribution Systems (LMDS) is being deployed in various countries, as an efficient means of meeting user needs for new services, interactivity and high bandwidth at a reasonable cost. LMDS architectures consist of star networks, with several slave cells monitored from a control and co-ordination centre via a master cell. The connection from the control centre to the master cell is usually wired, but from the master cell to the slave cells many types of connection are possible. The low cost argument for LMDS normally leads to radio link connections, but sometimes infrastructure and economical aspects will favour wired connections. LMDS is becoming an attractive solution for last mile distribution to households. As users will require more and more bandwidth in the future, it is natural to consider LMDS architectures employing optical fibres between base stations. At the same time, LMDS is often a good solution when remote locations need network connection, where optical fibre will represent superfluous capacity and excessive investments. Hence, a balanced deployment of optical fibre solutions has to be sought. New technological development in HFR will reduce the base station complexity and cost, and thereby make optical solutions increasingly attractive. Techniques based on radio frequency (RF) transmission over fibre, the possibility of light wave multiplexing and dynamic frequency allocation are key issues in this context.

II. OVERVIEW OF THE POSSIBLE ARCHITECTURES

LMDS is a generic system for local broadcast and interactive services covering both professional and entertainment services. To obtain the required flexibility LMDS must, to the extent possible, be implemented with a service independent architecture.

From a network and service point of view LMDS will interact with other networks. Although it is primarily an access network, it may also operate as a backbone or feeder network to other networks consisting of smaller cells. In areas with remote cell constellations radio, fibre or HFR may be used to connect base stations for an area covered by clusters of cells under the same management and co-ordination.

One possible realisation of LMDS is in case, when only one base station is connected to the transport network (represented by the LMDS Control Centre). The main co-ordination centre is the entrance point to the actual geographic area served by the LMDS. The cell in which they are located is defined as a master cell. All cells are individually fed from a LMDS base station connected to the co ordination centre. A base station will normally feed several cells when located at the periphery of a cell. This radio network connects to the different users within the cells and defines the LMDS access network for the cell. The distribution system of the cell is a star system with a Point to Multi-Point (PMP) down link and a point to point up link.

[1] Community of Yugoslav PTT, 11000 Beograd, Palmoticeva 2, Serbia and Montenegro, E-mail: zjptt@ptt.yu

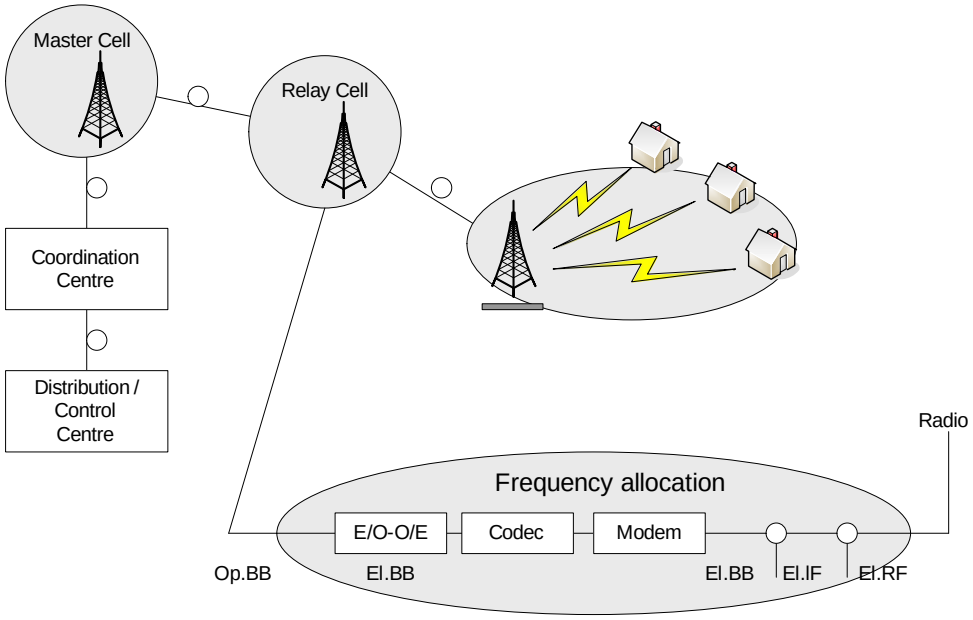

Fig. 1. LMDS with optical BB links

Normally, LMDS is operated as an interactive PMP radio access network. Both the down- an uplink is implemented via radio. The relation between the down- and uplink traffic may span between complete broadcast (no uplink) to symmetric systems. In some cases, the system is primarily used for video distribution. It is then called MVDS (Microwave Video Distribution System). In this case, the return channel (uplink) might not be implemented via the radio interface. It can be implemented in a number of other ways, depending on factors like capacity need, available technologies and cost.

There are three parts of a LMDS network where optical fibre may be an option:

- Optical fibre from a control centre out to a master cell
- Optical fibre also from the master cell out to the remote antennas
- Optical fibre for indoor distribution

Two classes of optical modulation technique are possible for LMDS systems; baseband digital (BB) and analogue radio frequency (RF). We have described some aspects connected to the use of the BB and RF techniques in the following.

A. LMDS with optical BB modulation

Optical baseband modulation signifies that the signal is conveyed through the fibre as a digital signal, and there will be a need for frequency conversion at the radio interface. Figure 1 shows a combination of optical fibre connections between LMDS base stations with radio connections to the more remote base stations.

The up-conversion from optical BB signal to RF radio signal will take place at the optical terminating LMDS base station. These base stations will have to be equipped with optical modulators and demodulators (E/O and O/E), signal processing equipment for radio links (codecs, modems, equalisers, synchronisers etc.) before up-conversion to RF signal, necessitating several local oscillators.

There are several disadvantages of such an approach however, stemming from its inherent inflexibility. There is no possibility of central, dynamic frequency allocation. Also, the LMDS base stations are relatively complex; all elements necessary for conversion between optical baseband and radio frequency waves are necessarily implemented in the base station. This is why the BB technique is not considered reliable in the LMDS case.

B. LMDS with analogue RF modulation

With RF modulation, the signal is analogue from the Control centre and is distributed at the radio frequency to be employed for the last mile radio transmission. In this case, no signal processing or frequency allocation is required at the LMDS base station, only the E/O and O/E conversions will be performed. The complexity of the LMDS base stations acting as repeaters, depends on whether baseband conversion is necessary in order to extract traffic for different destinations (i.e. for packet switching), or if this extraction can rather be based on extraction of optical carriers in a Wavelength Division Multiplex (WDM). scheme. If baseband conversion is necessary for switching, not much has been gained compared to the BB situation described previously. Therefore, extraction of optical carriers seems to be the most attractive solution for repeater base stations.

Figure 2 shows the same network as in figure 1, but now with use of RF modulation. We notice the simplicity of the LMDS base station compared to figure 1. Another advantage of this system is that the radio frequencies may be allocated at the co-ordination centre, enabling enhanced frequency reuse and more flexible bandwidth allocation.

The main disadvantage of this system is the current immaturity of the technology although systems like this will be conceivable in the future

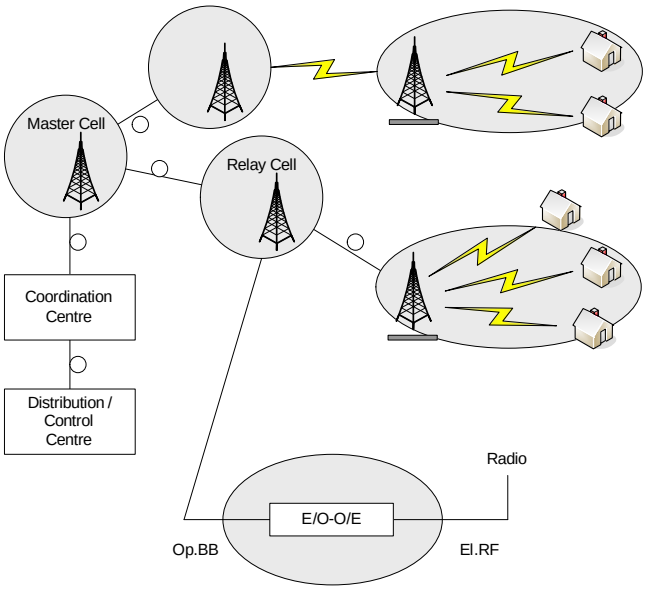

Fig. 2. LMDS with analogue RF modulation

III. Advantages of Dynamic Frequency Allocation

An important additional feature of using an optical HFR feeder system is the possibility to apply dynamic frequency allocation to meet the varying capacity demands. Following this approach an ideal architecture for a combined HFR-LMDS system is shown in Figure 3. All radio transceiver components for the LMDS system are concentrated in a central multi-cell base station serving a cluster of radio cells.

The base station contains also the HFR headend components, which transmit the radio carriers to the Remote Antenna Units (RAU) located at the cells. For LMDS, sectorisation is an important issue, and each RAU needs to be connected with one fibre per sector. The concentration of the active components in a single location allows us to assign radio carriers dynamically, following the actual capacity demand.

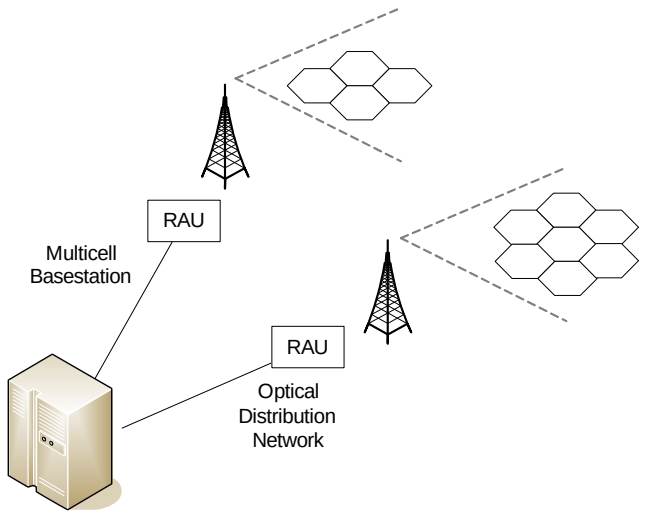

Fig. 3. Dynamic frequency allocation with HFR Feeder System

A HFR based distribution system provides the possibility of adding radio carriers without the need to modify or exchange the equipment at the RAU units and thus will allow a more flexible upgrade strategy for the network operator. This flexibility is particularly important for the roll-out of new services, where the demand is not known in advance.

The possible benefits of dynamic frequency allocation in LMDS systems depend on the absolute number of available radio carriers. It must be considered that a single operator may not own the total frequency band allocated for the LMDS service. However considering the high total frequency allocation of e.g. 2GHz in the 28 and 40GHz bands, there might be a high number of single radio carriers. The ETSI Recommendation [1] for symmetrical point to multipoint systems is based on n x 2Mbit/sec connections operating in channel widths from 3.5MHz to 112MHz. For a total bandwidth of 2GHz this relates to 18 to 572 radio carriers..

Related to the dynamic radio carrier allocation, is the relation between transmission capacity and radio bandwidth. The transmission capacity of a single channel depends on the modulation and coding format, which may be adaptive in some systems. Adaptive in this context means, that e.g. the system can switch from 4-QAM to 16-QAM in case of good transmission conditions, e.g. for near terminals. This corresponds to a twofold capacity increase using the same radio resources.

The absolute bit rate required by a customer is an uncertain factor in LMDS systems, as it will depend on the services and application scenarios. This is in particular true for the downlink/uplink asymmetry, which is a property of many applications like web browsing, audio and video-on-demand. This indicates that flexibility is an important feature and may even justify a higher installation cost for HFR components. While for video on demand, a bit rate of 4MBit/s downlink and 64kbit/s uplink might be sufficient, a business customer like a desk top publishing company might need bi-directional 100MBit/s. On the other hand the company will possibly use this high rate only for a short period of time per day. In a flexible LMDS-HFR system this capacity could be reused during the rest of the time to provide video-on-demand for another 25 customers, all using the same radio equipment.

An advanced application of dynamic frequency allocation in LMDS systems is to adapt the radio capacity to temporary customer movements. If the LMDS network detects a higher activity in a particular area, it may dynamically assign additional radio carriers to this area using the HFR feeder system.

IV. Optical Transmission Techniques Suitable for LMDS

Here we look at four of the most promising optical technologies for a wide variety of applications, suitable for LMDS. The candidate technologies are:

A. Digital baseband (BB)

Conventional optical link that is used extensively in transmission systems. Base station hardware must detect, demodulate, demultiplex, remodulate, and upconvert to the radio frequency. One transceiver is needed per carrier frequency. Dynamic reconfiguration of the signal format and number of transceivers is not possible.

B. Direct RF modulation of a single mode laser (DFB)

This is an Intensity Modulation–Direct Detection (IM-DD) link.

C. Optical single sideband (OSSB)

This is a special type of externally modulated optical link in which the modulator is driven in such a way that only one modulation sideband is produced [3]. This results in a link that is tolerant to fibre dispersion since only one signal is generated in the base station photodiode. Conventional IM-DD links use double sideband modulation that produces two signals in the base station photodiode that cause periodic fading in the presence of fibre dispersion, especially at high frequencies. OSSB is therefore suitable for systems requiring high frequency capability.

D. Electro-absorption modulator transceiver (EAM)

This is a new approach that avoids the need for a light source in the base station for the return path, which leads to the lowest complexity. The EAM device is an optical modulator that can also be used as a photo detector. As a base station transceiver, it acts as a photodiode for the send path and as a modulator for the return path. The light source for both directions is located in the central unit.

E. Comments on IHDN based on plastic fibres

In-house distribution networks (IHDN) based on optical plastic fibres have gained a lot of attention lately. The use of plastic fibres is convenient when short distances are involved and the price must be kept low. One of the main interests is that one single connection (antenna) can transmit all the traffic of the household. LMDS may then very well become the transport network carrying all the traffic into the house, In order for LMDS to become interesting as a provider for IHDN, HFR may very well be the solution.
The key features required of any HFR system are:

- Frequency range. Not all of the candidate technologies can support high radio frequencies. This is obviously of high importance to LMDS, which operates in bands around 30GHz.
- Dynamic range. Analogue optical links have limited dynamic range. This is not an important feature for LMDS however, since the path loss is not likely to change substantially once the radio link is in place.
- Flexibility. The ability to dynamically change the frequency plan, signal format and number of carriers is very attractive since it allows the network to be managed, reconfigured and upgraded effectively. Only the BB technology will not allow this.
- BS cost. The analogue technologies (BB, OSSB and EAM) have the potential to enable low BS cost since most of the system complexity is located in the Control Unit (CU).
- Reliability. If most of the system complexity is located in the CU then reliability will be increased. The analogue technologies are therefore relatively more reliable than BB digital.

V. CONCLUSION

We have investigated the possible use of Hybrid Fibre Radio techniques for Local Multipoint Distribution Systems. For analogue optical techniques, the advantages of such a combination were identified to be the simplicity of the base stations and the flexibility, in addition to the increased capacity, which is a valid argument both for analogue and digital optical modulation. The simplicity will reduce the base station cost and increase the reliability. Increased flexibility is illustrated by the possibility of dynamic frequency allocation. There are two restrictions connected to the analogue optical modulation, the first being the maturity of the technology, a second restriction is the need for baseband conversion in relay stations when packet switching systems are used. Of the optical modulation techniques analysed in this paper, only two were identified as of interest for the LMDS application; BaseBand and Optical Single SideBand. The BB technique is the digital technique employed in optical fibre systems today, whereas the OSSB is an analogue technique meeting the most important requirements of LMDS systems.

REFERENCES

[1] ETSI TM4: "Draft New Recommendation EN301 213 Point to multipoint digital radio relay systems in frequency bands in the range 24.25 - 29.5GHz"

[2] Balzaretti S., Janković M., Odadžić B., Szomolanyi T.: "Techno-economic analysis of Radio and Hybrid technologies for mobile networks", 3th Conference on the Design of Reliable Communication Networks-DRCN2001, Budapest, Hungary, October 2001, pp.78-83.

[3] G. H. Smith et al,.: "Technique for optical SSB generation to overcome dispersion penalties in fibre-radio systems", Electron. Lett. vol. 33, 1997.

[4] Paxal V., Janković M., Odadžić B., Gospić N.,: Hybrid Fibre Radio usability for future broadband wireless access, Proccedings of International Conference TELECOM 2000, Varna, Bulgaria, October 2000.

[5] E. Vergnol et al,: "Fully integrated millimetric single sideband light wave source", Electron. Lett., vol. 33, 1997.

[6] D. Wake, D. Johansson and D. G. Moodie : "Passive picocell - a new concept in wireless network infrastructure", Electron. Lett., vol.33, , 1997.

[7] ETSI BRAN : http://www.etsi.org/bran/

[8] Peha J.: Approaches to Spectrum Sharing, IEEE Communications Magazine, Vol 43, No 2., February 2005.

QoS Analysis of IEEE 802.11e EDCF

Marjan Davcevski, Toni Janevski

Abstract - **The scope of this paper is performance analysis of DCF and EDCF in 802.11 wireless LANs. The analyses are performed for EDCF with and without CFB, for different traffic types, such as voice, video and data. Using simulation methodology we have found that QoS parameters, such as throughput, packet delay and jitter, significantly depend upon the choice of the 802.11e parameters such as AIFS, CW, and TXOP.**

Keywords: **IEEE 802.11e, Quality of Service, Traffic**

I. INTRODUCTION

IEEE 802.11e Medium Access Control (MAC) is an emerging supplement to the IEEE 802.11 Wireless Local Area Network (WLAN) standard to support Quality-of-Service (QoS). The 802.11e MAC is based on both centrally-controlled and contention-based channel access. In this paper we evaluate the contention-based channel access mechanism, called enhanced distributed coordination function (EDCF), in comparison with the 802.11 legacy distributed coordination function (DCF) [1-4]. The EDCF provides differentiated channel access to frames with different priorities. We also consider an optional feature of the EDCF, called contention-free burst (CFB), which allows multiple MAC frame transmissions during a single transmission opportunity (TXOP). Furthermore, the CFB is found to enhance the EDCF performance by increasing the overall throughput and significantly decreasing delay, especially in case of transmission of video applications.

In this paper we compare the performance of the existing 802.11 MAC and the proposed 802.11e draft standard by simulating the protocols in Network Simulator v2.26 [5].

The paper is organized as follows. In the next two sections we describe briefly DCF and Enhanced DCF. Further, Section 4 gives details on CFB. Simulation analyses are presented in Section 5. Finally, Section 6 concludes the paper.

II. 802.11 DCF

The 802.11 standard specifies two channel access functions: the mandatory distributed coordination function (DCF) and optional point coordination function (PCF). Most of today's 802.11 devices operate in the DCF mode only. In this section we explain how the DCF works, because it is the basis for the Enhanced DCF (EDCF), which is the scope of our work in this paper. The diagram of DCF channel access is illustrated in Fig.1.

All authors are with the University "Sv. Kiril i Metodij", Faculty of Electrical Engineering – Skopje, Macedonia, E-mail: marjan@kabtel.com.mk, tonij@cerera.etf.ukim.edu.mk

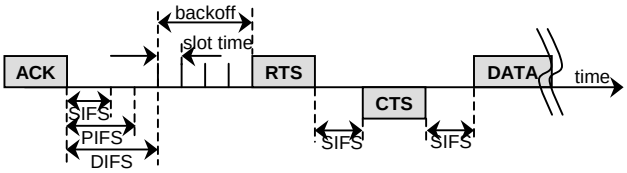

Fig.1 IEEE 802.11 DCF Channel Access

TABLE 1
MAC PARAMETERS FOR 802.11b PHY

Parameters	802.11b PHY
SIFS (μsec)	10
DIFS (μsec)	50
Slot Time (μsec)	20
CWmin	31
CWmax	1023

All of the MAC parameters including SIFS, DIFS, Slot Time, CWmin, and CWmax are dependent on the underlying physical layer (PHY). Table 1 shows these values for the 802.11b PHY. Irrespective of the PHY, DIFS is determined by SIFS+2·SlotTime, and another important IFS, called PCF interframe space (PIFS), is determined by SIFS+SlotTime. With 802.11b, the transmission rate is up to 11 Mbps.

III. 802.11E MAC ENHANCED DCF (EDCF)

EDCF enhances the original DCF to provide prioritized QoS, i.e. QoS based on priority of access to the wireless medium. Prioritized QoS is realized through the introduction of four access categories (AC), as given in Table 2. Each AC has its own transmit queue and its own set of AC parameters.

TABLE 2
PRIORITY TO ACCESS CATEGORY MAPPINGS

Priority	Access Category	Designation
1	0	Best Effort
2	0	Best Effort
0	0	Best Effort
3	1	Video Probe
4	2	Video
5	2	Video
6	3	Voice
7	3	Voice

As distinct from the legacy DCF, the EDCF is not a separate coordination function. Rather, it is a part of a single coordination function, called the Hybrid Coordination Function (HCF), of the 802.11e MAC [4]. The HCF combines the aspects of both DCF and PCF. All the detailed aspects of the HCF are beyond the scope of this paper as we focus on the

HCF contention-based channel access, i.e., EDCF. Fig.2 shows the timing diagram of the EDCF channel access.

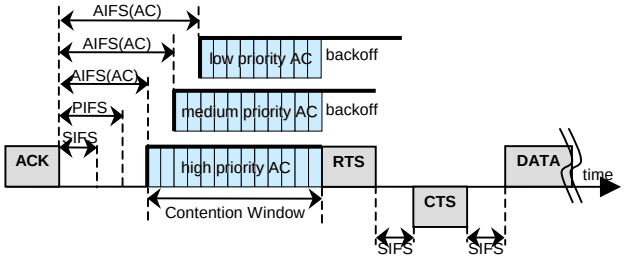

Fig.2 IEEE 802.11e EDCF channel access

The IEEE 802.11e defines a transmission opportunity (TXOP) as the interval of time when a particular station has the right to initiate transmissions. Along with the EDCF parameters of AIFS[AC], CWmin[AC], and CWmax[AP], the AP also determines and announces the limit of an EDCF TXOP interval for each AC, i.e., TXOPLimit[AC], in beacon frames. The AP can adapt these parameters dynamically depending on network conditions.

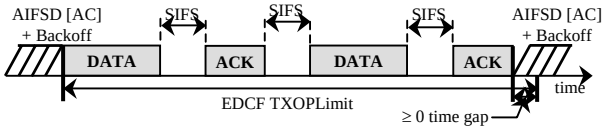

Fig.3. CFB timing structure

A single station may implement up to four transmission queues realized as virtual stations inside a station, with QoS parameters that determine their priorities. If the counters of two or more parallel ACs in a single station reach zero at the same time, a scheduler inside the station avoids the virtual collision. That is, the highest priority frame among the colliding frames is chosen and transmitted, and the others perform a backoff with increased CW values. There is then still a possibility that the transmitted frame collides at the wireless medium with a frame transmitted by other station.

IV. Contention Free Burst (CFB)

During an EDCF TXOP, a STA is allowed to transmit multiple MSDUs from the same AC with a SIFS time gap between an ACK and the subsequent frame transmission. We refer this multiple MSDU transmission to as Contention-Free Burst (CFB).

CFB was introduced to improve the performance for small packets (of timebounded services) in Wireless LANs by decreasing overhead and delay and by increasing the throughput. CFB basically uses the idea of a fragment burst (of 802.11 DCF) where a station sends small fragments of a large MSDU as a burst if it gains access to the medium. With CFB, not fragments of one large MSDU but a series of small MSDUs are transmitted in a burst. It is possible to send packets to different destinations in one burst frame. Between an ACK and the following packet only a time interval of SIFS is required. Therefore the station keeps control over the medium for the whole burst. Sending multiple small packets in a burst avoids contention for each single packet. This results in a higher efficiency and lower delay.

Fig.3 shows the transmission of two QoS data frames during an EDCF TXOP, where the whole transmission time for two data and ACK frames is less than the EDCF TXOP limit announced by the AP. As multiple MSDU transmission honors the TXOP limit, the worst-case delay performance is not affected by allowing the CFB. We show further that CFB increases the system throughput without degrading other system performance measures unacceptably as long as the EDCF TXOP limit value is properly determined.

V. Simulations

Our simulations are done with Network Simulator version 2.26. The scenario is consisted of one access point (AP) connected with server via switch from one side and eight wireless stations (WS) around it; each station except AP generates only a single type of traffic, and hence, for example, we refer to a station that generates video traffic as a video station. There are three possible directions of traffic stream: from a station toward the server (uplink), from the server towards a station (downlink) and from a station to a station. Most of the stations transmit towards server and receive from server too, except two voice stations that communicate among them.

TABLE 3
TRAFFIC TYPES AND CHARACTERISTICS

Type	Agent/ Application	Frame Size (bytes)	Data Rate (Mbps)
Voice	UDP/CBR	92	0.0368
Video	UDP/CBR	1464	1.4
Data	TCP/FTP	1500	1.0

TABLE 4
EDCF PARAMETERS 1

Type	AC	AIFS	CWmin	CWmax	TXOP Limit
Voice	3	1	7	15	0.003000
Video	2	1	15	31	0.006000
Video Probe	1	1	31	1023	0.003000
Data	0	2	31	1023	0

Two stations generate and receive the data traffic (with the lowest priority – AC0), two stations generate video probe signal (AC1) and receive the video traffic (AC2) and four stations generate and receive voice traffic (AC3). The AP transmit all kind of traffic (except video probe) generated from the server towards wireless nodes and receive all kind of traffic (except video) from wireless nodes towards server. Table 3 shows the traffic types and their characteristics that we used for our simulations. Basically, four different types of traffic are considered, namely, voice, video, video probe and data. Voice, video and video probe traffic is assumed to be of constant bit rate (CBR). Data traffic is assumed to be FTP traffic.

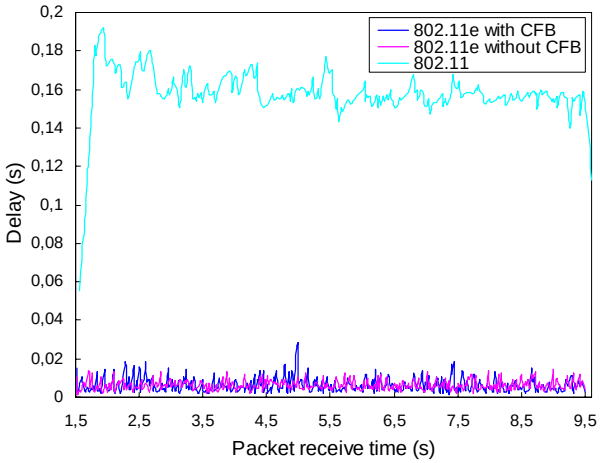

a) Delay for voice stations

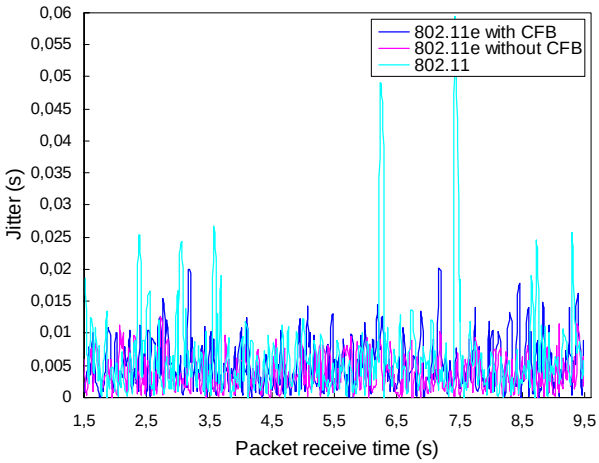

b) Jitter for voice stations

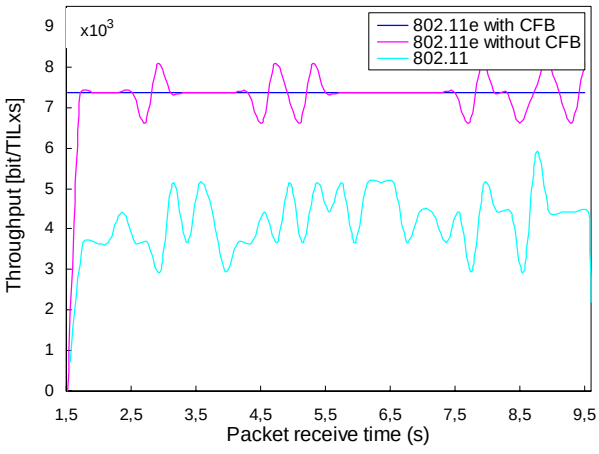

c) Throughput for voice stations

Fig.4. Comparison between 802.11, 802.11e with CFB and 802.11e without CFB for voice traffic

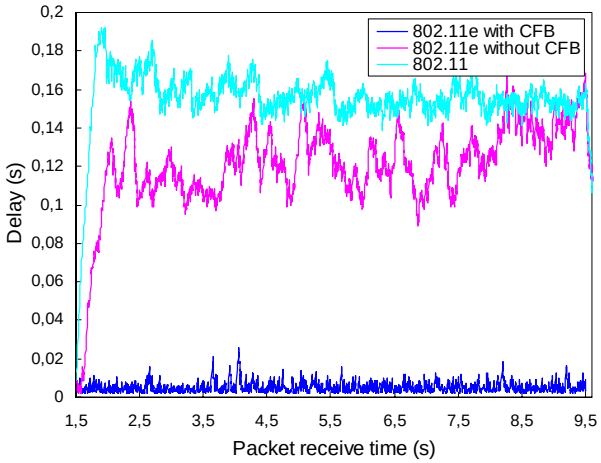

a) Delay for video stations

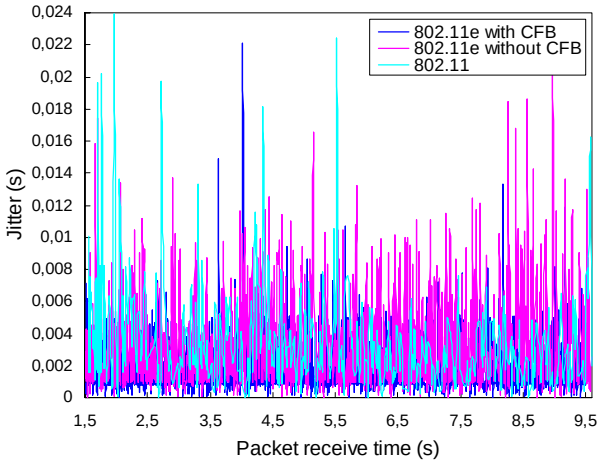

b) Jitter for video stations

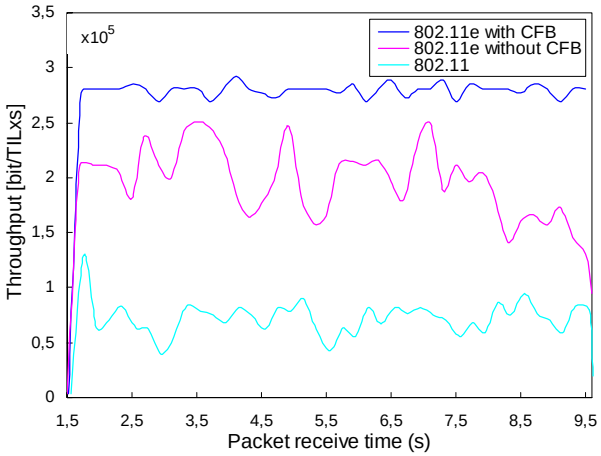

c) Throughput for video stations

Fig.5. Comparison between 802.11, 802.11e with CFB and 802.11e without CFB for video traffic

In our simulations we follow the behavior of the stations in the case of either DCF or EDCF implemented, i.e. the 802.11 stations versus QoS 802.11e stations. We measure the throughput, delay and the jitter of receiving bits in destination stations and evaluate the benefit of including different priorities for different kinds of traffic. We do the same simulations twice: first time with CFB not implemented, and the second time with CFB implemented in order to show the utility of the CFB.

We observe in Fig.4 that voice performance is significantly improved via the EDCF. Note that with the DCF, the voice frame delay sometimes goes over 250 ms, which is not acceptable in most cases. From the Fig.4c we can see that the curve representing throughput for the voice station with EDCF is almost flat. Thereat, the throughput with CFB is slightly better than without CFB.

The video performance is also improved remarkably with the EDCF. We now also observe from Fig.5a that the video delay performance is significantly improved with CFB as the video stations enjoy reduced overheads for backoff. The throughput is much better and varying much less with time then in case of DCF or EDCF without CFB (Fig.5c).

Regarding the data traffic, the results are very varying, as we expect it (Fig.6). Usually the throughput with the EDCF is better than one with the DCF, but the delay and jitter are worse, that is not surprising having in mind the 802.11e parameters for data traffic (Table 4). But delay and jitter are not critical for data traffic when compared to voice and video traffic, hence the EDCF does not make degradation of one kind of traffic in expense of the other.

VI. CONCLUSION

In this paper, we have analyzed the contention-based channel access scheme for QoS support, called the EDCF, of the IEEE 802.11e MAC. Based on the simulation, we compared the legacy 802.11 DCF and the 802.11e EDCF to show that the EDCF can provide differentiated channel access among different traffic types. We have also evaluated an optional feature called CFB, which allows a station to transmit multiple MSDUs with the SIFS time gaps within the time bound of the TXOP limit. The CFB is shown to improve the global system performance especially for the video traffic where the improvements are remarkable.

REFERENCES

[1] Sven Wietholter and Christian Hoene, “Design and Verification of an IEEE 802.11e EDCF Simulation Model in ns-2.26”, *Technical Report at TKN Telecommunication Networks*, November 2003.

[2] Simon Shung and Kamila Piechota, “Understanding the MAC impact of 802.11e”, 2003.

[3] Sunghyun Choi, Javier del Prado, Sai Shankar N, Stefan Mangold, “IEEE 802.11e Contention-Based Channel Access (EDCF) Performance Evaluation”, *in Proceedings of the IEEE ICC 2003*, Anchorage, Alaska, USA, May 2003.

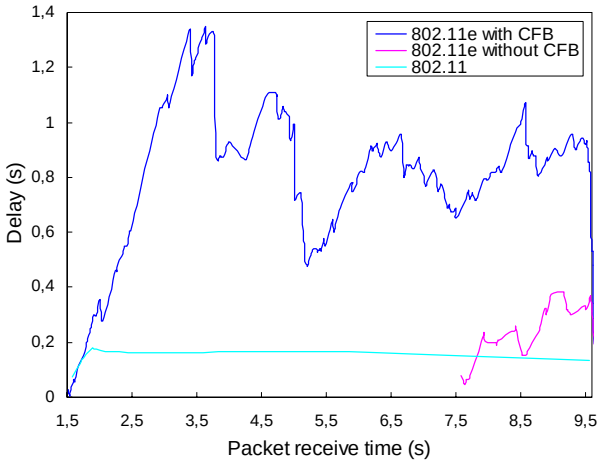

a) Delay for data stations

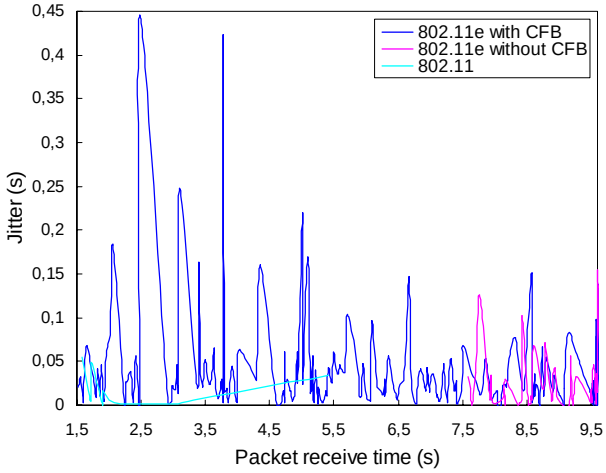

b) Jitter for data stations

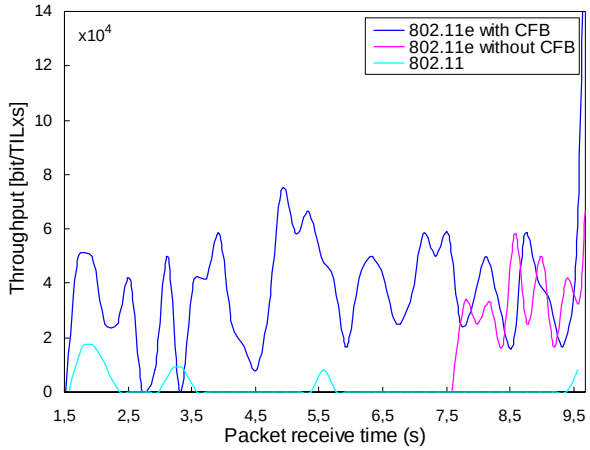

c) Throughput for data stations

Fig.6. Comparison between 802.11, 802.11e with CFB and 802.11e without CFB for data traffic

[4] Stefan Mangold, Sunghyun Choi, Peter May, Ole Klein, Guido Hiertz, Lothar Stibor, “IEEE 802.11e Wireless LAN for Quality of Service”, *in Proceedings of European Wireless 2002*, February 2002.

[5] “The Network Simulator”, http://www.isi.edu/nsnam/ns.

Determination of the Signal/Noise Ratio at the Input of Cable TV Amplifier Using Symmetrical N-Level Code

Kiril Koitchev[1], Stanimir Sadinov[2], Krasen Angelov[3]

Abstract – **The paper discusses the change in signal amplitude when interference is present during the transmission of a digital signal in the reverse channel of cable TV networks. We determine the level of noise and the signal/noise ratio as a function of the type of signals and the number of levels of the linear signal. This leads to the desired specifications of cable amplifiers, given a type of linear signal.**

Keywords – **N-level code, Signal-to-noise ratio, Amplifier, Bit error probability, Intersymbol interference.**

I. INTRODUCTION

Digital data transfer systems using the so-called "reverse channel" in coaxial CATV networks are being developed against the background of the existing analogue nets. This entails a flexible approach in the solution of the problems related to digital signal transfer.

The digital signal that is transmitted along the line is affected by noises, which bring about errors in certain symbols; the number of errors is expressed by the bit error rate [1].

Errors that appear during digital signals transmission are caused by noises and disturbances whose moment values exceed permissible boundaries, henceforth the appearance of many redundant pulses or the disappearance of those available. To avoid errors it is necessary to keep the proper signal-to-noise ratio at the input of the trunk line. When using multi-level signals errors could be generated whenever the moment value of noise exceeds the permissible level, and therefore, will have a sign opposite to that of the pulse itself. If the symbol "0" is accepted then the excess over the permissible level of noise is equally adverse for each polarity of this voltage.

Permissible noise voltage value B_0 should not exceed $0{,}5B_0$ [6], and the probability of excess over that quantity will determine the bit error rate at the input of any amplifier.

[1]Assoc. Prof. Ph.D. Kiril R. Koitchev is with the Department of Communications Technology and Equipment, Technical University of Gabrovo, Bulgaria, 5300 Gabrovo, str."Hadji Dimitar" № 4 Bulgaria, E-mail: koitchev@tugab.bg

[2]Ass. Stanimir M. Sadinov is with the Department of Communications Technology and Equipment, Technical University of Gabrovo, Bulgaria, 5300 Gabrovo, str."Hadji Dimitar" № 4 Bulgaria, E-mail: murry@tugab.bg

[3]Mag. Eng. Krasen K. Angelov is with the Department of Communications Technology and Equipment, Technical University of Gabrovo, Bulgaria, 5300 Gabrovo, str."Hadji Dimitar" № 4 Bulgaria, E-mail: kkangelov@mail.bg

II. EXPLANATION

Signal-to-noise ratio obtained in [1] is used to calculate the bit error rate and also allows to determine the properties which should be featured by given amplifier that is connected to the reverse channel of CATV networks at a preset signal $S_p(t)$. Signal-to-noise ratio according to [1] is determined by the following way:

$$b_0 = \frac{B_0}{2U_S}, \tag{1}$$

where $B_0/2$ is the permissible pulse amplitude and U_S is the effective value of noise voltage.

For symmetrical N-level code [6]:

$$B_0 = \frac{1}{(N-1)} \cdot S_p(t_1), \tag{2}$$

where t_1 is the moment of decision making. If there are disturbances between symbols, the amplitude of the signal will vary as the result of the impact of neighboring symbols.

The digital signal used in digital systems to transmit data is called isochronous which means that its symbols appear at intervals with period of appearance T_{TN}. This signal can be rendered as [2, 6]

$$S(t) = \sum_{n=-\infty}^{\infty} S_p\left(t_1 - nT_{TN}\right), \tag{3}$$

where n is the ordinal number of the symbol.

When reading the worst disturbances, caused whenever neighboring symbols obtain largest values, Eq. (3) will appear as:

$$B_0 = \frac{S_p(t)}{N-1} - \sum_{n=-\infty}^{\infty} S_p(t_1 - nT_{TN}), \tag{4}$$

The disturbance power at the point of decision-making, i.e. at the amplifier output, will be:

$$U_S^{\,2} = \frac{1}{2\pi} \int_{-\infty}^{\infty} p^2(\omega) n_{in}(\omega) d\omega, \tag{5}$$

However, the transfer characteristic of an amplifier could be written in the following kind [2, 4]:

$$S_p(\omega) = S_1(\omega) \cdot T(\omega) \cdot P(\omega), \tag{6}$$

from where:

$$P(\omega) = \frac{S_p(\omega)}{S_1(\omega) \cdot T(\omega)}. \tag{7}$$

Hence taking into account relationships Eqs. (1), (4), (5) and (7) the most unfavorable value of the ratio between signal power and noise power can be expressed in the following way:

$$b_0^{\,2} = \frac{\left\{ S_p(t) - (N-1)\sum_{n=-\infty}^{\infty} S(p)(t - nT_{TN}) \right\}^2}{(N-1)^2 \frac{2}{\pi} \int_{-\infty}^{\infty} n_{in}(\omega) \frac{S_p^{\,2}(\omega)}{S_1^{\,2}(\omega)} T^{-2}(\omega) d\omega} . \quad (8)$$

It is evident from Eq. (8) that the signal $S_p(t)$ should be selected in such a way that will help reduce symbol disturbances to the minimum level. Furthermore the spectrum signal $S_p(\omega)$ should be as narrow as possible because, in this way, the influence of noises n_{in} occurring at both inputs is reduced. At the same time, the input spectrum signal $S_1(t) - S_1(\omega)$ should be as large as possible in terms of noises n_{in}.

For most cables and especially coaxial ones, the transition characteristic $T(\omega)$ cane be expressed as [1, 6]:

$$T(\omega) = e^{-\alpha \sqrt{\frac{2\omega}{\omega_T}}} , \quad (9)$$

where α is the measured kilometer attenuation (in dB or Neper) for frequency that is numerically equal to the half value of the transfer rate of digital linear signal, and ω_T is clock frequency.

Setting Eq. (9) into Eq. (8) and assuming that the noise $n_{in}(\omega)$ is frequency independent (this is valid for the thermal noise which is the main reason for the noise caused in the coaxial channel) then the expression Eq. (8) could be written as:

$$b_{0N}^{\,2} = \frac{\left\{ S_p(t_1) - (N-1)\sum S_p(t_1 - nT_{TN}) \right\}^2}{(N-1)^2 n_{in} \frac{2}{\pi} \int_{-\infty}^{\infty} \frac{S_p^{\,2}(\omega)}{S_1^{\,2}(\omega)} e^{2A\sqrt{\frac{2\omega}{\omega_T}}} d\omega} . \quad (10)$$

By way of deduction it is possible to find the signal-to-noise ratio depending on $S_p(t)$ and $S_1(t)$ and the number of levels of the linear signal. Optimal decision is achieved for the signal $S(t)$ which is expressed by the Dirak function $h_1\delta(t)$ and signal $S(t)$ whereas for the signal $S_{ps}(t)$ adopting the kind shown below:

$$S_{ps}(t) = hp \frac{\sin \pi \frac{t}{T_{TN}}}{\pi \frac{t}{T_{TN}}} , \quad (11)$$

whose spectrum is expressed by [3, 4]:

$$S_{ps}(\omega) = \begin{cases} \frac{hp}{2} T_{TN} & for \ \ \omega \le \frac{\omega_{TN}}{2} \\ 0 & for \ \ \omega > \frac{\omega_{TN}}{2} \end{cases} . \quad (12)$$

The function $S_{ps}(t)$ shows that the intersymbol transfer disturbances at the moments of decision nT_{TN} are absent (at $t_1 = 0$) and the frequency band is limited by the quantity $\omega_{TN}/2$. By inputting the signals $S_{ps}(t)$, $S_{ps}(\omega)$, $S_1\delta(t)$, and also assuming that the mean value of the signal $h_1\delta(t)$ will be the same irrespective of the number of levels and equal to h_{1AV}, we get the following simplified expression of Eq. (10):

$$b_{0\delta NS}^{\,2} = \frac{h_{1AV}\, 2A \sqrt{\frac{f_{TN}}{f_T}}}{4 n_{in} f_{TN} (N-1)^2 e^{2A\sqrt{\frac{f_{TN}}{f_T}}}} . \quad (13)$$

It is evident from [2, 3] that with N-level linear code, the number of transferred states for a unit of time should be larger than the number of the possible states for a shared time in the transmitted binary code, i.e. to fulfill the inequality

$$\frac{N^k}{T} \ge \frac{2^M}{T} , \quad (14)$$

hence

$$K \log_2 N \ge M , \quad (15)$$

where K is the number of symbols expressed in N-level code which is used in the transfer of M symbols of binary code for a time period T. With the transformation of the binary code into linear we should use the condition

$$T_T M = T_{TN} K , \quad (16)$$

where T_T is the binary symbol duration, and T_{TN} – the N-level symbol duration.

From Eq. (16) follows that the transmission rate of the linear signal $f_{TN} = 1/T_{TN}$ will include

$$f_{TN} = \frac{K}{M} f_t , \quad (17)$$

where $f_T = 1/T_T$ is the binary signal transmission rate. Setting Eq. (17) in Eq. (18) we get the condition, which determines the linear signal transmission rate

$$f_{TN} \ge \frac{f_T}{\log_2 N} \quad (18)$$

or

$$f_{TN} = \frac{f_T}{\log_2 N}(1 + r) , \quad (19)$$

where r is the redundancy in linear signal

Taking into account Eqs. (17) and (19) and dividing the left part of Eq. (13) by $b_{0\delta 2S}^2$, and assuming that $r = 0$, we get:

$$\frac{b_{0\delta NS}}{b_{0\delta 2S}^2} = \frac{\sqrt{\log_2 N} \cdot e^{2A\left(1 - \frac{1}{\sqrt{\log_2 N}}\right)}}{(N-1)^2} . \quad (20)$$

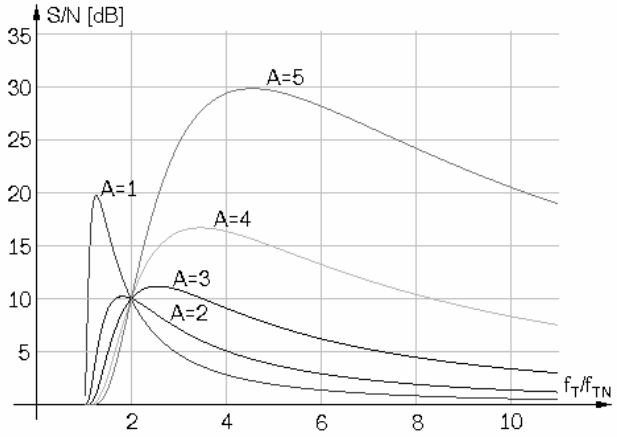

Fig. 1. Signal-to-noise ratio for multilevel code normalized in accordance with the quantity signal-to-noise for two-level signal.

This function has an extreme in relation to *N*, which depends on the quantity *A* (Fig. 1). The error in the result bay the use of the function $S_1(t)$ instead of function $S_1\delta(t)$ (instead of using in praxis rectangular impulse with working fill *50%*), amounts to, for example, *1dB*.

III. CONCLUSION

In the presence of signal $S_p(t)$, which causes intersymbol transitional disturbances, the results will be considerably better than those shown in Fig. 1 The difference will be greater in proportion with the level of symbols belonging to the linear signal. Consequently, by the transmission of multilevel digital signal correction in preamplifying stage of the line amplifiers should be carried out very precisely**.** Very effective in this case is the requirement for step reverse feedback with the regenerator output at the point of decision making. This helps to suppress intersymbol disturbances.

REFERENCES

[1] K. Koitchev, S. Sadinov, "Investigation of the Impact of Disturbances in Transmitting Digital Data Along the Return Channel in CATVs", *ICEST 2004 Conference Proceedings*, pp. 595-598, Bitola, Macedonia, 2004.

[2] J. Proakis, "*Digital Communications 3rd ed.*", McGraw-Hill, New York, 1995.

[3] J. Thomas, F. Edington, "*Digital Basics For Cable Television Systems*", Prentice Hall, 1999.

[4] В. Горянов, А. Журавлев, В. Тихонов, "*Статистическая радиотехника: Примеры и задачи*", Советское радио, М. 1980.

[5] Г. Бичев, "*Многоканални цифрови съобщителни системи*", С. Техника, 1980.

[6] "*Цифровые системы передачи*", Под ред. В. Романова, М. Связь, 1989.

A Model of Noise Influences in a Digital Communication Channel in Cable TV Networks

Krasen Angelov [1], Kiril Koitchev[2], Stanimir Sadinov [3]

Abstract – **In modern hybrid optical-coaxial cable networks, the cable cells support 150 to 300 subscribers. The lack of a physical separation of subscribers in a coaxial cell, leads to the accumulation of noise signals, which are of different types and are a function of time, geography, network architecture and so on. The successful localization and elimination of noise in the digital channel of a cable network requires knowledge of its spectrum profile and signature. This can be accomplished through modeling and studies using modern computer-aided methods.**

Keywords – **Model of noise influences, Bit error rate, Burst and impulse noise, Channel multipath reflections, Matlab.**

I. INTRODUCTION

Modern CATV networks tend to grow into larger structures. The rise in number of subscribers will normally cause an expansion of the area of coverage. This in turn brings forth a greater amount of disturbances and noises along the cable lines due to their extended length and also to the fact that most of these disturbances penetrate into the subscribers' part of the network.

Noises and disturbances affect in a greater extent the lower frequency area of the frequency range that is used in CATV networks, namely, the reverse channel range (from *5MHz* to *42MHz*). Noises tend to grow lower in loudness with the rise of frequency.

Several factors should be accounted for concerning the performance of the digital transmission channel:

- additive white Gaussian noise (AWGN);
- channel multipath reflections (echoes);
- burst and impulse noise;
- phase noise.

Bit Error Rate (BER) is used to estimate the fidelity of transmitted information when noises are available. BER stands for the ratio of wrongly received symbols to the total number of transmitted symbols [1].

In practice noise performance investigation is done over a definite period of time by means of a digital spectrum analyzer. Theoretical investigation of noise effects is conducted by means of state-of-the-art computer facilities, which implies preparation of relevant computer models and simulations in related software. Such models are essential since they appear to be individual ingredients of a larger model of a whole CATV network. Based on that model it is possible to develop another software or to improve the existing one for the purpose of optimum design or effective CATV networks control.

II. EXPLANATION

Additive white Gaussian noise is a regular noise that is characterized by a high rate of prognostication.

Multiple multipath reflections in the coaxial portion of the HFC network can severely degrade the propagating analogue or digital signals before they reach the subscriber home. Multipath reflections occur when two or more propagation paths exist between the transmitter and receiver sites. The various reflections relative to the directly transmitted signal as measured at the receiver are called echoes, which are characterized off man-made or natural structures, repeaters, or the multiple transmitters. Multiple echo degradation is not seen in the digitally demodulated picture until some "threshold" level of the digital signal is reached, resulting in a loss of the receiver synchronization. Uncorrected multipath echoes introduce intersymbol interference (ISI). The effect of multiple echoes is perceived as additional noise and causes degradation to the received SNR [2].

Burst noise is generated from different man-made or natural sources and its duration is longer than that of the $(symbol\ rate)^{-1}$. Impulse noise is similar to burst noise but its duration is less than the $(symbol\ rate)^{-1}$. Burst and impulse noises are generated from various man-made sources such as electric motors and power-switching devices. Although these sources produce burst/impulse noise events in the $5 \div 42$ *MHz* upstream frequency band. Naturally occurring burst/impulse noise events include lightning, atmospherics, and electrostatic discharge, which typically extend from *2kHz* up to *100MHz*. Part of the impulses are of repetitive character and various duration. Though impulse interferences are of broadband character their power is concentrated within the range below *10MHz*.

[1]Mag. Eng. Krasen K. Angelov is with the Department of Communications Technology and Equipment, Technical University of Gabrovo, Bulgaria, 5300 Gabrovo, str."Hadji Dimitar" № 4 Bulgaria, E-mail: kkangelov@mail.bg

[2]Assoc. Prof. Ph.D. Kiril R. Koitchev is with the Department of Communications Technology and Equipment, Technical University of Gabrovo, Bulgaria, 5300 Gabrovo, str."Hadji Dimitar" № 4 Bulgaria, E-mail: koitchev@tugab.bg

[3]Ass. Stanimir M. Sadinov is with the Department of Communications Technology and Equipment, Technical University of Gabrovo, Bulgaria, 5300 Gabrovo, str."Hadji Dimitar" № 4 Bulgaria, E-mail: murry@tugab.bg

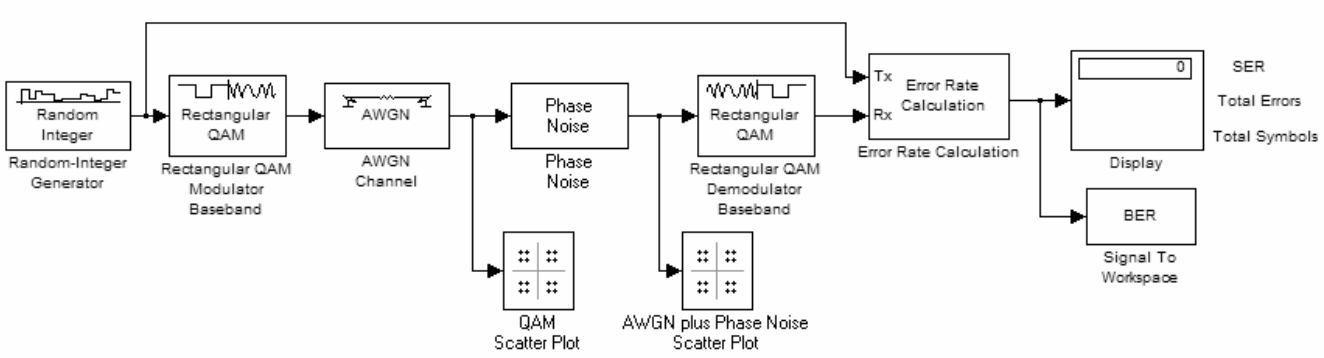

Fig. 2. Modeling the effect of additive white Gaussian noise and phase noise

The burst and impulse noise and the narrowband short-wave signals make up the so called ingress noise that is the most important and dominant noise source. In most cases narrowband short-wave signals are generated from short-wave radio transmitters whose signal penetrates the network through different poorly screened network elements. Other potential sources are short-wave radio broadcast stations and short-wave amateur stations, both of which operate within the range of *27MHz* (CB – Citizens Band) and pagers [3].

The observed increase in the ingress noise levels as the number of homes passed is increased in due to the so-called noise funneling effect. This effect is based on the assumption that the unwanted noise signals are located at the subscriber's location with time-dependent amplitude [2].

With the increase of phase noise the lowest necessary signal-to-noise ratio for effective transferring of information is shifted upwards, in other words, in order to keep the same level of the bit error rate it is necessary to reduce the noise level within the channel.

To investigate the effect of various types of noise we can use the following block schematic (Fig. 1):

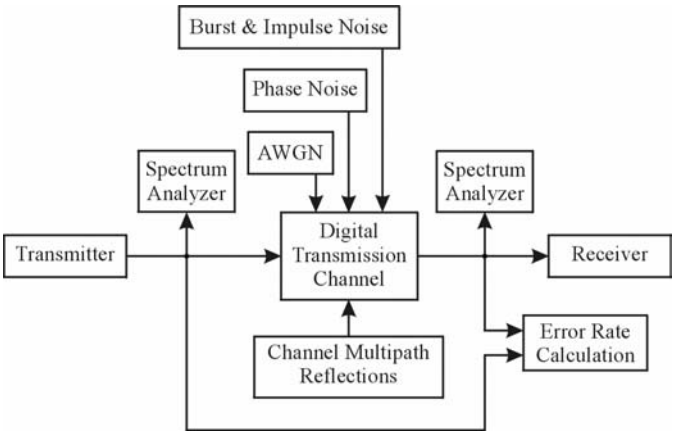

Fig. 1. Simplified block diagram for modeling of noise effect

The Maltab software includes ready functional blocks, which facilitate the implementation of simulation models that are made up according to the above block schematic. Additional functional possibilities are featured by the mechanisms for input and output of data arrays inside and outside the model. These allow to easy modify the parameters of the model and simulation as well as to facilitate the use of output data for further processing [4].

The model for simulation of the effect of additive white Gaussian noise and phase noise is relatively simple to implement (Fig. 2) [4].

Here, by using Maltab Command Window, it is possible to assign the automatic start of a series of simulations for a preset change in the signal-to-noise ratio which should result in the graphic dependence of the bit error rate on the average bit energy density relative to that of the noise – $BER = f(E_b/N_0)$. Fig. 3 shows the dependence $BER = f(E_b/N_0)$ when additive Gaussian noise is available. This dependence is obtained after four consecutive simulations corresponding to the four basic modulation formats used in CATV networks. The simulation was made with no presence of phase noise, i.e. without the use of Phase Noise block from Fig. 2.

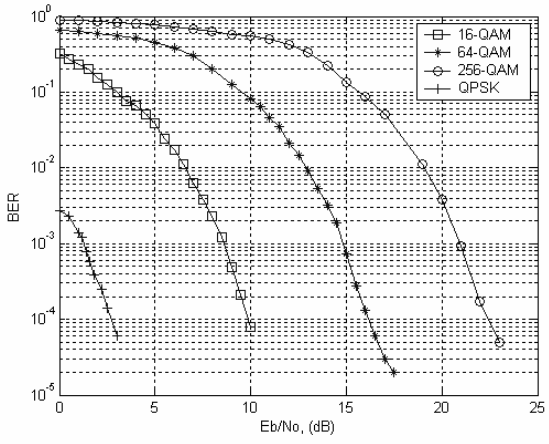

Fig. 3. $BER = f(E_b/N_0)$ for QPSK, 16-, 64- and 256-QAM modulation in presence of additive white Gaussian noise

Phase noise presence can be investigated in the same manner (by adding the Phase Noise block as shown at Fig. 2). Figs. 4 and 5 show exemplary results for 16- and 64-QAM modulation for the two different values of phase noise: *–66dBc/Hz* and *–80dBc/Hz*.

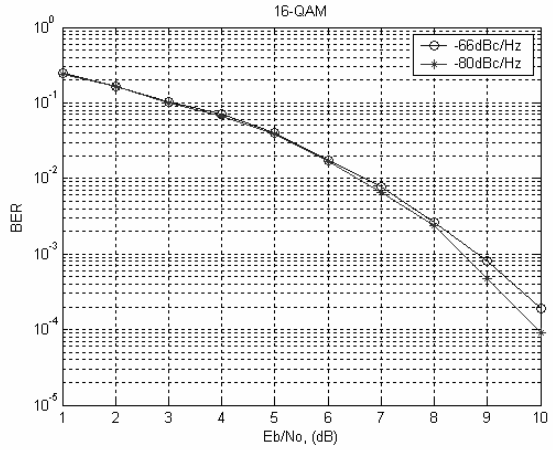

Fig. 4. *BER = f(E_b/N_0)* for 16-QAM modulation with two different values of phase noise

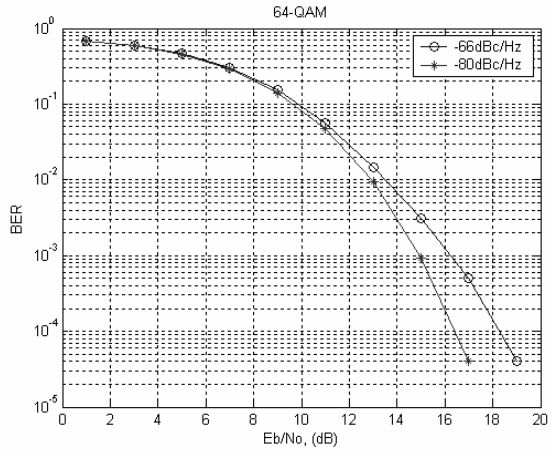

Fig. 5. *BER = f(E_b/N_0)* for 64-QAM modulation with two different values of phase noise

Impulse noise can be best described as an infinite series of interfering impulses with high level and short duration [3, 5]. For the purpose of modeling the effect of burst and impulse noise we use a model in which impulses occur periodically at a predetermined repetition rate. The three parameters in this model are the burst/impulse duration, the burst amplitude, and the repetition frequency [6]. This model can be further simplified resulting in impulses of pseudo-random character.

Modeling the effect of burst and impulse noise in a digital transmission channel is possible to obtain by means of the exemplary model shown in Fig. 6. In this model the impulse noise is entered by way of generating errors vector in which the presence of "0" means no errors whereas "1" means available error. The location and sequence of "1"s (the errors) in the errors vector can be predefined, but for the purpose of simplifying the model (the operations needed) we use errors vector each of whose entries independently takes the value zero with probability 1/2.

Figs. 7 and 8 show the signal spectrum with absence and presence of impulse noise in the transmission channel at 64-QAM modulation.

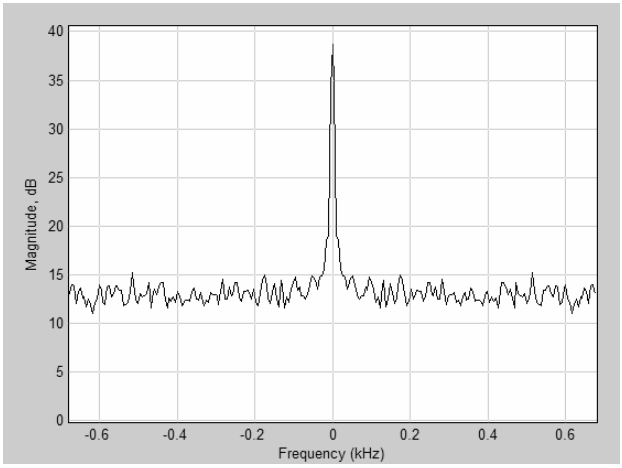

Fig. 7. Signal spectrum diagram with absence of impulse noise for 64-QAM modulation

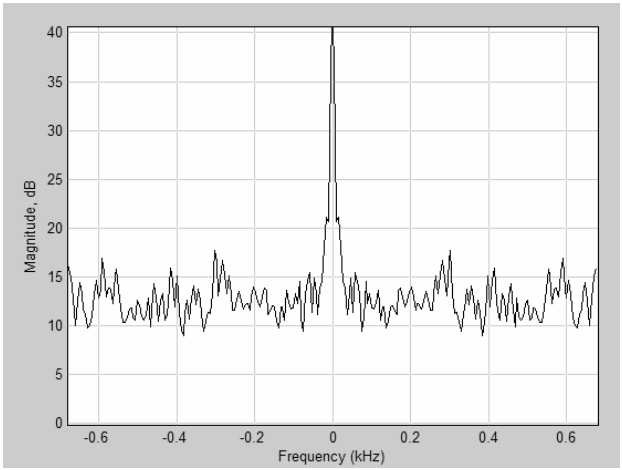

Fig. 8. Signal spectrum diagram with presence of impulse noise for 64-QAM modulation

As stated before, most disturbances penetrate through the subscribers' portion of the cable network. Noise sources appear to be TVs and the outputs of splitters, which are not connected to matched load. Another possible reason for noise interference is the poor matching of subscribers' receivers with the network, which result in the occurrence of strong channel multipath reflections in some sectors. The basic model for multipath reflections is to use a discrete channel model with 3 echoes – each consecutive echo being of a delay *T*, *2T*, *3T* respectively where *T* is a period of the symbol, and has attenuation *10dB*, *20dB*, *30dB* respectively below the main signal path. An illustration of the model of the effect of the channel mulltipath reflections in digital cable channel is shown on Fig. 9 where using the three blocks of Integer Delay it is possible to simulate the presence of echo inside the channel.

For 64-QAM modulation with input signal whose spectrum is shown in Fig. 7 we get at the model output a signal which is shown in Fig. 10 and which is the result of the impact of channel multipath reflections.

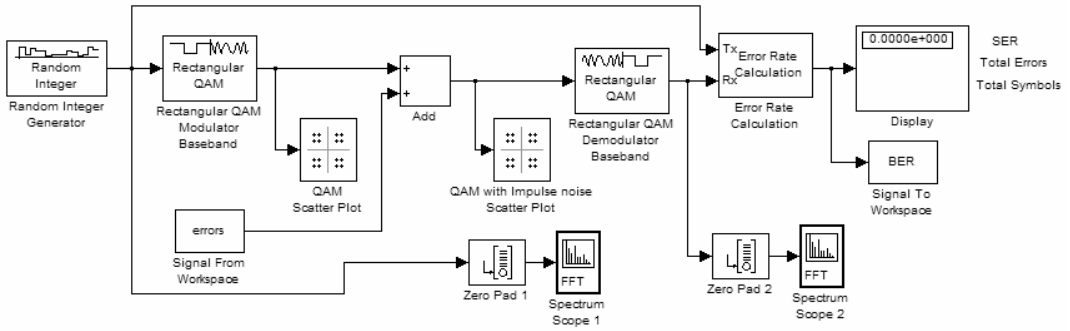

Fig. 6. Modeling the impact of burst and impulse noise

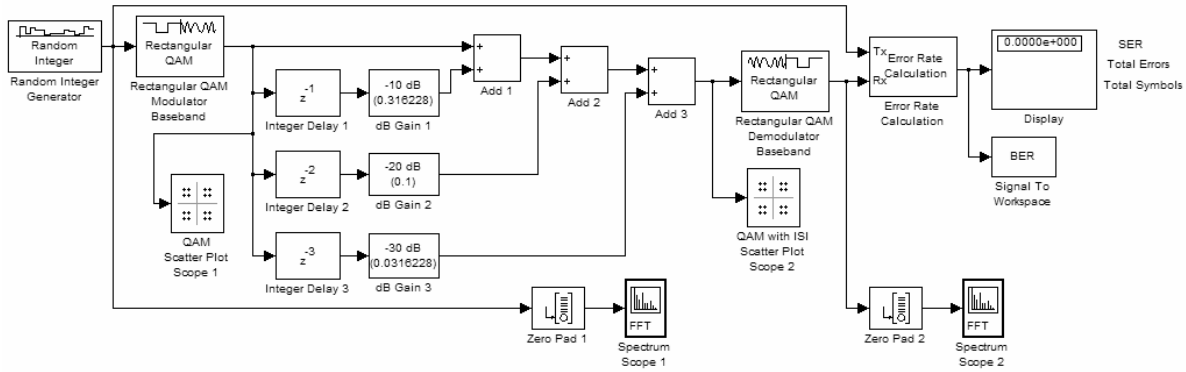

Fig. 9. Modeling the impact of channel multipath reflections

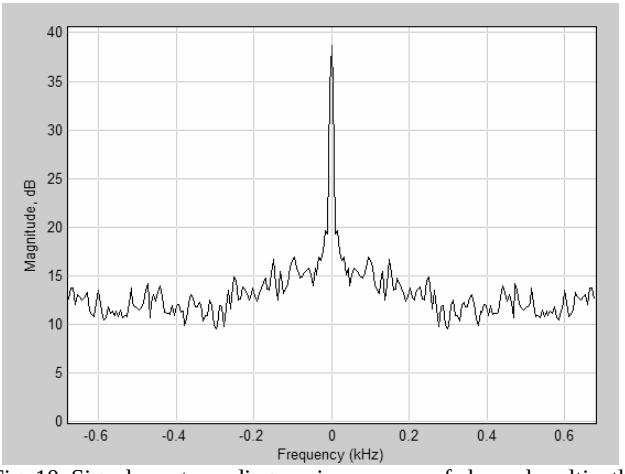

Fig. 10. Signal spectrum diagram in presence of channel multipath reflections for 64-QAM modulation

III. CONCLUSION

The effect of impulse noise can be very high and can certainly lead to communication errors. Applying appropriate error correcting techniques can reduce the effect of impulse noise. Since the peak power of impulse noise can be very high, increasing the power of transmitted signals will only slightly reduce the effect of impulse noise. On the other side, if it is accurately known how impulse noise disturbs the original signal, error correction can be used.

In the presence of Gaussian noise, the spectrum of the 64-QAM signal is essentially flat across most of the symbol rate bandwidth. If, however, multipath reflections are present, constructive and destructive interference of the reflected paths with the direct path will cause ripples in the otherwise flat spectrum. Even without the presence of multipath echoes, the use of various filters in the coaxial amplifiers typically generates group delay variation because of their nonflat frequency response. Note that placing the echo power at the maximum of the delay range produces the largest group delay variation, but not necessarily the worst effect of the transmitted signal. Breaking the echo power into multiple echoes within the time-delay range lowers the group delay variation, but actually has a worse effect on the transmitted signal due to higher peak-to-rms ratio for combining multiple echoes compared with a single echo.

REFERENCES

[1] K. Koitchev, S. Sadinov, “Investigation of the Impact of Disturbances in Transmitting Digital Data Along the Return Channel in CATVs”, *ICEST 2004 Conference Proceedings*, pp. 595-598, Bitola, Macedonia, 2004.

[2] S. Ovadia, “Broadband Cable TV Access Networks: From Technologies to Applications”, Prentice Hall, Inc., 2001.

[3] “Модернизация СКТВ для предоставления интерактивных услуг (Рекомендации tComLabs)”, *Кабельное телевидение 2004 - 2005*, vol. 7, pp. 89-93.

[4] “Using the Communications Blocksets”, MATLAB Help.

[5] R. Wolters, “Bi-directional Access on HFC CATV Networks: Design of a CDMA based Communications System”, Shaker Publishing, 1999.

[6] F. Buda, E. Lemios, H. Sari, “An Analysis of the TDMA and S-CDMA Technologies of DOCSIS 2.0”, NCTA and Juniper Networks, Inc., 2002.

Determination of the BER Characteristics with M-QAM Signal by Weibull Noise Distribution in Hybrid Cable TV Networks

Kiril Koitchev[1], Stanimir Sadinov[2], Krasen Angelov[3]

Abstract – **The paper discusses the influence of noise in hybrid cable TV networks with M-QAM signal. Non-linear distortions and thermal noise are unknown factors in CATV systems. This requires the determination of CSO and CTB levels, particularly with the use of digital signals. We use the properties of Weibull distribution to model the statistical properties of the "composite" distortions, leading to the BER characteristics of the M-QAM signal.**

Keywords – **BER, M-QAM, Weibull noise distribution, CSO, CTB.**

I. INTRODUCTION

The use of hybrid coaxial networks in CATV is a key technology in expanding the transferred services and in improving their performance quality [2, 4, 5]. Taking in consideration the use of M-array quadrature amplitude modulation (M-ary QAM) for transmitting data along with conventional amplitude modulation (AM) there should be some due attention paid to certain features, which occur with such modulations only. As is known the main line is built up by optic cable whose branches are coaxial lines [2, 3]. The optical part of the line causes the rise of thermal noise, nonlinear distortions and impulse noises. On the other hand the coaxial part of the network becomes the source of thermal noises, nonlinear distortions and low frequency noises.

Of all disturbances occurring in TV channels nonlinear distortions are best studied because they are active in both optical and coaxial part of the network.

Nonlinear products of the kind $f_m \pm f_n$ are called Second Order Intermodulation Distortion (IMD2) whereas those of the kind $f_m \pm f_n \pm f_p$ are called Third Order Intermodulation Distortion (IMD3). These distortions, coming from different channel signals, could come across some channel and by plying one over another cause additional phase distortions, which are known as "composite" distortions. In the existing CATV networks AM signal mixed with IMD2 is called Composite Second Order (CSO), and is in the area of *±1,25MHz* around the carrier of AM signal. Signal, which is mixed with IMD3, is called Composite Tipple Beat and is usually within the range of *±2,5MHz* around the carrier of AM signal. Generally, CSO cause most of the problems in the optic part of the net whilst CTB creates problems in the coaxial part. [5].

Nonlinear distortions as well as thermal noises are unknown factors in the Cable TV systems, which is why it is so important to determine the levels of nonlinear distortions, which would guarantee decent quality of digital service. The latter is closely related with the determination of the mean value of BER characteristic of the digital channel in presence of M-ary QAM signal. If the function of the random density of the probability distribution *P(u,v)* is used it will be possible to estimate the BER characteristic of M-ary QAM signal.

Investigation of CSO and CTB disturbances during digital data transfer proves that they are closer in semblance to noise rather than frequency divided harmonics and, also, their level differences are considerable [6].

In this case the noise can be regarded as such with limited frequency band and lending itself to statistical description. Normally "composite" distortions are regarded as noise which is distributed by the Gauss law [2] and not taking into account the function *P(u,v)* or the theoretical analysis of BER characteristic of M-ary QAM signals.

This article presents an optional use of statistical model of Weibull distribution whereby it is very convenient to model the mathematical features of "composite" distortions.

II. EXPLANATION

Weibull distribution of a random function is rendered by the formula [7]

$$P(x) = C.\alpha.x^{\alpha-1}.e^{-cx^{\alpha}}, \qquad (1)$$

where C and α are determining parameters.

It is evident that a Weibull distribution of the random quantity *P(x)* has the same form as that of a Reylei distribution which in fact is an amplitude distribution by Gaussian law. Accordingly, the Weibull distribution can be applied to all types of "composite" distortions by carefully selecting the level of asymmetry α no matter whether they have the same behavior or not.

A randomly selected Weibull variable could be rendered in a complex form by the following way

$$r = u + jv,$$

where u and v are the components "in phase" and "quadrature" of the variable. In this case the normal density of

[1]Assoc. Prof. Ph.D. Kiril R. Koitchev is with the Department of Communications Technology and Equipment, Technical University of Gabrovo, Bulgaria, 5300 Gabrovo, str."Hadji Dimitar" № 4 Bulgaria, E-mail: koitchev@tugab.bg

[2]Ass. Stanimir M. Sadinov is with the Department of Communications Technology and Equipment, Technical University of Gabrovo, Bulgaria, 5300 Gabrovo, str."Hadji Dimitar" № 4 Bulgaria, E-mail: murry@tugab.bg

[3]Mag. Eng. Krasen K. Angelov is with the Department of Communications Technology and Equipment, Technical University of Gabrovo, Bulgaria, 5300 Gabrovo, str."Hadji Dimitar" № 4 Bulgaria, E-mail: kkangelov@mail.bg

distribution of the probability *P(u,v)* could be rendered by the expression

$$P(u,v)=\frac{1}{2\pi\sigma^2}\cdot\frac{\alpha}{2}\left(u^2+v^2\right)^{\frac{\alpha}{2}-1}\cdot e^{-\frac{1}{2\sigma^2}\left(u^2+v^2\right)^{\frac{\alpha}{2}}}. \quad (2)$$

In Eq. (2) σ^2 is the signal dispersion. In this particular case it is the variable, which is connected to the power of the Weibull variable *r*.

By inserting in Eq. (2) the parameter

$$b=\sqrt[a]{2\sigma^2}, \quad (3)$$

then the relationship between a, b and energy E cane be expressed through the Γ-function

$$E\left(u^2+v^2\right)=\frac{2b^2}{a}\Gamma\left(\frac{2}{a}\right). \quad (4)$$

The left part of Eq. (4) cane be substituted for the alteration interval N_0 in case *u* and *v* have identical spectrum density of distribution:

$$E\left(u^2+v^2\right)=2N_0. \quad (5)$$

By substituting Eqs (3), (4) and (5) in Eq.(2) we get:

$$P(u,v)=\frac{a}{2}\cdot\frac{\left(u^2+v^2\right)^{\frac{a}{2}-1}}{n^{\frac{a}{2}}}\cdot\exp\left[\left(-\frac{1}{n^{\frac{a}{2}}}\right)\cdot\left(u^2+v^2\right)^{\frac{a}{2}}\right], \quad (6)$$

where $n=\pi\left[\frac{aN_0}{\Gamma\left(\frac{2}{a}\right)}\right]^{\frac{a}{2}}$.

Summarizing the expression for normal density of probability distribution we get:

$$P(u)=P(v)=\int_d^{+\infty}\int_{-\infty}^{+\infty}P(u,v)dudv=P_q. \quad (7)$$

It is well known that BER characteristic for M-QAM signal using the Gray code is expressed by [8]

$$P_e=\frac{2}{\log_2(M)}\left(\sqrt{M}-1\right)P_q, \quad (8)$$

where P_q is the probability for the undesired amplitude of the output signal to go beyond the appropriate level *q* of the coherent detector.

Then, by substituting Eqs. (6) and (7) in Eq. (8) we get Eq. (9) for the signal P_e:

$$P_e=\frac{2}{\log_2(M)}\left(\sqrt{M}-1\right)\int_d^{+\infty}\int_{-\infty}^{+\infty}P(u,v)dudv \quad (9)$$

i.e.

$$P_e=\frac{2}{\log_2 M}\left(\sqrt{M}-1\right)\times \times\int_d^{+\infty}\int_{-\infty}^{+\infty}\frac{a}{2}\frac{\left(u^2+v^2\right)^{\frac{a}{2}-1}}{n^{\frac{a}{2}}}\exp\left[\left(-\frac{1}{n^{\frac{a}{2}}}\right)\left(u^2+v^2\right)^{\frac{a}{2}}\right]. \quad (10)$$

Since *d* is the minimum distance between two adjacent symbols it can be expressed by Eq. (8) by means of the formula:

$$d=\sqrt{\frac{3T_S}{M-1}P_S}, \quad (11)$$

where P_S is the average power of M-QAM signal and *Ts* is the time needed for the appearance of a symbol.

If in Eq. (6) it is assumed that $k=\frac{aN_0}{\Gamma\left(\frac{2}{a}\right)}$, then from Eqs. (4) and (11) it follows:

$$\frac{d}{\sqrt{kN_0}}=\sqrt{\frac{3T_SP_S}{k(M-1)N_0}}=\sqrt{\frac{3\Gamma\left(\frac{2}{a}\right)\delta}{a(M-1)}}, \quad (12)$$

where $\delta=\frac{T_SP_S}{N_0}$.

In order to compare the results of both theoretical calculations and practical measurements, BER of 16-QAM signal for "composite" distortions were measured.

Figs. 1 and 2 show the results of BER measurement of 16-QAM signals for CSO and CTB and also the theoretical characteristics obtained in Eq. (10), which were compared with the BER characteristic of noise.

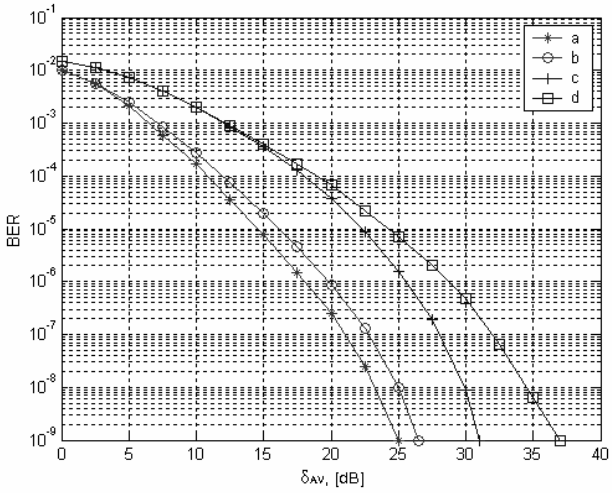

Fig. 1. BER as s function of δ_{AV} for 16-QAM signal in presence of CSO and random noise
a – theoretical results in presence of CSO
b – experimental results in presence of CSO
c – theoretical results in presence of random noise
d – experimental results in presence of random noise

From Fig. 1 it is evident that with values of error P_b for BER less than 10^{-3} the difference of δ_A with available noise and with CSO is about 2 dB. This result allows for the obtained properties of amplitude distribution of CSO and larger amplitudes with lower probabilities of occurrence than those of the noise itself.

The experimental results for BER of 16-QAM in presence of CTB are shown in Fig. 2

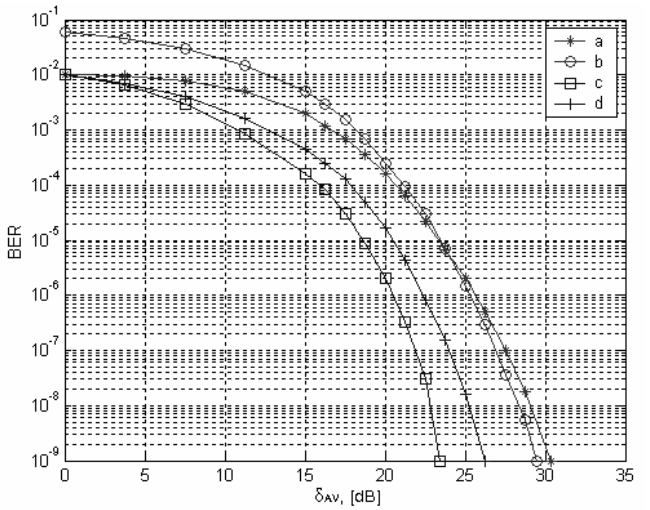

Fig. 2. BER as a function of δ_{AV} for 16-QAM signal in presence of CTB and random noise
a – theoretical results in presence of CTB
b – experimental results in presence of CTB
c – theoretical results in presence of random noise
d – experimental results in presence of random noise

It is evident that the results obtained for BER of CTB are very close to those of the noise for $P_b > 10^{-4}$, but after that they part smoothly. The connection between theoretical values and measured quantities is found in the fact that BER of the measured values are lower than the theoretical ones for $P_b > 10^{-5}$ and coincide for P_b in the area of 10^{-5} whereas for values $P_b < 10^{-5}$ it can be said that they fully coincide. For BER at $P_b < 10^{-5}$ the δ_{AV} for CTB have a *3dB* difference as compared with noise.

Accordingly, this model proves to be effective for BER at lower values.

III. CONCLUSION

The measured results for amplitude distribution show that the statistical properties of "composite" distortions are different from those of Gaussian process, i.e. Weibull distribution can be applied in calculating "composite" distortions. These results also show that the level of asymmetry of CSO is smoother than that of the noise unlike the asymmetry of CTB whose fluctuations of amplitude are much more uneven than those of the noise.

Also, the results obtained for BER show that the influence of CTB on these characteristics is stronger than noise. This is why it is important to give special attention to the CTB level control rather than to the level of both noise and CSO. The small difference between theoretical and experimental results in BER analysis by means of Weibull distribution indicates that such type of analysis is appropriate with CATV system design.

REFERENCES

[1] D. Gribb, "The Impact of digital compression in system rebuilds", *Commun. Eng. Design. Mag.*, pp. 51-56, August 1991.

[2] J. Thomas, F. Edington, "*Digital Basics For Cable Television Systems*", Prentice Hall, 1999.

[3] Q. Shi, "Asymptotic clipping noise and its impact an M-ary QAM transmission over optical fiber", *IEEE Trans. Commun.*, vol. 43, pp. 2077-2084, June 1995.

[4] P. Parsons, R. Frieden, "*The Cable and Satellite Television Industries*", Allyn&Bacon, 1998.

[5] J. Mattson, "Specifying AM fiber systems performance", *1990 NCTA Tech. Papers*, pp. 181-189.

[6] R. Prodan, M. Chelemal, T. Williams and C. Chamberlain, "Cable system transient impairment characterization", *1994 NCTA Tech. Papiers*, pp. 263-268.

[7] В. Горянов, А. Журавлев, В. Тихонов, "*Статистическая радиотехника: Примеры и задачи*", Советское радио, М. 1980.

[8] Lu Jianhua, K. Letaief, "M-PSK and M-QAM BER Computation Using Signal-Space Concepts", *IEEE Transaction of Communication*, vol. 47, no. 2, pp. 181-184, February 1999.

Session IP:

IMAGE PROCESSING

Image Deblur in Case of Symmetric Kernel

Georgi Gluhchev[1], Mladen Savov[2], Vesselin Velichkov[3]

Abstract - **An algebraic approach to image restoration is suggested. It is assumed that the blur is caused by a Gaussian type kernel of size 3x3. It is shown that the matrix of the obtained system of linear equations can be presented as a symmetric block-matrix consisting of symmetric blocks of same structure.**

Keywords – **Image deblur, Gaussian kernel, Algebraic approach.**

I. INTRODUCTION

The restoration of blurred images is one of the most important problems in the image processing. Due to different factors images could be distorted to a significant degree. The restoration techniques depend on the character of the distortion and nature of its sources. The image blur for example may be caused by the relative movement between the camera and the object when capturing the image, or due to not properly adjusted optics.

In image processing the blur effects are thought as a convolution of an ideal image *a(x,y)* with a kernel *k(x,y,α,β)* of specific parameters expressing the degradation process [1,2,3,4]. The regarded image *b*(α,*β)* is presented as the following convolution

$$b(\alpha,\beta)=\int_{-\infty}^{\infty}\int_{-\infty}^{\infty}a(x,y)k(x,y,\alpha,\beta)dxdy\,.$$

In case of discrete images the above formula takes the form

$$b(i,j)=\sum_{m=1}^{n}\sum_{l=1}^{n}a(m,l)k(m,l,i,j) \qquad (1)$$

Using the properties of the Fourier transform (FT) of the convolution of two functions the deconvolution process is determined as an inverse FT of the ratio of the blurred image spectrum and kernel spectrum, i.e.

$$a(x,y)=F^{-1}(B(u,v)/K(u,v))\,,$$

where F^{-1} is the inverse Fourier transform.

However, this simple mathematical approach known as inverse filtering faces some difficulties in its practical realization due to small or zero values in the denominator at some frequencies.

If additive noise is present it could be amplified significantly. In any case the original image could not be exactly restored. In practice the kernel k(x,y,α,β) is usually of small size and its spectrum contains a lot of zeros. To avoid this, a non-zero value (constant or optimal with respect to some criterion) is added to the denominator. Thus a family of Fourier domain filters has been developed leading to different types of Winner filters, requiring either direct or recursive operations. For incoherent imaging systems least squares based restoration filters may produce negative image values. This is not the case with the maximum entropy based or Bayesian theorem based restoration filters [1].

In this paper a straightforward approach in case of restricted and symmetric Gaussian type kernel, based on the solution of an algebraic system of linear equations, is described. For this the presentation (1) is used, where the blur effect alongside the image borders is evaluated using only the neighbor pixels from the image. The special type of the kernel allows avoiding the evaluation of determinants and matrices of large size because the inverse matrix of the system is a block (but not circulant) matrix which could be analytically evaluated.

II. THE APPROACH

Let the original, not blurred image, be of size *n*x*n* and the array of the pixels be denoted as $\boldsymbol{a}=\{a_{ij}\}$, (i,j = 1,2,…,*n*). Let the blur be caused by the kernel $\boldsymbol{k}$ of size 3x3 as shown in Fig. 1.

$$\boldsymbol{k}=\begin{Vmatrix}1&2&1\\2&4&2\\1&2&1\end{Vmatrix}$$

Fig. 1. Gaussian type kernel

We assume also, that the image is blurred placing the central element of $\boldsymbol{k}$ over every pixel of $\boldsymbol{a}$ and the blurred value is obtained as weighted sum of the pixels covered by the kernel. Thus, for a corner element only the element itself and its 3 neighbors will be used for the evaluation of the corresponding blurred value. For the border elements 6 pixels will be taken into account, while for the central elements 9 pixels will be used. The blurred image is of size *n*x*n* as well. Instead of using normalized weights we assume that the obtained blurred values are multiplied by 9, 12 and 16, respectively. As an illustration the following matrix of coefficients will be obtained for the case *n* = 3 (Fig.2):

[1]Georgi Gluhchev is with the Institute of Information Technologies, 2 Acad. G. Bonchev Str., Sofia, 1113, Bulgaria, E-mail: gluhchev@iinf.bas.bg

[2]Mladen Savov is a PhD student , E-mail: ihaiha99@abv.bg

[3]Vesselen Velichkov is a PhD student, E-mail: vesko@iinf.bas.bg

a_{11}	a_{12}	a_{13}	a_{21}	a_{22}	a_{23}	a_{31}	a_{32}	a_{33}
4	2	0	2	1	0	0	0	0
2	4	2	1	2	1	0	0	0
0	2	4	0	1	2	0	0	0
2	1	0	4	2	0	2	1	0
1	2	1	2	4	2	1	2	1
0	1	2	0	2	4	0	1	2
0	0	0	2	1	0	4	2	0
0	0	0	1	2	1	2	4	2
0	0	0	0	1	2	0	2	4

Fig. 2. Coefficient matrix of the system (1)

It could be presented as the following block-matrix **A**

$$\mathbf{A} = \begin{Vmatrix} \mathbf{2B} & \mathbf{B} & \mathbf{0} \\ \mathbf{B} & \mathbf{2B} & \mathbf{B} \\ \mathbf{0} & \mathbf{B} & \mathbf{2B} \end{Vmatrix}$$

where **0** is a 3x3 zero matrix and **B** is the following 3x3 matrix

$$\mathbf{B} = \begin{Vmatrix} 2 & 1 & 0 \\ 1 & 2 & 1 \\ 0 & 1 & 2 \end{Vmatrix}$$

For the determinant of **A** the following expression) holds

$$\det(\mathbf{A}) = 4^3 \det^3(\mathbf{B}).$$

For an arbitrary n the formula

$$\det(\mathbf{A}) = (n+1)^n \det^n(\mathbf{B}) \qquad (3)$$

will be obtained by induction.
In that case the matrix **B** looks as follows:

$$\mathbf{B} = \begin{Vmatrix} 2 & 1 & 0 & 0 & \dots & 0 & 0 & 0 \\ 1 & 2 & 1 & 0 & \dots & 0 & 0 & 0 \\ 0 & 1 & 2 & 1 & \dots & 0 & 0 & 0 \\ \dots & \dots & \dots & \dots & \dots & \dots & \dots & \dots \\ 0 & 0 & 0 & 0 & \dots & 1 & 2 & 1 \\ 0 & 0 & 0 & 0 & \dots & 0 & 1 & 2 \end{Vmatrix}$$

It is easily seen that det(**B**) = n+1. Thus

$$\det(\mathbf{A}) = (n+1)^{2n}. \qquad (4)$$

To solve the system (1) we have to evaluate the matrix $\boldsymbol{c}$ of adjuncts which is of size n^2 x n^2.

For $n = 2$ this matrix is as follows:

$$\boldsymbol{c} = \begin{Vmatrix} 36 & 18 & -18 & -9 \\ 18 & 36 & -9 & -18 \\ -18 & -9 & 36 & 18 \\ -9 & -18 & 18 & 36 \end{Vmatrix}, \quad \text{or}$$

$$\mathbf{c} = \begin{Vmatrix} C_{11} & C_{12} \\ C_{21} & C_{22} \end{Vmatrix} = \begin{Vmatrix} -2C & C \\ C & -2C \end{Vmatrix} \text{ with } C = \begin{Vmatrix} -18 & -9 \\ -9 & -18 \end{Vmatrix}$$

For $n = 3$ $\boldsymbol{c}$ is as follows:

$$\boldsymbol{c} = \begin{Vmatrix} 2304 & 1536 & 768 & 1536 & 1024 & 512 & 768 & 512 & 256 \\ 1536 & 3072 & 1536 & 1024 & 2048 & 1024 & 512 & 1024 & 512 \\ 768 & 1536 & 2304 & 512 & 1024 & 1536 & 256 & 512 & 768 \\ 1536 & 1024 & 512 & 3072 & 2048 & 1024 & 1536 & 1024 & 512 \\ 1024 & 2048 & 1024 & 2048 & 4096 & 2048 & 1024 & 2048 & 1024 \\ 512 & 1024 & 1536 & 1024 & 2048 & 3072 & 512 & 1024 & 1536 \\ 768 & 512 & 256 & 1536 & 1024 & 512 & 2304 & 1536 & 768 \\ 512 & 1024 & 512 & 1024 & 2048 & 1024 & 1536 & 3072 & 1536 \\ 256 & 512 & 768 & 512 & 1024 & 1536 & 768 & 1536 & 2304 \end{Vmatrix}$$

or

$$c = \begin{Vmatrix} C_{11} & C_{12} & C_{13} \\ C_{21} & C_{22} & C_{23} \\ C_{31} & C_{32} & C_{33} \end{Vmatrix} = \begin{Vmatrix} 3C & 2C & C \\ 2C & 4C & 2C \\ C & 2C & 3C \end{Vmatrix}, \text{ with}$$

$$C = \begin{Vmatrix} 768 & 512 & 256 \\ 512 & 1024 & 512 \\ 256 & 512 & 768 \end{Vmatrix}.$$

Similar relations between the elements of $\boldsymbol{c}$ hold for $n = 4, 5, \dots$ and they could be summarized as follows.

1. $\boldsymbol{c}$ is a symmetric matrix.
2. The elements of C_{11} are positive.
3. The sign ε_{ij} of C_{ij} changes according to the formula

$$\varepsilon_{ij} = (-1)^{n+1} sign(C_{i-1,j}) = (-1)^{n+1} sign(C_{i,j-1}), \qquad (5)$$

i.e., if $n = 2k + 1$ all sub-matrices C_{ij} consist of positive elements, otherwise the signs change alternatively.

4. The smallest absolute value in $\boldsymbol{c}$ is the value of $c_{n^2 1}$.
5. C is symmetric. Also, their elements are proportional to the smallest one and follow the rule:

$$C_{i,j} = 2C_{i+1,j} \text{ for } n - i < n - j + 1 \ (i,j = 1,2,\dots,n) \qquad (6)$$

Thus, the elements of C, and therefore all the elements of $\boldsymbol{c}$, could be easily evaluated if the element $c_{n^2 1}$ is known. But it is easy to check that

$$C_{n^2 1} = (-1)^{n+1} (n+1)^{2(n-1)}. \qquad (7)$$

The obtained results show that the solution of the linear system (1) does not require $n^2 \times n^2$ determinants of size $(n^2-1) \times (n^2-1)$ to be evaluated. Their values could be calculated straightforwardly according to the equations (3), (4), (5), (6) and (7).

The solution in a_{ij}, will be obtained according to the formula

$$a_{ij}=\frac{(-1)^{ni+j}}{\det(A)}\Big(\sum_{m=1}^{n}(-1)^{nm}\sum_{p=1}^{n}(-1)^{p}C_{m(p),i(j)}b_{mp}\Big) \tag{8}$$

Since the matrix $\boldsymbol{c}$ is of size n^2 x n^2 a lot of memory will be required to save it even in case of moderate value of n. However, the above formulated properties allow avoiding this problem. Knowing the smallest value $c_{n^2 1}$ all the elements $\boldsymbol{c}_{m(p),i(j)}$, where *m(p),i(j)* stands for the element (p,j) of the block $C_{m,i}$ of $\boldsymbol{c}$, could be evaluated according to the formula

$$C_{m(p),i(j)} = \varepsilon_{mi} i(n-m+1)\, j(n-p+1) c_{n^2 1}, \tag{9}$$

where

$$\varepsilon_{mi} = \begin{cases} 1, & if \quad n = 2k+1 \\ (-1)^{m+i}, & otherwise \end{cases}.$$

Formula (8) is valid for $m \geq i$ and $p \geq j$. If $m < i$ or $p < j$, m and i or p and j respectively, have to exchange their places in (8).

Including the expression (9) in formula (8) and performing elementary calculations the following formula for a_{ij} will be obtained:

$$a_{ij}=ij\frac{(-1)^{ni+j}}{(n+1)^2}\Big(\sum_{m=1}^{n}\varepsilon_{mi}(-1)^{nm}(n-m+1)\sum_{p=1}^{n}(-1)^{p}(n-p+1)b_{mp}\Big) \tag{10}$$

where i,j = 1,2,…,n.

III. Conclusion and Discussion

A straightforward algebraic approach to image deblur has been described provided an isotropic Gaussian type kernel of size 3x3 has caused the blur. The special kernel's type leads to direct evaluation of the determinant of the corresponding system of linear equations and its minors. Thus the heavy computational burden is overcome. This is the main advantage of the approach. The expression (3) shows that the system is always solvable and has a unique solution. The second advantage consists in the possibility of accurate restoration of the initially unblurred image if no round-off errors are present.

The third advantage stems from the integer arithmetic, which, in addition, will save computational resources and could allow for a fast parallel implementation.

However, the selected special type of the kernel is a shortcoming that will restrict the application of the approach.

It seems that similar results could be obtained with other isotropic kernels of larger size. This will be the next step in our investigation. Also, an interesting problem of great practical importance is the evaluation of the influence of the round-off errors and the possibility of its decrease. These errors are inevitable and stem from the integer output of the capturing devise. In [2] an illustration of the effect of round-off errors is present using one-dimensional signal of sinusoidal form of amplitude 25 presented with 30 points. The graph shows a significant offset from the original curve.

Acknowledgement

This investigation was supported by the Ministry of Education and Sciences in Bulgaria under contract No I-1302/2003.

References

[1] Jain, A. K., *Fundamentals of Digital Image Processing*, Prentice Hall, Englewood Cliffs, 1989

[2] Petrou M., P. Bosdogianni, *Image Processing*, John Wiley & Sons, Inc., 1999

[3] Parker J.R., *Algorithms for Image Processing and Computer Vision*, John Wiley & Sons, Inc., 1997

[4] Pratt, W. K. "*Digital Image Processing*" (Third Edition), John Wiley & Sons, Inc., 2001

Fast Algorithm for Color Space K-L Image Transform

Roumen Kountchev[1], Agata Manolova[2]

Abstract - **The *Karhunen–Loeve (KL) Transform* is an optimal transform among all discrete transforms, which is used in image processing and computer vision for several tasks such as face and object recognition. Its computational demands and its batch calculation nature have limited its application.**
In this paper, we will propose a new fast algorithm for *Karhunen-Loeve Color Space Transform* (KLCST) which will facilitate the computational process and will allow reducing the data redundancy in the color space. This algorithm is faster in typical applications and is advantageous for real time image processing.

Keywords **– Fast Karhunen-Loeve Color Space Transform, reduction of data redundancy, feature extraction, color segmentation, image compression.**

I. COLOR TRANSFORMS: STATE OF ART

The color space transform is critical for color feature extraction and data redundancy reduction. Many attempts have been made to model color perception by researchers of various fields: psychology, perception, computer vision, image retrieval, and graphics. Some of these resulted in well defined color spaces [1], [2]. The list of color spaces is almost endless. A few of the most important color spaces are:

- RGB – (Red, Green and Blue);
- YCbCr – (Luminance, Chrominance and Chrominance);
- HSV- (Hue, Saturation and Value);

In the present research, we adapt the W3C definition of color spaces: "A color space is a model for representing color numerically in terms of three or more coordinates." (http://www.w3.org/Graphics/Color/sRGB.html).

Each pixel of the image can be represented as a point in a 3D color space. Commonly used color space for image retrieval include RGB, YCbCr, HSV (or HSL, HSB). There is no agreement on which is the best.

RGB space is a widely used color space for image display. It is composed of three color components red, green, and blue. These components are called "additive primaries" since a color in RGB space is produced by adding them together.

YCbCr is a color space where Y represents the luminance of a color, while Cb and Cr represent the chromaticity of a color gray-vividness and brightness-darkness. One of the advantages of this transformation is that it reduces the psycho visual redundancy of an image.

In HSV (or HSL, or HSB) space is widely used in computer graphics and is a more intuitive way of describing color. The HSV depict the colors in a non linear space aiming closeness to the human perception. The three color components are *hue*, *saturation* (lightness) and *value* (*brightness*).

All these color transforms do not depend of the contents of an image except the Karhunen-Loeve transform. Karhumen-Loeve transform (KLT) is a unitary transform that diagonalizes the covariance or the correlation matrix of a discrete random sequence. The K-L transform has found many applications in traditional fields such as statistics and communication. In computer vision, it is used for a variety of tasks such as face recognition, object recognition, motion estimation, visual learning, and object tracking [3], [4], [5]. It is, however, used infrequently as it is dependent on the statistics of the sequence i.e. when the statistics change so also the KLT. Because of this signal dependence, generally it has no fast algorithm.

Our goal is propose a new fast algorithm for K-L optimal color transform which will facilitate the computational process and will allow the speed up of the process and the reducing of the data redundancy in the color space.

The first section of this paper introduces some of the most utilized color spaces and also presents a brief revue of the K-L transform. Afterwards in the second section we present the new algorithm for KLCST followed by the third section, where we present the evaluation techniques for this new algorithm. In section IV we will present the experimental results and a comparison between the performance of the KLCST and the introduced in section I color space transforms for reducing the data redundancy. We end this paper with plans for future research and the final conclusions.

II. ALGORITHM FOR FAST KARHUNEN-LOEVE COLOR SPACE TRANSFORM

KLT is utilized as a tool to extract the significant inter-component information and eliminate the redundancy. KLT is linear transformation which uses the signal statistics to define a rotation of the original images in such a way that the new axes are orthogonal to each other and point the direction of decreasing order of the variances. The transformation components are totally uncorrelated. KLT is a transform depending upon the data to be transformed. Its matrix consists of the eigenvectors derived from the covariance matrix, so a KLT matrix is an orthogonal matrix. This transform is the optimal statistic transform and the most effective technique for data decorrelation.

In this paper all the images used are in RGB color space. The work is realized in two section containing twelve steps [5]:

[1]Dr.Sc. Roumen Kountchev, Prof. is with the Faculty of Communications and Communications Technologies at the Technical University of Sofia, 8, Kliment Ohridski St. ,Sofia-1000, Bulgaria, E-mail: rkountch@tu-sofia.bg

[2]Agata H. Manolova, MsD, Ph. D student is with the Faculty of Communications and Communications Technologies at the Technical University of Sofia, 8, Kliment Ohridski St. ,Sofia-1000, Bulgaria, E-mail: amanolova@tu-sofia.bg

Section I – the direct transform algorithm:

Step 1. Calculate the mean values $\overline{R},\overline{G},\overline{B}$ for each color component of the S pixels, where S is the total number of pixels in the image; compare the calculated mean values with the corresponding threshold (T_{Green}, $T_{Red,}$ T_{Blue}); eliminate a mean value if smaller than the threshold (this step will be explained in section III of the paper).

Step 2. Calculate the elements of the covariance matrix $[K_c]$:

$$k_{11} = k_1 = \frac{1}{S}\sum_{s=1}^{S}(R_s - \overline{R})^2 \quad (1)$$

$$k_{22} = k_2 = \frac{1}{S}\sum_{s=1}^{S}(G_s - \overline{G})^2 \quad (2)$$

$$k_{33} = k_3 = \frac{1}{S}\sum_{s=1}^{S}(B_s - \overline{B})^2 \quad (3)$$

$$k_{12} = k_{21} = k_4 = \frac{1}{S}\sum_{s=1}^{S}(R_s - \overline{R})(G_s - \overline{G}) \quad (4)$$

$$k_{13} = k_{31} = k_5 = \frac{1}{S}\sum_{s=1}^{S}(R_s - \overline{R})(B_s - \overline{B}) \quad (5)$$

$$k_{23} = k_{32} = k_6 = \frac{1}{S}\sum_{s=1}^{S}(G_s - \overline{G})(B_s - \overline{B}) \quad (6)$$

Step 3. Find the three coefficients a, b and c of the principal component analysis equation:

$$\lambda^3 + a\lambda^2 + b\lambda + c = 0 \quad (7)$$

$$a = -(k_1 + k_2 + k_3) \quad (8)$$

$$b = k_1k_2 + k_1k_3 + k_2k_3 - k_4^2 - k_5^2 - k_6^2 \quad (9)$$

$$c = k_1k_6^2 + k_2k_5^2 + k_3k_4^2 - k_1k_2k_3 - 2k_4k_5k_6 \quad (10)$$

Step 4. Calculate the following values:

$$\varphi = \arccos\left[-q/2\sqrt{(|p|/3)^3}\right] \quad (11)$$

$$q = 2(a/3)^3 - (ab)/3 + c \quad (12)$$

$$p = -(a^2/3) + b \quad (13)$$

Step 5. Using the Cardano solutions for cubic equation calculate the three eigenvalues:

$$\lambda_1 = 2\sqrt{\frac{|p|}{3}}\cos(\frac{\varphi}{3}) - \frac{a}{3} \quad (14)$$

$$\lambda_2 = -2\sqrt{\frac{|p|}{3}}\cos(\frac{\varphi - \pi}{3}) - \frac{a}{3} \quad (15)$$

$$\lambda_3 = -2\sqrt{\frac{|p|}{3}}\cos(\frac{\varphi + \pi}{3}) - \frac{a}{3} \quad (16)$$

for $\lambda_1 \geq \lambda_2 \geq \lambda_3$

Step 6. Calculate the following intermediate values for each λ_m, for m=1, 2, 3;

$$M_m = k_5(k_2 - \lambda_m) - k_4k_6 \quad (17)$$

$$N_m = k_6(k_1 - \lambda_m) - k_4k_5 \quad (18)$$

$$P_m = (k_1 - \lambda_m)(k_2 - \lambda_m) - k_4^2 \quad (19)$$

$$A_m = \pm\sqrt{P_m^2 + M_m^2 + N_m^2} \quad (20)$$

Step 7. Calculate the eigenvectors $\vec{\Phi}_m = [\Phi_{1m}, \Phi_{2m}, \Phi_{3m}]^t$ of $[K_c]$:

$$\Phi_{1m} = M_m / A_m \quad (21)$$

$$\Phi_{2m} = N_m / A_m \quad (22)$$

$$\Phi_{3m} = P_m / A_m \quad (23)$$

Step 8. Define the transformed K-L color vector $\vec{L}_s = [L_{1s}, L_{2s}, L_{3s}]^t$ for each pixel.

$$\begin{bmatrix} L_{1s} \\ L_{2s} \\ L_{3s} \end{bmatrix} = \begin{bmatrix} \Phi_{11} & \Phi_{21} & \Phi_{31} \\ \Phi_{12} & \Phi_{22} & \Phi_{32} \\ \Phi_{13} & \Phi_{23} & \Phi_{33} \end{bmatrix} \begin{bmatrix} R_s \\ G_s \\ B_s \end{bmatrix} \quad (24)$$

Section 2 – the inverse transform algorithm:

Step 9. Chess board decimation of the L_2 and L_3 components, the L_3 component is decimated twice.

Step 10. Interpolation of the L_2 and L_3 components followed by filtering.

Step 11. Compute the inverse color transform and return to the original color space RGB.

Step 12. Calculate the MSE (Mean Square Error) and SNR (Signal to Noise Ratio) between the original image and the recovered image [6].

The samples to make the matrix $[K_c]$ may be all pixels in each image or all the pixels of all the images in a group [7]. The three eigenvalues are useful to determinate the concentration of the highest energy or which component is the most important. The larger the eigenvalues is the, the more important its corresponding component is [8].

III. Evaluation of the New KLCST Algorithm

For the evaluation of the effectiveness of the new KLCST algorithm we use the following characteristics:

A. Computation complexity

We have succeeded to reduce the complexity of KLCST. The proposed algorithm requires O(15xMN) operations, M and N being the dimensions of each of the color components of an image. We could accelerate more the computational

process by introducing three thresholds for each color component in Step 1 of the proposed algorithm:

$$T_{Green} > T_{Red} > T_{Blue} \quad (25)$$

After calculating the mean values of each color component, we compare their values with the corresponding threshold, if smaller than its corresponding threshold the mean value is put to 0 and ignored in the following steps. This way the computation complexity drops considerably. The values of the thresholds are chosen depending of the desired MSE (Mean Squared Error) to be achieved. The descending order of the thresholds is chosen using the distribution of the MacAdam's color spheres [1].

B. Quality of KLCST

For the evaluation of the quality of the KLCST we use the standard MSE and SNR [1], [6].

IV. Experimental Results

A. Color images – the database

In this paper, a database of 4 image groups is used. All of them are part of the database SCoPIe (http://www-mrim.imag.fr/projets/#scopie).

1. Deserts and beaches: Fig. 1 a) and b).
2. Forest: Fig. 1 c) and d).
3. Interiors: Fig. 1 e) and f)
4. Architectures: Fig. 1 g) and h).

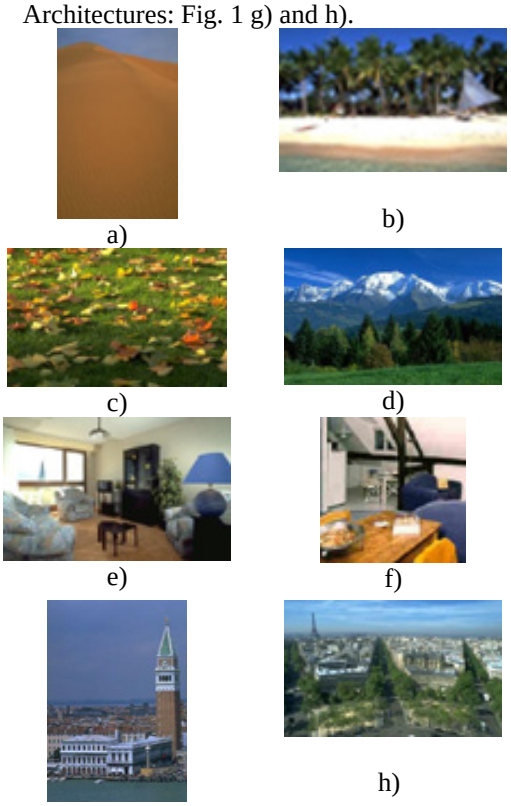

Fig. 1. Pictures in the database

B. Energy distribution

The goal of this experiment is to prove the effectiveness of the proposed algorithm:

- concentration of most of the energy in one component;
- decorrelation of the three components;
- minimization of the MSE;

We will also compare its performance with the performance of the YCbCr and HSV color transforms.

The K-L transform takes place in the RGB color space. The eigenvalues are sorted in the magnitude-descending order $\lambda_1 \geq \lambda_2 \geq \lambda_3$ and $\vec{\Phi}_1 = [\Phi_{11}, \Phi_{21}, \Phi_{31}]^t$ is the principal eigenvector. We calculate the relative power for each component of the transformed image. For better understanding the proportions between the energies concentrated in three transformed components, we introduce the value *eigPower*. This value represents the percentage of energies relative to the sum of all three.

We have obtained some very close results with individual image groups and even with some individual images. We have manually classified the images in four groups and in each group we observe that the principal eigenvector of each image is close to the principal eigenvector of the group. So instead of calculating a KLSCT for each image of each group we could calculate a single transform for all of the images in each group. We can observe the distribution of *eigPower* in the four groups on Table I:

TABLE I
DISTRIBUTION OF EIGPOWER IN THE THREE COMPONENTS FOR EACH IMAGE GROUP

Group	Component 1	Component 2	Component 3
Desert/Beach	64.30	18.40	17.30
Forest	76.99	21.63	1.38
Indoor	48.66	35.51	15.82
City	58.53	23.66	17.81

We have performed the color transforms YCbCr and HSV using the same database of color images and calculated the relative power for each of the three components of the color transforms. Fig. 2 a) represents the relation between the relative energies between the firs and the second component. Fig. 2 b) represents the relation between the relative energies between the firs and the third component.

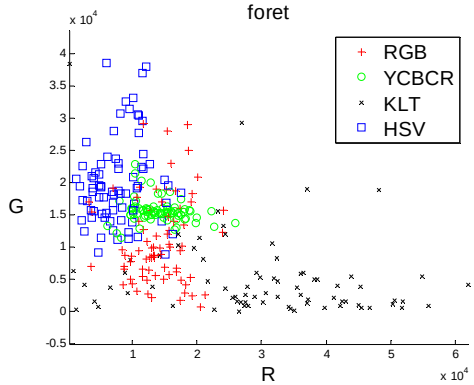

a)

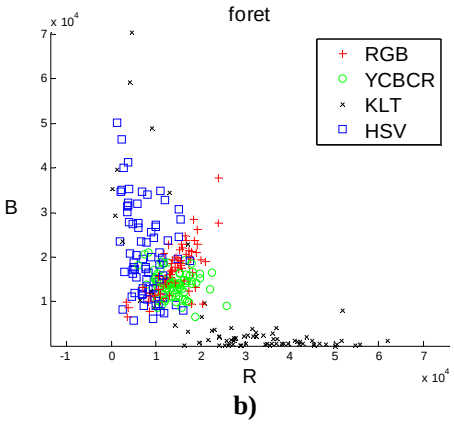

b)

Fig. 2. Distribution of energies of the color bands

We can observe that the relationship between the energies of the first and the second component for the color transforms YCbCr and HSV is close but this is not the same for the K-L color transform. As opposed to the other color transforms the energies of the three bands are principally uncorrelated. The most energy is concentrated in the first component; the energies in the second and third component are almost non existent. From the proportional percentages between the *eigPower*, we can assume that the significance between the components in the K-L color space is roughly 4:2:1, this means that the first component can be left untouched, the second is twice as small as the original and the third is four times as small as the original. Using this resolution we can achieve a SNR within the limits of 28 to 33 dB when we restore the image to the original RGB color space. This also looks very nice and very useful in image applications. The percentages of the three relative powers give the information, which can be used in image retrieval and image compression during quantization.

V. CONCLUSIONS

The proposed algorithm for KLCST is elegant and simplified to the maximum. Its advantages can be formulated as following:

- the algorithm can be adapted to the statistical properties of each image, meaning the algorithm could be accelerated using the thresholds.

- the K-L color space transform is useful for many applications such as image retrieval, image coding, color segmentation, object recognition.

All these applications could be executed in real-time.

We note that farther improvement of the KLCST algorithm performance can be achieved if the principles of distributed arithmetic are used. Also it will be interesting to apply the integer numbers arithmetic to the Eq. (24) and to calculate the KLCST for each group of images.

REFERENCES

[1] S. J. Sangwine, R. E. N. Horne, «The colour image processing handbook », Chapman & Hall, 1998.

[2] Pengwei Hao, Qingyun Shi, “Comparative study of color transforms for image coding and derivation of integer reversible color transform”, International Conference on Pattern Recognition, vol. 3, pp. 3228, September 2000.

[3] Avraham Levy, Michael Lindenbaum, “Sequential Karhunen-Loeve basis extraction and its application to images”, IEEE Transactions on Image Processing, vol. 9, No.8, August 2000.

[4] Dragana Carevic, Terry Caelli, “Region based coding of color images using K-L transform”, Graphical Models and Image Processing, vol. 59, No.1, pp.27-38, 1997.

[5] Roumen Kountchev, “Inverse pyramidal decomposition of images”, Doctoral Thesis, Sofia, 2002.

[6] David Salomon, “Data compression- The complete reference”, Spinger 2004.

[7] Charles Mathis, “Decorrelating transforms for color images”,http://ise.stanford.edu/class/ee368/projects2001/dropbox/project13/.

[8] Pengwei Hao, Qingyun Shi, “Reversible Integer KLT for progressive-to-lossless compression of multiple component images”, ICIP, vol. 1, pp. 633-6, September 2003.

Error Estimation of Adaptive 2D Interpolation of Images

Rumen P. Mironov[1]

Abstract - **An analysis of 2D adaptive interpolation filter frequency characteristics for halftone image processing is presented. The adaptation is based on the local information of processed images and interpolation order is changed with zero or bi-linear. Experimental surfaces suggest that the effective use of local information contribute to minimize the mean-square error.**

Keywords - **digital signal processing, 2D image interpolation, local adaptation, image processing.**

I. INTRODUCTION

The basic methods for 2D interpolation of halftone images are separated in two groups: non-adaptive (zero, bi-linear or cubic interpolation) and adaptive interpolation [1], [2]. For non-adaptive methods with the increasing of interpolation order the sharp of brightens transitions are decreased. In other side with decreasing of interpolation order the artifacts ("false" contours) in the homogeneous areas are depicted [3], [4]. To reduce them a local adaptive method for 2D interpolation of images is developed [5]. Based on local characteristics of brightness, the interpolation order (zero or bi-linear) is changed and reduction of image distortions are achieved.

In this paper analysis of frequency characteristics of the developed adaptive 2D interpolation filter and estimation of mean-square errors for two kinds of interpolation are described.

II. MATHEMATICAL DESCRIPTION

The input m-level halftone image of size *M* x *N* and the output interpolated image of size *pM* x *qN* can be represented by the matrices:

$$\begin{aligned}\mathbf{A}_{MxN} &= \{\mathbf{a}(i, j) \,/\, i = \overline{0,M-1};\ j = \overline{0,N-1}\},\\ \mathbf{A}^{*}_{pMxqN} &= \{\mathbf{a}^{*}(k,l) \,/\, k = \overline{0,pM-1};\ l = \overline{0,qN-1}\},\end{aligned} \quad (1)$$

where *p* and *q* are the interpolation coefficients in horizontal and vertical direction respectively [5].

The differences between each neighborhood pixels are given by the equations:

$$\begin{aligned}\Delta_{2m+1} &= \left|a(i+m,\, j) - a(i+m,\, j+1)\right|, \text{ for } m = 0,1;\\ \Delta_{2n+2} &= \left|a(i,\, j+n) - a(i+1,\, j+n)\right| \ , \text{for } n = 0,1.\end{aligned} \quad (2)$$

The four logical variables f_1, f_2, f_3 and f_4 are included, which depends from differences by the thresholds in horizontal (θ_m) and vertical (θ_n) directions as is shown in Eq. (3).

[1]Rumen P. Mironov is with the Faculty of Communication Technics and Techology, Technical University of Sofia, Kl.Ohridsky 8, 1000 Sofia, Bulgaria, E-mail: rpm@tu-sofia.bg

$$f_{2m+1} = \begin{cases}1, \ if: \Delta_{2m+1} \ge \theta_m\\ 0, if: \Delta_{2m+1} < \theta_m\end{cases}; \quad f_{2n+2} = \begin{cases}1, \ if: \Delta_{2n+1} \ge \theta_n\\ 0, if: \Delta_{2n+1} < \theta_n\end{cases}. \quad (3)$$

Then each interpolated pixel can by presented as linear convolution of 4 basic elements:

$$a^{*}(k,l) = \sum_{m=0}^{1}\sum_{n=0}^{1} w_{m,n}(r,t)\, a(i+m, j+n), \quad (4)$$

for $r = \overline{0,p}$; $t = \overline{0,q}$. Interpolation coefficients:

$$w_{m,n}(r,t) = F.Zr_{m,n}(r,t) + \overline{F}.Bl_{m,n}(r,t), \quad (5)$$

are dependent from the logical function F, which give the type of the interpolation (zero or bi-linear):

$$F = f_1 f_3 \cup f_1 \overline{f_2} f_4 \cup f_2 f_3 \overline{f_4}.$$

The zero or bilinear interpolation coefficients are defined by the equations:

$$\begin{aligned}Zr_{m,n}(r,t) &= \frac{1}{4}\left[1-(-1)^{m}\,\mathrm{sign}(2r-p)\right]\left[1-(-1)^{n}\,\mathrm{sign}(2t-1)\right]\\ Bl_{m,n}(r,t) &= (-1)^{m+n}\left[1-m-\frac{r}{p}\right]\left[1-n-\frac{t}{q}\right]\end{aligned} \quad (6)$$

The dependence of functions F from the kind of brightness transitions and the coefficients f_1-f_4 as are given in [5] are shown on Table.1.

No.	f_1	f_2	f_3	f_4	F	Transitions
0	0	0	0	0	0	
1	0	0	0	1	0	
2	0	0	1	0	0	
3	0	0	1	1	0	
4	0	1	0	0	0	
5	0	1	0	1	1	
6	0	1	1	0	0	
7	0	1	1	1	1	
8	1	0	0	0	0	
9	1	0	0	1	0	
A	1	0	1	0	1	
B	1	0	1	1	1	
C	1	1	0	0	0	
D	1	1	0	1	1	
E	1	1	1	0	1	
F	1	1	1	1	1	

The 2D interpolation process can by characterized by the generalized block scheme, shown on Fig.1.

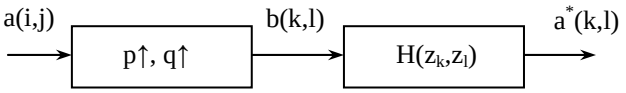

Fig.1 Generalized block scheme of the 2D interpolator

In the secondary sampling block the frequencies f_{sr} and f_{st} are increasing p and q times in the vertical and horizontal direction respectively. Consequently, the elements of the input image are added with zeros to receive b(k,l) from the equation:

$$b(k,l)=\begin{cases} a(k/p,l/q), \text{for } k=\overline{0,\pm(M-1)p}\ , l=\overline{0,\pm(N-1)q}, \\ 0\ , \text{for the other cases.}\end{cases} \quad (7)$$

The resulting image is processed by the 2D digital filter with z-transform function $H(z_k,z_l)$ and on our output the interpolated image $a^*(k,l)$ is received. From this the equation (4) can be presented as following:

$$a^*(k,l)=\sum_{m=0}^{1}\sum_{n=0}^{1} w_{m,n}(r,t).b\left(\left[\frac{k}{p}\right]+pm,\left[\frac{l}{q}\right]+qn\right), \quad (8)$$

where the operation $[x]$ is the largest integer not exceeding *x*.

Since the interpolation coefficients are repeating periodically, the distortion analysis can be accomplished for one block of the image. Then the amplitude and phase responses are described as following:

$$y(r,t)=\sum_{m=0}^{1}\sum_{n=0}^{1} w_{m,n}(r,t).x(pm,qn) \quad (9)$$

where x(pm,qn) are the basic elements in the current input block b(k,l) and y(r,t) are the interpolated elements in the output image block $a^*(k,l)$.

Zero interpolation characteristics.

After the 2D Z-transform of the equation (9) the result is:

$$H_{Zr}(z_r,z_t)=\frac{Y(z_r,z_t)}{X(z_r,z_t)}=\left[\frac{1-z_r^{-p}}{1-z_r^{-1}}\right]\left[\frac{1-z_t^{-q}}{1-z_t^{-1}}\right]. \quad (10)$$

After replacing of $z_r=e^{j\omega_r}$ and $z_t=e^{j\omega_t}$ in Eq.(10) the amplitude and phase responses are:

$$M_{Zr}(\omega_r,\omega_t)=\frac{\sin\left(\frac{p\omega_r}{2}\right)}{\sin\left(\frac{\omega_r}{2}\right)}\frac{\sin\left(\frac{q\omega_t}{2}\right)}{\sin\left(\frac{\omega_t}{2}\right)}=M_{Zr}(\omega_r)M_{Zr}(\omega_t)\ , \quad (11)$$

where $\omega_r=2\pi f_r/f_{sr}$ and $\omega_t 2\pi f_t/f_{st}$. By analogy for the phase is received:

$$\Phi_{Zr}(\omega_r,\omega_t)=\frac{p-1}{2}\omega_r+\frac{q-1}{2}\omega_t=\Phi_{Zr}(\omega_r)+\Phi_{Zr}(\omega_t)\ . \quad (12)$$

Bi-linear interpolation characteristics.

By analogy after the 2D Z-transform of the equation Eq.(9) the results are:

$$H_{Bl}(z_r,z_t)=\frac{Y(z_r,z_t)}{X(z_r,z_t)}=\frac{1}{pq}\left[\frac{1-z_r^{-p}}{1-z_r^{-1}}\right]^2\left[\frac{1-z_t^{-q}}{1-z_t^{-1}}\right]^2 \quad (13)$$

$$M_{Bl}(\omega_r,\omega_t)=\frac{\sin^2\left(\frac{p\omega_r}{2}\right)}{\sin^2\left(\frac{\omega_r}{2}\right)}\frac{\sin^2\left(\frac{q\omega_t}{2}\right)}{\sin^2\left(\frac{\omega_t}{2}\right)}=M_{Bl}(\omega_r)M_{Bl}(\omega_t)\ , \quad (14)$$

$$\Phi_{Bl}(\omega_r,\omega_t)=(p-1)\omega_r+(q-1)\omega_t=\Phi_{Bl}(\omega_r)+\Phi_{Bl}(\omega_t)\ . \quad (15)$$

On the base of equations Eq.(11) and Eq.(14) the frequency responses for the different values of p and q are analyzed. The amplitude responses corresponding to these received from 2D low-frequency filters for the frequencies, multiple to π/p and π/q. From the equations Eq.(12) and Eq.(15) follow that the phase characteristics are the planes crossing to the beginning of coordinate system width slope, defined by the variables p and q.

III. Experimental Results

For the analyzes of interpolation distortions the mean-square error can be used as a criterion. The input images have the uniform spectral characteristics in the spaces $-\pi\le\omega_r\le\pi$ and $-\pi\le\omega_{\le}\le\pi$. Then the equation can be expressed as following [3]:

$$\bar{\varepsilon}^2=\frac{1}{\pi^2}\int_0^{\pi}\int_0^{\pi}\left[1-M_n(\omega_r,\omega_t)\right]^2\partial\omega_r\partial\omega_t\ , \quad (16)$$

where:

$$M_n(\omega_r,\omega_t)=\frac{M(\omega_r,\omega_t)}{M(0,0)}=\frac{1}{pq}M(\omega_r,\omega_t)$$

is a normalized amplitude response of the adaptive 2D interpolator and

$$M(\omega_r,\omega_t)=\begin{cases} M_{Bl}(\omega_r,\omega_t)\ , \text{for } F=0\ ; \\ M_{Zr}(\omega_r,\omega_t)\ , \text{for } F=1\ . \end{cases}$$

After replacing equations Eq.(11) and Eq.(14) in Eq.(16) the following result is received:

$$\overline{\varepsilon^2}(p,q)=\begin{cases} 1-\frac{1}{pq}\left[\frac{8\Im(p)\Im(q)}{\pi^2}-1\right] \text{for } F=1, \\ 1-\frac{1}{pq}\left[2-\frac{(2p^2+1)(2q^2+1)}{9p^2q^2}\right] \text{for } F=0, \end{cases} \quad (17)$$

where $\Im(p)$ and $\Im(q)$ are integrals of the following kind:

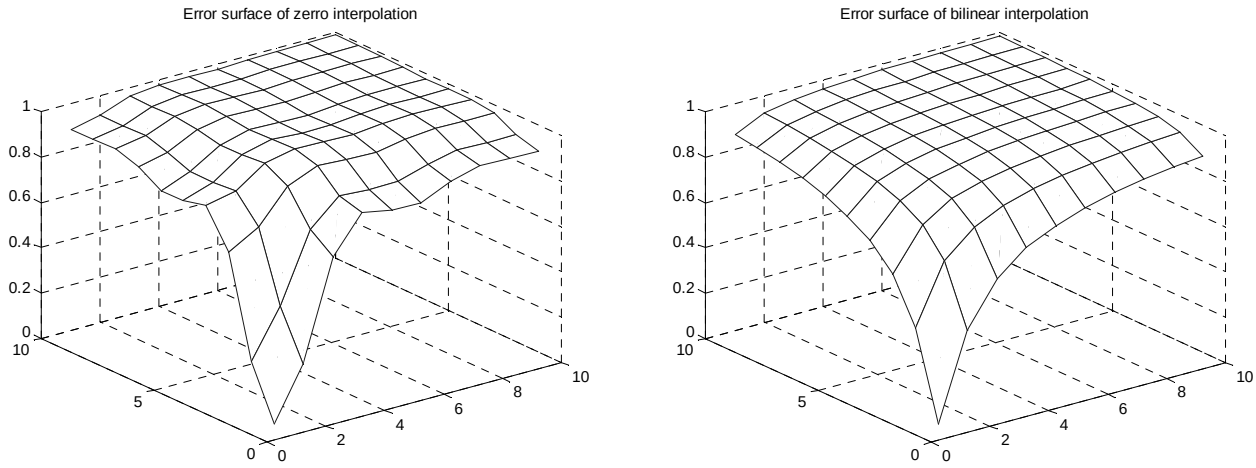

Fig.2. Error surfaces for zero and bi-linear interpolation

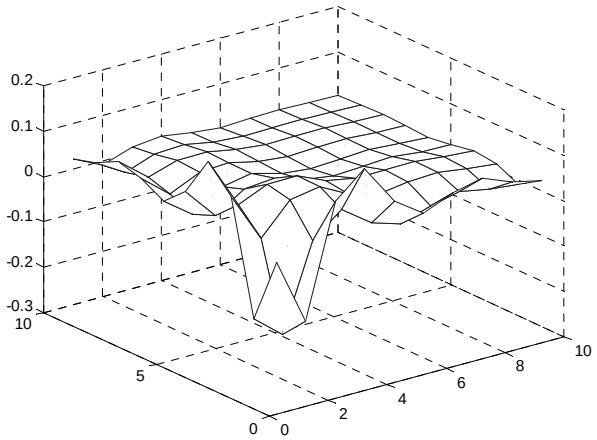

Fig.3. Difference error surface

$$\Im(u) = \int_0^{\pi/2} \frac{\sin(uv)}{\sin(v)} \partial v = \Im(u-2) + \frac{2\sin[(u-1)\pi/2]}{u-1}.$$

The error changing for the transition from zero to bi-linear interpolation, using equation Eq.(17), can be expressed as follows:

$$\Delta_{\overline{\varepsilon^2}}(p,q) \approx \frac{2}{pq}\left[\frac{4\Im(p)\Im(q)}{\pi^2} - 1\right] \quad . \qquad (19)$$

From equations Eq.(17) on Fig. 2 are presented the functions graph for mean-square errors, and on Fig.3 - their difference.

IV. CONCLUSION

On the base of error estimation for 2D adaptive interpolation on halftone images can be made the following conclusions:

- the digital interpolation filter doesn't include phase distortions in the processing images;
- to minimize mean-square error for p and q must be used variables in the space from 2 to 5;
- the maximal effective interpolation for the local characteristic of images can be achieved by using coefficients p,q=2-4.

ACKNOWLEDGEMENT

The authors thank the National Fund for Scientific Research of the Bulgarian Ministry of Education and Science for the financial support by the contract I-1101/2002.

REFERENCES

[1] P. Stucki. *Advances in Digital Image Processing*. N. J. Plenum Press, 1979.

[2] R. Crochiere, L. Rabiner. Interpolation and Decimation of Digital Signals - A Tutorial Review", *Proc. of IEEE*, Vol. 69, No. 3, March 1981.

[3] T. C. Chen, R. P de Figueiredo. "Image Decimation and Interpolation Techniques Based on Frequency Domain

Analysis", *IEEE Trans. on Communications*, vol. COM-32, No.4, April, 1984.

[4] Y. Wong, S. K. Mitra. "Edge Preserved Image Zooming", *Signal Processing IV:Theories and Applications*, EURASIP, 1988.

[5] R. Kountchev, R. Mironov. Analysis of Distortions for Adaptive 2D Interpolation of Halftone Images", XXV Science Session "Day of Radio'90", Sofia, Bulgaria, 7-8 may, 1990.

Digital Watermarking Using Complex Hadamard Transform and Phase Modulation

Roumen Kountchev [1], Vladimir Mirchev [2]

Abstract - **Image digital watermarking is the process of secretly embedding a short sequence of information inside the image without changing its perceptual quality. The bit sequence is embedded in a way that is difficult to find, modify or erase without a secret key. Standard image processing operations such as low pass filtering, JPEG compression, cropping, etc. should not remove the m[1]ark. We present a new digital watermarking method algorithm for copyright protection of still images. Watermark detection is done by comparing the watermarked image with the original one. The robustness to a JPEG image compression attack is demonstrated.**

Keywords - **watermarking, Complex Hadamard Transform, phase modulation**

I. INTRODUCTION

Image watermarking is an important technique for intellectual property protection of digital image information. Since the early 90's the area of watermarking has received a lot of attention from researchers in the signal, processing, security and multimedia communication communities. The rapid evolution of the Internet has lead to a growing concern about the protection of intellectual property. Since digital signals can easily be copied and reproduced in a way that is perceptually identical to the original, the chance of piracy of intellectual property has increased.

There are some requirements a good digital watermark must satisfy – robustness, perceptual invisibility and unambiguity. While this set of requirements is a must, others are also very important - high bit rate, security, constant bit rate, etc. There are a variety of watermarking techniques that have been proposed in the image digital watermarking literature. An overview of these techniques can be found in [4, 5].

It is known that much of the information that characterizes an image is contained in its phase. Most of the proposed algorithms use amplitude modulation techniques in order to embed the watermark bit sequence. Few of them use phase modulation [3].

In this article we describe a watermarking algorithm using phase modulation after applying a complex Hadamard transform. Similar to the watermarking technique described in [3], the phase components on selected transform coefficients are altered to convey the watermark information. It is well known that phase modulation possesses superior noise immunity when compared to amplitude modulation. One of the main differences between the algorithm described in [3] and the one proposed here is the choice of the CHT matrix used to perform the transform.

[1] Roumen Kountchev, Dr. Sc., Professor is with the Faculty of Communications and Communication Technologies, Technical University of Sofia, Climent Ochridski 8, Sofia, Bulgaria, E-mail: rkountch@tu-sofia.bg

[2] Vladimir Mirchev, PhD student is with the Faculty of Communications and Communication Technologies, Technical University of Sofia, Climent Ochridski 8, Sofia, Bulgaria, E-mail: vsmin@mail.bg

II. PROPOSED WATERMARKING ALGORITHM

In this section, a new watermarking algorithm is described. The technique is based on modifying the phase of image transform coefficients. The transform we are using in this article is Complex Hadamard Transform applied to 16×16 non-overlapping subblocks of the image. The basic principle of our watermarking technique is to set the phase of a coefficient according to value of the bit to be embedded. The choice of the coefficients is based on their type and amplitude – the coefficient must be complex, its module must be the highest one in the subblock and its module must be bigger than a chosen threshold. The calculation of the value of the threshold is done adaptively in order to increase the watermark detector's performance.

The Complex Hadamard transform we use in this algorithm is a rather new one. Although there are a few researches [1, 2, 3], its properties for the needs of digital signal and image processing are not studied well yet. The CHT matrices fulfill all the basic requirements expected from orthogonal transforms, such as linearity, uniqueness, complex convolution, etc. The CHT is confined to four complex values (±1 and ±j). In total, there are 64 CHT matrices that can be generated. The CHT matrix we use in our algorithm has several properties – all of the coefficients with both indexes even, have real values, the rest of the coefficients have complex values. Half of the complex coefficients are complex conjugates of the other half. This should be satisfied when altering a complex coefficient. The presence of real coefficients simplifies the calculations needed to perform the Hadamard transform. The integer arithmetic used in this transform is a big advantage compared to other complex transforms (e.g. DFT).

1	1	1	1
1	j	-1	-j
1	-1	1	-1
1	-j	-1	j

Fig. 1. $[CH_4]$ - Complex Hadamard Matrix 4x4

$[CH_2^{n-1}]$	$[CH_2^{n-1}]$
$[CH_2^{n-1}]$	$-[CH_2^{n-1}]$

Fig. 2. $[CH_2^n]$ - Complex Hadamard Matrix 2^n

Fig. 2 shows how to generate the complex matrices used to perform the CHT. We start with 4x4 matrix $[CH_4]$, shown in Fig. 1 and calculate higher order matrices $[CH_2^n]$ recursively from the previous ones.

The block scheme of our watermark embedding algorithm is shown in Fig. 3.

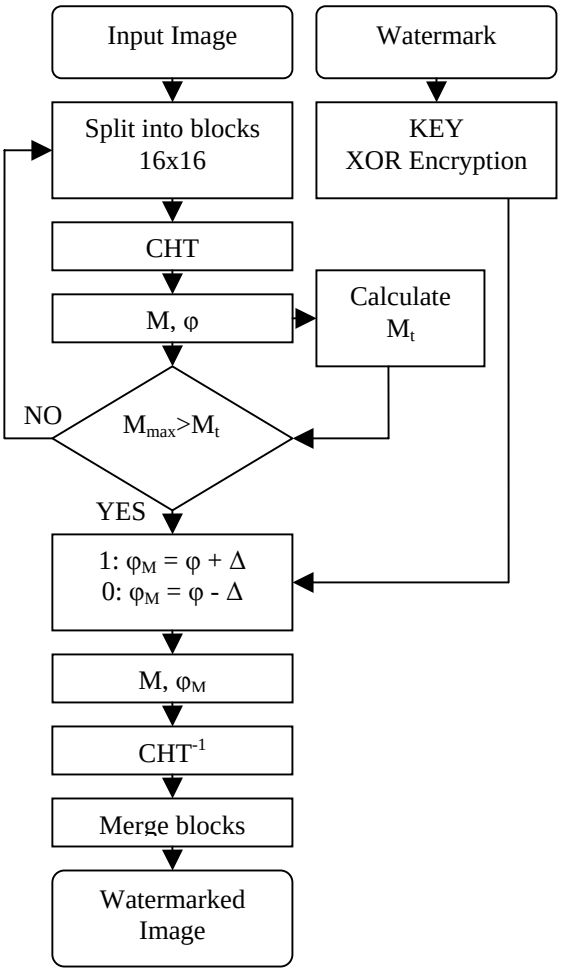

Fig. 3. Watermark encoder

First, we divide the input image into subblocks. We choose 16x16 pixels blocks so we can achieve high resistance to the popular JPEG image compression. Each subblock is processed by applying complex Hadamard transform. A translation from Decart to polar coordinate system is made. Then we find the complex coefficient *X[i, j]* with the highest module. If its magnitude is satisfies the chosen threshold value M_t, then an alteration of its phase is made according to the value of the current bit to be embedded. Higher magnitude transform coefficients are more immune to image processing operations than low magnitude coefficients. Furthermore, these coefficients preserve the most important information of the image and its integrity. The value of the threshold is adaptively calculated as an average value of the magnitudes of all complex coefficients in all of the previous blocks till and including the current one. The threshold condition guarantees that we will modify a coefficient in none homogenic image subblock. This leads to higher visual perceptibility. Alteration of the phase is made according (1):

$$\begin{cases} \varphi_M = \varphi + \Delta, \textit{ represents binary } 1 \\ \varphi_M = \varphi - \Delta, \textit{ represents binary } 0 \end{cases} \quad (1)$$

Where Δ is the depth of the watermark we embed. Choosing a bigger value for this parameter leads to higher robustness of the watermark, but also increases its visual perceptibility in the image and lowers the resulting PSNR.

The watermark bit sequence is encrypted by using a simple XOR operation with a randomly generated key. This insures that the information to be embedded has uniform probability distribution. This improves our algorithm in two aspects: first, one has to know both the encryption key and the watermark message in order to read the watermark, so the security of the watermark is higher; second, the potential autocorrelation in the watermark message is removed, thus improving the watermark resistance against various correlation detection attacks [4].

After that, an inverse CHT transform is made and the current subblock is replaced by the modified one.

The described process is successively made for all subblocks of the image. The result is a new watermarked image. The number of the subblocks that will stay unchanged due to the threshold condition can not be predetermined. That is, our watermark technique does not have the constant bit rate property and the amount of the embedded bits depends highly on the nature of the image to be watermarked.

The process of the watermark detection is shown in Fig. 2. The watermark extraction algorithm is very similar to the embedding one. The CHT transform is made twice – once for the subblock of the watermarked image and once for the corresponding subblock of the original image. The decision whether the current subblock is marked or not is made by taking the coefficient values from the original image, thus making it independent from the attacks applied to the watermarked image. If a subblock is found to be marked, the phase difference of the corresponding coefficients is calculated. According to the sign of the result the value of the current bit to be extracted is set (2).

$$\begin{cases} \varphi_M - \varphi > 0, \textit{ extracted binary } 1 \\ \varphi_M - \varphi < 0, \textit{ extracted binary } 0 \end{cases} \quad (2)$$

The resulting bit sequence is checked against the original one. If an error rate smaller than 25% is found, then the input image is claimed to be watermarked and the watermark message could be restored.

The decoding process in presence of geometric attacks is more involved. These attacks do not destroy the watermark, but rather disrupt the watermark synchronization. With the presence of the original image, an iterative search of set of inverse geometric operations can be made. Unfortunately, the iterative search approach is very computationally expensive and becomes even more so when the geometric attack does not introduce visible changes in the watermarked image. That's why, we often declare watermark is not present, when geometric attacks are applied.

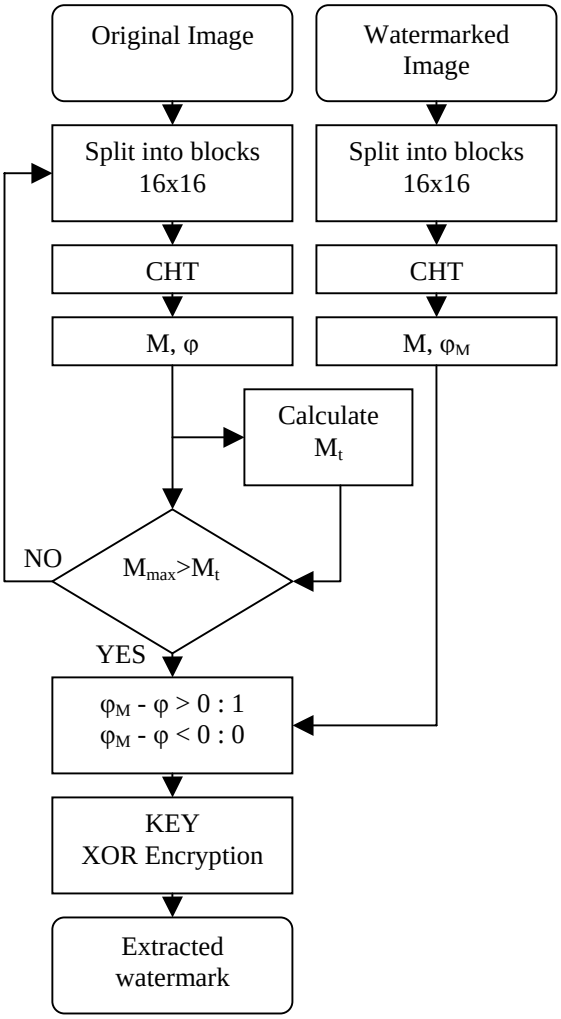

Fig. 4. Watermark decoder

III. SIMULATION AND RESULTS

A standard image was watermarked using the suggested algorithm. Figure 5 shows the original grey-scale image of 256×256 pixels. A block size of 16×16 pixels was used by the watermarking algorithm. The watermarked image is shown in Fig. 6. A total amount of 184 bits is embedded. Table 1 shows the amount of the embedded bits for four standard images. It proves that the watermark is embedded only in none homogenic areas of the image. Despite of the presence of the watermark no visible changes are made.

TABLE 1.
AMOUNT OF EMBEDDED BITS IN DIFFERENT IMAGES

Image name	Amount of embedded bits
Lena 256x256	184
Baboon 256x256	182
Camera 256x256	105
Peppers 256x256	179

Fig. 5 Original image “Lena”

Fig. 6. Watermarked image “Lena” at $\Delta = 12$

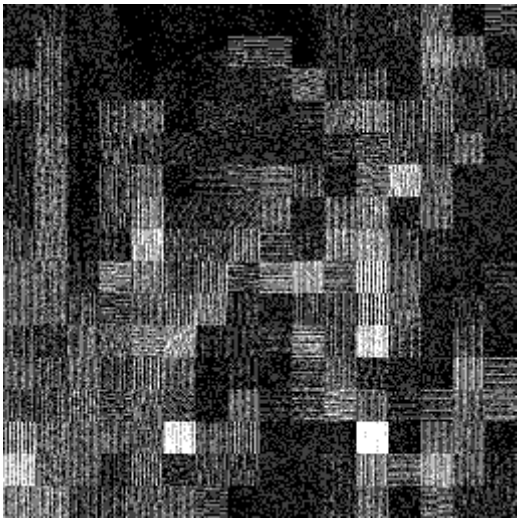

Fig. 7. Absolute difference image at scale factor 64

Figure 7 shows the absolute difference between the original image and the watermarked image “Lena” scaled by 64. As expected, the biggest difference occurs around edges.

In experiments the watermarked image is compressed using a JPEG encoder. Experimental results are shown in Fig. 8 and Fig. 9. Figure 8 shows the resulting PSNR at different values of the parameter delta. Bit error rate at different values of Δ and different JPEG quality factors is shown in Fig. 9.

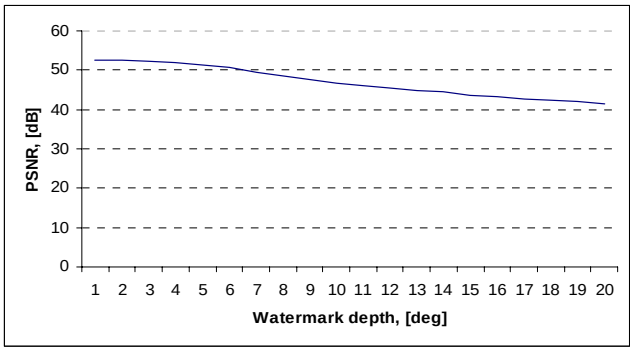

Fig. 8. PSNR results at different Δ

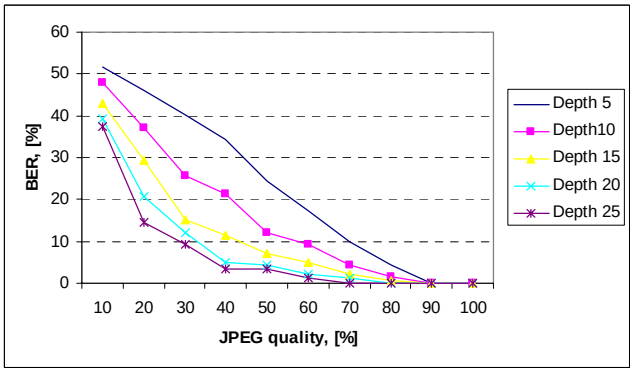

Fig. 9. BER versus JPEG quality

IV. Conclusion

In this paper, we present a new digital watermarking algorithm based on modifying the phase component of the selected coefficients. There is a lot of work to be done, but the test results indicate that using image phase information can lead us to designing very robust watermarks. In our algorithm we emphasize on achievement of low computational complexity, thus making it possible to perform real-time watermark embedding and detection.

Future work will concentrate in applying the phase alteration in more than one coefficient and at different phase steps, thus improving the amount of bits to be embedded in the image. In addition, novel techniques will be devised to make it possible to detect a watermark without requiring the original unmarked image.

There is a need of making an extended research on the properties of CHT transform. Finding algorithms for fast complex Hadamard transform is extremely important in order to lower the computational complexity, which will allow us to use CHT in pyramidal image decomposition. A pyramidal image decomposition using CHT will make it possible to embed different watermarks in each layer of the pyramid achieving the multilayer watermark property [6].

Another important research, that will be made, is the resistance of the watermark against various attacks – geometric transforms, filtering etc. In addition, a research on watermaking color images using the described algorithm will be made.

References

[1] S. Rahardja, B. Falkowski, Family of Unified Hadamard Transforms, IEE Transactions on circuits and systems-II: Analog and Digital Signal Processing, Vol. 46, No. 8, August 1999

[2] S. Rahardja, B. Falkowski, Complex Hadamard Transforms: Properties, Relations and Architecture, IECIE Trans. Fundamentals, Vol. E87-A, No. 8, August 2004

[3] S. Rahardja, B. Falkowski, Complex Composite Spectra of Unified Complex Hadamard Transform for Logic Functions, IEEE Transactions on circuits and systems-II: Analog and Digital Signal Processing, Vol. 47, NO. 11, November 2000

[4] M. D. Swanson, M. Kobayashki, and A. H. Tewfik, Multimedia data embedding and watermaking technologies, Proceedings of IEEE, vol. 86, no. 6, pp. 1064-1087, June 1998

[5] P. W. Wong, E. J. Delp, Security and Watermarking of Multimedia Contents, The International Society for Optical Engineering, San Jose, California, USA, 1999.

[6] R. Kountchev, M. Milanova, C. Ford, S. Rubin. Multimedia Watermarking with Complex Hadamard Transform in the Inverse Pyramid Decomposition. Proc. of the 2003 IEEE Intern. Conf. on Information Reuse and Integration, Las Vegas, USA, October 2003,pp.305-310

Face Extraction using 2D Color Histograms

Ognian Boumbarov[1], Diana Vasileva[2], Krasimir Muratovski[3]

Abstract: **Face extraction is first step of many applications including surveillance and security, human-machine interfaces, object-based video coding, virtual reality, automatic 3-D modeling and image database management. In this work we propose a face detection algorithm for color image sequences in presence conditions of varying lighting conditions and complex background. Our method finds skin regions and then generates face pixel candidates based on a histogram analysis of color space. The algorithm constructs face color map for verifying face pixels. The proposed approach consist thee parts: a color space selection, a modeling human skin with probability distribution and a human skin segmentation to identify probable regions corresponding human faces.**

Keywords: **Color space, 2D Color Histograms, Face detection**

I. INTRODUCTION

The analysis of human face images receives more interest in the field of image processing. The task of facial image analysis includes the face extraction and localization, the recognition of face and the analysis of facial expression or human mimics. Face detection is needed as preprocessing step for many applications, including surveillance and security, human-machine interfaces, object-based video coding, virtual reality, and automatic 3-D modeling. In addition, the robust face extraction is the first important step in a fully automated facial analysis system for static images and video sequences. There are many variations of image appearance such as pose variation (front and profile), occlusion, image orientation, lighting condition and facial expression [1], [2], which would bother face analysis and would be taken into account.

Various approaches to face detection are discussed in [1], [2], [3], [5]].

One of difficult problems in skin color detection is color constancy. Ambient light and shadows change the apparent color of an image. Different cameras affect the color value as well. A majority of skin detection algorithms in color image sequences use color histograms for segmentation [1], [2]. This approach relies on the assumption that skin colors form a cluster in same color measurement space.

In this work we propose an approach to automatic detection of faces in color image sequences. The proposed approach consists of three parts: a color space selection, a modeling human skin with probability distribution (2D histograms) and a human skin segmentation to identify probable regions corresponding human faces.

The paper is organized as follows. In the following Section (II.A) the choice of suitable skin color space is described. In Section II.B the use of 2D histograms in two variant - pixel-based skin color detection and face location using regional histogram ratio is discussed. The face skin color segmentation is given in Section II.C. The human skin segmentation employs a model-based approach to represent and differentiate the background colors and skin colors. Experimental results evaluating the performance of the algorithm are given in Section III.

II. MATHEMATICAL DESCRIPTION

A. Color space selection

Color information is an important feature of human faces. Using skin color as a feature for detecting face skin regions has several advantages. In particular, processing color is faster than processing other facial features. The more so as color information is invariant to face geometrical transformations. However, even under a fixed ambient lighting, people have different skin color appearance, but human skin forms a relatively tight cluster in color space[1].

Furthermore, to successfully use skin color for face detection, we need to choose color space, in which human skin colors cluster tightly together and reside remotely to background color[1], [2]. Color space is a method of color information obtained for a still image and video sequences. Human skin color tends to cluster in different color spaces. Different color spaces tend to enhance characteristics of images on expense of others[1], [3], [4]. Some color spaces are discussed in this paper.

The color space RGB (or the normalized color space RGB) is one of most widely used color spaces for processing and storing of digital image data [2], [3], [4]. However, high correlation between the color components, mixing of the chrominance and the luminance data make RGB color space not very favorable choice for color analysis and recognition.

In the color space YCbCr, the color is represented by luma, constructed as a weighting sum of RGB values, and two color difference values Cb and Cr that are formed by subtracting luma from RGB red and blue components [3], [4]. The transformation simplicity and explicit separation of luminance and chrominance components make this color space very attractive for skin color modeling.

The family of color spaces HSI (V, L) – Hue, Saturation, Intensity (Value, Lightness) was introduced when there was a need for the user to specify color properties numerically [2]. *Hue* defines the dominant color of an area; *saturation*

[1]Ognian Boumbarov is with Faculty of Communication Technics and Technology, Technical University of Sofia, Kl. Ohridski 8, 1000 Sofia, Bulgaria, E-mail: olb@tu-sofia.bg

[2]Diana Vasileva is a PhD student in Faculty of Communication Technics and Technology, Technical University of Sofia, Kl. Ohridski 8, 1000 Sofia, Bulgaria, E-mail: diana@engineer.bg

[3]Krasimir Muratovski is a student with Faculty of Communication Technics and Technology, Technical University of Sofia, Kl. Ohridski 8, 1000 Sofia, Bulgaria, E-mail: kraskoval@abv.bg

measures the colorfulness of an area in proportion to its brightness. The “intensity”, “lightness” or “value” is related to the color luminance. The explicit discrimination between luminance and chrominance components made this color spaces popular for skin color segmentation. Besides YCbCr color space, several other linear transform of the RGB color space was employed for human skin detection – YES, YUV and YIQ [2], [5].

Many works on face skin detection discard the luminance component of the color space. This decision seems logical, because this is a dimensionality reduction. The goal of any color-based approach is diminishing the influence of the lighting conditions. The chrominance-only color analysis will make the approach partially independent from the lighting conditions.

We choose YCbCr as the processing color space since it is perceptually uniform and separate the luminance and the chrominance components. In our implementation only the CbCr components are used to model the distribution of skin colors. The YCbCr space is of particular interest because it is widely used in still-images and video coding standards such as JPEG, MPEG, and H.263.

B. Modeling human skin with 2D histograms

The purpose of skin color modeling is to build a decision rule that will discriminate between skin and not-skin pixels. The techniques for skin color modeling in YCbCr space can be classifies into following categories: parametric, non-parametric, and semi-parametric. A parametric skin color model has a specific functional form [1], [2], [6] with adjustable parameters chosen to fit the model to the input data. A non-parametric model does assume any particular form (histogram thresholding) [5]. A semi-parametric approach applies a very general form with adaptive parameters systematically varied in number as well as in value in order to create flexible models [7].

Color histogram is the typical method to describe the distribution of chromatic component in the specified image. Histograms are created by equally by subdividing the color space (YCbCr) into a number of bins, and then counting the number of pixels falling into each of the bins. We choose a 2D histogram (Cb, Cr) to represent the skin tones. By using two parameters (Cb,Cr) of color system, which do not correspond to intensity or illumination, the histogram should be more stable with respect to differences in illumination and local variations caused by shadows.

Let a vector $\vec{C}$ = [Cb, Cr]^t represent a color pixel at spatial position (i,j) with chromatic components Cb(i,j), Cb(i,j)) be a color vector in a color space YCbCr. Let P(C/skin) and P(C/nonskin) be the conditional probability density functions of skin and nonskin color clusters. The color vector C is classified as skin color if

$$\frac{p(\vec{C} / skin)}{p(\vec{C} / nonskin)} \geq \Theta \qquad (1)$$

where Θ is a threshold. The left term is known as the likelihood ratio [12]. The theoretical value of Θ that minimizes the classification cost is determined by a priori probabilities P(skin) and P(nonskin). The probability P (skin) of obtaining skin pixels in the image is approximated by the fraction of pixels known to be skin

$$P(skin) = \frac{T_s}{T_t}, \qquad (2)$$

where Ts and Tt are total pixel counts contained in the skin regions and the whole image, respectively.

The threshold Θ can be computed from

$$\Theta = \frac{\lambda_f \; P(nonskin)}{\lambda_{rj} \; P(skin)}, \qquad (3)$$

where λd and λr are the cost of false detection and false rejection. The cost of correct classification [8] is assumed to be zero, but the value of Θ can be computed experimentally. Since the skin color and the nonskin color models are disjunctive to each other, the priori probability P(nonskin) can be computed from P(nonskin) = 1- P(skin).

Bayes rule states that the probability of skin given a color vector is

$$p(\vec{C} / skin) = \frac{H_{skin}(\vec{C})}{T_s} = \hat{H}_{skin}(\vec{C}), \qquad (4)$$

$$p(\vec{C} / nonskin) = \frac{H_{nonskin}(\vec{C})}{T_{ns}} = \hat{H}_{nonskin}(\vec{C}), \qquad (5)$$

$$p(skin / \vec{C}) = \frac{p(\vec{C} / skin).P(skin)}{p(\vec{C} / skin)P(skin) + p(\vec{C} / nonskin)P(nonskin)} \approx \approx \hat{H}_{ratio}(\vec{C}) \approx \frac{\hat{H}_{skin}(\vec{C})}{\hat{H}_{total}} \qquad (6)$$

The analysis in this subsection show, that Bayesian skin color model can be applied to any color space with good result.

There are some problems related with the histogram using for a color analysis. Firstly, it’s the change of illumination condition or influence of noise. Secondly, it cannot preserve spatial information. The other problem is that it required large feature vector and it is very important to simplify the histogram in some way. A color histogram used as a descriptor should be small enough to be managed, but it should produce correct results.

In other side, there are images with different content and chrominance but with equal or similar histograms.

There are several color features available. The color moments are proposed as color descriptor consisting of average, variance, and third-order moment. But it is difficult to evaluate these features and it is not possible to use them during real time processing.

Our approach employs a 2D color histogram H = [h(Cr,Cb)] for modeling skin color in Cb-Cr color space. After initial step - filtration and normalization of input face

images, it is computed the average 2D histogram of 30 faces (training set), which was used to create a common skin classifier working for all kinds of skin. Training is an off-line procedure that does not affect the on-line performance. Nevertheless, it is a time-consuming process in a sense that a human operator should manually mark all skin-colored pixels in the chosen training set. To obtain a training set that is capable of supporting detecting of various skin tones in images acquired from different cameras requires a large training set.

There are a few algorithms for modeling human skin with 2D histograms: "chromatic" *thresholding*, *histogram Lookup Table* and *histogram ratio Lookup Table.*

"Chromatic" Thresholding. A method that is often used and easy to implement is thresholding one or several channels of a color space with one or several thresholds, e.g., in the CbCr plane. This method used a minimum and maximum Cb and Cr components, respectively, i.e., define a skin region in YCbCr color space, it use two thresholds for Bayes classification.

Let Cb_{min}, Cb_{max} and Cr_{min}, Cr_{max} are minimum and maximum thresholds, respectively for chromatic components Cb and Cr in 2D average color histogram. The classification rules determine a rectangular area in CbCr chromatic plane.

The segmentation is obtained for current skin color vector $\vec{C}$ = [Cb, Cr]^t as $\vec{C} \in O_{bj}$ if are performed the conditions simultaneous $\begin{cases} C_b(ij) \in [C_{b\min}, C_{b\max}] \\ C_r(ij) \in [C_{r\min}, C_{r\max}] \end{cases}$,

here O_{bj} is segmentationed color region (face).

The thresholds are calculated from 1D color histograms for Cb and Cr color components. In the segmented areas faces are detected with limited color space. The skin area that is classified as a face is that used to calculate new thresholds that are adapted to that particular face these thresholds are then used to segment the face during tracking. The obvious advantage of this method is a simplicity of skin detection rules that conducts to a construction of very rapid classifier.

Histogram Ratio Lookup Table. This approach realizes a face location using a ratio of two 2D histograms. The main idea is localization of known face image in a known background based on colors. Let we determine the average color 2D histograms for face training set
Ho = [ho(Cr,Cb)] and for the background Hg = [hg(Cr,Cb)]. That the ratio of histograms is

$$R_{c_r c_b} := \min\left\{\frac{h_o}{h_g}, 1\right\} \quad \text{Cb, Cr=0,255,}$$

$$\text{with} \quad RH = \frac{H_0}{H_g} = \left[R_{c_b c_r}\right] \qquad (7)$$

C. Skin color segmentation

In order to detect a skin color region we must map the skin pixels into a region. Generating of skin/non-skin maps strongly depends on lighting conditions and the tuning of the camera. This is supported by the histograms of the normalized maps of expected skin regions, shown on Fig.5 and Fig.6**.**

III. EXPERIMENTAL RESULTS

Photos are usually taken under various lighting conditions. This is the reason why they have variations in quality, color, position, pose and facial expression. Our algorithm has been evaluated on various images from the World Wide Web. We present the evaluation on a set of images from our local database. The experiment took place in the following steps. First, a training set of skin samples is loaded, shown on Fig.2. Next, the sequence of original images is shown on Fig.1 and background Fig.3. After finding the optimal threshold value for every image we obtained a mask of the expected skin region, Fig.4. Using the mask we extract the expected skin region, ingnoring the non-skin regions of the image, as can be seen on Fig.4. Finally we use the limited region of the skin to search for facial features, with the algorithm described the previous section.

IV. CONCLUSION

We have presented a method for face detection in frontal images and feature extraction from a detected face region. First of all, our method generates a mask of authenticity of face region in the image. We use two algorithms of generating the mask. After generating an optimal mask, the face region is being extracted from the original image.

REFERENCES

[1] M.Yang, D. Kriegman, N. Ahuja, "Detecting Face in Image: A Survey, IEEE Trans. on PAMI, vol.1, pp. (34-58), January, 2002.

[2] V.Vezhnevets, V. Sazonov, A. Andreeva, "A survey on pixel-based skin color detection techniques", Proc. Graphicon-2003, September 2003.

[3] K. Sung, T. Poggie, Example-based learning for view-based human face detection, IEEE Trans. PAMI, vol.20, no.1, January 1998.

[4] W., Pratt, Digital Image Processing. AWiley-Intersc. Publication. John Wiley&Sons, Inc. 2001.

[5] E. Saber, A. Tekalp, Frontal-view face detection and facial features extraction using color, shape and symmetry based cost functions, Pattern Recognition Letters, vol.9, pp669-680, 1998.

[6] Rein-Lien Hsu, M. Abdel-Mottaleb, A. Jain, Face detection in color space, IEEE Trans. PAMI, vol.24, no.5, pp.696-706, 2002.

[7] S. Phung, D.Chai, A. Bouzerdoum, A universal and robust human skin color model using neural networks, IEEE, vol. pp.2844-2899, 2001.

[8] S. Theodoridis, K., Koutroumbas, Pattern Recognition, Academic Press, 2003

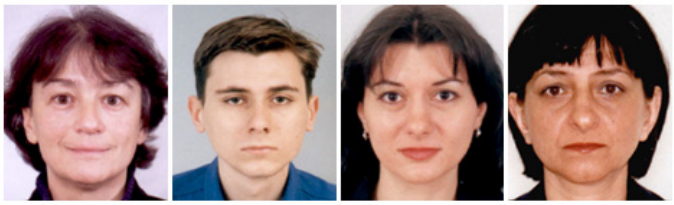

Fig.1 Original images of faces

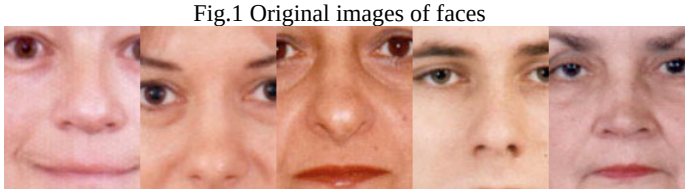

Fig.2 Experimental training set of faces

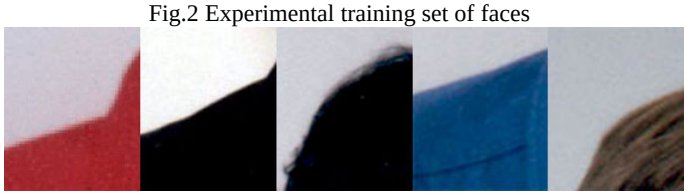

Fig.3 Original images of background

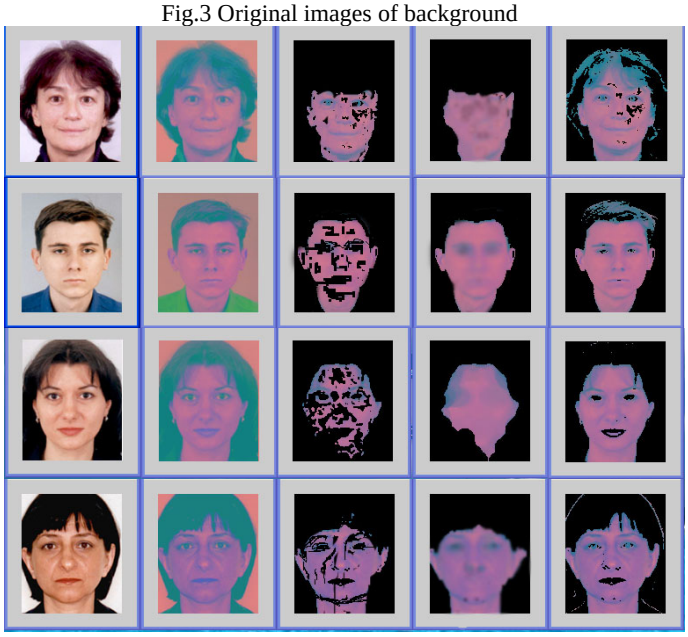

Fig. 4 Original images (RGB), Original images (YCrCb), Mask without smoothing, Mask after morphological filtering, Mask with smoothing;

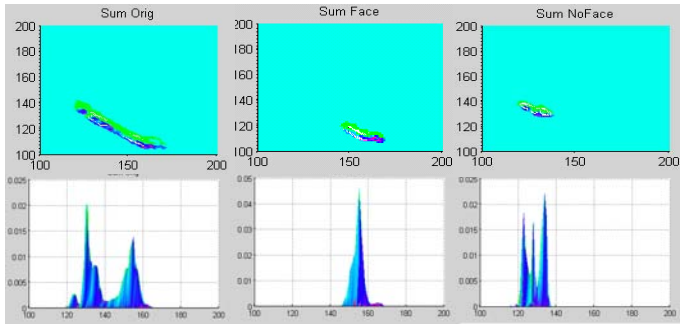

Fig.5 Histograms of original images, faces and background of training set

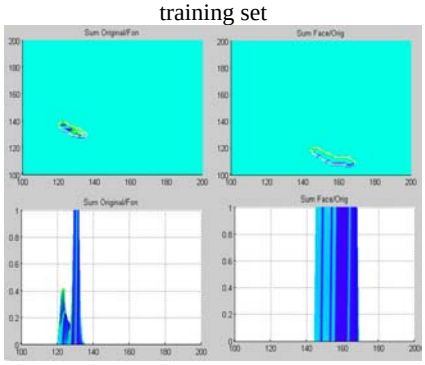

Fig.6 Histogram ratio of Faces/Background and Faces/Original images

An Improved Digital Watermarking Scheme for Image Copyright Protection using Morphological Skeleton and Wavelet Packets

Dragoş N. Vizireanu[1], Radu O. Preda[2]

Abstract – **In this paper we propose a robust blind private watermarking algorithm for image Copyright protection. The algorithm is based on Wavelet Packets. Our basic idea is to decompose the original image into a series of details at different scales by using Wavelet Packets; the skeleton of a binary image, used as the watermark, is then embedded into the different levels of detail. Experiments showed that our algorithm does only minimal degradation to the original image and can improve the robustness of watermarking against different attacks.**

Keywords – **Blind, private Watermarking, Wavelet Packets, Morphological skeleton.**

I. INTRODUCTION

Digital watermarking algorithms can generally be grouped into two main categories: those performed in the spatial domain and those in the frequency domain. Early techniques embedded the watermark in the least significant bits (LSBs) of image pixels [1]. However this technique and some other proposed improvements [2], [3] have relative low-bit capacity and are not resistant enough to lossy image compression, cropping and other image processing attacks. On the contrary frequency-domain-based techniques are more robust to attacks.

Procedures that can recover the hidden mark without the use of the original unmarked data are defined as *blind* decoding. Some of these blind techniques require access to a reference key to extract the mark. These are called *private*. Others, on the other hand, don't require the unmarked data either, nor do they need a key for decoding purposes. They are called public because everyone is allowed to access the watermarked data. From now on, the term DWT-based blind private watermarking technique should be meaningful.

The paper is organized as follows. In section II the Wavelet packets, a particular kind of wavelet decomposition that separates signals in symmetrical levels of detail is shortly described. Section III describes the mathematical morphology method used on the binary watermark image. Section IV presents the embedding and extraction strategies used by the proposed technique. Finally experimental results and conclusions are given in section V.

II. WAVELET ANALYSIS

The Discrete Wavelet Transform (DWT) is a special case of a subband transform, with a filter bank being the basic building block. The elements of the filter bank are a decomposition filter, a reconstruction filter, a downsampler and an upsampler. A multirate filter bank is a set of M parallel filters having either the same input or output. When the filters are used to split a common input x, it is referred to as an analysis filter bank. On the other hand, it is called a synthesis bank when it is used to form one common output.

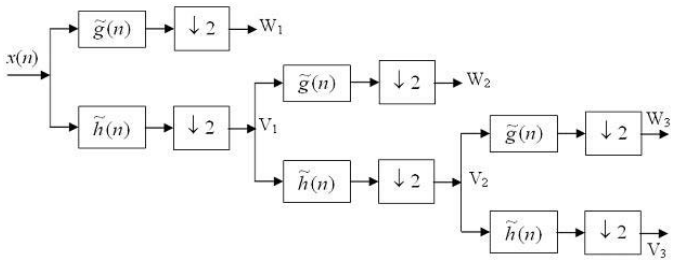

Fig. 1. Three level Wavelet decomposition

An important feature of multirate filter banks is that they split a signal into different frequency bands. Perfect reconstruction from the composition is maintained as long as specific filter requirements are fulfilled. Fig. 1 shows three levels of Wavelet decomposition using filter bank representation.

The multiresolution decomposition is described in terms of subspaces V_j and W_j, which relate to the intermediate signals at the output of the level j filter bank. As the number of decomposition levels used increases, the subspace number j increases as well.

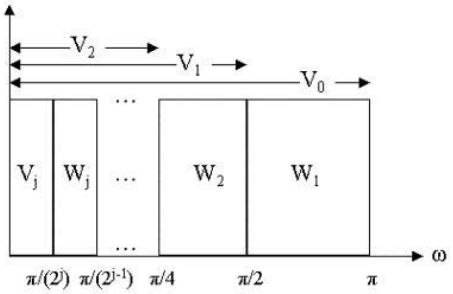

Fig. 2. Spectrum division after Wavelet decomposition

[1]Dragoş N. Vizireanu is witth the Electronics and Telecommunications Faculty, Bd. Iuliu Maniu Nr. 1-3, 061071 Bucharest, Romania, E-mail: nae@comm.pub.ro

[2]Radu O. Preda is with the Electronics and Telecommunications Faculty, Bd. Iuliu Maniu Nr. 1-3, 061071 Bucharest, Romania, E-mail: radu@comm.pub.ro

The Wavelet space W_j corresponds to the difference between the present scaling space V_j and previous one V_{j-1}. It means that $V_j \oplus W_j = V_{j-1}$ (see Fig. 2). The resulting decomposition bands are not of the same size, so we will try a different approach.

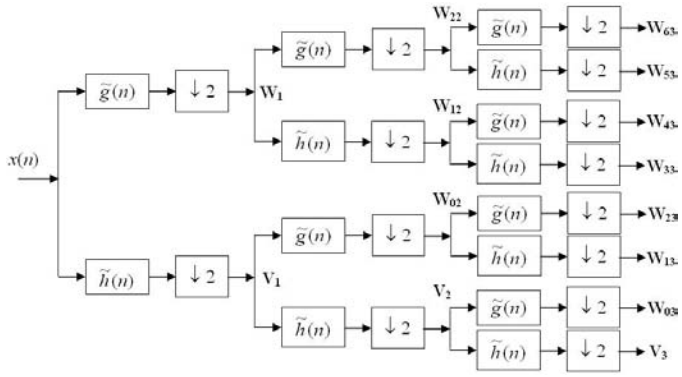

Fig. 3. Two level Wavelet Packets decomposition

One advantage of Wavelet Packets, important for our application, is the symmetry of the final decomposition bands. It means that all the bands are of the same size, and that the translation from frequency to time domain is much more staight-forward (see Fig. 4).

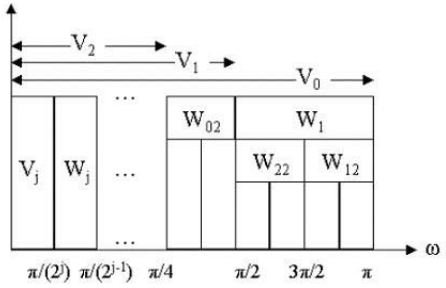

Fig. 4. Spectrum division after Wavelet Packet decomposition

III. MORPHOLOGICAL SKELETON

The skeleton is one of the main operators in mathematical morphology and it can be calculated entirely using the basic morphological operators.

Dilation and erosion are the fundamental operators of the Mathematical Morphology. The key process in the dilation and erosion operators is the local comparison of a shape, called structuring element, with the object to be transformed.

The structuring element is a predefined shape, which is used for morphological processing of the images. The most common shapes used as structuring elements are horizontal and vertical lines, squares, digital discs, crosses, etc.

The fundamental morphological operators are based on the operation of translation. Let B be a set contained in the Euclidean space E, and let x be a point in E. The translation of the set B by the point x, denoted B_x, is defined as follows:

$$B_x = \{b + x \mid b \in B\} \tag{1}$$

The dilation of the image X by the structuring element B, denoted $X \oplus B$, is defined by:

$$X \oplus B = \bigcup_{x \in X} B_x \tag{2}$$

For dilation: when the structuring element is positioned at a given point and it touches the object, then this point will appear in the result of the transformation, otherwise not.

The erosion of X by the structuring element B, denoted $X \ominus B$, is defined in the following way:

$$X \ominus B = \bigcap_{b \in B} X_{-b} \tag{3}$$

For erosion: when positioned at a given point, if the structuring element is included in the object, then this point will appear in the result of the transformation, otherwise not.

Based on the fundamental operators, two morphological operators are developed. These are the opening and closing operators. They are dual operators.

The opening operator, denoted "$\circ$", can be expressed as a composition of erosion followed by dilation, both by the same input structuring element:

$$X \circ B = (X \ominus B) \oplus B \tag{4}$$

The closing operator, denoted "$\bullet$", can be expressed as composition of dilation followed by erosion by the same input structuring element:

$$X \bullet B = (X \oplus B) \ominus B \tag{5}$$

Lantuejoul proved that the skeleton $S(X)$ of a topologically open shape X in Z^2 can be calculated by means of binary morphological operations, in the following way:

$$S(X) = \bigcup_{n>0} S_n(X) = \bigcup_{n>0} \{X \ominus nB - (X \ominus nB) \circ B\} \tag{6}$$

where B is a structuring element.

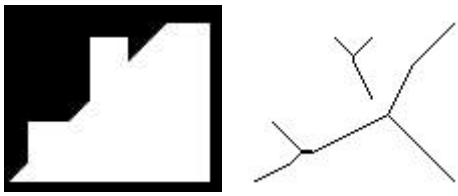

Fig. 5. The original image and its skeleton

In Fig. 5 a binary image and its morphological skeleton are shown. The skeleton is obtained using a cross as structuring element.

The compression rate for this example is about 4%. This means that, for the skeleton, we need 25 times less information in order to reconstruct the original image.

The reconstruction process needs additional information about the size of the structuring element for each point of the

skeleton. By adding the information about the structuring element to the skeleton, the resulting image can be considered as a greyscale image. In this case, the resulting image is shown in Fig. 6.

Fig. 6. The skeleton completed with structuring element information

The biggest problem with the skeleton representation is the fact that it contains many redundant points. These points are not needed for reconstruction, but appear in the skeleton.

The image representations obtained from these methods are called reduced skeletons: *RS*.

From the collection of subsets $\{S_n(X)\}_{n>0}$ and knowing the radius *n* for each pixel, the original shape *X* can be perfectly reconstructed in the following way:

$$X = \bigcup_{n\geq 0} S_n(X) \oplus nB \tag{7}$$

The Morphological Skeleton representation permits also partial reconstruction, yielding simplified versions of the original shape. This is obtained by eliminating from the skeleton the pixels with values smaller and equal to a given value *k*:

$$X \circ kB = \bigcup_{n\geq k} S_n(X) \oplus nB \tag{8}$$

The same results are obtained from the use of the reduced skeleton:

$$X = \bigcup_{n\geq 0} RS_n(X) \oplus nB \tag{9}$$

IV. The Wavelet Packets Based Watermarking Scheme

Our goal is to hide the Copyright information in the original image using the Wavelet Packets' domain for the watermark embedding. The author uses a unique (secret) binary identification key of 128 bits to allow the recovery of the mark. The main steps of our embedding technique are presented in the following.

a) First the owner's identification key of 128 bits is randomly generated. 128 bits are enough to grant uniqueness of the key and protect the owner. This key is stored and kept secret.

b) The first 8 bits in the secret key are used to select the wavelet decomposition scheme (the Wavelet functions used and the number of decomposition levels). The multitude of basis functions available increases the security of our scheme. The Wavelet families used are Coiflets, Daubechies and biorthogonal and the maximum level of decomposition is L.

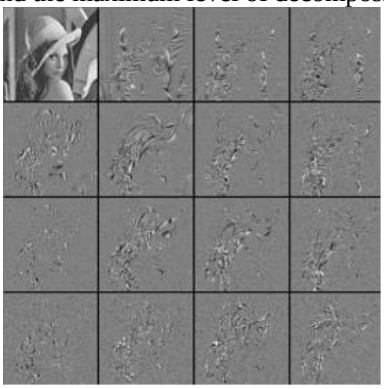

Fig. 7. Two level Wavelet Packet decomposition of image "Lena" using the Daubechies 12 Wavelet family

c) Using the specification extracted from the secret key the Wavelet Packets decomposition of the original image is performed. The multidimensional decomposition is done using successive filter banks. Fig. 7 shows a two level decomposition of the image "Lena" and the levels of detail.

d) The next 16 bits of the secret author's key indicate the size of the binary image used as the mark. The other bits of the key are used to identify the groups of coefficients, where the mark will be embedded. For every bit of the mark a group of *N* Wavelet Packet coefficients is identified. These groups of coefficients are evenly distributed in the bands of decomposition levels between 2 and L-1, where L is the maximum decomposition level of the original image.

e) For every group of coefficients the mean is individually computed. Then the individual quantization levels *q(i,j)* are obtained (see Equation 1) based on an optimal quantization step Δ. The quantization step is chosen so as to maximize the embedding weight, while minimizing the distortion introduced. Afterwards, each bit of the binary watermark image is inserted in the corresponding group of coefficients by the modification of the individual mean of the group. Rounding the mean to an even quantization level embeds a zero, while rounding the mean to an odd quantization level embeds a one. This is done by rounding the obtained quantization levels $q(i,j)$ to the nearest even / odd quantization levels (to form $q'(i,j)$) and then adjusting the mean of the Wavelet Packets coefficient regions to the computed values (as in Eq. 10 and 11).

$$q(i,j) = \left\lfloor \frac{mean(i,j)}{\Delta} \right\rfloor \tag{10}$$

$$\begin{aligned} mark(n) = 0 \;\rightarrow\; q'(i,j) &= \begin{cases} q(i,j) & if\ q(i,j)\ even \\ q(i,j)+1 & if\ q(i,j)\ odd \end{cases} \\ mark(n) = 1 \;\rightarrow\; q'(i,j) &= \begin{cases} q(i,j)+1 & if\ q(i,j)\ even \\ q(i,j) & if\ q(i,j)\ odd \end{cases} \end{aligned} \tag{11}$$

f) Finally, we apply the appropriate Wavelet Packet synthesis bank on the available coefficients – some modified and some not – to reconstruct the watermarked image. As

shown in Fig. 8, the image produced is visually identical to the original unmarked image.

Fig. 8. Original "Lena" image (left) and watermarked image (right)

At the other end of the communication channel or after the image has been stored, the watermark has to be extracted. The first four steps of the decoding procedure are identical to the embedding ones. The unique, secret key is used to decompose the image in levels of detail according to specific parameters. Then the groups of Wavelet Packets coefficients are selected. The groups of coefficients are examined. First the new mean $\hat{mean}(i, j)$ is computed. Then, using the knowledge of the optimal quantization steps, we can calculate the quantization levels and extract the watermarking data (see Eq. 12 and 13).

$$\hat{q}(i, j) = \left\lfloor \frac{\hat{mean}(i, j)}{\Delta} \right\rfloor \tag{12}$$

$$\begin{aligned} mark(n) &= 0 \quad if \quad \hat{q}(i, j)\ even \\ mark(n) &= 1 \quad if \quad \hat{q}(i, j)\ odd \end{aligned} \tag{13}$$

V. Experimental Results

This section describes the experimental results, which verify the capabilities of our watermarking scheme. For this purpose we used real square-size images of resolution greater than 256x256 pixels. We notice that our system is more suitable for photographic-like gray-scale images since they have more detail in which to hide a watermark. The binary images used as watermarks contained a text message and were less than 512 pixels big.

TABLE I
PSNR RESULTS FOR DIFFERENT WAVELET FUNCTIONS

Wavelet function	Average PSNR [dB]
Coiflets 12	40.23
Coiflets 24	39.87
Daubechies 12	40.12
Daubechies 16	40.28
Bior 4.4	41.72
Overall	**40.44**

First we have made sure that our embedding system does not introduce visual artifacts in images. We have first measured the visual quality of the marked images by qualitative observations. However, to produce more objective results, we have also used the Peak Signal to Noise Ratio (PSNR). The results obtained for 20 different original images are shown in Table I. We have obtained an average PSNR of 40.44 dB. This is above the usually tolerated degradation level of 40 dB.

The first goal of our project was to develop a watermarking scheme for Copyright protection, that can withstand a certain degree of image compression and resist a series of attacks. Generally speaking, JPEG recommends a quality factor between 75 and 95 for a compressed image to be visually indistinguishable from the original one, and between 50 and 75 to be merely acceptable. Table II and III show the robustness of our Wavelet Packets-based digital watermarking system to high and medium quality JPEG compression and to some attacks as blurring and sharpening.

TABLE II
RESISTENCE OF THE WATERMARKING SCHEME TO JPEG COMPRESSION

JPEG Quality Factor	50	60	70	80	90
PSNR after compression	33.7	34.5	35.7	37.4	40.6
Watermark extraction	96.2%	97.8%	98.5	99.4%	99.7%

TABLE III
RESISTENCE OF THE WATERMARKING SCHEME TO BLURRING, SHARPENING AND MIXED ATTACKS

Attack type	Blur	Sharpen	Blur+JPEG Comp. with Q=50	Sharpen+JPEG Comp. with Q=50
PSNR after attack (dB)	34.2	32.5	30.5	28.1
Watermark extraction	95.3%	98.4%	92.7%	94.2%

References

[1] R. G. van Schyndel, A. Z. Tirkel, and C. F. Osborne, "A digital watermark," in *IEEE Proceedings ICIP*, vol.2, pp. 86-90, 1994.

[2] N. Nikolaidis, and I. Pitas, "Copyright protection of images using robust digital signatures," in *IEEE Int. Conf. Acoustics, Speech Signal Processing*, vol. 4, pp.2168-2171, May1996.

[3] R. Wolfgang and E. Delp, "A watermark for digital image," in *IEEE ICIP*, vol.3, pp.211-214, 1996.

[4] M.-S. Hsieh, D.-C. Tseng, and Y.-H. Huang, "Hiding Digital Watermarks Using Multiresolution Wavelet Transform," in *IEEE. Trans. Industrial Electronics*, vol. 48, no. 5, pp. 875-882, 10/2001

[5] H. Daren, L. Jiufen, H. Jiwu, and L. Hongmei, "A DWT-based image watermarking algorithm," in *Proceedings IEEE Int. Conf. Multimedia and Expo*, Tokyo, 22-25/8/2001.

[6] R.R. Coifman and Y. Meyer, "Orthonormal wave packet bases", in Technical report, Dept. of Mathematics, Yale University, 1990.

[7] D.N. Vizireanu, C. Pirnog, "*Nonlinear Digital Signal Processing*", "Electronica 2000", Bucharest, 2001, Romania.

[8] D.N. Vizireanu, C. Pirnog, A. Vizireanu - "The Skeleton Structure - An Improved Compression Algorithm with Perfect Reconstruction", Journal of Digital Imaging, VOL. 14, NO. 2, June 2001, Orlando, Florida, USA, p. 241-242.

Improved Illumination Independent Moving Object Detection Algorithm in Infrared Video Sequences

Vesna Zeljkovic[1], Dragoljub Pokrajac[2]

Abstract – **Performance of moving objects detection algorithm on infrared videos is discussed. The algorithm consists of two phases: the noise suppression filter based on spatiotemporal blocks including dimensionality reduction technique for a compact scalar representation of each block and on the moving object detection algorithm resistant to illumination changes that detects and tracks the moving objects. The proposed method is evaluated on monochrome and multispectral IR videos.**

Keywords – **Video surveillance; Motion detection; Infrared videos.**

I. INTRODUCTION

In this paper, we evaluate the performance of motion detection algorithm introduced in [1]. Our main goal is to demonstrate that this novel technique is capable of successfully detecting moving objects in infrared videos.

Most of the moving object detection techniques are pixel based [2-5]. Recent approaches [6] are based on the spatiotemporal blocks. The pixel based techniques are resistant to the illumination changes [7] and prone to the influence of noise, while block-based methods are noise resistant [8,9]. We combined both approaches in our new improved method. The novelty introduced is image preprocessing similar to that used in the block-based method. We combine the pixel and region levels to a single level texture representation with 3D blocks and than we continue the image processing on such spatially-temporally filtered pixels. We decompose a given video into overlapping spatiotemporal blocks, e.g., 7x7x3 blocks centered at each pixel, and then apply a dimensionality reduction technique to obtain a compact representation of color or gray level values of each block as a single scalar value. We apply the principal component analysis and use the dominant eigenvector (corresponding to the largest eigenvalue) to obtain the coefficients of 3D filter, that we employ on every current frame. Such filtered images are subsequently treated with the moving detection algorithm based on pixel value [7].

The application of principal component projection instead of original pixels is expected to retain useful information while suppressing successfully the destructive effects of noise [10]. Proposed technique provides motion detection robust to various types of noise that may be present in infra-red video sequences.

[1]Vesna Zeljkovic is with with Delaware State University, Applied Mathematics Research Center, 1200 N DuPont Hwy, Dover, DE 19901, USA. E-mail: vesnaz@uzzpro.sr.gov.yu

[2]Dragoljub Pokrajac is with Delaware State University, CIS Dept and Applied Mathematics Research Center, 1200 N DuPont Hwy, Dover, DE 19901, USA. E-mail: dpokraja@desu.edu

II. METHODOLOGY

The technique for moving object detection consists of two major phases: 1) image filtering of a current frame with the noise removal filter coefficients extracted with the PCA analysis [10]; and 2) detection of moving objects applying the pixel based method for moving object detection resistant to illumination changes [1,7].

We treat a given video as three-dimensional (3D) array of gray pixels with two spatial dimensions *X*, *Y* and one temporal dimension *Z*. We use spatiotemporal (3D) blocks represented by *N*-dimensional vectors, where a block spans (2*T*+1) frames and contains N_{BLOCK} pixels in each spatial direction per frame $N=(2T+1)\times N_{BLOCK}\times N_{BLOCK}$. To represent the block vector by a scalar while preserving information to the maximal possible extent, we use principal component analysis [10]. For principal component analysis, we estimate sample mean and covariance matrix of representative sample of block vectors corresponding to the considered types of movies and use the first eigenvector of the covariance matrix **S** (corresponding to the largest eigenvalue) that represents the coefficients of the 3D filter that suppresses the noise. The 3D filter can be emulated by three 2D filters applied on frames *z*-1, *z* and *z*+1.

The fourth phase of the proposed method implies the application of a pixel based algorithm for moving object detection and tracking. We calculate the pixel variance in order to estimate the potential movement in the observed area incorporating the illumination compensation coefficient. The algorithm performs the analysis in time and space domains simultaneously, contributing to its resistance to the illumination changes and reducing the false detection, i.e. artifacts. We average estimated pixel variances for three successive pairs of frames and threshold this average to determine the presence of moving objects. This represents temporal aspect of analysis. The time analysis, additionally to space analysis, helps with correct moving object detection and augments the precision of the algorithm. Details of the algorithm are provided in [1,7].

III. RESULTS

In this paper, we demonstrate the performance of the proposed approach on two infrared video sequences. The first sequence, *RoofCam*, is obtained from Ohio State University Thermal Pedestrian Database [11]. Video was captured using a Raytheon 300D thermal sensor core with 75 mm lens.

Camera was mounted on an 8-story building overlooking a pedestrian intersection on the OSU campus. Image size is 360x240 and was captured at varying sampling rates. The second sequence, *RocketLaunch*[1], is false color thermal infrared sequence of Spitzer Telescope launch (25 August 2003 at 1:35:39 a.m. EDT from Cape Canaveral Air Force Station in Florida) taken from 3km distance. The original 45s video shows the rocket passing through a cloud including cooling of the rocket plume after the rocket flies out of flame. In our experiments we use T=1 and N_{BLOCK} = 5 for *RoofCam* and *RocketLaunch*. Processed video-sequences are available on our website: http://ist.temple.edu/~pokie/data/ICEST2005/.

Fig.1 contains two characteristic frames (40 and 194) with the results of the proposed moving objects detection for *RoofCam* video. The identified moving pixels are denoted by red. In the frame 40, four pedestrians appear in the "red" color in the scene. The algorithm is able to identify all four moving objects. The algorithm successfully identifies again all four pedestrians in the frame 194.

It should be pointed out that the proposed algorithm worked with no false alarms in spite of the relatively high level of noise in the considered IR video.

Fig. 2 contains two frames (350 and 450) of the *RocketLaunch* video sequence with indicated results obtained by the application of our moving objects detection algorithm. The frames show two characteristic phases of rocket launch. In the frame 350, the clouds are reflecting the bright infrared light of the hot rocket engines below so that clouds appear to light up and come down to meet the rocket. In this frame, this reflection is clearly identified by our algorithm (red-colored ellipsoid above the rocket top). The algorithm is also able to identify the base of the rocket flame in the frame 450, where the base of the jet appears through the cloud.

The proposed algorithm can identify movement in particular region of interest. To accomplish this, we first define rectangular spatial windows corresponding to the regions of interest and compute the following spatial-windows based evaluation statistics. We count the number of identified moving block within the spatial window and normalize it with the window size.

In Fig. 3a, we show the computed statistics for *RoofCam* sequence on the rectangular block [120:140, 110:130], annotated on Fig. 1. Visual inspection of the video sequence indicates the existence of two moving objects in the block: one in frames 6-65 and another in the frames 242-284. The values of motion statistics correspond to these two intervals, indicating two peaks of motion activity. Observe that the motion statistics value in the frame 40 is large, corresponding to the moving objects actually appearing in the frame within the observed rectangular block (see Fig. 1). Observe that the inertia of the proposed method is minimal; moving blocks cease to be identified in the observed rectangular regions as soon as the actual motion stops. Also, by thresholding the motion statistics, it is possible to get clear indication of the factual presence of the moving object in the rectangular region.

In Fig. 3b, we show the computed statistics for *RocketLaunch* sequence on the rectangular block [70:140, 70:140], annotated on Fig. 2. On frame 260, the base of the flame enters the block, which results in increase of the motion statistics. On frame 342, the cloud reflection appears and grows which results with rapidly augmenting motion statistics value. The reflection disappears at frame 370 and the level of the motion statistics becomes negligible. As we can see, the proposed motion statistics not only could be used to accurately detect the presence/absence of the moving object in the frame but also to distinguish different *phases* of motion.

IV. Conclusion

In this paper we have demonstrated that our illumination and noise-resistant moving object detection algorithm based on principal component filtering and spatiotemporal analysis can perform successful detection of moving objects in infrared videos. As a performance measure we, in addition to a visual evaluation, used spatial-windows based evaluation statistics and hand-labeled ground truth moving objects detection. The inertia of the proposed algorithm is negligible which make it suitable for detecting fast and sudden movement.

Our work in progress is concentrated on testing and improving its performance when background changes.

Acknowledgement

V. Zeljkovic has been partially supported by DoD HBCU/MI Infrastructure Support Program (45395-MA-ISP Department of Army).

D. Pokrajac has been partially supported by NIH-funded Delaware IDeA Network of Biomedical Research Excellence (INBRE) Grant, DoD HBCU/MI Infrastructure Support Program (45395-MA-ISP Department of Army), National Science Foundation (NSF) Infrastructure Grant (award # 0320991) and NSF grant "Seeds of Success: A Comprehensive Program for the Retention, Quality Training, and Advancement of STEM Student" (award #HRD-0310163).

[1]Video courtesy NASA/JPL-Caltech. Available at http://www.spitzer.caltech.edu/picturegallery/ir_launch.shtml

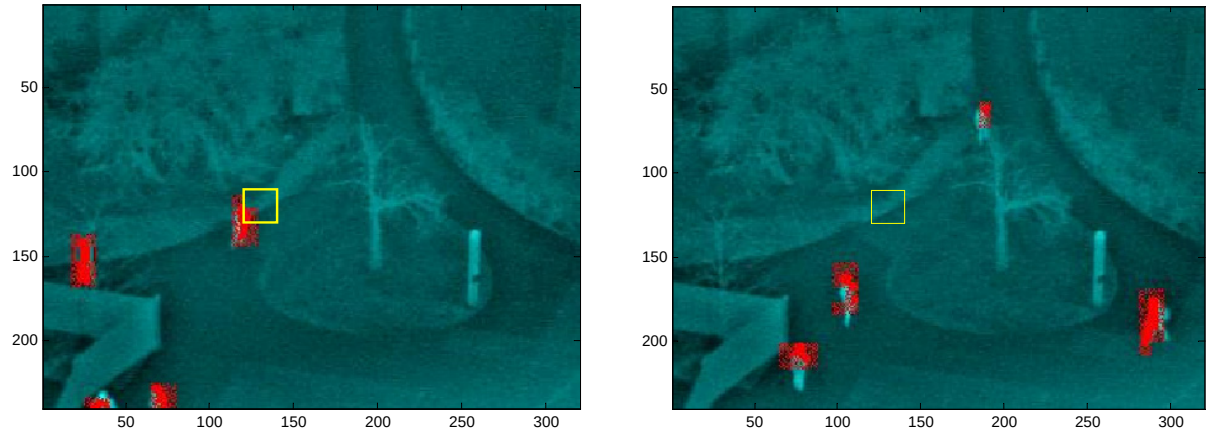

Frame 40 Frame 194

Fig. 1. Original frames 40 and 194 of *RoofCam* video with spatial block [120:140, 110:130] (yellow) and the result of moving objects detection (moving objects—red: background—navy).

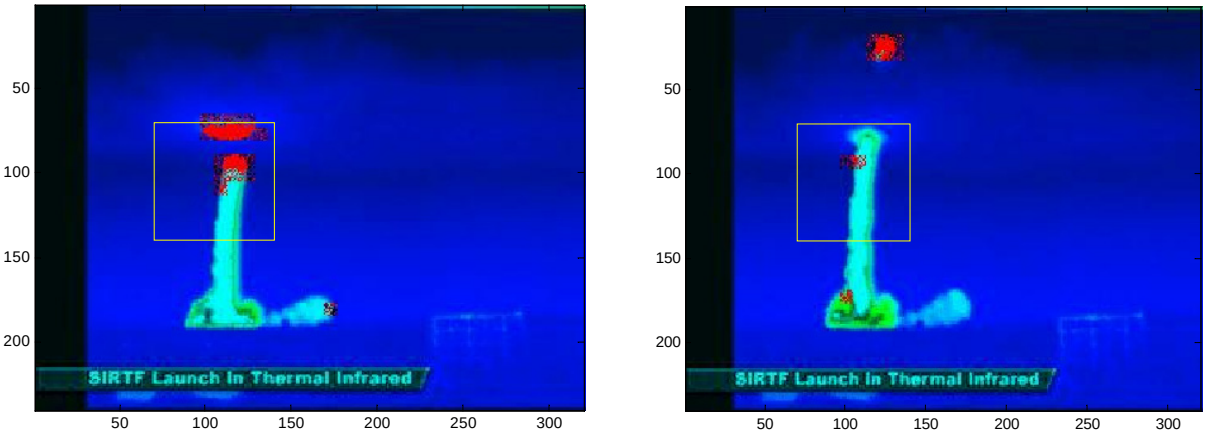

Frame 350 Frame 450

Fig. 2. Original frames 350 and 450 of *RocketLaunch* video with spatial block [70:140, 70:140] (yellow) and the result of moving objects detection (moving objects—red: background—blue).

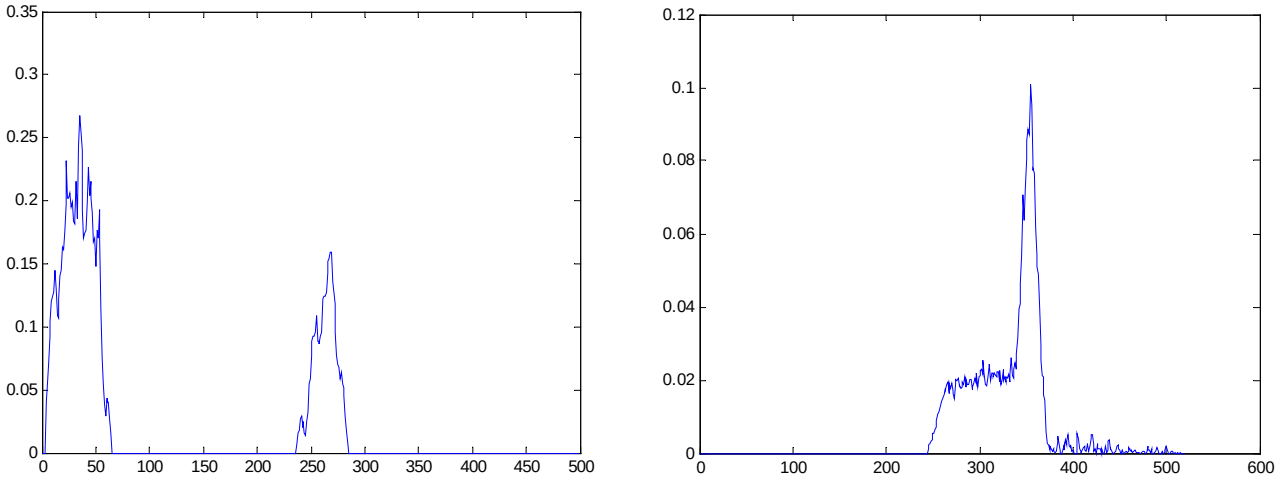

a) *RoofCam* b) *RocketLaunch*

Fig. 3. Motion statistics—Percentage of identified moving objects—at spatial blocks [120:140, 110:130] and [70:140, 70:140] calculated for the *RoofCam* and *RocketLaunch* sequence, respectively.

REFERENCES

[1] Pokrajac, D., Zeljkovic, V., "Influence of the Gaussian Noise on Spatial-Temporal Method for Moving Objects Detection", submitted to *11th International Conference on Computer Analysis of Images and Patterns.*

[2] DI. Haritaoglu, D. Harwood, and L. Davis, "W4: Real-Time Surveillance of People and Their Activities", IEEE Trans. Pattern Analysis and Machine Intelligence (PAMI) 22(8) (2000), pp. 809–830.

[3] N. M. Oliver, B. Rosario, and A. P. Pentland, "A Bayesian Computer Vision System for Modeling Human Interactions", IEEE Trans. Pattern Analysis and Machine Intelligence (PAMI) 22(8) (2000), pp. 831–843.

[4] Remagnino, P., G. A. Jones, N. Paragios, and C. S. Regazzoni, eds., Video-Based Surveillance Systems, Kluwer Academic Publishers, 2002.

[5] C. Wren, A. Azarbayejani, T. Darrell, and A.P. Pentland, "Pfinder: Real-time Tracking of the Human Body", IEEE Trans. Pattern Analysis and Machine Intelligence (PAMI) 19(7) (1997), pp. 780–785

[6] Pokrajac, D., Latecki, L. J. "Spatiotemporal Blocks-Based Moving Objects Identification and Tracking", In Proc. IEEE Int. Workshop Visual Surveillance and Performance Evaluation of Tracking and Surveillance (VS-PETS), Nice, France, 2003.

[7] V. Zeljkovic, D. Pokrajac, A. Dorado, and E. Izquierdo, **"**Application of the Improved Illumination Independent Moving Object Detection Algorithm on the Real Video Sequence", In Proc. 6th International Workshop on Image Analysis for Multimedia Interactive Services, WIAMIS 2005, in press.

[8] V. Zeljković, D. Pokrajac, L.J. Latecki, "Noise Robust Spatial-Temporal Algorithm for Moving Objects Detection", proc. 49th ETRAN Conf., 2005, in press.

[9] D. Pokrajac, V. Zeljković, L.J. Latecki, "Noise-Resilient Detection of Moving Objects Based on Spatial-Temporal Blocks", proc. 47th ELMAR Conf., 2005, in press.

[10] Jolliffe, I. T, Principal Component Analysis, 2nd edn., Springer Verlag, 2002.

[11] IEEE OTCBVS WS Series Bench; J. Davis and M. Keck, "A two-stage approach to person detection in thermal imagery" In *Proc. Workshop on Applications of Computer Vision*, January 2005

QMF Filtering Of Nuclear Medicine Heart Region Images

Cvetko D. Mitrovski[1] and Mitko B. Kostov[2]

Abstract – **In the paper we present our approach on pre-processing of NM heart-region images. The proposed method combines Discrete Wavelet Transform realized via near perfect reconstruction QMF bank with a specific strategy for selecting an appropriate threshold. The performance of the proposed method is demonstrated on real NM images.**

Keywords – **Nuclear medicine image, wavelets, thresholding, QMF.**

I. INTRODUCTION

Nuclear Medicine (NM) images are diagnostic digital images, which provide both anatomical and functional information. They present the projection of the distribution of radioisotope(s) in a body of a patient after injection of adequate dose of radioisotope(s). The raw NM images are created by accumulating the emitted gamma rays from a patient over a fixed observation period by computerized gamma cameras. They have a low signal-to-noise ratio (SNR) due to the nature of the gamma ray emission process and the operational characteristics of the gamma cameras (low count levels, scatter, attenuation, and electronic noises in the detector/camera). The noise obeys a Poisson law and is highly dependent on the space distribution of the image signal intensity. Therefore, a suitable image pre-processing must precede the NM images analysis in order to provide an accurate recognition of the anatomical data of the patient (the boundaries of the various objects – organs). This process of separating signal from noise is a rather difficult and much diversified task that should be adjusted to the organs and tissues, which physiology is to be investigated.

In [7], [8], [9] and [10] we proposed several approaches to cope with this problem. In [7], the whole process of spreading the radionuclide is divided in three successive phases and the images that belong to one specific phase are processed separate from the others. In addition, the image resolution is changed and autocorrelation technique is applied. In [8], the images are filtered by utilizing the wavelet shrinkage program, where the threshold is set to be same for all the wavelet coefficients in one level. In [9] the images processing is carried out by modifying images histogram. In [10] the denoising is tried by filtering the images in the direction that is normal to the spreading of the radionuclide.

In [5] a new method for designing optimal wavelet-domain filters for noise removal in photon imagery is proposed. The threshold adapts to the local noise level of the spatially varying Poisson process underlying the image and is different for every wavelet coefficient.

This paper presents a new approach on pre-processing of NM heart-region images. The images are processed in the discrete wavelet transform domain with linear phase QMF filters. The filters are designed to achieve both good image decomposition and near perfect reconstruction. The threshold in the wavelet shrinkage program is selected as proposed in [5].

The paper is organized as follows. In Section II the NM images creation process is modelled, and the problems due which raw NM images should be pre-processed, are formulated. Section III outlines the scheme used in wavelet filtering of NM images. Section IV presents suitable NM images filtration technique. The performance of the proposed method is demonstrated on real NM images in Section V. Conclusion is given in Section VI.

II. NM IMAGES CREATION PROCESS

The process of generating the NM images starts after injection of certain, small dose (for safety reasons) of suitably chosen radioactive material, into the body of a patient. The radionuclide spreads and mixes with the blood on its way to the heart through the vena cava superior. This results with some very complicated, fast changing function, $\rho(x, y, z, t)$. After passing through the heart, the blood-radioactivity mixture passes through the lungs, returns to the heart and proceeds with spreading toward each cell of the patient body through its arteries. This process could be recorded as a set of *N*, NM images (Fig. 1). Each image contains rather high level of noise caused by: a) mixing the radionuclide with the blood and the spreading of this mixture, b) hydrodynamic processes in the blood vessels caused by the pumping work of the heart, and c) by the randomness of the gamma rays emission and their detection by the gamma camera. Considering this, the raw images should be adequately preprocessed in order to extract the anatomy information about the position of the vena cava superior and the heart. According to this information, the optimal position (and the shape) of the regions of interest (ROI's) for the heart study could be proposed [1].

III. AN OVERVIEW OF THE DISCRETE WAVELET TRANSFORM

The Discrete Wavelet Transform (DWT) decomposes a signal into a set of orthogonal components describing the signal variation across the scale [2]. The orthogonal components are generated by dilations and translations of a prototype function ψ called *mother wavelet:*

[1]Cvetko D. Mitrovski is with the Faculty of Technical Sciences, I.L.Ribar bb, 7000 Bitola, Macedonia, E-mail: cvetko.mitrovski@uklo.edu.mk

[2]Mitko B. Kostov is with the Faculty of Technical Sciences, I.L.Ribar bb, 7000 Bitola, Macedonia, E-mail: mitko.kostov@uklo.edu.mk

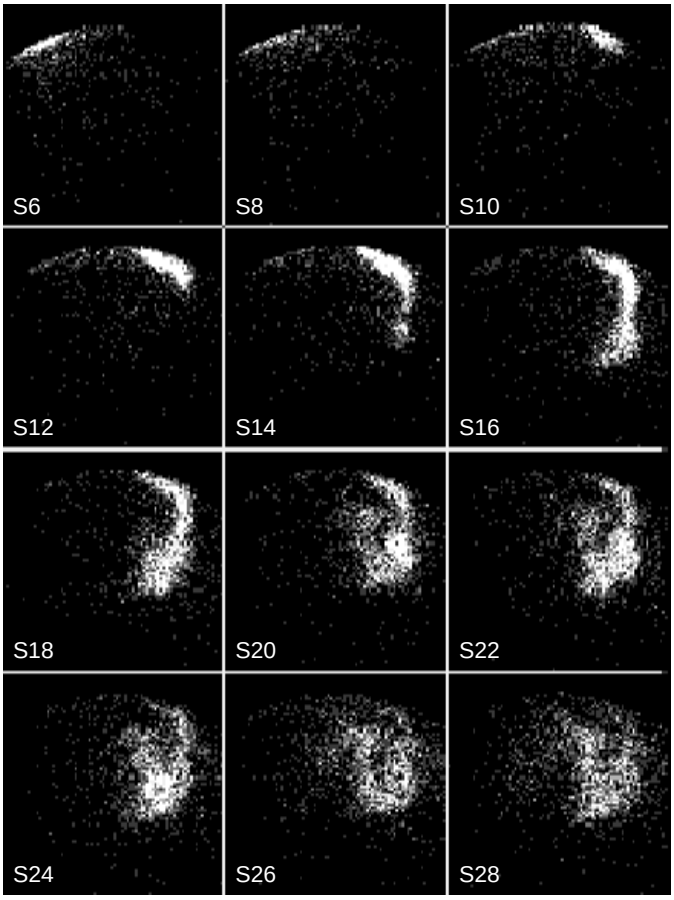

Fig. 1. Sequence of enhanced noised images (τ=0.4 s)

$$\psi_{i,k}(t) = 2^{-i/2}\psi(t/2^i - k), \quad k,i \in Z \tag{1}$$

The above equation shows that the mother function is dilated by the integer i and translated by the integer k. In analogy with other function expansions, a function f may be written for each discrete coordinate t as a sum of a wavelet expansion up to certain scale J plus a residual term, that is:

$$f(t) = \sum_{j=1}^{J} \sum_{k=1}^{2^{-j}M} d_{jk}\psi_{jk}(t) + \sum_{k=1}^{2^{-J}M} c_{Jk}\phi_{Jk}(t) \tag{2}$$

The estimation of coefficients d_{jk} and c_{Jk} is carried out through an iterative decomposition algorithm, which uses two complementary filters h_0 (low-pass) and h_1 (high-pass). Since the wavelet base is orthogonal, h_0 and h_1 satisfies the quadrature mirror filter conditions (QMF) [3]. The filter bank theory is closely related to wavelet decompositions and multiresolution concepts. For this reason, it is helpful at this point to view the scaling function ϕ as a low pass filter h_0 and wavelet function ψ as a high pass filter h_1. The mother and scaling functions are defined as follows [2]:

$$\psi(t) = \sum_n 2^{1/2} h_1 \psi(2t-n) \tag{3}$$

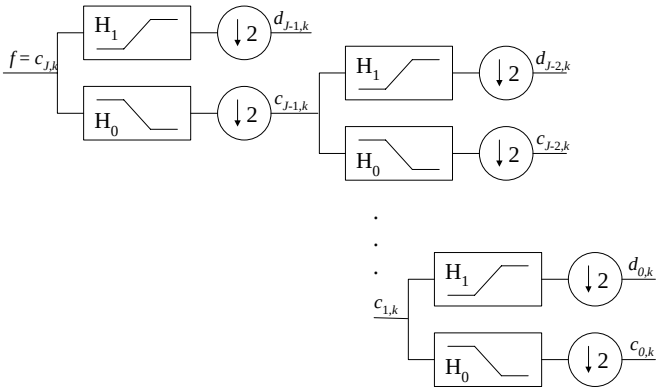

Fig. 2. Discrete Wavelet Transform Tree

$$\phi(t) = \sum_n 2^{1/2} h_0 \phi(2t-n) \tag{4}$$

For computation of wavelet transform, the following pyramidal algorithm is used:

The QMF bank decomposes the signal into low and high frequency components respectively. Convolving the signal with h_1 gives a set of wavelet coefficients $c_{J,k}$, while the convolution with h_0 gives the approximation coefficients $d_{j,k}$. Because of the redundancy of information, these filters are down-sampled, throwing away every other sample at each operation, thus halving the data each time. The approximation coefficients $d_{j,k}$ are then convolved again with the filters h_0 and h_1 to form the next level of decomposition. The backward algorithm simply inverts the process. It combines two linear filters with up-sampling operation. Fig. 1 shows the operation involved in the wavelet decomposition and synthesis of the signal.

At present, there exist no theoretical results that can predict which wavelet is suitable for a particular type of signal. Usually, the best wavelet is chosen by comparing the performances of several types of wavelets.

Wavelet Shrinkage

The most popular form of wavelet-based filtering is commonly known as *Wavelet Shrinkage*. The basic wavelet shrinkage algorithm involves computing of the discrete wavelet transform of the observation y (w = DWT(y)). The contribution of a particular wavelet basis function in the signal expansion can be filtered by weighting the corresponding coefficient w_i by a number $0 \le h_i \le 1$. That is, the wavelet coefficients are modified according to:

$$\hat{w}_i = w_i \cdot h_i \tag{5}$$

In the wavelet shrinkage program, the shrinkage filter corresponds to either the "hard threshold" nonlinearity

$$h_i^{(\text{hard})} = \begin{cases} 1, & \text{if } |w_i| \ge \tau \\ 0, & \text{if } |w_i| < \tau \end{cases} \tag{6}$$

or the "soft threshold" nonlinearity

$$h_i^{(\text{soft})} = \begin{cases} 1 - \dfrac{\tau \operatorname{sgn}(w_i)}{w_i}, & \text{if } |w_i| \geq \tau \\ 0, & \text{if } |w_i| < \tau \end{cases} \quad (7)$$

with τ a user-specified threshold level.

Finally, the signal is reconstructed (estimated) by computing the inverse wavelet transform from the processed data: $\hat{f}$ = IDWT($\hat{w}$).

IV. Filtration of NM Images

The heart region images contain quantum noise, which obeys a Poisson law and is highly dependent on the underlying light intensity pattern being imaged [5]. For denoising purposes, it is often advantageous instead of working in the spatial (pixel) domain to work in a transform domain. One possible choice for images transform is the discrete wavelet transform (DWT) domain. The DWT tends to concentrate the energy of a signal into a small number of coefficients, while a large number of coefficients have low SNR.

Motivated by the DWT tendency to produce coefficients with a high and low SNR, we apply the soft thresholding from the wavelet shrinkage program. But, if the noise was additive white Gaussian, the noise level would be uniform throughout the image and hence uniform across all the wavelet coefficients. Therefore, in a case when a signal contains additive white Gaussian noise a simple global noise threshold could be determined independently on the signal [4]. Unfortunately, the Poisson noise is signal-dependent and therefore wavelet-domain filtering based on a global threshold is inappropriate. Hence, for denoising this type of images we use the wavelet filter described in [5]:

$$h_I = \left(\frac{\hat{\theta}_I^{\,2}}{\hat{\theta}_I^{\,2} + \hat{\sigma}_I^{\,2}} \right)_+ \quad (8)$$

with

$$I = (i,j,m,n)$$

an abstract index for the four indices of the 2-d wavelets basis $\psi_{i,j,m,n}(k,l)$ and

$$\hat{\sigma}_I^{\,2} = \sum_{k,l} \psi_I^{\,2}(k,l) f_I(k,l)$$

an unbiased estimate of the noise power in the *I*-th wavelet coefficient, and

$$\hat{\theta}_I^{\,2} = \omega_I^{\,2} - \hat{\sigma}_I^{\,2}$$

an unbiased estimate of the signal power in the *I*-th wavelet coefficient, and $(\cdot)_+$ denoting the positive part (negative values set to zero).

In addition, due to the wavelet shrinkage program, some of the wavelet coefficients are discarded, so the perfect reconstruction is not possible. Hence, we propose to give up the perfect reconstruction at the very beginning. It means instead of using wavelet filters, to decompose the data using a filter bank with filters that have better characteristics. At the same time the QMF bank should be designed to achieve near perfect reconstruction (NPR). One possible choice for designing QMF NPR bank is using the algorithm in [6].

The algorithm for denoising chest region images can be summarized as following:

- apply the autocorrelation technique to the dynamical images [7];
- create a resultant image from the images obtained in the previous step;
- compute DWT of the image using a QMF NPR bank;
- compute the wavelet filter given with Eq. (8);
- apply the standard soft-thresholding;
- compute the inverse DWT by using modified wavelet coefficients.

V. Experimental Results

We use a set of real NM image matrices of resolution 128x128 shown in Fig. 1. Autocorrelation technique [7] is applied to remove the salt and paper noise from the images.

To design a suitable QMF bank we use the algorithm described in [6]. The obtained QMF bank has overall reconstruction error minimized in the minimax sense; the corresponding QMF filters have least-squares stopband error. The filters have linear phase, zero at π, good passband and narrow transition band. The decomposition filters magnitude response and the prototype filter coefficients are given in Fig. 3 and Table 1, respectively.

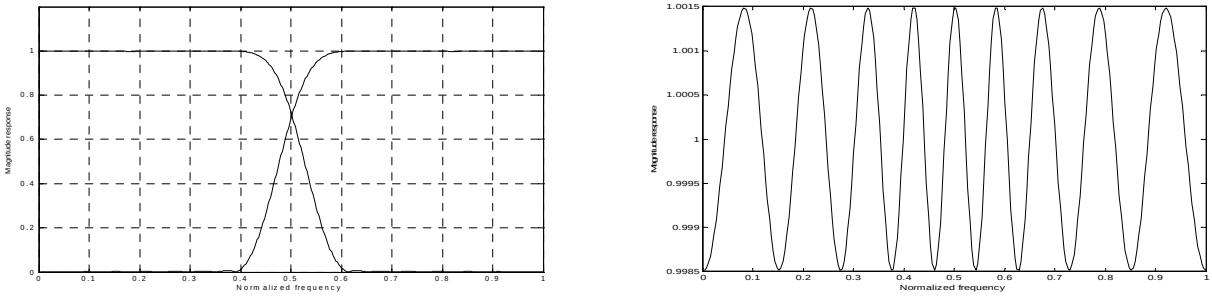

Fig. 3 a) Magnitude responses of the decomposing filters, b) Magnitude response of the QMF NPR bank

$h_0[0–15] = h_0[31–16]$	0.002722 -0.002856 -0.003194 0.007698 0.002690 -0.015823 0.000046 0.027907 -0.007397 -0.046104 0.023106 0.075651 -0.058667 -0.140412 0.184563 0.657174
$h_1[0–15] = –h_1[31–16]$	0.002722 0.002856 -0.003194 -0.007698 0.002690 0.015823 0.000046 -0.027907 -0.007397 0.046104 0.023106 -0.075651 -0.058667 0.140412 -0.184563 -0.657174
$f_0[0–15] = f_0[31–16]$	0.002722 -0.002856 -0.003194 0.007698 0.002690 -0.015823 0.000046 0.027907 -0.007397 -0.046104 0.023106 0.075651 -0.058667 -0.140412 0.184563 0.657174
$f_1[0–15] = –f_1[31–16]$	-0.002722 -0.002856 0.003194 0.007698 -0.002690 -0.015823 -0.000046 0.027907 0.007397 -0.046104 -0.023106 0.075651 0.058667 -0.140412 -0.184563 0.657174

Table 1 Filter coefficients of QMF bank filters

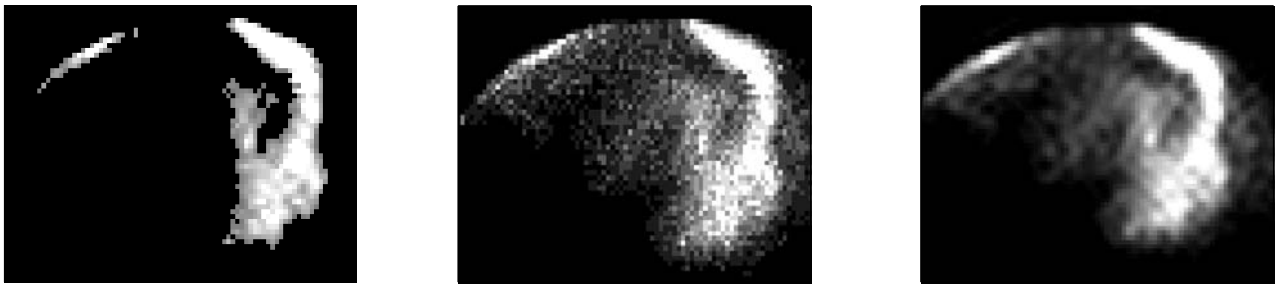

Fig. 4. The vena and the heart a) proposed approach b) conventional approach c) lowpass filtering of the image in b)

After applying the algorithm given in Section 4, we remove the shadow (pixels with low intensity) in the resultant image. Fig. 4 shows the resultant image without the shadow and the resultant image obtained by the conventional way of extracting anatomic information i.e. summing a number of sequential raw images. The image in Fig. 4-a) has sharp edges of the vein and the heart, while the image in Fig. 4-b) contains relatively high level of noise that blurs the edges of these objects. Therefore, the image in Fig. 4-a) is more suitable for an upgrading expert system that could provide automatic identification of optimal shapes and positions of regions of interest needed for further physiological diagnostics.

The quality of the image in Fig. 4-b) could be further improved by using certain low pass filtering techniques as shown in Fig. 4-c), but the projections of the vein and the heart would still suffer from certain deformations. These deformations could degrade the effects of an expert system for automatic identification of the optimal positions and shapes of regions of interest needed for further investigations.

VI. CONCLUSION

We present an approach on pre-processing heart region dynamical NM images. The aim of this approach is to determine anatomical data in order to upgrade the software with an expert system that could identify the optimal positions and the shapes of the regions of interest needed for the heart study. The images are processed in the wavelet transform-domain using linear phase QMF NPR filters. Due to the signal-dependence of the Poisson noise, an alternative approach for selecting the threshold is used. The performance of the proposed method is demonstrated on real NM images.

REFERENCES

[1] Cvetko D. Mitrovski, “Quantitative Determination of Left-Right Shunt at Heart Disease Patients”, *Proceeding of papers*, Faculty of Technical Sciences – Bitola, pp. 327-335, 1996;

[2] G. Strang and T. Nguyen, *Wavelets and Filter Bank*s. Wellesley-Cambrige Press, 1996;

[3] D. L. Donoho, "Wavelet Thresholding and W.V.D.: A 10-minute Tour", *Int. Conf. on Wavelets and Applications*, Toulouse, France, June 1992;

[4] D. L. Donoho and I. M. Johnstone, "Ideal Spatial Adaptation via Wavelet Thresholding", *Biometrika*, vol. 81, pp. 425-455, 1994;

[5] Robert D. Nowak, Richard G. Baraniuk, ”Wavelet-Domain Filtering for Photon Imaging Systems”, *IEEE Trans. Image Processing*, vol. 8, Iss. 5, p. 666-678, May 1999;

[6] Sofija Bogdanova, Mitko Kostov, and Momcilo Bogdanov, “Design of QMF Banks with Reduced Number of Iterations”, *IEEE Int. Conf. on Signal Processing, Application and Technology, ICSPAT ’99*, Orlando, USA, Nov. 1999.

[7] Cvetko D. Mitrovski and Mitko B. Kostov, “On the Preprocessing of Dynamic Nuclear Medicine Images”, *International Scientific Conference on Information, Communication and Energy Systems and Technologies ICEST 2002*, Nis, Serbia and Montenegro, 2002;

[8] Cvetko D. Mitrovski and Mitko B. Kostov, “A Wavelet Domain Approach On Noise Filtration Of Nuclear Medicine Images”, *International Scientific And Applied Science Conference Electronics ET’2002*, Sozopol, Bulgaria, Sept. 2002;

[9] Cvetko D. Mitrovski and Mitko B. Kostov, “An Approach For Extracting The Vein And Heart Boundaries From Raw NM Images”, *VI National Conference ETAI 2003*, Ohrid, Macedonia, Sept. 2003;

[10] Cvetko D. Mitrovski and Mitko B. Kostov, “On The Radionuclide Movement Depended Filtering Of Nuclear Medicine Images”, *Fourth International Conference for Informatics and Information Technology 2003*, Molika, Macedonia, Dec. 2003.

Session AN:

ANTENNAS

Field Analysis of the Eccentric Archimedean Spiral Antenna by the Least Square Boundary Residual Method

Ana Jovanović, Svetozar Jovićević[1]

Abstract: **This paper demonstrates the applicability of the least square boundary method (LSBM) in the eccentric Archimedean spiral antenna analysis. It appeared that the boundary condition is highly fulfilled by a small number of eigenfunctions, which makes the obtained results very reliable. The radiation field is found in the far zone.**

Keywords: **Spiral antennas, the least-squares boundary residual method**

I. INTRODUCTION

Radiation problem is certainly one of the most complex problem in linear electromagnetic. For a long time in the antenna analysis the method of moments has been most frequently used. Although this method is still very much employed (see f.e. [1], [2], [3]) it seems that in the last decade Finite-difference time-domain (FDTD) has become more popular (some of the recent references f.e. [4], [5], [6]). Any attempt to find solution in a closed form by using eigenfunctions of the wave equation even for a relatively simple structure such as circular loop [7] or conic [8] antennas leads to a rather cumbersome procedure.

In this paper for field analysis of the eccentric Archimedean spiral antenna the Least-squares boundary Residual method is applied. Magnetic vector potential is expressed as a linear combination of the wave equation eigenfunctions, the unknown expansion coefficients follow from the minimization of the square error in the boundary condition fulfillment. This method, in original or modified form, has been found as simple and highly accurate in wide range of electromagnetic problems ([9],[10],[11],[12],[13],[14]).

II. THEORETICAL ANALYSIS

There is an antenna's structure (figure 1) in xoy plane ($\theta = \frac{\pi}{2}$). Antenna is fed by a source of harmonic voltage with effective value U.

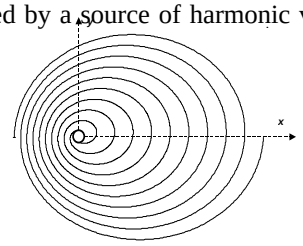

Fig. 1. Eccentric Archimedean spiral antenna

The antenna's structure such as Archimedean spiral has two arms described by the following equations in a spherical coordinate system:

$$r = a\varphi\sqrt{2K\cos\varphi + 1 + k^2} + b \quad 0 \le \varphi \le 2m\pi \quad \text{upper arm} \tag{1}$$

$$r' = a(\phi - \pi)\sqrt{-2K\cos\phi + 1 + k^2} + b \quad \pi \le \phi \le (2m+1)\pi \quad \text{lower arm}$$

where $a = \frac{\Delta}{2\pi}$ is a spiral constant, b is the initial point, k is eccentricity constant.

In a general case the field radiation, anywhere from the antenna does not belong to the TE and TM wave. All field components can be derived from the radial component of magnetic and electric vector potential.

$$A_r = \sum_m \sum_n C_{mn} B_n(kr) P_n^m(\cos\theta) e^{jm\varphi} \tag{2}$$

$$F_r = \sum_m \sum_n D_{mn} B_n(kr) P_n^m(\cos\theta) e^{jm\varphi}$$

where C_{mn} and D_{mn} are the unknown expansion coeficients, $B_n(kr)$ Bessel functions and $P_n^m(\cos\theta)$ Legandre polynoms.

Field components are given as [15]:

$$E_r = \frac{1}{j\omega\varepsilon}\left(\frac{\partial^2}{\partial r^2} + k^2\right)A_r \qquad H_r = \frac{1}{j\omega\mu}\left(\frac{\partial^2}{\partial r^2} + k^2\right)F_r$$

$$E_\theta = \frac{-1}{r\sin\theta}\frac{\partial F_r}{\partial\varphi} + \frac{1}{j\omega\varepsilon r}\frac{\partial^2 A_r}{\partial r\partial\theta} \qquad H_\theta = \frac{1}{r\sin\theta}\frac{\partial A_r}{\partial\varphi} + \frac{1}{j\omega\mu r}\frac{\partial^2 F_r}{\partial r\partial\theta} \tag{2.a}$$

$$E_\varphi = \frac{1}{r}\frac{\partial F_r}{\partial\theta} + \frac{1}{j\omega\varepsilon r\sin\theta}\frac{\partial^2 A_r}{\partial r\partial\varphi} \qquad H_\varphi = -\frac{1}{r}\frac{\partial A_r}{\partial\theta} + \frac{1}{j\omega\mu r\sin\theta}\frac{\partial^2 F_r}{\partial r\partial\varphi}$$

The boundary condition is the annulation of the tangential electric field components on the antenna's arms surfaces. In this case tangential components on the antenna's arms surfaces have E_φ and E_r components. The boundary condition for upper and lower antenna's arms are given as:

$$\left.\begin{aligned} E_{\varphi_t} + E_{r_t} &= E_i \quad za \quad 0 \le r \le b \\ E_{\varphi_t} + E_{r_t} &= 0 \quad za \quad r \ge b \end{aligned}\right\} \text{upper arm} \tag{3.a}$$

$$\left.\begin{aligned} E_{\varphi_t} + E_{r_t} &= -E_i \quad za \quad 0 \le r' \le b \\ E_{\varphi_t} + E_{r_t} &= 0 \quad za \quad r' \ge b \end{aligned}\right\} \text{lower arm} \tag{3.b}$$

where :

[1] Authors are with the Faculty of Electronic Engineering, Cetinjski put bb, 81000 Podgorica, Serbia and Montenegro, E-mail: anaj@cg.ac.yu

$$\left.\begin{aligned} E_{\varphi_t} &= E_\varphi \cos\alpha \\ E_{r_t} &= E_r \sin\alpha \end{aligned}\right\} \text{ upper arm, } \left.\begin{aligned} E_{\varphi_t} &= E_\varphi \cos\alpha' \\ E_{r_t} &= E_r \sin\alpha' \end{aligned}\right\} \text{ lower arm}$$

The angles between the tangent on the antenna lines and the field components are:

$$\alpha = arctg\frac{dr}{rd\varphi} \quad , \quad \alpha' = arctg\frac{dr'}{r'd\phi}$$

Inserting the electrical field components (2.a), into the boundary condition (3.a,b), the boundary condition is given as:
for upper arm

$$\sum_{n=1}^{N}\sum_{m=0}^{n}\left(C_{nm} f_{nm}^{(1)}\left(r,\frac{\pi}{2},\varphi\right) + D_{nm} f_{nm}^{(2)}\left(r,\frac{\pi}{2},\varphi\right)\right) = \begin{cases} E_i & za \quad 0 \le r \le b \\ 0 & za \quad r \ge b \end{cases} \tag{4.a}$$

where eigenfunctions are:

$$f_{nm}^{(1)}\left(r,\frac{\pi}{2},\varphi\right) = \left(\frac{n(n+1)}{yr^2} B_n(kr)\sin\alpha + \frac{jm}{yr}\frac{\partial B_n(kr)}{\partial r}\cos\alpha\right) P_n^m(\cos\theta) e^{jm\varphi}$$

$$f_{nm}^{(2)}\left(r,\frac{\pi}{2},\varphi\right) = \frac{B_n(kr)}{r}\frac{\partial P_n^m(\cos\theta)}{\partial\theta}\bigg|_{\theta=\frac{\pi}{2}} \cos\alpha \; e^{jm\varphi}$$

for lower arm

$$\sum_{n=1}^{N}\sum_{m=0}^{n}\left(C_{nm} f'^{(1)}_{nm}\left(r',\frac{\pi}{2},\phi\right) + D_{nm} f'^{(2)}_{nm}\left(r',\frac{\pi}{2},\phi\right)\right) = \begin{cases} -E_i & za \quad 0 \le r' \le b \\ 0 & za \quad r' \ge b \end{cases} \tag{4.b}$$

where eigenfunctions are:

$$f'^{(1)}_{nm}\left(r',\frac{\pi}{2},\phi\right) = \left(\frac{n(n+1)}{yr'^2} B_n\left(kr'\right)\sin\alpha' + \frac{jm}{yr'}\frac{\partial B_n\left(kr'\right)}{\partial r'}\cos\alpha'\right) P_n^m(\cos\theta) e^{jm\phi}$$

$$f'^{(2)}_{nm}\left(r',\frac{\pi}{2},\phi\right) = \frac{B_n\left(kr'\right)}{r'}\frac{\partial P_n^m(\cos\theta)}{\partial\theta}\bigg|_{\theta=\frac{\pi}{2}} \cos\alpha' \; e^{jm\phi}$$

To simplify the systems (4.a,b), we shall transform them into the following expressions:
for upper arm

$$\sum_n\sum_m S_{nm} F_{nm}\left(r,\frac{\pi}{2},\varphi\right) = \begin{cases} E_i & za \quad 0 \le r \le b \\ 0 & za \quad r \ge b \end{cases} \tag{5.a}$$

where are:

$$\left.\begin{aligned} F_{nm}\left(r,\frac{\pi}{2},\varphi\right) &= f_{nm}^{(1)}\left(r,\frac{\pi}{2},\varphi\right) \\ S_{nm} &= C_{nm} \end{aligned}\right\} za \quad n = 1,2....N \;\; i \;\; m = 0,.....,n$$

and

$$\left.\begin{aligned} F_{nm}\left(r,\frac{\pi}{2},\varphi\right) &= f_{n-N,m}^{(2)}\left(r,\frac{\pi}{2},\varphi\right) \\ S_{nm} &= D_{n-N,m} \end{aligned}\right\} za \quad n = N+1,.....2N \;\; i \;\; m = 0,...,n-N$$

for lower arm

$$\sum_n\sum_m S_{nm} F'_{nm}\left(r',\frac{\pi}{2},\phi\right) = \begin{cases} -E_i & za \quad 0 \le r' \le b \\ 0 & za \quad r' \ge b \end{cases} \tag{5.b}$$

where :

$$\left.\begin{aligned} F'_{nm}\left(r',\frac{\pi}{2},\phi\right) &= f'^{(1)}_{nm}\left(r',\frac{\pi}{2},\phi\right) \\ S_{nm} &= C_{nm} \end{aligned}\right\} za \quad n = 1,2....N \;\; i \;\; m = 0,.....,n$$

and

$$\left.\begin{aligned} F'_{nm}\left(r',\frac{\pi}{2},\phi\right) &= f'^{(2)}_{n-N,m}\left(r',\frac{\pi}{2},\phi\right) \\ S_{nm} &= D_{n-N,m} \end{aligned}\right\} za \quad n = N+1,.....2N \;\; i \;\; m = 0,...,n-N$$

We shall get system of algebraic equations for unknown coefficients S_{nm}, taking the F_{nm} as weighting functions:

$$\sum_n\sum_m S_{nm} a_{nm,n'm'} = b_{n'm'} \tag{6}$$

where :

$$a_{nm,n'm'} = \int_{gornjikrak} F_{nm}\; F^*_{n'm'}\, dl + \int_{donjikrak} F'_{nm}\; F'^{\,*}_{n'm'}\, dl'$$

$$b_{n'm'} = E_i\left(\int_0^b F^*_{n'm'}\, dl - \int_0^b F'^{\,*}_{n'm'}\, dl'\right)$$

The length elements of the upper and lower arms are:

$$dl = \sqrt{(rd\varphi)^2 + dr^2} \quad \text{i} \quad dl' = \sqrt{\left(r'd\phi\right)^2 + dr'^2}$$

As the space includes the point $r \to 0$, $B_n(kr)$ are spherical Bessel functions. Because of the radiation condition, in the far zone the field potentials and consequently the field components are to be expressed by the Hanckel's functions. So the field potentials are given as:

$$\begin{aligned} A_r &= \sum_m\sum_n \beta_{nm}^{(1)} H_n(kr) P_n^m(\cos\theta) e^{jm\varphi} \\ F_r &= \sum_m\sum_n \beta_{nm}^{(2)} H_n(kr) P_n^m(\cos\theta) e^{jm\varphi} \end{aligned} \tag{7}$$

where $\beta_{nm}^{(1)}$, $\beta_{nm}^{(2)}$ are the unknown explanation coefficients obtained by equalizing the expressions (2) and (7) on the sphere of radius $R = \max(r)$:

$$\begin{aligned} \beta_{nm}^{(1)} &= C_{nm}\frac{B_n(kR)}{H_n(kR)} \\ \beta_{nm}^{(2)} &= D_{nm}\frac{B_n(kR)}{H_n(kR)} \end{aligned} \tag{8}$$

Knowing that in the far zone $(r \to \infty)$ Hanckel's functions become $j^{(n+1)}e^{-jkr}$, the field component $E_r \to 0$, and the only existing components are E_φ and E_θ.

The radiation characteristics has a two components:

$$\widehat{F}_{\varphi}(\theta,\varphi)=\left|\sum_{n=1}^{N}\sum_{m=0}^{n} j^{n+1}e^{jm\varphi}\left(\frac{km}{y\sin\theta}\beta_{nm}^{(1)}P_n^m(\cos\theta)+\beta_{nm}^{(2)}\frac{\partial P_n^m(\cos\theta)}{\partial\theta}\right)\right|$$

$$\widehat{F}_{\theta}(\theta,\varphi)=\left|\sum_{n=1}^{N}\sum_{m=0}^{n} j^{n+1}e^{jm\varphi}\left(\frac{jk}{y}\beta_{nm}^{(1)}\frac{\partial P_n^m(\cos\theta)}{\partial\theta}-\frac{jm}{\sin\theta}\beta_{nm}^{(2)}P_n^m(\cos\theta)\right)\right|$$

III. NUMERICAL RESULTS

We analyzed eccentric Archimedean spiral antennas. On the figure 2.a,b radiation patterns of eccentric Archimedean spiral for two different spiral constant and two values of the eccentricity constants are given.

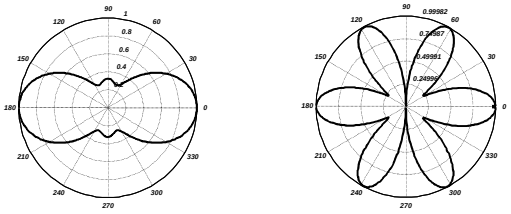

(a) $k = 0$

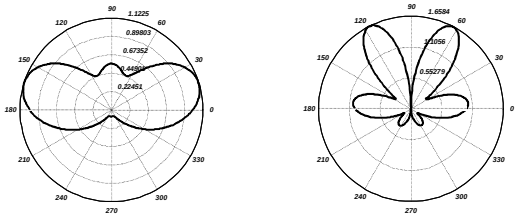

(b) $k = 0.4$

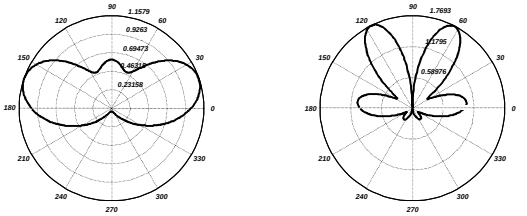

(c) $k = 0.8$

Fig. 2.a Radiation patterns of eccentricArchimedean spiral antenna.
(left column E_{φ} , right column E_{θ} ; $\Delta = 0.25\lambda$)

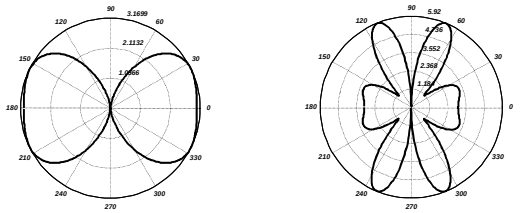

(a) $k = 0$

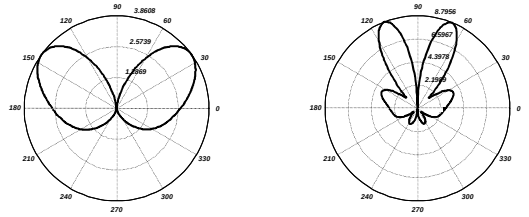

(b) $k = 0.4$

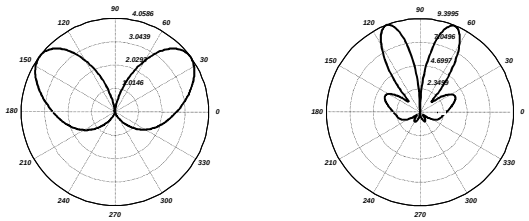

(c) $k = 0.8$

Fig. 2.b Radiation patterns of eccentricArchimedean spiral antenna.
(left column E_{φ} , right column E_{θ} ; $\Delta = 0.5\lambda$)

Radiation patterns of E_{φ} and E_{θ} are given in left and right columns. The patterns are normalized to the case $k = 0$, i.e. to the noneccentric antenna. The expected displacements of maximal radiations can easily be noticed and also that the greater eccentricity produces the grater displacement. The radiation characteristic for E_{φ} component in almost all cases has flater shape with small, in some cases even negligible side lobes. This is not so for E_{θ} component, which has very pronounced side lobes. All radiation patterns are plotted in the plane $\varphi = 0^{o}$.

The maximal gains for three spiral eccentricities are given in Table I.

TABLE I.

spiral geometry	$k = 0$	$k = 0.4$	$k = 0.8$
$\Delta = 0.25\lambda$, $0 \le \varphi \le 2\pi$	4.05 dB	5.22 dB	6.84 dB
$\Delta = 0.5\lambda$, $0 \le \varphi \le 2\pi$	3.99 dB	5.34 dB	7.18 dB

We can see that the larger eccentricity produces the greater gain in direction of maximal radiation.

Fig.3. gives the comparison of the results obtained by our theory and results of the theory discribed in [1].

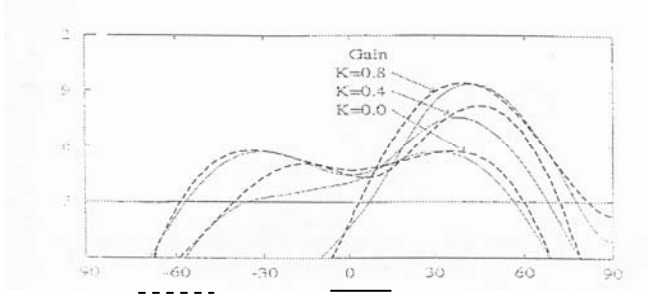

Fig. 3. Comparison of gains of the spiral with $a = 0.00144m/rad$, $90^{o} \le \varphi \le 1620^{o}$ *(our results, results from [1])*

A very good coincidence can be noticed for the case $k = 0$. The greatest deviation is for the spiral eccentricity $k = 0.4$

In all analyzed cases a very high accuracy in the boundary condition fulfillment is achieved with no more than twenty numbers of the series (2). As an example, the boundary condition error on upper and lower antenna arms is given on Fig. 4.

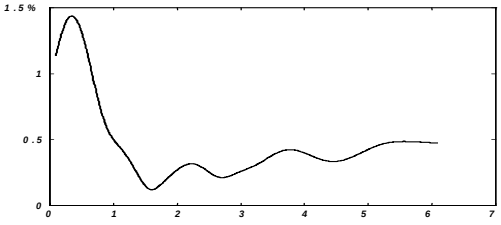

Fig. 4. The boundary condition error

IV. CONCLUSION

The applicability of the Least square boundary residual method to the analysis of eccentric Archimedean spiral has been demonstrated. The radiation patterns of eccentric spiral with two spiral constants and two eccentricities are obtained. Also, in all cases the directivities have been calculated. It was noticed that the enlargement of the spiral eccentricity produces higher gain in the direction of maximal radiation. The obtained gain patterns are compared with those given in Ref. [1]. A very good fulfillment of the boundary condition on the entire antenna was achieved with no more than twenty basic functions.

Therefore, we may conclude that in the analyzed cases the LSBR method turn to be accurate and relatively easy to be applied, which recommends it to even more complex radiation structures.

REFERENCES

[1] R.T.Gloutak, Jr. and N.G.Alexopoulos,"Two-Arm Eccentric Spiral Antenna", IEEE Trans. on Antennas and Propag.,vol.45, no.4, april 1997.

[2] S.K.Khamas and G.G.Cook,"Moment-Method Analysis of Printed Wire Spirals Using Curved Piecewise Sinusoidal Subdomain Basis and Testing Functions",IEEE Trans. on Antennas and Propag.,vol.45, no.6, jun 1997.

[3] H.Nakano, Y.Shinma and J.Yamauchi,"A Monofilar Spiral Antenna and Its Array Above a Ground Plane-Formation of a Circularly Polarized Tilted Fan Beam", IEEE Trans. on Antennas and Propag.,vol.45, no.10, october 1997.

[4] O.M.Ramahi,"Near-and Far-Field Calculations in FDTD Simulations Using Kirchoff Surface Integral Representation", IEEE Trans. on Antennas and Propag.,vol.45, no.5, may 1997.

[5] A.Shlivinski, E.Heyman and R.Kastner,"Antenna Characterization in the Time Domain", IEEE Trans. on Antennas and Propag., vol.45, no.7, july 1997.

[6] O.M.Ramahi," The Complementary Operators Method in FDTD Simulations",IEEE Trans. on Antennas and Propag. magazine, vol.39, no. 6, december1997.

[7] L.W.Li, M.S.Leong, P.S.Kooi and T.S.Yeo,"Exact Solutions of Electromagnetic Fields in Both Near and Far Zones Radiated by Thin Circular-Loop Antennas: A General Representation", IEEE Trans. on Antennas and Propag., vol.45, no.12, december 1997.

[8] S.N.Samadar and E.L. Mokole," Biconical Antennas with Unequal Cone Angles", IEEE Trans. on Antennas and Propag., vol.46, no.2, february 1998.

[9] LJ.Stanković, S.Jovićević," Modified least squares method with application to diffraction and eigenvalue problems", IEEE Procedings, vol.135, Pt.H, no.5, october 1988.

[10] LJ.Stanković, S.Jovićević,"A round-ridge waveguide", Ann.Telecommun., 43, n^o 9-10, 1988.

[11] LJ.Stanković, S.Jovićević," Boundary Condition Expansion of Basis Functions Method Implemented by Fast Fourier Transform Algorithms", IEEE Trans. on Microwave Theory and Techniques, vol.38, no.3, march 1990.

[12] A.Jovanović, S.Jovićević"A general Solution of the Thin Circular Loop Radiation", Electromagnetics, Vol. 23, no.1, january 2003.

[13] S.Jovićević, A.Jovanović,"The analysis of the biconical antenna by the Least-Squares Boundary Residual Method", Int. J. Electron. Commun. (AEU) 57 (2003), no. 6, 415-419.

[14] A.Jovanović, S.Jovićević,"Analiza žičanih antena metodom najmanjih kvadrata", XLII ETRAN sveska II, Vrnjačka Banja 1998.

[15] R.F.Harrihgton,Time-Harmonic Electromagnetic Fields, Mc Graw-Hill Book Company, New York 1961.

[16] L.W.Li, M.S.Leong, P.S.Kooi, T.S.Yeo,"Exact Solutions of Electromagnetic Fields in Both Near **and** Far Zones Radiated by Thin Circular-Loop Antennas: A General Representation", IEEE Trans. Antennas and Propag., vol. 45, no. 12, dec.1997.

Effect of Geometrical Aspect Ratio of a Rectangular Microstrip Element on Antenna Bandwidth

Nikola I. Dodov[1], Slavi R. Baev[2]

Abstract – **Analytical expressions based on the cavity model are used to evaluate some characteristics of the microstrip element. For the rectangular microstrip resonator these formulas provide clear information about the effect of the antenna geometrical dimensions on the bandwidth. When the dielectric substrate is very thin the accuracy of the formulas is sufficient which allows their use as approximate design expressions.**

Keywords – **antenna, microstrip resonator, bandwidth.**

I. INTRODUCTION

Microstrip antennas have a broad spectrum of applications in present-day communications due to their advantages like low volume and easy production technology. Main disadvantage of these antennas is the narrow bandwidth and many techniques for bandwidth enhancement have been developed. There are many publications [1-4] concerning the effect of the substrate parameters (dielectric permittivity, thickness) on the bandwidth, quality factor, radiation efficiency and other characteristics of the microstrip resonator.

The aim of the present publication is to analyze the relation between the bandwidth and the geometry of the microstrip resonator antenna. It has been found that some patch shapes have inherently low quality factor [1] – these are annular ring, square/rectangular ring, quarter-wave shorted patch and others. There is information about the strong dependence between the bandwidth and the geometrical aspect ratio (width to length ratio) of the rectangular patch [1], [5]. The analysis of this question is important because of the wide spread use of the rectangular microstrip element and the possibility for obtaining large bandwidth enhancement with simple variation of the antenna geometry.

In Section 2 of this publication are given basic expressions used in the analysis of microstrip resonator antennas. These analytical formulas are derived on the basis of the cavity model and include expressions for the resonant frequency, total quality factor, radiation efficiency and bandwidth. The formulas are given in form corresponding to the case of a rectangular microstrip patch and they provide insight into the effect of the geometrical aspect ratio on the antenna parameters. In Section 3 the above-mentioned expressions are used to obtain numerical results and a set of graphs for particular values of the dielectric permittivity, substrate thickness, resonant frequency and aspect ratio of the microstrip element.

[1]Nikola I. Dodov is with the Department of Radiotechnics, Faculty of Communications and Communications Technologies, Technical University – Sofia, 8 " Sv. Kliment Ohridski " Blvd., Sofia 1000, Bulgaria, E-mail: ndodov@tu-sofia.bg

[2]Slavi R. Baev is with the Department of Radiotechnics, Faculty of Communications and Communications Technologies, Technical University – Sofia, 8 "Sv. Kliment Ohridski " Blvd., Sofia 1000, Bulgaria, E-mail: rosislav@yahoo.com

II. THEORETICAL RELATIONS FOR THE RECTANGULAR MICROSTRIP PATCH

A rectangular patch is shown in Fig. 1. The designations are as follows: L – patch length, W – patch width, h – substrate thickness, ε_r – relative dielectric permittivity of the substrate material.

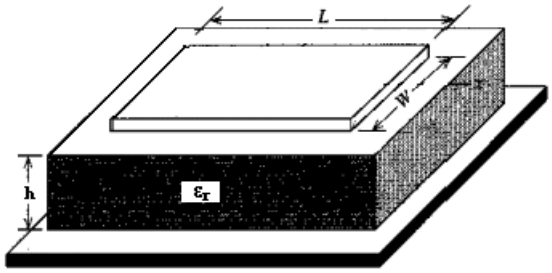

Fig. 1. Rectangular microstrip resonator

The analysis algorithm used for the purpose of this study is described next. All the expressions given in this section are derived for the dominant mode of a rectangular patch – TM_{010}, in which case the radiating edges are those with dimension W. Since the TM_{010} wave is used the most, the analysis shall be restricted only for this particular mode.

The effect of the aspect ratio on the resonant frequency can be evaluated with the expressions derived in [2]. From the resonance condition for the TM_{010} mode in the rectangular patch the following equation is obtained:

$$f_r = \frac{c}{2L\sqrt{\varepsilon_r}} \tag{1}$$

In this equation c is the speed of light in free space. When the resonant frequency f_r and the dielectric permittivity ε_r are given Eq. (1) can be used for determining the patch length. This formula does not account for the fringing effect, which leads to enlarged electrical area of the patch compared to the physical area. The including of the edge effects in Eq. (1) gives another value for the resonant frequency:

$$f_{rc} = \frac{c}{2L_e\sqrt{\varepsilon_{re}}} \tag{2}$$

L_e is the effective length of the patch and ε_{re} is the effective dielectric permittivity of the substrate. Expressions for L_e and ε_{re} are given in [2]:

$$\varepsilon_{re} = \frac{\varepsilon_r + 1}{2} + \frac{\varepsilon_r - 1}{2}\left(1 + 12\frac{h}{W}\right)^{-\frac{1}{2}} \tag{3}$$

$$L_e = L + 2\Delta L \tag{4}$$

$$\Delta L = 0{,}412h\frac{\left(\varepsilon_{re} + 0{,}300\right)\left(\frac{W}{h} + 0{,}264\right)}{\left(\varepsilon_{re} - 0{,}258\right)\left(\frac{W}{h} + 0{,}813\right)} \tag{5}$$

ΔL is the extension of the length on each side of the patch due to the fringing effects.

It is observed that if the values of L, ε_r, and h are kept constant the variation of the ratio W/L shall alter the resonant frequency and more precisely the increasing of W/L shall lower f_{rc}.

To evaluate the shift of the frequency f_{rc} from the specified operating frequency f_r the so called fringe factor (length reduction factor) can be used:

$$n = \frac{f_{rc}}{f_r} \tag{6}$$

This factor n is of importance because it is used for length correction of the patch. When the aspect ratio W/L increases the fringing effect also increases and the resonant frequency f_{rc} lowers. To compensate for this shift of the frequency f_{rc} compared to the given resonant frequency f_r the length of the patch L must be reduced. The following equation gives the reduced patch length:

$$L_c = L_e n - 2\Delta L \tag{7}$$

This dimension L_c must be taken into account in the calculations concerning the antenna parameters.

Next the losses, the Q-factors associated with them and then the radiation efficiency of the patch are determined. There are four loss mechanisms to be considered in the microstrip resonator: radiation, loss due to surface wave propagation, conductor loss and dielectric loss. The total quality factor of the system Q_t is given by:

$$\frac{1}{Q_t} = \frac{1}{Q_{rad}} + \frac{1}{Q_{sw}} + \frac{1}{Q_c} + \frac{1}{Q_d} \tag{8}$$

For very thin substrates ($h/\lambda_0 << 1$) the losses due to the surface waves and Q_{sw} can be neglected. Formulas for the other Q-factors are given in [2], [4]:

$$Q_d = \frac{1}{\tan\delta} \tag{9}$$

$$Q_c = h\sqrt{\pi f_r \mu\sigma} \tag{10}$$

$$Q_{rad} = \frac{2\varpi_r \varepsilon_0 \varepsilon_r}{hG_{t/l}} K \tag{11}$$

$tan\delta$ is the loss tangent of the substrate material, μ is the magnetic permittivity of the substrate, σ is the conductivity of the conductor used for the patch, ε_0 is the dielectric permittivity of free space, $G_{t/l}$ is the total conductance per unit length of the radiating aperture and:

$$K = \frac{\iint_{area} |E|^2 dA}{\oint_{perimeter} |E|^2 dl} \tag{12}$$

For a rectangular patch operating in the TM_{010} mode:

$$K = \frac{L_c}{4} \tag{13}$$

$$G_{t/l} = \frac{G_{rad}}{W} \tag{14}$$

G_{rad} is the radiation conductance of the equivalent slots. For thin substrates the expression for G_{rad} is [2]:

$$G_{rad} = \frac{I}{30\pi^3} \tag{15}$$

$$I = \int_0^{\pi}\int_0^{\pi}\left[\frac{\sin\left(\frac{k_0 W}{2}\cos\theta\right)}{\cos\theta}\right]^2 \sin^3\theta\cos^2\left(\frac{k_0 L_e}{2}\sin\theta\sin\varphi\right) d\theta d\varphi \tag{16}$$

The radiation efficiency of an antenna is defined as the power radiated over the input power or in terms of the Q-factors defined above:

$$e_r = \frac{Q_t}{Q_{rad}} \tag{17}$$

Eq. (16) allows evaluating the radiation efficiency as a function of the ratio W/L. In some publications [1], [3], [6] it is assumed that the radiation efficiency is almost independent of W/L. The results obtained in Section 3 prove that there is such dependency.

Next an expression for the bandwidth of a rectangular microstrip element is given. This equation clearly shows the dependence of the bandwidth from the substrate parameters, resonant frequency and geometrical aspect ratio. When the bandwidth is defined in terms of SWR (Standing Wave Ratio) and it is specified that SWR≤2 then the following expression for the bandwidth can be obtained [1], [6]:

$$BW = \frac{16}{3\sqrt{2}}\frac{p}{e_r}\frac{1}{\varepsilon_r}\frac{h}{\lambda_0}\frac{W}{L_c}q \tag{18}$$

$$p = 1 - \frac{0{,}16605}{20}(k_0 W)^2 + \frac{0{,}02283}{560}(k_0 W)^4 - 0{,}009142\,(k_0 L_c)^2 \tag{19}$$

$$q = 1 - \frac{1}{\varepsilon_r} + \frac{2}{5\varepsilon_r^2} \tag{20}$$

III. Results Of The Performed Simulation Analysis

The simulation analysis is performed according to the algorithm described in Section 2. Four substrate materials with different values of the dielectric permittivity ε_r are investigated: honeycomb (ε_r=1,07), duroid (ε_r=2,2), quartz (ε_r=3,8), alumina (ε_r=10). The first set of data is obtained for resonant frequency f_r=2 GHz and substrate thickness h=0,1588 cm. The initial value of the patch length is calculated by Eq. (1). The variation of the bandwidth BW and the radiation efficiency e_r is studied for a specified range of the aspect ratio (W/L=0,1÷3).

Fig. 2 shows the bandwidth BW as a function of W/L and some numerical values are given in Table I.

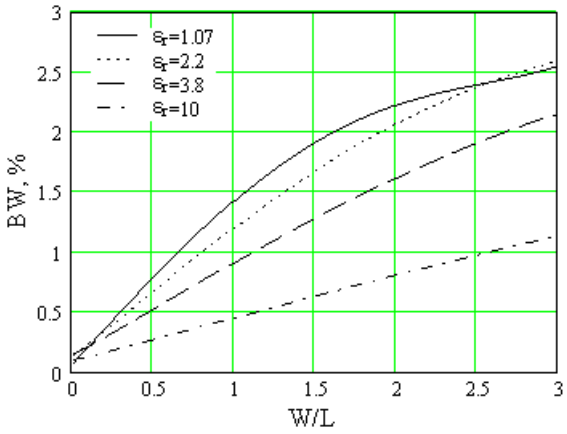

Fig. 2. Bandwidth as a function of the aspect ratio of the rectangular patch for four different substrates (h=0,1588 cm, f_r=2 GHz)

TABLE I

Bandwidth for different values of W/L and ε_r

W/L	BW,%			
	ε_r=1,07	ε_r=2,2	ε_r=3,8	ε_r=10
0,5	0,782	0,666	0,519	0,267
1,0	1,420	1,195	0,908	0,448
1,5	1,908	1,669	1,277	0,629
2,0	2,220	2,065	1,613	0,805
2,5	2,391	2,370	1,905	0,973

As can be seen from Fig. 2 the bandwidth increases almost linearly with W/L. This is due to the larger radiating edges of the wider patch, which leads to increased radiated power and radiation conductance G_{rad} and decreased values of Q_{rad} and Q_t. The patch bandwidth decreases inversely with the increasing of ε_r. Increased value of ε_r leads to reduced fringing field (the electromagnetic field concentrates in the substrate) and radiated power, simultaneously the surface wave power increases. As a result the quality factor of the patch becomes higher thus reducing the bandwidth. Interesting fact is that for lower value of ε_r the relative bandwidth enhancement decreases, i.e., the useful effect from widening the patch is reduced.

Fig. 3 shows the radiation efficiency as a function of W/L for the four investigated dielectric substrates. Eq. (17) is used for the calculation of e_r. The materials with higher dielectric permittivity ε_r have lower radiation efficiency due to the reduced radiated power and increased surface waves as described above. This result is also confirmed by other publications [1], [3], [6], but the assumption in these papers that the radiation efficiency is almost independent of the aspect ratio W/L is true only for low values of the dielectric permitivity and large ratios W/L (approximately W/L≥1,5). The growing shape of the graphs is explained by the increased radiation in space waves when the patch is wider.

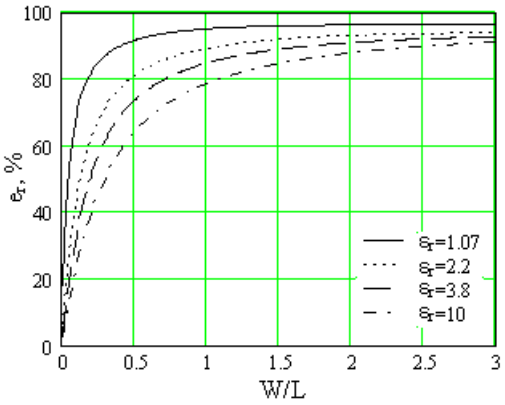

Fig. 3 Radiation efficiency as a function of the aspect ratio of the rectangular patch for four different substrates (h=0,1588 cm, f_r=2 GHz)

The next part of the study analyzes the effect of the aspect ratio W/L on the bandwidth BW of a rectangular microstrip resonator with dielectric permittivity of the substrate ε_r=2,2 and substrate thickness h=0,1588 cm for a range of resonant frequencies (f_r= 2, 4, 6, 8, 10 GHz). Fig. 4 illustrates the results.

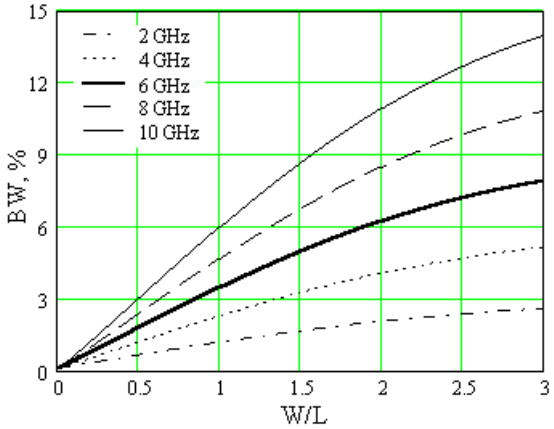

Fig. 4. Bandwidth as a function of the aspect ratio of the rectangular patch for five different frequencies (h=0,1588 cm, ε_r=2,2)

As can be seen the bandwidth increases with f_r. The higher value of the resonant frequency increases the electrical thickness of the substrate ($h\sqrt{\varepsilon_r}/\lambda_0$), radiation conductance and radiated power. Similar results are reported in [1] and [3]. For

low values of *W/L* the relation between *BW* and *W/L* is almost linear. The relative bandwidth enhancement increases with the frequency f_r. Table II contains values of *BW* for five ratios *W/L*.

TABLE II
BANDWIDTH FOR DIFFERENT VALUES OF *W/L* AND f_r

W/L	*BW,%*				
	f_r =2 GHz	f_r =4 GHz	f_r =6 GHz	f_r =8 GHz	f_r =10 GHz
0,5	0,666	1,204	1,778	2,382	3,018
1,0	1,196	2,290	3,450	4,679	5,981
1,5	1,671	3,264	4,958	6,757	8,671
2,0	2,068	4,077	6,219	8,500	10,933
2,5	2,373	4,704	7,193	9,851	12,692

IV. CONCLUSION

Theoretical formulas for the resonant frequency, radiation efficiency and bandwidth of the rectangular microstrip resonator are used to evaluate the variation of these parameters with the geometrical aspect ratio of the patch. The expressions in the present analysis can be used for obtaining quite accurate design data.

The results of the performed simulation clearly show that the increased patch width cause large bandwidth enhancement. This fact is explained by the increased radiating aperture and radiated power when the aspect ratio *W/L* is larger, which lowers the quality factor of the resonator. The bandwidth improvement of a wide rectangular patch (*W/L*=1,5) compared to a narrow patch (*W/L*=0,5) depends on the dielectric permittivity of the substrate and the resonant frequency and for the investigated values of these parameters it varies from 2,5 to 3 times. In other words the bandwidth can be changed to a great extent with a simple geometry variation. Interesting result is that the relative bandwidth enhancement becomes higher with the increase of f_r и ε_r, i.e., the useful effect of widening the patch is greater.

The main advantages of widening the rectangular patch are increased bandwidth, radiation efficiency, and directivity. This method for bandwidth improvement has also disadvantages, which must be taken into account for design purposes and which are not investigated in this study. These include larger patch size, generation of grating lobes in antenna arrays, effect on cross-polarization characteristics. In some papers [1], [4] it has been suggested that $W/L \leq 2$ for obtaining good aperture efficiency.

REFERENCES

[1] R. Garg, P. Bhartia, I. Bahl, and A. Ittipiboon, *Microstrip Antenna Design Handbook*, Norwood, Artech House, 2001.

[2] C. A. Balanis, *Antenna Theory (Analysis and Design)*, New York, John Wiley and Sons Inc., 1997

[3] P. Perlmutter, S. Shtrikman, and D. Treves, "Electric Surface Current Model for the Analysis of Microstrip Antennas with Application to Rectangular Elements", *IEEE Trans., Antennas and Propagation*, Vol. AP-33, pp. 301-311, Mar.1985.

[4] K. R. Karver, and J. W. Mink, "Microstrip Antenna Technology", *IEEE Trans., Antennas and Propagation*, Vol. AP-29 no. I, pp. 2-24, Jan.1981.

[5] D. M. Pozar, "A Review of Bandwidth Enhancement Techniques for Microstrip Antennas", in *Microstrip Antennas, The Analysis and Design of Microstrip Antennas and Arrays*, D. M. Pozar, and D. H. Schaubert(Eds.), New York, IEEE Press, pp. 157-166, 1995.

[6] D. R. Jackson, and N. G. Alexopoulos, "Simple Approximate Formulas for Input Resistance, Bandwidth, and Efficiency of a Resonant Rectangular Patch", *IEEE Trans., Antennas and Propagation*, Vol. AP-39, pp. 407-410, 1991.

Variations of the Axial Ratio of Microstrip Antenna for Circular Polarization with the Electrical Parameters of the Substrate

Nikola I. Dodov[1], Milko V. Stefanov[2]

Abstract – **Microstrip patch antenna with truncated corners is described. It is designed for 2GHz central frequency with different electrical substrate parameters – thickness and relative dielectric permittivity. It is shown that the Axial Ratio and the bandwidth are strongly dependent on the substrate parameters. The most proper combination between the parameters to achieve the best performance of the antenna is also discussed**

Keywords – **microstrip patch antenna, truncated corners, axial ratio, bandwidth.**

I. INTRODUCTION

Microstrip patch antennas are increasing in popularity for use in wireless applications due to their low-profile structure. Therefore they are extremely compatible for embedded antennas in handheld wireless devices such as cellular phones, pagers, GPS receivers etc. Some of their principal advantages are: light weight and low volume, low profile planar configuration, low fabrication cost, hence can be manufactured in large quantities, supports both, linear as well as circular polarization, can be easily integrated with microwave integrated circuits, capable of dual and triple frequency operations, mechanically robust when mounted on rigid surfaces. Microstrip patch antennas suffer from a number of disadvantages as compared to conventional antennas: narrow bandwidth, low efficiency, low Gain, extraneous radiation from feeds and junctions, low power handling capacity, surface wave excitation [1].

In many cases a circularly polarized antenna is desirable. For example, it may be difficult to know beforehand the required orientation of the antenna when linear polarization is used. Satellite-to-mobile ground-based or airborne links are a good example of this problem. In other situations, a circularly polarized antenna may make a system more user-friendly by avoiding the need lo line-up the antenna with the signal polarization. Right- and left-hand circular polarizations are orthogonal to each other. This can he employed to double the channel capacity on a link by having one signal use right-hand and the other left circular polarization [2].

[1] Nikola I. Dodov is with the Faculty of Communications and Communication Technologies, Technical University of Sofia, 8, Kliment Ohridski Str, 1756 Sofia, Bulgaria,
E-mail: ndodov@tu-sofia.bg

[2] Milko V. Stefanov is with the Faculty of Communications and Communication Technologies, Technical University of Sofia, 8, Kliment Ohridski Str, 1756 Sofia, Bulgaria,
E-mail: mvs@mail.bg

For example the GPS antenna in actuality needs to be a circularly polarized antenna. This not only eliminates the need to orient the antenna but also maximizes the received signal and can reduce the effects of multipath.

A circularly polarized wave has two orthogonal field components that are in phase quadrature. Microstrip antennas can be designed to radiate circular polarization with one feed. It is possible to excite the two modes with one feed by introducing a small perturbation in the patch shape [3]. Many types of perturbations are used. One of the most common used is a squire patch with two diagonally opposite truncated corners. The patch is fed at the center of one of its sides. The antenna is fed along a center line as with a linearly polarized patch.

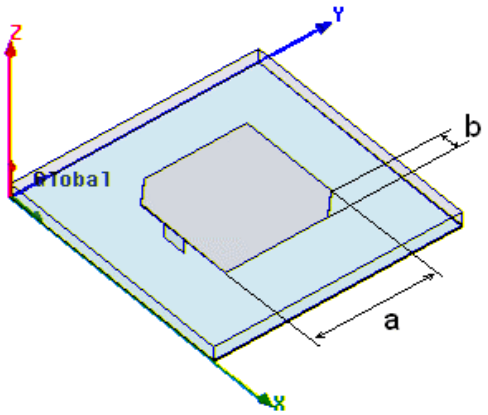

Fig.1. Circularly polarized microstrip antenna with truncated corners

The feed excites fields under the patch just as with a linearly polarized antenna. The signal injected by the feed tends to propagate in one direction, guided by the transmission line formed by the patch. In very approximate terms, the perturbation segment "scatters" [3] the feed fields into a mode that is spatially orthogonal. Because of the different patch geometry this scattered mode has a resonant frequency shifted slightly from that of the squire patch. To achieve circular polarization, these two modes must be made equal in amplitude and must differ in phase by 90 degrees. The equal amplitude is obtained by proper positioning of the feed. The creation of a 90-degree phase shift is due to two factors. One is again the feed position, but this time it involves the orientation of the feed with respect to the perturbation. Shifting from one side to the adjacent side changes the sense of the polarization for the truncated patch. The other factor is the size of the perturbation. For the singly-fed patch, only one

mode is excited by the feed. The perturbation scatters some of this into a mode similar to the first one. In actuality, the perturbation also modifies the original mode, creating two new modes [4].

In the field of the circular polarized microstrip antennas two bandwidths are defined [5]: impedance bandwidth and axial ratio bandwidth. These two bandwidths are connected but corners-truncated patch antennas are very narrowband. In the most cases the impedance bandwidth is wider then the axial ratio bandwidth when the impedance matching between the antenna and the feed line is performed.

II. CORNERS-TRUNCATED PATCH DESIGN

Dimensions design of a corners-truncated patch antenna includes calculation of the resonant length, input resistance at resonance, radiation efficiency, overall efficiency, and bandwidth for a rectangular patch. The basis for the calculations is a series of closed form expressions which were generated by curve fitting to full wave solutions. The closed form expressions calculate the patch resonant dimension and quality factor (Q). Formulas derived from patch cavity models determine Q's for conductor and dielectric losses. From all the Q values, the overall efficiency can be found. The overall Q also determines the bandwidth. The input resistance at resonance also follows from results derived from cavity models. Even though the solution is based upon full wave results, there are some limitations on certain parameters. The relative dielectric constant should be between 1 and 10. It is used a simulation software that iterates the element dimension until the correct resonant frequency is found. It stops iterating when the resonant frequency is within 0.001 GHz of the input value. The accuracy of the results is a few percent (2% to 3%). Unfortunately the bandwidth for good circular polarization may be 1% or less [4]. It may be necessary to use the model to establish initial dimensions. A combination of more model runs and some experiment may be needed to reach a final design.

As it was mentioned above there are not simple analytical expressions for synthesis and analysis of the corners-truncated microstrip antenna because of the complex character of the field in the antenna. That's why numerical methods for analysis as Moments Method, Finite Difference Method etc. have to be used. In the current analysis a model of a microstrip antenna with truncated corners by the medium of a software package, working with Finite Elements Method has been designed.

The feeding of the corners-truncated patch antenna can be realized by several methods: by microstrip line, by coaxial probe, by proximity coupling etc. In this analysis the antenna is fed by a microstrip line but similar results can be achieved with using of a coaxial probe.

III. RESULTS FROM THE ANALYSIS

On the basis of models of corners-truncated microstrip antennas designed for operation at central frequency of 2 GHz are obtained the variations of the axial ratio with the parameters of the substrate.

Fig. 2, 3 and 4 show the variations of the axial ratio with the frequency for different values of the substrate thickness h. On these plots the axial ratio bandwidth can be determined as the difference between the frequencies for which the axial ratio has value of 3dB. With the increasing of the thickness the bandwidth becomes wider. That is due to the variations of the geometrical dimensions of the patch. As it can be seen from Table I the nominal patch size (a) decreases but the size of perturbation (b) increases.

The curve of the axial ratio on the plots has two minimums, which improve approximately 0dB but there is a maximum between the minimums. This maximum shows that at the central frequency the axial ratio has a value grater than 0dB. The two minimums are obtained for the resonance frequencies of the modes. For these frequencies the polarization is almost circular. The effects of increasing the axial ratio due to the resonance character of the field from the two excited modes and to the feeding of the antenna. As it was mentioned above one of the requirements to achieve circular polarization is the two excited modes to be equal in amplitude. This is difficult to realize and as a result of the difference in the amplitudes the axial ratio increases at the central frequency. This disadvantage can be avoided by some changes of the dimensions of the patch but that leads to reduction of the bandwidth. To operate the antenna with wider bandwidth the increasing of the axial ratio can be neglected but only when the maximal value is less than 3dB.

TABLE I
NUMERICAL RESULTS

h, mm	ε_r	a, mm	b, mm	BW, MHz
1.1	2.2	49.450	4.057	37
1.5	2.2	49.120	4.577	43
2	2.2	48.782	5.178	65
1.4	2.2	49.245	4.453	41
1.4	5	32.813	2.344	31
1.4	7.5	26.838	1.779	26

The impedance bandwidth of a microstrip antenna increases with larger substrate thickness. That is attended by some disadvantages – presence of higher level surface waves that degrade the radiation pattern, polarization characteristics and leads to poor radiation efficiency; higher antenna profile and higher level of the maximum in the axial ratio within the operating bandwidth.

Fig. 5, 6 and 7 illustrate the variations of the axial ratio with the frequency for different values of the relative permittivity of the substrate. It can be seen that the bandwidth decreases for higher ε_r but the patch dimensions are reduced. The maximum level of the axial ratio also decreases. The impedance bandwidth decreases because more energy is stored within the dielectrics with high ε_r. The energy of the surface waves is also increased. As a result the radiation losses are reduced and radiation quality factor increases. On the other hand when ε_r increases, the patch dimensions decreases (see Table I). That is an advantage because microstrip antennas are commonly used in antenna arrays and rarely as single radiators. Then the patch size is important.

Microstrip antennas are printed antennas. When they are fed by a microstrip line the dielectric of the antenna and transmission line is common. Microstrip line must guide the energy and it should not radiate but this can be achieved with higher values of ε_r. In the same time the antenna must radiate and wide bandwidth is the most important purpose. Therefore the optimal value of ε_r, which partially satisfies all requirements, should be accepted.

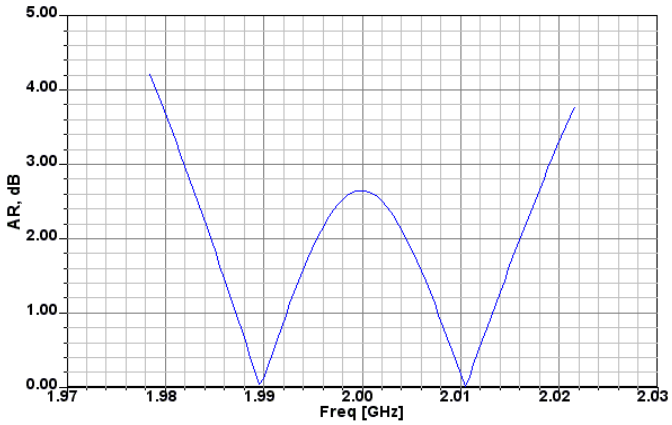

Fig.2. Axial Ratio versus frequency, ε_r =2.2, h=1.1 mm

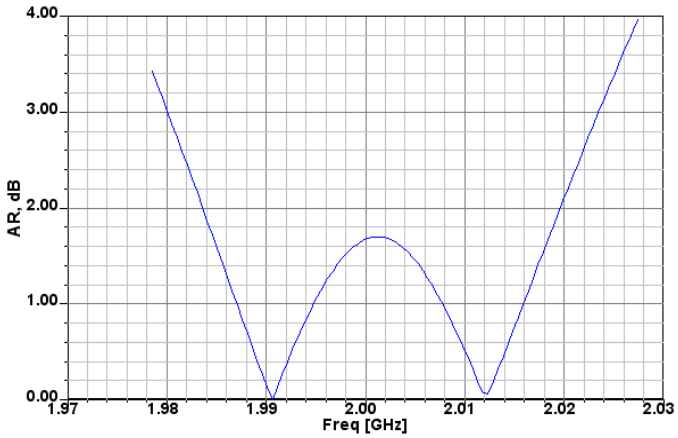

Fig.3. Axial Ratio versus frequency, ε_r =2.2, h=1.5 mm

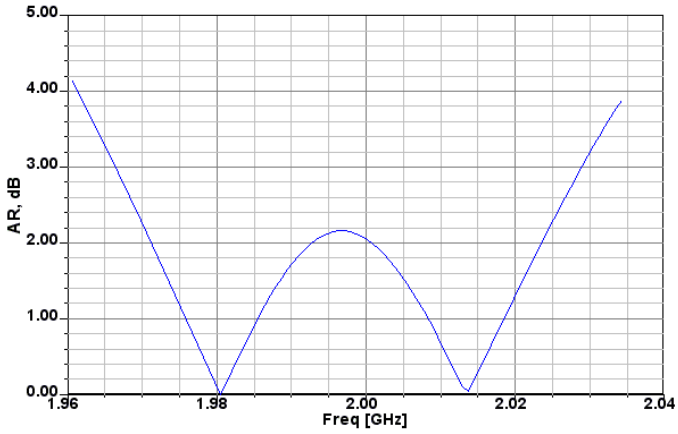

Fig.4. Axial Ratio versus frequency, ε_r =2.2, h=2 mm

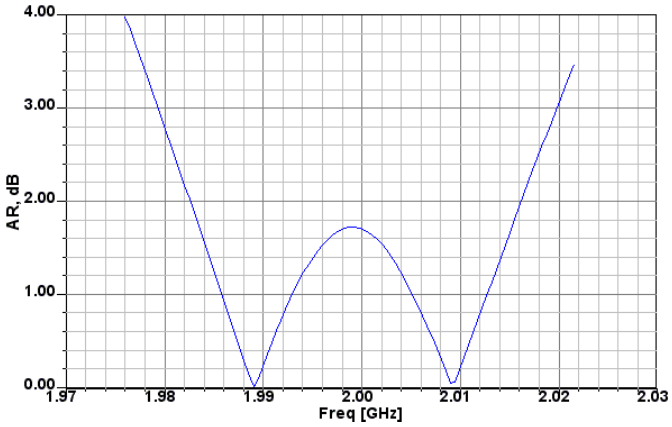

Fig.5. Axial Ratio versus frequency, ε_r =2.2, h=1.4 mm

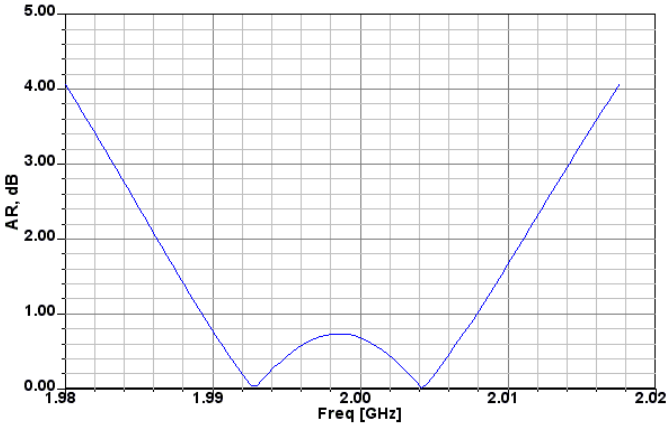

Fig.6. Axial Ratio versus frequency, ε_r =5, h=1.4 mm

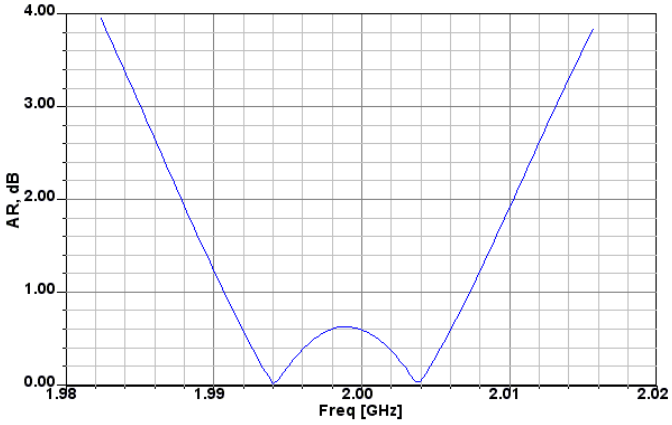

Fig.7. Axial Ratio versus frequency, ε_r =7.5, h=1.4 mm

IV. Conclusion

In this paper a circularly polarized antenna with truncated corners has been analyzed from the view point of the polarization characteristic – Axial Ratio and respectively Axial Ratio Bandwidth. The widest bandwidth is obtained with larger thickness and lower relative permittivity of the substrate.

That is attended by several undesired effects – high level of the axial ratio for the central frequency, transformation of more energy to surface waves, larger antenna dimensions and surface profile. Some of these disadvantages can be reduced

by different modifications of the geometry and feeding system.

REFERENCES

[1] C. A. Balanis, *Antenna Theory: Analysis and Design*, second edition, John Wiley & Sons, New York, 1997.

[2] P. C. Sharma, K. C. Gupta, "Analysis and optimized design of single feed circularly polarized microstrip antennas", IEEE Trans. Antennas Propagat., AP-31, pp. 949-955, 1983.

[3] R. A. Sainati, *CAD of Microstrip Antennas for Wireless Applications*, Artech House Inc., 1996.

[4] P.S.Hall, "Review of techniques for dual and circularly polarized antennas", invited review in Pozar, D.M.and Schaubert, D.H. (eds), *Microstrip Antennas*, IEEE Press, New York, 1995.

[5] Kin-Lu Wong, *Compact and Broadband Microstrip Antenna*, A Wiley- InterScience Publication John Wiley & Sons, Inc.2002.

Determination of Optimal Values of the Substrate Parameters in Microstrip Antennas

Nicola I. Dodov[1] and Peter Zh. Petkov[2]

Abstract –**This paper presents results of research into the resonant properties of the printed antennas. The research has been carried out by means of varying relative dielectric permittivity and the thickness of the substrate. A field of unsuitable values of dielectric permittivity and substrate thicknesses have been noted. The values of the impedance bandwidth were examined as a function of substrate parameters.**

Keywords – **bandwidth, radiation Q, substrate thickness, microstrip antenna.**

I. INTRODUCTION

Microstrip antenna arrays are widely used in modern telecommunication systems. Along with their advantages – ease of manufacturing, functionality, low cost they have some significant disadvantages. The main shortcoming is their narrow working frequency band. This property is determined by the resonant character of this type of antennas. There are several electrical models that describe the resonant behavior of the microstrip resonator. Most commonly used are the transmission line model (TLM) and the cavity model. The working bandwidth (BW) of the antenna mainly depends on the total quality factor (Q_{tot}) of the resonant system, and on VSWR. Their relationship is defined by Eq. 1:

$$BW = \frac{VSWR - 1}{Q_{tot}\sqrt{VSWR}} \tag{1}$$

When the microstrip antenna is properly matched, the working impedance bandwidth depends entirely on the feeding type and the total quality factor of the resonant system. The present paper investigates the behavior of the Q_{tot} in conditions of different substrate parameters.

II. EMPIRICAL AND THEORETICAL MODELS

The Q_{tot} is a function of several components. From the microstrip antenna theory there are well known formula (Eq2):

$$\frac{1}{Q_{tot}} = \frac{1}{Q_{rad}} + \frac{1}{Q_{sw}} + \frac{1}{Q_{di}} + \frac{1}{Q_c} \tag{2}$$

Where Q_{sw} is surface waves related quality factor component, $Q_{di}=1/\tan(\delta)$ – dielectric losses quality factor component, Q_c is the component associated with the Ohmic loses in the resistance of the metal plate and Q_r is radiation quality factor, defined as fraction of energy stored at resonance and the associated power loss [1]. These components have a different contribution to the total quality factor. The data presented on Fig. 1 makes it clear that the radiation quality factor Q_{rad} has the most important role.

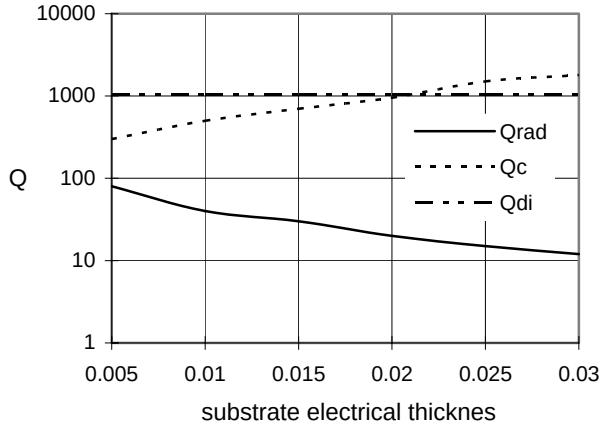

Fig. 1. Variation of Q_{rad}, Q_c and Q_{di} versus relative substrate thickness (h/λ), after K. R. Carver, [2]

There is theoretical low limit of the Q_{rad} and it can be determined by Eq. 3:

$$Q_{rad} = \frac{1}{k^3 a^3} + \frac{2}{ka} \tag{3}$$

Where k is $2\pi/\lambda$ and **a** is the radius of a sphere enclosing the maximum dimension of the antenna. It has been calculated that typical value of that factor is between 0.5 and 100. The first value is for relatively electrical large antennas, and second value - for electrical small antennas (with dimensions smaller than $\lambda/2\pi$). These limits cannot be reached because of the resonant character of the radiating edges. Hence the typical values for the relative impedance bandwidth of the microstrip antenna are between 0.7 ÷ 1.5%, depending on dielectric permittivity

[1]Nicola I. Dodov is with the Faculty of Communication Technique and Technologies. TU-Sofia, 8 Kliment Ohridski Blv., 1000 Sofia, Bulgaria. E-mail: ndodov@tu-sofia.bg

[2]Peter Zh. Petkov is with the Faculty of Communication Technique and Technologies TU-Sofia, 8 Kliment Ohridski Blv., 1000 Sofia, Bulgaria. E-mail: pjpetkov@tu-sofia.bg

III. RESULTS

The analysis has been performed at frequency of 5.7 GHz, with electromagnetic simulator using the method of moments. It can be seen that there is an area where Q_{rad} has definite extreme value (Fig.2). At that area of dielectric permittivity the expected reduction in impedance bandwidth is about 20 to 500 times and the related BW values range between 0.01 and 0.001%. This sharp resonant character is extremely undesirable. It not only leads to reduction of the working bandwidth, but also to instability of the central frequency of the antenna, caused by the coefficient of thermal expansion of the substrate.

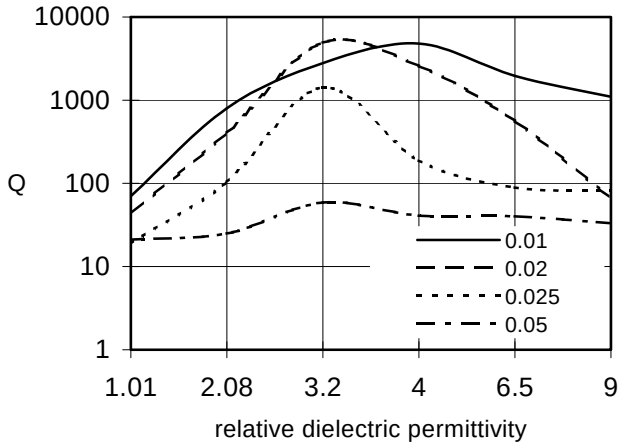

Fig. 2. Q_{rad} as function of ε_r for different substrate thicknesses (in h/λ).

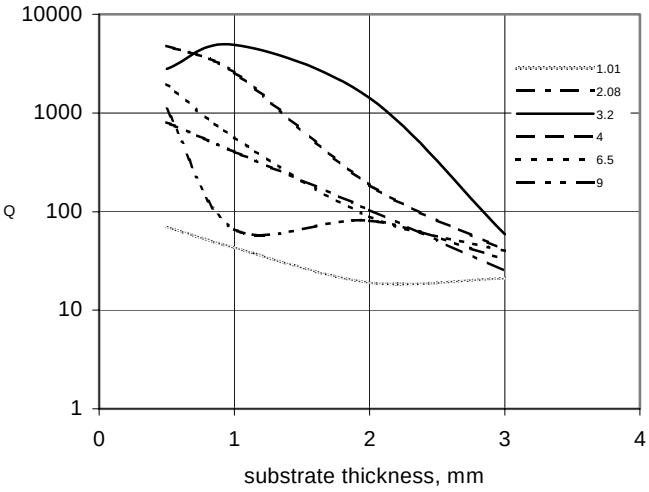

Fig. 3. Q_{rad} as function of substrate thickness (h) for different dielectric permittivity

Since these extremes depend on the relative dielectric permittivity, but not on the substrate thickness - h (Fig. 3), it can be concluded that in rectangular microstrip antenna there are types of substrate that should be avoided. Undesirable areas exist in all types of substrates (in terms of thickness) and should be carefully defined and avoided. Similar results are achieved with circular patches. Another effect that limits the choice of substrate is the lost of radiation efficiency. On Fig 4 we can see that in substrates with dielectric permittivity above 2 there is significant lost of efficiency. On the other hand, additional loss of efficiency can be expected in cases of substrates with higher thickness and permittivity because of excitation of the surface waves.

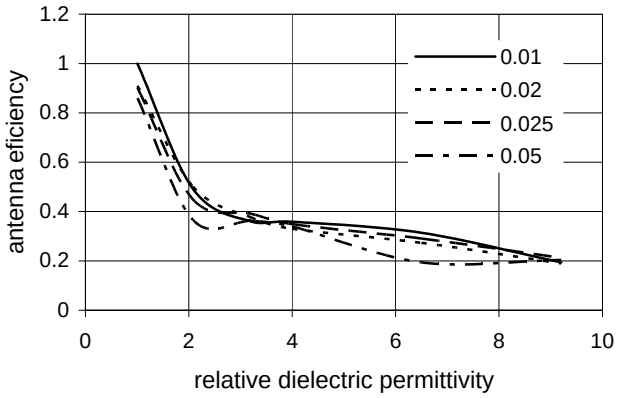

Fig. 4. Radiation efficiency as function of dielectric permittivity for different substrate thicknesses (in h/λ).

That effect is very well examined and explained in previous publications and also by other authors [3], [4]. A recommended method of suppression of the surface waves is the use of PBG (Photonic Bandgap Structures). Yet another unwanted effect of broadbanding achieved by increased substrate thickness is the complex impedance of the feeding probe that makes the matching complicated and narrowband. In conclusion, as a general rule of thumb in cases when precise analysis cannot be performed, we recommend substrates with permittivity below 2. The choice of substrate thickness should be made taking into account the degree of complexity of the feeding system.

IV. CONCLUSION

This paper examines the problems of broad banding in printed microstrip antennas. The study defines empirically an area of undesirable substrate dielectric permittivity and thicknesses. In this area energy stored in the resonating element is much higher than radiated; hence this area should be avoided. It also emphasizes the theoretical limit in broadband abilities which is determined by the physical size of the radiating element and it resonant abilities. Increasing further the frequency band over these limits is possible through changing the shape of the radiating element (fractalization) or by using parasitic elements.

REFERENCES:

[1] R. Garg, P. Bhartia, I. Bahl and A. Ittipiboon, "Microstrip design antenna handbook". Norwood MA, Artec House, 2001

[2] K. R. Carver and J. W. Mink, "Microstrip antenna technology", IEEE Transactions on Antennas and Propagation, Vol. 29, No. 1, pp. 2-24, January 1981

[3] N. I . Dodov and P. Zh. Petkov, "Surface wave's impact on mutual coupling in microstrip antennas", ICEST 2002 Conference, Nis, Serbia and Montenegro, Oct. 2002

[4] D. Pozar, "Input impedance and mutual coupling of rectangular microstrip antennas", IEEE Trans. Antennas Propagat., vol. A-P 30, pp. 1191-1196, Nov. 1982

Suppressing Mutual Coupling of Microstrip Antenna with Photonic Band-Gap Substrate

Nikolay Mitrev Stoyanov

Abstract – **In this paper is made a simulative investigation of suppressing mutual coupling of microstrip antenna array with photonic band-gap substrate (PBG). PBG substrate to minimize surface wave effects is analyzed for a high ε_r of the substrate. Conventional PBG with drilled dielectric substrate and 2-D PBG microstrip antennas are compared. The received results can be used of design of microstrip antennas with low mutual coupling between the elements.**

Keywords – **Microstrip antennas, mutual coupling, surface wave, Photonic band-gap structures**.

I. INTRODUCTION

Surface wave propagation in dielectric substrates often negatively affects the performances of microwave and millimeter wave circuits. For instance, it may reduce the efficiency of planar antennas on high dielectric constant substrates or may produce unwanted coupling between different parts of circuits. It is difficult to evaluate this latter effect in the design stage since it can be accurately assessed only using computational intensive full-wave: numerical techniques to analyze the whole circuit[1].

Suppression of unwanted surface waves and control of their propagation is desirable not only to improve circuits performances. It can also lead to realization of antenna arrays structures, particularly use at millimeter wave frequencies where metallic losses in microstrips or coplanar waveguide become significant.

The surface waves excited in the process of radiation of these antennas are radiated more efficiently into the structure than the air side. This due to the fact of the substrate dielectric constant to be greater than the unit. Thus, the substrate works as a storage device of propagating modes on the ground plane of the antenna. If the interface between two media is perfectly plane, these waves will not contribute to the radiation process. However, the antenna edges, in this case, diffract or scatter the waves that reach there, giving origin to end-fire lobules.

Further more, if a system is formed by multiple antennas (array), all sharing the same substrate and ground plane, the currents that will come up, due to the conducting properties of the ground plane, may cause coupling of fields, which reduce even more the efficiency of the antenna.

Nikolay M. Stoyanov is with the Faculty of Communications and Communications Technologies, Technical University of Sofia, 8, Kliment Ohridski St. Sofia-1000, Bulgaria
E-mail: n_m_stoyanov@abv.bg

II. DESIGN OF PHOTONIC BAND GAP SUBSTRATE

Two different kinds of periodically loaded, grounded dielectric slabs have been investigated. The first kind is realized by drilling holes in the dielectric, while the second is with 2-D PBG structure with metal lattice.

The values of dielectric constant and thickness of grounded slabs used as substrates for microwave and millimeter waves circuits is such that only the fundamental TM_0 surface wave mode can propagate in the substrates when excited by discontinuities, or by planar antennas. Then, this is the mode that the designer may want to be able to forbid, without allowing propagation for the other modes at the same time. If we assume that f_0 is the center frequency of the desired stop-band so TM_0 can be suppressed by using triangular (fig.1 a) or square lattice of hole (fig. 1 b).

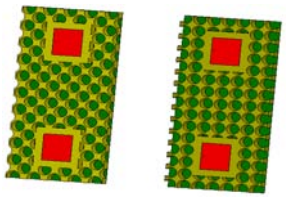

a b

Fig.1. Triangular lattice of holes 1a) and square lattice of holes 1b) in a grounded dielectric slab. The ground plane is not pierced;

The triangular lattice is chosen because it has proved capable, in the simpler case of a two-dimensional photonic crystal, of providing a stop-band for any in-plane direction of propagation due to the high symmetry of the Brillouin Zone (BZ) associated to it [2]. This latter is the hexagon shown in Fig. 2. The band-gap in the dispersion curves will show up at the edges of the BZ. We can focus our attention on the two directions of propagation corresponding to the edges ΓK and ΓM of the BZ. The gaps should appear at the vertexes M and K. Frequency values corresponding to a propagation vector pat points M or K are generally unknown for the actual periodic structure. In the case of small perturbations, i.e. for small values of the *R/a* ratio, they can be estimated using the propagation constant in the unperturbed structure.

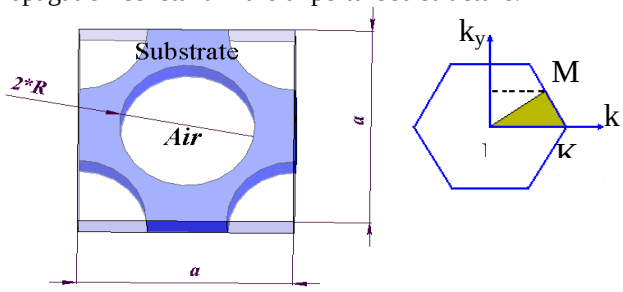

Fig. 2. Irreducible Brillouin zone in the ***k*** vector for triangular

Assessing the width of the band-gap is a more difficult task. However, the general trend is that the stronger the perturbation, the wider the band-gap. Thus, high values of the ratio are needed to realize substrates featuring a complete stop-band.

Another type structure is the 2-D PBG which will be analyzed (fig.3). It consists of four parts: a ground plane, a dielectric substrate, metallic patches, and connecting vias. This EBG structure exhibits a distinct stop-band for surface-wave propagation [3].

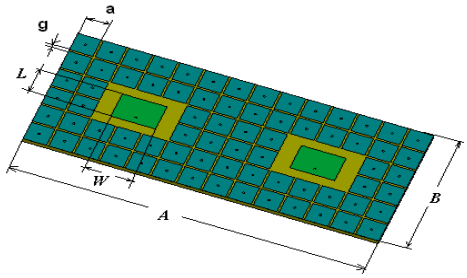

Fig.3 Two Elements microstrip antenna with 2-D PBG substrate

The operation mechanism of this EBG structure can be explained by an LC filter array: the inductor results from the current flowing through the vias, and the capacitor due to the gap effect between the adjacent patches. For an EBG structure with patch width, gap width, substrate thickness and dielectric constant, the values of the inductor and the capacitor are determined by the following formula [4]:

$$L = \mu_0 h \tag{1}$$

$$C = \frac{a(\varepsilon_1 + \varepsilon_2)}{\pi}.\cosh^{-1}\left(\frac{l}{g}\right) \tag{2}$$

$$\omega = \frac{1}{\sqrt{LC}} \tag{3}$$

where h is the high of the dielectric substrate, ε_1 and ε_2 relative dielectric permittivity of the air and substrate respectively, l is constant of lattice, g is the gap between patches of lattice and ω is the angular frequency.

III. Results

Two type antennas were designed one with PBG triangular lattice of holes (fig. 1a) and second planar PBG with 2-D metal rectangular lattice respectively (fig. 3). These antennas were optimized to suppress TM_0 mode of surface waves. The received results are compared with the classical microstrip antenna which is built on the same dielectric substrate.

The parameters of antenna with PBG triangular lattice of holes (fig. 1a) are the next: relative dielectric permittivity $\varepsilon_r = 10,2$; the normalize angular frequency $\omega_{norm} = a/\lambda = 0,23$; *h*igh of the dielectric substrate $h = 0,2a$; *r*adius of the hole $R = 0,28a$;

The parameters of second structure (2-D metal lattice of patches, fig.3) are: width of patches $a = 3,26mm$; high of substrate $h = 1mm$; the gap between patches $g = 0,54mm$, $\varepsilon_r = 10,2$.

The microstrip resonators are placed in H-plane with distance between them $\lambda_0/2$.

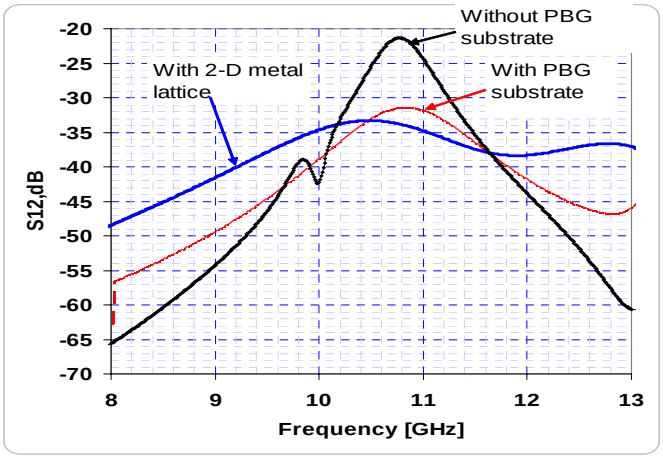

Fig.4. S-parameters of the tree microstrip antennas: the classical structure and antenna with triangular lattice of holes and with 2-D rectangular metal lattice

The mutual coupling results are shown in Fig. 4. Without the PBG structure, the antennas show a strong mutual coupling of 21 dB. If the PBG (EBG) structures are employed, the mutual coupling level changes. By using two kinds structure can by reached reducing of mutual coupling between the elements compared to the conventional antenna with above 10dB.

IV. Conclusion

In this paper, two type PBG structures are implemented in the design of microstrip antenna arrays to reduce the strong mutual coupling caused by the high permittivity substrate without sacrificing the compact size or bandwidth of the antenna elements. The PBG structures are analyzed using the FEM method. The strongest mutual coupling happens in the E-plane coupled antennas with high permittivity substrate due to the pronounced surface waves.

The PBG structure is then inserted around the antenna elements to reduce the mutual coupling. This mutual coupling reduction technique can be used in various antenna array applications.

References

[1]. H. Fernando, A. Roche, “Analysis of antennas wit PBG substrate”, IEEE proceeding, MTT-IMOC 2003.

[2]. H. Rong, Z. Xuexia,“A novel 2-D PBG structure and its application in monopoles”, 3rd International Conference on Microwave and Millimeter Wave Technology, Proceeding 2002

[3]. D. Debasis,Y. Ohashi,”A novel Electromagnetic Band Gap Metal Plate for Parallel Plate Mode Suppression in Shielded Structure,” IEEE Microwave and Wireless Component Letters, vol. 12, No. 5, May 2002

[4]. D. F. Sievenpiper, “High-impedance electromagnetic surfaces,” Ph.D. dissertation, UCLA, 1999.

Modelling of Microstrip Antennas using TLM Method

Tijana Ranđelović, Mila Stojanović, Vera Marković

Abstract - **In this paper, several patch antenna configurations are analyzed by using 3D TLM software in order to investigate possibilities of TLM method for modeling complex structure patch antennas with excitation in the form of wire conductor loaded in the substrate. Good agreement has been achieved between results obtained by using TLM method and those obtained by using the other numerical approaches, which indicates good modeling of antennas using TLM method.**

Keywords - **TLM method, TLM wire node, slotted patch antenna, H-shaped antenna, circular microstrip antenna**

I. Introduction

Microstrip and printed circuit antennas have gained prominence over the past two decades as viable and desirable antenna elements and arrays. The interest in these antennas stems directly from advantages such as low profile, low cost, light weight, conformity to surface, mass production, dual-frequency operation possibilities and direct integrability with microwave circuitry. There are some limitations, however, principally in characteristics such as low gain and narrow bandwidth.

Patch antennas have recently received much attention for application in mobile communication systems since they can provide advantages over traditional whip and helix antennas in terms of high efficiency, low EM coupling to the human head, and increased mechanical reliability. In many applications, the requirements on both bandwidth and physical size are quite stringent, [1].

TLM (Transmission Line Modelling) method is a general, electromagnetic based numerical method that has been applied successfully to the wide range of problems. For example, it has been applied to the modelling of metallic cavities [2]. By using a real feed probe for establishing desired field distribution in the modeled cavity the deficiencies of impulse excitation could be avoided. With some recent improvements in TLM method, it is possible to model a probe inside the cavity using TLM wire node [3] and to investigate the influence of the real excitation to the resonant frequencies and field distributions in the cavity [4, 5].

TLM method has been also successfully applied to the modeling of planar electromagnetic structures. For instance, it has been used for the analysis of a simple rectangular patch antenna [6] and of a U-shaped patch antenna [7].

Tijana Ranđelović, Mila Stojanović and Vera Marković are with the Faculty of Electronic Engineering, Aleksandra Medvedeva 14, 18000 Nis, Serbia and Montenegro, E-mail: [tijana, milas, vera] @elfak.ni.ac.yu

The goal of this paper is to investigate the possibilities and effectiveness of TLM method for modelling of up-to-date microstrip antennas with complex geometries that have significant application in modern wireless communication systems. Using TLM wire node it is possible to model coaxial feed and include the influence of the real excitation in the antenna model.

II. Modelling Procedure

In TLM method, a 3D electromagnetic (EM) field distribution in a microwave structure is modelled by filling the space with a network of transmission lines and exciting a particular field component in the mesh by voltage source placed on the excitation probe. EM properties of a medium in the patch antenna are modelled by using a network of interconnected nodes. A typical node structure is the symmetrical condensed node (SCN), which is shown in Fig. 1. To operate at a higher time-step, a hybrid symmetrical condensed node (HSCN) [8] is used. An efficient computational algorithm of scattering properties, based on enforcing continuity of the electric and magnetic fields and conservation of charge and magnetic flux [9], is implemented to speed up the simulation process.

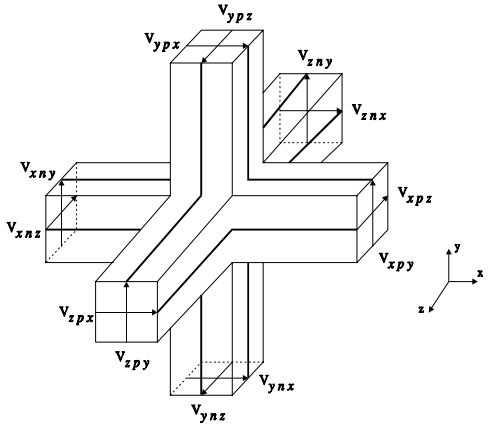

Fig. 1. Symmetrical condensed node

For accurate modelling of this problem, a finer mesh within the substrate and cells with arbitrary aspect ratio suitable for modelling of particular geometrical features are applied.

In TLM wire node, wire structures are considered as new elements that increase the capacitance and inductance of the medium in which they are placed. Thus, an appropriate wire network needs to be interposed over the existing TLM network to model the required deficit of electromagnetic parameters of the medium. In order to achieve consistency with the rest of the TLM model, it is most suitable to form wire networks by using TLM link and stub lines (Fig. 2) with characteristic impedances, denoted as Z_{wy} and Z_{wsy}, respectively.

An interface between the wire network and the rest of TLM network must be devised to simulate coupling between the electromagnetic field and the wire.

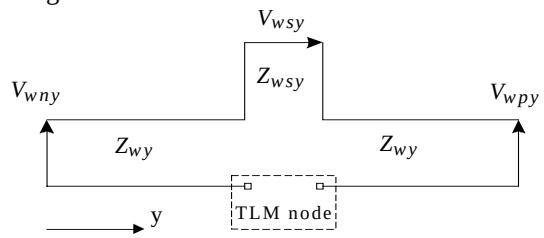

Fig. 2. Wire network

In order to model wire junction and bends, wire network segments pass through the centre of the TLM node. In that case, coupling between the field and wire coincides with the scattering event in the node which makes the scattering matrix calculation, for the nodes containing a segment of wire network, more complex. Because of that, an approach proposed in [10], which solves interfacing between arbitrary complex wire network and arbitrary complex TLM nodes without a modification of the scattering procedure, is applied to the modelling of planar antennas.

III. Numerical Analysis

Different patch antenna configurations are analyzed using 3D TLM software in order to investigate possibilities of TLM method for modelling complex patch antennas with excitation in the form of wire conductor loaded in the substrate.

A. Slotted Patch Antenna

A slotted patch antenna with the possibility to control the input impedance (Fig. 3) is considered first.

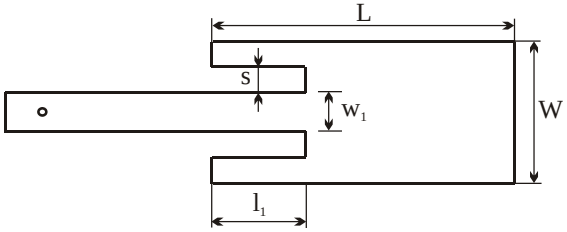

Fig. 3. Slotted patch antenna

Three configurations presented in [11], which have been designed for frequencies 13, 26 and 38GHz, whose dimensions are given in Table 1, are examined.

TABLE I
Dimensions of the Patch Antennas

f [GHz]	W [mm]	L [mm]	w_1 [mm]	l_1 [mm]	s [mm]
13	9.2	7.55	0.5	0.8	0.3
26	4.6	3.6	0.5	0.8	0.4
38	3.1	2.45	0.3	0.825	0.2

The antennas are built on substrate with following characteristics: relative dielectric constant ε_r = 2.17, thickness h = 0.508 mm, conductor thickness T = 0.017 mm and loss tangent of dielectric $tan\ \delta$ = 0.002.

The results for the return losses of these antennas obtained by using 3D TLM method are shown in Fig. 4. A real feed probe loaded in the substrate with radius of 0.05 mm is used as an excitation for all cases.

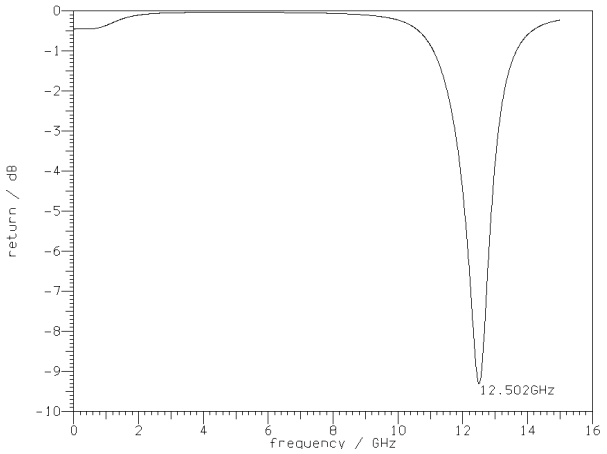

a)

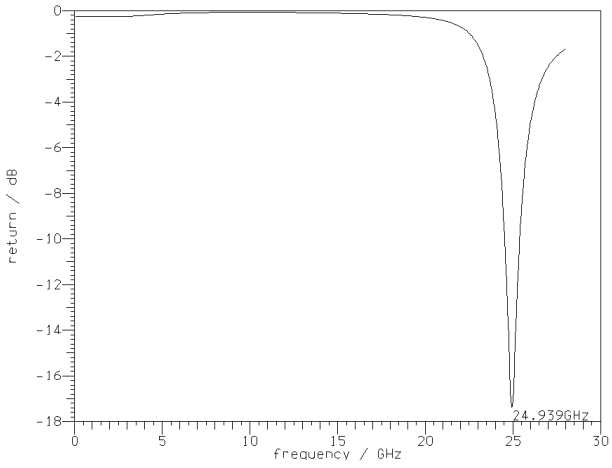

b)

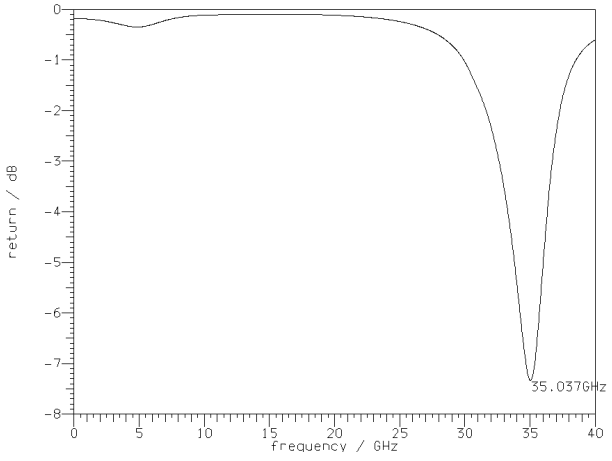

c)

Fig. 4. Results of patch antenna analysis by using TLM for a) 13 GHz, b) 26 GHz, c) 38 GHz

As it can be seen from Fig. 4 resonance frequencies are slightly below the expected ones. This may be caused by the problem of the accurate edge-effects modelling appearing because of slots. The values of resonant frequencies that are somewhat closer to the nominal values can be obtained by using a mesh with smaller TLM nodes, but it increases time of simulation in return.

B. H - Shaped Antennas

Short-circuited H-shaped antennas are very suitable for MMIC active antenna applications because they take only a fraction of the substrate area of conventional patch antennas and have a convenient shape enabling the active circuits to be integrated within the antenna, taking no additional substrate area. In this section, a quarter wavelength H-shaped antenna at 5 GHz [12] is examined by using 3-D TLM method. In that example, the substrate is a glass loaded PTFE substrate with the relative dielectric constant ε_r of 2.2 and with the thickness of 0.508 mm. The length L and the width W of the antenna are 9.5 mm and 11 mm, respectively. The lengths L_1 and L_2 have been chosen to be 2.5 and 2.9 mm, respectively. Ten shorting pins of 0.1 mm thickness are used for making the short to the ground. The substrate and the ground plane size is 50 mm x 50 mm. The antenna layout is presented in Fig. 5.

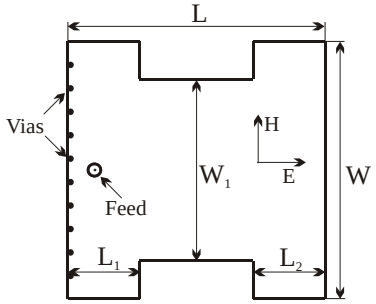

Fig. 5. The layout diagram of short circuit *H*-shaped antenna

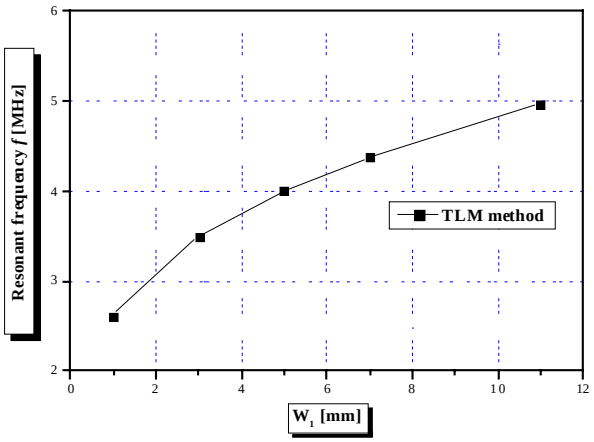

Fig. 6. The resonant frequency of a H-shaped antenna for different values of W_1 (L = 9.5 mm, W = 11 mm, L_1 = 2.5 mm, L_2 = 2.9 mm, substrate ε_r = 2.2 and thickness = 0.508 mm)

The effect of varying the middle width (W_1) on the resonance frequency is investigated by using the above discussed TLM procedure that includes the wire node application. Five antennas with middle width (W_1) of 1, 3, 5, 7 and 11 mm are considered. In all cases, the feed position is chosen to be 0.8 mm from the shorted end.

The results show that the width W_1 has a significant effect on the resonant frequency of the antenna. In Fig. 6, the resonant frequency of the *H*-shaped antenna versus W_1 is presented. It can be seen that the resonant frequency of the antenna reduces by more than 40% when the width W_1 is reduced to 1 mm.

It should be pointed that very good agreement has been achieved between results for the short-circuited H-shaped antennas obtained by using TLM method and those obtained by a FDTD software as well as a commercial HP Momentum electromagnetic simulator [12].

C. Circular Microstrip Antenna

Accurate prediction of input impedance of a coax-fed circular patch antenna is very important for the attempts to improve the antenna performance. In this section, an example of the application of the TLM method to the analysis of circular microstrip antennas is presented. It is investigated how feed position influences resonant frequencies of an circular-shaped antenna built on substrate with relative dielectric constant ε_r = 2.32, loss tangent $tan\ \delta$ = 0.001 and with the thickness h = 1.59 mm (Fig. 7). The radius of the circular patch is a = 50 mm. As an excitation, wire conductor loaded in the substrate with diameter d_0 = 1.27 mm is used. The example of antenna is taken from [13].

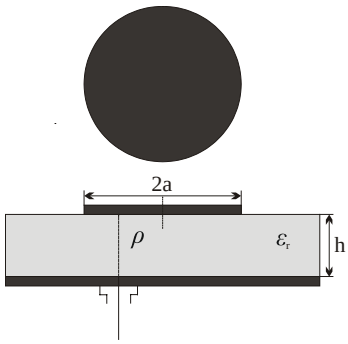

Fig. 7. Coax-fed circular microstrip antenna

TLM analysis has been done for five different feed positions. Normalized feed locations are ρ/a = {0.2, 0.4, 0.6, 0.8, 0.95}. In Fig. 8 the resonant frequencies for two cases, ρ/a = 0.2 and ρ/a = 0.95, are shown. It can be seen that the resonant frequency changed not significantly when the feed location is varied.

On the other hand, the analysis shows that the influence of the feed location to the reflection characteristics is much more expressed. In Fig. 9 is given the variation of parameter S_{11} of the considered coax-fed circular microstrip antenna as a function of normalized feed position ρ/a.

IV. Conclusion

In this paper, several patch antenna configurations are analyzed by using 3D TLM approach. It has been shown that the application of the TLM method including the wire node is

very convenient for modelling complex patch antennas with an excitation in the form of wire conductor loaded in the substrate. Three different examples of patch antennas are examined: slotted patch antenna, H-shaped patch antenna and circular microstrip antenna. Good agreement has been achieved between results obtained by using TLM method and those obtained by using the other numerical approaches.

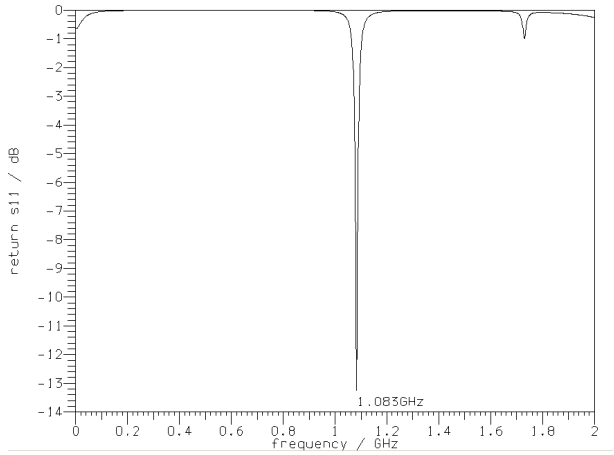

a)

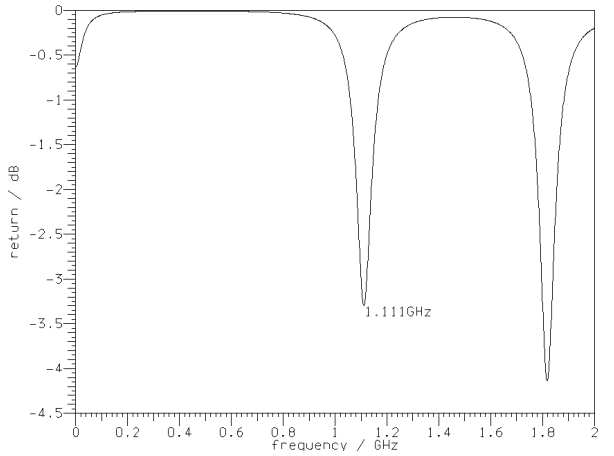

b)

Fig. 8. Resonant frequencies of circular patch antennas for a) ρ/a = 0.2, b) ρ/a = 0.95

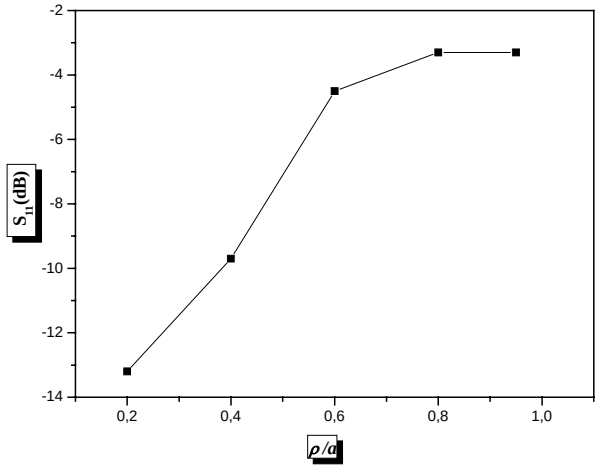

Fig. 9. S_{11} versus normalized feed-location ρ/a

REFERENCES

[1] P. Bhartia, K.V.S. Rao, R.S. Tomar, "Millimeter-Wave Microstrip and Printed Circuit Antennas", *Artech House*, Inc, 1991

[2] N. Dončov, "Microwave structures analysis using 3-D TLM method", *M.Sc thesis*, *Faculty of Electronic Engineering*, *University of Niš*, 1999

[3] V.Trenkić, A.J.Wlodarczyk and R.A.Scaramuzza, "Modelling of Coupling between Transient Electromagnetic Field and Complex Wire Structures," *International Journal of Numerical Modelling: Electronic Networks*, Devices and Fields, Vol.12, No.4, pp.257-273, 1999

[4] B. Milovanović, N. Dončov and J. Joković, "Real Excitation Modeling in a Loaded Cylindrical Metallic Cavity Using 3-D TLM Method," *Proceedings of the 5th IEEE TELSIKS 2001 Conference*, Niš, Yugoslavia, pp. 213-216, 2001

[5] B. Milovanović, A. Marinčić, J. Joković, A. Atanasković and A. Mitić, "Real Excitation Modeling in Cylindrical Metallic Cavity with Circular Cross-section Using 3-D TLM Method," *Proceedings of the XXXVII ICEST 2002 Conference*, Niš, Yugoslavia, pp. 217-220, October 2002.

[6] J. Joković, "Modeling and Analysis of the Patch Antenna by Using 3D-TLM Method" (in Serbian), *Proceeding of the XLVII ETRAN Conference*, H. Novi, Serbia & Montenegro, pp. 289-292, June 2003.

[7] J. Jokovic, T. Randjelovic, "Modeling of U-shaped dual band patch antenna using 3D TLM method", *Proceedings of the 6th International Conference TELSIKS 2003.*, pp. 60-63, Oct. 2003.

[8] C. Christopoulos, "The Transmission-Line Modelling Method", *IEE/OUP Press*, 1995.

[9] V. Trenkić, "The Development and Characterization of Advanced Nodes for TLM Method" *Ph.D. Thesis*, University of Nottingham, 1995.

[10] V. Trenkić, C. Christopoulos, "An Efficient Implementation of Wire Nodes in TLM", *Proceedings of the 2nd International Workshop on TLM Modelling-Theory and Applications*, Munich, Germany, pp.60-67, 1997.

[11] D. Radulović, A. Nesic, "Impedance of Patch Antenna for Active Antenna's Structures", *Proc. XLVIII ETRAN Conference*, Čačak, June 6-10, 2004, Vol. II, pp: 286-289

[12] D. Singh, C. Kalialakis, P. Gardner, P. S. Hall, "Small H-Shaped Antennas for MMIC Applications", *IEEE Transactions on Antennas and Propagation*, Vol.48, No. 7, pp: 1134-1141, jul 2000.

[13] Siddiqui, J.Y.; Guha, D., "Improved formulas for the input impedance of probe-fed circular microstrip antenna", *Antennas and Propagation Society International Symposium*, 2003. IEEE, Volume: 3 , 22-27 June 2003, pp:152 - 155 vol.3

Television Antenna Curtain

Dimitor Dimitrov[1], Alexander Bekiarski[2]

Abstract: **In the article are observed technology of construction, production and measurement of full-length television antenna curtain with one basic aim – to achieve the necessary exploitation parameters. The production is ensured by Bulgarian joint-free steel pipes. Construction method is precise and is achieving high technological sustainability and reproduction in log life cycle of exploitation. By these television curtains are equipped television retranslators (relays) and transmitters. Foreseen is exploitation of antenna systems in conditions of dissemination of ground digital television (DVB-T).**

Key words: **antenna, gain, curtain, broadcasting, wavelength, VHF-band, voltage standing – wave radio – VSWR, methodology.**

The calculation methods are optimized step by step [1, 2] in conformity with the requirements of the ISO 9000 standard and restrictive conditions are formulated [3, 4, 5, 6] from the shot diagram of direction (Fig 1) during the building of complex antenna systems (Fig 2) aiming at their exploitation and in regard to the inculcation of the ground digital television dissemination.

The developed construction and technologies of production are realized experimentally accompanied by detailed measurements and comparison with similar transmitting antennas [7].

The sequence of the calculating operations is related to the average length of the wave λ_{AV} for III VHF – Very High Frequency (170 to 230 MHz) and is related to asymmetric supply of antenna curtains through concerted transformer Tp1 (Fig 3).

The letters given for geometric dimensions are responding to the construction of Fig 4.

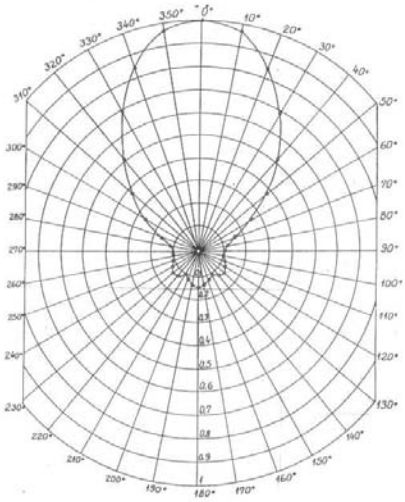

Fig. 1

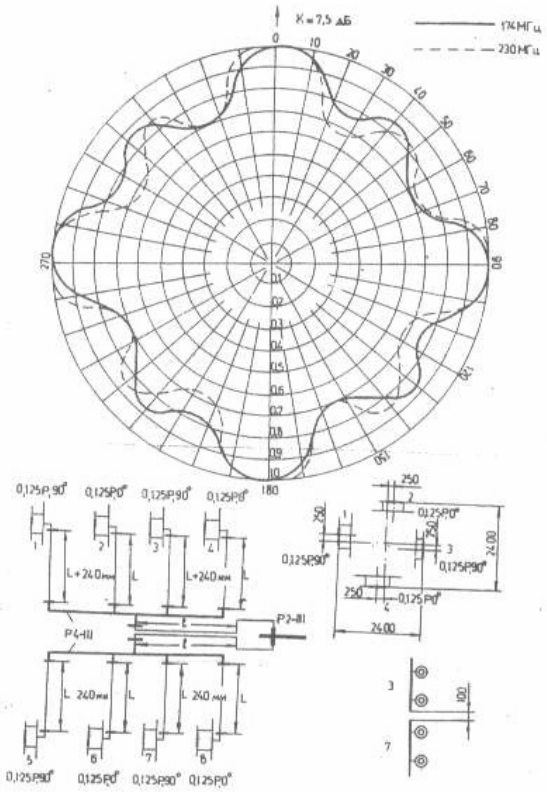

Fig. 2

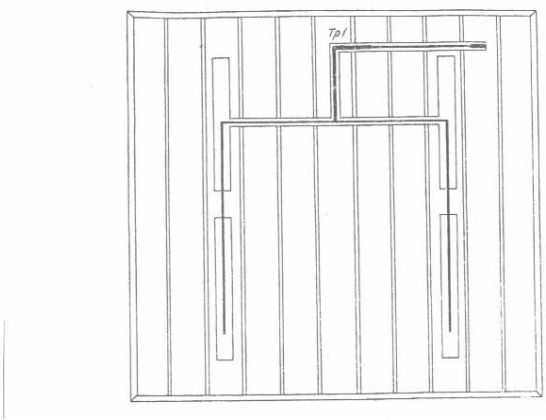

Fig. 3

[1] Dimitar I. Dimitrov, Ph. D., is with the Faculty of Communication Technology, Technical University – Sofia, Kliment Ohridski 8, 1000 Sofia, Bulgaria, e-mail: ddim@tu-sofia.bg

[2] Aleksander B. Bekiarski, Ph. D. is with the Faculty of Communication Technology, Technical University – Sofia, Kliment Ohridski 8, 1000 Sofia, Bulgaria, e-mail: aabbr@tu-sofia.bg

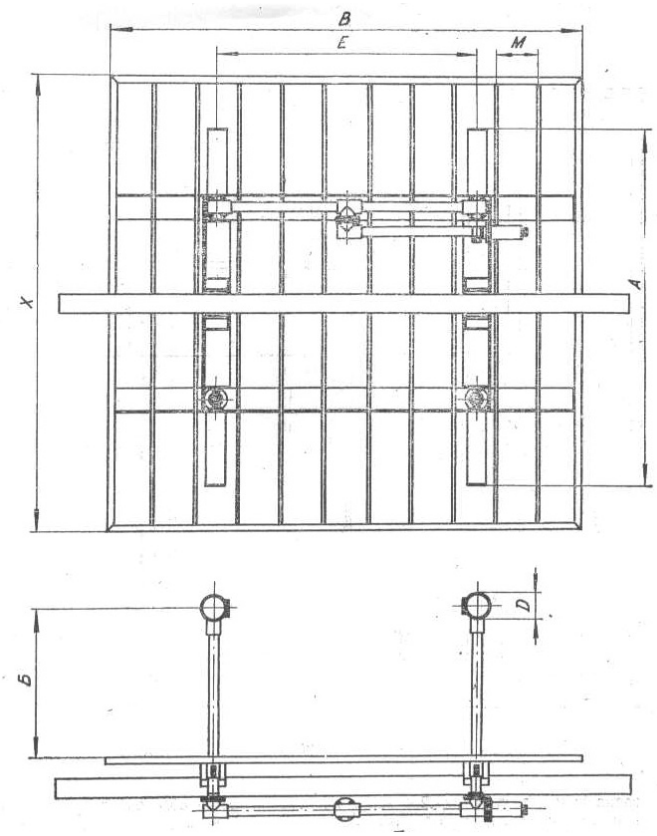

Fig 4

Rest (fulcrum) wave length for III VHF is determined:

$$\lambda_{AV} = 1480 \text{ mm} \quad (1)$$

the length of the two mutually dependant dipoles in antenna curtain is determined by:

$$A = K_C \cdot \lambda_{AV} \quad (2)$$

Where K_C is general coefficient of curtail (shortening), that reports the influence of the diameter D of the joint-free steel pipe, i. e.

$$D = 0{,}04\ \lambda_{AV} \quad (3)$$

A standard size is calculated D = 60/3 mm.
One-direction emission with great coefficient face/back (Fig 1) is ensured by the distance B dipol-reflector grid (Fig 4) depending on the optimal coefficient of the standing wave (VSWR), i. e.:

$$B_{opt} = \varphi\ (VSWR) \quad (4)$$

The coefficient of the standing wave VSWR is defined by the expression:

$$VSWR = \frac{U_i + U_r}{U_i - U_r} = \frac{U_{max}}{U_{min}} = \frac{1+r}{1-r} = \frac{1+r}{t} \quad (5)$$

Where U_i is the straight wave voltage, U_r is the reflected wave voltage, $r = U_r/U_i$ is coefficient of reflection when the coefficient of the transmission of the efficient signal $t = 1 - r$.
Experimental subjection of the distance B:

$$B = (0{,}26 \div 0{,}3)\ \lambda_{AV} \quad (6)$$

The results of the experiments are given in Table 1

TABLE 1

B[mm]	400		430		460		700		730	
f[MHz]	r	VSWR	r	VSWR	r	VSWR	r	VSWR	r	VSWR
175	0,09	1,21	0,06	1,14	0,06	1,14	0,04	1,08	0,03	1,06
180	0,06	1,14	0,05	1,12	0,05	1,12	0,04	1,08	0,04	1,07
190	0,04	1,09	0,03	1,06	0,02	1,04	0,03	1,06	0,02	1,04
200	0,05	1,11	0,03	1,06	0,02	1,04	0,03	1,06	0,03	1,06
220	0,03	1,06	0,02	1,04	0,01	1,02	0,02	1,04	0,01	1,03
230	0,01	1,03	0,02	1,04	0,02	1,04	0,02	1,04	0,01	1,03

The distance E between the two full length dipoles, forming the system of dipole antenna curtain, influences the coefficient of gain $D_{H,V}$ expressed visually on the horizontal vertical diagram of direction, i. e.:

$$D_{H,V} = \varphi\ (E) \quad (7)$$

From the experimental research we have received the following expression:

$$E = (0{,}5 \div 0{,}65)\ \lambda_{AV} \quad (8)$$

In this case the B size is:

$$B = (1{,}8 \div 2)\ E \quad (9)$$

And for the X the following expression is valid:

$$X(1{,}2 \div 1{,}45)\ A \quad (10)$$

To ensure effectiveness of the reflector grid, i. e. minimal back of the diagram of direction (Fig 1) joint-free steel pipes with standard diameter 10/3 mm are fixed (put) on the distance M (Fig 4) and following the experimental research is received this expression:

$$M = (0{,}1 \div 0{,}08)\ \lambda_{AV} \quad (11)$$

In this case on the face of the diagram of direction gain G > 10 dB is received.
Maximum admissible power reaches 1 kW.
The input resistance of the sequence transformer Tp1 (Fig 3), that ensures asymmetric power supply of the two full-length dipoles, is between 50/75 Ω.
The maximum wind loading reaches 255 kg/m^2 when the mass (weight) of the antenna is 65 kg and dimensions are 1450 x 1395 x 730 mm.
The quality control in production and diagnosis are realized in following conditions:
- noise coefficient N = 4 of the receiver;
- the coefficient of power gain in numbers is G = 4;
- the fulcrum tension of the electrical field is E_{AV} = 82 [μV/m];
- the minimum ratio signal/noise (S/N) for quality receiving of TV image in analog television is compared to the ratio carrying coefficient of the image/noise (C/N) for the quality image and in digital ground television [3, 4, 5], i. e.:

$$N/S = C/S = 20 \text{ dB} \quad (12)$$

These relations are controlled by the extract of 50 full-length antenna curtains taken from production on casual method. This ensures a possibility of big enough number of independent measurements of the chosen parameter for control – field tension E [μV/m];

The received variation order has the following scope (range):

$$R = E_{max} = E_{min} = 85 - 79 = 6\ [\mu V/m] \quad (13)$$

When grouping 50 measured field tensions in interval order this gives information for correlation subjection between technological sustainability and reproduction of the antenna.
In Table 2 in interval order are given measured values of field tension.

TABLE 2

E [μV/m]	$E_1 = E_{min}$ 79	E_2 80	E_3 81	$E_{AV} = E_4$ 82	E_5 83	E_6 84	$E_7 = E_{max}$ 85
Number of hits n_i	4	5	5	10	15	4	5
$\sum n_i = 50$							
Probability of hits in the interval $P_i = n_i/\sum n_i$	0,08	0,1	0,2	0,14	0,08	0,1	0,1
$\sum P_i = 1$							

The diversion of the nominal fulcrum value $E_{AV} = 82$ [μV/m] is under 5 %, where the nominal value is:

$$Emax = EAV + 3\ \% \quad (14)$$

And the minimal is:

$$Emin = EAV - 4\ \% \quad (15)$$

CONCLUSIONS

1. Developed is relevantly precise methodology for calculation, construction and production technology of full-length antenna curtain with control and quality diagnostic.
2. The analysis and quality control are developed using statistical method in group extract of 50 numbers for proving the technological sustainability and reproduction.
3. Measured are television antenna system from full-length antenna curtains for proving compatibility of dissemination of ground and digital television.
4. The researches show the possibilities for creation of methods and means for measuring quality of joint-free steel pipes.
5. The produced full-length antenna curtains have proved life over 30 years in non-stop regime of work.

REFERENCES

[1] Dimitrov D., Methods for calculation of dipole antenna "curtain" type for III television range (III VHF-band). Radio, Television, Electronics, No 9, 1971, pp. 262-264.

[2] Dimitrov D., Television transmitting antennas. Radio, Television, Electronics, No 2, 1972, pp. 17-18.

[3] Dimitrov D., V. Mitkov, Television- and video-technics. Rousse University "Angel Kanchev, Rousse, 2000, pp. 80-86.

[4] Dodov N., Antennas and UHF devices. Technica, Sofia, 1989, pp. 220-222.

[5] Konov K., Digital television. Dios, Sofia, 2004.

[6] Vassileva Ts., St. Popov. Bulgarian telecommunications company, methodology for the technical performances of the radio- and TV equipment and systems and the quality of the transmitted and emitted signals, Sofia, 1999.

[7] Rode and Shwarz and Katerin, Company's materials and models.

Session MS:

MEASUREMENT SYSTEMS

Device for Measuring The Level of Bulk Materials in Bunkers

Ventseslav D. Draganov[1] , Ilya T. Tanchev[2]

Abstract - **The problem for measuring the level of bulk materials in bunkers is solved by selecting the method at constriction and scheme decision, the capacities converter at allows detection of small changes of capacities, the high sensitivity and stability. This method enabled for calibration in two parts, one for manufacture and second for device exploiting.**

Keywords - **Level of bulk material.**

I. INTRODUCTION

A necessary condition for the automatic control of transport lines in glass production and their normal work is to ensure the control over the level of bulk material in silos and material mixture in bunkers.

The silos which provide the dozing line with material need signaling when the lowest (minimum) and highest (maximum) levels of material are reached and at the same time a command should come for a stop of unloading or loading.

To get the exact information for the level of material used in glass production (sand, soda, dolomite, feldschpad, limestone etc.), the primary converters of level into electrical signal, it is necessary for them:

- to function reliably in an environment of a lot of dust, noise and vibrations;
- to be in accordance with the peculiarities of the material: chemical activity, abrasives, hygroscopic capacity, humidity, .adhesion etc.
- to be located in immediate proximity to or inside the silos, within a wide temperature range from -15°C to +45°C;
- to be in accordance with the way the silos and bunkers are loaded with material and material mixture - from transport pipes loading the material in the middle of the silos i.e.the profile of the material is at its maximum in the center of the silo;
- to be in accordance with the shape of the silo and the material from which its walls and bottom were made.

The main problem in designing the device to control the minimum and maximum levels of material in silos to be used in glass production is the choice of method for measuring the level of the material as well as the concrete engineering design of a primary converter.

[1]Ventseslav D. Draganov is from the Faculty of Electronics at the Technical University - 1, Studentska Str., Varna, Bulgaria, E-mail address: itta@ms3.tu-varna.acad.bg

[2]Ilya T. Tanchev is with the Faculty of Electronics at the Technical University - 1, Studentska Str., Varna, Bulgaria, E-mail address: itta@ms3.tu-varna.acad.bg

II. EXPOSITION

A. Choice of a method to control the minimum and maximum levels of bulk material in silos for the needs of glass production

A large number of methods for measuring the level of bulk material in covered vessels are applied in practice. The instruments for measuring and control are rated in four groups - weight, hydrostatic, electromechanical and electrical.

The largest groups of devices, whose sensitive units function on the principle of converting certain qualities of the controlled environment into respective signals for the level, are the electrical level meters: resistance, capacitive, inductive, photoelectrical, thermal, acoustic, radar, laser radar, radioactive etc.

The great variety of methods and equipment for positional and uninterrupted control of the level of bulk material doesn't make the choice of just one of them for a particular application easier. Most of these methods have certain disadvantages, which make them inapplicable, and some of them can only have limited application - for instance only as positional ones and only for maximum or for minimum level at that.

With the choice of method it is necessary to take into consideration all the requirements concerning the concrete working conditions of the primary converters.

On the basis of the examination of all the devices for constant and positional control of the level of bulk material and after a large number of laboratory and factory experiments, the capacity method for positional control of the level has been chosen.

The chosen method has a wide range of advantages in comparison with the other methods in use - the simple and technological design providing great mechanical strength as well as the lack of movable parts which is a prerequisite for high reliability.

The main problem, which arises when capacity converters for level control are used, are the very small values of dialectical permeability ε of bulk material for glass production. The dialectical permeability ε is different for the different materials and it is very close to that of air. It depends on the temperature, the humidity and thickness of the materials. This dependence leads to the need to use a method and a scheme allowing for a stable control over the variation of very small capacities.

There are plenty of methods for measuring small capacities. The disadvantages of the existing methods are their comparatively low sensitivity and insufficient stability in registering the very small variations of capacity.

B. Choice of a concrete engineering solution

1. *Choice of a scheme solution*

The solution of the problem for registering very small variations of capacity, with high sensitivity and stability, is based on the possibility for the frequency of a crystal oscillator to change within a small range when the capacity of a capacitor is changed, and it (the capacitor) is connected in the chain of the crystal oscillator; at the same time the stability of the generated variations depend on the stability of the oscillator.

When this change in frequency of the generated variations is registered in a certain way, a possibility arises for registering very small variations of the capacity connected to the scheme.

Device [1], is offered for the control of the level of bulk material and material mixture in bunkers. It consists of 2 parts: converter block **1** and measuring - converter block **5.**

The scheme of the device is shown in Fig.1.

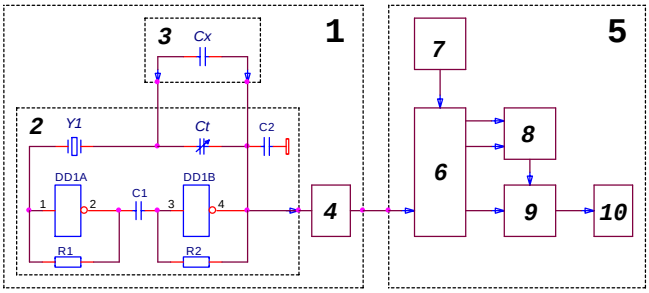

Fig.1. Device for the control of the level of bulk material

Converter block 1:

3 - primary converter "level-capacity";
the design is shown in [1],
in the scheme it is replaced with the capacitor C_X.
Parallel to the C_X capacitor the adjusting C_t is also connected.

2 - secondary capacitor "capacity - frequency", made according to the classical scheme of a crystal oscillator with logical elements;

4 - connecting block;

Measuring - converter block 5:

7 - second crystal oscillator;

6 - control block;

8 - comparing block;

9 - memory;

10 - indication block

The operation of the device is as follows.

When the capacity is connected in series with the crystal oscillator Y1 between the electrodes of the primary converter "level - capacity" Cx, the frequency of the series resonance of the crystal oscillator is changed to the following value:

$$f_S' = \frac{1}{2\pi.\sqrt{L_S.\frac{C_S.C_X}{C_S + C_X}}} \qquad (1)$$

where:

$\boldsymbol{C_S}$ - dynamic capacity from the equivalent replacing scheme of the crystal resonator;

$\boldsymbol{L_S}$ - dynamic induction of the equivalent replacing scheme of the crystal resonator.

When the level of the bulk material is changed between the electrodes of the measuring capacitor Cx the dialectical permeability ε of the environment between them is changed, and respectively - the capacity of the measured capacitor as well:

$$C_X = C_{X0} + \Delta C_X \qquad (2)$$

This leads to a frequency change in the crystal oscillation stabilizer **2**, which is registered by the comparing block **3**. Block **8** is a digital comparator. Its output signal is determined by the rate of the frequencies of the two generators - **2** and **7**. The output information is recorded in the memory **9** and is registered by the indication **10**. Blocks **8** and **9** are controlled by block **6** through the impulses coming from the second crystal oscillation stabilizer **7**.

The dependency of the frequency of the generated variations Eqs. (1) on the level of the bulk material between the electrodes of the primary converter, and respectively on its capacity, is non-linear:

$$f_S'' = \frac{1}{2\pi.\sqrt{L_S.\frac{C_S.(C_{X0} + \Delta C_X)}{C_S + C_{X0} + \Delta C_X}}} = f_S.\sqrt{1 + \frac{C_S}{C_{X0} + \Delta C_X}} \approx f_S.\left(1 + \frac{1}{2}.\frac{C_S}{C_{X0} + \Delta C_X}\right) \qquad (3)$$

The sensitivity is having maximum with materials that have very small dialectical permeability.

To ensure high technological qualities of the device during its operation, the trimmer capacitor C_t is connected parallel to the measuring capacitor Cx. It regulates the sensitivity of the scheme - for the different materials with different dialectical permeability **ε**.

To lessen the temperature instability of the generated variations it is necessary to select a suitable crystal resonator. Best results will be reached with the use of a crystal resonator with the so called "*AT - section*" [2], having frequency - temperature characteristic in the form of a cubic parabola. It is characterized with very low temperature instability ($\Delta f/f \leq \pm 15.10^{-6}$) within a wide temperature range (-60°C ÷ 100°C). With a selected, in the production of the crystal resonator, variation of the section angle, the temperature instability can be lessened additionally (to $\Delta f/f \leq \pm 5.10^{-6}$) within the temperature range (-30°C ÷ 60°C).

For an additional lessening of the temperature instability of the crystal generator traditional methods can be used: schemes for temperature compensation (for instance - connecting an additional capacitor with a selected temperature coefficient, parallel or in series to the primary converter "level - capacity" *Cx*; this role may be played by the trimmer capacitor *Ct*). Possibility used passive or active thermostat. Also this case complicated device and construction.

2. Choice of a construction for the primary converter "level - capacity"

Device [1] is offered for the control of the level of bulk material in silos and material mixture in bunkers. It uses a primary converter "level - capacity".

Its construction is shown in Fig.2.

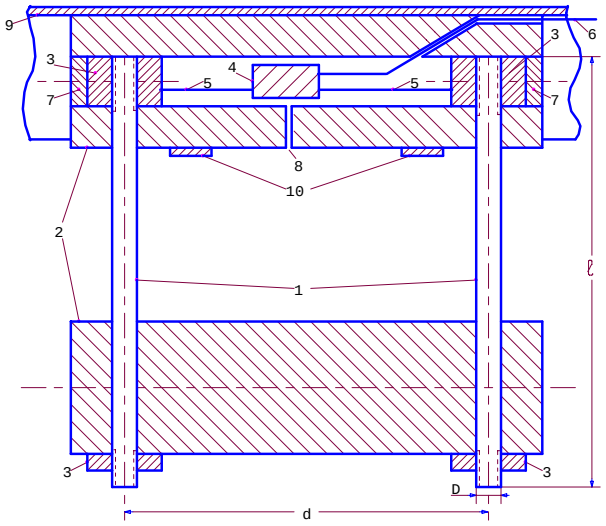

Fig.2. Construction of the primary converter "level-capacity"

The main part of the construction are the electrodes **1** of the measuring capacitor - two pieces of stainless steel pipes, joined in one construction with two insulating rods **2** made of textolite. The materials used in the construction elements as well as the construction itself meet the requirements for sufficient mechanical strength and resistance to the chemical and abrasive influence of the controlled bulk material.

The capacity of the thus constructed capacitor with cylindrical electrodes, with air used as dielectric, is determined with the following expression [2]:

$$C = \varepsilon_o . \varepsilon_в \frac{l}{4.\ln\frac{2.d}{D}} \text{ [F]}, \qquad (4)$$

where:

- $\varepsilon_o \approx 8{,}85.10^{-12}$ - the absolute dielectric permeability;
- $\varepsilon_в = 1{,}000594$ - relative dielectric permeability of the air;
- ℓ [m] - length of the electrodes;
- d [m] - distance between the electrodes;
- D [m] - diameter of the electrodes.

The distance between the electrodes is selected making a compromise between the concerns for sufficient mechanical strength of the construction and avoiding the adhesion of the material between them at high humidity or in case of eventual freezing? Electrode dimensions and distances between them are with the peculiar characteristics of any of the measured materials.

The fixing of the electrodes to the insulating rods is made with steel insertions ***3***, accommodated in the recess of the upper insulating rod ***2***. The insulating washers **7** protect the recess from permitting material and humidity.

The construction of the converter "level - capacity" is fixed with steel clamps **10** to the steel girder **9** with Π - shaped profile which is intended to ensure and protect the construction against mechanical attacks when filling the bunker. The steel girder is fixed to the walls of the bunker in a way providing the location of the constriction along its axis.

In the upper insulating rod there is one main opening along its axis, with the circuit board **4**, where the components of the secondary converter **2** are located. The metal electrodes **1** are connected through short conductors **5** to the circuit board **4**, thus providing a minimum mounted capacity. The output signal from the crystal oscillation stabilizer mounted onto the circuit board **4** is sent to the measuring - converter block **5** (from Fig.1) via coaxial cable **6** to the control block thus suppressing to a great extent the possible external interference.

The upper insulation rod has a second opening **8** for adjusting the secondary converter **2** during the device production as well as during its mounting in the silo.

Additional lowering of the temperature instability of the generated variations can also be done with a certain alteration of the device construction - when mounting the components of the second crystal oscillation stabilizer **7** onto the circuit board **4** together with components from the secondary converter "capacity - frequency" **2**. The use of two generators with components having the same parameters provides constant rate of the frequencies of both generators, with a change in temperature as well as under the influence of other destabilizing factors (for example, ageing of the components). However, this makes the construction more complicated to a certain extent as a second signal cable is needed.

III. Conclusion

The offered method and the scheme and construction of the device for controlling the minimum and maximum levels of bulk material in silos provide very high sensitivity and stability of the received results under the influence of destabilizing factors - temperature, ageing, interference etc. The device construction meets the requirements for sufficient mechanical strength and resistance to the abrasive and chemical influence of the controlled material.

The application of the offered method for measuring the level of bulk material is recommended above all for positional control, due to the non-linear dependency of the frequency of the generated signal on the level of the material.

The device can also be used for uninterrupted control, under limited conditions - connecting additional devices for linearization of the dependency of the generated signal frequency on the level of material, temperature stabilization or compensation of the instability of the generated signal etc. In this case the electrodes' length should be in accordance with the height of the silo.

The device has been introduced in the glass production of the Republic of Bulgaria and has its own patent licence [1].

References

[1] Draganov, V. e.t. "*Device of Level Measuring*"Author certificate № 45168 (МПК – С 01 Г 23/26) with priority since 08.01.1988, entered in the state rregister for applications for inventions ref. .№ 82569/1988г.

[2] Тихчев Х. Г. – "*Радиопредавателни устройства*" – "Техника", София, 1992

Magnetic Hysteresis Measurement Using Virtual Instrumentation

Boyanka M. Nikolova[1], George T. Nikolov[2], Marin B. Marinov[3]

Abstract – **In this paper the approach of improving a laboratory experiment of magnetic hysteresis measurement is presented. In order to achieve targets, the modern tools of software design and coding such as unified modeling language and graphical programming are implemented. The concepts of virtual instrumentation are applied to create laboratory workbench.**

Keywords – **Virtual Instrumentation, LabVIEW, Magnetic Hysteresis, UML.**

I. INTRODUCTION

One of the base magnetic features of ferromagnetic materials is its hysteresis loop. To identify the hysteresis parameters, it is necessary to measure these characteristics as great accuracy as possible. In magnetic materials, the relationship between *H* and *B* is usually nonlinear and is expressed graphically by the *BH* curve of the material. For a cyclic, input current waveform, a typical *BH* curve of a magnetic material can be observed.

Many laboratories still use old swept sine measurement systems consisting of separate standalone hardware linked together by set of cables. In a traditional hardware-based test system (see Figure 1) [1], a sine generator performs a continuous sweep through the amplitude range of interest. The investigated ferromagnetic material has toroidal shape because of the demagnetizing field. The examined material contains two coils. The *BH* curve can easily be obtained if the magnetic circuit is operated on alternating current. In the circuit, *H* is proportional to this current flowing in the winding, and B is proportional to the integral of the voltage (*v*) across the winding.

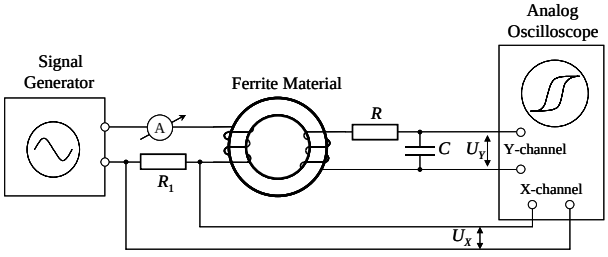

Figure 1 Traditional hysteresis measuring setup

The first coil is the excitation coil, which controlled by the signal generator. The second coil is used for measuring the effect of excitation; in this case the induced voltage of coil is measured. The amplitude of excitation current can be measured as a voltage of the R_1 resistance. The value of resistance R_1 is prescribed and constant independently the temperature and voltage. This resistor is kept small in comparison with the inductive reactance of the wound sample. Flux density of the cores is determined by integrating the secondary voltage using the *RC* circuit. The excitation (U_X) and induced (U_Y) voltages on the measuring coil can be observed by two-channel oscilloscope. The curves depicted in oscilloscope's tube are in scale to *BH* curve according to the following equations [1, 5]:

$$U_X(t) = R_1 \frac{l}{N_1} H(t), \tag{1}$$

$$U_Y(t) = \frac{1}{RC}\int_0^t v(t)dt = \frac{N_2 S}{RC} B(t), \tag{2}$$

where N_1 is the number of turns of the excitation coil, l - effective length of the magnetic core, N_2 - the number of turns of the second coil and S - the cross-sectional area of the magnetic core.

As disadvantages of this traditional measurement systems for education and research applications can be noted:

- Low resolution;
- Unattractive visualization;
- A lot of fatiguing mathematical calculations necessity;
- The experiment's equipment complexity distract attention of the students from essence of the magnetic quantity;
- Impossibility to compare the magnetic hysteresis loops of different materials in the same time.

II. THE BENEFITS OF VIRTUAL INSTRUMENTATION

Recent developments and applications, specifically the computer-based applications, have shown that many pure lecture-based engineering courses and conventional experiments (which are heavily dependant upon specialized instruments) can be updated and integrated with custom-written virtual instrumentation (VI), and can be delivered by computers [4]. In addition to this, the courses and experiments can be delivered remotely without having multiple copies of the experimental setups. Additional scientific visualizations and advanced analysis can also be added in the form of virtual instruments with minimal cost, which is limited or not possible in the conventional laboratory practice. Moreover, the virtual instrumentation approach is open to further improvements and developments, which may increase the student participation and enthusiasm while providing ideal delivery environment.

[1]Boyanka M. Nikolova - Faculty of Communications, Technical University of Sofia, 8 "Kliment Ohridski" Blvd., Sofia, Bulgaria, E-mail: bnikol@tu-sofia.bg
[2]George T. Nikolov - Faculty of Electronics, Technical University of Sofia, E-mail: gnikolov@tu-sofia.bg
[3]Marin B. Marinov - Faculty of Electronics, Technical University of Sofia, E-mail: mbm@tu-sofia.bg

However, due to the diverse nature of the lectures and the laboratory courses in every institution, custom-built software and hardware development is required most of the time. In addition, due to the fast developments in technology, the choice of the software and hardware should be considered carefully along with the cost.

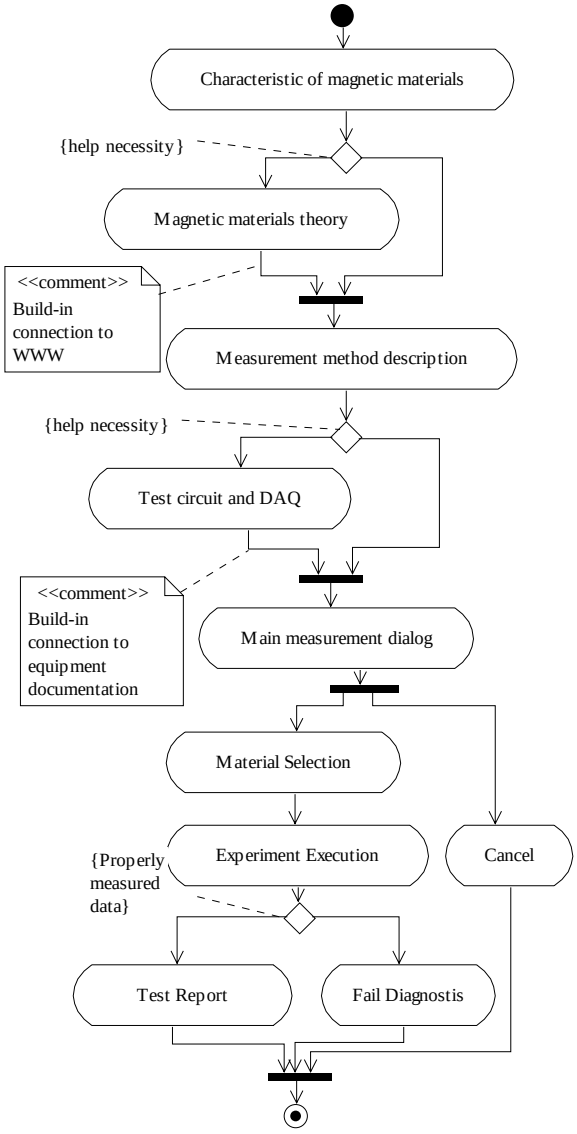

Fig. 2 The activity diagram for hysteresis experiment modeling

A number of interactive computer-delivered simulation, control, and scientific visualization software solutions are available in the market. It is found that the number of criteria may be contemplated for selecting application software to build virtual instrumentation used in engineering education. Because of its overall versatility as an engineering tool, the software package LabVIEW is chosen to create virtual workbench for magnetic hysteresis measurement. It is a graphical programming language that allows engineers and scientists to develop their own virtual instrument, which is flexible, modular and economical [3]. Furthermore, the software meets most of the software selection criteria, and it not only does the data manipulation, analysis, and control, but also has some multimedia authoring capabilities with the help of the add-on tools. The LabVIEW software allows for the creating of application-specific templates (sub-virtual instruments) to reduce the production time for the identical subjects. Many useful functions can be incorporated with the LabVIEW programs to perform very useful tasks in a laboratory virtual instrumentation system design.

A virtual test system is proposed that operates on the same principles as a traditional measurement system consisting of a sine generator, and two-channel oscilloscope. The main difference is that all these functions are implemented in multifunctional data acquisition system (DAQ), power voltage to current converter and software ADE as LabVIEW. This virtual system uses a similar but improved approach, for magnetic hysteresis measuring. By the way the automated magnetic hysteresis measurement is controlled by a personal computer. For the measurement experiment the NI 6024 multifunctional DAQ is used. The data acquisition and the generation of excitation current can be performed simultaneously.

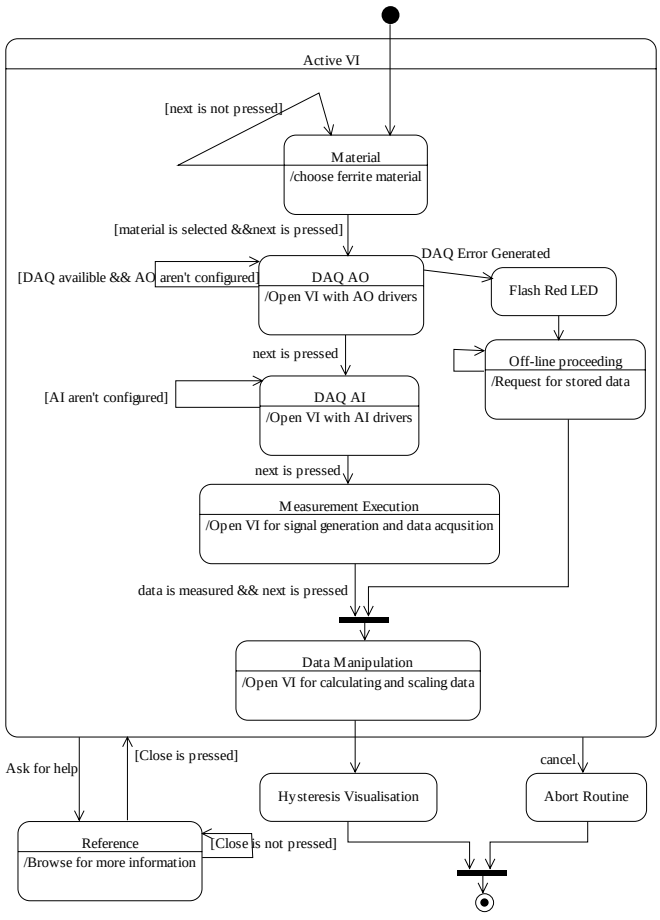

Fig. 3 The state diagram modelling execution of measurement experiment

The VI Generate_Sine.vi generates a sinewave analog output waveform on the DAQ board specified. It is the simplest form of continuous waveform generation. A sine wave is computed using the trigger functions in a “for loop”.

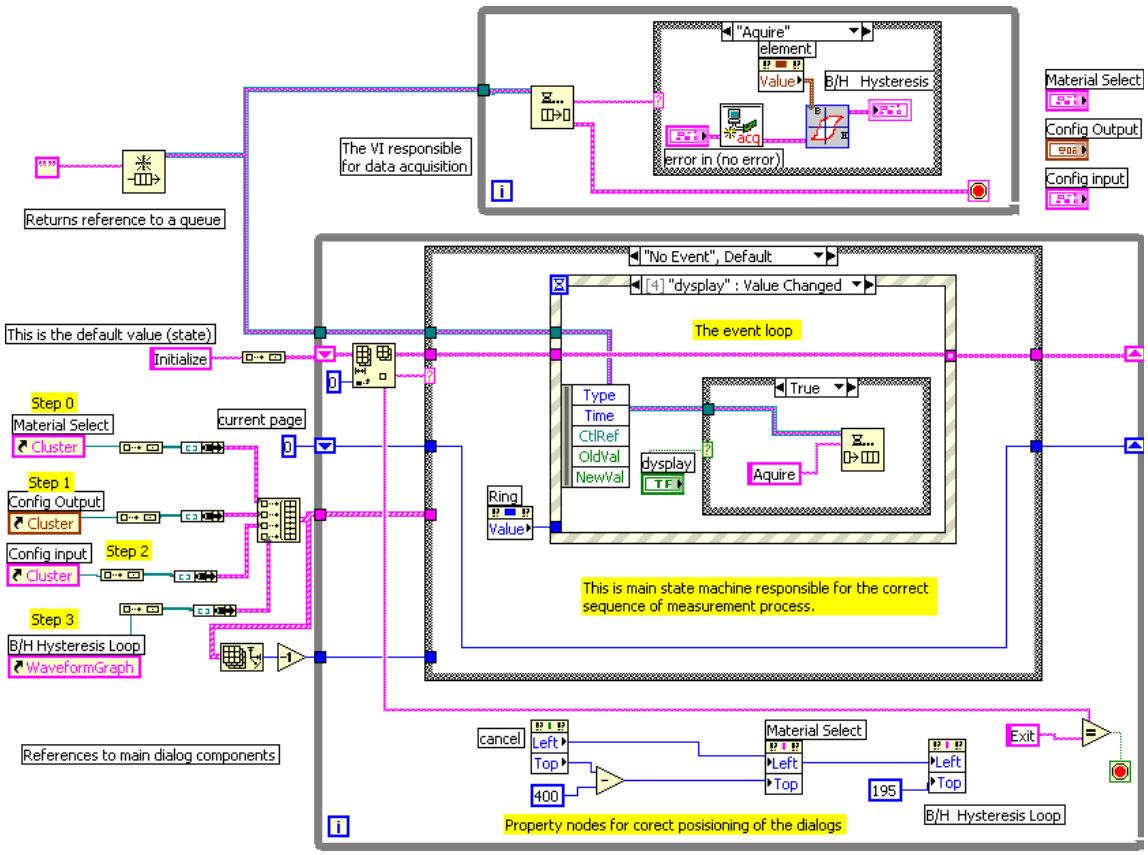

Fig. 4 LabVIEW block diagram for execution of measurement **experiment**

The analog output channel and buffer is initialized, the waveform written to the waveform buffer and continuous waveform generation is initiated at the specified update rate.

The Acquire_Data.vi VI retrieves the specified amount of data from two analog input channels. The VI is a timed acquisition, meaning that a hardware clock is used to control the acquisition rate for fast and accurate timing. It is also a buffered acquisition. Data are stored in an intermediate memory buffer after they are acquired from the DAQ board. Once the data have been acquired, LabVIEW retrieves the data from that buffer and displays it.

III. Designing the Experiment Sequence

Modeling is a proven and well-accepted engineering technique. Engineers study models to assess the impact of environmental forces and anticipate the behavior of actual structures. The Unified Modeling Language (UML) is a modeling language for specifying, visualizing, constructing and documenting the artifacts of a system-intensive process.

The UML [3] has become the standard for documentation and high-level design of modern software. As an example of this approach the application layer of the magnetic hysteresis measurement system based on concept of virtual instrumentation is presented. UML defines nine types of diagrams. The most appropriate to hysteresis measurement experiment modeling are activity and state diagrams.

Activity diagrams illustrate the dynamic nature of a system by modeling the flow of control from activity to activity. An activity represents an operation on some subVI in the system that results in a change in the state of the system. Activity diagrams are used to model workflow and internal operation. The dynamic behavior of the virtual workbench modeled by activity diagram is shown in fig. 2.

Statechart diagrams describe the dynamic behavior of a system in response to external stimuli. Statechart diagrams are especially useful in modeling reactive objects whose states are triggered by specific events. The state diagram that is used to model execution of measurement experiment is shown in fig. 3.

IV. LabVIEW Coding

Recently widely treated in realm of software engineering is the term “pattern”. Design patterns represent techniques that have proved themselves useful time and time again. They typically have evolved through the efforts of many developers and have been fine-tuned for simplicity, maintainability and readability. Furthermore, as a pattern gains acceptance, it becomes easier to recognize. This recognition alone helps other developers to read and make changes to the code.

The state machine pattern is one of the most widely recognized and highly useful design patterns for LabVIEW. This pattern neatly implements any algorithm explicitly described by a state diagram. A state machine usually illustrates a moderately complex decision making algorithm, such as a diagnostic routine or a process monitor.

The standard LabVIEW state machine consists of a large “while loop”, a shift register to remember the current state, and a case structure that holds separate code to run for each state.

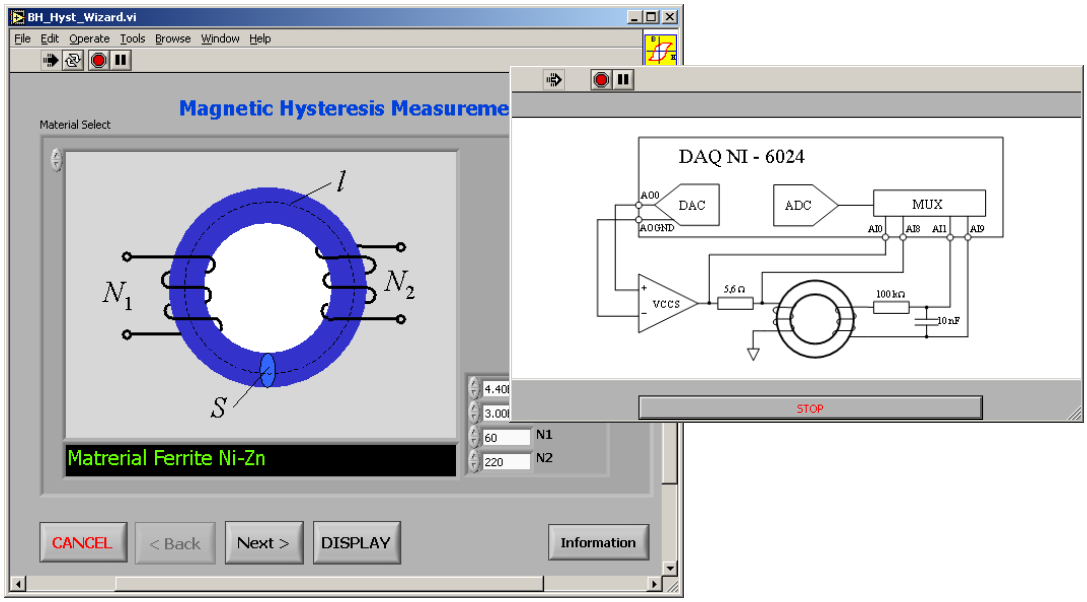

Fig. 5 Front panel for selection of ferrite material

The state machine that is created following the UML consideration (fig.3) is shown in fig.4. This programming code is responsible to ensure the correct sequence of measurement process.

Another design pattern, so called "event loop", is applied in software code and can be seen also in fig.4. As the state machine it is suggested by UML modeling also. The event loop is a powerful and efficient method for handling user interaction with a LabVIEW program. Because the event loop wakes up precisely when an event happens and sleeps in between, it is not needed to read control values over and over again in order to detect when a user presses a button. This will allow using the processor much less without risking loss of interactivity.

Of course, to complete the full LabVIEW program many other build-in functions and subVI are used, which are less or more described in appropriate documentation [4].

V. Realization of Virtual Laboratory Workbench

In order to illustrate some of benefits offered by virtual instrumentation in this topic the user interface (front panels) is appended. This user interface corresponds of state diagram shown in fig.3 and program code (block diagram) of fig. 4.

The first step of magnetic hysteresis measurement – selection of ferrite is shown in the fig. 5. In the right of figure is shown the opportunity to investigate the experiment's details without leave the working environment. As can be seen the great representational possibility of LabVIEW focus attention of the user in the base objective of experiment.

In the next figure 6, the successful completion of the measurement procedures are shown. The user can to turn of profit the build-in markers for desired magnetic parameter extraction.

VI. Conclusion

The design and development a set of virtual instruments measuring magnetic hysteresis is presented. The modern software technologies namely the unified modeling language and graphical programming are implemented in order to complete laboratory workbench. The exposed material can be useful for test and design engineers that going to involve the virtual measurement technologies into theirs practice. The applications of introduced modeling approach and software code cover – design of behavioral models for relatively large virtual instruments; using design patterns; magnetic materials characterization and measuring; engineering education; etc. It is relevant to remark that LabVIEW and UML have provided the educator with excellent opportunities to deliver curricula: in the hardware laboratory, to provide student self study resources, or for research purposes.

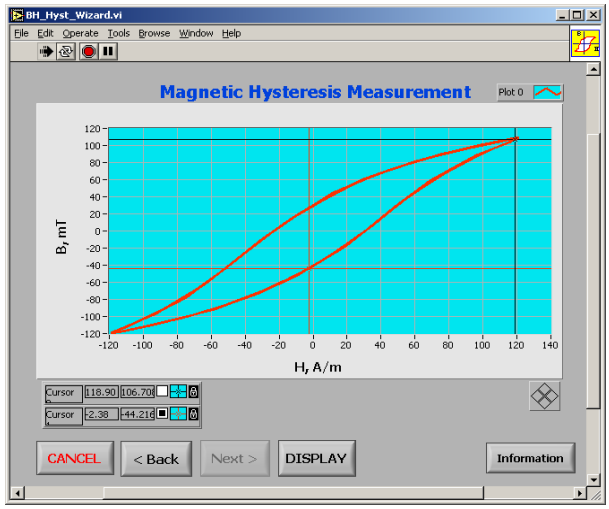

Figure 6 Measured hysteresis

References

[1] STEWARD, "Ferrite Property Measurement", Transformer & Filter Cores Application Guide, 2004.

[2] Kis P., A. Iványi, "Computer Aided Magnetic Hysteresis Measurement in LabVIEW Environment", Journal of Electrical Engineering, Vol 53. No 10/S, 2002, 10-11.

[3] OMG Unified Modeling Language Specification, Version 1.5, March 2003.

[4] National Instruments "LabVIEW Development Guidelines", 2000.

[5] Ertugrul N., "Hysteresis Characteristics of Magnetic Circuits", Department of EEE, University of Adelaide, National Instruments, 2000.

Test Set for Measuring Railway Weight under Condition of Movement

Georgy S. Mihov[1], Nencho G. Nenov[2], Emil N. Dimitrov[3]

Abstract – **The subject of the paper is the methodology for railway weight measuring under condition of moving. A smart strength sensor for measuring the wheel load is applied. Specific measurement channel for wheel static load determining is used as a test set for dynamic measuring. Collected data of wheel load is analysed and a proper algorithm is offered.**

Keywords – **Railway weigh, Dynamic load, Force sensor, Analog data treating.**

I. INTRODUCTION

Measuring carriage weight is an important process for railway transport in two aspects. First of all, the measuring allows to determine the dead or full load of railway carriages and to avoid the overcharging as well. Secondly, the measuring permits to know the distribution of the load among the wheels.

The difference of the wheel loads changes the process of the railway carriage interaction with the railroad. Moreover, this difference changes also the parameters of the above-spring construction dynamic part. As a consequence: the reaction of the vehicle mechanical system is increased; the limitation in the cohesion of the drive and brake forces is lowered; the intensity of wheel wearing-out is increased; the wheel axle directing ability is decreased; and the reliability of some important elements of the vehicle running part is decreased.

The measurement of the wheel load can be realised by special static test set, but it requires an individual measurement unit for each carriage wheel. Another way of carriage weight measuring is to use just two measurement units and to complete measurement process under condition of carriage moving.

The presented in the paper investigation aims to collect a practical data from measuring of vehicle weights under condition of movement and to offer a suitable method for data treating and calculating the load of each passing wheel.

To perform the carriage weight measuring under condition of movement, we used existing equipment for static load measuring of railway carriage wheels [1]. It consists of a specific measurement channel and a computer based data acquisition system. This equipment is used primary for locomotive spring system adjustment. The measurement channel is a typical railway channel with force measurement devices placed under each locomotive wheel. That allows the load of all the railway vehicle wheels to be measured at one and the same time. The number of measurement devices is 12 (for a 6-axles locomotive).

Each measurement device is an immovable sensor being part of railway [2]. It is built on a peace of standard rail type P49 with length of 1140 mm. On milled pads in the niche area of the peace of rail are mounted two full bridge of strain gauges [3, 4]. The distance between the bridges is 700 mm.

II. EXPERIMENT EQUIPMENT

To complete the experiment, we engage just two interface placed measurement devices, that form a measurement couple for the load of two wheels, belonging to a single axle. The first couple of measurement devices, that is suited at the beginning of the channel is chosen.

Each measurement device is a smart force sensor provided with embedded microcontroller. The force sensor is connected through industrial network (standard RS485) to the central computer. The experiment was planed preliminary. We completed the needed software for the smart force sensor and for the central computer as well. We decided the experiment to be completed by the following technology:

1. The central computer sends a command for starting the process of measuring. The force sensor measures periodically forces applied to both strain gauge bridges and stores them into an internal buffer (data segment – RAM). The measurement continues until the buffer is filled or a command for stopping the measuring is received from the central computer.

2. The railway carriage passes upon the force sensor and the measuring of the wheel load is being performing in progress.

3. After the measuring, the stored data is downloaded from the force sensor and is saved in a file at the central computer.

4. Off-line, the saved information is processed and analyzed and a technology for the individual wheel load determining is specified.

The preparation of the experiment includes creation of specific software:

1. Experimental software for the smart sensor: software designed for periodic measuring of voltage values generated by strain gauge bridges and storing the data into an internal buffer; software for the command interpreter completed with commands for starting the measuring, stopping the measuring and sending the collected data; software for loading the data on the central computer.

[1]Georgy S. Mihov is with the Faculty of Electronic Engineering, and Technologies, TU – Sofia, 1797, Sofia, Bulgaria, E-mail: gsm@tu-sofia.bg

[2]Nencho D. Nenov is with the Higher School of Transport, 1574, Sofia, Bulgaria, E-mail: rector@vtu.bg

[3]Emil N. Dimitrov is with the Faculty of Electronic Engineering, and Technologies, TU – Sofia, 1797, Sofia, Bulgaria, E-mail: edim@tu-sofia.bg

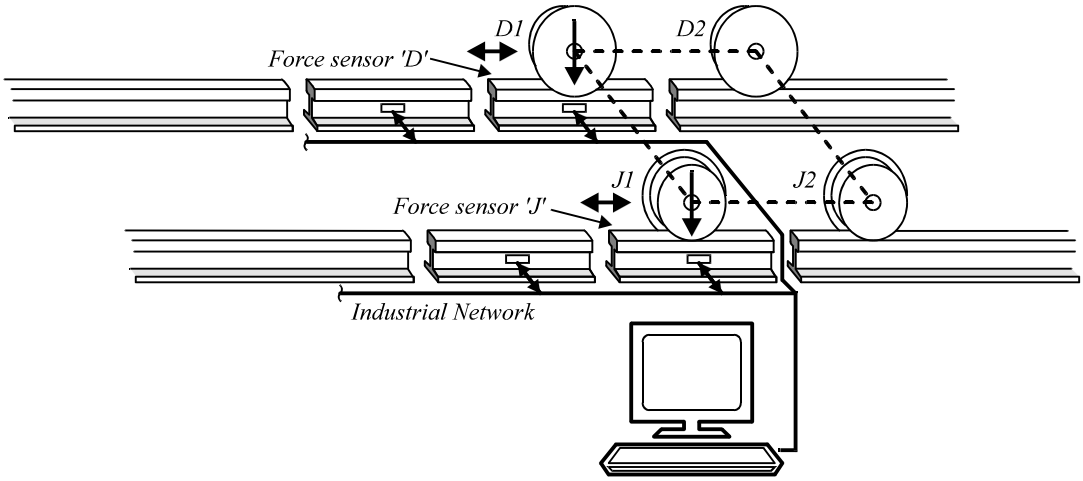

Fig. 1. Experimental test set for measuring wheel load under condition of movement.

2. Experimental software for the central computer: adding to the command interpreter commands for starting the measuring, stopping the measuring and receiving the data collected by the force sensor; software for saving data into a file with MS EXCEL compatible format.

The created experimental software was laboratory tested. The experiment was performed on the 21 of February in Locomotive Shed Ltd. in Sofia, Bulgaria. The experimental software was loaded on the used force sensors. The central computer was loaded with specialized software for testing and demonstration.

A locomotive (Series 46) passed with low speed upon the used force sensors (named 'D' and 'J'). When the locomotive was passing, the digital signals of the wheel load from the two wheel-axles were recorded. The movement was firstly directed from right to left and after that reversed from left to right. The recorded data is sent to the central computer, stored into a file and later – processed and analyzed with MS Excel.

III. Results

Two different sampling rates were applied for analog-to-digital (AD) conversion. They are the minimal and the maximal allowed frequency of sampling for the embedded in the force sensors AD Converter. The analysis of the sampled data with the maximal frequency said that it is unusable, due to the low number of samples in so-called active measurement zone of the force sensors. The recorded data at the maximal sampling rate is suitable for analysis. The records are shown in fig. 3. The sequence of forms correspond to the wheel load movement D1 and D2 (left movement) and D2 and D1 (right movement) from the first picture. The sequence of forms in the second picture is analogous to the first, but for the sensor 'J' –wheel load J1 and J2 (left movement) and J2 and J1 (right movement).

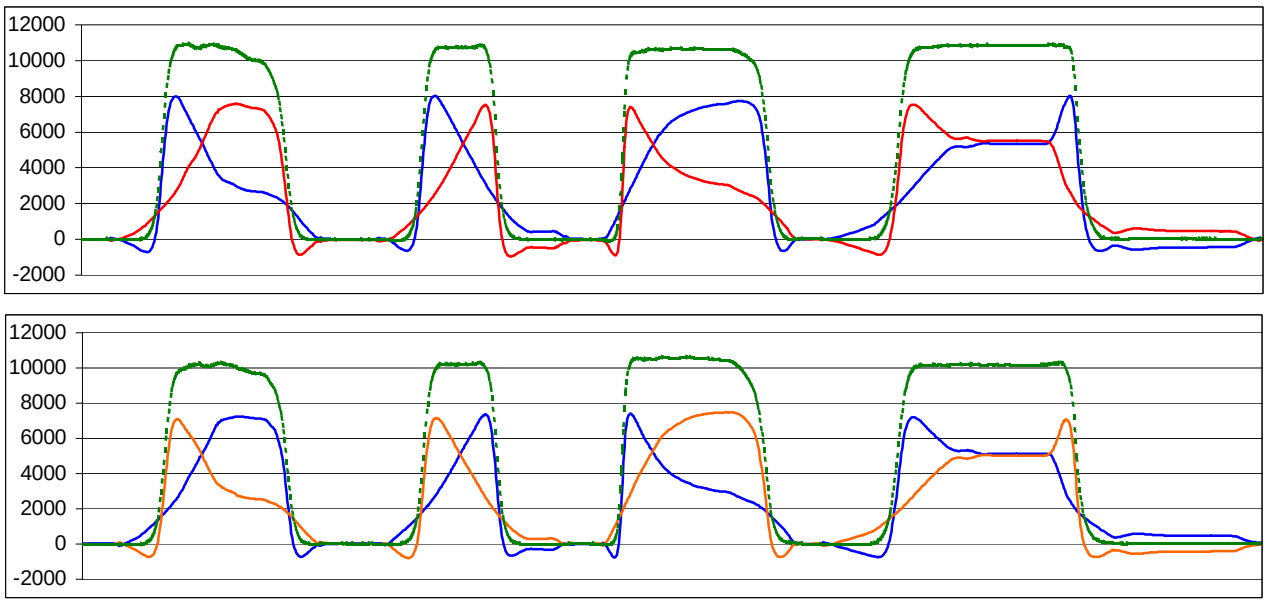

Fig. 2. Primary data sampled by force sensors D (first picture) and J (second picture). Y dimensions are displayed in kg.

Except the recorded signals from the couple of strain gauge bridges, in pictures on figure 2 is shown full passed weights. The full weight is calculated as a sum of signals from one couple strain gauge.

IV. ALGORITHM FOR WEEL LOAD ESTIMATING

A specific algorithm for processing the collected data is created. It aims to localise the zone of proportionality [5]. In this zone the calculated value of the force (weight) does not depend on its applied point. Its place is experimentally determined of ±250 mm according the centre of the force sensor.

The determination is done by detecting the value of the signal, corresponding to 90% of the maximum of the signal from strain gauge bridges (fig. 3). The next figures demonstrate the different stages of the algorithm, visualizing the results of the signals from wheel D2, moving leftward.

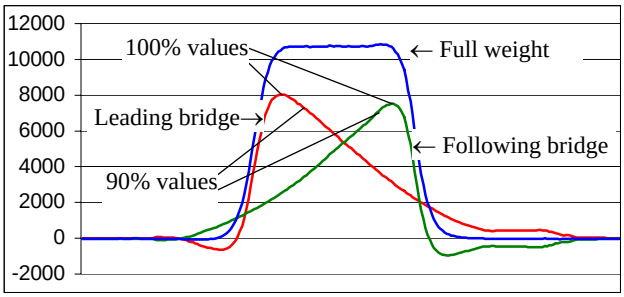

Fig. 3. Primary signal for D2 wheel (left movement).

This algorithm is one directional, i.e. it processes the signals in the same sequence as they arrive. It is impossible to know 90% of the maximal value of the following strain gauge bridge, because the maximum value is situated later in time. Thus it is accepted that the both 90% values are approximately equal, so this one, which is calculated first, is used for both of the bridges.

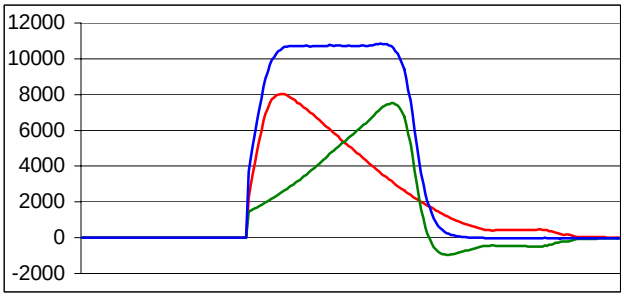

Fig. 4. Omitting samples below 2000 kg threshold.

The realization of the algorithm is made by a state machine with 5 stages:

1. The accounts of both of the bridges are being kept clear, until the leading one indicates value lesser than the given level. For the aims of the experiment, this level is set to 2000 kg, which is approximately 20% of the maximal weight, something that can be expected. Results are shown on fig. 4.

2. The maximal value of the signal in the leading bridge is being searched, and till the moment it is determined, the accounts of both bridges are being kept clear. When the maximal value is determined, it is calculated 90% of its value. The result is shown on fig. 5.

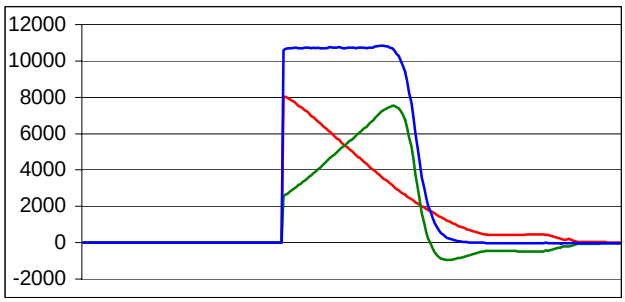

Fig. 5. Omitting samples before maximum in the left bridge.

3. The first account from the leading bridge which is lesser than the preliminary calculated 90% value of the maximum, is being searched. The accounts of both of the bridges are cleared. The result is shown on fig. 6.

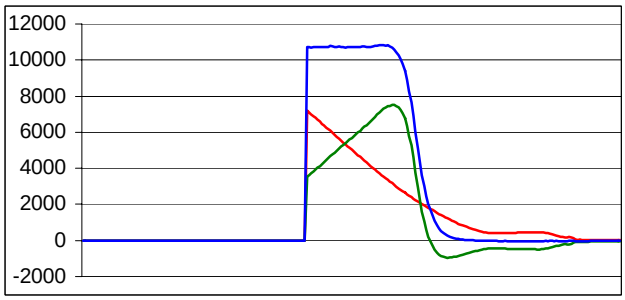

Fig. 6. Omitting samples above the 90% values in the left bridge.

4. The first account from the following bridge which exceeds the preliminary calculated 90% value of the maximum, is being searched. The accounts taken till that moment are being averaged and the result represents the passed load.

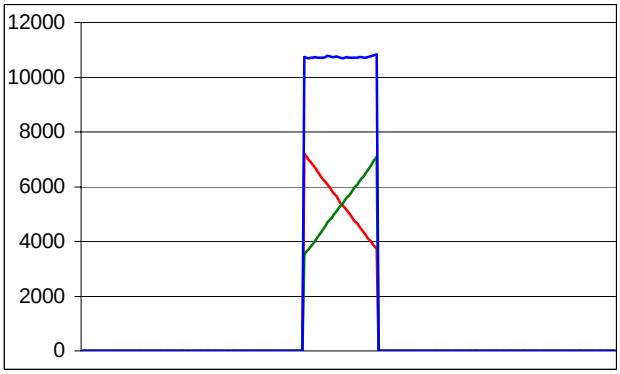

Fig. 7. Omitting samples after the 90% value in the right bridge.

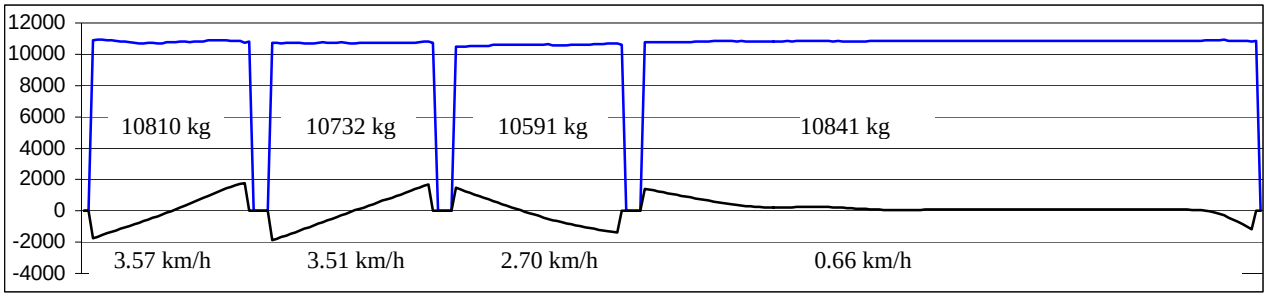

Fig. 8. Final results after completing the offered algorithm.

The algorithm ends with calculating the average load of the wheels for the determined sections.

5. The first account from the followed bridge which is lesser than the preliminary given measurement level (2000 kg), is being searched. The accounts of both of the bridges are cleared.

6. The procedure starts again from stage 1 and the accounts of both of the bridges are being kept clear until new measurement level is reached or the buffer ends. The result is shown on fig. 8.

The two graphics from the figures correspond to the total weight of the passed load (sum of the data from the bridges) and the speed of the load passing over the sensor, respectively.

By comparison of the data for the movement of one and the same wheel in both directions, a difference in the registered total weight is noted. This diversion for wheel D1 is –0,28 %, while for wheel D2 it is +1,31 %.

There is no explanation for this difference for now. Probably it appears due to an aperture error of the ADC or to the force sensor inertia. We intend to continue the research and the experiments in order to eliminate or compensate the discrepancy found.

V. CONCLUSION

An experiment has been planned for sampling and taking data from smart strength-sensor under condition of weight moving, for the purposes of the railway transport. An existing test set has been used for determining the static loading of locomotive wheels, which comprises the same sensors. The experiment used data from only two of all sensors.

Experimental software for the smart sensor and the central computer has been developed.

The experiment has been made as the data obtained by the two strain gauge bridges has been saved in a file.

On the basis of the data-file analysis has been developed an experimental algorithm for determination each wheel load in progress.

In addition the algorithm determines the speed of the load passing upon the sensor.

ACKNOWLEDGEMENT

We want to thanks to the staff of Locomotive Shed Ltd. in Sofia and mention the name of Eng. J. Jordanov for the kind support and the valuable help, that contributed the success of our experiments and investigations.

REFERENCES

[1] N. Nenov, T. Rouzhekov, G. Mihov, E. Dimitrov, “Technology of Locomotive Spring System Adjustment”. *11th International conference ‘Science, Education and Society’*, pp. 51-54, Žilina, Slovak Republic, 2003.

[2] N. Nenov, T. Ruzhekov, E. Dimitrov, G. Mihov. “Sensor of Strength for Measuring Wheel Load of Railway Carriages”, *25th International Spring Seminar on Electronics Technology*. pp. 105-108, Prague, Czech Republic, 2002.

[3] K. Hoffman, “An Introduction to Measurements using Strain Gages”, *HBM GmbH*, Darmstadt, 1989.

[4] B. Espion, P. Halleux, “Sameexperimental rezults on long-term stability of stran gauge load cells”, *Proceedings of the Int. Conference on Material Engineering*, Lecce, pp.729-736, 1996.

[5] G. Kolarov: “Methods of Finite Integral Transformations and Methods of Finite Elements in Some Problems in Theory of Elasticity”, *Author’s Paper on Doctorial Thesis*, Sofia, Bulgaria, 1990 (in Bulgarian).

[6] N. Nenov, T. Rouzhekov, G. Mihov, E. Dimitrov, “Strength Sensor for Dynamic Wheel Load Measuring of Railway Carriages”, “*26th International Spring Seminar on Electronics Technology*”. pp. 260-265, High Tatras, Slovakia, Czech Republic, 2003.

[7] G. Mihov, E. Dimitrov, N. Nenov, “Temperature Errors Compensation of Force Sensor for Railway Carriages Wheel Load Measuring”. *27th International Spring Seminar on Electronics Technology*. pp. 486-490, Bankya, 2004.

Virtual Instrument Applied to Energy Meters Gauging

Božidar B. Dimitrijević[1], Dragan B. Živanović[2] and Ivana S. Ranđelović[3]

Abstract - **Virtual instrument developed for metrological assurance of gauging procedure in electronic energy meters production as a product of the project sponsored by the Ministry of science and technology in Serbia is described in this paper. Multi-channel microcomputer acquisition card generates voltage and current three phase waveforms. Amplifiers provide required voltage and current levels for energy meters calibration. Output information from the current shunt, as well as those from AC dividers, across the ADC converter are returned to the PC computer, where the kWh parameter correction is done. Virtual instrument software is developed in graphical programming language LabVIEW. He is a part of feedback which in real time regulates a voltages, currents and phases in order to eliminate instability of applied amplifiers.**

Keywords - **virtual instrument, automated calibration, energy meters, LabVIEW**

I. INTRODUCTION

The rapid development of intelligent data acquisition and high-performance computing systems permits the successful application of more effective, sensitive and accurate methods in many different fields, from manufacturing and environmental monitoring, to medical systems and instrumentation. However, it has also introduced some urgent problems in the area of metrological assurance of these systems [1]. These problems concern in particular: choosing the right method for characterization of metrological properties of the system, automatic evaluation of the final results' uncertainties, and testing of both software and hardware means for metrological automatic support.

Various systems of this kind are employed worldwide, with a final goal of complete automation. Automated process, based on application of PC computer and virtual instrumentation software would significantly save time needed for calibration and presentation of results obtained during that process. There are already few completely automated systems employed in the world, and in our country, with similar characteristics [2, 3]. For example, the System Century Controls Company from India now offers a fully automatic energy meter calibration [4].

National Instruments LabVIEW [6] is a graphical development environment for designing test, measurement, and control systems, which gives the flexibility of a programming language without the complexity of traditional development tools.

[1] Božidar B. Dimitrijević is with the Faculty of Electronic Engineering, University of Niš, Aleksandra Medvedeva 14, 18000 Niš, Serbia and Montenegro, e-mail: dimitrijevic@elfak.ni.ac.yu

[2] Dragan B. Živanović is with the Faculty of Electronic Engineering, University of Niš, Aleksandra Medvedeva 14, 18000 Niš, Serbia and Montenegro, E-mail: dzile@elfak.ni.ac.yu

[3] Ivana S. Ranđelović is with the Faculty of Electronic Engineering, University of Niš, Aleksandra Medvedeva 14, 18000 Niš, Serbia and Montenegro, E-mail: rivana@elfak.ni.ac.yu

The basic building block of a LabVIEW application is a virtual instrument (VI), which consists of a front panel, where you design a user interface, and a block diagram, where you create graphical code. LabVIEW is the graphical development environment designed specifically for engineers and scientists who need to create flexible and scalable test, measurement, and control applications rapidly and at minimal cost. LabVIEW is a fully functional graphical programming language with the flexibility of a traditional, text-based language, [6].

In the framework of our project an automated system for gauging of new type of kWh meters, which are produced in the Ei - "Professional Electronics" factory in Niš, is being developed. The principal goal of our project is to develop a new traceability/calibration procedure for metrological assurance of the automated gauging system in the production of a new type of electronic kWh meters, [5].

II. TECHNICAL CHARACTERISTICS AND FUNDAMENTALS METHODS OF THE GAUGER

The gauger is designed for automated and semiautomatic simultaneous calibration and gauging up to twenty kWh meters of following types:

- Direct mono-phase kWh meters for reactive and active electrical energy measurement;
- Direct three-phase kWh meters for reactive and active electrical energy measurement;
- Indirect kWh meters for reactive and active electrical energy measurement;

There is a possibility of simultaneous calibration of kWh meters with same characteristics and of different type, e.g.:

- Mechanical kWh meters which obtain the information about the measured energy using optical reading head;
- Electronic kWh meters which obtain the information about the measured energy at the test output;
- Digital kWh meters, which obtain the information about the measured energy at the optical port, [7].

Use of PC computer and virtual instrumentation software significantly saves time needed for calibration and presentation of results obtained during that process, as well as it provides secure level of quality, reliability, and accuracy appointed by the corresponding standards for measuring of electrical energy, [5, 7].

The goal of developed virtual instrument is to generate voltages and currents for three-phase kWh meters calibration. The voltage and current waveforms are obtained from DAQ acquisition card NI PCI 6713, [8]. Then, signals of

appropriate amplitude for energy meters testing are generated by appropriate voltage and current amplifiers. Measuring transducers provide information about momentary values of voltage and current. Results are fit to input of ADQ acquisition card ED428, [9], i.e. in range at ±10V. According to measured voltage and current values, a regulation is done in loop, i.e. computation of new values that are generated by DAQ card, with purpose to get wanted values of amplitude and phase generated voltages and currents.

III. PROGRAM SUPPORT DEVELOPED BY LABVIEW

A program support is organized within of the "**Bazdarnica_glavni_ampfaz.vi**" programme. This "virtual instrument" is developed by LabVIEW version 6i. Control panel, i.e. working panel of this programme is shown on figure 1. It is alowed to the user to set effective values of voltages and currents,and also a frequency of generated signals. He can choose if to perform PID regulation of amplitudes and phases or to generate precalculated value, i.e. without regulation. Waveforms of generated and measured signals, and generated and measured values of signal amplitudes and phases are shown in front panel. Deviations of effective values in time are presented at small graphic (in the upper part of display).

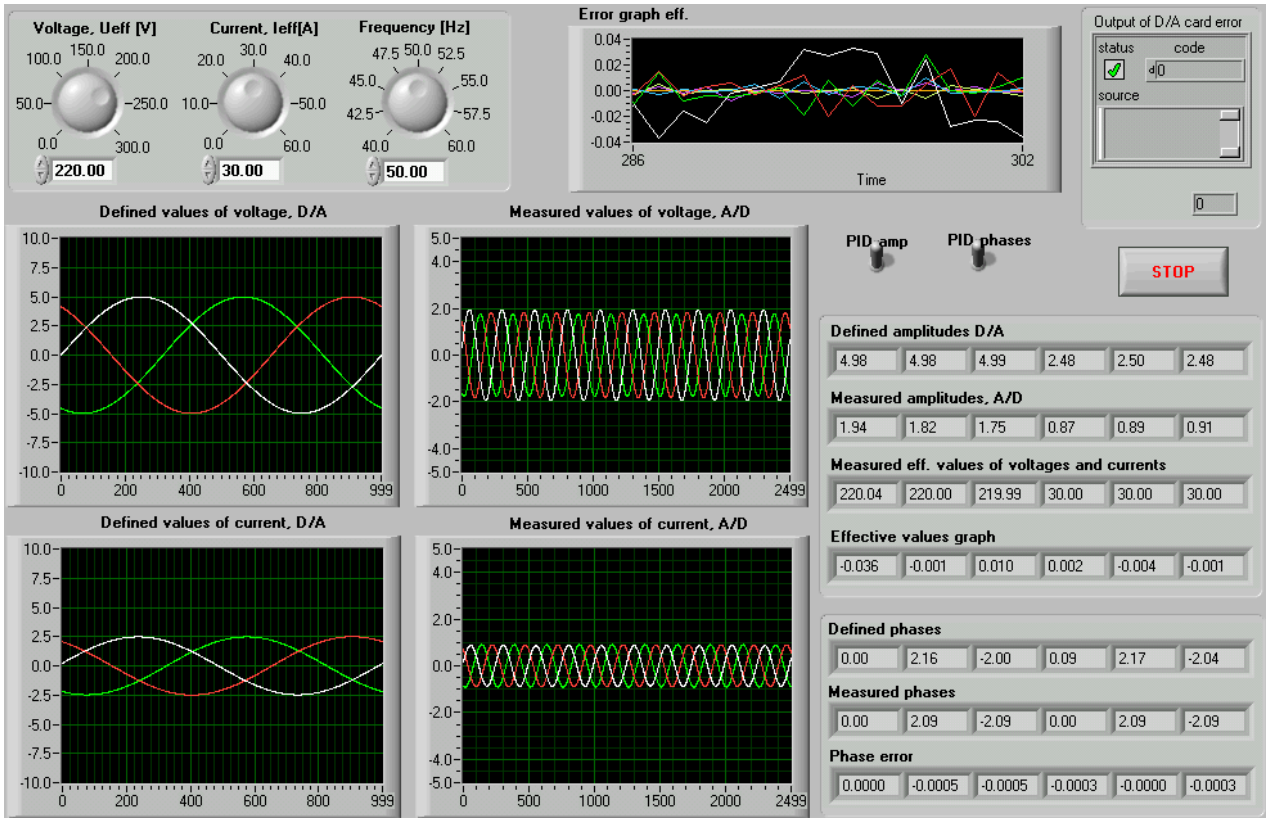

Figure 1. Virtual instrument displey

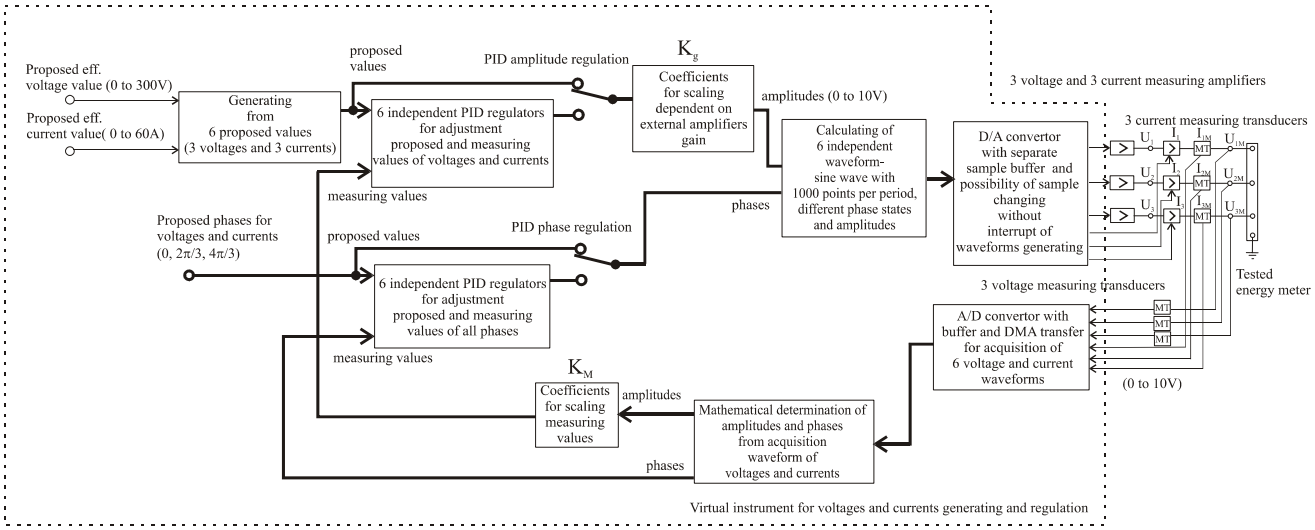

Figure 2. The system blok sheme

The block sheme of realized programme and whole system is shown on figure 2., and developed realization of LabVIEW programme is shown on figure 3. On those pictures thicker lines represent a flow with 6 data simultanously, i.e. transfer of data row. Regulation of signal amplitudes and phases is performing within the PID regulator block. Thus, 12 PID regulation loops run simultaneously, apart for all 6 amplitudes and 6 phases. PID regulators try to equal defined and measured values of amlitudes and phases, there in using *P, I* and *D* coefficients are set in programme (*P*=0,2 *I*=2 i *D*=0,01). PID regulator coefficients are choosen experimentally (they are the same for all 12 PID regulators) and it should be defined depend on the speed of the programme main loop running.

Then, the new amplitude and phase values are multiplied with coefficients K_g, so that required maximal values for generating are in range to 10V. Coefficients K_g is calculated so that signal after DA convertor, and applied external signal amplifiers, have effective value as those which are defined by programme.

SubVI **"Data_Generator_with_phases.vi"** calculates a array of samples in order to get for all 6 waveforms exactly one sinusoidal periode with proposed amplitude and phase, with already determined number of samples per period (now it is 1000 samples). D/A card circularly generates voltage for all channels based on already defined values of samples, which holds in internal baffer. SubVI **"AO Continuous_Gen_(scaled array).vi"** is using for bafer charging and D/A card initalization, which is obtained attained with card i.e. at driver installation for that card. Very important feature of this procedure, and chosen D/A card, is that new bafer charging doesn't interrupt generating, but it is executed syncronically with current generated period i.e. it is possible to continually changed values of samples, and this will not produce discontinuitet in generated sinusoids.

Accuracy of generated signals in forward loop depends on measurement accuracy of instant voltage and current values. Those informatons we get by external measurement transducers of voltages and currents. Waveforms of generated signals are gotten by acqusition in subVI-**"DMA_one_measurement.vi"**. This subVI is provided by accomodation of appropriate test programmes delirevied within Masterlink library, with A/D card. Based on calculated waveforms in range ±10V, subVI **"Amplitudes_and_phases_of_all_channels.vi"** estimates values of amplitudes and phases for all channels. True measuring values of voltages and currents are gotten after multiplying with coefficients K_m, so that measuring results are consistent to proposed effective values about 220V and to 60A. On this way, PID regulators use obtained values in next iteration, i.e. at next loop executing of main programme, to define a deviation from rezuired values of voltages and currents.

Phases of signals don't need multiplying with some coefficients, but all are calculated in relation to first channel, i.e. its phase is subtracted from the others. This is necessary to perform, because by A/D card acquisition we get reliable information only about interrelated phase of all channels, while absolute phase of measured sinusoids continually change value depends from momentary delay between generating signal start and acquisition start of same. This delay is not allways constant, and it is not syncronical with proposed frequency, i.e. signal period.

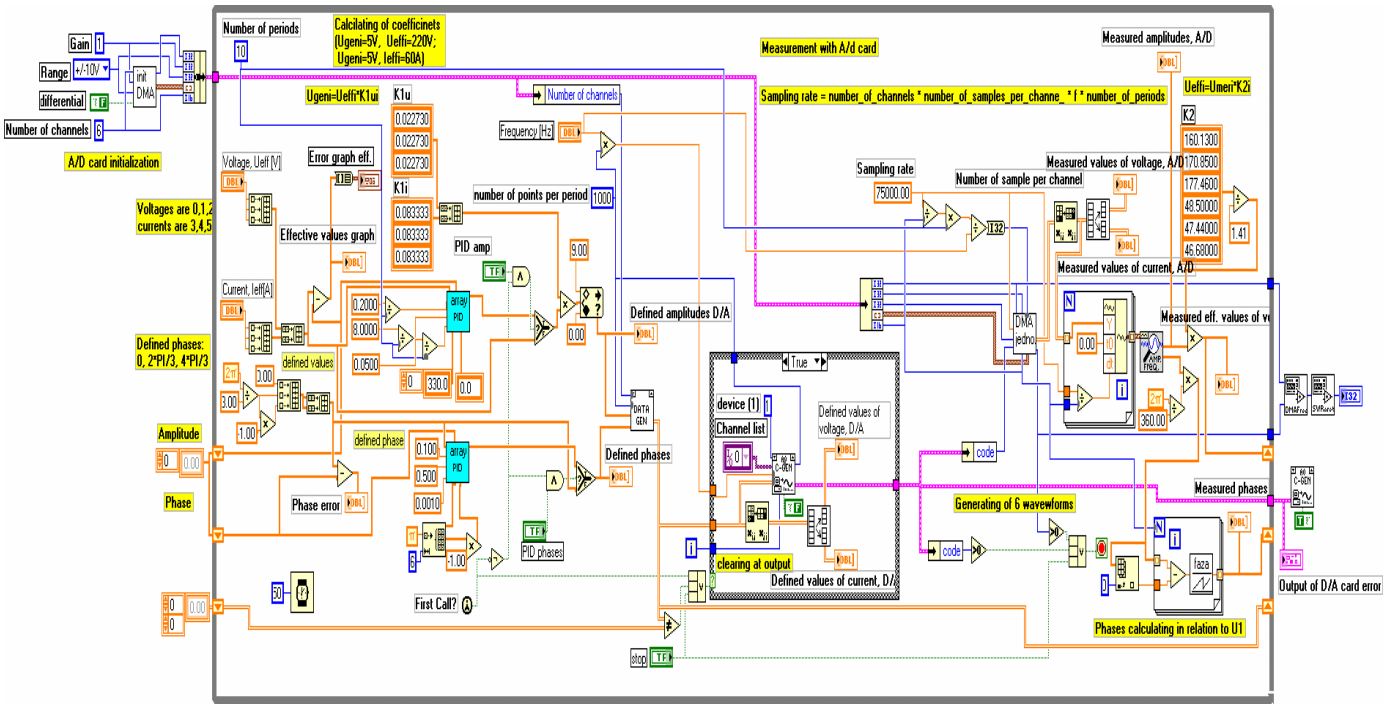

Figure 3. Blok diagram "Bazdarnica_glavni_ampfaz.vi"

IV. Conclusion

Virtual instrument developed for metrological assurance of gauging procedure in electronic energy meters production as a product of the project sponsored by the Ministry of science and technology in Serbia is described in this paper. Virtual instrument is used to generate three phase waveforms. It is also a part of feedback which in real time regulates a voltages, currents and phases in order to eliminate instability of applied amplifiers. Multi-channel microcomputer DAQ acquisition card NI PCI 6713 generates voltage and current three phase waveforms. Measuring transducers provide information about momentary values of voltage and current, which are fit to input of ADQ acquisition card ED428. According to measured voltage and current values, a regulation is done in loop, computation of new values that are generated by DAQ card, with purpose to get required values of amplitude and phase generated voltages and currents. Virtual instrument software is developed in graphical programming language LabVIEW.

References

[1] Vladimir Sobolev, Olli Aumala, “Metrological Automatic Support of Measurement Results in Intelligent Measurement Systems”, Elsevier Science Ltd. Computer Standards & Interfaces, Measurement Vol.17.- No. 3.- pp.151-159, 1996.

[2] Fluke Corporation, Using the 6100A Electrical Power Standard to calibrate energy meters, Application Note.

[3] Cronin L. B., Electrical measurement accreditation of automated calibration systems.

[4] Fully Automatic Energy Meter Calibration, System Century Controls, 28/2, 2nd Main Road, Seshadripuram, Bangalore 560 020, India.

[5] Ranđelović I, Rančić M., Dimitrijević B., "Metrology Assurance of the Automated Gauger in the Energy Meter Production", VIII Triennial International SAUM Conference, Conference proceedings, pp. 154-159, 5-6 November 2004.

[6] LabVIEW, User's Manual, National Corporation, USA, 2000.

[7] Dimitrijević B., Ranđelović I, Rančić M., "Metrological Support of Electronic Energy Meter Production", ICEST 2004, Conference proceedings, pp. 541-544, 16-19 June 2004.

[8] DAQ 6711/6713/6715 User Manual, Analogue Voltage Output Device for PCI/PXI/CompactPCI/PCMIA/1394 Bus Computers, National Corporation, 2003, USA.

[9] Multi-channel ISA modul for acquisition, measurement and control, ED428, Electronic Design, Belgrade, Serbia and Montenegro.

New Type of Linear and Angular Displacement Transducer Based on Pseudorandom Encoding

Dragan B. Denić[1], Ivana S. Ranđelović[2], Jelena R. Đorđević[3] and Goran S. Miljković[4]

Abstract - **Pseudorandom encoder as a new type of absolute encoder with one code track coded by applying pseudorandom binary sequences, is considered in this paper. A method for parallel reading of pseudorandom code using photodetector array is proposed. Simultaneously a problem of zero position adjustment at encoder installation is considered and a concrete solution in accordance with requests of high technologies encoders is proposed.**

Keywords - **Position measurement, Pseudorandom encoder, Pseudorandom binary sequence, Zero position adjustment.**

I. INTRODUCTION

Digital linear and angular displacement sensors, well - known as a encoders, are electromechanical components, whose basic function is providing measurement information about sensor head position in relation to measuring scale. One good alternative to the classical absolute encoder is absolute encoder which uses a technique of longitudinal coding. By using of one code track an absolute position is coded by using of pseudorandom binary sequence so that each groupe of *n* successive bits represents the unique code word. Two successive code words overlap and differ in only one bit [2, 3]. Instead of *n* bits per quantization step now we have only one bit and in that way it is opened a possibility of achieving greater accuracy of position measurement besides eliminating problem of great number of code tracks.

There are some special applications where it is impossible to demand such initial movement of the movable system (MS), such as systems for level measurement using digital position converters. It can achieve by applying detectors with integrated photodetector array [1], or using CCD cameras [4]. Since there is a great need for such a solution, an algorithm for reducing its performance time, using linear integrated photodetector array for parallel pseudorandom code reading, will be considered in this paper. Such way of coding opens a possibility of serial pseudorandom code reading by using only one detector [10, 11]. For new position defining it is enough to read only one next bit on code track. Such encoders exist on market under term the virtual encoder [12].

[1] Dragan B. Denić is with the Faculty of Electronic Engineering, University of Niš, Aleksandra Medvedeva 14, 18000 Niš, Serbia and Montenegro, e-mail: ddenic@elfak.ni.ac.yu

[2] Ivana S. Ranđelović is with the Faculty of Electronic Engineering, University of Niš, Aleksandra Medvedeva 14, 18000 Niš, Serbia and Montenegro, E-mail: rivana@elfak.ni.ac.yu

[3] Jelena R. Đorđević is with the Faculty of Electronic Engineering, University of Niš, Aleksandra Medvedeva 14, 18000 Niš, Serbia and Montenegro, E-mail: jelenadj@elfak.ni.ac.yu

[4] Goran S. Miljković is with the Faculty of Electronic Engineering, University of Niš, Aleksandra Medvedeva 14, 18000 Niš, Serbia and Montenegro, E-mail: goranm@elfak.ni.ac.yu

Their basic disadvantage is in fact that they request initial movement at system starting in order to collect first n bits from code track which define the first position.

II. PARALLEL CODE READING OF PSEUDORANDOM CODE AND ITS USAGE IN POSITION ENCODERS

One of the important features of pseudorandom binary sequence (PRBS) is based on the "window property" which is represented as *{S(p)/p=0, 1 ,..., 2^n-2}*. Window of width *n* gives *n*-bit code word *{S(p+n-k)/k=n,...,1}* which is unique and may fully identify window's absolute position *p* relative to the beginning of sequence, Fig. 1. Code words are now arraying linearly or longitudinally (but not transversely as in the case of classic coding), and they overlap. The first *(n-1)* bits of such code word are identical to the last *(n-1)* ones of the previous code word.

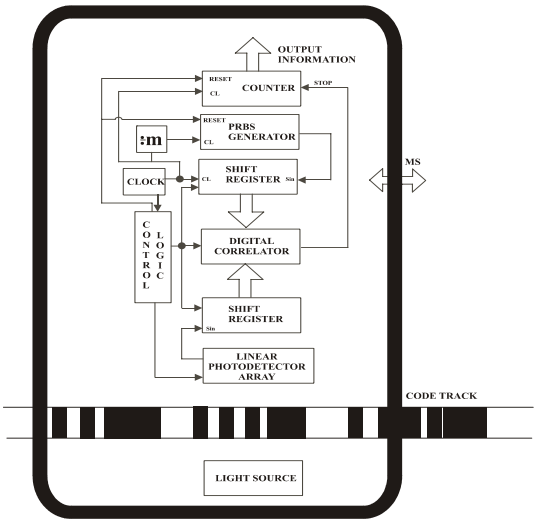

Fig. 1. High-resolution pseudorandom encoder with applied method of parallel code reading

For realizing of true pseudorandom absolute encoder, it is needed to apply any kind of parallel code reading method and in order to avoid a need for initial movement. A usage of *n* particular detectors is unacceptable to encoders with high measurement resolution. It is problem to dispose those *n* detectors on such little space [12]. One of the possibility is applying of integrated photodetector arrays for pseudorandom code reading. Integrated photodetector arrays are available on the market with different intervals between photodetectors. Those intervals are 13μm, 10μm, 7μm and smaller. It should use a large number of photodetectors in order to increase absolute position measurement precision. On Fig. 1 is shown one solution which represents the basic principles of parallel

reading solutions until now as based on using of linear photodetector array so as those represented in references [1,5].

Reading of the code track is with a light source at one side and an integrated circuit which consists linear photodetector array, at the other side. A state read after *k* tact pulses puts into the shift register. Let us read (*n+c*) bits and let nominal value of photodetectors number per one code bit be *m* and *n* is a number of bits needed for detecting the absolute position. Usually *c* is one additional bit and it increases a system redundancy, which provides detection of code reading errors. A condition $k \geq (n+c)\ m$ is always accomplished. Read code word is in the following form {00000111...1100 00111...1100....}. A transition is detected at the border of two elements. In the ideal case, a number of consecutive "1" or "0" per one bit equals *m*. It may occur a deviation due to not ideal drift of code elements on code track. Conversion into natural code is done after the reading of total output code. A generator of used PRBS starts from the code word that corresponds to initial "0" position on the code track. Generator core is a shift register with appropriate feedback. With each tact that conduces generating of next PRBS byte, *m* tacts from the shift register are performed. A code identical to the one that would be read in the case of continuous MS movement from the position "0", is obtained that way. In an ideal case, after a certain number of register shifts, a code word identical to the read one would be obtained. That correspondence could be simply detected by digital comparator circuit. A number of steps counted by a counter until the moment of correspondence represents output position information in the natural code. Unfortunately, as said before, an error would often occur in practice, and it is enough that one bit is read from (*m+1*) detectors and the PRBS generator will not generate such code word, thus, a correspondence will not be detected. This is why a digital correlator is used, although it is a much complex solution, but it solves the problem, Fig. 1. Accuracy of the detected code is increased introducing a greater value for *c*. Accuracy of correlator output does not depend much on the accuracy of defining boundary locations of code elements. Let us observe the following example. Let the distance between code element locations be 0.5mm and let the 11-bit PRBS (2047 quantization steps) be applied. In this case, a measurement range of 1m is realized. Now, let the distance between code elements be 10μm, which means that for the range of 1m, 100000 positions are required. This could be achieved using a 17-bit code. At least (17+1)10μm=180μm of code track should be read by photodetector array. An optical system for enlargement of the figure can be applied here. If the figure is enlarged 10 times, a photodetector circuit of at least 1800μm is required. If distance of 10μm between detectors is satisfied with an array of 256 photodetectors, total space resolution is now 1μm. In the worst case, the shift register connected to the PRBS generator, should make 10x100000 shifts until the moment it detects the correspondence. It is altogether 0,1s at the tact of 10MHz, i.e. 100ms. That makes the boundary work frequency of the system 10Hz, which is inadmissibly small even for general purpose encoders. In the reference [5] it is pointed to a possibility that a classic pseudorandom/natural code conversion is done using a simple digital comparator. Additional fine position could be defined based on the detected, defined transitions. Further in the paper, this idea will be elaborated and with some additional modifications, we will attempt to realize a solution where it is not necessary to define rough position for each new code reading.

III. NEW ALGORITHM WITH REDUCED PROCESSING TIME

The same function can be done using microprocessors and the appropriate software. A realization using one modern programmable logical circuit is possible. An example of a possible algorithm realization of a new solution proposed here is shown in Fig. 2. The basic idea is to exclude the digital correlator because it leads to a more complex system. Our goal is to achieve shorter time for PRBS reconstruction read from the track, and then use the well-known algorithm of pseudorandom/natural code conversion. The other idea does not consider constant determination of the rough position, but only for certain values of the fine ones. The fine position is defined by a number of rightmost photodetectors. A momentary position of the movable system is directly obtained without using any arithmetical operations, with the fine position resolution defined by the distance of two consecutive photodetectors in the photodetector array circuit.

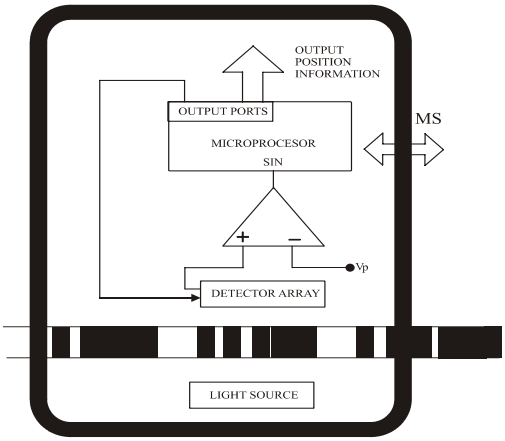

Fig. 2. An example of an encoder realization using a microprocessor

As it is shown in Fig. 2., a microprocessor defines the operation of photodetector array circuit using control signals. A reading of the recorded PRBS sequence is done in a way that series of voltage levels, which indicate a light intensity on the corresponding elements of the photodetector array, is lead to the input of a comparator. On that way, with a defined voltage level V_p, this series of voltage levels is converted to a series of logical "0" and "1" at the comparator output, that is then lead to a serial microprocessor port. Afterwards, the microprocessor performs the functions according to the software whose algorithm is shown in Fig. 3.

Bits obtained on this way are memorized and then analyzed. Memorized binary code word is in the form of {...000111...1111000...}, considering that *m* consecutive detectors are used for reading of one bit. However, as it is previously mentioned, it is possible that some deviations occur - {...0001011...1101000...}. Detector ordinals are then

determined. Since nominal period (a number of detectors per one bit) is known, a difference of two consecutive detector ordinals is approximately *dm*, *d={1,2,..., n}*. All deviations greater then this one can be updated, but the periods between the transitions will be different afterwards.

In any case, a calculation of period mean value is proposed here. In the ideal case, obtained mean period (meaning the integer part of the mean value) will be equal to the nominal period. In reality, there will be deviations, and if they are greater than the proposed value *k*, the user should be informed. The system can track down those deviations and perform diagnostics in the part of additional functions. Based on the estimated mean period, certain corrections are eventually performed and the detector ordinals are determined. Fine position is now simply evaluated as a number of detectors that are outside of the last determined transition. The MS movement direction is determined based of the previous value of the fine position. When the boundary between bits is known, it is easy to perform the reconstruction of the read part of PRBS and then the pseudorandom/natural code conversion. The value of the rough position is that way determined. Since the rough position has the same values for a great number of simultaneous code readings, there is no need for permanent performing of this, according to the necessary time, the most important part of the algorithm. Initial idea about the moment of rough position determination, which is completely logical, imposes as the natural first one, and considers rough position determination whenever the fine position equals 0. However, detail elaboration of this idea indicates various additional problems. Firstly, during the MS movement to the left, the next fine position value is *m-1*, and it is necessary to decrease the rough position value by one. This correction of position value by one is a well known problem which occurs in the case of all parallel code reading methods, and it is solved by implementing correction logic as shown in [8]. Additional problem is that the correction is not to be done always, but only in specific moments. All this could be solved, but the complication of the algorithm would be significant, and it would even be necessary to record the preceding fine position value. Secondly, it is possible, for some reason, to skip value *fine position=0*, which way the rough position determination would also be skipped. Naturally, detection of this kind of situation would further complicate the proposed algorithm. The idea which avoids mentioned problems considers the rough position determination whenever the leap of fine position occurs. During the MS movement to the right, the fine position leaps from value *"fine position = m-1"* to *"fine position = 0"*. When the leap is detected, the fine position will equal 0, and the rough position will be determined then, which is identical to the above-described approach. However, during the MS movement to the left, the fine position leaps from value *"fine position = 0"* to *"fine position = m-1"*. The rough position is now determined for the value *"fine position = m-1"* and will be decreased by one relative to the case when it is determined for the value *"fine position = 0"*. This means that the correction logic is no longer needed, which way the system is simplified and its reliability increased. If the leap *"fine position = 0"* or *"fine position = m-1"* occurs, this will not affect system performance, because the rough position determination is no longer linked to a specific value of the fine position. At the end, this kind of system is immune to errors that cause fine position leap. In these cases, after such error occurs, the system automatically determines the rough position, which is necessary to be done after occurrence of every error.

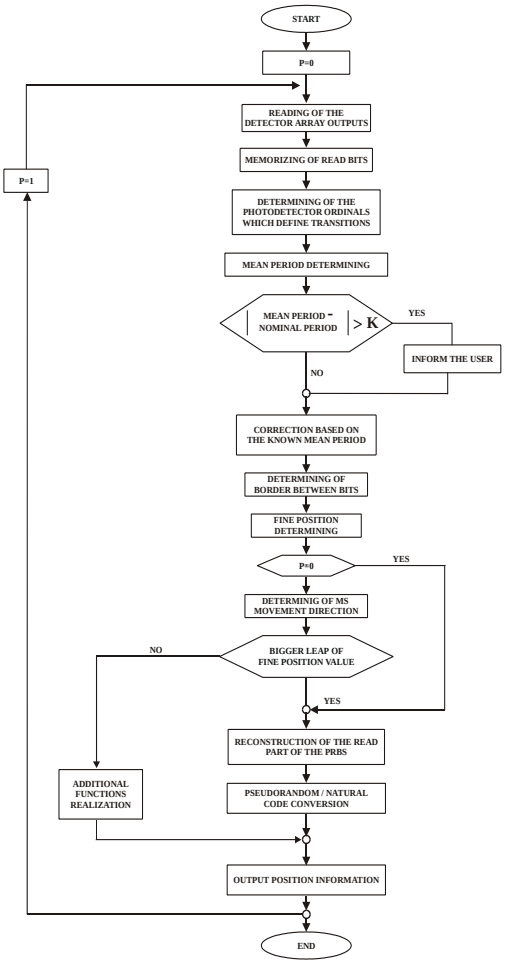

Fig. 3. Algorithm of the proposed solution

IV. DETERMINING OF MOMENTARY POSITION WITH DIRECT ADJUSTED ZERO POSITION

It comes to the unmatchings in the starting positions when installs an absolute encoder on movable system shaft. Therefore it is needed to adjust that zero position of position encoder corresponds to zero position of movable system, respectively directly accomplishing of zero position adjusting.

One of the leader factory in the world for production of new encoder generation, Stegmann, presented on the market a great choice of the incremental and absolute encoders with a different mechanical interface, resolution and with the new electronic features which are in the scope of the regular standards [9]. Today, it requests from encoders a flexibility, a reliability, a simple installation, and based on that it is created a new technology for the encoder production which enables directly adjusting of zero pozition. On Fig. 4. it is shown an example of the absolute encoder with such possibility.

If at installation of encoder CA6S on shaft of the movable system exists an umatching in the starting positions, directly adjusting of the starting position is done by pressing a taster. According to the function method of classical encoders, this solution is most probably based on storing of the correction parameters which almost figuring within function algorithm of such encoder.

Fig. 4. Stegmann absolute encoder, CA6S

Most probably and most natural is that momentary position of encoder for zero position of the movable system exactly represents that memory correction value. Anyway, this approach requests an additional operation in each subsequent process of the position measurement, and that operation is a correction of each read new position. That points out to the fact that with such approach time of position measurement increases. That disadvantage is certainly less important in relation to the big quality which is obtained by possibility of direct adjusting of zero position. A necessity of permanent memory existing doesn't represent the additional system complexing with respect that modern encoder should represent or in future will represent the intelligent sensor. In that case standard dictates that it comprises a memory element with permanent record in which are occured a factory number, a detecting and deciding to whom defined area quantity belongs, a processing of measured data, upkeep and identification of address, acceptance of command/data and generating data/command, autocalibration, zero and offset adjusting, and autotesting, besides a measurement of the physical quantity. Furthermore, from the modern encoders are requested or will be certainly requested an independence in deciding at control, local processing and statistic besides direct installation on the spot. Therefore, the existing of permanent memory element is or will be something necessarily and dictated with standard.

In order to direct adjusting of zero position, in paper is proposed solution that with pressing the taster, read code word is addopted for starting code word. It stores as such in flash memory of encoder itself as starting code word and in relation to it code conversion is perfomed, with respect to that can take anyone code word in relation to who, code conversion will perform. With direct adjusting of zero position by users with pressing the taster and by addopting of read code word for starting code word, doesn't request a mechanical movement or encoder rotation if exists an unmatching in starting positions during encoder installation on shaft of the movable system. This has a great importance in environments where encoder is used and where is very hard performing of encoder mechanical movement, with respect that a usage of encoder is wide. Therewith, the additional operation is eliminated, respectively a correction of each read value, because if on this way read code word wouldn't addopt for started, it would represent a correction factor which in each subsequent process of position measurement would add or substract from current read value. Addopting of read code word for starting is especially important and for time saving of position measurement, with respect that needed time for position measurement performing is one of the basic problems at pseudorandom encoders. By using of this solution it doesn't come to the encoder complexing besides it significally gets on time saving of position measurement. After storing of code word in flash memory, that memorizes as starting code word, it performs a code conversion pseudorandom/natural, according to the algorithm which is shown on Fig. 3.

V. Conclusion

There are usages where an initial movement of movable system after power is turned on, is unacceptable or even impossible. Then it is neccessary to perform parallel code reading and for case of high measurement resolutions the linear detector arrays or CCD sensors are used. In paper is suggested the solution which significally decreases a basic problem, and that is significant time needed for performing of position measurement. Simultaneously proposed solution provides in the simple way direct adjusting of zero position. Read code word for that arbitrary position is memorised as starting code word and in relation to it code conversion is performed, according to algorithm which is shown in the paper. On this way, additional operation is eliminated.

References

[1] J.T.M Stevenson and J.R. Jordan, "Absolute position measurement using optical detection of code patterns", *J. Phys E. Sci. Instrum. 21*, 1140-1145, 1988.

[2] Jones B.E. and K. Zia, "Digital Displacement transducer Using Pseudorandom Binary Sequences and a Microprocessor", *IMEKO/IRAC, Symposium Proceedings*, pp. 368-379, London, 1980.

[3] Arsić, M., Denić, D.: "Position measurements based upon the application of pseudorandom encoding", *Facta Universitatis, Ser. Electronics and Energetics*, no. 6, pp. 13-23, 1993.

[4] Khalfallah, H., Petriu, E.M., Groen, F.C.A.: "Visual position recovery for an automated guided vehicle", *IEEE Trans. Instrum. and Meas.*, vol. 41, no. 6, pp. 906-910, 1992.

[5] Johnston J. S. "Position measuring apparatus", UK Patent Application no GB 2126 444A.

[6] Arsić, M., Denić, D.,: "Code convertor pseudorandom/natural applied at position encoders", *ETRAN, Ser. Elektronika*, pp. 164-167, 1995.

[7] Denić, D., Pešić, M., Arsić, M.: "New algorithm of code conversion pseudorandom/natural", Proceedings *ETAN*, II sveska, pp. 39-44, Belgrade, 1993.

[8] Petriu, E.M., Basran, J.S.: "On the position measurement of automated guided vehicles using pseudorandom encoding", IEEE Trans. Instrum. and Meas., vol. 38, no. 3, pp. 799-803, 1989.

[9] http: // www.stegmann.com

[10] Arsić, M., Denić, D.,: "New pseudorandom code reading method applied to position encoders", *Electronic letters* no. 10, vol. 29, pp. 893-894, 1993.

[11] Denić, D., Ranđelović I., M., Arsić, M.: "Absolute position measurement using the method of pseudorandom code parallel reading", *ICEST 2003 Conference Proceedings*, pp. 394-397, Sofia, Bulgaria, 2003.

[12] Denić, D., Ranđelović I., Rančić M.: "High-resolution pseudorandom encoder with parallel code reading", *ISSN 1392-1215 Elektronics and electrical engineering* Nr 7(56), pp. 9-14, Kaunas, Litvania, 2004.

Research with Modeling of Temperature Regime of Electronic Components in Middle and Deep Vacuum

Asoc. Prof. Dr Eng. Ivan Evstatiev[1], Dr Eng. Dimitar Dimitrov[2]

Abstract: **A research of the parameters influence of an electronic model that works in conditions of middle and deep vacuum. We discus the changes in the energy characteristics. Using a physical model, that describes the processes in the system. Using this model is we develop a software model on a personal computer and we analyze the changes in the physical model. A research of the power consumption, the mass, the surface, the environment temperature, the blackness etc. The results are given on following graphics.**

Keywords: **mathematical model, electronic components, vacuum**

The valuation of the influence of the parameters of an electronic module and the parameters of the environment in middle and deep vacuum is a precondition of choosing the rights regimes of module power loading and a regime of backing of its parameters in the established regime.

The research is based on a given algorithm [1]. Using this algorithm a software for a personal computer has been made. We made the research using this software. The software gives an information window on the computer screen. This window consists of graphics zone, key zone for starting the four graphic conditions and zone for giving the parameters used in the research.

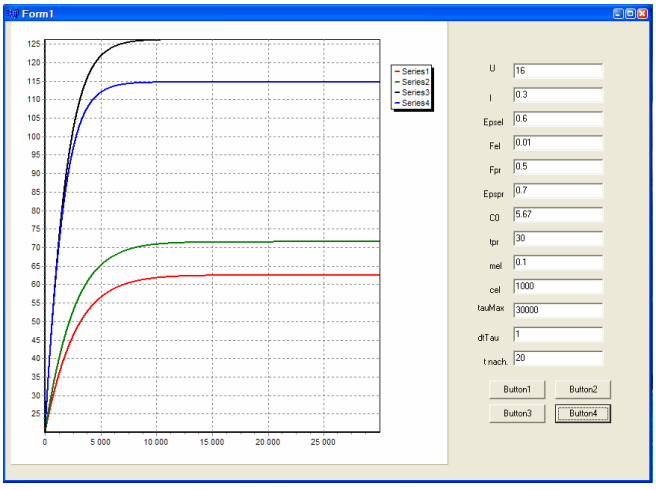

Figure 1. Software's information window

Using simultaneously giving of the four graphs we can compare four different regimes of operation.

I. Research Methods

Power consumption over the caloric effect of the module.

We presume that all consumed energy transforms into heat [1]. We test the influence of the power supply voltage and the current consumed over the caloric effect of the module. We use two power supply voltages and two different currents consumed – graphic 1 – 5 V/0,1 A, graphic 2 – 5 V/ 0,2 A, graphic 3 – 10 V/ 0,1 A and graphic 4 – 10 V/ 0,2 A.

Investigation of influence of the level of black of the electronic model and the environment.

We give four levels of black of the electronic module E_{psel} = 0,2; 0,4; 0,6 and 0,8. We change the levels of black of the enclosure too (E_{pspr} = 0,2: 0,4: 0,6 and 0,8).

Research of the influence of the radiation surface of the module and the enclosure.

We change the surface of the electronic module (F_{el} = 0,01; 0,02; 0,03 and 0,04 m^2) and the enclosure (F_{pr} = 0,5; 1; 1,5 and 2 m^2).

To analyze the mass action of the module and its thermal capacity coefficient they change as follows (m_{el} = 0,1; 0,2; 0,3 and 0,4) and (c_{el} = 1200; 1400; 1600 and 1800 $J.kg^{-1}.K^{-1}$).

II. Results

Research of the power consumption over the caloric effect of the module.

According to the methods the received dependences are shown in figure 2.

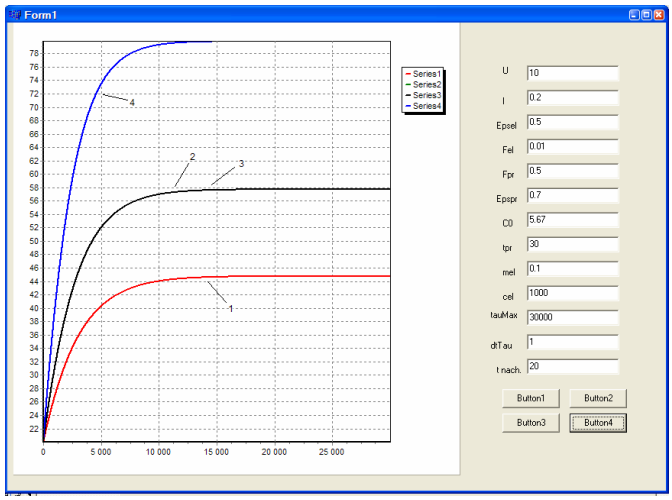

Figure 2. Power consumption influence over the caloric effect of the module

[1] Ivan Evstatiev, University of Rousse "Angel Kanchev", Faculty of Electro technique, Electronics and Automatics. e-mail: ievstatiev@ecs.ru.acad.bg, address: Bulgaria, Russe 7017, ul. "Studentska" 8.

[2] Dimitar I. Dimitrov, Ph. D., University of Rousse and the Faculty of Communication Technology, Technical University – Sofia, Kliment Ohridski 8, 1000 Sofia, Bulgaria, e-mail: ddim@tu-sofia.bg

As you can see from the figure above the temperature change is proportional to the brought energy of the module. The time needed to reach the established regime is about 2,7 hours practically does not depend on the energy.

Figure 3 gives the influence of the level of black of the module over the thermal regime is given in figure 3.

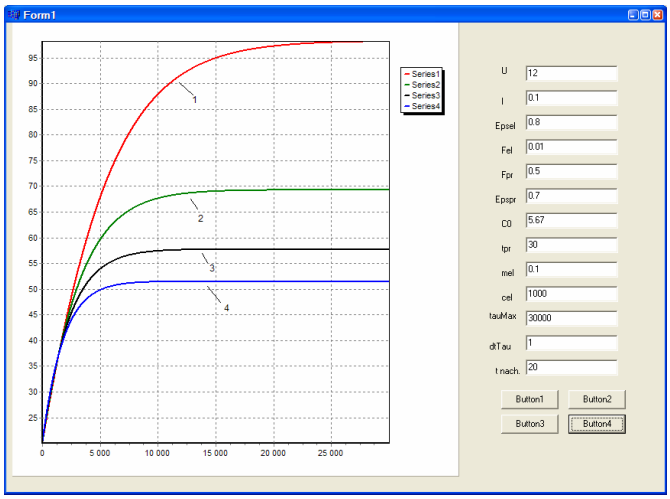

Figure 3. Influence of the value of black of the module over the thermal regime

Using the dependences we can generalize that increasing the value of black of the electronic module, almost exponent decreases the module temperature after reaching the established process. Increasing the value of black of the electronic module, the time for reaching the established regime decreases.

The result of the investigation of the influence of the level of black of the environment is given in figure 4.

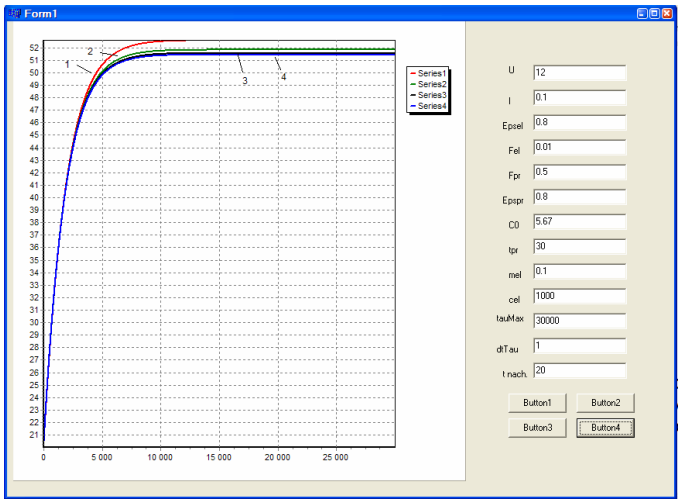

Figure 4. An influence of the level of black of the environment over the temperature regime

The value of black of the environment practically does not influence on the thermal regime and the dynamics of its changes.

The influence of the radiation surface of the module is shown in figure 5. The influence of the environment in figure 6.

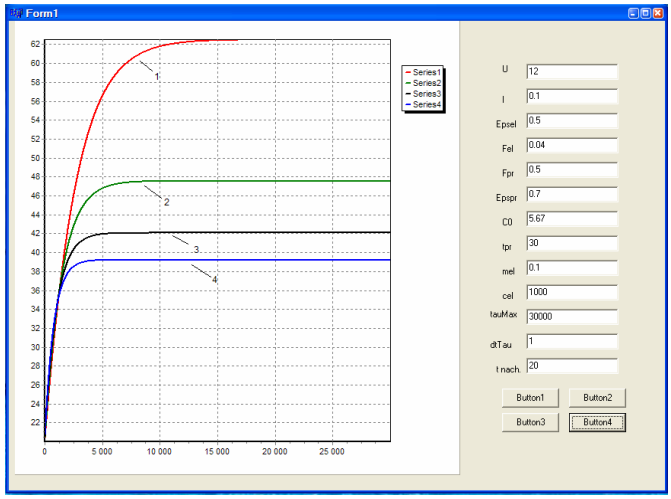

Figure 5. The influence of the radiation surface over the temperature regime

As shown in figure we can assume that increasing the radiation surface of the electronic module decreases exponent its temperature. Using module with bigger surface we reach the established regime faster.

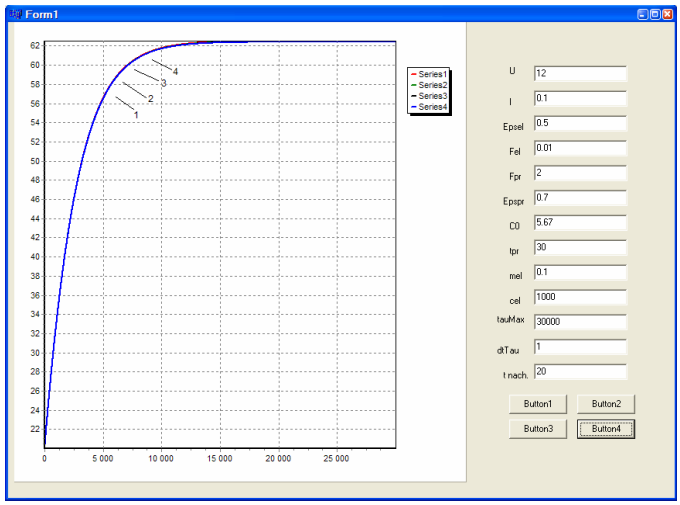

Figure 6. The influence of the radiation surface of the environment over the temperature regime

The radiation surface of the environment does not effect on the thermal regime and over the dynamics of changing module's temperature.

The analyses of the influence of mass of the module is shown in figure 8. The thermal capacity is given in figure 8.

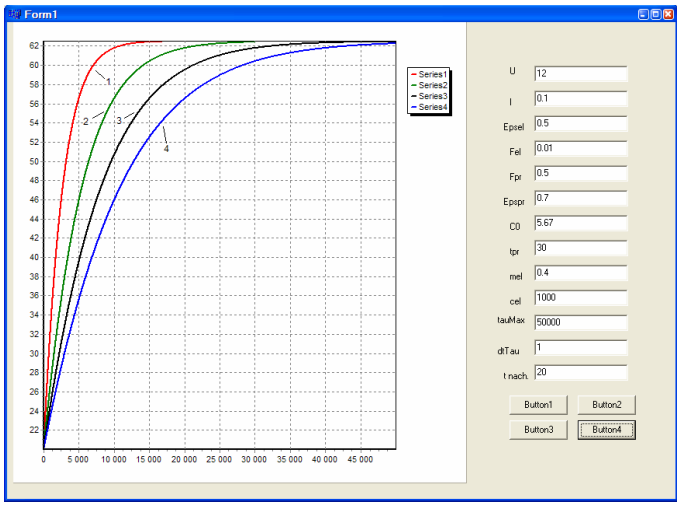

Figure 7. The influence of the module's mass over the thermal regime

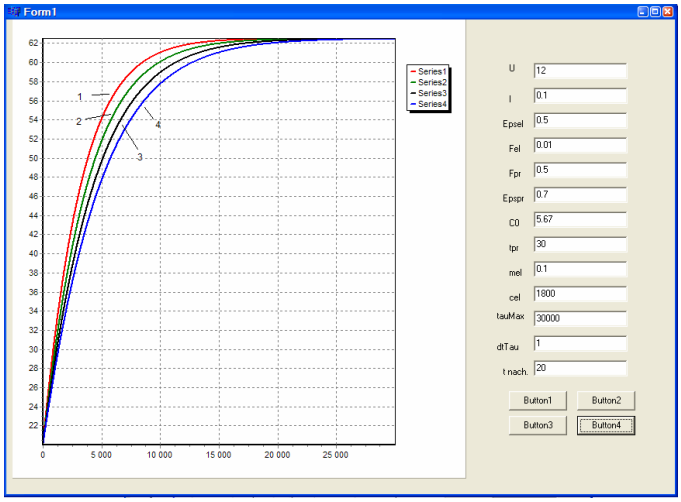

Figure 8. Influence of the thermal capacity coefficient of the electronic module over the temperature regime

Increasing the module's mass increases the time constant of the process and increases time for reaching the established regime.

Changing the thermal capacity coefficient of the electronic module changes the dynamics of the process.

III. CONCLUSIONS

The following parameters influence electronic module working in middle and deep vacuum conditions:

- Increasing power consumption increases exponentially its temperature
- Increasing the level of black of the electronic module and its radiation surface exponentially decrease its temperature
- Changing the electronic module mass and its thermal capacity coefficient change the dynamics of temperature changes, but do not change the temperature of the established regime
- The level of black of the environment and the radiation surface effect weekly over the heat exchange

REFERENCES

[1] Evstatiev I., D. Dimitrov, Temperature Sweep Modeling of Electronic in Medium and Deep Vacuum Conditions, ICEST 2004, Bitola, Macedonia, 16-19 June, 2004.

Session WC:

WIRELESS COMMUNICATION

Interactive Broadcasting: Solution for a DVB-T / WCDMA Hybrid Wireless Access

Serban Obreja[1], Octavian Fratu[2], Simona Halunga[3], Ioana Berca[4]

Abstract - **The latest developments in the area of wireless systems are placing the accent on the interactive services related to mobile Internet services and digital TV services. In order to use the DVBT link for data transmissions as well as or digital TV programs, an uplink channel has to be defined for interactive services. A possible solution might be the use of a hybrid system DVB-T/UMTS, in which the uplink is ensured by the UMTS while the downlink might be shared between UMTS and DVB-T, increasing thus the capacity of the overall system. This paper presents a possible interconnection scenario, which takes benefit of the advantages of both systems in order to realize an improved, high capacity fully mobile communication link. The development of a simulator for the overall system is under development but partial solutions, obtained from the DVB-T system simulation are presented.**

Keywords – **Interactive broadcasting, DVB-T, UMTS, WCDMA**

I. INTRODUCTION

The Digital Switchover process, which implies switching from analogue type broadcasting systems to digital broadcasting ones (DAB, DVB), offers the possibility to introduce supplementary data services in the remaining bandwidth. Those systems can be used as flexible digital multimedia content-broadcasting platforms. They enable access not only to multiple TV and radio channels sources, but to data services as well, which, on their turn, can be a mixture of video, audio and text content. A second trend in broadcasting services is interactivity and personalization: the users should have many degrees of freedom, to choose the content and the form of the selected program, before or during the presentation, in an interactive manner.

In the same time the mobile networks evolved form narrowband telephone / audio services to complex multimedia services. The UMTS has been adopted as the global wireless multimedia network standard at the beginning of 2000.

[1] Serban Obreja, Electronics and Telecommunications Faculty, Str. Iuliu Maniu 1-3, Bucuresti, Romania
E-mail:serban@radio.pub.ro
[2] Octavian Fratu, Electronics and Telecommunications Faculty, Str. Iuliu Maniu 1-3, Bucuresti, Romania
E-mail: ofratu@elcom.pub.ro
[3] Simona Halunga, Electronics and Telecommunications Faculty, Str. Iuliu Maniu 1-3, Bucuresti, Romania
E-mail: simona.halunga@elcom.pub.ro
[4] Ioana Berca, Electronics and Telecommunications Faculty, Str. Iuliu Maniu 1-3, Bucuresti, Romania
E-mail: bodita_79@yahoo.com

Due to its flexible system design, UMTS offers a large variety of services, with various data rates, from speech telephony and pure voice applications to high rate data applications such as web-browsing, as well as to interactive communication and entertainment services.

A new challenge might be the integration of all these new technologies, very different as applications and data processing algorithms in a hybrid system. The system might provide in this way more flexibility, new applications and a better quality of the existing services. For example, broadcasting technologies are ideal for the delivery of one-to-many services, such as video streaming. In exchange, the mobile telecommunication technologies offer good symmetrical bi-directional communication link as well as a complex billing systems, which might constitute a drawback of the broadcasting technologies lack.

II. DVB-T SYSTEM

DVB-T is the standard for Digital Television Terrestrial Broadcasting defined for Europe. The DVB family standards allows for digital video and audio broadcasting as well as transport of multimedia services. For terrestrial broadcasting the system was designed to operate within the existing UHF spectrum allocated for analogue television. The system was developed for 8MHz channels but it can be reconfigured to work on 7 or 6MHz channels as well.

The achievable data-rates of DVB-T range from 3.7 - 23.8 Mbit/s for a 6 MHz channel and from 4.9 - 31.7 Mbit/s for an 8 MHz channel. The maximum achievable data-rate depends on the channel quality expressed as the signal-to-noise ratio observed at the receiver. This trade-off between SNR and achievable data-rate gives broadcasters a great flexibility in the system design. For instance, a broadcaster can decide between wide-area coverage at medium data rate, that can operate at higher SNR's, or local-area coverage at high data-rate, which assumes low SNR's.

The DVB data broadcasting specification is designed to allow software downloads over satellite, cable or terrestrial links, to deliver Internet services over broadcast channels (using MPE encapsulation), and to provide interactive TV. The specification is based on a series of four profiles, each corresponding to an application area. The four application areas covered by the DVB data broadcasting specification are as follows [2]:

- *Data Piping* – This is the simplest, asynchronous, end-to-end delivery of data through DVB compliant broadcasting networks;

- *Data Streaming* –supports data broadcast services that require a streaming-oriented, end-to-end delivery of data in either an asynchronous, synchronous or synchronized way through DVB-compliant broadcast networks;
- *Multiprotocol Encapsulation* – supports data broadcast services that require the transmission of datagrams of communication protocols via DVB-compliant broadcast networks;
- *Data Carousels* –supports data broadcast services that require the periodic transmission of data modules through DVB-compliant broadcast networks.

III. UMTS

Third-generation mobile communication systems are characterized by offering:

- wideband multimedia services, which include both data and voice services;
- real-time as well as non real-time support;
- dynamic user bandwidth and services;
- IP connectivity from end to end.

The UMTS system can deliver high-speed data, Internet services and mobile multimedia as well as simple audio services to any fixed or mobile user. The system has been develop in such a way to maintain the compatibility with previous mobile systems (like second generation digital cellular systems, cordless telephones, etc.) providing also increased capacity, larger data ranges and supplementary services in order to make it more attractive.

UMTS provides an increased data rate capability, depending on the speed the user is moving: a rate of at least 144 kbit/s for full mobility applications in all environments is ensured, at least 384 kbit/s for limited mobility applications in macro and micro cellular environments and at least 1.92 Mbit/s for low mobility applications particularly in micro and pico cellular environments. The 1.92 Mbit/s rate may also be available for short range or packet radio applications in the macro cellular environment, depending on deployment strategies, radio network planning and spectrum availability.

The frequency bands allocated by ERC to terrestrial UMTS services are 1900-1980 MHz, 2010-2025 MHz and 2110-2170 MHz.

IV. SYSTEM ARCHITECTURE

The proposed system architecture, shown in figure 1, is composed by two main parts: the DVB-T system and UMTS system. The DVB-T system main components are:

- the DVB-T transmitter;
- the TS multiplexer - it multiplexes the transport streams coming from different sources: TV studios, IP /DVB-TS encapsulated streams;
- MPE encapsulation block – encapsulates others communications protocols into DVB-TS stream.

The system blocks that are specific to this architecture are the routing block and the mobile station. The routing block must be able to separate the IP traffic which will be transmitted over DVBT and the traffic transmitted over UMTS. The routing block rule should transmit the multicast traffic over the DVB-T (being addressed to multiple users). The remaining bandwidth will be shared for unicast traffic. The routing block should implement also a bandwidth management block which will decide the way the total bandwidth (the DVB-T remaining bandwidth and the UMTS bandwidth) will be distributed among users. The mobile station must have two wireless interfaces, one for DVB-T and the other UMTS. The mobile station could be a hand held device, a notebook or a computer attached to a mobile vehicle.

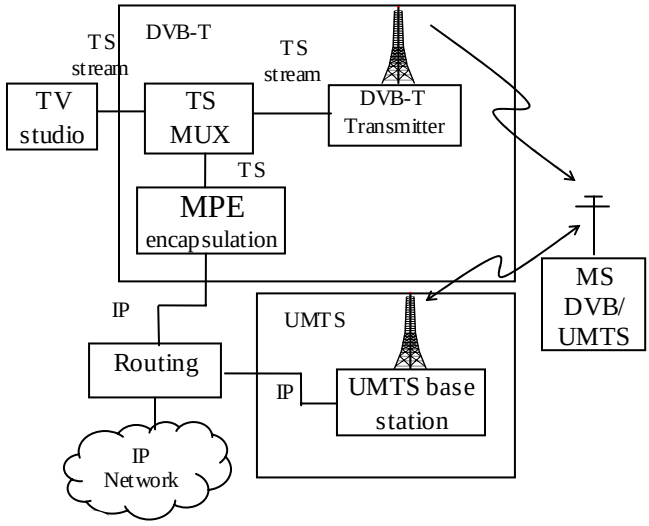

Fig. 1. DVB-T/UMTS system architecture

The architecture in figure 1 presents the way the DVB-T and UMTS are combined in order to realize an improved, high capacity, multimedia communication link. Another challenge for such a system is to deploy a fully mobile solution. It means that the user can move all over the coverage are and is able to have uninterrupted access to mobile services. For the UMTS system the global coverage problems is solved; the user cold have, from this point of view, a global access. For broadcasting services the availability is also global because, wile moving from one cell to another, the user could receive the programs without interruptions. The mobility aspects taken into account here refers the cases when the mobile switch from one UHF channel to another (figure 2) and when there is a transition from a DVB-T coverage area to a UMTS coverage area, which implies the reception of IP data to be switched from DVB-T to UMTS or opposite (figure 3).

In figure 3 the mobile moves from DVB-T to UMTS cell 2. In DVB-T cell it received an IP service via DVB-T downlink channel. In UMTS cell 2 there is no DVB-T coverage but it is via UMTS2 channel. So the traffic must be translated over UMTS2 channel.

In this respect, a traffic policy mechanism is required, which, in collaboration with the bandwidth management system, will route/direct the data traffic destined to a specific citizen, via the appropriate DVB-T stream (proper UHF channel within the same area or among different territories), in order to provide seamless access to the targeted services, besides enabling for any-time, any-where ubiquitous services distribution.

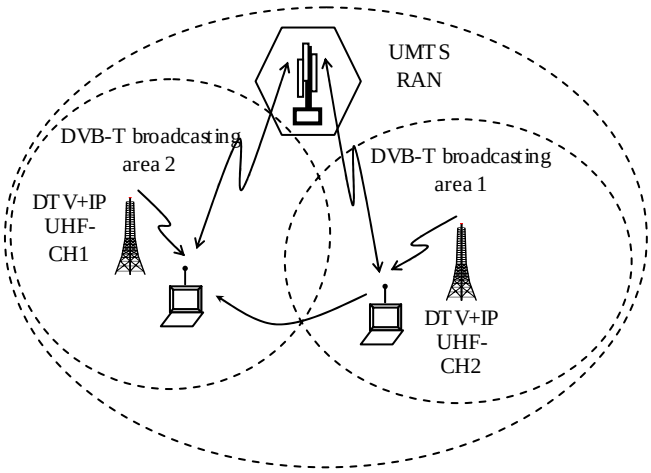

Fig. 2. Handover between different UHF DVB-T channels

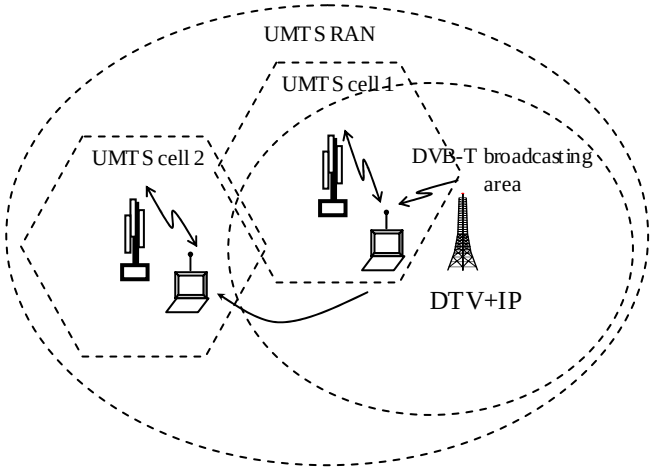

Fig. 3. Handover between DVB-T and UMTS

V. SYSTEM MOBILITY

A typical interactive broadcasting system has to deal with two types of mobility: the network layer mobility and data link layer mobility.

The network layer mobility implies that the mobile device can be found as an IP device when it moves. While moving it could travel across multiple IP networks (having different IP network addresses). It could be found in each network it crosses if it has an IP address belonging to that network. This implies that the mobile device must change its address while it moves from one network to another. Changing the IP address will cause the connection to be disrupted and lost.

The solution proposed for this kind of mobility is the Mobile IPv6. Mobile IP (RFC 2002), a standard proposed by a working group within the Internet Engineering Task Force, was designed to solve this problem by allowing the mobile node to use two IP addresses: a fixed home address and a care-of address that changes at each new point of attachment.

In Mobile IP, the *home address* is static and is used, for instance, to identify TCP connections. The *care-of address* changes at each new point of attachment; it indicates the network number and thus identifies the mobile node's point of attachment with respect to the network topology. The home address makes it appear that the mobile node is continually able to receive data on its *home network*, where Mobile IP requires the existence of a network node known as the *home agent*. Whenever the mobile node is not attached to its home network (and is therefore attached to what is termed a *foreign network*), the home agent gets all the packets destined for the mobile node and arranges to deliver them to the mobile node's current point of attachment.

When the mobile node moves, it *registers* its new care-of address at its home agent. The packets addressed the mobile user are sent to its home address firstly. It is the home agent task to forward the packets to the care of address. The further delivery requires that the packet be modified so that the care-of address appears as the destination IP address. This modification can be understood as a packet transformation or, more specifically, a *redirection*. When the packet arrives at the care-of address, the reverse transformation is applied so that the packet once again appears to have the mobile node's home address as the destination IP address.

For data link layer mobility we adopt the solution proposed by [4]. For seamless reception and uninterrupted access to the provided services i) the user must switch his DVB-T receiver device to the new UHF channel, and ii) the core infrastructure must redirect the IP traffic (targeted to him) from DVB-T cell 1 to the DVB-T cell 2 platform. In this respect, a handover policy mechanism is required for enabling efficient redirection of the IP traffic and fast transition from one UHF channel to another. The solution is based on a Location Aided DVB-T Handover (LADH) policy mechanism, capable of providing DVB-T mobility. The mobile transmits periodically information about its current location via UMTS. This information is processed by the LADH module and, if it decides that the mobile is about to enter another broadcast area, it will inform the Traffic Policy Manager (TPM) that the mobile user needs to switch to the new UHF channel. The TPM will transmit the control data (new UHF channel, communication parameters, etc) to the mobile user via DVB-T downlink channel. It will also reroute the traffic to the new DVB-T area. As a result the mobile user will switch to the new UHF channel

When switching from DVB-T to UMTS the LADH module will inform the mobile user that the broadcasted services will be lost. Also it will inform the TPM to reroute the IP data traffic (dedicated traffic) via UMTS, with a possibly decrease in QoS. The broadcasted services could be available at lower quality in UMTS also.

VI. SIMULATION RESULTS FOR DVB-T SYSTEM

The DVB-T transmitter and receiver system have been implemented in Simulink [8]. We didn't include in our model The synchronization block was not included in the simulated model. Different system configurations was considered: 2k mode for OFDM signal with 3/4 code rate for the convolutional coder, 64 QAM modulation and ½ code rate, 16 QAM modulation and 8k mode with ½ code rate and 16 QAM modulation.

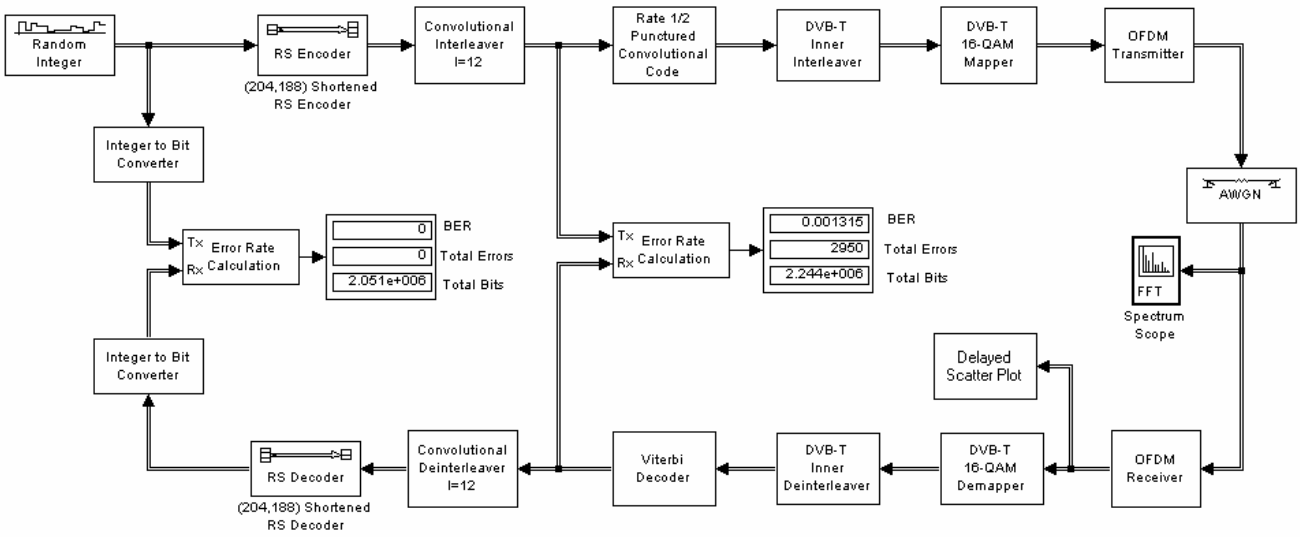

Figure 4 – DVB-T system simulink model

For radio transmission we used an AWGN channel model.

The simulation results are presented in figure 5 and figure 6. The BER is calculated after the Viterbi decoder

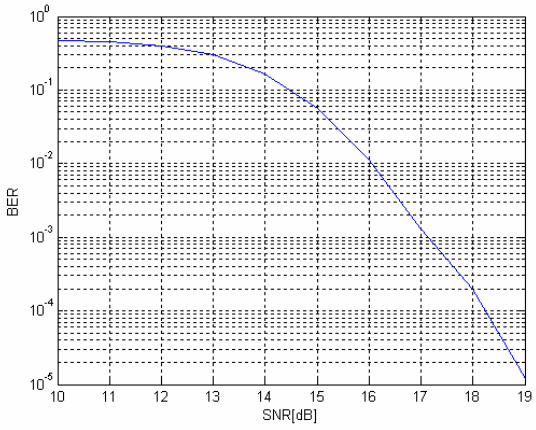

Figure 5 – BER for DVB-T (2k, 64QAM, 3/4)

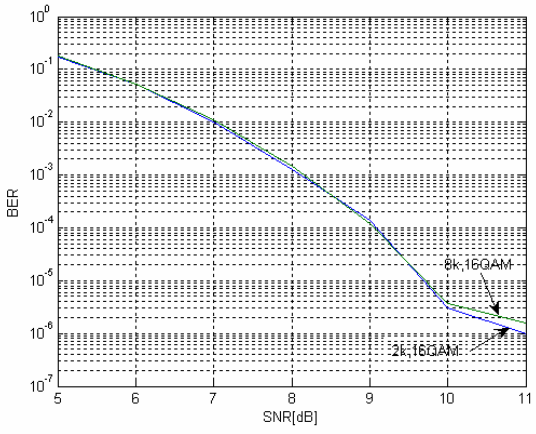

Figure 6 – BER for DVB-T (2k and 8k, 16QAM, 1/2)

VI. CONCLUSIONS

In this paper was presented an interactive broadcasting system solution based on DVB-T and UMTS hybrid access. The system architecture and the mobility aspects have been analyzed. Also some results obtained from DVB-T communication system simulations was highlighted. These simulations are part of an exhaustive set of simulations for the DVB-T system in order to have a better knowledge of its capacity and limitations, as well as to be able to verify their parameters in conjunction with an UMTS system.

REFERENCES

[1] S. Deering and R. Hinden, "Internet Protocol, Version 6 (IPv6) Specification", *RFC 2460*, December 1998.

[2] G. Fairhurst, H. D. Clausen and H. Linder, "Requirements for transmission of IP datagrams over MPEG-2 networks", *Internet Draft, draft-fair-ipdvb-req-04.txt*, work in progress, December 2003.

[3] ETSI: "Digital Video Broadcasting (DVB); DVB specification for data broadcasting", *European Standard EN 301192*.

[4] D. Negru, Y. Hadjadj-Aoul, A. Mehaoua, A. Kourtis, "IPv6 over DVB-T: Mobility Issues and Challenges".

[5] ETSI: "Digital Video Broadcasting (DVB); framing structure, channel coding and modulation for digital terrestrial television", *European Standard EN 300 744*.

[6] ATHENA Report: "ATHENA Digital Switchover: Developing Infrastructures for Broadband Access", August 2003.

[7] D. Johnson, C. Perkins and J. Arkko, "Mobility Support in IPv6", *Internet Draft, draft-ietf-mobileip-ipv6-24.txt*, work in progress, June 2003.

[8] *** - *Matlab 6.5 and 7.0 Manuals*, Mathworks Inc., http://www.mathworks.com .

Performance Analysis of Diversity Systems in Land Mobile Satellite Channels

Milan Živković[1], Nenad Milošević[2], Bojan Dimitrijević[3], Zorica Nikolić[4]

Abstract - **We present the analysis of LMS channel performances in the presence of multiple interferers employing various diversity receivers, including SC, MRC, and OC. The dependence of the BER of the average SNR/bit per branch is used as the measure of performances.**

Keywords – **BPSK signaling, SC, MRC, OC, Rayleigh fading, log-normal shadowing, diversity combining, cochannel interference.**

I. INTRODUCTION

Land Mobile Satellite (LMS) systems are becoming important part of today digital wireless systems. They offer a great number of applications and can serve many users over a wide area with low cost. It is very important to develop an accurate statistical model for the LMS channel between satellite and mobile user because the overall performances of LMS system strongly depends on it. In this paper we describe one single model of LMS channel in the presence of multiple cochannel interference and additive white Gaussian noise (AWGN). In a single model, the channel is characterized by a single statistical distribution, while a mixture model refers to a combination (weighted summation) of several statistical distributions. Single models are valid for stationary conditions, where the channel statistics remain approximately constant over the time interval of interest in a small area.

Namely, digital signaling is often followed by presence of fading and shadowing. Fading is the term used to describe the rapid fluctuations in the amplitude of the received radio signal over a short time interval caused due to the interference between two or more versions of the transmitted signals which arrive at the receiver at slightly different times [1]. The resultant received signal can vary widely in amplitude and phase, depending on various factors such as the intensity, relative propagation time of the waves, bandwidth of the transmitted signal etc... In mobile environments transmitted signal can be also affected by effect of shadowing which results in the long- term attenuation of received signal due to specific propagation environment (vegetation, buildings). The shadow fading can be classified on the line-of-sight (LOS) shadow fading and multiplicative shadow fading. LOS shadow fading affects only LOS component of received desired signal and attenuate it, while multiplicative fading affects both the LOS and scattered component of received desired signal attenuating the total power of desired signal.

Authors are with the Faculty of Electronic Engineering, Aleksandra Medvedeva 14, 18000 Nis, Serbia and Montenegro, E-mail: {mikaz, nemilose, zora}@elfak.ni.ac.yu,

In this paper we consider LMS channel with LOS shadowing modeled with Nakagami distribution, while fading is modeled with Rice distribution with shadow effect on LOS component. This model is modification of Loo's model widely used in literature where shadowing is modeled by lognormal distribution. Also, multiple interfering signals affected the desired multipath signal is modeled with Rayleigh distribution. Some simulation results are given in order to show improvement attained by implementing various types of diversity receivers including Selection Combining (SC), Maximal Ratio Combining (MRC) and Optimum Combining (OC).

II. SYSTEM MODEL

Consider BPSK signaling in LMS channel with AWGN and additional cochannel interference and corresponding diversity receiver. Let L be the number of diversity branches which is assumed to be independent and M is the number of independent interference signals. The received signal in matrix notation may be written as [2]

$$\mathbf{r} = \mathbf{u}_s \cdot x_s + \sum_{j=1}^{M} \mathbf{u}_j \cdot x_j + \boldsymbol{\eta} \tag{1}$$

where

$\mathbf{u}_s = \left[\alpha_{s,1}(t), \alpha_{s,2}(t), ..., \alpha_{s,L}(t)\right]^T$ - L-dimensional vector of fading amplitudes of desired signal.

$\mathbf{u}_j = \left[\alpha_{j,1}(t), \alpha_{j,2}(t), ..., \alpha_{j,L}(t)\right]^T$ - L-dimensional vector of fading amplitudes of jth interfering signal.

x_s - desired signal equals $\sqrt{E_b}$ or $-\sqrt{E_b}$ with *a priori* probability ½.

x_j - jth interfering signal equals $\sqrt{E_b}$ or $-\sqrt{E_b}$ with *a* priori probability 1/2.

$\boldsymbol{\eta} = \left[\eta_1(t), \eta_2(t), ..., \eta_L(t)\right]^T$ - L-dimensional vector of additive complex Gaussian noises.

E_b - energy per bit.

LMS channel model we consider [1] models fading amplitudes of desired signal with lowpass-equivalent complex envelope of the stationary narrowband shadowed Rice singled model which can be written as

$$\alpha_{s,l}(t) = \left|A_l(t) \cdot \exp\left[j\alpha_l(t)\right] + S_l(t) \cdot \exp\left[j\zeta_{l0}\right]\right|, \; l = 1, ...L \tag{2}$$

where $\alpha_l(t)$ is the stationary random phase process with uniform distribution over $[0,2\pi)$, while ζ_{l0} is the deterministic phase of the LOS component. The independent stationary random processes $A_l(t)$ and $S_l(t)$, which are also independent of $\alpha_l(t)$, are the amplitudes of the scatter and the LOS components, following Rayleigh and Nakagami distributions, respectively

$$p_A(a)=\frac{a}{b_s}\exp\left(\frac{-a^2}{2b_s}\right), \quad a\geq 0, \tag{3}$$

$$p_S(s)=\frac{2m^m}{\Gamma(m)\Omega^m}s^{2m-1}\exp\left(\frac{-ms^2}{\Omega}\right), \quad s>0 \tag{4}$$

where we except subscript *l* denoting the diversity branches.
If we consider Loo's model, the LOS component is modelled by lognormal distribution

$$p_S(s)=\frac{1}{\sqrt{2\pi}\sigma_s s}\exp\left(-\frac{(20\log s-\mu)^2}{2\sigma_s^2}\right) \tag{5}$$

where $\mu[dB]=E[20\log s]$ i $\sigma_s[dB]=Var[20\log s]$.
The corrensponding relation between sets of parameters for Nakagami na lognormal distribution is as follows [3]:

$$\mu[dB]=10*\left(\log\left[\frac{\Omega}{m}\right]+\frac{\Psi(m)}{\ln 10}\right) \tag{6}$$

$$\sigma_s[dB]=\frac{10}{\ln 10}\sqrt{\Psi'(m)} \tag{7}$$

where $\Psi(\cdot)$ is psi function and $\Psi'(m)$ is its first order derivativ.
As we consider model where changes of fading amplitudes are sufficently slow during one bit interval, we assumes that they are constant during one bit interval.
Quantity $E[A^2]=2\cdot b_s$ denotes the average power of the scatter component, $\Omega_s=E[S^2]$ denotes the average power of the LOS component, $\Gamma(m)$ is the gamma function, and *m* is Nakagami parameter (case *m* = 1 corresponds Rayleigh distribution), which determines the magnitude of obstruction of of the LOS. Smaller values of *m* correspond to urban areas, moderate values correspond to suburban and rural areas, while bigger values of this parameter correspond to open areas with no obstruction of the LOS.
After some algebraic manipulations, using (3) and (4) we obtain fading envelope pdf of desired signal, which is

$$p_{\alpha_s}(\alpha_s)=\left(\frac{2b_s m}{2b_s m+\Omega_s}\right)^m\frac{\alpha_s}{b_0}\exp\left(-\frac{{\alpha_s}^2}{2b_s}\right)\cdot {}_1F_1\left(m,1,\frac{\Omega_s{\alpha_s}^2}{2b_s(2b_s m+\Omega_s)}\right), \quad \alpha_s\geq 0 \tag{8}$$

where ${}_1F_1(\cdot,\cdot,\cdot)$ is the confluent hypergeometric function. For $m=0$, (8) simplifies to the Rayleigh pdf, while for $m=\infty$, it simplifies to the Rice pdf.
In order to derive system performances in sense of dependency of the average Bit Error Rate (BER) of the average signal-to-noise ratio (SNR), we must concern the second moment of fading anvelopes pdf, which is

$$E[\alpha_s^2]=\Omega_s+2b_s. \tag{9}$$

If we define instant SNR/bit as $\gamma_b={\alpha_s}^2\frac{E_b}{N_0}$, where $N_0(W/Hz)$ denotes one-sided spectral power density of additive whitte Gaussian noise, then average SNR/bit can be written as $\bar{\gamma}_b=E[\alpha^2]\frac{E_b}{N_0}=(\Omega_s+2b_s)\frac{E_b}{N_0}=2b_s(K_s+1)\frac{E_b}{N_0}$ where $K_s=\frac{\Omega_s}{2b_s}$ denotes Rice factor of desired signal fading anvelope..

Also, in this paper, we assume interference model where fading amplitudes of interfering signal is modeled as [2]

$$\alpha_{j,l}=a_{j,l}\cdot\cos(\phi_{j,l}), \quad j=1,...,M, \quad l=1,...,L \tag{10}$$

where $\phi_{j,l}$ denotes random phase of *j*th interfering signal in *l*th diversity branch, assumed to be uniformly distributed over the interval $[0,2\pi)$, and $a_{j,l}$ denotes fading anvelope of *j*th interfering signal in *l*th diversity branch that has Rayleigh pdf

$$p_{a_j}(a_j)=\frac{a_j}{b_j}\exp\left(\frac{-a_j^2}{2b_j}\right), \quad a_j\geq 0. \tag{11}$$

where average power of interfering signal fading anvelope is $E[a_j]=2\cdot b_i$
In this analysis we assume that fading anvelope of interfering signals are identically distributed with equal average power so $b_j=b_i$, for $j=1,...,M$.

TABLE 1
CHANNEL PARAMETERS FOR THREE DIFFERENT SCENARIOS, TAKEN FROM [2]

Channel type	b_s	m	Ω_s	$K_s[dB]$
Channel 1 (light shadowing)	0.158	19.4	1.29	6.1
Channel 2 (heavy shadowing)	0.063	0.739	$8.97\text{x}10^{-4}$	-21.48
Channel 3 (average shadowing)	0.126	10.1	0.835	5.2

III. THE SYSTEM PERFORMANCES

We analyze performances of proposed model of LMS channel with multiple cochannel interferers involving the three sets of parameters estimated from experimental measurements, which is taken from [3]. These parameters is given in Table 1. Channel 1 corresponds to light shadowing scenario which is associated with bigger values of parameters m and K_s. Channel 2 is used for description of heavy shadowing scenario corresponding with smaller values of m and K_s, and channel 3 is associated with average shadowing conditions. Percentage of time received desired signal level is greater than apscisa is given on Fig.1. This quantity is analytically derived using (8) as

$$P(\alpha_s > \alpha_{st}) = \int_{\alpha_{st}}^{\infty} p_{\alpha_s}(\alpha_s) d\alpha_s \,. \qquad (12)$$

Results derived by computer simulation of these quantity is also depicted in Fig. 1, and they agree with analytical results. We also presents some results derived by simulation of described LMS channel in the presence of multiple interferers employing diversity receivers. They are depicted on Figs. 2. - 4. for three analyzed types of LMS channels. We consider three techniques of diversity reception involving Selection Combining (SC), Maximal Ratio Combining (MRC) and Optimum Combining (OC).

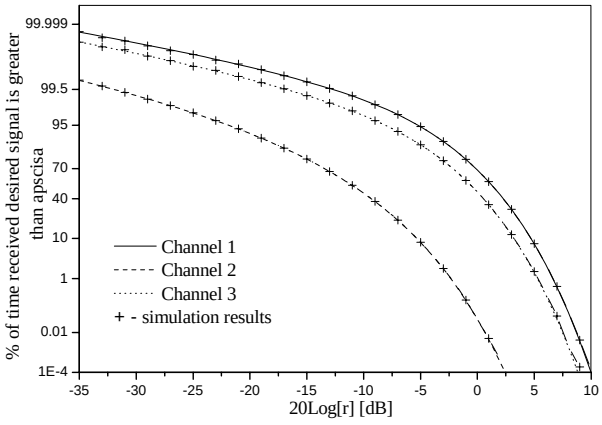

Fig. 1. Percentage of time received desired signal level is greater than apscisa

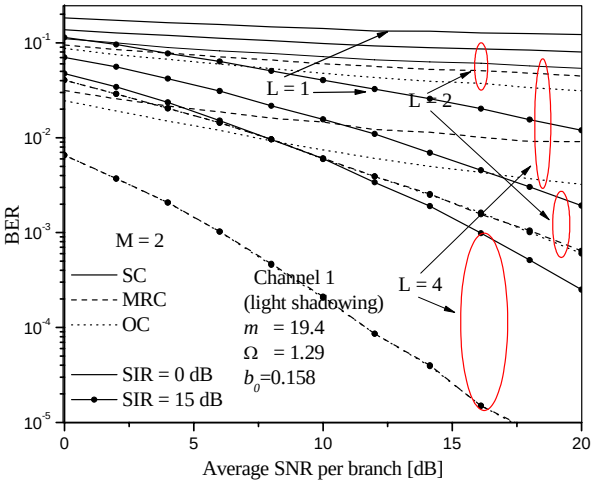

Fig. 2. BER dependency of average SNR/bit per branch for M =2 and $SIR_{per\ branch}$ = 0 and 15 [dB] in channel 1

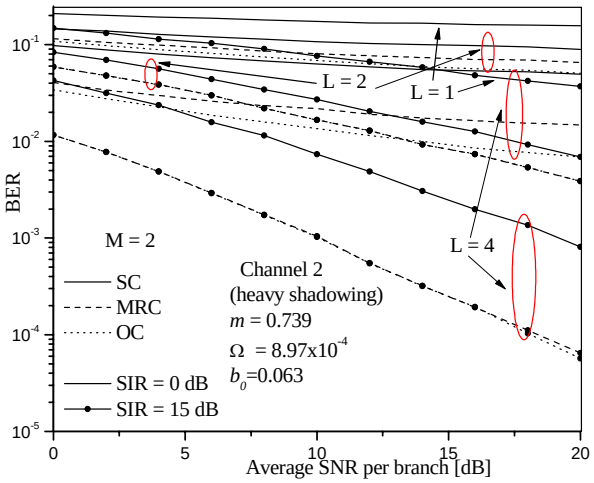

Fig. 3. BER dependency of average SNR/bit per branch for M =2 and $SIR_{per\ branch}$ =0 and 15 [dB] in channel 2

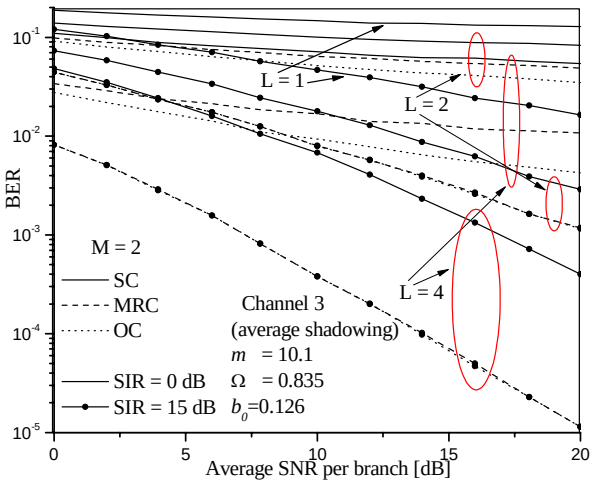

Fig. 4. BER dependency of average SNR/bit per branch for M =2 and $SIR_{per\ branch}$ =0 and 15 [dB] in channel 3

SC selects, among the L diversity branches, the branch providing the largest SNR ratio (or largest fading amplitude). In MRC the signals from all the branches are co-phased and individually weighed by fading amplitude of desired signal and than added. Weighting MRC vector is

$$\mathbf{w} = \mathbf{u}_s \tag{13}$$

so the signal at the output of combiner is

$$y = \mathbf{w}^H \mathbf{r} = \left|\mathbf{u}_\mathbf{s}\right|^2 \cdot x_s + \sum_{j=1}^{M} \mathbf{u}_s^H \mathbf{u}_j \cdot x_j + \mathbf{u}_s^H \boldsymbol{\eta} \tag{14}$$

This technique is optimal in environments without interference in sense of maximizing SNR and combating fading effect at the output of receiver, but it ignores the effect of cochannel interference [7]. OC addresses both effects of fading of desired signal and the presence of cochannel interference and optimize the signal-to-interference-plus-noise ratio (SINR) at the output of receiver [8]. Weighting OC vector is [7]

$$\mathbf{w} = \mathbf{R}^{-1}\mathbf{u}_s \tag{15}$$

where $\mathbf{R}$ is the interference-plus-noise covariance matrix across the array's elements

$$\mathbf{R} = E\left[\left(\sum_{j=1}^{M} \mathbf{u}_j \cdot x_j + \boldsymbol{\eta}\right)\left(\sum_{j=1}^{M} \mathbf{u}_j \cdot x_j + \boldsymbol{\eta}\right)^H\right]. \tag{16}$$

Note that OC weight vector is conditioned on desired signal fading amplitudes vector $\mathbf{u}_s$, interference signals fading amplitudes vectors $\mathbf{u}_j$, $j = 1,...,M$ and AWGN vector $\boldsymbol{\eta}$, while MRC weight vector is conditioned only on desired signal fading amplitudes vector $\mathbf{u}_s$.

As parameter we use different number of diversity branches (L = 1, 2, 4), M = 2 intefering signals and values of $SIR_{per\ branch}$, 0 and 15 [dB]. This quantity is defined as

$$SIR_{perbranch} = \frac{E[\alpha_s^2]}{M \cdot E[\alpha_j^2]} = \frac{\Omega_s + 2b_s}{2b_i} = 10\log\frac{b_s(K_s+1)}{b_i}[dB] \tag{17}$$

It can be seen that in case that responds to bigger value of $SIR_{per\ branch}$ = 15 [dB] MRC and OC performs equal, while in case with $SIR_{per\ branch}$ = 0 [dB], which responds to greater power of interfering signals, OC outperforms MRC. Also, differences between SC and optimal techniques become more significant in light shadow environment (channel 1) than in heavy shadow influenced channel 3.

IV. CONCLUSION

We present the analysis of LMS channel performances in the presence of multiple interferers employing various diversity receivers, including SC, MRC, and OC. Simulation results is given for different values of diversity branches (L = 1, 2, 4) and $SIR_{per\ branch}$ (0 and 15 [dB]) for three types of communication channel which parameters is taken from literature. It can be seen that in case that responds to bigger value of $SIR_{per\ branch}$ = 15 [dB] MRC and OC performs equal, while in case with $SIR_{per\ branch}$ = 0 [dB], which responds to greater power of interfering signals, OC outperforms MRC. Also, differences between SC and optimal techniques become more significant in light shadow environment (channel 1) than in heavy shadow influenced channel 3.

REFERENCES

[1] J.G. Proakis, Digital Communications, 3rd ed. New York: McGraw-Hill, 1995.

[2] M. G., Simon, M.-S., Alouini, *Digital Communication over Fading Channels: A Unified Approach to Performance Analysis*, New York: Wiley, 2000

[3] W. C., Abdi, M.- S., Alouini, M., Kaveh, "A New Simple Model for Land Mobile Satellite Channels: First- and Second-Order Statistic", IEEE Trans. Wireless Commun., vol. 2, No. 3, pp. 519-527, May 2003.

[4] C., Loo, C., "Digital Transmission Through a Land Mobile Satellite Channel", IEEE Trans. Commun., vol. 38, pp. 693-697, May 1990.

[5] C., Loo, "A Statistical Model for a Land Mobile Satellite Link", IEEE Trans. Veh. Technol., vol. VT-34, pp. 122-127, 1985.

[6] E., Lutz, D., Cygan, M., Dippold, F., Dolainsky, W., Papke, "The Land Mobile Satellite Communication Channel-Recording, Statistics and Channel Model", IEEE Trans. Veh. Technol., vol. 40, pp. 375-386, 1991.

[7] A., Shah, A. M., Haimovich, "Performance Analysis of Maximal Ratio Combining and Comparison with Optimum Combining for Mobile Radio Communications with Cochannel Interference", IEEE Trans. Veh. Technol., vol. 49, pp. 1454-1463, July 2000.

[8] R. K., Mallik, M. Z. Win, M. Chiani, A. Zanella "Bit Error probability for Optimum Combining of Binary Signals in The Presence of Interference and Noise", IEEE Trans. Wirel. Technol., vol. 3, pp. 395-407, June 2004.

Neural Models for Electromagnetic Field Strength Level Prediction – Application in RF Communications

Bratislav Milovanović, Zoran Z. Stanković, Maja Sarevska, Aleksandar V. Jovanović

Abstract – **New approaches of modelling in RF Communications using neural networks are presented in this paper. For that purpose new neural models are presented in a way that can integrate current empirical or semi-empirical knowledge from the problem domain which highly increases the efficiency of modelling. Possibilities of application presented neural models is demonstrated through results of modeling in the area of RF communications and mobile communications which have been realised in the Laboratory for Microwave Technique and Satellite Communications at the Faculty of Electronic Engineering in Niš.**

Keywords – **RF Communications, neural networks, modelling, neural model.**

I. INTRODUCTION

Today expansion of RF Communications, utilization of more complex RF equipment and systems and setting up more and more severe requests concerning performance and quality of their services certainly leads in appearing of a faster, more reliable and accurate tools for designing adequate reliable models. Methods for designing that are based on detailed physical-electromagnetic models are complex and very requesting concerning hardware platform and needed computation time. Simpler models, whether they are empirical, semi-empirical or statistical, usually have limitations, like achieved accuracy. The reason for that is the approximation used as a tool for simplification.

As a good alternative to go beyond these problems can be RF modelling based on artificial neural networks (ANNs) [1]. Encouraging results that have been achieved in this area showed that neural models can be much faster than EM models and also more accurate than different empirical and approximate models. There are two main characteristics of ANN. The first is that it represents highly parallel distributed architecture which is built from highly connected small processing units – neurons. This enables the modelling of a highly dimensional and highly nonlinear problems using fast data transfer from input to output of the neural model. The second characteristic is that ANN is not programmed to execute functional dependences designated in advance. These functional dependences are learnt on the basis of group of solved examples.

When the learning process of ANN is finished, it doesn't give good results just for solved examples that have been presented to it during the process of learning. It is also used for predicting solutions and examples that have not been presented during the training process. This is called a generalization characteristic.

Bratislav Milovanović, Zoran Stanković, Maja Sarevska and Aleksandar Jovanović are with the Faculty of Electronic Engineering, Aleksandra Medvedeva 14, 18000 Niš, Serbia and Montenegro, E-mail: [bata, zoran, jalex]@elfak.ni.ac.yu

This enables modelling of problems whose electromagnetic nature is not known enough by model based on ANN.

Great amount of encouraging results have been already achieved in the area of applying neural networks in EM wave's propagation modelling and designation of service areas of broadcasting and mobile communication systems [2-8]. In the past few years neural networks are applied in the area of modelling of a passive [9-12] and active [13-16] RF/microwave components, as well as RF microwave circuits modelling [17,18]. Certain success is achieved in the area of applying neural networks in antenna modelling [19,20] and in radar techniques concerning problem of detection and tracking radar targets [21]. Results that are derived by scientists from Laboratory for Microwave Technique and Satellite Television at the Faculty of Electronic Engineering in the area of broadcasting and mobile communications will be presented in this paper.

II. MAIN CONCEPT OF NEURAL NETWORKS AND TYPES OF NEURAL MODELS

Owing to the capability of a functional dependence's modelling exclusively on the basis of input data, Multilayer Perceptron Network (MLP) is a type of neural network that can be successfully applied in the modelling of a large number of RF communication problems.

If we want to obtain accurate MLP model we should provide large number of samples for training process when just MLP network is used as neural model. This may lead to big problems in using MLP neural models. The first one is that obtaining such a large number of samples can be difficult because they usually can be generated by time-consuming numerical methods or obtained by complex measurements. The second is that training of MLP neural network with such large number of samples can have implementation limitations, and can take much time without knowing the final results.

If there is certain knowledge about the problem that is modelled, it can be built in neural model aiming to significantly decrease the number of training samples that is needed for neural network and also to provide more efficient modelling process. This knowledge is presented by known empirical or semi-empirical functions that represent connections between input and output parameters. Those functions don't have to describe influence of all input parameters and to cover whole range of input values, but they have importance to help neural network to model all desirable functional dependences, even when there are limited and small number of training samples. Model that uses this knowledge can much faster and more reliable solve the problem that is modelled.

We can apply two different approaches in realization of such model. The first one is using hybrid empirical-neural model (HEN). Basic idea in using HEN model is that with

appropriate connection with neural model, empirical model can enlarge generalization and extrapolation capabilities of the

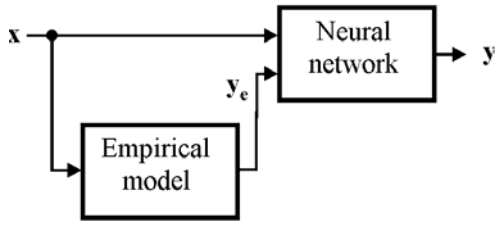

Figure 1.Hibrid empirical-neural model based on Input knowledge

neural network by presenting to it additional information about functional dependences of the problem.

Depending on which way empirical and neural model are connected in hybrid model we can differentiate two types of

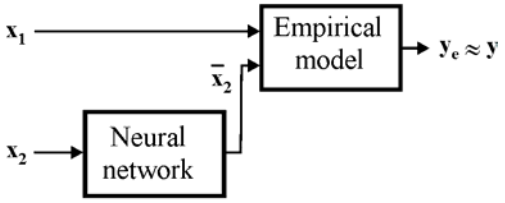

Figure 2 .Hibrid empirical-neural model based on mapping the input values

models that we used: HEN model based on input knowledge and HEN model based on mapping the input range.

HEN model which is based on input knowledge[18] (Fig. 1) is realized by taking the output from the empirical model as an additional input in neural network that models the problem. It can be so presented as:

$$\mathbf{y = y(x,w,b,y_e(x))} \quad (1)$$

Additional input in neural network is called the input of knowledge because empirical model use it to present empirical pre-knowledge about the problem that is modelled to neural model.

HEN model which is devised on mapping the input values (Fig. 2) consist of neural network that have to map values of one part of input parameters $\mathbf{x_2}$ into new values $\bar{\mathbf{x}}_\mathbf{2}$ that will enable the output of empirical model to be approximately equal to desired ones. This HEN model can be functionally described as:

$$\mathbf{y \approx y_e = y_e(x_1, \bar{x}_2(w, b, x_2))} \quad (2)$$

III. Application of Neural Networks in Broadcasting

The development of models for electromagnetic field level prediction, which properly describe realistic propagation conditions, is very important for designing of modern broadcasting systems. Large number of global and local parameters such as relief, object along propagation path, climate zone, refraction coefficient in atmosphere, multi-path propagation etc., have great influence on electromagnetic wave propagation. Existing statistical or deterministic models mostly take partially in consideration those influences. Among current statistical models for electromagnetic field level predicting in broadcasting, the most often applicable method is proposed by ITU-R, proposal 370-7[2,3]. This method is based on visual reading of electromagnetic field level directly from the curve which gives dependence of field strength level from distance and effective height of antenna. This read values has to be then corrected in accordance with values read from the curve which gives correction according to undulation of terrain, and values read from the curve which gives correction according to clearance angle of terrain. The main disadvantage of this method is that visual reading is time-consuming and inaccurate. It can be eliminated by automatisation by neural models developed in [2-4].

Empirical or semi-empirical propagation models for urban area which are mostly used today are based on too rough approximations without including in an appropriate manner the properties of the environment through which the signal is propagating. Frequently used COST 231 Walfisch-Ikegami model assumes that all streets in propagation area are parallel with the same width; all buildings are of the same height and equally spaced. In paper [5] is presented the architecture of HEN model which maps the input values. It takes into consideration parameters that characterize specificity of the propagation area through which signal propagates. Urban environment is divided into areas in which a particular type of objects is dominating (low buildings-houses, high buildings, green areas), characteristic parameters for every type of area are defined, and then every type is modelled by specific HEN model. In [5] is developed approximate model which is based on measurements obtained in Niš (80-120 measurements for specific area) and which is used as empirical model in HEN model. According to this model the path loss of propagation area is:

$$A = \sqrt{\rho_k}\,\Delta r\,\bar{X} + 5n\log\Delta r \quad (3)$$

where A is the path loss value along the section with the length Δr from the beginning of the area with the mean building density ρ_k, average partial loss of single building $\bar{X}$ and exponential loss index n. Parameters $\bar{X}$ and n can be obtained according to measured values. The approximate model presumes that the signal loss induced by a single building is the same along the whole section in the propagation area. However, during the propagation, electromagnetic wave encounters objects with different geometries and compositions, so the average partial loss of a single building $\bar{X}$ changes with the distance Δr.

Neural network in HEN model (Fig. 3.a) is used to correct this weakness of approximate model by modelling the partial loss of a single building, which changes according to function:

$$X = f(\bar{X}, \Delta r) \quad (4)$$

New value of partial loss X which is brought to approximative model can correct its accuracy by providing more accurate value for propagation loss.

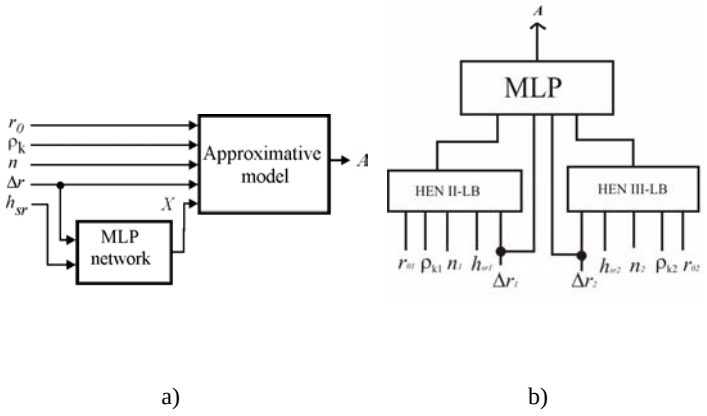

Figure 3. Hybrid empirical neural model of propagation area a) and two HEN models integrated in complex HEN model b)

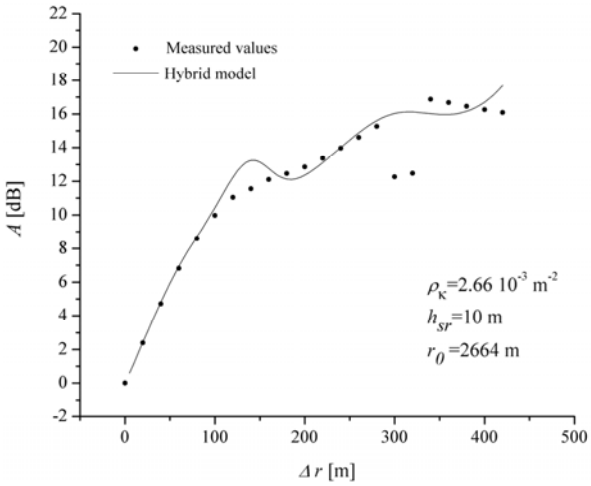

Figure 4. Comparison of results obtained by approxmatiive and HEN model with measured values for area L-III

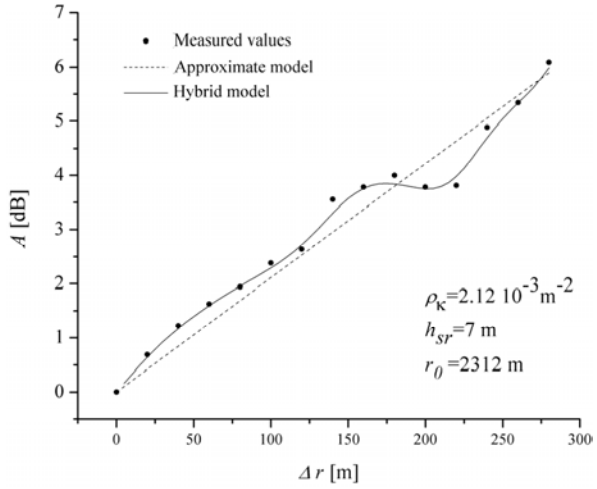

Figure 5. Comparison of results obtained by approximative and HEN model with measured values for L-II area

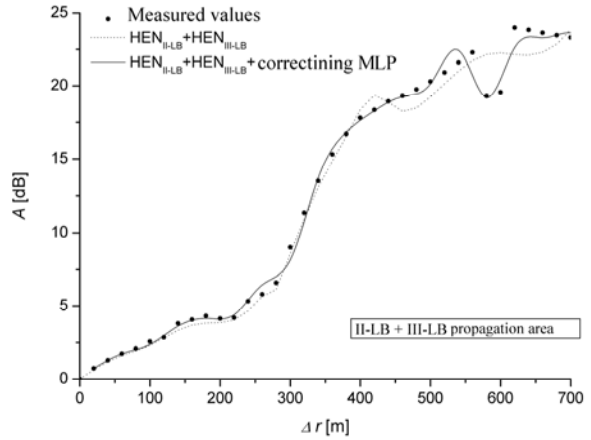

Figure 6. Propagation loss of area that passes through propagation area II-LB i III-LB obtained by HEN models and complex HEN model

TABLE 1- PARAMETERS OF LOW AND HIGH BUILDINGS AREA

Oblast	Low buildings				High buildings			
	L-I	L-II	L-III	L-IV	H-I	H-II	H-III	H-IV
ρ_k [10^{-3} m^{-2}]	1.88	2.12	2.66	3.23	0.32	0.38	0.58	0.73
h_{sr} [m]	13	7	10	9	24	22	30	20
d [m]	420	280	420	420	250	200	250	160
r_0 [m]	2350	2312	2664	2236	1224	1792	1064	3056

Parameters of urban propagation area of Niš with low and high buildings, that HEN models are developed for, are showed on table 1. Comparison of results obtained from approximative and HEN model with measured values for one area with low buildings is presented on Fig. 4. Results obtained by HEN model in area where measurements for checking accuracy and not for realization were taken out are showed on Fig. 5. Good results in this area show that HEN model can be applied for electromagnetic field level prediction in the area where no measurements are taken out which is the main advantage of this model. Propagation loss on path which passes through two or more area of different type can be obtained by addition of propagation losses of each area. Better results are obtained when each HEN model is connected to correctioning MLP network (Fig. 3.b) for whole propagation area. Obtained model is called complex HEN model.

IV. APPLICATION OF NEURAL NETWORKS IN MOBILE COMMUNICATIONS

Enlarging covering area, number of subscribers and the quality of subscriber services is not possible without effective interference problem solving between subscribers. One way to solve this problem is to apply the DOA (*Direction of arrival*) algorithm in order to determine the direction of electromagnetic radiation. DOA algorithm in first step is used for determination of the locations of mobile subscribers between which can interference arises, and then in second step using adaptive antenna array radiation is routed to desired subscribers. The most often used algorithm for DOA estimation is MUSIC algorithm (*Multiple signal classification*). It is hard to be implemented it in real time because of its extremely difficult computation. The good alternative for DOA estimation can be neural networks.

Architecture of RBF (*Radial basis function*) neural networks for DOA estimation of *U* mobile subscribers in the radiation area of *M* - element antenna array is showed at Fig.7 [6,7]. It models THE mapping $F:C^M \rightarrow R^U$ of output values of antenna array $\{x(t)=[x_1(t),...,x_M(t)]\}$to values in DOA space $\{\theta=[\theta_1,...,\theta_U]\}$where $x_i(t)$ is signal at the output of the *i-th* element, and θ_m is azimuth of the *m*-th subscriber. Signal $x_i(t)$ is determined as:

$$x_i(t) = \sum_{m=1}^{U} s_m(t) \cdot e^{-j(i-1)\cdot(\omega_0 d/c)\cdot\sin(\theta_m)} + n_i(t) \qquad (5)$$

where $s_m(t)$ is the signal of *m*-th subsriber, $n_i(t)$ is noise at *i*-th antenna element, and *d* is distance between elements of antenna. The output of antenna $x(t)$ is changable in time so during the preprocessing of data spatial correlation matrix $R=E\{x(t)x^H(t)\}$is formatted and brought at the input of the network [7]. Effficiency of the DOA estimation can be multiplied if instead one RBF network hierarchical neural model (HN) is used where the space of mobile subscribers is divided in sectors which are modelled by special networks. At Fig. 8 is presenting HN model which in first level detects subscriber in *i*-th sector by network based on probability (PNN-*Probabilistic* NN), and then in second level its DOA estimation is performed by RBF network of *i*-th sector which is activated by the output of the PNN network. In Fig. 9 are presented the results of simulation by HN model. (dashed line) with referent values (prompt line) for two mobile subscribers which change their mutual distance from 4° to 2° (with step 0.5°) with *M*=10 elements and *SNR* ratio is 10 dB.

V. CONCLUSION

New approaches of modelling in RF communications based on neural networks application can go beyond different kind of limitations in application of existing electromagnetic and empirical models. For that purpose are suitable neural models that have ability to use existing empirical or semi-empirical knowledge from the problem domain, which can make neural modelling very efficient. Results that are presented in this paper support this fact.

REFERENCES

[1] S. Haykin, *Neural Networks*, New York, IEEE, 1994.

[2] Z. Stanković, N. Vasić, "Neuronski pristup u modelovanju propagacionih krivih iz ITU-R P.370-7 preporuke", Zbornik radova XLVII konferencije ETRAN 2003, Herceg-Novi, jun 2003, sveska II, str. 269-272.

[3] B. Milovanović, Z. Stanković, A. Stošić "Prediction of the Electromagnetic Field Strength Level using Neural Model", *TELSIKS 2003 Conference Proceedings*, 1-3 october 2003, pp. 687-690.

[4] B. Milovanović, Z. Stanković, A. Đorđević, M. Veljković, "Neuronski model za predikciju nivoa EM polja u radio difuziji", *Zbornik radova YUINFO 2004 Konferencije*, Kopaonik, mart 2004.

[5] Z. Stanković, B. Milovanović, M. Veljković and A. Đordjević, "The Hybrid Neural-Empirical Model for the Electromagnetic Field Level Prediction in Urban Environments", *NEUREL 2004 Conference Proceedings*, Beograd, 23-26 september 2004, pp. 189-192.

[6] A.H. El Zooghby, C.G. Christodoulou, and M. Georgiopoulos, "A neural network-based smart antenna for multiple source tracking", *IEEE Trans. Antenna Propagat*., vol. 48, no.5, May 2000.

[7] M. Sarevska, B. Milovanović, and Z. Stanković, "Alternative Signal Detection For Neural Network-Based Smart Antenna", *NEUREL 2004 Conference Proceedings*, Beograd, 23-26 september 2004, pp. 85-89.

[8] A. Nešković, N. Nešković, Đ. Paunović "Microcell Coverage Prediction Using Artificial Neural Networks", *NEUREL 2002 Conference Proceedings*, Beograd, 23-26 september 2004, pp. 85-89.

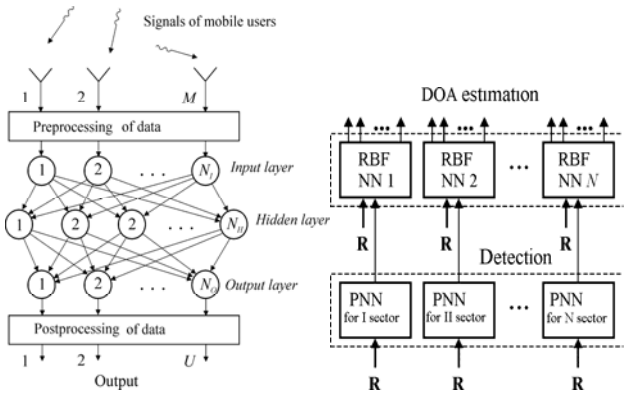

Figure 7. RBF neural network for DOA estimation

Figure 8. HNM for detection and DOA estimation of EM waves

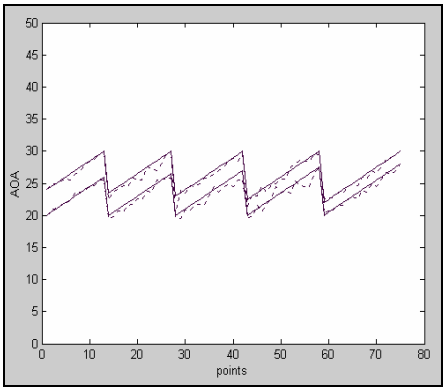

Figure 9. Results of simulation by HN model for two users at distance 4°, 3.5°, 3°, 2.5°, and 2°

[9] G. L. Creech, B. J. Paul C. D. Lesniak, T. J. Jenkins, and M. C. Calcatera, "Artifical neural networks for fast and accurate EM-CAD of microwave circuits", *IEEE Trans., MTT*, vol. 45, no. 5 pp. 794-802, 1997.

[10] Z. Stankovic, B. Milovanovic, V. Stankovic, "Microwave Planar Circuits Modeling with Knowledge-Based Neural Networks", *Zbornik radova YUINFO '99 Konferencije*, Kopaonik, Yugoslavia, mart 1999.

[11] B. Milovanović, Z. Stanković and S. Ivković, "Modelling of the Cylindrical Metallic Cavity with Circular Cross-Section using Neural Networks", *10th Mediterranean Electrotechnical Conference MELECON 2000*, Cyprus, pp. 449-452, vol.2, 2000.

[12] Z. Stanković, B. Milovanović and S. Ivković, "Microwave Cylindrical Cavity Applicators Modelling using Knowledge Based Neural Network", *TELSIKS 2001 Conference Proceedings*, september 2001, Niš, pp. 687-690.

[13] V. B. Litovski, J. I. Radjenovic, Z. M. Mrcarica, S. L. Milenkovic, "MOS Transistor Modeling using Neural network", *Electron. Lett.*, Vol. 28, No-18, 1992, pp. 1766-1768.

[14] V. Marković, O. Pronić and Z. Marinković, "Noise Wave Modeling of Microwave Transistors Based on Neural Networks", *Microwave and Optical Technology Letters*, Vol. 41 No. 4, May 2004, pp. 294-297.

[15] V. Markovic, Z. Marinkovic, "HEMT Noise neural model based on bias conditions", *COMPEL-The Inter. Journal for Computation and Mathematics in Electrical and Electronic Engin*., Vol. 23, Iss. 2, 2004, pp. 426-435.

[16] Z. Marinkovic, V. Markovic, "Neural Networks in Microwave Low-Noise Transistor under Various Temperature Conditions", *NEUREL 2004 Conference Proceedings*, Beograd, 23-26 september 2004, pp. 199-203.

[17] A. Veluswami, M. S. Nakhla, Q. Zhang "The Application of Neural Networks to EM-Based Simulation and Optimization of Interconnetcts in High-Speed VLSI Circuits", *IEEE Trans., Microwave Theory Tech*.,vol. 45, no. 5, 1997, pp. 712-723.

[18] B. Milovanović, V. Marković, Z. Marinković, Z. Stanković, "Some Applications of Neural Networks in Microwave Modeling", *JAC - Journal of Automatic Control*, Univeristy of Belgrade, Vol. 13(1), 2003, pp 39-46.

[19] H. L. Southall, J. A. Simmers, T. H. O'Donnell, "Direction finding in phased arrays with neural network beamformer", *IEEE Trans. on Antennas and Propagation*,, vol. 43, no. 12, pp. 1369-1374, 1995.

[20] G. Washington, "Aperture antenna shape prediction by feed forward neural networks", *IEEE Trans. on Antennas and Propagation*, vol. 45, no. 4, pp. 683-688, 1997.

[21] Q. Zhao, Z. Bao, "Radar target recognition using a radial basis finction", *IEEE Trans. on Neural Networks*, vol. 9, no. 4, pp. 709-720, 1996

Automatization of Electromagnetic Field Level Measurement in Broadcasting using GIS-MW Software

Zoran Stanković, Bratislav Milovanović, Marija Milijić, Aleksandar Atanasković

Abstract − **This paper presents a principle of automatization of electromagnetic field level measurement in broadcasting based on use of specialized GIS software package GIS-MW. This software package, developed in Laboratory for Microwave Technique and Satellite Television at Faculty of Electronic Engineering Niš, enables automatic measurements of EM field level, measurement results storage in space-relational database and their appropriate presentation in georeferenced space**.

I. INTRODUCTION

For work analysis and development of actual microwave systems, it is very important to strictly determine covering zones of their transmitters. If this is done successfully, EM field level measurements will be done in large number of different locations, especially in urban area. These measurements enable modeling of EM waves propagation using some empiric or neural model to improve broadcasting systems analysis [1,2]. These measurements should be correct and they should be finished for a certain period of time in the large number of locations. These requirements are not easily realized if the measurements are done manually, if the standard geographic maps are used and if the measurements results are saved as usual file.

Recently, majority of measurement systems have been automated and controlled by the computer while space-relational databases have been used for results storage and their representation. This improving has many benefits. Automation of measurement systems can give ability of using the large number of mathematical functions with measurement data, generation professional reports, synchronization of instruments and big speed of measurement process and many others benefits. Automated measurement place need less engineer time, which induces both effectiveness increasing and measurement cost decreasing. Use of space-relational database minimizes development time of application, increments level of data updating, the new information requirements are easily accepted and unification of reports and of data is enabled.

The problem of automatization of EM field level measurement is analyzed by two approaches concurrently: approach of maximal automation of measurement place (vertical automation) and approach of space automation (horizontal automation) with software support of specialize GIS (Geographic Information System) application which is named GIS-MW (Fig. 1) [3-6]. This GIS-MW software, which is presented in this paper, is improved version of previous GIS application [7].

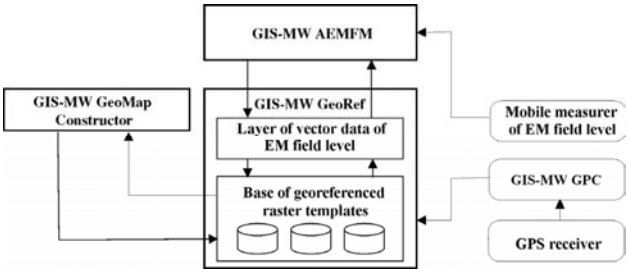

Fig. 1. Special GIS software package for automatization of EM field level measurement

Automation of measurement place is done by connecting notebook computer with removable manually EM field level measure equipment. Managing of measurement procedure and processing of measurement results are controlled entirely by software, which is executed by notebook computer. Ability of software package to strictly determine both measured signal level by GPS receiver and accurate geographic location of measurement place has enabled that this software has become one specialize GIS application.

GIS-MW software package for automatization of EM field level measurement, developed in Laboratory for Microwave Technique and Satellite Television in Electronic Faculty in Niš, is unique measuring system which consists of relational information system and different geographic data, as many geographic information systems. This application has been developed with maximal exploitation of processor power and integrated memory for effective processing large amount of complex type data, which is, in this case, elements of digital maps (bitmap pictures) obtained by scanning of geographic maps of measurement place and data obtained by mobile measure equipment of EM field level. Digital maps represent template in which accurate location of measurement place is determined by technique of signal processing from GPS device. Both location and level of measured signal are stored in local database and they are basis for latter graphical display of signals levels from different geographic locations.

Measuring equipment consists of notebook Pentium IV (2.5 GHz, 512 MB RAM) in which GIS MW software package is executed, GPS device Garmin 35PC, and mobile measure equipment of electromagnetic field Sperry RF-3200. First

Authors are with the Faculty of Electronic Engineering, Aleksandra Medvedeva 14, 18 000 Niš, Serbia and Montenegro
e-mail: [zoran, bata, marijam, beli]@elfak.ni.ac.yu

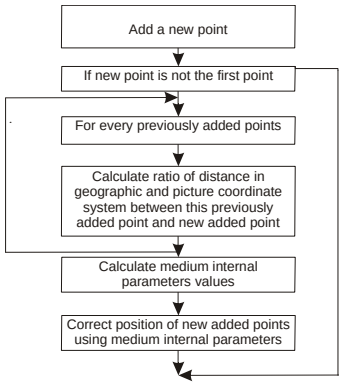

Fig. 2 Algorithm for correction of geographic point position

measurements, performed in wider area of city Niš, are used for testing of currently version of software systems.

II. GIS-MW SOFTWARE PACKAGE PARTS

GIS-MW software package for automatizated measurement of EM field level consists of four modules cooperating. First module is used for preparing georeferenced templates (*GIS-MW GeoMap Constructor*), second module is used for managing georeferenced system and for positioning in it (*GIS-MW GeoRef*) and the third module is used for data acquisition from field measure equipment and GPS device and their storage in database and their representing in the proper way in georeferenced space (*GIS-MW AEMFM*) (Fig. 1). Accuracy of position of measured geographic points is very important for GIS-MW software package whose previous version is improved with module GIS-MW GPC (Geographic Points Correction). This module corrects points positions and it increases accuracy of GIS-MW software package. In the first phase, different components have been developed almost entirely independently and they have been integrated in the second phase.

A. GIS-MW GPC (Geographic Points Corrector)

Accuracy of position of geographic points obtained by GPS device determines accuracy of whole *GIS-MW* software package. This accuracy depends of measuring device accuracy but it is not greater than it. To decrease overall system error, this program owns special statistic processing which is based on relationship between measured points in one area (Fig. 2). This module, for every two measured points, calculates ratio of distance between these two points in picture coordinate system and distance between these two points in geographic coordinate system and it minimizes overall error using medium value of pixel per meter. In that way, values of medium internal parameters are calculated and points coordinates correction is done using these values. Both accuracy of transformation of geographic coordinate system into picture coordinate system and accuracy of EM field measuring and representing of measuring results increase.

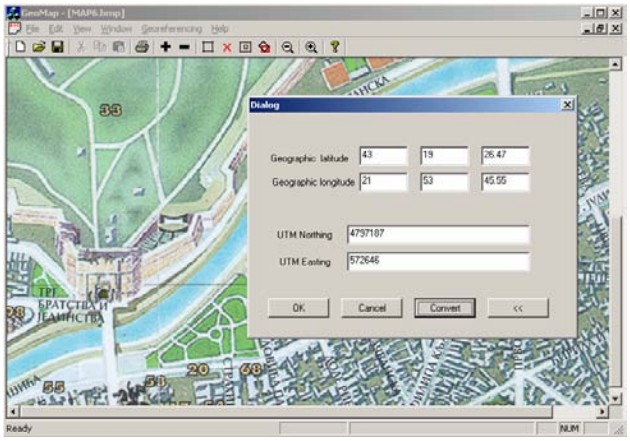

Fig. 3. Input parameters of essential points using GIS-MW GeoMap constructor module

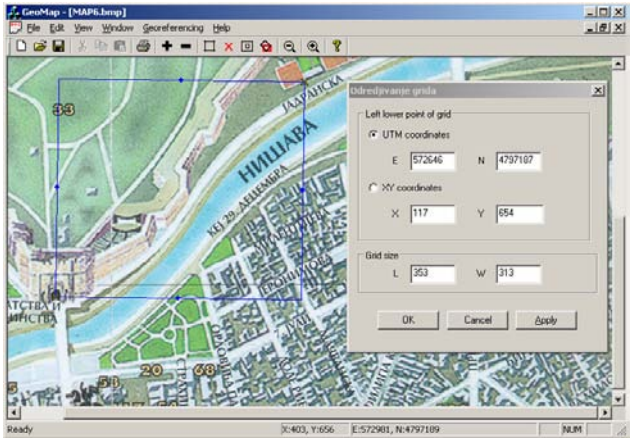

Fig. 4. Definition of UTM cells in software module GIS-MW GeoMap constructor

B. *GIS-MW GeoMap Constructor*

The principle of operating of this software module is based on transformation digital geographic maps into 2-dimensions bitmaps, which are projected by *Universal Transverse Mercator* (*UTM*) projection (term *Gaus-Krigerova* projection is used in German literature).

UTM projection defines position of every point at the surface of Earth on the basis of *Easting* and *Northing*, which are equivalent of geographic longitude and latitude [8]. *Northing* is distance of equator in meters, and *Easting* is distance of Central meridian in meters. Entire Earth surface is divided into 60 zones, each covers 6 degrees of geographic longitude and 8 degrees of geographic latitude with same exceptions. Central meridian, defined for every UTM zone, whose *Easting* is known and it is used for calculating *Easting* distance inside the zone. Transformation formula involves specialize *scale* factor which is the same for every zone (0,9996) at the Central meridian. Our country is in 33T zone where there are not system deviations.

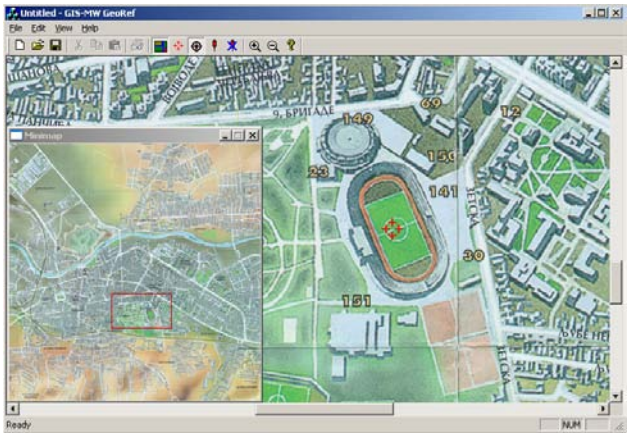

Fig. 5. Defining accurate position of selected geografic point using GIS-Mw GeoRef module

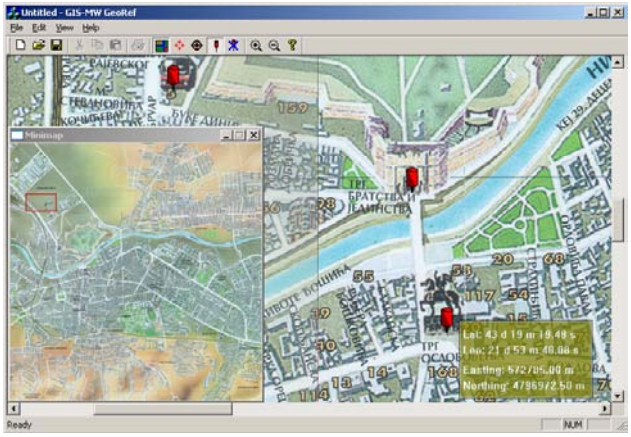

Fig. 6. Positioning of references points in GIS-MW GeoRef module

Digital maps (previously digitized by process of scanning or by some other way), where relevant points are assigned, represent input in this program. Output from program is group of maps, transformed into UTM orthogonal system. These maps make base of raster template of GIS-MW software package. Every raster template is mosaic group of UTM cells, which are 2-dimensional bitmap with equal resolution. Geographic coordinates of relevant points are input value in transformation formula and coordinates of other points in the map are determined by using them. Coordinates of relevant points are obtained by measuring geographic longitude and latitude by GPS device in different location of original map. The system error decreases using GIS-MW GPC module. Input digital map consists of pixels which position is defined in two coordinate systems:

1) *Picture coordinate system* – each pixel is defined by sorted couple of (x,y) coordinates.
2) *Geographic coordinate system* – each pixel is defined by geographic longitude and latitude in geographic map.

Operating with *GIS-MW GeoMap Constructor* module starts with labeling essential points in map, which should be transformed, and input their measuring values of geographic longitude and latitude (Fig. 3). These input parameters determine both internal transformation parameters and system accuracy, and GIS-MW GPC module is used to minimize transformation error. After that, the area, which should be transformed in one UTM cell, is denoted. Using suitable options in module, user can define resolution, width and length in pixels of UTM bitmap in which denoted area will be translate (Fig. 4). Transformation process involves processing started picture, which is named as orto-rectification process. This processing should eliminate both effect of picture distortion and rotation and some others noises which can occur during process of scanning and other way digitalizing of digital map.

After transformation, orto-rectificated picture is retrieved in UTM system. This picture is one element of collective pictures group, which represents georeferenced system, and after such editing, it should be treated by different processes.

C. *GIS-MW GeoRef*

GIS-MW GeoRef software module is used for managing georeferenced system of previously prepared geographic maps and for positioning in this system. This module uses group of two-dimensional raster pictures (i.e. bitmapped templates) which form unique electronic map with suitable interface for diapason of operations. This diapason of operations involves: manual (fine) scrolling throughout georeferenced space, system of fast scrolling using minimap, determining accurate position of selected geographic point (Fig. 5), reading position by input suitable geographic longitude and latitude and setting up adequate referenced points in georeferenced space (GIS markers) to enable easier performing same spacing operations (Fig. 6). This module manages superiors layer, composed of vector data which concern measuring of electromagnetic field and which are represented in georeferenced coordinate system. Positioning can be guided by information, which GPS receiver transmits.

D. *GIS-MW AEMFM (Automatic EM Field Measurement)*

GIS-MW AEMFM is module for automatic measurement of electromagnetic field level and for storing measurement results in vector layer of GIS software package. Also, this module must represent measurement results in georeferenced space using isofield lines in city map. Module manages mobile measurer of EM field level and it cooperates with *GIS-MW GeoRef* to get information about current position.

This vector layer is advanced layer, which is above level of geographic maps. In this case, vector layer consists of information concerning EM field level and place in the geographic map where this level has been measured. Using mobile measuring device of electromagnetic field, value of EM field is determined in the current position and GPS device gives information about current geographic coordinates. These measurement results are sent to notebook computer, GIS-MW GPC module corrects their position accuracy and they are written in database. During writing, geographic coordinates are translated into picture coordinates, and EM field zone, where measured EM field belongs, is determined. When the measurements are done, results are represented and isofield lines for this measuring area are drawn (Fig. 7).

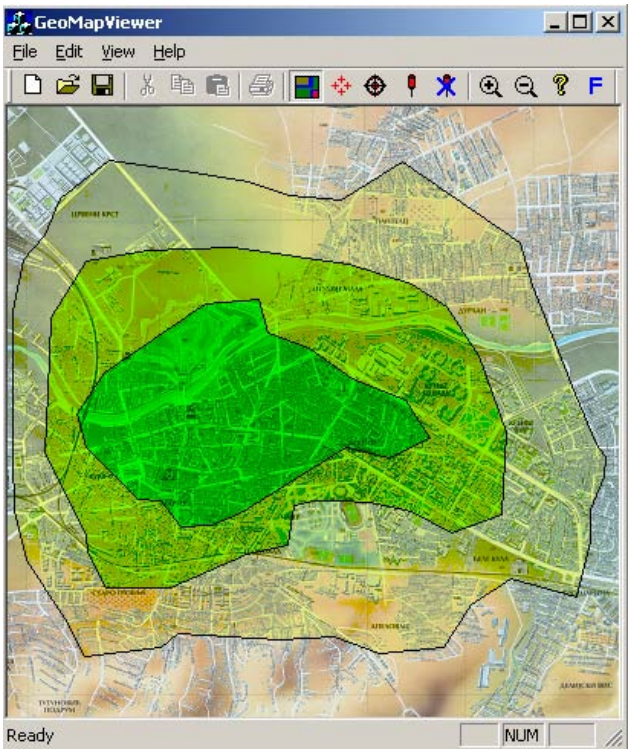

Fig. 7. Representing measurement results for total area of city Niš

III. INTEGRATED GIS-MW SOFTWARE PACKAGE FOR EM FIELD MEASUREMENT

The integration of *GIS-MW GeoMap Constructor*, *GIS-MW GeoRef* and *GIS-MW AEMFM* modules gets GIS-MW software package, which enables automatization of EM field level measurement in broadcasting (Fig. 1). Links between particular modules are direction of data exchange between software modules in the same time. Particular components are clearly isolated to see their roles in system. Central part of system is module *GeoRef* which manages georeferenced template, which is one of more complex problem. Communication with user and editing of digital maps are established by module *GeoMap Constructor*. Collection of data from measuring instruments and their final processing and storing are done by *AEMFM* module. Also, *GIS-MW GPC* module is very important because it determines accuracy of whole system.

Each components of the system can work relatively independently. The current reached version of *GeoMap Constructor* module can process digital picture and it can be enlarged with new functions. *GeoRef* module depends of previous module, but it can be enlarged with specific function for operating with *GeoTiff* formats picture which enable maps in different projections and which are useful instrument for exchanging information between independent GIS packages. *AEMFM* module collects data and processes data transmission.

IV. CONCLUSION

For analysis of transmitter operating in modern broadcasting systems, it is necessarily to do accurate measurements of EM field level in the large number of different locations and then to process these results effectively. Manual measurement needs a lot of time, errors can occur and preparing measurement results for processing is difficult. Automation of these measurements can reduce remarkably these problems and it can make analysis of broadcasting systems very fast and effective. Automated system for EM field level measurement, which is presented in this paper, introduces space component in data processing (space automation) by combining measurement results and space-geographic data. In this way, this system becomes one powerful geographic information system with many advantages. Characteristic of this system is its mobile. Also, it can be enlarged with many automated mobile measuring units, which can do data transmission by *wireless* link into *mainframe* computer in control room where data should be processed. Rate and quality of processing of measurement data get better and they make analysis more effective. Entire system can be serviced by several people, which may not have some computer knowledge, although they should have knowledge from their specific domain.

System precision and accuracy depend on measurement equipment quality because information, which is obtained by these instruments, is the majority source of data for this automated measurement system.

REFERENCES

[1] Lal Chand Godara “Handbook of Antennas in Wireless Communications”, Chapter 3, CRC Press, 2002.

[2] Bratislav Milovanović, Zoran Stanković, Aleksandar Stošić "Prediction of the Electromagnetic Field Strength Level using Neural Model", TELSIKS 2003 Conference Proceedings, Niš 2003, pp.457-46.

[3] http://www.gis.com.

[4] Đorđević-Kajan, S., Stojanović D., Petković M., Stoimenov L., "GIS tehnologije u telekomunikacionom i poštanskom saobraćaju", XVI Simpozijum o novim tehnologijama u poštanskom i telekomunikacionom saobraćaju, Beograd, 1998, 215-224.

[5] NCGIA National Center for Geographic Information and Analysis, http://ncgia.umesve.maine.edu.

[6] http://www.livonagis.co.yu.

[7] Zoran Stanković, Bratislav Milovanović, Marija Milijić, Aleksandar Atanasković, Automatizacija merenja nivoa elektromagnetnog polja u radiodifuziji korišćenjem GIS-MW softverskog paketa, YU-Info 2005 konferencija, Kopaonik, Srbija i Crna Gora, Mart 7.-11., 2005.

[8] http://hosting.soonet.ca/eliris/gpsgis/Lec2Geodesy

QoS Architecture over Heterogeneous Wireless Access Networks

Zoran S. Bojkovic[1], Bojan M. Bakmaz[2]

Abstract – **This article discussed the process of establishing end-to-end quality of service QoS and focused on the architecture over heterogeneous wireless access networks. The cross-layer QoS architecture for video delivery over multimedia wireless channel is presented and analyzed. There are several important blocks like QoS interaction between coding and transmission modules, QoS mapping and adaptation, as well as source rate constraint. This architecture enables to perform QoS mapping between statistical QoS guaranties at the network level to a corresponding priority class with different quality requirements.**

Keywords – **Quality of service QoS, Wireless access networks, rate constraint, transmission module, cross-layer QoS.**

I. INTRODUCTION

Quality of service QoS is a topic that attains a lot of attention in the wireless world. On the other hand, the future networking environment will be strongly characterized mainly by the heterogeneity of networks, especially regarding the network access part, although having IP as the common denominator. The end-to-end part will first traverse one access network that may be a high-speed wired segment (e.g., digital subscriber line DSL), a wireless local area network LAN, a wireless wide area network WAN (e.g., Universal Mobile Telecommunication System UMTS), or even a satellite one [1]. These segments will be supported by an IP-based core network, which will at least supply end devices with Internet Protocol IP connectivity, and include a gateway to the Internet backbone [2]. In heterogeneous, overlopping networks, a handover to a more suitable access point offer more capabilities needed to enable additional services [3]. For example, when passing by a wireless hot spot, one can perform a handover to this access point for a short period of time to facilitate some demanding service, such as download of bulk data or video conferencing. In many cases the availability of resources at the potential access point is not known before handover is performed. For QoS this means that the resources at the new access point should be allocated before attaching to the new network. This is often called anticipated or planed handover. This kind of handover offers two advantages. First, it reduces handover latency, because most signaling to set up resources in the new path is carried out in advance. Second, it avoids unsuccessful handovers or unnecessary periods of QoS degradation because handovers should only be performed if the resources are actually available.

QoS signaling architecture integrates resource management with mobility and location management. Resource management has to take care of admission control and release of requested resources. To ensure QoS on the data path, there are several techniques such as differentiated services or integrated services. Differentiated services (DiffServ) are a recent approach defined by the Internet Engineering Task Force (IETF). Instead of manipulating per-flow state at each router in a network, QoS preferences or guarantees at the network edges [4,5]. This requires the marking of packets in a special field of the IP header. Resource manager approach fulfills the main requirements of future mobile networks. It is flexible regarding heterogeneous networks with different QoS capabilities and mobility models. Mobility management protocols like Mobile IP ensure that a mobile device is reachable by a home address, although the local IP address may change during handover.

Traffic generated by the different services will not only increase traffic loads on the networks, but will also require different QoS requirements (call loss rate, delay and jitter) different streams (e.g., video, voice, data). Delivering multiple QoS to different types of traffic while maintaining high utilization of the bandwidth is the objective of efficient traffic management, which encompasses technologies like call admission control, policing, scheduling, buffer management and congestion control.

The article is organized as follows. We present important problems in mapping QoS parameters. We address cross-layer QoS architecture issues over wireless channel. We then introduce and explain substream rate constraint in the priority transmission module.

II. IMPORTANT ISSUES

With the development of third generation (3G) and fourth generation (4G) wireless standards, new broadband applications can be offered to mobile users [6]. In addition to delivering high bit rate applications, 3G and 4G systems are also expected to provide multiple QoS guarantees to different types of user applications. For example, the packet switched connection in the UMTS provides four different services differentiated by delay sensitivity conversational, streaming, interactive and background classes.

An important issue in providing multiple QoS guarantees to video applications in wireless systems is dynamic QoS management for services with mobility support. A dynamic

[1]Zoran S. Bojkovic is with the Faculty of Transport and Traffic Engineering, Vojvode Stepe 305, 11000 Belgrade, Serbia and Montenegro, E-mail: zsbojkovic@yahoo.com

[2]Bojan M. Bakmaz is with the Faculty of Transport and Traffic Engineering, Vojvode Stepe 305, 11000 Belgrade, Serbia and Montenegro, E-mail: bakmaz78@eunet.yu

QoS management system allows video applications and the underlying prioritized transmission system to interact with each other in order to cope with service degradation and resource constraint in a time-varying wireless environment.

Wireless networks have time-varying and nonstationary links due to:

- fading effects coming from path loss, large scale fading and small scale fading,
- roaming between heterogeneous mobile networks (e.g., from wireless LAN to wireless WAN),
- the variation in mobile speed, average received power and surrounding environments.

Consequently, the quality of wireless link varies, which can be measured by the variation of the signal-to-noise ratio (SNR) or the bit error rate (BER). These variations result in time-varying available transmission bandwidth at the link layer. This is also called the channel service rate. Since the buffer size at the link layer is typically finite, the time-varying channel service rate can induce buffer overflow and therefore packet loss, due to the bit rate mismatch between the transmitting packet and the channel service rate. At the application layer, due to variation in arrival time of video packets, some packets may become useless during playback if its arrival time exceeds certain threshold [4].

To coordinate effective adaptation of QoS parameters at video application layer and QoS mechanism are required. Generally speaking, a good cross-layer QoS mapping and adaptation mechanism that offers a good compromise between the video quality requirement and the available transmission resource is a challenging task. Namely, at the priority transmission layer, QoS is expressed in terms of probability of buffer overflow and/or the probability of delay violation at the link layer. On the other hand, at the video application layer, QoS is measured objectively by the mean squared over (MSE) and/or the peak signal-to-noise ratio (PSNR).

III. Additional Remarks

There are some important problems in mapping QoS parameters. These problems can be summarize as follows:

- A QoS-based adaptation model, which shows how QoS parameters of both priority transmission systems and video applications should be adjusted based on time-varying wireless channel.
- A coordination mechanism between priority transmission system and video applications, which provides interaction between two layers.
- A resource allocation within the priority transmission system, which provides soft QoS guarantees based on time-varying wireless channel.

In an attempt to take into account the problem statement, we will use QoS mapping architecture that will address cross-layer QoS issues for video delivery over wireless networks. Details for each important building blocks include: (a) the derivation of the rate constraint of a priority of transmission system; (b) the development of a QoS mapping mechanism that optimally maps video classes to statistical QoS guaranties of a priority transmission system and (c) the QoS interaction procedure between video applications and the priority transmission system to provide the best tradeoff between the video application quality and the transmission capability under time-varying wireless channel. To address these problems, we need a QoS mapping architecture that address cross-layer QoS issues for video delivery over wireless networks.

IV. Cross-layer QoS Architecture over Wireless Channel

This architecture considers an end-to-end delivery system for a video source from the sender to the receiver, which includes source video encoding module, cross-layer QoS mapping and adaptation module, link layer packet transmission module, wireless channel which is time varying and nonstationary, adaptive wireless channel modeling module, and decoder output at the receiver. Cross-layer QoS architecture for video delivery over multimedia wireless channel is shown in Fig. 1.

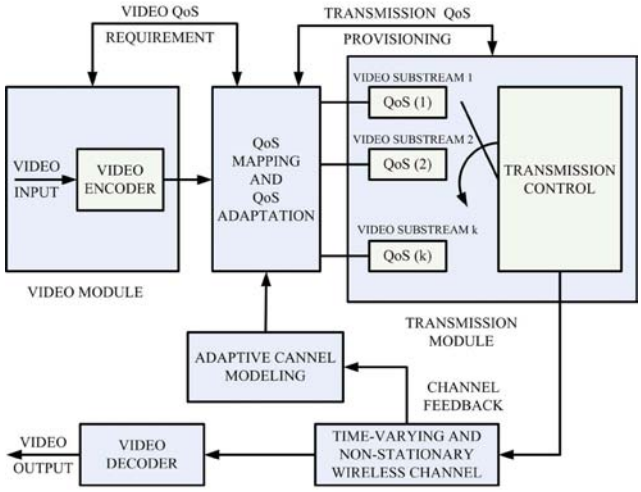

Fig. 1. Cross-layer QoS architecture for video delivery over multimedia wireless channel

The wireless channel is modeled at the link layer, since modeling of this layer is more amenable for analysis and simulations of the QoS provisioning system (e.g., delay bound or packet loss rate). The wireless link is expected to be fading, time-varying and nonstationary, which will provide a time-varying available transmission bandwidth for video service. The characteristics of the wireless channel can be modeled by a discrete-time Markov model, where each state represents the available transmission rate under current channel conditions. The channel modeling process is performed by the adaptive channel modeling module.

The QoS mapping and adaptation module is the key component to achieve cross-layer QoS mapping in the video delivery architecture. Unlike the adaptive channel modeling module and link-layer transmission module, the QoS mapping and adaptation module is application specific. It is designed to optimally match video application layer QoS and the underlying link-layer QoS. At the video application layer, each video packet is characterized based on its loss and delay properties, which contribute to the end-to-end video quality and service. Then, these video packets are classified and

optimally mapped to the classes of link transmission module under the rate constraint. The video application layer QoS and link-layer QoS are allowed to interact with each other and adopt along with the wireless channel condition. The objective of these interaction and adaptation is to find a satisfactory QoS tradeoff so that each end user's video service can be supported with available transmission resources.

In the link-layer transmission control module, we employ a class-based buffering and scheduling mechanism to achieve differentiated services. A strict priority scheduling policy is employed to serve packets among the classes. That is, packets in a higher priority queue will always be sent first: packets in the lover priority queue will be sent only if there is no packet in the higher priority queues. Also, packets within the same class queue are served in a firs-in-first-out (FIFO) manner. Based on the class-based buffering and strict priority scheduling mechanism, we expect that each QoS priority class will have some sort of statistical QoS guarantees in terms of probability of packet loss and packet delay.

V. Substream Rate Constraint in the Priority Transmission Module

The rate constraint specifies the maximum input data rate to a particular buffer class that can be transmitted with certain statistical QoS guarantee. It will be used as the basis to allocate the channel bandwidth for data transmission. Since the wireless channel is expected to be fading, time-varying and nonstationary we will start with characterizing time-varying nonstationary wireless channel rate.

Suppose that the service rate for the time-varying wireless channel can be modeled by a first-order L-state Markov model, within each small time interval "g". Denote $X_C(u)$ as the state of the channel at time "u" and $X_C(u) \in \{1,..., L\}$. Each state $X_C(u)=i$ corresponds to a channel link condition, which can be characterized by an achievable channel transmission rate r_i. The channel transmission rate at state i can be computed as

$$r_i = R \cdot \log_2(1+\gamma_i) \tag{1}$$

in bits per second. Here, R is the transmission bandwidth in Hz and γ_i is the SNR value of the wireless channel condition at state i (physical layer parameter). For the L-state discrete-time Markov chain, denote p_{ij} as the state transition probability from state "i" (at time u-1) to state "j" (at time u) with a transition time interval of 1 time unit and 1<g. It means that $p_{ij}=P\{X_C(u)=j/\ X_C\ (u-1)=i\}$. Then, the L-state Markov chain can be completely characterized by the L×L state transition matrix which can be written in the form [8]

$$P_{transition} = \begin{pmatrix} p_{11} & \cdots & p_{1L} \\ \cdots & & \cdots \\ p_{L1} & \cdots & p_{LL} \end{pmatrix} \tag{2}$$

We can calculate the state probability for Markov model within the time interval g, which we denote in the form $[p_1, p_2, ..., p_L]$. Therefore, the expected link-layer transmission rate $r_{channel}$ during this time interval g is

$$r_{channel} = \sum_{i=1}^{L} r_i \cdot p_i \tag{3}$$

where r_i is the achievable link layer transmission rate given by Eq. (1). At the end of each time interval g, the state transition matrix in Eq. (2) will be updated by the adaptive channel modeling module to reflect the nonstationay nature of the wireless environment.

Fig. 2 shows a queueing system for time-varying source rate and channel service rate. The amount of data generated by the source from time "0" to "t" is a random variable of the form

$$A(t) = \int_0^t \alpha(u)du \tag{4}$$

where α(u) is the source data generated rate. The amount of data A(t) will be stored in the buffer of size B^{max} awaiting for transmission. On the other hand, the accumulated channel service from time "0" to "t" is of the form

$$S(t) = \int_0^t \alpha^{(c)}(u)du \tag{5}$$

where $\alpha^{(c)}(u)$ is the channel service rate at time "u". The time-varying channel service rate has been modeled by a L-state discrete time Markov chain, where $\alpha^{(c)}(u) \in \{r_1, r_2, ..., r_L\}$.

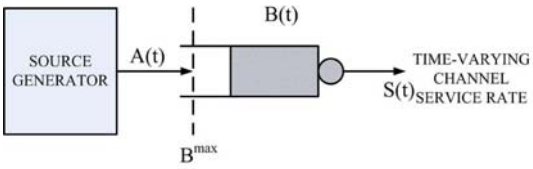

Fig. 2. A queueing system for time-varying source rate and channel service rate

The stochastic behavior of the accumulated channel service S(t) can be described by the concept of effective capacity, which can be written in the form [9]

$$\mu(\theta) = -\frac{\Lambda^{(c)}(\theta)}{\theta} \tag{6}$$

where $\Lambda^{(c)}(\theta)$ is the asymptotic log-moment generating function of S(t), defined as

$$\Lambda^{(c)}(\theta) = \lim_{t\to\infty} \frac{E\left[-\theta\ S(t)\right]}{t}$$

where θ is the QoS exponent of transmission service. It is called the QoS exponent to the effective capacity μ(θ). The

parameter θ is related to the statistical QoS guarantee, e.g., packet loss probability of the time-varying channel. The statistical QoS guarantee in terms of packet loss probability can be derived as a function of θ in the form

$$P\{B(t) > B^{\max} \mid \theta\} \approx \xi \cdot e^{-\theta \cdot B^{\max}} \quad (7)$$

Here, B(t) represents the buffer occupancy at time t, B^{max} is the maximum buffer size, ξ is the probability that the buffer is not empty and $\xi \cdot e^{-\theta \cdot B^{\max}}$ is the approximate packet loss probability guarantee. As it can be seen, the effective channel capacity is related with the statistical QoS guarantee through the QoS exponent θ. Effective capacity μ(θ) in Eq. (6) imposes a limit for maximum amount of data that can be transmitted over time-varying channel with statistical QoS guarantee in (7). The statistical QoS guarantee required by the may mismatch with the statistical QoS guarantee provided by the channel [10]. In particular, if the source generating rate corresponding to the effective capacity of the QoS exponent "k" of the generated source, is grater than the effective channel capacity, i.e., μ(k)>μ(θ), part of the source rate would be expected to be cut-off or shaped. Here, θ represents QoS exponent of transmission service.

The maximum source rate that can be transmitted when there is a mismatch between the QoS exponents corresponding to the source and channel

$$\mu(k) = \begin{cases} \mu(\theta), & 0 \le k \le \theta \\ \mu(\theta)\dfrac{\theta}{k} + \dfrac{k-\theta}{k} e_{S(t)}(k-\theta), & k > \theta \end{cases} \quad (8)$$

where k>0 is the QoS exponent corresponding to the packet loss probability required by the source generation rate, while μ(k) is the source generation rate with QoS exponent k. At the same time

$$e_{S(t)}(k-\theta) = \frac{\Lambda^{(c)}(\theta - k)}{k-\theta}$$

can be viewed as the effective bandwidth with the QoS exponent k-θ.

The rate constraints for multiple priority classes are dependent on each other. Channel occupation by higher priority classes, i.e., rate constraints affect the rate constraints of lower priority classes, the lower opportunity of channel resource usage from lower priority ones.

VI. Concluding Remarks

The necessity to support high-capacity bursty traffic in extremely unpredictable wireless channels has posed a great challenge to all existing air link technologies based on time-division multiple access (TDMA) or code-division multiple access (CDMA) alike. Many research initiatives have been underway to investigate the issues in which type of multiple access technologies could be most suitable for wireless applications. A new wave of worldwide research is on the way to search for next generation multiple access technologies, which should effectively address all the constraints and problems existing in current TDMA and CDMA technologies, such as poor bandwidth efficiency, strictly interference-limited capacity, difficulties in performing rate-matching algorithms, and complexity in implementing fast adaptive equalizers. As we know, the access link remains the primary bottleneck in the network due to a number of existing economical and technological factors. As the available access bandwidth increases and more flexible operations management, administration and provisioning tools become available, new user applications requiring broadband connectivity become more attractive and economically viable. In some cases, these applications are bandwidth-intensive, such as video on demand. In other cases, broadband access allows less efficient use of the line in order to gain efficiencies in other portion of the network. Voice over IP is an example of the latter. A QoS mapping architecture that address cross-layer QoS issues for delivery over wireless networks include: rate constraint of a priority transmission system, the development of a QoS mapping mechanism that optimally maps video classes to statistical QoS guarantees of a priority transmission system and QoS interaction procedure between applications.

References

[1] K. R. Rao, Z. S. Bojković, D. A. Milovanović, *Introduction to Multimedia Communications: Applications, Middleware, Networking*, Wiley, 2005.

[2] K. R. Rao, Z. S. Bojković, D. A. Milovanović, *Multimedia Communication Systems: Techniques, Standards and Networks*, Prentice-Hall, 2002.

[3] Z. Bojković, B. Bakmaz, "Quality of Service and Security as Frameworks toward Next-Generation Wireless Networks", *Proceedings of the 6th WSEAS International Conference on Automation and Information ICAI'05*, Buenos Aires, Argentina, March 2005., http:/www.wseas.org

[4] K. R. Rao, Z. S. Bojković, *Packet Video Communications over ATM Networks*, Prentice-Hall, 2000.

[5] Z. Bojković, B. Bakmaz, "Quality of Service in DiffServ IP-based Networks", *WSEAS Transactions on Communications*, issue 1, vol. 4, pp. 30-35, January 2005.

[6] A. Jamalipour, T. Wada, T. Yamazato, "A Tutorial on Multiple Access Technologies for Beyond 3G Mobile Networks", *IEEE Commun. Mag.*, vol. 42, no. 2, pp. 110-117, Feb. 2005.

[7] D. Wu, R. Negi, "Effective Capacity: A Wireless Link Model for Support of Quality of Service", *IEEE Transactions on Wireless Commun.*, vol. 2, pp. 630-643, July 2003.

[8] H. Wang, N. Moayeri, "Finite-state Markov Channel-a Useful Model for Radio Communication Channels", *IEEE Trans. Vehicular Tech.*, vol. 44, pp. 163-171, Feb. 1995.

[9] C. S. Chang, J. A. Thomas, "Effective Bandwidth in High Speed Digital Networks", *IEEE Journal on Selected Areas in Commun.*, vol. 13, pp. 1091-1100, Aug. 1995.

[10] Z. Bojković, "Challenges in Multimedia Across Wireless Broadband", *Invited plenary lecture presented at the 6th WSEAS International Conference on Automation and Information ICAI'05*, Buenos Aires, Argentina, March 2005.

Capacity Evaluation of CDMA Downlinks Using Optimum Orthogonal Code Allocation Scheme

Stiliyan Y. Paunov[1]

Abstract – **This paper presents an optimum orthogonal code allocation in case of the multiple-scrambling-code approach. The multiple-scrambling-code approach that was used in the aforementioned capacity results for the code limitation cases fully utilizes the soft capacity feature of CDMA. If the orthogonal code is short in a cell, then a new orthogonal code set is made appending a new scrambling code. However, we can no longer expect to avoid intracell interference between signals assigned different scrambling codes, and therefore the assignment of the orthogonal codes to the respective signals is an important study item if we continue to consider the multiple-scrambling-code approach. Finally, the numbers of mobile stations for the optimum code allocation were compared with those for the worst code allocation.**

I. INTRODUCTION

The orthogonal code limitation affects CDMA (Code-division multiple access) performance: The fewer the orthogonal codes, the smaller the capacity. This code limitation problem is also discussed extensively in [1], which takes a theoretical approach.

Two general approaches are used to cope with the code limitation: the call-blocking approach and the multiple-scrambling-code approach. In call blocking, the arrival of a new call is blocked if the number of MSs (mobile stations) connected exceeds the number of orthogonal codes available. This approach sacrifices some of the soft capacity feature of CDMA because a call will be rejected in case of orthogonal code shortage even though the interference has not reached the specified limit. However, the multiple-scrambling-code approach that was used in the aforementioned capacity results for the code limitation cases fully utilizes the soft capacity feature of CDMA; if the orthogonal code is short in a cell, then a new orthogonal code set is made appending a new scrambling code. However, we can no longer expect to avoid intracell interference between signals assigned different scrambling codes, and therefore the assignment of the orthogonal codes to the respective signals is an important study item if we continue to consider the multiple-scrambling-code approach.

In cellular CDMA systems, downlink signals are spread by orthogonal spreading codes in order to minimize the interference between the signals [2]. However, because the number of orthogonal codes is limited, the downlink capacity is also limited once the number of MSs connected exceeds the number of orthogonal codes available. The impact of code limitation depends on such factors as the data transmission rate and the forward error control coding rate and is especially significant when soft handoff is used. This is because soft handoff accelerates the consumption of the orthogonal codes in accordance with the number of base stations connected to an MS. The number of downlink channels can be increased by enabling multiple scrambling codes to be allocated to a single BS. But a downlink signal is then subject to strong interference from the other signals assigned different scrambling codes. In this paper we discuss, with the help of a general genetic algorithm toolkit implemented in Java , an optimum code allocation maximizing the average SIR(Signal-to-interference power ratio) measured at MSs within a cell. A genetic algorithm is a search/optimization technique based on natural selection. Successive generations evolve more fit individuals based on Darwinian survival of the fittest. The genetic algorithm is a computer simulation of such evolution where the user provides the environment (function) in which the population must evolve [3].

II. AVERAGE SIR

The term *code allocation* throughout this section means an allocation of codes given as products of the multiplication of a basic orthogonal code set and multiple scrambling codes. We denote as *S* the number of basic orthogonal codes and denote as N the number of orthogonal code sets provided for a cell. The transmission power for downlink signals is fixed, and the orthogonal code occupancy ratio k_i is the ratio of the number of MSs assigned the *i*th orthogonal code set to the number *n* of all MSs within a cell, where the sum of k_1 , k_2 ,……., and k_N is 1. Defining the code occupancy ratio vector of k = *(*k_1, k_2,……, k_N*)*, we can write the following equation for the average SIR measured at MSs within a cell:

$$\bar{\Gamma}(k)=\sum_{i=1}^{N}k_i\frac{P_g}{\varepsilon k_i n+(1-k_i)n}=\frac{P_g}{n}\sum_{i=1}^{N}\frac{1}{\varepsilon+1/k_i-1} \quad (1)$$

where P_q and $\in$ denote the processing gain and the interference figure. The value of $\in$ ranges from 0 to 1, and $\in$ = 0 denotes no multipath distortion in the downlink channel. In (1), $\in$ = 1 is assumed between downlink signals assigned different scrambling codes, hence the signals with different scrambling codes interfere completely with each other. We also assume in (1) a single-cell environment, that is, we exclude the intercell interference in measurement of the average SIR.

[1]Stiliyan Paunov is with the Faculty of Communication, Technology, Sofia, Bulgaria, E-mail: stp@tu-sofia.bg

III. EXTREME VALUE OF AVERAGE SIR

When k* = $(k_1^*, k_2^*,\ldots,k_N^*)$ is the code occupancy ratio vector giving an extreme value of $\overline{\Gamma}(k)$ and when

d = $(d_1, d_2,\ldots, d_N)$ is the variation vector, the equation

$$\frac{d\overline{\Gamma}(k^* + \alpha d)}{d\alpha}\Big|_{\alpha=0} = 0 \qquad (2)$$

is satisfied for an arbitrary variation vector d because $\overline{\Gamma}(k)$ takes an extreme value at k = k*. From (1) and (2), we can derive

$$\frac{P_g}{n}\sum_{i=2}^{N} d_i\left[-1/\left\{(\varepsilon-1)\left(1-\sum_{j=2}^{N}k_j^*\right)+1\right\}^2 + 1/\left\{(\varepsilon-1)k_i^*+1\right\}^2\right]=0 \qquad (3)$$

which is an identical equation with respect to d_i because the equation must be satisfied for an arbitrary variation vector d, and hence all coefficients of d_i must be 0. Eventually, simultaneous equations with respect to k_i are given as follows:

$$-\frac{1}{\left\{(\varepsilon-1)\left(1-\sum_{j=2}^{N}k_j^*\right)+1\right\}^2} + \frac{1}{\left\{(\varepsilon-1)k_i^*+1\right\}^2} = 0 \qquad (4)$$

Solving simultaneous equations led by (4), we have

$$k_i^* = 1-\sum_{j=2}^{N}k_j^* = k_1^* \qquad \because i = 2 \sim N \qquad (5)$$

which leads to a unique solution to the simultaneous equations of interest, k* = *(1/N, 1/N, ..., l/N)*. To determine which k* = *(1/N, 1/N, ..., l/N)* gives a minimum or maximum SIR, we use Figure 1, which is a plot of the average SIR against k_1 and k_2 in the case for which N = 3 is assumed. The assumed case gives k* = (k_1, k_2, k_3) = (1/3, 1/3, 1/3). From Figure 1, we can see that the point at (k_2, k_3) = (1/3, 1/3) shows the lowest SIR. The sequence developed so far tells us that the average SIR is smallest when each orthogonal code set is equally used.

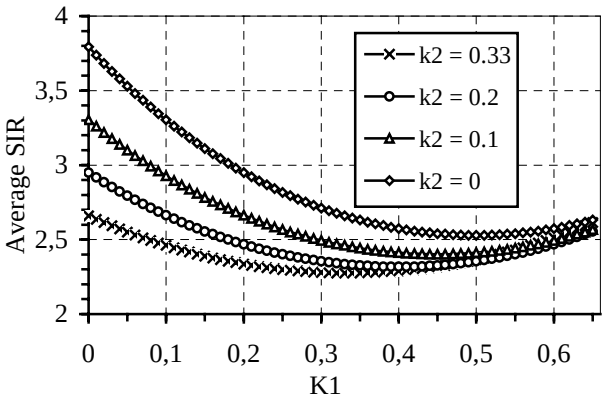

Figure 1. The average SIR for N = 3.

IV. OPTIMUM CODE ALLOCATION

Figure 1 and Table 1 also shows that the average SIR $\overline{\Gamma}(k^* + \alpha d)$ becomes larger as the absolute value of α increases. There is, however, a limit to the value of α because all elements of the vector k* + αd have to be between 0 and *S/n* *(n ≥ S)*. Defining the limit of α as α_l, we can write the code occupancy vector k* + α_ld at α_l as

$$k^* + \alpha_l d = \left(\frac{S}{n},\frac{S}{n},\ldots,\frac{S}{n},r_1,r_2,\ldots,r_R,0,0,\ldots,0\right) = k_r \qquad (6)$$

where $0 < r_1 < r_2 < \ldots < r_R < S/n$. We call k_r a code occupancy bound vector, and the code occupancy vector maximizing $\overline{\Gamma}$ is one of these code occupancy bound vectors.

From Figure 1and Table 1 we can see that as the number of fully occupied orthogonal code sets increases, the average SIR can be larger and also as the number of empty orthogonal code sets increases, and hence as the use of scrambling codes is reduced, the average SIR can be larger.

Finally, an optimum code allocation can be described as follows: Optimum code allocation is an allocation scheme that maximizes the number of code sets fully occupied and minimizes the use of scrambling codes.

TABLE 1
AVERAGE SIR AGAINST N FOR S = 128, n = 270, Pg = 512 end ∈ = 0.5.

N	2	3	4	5	8	10
Average SIR, dB	4,03	3,57	3,36	3,24	3,06	3,00

V. DOWNLINK CELL LOAD IN CDMA SYSTEM

The ability of a given mobile station to recover a signal that is destined for that mobile station is dependent upon how many other signals are being sent to other mobile stations in the cell. In the other words, for a given user, j, the signals that are being sent from the base station to the other users are simply interference. The more such signals, the greater the interference. There is also interference caused by other base stations. In the case of interference from other base stations, the amount of interference will depend upon the individual user's location. A user that is close to the serving base station is less likely to experience as much interference from neighboring cells as a user that is near the border between cells.

Finally, we need to factor in orthogonality. In the downlink, for a given scrambling code, transmissions to different users are sent using different channelization codes, which are chosen such that the codes are orthogonal. If the transmission from the base station to a single user arrives over multiple paths, however, and the delay spread across those paths is sufficiently large, the mobile station will directly recover only a part of the signal from the base station. The other pert of the signal, which arrives over a long delay path, will be seen as interference. This phenomenon needs to be

accounted for in our calculation of downlink loading. The equation for downlink load factor LF is

$$\text{LF} = \sum_{j=1}^{N} L_j.(1-\alpha_j + i_j)$$

$$= \sum_{j=1}^{N} (1-\alpha_j + i_j)/\left[1+\left(C/a_j.R_j.(E_b/N_o)_j\right)\right] \qquad (7)$$

where Lj is the load factor of a single user (j) and we assume N users in the cell, C is the chip rate, aj is the activity factor (such as about 65 percent for voice and 100 percent for data).

Rj is the user data rate, α_j is the orthogonality factor related to user j and ij is the interference from neighboring cells experienced by user j.

As in the case in the downlink, for more services, the term $C/(a_j.R_j.(E_b/E_o)_j)$ is far greater than 1, which means that the equation (7) can be simplified. Moreover, it is not realistic to determine the orthogonality factor for each mobile station in the cell as this will depend on the exact user location and multipath profile. Nor is it realistic to determine the intercell interference experienced by each user as that also depend on the user's exact location. Thus, we need to consider average values of orthogonality (α) and intercell inter-ference (i). A typical value for α is 0.4 and for i is 0.5.

Including these considerations, the load equation (7) becomes

LF =

$$(1-\alpha+i)\cdot\sum_{j=1}^{N} L_j = (1-\alpha+i)\cdot\sum_{j=1}^{N} 1/\left[C/\left(a_j.R_j.(E_b/N_o)_j\right)\right] \qquad (8)$$

VI. Evaluation of Optimum Code Allocation

The average SIRs for the optimum code allocation were compared with those for the worst code allocation in which every orthogonal code set enabled by multiple scrambling codes is equally occupied. When N = 5, S = 128, n = 270, P_g= 512, and ϵ = 0.5, the average SIR was found to be 3.24 dB for the worst allocation and 3.90 dB for the optimum allocation. That is, the optimum code allocation improved the average SIR by about 0.7 dB. And when N = 2, S = 128, n = 150, P_g = 512, and ϵ = 0.5, the average SIRs given by the optimum and worst code allocations, respectively, were 6.58 and 7.50 dB; the average SIR was about 1 dB better with the optimum allocation.

VII. Capacity Evaluation of CDMA Downlink Using Optimum Code Allocation

We calculate the cell loading as a function of the number of users for the worst code allocation (WCA) and for the optimum code allocation (OCA) assuming that all users are using standard voice service – Table 2.

Assumptions:

a_j = 0.65 for all users ; C = 3.84 Mcps ;

R_j= 7.4 Kbps for all users;

E_b/N_o = 3.24 dB (=2.1) for the worst code allocation or 3.90 dB (=2.45) for the optimum allocation.

α = 0.4, i = 0.5

Because of the fact that all users have the same characteristics, equation (8) becomes

$$\text{LF} = N.(1-\alpha+i)/\left[C/\left(a.R_j(E_b/N_o)\right)\right] \qquad (9)$$

TABLE 2

Cell loading as a function of the number of users for the WCA and for the OCA scheme

LF, %	0	20	40	60	80
Number of users for the WCA	0	69	138	207	276
Number of users for the OCA	0	79	158	238	317

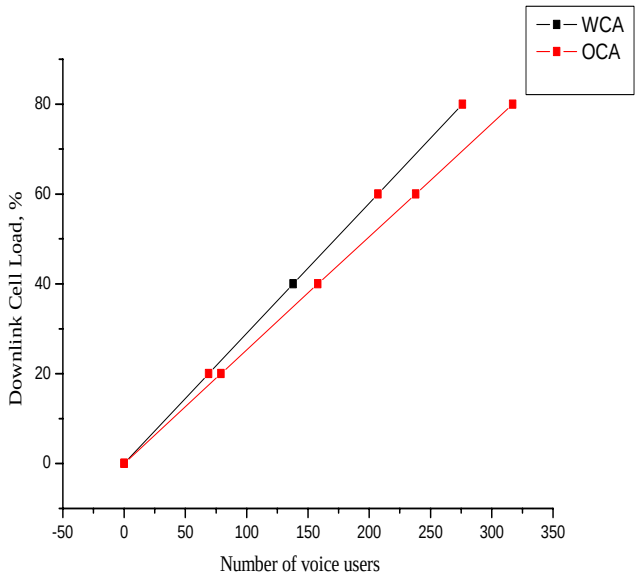

Fig. 2. Cell loading as a function of the number of users for the WCA and for the OCA scheme

VIII. Conclusions

Thus, for a downlink load factor of 60 percent, we can accommodate approximately 207 simultaneous voice users for the WCA scheme, and approximately 238 simultaneous voice users for the OCA scheme. Figure 2 and Table 2 also shows that with improved the average SIR by about 0.7 dB, we can accommodate approximately 15 percent more voice users.

Optimum code allocation scheme in downlink can significantly improve system capacity. This is of particular importance because UMTS services can be asymmetrical and the 3G system thus must offer high-capacity downlinks that can accommodate for instance multimedia traffic.

REFERENCES

[1] Furocawa, H., “Theoretical Capacity Evaluation of Power Controlled CDMA Downlink“, *Proc. VTC 2000-Spring*, Vol. 2, May 2000, pp. 997-1001.

[2] Adachi, F., “ Effects of Orthogonal Spreading and Rake Combining on DS-CDMA Forward Link in Mobile Radio, “ *IEICE Trans. On Communication*, Vol. E80-B, No. 11, Nov. 1997, pp. 1703-1712.

[3] Goldberg,David "*Genetic Algorithms in Search, Optimization and Machine Learning*," Addison-Wesley, 1989.

[3] Furocawa, H., “ An Optimum Code Allocation Scheme for CDMA Downlink , “ *Proc. IEICE Nat. Conf.*, B-5-93, Oct. 2000.

[4] Wang, J., Ng, TS., “*Advances in 3G Enhanced Technologies for Wireless Communications*“ Artech House, 2002.

Loosely-Coupled Interworking of GSM/GPRS Mobile Networks and Wireless LANs

Toni Janevski[1], Aleksandar Tudzarov[2], Dusko Temkov[3], Perivoje Stojanovski[4]

***Abstract* – In this paper we propose a solution for interworking of cellular networks, such as GSM/GPRS networks, and Wireless LAN. Proposed interworking is based on so-called loosely-coupled architecture, where the integration is based on the Authentication, Authorization and Accounting i.e. AAA. The applicative solution for GSM/GPRS-WLAN integration includes development of several network nodes, such as WLAN Access Controller and WLAN AAA charging gateway. The proposed solution provides possibility for efficient deployment of WLAN network to existing GSM/GPRS system of the mobile operator.**

***Keywords* - AAA, Cellular, Internetworking, Mobile networks, Wireless LAN.**

I. INTRODUCTION

Wireless LAN (WLAN) is a complementary service offering for mobile operators. Mobile operators using GSM and GPRS already have infrastructure that covers wide-area. However, they lack the higher data rates for Internet services that are demanded by most of the users, which are accommodated to the wired Internet and expect similar offer in a wireless environment. WLAN may be deployed in Public, Corporate or Residential environments, where GSM/GPRS systems already are accommodated. In particular it is suitable for indoor public hot spots, hotels, exposition areas, and corporate business. Hence, with a little additional investment mobile operators can further expand the packet (i.e. Internet) service by adding throughput and capacity in hot spots by using WLAN.

General Packet Radio Service (GPRS) is a development of GSM that provides packet switched data communications. On the other side, Wireless LAN (WLAN) is a relatively cheap technology and provides many times higher bandwidth than GPRS for packet traffic, but with many times smaller cells (up to 50-100 meters).

[1] Toni Janevski is with Faculty of Electrical Engineering, University "Sv. Kiril i Metodij", Karpos 2 bb, Skopje, R.Macedonia, E-mail: tonij@etf.ukim.edu.mk
[2] Aleksandar.Tudzarov is graduate student at the Faculty of Electrical Engineering, Skopje, R.Macedonia,
E-mail: Aleksandar.Tudzarov@mobimak.com.mk
[3] Dusko Temkov is graduate student at the Faculty of Electrical Engineering, Skopje, R.Macedonia,
E-mail: Dusko.Temkov@mt.com.mk
[4] Perivoje Stojanovski is graduate student at the Faculty of Electrical Engineering, Skopje, R.Macedonia,
E-mail: pstojanovski@mt.net.mk

The most used WLAN standard today is IEEE 802.11b, which is relatively cheap and offers high data rate up to 11 Mbps. Wireless LANs IEEE 802.11b are already widely deployed in developed countries and also in some companies in Macedonia. Other currently available WLAN standard for interworking are 802.11a and 802.11g, which offer data rates up to 54 Mbps.

Due to interest for WLAN considering lower price than classical cellular infrastructure, large vendors on the telecommunication market have created different solutions for Wireless LAN operated by mobile operators. Some of these solutions are described in [1-51].

In this paper we propose and describe in details efficient and cost-effective system for unified Authentication, Authorization and Accounting (AAA) for loosely-coupled PLMN-WLAN internetworking, in particular, for the scenario where PLMN operator adds its own WLAN network to offer WLAN service.

The paper is organized as follows. In Section II we discuss architectures for PLMN-WLAN interworking. Proposed AAA solution is given in Section III. Finally, Section IV concludes the paper.

II. ARCHITECTURE FOR PLMN-WLAN INTERWORKING

Depending on the degree of inter-dependence that one is willing to introduce between the PLMN network and the 802.11 network, there are two different ways of integrating the two wireless technologies. They are usually defined as [16]:

- Loosely-coupled internetworking (loose coupling)
- Tightly-coupled internetworking (tight coupling).

There are several advantages to the loosely-coupled integration approach. First, it allows independent deployment and traffic engineering for PLMN and WLAN networks. Second, loosely-coupled solution has lower costs and complexity compared to tightly-coupled one. Furthermore, loosely-coupled internetworking provides easy access to WLAN services for all potential types of users, such as postpaid and prepaid users of the mobile operator, as well as provides possibility to use WLAN services to users that have no subscription made with the mobile operator by using WLAN vouchers. Also, tightly-coupled approach demands additional investments in end user equipment for WLAN access (besides traditional 802.11 network cards), while loosely-coupled solution does not.

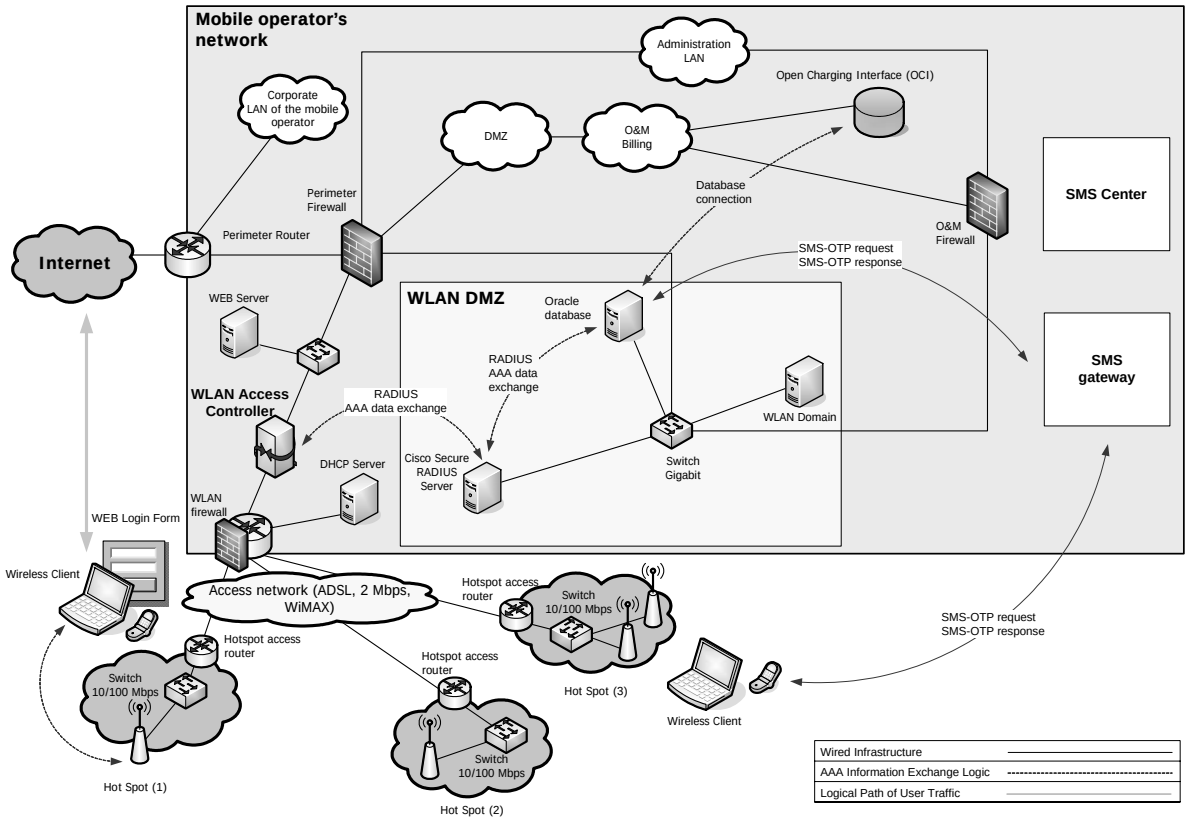

Fig. 1 Architecture for PLMN-WLAN interworking

From the discussion above it is clear that loosely-coupled solution offers several architectural advantages over the tightly-coupled approach, with no drawbacks. Furthermore, in loosely-coupled solution we may distinguish two main access methods:

- Universal Access Method – UAM, which is dominant today; and
- Secured access method, which should be implemented for users that care about the security

Because one WLAN access method is secured by using 802.1X and an encryption protocol, and other is not (i.e. UAM), we need to separate both types of access methods. Solution for this is to use Wireless Virtual LAN – WVLAN, which is based on 802.1Q standard [21]. In such approach, one Virtual WLAN will be used for UAM, and other (or others) will be used for secured WLAN access method.

Our PLMN-WLAN internetworking framework is based on loosely-coupled architecture (Fig. 1). Both, user data traffic and control traffic (e.g. AAA control signaling) aggregate at WLAN perimeter router. Traffic from hotspots (and vice versa) may aggregate in a switch (from the WLAN side of the network) that is plugged into the WLAN router.

III. Authorization, Authentication and Accounting for PLMN-WLAN

Security solution provided for a wireless LAN environment depends upon the purpose of the WLAN. In that sense, the solution differs for public WLAN network and corporate WLAN. While corporations give security a preference over easiness of use, an ordinary Internet user may prefer simplicity than security. There is always a balance that should be achieved between system security and user friendliness, especially in public WLAN access network.

The IEEE 802.11 standard defines two authentication mechanisms in the wireless interface, i.e. Open System and Shared Key, as well as a privacy method called Wired Equivalent Protocol (WEP). The standard mandates use of the authentication for the infrastructure BSS mode (it is optional for the ad-hoc mode), while WEP is optional in all cases.

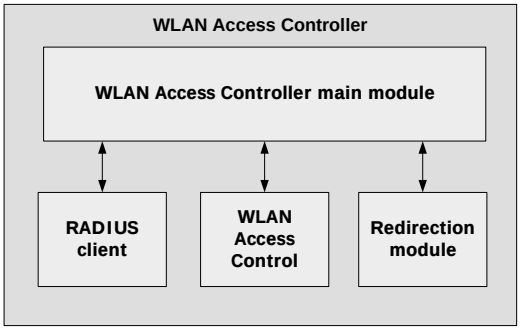

Fig. 2 WLAN Access Controller

Most common method for controlling Internet access for WLAN networks is to filter packets based on IP address and/or MAC address [43]. This method refers mainly to UAM, but it may be applied to the secured access as well. This method is based on limiting the user's access to only a set of designating destinations, which is usually web server with web-login page in the operator's WLAN backbone

network. This is referred to as browser redirection. However, the implementation of this access control is a proprietary solution, because there is no standardized one.

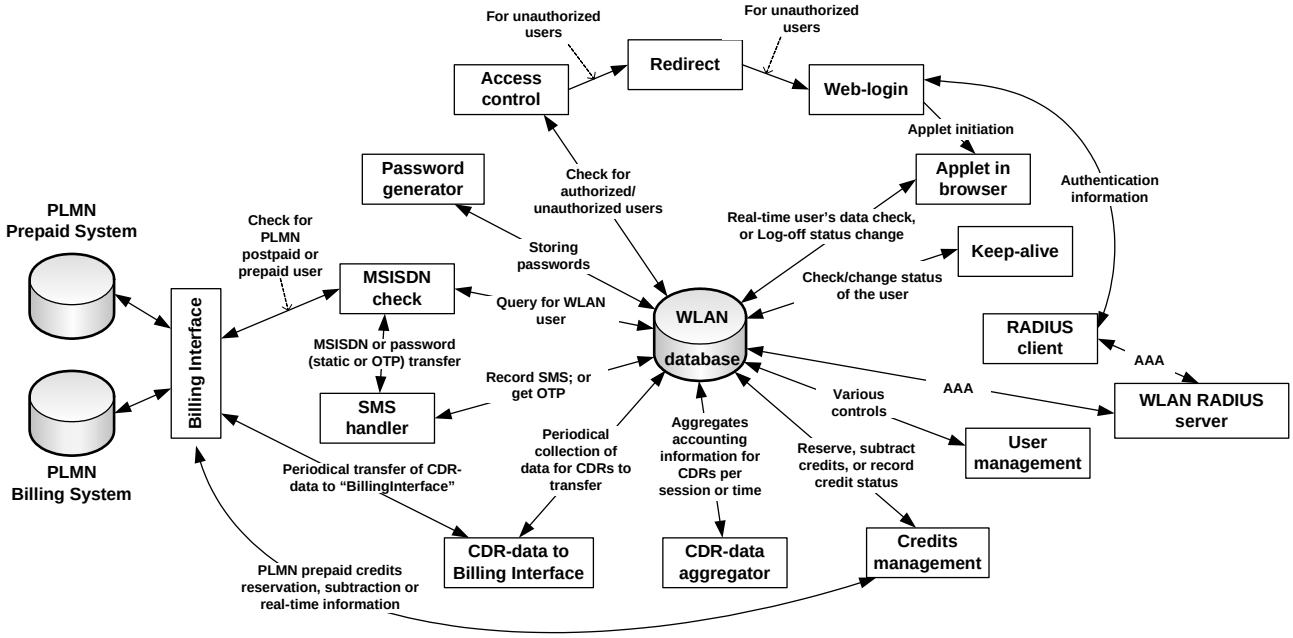

Fig. 3 Solution for PLMN-WLAN integration: software modules and interfaces

In the solution for mobile operator's WLAN network, we use dynamic packet filtering method for access control in the network access control server. The machine used for Access Control (i.e. gateway) has two Ethernet cards, one on the side of the WLAN access network, and the second out on the side to the external packet network (i.e. Internet). WLAN Access Controller is shown in Fig. 2. It is consisted of the following main modules:

- *RADIUS client* -for communication with RADIUS server
- *Access Control module* -for controlling the access of WLAN clients
- *Redirection module* -for redirection of unauthenticated users to the web-login server
- *WLAN web-login interface* -used as an user interface in the authentication process

The environment for the WLAN Access Controller is shown in Fig. 3.

When a user opens a browser his browser will be redirected to the web-login page of mobile operator's WLAN. There postpaid user will find information that he should send an SMS to a designated number to obtain access to the WLAN network (if he does not have such information in advance).

The SMS-Center of mobile operator receives the SMS and forwards it to a machine connected to IP backbone network of mobile operator by using the SMPP protocol for that purpose. An application receives that request for an OTP via SMS, and triggers check of the MSISDN number of the user (whether it is a mobile operator subscriber or not). The MSISDN check is necessary because there can be also roaming users from other operators. It is performed by an analysis of the number of the SMS sender.

After a positive check of the user's MSISDN, the application will trigger generation of OTP for that user. Then, the MSISDN and OTP are stored in the SQL database for WLAN users. Further, the OTP is sent to the user in a SMS via mobile operator's SMS-Center by using SMPP for communication between the application and the SMS-C (we refer to this OTP as Sent OTP i.e. S-OTP). The user receives the SMS-OTP and enters his MSISDN and the Received OTP (R-OTP) as his username and password. These credentials are sent to the WLAN RADIUS AAA server via the AP. Then, the Received OTP (R-OTP) is compared with Sent-OTP (S-OTP), which is in the WLAN users' database. After successful match of credentials given by the user and those recorded in the database, the user is granted access to the Internet, and accounting process starts. RADIUS server is also an accounting server and it receives all accounting messages (Accounting Start, Interim Accounting, Accounting Stop etc.). After session ends, RADIUS server records the accounting data into the SQL database. Also, all start, stop, and interim accounting messages are stored in the WLAN database.

Each accounting message triggers the WLAN database to send request to the mediation node i.e. PLMN charging mediation node (i.e. charging interface). From the accounting data recorded into the OCI database, an application periodically creates CDRs from the accounting data for completed sessions. All created CDRs are periodically sent to the Billing System of the mobile operator over FTP.

IV. CONCLUSIONS

In this paper we have described our solution for PLMN-WLAN interoperability based on loosely-coupled architecture. We have made a choice for loosely-coupled PLMN-WLAN integration as a dominant scenario today worldwide and we have justified its advantages over the tightly-coupled approach.

Further, we presented the developed WLAN Access Controller, which works as a gateway between WLAN segment and mobile operator's cellular network. Also, we have developed PLMN-WLAN AAA charging gateway, which is based on SQL database and carries all charging and billing functionalities for WLAN users.

The created solution is cost-effective and provides all needed functionalities for efficient charging and billing, as well as access control for WLAN. It is suited to be used for the scenario where PLMN operator adds WLAN as an additional service.

REFERENCES

[1] Alcatel, "Public Wireless LAN for Mobile Operators: WLAN beyond the enterprise", White paper, 2003.

[2] Flash Networks, "NettGain 1200 Flash Networks", www.adjungonet.com

[3] M. T. Bostrom, A. Norefors, "Ericsson Mobile Operator WLAN", Release 1 Technical Description, February 2002.

[4] M.Ritter, "Billing WLAN to macro-networks", White paper, Mobility Networks, www.mobilitynetworks.com, 2003.

[5] The Wireless Directory, "Hotspot Locations", http://www.hotspot-locations.com/modules.php?name=HotSpots, accessed June 2004.

[6] "Huawei to provide WLAN for China Mobile", http://www.ciol.com/content/news/repts/102112206.asp, accessed May 2004.

[7] WeRoam – WLAN and PLMN united, www.weroam.com, accessed June 2004.

[8] Swisscom-Eurospot, http://www.swisscom-eurospot.com, accessed June 2004.

[9] Telia HomeRun, http://www.homerun.telia.com, accessed June 2004.

[10] BT Openzone, http://www.btopenzone.com, accessed June 2004.

[11] T-Mobile International, http://www.t-mobile-international.com, accessed June 2004.

[12] T-Mobile US, http://www.t-mobile.com/hotspot/, accessed June 2004.

[13] "TDC Mobil" official WiFi/3G offer, www.tdcmobil.dk, accessed April 2004.

[14] VIPonline, https://airlink.vip.hr/hotspot/, accessed June 2004.

[15] Era Hot@Spot, http://www.erahotspot.pl, accessed June 2004.

[16] M. Buddhikot, G. Chandranmenon, S. Han, Y. W. Lee, S. Miller, L. Salgarelli, "Integration of 802.11 and Third-Generation Wireless Data Networks", Infocom 2003, San Francisco, USA, March 30 – April 3, 2002.

[17] Portal Software Inc., "Overcoming Wireless LAN Billing Challenges", 2003.

[18] Wi-Fi Alliance (2003) "Wi-Fi Alliance Wireless ISP Roaming Best Practices Document". http://www.Wi-Fialliance.org/opensection/

[19] Intel, "Wireless LAN (WLAN) End To End Guidelines for Enterprises and Public HotSpot Service Providers", Release 1.0, October 2002.

[20] IEEE 802.1X standard, "IEEE standard for local and metropolitan area networks – Port-Based Access Control", July 2001.

[21] IEEE 802.1Q standard, "IEEE standard for local and metropolitan area networks - Virtual Bridged Local Area Networks", May 7, 2002.

[22] C. Rigney, S. Willens, A. Rubens, W. Simpson, "Remote Dial-In User Authentication Service (RADIUS)", RFC 2865, June 2000.

[23] C. Rigney, "RADIUS Accounting", RFC 2866, June 2000.

[24] C. Rigney, W. Willats, P. Calhoun, "RADIUS Extensions", RFC 2869, June 2000.

[25] Cisco, "Single-User Network Access Security TACACS+", http://www.cisco.com/warp/public/614/7.html, accessed June 2003.

[26] P.Calhoun et al, "DIAMETER base protocol", IETF, RFC 3588, September 2003.

[27] C. Finseth, "An Access Control Sometimes Called TACACS", RFC 1492, July 1993.

[28] The Unofficial 802.11 Security Web Page, http://www.drizzle.com/~aboba/IEEE/, accessed June 2003.

[29] Wi-Fi Alliance, "Q&A Wi-Fi Protected Access", http://www.wi-fi.org/OpenSection/pdf/Wi-Fi_Protected_Access_QA.pdf , March 28, 2003.

[30] Frank Ohrtman, Konrad Roeder, "Wi-Fi Handbook: Building 802.11b Wireless Networks", McGraw-Hill, 2003.

[31] US Department of Commerce, "Advanced Encryption Standard (AES)", Federal Information Processing Standard (FIPS), Publication 197, November 2001.

[32] L.Blunk, J.Vollbrecht, "PPP Extensible Authentication Protocol", IETF, RFC 2284, March 1998.

[33] T. Dierks, C. Allen, "The TLS Protocol", RFC 2246, January 1999.

[34] T. Wu, "The SRP Authentication and Key Exchange System", RFC 2945, September 2000.

[35] IEEE 802.1X standard, "IEEE standard for local and metropolitan area networks – Port-Based Access Control", July 2001.

[36] W. Simpson, "PPP Challenge Handshake Authentication Protocol (CHAP)", August 1996.

[37] RFC 2716, "PPP EAP TLS Authentication Protocol", Internet Engineering Task Force (IETF), October 1999.

[38] J. Edney, W.A. Arbaugh, "Real 802.11 Security: Wi-Fi Protected Access and 802.11i", Addison Wesley, July 2003.

[39] J. Hammond et al., "Wireless Hotspot Deployment Guide", Intel in Communications, December 2003.

[40] Palekar, et al, "Protected EAP Protocol (PEAP) Version 2", draft-josefsson-pppext-eap-tls-eap-00, October 2003.

[41] N. Cam-Winget, D. McGrew, J. Salowey, H. Zhou, "EAP Flexible Authentication via Secure Tunnelling (EAP-FAST)", draft-cam-winget-eap-fast-00, February 2003.

[42] H.Haverinen, et al., "EAP SIM Authentication", draft-haverinen-pppext-eap-sim-13, April 5, 2003.

[43] P.Iyer at el, "Public WLAN Hotspot Deployment and Internetworking", Intel Technology Journal Vol. 7, August 19, 2003.

[44] Microsoft 802.1x Authentication Client, www.microsoft.com/windows2000/server/evaluation/news/bulletins/8021xclient.asp, December 13, 2002.

[45] Open Source Implementation of IEEE 802.1x, www.open1x.org/, accessed June 2003.

[46] IEEE 802.1Q standard, "IEEE standard for local and metropolitan area networks - Virtual Bridged Local Area Networks", May 7, 2003.

[47] SMPP Protocol Specification v4.0, http://www.smsforum.net/doc/public/Spec.

[48] ETSI TS 101 393 – Digital cellular telecommunications system (Phase 2+); General Packet Radio Service (PLMN); PLMN Charging, 3GPP TS 12.15 version 7.7.0 Release 1998.

[49] Ericsson Radio System AB, "PLMN System Description", PLMN Customer Documentation, 1551-AXB 250 01/1 Uen, 1999.

[50] PLMN Association, "Services, Ease of Use, and Operator Considerations in Interworked WLAN-Cellular Systems", PRD SE. 27, May 28, 2003.

Two Samples per Bit Interval Detection of NCFSK Signal in Presence of White Gaussian Noise and Interference

Petar C. Spalevic[1], Selena Z. Stanojcic[2], Hana Z. Popovic[3], Srdjan M. Jovkovic[4]

Abstract – **In this paper, an analysis of non – coherent FSK signal in the presence of Gaussian noise and channel interference has been performed. In receiver, decision is made on the bases of two samples during one bit – interval. We express the conditional probability density function for signals in both detector branches. Also, bit error probability versus signal to noise ratio, for different values of signal to interference ratio, is plotted.**

Keywords – **NCFSK receiver, White Gaussian noise, Interference, Bit error probability.**

I. INTRODUCTION

Frequency shift keying (FSK) is commonly used form of digital modulation in the high-frequency radio spectrum, and has important applications in telephone circuits. Binary FSK (usually referred to simply as FSK) is a modulation scheme allowing the data transmission by shifting the frequency of a continuous carrier in a binary manner to one or the other of two discrete frequencies. One frequency is designated as the "mark" frequency and the other as the "space" frequency. The mark and space correspond to binary one and zero, respectively. By convention, mark corresponds to the higher radio frequency. FSK modulation (Frequency Shift Key) is commonly believed to perform better than ASK and PSK in the presence of interfering signals. However, it is usually more difficult and expensive to implement. [1]

FSK signal can be transmitted coherently or noncoherently. Coherency implies that the phase of each mark or space tone has a fixed phase relationship with respect to a reference. Coherent FSK is capable of superior error performance but noncoherent FSK is simpler to generate and is used for the majority of FSK transmissions. Noncoherent FSK has no special phase relationship between consecutive elements, and, in general, the phase varies randomly.

Noncoherent FSK modulation is based on the system modeled with two matched filters centered at ω_0 and ω_1 with envelope detectors summed to a decision circuit [2].

[1]Petar C. Spalevic is with Faculty of Technical Sciences, Kneza Milosa 7, 38200 Kosovska Mitrovica, Serbia and Montenegro, E-mail:pspalevic@ptt.yu

[2]Selena Z. Stanojcic is with Faculty of Electronics Engineering, Aleksandra Medvedeva 14, 18000 Nis, Serbia and Montenegro, E-mail: selena1@ptt.yu

[3]Hana Z. Popovic is with High School of Electrical Engineering, Vojvode Stepe 2 83, 11000 Belgrade, Serbia and Montenegro, E-mail:hanap@eunet.yu

[4]Srdjan M. Jovkovic is with Faculty of Electronics Engineering, Aleksandra Medvedeva 14, 18000 Nis, Serbia and Montenegro, E-mail: srdjanjv@ptt.yu

This model suggests that non-coherent FSK modulation can be treated as two ASK signals, one at frequency ω_0 and the other at frequency ω_1.

Optimum demodulation of non-coherent FSK can be achieved by envelope detection of the signal filter outputs in a filter-type demodulator. The outputs of the mark and space filters are envelope-detected and then compared to determine which has greater magnitude.

The phase information is not required. With the "right" filter shape, performance of this type of demodulator approaches the theoretical optimum for noncoherent FSK. The "right" filter shape for a white noise interference environment is one that has the same spectral shape as the transmitted signal. For the "rectangular" modulation of FSK, the right shape is a function (sin x)/x bandpass filter centered about the desired mark or space tone.

II. THE SYSTEM ANALYSIS

Gaussian noise and disturbances are inevitable in telecommunication systems. Typical interferences usually have sinusoidal form. It is interesting to analyze the influence of sinusoidal interferences and Gaussian noise on the system error.

This paper presents an analysis of the digitally modulated signal with two symbols in presence of Gaussian noise and sinusoidal interference. In Figure 1. the block diagram for noncoherent detection of FSK signal is shown.

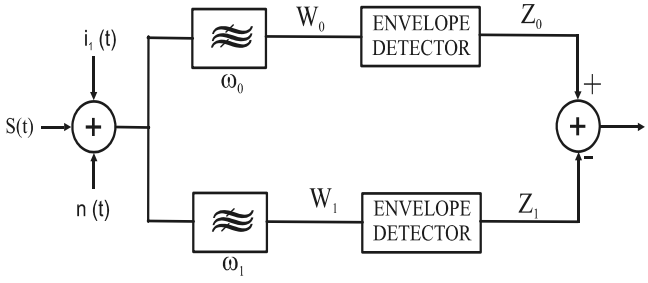

Fig. 1. Block diagram of the receiver for noncoherent detection of 2 - FSK signal

We supposed that filter in the upper branch passes just the elemental signal of ``1``, while the filter in the lower branch passes the elemental signal of ``0``. Besides, the central frequencies ω_0 and ω_1 are sufficiently spaced so the bands of these filters are not overlapping in the frequency domain.

Each branch contains an ideal envelope detector after filter. In the moment of decision making (if ``0`` or ``1`` is sent), the instantaneous difference of the two envelopes is compared to the decision threshold.

We consider a signal containing two components at frequencies ω_0 and ω_1 and presented with two pulses of duration T.

In real systems it is generally T >> T_0, T_1, so the modulated carrier signal can be analytically presented as:

H_0: ``0`` is sent:

$$\begin{aligned} S(t) &= A\cos\omega_0 t \quad 0 \le t \le T/2 \\ S(t) &= A\cos\omega_1 t \quad T/2 < t < T \end{aligned} \tag{1}$$

H_1: ``1`` is sent:

$$\begin{aligned} S(t) &= A\cos\omega_1 t \quad 0 \le t \le T/2 \\ S(t) &= A\cos\omega_0 t \quad T/2 < t < T \end{aligned} \tag{2}$$

Gaussian noise can be analytically presented as:

$$n(t) = \sum_{i=1}^{\infty} N\cos(2\pi i\Delta f + \theta_i) \tag{3}$$

A disturbance signal generally interferes with one of the components, so it can be taken as:

$$i_1(t) = A_1\cos(\omega_0 t + \theta_1) \tag{4}$$

Filtering the signal at the output of band pass filter at ω_0 results in component of the signal at frequency ω_0, narrow band noise and disturbance at frequency ω_0. Likewise, the output of band pass filter at ω_1 consists of the signal at frequency ω_1 and narrow band noise, since the disturbance is eliminated. In proposed cases, this can be written as:

H_0:

$$W_0(t) = (A\cos\omega_0 t + x\cos\omega_0 t + y\sin\omega_0 t + A_1\cos(\omega_0 t + \theta_1))(h(t) - h(t - T/2)) \tag{5a}$$

$$W_0(t) = (x\cos\omega_0 t + y\sin\omega_0 t + A_1\cos(\omega_0 t + \theta_1)(h(t - T/2) - (t - T)) \tag{5b}$$

$$W_1(t) = (x\cos\omega_1 t + y\sin\omega_1 t)(h(t) - h(t - T/2)) \tag{5c}$$

$$W_1(t) = (A\cos\omega_1 t + x\cos\omega_1 t + y\sin\omega_1 t)(h(t - T/2) - h(t - T)) \tag{5d}$$

H_1:

$$W_0(t) = (x\cos\omega_0 t + y\sin\omega_0 t + A_1\cos(\omega_0 t + \theta_1))(h(t) - h(t - T/2)) \tag{6a}$$

$$W_0(t) = (A\cos\omega_0 t + x\cos\omega_0 t + y\sin\omega_0 t + A_1\cos(\omega_0 t + \theta_1))(h(t - T/2) - h(t - T)) \tag{6b}$$

$$W_1(t) = (A\cos\omega_1 t + x\cos\omega_1 t + y\sin\omega_1 t)(h(t) - h(t - T/2)) \tag{6c}$$

$$W_1(t) = (x\cos\omega_1 t + y\sin\omega_1 t)(h(t - T/2) - h(t - T)) \tag{6d}$$

In the frequency domain, the envelope detector translates the spectrum of the useful signal from the region of the high frequencies to baseband. In the time domain, it forms a sequence of pulses containing the modulating digital signal.

Digital signal envelope detectors contain also a decision block, which generates a sequence of pulses, despite of presence of noise and disturbances. The output of envelope detector in the upper branch in case of hypothesis H_0 is the symbol 1 in the first half - period and 0 in the second, and in case of hypothesis H_1 it will be 0 in the first half - period and 1 in the second. Likewise, the envelope detector output in the lower branch will be 0 in the first and 1 in the second half - period in the case of hypothesis H_0, and 1 in the first and 0 in the second half period in the case of hypothesis H_1.

III. Determination of the Probability Density Function

At the output of the envelope detector, the signals z_{ijk} are analyzed. In this case we can use the following notations:

i = {0, 1}, whether 0 or 1 is sent; (code domain)

j = {0, 1} whether upper or lower branch with bandpass filter is considered; (space domain)

k = {1, 2} whether the first or the second half - period is considered; (time domain).

Since both branches are subject to noise and one is subject to disturbance, we derive joint conditional probability density functions for different hypothesis in time and space domains.

$p(z_{001}, z_{002})$- represent combined probability density function of the signal “0” in upper branch during the whole period given by:

$$p(z_{001}, z_{002}) = \int_{-\pi}^{\pi} d\varphi_1 \int_{-\pi}^{\pi} d\varphi_2 \int_{-\pi}^{\pi} d\theta\ p(\theta) \frac{z_{001} z_{002}}{(2\pi\sigma^2)(1-R)} \times \tag{7}$$

$$\times \exp\left\{ -\frac{(z_{001}\cos\varphi_1 - A - A_1\cos\theta)^2 + (z_{001}\sin\varphi_1 + A_1\sin\theta)^2}{2\sigma^2(1-R)^2} \right\} \times$$

$$\times \exp\left\{ \frac{(z_{002}\cos\varphi_1 - A_1\cos\theta)^2 + (z_{001}\sin\varphi_2 + A_1\sin\theta)^2}{2\sigma^2(1-R)^2} \right\} \times$$

$$\times \exp\left\{ -\frac{2R(z_{001}\cos\varphi_1 - A - A_1\cos\theta)(z_{002}\cos\varphi_2 - A_1\cos\theta)}{2\sigma^2(1-R^2)} \right\} \times$$

$$\times \exp\left\{ \frac{2R(z_{001}\sin\varphi_1 + A_1\sin\theta)^2 + (z_{002}\sin\varphi_2 + A_1\sin\theta)^2}{2\sigma^2(1-R^2)} \right\}$$

R represents reference parameter of the envelope for both sampling moments. We suppose the uniform distribution of $p(\theta)$. φ_1 and φ_2 represent the refererent phasing for the z_0 and z_1 processes. They are given by the following expressions:

$$\varphi_1 = arctg\frac{y - A_1\sin\theta_1}{A + x + A_1\sin\theta_1}$$
$$\varphi_2 = arctg\frac{y - A_1\sin\theta_1}{x + A_1\sin\theta_1} \quad (8)$$

$p(z_{011}, z_{012})$- combined probability density function of the signal "0" in lower branch during the whole period and is given by:

$$p(z_{011}, z_{012}) = \frac{z_{011}z_{012}}{(2\pi\sigma^2)(1-R^2)} \times$$
$$\times \exp\left(-\frac{z_{012}^2 + z_{012}^2 + A^2}{\sigma^2(1-R^2)}\right) \times$$
$$\times \int_{-\pi}^{\pi} \exp\left(-\frac{z_{011}RA}{\sigma^2(1-R^2)}\right)\cos\varphi_1 d\varphi_1 \times \quad (9)$$
$$\times \int_{-\pi}^{\pi} \exp\left(\frac{z_{012}A\cos\varphi_2}{\sigma^2(1-R^2)} + \frac{z_{011}z_{012}\cos(\varphi_1 - \varphi_2)}{\sigma^2(1-R^2)}\right)d\varphi_2$$

$p(z_{101}, z_{102})$ - combined probability density function of the signal "1" in upper branch during the whole period. It is given by:

$$p(z_{101}, z_{102}) = \int_{-\pi}^{\pi} d\varphi_1 \int_{-\pi}^{\pi} d\varphi_2 \int_{-\pi}^{\pi} d\theta\, p(\theta) \frac{z_{101}z_{102}}{(2\pi\sigma^2)(1-R^2)} \quad (10)$$
$$\times \exp\left\{-\frac{(z_{101}\cos\varphi_1 - A_1\cos\theta)^2 + (z_{101}\sin\varphi_1 + A_1\sin\theta)^2}{2\sigma^2(1-R^2)}\right\} \times$$
$$\times \exp\left\{\frac{(z_{102}\cos\varphi_1 - A - A_1\cos\theta)^2 + (z_{102}\sin\varphi_2 + A_1\sin\theta)^2}{2\sigma^2(1-R^2)}\right\} \times$$
$$\times \exp\left\{-\frac{2R\{(z_{101}\cos\varphi_1 - A_1\cos\theta)(z_{102}\cos\varphi_2 - A - A_1\cos\theta)\}}{2\sigma^2(1-R^2)}\right\} \times$$
$$\times \exp\left\{\frac{+(z_{101}\sin\varphi_1 + A_1\sin\theta)(z_{102}\sin\varphi_2 + A_1\sin\theta)}{2\sigma^2(1-R^2)}\right\}$$

$p(z_{111}, z_{112})$ - Combined probability density function of the signal "1" in lower branch during the whole period and it is given by:

$$p(z_{111}, z_{112}) = \frac{z_{111}z_{112}}{(2\pi\sigma^2)(1-R^2)} \exp\left(-\frac{z_{111}^2 + z_{112}^2 + A^2}{\sigma^2(1-R^2)}\right) \times$$
$$\times \int_{-\pi}^{\pi} \exp\left(\frac{z_{111}A}{\sigma^2(1-R^2)}\cos\varphi_1\right)d\varphi_1 \times \quad (11)$$
$$\times \int_{-\pi}^{\pi} \exp\left(-\frac{z_{112}AR\cos\varphi_2}{\sigma^2(1-R^2)}\right)\exp\left(\frac{z_{111}z_{112}\cos(\varphi_1 - \varphi_2)}{\sigma^2(1-R^2)}\right)d\varphi_2$$

The system output during the whole period in case the symbol "0" is sent, is:

$$H_0: \quad \begin{aligned} z_1 &= z_{001} - z_{011} \quad \rightarrow \quad z_{001} = z_1 + z_{011} \\ z_2 &= z_{002} - z_{012} \quad \rightarrow \quad z_{002} = z_2 + z_{012} \end{aligned} \quad (12)$$

Combined probability density function for symbol "0" is therefore:

$$p_0(z_1, z_2) = \int_{z_{011}} \int_{z_{012}} p_1(z_1 + z_{011}, z_2 + z_{012}) \times \quad (13)$$
$$\times\, p_2(z_{011}, z_{012})dz_{011}dz_{012}$$

The output during the whole period if the symbol "1" is sent will be:

$$H_1: \quad \begin{aligned} z_1 &= z_{101} - z_{111} \quad \rightarrow \quad z_{101} = z_1 + z_{111} \\ z_2 &= z_{111} - z_{112} \quad \rightarrow \quad z_{111} = z_2 + z_{112} \end{aligned} \quad (14)$$

Combined probability density function for symbol "1" is therefore:

$$p_1(z_1, z_2) = \int_{z_{111}} \int_{z_{112}} p_1(z_1 + z_{111}, z_2 + z_{112}) \times \quad (15)$$
$$\times\, p_2(z_{111}, z_{112})dz_{111}dz_{112}$$

The decision area $\Im_1$, for symbol "1", contains all the (z_1, z_2) pairs giving the likelihood ratio $\lambda(r) > \lambda_0$ [3]. On the other side, the decision area $\Im_0$, for symbol "0", contains all the (z_1, z_2) pairs giving the likelihood ratio $\lambda(r) < \lambda_0$. From these equations the error probability can be determined [4]..

IV. The Bit Error Probability

The main parameter that characterizes the system performances, that is, the quality of telecommunication service, is the bit error probability. Analytical expression for the bit error probability *Pe* is derived directly from previous equations:

$$Pe = P(H_1)\iint_{\Im_0} p_1(z_1, z_2)dz_1dz_2 + \quad (16)$$
$$+ P(H_0)\iint_{\Im_1} p_0(z_1, z_2)dz_1dz_2$$

where $p_0(z_1, z_2)$ and $p_1(z_1, z_2)$ represent probability density functions for H_0 and H_1, respectively. Integrals $\iint_{\Im_0}$ and $\iint_{\Im_1}$ represent the probabilities that ``0`` is detected when ``1`` is sent, and that ``1`` is detected when ``0`` is sent,

respectively. The decision area is obtained relative to the likelihood ratio $\lambda(r) > \lambda_0$ [5].

The bit error probability dependence on SNR, for three values of signal to interference ratio, is given in Figs. 2 and 3.

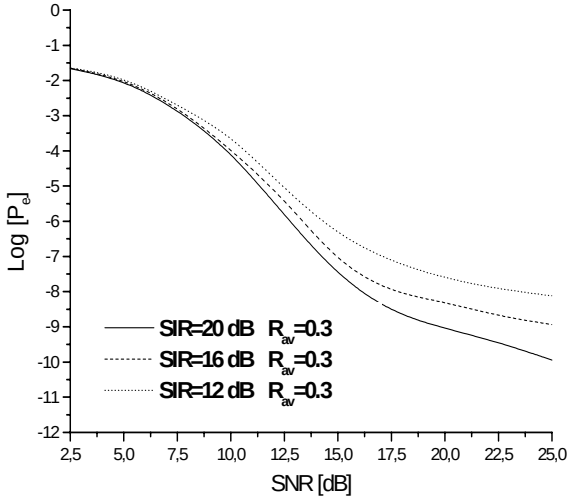

Fig. 2. The bit error probability of the system with respect to SNR, for three different values of SIR and parameter R_{av} = 0. 3.

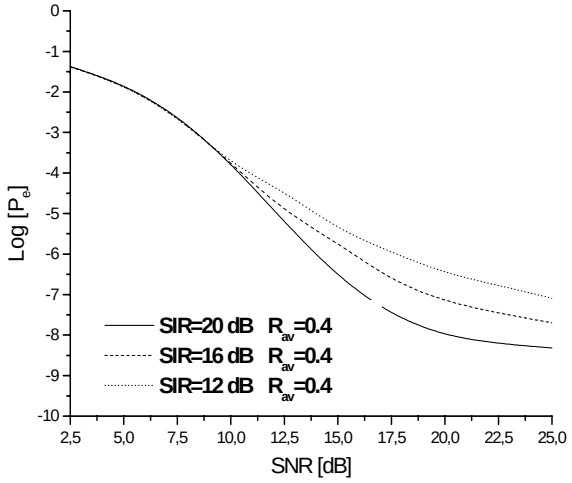

Fig. 3. The bit error probability of the system with respect to SNR, for three different values of SIR and parameter R_{av} = 0. 4.

These plots show that increasing the SNR results in decreasing the bit error probability. The best performances are gained for SIR = 20 dB

V. CONCLUSION

This paper presents expressions to evaluate the bit error probability for noncoherent frequency shift keying (NCFSK) system over digital channel with white Gaussian noise and channel interference. In receiver, decision is made on the bases of two samples per bit interval. The probability density function with respect to whether ``0`` or ``1`` is sent, is determined for both cases.

The system performances, i.e. the bit error probability is discussed in terms of different values of the SNR. As expected, the bit error probability is decreasing (the performances are better) when rising of SNR. Such system gives significantly better performances but is somewhat less cost effective.

REFERENCES

[1] M. Ilic, A. Vidovic, D. Petrovic, M. Stefanovic, 'Noncoherent Detection of FSK Signal in Presence of Gaussian noise and Cochannel Interference'', *Proceedings of the Symposium of Electronics and Telecomunications*, Vol. I, pp. 128 – 131, Temisvar, Romania, 17-18 September, 1998.

[2] M. Schwartz, *Information Transmission, Modulation and Noise*. New York: McGraw-Hill, 1980.

[3] M. C. Stefanovic, ''Performances ofdigital telecommunication systems - edition'',, p. 341 - 348, Nis, Faculty of Electronics Engineering, 2004.

[4] M. P. Fitz, ''Further results in the unified analysis of digital communication systems", *IEEE Trans. Commun.*, vol. 40, pp. 521–532, Mar. 1992.

[5] Y. Ma. , T. J. Lim, '' Bit Error Probability for MDPSK and NCFSK over Arbitrary Rician Fading Channels'', *IEEE Journal on Selected Areas in Comm.*, vol. 18, no. 11, pp. 2179-2189, 2000.

Session CSA:

COMPUTER SYSTEMS AND APPLICATIONS

Computing Minimum Cost Spanning Tree on Linear Unidirectional Systolic Array

E. I. Milovanović[1], I. Ž. Milovanović[2], B. M. Randjelović[3]

Abstract –**A problem of finding MCST of a given graph is considered. The problem is partitioned into two parts. First, we compute a wighted matrix, $D^{(n)}$, according to weighted matrix, $D^{(0)}$, of a given graph. Second, MCST is determined by comparing matrices $D^{(n)}$ and $D^{(0)}$. To solve the first problem we designed unidirectional linear systolic array with optimal number of PEs and minimize the execution time. The secdond is performed by the host computer.**

Keywords – **Systolic array, Minimum cost spanning tree.**

I. INTRODUCTION

The minimum cost spanning tree (MCST) of a graph defines the cheapest subset of edges that keeps the graph in one connected component. The MCST problem arises in a number of applications, both as a stand-alone problem and as a sub problem in more complex problem settings. It is perhaps the simplest, and certainly one of the most central, models in the field of network optimisation.

The problem of finding MCST can be formulated as follows. Consider a connected undirected or directed graph, $G=(V,E)$, where $V=\{1,2,...,n\}$ is the set of vertices and E is the set of edges. Associated with each edge (i,j) in E is a cost d_{ij}. Thus, weighted matrix $D^{(0)}=(d_{ij}^{(0)})$ of order nxn which corresponds to graf G can be described as

$$d_{ij}^{(0)}=\begin{cases} d_{ij}, & if\ \{i,j\}\in E \\ +\infty, & if\ \{i,j\}\notin E \\ 0, & if\ i=j \end{cases},$$

for each $i=1,2,\ldots,n$ and $j=1,2,\ldots,n$. The problem is to find a rooted spanning tree, $G=(V,E')$ where E' is a subset of E such that the sum of d_{ij} for all (i,j) in E' is minimized. The spanning tree is defined as a graph which connects, without any cycle, all nodes with n-1 arcs, i.e., each node, except the root, has one and only one incoming arc. Note that a minimum cost spanning tree is not necessarily unique. This problem can be solved by many different algorithms. The first algorithm for finding MST was developed by Czech scientist Otakar Boruvka in 1926 [1-2]. Now, there are two algorithms commonly used, Prim's algorithm and Kruskal's algorithm [3], [4]. In this paper we will use an algorithm equivalent to Warshall's [5] and Floyd's algorithms [6] for computing transitive closure and shortest path in a given graph.

[1]E. I. Milovanović, [2]I. Ž. Milovanović, [3]B. M. Randjelović are with the Faculty of Electronic Engineering, Aleksandra Medvedeva 14, 18000 Nis, Serbia and Montenegro E-mail: ema@elfak.ni.ac.yu, igor@elfak.ni.ac.yu, bane@elfak.ni.ac.yu

In order to find MCST we start from the matrix $D^{(0)}=(d_{ij}^{(0)})$ and compute a series of matrices $D^{(k)}=(d_{ij}^{(k)}), k=1,2,\ldots,n$, according to the following algorithm:

Algorithm_1
for k:=1 **to** n **do**
for i:=1 **to** n **do**
for j:=1 **to** n **do**
$d_{ij}^{(k)}:=\min\{d_{ij}^{(k-1)},\max\{d_{ik}^{(k-1)},d_{kj}^{(k-1)}\}\}$

In the second step matrix $D^{(0)}$ is compared with matrix $D^{(n)}$. An edge (i,j), $(i,j)\in E$, is added to MCST if and only if $d_{ij}^{(n)}=d_{ij}^{(0)}$ for $i=1,2,\ldots,n$ and $j=1,2,\ldots,n$.

In this paper we are interested in finding matrix $D^{(n)}$, only. The comparison and computation of the cost is left for the host computer. In order to compute $D^{(n)}$ we use unidirectional linear systolic array (ULSA). Because of the problem dimension and data dependencies in the corresponding data dependency graph, Algorithm_1 is not suitable for direct synthesis of ULSA. To overcome this problem we partition the computations in Algorithm_1 into appropriate number of two-dimensional entities which are then computed on the ULSA The final result is obtained by repeating the computation n times on the designed ULSA. We require that designed ULSA is space-optimal with respect to a problem size and the execution time should be as minimal as possible for a given size of ULSA.

II. THE SYSTOLIC ALGORITHM

In order to obtain two-dimensional entities suitable for the synthesis of ULSA with desired properties, it is obvious that one of index variables in Algorithm_1 should be fixed on some constant value. The computation in Algorithm_1 does not depend on whether it is performed first on index variable i or j. In other words the loops on index variables i and j can be permuted. Therefore, without lost of generality, assume that index variable i is outer and fixed to some constant value. Two-dimensional entities obtained by setting i to some constant value in Algorithm_1 are $M_i=(d_{ij}^{(k)}), i=1,2,...,n$. The dependencies between different $M_i, i=1,2,...,n$ are very complex. Namely, it is not possible to compute M_i only according to $M_t, 0\le t\le i-1$. Therefore, the computation of different M_i is not suitable for systolic implementation. The same conclusion would be obtained if j is fixed. Therefore, only index variable k has left. Let us note that index variable k is an iterative one in Algorithm_1. The computations in SA

are usually performed such that resulting elements are pipelined through the array unless SA with fixed number of PEs is concerned or the array where resulting elements are accumulated in PEs. We do not use neither of the approaches in this paper. Instead, we partition the computations in Algorithm_1 into two-dimensional entities $D^{(k)} = (d_{ij}^{(k)})$, for some fixed k=1,2,...,n. The computation of $D^{(k)}$ depends only on $D^{(k-1)}$. This means that the computations of $D^{(1)}$,..., $D^{(n)}$ can be performed successively, which is very important for our approach. It is enough to synthesize ULSA that computes $D^{(1)}$ and then use it to compute $D^{(n)}$ by repeating the computations n times.

To ease the presentation we use the following denotation

$$a(i,0,1) = d_{i1}^{(0)}, b(0,j,1) = d_{ij}^{(0)}, c(i,j0) = d_{ij}^{(0)}, c(i,j,1) = d_{ij}^{(1)} \quad (1)$$

for i=1,2,...,n and j=1,2,...,n. The corresponding systolic algorithm has the following form

Algorithm_2
for i:=1 **to** n **do**
f**or** j**:=**1 **to** n **do**
$a(i,j,1) := a(i,j-1,1)$
$b(i,j,1) := b(i-1,j,1)$
$c(i,j,1) := \min\{c(i,j,0), \max\{a(i,j,1), b(i,j,1)\}\}$

The inner computation space of Algorithm_2 is

$$P_{\text{int}} = \{(i,j,1) \mid 1 \le i \le n, 1 \le j \le n\} \quad (2)$$

and the corresponding dependency matrix is

$$D = \left[\vec{e}_b^{\,3} \quad \vec{e}_a^{\,3} \quad \vec{e}_c^{\,3}\right] = \begin{bmatrix} 1 & 0 & 0 \\ 0 & 1 & 0 \\ 0 & 0 & 1 \end{bmatrix} \quad (3)$$

Different linear SAs can be obtained by mapping (D, P_{int}) along different projection direction vectors. Namely, each projection direction vector is associated with the corresponding space-time transformation matrix T which maps a computational structure of the algorithm (D, P_{int}) into a systolic implementation. Matrix T is of the form [9]:

$$T = \begin{bmatrix} \vec{\Pi} \\ S \end{bmatrix} = \begin{bmatrix} t_{11} & t_{12} & t_{13} \\ t_{21} & t_{22} & t_{23} \\ t_{31} & t_{32} & t_{33} \end{bmatrix}$$

where $\vec{\Pi}$ determines time scheduling, while S is space transformation which maps (D, P_{int}) into 1D systolic array. ULSA can be obtained for the direction projection vector $\vec{\mu} = [1 \quad -1 \quad 0]^T$ (see, for example [7-8]). However, this direction is not a permissible one for the Algorithm_2. Namely, if from the set of possible transformation matrices for this direction the following one

$$T = \begin{bmatrix} \vec{\Pi} \\ S \end{bmatrix} = \begin{bmatrix} 2 & 1 & 1 \\ 1 & 1 & 0 \\ 0 & 0 & 1 \end{bmatrix} \quad (4)$$

is chosen arbitrarily, then according to mapping $S : D \to \Delta$, i.e. according to

$$\Delta = S \cdot D = \left[\vec{e}_b^{\,2} \quad \vec{e}_a^{\,2} \quad \vec{e}_c^{\,2}\right] = \begin{bmatrix} 1 & 1 & 0 \\ 0 & 0 & 1 \end{bmatrix} \quad (5)$$

which represents the direction of data flow in the systolic array, we conclude that $\vec{e}_b^{\,2} = \vec{e}_a^{\,2} = [1 \quad 0]^T$ meaning that elements of vectors $\vec{b}$ and $\vec{a}$ propagate through the array in the same direction. This will cause that the same partial product is computed in all PEs, leading to incorrect computation. One way to solve this problem is to introduce the delay elements between neighbouring PEs. This will result in different data speed of $\vec{b}$ and $\vec{a}$ elements through the array. If we put delay elements on $\vec{b}$ path, then $\vec{e}_b^{\,2}$ will be half of the $\vec{e}_a^{\,2}$ i.e. $\vec{e}_b^{\,2} = \frac{1}{2}\vec{e}_a^{\,2}$. From the algorithmic point of view, we need to introduce additional index space,

$$P_d = \{(i - \frac{1}{2}, j, 1) \mid 1 \le i \le n, 1 \le j \le n\} \quad (6)$$

and new dependency matrix

$$D = \left[\vec{e}_b^{\,3} \quad \vec{e}_a^{\,3} \quad \vec{e}_c^{\,3}\right] = \begin{bmatrix} \frac{1}{2} & 0 & 0 \\ 0 & 1 & 0 \\ 0 & 0 & 1 \end{bmatrix} \quad (7)$$

Let us note that in index points of space P_{d} no computation is performed. Elements of vector $\vec{b}$ are just copied (i.e. delayed for one cycle). Now, according to (2), (6) and (7) we construct a new systolic algorithm, equivalent to Algorithm_2 which computes $D^{(1)}$, for which the direction $\vec{\mu} = [1 \quad -1 \quad 0]^T$ is a permissible one. The algorithm has the following form

Algorithm_3
for i:=1 **to** n **do**
f**or** j**:=**1 **to** n **do**
$b(i - \frac{1}{2}, j, 1) := b(i-1, j, 1)$
$b(i, j, 1) := b(i - \frac{1}{2}, j, 1)$
$a(i,j,1) := a(i,j-1,1)$
$c(i,j,1) := \min\{c(i,j,0), \max\{a(i,j,1), b(i,j,1)\}\}$

The ULSA obtained according to Algorithm_3 computes $D^{(1)}$ correctly, but according to P_{int}, defined by (2) and space transformation S, defined by (4), it has $\Omega = 2n-1$ PEs which is too large for a given problem size. Space-optimal ULSA should have n PEs. In order to obtain ULSA with optimal number of PEs, the inner computation space P_{int} has to be accommodated to the projection direction $\vec{\mu} = [1 \quad -1 \quad 0]^T$ (see, for example, [7-9]). The accommodation is performed by mapping P_{int} into a new according to the following

$$\begin{bmatrix} U \\ V \\ 1 \end{bmatrix} = \begin{bmatrix} 1 & 0 & 0 \\ -1 & 1 & 0 \\ 0 & 0 & 1 \end{bmatrix} \cdot \begin{bmatrix} i \\ j \\ 1 \end{bmatrix} + \begin{bmatrix} 0 \\ n \\ 0 \end{bmatrix} = \begin{bmatrix} i \\ j - i + n \\ 1 \end{bmatrix}$$

for each i=1,2,...,n and j=1,2,...,n. Now, the new inner computation space is

$$P_{\text{int}} = \{(i, j-i+n,1) \mid 1 \le i \le n, 1 \le j \le n\}\ , \qquad (8)$$

and the corresponding space of delay elements is

$$P_d = \{(i-\frac{1}{2}, j-i+n,1) \mid 1 \le i \le n, 1 \le j \le n\}. \qquad (9)$$

Now, according to (7), (8) and (9), we can define the new systolic algorithm that is adjusted to direction $\vec{\mu} = [1 \quad -1 \quad 0]^T$ and equivalent to Algorithm_3. It has the following form

Algorithm_4
for i:=1 **to** n **do**
for j:=1 **to** n **do**

$$b(i-\frac{1}{2}, j-i+n,1) := b(i-1, j-i+n,1)$$
$$b(i, j-i+n,1) := b(i-\frac{1}{2}, j-i+n,1)$$
$$a(i, j-i+n,1) := a(i, j-i+n-1,1)$$
$$c(i, j-i+n,1) := \min\{c(i, j-i+n,0), \max\{a(i, j-i+n,1), b(i, j-i+n,1)\}\}$$

where $a(i,j,1) \equiv a(i,0,1)$, $b(0, j+n,1) \equiv b(0, j,1)$, $c(i, j+n,0) \equiv c(i, j,0)$, $c(i, j+n,1) \equiv c(i, j,1)$, for i=1,2,...,n and j=1,2,...,n.

III. THE ULSA SYNTHESIS

The ULSA that computes matrix $D^{(1)}$ according to Algorithm_3 is obtained by mapping (P_{int}, P_{d}, D) using transformation S defined by (4). The (x,y) coordinates of the PEs in ULSA are obtained by mapping P_{int}, defined by (8), according to the following equations

$$PE \rightarrow \begin{bmatrix} x \\ y \end{bmatrix} = \begin{bmatrix} j+n \\ 1 \end{bmatrix} \qquad (10)$$

for each i=1,2,...,n.

Positions of delay elements in the (x,y) plane are determined by mapping set P_{d}, defined by (9), using transformation S defined by (4), i.e. according to

$$P_d \rightarrow \begin{bmatrix} x \\ y \end{bmatrix} = \begin{bmatrix} j+n-\frac{1}{2} \\ 1 \end{bmatrix} \qquad (11)$$

for each i=1,2,...,n.

The communication links between the PEs in the ULSA are implemented along the propagation vectors

$$\Delta = S \cdot D = \begin{bmatrix} \vec{e}_b^2 & \vec{e}_a^2 & \vec{e}_c^2 \end{bmatrix} = \begin{bmatrix} \frac{1}{2} & 1 & 0 \\ 0 & 0 & 1 \end{bmatrix}, \qquad (12)$$

where D is defined by (7) and S by (4).

The initial (x,y) positions of input data items at the beginning of the computation in the ULSA are obtained according to

$$a(i,01) \rightarrow \begin{bmatrix} x \\ y \end{bmatrix} = \begin{bmatrix} 1+n-i \\ 1 \end{bmatrix} + rn \begin{bmatrix} 1 \\ 0 \end{bmatrix}$$
$$b(0, j-i+n,1) \rightarrow \begin{bmatrix} x \\ y \end{bmatrix} = \begin{bmatrix} \frac{j-i+2n+1}{2} \\ 1 \end{bmatrix} + rn \begin{bmatrix} \frac{1}{2} \\ 0 \end{bmatrix}, \qquad (13)$$
$$c(i, j-i+n,0) \rightarrow \begin{bmatrix} x \\ y \end{bmatrix} = \begin{bmatrix} j+n \\ 2-i-j \end{bmatrix} + rn \begin{bmatrix} 0 \\ 1 \end{bmatrix}$$

for each i=1,2,...,n and j=1,2,..., n. The parameter r is determined for each pair (i, j) as greater of the integers from the set {0,1} for which the following is valid

$$2-i-j+rn \ge 0\ .$$

The role of parameter r is to minimize the execution time of Algorithm_4. An example of ULSA that computes $D^{(1)}$ for the case n=3 is depicted in Fig. 1. Denotation introduced in (1) is used.

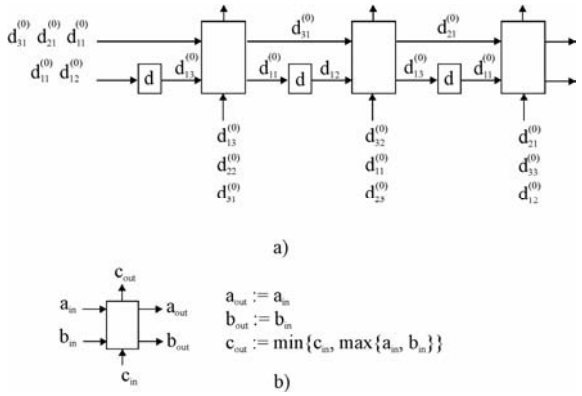

Fig.1. a) Data flow in the ULSA during the computation of $D^{(1)}$ for the case n=3. b) Functional property of the PE.

IV. PERFORMANCE ANALYSIS

According to (10) it is not difficult to conclude that obtained ULSA has $\Omega = n$ PEs, which is optimal number for a given problem size. Assume that time needed to perform an operation of type finding a minimum and maximum of two values (min and max) represents one time unit. Denote with t_{in} initialization time, t_{exe} execution time, t_{out} output time, and t_{tot} the total execution time of Algorithm_4 on the ULSA. According to (13) we have that $t_{in}=2n-2$, $t_{exe} = n$ and $t_{out}=2n-2$. Since $t_{tot} = t_{in} + t_{exe} + t_{out}$ we have that $t_{tot}=5n-4$. Recall that we have designed ULSA that implements Algorithm_4, i.e. computes $D^{(1)} = (d_{ij}^{(1)})$. Matrix $D^{(n)}$ is obtained by computing $D^{(1)}, D^{(2)}, ..., D^{(n-1)}, D^{(n)}$, such that elements $D^{(k)} = (d_{ij}^{(k)})$ are used as inputs for computing $D^{(k+1)} = (d_{ij}^{(k+1)})$, for k=0,1,...,n-1. During the computation the output time of k-th iteration is overlapped with the input time of (k+1)-st iteration. This is illustrated in Table I for the case n=3. Having this in mind, the total time required to compute matrix $D^{(n)}$, on the ULSA is $T_{tot} = n(3n-2)$. The efficiency of the ULSA is $E = \frac{n}{3n-2}$, $0.33 \le E \le 0.5$, which is considered as good efficiency.

TABLE I
STEP BY STEP TIMMING DIAGRAM

clk	d	PE1	d	PE2	d	PE3
0	$d_{11}^{(0)}$					
1	$d_{13}^{(0)}$	$0 \coloneqq \min\{0, \max\{0, d_{11}^{(0)}\}\}$				
2	$d_{12}^{(0)}$	$0 \coloneqq \min\{0, \max\{0, d_{13}^{(0)}\}\}$	$d_{11}^{(0)}$			
3	$d_{11}^{(0)}$	$0 \coloneqq \min\{0, \max\{d_{21}^{(0)}, d_{12}^{(0)}\}\}$	$d_{13}^{(0)}$	$0 \coloneqq \min\{0, \max\{0, d_{11}^{(0)}\}\}$		
4	$d_{13}^{(0)}$	$0 \coloneqq \min\{0, \max\{d_{31}^{(0)}, d_{11}^{(0)}\}\}$	$d_{12}^{(0)}$	$0 \coloneqq \min\{0, \max\{d_{21}^{(0)}, d_{13}^{(0)}\}\}$	$d_{11}^{(0)}$	
5	$d_{12}^{(0)}$	$d_{13}^{(1)} \coloneqq \min\{d_{13}^{(0)}, \max\{d_{11}^{(0)}, d_{13}^{(0)}\}\}$	$d_{11}^{(0)}$	$d_{32}^{(1)} \coloneqq \min\{d_{32}^{(0)}, \max\{d_{31}^{(0)}, d_{12}^{(0)}\}\}$	$d_{13}^{(0)}$	$d_{21}^{(1)} \coloneqq \min\{d_{21}^{(0)}, \max\{d_{21}^{(0)}, d_{11}^{(0)}\}\}$
6	$d_{11}^{(0)}$	$d_{22}^{(1)} \coloneqq \min\{d_{22}^{(0)}, \max\{d_{21}^{(0)}, d_{12}^{(0)}\}\}$	$d_{13}^{(0)}$	$d_{11}^{(1)} \coloneqq \min\{d_{11}^{(0)}, \max\{d_{11}^{(0)}, d_{11}^{(0)}\}\}$	$d_{12}^{(0)}$	$d_{33}^{(1)} \coloneqq \min\{d_{33}^{(0)}, \max\{d_{31}^{(0)}, d_{13}^{(0)}\}\}$
7	$d_{11}^{(1)}$	$d_{31}^{(1)} \coloneqq \min\{d_{31}^{(0)}, \max\{d_{31}^{(0)}, d_{11}^{(0)}\}\}$	$d_{12}^{(0)}$	$d_{23}^{(1)} \coloneqq \min\{d_{23}^{(0)}, \max\{d_{21}^{(0)}, d_{13}^{(0)}\}\}$	$d_{11}^{(0)}$	$d_{12}^{(1)} \coloneqq \min\{d_{12}^{(0)}, \max\{d_{11}^{(0)}, d_{12}^{(0)}\}\}$
8	$d_{13}^{(1)}$	$0 \coloneqq \min\{0, \max\{0, d_{11}^{(1)}\}\}$	$d_{11}^{(0)}$	$0 \coloneqq \min\{0, \max\{d_{31}^{(0)}, d_{12}^{(0)}\}\}$	$d_{13}^{(0)}$	$0 \coloneqq \min\{0, \max\{d_{21}^{(0)}, d_{11}^{(0)}\}\}$
9	$d_{12}^{(1)}$	$0 \coloneqq \min\{0, \max\{0, d_{13}^{(1)}\}\}$	$d_{11}^{(1)}$	$0 \coloneqq \min\{0, \max\{0, d_{11}^{(0)}\}\}$	$d_{12}^{(0)}$	$0 \coloneqq \min\{0, \max\{d_{31}^{(0)}, d_{13}^{(0)}\}\}$
10	$d_{11}^{(1)}$	$0 \coloneqq \min\{0, \max\{d_{21}^{(1)}, d_{12}^{(1)}\}\}$	$d_{13}^{(1)}$	$0 \coloneqq \min\{0, \max\{0, d_{11}^{(1)}\}\}$	$d_{11}^{(0)}$	$0 \coloneqq \min\{0, \max\{0, d_{12}^{(0)}\}\}$
11	$d_{13}^{(1)}$	$0 \coloneqq \min\{0, \max\{d_{31}^{(1)}, d_{11}^{(1)}\}\}$	$d_{12}^{(1)}$	$0 \coloneqq \min\{0, \max\{d_{21}^{(1)}, d_{13}^{(1)}\}\}$	$d_{11}^{(1)}$	$0 \coloneqq \min\{0, \max\{0, d_{11}^{(0)}\}\}$
12	$d_{12}^{(2)}$	$d_{13}^{(2)} \coloneqq \min\{d_{13}^{(1)}, \max\{d_{11}^{(1)}, d_{13}^{(1)}\}\}$	$d_{11}^{(1)}$	$d_{32}^{(2)} \coloneqq \min\{d_{32}^{(1)}, \max\{d_{31}^{(1)}, d_{12}^{(1)}\}\}$	$d_{13}^{(1)}$	$d_{21}^{(2)} \coloneqq \min\{d_{21}^{(1)}, \max\{d_{21}^{(1)}, d_{11}^{(1)}\}\}$
13	$d_{11}^{(1)}$	$d_{22}^{(2)} \coloneqq \min\{d_{22}^{(1)}, \max\{d_{21}^{(1)}, d_{12}^{(1)}\}\}$	$d_{13}^{(1)}$	$d_{11}^{(2)} \coloneqq \min\{d_{11}^{(1)}, \max\{d_{11}^{(1)}, d_{11}^{(1)}\}\}$	$d_{12}^{(1)}$	$d_{33}^{(2)} \coloneqq \min\{d_{33}^{(1)}, \max\{d_{31}^{(1)}, d_{13}^{(1)}\}\}$
14	$d_{11}^{(2)}$	$d_{31}^{(2)} \coloneqq \min\{d_{31}^{(1)}, \max\{d_{31}^{(1)}, d_{11}^{(1)}\}\}$	$d_{12}^{(1)}$	$d_{23}^{(2)} \coloneqq \min\{d_{23}^{(1)}, \max\{d_{21}^{(1)}, d_{13}^{(1)}\}\}$	$d_{11}^{(1)}$	$d_{12}^{(2)} \coloneqq \min\{d_{12}^{(1)}, \max\{d_{11}^{(1)}, d_{12}^{(1)}\}\}$
15	$d_{13}^{(2)}$	$0 \coloneqq \min\{0, \max\{0, d_{11}^{(2)}\}\}$	$d_{11}^{(1)}$	$0 \coloneqq \min\{0, \max\{d_{31}^{(1)}, d_{12}^{(1)}\}\}$	$d_{13}^{(1)}$	$0 \coloneqq \min\{0, \max\{d_{21}^{(1)}, d_{11}^{(1)}\}\}$
16	$d_{12}^{(2)}$	$0 \coloneqq \min\{0, \max\{0, d_{13}^{(2)}\}\}$	$d_{11}^{(2)}$	$0 \coloneqq \min\{0, \max\{0, d_{11}^{(1)}\}\}$	$d_{12}^{(1)}$	$0 \coloneqq \min\{0, \max\{d_{31}^{(1)}, d_{13}^{(1)}\}\}$
17	$d_{11}^{(2)}$	$0 \coloneqq \min\{0, \max\{d_{21}^{(2)}, d_{12}^{(2)}\}\}$	$d_{13}^{(2)}$	$0 \coloneqq \min\{0, \max\{0, d_{11}^{(2)}\}\}$	$d_{11}^{(1)}$	$0 \coloneqq \min\{0, \max\{0, d_{12}^{(1)}\}\}$
18	$d_{13}^{(2)}$	$0 \coloneqq \min\{0, \max\{d_{31}^{(2)}, d_{11}^{(2)}\}\}$	$d_{12}^{(2)}$	$0 \coloneqq \min\{0, \max\{d_{21}^{(2)}, d_{13}^{(2)}\}\}$	$d_{11}^{(2)}$	$0 \coloneqq \min\{0, \max\{0, d_{11}^{(1)}\}\}$
19	$d_{12}^{(2)}$	$d_{13}^{(3)} \coloneqq \min\{d_{13}^{(2)}, \max\{d_{11}^{(2)}, d_{13}^{(2)}\}\}$	$d_{11}^{(2)}$	$d_{32}^{(3)} \coloneqq \min\{d_{32}^{(2)}, \max\{d_{31}^{(2)}, d_{12}^{(2)}\}\}$	$d_{13}^{(2)}$	$d_{21}^{(3)} \coloneqq \min\{d_{21}^{(2)}, \max\{d_{21}^{(2)}, d_{11}^{(2)}\}\}$
20	$d_{11}^{(2)}$	$d_{22}^{(3)} \coloneqq \min\{d_{22}^{(2)}, \max\{d_{21}^{(2)}, d_{12}^{(2)}\}\}$	$d_{13}^{(2)}$	$d_{11}^{(3)} \coloneqq \min\{d_{11}^{(2)}, \max\{d_{11}^{(2)}, d_{11}^{(2)}\}\}$	$d_{12}^{(2)}$	$d_{33}^{(3)} \coloneqq \min\{d_{33}^{(2)}, \max\{d_{31}^{(2)}, d_{13}^{(2)}\}\}$
21		$d_{31}^{(3)} \coloneqq \min\{d_{31}^{(2)}, \max\{d_{31}^{(2)}, d_{11}^{(2)}\}\}$	$d_{12}^{(2)}$	$d_{23}^{(3)} \coloneqq \min\{d_{23}^{(2)}, \max\{d_{21}^{(2)}, d_{13}^{(2)}\}\}$	$d_{11}^{(2)}$	$d_{12}^{(3)} \coloneqq \min\{d_{12}^{(2)}, \max\{d_{11}^{(2)}, d_{12}^{(2)}\}\}$
22						

V. CONCLUSION

A problem of finding MCST of a given graph was considered. The problem is partitioned into two parts. First, we compute a wighted matrix, $D^{(n)}$, according to weighted matrix, $D^{(0)}$, of a given graph. Second, MCST is determined by comparing matrices $D^{(n)}$ and $D^{(0)}$. To solve the first problem we designed unidirectional linear systolic array with optimal number of PEs and minimize the execution time. The efficiency of the designed array is in the range [0.33, 0.5]. Second task is performed by the host computer.

REFERENCES

[1] O. Boruvka, "About a certain minimal problem", *Prace Mor.Prirodoved.Spol.v Brne,* vol. III, no. 3, pp. 37-58, 1926.

[2] J. Nešetril," A few remarks on the history of MST-problem", *Archivum Mathematicum (Brno),* 33, pp. 15-22, 1997.

[3] R. C. Prim, "The shortest connecting network and some generalisations", *Bell Syst. Tech. J.*, no.36, pp. 1389-1401, 1957.

[4] J. B. Kruskal, " On the shortest spanning subtree of a graph and the travelling salesman problem", *Proc. Amer. Math. Soc.*, no 7, pp. 48-50, 1956.

[5] S. Warshall. "A theorem on Boolean matrices", *J. ACM*, no. 9, pp. 11-12, 1962.

[6] R. W. Floyd,"Algorithm 97, Shortest path", C. ACM, no. 5, pp. 5, 1962.

[7] E. I. Milovanović, I. Ž. Milovanović, B. M. Randjelović, M. K. Stojčev, "Systolic implementation of nonlinear transformation of two sequences", *TELSIKS '03 Conference Proceedings*, pp.592-595, Nis, Serbia & Montenegro, 2003.

[8] E. I. Milovanović, M. P. Bekakos, Ć. Dolićanin, I. Ž. Milovanović, "Computing transitive closure on unidirectional linear systolic array, *J. Electrotehn. Math*., vol. 9, no 1, pp.19-28, 2004.

[9] M. Bekakos, E. Milovanović, N. Stojanović, T. Tokić, I. Milovanović, I. Milentijević, "Transformation matrices for systolic array synthesis", *J. Electrotehn. Math*., vol. 7, no 1, pp.9-15, 2002.

Performance of a Dynamic Small-size HPC Platform

D. Kehagias, M. Grivas, G. Pantziou

Abstract - **The dynamic cluster that we proposed in a previous work, matured to a full-scale research tool, that proved its abilities and its potentials. In order to justify its existence, we produced a qualitative performance examination, based on simple techniques and benchmarking tools and programs. The measurements demonstrated that the proposed platform indeed provides a powerful highperformance computing environment, capable of supporting quite large problem solving. It also showed that the advantages of the NoW as a dynamic pool of processors, provides extra on-demand power .**

Keywords - **Beowulf Clusters, NoW, dynamic Cluster, Linux Cluster performance enhancement.**

I. INTRODUCTION

Our previous work on clusters and NoWs concluded to a dynamic, high-performance, versatile, multi-computer complex, that exhibited dynamically adapted performance, ensured cluster-level minimal performance and availability, as well as an interesting Grid resemblance. The complex was used primarily as an educational platform ([1]). Nevertheless, as a dynamic platform, it provides high-performance that can be used for research purposes, too. Its potentials are valuable, since the minimum cluster ensures availability, but the dynamic, ondemand or when available expansion of performance over the NoW, offers a significant power for several kind of scientific problems.

In this paper we present the results of various performancewise test run on the aforementioned platform. It proves its ability to produce high-performance computing, with simple configuration and reuse of existing equipment. To justify that, we ran a set of tests on the platform, in many phases of available nodes. We measured how performance scales within the cluster and when the NoW nodes become available.

The following section describes the platform as used. Next, we explain the set of tests we used and follows the section with the results. We conclude with next steps in this research.

II. CONFIGURATION

The setup we use in the original form of the dynamic cluster is depicted in fig. 1. It includes a small Beowulf-class cluster and a NoW. The cluster consists of 8 PCs, employing Pentium 4 and 512 MB RAM, and a dedicated 100 Mbps Ethernet. No swap is used. The NoW configuration is based on the PC equipment of the Microcomputers laboratory, consisting of 18 PCs connected to a 10/100 Mbps Ethernet. Through a gateway, the laboratory LAN connects to the Institution (TEI) backbone and to the Internet.

The cluster PCs are dedicated to the parallel processing. On the other side, workstations that are members of the NoW may be used by students. Such use may consist of laboratory operation that can be light, moderate or heavily burdening nodes processors, such as compiling, graphics etc. In addition, students may overload the network (downloading large files) or the workstation (complex software, games etc). Last but not least, workstations may stack or reboot any time, without prior notice. Hence, NoW nodes cannot be considered totally available. Instead, they can assist dynamically to increase computing power, especially when no workshop sessions take place.

The parallel processing media is the message passing interface (MPI) and specifically LAM, an open-source implementation of MPI. One of the cluster PCs plays the role of the central controller for both the cluster and the NoW. This PC carries two NIC cards, one for the cluster s LAN and one that connects to the laboratory LAN. As explained in [2], this configuration ensures high security, availability and dynamic high performance.

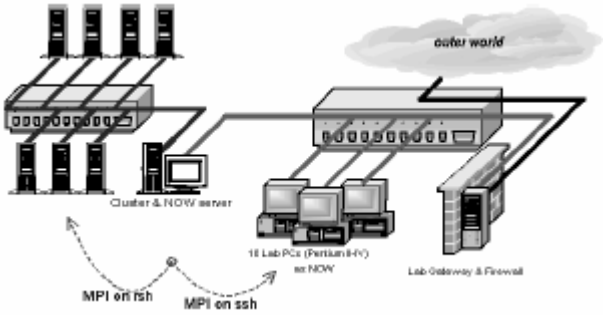

Fig.1. The dynamic cluster.

The cluster LAN is physically isolated from the rest; only the central controller may communicate with the cluster nodes. Hence, their communication happens without any security measurements. Packets encoding or cryptography would impose an impediment to performance, introducing higher latencies and limited bandwidth, as well as wasting CPU cycles. For that, there is no secure shell or SSL installed in cluster nodes. On the other side, security is of prime importance on the NoW, where all systems are exposed to Internet communications, that imply external and internal attacks. A multi-layered protection scheme in the Institution (TEI) enforces protection and therefore external attacks are hard to happen. However, students that work on the NoW nodes may, intentionally or unintentionally, expose the system to attacks, over their workstations. Therefore, security on this

D.Kehagias, M.Grivas and G.Pantziou are with the Department of Informatics, Technological Educational Institution (TEI) of Athens 122 10 - Athens, Greece.
Emails: dkehayas@teiath.gr, mgrivas@cs.teiath.gr
pantziou@teiath.gr

side has to be enforced. Using ssh has been proved a feasible and adequate solution that does not degrade severely nodes and network performance.

III. TESTS

The sole objective in this work is to measure -and ensurethe performance of our proposed platform. At the moment, the possible jobs are limited to computational tasks, although both NoW and cluster nodes employee hard disk and could assist in other distributed computing facilities, such as databases, file management etc.

For the measurements of performance in clusters, many researchers have proposed different techniques and approaches. Some study in details specific factors and their influence to overall performance. Such specifics include network details ([3]), computational or communication needs of tasks ([4]), individual systems performance and heterogeneity ([5][6]), MPI performance and others. Because of the multiple factors that get into account, it is not always possible -or at least easyto identify the factors that affect more overall performance or the way they interact with other factors. It seems that with a large-scale statistical analysis in user-level programs, one cannot identify immediately such factors but may have a very clear picture of the system s performance and the circumstances that affect it.

Many researchers propose simple, user-level tasks as measuring facilities that shows the overall system performance in specific kinds of tasks ([7],[8]). From the differentiation among different kinds and several factors, one can better isolate the influencing factors. Such program metric programs include simple tasks like array multiplication, or more complex sets of measuring tasks that extract immediately sets of results for several values, such as NAS, HPL, HINT and the Pallas Benchmarks.

Our work has been guided by the research interests of influencing colleagues. Specifically, our current research emphasises the use of cluster for load balancing studies, image analyses and information retrieval. Thus, we ensured that performance distribution among different values will depict an analogy for our real tasks. Another important factor, due mainly to the educational perspective, was simplicity in con- figuration and results extract. We concluded in using the NAS benchmarks.

The NAS benchmarks suite was developed by NASA to measure the performance of parallel systems. It consists of 8 tests, namely the Block Tridiagonial (BT), the Conjugate Gradient (CG), the Embarrasingly Parallel (EP), the Fourier Transform (FT), the Integer Sort (IS), the LU Decomposition (LU), the Multi-Grid (MG) and the Scalar Pentadiagonal (SP). Details, articles and information can be seeked at the official site: http://www.nas.nasa.gov/NAS/NPB.

A crucial issue is the scalability of the platform in the form of gain by adding more processors from the NoW. Since the Beowulf-class cluster is a very well known -and very much studied- platform, we do not emphasize the cluster benchmarks, apart from a regular test that runs for measuring and configuration validity. Then, any test focuses on the merits of the NoW to the overall performance, proportionally to the cluster performance.

For our studies, the most interesting tests are EP and FT, that are more compute-intensive. Some other tests (i.e. LU, CG, MG) are used only for informational purposes, because they focus on issues that are not of interest, like blocking communication. BT, SP, IS were not eligible at all, since their requirements are beyond the form or scope of our platform. Those test run as-is, without any optimization or adaptation; neither did any optimization happen to the cluster software. Regarding the size of problems, it is recommended that size B or higher should be used accurate, exact performance comparisons. A is considered very small and may be affected by other factors that are irrelevant to ones study. Size W is a workstations (single machine) version, that is very small and not properly parallelized, mainly for comparison reasons. We used B size since C is very demanding and may not run in all of our equipment.

The common procedure for measuring performance is through the speedup value, that is the amount that the program will run faster than if it was running in a single machine. The most famous approach comes from the computer scientist Amdahl, back in 1967 ([9]). Apart from the speedup factor, he also introduced a formula that produces the upper limit of speedup, known as Amdahl s Law :

$$Speedup_N = \frac{T_{ser} + T_{par}}{T_{ser} + \frac{T_{par}}{N}} = \frac{1}{T_{ser} + \frac{1-T_{ser}}{N}}$$

where T_{ser} is the time to complete the serial portion of the program, T_{par} is the time for the parallel portion and N is the number of processors. If f is the serial fraction of the program then $T_{ser} = fT_1$, where T_1 is the time to execute in a single processor, and

$$Speedup_N = \frac{\mathrm{N}}{\mathrm{fN} + (1-f)}$$

Triggered by results on MPP that surpassed the limits of Amdahl Law, a newer study, [10], concluded with a different formula named Gustafson-Baris Law:

$$ScaledSp_N = \frac{T_{ser} + NT_{par}}{T_{ser} + T_{par}} \text{ or } ScaledSp_N = N + (1-N)T_{ser}$$

However, those laws were made for parallel systems and a long time ago, ignoring communication latencies between processors and other elements, operating system buffering, memory management and other delays. This is by far not the case in distributed systems, like clusters. Several attempts have been made to embed communication and other latencies into the above laws (for example [11]).Clusters perform better under specific circumstances, with a major factor being the computational effort needed for each parallel task. After all, in both the aforementioned laws, latencies can be considered as part of the serial portion. If the parallel portion is by far bigger (i.e. the parallelizable tasks are very big), then $f << 1 - f$ and practically Amdahl s law reaches the optimal N. Thoughts and information on behaviour of clusters can be seen in [12].

IV. RESULTS

The standard metrics is the time it takes for the systems to finish with a specific task. Since the nodes are homogeneous, we can compare their performance to a single computer and specifically the central controller. It should be noticed that each task tried is vastly parallelizable, since our research tasks later will be parallel, too. There was no meaning for a comparison against a simplified, serial algorithm for each measuring program. A single machine setup means that a single PC runs the same program, not that the program is single-threaded or serial. The performance penalty regarding scheduling, multi-tasking and local latencies is out of the scope of this work, which does not include different algorithms. In general, such issues do not affect a beowulf cluster s performance, since communication latencies of commodity networks are many orders of magnitude bigger.

In table I, we compare the cluster against a single machine, for 2 different tests (EP and FT) and for 3 problem sizes each. Our results ensure the validity of our configuration and study the merits in performance to the whole system when adding NoW nodes. The cluster, apart from the validity check, is considered as one step above the single system. The FT test in B size is very large and this is likely the reason that it could not run in the single machine configuration, since we do not use any swap space. However, the most important is that FT exhibits large communication overhead in one of its stages and therefore does not earn as much from the usage of the cluster. As seen in other works, FT can have superlinear scaling on platforms with very fast communication infrastructures, such as InfiBand, Myrinet or SCI. However this is not our case and, hence, FT performance faces a severe bottleneck in the data exchange phase. In addition, since our tasks are more process-oriented, we emphasize EP test.

TABLE I
CLUSTER PERFORMANCE RESULTS FOR DIFFERENT TESTS AND SIZES

Test & size	Single - Mops	Cluster - Mops
FT (W)	34	62
FT (A)	7	32
FT (B)	-	59
EP (W)	1.3	10.4
EP (A)	1.3	10.3
EP (B)	1.1	8.9

Another validity test is the scalability of performance within the cluster (table II). Although there are many studies about scalability within a Beowulf-class cluster, before going to the larger and more unpredictable situation we should ensure that the basis of our configuration follows the norm.

TABLE II
PERFORMANCE SCALABILITY IN THE CLUSTER

# of nodes	EP (B)	FT (A)
Single	1.1	7
2	2.2	10
4	4.5	18
8	8.9	56

Indeed, table II shows that performance within the cluster increases as expected. We should notice that our primary type of tasks (EP) increase linearly and do not exhibit any anomalies, like superlinearity etc.

Then, we study scalability when new computers are introduced, over the existing cluster. We consider the new PCs as available (idle), with a lightly loaded network as it happens off working periods. In table III, after cluster results, each row shows how many more PCs participate. The maximum number (16) is the number of workstations in the laboratory. In future versions, we will have the opportunity to include other laboratories, increasing the number significantly.

After all, the way of connection, i.e. over a separate LAN, using encoding etc, does not allow for an analogous linear scaling of performance. The most interesting detail is that additional nodes exhibit linearity as an independent part, meaning that NoW presents a function of independent cluster that works in parallel to -and complementing- the basic cluster.

TABLE III
PERFORMANCE SCALABILITY WITH NOW

# of nodes	EP (B)
single	1.1
cluster (8)	8.9
+2	9.1
+4	11.4
+8	14.3
+16	20.1

The performance increment is significant. Especially in large problems the merits in perormance can be more than visible. The only drawback is that processes should minimise information exchange, like EP that does not perform any interprocess communication. For such kind of tasks, time of execution can be significantly reduced. The following table IV shows the merits in terms of time gained for the EP test.

TABLE IV
TIME NEEDED TO COMPLETE TASK EP, SIZE B

# of nodes	EP (B)
single	682
cluster (8)	86
+2	80
+4	53
+8	35
+16	22

The following figures depict the improvement in the platform s performance: fig 2 shows the performance in Megaoperations per second (Mops) as a function of the number of nodes within the cluster for both FT (size A) and EP (size B), fig. 3 shows the performance in Mops for EP (size B) test within the cluster and beyond, including NoW nodes, as well as the time in sec.

V. CONCLUSION

In this paper we have studied the performance of our proposed complex, dynamic, multi-computer platform. These first results are very encouraging. Apart from an educational

tool, it exhibits real merits to research related to parallel algorithms and HPC studies. They enable us to continue investigation about the performance and the potentials of this platform.

Forthcoming investigation includes the extension of the platform by adding more computers, more laboratories and other individual clusters that will break the homogeneity and will introduce new problems. In a another direction, parallel algorithms regarding Information Retrieval, cluster and Grid scheduling and other parallel tasks will be produced to the platform. This will allow studies on performance of parallel programs over unstable connections and unpredictable latencies. Finally, more fine-grained and optimized tests will run to produce detailed results, specific to each participant element of the cluster, i.e. communication infrastructure, processing elements, memory usage, nodes performance and others.

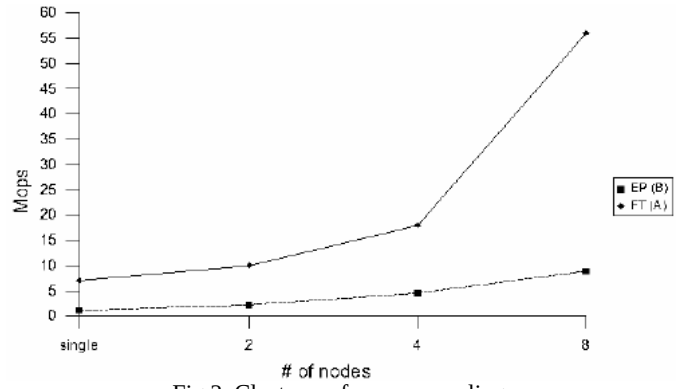

Fig.2. Cluster performance scaling.

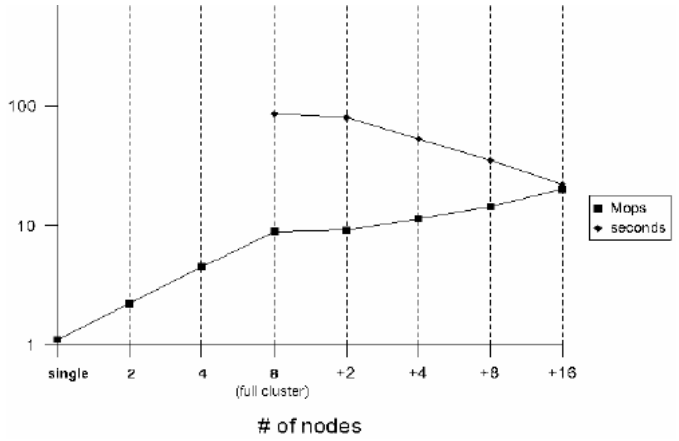

Fig.3. NoW - improving performance, minimizing time.

ACKNOWLEDGEMENTS

This work has been partly supported by the 3rd European Support Framework: Operational Programme in Education and Initial Vocational Training II, programme Archimedes.

REFERENCES

[1] D. Kehagias, M. Grivas, G. Meletiou, G. Pantziou, B. Sakellarios, D. Sterpis, and D. Ximerakis, " low-cost dynamic clustering system for education and research", in *Proceedings of TEMPUS Workshop*, Jan. 2004.

[2] D. Kehagias, M. Grivas, G. Meletiou, G. Pantziou, B. Sakellariou, D. Sterpis, and D. Ximerakis, "Building a low-cost high-performance dynamic clustering system", in *6th International Conference on Telecommunications in Modern Satelite, Cable and Broadcasting Services (TELSIKS 2003)* (B. D. Milovanovic, ed.), vol. 2, pp. 608 613, IEEE and Faculty of Electronic Engineering, Nis, Serbia, October 1-3 2003.

[3] J. Mache and V. Lo, "Dispersal metrics for non-contiguous processor allocation", *tech. rep*., University of Oregon, 1996.

[4] D. G. Feitelson, "The forgotten factor: Facts on performance evaluation and its dependence on workloads"

[5] S. Ali, J.-K. Kim, Y. Yu, S. B. Gundala, S. Gertphol, H. J. Siegel, A. A. Maciejewski, and V. Prasanna, "Utilization-based heuristics for statically mapping real-time applications onto the HiPer-D heterogeneous computing system", in *11th IEEE Heterogeneous Computing Workshop (HCW 2002)*, Apr 2002.

[6] F. D. Berman, RichWolski, S. Figueira, J. Schopf, and G. Shao, "Application-level scheduling on distributed heterogeneous networks", in *Supercomputing 96 Conference Proceedings, New York*, pp. 17 22, ACM Press and IEEE Computer Society Press, 1996.

[7] H. Dail, H. Casanova, and F. Berman, "A decoupled scheduling approach for the grads program development environment", 2002.

[8] A. S. Carsten Ernemann, Volker Hamscher and R. Yahyapour, "Enhanced algorithms for multi-site scheduling", in *Proceedings of 3rd IEEE/ACM International Workshop on Grid Computing (Grid 2002) at Supercomputing 2002, Baltimore*, USA, 2002.

[9] G. Amdahl, "Validity of the single processor approach to achieving large scale computing capability", in *Proceedings of the on AFIPS Spring Joint Computer Conference (Reston, Va.)*, pp. 483 485, AFIPS Press, Arlington, VA, 1967.

[10] R. Benner, J. Gustafson, and G. Montry, "Development and analysis of scientific application programs on a 1024-processor hypercube", *Tech. Rep. SAND 88-0317*, Sandia National Laboratories, Feb. 1988.

[11] K.-J. Andersson, D. Aronsson, and P. Karlsson, "An evaluation of the system performance of a Beowulf cluster", *Tech. Rep. 2001:4*, Dept. of Scientific Computing, Uppsala Uni., 2001.

[12] R. S. Morrison, "Cluster computing architectures, operating systems, parallel processing and programming languages", 2 April 2003.

Language Support for Parallel Discrete Event Simulation

Hristo Valchanov[1], Nadezhda Ruskova[2], Trifon Ruskov[3]

Abstract – **Parallel discrete-event simulation (PDES) requires in-depth knowledge of the mapping process from the physical model to the simulation model and underlying synchronization protocols in use. Languages for PDES could significantly reduce the development effort by providing the user with a set of well-defined language constructs for designing simulation models. In this paper we present an object-oriented language for PDES, called SIMOPAL. Basic features of the language and its distributed implementation are discussed.**

Keywords – **Simulation languages, Distributed Simulation, PDES.**

I. INTRODUCTION

For the past few years Parallel Discrete Event Simulation (PDES) has been regarded as a broad field for scientific research. The interest for it has been dictated by the need for increasing the processing speed in the complex systems analysis. The main reasons thereof are two: the use of parallel processors presumes simulation speed increase, on the one hand, and the large memory space of the parallel processors allows for realization of larger simulation models compared to the memory of single-processor machines, on the other hand. Due to the asynchronous nature of events occurrence and the distributed nature of the model's components performance, the main problem with PDES is ensuring of correct events processing with respect to model time. There are two main approaches for complying with this requirement: conservative and optimistic [2]. With both approaches the simulation model is presented as an aggregate of logical processes, each modeling a separate physical process of the modeled system. The logical processes exchange messages for the events taking place at certain moments of the model time.

The transition from sequential to distributed simulation needs to be as smooth as possible. The user has to focus his skills on the modeling process, free of the necessity to know the used synchronization protocols or their influence. This is what the main goal in the design and development of frameworks for PDES is.

A typical feature of these frameworks is the presentation of the PDES means – in the form of simulation language or as a library. The motivation for the development of languages for PDES instead of function libraries is in the fact that the users do not have to be familiar with the used synchronization protocols or the peculiarities of the runtime environment.

II. RELATED WORK

There are a number of requirements to the PDES languages as regards the model of: presentation of the modeled system; the framework; the synchronization protocols and the runtime environment.

The simulation languages require that the user models the physical environment in a certain way. In the terminology of PDES, the program interface by which the user can describe the modeled environment is known as 'world view'. In the PDES languages two main concepts for the 'world view' are used: event scheduling and process interaction.

Under the approach of event scheduling, the development of the model is described as a sequence of events ordered by their time of occurrence. A procedure corresponds to each event. The occurrence of the event is interpreted by executing of the corresponding procedure and has influence on certain variables of the model state. Typical representatives of this approach are the systems for PDES SPEEDS [3], TWOS [4] and WARPED [5].

The second approach considers the modeled system as an aggregate of parallel interacting processes. The actual components of the modeled system may share the same characteristics which allows for them to be combined in a class. The behavior of each class of components is described by a class process. The interaction between the processes is carried out by an exchange of messages interpreting the occurrence of certain events. Representatives of this approach are the simulation languages of the type of APOSTLE, ParSec, ModSim and YADEES [6].

The PDES languages can provide to the user both the traditional structural programming approach and the object-oriented approach. The advantage of structural programming is the simplified realization of the runtime system and the better time-saving characteristics of the model implementation. However, the object-oriented languages allow for the time of applications development to be significantly reduced and an easier modification and a reusing of the program code to be achieved. APOSTLE and ModSim provide to the users an object-oriented environment for development of their applications, whereas Parsec is a representative of the structural languages for PDES, being a language extension of C. YADDES, on its part, is a descriptive language of the type of Lex and Yacc, providing a minimum set of language structures.

The researches in the filed of PDES for the last 15 years have resulted in the development of a series of

[1]Hristo Valchanov is with the Computer Science Department, Technical University, 9010, Studentska Str., Varna, Bulgaria, E-mail: hristo@tu-varna.acad.bg

[2]Nadezhda Ruskova is with the Computer Science Department, Technical University, 9010, Studentska Str., Varna, Bulgaria, E-mail: ruskova@tu-varna.acad.bg

[3]Trifon Ruskov is with the Computer Science Department, Technical University, 9010, Studentska Str., Varna, Bulgaria, E-mail: ruskov@tu-varna.acad.bg

synchronization protocols [1]. Yet no adequate solutions are known allowing the user to choose the appropriate synchronization protocol. The simulation model can very often derive much better efficiency from a synchronization protocol, but with productivity dramatically reduced when using another one. Some of the simulation languages presented are based on the conservative approach while others use optimistic synchronization methods.

The PDES systems developed in the recent years are largely architecturally dependent, which is influenced by their use by a limited area of researches of the scientific community. For instance, APOSTLE has been developed for the Meico CS-2 multiprocessor system. WARPED has been developed for Intel Paragon and a network of Sun Sparc workstations. Parsec has been developed for IBM SP and for a network of Sun Sparc workstations. The spread of local area computer networks (LAN) provides new possibilities for organizing of large computing resources for acceleration of the simulation process as well as for its popularization. LAN are of low cost and provide a possibility for easy reconfiguration unlike the multiprocessor systems with shared memory traditionally used for the purposes of PDES. At the same time LAN use the widely spread hardware and software which makes them accessible to a wide area of users. The distribution LAN based systems allow for effective use of the available unloaded processors and for an increase of the number of computers in the network, creating conditions for the implementation of simulation models with sufficiently high degree of parallelism.

The article present the typical features of an object-oriented language for PDES – SIMOPAL, providing a possibility for organizing shared memory on distributed memory systems, at the same time ensuring transparency as regards synchronization protocols. Its potential for describing of complex systems as well as its realization has been demonstrated.

III. THE LANGUAGE SIMOPAL

In the model of SIMOPAL (SIMulation Object-oriented Paralel Language) the modeled system is presented in the form of object-oriented parallel system, considered as an aggregate of objects and messages. The object is an abstract description of an independent processing element, possessing local memory. The only admissible interaction between the objects is the asynchronous exchange of messages. These typical features of the model fully satisfy the requirements of PDES to the modeling languages in terms of: maximum performance parallelization; adequacy of describing the modeled system taking account of its inherent parallelism; a possibility for applying the object-oriented approach in view of reducing the process of models description; convenient and effective model implementation on various parallel architectures.

SIMOPAL language is based on the concept of ‘world view’ by means of interacting processes, with elements of the other events processing approach added. The modeled system is described as an aggregate of class instances. A class instance simulates a specific physical process of the modeled system. In the ideal case, each process is executed independently of the rest, on a separate processor in the distributed runtime environment. The executing of each instance (process) is determined depending on the occurrence of specific events. The occurrence of an event may result in one of the following three actions: change in the attributes of a process; scheduling of a new event in the simulation model; creation of a class instance.

SIMOPAL program is an aggregate of class declarations and an initiating section. The declarations are used for structural description of the components and features of the modeled program. The initiating section is used for initial establishment and starting of the simulation and is implicitly interpreted by the runtime system as a virtual initial process.

III.1. CLASSES

A class declaration specifies a pattern of the structure (attributes) and behavior (rules on event processing) of its instances (objects). The class instances are created dynamically during the process of simulation and are interpreted by the runtime system as active components (processes). The values of the attributes of each instance reflect its current state while the aggregate of values of the attributes of all instances determines the current state of the entire modeled system. Each attribute may be of a specific type. Due to the experimental nature of the language, only simple data types are supported: integers (**int**), reals (**real**), boolean data (**bool**), symbol data (**char**), strings, object identifiers (**oid**) as well as a structured type – array.

The class declaration includes a declaration of events, too. The events are the main component of the PDES model, reflecting the change in the state of the modeled system. The events are interpreted by the runtime system as exchange of messages between the class instances (processes). A simulation time (timestamp) simulating the moment of occurrence is associated with each event. An event may contain typified parameters. It allows implementation of an information exchange between the class instances by means of the mechanism of events scheduling in the simulation model and their handling by the processes. The events declared within a class have a local scope of visibility and are only accessible by the objects in this class. If any processing of events between objects of various classes is necessary, then these common events should be declared in a common basic inheritable class.

The execution of the simulation model (change in the current state of the simulation system) is the result of the occurrence of a certain series of events during the model time. The simulation process requires that these events are processed by the active components – the class instances (processes). The class declaration includes a pattern of the behavior of the class instances, too, specified by means of behavior rules. Each rule is defined by an **isevent** statement and refers to a single event of specific type. The algorithm of a process functioning comprises a sequential checking for received message of scheduled event by the order of rules defining. In case of coincidence, that is, when the respective rule is satisfied, the process performs the actions described.

Fig. 1 shows a program fragment of *Router* class declaring with two attributes of the *int.* type. The objects of this class may communicate with one another by means of two types of events, performing certain actions depending on the specific event received.

```
typeclass Router () {
   int hops;
   int length;

   event Update { int hop };
   event Resume { };

   isevent (Update u) {
        length = length + u.hop;
        ...
   };
   isevent (Resume r) {
        ...
   };
};
```

Fig.1. Declaration of Router class

During event processing, additional conditional behavior may be introduced by assigning a guard in the **isevent** statement. An event rule **e** with a guard **b** is satisfied if the process has received a message of event **e** occurrence and the result of guard **b** calculation is true. Fig. 2 shows an example of using a guard.

```
   isevent (Update u) when (length > 0) {
        length = length + u.hop;
        ...
   };
```

Fig.2. Using a guard

III.2. EVENT SCHEDULING

The objects behavior and hence the executing of the simulation model are determined by the occurrence of certain events. The events in SIMOPAL are explicitly scheduled by the instances in the simulation environment by means of **deposit** statement. Such explicit scheduling provides a possibility for the user to describe the functioning of the real modeled system more adequately.

By default, each new event is scheduled with a timestamp equal to the current value of the local simulation time of the process. SIMOPAL provides a possibility for the events occurrence time control by inputting a offset against the current local time of the process. Fig. 3 shows the scheduling of a *Resume* event to a process with *next_router* identifier which is to occur after 100 units of simulation time.

```
   deposit ( next_router, Resume, 100 );
```

Fig.3. Event scheduling

SIMOPAL provides a possibility for special scheduling of events (Fig. 4):

- object to itself – the keyword **self** is specified as first argument. This allows for simulation of timeout events or for generators of events;
- to all objects in the simulation system – the value of **nil** is specified as first argument. Simulation of broadcast exchange is allowed;
- to a group of objects in the simulation system – a composition of objects identifiers is specified as first argument by means of + operator. If a class identifier or a composition of class identifiers is specified, depositing of the event will concern all objects of this class or composition of classes.

```
(* Timeout event to self after 100 time units *)
   deposit ( self, Timeout, 100 );

(* Event Transfer to all processes immediately *)
   deposit ( nil, Transfer );

(* Event Route to all objects of class *)
(* OSPF_router and BGP_router *)
   deposit ( OSPF_router + BGP_router, Route );
```

Fig.4. Special scheduling of events

Depositing of events to multiple objects is one of the features of SIMOPAL which has not been realized in any of the above-mentioned simulation languages.

III.3. CLASS INHERITANCE

SIMOPAL ensures multiple class-to-class inheritance. The current class inherits the immediate superclasses of a list. The inheriting allows setting up of class hierarchy. An object of a given class inherits both the structure (attributes) and the behavior (rules) of its superclasses.

Fig. 5 shows an example of relations between three classes.

Class C is subclass of classes A and B. When inheriting, all attributes (*Attr)*, rules *(Rules)* and declarations of events (not shown on the diagram) of its superclasses A and B are added without changes. Any new properties of class C object may be additionally specified in the C declaration. If classes A and B on their part are a subclass of other superclasses, the above inheritance principle will be valid for them, too.

One of the main applications of inheritance is the expansion of the visibility scope of the identifiers in a SIMOPAL program. By default, only the class identifiers are global, while all declarations within their bodies are local. Due to the absence of global data in the distributed simulation model, objects of different classes may exchange information only by means of the events mechanism. The declarations of used events may be set apart in a superclass which on its part is to be inherited by the above-mentioned classes.

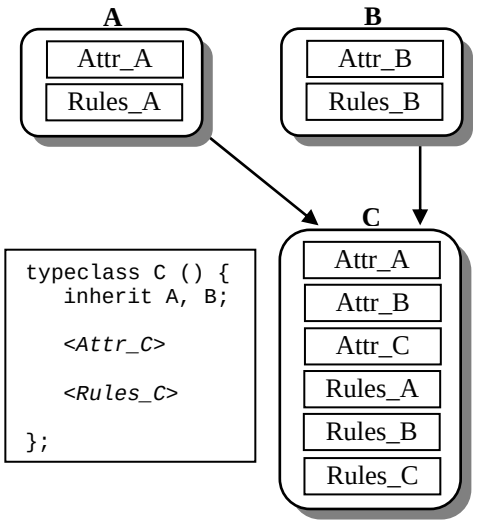

Fig.5. A class inheritance hierarchy

IV. IMPLEMENTATION OF THE LANGUAGE

The distributed runtime system of SIMOPAL language has been realized on a network of workstations, each functioning under the control of OS Linux. Its structure is of cluster organization, with a cluster of logical processes executed by a separate workstation. Each logical process (LP) interprets the functioning of a specific instance of a process defined in the language. The execution of LP in each cluster is controlled by a local dispatcher. Realization of the logical processes within a single Linux process reduces switching of the processes context to a significant extent, which increases the simulation efficiency. The communication between the individual clusters is carried out by a communication subsystem with possibilities for use of both the MPI communication standard and the SCTP protocol [7].

The distributed runtime system is based on optimistic synchronization protocol TimeWarp with aggressive and lazy message cancellation.

V. CONCLUSION

The SIMOPAL language for distributed simulation has the following characteristics:

- object orientation;
- compact and convenient description of the modeled system;
- transparency for the user as regards the distributed nature of modeling allowing for sequential or distributed simulation of the models without changing the program code;
- it is oriented to a wide area of conceptual synchronization models in PDES;
- it is realized on a distributed runtime system with transparency as regards the load balancing of logical processes;
- a possibility for logical organization of a shared memory on a distributed architecture.

In our future work we will focus on the development of graphic user interface and libraries to help accelerate the process of creation of program models in specific areas of application.

REFERENCES

[1] Ferscha A. Parallel and Distributed Simulation of Discrete Event Simulation. In Handbook of Parallel and Distributed Computing, Mc-Graw Hill, 1995.
[2] Fujimoto R.M. Parallel Discrete Event Simulation. Communications of the ACM, vol.33, N10, pp.41-52, 1990.
[3] Steinman J. SPEEDES: A Multiple Synchronization Environment for Parallel Discrete Event Simulation. Int. Journal in Computer Simulation, v.2, N3, pp.251-286, 1992.
[4] Rich D.O., Michelsen R.E. “An Assessment of the ModSim/TWOS Parallel Simulation Environment.” In Proc. of the 1991 WSC, pp. 509-518, 1991.
[5] Dale E., Wilsey P., Timothy J. WARPED Simulation Kernel Documentation, 1995.
[6] Low Y., Lim C. Cai W., Huang S., Turner S. Survey of Languages and Runtime Libraries for Parallel Discrete Event Simulation. Tech. Report, Simulation, pp.1-15,1999.
[7] H. Valchanov, I. Ruskov, N. Ruskova. A Communication Kernel of a Cluster System for Distributed Simulation. In Proc. of the CompSysTech2004, pp.IIIB.19-1 – IIIB19-5 , 2004.

DRAM Controller with a Simple Predictor

Vladimir V. Stankovic[1], Nebojsa Z. Milenkovic[2]

Abstract – **In the arsenal of resources for computer memory system performance improvement, predictors have gained an increasing role in the past years. They enable hiding the latencies when accessing cache or main memory. In paper [1] it is shown how temporal parameters of cache memory access, defined as live time, dead time and access interval could be used for prediction of data prefetching. In this paper a possibility of applying an analog technique on controlling DRAM memory opened rows closing, is being researched. Obtained results confirm such a possibility, which served us to propose a simple predictor. Using such a predictor can significantly decrease the average DRAM latency.**

Keywords – **DRAM, memory, latency, DRAM controller, DRAM controller policy, predictor, bank, row.**

I. INTRODUCTION

A desire for better potential utilization of processors, which are becoming faster and faster, demands a memory system with similar performances. A critical ring in the hierarchically organized memory system is the main memory, implemented with chips of dynamic memory (DRAM – Dynamic Random Access Memory). In order to achieve as large bandwidth as possible, the chips of contemporary DRAM memories are organized with several independent memory banks, allow memory accesses pipelining, and buffer the data from the last activated row in each bank. Although increasing the memory bandwidth, these solutions make the contemporary DRAM memories performances dependable on memory access patterns. Contemporary DRAM memories are not really random access memories, characterized with identical access times to all locations in them. They are actually three-dimensional memories, with banks, rows, and columns as dimensions. DRAM data access with row opening demands the following time:

$$Ta = Tpr+Tra+Tca \quad (1)$$

where

- Tpr – is precharge time,
- Tra – is row access time,
- Tca – is column access time.

Using of read and write commands with autoprecharge eliminates the precharge time when next access occurs, reducing the access time to Tra+Tca. Data accesses into already opened rows eliminate the precharge time and row access time, reducing the access time to Tca. The result is that consecutive accesses to different rows into single memory bank have larger latencies than consecutive accesses into the same row. Performance maximization of DRAM memories demands minimization of participation of precharges and rows openings.

This makes that we can influence DRAM memory performances (latency) by controlling the data placement into banks and rows. This is the basis of papers in which address remappings are considered, which transform memory addresses into banks, rows and columns that optimize DRAM performances for certain memory access patterns [3, 4].

DRAM memory latency can be decreased if the opened row is closed just before the next data access directed to the same bank, but to different row, occurs. In that way the precharge time Tpr is being hidden, so the latency is practically reduced to Ta = Tra+Tca. The latency could be additionally reduced to Ta = Tca, by hiding the row access time. This demands the next row that is going to be accessed, to be opened in advance. In-time closing of the opened row demands a prediction *when* to close the opened row. Opening in advance the next row to be accessed demands a prediction *which row* to open and *when*.

Papers [1, 2] deal with possibilities to predict the moment when the data block in the cache memory is to be declared 'dead' (i.e. unnecessary present in the cache, because it is not to be used in the near future) and when and which data block to prefetch to the cache. Those ideas maybe could be applied to DRAM memories. That inspired us to investigate the possibilities of applying some of those ideas on DRAM memory performance optimization. In this paper we have restrained on ideas from [1], which relate to applying metrics of characteristic time parameters of data blocks transferred to cache memory. Analogically, we have defined proper characteristic time parameters for DRAM memories. By simulation, we have concluded that DRAM memory accesses have some regularities that can be used for prediction when to close the opened row. Based on those results, we have proposed a predictor, which could be integrated into existent DRAM memory controllers.

The paper is organized as follows. In section II we consider the existent DRAM controller policies and the basic idea. In section III the used simulation model is exposed. Section IV gives a review of the obtained results, and section V is the conclusion.

II. WHAT PREDICTION IS BASED ON?

A classic DRAM controller uses two possible policies (strategies): Open Page (Row) Policy (Optimistic Policy) and Close Page (Row) Autoprecharge Policy (Pessimistic Policy). When using the first one, the row is kept opened, which decreases the latency if the next DRAM access is directed to

[1]Vladimir V. Stankovic is with the Faculty of Electronic Engineering, Aleksandra Medvedeva 14, 18000 Nis, Serbia and Montenegro, E-mail: svlada@elfak.ni.ac.yu

[2]Nebojsa Z. Milenkovic is with the Faculty of Electronic Engineering, Aleksandra Medvedeva 14, 18000 Nis, Serbia and Montenegro, E-mail: nmilenko@elfak.ni.ac.yu

the same row as the previous, and increases the latency if the next DRAM access is directed to some other row. In the first case the latency is equal to Tca, and in the second it is equal to the sum Tpr+Tra+Tca. When using the second policy, a row is being closed after every access, so the latency is always the same – the sum Tra+Tca. The Open Row Policy gives good results if there is a good memory access locality, and the Close Row Autoprecharge Policy gives good results if DRAM accesses have mostly random character. In our previous papers [4, 5] we have already considered various possibilities of obtaining hybrid policies, which use the advantages of both policies. The goal is to achieve a policy more efficient than both the Open Row and Close Row Autoprecharge Policy, and in that way, decrease the DRAM latency. In ideal case the opened row should be kept open for as long as there are accesses into it, and not to some other row, and it should be closed after the last access into it. In that way the system would be prepared for the next row access. In that case the precharge time could be hidden every time the row is changed, which would decrease the latency. In this paper we consider a hybrid policy which strives to predict the moment when to close the opened row.

Since we want to apply the metrics analogous to those from [1] in order to improve DRAM memory performances, let us first define those metrics related to DRAM memory. Live time is a time interval that elapses from opening the row in a bank until the last access into that row before its closing. Dead time is a time which elapses from the last access to open row until the moment of its closing. Access interval is a time interval which elapses between two consecutive accesses to open row in a bank. A live time of an open row is called a zero live time, if after its opening there are no further accesses to that row till its closing. If there is at least one access to already open row before its closing, then that row's live time is not a zero live time.

An insight of open row entering into dead time is a signal for the DRAM controller to close that row, and eventually open some other row in the same bank. It would also be preferable for the DRAM controller to be able to recognize (i.e. to predict) opening row with zero live time, since in that case that row should be immediately closed.

III. System simulation model

For simulation we have used the program Sim-Outorder from the Simplescalar Tool Set [6]. We have integrated this simulator with programs that simulate DRAM memories, written by ourselves. The characteristics of the simulated processor are: a superscalar processor that issues at most 4 instructions on every clock cycle and supports out of order instruction execution. The processor clock frequency is 2 GHz. As a branch predictor a two-level branch predictor was used. There are two levels of cache memories. The first one contains separate instruction and data caches. They are both 16KB large; use direct mapping and have line size of 32B. The second level contains a unified cache, 1MB large, with set-associative mapping - associativity of 4, and line size of 128B. All the cache memories use write-back policy.

The simulated DRAM memory has the following characteristics: there are 4 banks in one chip, 4096 rows in a bank, the row capacity is 1KB, the precharge time, row access time, and column access time are 20 processor clock cycles each, the memory bus has 128 data lines.

We have simulated executions of 6 benchmark programs from the SPEC95 suite: cc1, compress, ijpeg, li, m88ksim, and perl. The characteristics of those programs can be found in our previous papers [4, 5].

IV. Results

As a start, we have measured the following parameters: open row hit probability, number of zero live times, number of non zero live times, and average values for access interval, live time and dead time, measured in processor clock cycles. The results are shown in Table I. It can be seen that in benchmark programs with small open row hit probability (cc1, ijpeg, perl) number of zero live times is much greater than number of non zero live times, which is reasonable. In benchmarks with large open row hit probability (compress, li, m88ksim) there are much more non zero live times than zero live times. These results recommend to try researching the possibilities of designing a predictor which, when opening a row, predicts its live time as zero or nonzero. This will, probably, be a subject of our future work. If the other parameters are observed, it can be noticed that in all the cases, not dependable on the open row hit probability, the average value of access intervals is much less than the average value of dead times. This suggests a possibility of defining a simple predictor. If, from the last access to open row, a certain amount of time (equal to some boundary value) has elapsed, then that row should be closed, since it has probably entered the dead time. If that amount of time has not yet elapsed, the row is to be kept open. As a boundary, a value that is the same order of magnitude as the last access interval should be used. For instance, it could be the last access interval multiplied by 2 or 4.

TABLE I
MEASURED CHARACTERISTICS OF BENCHMARK PROGRAMS

Benchmark	cc1	compress	ijpeg
Open row hit probability	0.34	0.84	0.31
Zero live times	58662	51	28895
Non zero live times	15811	587	2621
Access interval	65833	2889	28692
Live time	165718	17773	155700
Dead time	1243661	161594	580286

Benchmark	li	m88ksim	perl
Open row hit probability	0.76	0.83	0.07
Zero live times	59	101	1174201
Non zero live times	236	794	44955
Access interval	839903	643307	43078
Live time	3420116	3712389	97176
Dead time	18495793	19202689	135064

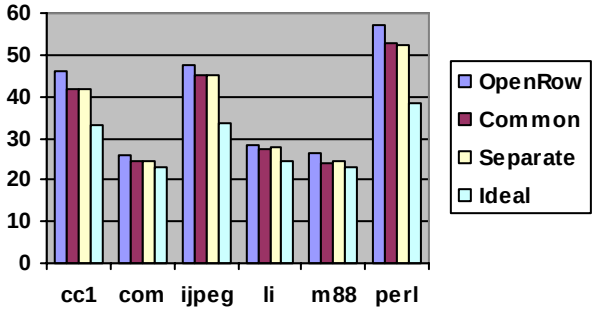

Fig. 1. Average latencies in processor clock cycles for rgbc

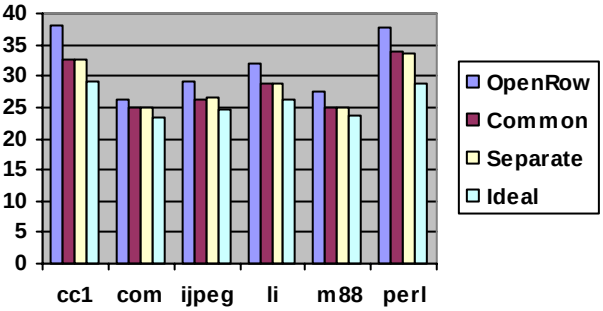

Fig. 2. Average latencies in processor clock cycles for rgrbcx

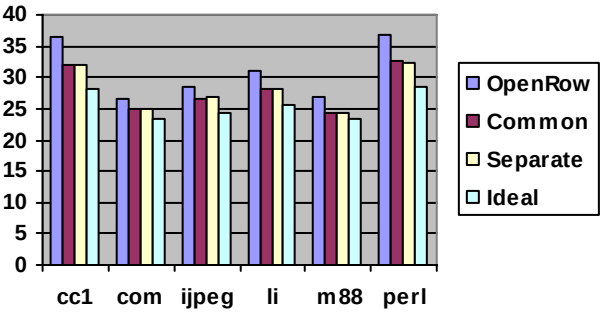

Fig. 3. Average latencies in processor clock cycles for rbrgcx

We have tried 2 variants for boundary levels – the last access interval multiplied by 2 and 4. The results are practically the same; i.e. the differences are insignificant. In this paper we show the results when the boundary value is equal to the access interval multiplied by 2. In paper [4] we have considered various address remappings, which increase the open row hit probability. In order to gain as objective evaluation as possible, we have tried 3 variants. The first one is a classical page interleaving scheme, which also can be named as row-group-bank-column (rgbc) by the sequence of meaning of the address bits, and the other two are the two address remappings from the mentioned paper that have showed as the best: rgrbcx and rbrgcx. For all of the named combinations we have tried two possible solutions. The first one uses only one common value of access interval, which is defined by every appearance of new access interval in any bank. In the second solution there is one value of access interval for each bank in the system.

The average DRAM latencies, in processor clock cycles, are shown in Figs. 1, 2 and 3. These Figs. show average DRAM latencies when using Open Row Policy (Open Row), policies with the proposed simple predictor with a common value and with separate values of access interval (Common and Separate), and a policy with an ideal predictor, i.e. a predictor whose prediction accuracy would be 100% (Ideal). It can be seen that the proposed solutions, although simple, give rather good improvements. The encouraging thing is that improvements are obtained not only for the basic rgbc scheme, but also for the both address remapping schemes. This means that it is possible to apply the address remappings, which already give respectable improvements, together with the considered predictor to additionally increase the improvements.

If we compare the solutions with a common value and with separate values of access interval, there are almost no differences among them. In the solution with a common value there are access interval interferences from different banks. That interference is removed when using separate values for each bank. This interference is not significant in a single program environment, which was the case of our simulations (this is why there are practically no differences in the results). In some cases (li and m88ksim with rgbc and ijpeg with rgrbcx and rbrgcx) worse results for Separate than Common could be explained by longer negative influences of extreme, relative to average, values of access interval. In a multiprogram environment access intervals of different programs can differ a lot. In that case the interference influence in the solution with a common value would dominate, which would certainly decrease the prediction accuracy, so this solution would show less performance improvement. We can conclude this from Table I, which shows that average access interval values for different programs can range up to 1 to 290 (for compress and li).

Table II shows the prediction accuracy and coverage when using one common register for all the banks. The coverage is the part of accesses for which the predictor made a certain prediction, starting from the first appearance of access interval value. The prediction accuracies and coverages when using separate values for each bank are very similar to these ones, so we omit them. In Table II cr (close row) is the probability of the accurate prediction that the row should be closed, and ncr (not close row) is the probability of the accurate prediction that the row should be kept open. The proper coverages are given in the parenthesis. By simple addition of these coverage percentages it can be concluded that the percentage of the accesses not involved by the predictor is negligible – in almost all the cases it is about 1% or less. Only in case of li using basic page interleaving scheme this percentage is about 5%. These accesses not involved by the predictor comprises all the first accesses which are zero live times, till the appearing of the first non zero live time, i.e. the first value for access interval, which is the moment when the predictor starts with the prediction process. If we see the prediction accuracies themselves it can be seen that in 29 of 36 cases they are more than 70%, and in 19 of 36 cases are more than

80%. These are rather good values. The high prediction accuracies also have high coverages in most of the cases. It happens, however, the predictions that the row should be kept open, to be very low, and to have rather high coverages, when using the basic page interleaving scheme, in the benchmarks with low open row probabilities (cc1 - 0.43 (63%), ijpeg - 0.34 (80%) and perl - 0.08 (78%)). These cases deserve an attention to look for improvements – probably the mentioned predictor which predicts zero live times could give needed improvements.

TABLE II
PREDICTION ACCURACY AND COVERAGE FOR COMMON

Benchmark	cc1	compress	ijpeg
cr – rgbc.	0.79 (37%)	0.63 (21%)	0.80 (20%)
ncr – rgbc	0.43 (63%)	0.99 (78%)	0.34 (80%)
cr – rgrbcx.	0.78 (48%)	0.66 (21%)	0.79 (25%)
ncr – rgrbcx	0.85 (52%)	0.97 (79%)	0.96 (75%)
cr – rbrgcx.	0.74 (48%)	0.68 (21%)	0.70 (24%)
ncr – rbrgcx	0.89 (52%)	0.98 (78%)	0.94 (76%)

Benchmark	li	m88ksim	perl
cr – rgbc.	0.60 (27%)	0.78 (18%)	0.95 (22%)
ncr – rgbc	0.96 (68%)	0.99 (80%)	0.08 (78%)
cr – rgrbcx.	0.78 (29%)	0.86 (18%)	0.82 (30%)
ncr – rgrbcx	0.90 (70%)	0.96 (81%)	0.72 (70%)
cr – rbrgcx.	0.73 (31%)	0.82 (19%)	0.82 (32%)
ncr – rbrgcx	0.94 (67%)	0.98 (80%)	0.77 (68%)

Let us now consider how the implementation of the considered predictor would influence the complexity and price of the DRAM controller. The controller should have a counter for each bank (to take care of the elapsed time since the last access), one common register for all the banks in the system or separate registers, one for each bank, (for storing the last access interval value), and one comparator for each bank (for comparing the access interval register value(s) with the counters). In order to minimize the length of the counters, they could be triggered with a signal derived by dividing the DRAM's clock. A simple shift operation by 1 or 2 positions over the access interval register(s) would be needed for defining the boundary value(s). By comparing this value with the counters the controller would decide whether to issue a precharge command or not. The controller that implements the Open Row Policy has a register for each bank for storing the last open row index, and comparators for comparing the index of the row to which the current access occurs with those registers. Compared to that, we could say that the controller with the proposed predictor would have similar complexity and price.

V. CONCLUSION

In this paper we have considered performances of DRAM memory with a controller that uses a simple predictor which predicts whether the opened DRAM row should be further kept open or it should be closed. The considered two solutions (the first one, with a common register, and the second one, with separated registers, for access intervals storing) are rather simple, and give good performance improvements, for all the three considered variants (the basic page interleaving scheme and the two address remapping schemes). The implementation of the considered solutions would be simple and with acceptable price. It is expected that the considered predictor, amplified with a predictor that predicts whether the live time is going to be a zero live time, would give additional performance improvements. This will be a subject of our further research. Also, we will focus our attention on designing a predictor which predicts which is the next row to be opened, after closing the current row. That kind of solution would additionally decrease the DRAM memory latency.

REFERENCES

[1] Z. Hu, S. Kaxiras, M. Martonosi, "Timekeeping in the Memory System: Predicting and Optimizing Memory Behavior", The 2003 IEEE International Solid_state Circuits Conference (ISSCC 2003), February 2003.

[2] A. Lai, C. Fide, B. Falsafi, "Dead-Block Prediction and Dead-Block Correlating Prefetchers", Proc. 28th ISCA, June 2001, pp. 144-154.

[3] Zhang Z., Z. Zhu and X. Zhang "A permutation-based page interleaving scheme to reduce row-buffer conflicts and exploit data locality" Proc. 33rd AIS on Microarchitecture, (Micro-33), Monterey, Calif. 2000.

[4] V. Stankovic, N. Milenkovic, "Access Latency Reduction in Contemporary DRAM Memories", Facta Universitatis, series: Electronics and Energetics, Vol. 17, No. 1, April 2004, pp. 81-97.

[5] V. Stankovic, N. Milenkovic, "Two New DRAM Controller Policies", Yu Info 2004, Kopaonik, March 2004.

[6] Burger D and T.M.Austin, "The SimpleScalar Tool Set, Version 2.0", University of Wisconsin-Madison Computer Sciences Department Technical Report #1342, June 1997.

An Organization of System for Access Sharing to Information Resources

Radi Romansky[1], Iva Nikolova[2]

Abstract – **This paper examines and describes some organizational issues of the design of decentralized distributed information space that allows information resources as files to be shared in a synchronized and consistently manner amongst the distributed users. Our work focuses mainly on presenting some of the principles and technical approaches to the implementation of the networking and the system infrastructures, as well as on the possible approaches for optimization of the information access and effective scheduling of the distributed processes.**

Keywords – **peer-to-peer networks, distributed systems, distributed content sharing, file sharing, access sharing, collaboration**

I. INTRODUCTION

Organizing access to resources and deploying the computer and communication networks that underpin this access presents a number of challenges.

The sharing and coordinated use of resources is fundamental to an increasing range of computer applications. This sharing may involve not only file exchange, but also direct access to computers, software, data, and other resources, as is required by a range of collaborative problem-solving and resource-brokering strategies [1-3].

In the recent years, a lot of research interests focus on the content sharing networks and technologies [4-7] and their analysis and application. More and more popular become the computer applications that rely on the decentralization and equality of participants [8 -15].

The object of our current research interest is the design and organization of decentralized and dynamic, distributed information space, which to integrate the information resources that are shared by a group of users for support of research and educational process within the intranet network. The aim is to form a collaborative group of the PC's of the participants, in which the users are not only consumes of resources, but also are providers of such resources.

The main goal of this work is to offer an organization and implementation of collaborative application, in which the users can exchange information, such as educational materials. The problem actuality is verified by the work discussed in [11], [13], [14]. The computer application we consider here, represent a small file-sharing system. Its implementation is based on the architectural paradigm of the decentralized peer-to-peer network topologies [15].

The use of a collaborative environment based on peer-to-peer approach enables to take advantage of the following characteristics of the decentralized P2P systems: (1) *scalability* – constant complexity of the system regardless of number of nodes in the system; (2) *reliability* – peer nodes are connected directly without the need of a master server's arrangement, creating a flat, ad-hoc network topology, thus the malfunction on any given node will not effect the whole system. Only the data that has been stored on the peer that crashed gets lost. The rest of the system works as before.

Therefore, in the process of building of such distributed information space an important moment is the design of the policies of the system and very well understanding of all the scenarios that might occur. Following that principle, in the next sections, we will describe the main organizational features and technical aspects of implementation of the networking and the system infrastructures.

II. AN ORGANIZATION OF THE NETWORKING INFRASTRUCTURE

As it is well known the networking infrastructure sets up the base of all high-level operations.

The distributed information space is formed by the network integration of the PCs of the participants, called *member peer nodes* or only *peer nodes*. The system architecture, shown in Figure 1, is based on the decentralized model of P2P content-sharing networks [15]. It has a *Server-Client* structure where there is no centralized servers exists. All peer nodes are connected directly and are equal i.e. each peer node that is member of the collaborative group is empowered as both, a server of files and also as a client that can request files from other members, hence creating a flat network topology.

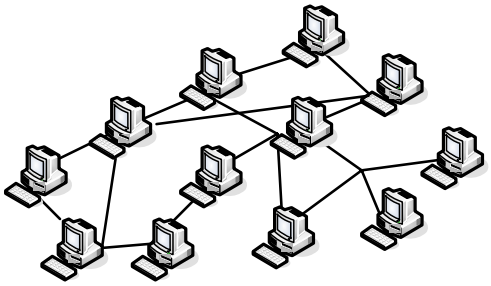

Fig.1. An illustration of the decentralized topology of the system

The system is designed to support two type operations – *join operations* and *file operations*. In order to join the network, a peer node must contact a node that is always

[1] Radi Romansky, Faculty of Computer Systems and Control, Computer Systems Department, Technical University of Sofia, Bulgaria E-mail: rrom@tu-sofia.bg

[2] Iva Nikolova, Faculty of Computer Systems and Control, Computer Systems Department, Technical University of Sofia, Bulgaria E-mail: inni@tu-sofia.bg

online, which give the joining peer the IP address of one the existing peer nodes that are already a members of the group. Each peer, however, will only have information about its neighbors, which are peers that have a direct edge to it in the network.

When the joining is made, a peer node can send its query (e.g searching for a particular file) to the other peer nodes in the network. File transfers made between member peer nodes are always done directly through a data connection that is made between peer sharing the file and the peer requesting for it.

The requirement for support of group working means that online resources may be shared and used by multiple concurrent readers and writers.

The collaboration amongst peer nodes can take two forms:

(a) each peer node can request local files, shared from remote peer node;

(b) each peer node can serve requests of remote peer nodes for local files it owns.

This form of collaboration between peer nodes requires concurrency control and usual concerns with liveness, safety and fairness [15].

To achieve a multiple concurrent queries for files to be processed simultaneously by a peer node, the network infrastructure is implemented as a multithread model. The simultaneously access of the multiple threads to the file directories is ensured by using critical section objects for each data structure.

Communications are built in the basis of numerous *messages passing*. A given message contains the request type and returned answer.

Two types of threads are empowered to take care of the system operations: *client* and *server* threads. The first ones are charged with client-side processing, forming the requests toward the server threads, and with the receiving the responses. They are created either by the main interface thread of the application or by other client threads. The second ones are created to correspond to the identity of the requesting threads and are responsible for the server-side processing. They accept all incoming connection requests and take the appropriate actions to their processing.

Join Process

As it was mentioned above, if a peer node wants to join the network, it needs to know the IP address of a peer node that is already a member of the group. The peer nodes will connect to each other and execute *Join Algorithm*. At its end, all the members of the collaborative group will know about the new member and the files that it has to share, and the new member will know about all the existing members and the files they have share.

We consider two steps join process: *Initial join* and *Group join*. The concept of the Initial join process is illustrated in Figure 2, where: *(1)* New peer node A connects to the Host Cache to get the list of available online member peer nodes already connected in the network; *(2)* The Host Cache sends back the list with member peer nodes to the peer node A; *(3)* Peer node A sends the connection request message to one of member peer nodes, for example peer node B; *(4)* Member peer node B replies with message granting peer node A to join the network. Next, new peer node A automatically receives a list with the IP addresses of all member peer nodes that are online. With these member nodes it begins the second step of the join process – *Group Join*. During that phase a connection with each of these nodes in the list is established. At its end, all the members will have information about the list of files that are available locally at the new peer node, as well as the new peer node will receives a list of files that are at the remote node.

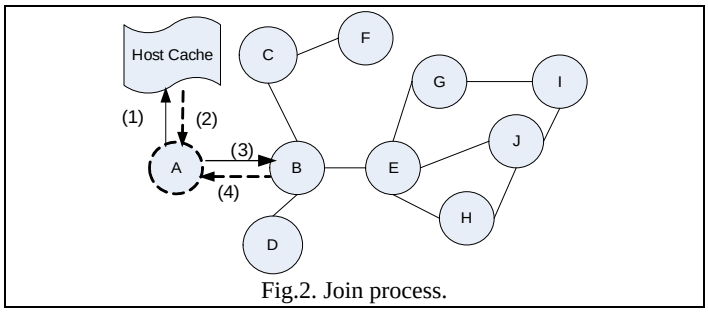

Fig.2. Join process.

From the point of view of the multithread model, there is a client and server parts of the join process that are implemented as client and server threads.

On receipt of the user's request to join in the group, the user interface server thread creates a *Initial Join Client Thread* (IJCT), maintained by *IJoinClientThreadProc()* function that sends a connection request *initial_join* to the listener server thread on the chosen remote peer node. As a result the server *AcceptThread* creates a new thread to serve that connection request. This server tread (IJST) is maintained by *IJoinServerThreadProc()* function.

The IJCT begins the join process by sending its computer name to the IJST. In return, the IJCT receives a list of the computer names of the existing member peer nodes. Next, the IJCT creates separate threads called *Group Join Client Thread* (GJCT) that establishes a connection with each of the peer nodes in the list. A *Group Join Server Thread* (GJST), maintained by G*JoinServerThreadProc()* function is created at each member peer node to correspond with the GJCTs on the non-member node. Then, by accessing a global data structures a GJCT receives a list of files that are available locally at that peer. This list is sent to the corresponding GJST. Mutually exclusive mechanisms and critical sections objects control the access to the global data structures, containing the identification of all member peer nodes and their files. These connections are broken with competition of join threads 'executions.

III. DESIGN OF THE SYSTEM INFRASTRUCTURE

To construct such a versatile working environment, in which the participated peer nodes can share and use information resources among themselves without relying on a dedicated server it is necessary all member nodes of the collaborative group to maintain information about all the members peer nodes and the files that they own. Additionally, in the context of the decentralized management, a natural

tendency of such environment is to evolve over time (for example, with joining and leaving peer nodes along their resources). We are thus motivated to study how to improve the availability of shared files, so that users can access any file regardless of the current subset of online member peer nodes. Maintenance replicas of a particular file can achieve this. If replicas of files exist, they will serve the purpose of increasing concurrent reads. When member peer nodes need to download the latest copy of the file they can do from any location that holds a valid replica.

Figure 3 illustrates an example scenario of the collaboration amongst the member peer nodes: (1) Member peer node B and Peer node D collaborate on file; (2) Peer A access file on D.

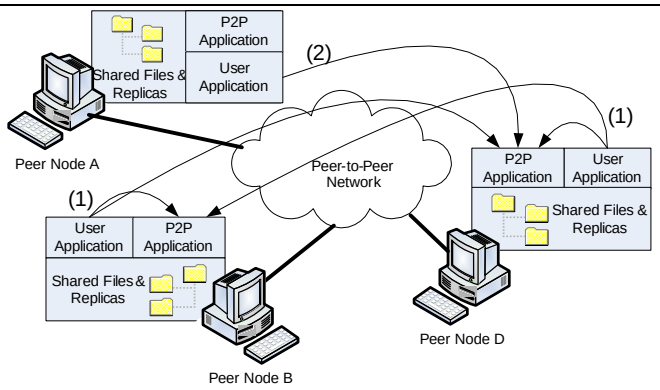

Fig.3. Example Scenario of collaboration

In reference to this, we consider the following system design features:

- All peer nodes must dedicate folders on their hard disks to store shared files or replicas. Before a peer node is ready to join the network, all the local files must be registered by creating replica lists for each file.
- Files present in the dedicated folder can be viewed or modified by all member peer nodes except in the case if a write operation is requested by a peer node for a file that is being written to by another peer node or that files are not valid replicas.
- When a peer node modifies a file, all previous replicas of that file lose their status of being a replica and become old copies of the file. Subsequent requests to use these old copies of the file will cause to download the latest copy of the file so that the users always work on a valid replica.
- When a peer nodes need to download the latest copy of a file they can do so from any locations that hold a valid replica. A concurrency can be improved by allowing a read operation on a file that is being written to. In this case the user should be warned that the copy being read might not be valid for too long. To optimize the number of file transfers that occur between peer nodes it considers a transfer to be only performing after comparing the local replica of file with the original file.

The system supports the following actions with shared files: adding a new files; removing files; reading a file that belongs to another member peer node; writing to a file that belongs to another peer node; reading a remote file by fetching it from one of its replica locations; choosing a location from where to fetch the replica of a file; getting "*Read*" permissions for a file that is currently being written to.

The following data structures are necessary to support these functional requirements. We will present here with a view of the object-oriented approach of the system implementation:

- Class *CPeerInfo* – each of the class objects contains the name of member peer node, node's IP address, a list of the files, shared by this node;
- Class *CFileInfo* – each of the class objects contains information about one of files, shared by a member peer node;
- *Class CreplicaInfo* – each of the class objects contains data about various locations, where copies of a particular file might exist.

The objects described are sorted in the linked lists:

- *Class CPeerInfoList* - contains the list of group members
- *Class CfileInfoList* – contains the list of all files, shared by a peer node
- *CReplicaInfoList* - contains the list of all peer nodes that have valid copies of a particular file. The first node in the list usually contains the identity of the owner of the file.

IV. SYSTEM FUNCTIONALITY TESTS

The P2P application has been developed on the top of the architecture described for file exchange. The actual file transfer happens over a direct TCP connection between the requester and the owner nodes. Socket classes are used to represent the connection between a client and server side.

The system is currently in a testing stage. It is completely developed in MS Visual C++. The graphical user interface has been programmed, using, document-view architecture, given by MFC, as a SDI Windows Explorer Style application.

System functionality was tested in the real conditions of the local computer nodes. The tests are carried out Windows XP Professional, using 12 computers connected via 100Mbps Ethernet LAN. The main purpose of the testing process was to check the correctness of our implementation of the algorithms and data structures in order to achieve the system functionality. In Figures below are shown screen shots of the tests we carried out with the application.

Bellow are presented some results of the experiments we are carried out to observe the system functionality:

- Testing the execution of the Join Algorithm (Fig. 4)

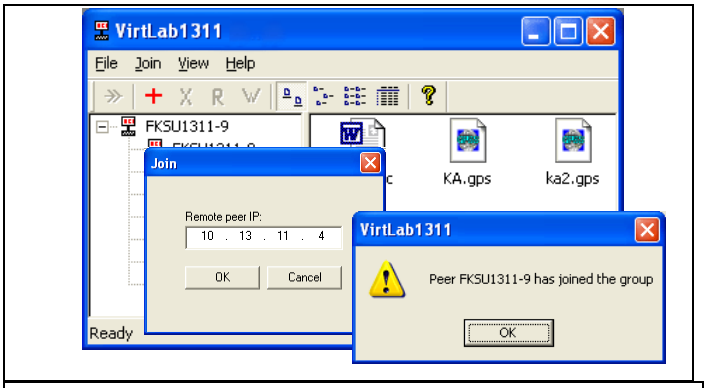

Fig.4. New Peer Join - a node FKSU1311-9 joins to the node FKSU1311-4 and both form a group.

• Reading a file from remote peer (Fig.5) by fetching it from one of its replica locations

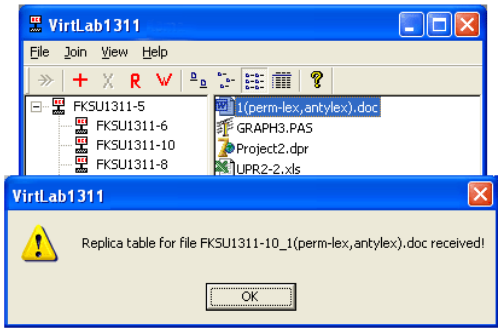

Fig.5. Receiving a replication table for a file, requested from node FKSU1311-5.

• Choosing a location from where to fetch the replica file (Fig.6).

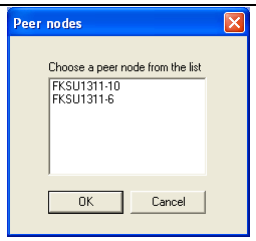

(a) Choose a location

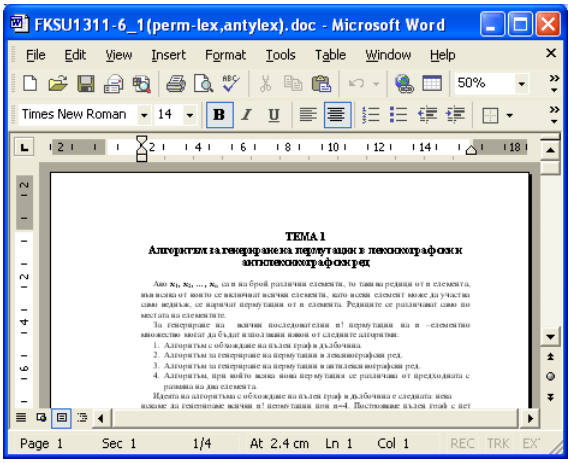

(b) Read a file that is fetched from FKSU1311-6

Fig.6. Choice of location

V. CONCLUSIONS

This paper describes some aspects of the organization of decentralized file sharing system, which allows users to contribute and to share information resources amongst them. Our goal was to explore the feasibility of and the technical approaches to the implementation to some of the benefits of the architectural paradigm of the decentralized peer-to-peer network topologies. We have tried to build a collaborative group for a small number of peers as well as to outline the principal tasks of the design and development of the network and the system infrastructures, and the user interface that implements the system functionality. In reference to this, it is discussed some of the base algorithms and their implementation along with the required data structures in order to achieve the system functionalities.

There are several possible directions in expanding this application that might be a challenge, interesting to solve in the future: system performance characterization; providing of search mechanisms (discovering the desired information resources, giving its description); designing mechanisms that ensure robustness, security, file authenticity and access control. In the current implementation it considers that peer trust each other and there is no need for any authentication or encryption; User-level (instead of device-level) security and authentication.

REFERENCES

[1] Foster, I., Kesselman, C. & Tuecke, S. (2001) “The Anatomy of the Grid: Enabling Scalable Virtual Organizations”, International Journal of High Performance Computing Applications, 15 (3), p 200-222, 2001.

[2] K. Czajkowski, S. Fitzgerald, I. Foster, and C. Kesselman (2001), “Grid information services for distributed resource sharing”. In 10th IEEE International Symposium on High Performance Distributed Computing, 2001, San Francisco CA, IEEE Press.

[3] C. Shahabi, F. Banaei-Kashani (2002). “Decentralized Resopurce Management for a Distributed Continuous Media Server, IEEE Transactions on Parallel and Distributed Systems, Vol. 13, #6, June 2002.

[4] Open Source Community. The free network project – rewiring the internet. In http://freenet.sourceforge.net, 2001

[5] Fast Track Peer-to-peer technology company. In http://fasttrack.nu/, 2001

[6] KaZaA file sharing network. In http://www.kazaa.com, 2002

[7] Gnutella. In http://gnutella.wego.com 2001

[8] S. Ratnassamy, P. Francis, M. Handley, R. Karp, and S. Shenker (2001), “A scalable content-addressable network”. In Proceedings of the ACM SIGCOMM’01 Conference, 2001

[9] Nejl, W., Wolf W. et al “EDUTELLA: a P2P Networking infrastructure based on RDF”. In Proc. Of the 11th World Wide Web Conference (Hawaii, USA, May, 2002)

[10] Cuenca-Acuna, F. M., Peery, C., Martin, R. P., Nguyen, T. D. (2002), “PlanetP: using gossiping to build content addressable peer-to-peer information sharing communities”. Technical Report DCS-TR-487, Dept. of Computer Science, Ruthgers Univ. (2002)

[11] Vassileva J. (2002): Supporting Peer-to-Peer User Communities, in R. Meersman, Z. Tari et al. (Eds.) Proc. CoopIS, DOA, and ODBASE, LNCS 2519, Springer: Berlin, 230-247 (2002).

[12] Kan, G. (2001) “Peer-to-Peer: Harnessing the Power of disruptive technologies”, A. Oram (ed.), O’Reilly Press, USA, 2001.

[13] Bretze H., Vassileva J. (2003) “Motivating Cooperation in Peer to Peer Networks” Proceedings User Modeling UM03. Johnstown, PA, June 22-26, 2003, p. 218-227.

[14] Vassileva J. (2004) “Harnessing P2P Power in the Classroom”, In Proc. Of ITS’2004, Braazil, August 2004.

[15] Peter, B., Tim, W., Bart, D., & Piet, D., (2002), “A Comparison of Peer-to-Peer Architectures”, Broadband Communication Networks Group (IBCN), Department of Information Technology (ITEC), Ghent University, Belgium, 1-2, 2002.

Semi-Automatic Karyotype Generation System "Chromosomes"

Nenad V. Ilijic[1], Nemanja B. Grujic[2], Dragan Jankovic[3]

Abstract – **This work points out the problems that occur during the manual karyotype generation. A short explanation of medical statistical data and implications of this problem is included. Software package using new segmentation algorithm is presented. It presents the tool for semi-automatic karyotype generation. The main functionalities of package are presented.**

Keywords – **Karyotype, segmentation algorithm.**

I. INTRODUCTION

There are well known software packages for the karyotype generation in the market [5], [6]. They are characterized by very high market price. The goal of this project is to create a system which will significantly speed up the karyotype generation process and contribute to early detection of genetic malformations in prenatal diagnostics. Karyotype generation system should enable faster karyotype determining process without decreasing the flexibility a user has during the manual processing. This system is the result of karyotype generation and segmentation algorithm research made by the authors in past two years. A new segmentation algorithm is developed for purpose of karyotype generation. Importance of karyotype generation problem, and statistical data which implies it, are shown in the chapters II and III.

II. GOALS AND ACHIEVEMENTS

Number of anomalies in newborn children is increasing every year, which makes karyotype determining a very important procedure conducted by citogenetic laboratories. Citogenetic laboratories in our country perform this procedure manually. Some notable manual processing deficiencies are:

1. Extremely long image analysis process,
2. Increased error probability compared to application of specialized software packages,
3. Difficult data organization and categorization, especially when dealing with images in digital format.

The karyotype generation system is expected to facilitate:

1. Chromosome segmentation from preparation image.
2. Flexible manual manipulation of separated chromosomes.
3. Automatic generation of initial state of karyotype.
4. Possibility of simultaneous processing of several preparations.
5. Storing and printing of karyotype.
6. Differential diagnostic possibilities.

"Chromosomes" software package was developed in Microsoft Visual Studio .NET environment, using C# programming language and ActiveX technology, for Windows operating systems [3].

Focusing on solving afore mentioned problems, software package implements the following functionalities:

1. Workspace creation and reading of arbitrary number of digital images and their descriptive representation.
2. Application of automatic segmentation algorithm on the current image.
3. Manual chromosome separation using the available tools.
4. Automatic extraction of chromosomes from the resulting image which can be individually manipulated.
5. Automatic orientation and zooming of chromosomes.
6. Automatic karyotype proposition.
7. Manual classification of chromosomes into groups.
8. Free rotation and zooming of chromosomes.
9. Breakdown of groups of chromosomes into individual chromosomes.
10. Marking of non-chromosomal objects and their transfer to a list.
11. Restoration of chromosomes that were automatically removed.
12. Saving the entire workspace (input and output data) as a single project.

III. STATISTICAL DATA AND IMPLICATIONS

According to some statistical data, 2-4% or newborns has at least one chromosomal aberration in the karyotype, while in adults this percentage is lower 0.5-1%. This is because the newborns with chromosomal aberrations are less likely to reach adulthood. It is speculated that at least 7% of human zygotes has chromosomal aberrations, which would be the reason for a high percentage of spontaneous abortions. [1].

[1]Nenad V. Ilijic is with the Faculty of Electronic Engineering, Nikoletine Bursaca 16, 18000 Nis, Serbia and Montenegro, E-mail: ni@ulfserk.com

[2]Nemanja B. Grujic is with the Faculty of Electronic Engineering, Aleksinacka 28, 18000 Nis, Serbia and Montenegro, E-mail: jagru@bankerinter.net

[3]Dragan Janković is with the Faculty of Electronic Engineering, Aleksandra Medvedeva 14, 18000 Nis, Serbia and Montenegro, E-mail: gaga@elfak.ni.ac.yu

This statistics clearly implies the impact of genetic consultancies and software tools which will speed up the process of predicting possible malformations and make it a lot more efficient.

The role of genetic consultancy is to provide the patient and family members with information about type and nature of ailment, the development of ailment, possible consequences and therapies, mechanism of inheritance and possible prevention. Genetic consulting also provides risk estimates of the child being born with an inherited disease, as well as directing to prenatal diagnostics in cases where such risk is high.

This software package can be applied in several specific techniques used in prenatal diagnostics [2]:

1. Amniocentesis
2. Chorionic villi sampling
3. Citogenetic analysis
4. Cell culture in Vitro

IV. Program Functionality

"Chromosomes" software package satisfies several functional demands which give the advantage compared to the manual karyotype generation. Also, because of its modular build, it is easily upgradeable. The advantages of using this software solution are the following:

1. Faster image processing and karyotype generation.
2. Decreased error occurrence.
3. Organizing of data as projects.
4. Can be used as a starting point for the development of a more complex system (differential diagnostics methods).
5. With minor modifications, possible application in other areas where sample recognition plays a vital role (blood analysis).

Current level of functionality deals with organization of microscope acquired digital images as logical units (Workspaces), in order to achieve desired classification by responsible staff or patients. Each of the resulting images can be processed individually, so it is possible to store more processing results in one workspace (Figure 1). Once saved, a project is no longer depending on the source images, but is built in a workspace.

An automatic analysis can be performed on loaded images resulting in individual chromosomes (Figure 2). This analysis is achieved by use of several techniques for efficient chromosome separation. Input data is a digital image acquired from the microscope, and output data is an image with background and unwanted objects removed, as well as a list of chromosomes organized as individual projects.

Fig. 1. Working environment with several loaded images

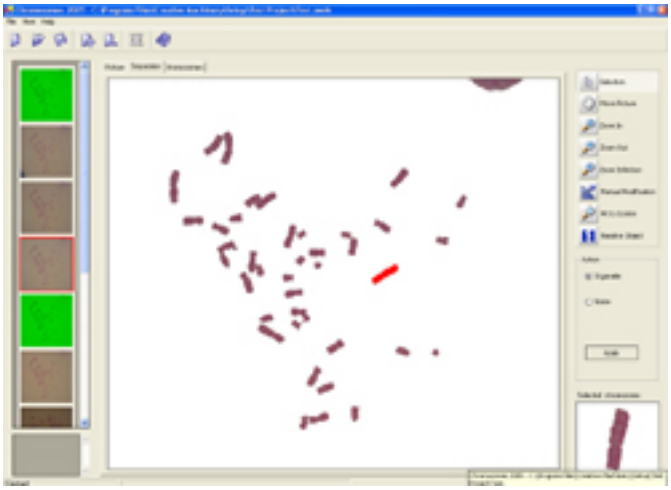

Fig. 2. Result of automatic separation applied on the previous example (Figure 1)

After the first pass all objects in the viewing area at the moment of image capture are extracted. There can be quite a lot of these unwanted objects, and coupled with equipment imperfections a consequence might be impossibility to place only chromosomes in the viewing area.

Among the chromosomes we can find:

1. Cell organelles,
2. Air bubbles,
3. Interference due to imperfections in optical equipment,
4. Local fluctuations in cytoplasm colour.

Because of this, during system implementation we must take into consideration the extraction of all these unwanted subjects. Irregularities, such as variable lighting can be seen on input images, which can make the differentiation of objects and background more difficult. Since there are more ways to colour the samples, the program must not make the difference between images made by different methods.

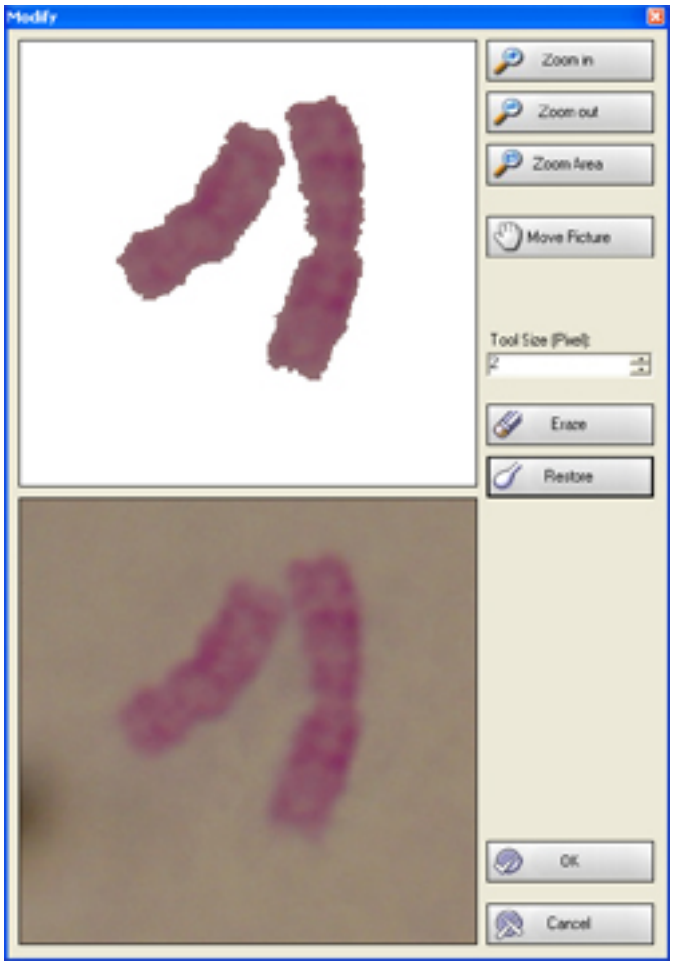

Fig. 3. Result of use of the tool for manual manipulation of digital images

Judging by the results of test samples, a chromosome is never removed as an unwanted object (noise); and the noise (either organelle or chromosome) is never marked as a valid object. In certain cases organelles similar in size and colour to a chromosome might be marked as a chromosome.

The biggest problem an algorithm might encounter is the overlapping or connection between the chromosomes, which results in those two chromosomes being extracted as a single unit; however an option of manual ungrouping is offered, and an automatic option is planned, too.

All unwanted phenomena can be removed by system of manual image manipulation. (Figures 3 and 4). User has two tools available, as well as several customary auxiliary tools:

1. Tool for removal of unwanted objects.
2. Tool for restoration of image parts that were removed by mistake.
3. Zooming tool (with centring or selection of a region to be magnified).
4. Image moving tool in order to focus the necessary part in the viewing area.

Fig. 4. Tool for manual manipulation of digital images

In order to facilitate this process, a user can work both on input and output image and user can copy contents from input image to an output image. All changes done in this manual image processing phase are reflected in the generated karyogram.

Next phase is work with output data acquired as a result of separation (both manual and automatic). The result might be:

1. Chromosomes,
2. Groups of chromosomes and
3. Possibly unwanted objects.

At the beginning of this phase all extracted objects are in the common list. Automatic karyotype proposal option is enabled, but this option makes sense only if the user is sure about the accuracy of the output results. Actually, this option should not be used if there are overlapped chromosomes and organelles in the list. Also, it is possible to manually assign chromosomes to the groups they belong to, by dragging from the common list of chromosomes to the corresponding group.

In the last phase of processing the user has several tools for manual processing of acquired data and upon their successful use the final list can be minimized to the array of chromosomes free of noise.

Those are:

1. Possibility of marking unwanted objects so they are treated as organelles or noise later on.
2. Separation of overlapped chromosomes.
3. Restoration of damaged chromosome parts.
4. Restoration of chromosomes that were marked as organelles or noise during the automatic separation phase.

Selected chromosome can be removed from the list of obtained chromosomes by being marked as an organelle or noise. That doesn't mean it's completely removed from the list of obtained objects, which can be reviewed at any time and the marked objects from it can be restored.

If there were overlapped chromosomes on the original image, they will be extracted as individual objects which can be separated into individual chromosomes in the last phase. This is done by the same means of manipulation that is being used in the manual processing of the entire output image. In the case of chromosomes being damaged by the algorithm, damaged parts of the chromosome can be restored from the original image.

Fig. 5. Result of automatic karyotype proposal on separated chromosomes

As mentioned above, after the generation of the final list of chromosomes, it is possible to manually assign chromosomes to the groups they belong to, but it is also possible to apply the automatic karyotype proposal option (Figure 5).

We can perform rotation and scaling of the extracted chromosomes, and those actions can be performed locally (on one chromosome) or globally (on all chromosomes).

Algorithm will automatically attempt to orientate all chromosomes vertically and to maintain their relative proportions (by magnifying them relative to the largest chromosome).

V. Conclusion

The problem of automatic karyotype generation, and especially segmentation of chromosomes from a digital image, is a very complex problem which requires practically years of work and efforts by whole teams of experts [4]. This area is still open for research and there is still no complete and fully functional solution for this problem, based on undefined nature of object recognition in general. "Chromosomes" software package should be a step forward towards the more efficient resolution of this problem. It yields results with monochromatic input images, meaning that it can be used without the need for expensive aparatus used for multispectral coloring of chromosomes. Since it's organized as a completely functional environment it is suitable for work in healthcare establishments and also commercial application.

References

[1] *Stevo Najman*, OSNOVE MOLEKULARNE I HUMANE GENETIKE, Niš, Savez studenata medicinskog fakulteta, 2002.

[2] *Živojin Stanković, Jelena Živanov-Ćurlis, Stevo Najman*, BIOLOGIJA SA HUMANOM GENETIKOM, Niš, Autori, 2001.

[3] *Jacon Price, Mike Gunderloy*, VISUAL C# .NET, Sybex, 2003.

[4] *Zixiang Xiong, Qiang Wu, and Kenneth R. Castlemen*, "Enhancement, Classification and Compression of Chromosome Images",

www.gensips.gatech.edu/proceedings/Contributed/CP2-03.pdf

[5] MetaSystem's karyotyping system Ikaros http://www.metasystems.de/products/ikaros/ikaros3.htm

[6] Spectral Imaging - BandView® EXPO System http://www.spectral-imaging.com/BandView.asp

Application of Glscene Technology in Satelitte Tracking Software

Dušan Vučković[1], *B.Sc.*, Petar Rajković[2], *B.Sc.*, Dragan Janković[3], *Ph. D.*

Abstract – **GLScene is a library which provides all the components and support classes to build 3D scenes and display them on the screen. Basically , what GL Scene represents is an OpenGL extension to be used with Borland Delphi compilers. This paper will show one of the possible implementations in Satellite Tracking Software.**

Keywords - **GLScene, Satellite, Tracking, OpenGL, Delphi**

I. INTRODUCTION

In the past, Delphi programmers, unlike ones using Visual C++ or any other Microsoft development tools, had to deal with a problem of making 3D animations and rendering 3D scenes. DirectX or OpenGL solutions were in most cases turned towards C++ programming audience.

GLScene is a open source project which has started in 1998. Even though it has been a while since development started, GLScene has not yet reached version 1.0.

Although its' origin use isn't to create 3D games, one may try to write some successfully. The focal points, however, lie in other areas, mainly GUI (graphical user interface).3D components can be built and look really natural, scene editors for the games, screen savers or even 3D logo for WWW home page. Limits are only given by ones' imagination.

After many hours of working with OpenGL, the Open Graphics Library from Silicon Graphics Inc., open source society managed to wrap it into an object-oriented shell using Delphi.

Since Delphi versions 8 and 9 are based on Microsoft .Net framework, writing a code to support 3D object rendering and movement shouldn't be a problem. So, the focal point of GLScene is Delphi version 7 or lower.

II. GLScene features

Among all of the features GLScene provides the most important ones are :

- hierarchical scene management;
- optimized transformation and object handling to get out the highest speed possible;
- optimized floating point assembler routines for geometric calculations;
- multiple viewers for one or more scenes, easy change of viewpoint by just changing one property (Camera);
- well working camera model using focal length and target resolution (screen, bitmap, printer) instead of field of view and far/near plane parameters;
- as many objects as memory allows;
- predefined objects (cube, disk, sphere, cylinder, cone, torus, 3D text, mesh, free form, teapot, dodecahedron), easily extendable;
- more than 150 predefined colors like clrCornflowerBlue or clrCoolCopper, easily extendable;
- polymorphic object creation with one function;
- render to a file, a bitmap or to the printer in any color and pixel resolution;
- full screen support with dynamic resolution changes;
- viewer window transparency simulation;
- various image formats support (*.jpg, *.tif, *.tiff, *.pic ...);
- precise frame speed determination;
- 3D Studio file import with automatic and precise normal vector calculation (using the given smoothing groups of the file) and texture coordinate import.

For OpenGL is, in opposition to DirectX, supported on almost all operating systems available today (Windows95, Windows NT from version 3.51, all kinds of Unix , OS/2 and even the Macintosh) porting applications to operating systems like Linux wouldn't be a problem, specially with the upcoming Kylix 2, Linux version of Delphi. [2].

[1]Dusan Vuckovic is associate of faculty of Electronic engineering, Aleksandra Medvedeva 14, 18000 Nis, Serbia and Montenegro, E-mail: dvuckovic@elfak.ni.ac.yu

[2]Petar Rajkovic is junior assistant at faculty of Electronic engineering, Aleksandra Medvedeva 14, 18000 Nis, Serbia and Montenegro,
E-mail: rajkovicp@elfak.ni.ac.yu

[3]Dragan Jankovic is professor at faculty of Electronic engineering, Aleksandra Medvedeva 14, 18000 Nis, Serbia and Montenegro, E-mail: gaga@elfak.ni.ac.yu

III. User Interface

There are two basic components to be placed on the form. TGLScene and TSceneViewer [1]. TGLScene is the scene manager, responsible for holding the tree structure and other lists describing the scene. TSceneViewer (Fig.1) is the viewing window used to actually display a scene. It's connected via a camera which determines the look direction, focal length and other things; with scene viewers one can render the same scene from different locations or different scenes as well.

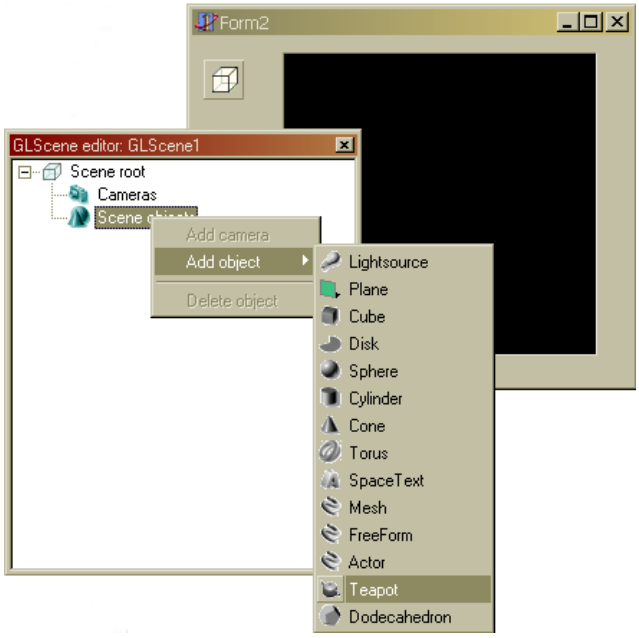

Fig. 1. User interface example

There's a large number of predefined objects, ready to be used in application. An object can simply be added to the scene from the Add object menu. More complex objects can be defined using OpenGL sintax, or imported from 3D Studio®.

Object's properties can be edited, so any shading or material can be applied and combined with several types of light sources.

IV. Application in Satellite Tracking Software

Most objects in space are small, but quite a few are large enough to be seen with the unaided eye. It appears that some, like the Space Shuttle and the Russian Mir space station, are very large and very bright.

There are over 7,000 objects in space for which orbital information is kept by military and civilian space organizations.

Satellites can only be seen when sunlight reflects of their surface, since they do not give off light of their own. But the daytime sky is too bright for their reflected light to be seen. Therefore only during a comparatively brief period after sunset and before dawn, when the sun is below the horizon for Earth based observers but is still illuminating space overhead, they reflect light in a dark sky. For that hour to hour-and-a-half it is easy, if patient, to see artificial satellites. Obviously, darker the sky and more is revealed to the observer's eye.

Determination of what satellite one is viewing can be difficult task. But, if one knows an orbit tracking program and updated spacecraft orbital elements, it is usually pretty easy to figure it out. Bright objects like the shuttle and Mir space station can be viewed from even light polluted city skies at certain time.

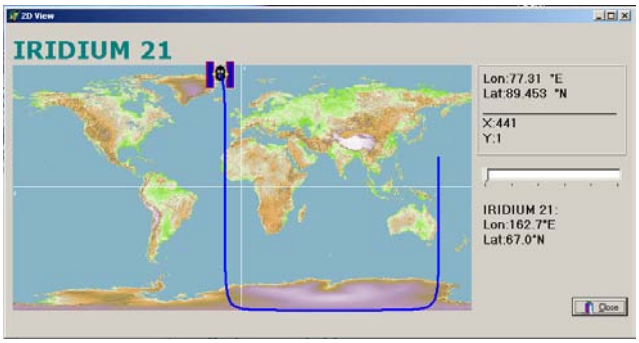

Fig. 2. 2D Display

Also, there are orbit tracking programs for Macintosh and IBM compatible computers. They are either free or shareware and can be obtained from public access sites via a modem or Internet connection. They require updated orbital elements which can also be easily obtained.

Orbit tracking programs requires information about the shape and orientation of satellite orbits. These data are known as "Keplerian elements," named for Johannes Kepler. There are two forms of Keplerian elements; the long version which has each value described, and the short form or "two-line elements" (tle) which are a standard way of formatting the data so computer programs can read them automatically. [5].

This satellite tracking software is based on mathematical SGP4/SDP4 model [3]. The whole model is encapsulated in ActiveX® control, so it acts like a black box. The data is provided from two elements set and on the other end viewport coordinates are calculated. The software provides detailed information on satellite, restored from the two line elements set. (Fig. 3).

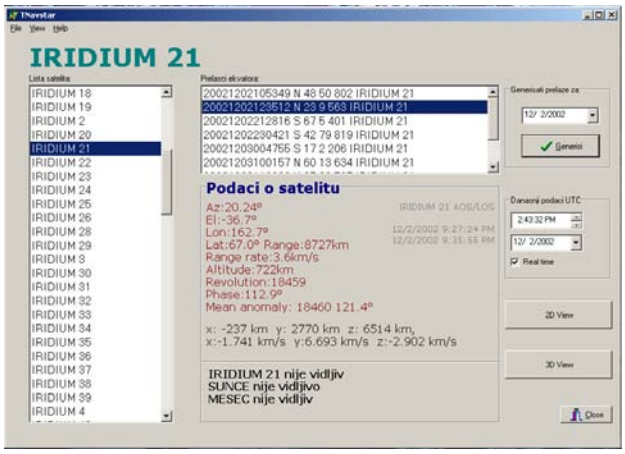

Fig. 3. Satellite list

Also, satellite 2D footprint tracking is available, as well as 3D view. It is possible in 3D view to make prediction on satellites position in the future, or to see its' position in the past. All is based on the information gathered from TLE's . [4].

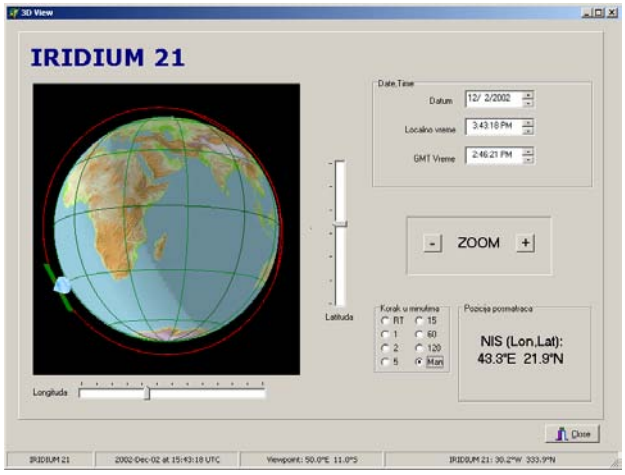

Fig. 4. 3D View made with GL Scene

In 3D View, options for variable view angle, zoom and time increment are implemented. This gives user ability to view satellite from all angles and opportunity to see the path (orbit), area on Earth covered by its' signal (in a form of beam) and real-time movement, as well as possible faster movement caused by time speed up.

The part of Earth not covered with Sun light is dimmed on the globe, so the user is able to predict when it will be possible to see the satellite by naked eye.

The software was tested in parallel with Maghelan GPS device and it acted very well. The coordinates of the satellite given by the GPS device matched with data provided by NAVSTAR software perfectly. At night it was possible to observe low-orbit satellites visually since they regularly reflect light in various directions due to the rotation. That was the third way to check software's prediction capabilities.

V. Conclusion

GLScene is library that finally eases the process of creating 3D animations and scene rendering in Delphi applications . Although it has not yet reached version 1.0 it represents a very usable tool. The fact that it's freeware helps in deciding whether or not should you use it.

References

[1] Dipl. Ing. Mike Lischke , "*GLScene Library*", glscene.org publication, p3-14..

[2] Jon Jacobs, "Delphi Developer's Guide to Open GL", Wordware Publishing inc., p61-63, p79-98

[3] R.E.Burns, "*Solution of the angles-only satellite tracking problem"*, National Aeronautics and Space Administration, Marshall Space Flight Center National Technical Information Service, 1997.

[4] Peter Drake Thompson, Jr., "*A General Technique for Satellite Tracking"*, QST, November 1975, p. 29.

[5] Dr. T.S. Kelso, *"Orbital Data on the WWW."* *Satellite Times*, 2, no. 5 (May/June 1996): p80-81.

PKI Smart Card Technology

Dragan M. Spasić[1]

Abstract - **Hardware-based cryptography is more secure than software-based cryptography, because cryptographic operations are performed and private keys stored on the cryptography devices (such as smart cards). This paper provides a description of a digital ID, cryptographic keys and digital certificates, creating a digital ID, Microsoft CryptoAPI, and PKI smart card structure and operations. Included in this description is also the Philips Smart Card P8WE5032 chip.**

Keywords - **Public Key Infrastructure (PKI), digital certificate, smart card, Microsoft CryptoAPI.**

I. Introduction

Users submit transactions via the Internet only when they are confident that their personal information, such as credit card numbers and financial data, is secure. The Public Key Infrastructure (PKI) [1, 2, 3] is the basis for every e-business (e-commerce, e-banking, e-government…) trust infrastructure. PKI cryptography, digital signature, and smart card technology, applied via digital certificates, provide the authentication, data integrity, nonrepudiation and privacy (confidentiality) necessary for e-business.

PKI smart card is hardware-based cryptography device for securely generating and storing private and public keys, digital certificates and performing cryptographic operations, such as digital signing and key exchange. Only someone who possesses the smart card, the smart card reader and knows the Personal Identification Number (PIN) can use the smart card.

Smart card vendors provide interface software, such as Cryptographic service provider module (CSP), for use with Microsoft CryptoAPI, or they use a PKCS#11 module. Support for Gemplus GemSAFE smart card, and Schlumberger-Axalto Cryptoflex smart card [4] is included with the Windows 2000/XP installation. Additional smart card CSPs might be developed and certified for use with Windows 2000/XP (for example, Datakey RSA CSP).

II. A Digital ID and Media

A digital ID is a set of electronic credentials that uniquely identify a person. There are two parts to a digital ID: an asymmetric private key and a digital certificate (asymmetric public key).

Asymmetric keys come in pairs. PKI uses asymmetric keys in both encryption and digital signature operations. In the encryption operation, there is an encryption public key and a decryption private key. The decryption private key decrypts data that has been encrypted with the corresponding encryption public key.

In the digital signature operation, there is a signing private key and a verification public key. The verification public key is used to decrypt a hash value that has been encrypted with the signing private key.

PKI X.509 digital certificate is the public part of digital ID. Each digital certificate contains at least the following fields [5]:

- Version. Version of the certificate format (for example, version 3).
- Serial number. The unique serial number that is assigned by the issuing CA (the entity that issued the certificate).
- Signature algorithm. The message digest (hash) and public key cryptography algorithms that are used by the issuing CA to digitally sign the certificate.
- Issuer. The name of the issuing CA.
- Validity period. The certificate's start and expiration dates. These define the interval during which the certificate is valid, although the certificate can be revoked before the designated expiration date.
- Subject. The name of the subject (owner) of the certificate.
- Subject public key information. The public key and the public key cryptography algorithm.
- Digital signature. The CA's digital signature, which is created as the last step in generating the certificate.

The following media can be used for storing digital ID:

- Hard disk, CD-ROM, floppy disk, or other removable media.
- PKI smart card (Fig. 1.).
- PKI USB smart token (Fig. 2.). It plugs directly into a USB port (no smart card reader required).

Smart cards and USB tokens provide a number of benefits [6]:

- Security: Private key never leaves the card, and is protected by two-factor security: something that is owned (the card) and something that is known (the card PIN or PassPhrase).
- Portability: Digital ID can go wherever user (owner) go.
- Flexibility: A card can be used to store a variety of data, including private keys, public keys, digital certificates, user names and passwords, etc.
- Simplicity: Many passwords can be stored on a single card. In addition, user is less likely to lose a card than forget a password.

Dragan M Spasić is with the Public enterprise of PTT communications "Srbija" (Post Serbia), Katićeva 14-18, 11000 Belgrade, SCG, E-mail: dspasic@ptt.yu

- Ease of use: A card is simply inserted into a card reader to activate an application. Also, one card can be used for several applications.

Fig. 1. Smart card and smart card reader

Fig. 2. USB smart token

III. Creating a Digital ID

Digital ID is created in a three-step process (Fig. 3.) [7]:

1. Private and public keys are generated on a smart card. This is done directly on a card. The private key is permanently stored on a card. It never leaves a card. The public key is sent to a Certificate Authority (CA).
2. The CA verifies the public key really belongs to user. If the verification succeeds, it creates a digital certificate for user and sends codes to user to download the certificate.
3. User then downloads the digital certificate on a card, completing the digital ID.

This three-step process is very simple for end user, because, most of the details are transparent.

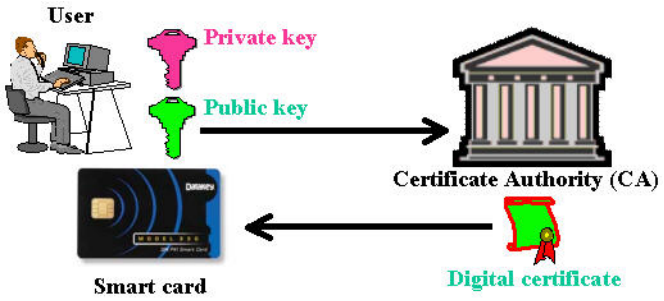

Fig. 3. Creating a digital ID

IV. Microsoft CryptoAPI

The basic cryptographic element of the Windows 2000/XP architecture is the Microsoft Cryptographic Application Programming Interface, or Microsoft CryptoAPI, or CAPI. All major application elements of Windows 2000/XP make use of the Microsoft CryptoAPI for their cryptographic services. The Microsoft CryptoAPI model consists of (Fig. 4.):

1. Applications.
2. Microsoft CryptoAPI (CAPI).
3. Cryptographic Service Provider (CSP) modules.
4. Smart cards.

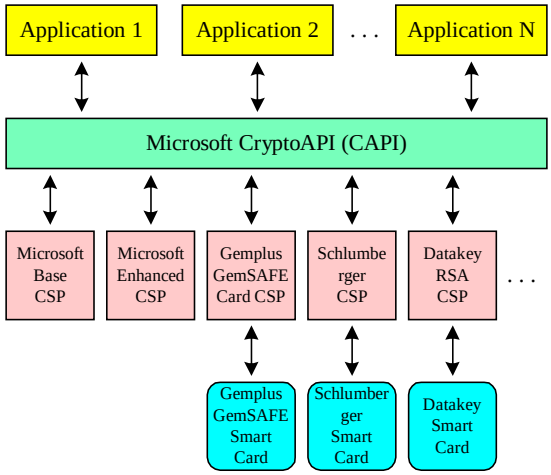

Fig. 4. Microsoft CryptoAPI model

Microsoft CryptoAPI provides a set of functions that allow applications to encrypt or digitally sign data in a flexible manner while providing protection for private keys. Cryptographic operations are performed by independent modules known as cryptographic service providers (CSPs). Any Windows 2000/XP application can request cryptographic operations from a CSP. CSPs can be implemented in software as well as in hardware (such as smart card CSPs).

Using Microsoft CryptoAPI, developers can easily integrate strong cryptography into their applications. Cryptographic service provider (CSP) modules interface with CryptoAPI and perform several functions [8]:

- Create and manage private and public keys.
- Create and manage digital certificates.
- Encrypt and decrypt messages, files, programs, passwords, forms, credit-card numbers or any other data either residing locally on a computer or being transmitted over a network, including the Internet.
- Digitally sign a message or data to ensure that a recipient knows the identity of its creator and that the data hasn't been tampered with or altered.

Microsoft provides two distinct CSP modules with Windows 2000/XP configurations:

1. Microsoft Base Cryptographic Provider, which provides basic cryptography support (RSA key length: 512 bits).
2. Microsoft Enhanced Cryptographic Provider, which provides strong cryptography support (RSA key length: 1024 bits).

For these Microsoft CSPs, all cryptographic operations are provided through software within the CSP. No cryptographic hardware, including smart cards, is supported. Both CSPs use RSA technology. Microsoft CSPs have received the Federal Information Processing Standard (FIPS) 140-1 Level 1 certification by the National Institute of Standards and Technology (NIST).

Vendors can develop hardware or software CSPs that support a wide range of cryptographic operations and technologies. However, Microsoft must certify and digitally sign all CSPs. CSPs do not work in Windows 2000/XP unless they have been digitally signed by Microsoft.

Windows 2000/XP includes smart card CSPs from two vendors: Gemplus (http://www.gemplus.com) and Schlumberger-Axalto (http://www.axalto.com). The Gemplus GemSAFE Card CSP and the Schlumberger CSP support cryptographic operations for the Gemplus and Schlumberger-Axalto smart cards, respectively. Additional smart card CSPs might be developed and certified for use with Windows 2000/XP (for example, Datakey RSA CSP).

V. Smart Card Structure

The PKI smart card is a credit card-sized device that is used to securely generate and store private and public keys, digital certificates and to perform cryptographic operations, such as digital signing and key exchange. It contains [7]:

1. Chip or integrated circuit (IC). The chip includes (for example, Fig. 5.): CPU (Central Processing Unit) - perform cryptographic operations, ROM (Read-Only Memory) - memory for containing the smart card operating system, RAM (Random Access Memory) - memory that can be read and written by the CPU, EEPROM (Electronically Erasable and Programmable Read-Only Memory) - memory to securely store private and public keys, digital certificates and other data as required, etc.
2. Smart card contact. The smart card contact has 8 contacts [9].
3. Smart card body. The smart card is credit card-sized plastic card.

The PKI smart card is protected from misuse by the Personal Identification Number (PIN) or PassPhrase, which is known only to the owner of the smart card. To use the smart card, a user inserts the card in a smart card reader that is attached to a computer and, when prompted, enters the PIN. The smart card locks after only a few failed attempts to guess the PIN.

A smart card reader (Fig. 1.) attached to the computer reads the smart card. Smart card readers attach to standard personal computer peripheral interfaces such as RS 232, PS/2, Universal Serial Bus (USB), and PCMCIA.

Each smart card vendor provides software that user must install and use to initialize and configure smart card before it can be deployed. User can use the vendor's software to configure PIN, label, inactivity timer, etc.

This section provides description of the Datakey smart card package. It includes:

1. A blank Datakey smart card.
2. A smart card reader with the selected format.
3. The Datakey CIP (Cryptographic Interface Provider) interface software (middleware) version 4.7.

There are the following Datakey smart cards (http://www.datakey.com): Model 330 Smart Card, Model 330u User PIN unblocking enabled Smart Card, Model 330i Smart Card for the Identrus System, Model 330g GSA compatible Smart Card, Model 330m Biometric-enabled Smart Card, Model 330j Java-based Smart Card.

The standard Datakey Model 330 smart card is a file-system card with an embedded chip (the Philips P8WE5032 smart card chip; see Section VI.) that contains Datakey's DKCCOS operating system. The following technical features is specific to the Datakey Model 330 smart card:

- 8-bit CPU (80C51) for performing cryptographic operations.
- DKCCOS smart card operating system (Datakey Cryptographic Card Operating System) in 32 KBytes ROM.
- 32 KBytes EEPROM for secure storage of private and public keys, digital certificates and other data such as passwords, notes, etc. Read cycles: unlimited; write/erase cycles: 100000.
- Supports both on-card key generation and key injection.
- All sensitive operations performed on-card. It means that all private key operations are performed within the smart card's chip: digital signatures and decryption of symmetric encryption keys ("unwrapping").
- Algorithms supported: RSA (key lengths: 512, 1024, 1536, 2048 bits), DSA (key lengths: 512, 1024 bits), Diffie-Hellman (primes from 512 bits to 2048 bits, and exponents from 128 bits to 256 bits), 3 DES and DES. In practice, however, 3 DES and DES are performed in the Datakey CIP software for performance reasons.
- Implements public key functions: RSA and DSA key generation, RSA and DSA for digital signature, RSA and Diffie-Hellman key exchange.
- Validated for FIPS 140-1 Level 2 (Validation Certificate No. 94).
- ISO 7816 (Identification cards - Integrated circuit(s) cards with contacts) compliant.
- PKCS#11 (Public Key Cryptographic Standard 11: Cryptographic Token Interface Standard, commonly called "Cryptoki") and Microsoft CryptoAPI

(Cryptographic Application Programming Interface) compliant.
- Supported operating systems: Windows 98, NT, 2000, XP, 2003.
- Microsoft PC/SC (Personal Computer/Smart Card specification) compliant.
- "Entrust-Ready". It can be used with Entrust applications (Entrust/Authority, Entrust/RA, Entelligence, ICE, Express, SignOn, etc).

Datakey smart cards are compliant with a wide range of smart card readers. Datakey readers are available in serial port, USB port, and PCMCIA versions.

The Datakey CIP interface software which functions as the "middleware" between a user's cryptographic smart card and their computer is designed to enhance the security of applications that support PKCS#11 (versions 1.0 and 2.01) or Microsoft CryptoAPI (version 2.0) standard cryptography.

Popular applications that support this standard include Microsoft applications (Internet Explorer, Outlook, Outlook Express, Word 2002/2003, Excel 2002/2003, PowerPoint 2002/2003…), Entrust applications, Netscape Communicator, etc.

VI. The Philips P8WE5032 Smart Card Chip

The Philips Smart Card Controller P8WE5032 is a single chip secured 8-bit microcontroller. It is specifically designed for secured conditional access applications and transactions in smart card environments or other security applications.

The Philips P8WE5032 chip or integrated circuit (IC) includes (Fig. 5.) [9]:
- 8-bit 80C51 CPU.
- 32 KBytes of ROM.
- 2304 bytes of RAM.
- 32 KBytes of EEPROM.
- Triple-DES co-processor:
  - 3 DES calculation time (including key load) < 200 μs.
  - DES calculation time (including key load) < 100 μs.
- Crypto co-processor Fame X (Fast Accelerator for Modular Exponentiation - eXtended) optimized for public key cryptographic calculations:
  - The major Public Key Cryptosystems like RSA, El'Gamal, DSS, Diffie-Hellmann, Guillou-Quisquater, Fiat-Shamir and elliptic curve are supported.
  - 4032 bits maximum key length for RSA with randomly chosen modulus.
  - < 450 ms typical encryption time of 1024-bit RSA with randomly chosen modulus.
  - 32-bit key length increments.
  - Boolean operations for acceleration of standard, symmetric cipher algorithms.
- True random number generator in hardware, etc.

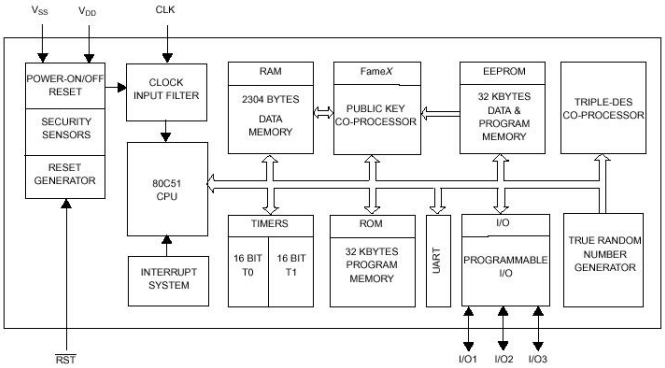

Fig. 5. The Philips P8WE5032 smart card chip diagram [9]

VII. Conclusion

Public key cryptography can be software-based, hardware-based (such as smart card), or a combination of both. For software-based cryptography, cryptographic operations occur in the computers operating system memory. Also, software-based cryptosystems store private keys on local hard disks. Attackers might be able to do memory or hard disk dumps to obtain private keys.

Hardware-based cryptography and key management is more secure than software-based cryptography and key management, because cryptographic operations are performed and private keys stored on the cryptography devices (smart cards), isolated from the operating system, computer memory and applications. On the other hand, cryptography devices store only a limited number of private and public keys and digital certificates, can take a more time to generate keys and perform cryptographic operations, and require additional costs (for smart cards, smart card readers and interface software).

References

[1] D. Spasić, "Electronic Business and PKI System of the Post Serbia", XXXIX Conference "ICEST 2004", Conference Proceedings, pp. 321-324, Bitola, Macedonia, June 2004.

[2] D. Spasić, "The Post Certification Authority", V Conference "Postfest 2004", Conference Proceedings, pp. 673-684, Zlatibor, SCG, May 2004.

[3] "Entrust Authority Security Manager Comprehensive", Entrust Technologies, 2002.

[4] D. Spasić, "Importing Entrust Web Certificate into Cryptoflex Smart Card", IX Conference "JISA 2004", Conference Proceedings (CD-ROM), Herceg Novi, SCG, June 2004.

[5] "Public enterprise of PTT communications "Srbija" Certification Practice Statement", Version 1.0 (Serbian), 8.10.2004. (http://www.cepp.co.yu/ca).

[6] Datakey CIP 4.7 User's Guide, Datakey, 2003.

[7] D. Spasić, "Digital Certificates of the Post Certification Authority on Smart Cards and USB Tokens", XXII Conference "PosTel 2004", Conference Proceedings, pp. 155-164, Beograd, SCG, December 2004.

[8] "Microsoft Releases Beta Version of CryptoAPI 2.0", Microsoft PressPass, 1996.

[9] "Secure 8-bit Smart Card Controller P8WE5032", Revision 1.0, Philips Semiconductors, July 2000.

Session SCI:

CONTROL SYSTEMS I

Development of Data Acquisition and Control System for Electrothermal Processes, Based on the Structure of Fuzzy Knowledge – Based Controller

Ivan G. Babatov [1]

Abstract – **This paper presents the development of Data acquisition and control system, based on the structure of Fuzzy Knowledge- Based Controller (FKBC). The system is intended for testing the applicability and efficiency of a new software model of a fuzzy system, built according to the principles of the Object- Oriented Programming.**

Keywords **– Fuzzy control system, FKBC, Embedded control system, Object-Oriented Programming.**

I. INTRODUCTION

The control systems, utilizing the principles of the Fuzzy Set Theory and Fuzzy Logic have been a matter of interest for many scientists and engineers during the past decade. It has been proved, that in many cases these systems perform better than the conventional ones and can cope with nonlinearities and run-time changes in the controlled object's properties that normally render the control system ineffective.

In spite of their benefits, these systems still are not widely used, due to a variety of reasons, spreading from classical control scientist's mistrust to purely mathematical stability problems that may occur in some algorithmic implementations of such systems.

One of the basic problems that one meets while designing a fuzzy system to be used in practice, i.e. not only in theory is that of converting the continuous equations into discrete ones and optimizing them for use with integer arithmetic, so that they can be implemented in a microcontroller unit and run concurrently in real-time conditions. This process follows the symbolic-to-meaning translation process (identified by the dotted arrow in Fig. 1).

Normally this problem is solved by simplifying the model of the system and its conversion to a set of tables and a simple algorithm for mapping a vector of output values to each vector of input values according to the entries in the tables.

Although being computationally effective and suitable for automation, this method has the disadvantage of highly reducing the information, built in the rulebase, since not the rules and the linguistic representations of the process variables are stored, but just a set of numbers, calculated according to them. Thus the basic form of the expert knowledge is stripped from the system prior to its implementation.

The basic goal of our research is to find a new method of translation that will allow for the linguistic information to be stored in the embedded system, rather than just used for creation of the tables and input- output mapping rules.

[1]eng. Ivan G. Babatov is a PhD student in the Department of Electronics, Technical University of Gabrovo. 5300 Gabrovo, 4 H. Dimiter str., Bulgaria. E-mail: babatow@yahoo.com

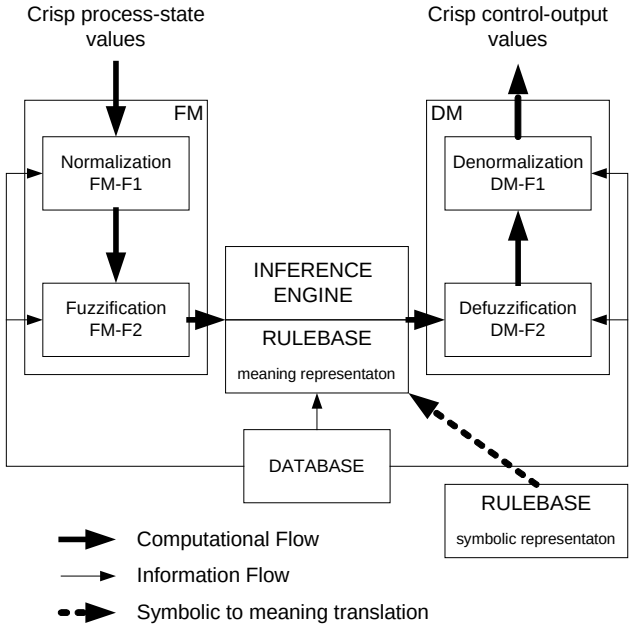

Fig. 1. The structure of a Fuzzy Knowledge-Based Controller [1]

The research is done in two stages:

1. Development of an Object-Oriented model of the Fuzzy Set Theory and Fuzzy Logic's basic concepts and its use for implementation of Fuzzy Control Systems;
2. Development of prototype embedded data acquisition and control system for model testing and verification.

The basic structure of the class hierarchy of the model is presented in [2]. This paper presents the structure and basic characteristics of the prototype embedded data acquisition and control system.

II. SYSTEM DEVELOPMENT

The system of discourse is intended for use for data acquisition, monitoring and control of electrothermal processes. It can monitor and control a variety of plants, spreading from domestic heaters and air- conditioning systems to induction- heating equipment. This wide spectrum of target devices is needed in order to test the applicability and reliability of the designed program model. Along with the relatively high computational complexity, implied by the model this leads to the necessity of separating the low- level data acquisition and control tasks, such as analog- to digital conversion of the process variables and waveform generation for the control output signals from the main control algorithm.

The need for on-line monitoring of the process and control activities in its turn require intense communication between the system and a host device, such as personal computer or industrial network concentrator.

The requirements, stated above lead to the idea of building several autonomous subsystems, each managing a distinct set of low- level tasks, and controlled by a kernel module (or subsystem) which carries out the main control algorithm and system-wide synchronization functions. The structure of the developed system is shown in Fig. 2.

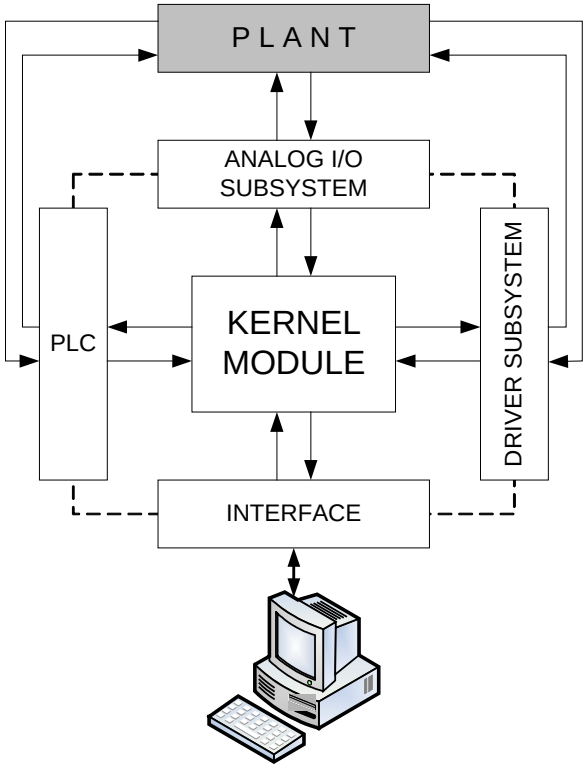

Fig. 2. System architecture

As shown, the system consists of four autonomous subsystems, controlled by a kernel module. The subsystems are as follows:

- Analog Input- Output subsystem;
- Driver subsystem;
- Interface subsystem;
- Programmable Logic Controller (PLC) subsystem.

The kernel module is the one that implements the structure of the Fuzzy Knowledge- Based Controller (FKBC), presented on Fig. 1 (redrawn from Drjankov *et al.* [1]). The controller consists of two- stage **fuzzification module** (FM), which basic functions are *input normalization*, carried out in the FM-F1 stage, which maps the physical values of the process variables into a normalized universe of discourse (normalized domain), and *fuzzification* (in FM-F2 stage), which converts a point-wise (crisp) current value of a process variable into a fuzzy set, in order to make it compatible with the fuzzy set representation of the process state variable in the rule- antecedent. These actions in the kernel are actually performed by instances of dedicated classes (TInputValue), responsible for handling the values of input variables.

The inverse operations are carried out in the **defuzzification module** (DM), which also consists of two stages: DM-F2, which performs the *defuzzification*, which converts the set of modified control output values into a single point-wise value. The second stage, DM-F1 performs an output *denormalization*, which maps the point-wise value of the control output onto its physical domain. The actual processing for the defuzzification module is carried out by instances of the TOutputVariable class from the model.

The **knowledge base** is the basic data repository of the FKBC. It consists of *database* and *rule base*.

The basic function of the database is to provide the necessary information for the proper functioning of the fuzzification module, the rule base and the defuzzification module. This information includes the membership functions, representing the meaning of the linguistic values of the process state and control output variables and the physical domains and their normalized counterparts together with the normalization/denormalization (scaling) factors.

In the current implementation these functions are built-in the very representation of the variables by means of instances of the classes, representing the concepts of fuzzy set and linguistic variable.

The rule base represents in a structured way the control strategy of an experienced process operator and/or control engineer in the form of a set of production rules in the form

$$if \ \langle process\_state \rangle \ then \ \langle control\_output \rangle \qquad (1)$$

The *if*- part of the production rule is called the *rule antecedent* and the part following the *then – rule consequent*. In the current implementation of the kernel the rule base is presented by a list of instances of the class, representing the production rule concept.

The **inference engine** is the part of the controller that mimics the human reasoning. It is here, where the input values are combined with the knowledge from the knowledge base and in logical way produce the output values. There are several types of fuzzy inference with Mamdani and Gödel being the most common. The model that will be tested with the system has means of representing both of them by using various inference classes.

Along with the main control algorithm, the kernel module performs various system- level functions as:

- System power-up testing;
- Nonvolatile memory (DataFLASH) management;
- Real- time clock tracking;
- Basic communication functions;
- Initialization and control of the autonomous subsystems;

The subsystems are connected to the kernel module via high- speed serial system bus, utilizing up to 1Mbps throughput between any two devices. At every instant of time only one subsystem is enabled to communicate with the kernel and their simultaneous communication is performed by means of time- sharing algorithm, run by the kernel module.

Each subsystem, however, has a means of generating interrupt requests to the kernel and the priorities of these requests are programmable, so that in different applications different time- sharing and response strategies can be implemented.

The kernel subsystem is based on the ATMega128 High-performance RISC microcontroller unit, produced by ATMEL Corporation.[3] This MCU has 8-bit architecture, utilizes 128KB of reprogrammable program memory, 4KB on-chip data RAM, and is capable of driving up to 64KB external RAM. This allows for creation of memory-intensive dynamic data structures, such as lists and object collections, and also provides enough space for buffering the incoming data from other subsystems before sending it up the communication interface to the host device.

The kernel subsystem is equipped with 4MB of non-volatile data memory (a DataFLASH® device) which allows for off- line monitoring of the system operation process. Depending on the amount of data and the frequency of recording, this device is capable of storing information about the system activities for more than a week of continuous operation.

The system is equipped with real- time clock that keeps track of the astronomical time, and, if programmed to, will form the time- base for the operating system task switching.

The kernel runs real- time multitasking operating system, also built upon the principles of the Object- Oriented Programming. This operating system allows for virtually simultaneous execution of several tasks of various priorities, and is the basic feature that secures the operation of the entire instrument.

All four peripheral subsystems are built upon the ATMega32 microcontroller units, produced by ATMEL Corporation. Their functions are as follows:

The **analog input- output subsystem** structure is shown on Fig.3. It performs the low- level data acquisition and analog control functions. It consists of eight programmable gain single- ended voltage measurement channels with ranges from (0÷10) mV, (0÷50) mV, (0÷100) mV, (0÷500) mV, (0÷1000) mV, (0÷5) V and (0÷10) V. Additional adaptors can be used for measurement of resistance and/or cold- end compensation of thermocouple sensors if needed.

The voltages are normalized and filtered by analog circuitry, and digitized by 12-bit analog-to-digital converter. The samples are then packed into blocks and sent to the kernel on request.

This subsystem also has 4- analog outputs, produced by 12-bit digital-to-analog converter. The outputs are passed through programmable gain amplifiers, thus capable of producing voltages within the ranges (-1 ÷ 1) V, (0 ÷ 1) V, (-5 ÷ 5) V and (0 ÷ 10) V. The maximum load of each analog output is 1A.

The **driver subsystem** (Fig. 4) contains the circuitry, needed to control two independent solid- state pulse-width modulated (PWM) outputs, full- bridge autonomous inverter and controlled monophase bridge rectifier. This subsystem includes all the circuitry for obtaining the feedback signals from the controlled devices, and thus is capable of operation as autonomous servo- control system.

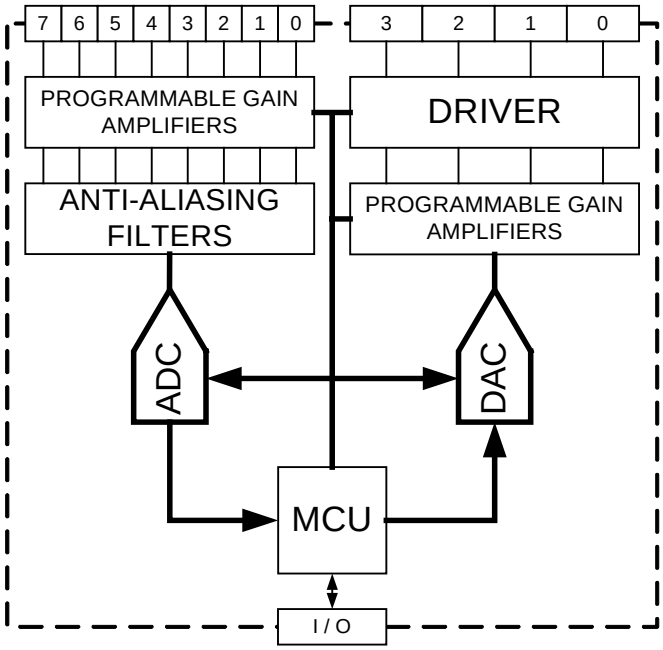

Fig. 3. Analog Input – Output Subsystem architecture

The distribution of the control signals and protection mechanisms are highly configurable due to the use of Complex Programmable Logic Device (CPLD) XC9572, produced by XILINX Corporation.

The driver subsystem is designed to act as a stand- alone programmable controller, capable of driving single electrothermal process. In this way it is possible to set the kernel module to supervisory control only, which will allow for testing variety of indirect control modes of the fuzzy knowledge- based controller.

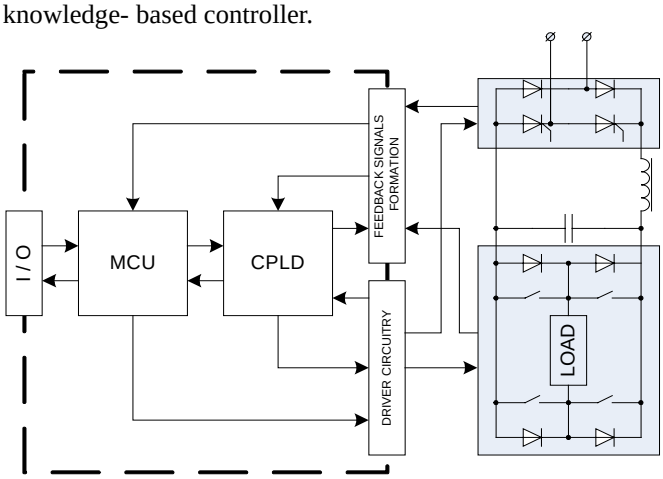

Fig. 4. Driver subsystem architecture

The **programmable logic controller (PLC) subsystem** is basically digital input – output system, capable of running its own control algorithm, along with serving the kernel subsystem. It is designed to extend the control capabilities of the kernel as well as performing stand-alone non- fuzzy control on certain parts of the plant. The control algorithm for the PLC is coded in simplified statement language (STL) form. At the programmer's disposal are logic, basic arithmetic and trigger functions, as well as timers and two independent analog inputs. The PLC program is loaded into the subsystem

by the kernel unit and is stored in a battery backed- up memory.

The **interface subsystem** provides the user interface to the system. It consists of 4 line LCD display and a control keypad.

The interface subsystem implements insulated RS-232 interface to personal computer, which is used to perform process monitoring, system optimization and control. A front-end PC application for system maintenance is in a process of development.

III. CONCLUSION

The prototype system, presented in this paper is still under development, but most of its hardware modules are designed and are in process of manufacturing. The real- time operating system, which the kernel and the peripheral subsystems will run is developed and tested on a prototype controller, built on the ATMega8 microcontroller unit.

After its complete development, the system will have the following basic features:

1. Capability of control and monitoring of various electrothermal processes, spreading from domestic heaters to induction – heating systems.

2. Capability of control and monitoring of distributed technological processes by means of autonomous intelligent peripheral units, connected in industrial network.

3. Capability of on-line and off-line monitoring of the process from host device such as personal computer or network concentrator. The process data will be exported in format, suitable for further analysis by means of dedicated software applications such as MATLAB.

4. The basic goal of the system is to verify the applicability of the object – oriented hierarchical model of the fuzzy set theory and fuzzy logic that was developed and to test its efficiency, compared to the conventional control methods.

5. The presumable possibilities for integration of module for self- optimization in the model implementation will be tested upon the system.

6. The possibilities for application of this control system architecture to other types of processes (such as motion control) will be tested.

7. The system will allow for testing of various control algorithms of a certain plant, with the possibility of off-line analysis of the results. This will help in optimizing the control algorithm to minimize the computational overhead and hardware requirements. The results of this optimization can be used in simpler controllers for commercial purposes.

8. As a result of the previous item, the system can be of use in the education process in control engineering, data acquisition and microprocessor systems.

REFERENCES

[1] Driankov D., H. Hellendoorn, M. Reinfrank, *An Introduction to Fuzzy Control*, Springer-Verlag, 1996 (2nd ed.)

[2] Babatov I., *Object- Oriented Model of the Fuzzy Set Theory for Direct Implementation of Embedded Control Systems*, UNITECH'04, *Confence Proceedings - Volume I*, pp. I-213 - I-218, Gabrovo, Bulgaria, 2004.

[3] *ATMega128 - 8-bit Microcontroller with 128K Bytes In-System Programmable Flash*. Datasheet. 2467E–AVR–05/02. Atmel Corporation, 2002.

Reduction of the Control Rule Numbers in the Knowledge Base of an Expert System for Fuzzy Control

Valentin G. Stanchev [1]

Abstract – **In the paper is presented a method for reduction of the fuzzy control rule (FCR) numbers in knowledge base of an expert system for fuzzy control. In the reduction process valid is proceeded from complicated to complicated-composite FCR; as a result is obtained a minimization of the knowledge base and maximum quickness of the conclusion logics in real-time mode. The reduction is realized by: estimation of the nearness between the complicated FCR, fuzzy likeness relation, FCR grouping in equivalence classes and replacement of every class with one complicated-composite FCR.**

Keywords – **Fuzzy Control, Control rules**

I. INTRODUCTION

The fuzzy control algorithms, received through application of the fuzzy sets theory for expert knowledge formalization are one form of an expert control systems. In the expert systems for fuzzy control (ESFC) in real time mode the correct structurization and minimization of the knowledge base are important for achieving quickness of the conclusion logic (control impact). Basically in the knowledge base (KB) of the ESFC there are data for membership functions (MF) to the terms of the linguistic variables (LV) used for the control and preliminarily defined numbers (list) of linguistic fuzzy control rules (FCR) with complicated structure. The numbers of these FCR can be great, depending radically from the numbers of terms for LV values. The great number of FCR makes worse ESFC quickness, which leads to the unsatisfactory dynamic precision of the control.

Because of this it is desirous to reduce and decrease the numbers of FCR with complicated structure in the KB. During reduction it well-funded proceeds from complicated to complicated-composite FCR.

II. THE CORE OF THE PROPOSED METHOD

The main difficulty in the creation process of an ESFC actually reduces to synthesis of FCR in the KB of the system. The set of FCR describes the relation between control error and control signal at the controlled plant input. For obtaining of more precise control, besides control error as input information in the precondition (left part) of every FCR it is included second condition for error variation rate. That way one elementary FCR has the following complicated structure:

$$R_i: \quad If\ A\ is\ A_i\ \ and\ \ B\ is\ B_j\ ,\ then\ C\ is\ C_\kappa\ , \qquad (1)$$

where: A – control error; B – error variation rate; C – control signal; A_i and B_j are terms (values) of the LV – L_A and L_B with fuzzy subsets Q_i^A and Q_j^B, defined on the corresponding universal sets (US) U_A and U_B; C_κ is term of the output LV - L_C with fuzzy subset Q_κ^C on the US - U_C. Every FCR reflects determinate dynamic particularity of the process flowing in the plant which is the subject of control.

There are different methods for the FCR synthesis [2], one of them is the method, using experimental information and described in details in the [3]. Its basic advantage is that at the synthesis process it is not used expert judgment and it is not necessary to find expensive experts well-knowing the object of the control. At the same time the subjective errors which are result of evidenced expert incompetence during FCR synthesis are avoided. Because of these causes this method is preferred to the other methods, using only expert knowledge.

Experimental information for FCR synthesis is collected in the conditions of passive experiment or by simulation analog modeling. It consists in two random realizations of the plant input (the control signal) and the plant output (the output signal) of the subject of control measurements. From them are received three discrete data realizations with equal length $T = N.\Delta t$ and time quantization step Δt, respectively for error signal, its variation rate and control signal. Universal sets U_A, U_B, U_C and the term sets $\{A_i\}$, $\{B_j\}$ and $\{C_k\}$ are determined. After that from the control error values, its variation rate and control signal for every quantization moment is formed at the rate of one FCR with structure (1). That way is obtained the set {R}, including the preliminary list of n numbers FCR.

The input-output realizations are random processes wich have to be with big continuance, because of that the number of obtained FCR is very high. This embarrasses the work of ESFC conclusion mechanism. Moreover among the list of FCR there are identical and close by meaning and action rules, which allow reduction of their numbers with the purpose of KB minimization.

The reduction is realized by evaluation of the closeness between detached rules through fuzzy similarity relation. To this end complicated FCR complying with the condition of the fuzzy similarity relation are grouped in equivalent classes through constructing of simply similarity relations at the level α ($0 < \alpha \leq 1$) on the fuzzy relation. As an effect every equivalency class is substituted by one FCR with complicated-composite structure

$$R_i: \quad If\ A\ is\ A_i\ \ and\ \ B\ is\ B_l\ or\ B_m\ ,\ then\ C\ is\ C_{\kappa 1}\ . \qquad (2)$$

It is possible for some of FCR to remain alone in a class as a result of grouping process if in the preliminary list there are not rules close enough to them. Such FCR save their initial complicated structure.

[1]Valentin Georgiev Stanchev, Technical University of Sofia, "Kliment Ohridski Blvd, 1000 Sofia, Bulgaria, E-mail: stanchev@tu-sofia.bg

The fuzzy binary relation of similarity ρ^R is used for evaluation of the closeness between FCR and their grouping in different classes is defined as:

$$\rho^R: R_i \ \rho \ R_j \Leftrightarrow A_i = A_j \ u \ / B_i - B_j / \leq \delta, \qquad (3)$$

where R_i (A_i, B_i ,C_i) is i rule and R_j (A_j, B_j ,C_j) is j rule from the list.

The relation conditions, described in (3), are: a) equal terms for control error; b) the absolute value of deviation between error rate terms to be smaller than preliminary given quantity - δ. The value of the deviation δ is determined accordingly the characteristics of the controlled plant and technology. In the particular case it is accepted this deviation referenced to the error rate to be one term. If this choice does not lead to good results at the reduction, it is necessary to reduce the value of δ. This is achieved by increasing the numbers of the terms B_j in the set $\{B_j\}$ keeping the range of the error rate in the universal set - U_B. At the determination of the relation ρ^R , the conclusion terms for control signal –C_i and C_j do not take part, because they have to be determinate after the reduction for united complicated-composite FCR.

For every FCR with equal terms for A is constructed one similarity relation ρ^R. Similarity relation between FCR R_i and R_j has as a bearer the similarity coefficient– K_{ij}, which can be determined from the dependence:

$$K_{ij} = 1 - \frac{\left| Y_i - Y_j \right|}{\left| Y_i - Y_j \right|_{max}}, \ 0 \leq K_{ij} \leq 1, \qquad (4)$$

where Y_i (Y_j) recalculated on US U_B evaluation of measured (calculated)error rate for i and j FCR. The denominator $|Y_i - Y_j|_{max}$, for determinate plant is constant and can be accepted equal to the range of the error rate US U_B. The similarity coefficient has a sense only for FCR with equal terms for control error. It is not difficult to see that $K_{ij} = K_{ji}$, i.e. the similarity coefficients can to be consider as similarity rate between rules [1]. If {R} is set of N numbers of FCR, within it exists a fuzzy binary relation ρ^R with membership function μ_ρ (R_i, R_j) = K_{ij}. This relation is reflective and symmetric, i.e. it really can be accepted as similarity relation alloying to evaluate the closeness between the rules. At the same time in [1] is proved that the transitive envelope $\hat{\rho}^R = \rho \cup \rho^2 \cup \rho^3 \ldots$ of the relation ρ^R is the smallest transitive equivalency relation compatible with ρ^R and

$$K_{ij} = \mu_\rho(R_i, R_j) \leq \mu_{\hat{\rho}}(R_i, R_j), \qquad (5)$$

i.e. the preliminary defined similarities are kept and into the transitive envelope.

The numbers of relation ρ^R is equal to the number of the terms in the term set $\{A_i\}$.

For every constructed relation ρ^R is found the transitive envelop $\hat{\rho}^R$. Into the envelop $\hat{\rho}^R$ are kept the preliminary determined into ρ^R correlations. The transitive envelop characters allow us in need a transpose of rows and columns, without a change of the correlations. This transposition can be necessary during grouping of the FCR in distinguish classes. The grouping process is realized by construction of simple relations $\hat{\rho}_\alpha$ at level α on the transitive envelop $\hat{\rho}^R$ of the fuzzy relation на ρ^R. The membership function - $\mu_\rho^R(R_i, R_j)|_\alpha$ to the simple relation at level α is:

$$\mu_\rho^R(R_i, R_j)|_\alpha = \begin{cases} 1 \ if \ \mu_{\hat{\rho}}^R(R_i, R_j) \geq \alpha \\ 0 \ if \ \mu_{\hat{\rho}}^R(R_i, R_j) < \alpha \end{cases} \qquad (6)$$

At every separate case of the relations ρ^R the choice of α is different. It depends of that to what summarization can we reach in the process of the rule coalescence in separate classes, complying with the laid in (3) restrictions. After achieving the admissible summarization and the replacement of every class with one FCR with structure (2), the reduction process finishes. Application of the described reduction leads to decrease of the numbers of FCR in the KB.

After the reduction it is necessary to determine corresponding terms C_{k1} for conclusion in the right side of all substitute FCR with complicated-composite structure (2). The determination of these terms can be executed by different approaches but the best way is to use expert judgment.

III. DEMONSTRATIVE EXAMPLE OF DESCRIBED METHOD APLICATION

The described method for FCR numbers reduction is tested in the synthesis of the ESFC for energy object – mill-ventilator MB 3300. The controlled quantity is aero-mixture temperature – T at the mill output, the control error is the deviation of T from predefined value - ΔT, the control signal is the change of the rotation speed Δn of their mill-ventilator. The automatic control system is stabilizing at basic outside disturbance – the coal quality at constant load of the steam generator. The examined plant has a delay at dynamic channel "Δn - ΔT". By this reason the information about error rate ΔT′ has a significant role for stabilization or the controlled quantity. This supposes decreasing of δ in (3) as permissible condition for the closeness of FCR evaluation. For the three quantities ΔT, ΔT′ and Δn was selected 7 similar by name terms (NB, NM, NS – negative big, middle, small; Z – zero; PS, PM, PB – positive small, middle, big). All terms have equal overlapped triangular membership functions. The universal sets are normalized in the interval 0 ÷ 100 %. For the obtaining of FCR is applied the method using experimental information from simulative analogical modeling with scales range for output quantities 0 ÷ 100 units. The quantization step at measuring of ΔT and Δn and ΔT′calculation was selected equal to Δt = 10 s. At synthesis of the FCR for every one term is accepted interval in which it

is dominating over the two adjoining. These intervals are evaluated at % in relation to US and they are respectively equal: NB – 0 ÷ 9 %, NM - 9 ÷ 26 %, NS - 26 ÷ 42 %, Z - 42 ÷ 58 %, PS - 58 ÷ 74 %, PM - 74 ÷91 % и PB - 91÷100 %.

In the treatment of the realizations with length more then 1800 s a preliminary list of rules was received. After the sinking of the equal and removing of the inconsistent rules 78 FCR with complicated structure are obtained. In this FCR the values for ΔT fault into six terms (for term NB rules were not obtained). This allowed the construction 6 fuzzy binary similarity relations - ρ^R.

As an example for reduction of the numbers FCR trough the described method we will exercise the relation ρ^{PB} for term of the control error of the PB. It includes 4 FCR with numbers from № 27 to № 30, for which ΔT falls in the term PB. For these rules the values of ΔT and ΔT′ in % of US and their relevant terms are given in table 1.

TABLE 1
VALUES OF ΔT AND ΔT′ IN % AND TERMS FOR 27, 28, 29 AND 30 FCR

№ of FCR	ΔT [%]	Term	ΔT′ [%]	Term
R_{27}	94,62	PB	97,79	PB
R_{28}	99,79	PB	75,37	PM
R_{29}	100,0	PB	51,01	Z
R_{30}	96,11	PB	30,95	NM

The similarity relation ρ^{PB} with bearer the similarity coefficient - K_{ij} , defined by (4) has the following form:

$$\rho^{PB} = \begin{array}{c|cccc} & R_{27} & R_{28} & R_{29} & R_{30} \\ \hline R_{27} & 1 & 0,7758 & 0,5322 & 0,3316 \\ R_{28} & 0,7758 & 1 & 0,7564 & 0,5557 \\ R_{29} & 0,5322 & 0,7564 & 1 & 0,7994 \\ R_{30} & 0,3316 & 0,5557 & 0,7994 & 1 \end{array}.$$

The transitive envelop - $\hat{\rho}^{PB}$ for the above relation is equal to:

$$\hat{\rho}^{PB} = \begin{array}{c|cccc} & R_{27} & R_{28} & R_{29} & R_{30} \\ \hline R_{27} & 1 & 0,7758 & 0,7564 & 0,7564 \\ R_{28} & 0,7758 & 1 & 0,7564 & 0,7564 \\ R_{29} & 0,7564 & 0,7564 & 1 & 0,7994 \\ R_{30} & 0,7564 & 0,7564 & 0,7994 & 1 \end{array}$$

We choose the alteration step for α, in decreasing direction, equal to Δα = 0,1. at this step for the levels α = 0,9 and α = 0,8 the simple relations $\hat{\rho}_\alpha$ have one and the same form:

$$\hat{\rho}^{PB}_{0,9} = \hat{\rho}^{PB}_{0,8} = \begin{vmatrix} 1 & 0 & 0 & 0 \\ 0 & 1 & 0 & 0 \\ 0 & 0 & 1 & 0 \\ 0 & 0 & 0 & 1 \end{vmatrix}.$$

These relations concur with one of the border condition in case of α = 1,0 of the usual relation $\hat{\rho}_\alpha$. At this case every rule forms one class - f_i , i = 1, 2, 3, 4. The rule in the class does not change and the number of rules doesn't decrease. Practically there is no reduction.

For level α = 0,7 the usual relation $\hat{\rho}_\alpha$ has the following mode:

$$\hat{\rho}^{PB}_{0,7} = \begin{vmatrix} 1 & 1 & 1 & 1 \\ 1 & 1 & 1 & 1 \\ 1 & 1 & 1 & 1 \\ 1 & 1 & 1 & 1 \end{vmatrix}.$$

In case of level α = 0,7 every FCR belong into one class - f, т.к. $\alpha \le \min \mu_{\hat{\rho}}(R_i, R_j)$ – second border condition. This isn't acceptable because of the failure in observing the second condition for the terms of ΔT′ in the relation of similarity, described in (3). In this unique class the diversion $|B_i - B_j|$ is equal to 5 terms, including the term ΠM for ΔT′ or $|B_i - B_j| > \delta$ (the given quantity δ is one term). Reason for passing from the one (α = 0,8) to the other border condition (α = 0,7) is the big step for change of α. It is necessary the step Δα for the change of α under 0,8 to be decreased. We choose step Δα = 0,01.

In the case of α = 0,79 the relation $\hat{\rho}_\alpha$ concur with this for α = 0,80 or $\hat{\rho}^{PB}_{0,79} = \hat{\rho}^{PB}_{0,8}$.

In the case of α = 0,78 the matrix of the usual relation has the following mode:

$$\hat{\rho}^{PB}_{0,78} = \begin{array}{c|cccc} & R_{27} & R_{28} & R_{29} & R_{30} \\ \hline R_{27} & 1 & 0 & 0 & 0 \\ R_{28} & 0 & 1 & 0 & 0 \\ R_{29} & 0 & 0 & 1 & 1 \\ R_{30} & 0 & 0 & 1 & 1 \end{array}.$$

At this level the four FCR fall in 3 classes and reduce themselves to 3 rules. The reduction isn't completely fulfilled because FCR R_{27} and R_{28} has valuations for ΔT′

distinguished with one term and they have to get into one class. It is obvious that α has to be decreased more. In the case of α = 0,77 we receive:

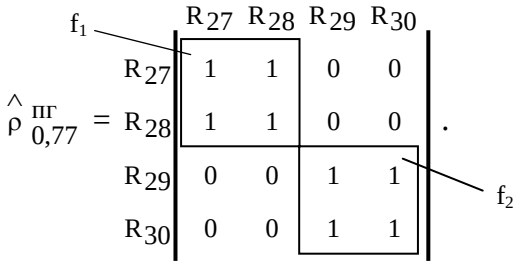

$\hat{\rho}_{0,77}^{\text{пг}} = R_{28}$.

At that level the four FCR group themselves into two classes f_1 and f_2 and reduce themselves to two rules R_k и R_m with complicated-constituted structure (2). Every two FCR в one class (R_{27} and R_{28} in class f_1 as well as R_{29} and R_{30} in class f_2) are with a degree of similarity not smaller than 0,77. After assignment of the terms for the regulating influence (conclusion) in the right part of the rules R_k and R_m, they can be written in the following manner:

R_k: If ΔT is PB and ΔT′ is PM or PB, then Δn is C_{k1}

R_m: If ΔT is PB and ΔT′ is Z or NS, then Δn is C_{m1}

The following diminution of α doesn't lead to a better result.

The applying of the described procedure reduces FCR from the number of 78 to 29.

IV. Conclusion

1. The passing from fuzzy relation of similarity to an usual relation at level α has the following border conditions:
   a) If α = 1 every element from the multitude {R} of the relation $\hat{\rho}_\alpha$ is equal to itself and forms its own class including only one rule;
   b) If $\alpha \le \min \mu_{\hat{\rho}}$ (R_i , R_j), all elements from the relevant relation ρ^R are equal between themselves and form one total class, which includes all the rules.

2. For every α ∈ [0, 1] there are exactly determinate number of classes – f in the interval 1≤ f ≤ N, but if f is given previously, it can result that doesn't exist any α for which the relation $\hat{\rho}_\alpha$ consists of exactly of classes.

3. If after the assignment of the terms for the conclusions (C_{k1} , C_{m1}) of the complicated-constituted FCR rules with same terms for the second condition in the precondition - B and for C and adjoining terms for the error of regulating – A are obtained, so they can, in need, to be combined into one new FCR. This union leads to a better result, if a bigger number of terms is used.

References

[1] Georgeva Sv., V. Mladenov, Method for classification based on the foundation of a fuzzy similarity relation., II Scientific conference for automation of biotechnological processes, 1986.

[2] Kafarov, V. V. and others., "System analysis of the processes of the chemical technology (fuzzy sets method application)", M., Science, 1986.

[3] Stanchev V., Al. Grigorov, A method for formation of fuzzy managing rules trough using experimental information, International Scientific conference EMF'2000, v. I, Varna, June 25-28. 2000.

Fuzzy Logic Controller for the Inverted Pendulum

Vesna Ranković[1], Ilija Nikolić[2]

Abstract - **In this paper we propose a Takagi-Sugeno (TS) type Fuzzy Logic Controller (FLC) to stabilize a inverted pendulum. Moreover there is a need for developing efficient methods to tune membership functions i.e. to obtain optimal shapes, ranges and number of member function. In this work is used ANFIS (Adaptive-Network Based Fuzzy Inference System).**

Keywords - **inverted pendulum, fuzzy, control**.

I. INTRODUCTION

The classical problem of the inverted pendulum controlled using linear quadratic regulator has been extensively studied and implemented. The linear quadratic regulator design is based on a linear model of the system and a quadratic performance index. The result is a linear feedback of the state variable of the system multiplied by a set of gains.

The nonlinear Ljapunov-based controller is proposed [1] to stabilize the cart-pole system. The novelty is in the use of two-loop cascade controller.

Fuzzy logic, neural network and neuro-fuzzy systems have been applied to identification of nonlinear dynamics and to stabilize a inverted pendulum. Justification for using neural networks and neuro-fuzzy systems lie in their capability in learning and generalizing any complicated mapping from training examples.

In [2] is used a control scheme that combines neural control and linear quadratic regulator together. The output from neural network is used to compensate the output from a linear quadratic regulator to stabilize the pendulum when it is near the orign.

In [3] is presented a Takagi-Sugeno type fuzzy logic controller for a 4 dimensional inverted pendulum system. The rule antecedents of this controller is extracted from a cell state space based optimal control table.

In [4] is examined the problem of learning an efficient fuzzy logic rule set for the control of the inverted pendulum using an evolutionary algorithm.

[5] presents a hybrid system controller, incorporating a neural and an linear quadratic regulator. The neural controller has been optimized by genetic algorithms directly on the inverted pendulum system.

In this work is used the Takagi-Sugeno controller implemented within the framework of the adaptive network to stabilize a inverted pendulum. Takagi-Sugeno fuzzy controllers are today one of the most promising technique to describe input-output relations of nonlinear systems using fuzzy rules. A number of algorithms have been developed that address this problem of learning fuzzy rules and tuning membership function in a neural network architecture. In this work is used ANFIS (Adaptive-Network Based Fuzzy Inference System) ([6]). The learning rule proposed for this method is basically a hybrid of the gradient-descent method and the least square technique. ANFIS and all ANFIS-like systems extract fuzzy if-then rules such that the premises are connected by a t-norm. The t-norm being used is the product, because it is continuous and all over differentiable.

In the second section of the paper is presented the inverted pendulum system. In the third section are presented simulation results. The fourth section contains the concluding remarks.

II. INVERTED PENDULUM SYSTEM

The system of an inverted pendulum on a cart is depicted in Fig. 1. The force delivered to the cart is always in horizontal direction. Assume the mass of the pole is evenly distributed along the pole. The positive direction of force F, cart displacement x, and pole angle θ are defined in Fig. 1.

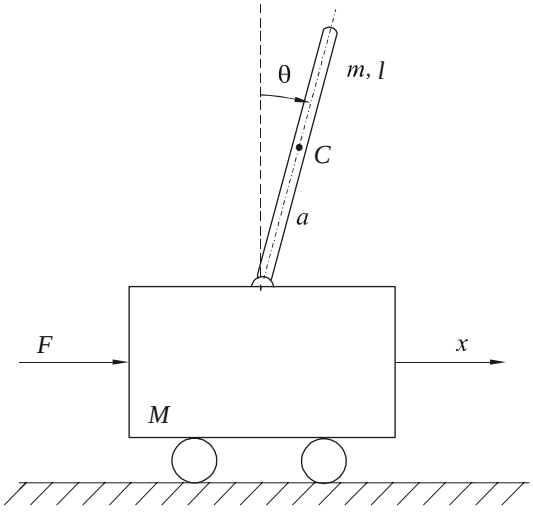

Fig. 1. Cart-pole inverted pendulum system

From the Langrangian, the general equations of motion are:

$$(M+m)\ddot{x} + ma\ddot{\theta}\cos\theta - ma\dot{\theta}\sin\theta = F \qquad (1)$$

$$\left(ma^2 + \frac{1}{12}ml^2\right)\ddot{\theta} + ma\ddot{x}\cos\theta - mga\sin\theta = 0 \qquad (2)$$

Where m and M are the masses of the pole and cart, respectively, g is the gravitational acceleration and a is

[1]Vesna Rankovic is with the Faculty of Mechanical Engineering, Sestre Janjic 6, 34000 Kragujevac, Serbia and Montenegro, E-mail: vesnar@kg.ac.yu

[2]Ilija Nikolic is with the Faculty of Mechanical Engineering, Sestre Janjic 6, 34000 Kragujevac, Serbia and Montenegro, E-mail: inikolic@ptt.yu

distance from the pivot to the centre of mass of the pendulum.

The control objective of the inverted pendulum is as follows: given initial conditions $\boldsymbol{x}(\mathbf{0}) = \boldsymbol{x_0}$ where $\boldsymbol{x_0}$ is the state variables θ, $\dot{\theta}$, x, $\dot{x}$ at time $t = 0$, find the control F to bring the system to point $\boldsymbol{x_e}$ where $\theta = 0$ and $x = x_d$.

We propose a Takagi-Sugeno type fuzzy logic controller to attain the control aim.

III. Application of Takagi-Sugeno fuzzy controller to stabilize inverted pendulum system

Simulation were performed with the program package MATLAB, by using the fuzzy toolbox. Fig. 2 are shown block diagram of the control system used in simulation. In Fig. 3 are shown SIMULINK model of inverted pendulum. The input and the output variables of the Takagi-Sugeno fuzzy controller to stabilize inverted pendulum system are shown in Fig. 4.

The inputs variables of the fuzzy logic controller:

x - cart displacement

$\dot{x}$ - cart velocity

θ - pole angle

$\dot{\theta}$ - pole angular velocity

e -cart position error ($e = x_d - x$, x_d -desired position)

and $\int_0^t edt$.

The fuzzy partitioning of the input variables of the fuzzy logic controller is realized by selection of 2 primary fuzzy sets. Selected are the Gaussian membership functions, since the best results are achieved with them.

For the system with 6 inputs and one output, set of linguistic rules is defined in the form:

R_1: if x_1 is A_{11} and x_2 is A_{12} and x_3 and is A_{13} and x_4 is A_{14} and x_5 is A_{15} and x_6 is A_{16} then

$f_1 = p_{11}x_1 + p_{12}x_2 + p_{13}x_3 + p_{14}x_4 + p_{15}x_5 + p_{16}x_6 + c_1$

R_2: if x_1 is A_{11} and x_2 is A_{12} and x_3 and is A_{13} and x_4 is A_{14} and x_5 is A_{15} x_6 is A_{26} then

$f_2 = p_{21}x_1 + p_{22}x_2 + p_{23}x_3 + p_{24}x_4 + p_{25}x_5 + p_{26}x_6 + c_2$

...

R_{64}: if x_1 is A_{21} and x_2 is A_{22} and x_3 and is A_{23} and x_4 is A_{24} and x_5 is A_{25} and x_6 is A_{26} then

$f_{64} = p_{641}x_1 + p_{642}x_2 + p_{643}x_3 + p_{644}x_4 + p_{645}x_5 + p_{646}x_6 + c_{64}$

Linguistic variables x_i are A_{1i}, A_{2i}, $i = 1,6$.

The number of liguistic rules is: $p = 2^6$.

The total number of parameters, which are being adapted is 484, out of which 36 are premise parameters and 448 are consequences parameters.

The output from Takagi-Sugeno controller is:

$$y = \frac{1}{\sum_{i=1}^{64} u_i} \sum_{i=1}^{64} u_i \left(\sum_{j=1}^{6} p_{ij} x_j + c_i \right) \tag{3}$$

where:

$u_1 = \mu_{11}(x_1) * \mu_{12}(x_2) * \mu_{13}(x_3) * \mu_{14}(x_4) * \mu_{15}(x_5) * \mu_{16}(x_6)$

$u_2 = \mu_{11}(x_1) * \mu_{12}(x_2) * \mu_{13}(x_3) * \mu_{14}(x_4) * \mu_{15}(x_5) * \mu_{26}(x_6)$

...

$u_{64} = \mu_{21}(x_1) * \mu_{22}(x_2) * \mu_{23}(x_3) * \mu_{24}(x_4) * \mu_{25}(x_5) * \mu_{26}(x_6)$

* denotes certain *T*-norm.

If the membership function are taken in the Gaussian then:

$$\mu_{ij} = \frac{1}{1 + \left[\left(\frac{x_j - a_{ij}}{c_{ij}} \right)^2 \right]^{b_{ij}}}, \; i = 1,2, \;\; j = 1,6 \tag{4}$$

Characteristic values of the inverted pendulum: $M = 0.5\ kg$, $m = 0.2\ kg$, $l = 0.6\ m$, $a = 0.3\ m$. In Fig. 5, Fig. 6, Fig. 7, Fig. 8 , Fig. 9, Fig. 10 are shown the membership functions of primary fuzzy sets of variables x, $\dot{x}$, θ, $\dot{\theta}$, e, $\int_0^t edt$, respectively, after learning. In Fig. 11 is presented variation of the pole angle, and in Fig. 12 is given the force variation.

IV. Conclusion

Design of a fuzzy logic controller is accompanied certain problems regarding design of membership functions and choosing appropriate fuzzy rules. A number of algorithms have been developed that address this problem of learning fuzzy rules and tuning membership function in a neural network architecture. In this work is used ANFIS.

Results of simulation, presented in this paper, show that the application of the neuro-fuzzy (Takagi-Sugeno) system to stabilize inverted pendulum gives satisfactory results.

The traditional approach to building system controllers requires a priori model of the system. The quality of the model, that is, loss of precision from linearization and uncertainties in system's parameters negatively influence the quality of the resulting control.

At the same time, methods of soft computing such as neural network, fuzzy logic or neuro-fuzzy systems possess non-linear mapping capabilities, do not require an analytical model and can deal with uncertainties in the system's parameters.

Structure of the Takagi-Sugeno controller implemented within the framework of the adaptive network is similar to the structure of the RBF neural network

The controller drive the cart and the pole to its desired position (Fig. 11, Fig. 12).

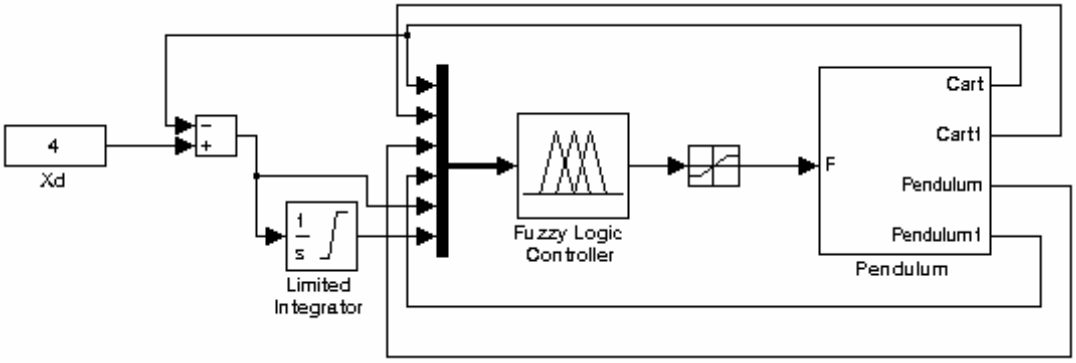

Fig. 2. Block diagram of the control system used in simulation

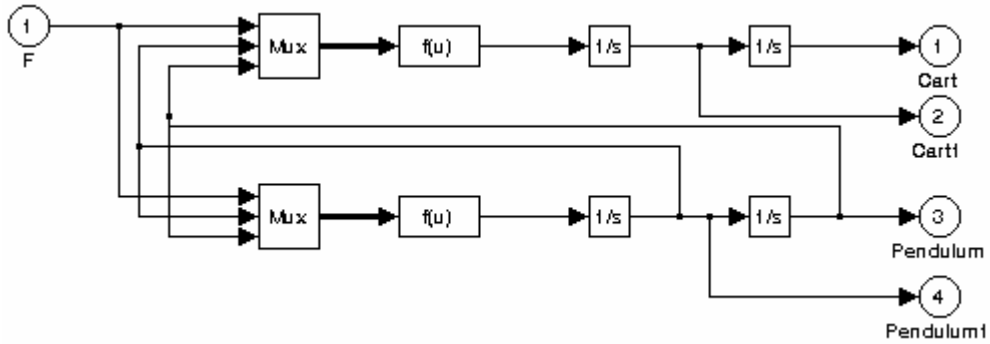

Fig. 3. SIMULUNK model inverted pendulum system

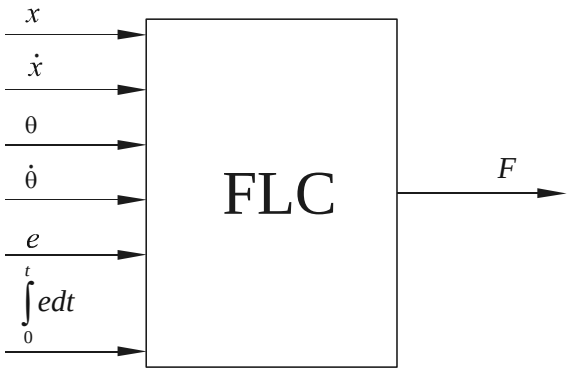

Fig. 4. Illustration of the input and output vatiables of Takagi-Sugeno fuzzy controller

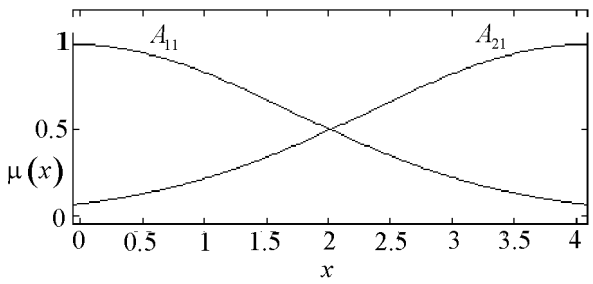

Fig. 5. Membership function of variables x after learning

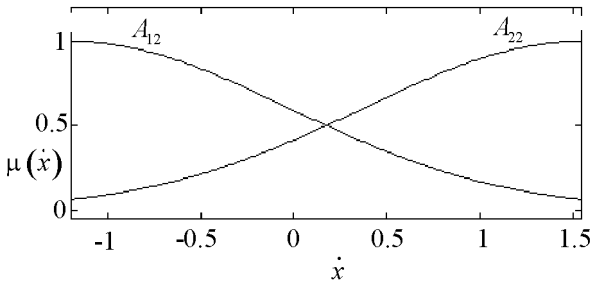

Fig. 6. Membership function of variables $\dot{x}$ after learning

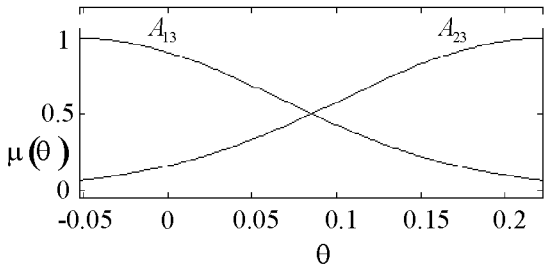

Fig. 7. Membership function of variables θ after learning

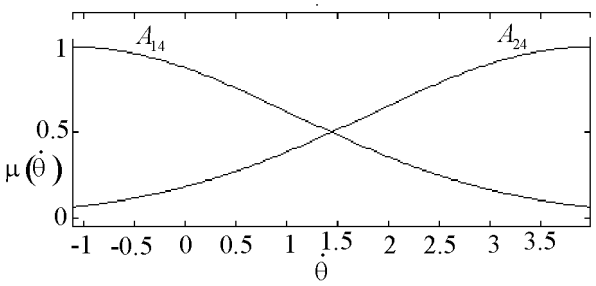

Fig. 8. Membership function of variables $\dot{\theta}$ after learning

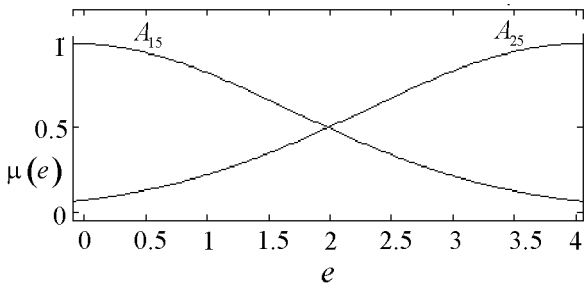

Fig. 9. Membership function of variables e after learning

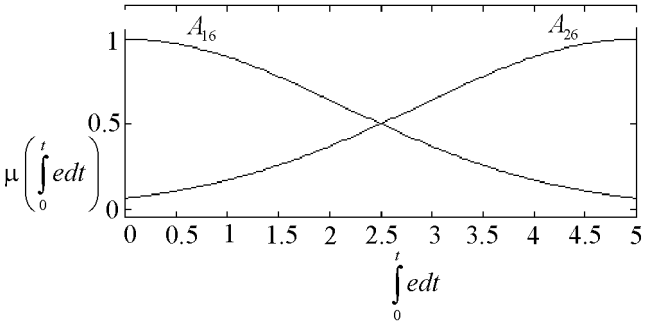

Fig. 10. Membership function of variables $\int_0^t edt$ after learning

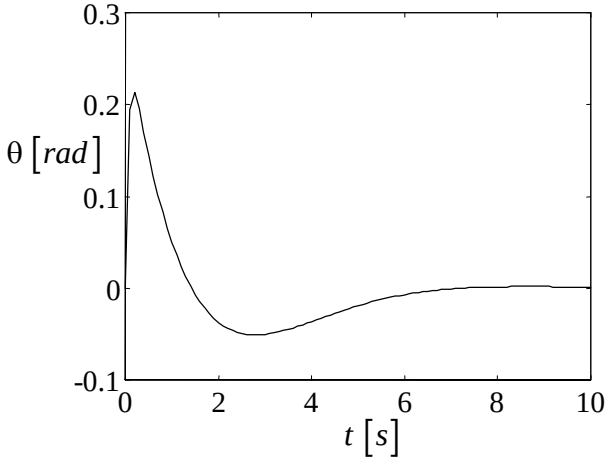

Fig. 11. Variation of the pole angle

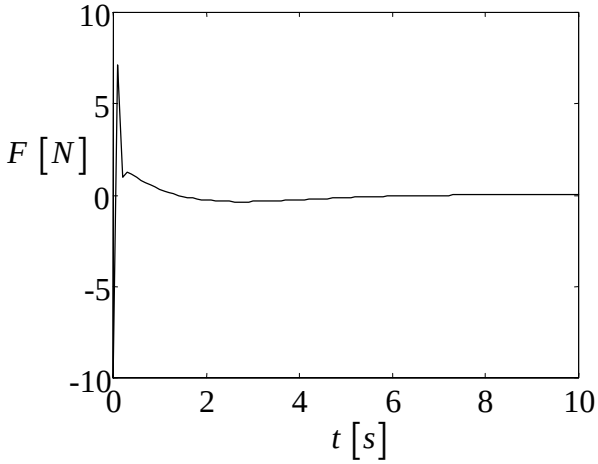

Fig. 12. Variation of the force

ACKNOWLEDGEMENT

This resarch was supported by the Ministry of Science, Tehnology and Development Republic of Serbia, Project 1616.

REFERENCES

[1] A. Benaskeur, A. Desbiens "Application of adaptive backstepping to the stabilization of the inverted pendulum" Proceedings of IEEE Canadian Conference on Electrical and Computer Engineering, pp. 113-116, Waterloo, Canada, 1998.

[2] S. Omatu, T. Ide "Stabilization of Inverted Pendulum by Neuro-Control" Proceedings of IEEE International Conference on Neural Networks, pp. 2367-2372, Orlando, FL, 1994.

[3] F. Song, S. Smith "A Takagi-Sugeno Type Fuzzy Logic Controller with only 3 Rules for a 4 Dimensional Inverted Pendulum System" Proceedings of IEEE International Conference on System, Man and Cybernetics, pp. 3800-3805, Nashville, Tennessee, 2000.

[4] R. J. Stonier, A. J. Stacey, C. Messom "Learning fuzzy control laws for the inverted pendulum" Proceedings of ISCA 7th International Conference on Intelligent Systems, pp. 64-67, Melun, Paris, July, 1998.

[5] E. S. Sazonov, P. Klinkhachorn, R. Klein "Hybrid LQG-Neural Controller for Inverted Pendulum System" Proceedings of 35th Southeastem Symposium on System Theory, pp. 144-148, Morgantown, WV, 1993.

[5] E. S. Sazonov, P. Klinkhachorn, R. Klein "Hybrid LQG-Neural Controller for Inverted Pendulum System" Proceedings of 35th Southeastem Symposium on System Theory, pp. 144-148, Morgantown, WV, 1993.

[6] J.-S. R. Jang "ANFIS: Adaptive-Network-Based Fuzzy Inference Systems", *IEEE Transactions on Systems, Man, and Cybernetics*, Vol. 23, No. 3, pp. 665-685, 1993.

Identification of Dynamic Systems using Spline Neural Networks

B. Danković[1], M. Milojković[2], Z. Jovanović[3]

Abstract- **This paper demonstrates how spline neural networks can be used for identification of dynamic systems. A neuron is utilized to build spline networks with locally distributed dynamics to identify input/output models of dynamic processes. For static neural network design, cubic splines are used; for dynamic part, orthogonal Malmquist rational functions are used.**

Keywords- **Identification, Spline, Neural Network**

I. Introduction

Artificial neural networks represent nonlinear parametric models which process signals without requiring a specified model structure. They are employed to a wide spectrum of problems as different as pattern recognition, communication, artificial vision and system control. They have great importance for system analysis and automatic control problems such as control tasks, fault diagnosis, real-time simulations and system identification.

A subclass of artificial neural networks, so-called mapping neural networks, perform mathematically a mapping action from a domain of its input space to the output space. The mapping task is labelled static (or spatial) if there is no time-dependency involved within the mapping action. In general, neural networks belonging to this category are capable of approximating a mathematical function to any desired degree of accuracy based upon training data pairs and thus can be applied to identify static nonlinearities. As regards the identification of static (memory-less) systems, the multilayer perceptron (MLP) an radial basis function (RBF) networks are the most commonly applied types [3], [6]. Both networks belong to the subcategory of spatial mapping neural networks, and are proved to be universal approximators of static nonlinearities [3], [6]. Therefore, the networks can fit a function to the measurements of a memory-less system to any degree of accuracy.

In this paper, spline neural networks are used instead of RBF networks. Approximating functions with splines gives smoothness during approximation, i.e. sustain continuance of function and her derivates (up to three for cubic splines).

[1]Prof. dr Bratislav Dankovic is with the Faculty of Electronic Engineering, Aleksandra Medvedeva 14, 18000 Nis, Serbia and Montenegro, E-mail: dankovic@elfak.ni.ac.yu

[2]Marko Milojkovic is with the Faculty of Electronic Engineering, Aleksandra Medvedeva 14, 18000 Nis, Serbia and Montenegro, E-mail: milojkovic@elfak.ni.ac.yu

[3]Mr Zoran Jovanovic is with the Faculty of Electronic Engineering, Aleksandra Medvedeva 14, 18000 Nis, Serbia and Montenegro, E-mail: zoki@elfak.ni.ac.yu

Several approaches were proposed to introduce dynamics to artificial neural networks to identify dynamic systems. The networks are essentially subdivided into structures with lumped dynamics and distributed dynamics. Structures with lumped dynamics suffer from extensive memory menagement problems since the input space dimension and training times increase with the used number of lagged measurements. Figure 1 shows the process of identification using neural networks.

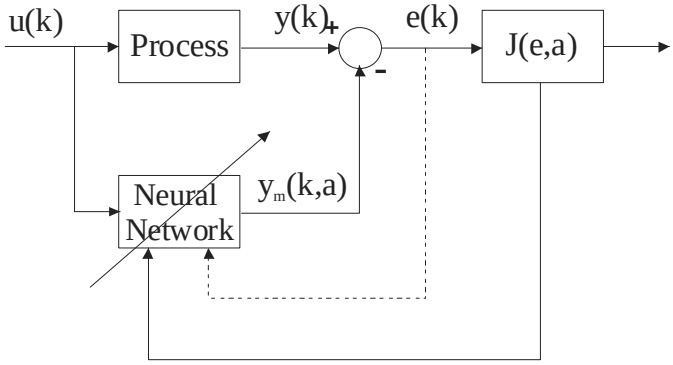

Fig 1 Process identification using neural networks

Contrary to these approaches with lumped dynamics, a novel class of neural networks arose with locally possess dynamic elements embodied within the neurons [6], [7], [8]. This class is labeled networks with distributed dynamics. In this paper, splines are used for static part of neural network; orthogonal Malmquist filter is used for dynamical part of the network instead of usual ARMAX filter [6].

II. Dynamic Spline Units

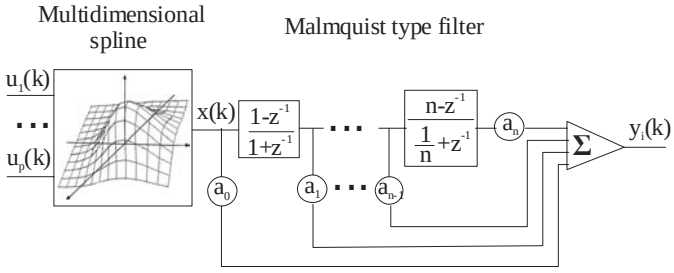

Fig. 2 Dynamic processing unit with spline function in state space representation with *p* inputs and one output

Figure 2 shows the modified structure of the dynamic neuron where spline cubic fuctions are used instead of RBFs. Instead of ARMAX filter, orthogonal Malmquist filter is used [9]. The filter input x(k) is calculated as a function of the *p* neuron inputs u_p(k) by a multidimensional spline basis function [1], [2], with different biases with respect to each input. The mapping function of the spline function is given as:

$$M_i(x)=\begin{cases}0, x>2\\ \frac{1}{6}(2-x)^3, 1\le x\le 2\\ \frac{1}{6}\left[1+3(1-x)+3(1-x^2)-3(1-x)^3\right], 0\le x\le 1\end{cases} \quad (1)$$

Let $M_{ij}(x)=M_i(x-x_j)$, where x_j represents j-th bias

Function approximation using splines has a form [4]:

$$S_{iN}(x)=\sum_{l=0}^{N} C_l M_{ij}(x) \quad (2)$$

where C_l is unknown coefficient which can be determined by solving equation:

$$\mathbf{AC}=\mathbf{F} \quad (3)$$

where:

$$\mathbf{A}=\begin{bmatrix} \frac{2}{3} & \frac{1}{6} & \dots & \\ \frac{1}{6} & \frac{2}{3} & \frac{1}{6} & \dots \\ \dots & \frac{1}{6} & \frac{2}{3} & \dots \\ & \dots & \dots & \end{bmatrix}$$

$$\mathbf{F}=\begin{bmatrix} x_0 & x_1 & \dots & x_n \end{bmatrix}^T$$

$$\mathbf{C}=\begin{bmatrix} c_0 & c_1 & \dots & c_n \end{bmatrix}^T$$

for *p* inputs, we obtain:

$$x_q(k)=\prod_{i=1}^{p} M_{ij}(u_i) \quad (4)$$

where *q=1,...,M*.

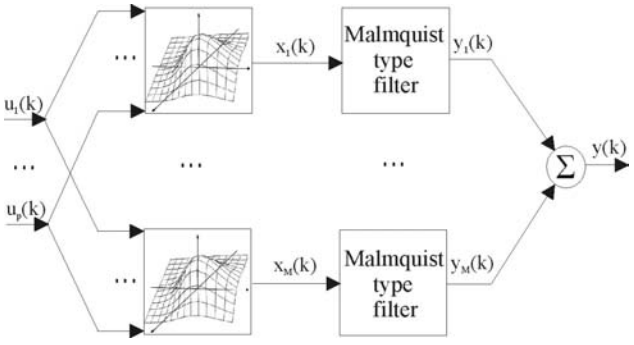

Fig. 3 Spline network with P inputs and one output

Linear part of the network is given by Malmquist orthogonal filter:

$$y(k)=a_0+\sum_{m=1}^{n} a_m \prod_{q=1}^{m} \frac{q-z^{-1}}{\frac{1}{q}+z^{-1}} \quad (5)$$

where *N* is order of the linear part.

Fig. 3 shows spline network with *P* inputs and one output comprising *M* dynamical spline units.

III. Parameters Optimization

Aim of algorithm for parameters optimization is to determine optimal parameter set which minimizes a quadratic performance index.

Model output has a form:

$$y_m=\sum_{i=1}^{N} y_i \quad (6)$$

where *N* is a number of spline units.

Output from *i*-th spline unit:

$$y_i=\sum_{j=1}^{Q} a_j M_j(\mathbf{U}) \quad (7)$$

where *Q* represents approximation order.

Mean square error:

$$J(\mathbf{a})=\frac{1}{2}\sum_{l=1}^{L}\left(y(k)-y_m(k,\mathbf{a})\right)^2=\min \quad (8)$$

where ***a*** is unknown parameter set which should be determined.

$$\mathbf{a}=(a_1,a_2,...,a_n)$$

Optimal parameters can be obtained in following way:

$$\frac{\partial J(a_i)}{\partial a_i}=0, \quad (\text{i=1,...,n}) \quad (9)$$

From (9) we obtain:

$$M^T M\mathbf{a}=M^T y_m \quad (10)$$

Where:

$$M=\begin{bmatrix} M_1(u_1) & M_2(u_1) & \dots & M_Q(u_1) \\ M_1(u_2) & M_2(u_2) & \dots & M_Q(u_2) \\ \dots & \dots & \dots & \dots \\ M_1(u_p) & M_2(u_p) & \dots & M_Q(u_p) \end{bmatrix}$$

From (10) we obtain [5], [6]:

$$\mathbf{a}=[M^T M\ ]^{-1}M^T y_m \quad (11)$$

IV. Conclusion

Further studies of the proposed neural structure with respect to the identification properties have shown that the network is capable of approximating an accurate input/output model of physical processes where the nonlinearity is a function of the process inputs. For a first time, multidimensional splines for static part and Malmquist orthogonal filters for dynamic part of neural network are introduced. The final results are: smoother approximation and more accurate identification.

References

[1] Ahlberg J.H., *The Theory of Splines and their Applications*, Ac. Press, New York, 1987.

[2] Schumaker L.L., *Approximation by Spline Functions*, Ac. Press, New York, 1991.

[3] Gupta M.M., Jin L., Homma N., *Static in Dynamic Neural Networks*, John Willey and Sons, 2003.

[4] Kocic Lj., Dankovic B., "Process Identification using B-splines", *Numerical Methods and Approximation*, Nis, 1987.

[5] Dankovic B., Antic D., Jovanovic Z., *Process Control-Process Identification*, Faculty of Electronic Engineering, Nis, 1996.

[6] Ayoubi M., Isermann R., "Radial Basis Function Networks with Distributed Dynamics for Nonlinear Dynamic Systems Identification", *EUFIT*, Aachen, Germany, 1995.

[7] Ayoubi M., "Nonlinear Dynamic Systems Identification with Dynamic Neural Networks for Fault Diagnosis in Technical Processes", *IEEE Int Conf on Systems, Man and Cybernetics*, USA, 1994.

[8] Chassiakos A., Kosmatopoulos E. and Christodoulou M., "Identification of Robot Dynamics by Neural Networks with Dynamic Neurons", *Workshop on NN in Robotics*, 1991.

[9] B. Dankovic, G.V.Milovanovic, S. Rancic, "Malmquist and Muntz Orthogonal systems and applications, in Th. M. Rassias (Ed.), *Inner Product spaces and Applications*, Addison-Wesley, Harlow, pp. 22-41,1997.

Improvement of Heating System Performance Using Fuzzy Logic

Marija M. Živković[1], Milica B. Naumović[2]

Abstract – **This paper deals with the possibilities of applying fuzzy controllers in heating systems. The heating plant «Krivi vir» in Niš, is considered as an example. The study involves the possibility of applying fuzzy approach both on higher and lower hierarchy level, as whole plant controller with load management optimization function, and on a boiler load controller, respectively.**

Keywords - **fuzzy controller, boiler, thermal load**

I. Introduction

Complex, nonlinear, multivariable and partially known systems with many disturbing influences, encountered for example in the chemical process industry, biotechnological processes or climate control objects, present great challenges for control engineering. Fuzzy logic controllers have emerged as very useful for control of processes that are complex and ill-defined. The main advantage of fuzzy logic techniques is the ability of control system design without precise mathematical model. Namely, the design approach is based on real or simulation trial and error experiments. It is very important when the mathematical modelling is difficult, or the model-based calculation is not possible in real time.

Numerous examples of fuzzy logic application in heating systems can be found in the literature (the control of drives like valves, pumps and fans, both on/off and frequency regulation, boiler and entire combustion process control, for example) [1]. Very interesting are the efficient studies about fuzzy logic application at miscellaneous climate state variables combining in order to find an optimal working regime of the heating plant [2], [3]. Moreover, in the special fuzzy-neuro control systems, the mutual influences of some variables are treated by fuzzy logic, and previously experience is incorporated by neuro techniques [4]. Our consideration related to the application of fuzzy logic in heating plant "Krivi vir" was inspired by these studies.

Some structures of fuzzy controllers, which are efficiently applied in simulation model, are presented in this paper. The study results are presented as follows. Section II presents a short technology description and some requirements, which must be fulfil during the work with masut. The structure of the fuzzy controller, that assigns the function of boilers during the thermal load management, is completely presented in section III. Section IV is devoted to the fuzzy controller structures for particular boiler load control and some simulation results. The general goals for the further development of heating control system, and odds of fuzzy logic application by that realization are presented, as a conclusion, in section V.

[1]Marija M. Živković is with JKP "Gradska toplana", Blagoja Parovića 3, 18000 Niš, Serbia and Montenegro,
E-mail: marija.milenovic.zivkovic@nitoplana.co.yu

[2]Milica B. Naumović is with the Faculty of Electronic Engineering, Aleksandra Medvedeva 14, 18000 Niš, Serbia and Montenegro, E-mail: nmilica@elfak.ni.ac.yu

II. Technology Description

The following requirements must be fulfil to ensure the necessary temperature of supply water and to achieve the maximal efficiency degree of the heating plant.

The necessary supply water temperature is determinate by heating plant-working diagram, which refers to environment temperature. The base for the work of the heating plant is temperature regime of 135/75 ^{o}C and the maximal possible load of boilers (boiler 1 – 35 MW, boiler 2 – 35 MW and boiler 3 – 58 MW).

By working with masut, boilers must be activated according to the most optimal sequence. The requirement is the activation of minimal boiler numbers that work with as large as possible load. The sequence means that there is a concept of leader and following boilers. After achievement of max load with the leader boiler, the next (first following) boiler will be activated and it will supplement the work of former boiler. Notice that the former boiler works at a full load, but the next one has only supplementing task. The same principle is applied on the relation first following - second following boiler.

The selection which boiler will be activated is guided by the criterion of correct function of boilers.

Also, by working with masut, the request is that a boiler unit stays as long as possible, as a substitute, inactivated (it is one criterion for boiler including, after the priorities work diagram and boilers' correct functions).

III. Load Management Optimization

Based on the simulation model and the equations obtained from mechanical project [7], the following recapitulation can be made: 1. The 35 MW boiler covers from +15°C up to +10°C; 2. The 58 MW boiler covers from +15°C up to 4°C; 3. Two 35 MW boilers cover from +10°C up to +1°C (leading boiler is of 35 MW); 4. The boilers of 35 MW and 58 MW cover from +10°C up to -6°C (leading boiler 35 MW); 5. The boilers of 58 MW and 35 MW cover from +3°C up to -6°C (leading boiler 58 MW); 6. Two boilers of 35 MW and the boiler of 58 MW cover from 0°C up to -15°C (leading boilers 2x35 MW); 7. The boilers of 35 MW, 58 MW and 35 MW cover from -5°C to -15°C (leading boilers 35 and 58 MW).

The question is which combination should be select as optimal one in order to fulfil all mentioned requirements given in section II.

The fuzzy controller, which is successfully used for load management and boilers function assignment tasks, is the Takagi-Sugeno type zero-order controller [5], with characteristics:

The controller has 7 inputs: 1. required thermal load of whole heating plant, 2. boiler 1 serviceability, 3. boiler 2 serviceability, 4. boiler 3 serviceability, 5. boiler 1 previous work, 6. boiler 2 previous work and 7. boiler 3 previous work. Based on working diagram equations, the required thermal load of complete heating plant, range [0 MW – 128 MW], is determined by outside temperature, range [$+15^0$C ÷ -15^0C].

Five membership functions, as shown in Fig. 1, are assigned to the first controller input, which is the required load of complete heating plant. The operational range is [0, 128] MW. Appropriate membership functions are chosen according to maximal boilers load: 1. 0–35 (trapezoidal type), 2. 35–58 (triangular type), 3. 58–70 (triangular type), 4. 70–93 (triangular type) and 5. 93–128 (trapezoidal type).

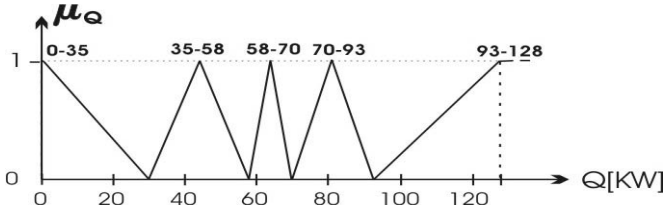

Fig. 1: Membership functions for input 1

The inputs 2-7 can be defined by operator or generated in working process. They are especially important for load ranges, which can be covered by several combinations of boilers working. The operational range is [0, 1]. The same membership functions are assigned to all inputs 2-7: 1. NO (trapezoidal type) and 2. YES (trapezoidal type), Fig 2.

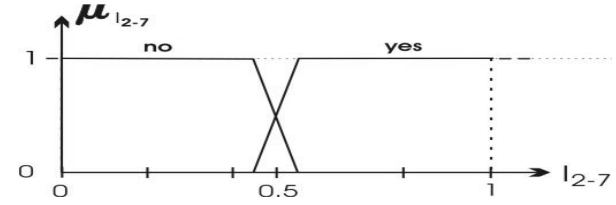

Fig. 2: Membership functions for inputs 2-7

The controller has 3 outputs that are function of load management for boiler 1, boiler 2 and boiler 3, respectively.

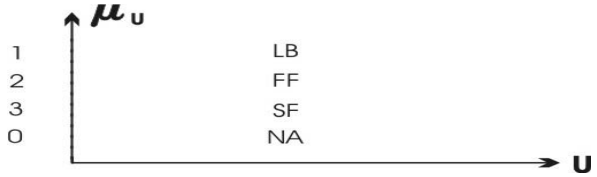

Fig. 3: Membership functions for outputs 1-3

The same membership functions, singleton type, are assigned to all outputs 1-3, Fig. 3: 1. NA – a boiler will not be activated (constant 0), 2. SF – a boiler will be activated as second following (constant 3) 3. FF – a boiler will be activated as first following (constant 2) and 4. LB – a boiler will be activated as leader (constant 1).

After input/output determination by fuzzy sets, the appropriate rules between inputs and outputs should be defined. The rule base presents set IF-THEN rules that include occasional expert's description how to control the process in an optimal way. A complete list of 44 rules for the applied fuzzy controller is given in Table I.

Beside described membership functions and fuzzy rules, the following methods typical for a fuzzy approach were selected:

- Decision method for fuzzy logic operators AND: PROD
- Decision method for fuzzy logic operators OR: PROBOR
- Implication: MIN
- Aggregation: MAX
- Defuzzyfication: The mean of maxima method

Based on determinate function of boilers and rule – work of boiler with maximal possible load, it is easy to set required thermal load by boilers.

IV. Boiler's Load Control

The control loop is presented in Fig. 4. The control system must track boiler's setup load. Setup point is variable in time, according to conditions, which are treated on higher hierarchy level of control. As example, boiler 1 is considered.

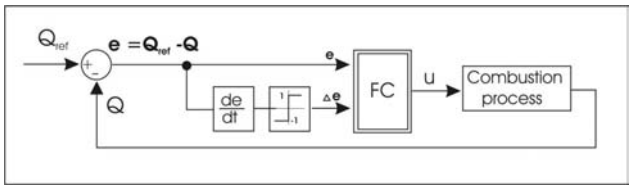

Fig. 4: Boiler's load regulation

The fuzzy controller is Mamdani type with following characteristics [5]:

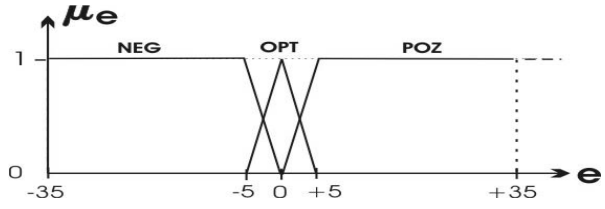

Fig. 5: Membership functions for input 1

The controller has two inputs, which are important for dynamic characteristics. First input is control error e = Q_{ref} – Q, the operational range is [-35, +35] and the membership functions, that are assigned to input 1, are presented on Fig. 5: 1. NEG –negative error (trapezoidal type), 2. OPT–optimal error (triangular type) and 3. POZ – positive error (trapezoidal type).

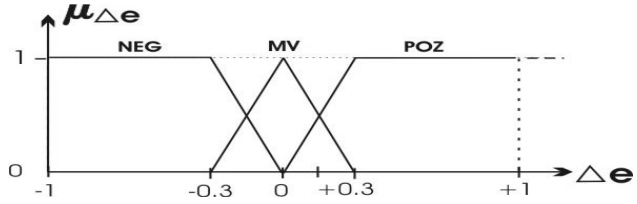

Fig. 6: Membership functions for input 2

The second input is error derivate, Δe. There is limit of this variable so its operational range is [-1 1]. Membership functions that are assigned to input 2 are presented on Fig.6: 1. NEG – negative Δe (trapezoidal type), 2. MV – mean value Δe (triangular type) and 3. POZ – positive Δe (trapezoidal type).

The controller output is signal for increasing / decreasing boiler load, with assigned membership functions, as shown on Fig. 7: 1. FD – fast decreasing (trapezoidal type), 2. SD- slow decreasing (triangular type), 3. NA – no action (triangular type), 4. SI – slow increasing (triangular type) and 5. FI – fast increasing (trapezoidal type).

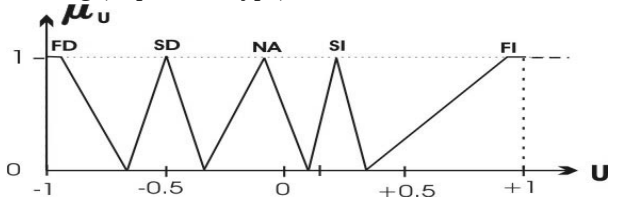

Fig. 7: Membership functions for output

The appropriate rule base is formed and given in Table II.

TABLE II
FUZZY RULE BASE FOR CONTROLLER 2

e / Δe	NEG	OPT	POZ
NEG	FD	SI	FI
MV	FD	NA	FI
POZ	FD	SD	FI

The following methods in fuzzy approach were selected:

- Decision method for fuzzy logic operators AND: PROD
- Decision method for fuzzy logic operators OR: PROBOR
- Implication: PROD
- Aggregation: PROBOR
- Defuzzyfication: The centre of gravity method

Two properties of the fuzzy controller can be mentioned.

1. The fist one is local reduction – the reduction effect is blocked if the system error is big, so the system response is fast. The reduction effect increases progressively with approach the error value to zero. This behaviour is similar to time optimal bang-bang control and it is not possible to be realized by linear PID controller.

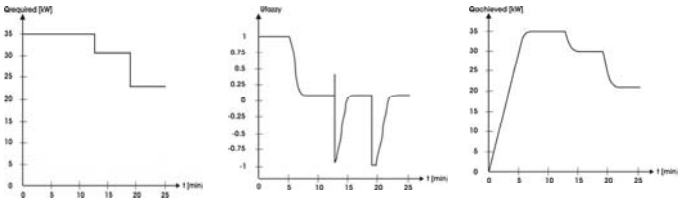

a) b) c)

Fig. 8: a) Reference value with suddenly changes,
b) Fuzzy control sygnal
c) Boiler load

2. The second property related to different velocities. Namely, the velocities for load decreasing/increasing are sited differently by definition membership functions variously. This property is desired and motivated by technology process of boiler, and cannot be provided by the linear PID control.

To verify the usefulness of suggested fuzzy controller the complete system has been simulated. One of simulation results is presented in Fig. 8. The traces show the satisfactory properties of fuzzy controller in the case of fast changes of reference signal.

V. CONCLUSION

Nowadays, the heating plant "Krivi vir" in Niš is in process of reconstruction and automatization with goal to increase energy efficiency of complete heating systems. Newly installed equipment (Control Systems SIMATIC S7 and SIMATIC WinCC) can be updated by Fuzzy Control++ software, [6]. This software can be used on all automatization levels – from single control loop to optimal control of complete heating plant. In addition, Fuzzy Control++ can be combined with conventional PID control in order to exploit all advantages.

Bearing in mind that any savings at one efficiency level represents more 10,000€ per year, all possible measures must be undertaken. The ultimate level is adaptive control, with ability of adjustment in the case of all environment changes. The master variable will be outside temperature combined with other variables such as wind, solar radiation, relative humidity, etc. After making of a reliable control system infrastructure, the further improvements are possible by software changes only. In that way, the idea of including the artificial intelligence and expert system will be also possible. The proposed adaptive system configuration should be state of the art.

REFERENCES

[1] S.K Kim and S.U Kim, "A Study on Fuzzy Control Simulator of Naturally Circulated Boiler", Korea University of Technology and Education, Internal Report, 2001.

[2] Th.Bernard and H.-B.Kuntze, "Multi-objective optimization of building climate control systems using fuzzy-logic", *European Control Conference ECC'99*, F0851, Karlsruhe, Germany, 1999.

[3] H. Feriadi and W. N. Hien, "Modelling thermal comfort for tropics using fuzzy logic", *Eighth International IBPSA Conference*, pp. 323-330, Eindhoven, Netherlands, 2003.

[4] M. El-Khoury, J. Krauss, M. Bauer and N. Morel, "NEUROBAT Predictive Neuro-fuzzy Building Control System", Project No. 51'565 supported by the Swiss Federal Office of Energy, Final Report, 1998.

[5] R-E. Precup, S. Preitl, Fuzzy controlers, Timişoara: Orizonturi Universitare, 1999.

[6] Siemens Catalog ST 70, Simatic Components for Totally Integrated Automation, 2001.

[7] Đ. Delikladić, Glavni mašinski projekat promene hidraulike u toplani «Krivi vir», Niš, 2003.

TABLE I
FUZZY RULE BASE FOR CONTROLLER 1

Ordinal		Qreq (KW)	ST B1	ST B2	ST B3	P.W B1	P.W B2	P.W B3		Func B1	Func B2	Func B3
1.			yes	no	yes/no	yes/no	yes/no	yes/		LB	NA	NA
2.			no	yes	yes/no	yes/no	yes/no	yes/no		NA	LB	NA
3.			yes	yes	yes/no	yes	no	yes/no		LB	NA	NA
4.	**IF**	**≤ 35**	yes	yes	yes/no	no	yes	yes/no	**THEN**	NA	LB	NA
5.			yes	yes	yes/no	yes	yes	yes/no		LB	NA	NA
6.			no	no	yes	yes/no	yes/no	yes/no		NA	NA	LB
7.			no	no	no	yes/no	yes/no	yes/no		NA	NA	NA
8.			yes/no	yes/no	yes	yes/no	yes/no	yes/no		NA	NA	LB
9.		**> 35**	yes	yes	no	yes/no	yes/no	yes/no		LB	FF	NA
10.	**IF**	**and**	yes	no	no	yes/no	yes/no	yes/no	**THEN**	LB	NA	NA
11.		**≤58**	no	yes	no	yes/no	yes/no	yes/no		NA	LB	NA
12.			no	no	no	yes/no	yes/no	yes/no		NA	NA	NA
13.			yes	yes	no	yes/no	yes/no	yes/no		LB	FF	NA
14.			yes	no	yes	yes/no	yes/no	yes/no		FF	NA	LB
15.			no	yes	yes	yes/no	yes/no	yes/no		NA	FF	LB
16.			no	no	no	yes/no	yes/no	yes/no		NA	NA	NA
17.			no	no	yes	yes/no	yes/no	yes/no		NA	NA	LB
18.		**> 58**	no	yes	no	yes/no	yes/no	yes/no		NA	LB	NA
19.	**IF**	**and**	yes	no	no	yes/no	yes/no	yes/no	**THEN**	LB	NA	NA
20.		**≤70**	yes	yes	yes	yes	yes	yes/no		LB	FF	NA
21.			yes	yes	yes	no	yes	yes		NA	FF	LB
22.			yes	yes	yes	yes	no	yes		FF	NA	LB
23.			yes	yes	yes	no	no	no		LB	FF	NA
24.			yes	yes	yes	no	no	yes		FF	NA	LB
25.			yes	yes	yes	no	yes	no		LB	FF	NA
26.			yes	yes	yes	yes	no	no		LB	FF	NA
27.			yes	no	yes	yes/no	yes/no	yes/no		FF	NA	LB
28.			no	yes	yes	yes/no	yes/no	yes/no		NA	FF	LB
29.			yes	yes	yes	yes	no	yes/no		FF	NA	LB
30.		**> 70**	yes	yes	yes	no	yes	yes/no		NA	FF	LB
31.	**IF**	**and**	yes	yes	yes	yes	yes	yes/no	**THEN**	FF	NA	LB
32.		**≤93**	yes	yes	no	yes/no	yes/no	yes/no		LB	FF	NA
33.			yes	no	no	yes/no	yes/no	yes/no		LB	NA	NA
34.			no	yes	no	yes/no	yes/no	yes/no		NA	LB	NA
35.			no	no	no	yes/no	yes/no	yes/no		NA	NA	NA
36.			no	no	yes	yes/no	yes/no	yes/no		NA	NA	LB
37.			yes	yes	yes	yes/no	yes/no	yes/no		FF	SF	LB
38.			yes	no	yes	yes/no	yes/no	yes/no		FF	NA	LB
39.		**> 93**	no	yes	yes	yes/no	yes/no	yes/no		NA	FF	LB
40.	**IF**	**and**	no	no	no	yes/no	yes/no	yes/no	**THEN**	NA	NA	NA
41.		**≤128**	no	no	yes	yes/no	yes/no	yes/no		NA	NA	LB
42.			no	yes	no	yes/no	yes/no	yes/no		NA	LB	NA
43.			yes	no	no	yes/no	yes/no	yes/no		LB	NA	NA
44.			yes	yes	no	yes/no	yes/no	yes/no		LB	FF	NA

Control of Chaotic System by Combined Synchronization

Radoslav H. Radev[1], Dragomir P. Chantov[2]

Abstract – **In this paper synthesis of a relay-based control of chaotic systems is proposed for the cases when only one of the state variables is accessible. A second identical chaotic system is constructed and the two systems are synchronized on the basis of the accessible variable. A combined approach is proposed to achieve synchronization, which combines the advantages of two of the known synchronization methods. Only variables of the second system take part in the control.**

Keywords – **chaotic systems, chaotic synchronization, control, Pontryagin's maximum principle.**

I. Introduction

The chaotic systems are nonlinear continuous or discrete systems which possess complex dynamical behaviour by certain conditions and this behaviour is characterized by a strange attractor in the state space, a positive Lyapunov exponent and a specific type of Poincare section. The main feature of these systems is their extreme sensitivity of the initial conditions. Due to their character, the chaotic systems are for long time considered as non-controllable systems. Ott, Grebogi и Yorke [1] however suggest a method for their control and since then the proposed methods for control and stabilization of chaos increase continuously. On the other hand in the last years there is a growing interest to another phenomenon from the field of the chaotic dynamics - this is the so called chaotic synchronization. The aim here is to connect two chaotic systems in such a way that the dynamics of one of the systems to be dependent of the dynamics of the other. As the control as well as the synchronization of chaotic systems find application in different fields of the technics [2,3].

In this paper a specific task is considered, which involves a combination of the problems about chaotic control and synchronization. The main idea is to construct control functions which will stabilize a given chaotic system on the basis of the Pontryagin's maximum principle. A second (auxiliary in this case) identical chaotic system is built, which is synchronized with the main one by a connecting function in which only one of the state variables takes part. After identical synchronization between the two systems is achieved, the control function, in which only variables from the auxiliary system take part, is applied to the first system. This control function stabilizes the main chaotic system into a preliminarily selected unstable fixed point. To exemplify the proposed control approach we choose the Willamowski-Rossler chaotic system, which describes the processes in a chemical reactor.

[1] Radoslav H. Radev is with the Faculty of Electrical Engineering and Electronics, Technical University - Gabrovo, 4 H.Dimitar Str., 5300 Gabrovo, Bulgaria, E-mail: radev@tugab.bg

[2] Dragomir P. Chantov is with the Faculty of Electrical Engineering and Electronics, Technical University - Gabrovo, 4 H.Dimitar Str., 5300 Gabrovo, Bulgaria, E-mail: dchantov@yahoo.com

II. Control and Synchronization of Chaotic Systems

Control In the general case a continuous chaotic system can be described by the following nonlinear equation:

$$\dot{\mathbf{x}}(t) = \mathbf{f}(\mathbf{x}, \mathbf{p}), \quad (1)$$

where $\mathbf{x} \in \Re^n$ is the state variables vector of the system, $\mathbf{p} \in \Re^k$, $k<n$ is the parameters vector and $\mathbf{f}$ is a nonlinear function.

There exist different methods to control the chaotic systems. In this paper control synthesis, based on the Pontryagin's maximum principle, is proposed. On the basis of the necessary conditions of the maximum principle [3] we will seek an external force control of the type:

$$\dot{\mathbf{x}}(t) = \mathbf{f}(\mathbf{x}) + \mathbf{B}\mathbf{u}, \quad (2)$$

where $\mathbf{B}$ is a column-vector of the type:

$$\mathbf{B} = \begin{bmatrix} b_1 \\ \vdots \\ b_i \\ \vdots \\ b_n \end{bmatrix}$$

We will say the control is an *i-th input control*, if $b_i \neq 0$ and $b_j = 0$ for $\forall j \neq i$. An auxiliary vector

$$\boldsymbol{\lambda}(t) = \begin{bmatrix} \lambda_1 \\ \lambda_2 \\ \vdots \\ \lambda_n \end{bmatrix}$$

is introduced for the formulation of the maximum principle. Then the so called Hamiltonian function is composed:

$$H(\mathbf{x}, \mathbf{u}, t, \boldsymbol{\lambda}) = \boldsymbol{\lambda}^T(t)\mathbf{f}(\mathbf{x}, \mathbf{u}, t) \quad (3)$$

From the maximum principle [3] the Hamiltonian function has a maximum over the optimal system trajectory, i.e.:

$$\frac{\partial H}{\partial \mathbf{u}} = 0, \quad (4)$$

from which for λ_i we obtain

$$\lambda_i = 0.$$

(For each t with exception of the interruption points of **f** and **u** the following condition is fulfilled over the optimal trajectory:

$$\frac{d\boldsymbol{\lambda}(t)}{dt} = -\frac{\partial H}{\partial \mathbf{x}} = 0 \qquad (5)$$

If the terminal time is not given, the additional condition:

$$H(\mathbf{x}, \mathbf{u}, \boldsymbol{\lambda}) = 0 \qquad (6)$$

is imposed.

It follows from (4) that the control will be relay-based from the type:

$$u = k\, sign\, s_i(\mathbf{x}), \qquad (7)$$

where s_i are the control functions, which satisfy the condition for a non-zero vector $\boldsymbol{\lambda}$.

By taking into consideration (4), (5) and (6) for third-order systems and *i*-th input control only one variant of control function s_i for each i is possible. It is obtained from the following system:

$$\det\begin{bmatrix} f_l(\mathbf{x}) & f_k(\mathbf{x}) \\ -\dfrac{\partial f_l(\mathbf{x})}{\partial x_i} & -\dfrac{\partial f_k(\mathbf{x})}{\partial x_i} \end{bmatrix} = 0 \quad \text{for } k \neq i \text{ and } l \neq i\,. \qquad (8)$$

From (8) the control function is:

$$s_i(\mathbf{x}) = f_k(\mathbf{x})\frac{\partial f_l(\mathbf{x})}{\partial x_i} - f_l(\mathbf{x})\frac{\partial f_k(\mathbf{x})}{\partial x_i} = 0\,. \qquad (9)$$

Synchronization. In the general case when speaking of chaotic synchronization we take two connected chaotic systems of the type:

$$\dot{\mathbf{x}} = \mathbf{f}(\mathbf{x}), \qquad (10)$$

$$\dot{\tilde{\mathbf{x}}} = \tilde{\mathbf{f}}(\tilde{\mathbf{x}}), \qquad (11)$$

with the corresponding solutions $\mathbf{x}(t, t_0, \mathbf{x}(t_0))$ and $\tilde{\mathbf{x}}(t, t_0, \tilde{\mathbf{x}}(t_0))$, where $\mathbf{x} \in \Re^{n_1}$, $\tilde{\mathbf{x}} \in \Re^{n_2}$, and the initial conditions of the two systems are $\mathbf{x}(t_0)$ and $\tilde{\mathbf{x}}(t_0)$. For $n_1 = n_2$ and $\tilde{\mathbf{f}}(\tilde{\mathbf{x}}) = \mathbf{f}(\mathbf{x})$ the two systems are identical. The solutions $\mathbf{x}(t, t_0, \mathbf{x}(t_0))$ and $\tilde{\mathbf{x}}(t, t_0, \tilde{\mathbf{x}}(t_0))$ of the systems (10) and (11) with initial conditions $\mathbf{x}(t_0)$ and $\tilde{\mathbf{x}}(t_0)$ are *identically synchronized* [2,4] if the following function

$$Q_t = Q_t[\mathbf{x}(t), \tilde{\mathbf{x}}(t)] = \|\mathbf{e}(t)\| \equiv 0 \qquad \forall t > 0\,, \qquad (12)$$

where $\mathbf{e}(t)$ is the difference function between the two systems:

$$\mathbf{e}(t) = \mathbf{x}(t, t_0, \mathbf{x}(t_0)) - \tilde{\mathbf{x}}(t, t_0, \tilde{\mathbf{x}}(t_0))\,. \qquad (13)$$

The equality (12) means that after starting the two systems from different initial conditions, some time later they will begin to oscillate identically in the generalized state space. However this will only be possible if the synchronization process is stable. Measure of the stability of the synchronization give the *conditional Lyapunov exponents*. It is also accepted to refer to the system (10) as Master, and to system (11) as Slave.

The two main approaches for chaotic synchronization are the decomposition methods and the feedback ones. The common between them is that they define some type of connection between the two systems. By the decomposition methods one mentally "decomposes" the Master system into two or more parts, one of which drives the Slave system by direct substitution of some of its variables with the variables of the driving part of the decomposed Master system. Generally the two systems are described by the following equations [2,4]:

$$\textbf{Master}\ \ \dot{\mathbf{x}} = \mathbf{f}(\mathbf{x}, \mathbf{h}(\mathbf{x})), \qquad (14)$$

$$\textbf{Slave}\ \ \dot{\tilde{\mathbf{x}}} = \mathbf{f}(\tilde{\mathbf{x}}, \mathbf{h}(\mathbf{x})), \qquad (15)$$

where $\mathbf{h}(\mathbf{x})$ is the driving part of the decomposed Master which drives the Slave system.

In the case of the feedback methods with one-way coupling a signal, proportional to the difference between the two systems, is added to the Slave system [4]:

$$\textbf{Master}\ \ \dot{\mathbf{x}} = \mathbf{f}(\mathbf{x}), \qquad (16)$$

$$\textbf{Slave}\ \ \dot{\tilde{\mathbf{x}}} = \mathbf{f}(\tilde{\mathbf{x}}) + \alpha\mathbf{E}(\mathbf{x} - \tilde{\mathbf{x}}), \qquad (17)$$

where α is the feedback gain and **E** is the coupling matrix with a proper dimension.

In the present paper we suggest a concurrent application of the two approaches [5]:

$$\textbf{Master}\ \ \dot{\mathbf{x}} = \mathbf{f}(\mathbf{x}, x_i), \qquad (18)$$

$$\textbf{Slave}\ \ \dot{\tilde{\mathbf{x}}} = \mathbf{f}(\tilde{\mathbf{x}}, x_i) + \alpha\mathbf{E}(\mathbf{x} - \tilde{\mathbf{x}}), \qquad (19)$$

where the decomposition part of the coupling is restricted to the *partial replacement* method, where the connection is only by a single variable x_i, substituted only in one place in the Slave system. The second part of the connection (the feedback coupling) can be selected in such way that only the same variable x_i to take part in it and the whole connection between the Master and the Slave system to be only with one variable.

Control by synchronization. The idea about control of chaotic systems by means of a synchronized system is shown on fig.1.

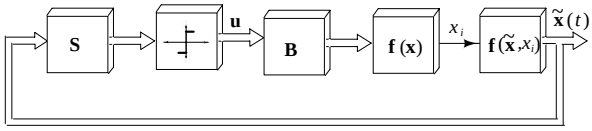

Fig.1. Control by synchronization

If we suppose that only one variable x_i of the Master system is accessible and the aim is to stabilize this system, the control functions (9), in which in the general case all state variables of the Master system take part, can not be obtained. In such a case we can construct a Slave system and synchronize the two systems by the accessible variable x_i. Then the proposed by us combined approach for synchronization (18) and (19) has the advantage that it permits many different variants of connection, even with only one variable. From all these variants we can choose that with the shortest transient process and to control the Master system again with control of type (7), but now the control function (9) is:

$$s_i(\tilde{\mathbf{x}}) = f_k(\tilde{\mathbf{x}})\frac{\partial f_l(\tilde{\mathbf{x}})}{\partial \tilde{x}_i} - f_l(\tilde{\mathbf{x}})\frac{\partial f_k(\tilde{\mathbf{x}})}{\partial \tilde{x}_i} = 0\,. \qquad (20)$$

The proposed approach for control by synchronization will be illustrated with a concrete third-order chaotic system,

since most of the known chaotic systems are relatively simple third-odred nonlinear continuous systems.

III. WILLAMOWSKI-ROSSLER SYSTEM

The Willamowski-Rossler (WR) [6, 7] describes the processes in a chemical reactor and is given with the following equations:

$$\begin{aligned}\dot{x}_1 &= f_1(\mathbf{x}) = k_1 x_1 - k_{-1}x_1^2 - k_2 x_1 x_2 + k_{-2}x_2^2 - k_4 x_1 x_3 + k_{-4},\\ \dot{x}_2 &= f_2(\mathbf{x}) = k_2 x_1 x_2 - k_{-2}x_2^2 - k_3 x_2 + k_{-3},\\ \dot{x}_3 &= f_3(\mathbf{x}) = -k_4 x_1 x_3 + k_{-4} + k_5 x_3 - k_{-5}x_3^2,\end{aligned} \quad (21)$$

where the variables x_i are the concentrations of the species in the reactor and they can take only positive values. The system has 10 parameters $k_{\pm i}$, with nominal values, by which chaos is present in the system:

$k_1 = 31.2,\ k_{-1} = 0.2$, $k_2 = 1.572$, $k_{-2} = 0.1$, $k_3 = 10.8$,

$k_{-3} = 0.12$, $k_4 = 1.02$, $k_{-4} = 0.01$, $k_5 = 16.5$ i $k_{-5} = 0.5$

For these values the system evolves chaotically, which is evident by the presence of a typical chaotic attractor in the system state space, which is shown on fig.2.

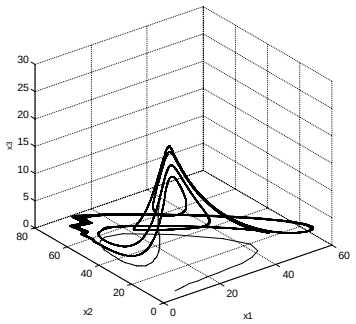

Fig.2. Chaotic attractor of the WR system

When analizing a chaotic system it is important to find its equilibrium or fixed points, i.e. the points for which:

$$\mathbf{f}(\mathbf{x}) = 0. \quad (22)$$

By means of the program Matlab the fixed points of the WR system are calculated for the nominal values of the system variables and we find that the system has eight fixed points (27):

$\mathbf{x}_1^* = [84.21\ \ 1216\ \ -139]^T$, $\mathbf{x}_2^* = [8.31\ \ 22.7\ \ -1e-3]^T$,

$\mathbf{x}_3^* = [-3e-4\ \ 0.01\ \ -6e-4]^T$, $\mathbf{x}_4^* = [-701\ \ -11130\ \ -1e-5]^T$,

$\mathbf{x}_5^* = [156\ \ -5e-4\ \ 7e-5]^T$, $\mathbf{x}_6^* = [7.354\ \ 7.354\ \ 17.99]^T$,

$\mathbf{x}_7^* = [1.32\ \ 0.014\ \ 30.32]^T$, $\mathbf{x}_8^* = [0.004\ \ 0.01\ \ 32.99]^T$.

Only the points $\mathbf{x}_6^* \div \mathbf{x}_8^*$ have real meaning (there aren't negative concentrations x_i). The point $\mathbf{x}_8^*$ is a stable fixed point (the eigenvalues of the $[p\mathbf{I} - \mathbf{J}_8]$ matrix are all negative, $\mathbf{J_8}$ is the system Jacobian in this point) and hence this point is not of interest for the control, where the purpose is to stabilize the system into an unstable fixed point. the point $\mathbf{x}_7^*$ due to its proximity to $\mathbf{x}_8^*$ is also not of interest notwithstanding the fact that it is unstable. Then we set the aim of the control to stabilize the system into the unstable fixed point $\mathbf{x}_6^*$. We can evaluate the controllability of the system around this point from the matrix:

$$\mathbf{Q}_{6i} = [\mathbf{B}_i \quad \mathbf{J}_6\mathbf{B}_i \quad \mathbf{J}_6^2\mathbf{B}_i], \quad (23)$$

where $\mathbf{J_6}$ is the system Jacobian in the point $\mathbf{x}_6^*$. For each i the matrix is of full rank, i.e. the system is controllable around the point $\mathbf{x}_6^*$.

IV. SYNCHRONIZATION AND CONTROL BY SYNCHRONIZATION OF THE WR SYSTEM

A Slave system according to (19) is synthesized. For the synchronization we choose a combination of the methods of the partial replacement, by which one variable x_i from the Master system substitutes its corresponding variable of the Slave system only in one place; and the standard one-way coupling, by which there are three variants for the **E** matrix:

$$1.\mathbf{E} = \begin{bmatrix}1&0&0\\0&0&0\\0&0&0\end{bmatrix};\ 2.\mathbf{E} = \begin{bmatrix}0&0&0\\0&1&0\\0&0&0\end{bmatrix};\ 3.\mathbf{E} = \begin{bmatrix}0&0&0\\0&0&0\\0&0&1\end{bmatrix}. \quad (24)$$

With these limitations imposed, there exist 45 different variants of connection between the two systems, which are examined in detail in [5]. 12 of them are with a connecting signal, in which only one state variable is present and the synchronization scheme is stable (the calculated conditional Lyapunov exponents [2] are all negative). To illustrate the proposed in part II control approach we will examine one variant in detail. By this variant the Master system is given by (21) and the slave system is:

$$\begin{aligned}\dot{\tilde{x}}_1 &= k_1 \underline{x_1} - k_{-1}\tilde{x}_1^2 - k_2\tilde{x}_1\tilde{x}_2 + k_{-2}\tilde{x}_2^2 - k_4\tilde{x}_1\tilde{x}_3 + k_{-4} + \underline{\alpha(x_1 - \tilde{x}_1)},\\ \dot{\tilde{x}}_2 &= k_2\tilde{x}_1\tilde{x}_2 - k_{-2}\tilde{x}_2^2 - k_3\tilde{x}_2 + k_{-3},\\ \dot{\tilde{x}}_3 &= -k_4\tilde{x}_1\tilde{x}_3 + k_{-4} + k_5\tilde{x}_3 - k_{-5}\tilde{x}_3^2.\end{aligned} \quad (25)$$

For $\alpha = 10$ the calculated conditional Lyapunov exponents are $\lambda_{1,2} = -4.73$, $\lambda_3 = -47.07$, i.e. stable synchronization between the two systems will exist. This is shown on fig.3, which depicts the differences $e_i(t) = x_i(t) - \tilde{x}_i(t)$. The initial conditions of the systems are $\mathbf{x}(0) = [5\ \ 2\ \ 1]^T$ and $\tilde{\mathbf{x}}(0) = [6\ \ 1\ \ 0]^T$.

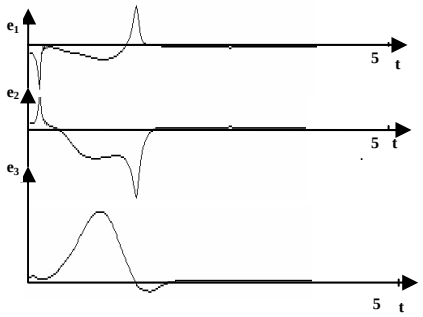

Fig.3. Differences $e_i(t) = x_i(t) - \tilde{x}_i(t)$

After identical synchronization between the two systems is achieved, we can use the Slave system to stabilize the Master system according to fig.1. The control functions for

first-, second- and third-input control are calculated according to (20) with the Slave system variables:

$$s_1(\tilde{\mathbf{x}}) = a\tilde{x}_2 + b\tilde{x}_3 + (c - d\tilde{x}_3 - f\tilde{x}_2)\tilde{x}_2\tilde{x}_3, \quad (26)$$

$a = k_2k_{-4}$, $b = k_{-3}k_4$, $c = (k_2k_5 - k_3k_4)$, $d = k_2k_{-5}$, $f = k_{-2}k_4$,

$$s_2(\tilde{\mathbf{x}}) = (-k_2\tilde{x}_1 + 2k_{-2}\tilde{x}_2) f_3(\tilde{\mathbf{x}}), \quad (27)$$

$$s_3(\tilde{\mathbf{x}}) = -k_4\tilde{x}_1 f_2(\tilde{\mathbf{x}}). \quad (28)$$

The control is relay-based of the type (7). The controlled Master system has the form (2).

We choose to apply the concept of the so called *local control* [3] for each-input control. The sense of the local control is that by this type of control the control function is not applied immedeately to the controlled system, but the system is let to run free and only when the system trajectory enters into a sphere in the state space with a center - the chosen for the stabilization fixed point and radius - *R*, defined by us, we will apply the control. We will say that the system is stabilized in the point $\mathbf{x}_6^*$ when the trajectory enters into another small sphere with the same center $\mathbf{x}_6^*$ and sufficiently small radius $r<R$.

V. Experimental Results

The results shown are for the synchronization scheme (25). The other synchronization variants between the Master and the Slave systems give similar results, the only difference is the length of the transient until the stabilization of the Master system. Fig.4 depicts the state space of the controlled Master system and the control (7) for first-input control with a control function (26). The initial conditions of the two systems are $\mathbf{x}(0) = [5 \quad 2 \quad 1]^T$ and $\tilde{\mathbf{x}}(0) = [6 \quad 1 \quad 0]^T$. The big and the small spheres of the local control are with radii R = 6 and r = 0.8, the control gain is k = -20. The system stabilizes in the point $\mathbf{x}_{61}^* = [7.65 \quad 7.26 \quad 18.67]^T$.

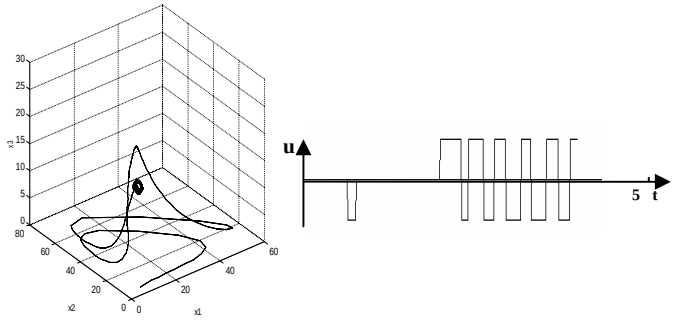

Fig.4. First input control - state space and control function u(*t*).

The same characteristics are shown on fig.5 for the second-input control with a control function (27). The systems are started from the same initial conditions. The spheres are with radii R = 6 and r = 0.3, the control gain is k = 10. The system stabilizes in the point $\mathbf{x}_{62}^* = [7.6 \quad 7.27 \quad 18.1]^T$.

Fig.6 shows the state space and the control for the third-input control with a control function (28) and the same initial conditions. The spheres are with radii R = 6 and r = 0.5, the control gain is k = -20. The system stabilizes in the point $\mathbf{x}_{63}^* = [6.87 \quad 7.45 \quad 17.94]^T$.

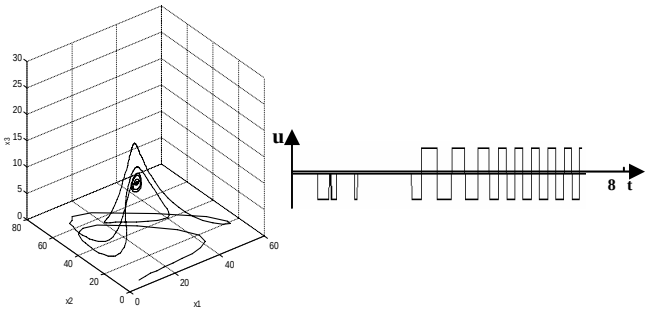

Fig.5. Second input control - state space and control function u(*t*).

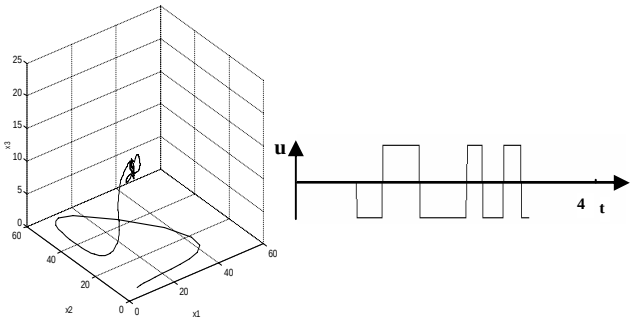

Fig.6. Third input control - state space and control function u(*t*).

VI. Conclusion

In this article an approach for the stabilization of chaotic systems, based on the phenomenon chaotic synchronization, is proposed. We also propose a synchronization method, which offers a great number of variants of connection between the Master and the Slave systems and by some of them the connection is only by one variable. This gives us the opportunity to choose the best variant in terms of speed of synchronization and starting from it, to realize a proper control to the Master system on the basis of the maximum principle, which will stabilize the system into a preliminarily chosen unstable fixed point.

References

[1] Ott,E., C.Grebogi, J.Yorke, Controlling chaos, Phys.Lett, vol.64, pp.1196-1199, 1990.

[2] Boccaletti, S. et al , The synchronization of chaotic systems, Phys.Reports 366, 2002, pp.1-101.

[3] Radev, R., Chaos and control, U.P. "V.Aprilov", Gabrovo, Bulgaria, 2004

[4] Pecora, L., T.Carroll, Synchronization in chaotic systems, Phys.Rev.Let., Vol.64, No8, 1990, pp.821-824.

[5] Radev, R., D.Chantov, Synchronization of the Willamowski-Rossler chaotic system, Int.Conf. Automatics and Infromatics'04, 6-8 Oct. 2004, Sofia, Bulgaria.

[6] Wu, X., R.Kapral, Internal Fluctuations and deterministic chemical chaos, Phys.Rev.Letters, Vol.70, No13, 1993, pp.1940-1943.

[7] Guemez, J., M.Matias, Internal fluctuations in a model of chemical chaos, Phys.Review E, Vol.48, No4, 1993, pp.2351-2353.

Session TS:

TELECOMMUNICATION SYSTEMS

CATV Systems – Parameter's Optimization

Oleg Borisov Panagiev[1]

Abstract – **This paper aims to provide an exact expressions for the BER performance of the HFC (Hybrid Fiber Coaxial)/CATV (CAble TeleVision) systems in the presence of an additive mixture of infrequent clipping impulse and Gaussian background noise. The clipping noise model employed here is presented as Weibull distributions.**

Keywords – *CATV* (**cable television), optimization, HFC networks, BER.**

I. INTRODUCTION

CATV systems are traditionally one-way and broadcasting infrastructure for residential area TV distribution. Whit the population of Internet services, cable services providers are interested in providing these Internet services. Such a good solution is a hybrid transmission on analogue and digital signals by means optical fibers and coaxial cables. In fact, the hybrid transmission of existing AM/VSB and new digital signals is essential for developing future expandable and cost-effective CATV systems. The HFC topology is considered as a bi-directional broadband communication infrastructure. A group of 500 to 2000 subscribers are served by a fiber that comes from the HEADEND to a fiber node (FN), as shown in Fig.1. Moreover, signals are transmitted electrically from FN to home by coaxial cable through some amplifiers and splitters. Stations attached to the cable transmit and receive signals over different frequencies, named as upstream and downstream channels.

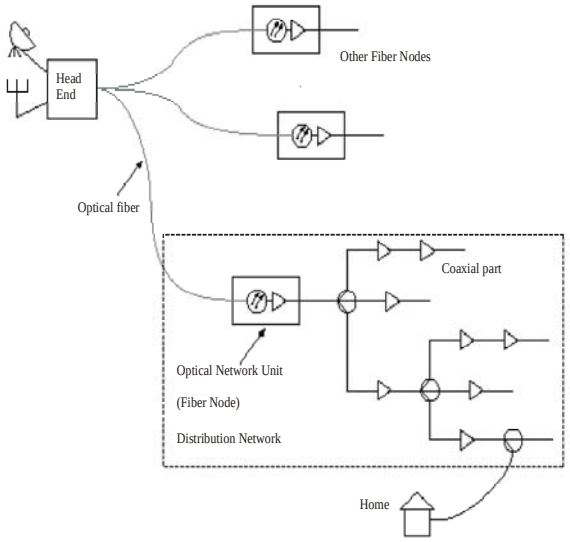

Fig.1. HFC/CATV system

[1]O. B. Panagiev is a system engineer at the Technical University of Sofia, e-mail: olcomol@yahoo.com

HFC/CATV systems are ones of the attractive systems, since M-QAM is expected to be able to offer both high spectral efficiency and robustness to noise and non-linearity. But, the clipping noise generated by the laser diode (DFB – distributed feedback) threshold results in a severe BER (Bit Error Rate) performance degradation in the transmission of digital signals because of its impulsive nature, although the impact on the analogue video transmission is much more tolerable.

II. HFC SYSTEMS – FEATURES, ADVANTAGES AND PARAMETERS

The topology of HFC/CATV system (Fig.1) presents some inherent problems and limitations. For instance, a large number of broadband amplifiers are required to operate in cascade. Each amplifier adds noise and intermodulation distortions to the signal, the number of cascaded trunk amplifiers in the primary lines is thus limited to 40 to 45, in order to ensure a good reliability of the network and a good quality of the signal delivered to the subscribers. In order to provide other services such as digital television, it is necessary to increase the capacity of existing networks.

Large bandwidth, low losses and lightweight make optical fibre a unique candidate for designing CATV systems. One constraint, which has to be taken into account, is the considerable investment, which has been needed to build the existing coaxial CATV networks. It thus seems obvious that one has to search for ways to apply the fibre technology to an hybrid optical fiber-coaxial cable system which makes use of the existing plant structures, at the same time, uses the optical fibre advantages for suppressing the most serious weaknesses of current networks.

Features and advantages

- Remote location light-source for easy maintenance.
- Heat – free light: cold light emission points, Infrared spectrum are not transmitted.
- Color control/change: certain light sources use color or dimming programs with local or remote control lines.
- Focusable light: directional lighting / high contrast ratio: control of beam size by selection of suitable end-fittings for high object contrast ratio.
- Dimmable light.
- Moving and colored light.
- Conservation lighting: UV-filtered light.
- Intrinsic safety: Electricity- free lighting: no electric or electromagnetic interference.
- Low maintenance.
- Low running costs.
- Ecologically desirable.

- Providing designers with great flexibility and versatility in meeting the growing challenges.

B. Fiber optic link: transmissions-system parameters

- Direct laser modulation
- OMI - optical modulation index
- RIN - relative intensity noise
- Optical signal parameters
- Signal quality
- Carrier to noise ratio (CNR)
- Signal to noise ratio (SNR)
- Bit error rate (BER)
- CSO (Composite Second Order)
- CTB (Composite Triple Beat)
- Interference of audio-video channels
- Average transmitter life-time
- External modulation

III. PARAMETER'S OPTIMIZATION

A. General principles

In this part we described four cases for optimizations on parameters HFC network. These parameters define her reliability and quality transmitting signals – analog (AM/VSB) and digital (M-QAM).

The nonlinear distortions, as with thermal noise, are inevitable impairments in CATV systems; therefore, it is necessary to specify levels of distortions that can guarantee desirable picture quality for in-service programs. Many efforts to clarify the impact of these distortions on the AM/VSB signal have been made, and the required distortion levels for the AM signal have been established. Furthermore, composite distortions are ones of the most important narrow-band interferences when considering the digital channel quality of CATV systems. Accordingly, should be taking into account to it in order to specify not only system performance but also the requirements for system components, such as optical transmitters/receivers, trunk amplifiers, brides and etc.

B. Essences and algorithms

The averaged BER of the digital channel (M-QAM signal) must be specified to guarantee the picture quality of digital channels when discussing composite distortion levels. The PDF (probability density function) of the distortions is necessary in evaluating the BER of the M – QAM signal; accordingly, the required composite distortion levels in the digital channel can be determined by using a BER analysis method that takes into account this PDF.

The Weibull distribution has been used in [5,6] in order to examine the composite distortions' statistical features, where PDF [6] is

$$P_e = \frac{1}{2} K_1^M \cdot \exp\left[-\frac{3}{2} \cdot \frac{CNR}{M-1} + \gamma \right] \quad (1)$$

The BER of M - ary QAM is evaluated in terms of optical modulation indexes of M - QAM and AM/VSB signals which in turn specify CNR, impulsive index γ (clipping index) of the clipping noise, and power ratio of the Gaussian noise to the clipping noise.

K_1^M is a ratio depending on the M-ary quadrature amplitude modulation and the Gray's code:

$$K_1^M = (2/\log_2 M) \cdot (1 - 1/\sqrt{M}) \quad (2)$$

$$\gamma = \lambda/B \quad (3)$$

$$\lambda = \sqrt{\frac{f_H^2 + f_H . f_K + f_K^2}{3}} \cdot \exp\left[-\frac{1}{N.m_{AM}^2} \right] \quad (4)$$

We should be optimizing CATV system by following primary data:

f_H = 47 MHz; f_K = 470 MHz; F = 0,69mA;

RIN = -150dB/Hz; $i_n = 24.10^{-12}$ A/$\sqrt{Hz}$.

1. First case P_e = func (CNR, M):

$$P_e = 1{,}002 .((1 - 1/\sqrt[5]{M}) . \exp(-1{,}5 . 10^{0,1CNR} /(M-1)) /\log_2 M)) \quad (5)$$

where B = 10 MHz is channel bandwidth;
N = 42 - number of channels (AM/VSB);
m_{AM} = 5% is modulation index of AM/VSB signals;
M = 16 to 256;
CNR = 30 to 50 dB.

In fig.2 is given a graphic of the dependence $P_e = func(CNR, M)$ in the three-dimensional space.

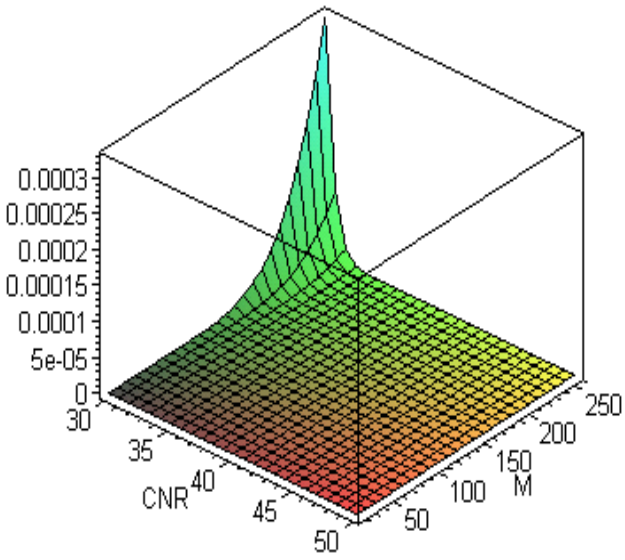

Fig.2. P_e = func (CNR, M)

2. Second case P_e = func (CNR, N):

$$P_e = 0{,}1875.\exp(-0{,}1.10^{0{,}1CNR}).\exp(28{,}6.\exp(-400/N)) \quad (6)$$

In fig.3 is given a graphic of the dependence $P_e = func(CNR, N)$ in the three-dimensional space for the following values of:

B =10 MHz; m_{AM} = 5%; M = 16; N = 1 to 50;
CNR = 21 to 30 dB.

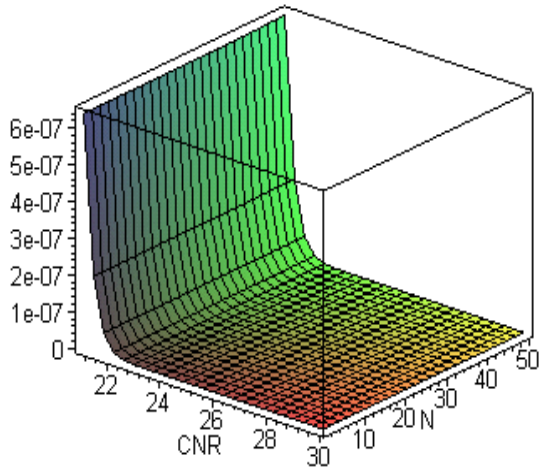

Fig.3. P_e = func (CNR, N)

3. Third case P_e = func (CNR, m_{AM}):

$$P_e = 0{,}1875.\exp(-0{,}1.10^{0{,}1CNR} + 28{,}6.\exp(-0{,}0238/m_{AM}^2)) \quad (7)$$

In fig.4 is given a graphic of the dependence $P_e = func(CNR, m_{AM})$ in the three-dimensional space for the following values of:

B =10 MHz; M = 16; N = 42; CNR = 21 to 30 dB; m_{AM} = 1 to 10%.

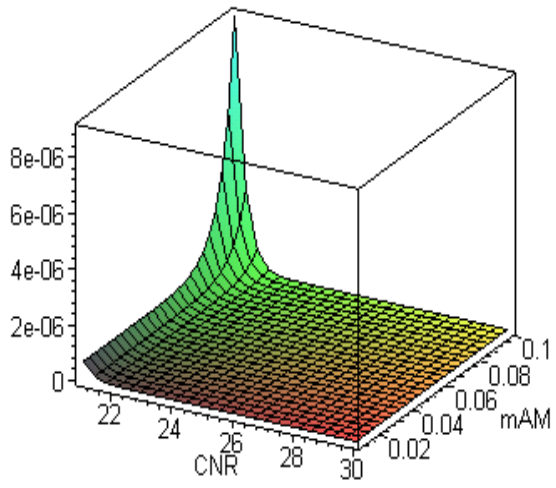

Fig.4. P_e = func (CNR, m_{AM})

4. Fourth case P_e = func (CNR, B):

$$P_e = 0{,}1875.\exp(-0{,}1.10^{0{,}1CNR}).\exp(20903{,}938/B) \quad (8)$$

In fig.5 is given a graphic of the dependence $P_e = func(CNR, B)$ in the three-dimensional space for the following values of:

M = 16; N = 42; m_{AM} = 5%; CNR = 21 to 30 dB; B = 5 to 12 MHz.

The calculation of P_e and the drawing of the graphics is done by the program product MAPLE.

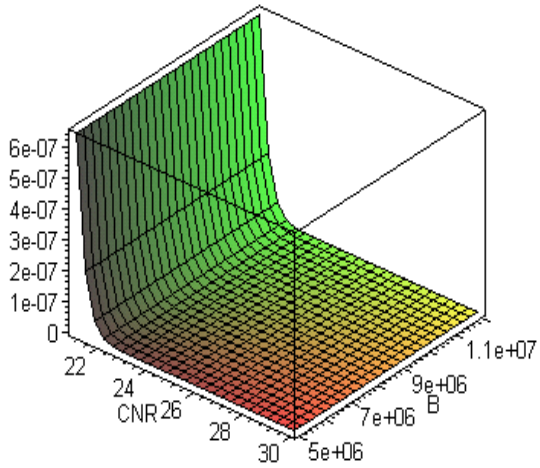

Fig.5. P_e = func (CNR, B)

IV. CONCLUSION

We have presented results of investigation of M-ary QAM (BER) performances in a HFC/CATV system. The results show that the BER performance of the M-QAM signals in such environments can be significantly degraded in the presence of the clipping noise distortion generated by occasional laser clipping of the AM signals. By modeling the clipping noise as a Weibull distributions, we have obtained the asymptotic distribution of the clipping noise plus the additive Gaussian noise and evaluated the BER`s of the M - QAM signals, under various clipping conditions (CNR, m_{AM}) and the parameters B, N and M. The results show a significant increase in BER by lower value on CNR and higher values on m_{AM} and M. The results also show, that BER independed from B and N for high values on CNR.

REFERENCES

[1] Wtm.wemif.pwr.wroc.pl
[2] S.S. Sheu M.H. Chen, "A network architecture with intelligent node (IN) to enhance IEEE 802.14 HFC Networks", IEEE Transactions on broadcasting, VOL.45, NO.3, Sept. 1999
[3] www.telecom.fpms.ac.be
[4] V.Germanov, "The impact of CSO/CTB Distortion on BER Characteristics by Hybrid Multichannel Analog/QAM Transmission Systems", IEEE Tr. on Broadcasting, VOL.45, NO.1, Mart 1999
[5] K. Maeda., K. Utsumi, "Bit-error rate of M-QAM Signal and Its Analysis Model For Composite Distortions in AM/QAM Hybrid Transmission", IEEE Tr. on comm., vol. 47, No. 8, Aug. 1999, pp. 1173 – 1180.
[6] O. Panagiev "Composite distortions in the hybrid fiber coaxial networks" BTEBIZ' 2002, 15-18 Sept. 2002, Albena, Bulgaria.

Measuring Cable System Distortions

Oleg Borisov Panagiev[1]

Abstract **- The aim of this measurement is to exactly measure the video carrier level, and then just as exactly measure the average power of the distortion products in the video bandwidth. The difficult part of the measurement is precisely determining the level of the distortion products in the presence of noise and video modulation. The most exact method for measuring distortion requires the removal of the video modulation for CSO and the removal of the video carrier for CTB.**

Keywords **– CSO (composite second order), CTB (composite triple beet), CATV, nonlinear products**.

I. INTRODUCTION

Each Cable television (CATV) system contains active devices: amplifiers, modulators, converters and etc. Under certain conditions [1], one or more devices go in nonlinear mode. Consequently in output subscriber`s outlets has been appear nonlinear products, which worse picture quality. The knowing and measuring these nonlinear products is important step to limitation and decrease to them.

When a distortion product is due to components of different order, and/or different order products occur within the bandwidth of the device used to measure the level of distortion products, then the measured level will not follow a standard level variation [2].

In principle, an infinite number of terms are necessary for a complete description of a non-linear characteristic. However, considering the standard level variation of terms of different order, the relative contribution of higher order terms increases with the level of input signals. Conversely, if signal levels are low enough, only a few of the lowest order terms will produce significant contributions at the output.

If all input signals are limited to a frequency band of less than one octave, the frequencies of all second order terms will fall outside the band limits. Signal frequencies can also be allocated in two or more non-contiguous bands in a manner that will place all second order products outside the bands.

Third order distortion products, in particular some of the products that occur at frequencies represented by $\omega_1 \pm \omega_2 \pm \omega_3$ cannot be kept out of the band that contains the input signals. The accumulation of third order distortion products may therefore be a limiting factor in the performance of a wideband multi-channel distribution system.

The video carrier must be at least 60 dB above any interfering signals, except in a system with harmonically related carriers (HRC). In an HRC system, the video carrier must be at least 56 dB above the distortion product that falls at the video carrier frequency (CTB). This higher level of distortion is allowed because the synchronous nature of the CTB in an HRC system is less objectionable to the viewer than the asynchronous beat in a non-HRC system [3], [4].

[1]O. B. Panagiev is a system engineer at the Technical University of Sofia, e-mail: olcomol@yahoo.com

II. SYSTEM PERFORMANCES

The system and equipment requirements are matched to each other in such a way that the minimum requirements for signal quality at the subscriber's outlet can be met with a minimum of technical effort. In addition, requirements that result from use of both analog and digital signal transmission have also been taken into account. The EN 50083 standards provide the network operator, planner and installer with concrete guidelines for network design and selection of appropriate network components.

When the amplifier is designed for sloped operation, measurements shall be carried out with sloped output.

The tests outlined are applicable to various categories of amplifiers as follows.

1. For wideband amplifiers intended for operation with more than 10 television channels in the range below 862 MHz: composite triple beat, composite second order and composite cross modulation.
   Note: Manufacturers may also publish second order and third order intermodulation performance.
2. For amplifiers intended for operation with less than 10 television channels in the range below 862 MHz, including return path amplifiers below 70 MHz: second order and third order distortion.
   Note: The maximum number of channels shall be clearly stated in the specification.

For all cases on distortions: *second* and *third order, composite triple beat (CTB)* and c*omposite second order (CSO)* shall be published the worst-case value as the output level in dBμV, that gives 60 dB signal to distortion ratio.

Note: For some amplifiers (e.g. feed forward) it may not be possible to measure 60 dB distortions. In these cases, the output level for a greater signal to distortion ratio may be stated.

III. METHOD FOR MEASURING ON CTB AND CSO

A. Composite triple beat (CTB).

The method of measurement of composite triple beat using CW (continuous wave) signals is applicable to the measurement of the ratio of the carrier to composite triple beat at a specified point in a cable network. The method can also be used to determine the composite triple beat intermodulation performance of individual items of equipment.

When the input signals are at regularly spaced intervals (as is common in most allocations for TV channels), the various distortion products tend to cluster in groups, close to the TV

channels. The number of different products in each cluster increases rapidly with the number of channels, and they combine in different ways, depending on the degree of coherence between generating signals, and the relative phases of the different distortion products.

The method described in this sub clause measures the non-linear distortion of a device or system by the composite effect of all the beats clustered within ±15 kHz of the video carrier of a TV channel. During the measurement, the video carrier of that channel shall be turned off, so that the composite triple beat measured is that generated by all the carriers except that of the measured channel.

B. Composite second order (CSO)

Practically everything called for CTB have a bearing on CSO except that the second order beats are not clustered (±15 kHz) about the exact carrier frequencies but may be clustered (±10 kHz) at ±0,75 MHz or ±0,25 MHz from them. The carrier/composite second order distortion ratio can be read directly off the screen of the spectrum analyzer.

For composite second order it is also necessary to measure the beats close to the channel at 48,25 MHz or, where this is not possible with the equipment under test, at the lowest frequency available. Although it is not essential to have the carrier present at this frequency, it may be useful for reference purposes. In this case, the second order beats are clustered around 48,00 MHz ±10 kHz and so again may be read directly off the screen of the spectrum analyzer.

The worst case maximum output level giving the required signal to composite second order distortion ratio shall be noted for publication.

C. Measurement procedure

The measurement procedure comprises the following steps:

1. Connect point A directly to point B and disconnect the band pass (BP) filter (see Fig.1). Adjust the level of each generator for an output level at point A equal to that, which will be present when the system or device under test (DUT) is connected.
2. Adjust the spectrum analyzer as follows:
   - IF bandwidth 30 kHz
   - Video bandwidth 10 Hz
   - Scan width 5 kHz/div
   - Vertical scale 10 dB/div
   - Scan time 0,2 s/div.
3. Tune the spectrum analyzer so that the video carrier of the channel in which the measurement is to be made is centered on the display screen.
4. Adjust the sensitivity of the spectrum analyzer together with its internal and external input attenuator (75Ω/step 1 dB) in such a way that the response to the video carrier corresponds to a full-scale reference.

   At the same time the noise level shall be at least 10dB lower than the distortion level expected.
5. Insert the band pass filter corresponding to the channel to be measured and adjust the input attenuator to correct for the attenuation of the filter.
6. Disconnect the generator for the channel to be measured and terminate the combiner with its nominal impedance.
7. Verify that the intermodulation products generated in the spectrum analyzer over the entire channel are at least 20 dB below the distortion ratio required. If this is not the case, disconnect the band pass filter and repeat the steps 4 to 7 of this procedure with decreased sensitivity of the spectrum analyzer.
8. Note the setting of the sensitivity control.
9. Connect the signal generator again and repeat steps 3 to 8 of this procedure for all channels.
10. Connect the device to be tested between points A and B and reset the signal generators (SG) to obtain the required output levels at point B.
11. Adjust the center frequency of the spectrum analyzer as in step 3 and insert the appropriate band pass filter.
12. Adjust the input attenuator (internal or external) to return the response of the spectrum analyzer to the video carrier to full scale with the appropriate setting of its sensitivity control (see step 8).
13. Disconnect the generator for the channel to be measured and terminate the combiner with its nominal impedance.
14. The composite triple beats are clustered within ±15 kHz of the video carrier, so the signal/composite triple beat ratio can be read directly off the screen of the spectrum analyzer.
15. Adjust the attenuator Al of Fig. 1 to obtain the required signal/composite triple beat ratio and compensate for the change in output level by using attenuator A2.
16. Measure the signal level at the output of the device under test.
17. Repeat the steps 11 to 16 of this procedure for every channel used in this test.
18. The worst case maximum output level giving the required signal to composite triple beat ratio shall be noted for publication.

IV. EXPERIMENTAL SETUP

Fig.2 shows the experimental setup, where SGi have been replacing with signals from Head end's up-converters. DUT is CATV system on Technical University of Sofia. Channel number is 47. First channel is 49,75 MHz and last channel is 495,25 MHz.

Spectrum analyzer is PROMAX AE-476.

TABLE I presents experimental results for CTB and CSO by carrier frequencies from channel allocation on CATV system.

Fig.3, Fig. 4 and Fig.5 present the results from measurements of signals for channel 12 (223.25 MHz, standard D/K) and put him non-linear distortions.

TABLE I

Frequency MHz	CTB dB	CSO dB
49.75	61	64
119.25	62	62
175.25	61	61
191.25	62	62
207.25	62	62
223.25	63	63
231.25	61	66
247.25	61	63
263.25	62	63
287.25	62	64
311.25	61	63
327.25	61	61
343.25	60	61
359.25	60	61
375.25	61	63
391.25	62	63
407.25	62	63
479.25	61	62
495.25	62	61

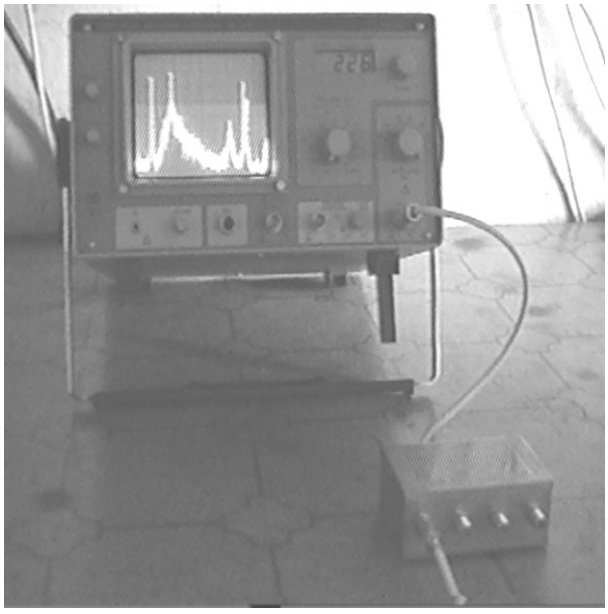

Fig.2. Measurement setup with a screen image of signals channel 12 (223.25 MHz, standard D/K)

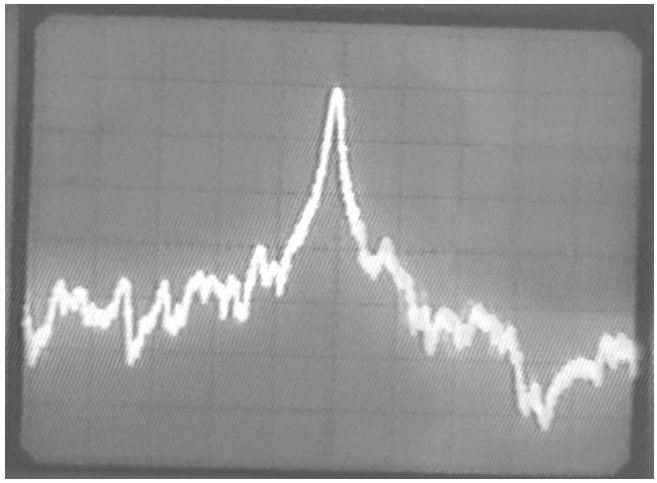

Fig.3.AM video signal (channel 12,D/K) with put non-linear products. Span 1 MHz, input level 80 dBμV, step 10 dB/div

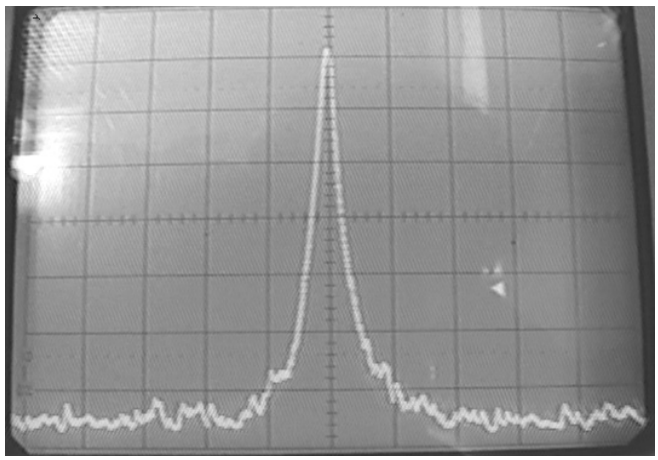

Fig.4. Videocarrier (223.25 MHz, D/K) with CSO and noise. AM absent

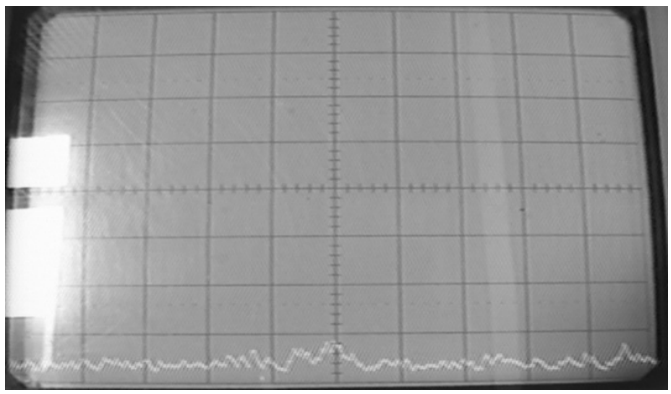

Fig.5. CTB and noise (channel 12,D/K). Videocarrier absent

V. CONCLUSION

The method is used to support a specification of the following general format:

The composite triple beat ratio for groups of carriers in channel (A) at (B) dBμV is (C) dB, where

(A) Designates the channel in which the test is made. If omitted, the specification is understood to be a minimum specification for measurements at all the channels specified by the list of carriers.

(B) Is the reference level at which all the carriers should be set during the measurement, unless otherwise specified. If all the carriers are not at the same level, the specification should clearly indicate the level of each carrier relative to the reference level.

(C) Is the composite triple beat ratio, usually given as a minimum specification.

Because of the large variety of frequency plans in use throughout Europe and the need to compare readily performance specifications of different manufacturer's equipment, the measurement shall be made with the carriers listed in Annex C, [2]. The carriers are all in an 8 MHz raster.

The video carrier frequencies are arranged in groups and only complete groups shall be used, except as stated below:

- Group A for amplifiers specified up to 450 MHz.
- Groups A and B shall be used if specified up to 550 MHz.
- Groups A, B, C, D and E shall be used if specified up to 862 MHz.

Group A also can be used in part, dependent on the specified bandwidth of the equipment under test. The frequencies deleted shall be stated. For all pass bands, the performance shall be quoted for the maximum possible number of complete groups. The manufacturer may, in addition, provide a performance figure for a larger number of carriers. The frequencies deleted shall be stated.

REFERENCES

[1] O.B Panagiev, "Nonlinear products, spring up active devices by transferring of modulated video signals", Proc.of Intern. Scient. Confer. EIST' 2001, vol.II, Bitola, June 7-8, 2001

[2] European standard "EN 50083-3", aug.1998.

[3] http://www.gemini-inc.com

[4] Catalog "Hirschmann" , 2003.

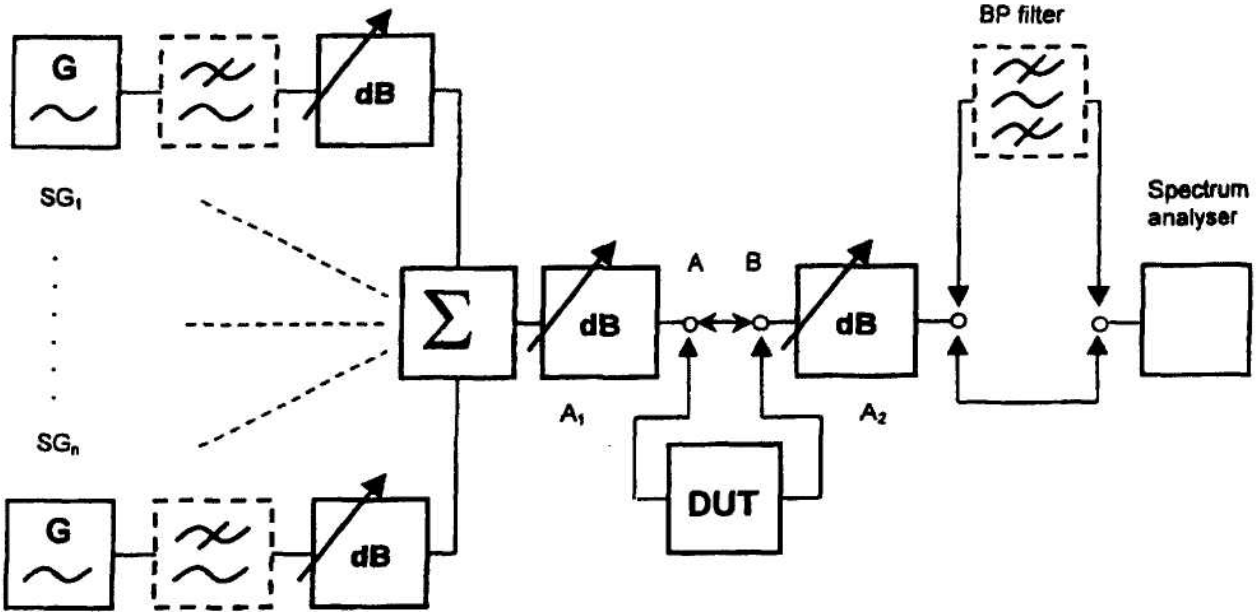

Fig.1. Connection of test equipment for the measurement of non-linear distortion by composite beat

Improving the Quality of Analog TV Signals in Cable TV Networks through Optimization of the Number and Parameters of Amplifiers in the Network

Stanimir Sadinov[1], Kiril Koitchev[2], Krasen Angelov[3]

Abstract – **We study a transmission line by performing experiments varying the signal/noise ratio (S/N), non-linear distortions (CSO, CTB), amplification coefficient (K_U) and the number of transmitted TV channels.**
We exhibit graphical relationships, which allow easy determination of the required number of amplifiers in order to compensate for transmission line losses, given the signal/noise ratio. We optimise a structure with the smallest amplification coefficient, maximum signal level at the output that results in high signal quality.

Keywords – **Signal/noise (S/N), non-linear distortions (CSO, CTB), amplification coefficient (K_U)**

I. INTRODUCTION

Each CATV is designed to supply its subscribers with quality signal. Application reveals that there are a number of difficulties encountered in the translation of many channels. The passing of a signal along the whole line, through active and passive elements, causes its modification. Distortions, degrading and noises appear whose norms are given in detail in the standards [2, 3].

Basically, they are divided into linear and nonlinear [1, 2]. Nonlinear include the irregularity of group delay time (channel distortions) and the amplitude frequency response of the individual channel and as a whole [4, 6].

II. NONLINEAR DISTORTIONS ANALYSIS

Nonlinear distortions re caused by active devices (amplifiers). In practice we have multifrequency impact at their input – these are the carriers of the individual channels – ω_1, ω_2,… ω_n [1, 2]. CATV amplifier can be regarded as an active four pole piece whose input signal is "*x*" and the output signal is "*y*".

[1]Ass. Stanimir M. Sadinov is with the Department of Communications Technology and Equipment, Technical University of Gabrovo, Bulgaria, 5300 Gabrovo, str."Hadji Dimitar" № 4 Bulgaria, E-mail: murry@tugab.bg

[2]Assoc. Prof. Ph.D. Kiril R. Koitchev is with the Department of Communications Technology and Equipment, Technical University of Gabrovo, Bulgaria, 5300 Gabrovo, str."Hadji Dimitar" № 4 Bulgaria, E-mail: koitchev@tugab.bg

[3]Mag. Eng. Krasen K. Angelov is with the Department of Communications Technology and Equipment, Technical University of Gabrovo, Bulgaria, 5300 Gabrovo, str."Hadji Dimitar" № 4 Bulgaria, E-mail: kkangelov@mail.bg

By approximating by power order of Taylor's function we get $y = f(x)$, where f stands for the translation characteristic at point

$$y = f(x_0) + \sum_{n-1}^{\infty} f^{(n)}(x_0).(x - x_0)^n \quad . \tag{1}$$

Where $f^{(n)}(x_0)$ is the derivative of translational characteristic at operating point x_0.

If we are confined to two signals

$$x = x_0 + a_1 \cos \omega_1 t + a_2 \cos \omega_2 t \quad . \tag{2}$$

Actually only the distortion products of the first two orders are evaluated: IMA2 (second order) and IMA3 (third order – Inter Modulation Amplitude).

2.1. Inter Modulation products analysis

One of the consequences of the linear irregularity is the decrease of the amplification coefficient when the level of the input signal is boosted (Fig. 1).

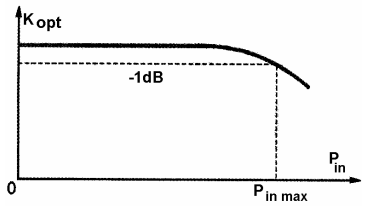

Fig. 1

In fact, if an input signal $x = \alpha_1 \cos \omega_1 t$; output signal $y = f'\alpha_1 + \frac{1}{8} f'''\alpha_1^2$ and the coefficient of amplification is $f' + \frac{1}{8} f'''\alpha_1^2$. Accordingly, by entering amplification coefficient of relatively weak signal function f', equal to $1 + \frac{1}{8}\frac{f'''}{f'}\alpha_1^2$ then it will increase in proportion to the square value of the input signal amplitude ($f' > 0$, $f''' < 0$).

As much as the output power in the reference frequency of the second and third harmonic increments with the increase of the input power, the dependencies $P_{out}=f(P_{in\omega 1})$ intersect at some values of input power P_{ip} (Fig. 2). The values of these intersection points allow finding the levels of the harmonic at the amplifier input with a certain level of input signal. The ratio which combines output power with basic power ($P_{1\omega 1}$), the double frequency ($P_{2\omega 1}$) and the output power of the third order with the output power in the basic frequency at the point of intersection P_{ip} (Intercept Point), is of two kinds:

$$P_{2\omega 1} = 2P_{1\omega 1} - P_{ip}\,(dBm);$$
$$P_{3\omega 1} = 3P_{1\omega 1} - 2P_{1}. \qquad (3)$$

Thus, on the ground of the discussed subject (3) it is possible to draw the following conclusion: when boosting (decreasing) the output level of the amplifier signal ΔdB the intermodulation components of second order (IMA2) will rise (decrease) also to ΔdB whereas the intermodulation components of the third order (IMA3) will rise (decrease) to $2\Delta dB$.

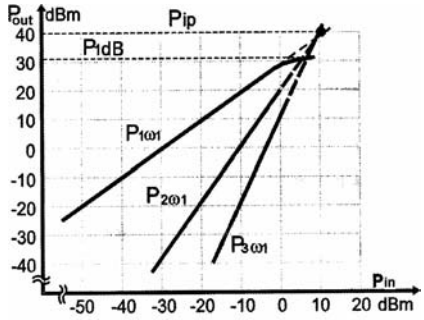

Fig. 2

2.2.Calculation of nonlinear distortions

To determine the maximum level of the output signal during translation of a large number of channels according to [5, 7] the usual procedure is to estimate intermodulation components by the composite beat of second CSO (Composite Second Order) and third CTB (Composite Triple Beat). In addition, it is known that for amplifiers having upper frequency of *606MHz* test trials are conducted with *29* channels whereas for amplifiers with upper frequency *862MHz* the number of channels is *42*. Estimations of CSO and CTB are carried out along the worst performing channel with predetermined frequency disposition of the channel.

Calculation of maximum output level of the amplifier U_{maxN} (*CTB = 60dB*) for distortions of the third order during translation of *N* number of channels is done by the formula:

$$U_{\max N3} = U_{\max 3} - 10\lg(N/2). \qquad (4)$$

Formula (4) shows that with the increase in the number of channels we get the maximum level of the output channel U_{maxN3} drop to (see Table 1) the value of $\Delta U_{1(3)}$. By virtue of this when studying the instruction manuals of the selected type of amplifier special note should be taken concerning the assigned values U_{max3}(*IMA = -60dB, 2* channels) and U_{maxN3} (*CTB = -60dB, 42* channels). The difference between them should be about *13 ÷ 14 dB*. If that difference is higher or less than the assigned value, check carefully the parameters in the manuals.

A similar dependence can be derived for a product of the second order (*CSO = -60dB*) by the empirical expression:

$$U_{\max N2} = U_{\max 2} - (3{,}5...4{,}3)\lg(N/2) \qquad .(5)$$

Table 1 contains the results from calculations concerning the decrease of the maximum output level U_{max2} (for average cases) with increased number of translated channels (*CSO = -60dB*). When conducting real calculations with a large number of channels (*N* >20) it is preferable to use values close to that recommended by the manuals U_{maxN2} and U_{maxN3} (i.e, according to criterion *CSO = 60dB* and CTB=60*dB*).

$$U_{\max N2} = U_{\max SCO} + (3{,}5...4{,}3)\lg(42/N) \qquad (6)$$

TABLE1

N	$DU_{1(3)}$, *dB*	$DU_{1(2)}$, *dB*
1	+3,0	+1,1
2	0	0
4	-3,0	-1,1
6	-4,8	-1,8
8	-6,0	-2,3
10	-7,0	-2,7
20	-10,0	-3,8
40	-13,0	-4,9
60	-14,8	-5,6
80	-16,0	-6,1

$$U_{\max N3} = U_{\max CTB} + 10\lg(42/N). \qquad (7)$$

Example 1. Determination of maximum output level of amplifier GPV 841 U_{maxN3} for *29* channels with reference value U_{maxCTB} = *108dBμV* (*42* channels, *CTB = 60dB*).

Solution: By using formula (7) we get:

$$U_{\max N3} = 108 + 10\lg(42/29) = 109dB\mu V$$

which is similar to the reference value *110dBμV*.

Distortions with random output level of the amplifier. By way of analogy with distortions IMA2 and IMA3 with the increase (decrease) of output level of the amplifier signal *DdB*, the intermodulation components of the second order (CSO) are boosted (drop down) to same *DdB* whereas intermodulation components of third order IMA3 are boosted to *2DdB*, i.e.:

$$CSO = 60 + (U_{\max CSO} - U_{out}),$$
$$CTB = 60 + 2(U_{\max CTB} - U_{out}). \qquad (8,9)$$

Example 2. Determination of values and CTB when GHV 835 (Hirschmann) amplifier is used with reference parameters U_{maxCSO} = *104dBμV* and U_{maxCTB} = *102dBμV* (*42* channels, *CTB = CSO = 60dB*) at U_{out} = *95dBμV*.

Solution: By using formulae (8) and (9) we get:

$CSO = 60 + (104 - 95) = 69dB,$

$CTB = 60 + 2(102 - 95) = 74dB.$

General case. In this way by using formulae (6 ÷ 9) we get experessions for calculation of CTB including a random number of channels and random output operating level:

$$CSO = 60 + (U_{\max CSO} - U_{out}) + 4{,}3\lg(42/N), \qquad (10)$$
$$CTB = 60 + 2[U_{\max CTB} - U_{out} + 10\lg(42/N)]. \qquad (11)$$

Example 3. We find the values for CSO and CTB for amplifier YCM-800-2737 (Standard telecom) of U_{maxCTB} = 114*dBμV* and U_{maxCSO} = 110*dBμV* (*42* channels *CTB = CSO = 60dB* and balance between channels of *9dB*) for translation of *50* channels at U_{out} = *105dBμV*.

Solution: By altering the numeric values in (10) and (11) we get:

$$CSO = 60 + 110 - 105 + 4{,}3\lg(42/50) = 64{,}7dB,$$

$$CTB = 60 + 2[114 - 105 + 10\lg(42/50)] = 77{,}8dB.$$

Accumulation of distortions along the lines is effected by formulae:

$$CSO_{\Sigma} = -10\lg(10^{-CSO1/10} + 10^{-CSO2/10} + ... + 10^{-CSOi/10}), \quad (12)$$

$$CTB_{\Sigma} = -10\lg(10^{-CTB1/20} + 10^{-CTB2/20} + ... + 10^{-CTBi/20}), \quad (13)$$

Formulae (12) and (13) indicate that distortions of third order (CTB) are generated quite easily as compared to distortions of the second order (CSO). For *n* amplifiers switched on in cascade with equal values of CTB and CSO the total number of distortions is determined by the formula

$$CSO_{\Sigma} = CSO10\lg n, \quad (14)$$

$$CTB_{\Sigma} = CTB - 20\lg n. \quad (15)$$

Thus for *5* amplifiers in a series (example 3) CSO_{Σ} = *57,7dB* (decrease to *7dB*) and CTB_{Σ} = *63,8dB* (decrease to *14dB*).

Lets consider another example.

Example 4. We find the extreme values CTB_{Σ} and CSO_{Σ} provided that the inherent values of CSO and CTB are known at the output of each active device. Main station *CSO = 72dB, CTB = 84dB* optic system: *CSO = CTB = 65dB*; highway amplifiers: *CSO = 74dB, CTB = 82dB*; subscriber amplifiers: *CSO = 72dB, CTB = 66dB*

Solution: By substituting numeric values in (12) and (13) we get:

$$CSO_{\Sigma} = 62{,}5dB,\ CTB_{\Sigma} = 57{,}3dB.$$

Example 5. How many amplifiers of one type can be switched on in a series if their individual CTB_i = *84dB* (conducted system calculation) with CTB_{out} = *-57dB*. Total CTB of all other devices is CTB_{Σ} = *64dB.*

Solution: We calculate the permissible value of distortion *ΔCTB* entering the highway amplifiers from (11):

$$\Delta CTB = -20\lg(10^{-CTB_{ucx}/20} - 10^{-CTB_{\Sigma}/20}) = \\ = -20\lg(10^{-57/20} - 10^{-64/20}) = 62{,}1dB.$$

This means that such CTB are permissible for all highways for storing of final CTB_{out} = *57dB*

2. We find the maximum number of highway amplifiers (15):

$$n \le 10^{(CTB_i - \Delta CTB)/20} = 10^{(84-62{,}1)/20} = 12{,}4,$$

i.e., we found 12 equal amplifiers each of which has *CTB=84dB.* This guarantee final CTB_{out} > *57dB*. For requirement (*CTB* > *57dB*). Up to 21 amplifiers can be switched on at any equal terms.

Measuring CTB and CSO by [3] are different in the methods they employ, however, all sets of methods boil down to the following:

1. *At the amplifier input or the main station we enter* N_{test}. *unmodulated carrying signal whilst at the output of the tested object we switch on a spectrum analyzer*

2. *The spectrum analyzer helps fix the levels of useful signal in the tested channel.*

3. *The spectrum analyzed is set to a maximum sensitivity mode. Combination components are observed, video carriers (by rule they are divided by frequencies which withstand from the carrier by 0, 0.25 and 0,5 MHz) and then their levels are fixed The difference in levels is expressed in dB and make up the CSOs and CTBs*

III. Optimization of Amplifier Output Level

By analyzing the above formulae we draw the following conclusion: the lower the output level of the amplifier the lesser its nonlinear distortion. From this follows that it is enough to transmit TV signals at lower input/output levels to solve the problems. In fact it is just the opposite. Apart from the observed nonlinear distortions ther is the requirement which states that the signal to noise (S/N) ratio should not be lower than 44dB [3]. S/N at the output depends on the noise parameters of the source itself, the noise parameters of the main station, the optic system, amplifiers, operational modes and their values.

This dynamic range is a convenient value for conducting system calculations and shows the magnitude of S/N ratio, which is generated at the amplifier output when "ideal" "quiet" signal is entered at its input. [5]

$$S/N_{[dB]} = U_{out[dB\mu V]} - K_{[dB]} - F_{[dB]} - 2{,}4 \quad (16)$$

It is evident that U_{out} *-K* indicates the level of input signal that is entered directly through the first amplifier (no account is taken for the losses of the input device – attenuator and equalizer). From (16) it is evident that the larger the amplifying coefficient the lower its *S/N* ratio. We discussed the means of selecting proper amplifier in [4]. Here will note that for most highways which employ *7 ÷ 10* amplifiers, when it is necessary to keep maximum possible output *S/N* ratio amplifiers with smaller amplifying coefficients should be selected. This, however, is very expensive due to the large number of amplifiers switched in series.

Noise accumulation along highways. When amplifiers are connected in series with individual S/N_i ratios, the sum total of output S/N_{Σ} ratio will be :

$$S/N_{\Sigma} = -10\lg(10^{-(S/N_1)/10} + 10^{-(S/N_2)/10} + ... + 10^{-(S/N_n)/10}). \quad (17)$$

In this way it is possible to calculate for a cable TV if at its antenna system *S/N = 54dB* at the main station : *S/N = 54dB* at the optic line *S/N = 52,2dB* for the three highway amplifiers *S/N = 58,6dB* then the output S/N_{Σ} = *45,5dB*

From (17) it follows that if the highway contains *n* number of switched on devices with similar mode of operation then S/N_{Σ} will be determined by:

$$S/N_{\Sigma} = S/N - 10\lg(n) \quad (18)$$

So when two similar highway amplifiers are on then the output S/N_a will drop with 3*dB.*

Subscribers amplifiers should be able to ensure the required level of the signal. In reality it turns out that subscribers' amplifiers are the cause for the maximum number of distortions CSO and CTB, To ensure less nonlinear products it is necessary to keep lower signal levels = *92÷100dBμV*. The number of channels should also be taken into account as well

as the dynamic range of the amplifier plus the number of amplifiers, which are connected in series. Fig. 3 shows the dependence of permissible levels of output signal on the number of amplifiers which are connected in series.

Graphics are draw by formulae (15,18). *CTB= 60÷70 dBμV* is selected as criterion whereas the preventive interval *S/N=46dB*. From the analyzed result it is evident that the output level is within the range *91÷102dBμV* (for *CTB=70dB*) or *91÷107dBμV* (for *CTB=60dB*). For the lowest point at *91dB, S/N≥46dB* and peak value *102dBμV* (*CTB≥70dB*) by taking into account the reserve we get: *S/N=46+11+57 dB.*

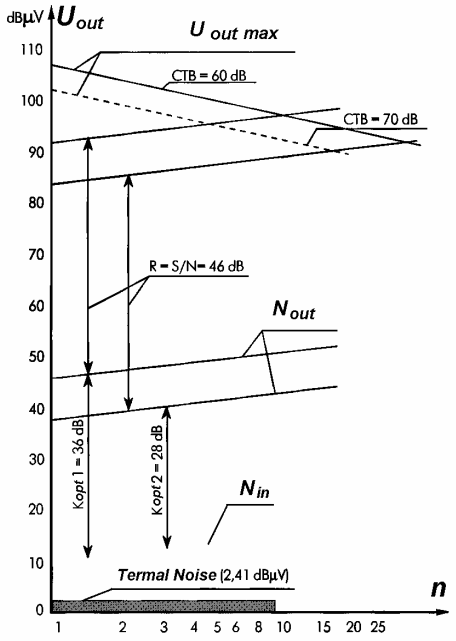

Fig. 3

In cases of increased number of amplifiers it is evident that the difference between permissible levels is being reduced due to the fact that a lot of noises and distortions have been accumulated. For example, amplifiers of the type GPV 839, having coefficient of amplification 36 dB, is possible it be connected up it 10 units in series (*CTB = 60dB*) thus we can recover line losses to approximately 360*dB*. If the amplification coefficient is reduced to 28 then the maximum number of amplifiers connected in series grow to *25dB* which is equivalent of line losses recovery of approximately 700*dB* (Fig. 4).

With *CTB*=70*dB* we observe an opposite trend since the maximum number of amplifiers is only 5 (with k_0=36*dB*). These graphic result are indicative of the importance of parameters such as maximum output level of the signal and amplification coefficient.

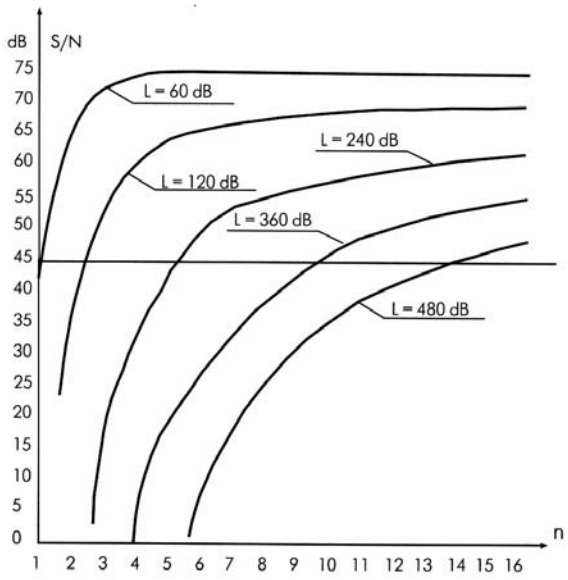

Fig. 4

IV. CONCLUSION

The optimum level is that output level, which allows for technological reserves (for example, climate conditions when effecting overhead laying of cables) as well as of intermodulational distortions *CTB* and *CSO*. Another important factor is the proper *S/N* ratio when designing and laying CATV networks. Then optimum operating output level for amplifiers could be found by the formula:

$$U_{outopt} = \frac{U_{max} + 2U_{min}}{3} \quad , \tag{19}$$

where U_{max} is the maximum permissible value of the amplifier output level provided *CTB* and *CSO* were carefully considered while designing the network. U_{min} is the minimum permissible value at the amplifier output, which is effected if the *S/N* ratio is protective. Thus for our example we get $U_{out\ opt}$= 95 *dBμV*

REFERENCES

[1] Koitchev K., Sadinov St. Maximum Value Determination of Non-linear Products in Cable Television Networks. IEEE Transactions on Broadcasting, March 2003.

[2] Песков С. Н. Рабочий вьиходной уровень усилителей в широкополосьих телевизионньих сетях. “Телеспутник”, 2004г., №2

[3] European Standart CENELEC EN 50083. Cabled distribution systems for television, sound and interactive, December 2002.

[4] Sadinov St.,Koitchev K. About a Possible Way of Optimizing the Number of Amplifiers in CATVs. XXXIX International Scientific Conference Information, Communication and Energy Systems and Technologies – ICEST 2004.

[5] Койчев К., Садинов Ст. Проектиране на кабелни телевизионни мрежи. AMI, Габрово, 2001.

[6] Ciciora W., J. Farmer, D. Large. Modern cable television technology. San Francisco, MK Publishers, Inc., 1999.

[7] S. Ovadia, “Broadband Cable TV Access Networks: From Technologies to Applications”, Prentice Hall, Inc., 2001.

Power Utility Companies as Telecommunication Service Operators

Igor Vujicic[1], Natasa Gospic[2]

Abstract – **After structural reform of Electricity sector in Bosnia and Herzegovina, electricity distribution companies consider possibilities to enter liberalized telecommunication market as alternative telecom operators using some of available models for provisioning telecom services. The paper presents use of Broadband Power Line (BPL) technology as a model for delivering broadband services to the End-users**.

Keywords – **electricity companies, alternative telecom operators, BPL models, Access network, In-Home network**

I. INTRODUCTION

Deregulation and liberalization of Electricity sector will causes entrance new players in the electricity supply segment of market. The onset of growing competition in the supply segment will drive electricity distribution companies to investigate and develop strategies that will differentiate their service and be able to provide competitive advantage in the marketplace. One strategy is entering the telecommunication market.

Electricity sector in Bosnia and Herzegovina is faced with ongoing structural reform. Separation of Transmission Company from other parts of system is main step. Power Generating Companies will form one holding, and Power Distribution Companies will remain as independent market entities. Following the examples from countries, which already finished such reforms, electricity companies in Bosnia and Herzegovina exploring their own capabilities for providing telecom services on liberalized telecom market.

In Bosnia and Herzegovina the electrical power distribution grid is divided into three sections with high (HV) voltage level refers to 400 kV, 220 kV and 110 kV, medium (MV) voltage level refers to 35 kV and 10 kV, and low (LV) voltage level refers to 400 V. Three still existing power utilities (EPBiH, EPHZHB and ERS), within the SCADA/EMS Project for Bosnia and Herzegovina, have already implemented and design telecommunication systems for their own needs. The general approach was to design and build a communications system that would satisfy the current and future communications requirements. The network architecture was developed to support a wide range of utility information exchanges as well as integration with regional utility operations and possible interfaces with external markets, users and third party service providers. It is about modern communications systems based on SDH technology with STM-4 and STM-16 multiplexing equipment and realized mostly using OPGW cables. OPGW cables are installed or will be installed during reconstruction for all HV and MV (down to 10 kV).

Depending on the shape and operations of an electricity company, there are various paths that can be taken in order to enter telecommunications market. These paths cover a wide area of telecom services, ranging from basic property leasing land for mast builds, to complex managed services such as the provision of telecommunication data services using IP VPN. Generally, there are three basic models that can be defined for entering telecommunications market:

- Model 1: Fixed networks – unmanaged services *(Rights-of-way; Duct space; Dark fibre; Lit fibre-Wavelength)*
- Model 2: Fixed networks – managed services *(Co-location; Managed transmission; Non-IP and IP wholesale; End-user services)*
- Model 3: Mobile network services *(Leasing: existing land, rooftops, towers; Build towers: new business or partner; Backhaul provision, MVNO-Mobile Virtual Network Operator; Mobile Network Operator)*

There are several options in each model, which may be used by electricity distribution companies, but this paper is focused on the Model 2 for providing telecom services to the end-users.

After the signals is transmitted over fibre network to the 10 kV power network or in some cases to the 10/0,4 kV/kV transformers there is still problem how that signals forward to the users premises. One solution is employing *Broadband Power Line - BPL* technology on MV and LV segments of power network, for delivering broadband services to their customers.

II. BPL OVERVIEW

Broadband over Power Lines (BPL), also known as Power Line Communications (PLC), is a rapidly evolving technology that utilizes electricity power lines as "Local Loop Access Medium", for the high-speed transmission of data services. BPL works by transmitting high frequency data signals through the same power cable network used for carrying electricity power to household users. Simultaneous transmission electricity and data over same power lines is possible due to transmission over different frequencies. Electricity is transmitted at low frequencies (50 Hz), whereas data signals are at range 1,7 to 30 MHz).

The new low-power, unlicensed access BPL systems couple RF energy onto the existing electric power lines and carry high-speed data signals outdoors over the medium voltage line from a point where there is a connection to a telecommunications network. This point of connection may be

[1] Igor Vujicic is with the Elektro-Bijeljina AD, Majevicka 97, 76300 Bijeljina, Bosnia and Herzegovina, E-mail: vigor@rstel.net

[2] Natasa Gospic is with the Faculty of Transport and Traffic Engineering, Vojvode Stepe 305, 11000 Belgrade, Serbia & Montenegro, E-mail: n.gospic@sf.bg.ac.yu

at a power substation or at an intermediate point between substations, depending on the network topology. Within a residential neighborhood, most access implementations employ a coupler or bridge circuit module at the low-voltage transformer to enable the transfer of high-frequency digital signals across the distribution transformer (the low voltage transformer is a poor conduit for high-frequency digital signals, as it is intended to conduct 50 Hz signals). The broadband communication signals are then brought into the home over the exterior service power cable from the coupler/bridge, either directly, or via an access BPL adaptor module.

Some access BPL implementations use the medium voltage lines to bring the BPL signals to neighborhoods and employ a wireless link between a transceiver mounted on the power pole and a companion transceiver located inside the end user's premises to complete the connection. Typically, the medium voltage lines are carried overhead on transmission poles or tower mountings; however, in some locations they are enclosed in underground conduits and only the distribution transformers are mounted above ground on a pad, inside a metal housing.

In addition, BPL systems can be used by electric utilities to manage their electric power networks more efficiently. Utility company application may include AMR (automatic meter reading), voltage/VAR control, SCADA (supervisory control and data acquisition), equipment monitoring, energy management, remote connect / disconnect and power outage notification, along with collecting power usage information to be used to bill customers. BPL is simply data transfer via a combination of the power network within the home or office, the metropolitan power distribution grid, and a means of getting the data signal from the Internet Service Provider – ISP to the "last mile" point of injection on the power line or grid. Most important is that there are no needs to install new wires in the "last mile", and BPL takes advantage of one of the largest networks on earth - the power grid.

III. Defining BPL Models

BPL systems are categorized in two segments. These segments can be considered as two models for application:

- Model 1 – External system (Access BPL)
- Model 2 – Internal system (In-House BPL)

External system (Access BPL)

Access BPL equipment consists of injectors (also known as concentrators), repeaters, and extractors. BPL injectors are connected to the Internet backbone via fiber or T1 lines and interfaced to the MV power lines feeding the BPL service area. MV power lines may be overhead on utility poles or underground in buried conduit. Overhead wiring is attached to utility poles that are typically over 10 meters above the ground. MV distribution circuits running from substation comprises three-phase wiring. One or all three-phase lines (in most cases) branch out from the three-phase lines to serve a number of customers. A grounded neutral conductor is generally located below the phase conductors and runs between distribution transformers that provide Low Voltage (LV) electric power for customer use.

BPL signals may be injected onto MV power lines between two-phase conductors, between a phase conductor and the neutral conductor, or onto a single phase or neutral conductor, depending upon the application being utilized. Extractors provide the interface between the MV power lines carrying BPL signals and the households within the service area. BPL extractors are usually located at each LV distribution transformer feeding a group of homes. Some extractors boost BPL signal strength sufficiently to allow transmission through LV transformers and others relay the BPL signal around the transformers via couplers on the adjoining MV and LV power lines. Other kinds of extractors interface with non-BPL devices (*e.g.*, WiFi) that extend the BPL network to the customers' premises.

For long runs of MV power lines, signal attenuation or distortion through the power line may lead them to employ repeaters to maintain the required BPL signal strength and fidelity (typical distance without a repeater is from 300 to 500 meters). Figure 1 illustrates the basic BPL system, which can be deployed in cell-like fashion over a large area served by existing MV power lines.

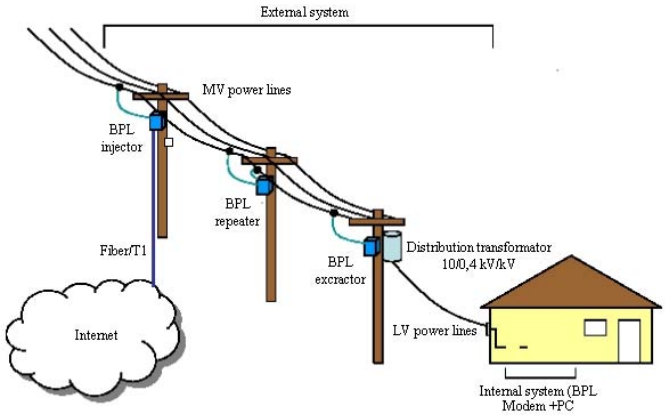

Figure 1. External BPL System

Internal system (In-Home BPL)

In-House BPL utilizes a building's existing electrical wire as a local area network (LAN). By simple plugging a modem into an electrical outlet, a user can communicate with other computers and printers on the same network within the building without any new wiring. Since nearly every room in a house or building has an electrical outlet, this allows for a very extensive and flexible network. Current technologies support speeds up to 14 Mbps, but theoretically should be able to surpass 100Mbps. Cost reductions, particularly in semiconductor chips, has allowed prices for power line modems to become affordable at €50-€70. Figure 2 illustrates internal BPL system (In-Home network), which uses home electrical installations as computer network.

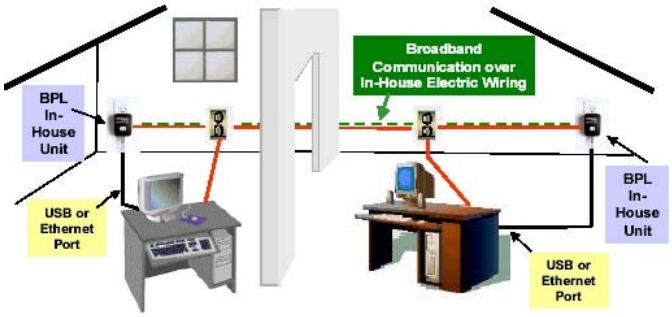

Figure 2. Internal BPL System

IV. ADVANTAGES

One of the major advantages of BPL is that the basic infrastructure is already in place. This allows the power companies to roll out the service faster and reduces the amount of capital expenditures required. Significant is the fact that other broadband technologies currently available on the market, such as fiber optic, Wireless Local Loop, UMTS, xDSL, CaTV, etc., can yield comparable or higher throughput than BPL but generally do not have a fully deployed infrastructure with which they can reach a mass market in such a short timeframe. Penetration of power lines to homes and businesses of potential users is very near 100%. BPL service is a potentially attractive and cost-effective way to reach rural customers that do not have access to cable or DSL. Estimates are €130-€250 (depending on technology) per house/building passed to upgrade power lines and provide BPL access. This allows the service to be offered to the consumer at lower prices than DSL or cables. Preliminary estimates are in the €25-€50 range. This attractive price point could influence customers that already have cable or DSL to switch to BPL and should make the service an easy decision for rural customers. BPL technology has the capability to deliver speeds up to 54Mbps, but current testing delivers reliable signals in the 2 to 5Mbps range. From the government's point of view, BPL increases national security. Wide scale BPL would provide another layer of redundancy for communications systems and allow more careful monitoring of the power grid. Overall the implementation of BPL could offer both consumers and ISPs a third broadband access solution

V. DISADVANTAGES

One of the biggest issues is potential interference with other electronic equipment. Power lines were designed to carry electricity and not data. Therefore, signals transmitted across power lines could leak out and cause interference. Conducted energy can cause harmful interference to radio communications by two methods. The first is radio frequency (RF) energy may be carried through electrical wiring to other devices also connected to the electrical wiring. This poses a problem with In-House BLP. Other devices plugged into the electrical wiring could pick-up interference from the network. Second, at frequencies below 30 MHz, where wavelengths exceed 10 meters, long stretches of electrical wiring can act as an antenna, permitting the RF energy to be radiated over the airwaves.

As a result of low propagation loss at these higher frequencies, the radiated energy can cause interference to other services even at large distances. Solution is in using orthogonal frequency-division multiplexing (OFDM), a technology similar to that used in DSL. This creates a low power signal by spreading the signal over a very wide bandwidth. Using OFDM substantially reduces the chance of producing interference. In addition, most new BPL equipment has the ability to blocking frequencies that may conflict with nearby devices.

VI. BPL POTENTIAL IN BOSNIA AND HERZEGOVINA

Considering BH telecommunications market liberalization level as well as power company's assets for providing services as alternative telecom operators, it could be understand that BH power companies may use options from Model 1 and Model 2 for entering BH telecom market.

BPL technology has unique potential for BH power distribution companies either they leasing bandwidth (end-to-end connections) or they providing broadband services to the end users (Internet services for example). Figure 3 illustrates network architecture for providing such services using combination of optical and BPL technologies. Target consumers are various financial, government, cultural and educational institutions and organizations, which has geographically dispersed subsidiaries all over the country. Figure 3 represents example of linking couple subsidiaries with NOVA BANKA A.D head office.

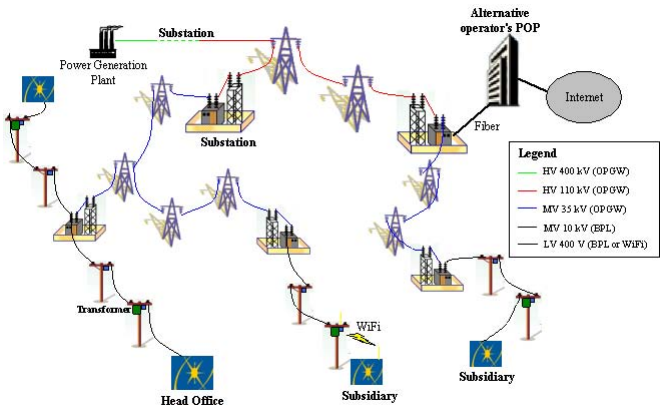

Figure 3. BPL example for NOVA BANKA AD networking

Although, the broadband access is the future for communication services, in the Bosnia and Herzegovina, across all technologies, the penetration is very low. In this case, the total and especially rural market for BPL might not be as large as expected. Power companies, alone or with partners, would potentially have to go after current broadband users to create a profitable business model. One solution might be bundling strategy (one-bill for electricity and telecommunication services), with competitive prices for broadband access.

VII. CONCLUSION

After structural reform of Electricity sector in Bosnia and Herzegovina, electricity distribution companies will get possibilities for entering liberated telecommunication market as alternative telecom operators using some of available models for provisioning telecom services.

Beside the fact that power utilities in BH has already designed and implemented modern telecommunication system based on optical SDH technology, there are still problem of "last mile access" for provisioning services to the end users. To overcome this problem application of the BPL technology over MV and LV segment of power network is recommended.

In order to perform a set of measurements of BPL channel under practical power line noise and impedance loading, and to investigate commercial viability of such appliance a pilot projects are planed and will start in near future, in Bosnia and Herzegovina, within regional electricity company operating in Sarajevo.

REFERENCES

[1] I. Vujicic, N. Gospic, "Broadband Services over Power Lines", Telfor2004 Conference Proceedings, paper 1.10, Belgrade, Serbia & Montenegro, 2004.

[2] H. Akkermans, D. Healey, and H. Ottoson, "The Transmission of Data over Electricity Power Lines", 1998 (http://www.enersearch.se)

[3] C.N. Krishnan, P.V. Ramakrishna, T.V. Prasad, and S. Karthikeyan "Power Line as Access Medium", 3rd International Symposium on Power-line Communications and its Applications, Lancaster, UK, 1999

[4] S. Wilt, "Broadband over Power Lines", NARUC Summer Meetings, Salt Lake City, Utah, 2004.

[5] I. Vujicic, "Models for power companies for entering telecommunication market and Power Utility of Republic of Srpska's capabilities", Master Thesis, Faculty of Transport and Traffic Engineering, University of Belgrade, Serbia & Montenegro, 2004.

A Study of the Effect of Land Relief on the Design of Wireless GSM Coverage

Stanimir Sadinov [1], Kiril Koitchev [2], Krasen Angelov [3]

Abstract – **The paper summarizes the basic steps in the design of a GSM network. We consider a hypothetical design using EDX-SignalPro software. We select an area from the digital map generated by the software. We conduct a study of traffic patterns, demography and the land surface suitability in a given area in order to select the number and location of base stations. The network parameters are entered into the software package, generating a visual results exhibit. We demonstrate the advantages of computer-aided design using software such as EDX-SignalPro, which include greatly reduced cost and time spent on the design process.**

Keywords – **Design, Wireless, GSM network, EDX-SignalPro software**

I. INTRODUCTION

Proper planning of network is essential for obtaining largest possible coverage, appropriate level of service and lowest possible cost. Assume that there is a permission for the make-up of a certain cellular system in a corresponding consumer field. To begin with, it is necessary to determine two elements: the standards and norms in the selected country/area and the current situation on the target market [1, 2].

The aim is to cover the largest cities first, then the busiest highways and border checkpoints. Due to economic considerations it is not expedient to ensure a *100%* of quality coverage.

It is a widespread practice to determine the coverage zones on the basis of *90%* (*10%* are allotted for poor quality communications).

II. STEPS OF EFFECTING NETWORK MAKE - UP

1. Selection of areas to be covered and stages of network construction.

2. Selection of location of components. Selection of points for BTS. A good knowledge of the area map and the available TV towers is of vital importance.

[1]Ass. Stanimir M. Sadinov is with the Department of Communications Technology and Equipment, Technical University of Gabrovo, Bulgaria, 5300 Gabrovo, str."Hadji Dimitar" № 4 Bulgaria, E-mail: murry@tugab.bg

[2]Assoc. Prof. Ph.D. Kiril R. Koitchev is with the Department of Communications Technology and Equipment, Technical University of Gabrovo, Bulgaria, 5300 Gabrovo, str."Hadji Dimitar" № 4 Bulgaria, E-mail: koitchev@tugab.bg

[3]Mag. Eng. Krasen K. Angelov is with the Department of Communications Technology and Equipment, Technical University of Gabrovo, Bulgaria, 5300 Gabrovo, str."Hadji Dimitar" № 4 Bulgaria, E-mail: kkangelov@mail.bg

3. Prognostication of field *E* intensity, i.e. what is the distance that will ensure quality connection (the size of the cell)

4. Evaluation of prospective communications traffic in the area which is covered by one BTS

5. From item 4. we get the number of radio channels required for the proper service within the zone covered by a single cell.

6. Estimation of mutual interferences (what is the extent to which other transmitters interfere with this or other particular frequencies). These also depend on the intensity of the communications traffic. When estimating interferences it should be taken into account that the range of two adjacent cells will overlap to a certain extent – (interference prognostication)

7. Structure of radio channels is made up on the basis of item 6. (what is the distance that will allow for an identical frequency to be repeated). After that *D* is determined (the distance between cells which share channels) and the number of cells in a group.

8. Then comes the channels distribution for all cells and investigation of probable lockings of each cell within the BTS as well as its recovery.

Applicable check up of the lay-out (blueprint) requires a good knowledge of both techniques and conditions for distribution within a certain network. In reality there are always some unserviced zones (recovery measures include: addition of cells, splitting a cell into sectors, use of directed antennae) [1, 2, 3].

2.1. Prognostication of the mean value of field E_{mean}

When prediction is made of *E* field of a certain cell, it should be divided into small enough sectors, which will allow predicting the average square value of signal for each sector.

Now the average square value of E_{mean} at a certain point (sector being determined by averaged values) will depend on the following:

1. Frequency *f*
2. Distance *d.*
3. Height of the antenna over the ground (*H base*)
4. Height of receiver's antenna over the ground
5. Average altitude of the terrain
6. Landscape features and peculiarities of the terrain (sea, land, forest, barriers)

Prediction database for E_{mean}

1.Topographic (average altitudes)

2.Database for specific terrain (through satellite mapping-field, forest, etc.)

a) densely populated city

b) suburban or country area

d) forests and fields- pure forest terrain; mixed terrain – fields and forests(parks), green patches, agricultural areas

e) others: rock, sands, roads, tarmacs, water surface

Since prediction by utilizing theoretic formulae is very difficult to achieve, some other practical models are used instead [1, 4].

2.2. Estimation of probable communications traffic in a certain area covered by one BTS

Network planning basis involves traffic requirements such as the number of subscribers in the network and the amount of traffic they could possibly generate. The unit of traffic intensity is Erlang (*E*). Generated traffic is calculated by the following formula:

$$A=n.T/3600 Erlangs,$$

Where *A* is the traffic generated by one or more subscribers in the system, *n* is the number of calls per hour and *T* is the average duration of a call in seconds.

Geographical distribution of traffic can be calculated by employing specific data such as:

- distribution of population
- distribution of the use of vehicles
- distribution of incomes among the population
- agricultural and other kinds of use of the land
- statistic surveys of the use of telephones
- other factors such as subscription fees and cost of mobile phones [1, 4].

III. PLANNING AND DEVELOPMENT OF MODEL PROJECT BY MEANS OF "EDX-SIGNALPRO" SOFTWARE

"EDX-SignalPro" offers computer modeling of radio networks, pertaining to all known systems, by preassigned digitalized map or by a map generated through the software. In the particular case of study the total area amounts to *36370 km²*. Out of this area is picked a region of *7000 km²* of specific relief which allows simultaneous investigations of the signal in a plain, urban, semimountainous, mountainous and rural regions For the sake of getting a better impression of the relief it would be a good idea to make a 3D image. Colours are selected to correspond to the relief and altitude printed on standard maps. Each image is supplied with a legend, which indicates the boundaries of individual colours and the perimeters they correspond to. In this way we get detailed information for the investigated area. In our particular case forests and mountainous areas occupy *5900,25 km²* (*82,27%*) Areas of arable land are *675,50 km²* (*10,29%*), *292,2 km²* or *4,46%* pertain to residential areas whereas industrial areas are equal to *48,5 km²* (*0,74%*), open spaces amount to *9,25 km²* (*0,14%*); and water bodies are *124 km²* or (*1,87%*)

3.1. Selecting the location of BTSs

Initial cellular plan indicates the locations of BTSs, each antenna coverage, and the distribution of frequencies among the cells. Factors such as these are based on traffic prediction so that after having tuned the layer according to the relief another layer, that of traffic intensity, is generated as well as a layer of the population distribution (number of persons per *km²*). Both investigations make it evident that high traffic intensity corresponds to high population concentrations in the separate areas.

Basic parameters that are taken into account in selecting the sites and the number of BTSs include traffic intensity, utilization of land, demographic distribution and the relief of the landscape. Five stations have been selected (BTS1, BTS2, BTS3, BTS4 and BTS5) and located at vantage sites of suitable altitude, as close as possible to densely populated settlements with high traffic intensity. Fig. 1 shows the locations of BTSs as a proof of above statement.

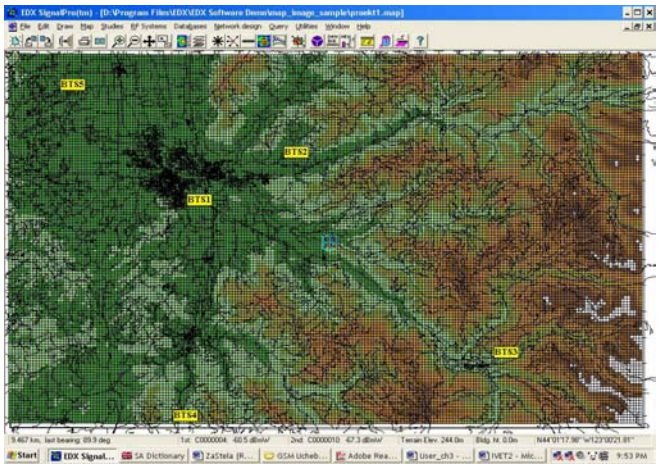

Fig.1. Locations of BTSs

The next parameter to be taken into account is the height of the equipment, which is in direct dependence on location (Table 1). In this case the recommended location from Table 1 is not kept for all BTSs because selected locations in real settings are properly made and that could bring to considerable cost cuts.

TABLE 1
GSM900

Parameters of BTS	Rural zone (plain terrain)	Rural zone (quasi plain terrain)	Urban area
Height of BTS, *m*	100	100	50
Height of MS, *m*	1,5	1,5	1,5
Hata's formula of losses (*d* is in *km*)	90,7+31,8*lg*(*d*)	95,7+31,8*lg*(*d*)	123,3+33,7*lg*(*d*)
Losses within the building (internal), *dB*	10	10	15

3.2 Assigning the parameters of the mobile unit

The parameters of the mobile station are assigned by standard values (Fig .2) [4] such as type of antenna (cross/ guided) average antenna (height above ground)

$$h.a.g = 1,5m,$$

gain = 3dB, maximum transmission power *ERP = 2W*, minimum permissible signal to noise ratio, intermodulation distortions:

$$C/(I+N) = 16\ dB.$$

Maximum permissible receiver noise level - *R.n.l. = -122 dBmW*.

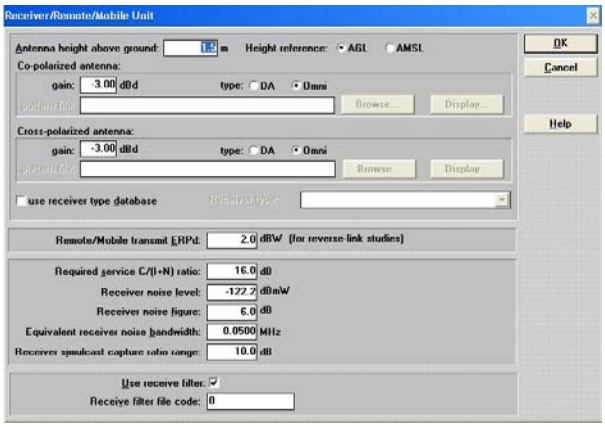

Fig.2. Window for tuning of mobile unit parameters

It is recommendable to make a preliminary estimation of field intensity for each BTS in order to find out whether the tunings are appropriate and, if not, to make necessary corrections [4].

3.3. Investigation results

Fig.3 shows the window for defining of investigation parameters whereby most measurements that underlie coverage quality are made. These are received power at remote (the level of signal i.e., power gain at the mobile unit antenna), field strength at remote (levels of field intensity), Shadow map (direct visibility zones and the zones of signal reflected by the environment). All have been selected from Area study type menu.

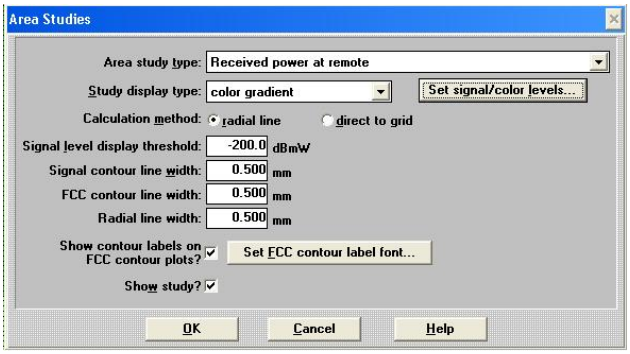

Fig.3. Defining investigation parameters

Signal power, which comes to the mobile unit in *dBmW* is shown in Fig.4. Graded colours are used for the purpose of better visualization. Minimum usable level which allows standard quality connection is [3, 4]: *m.u.l.= -104 dBmW*.

The figure makes clear that a very good coverage is achieved in densely populated areas (red and yellow), the power values being far above the minimum required for quality connection. Lower power areas are marked with green. However, it is sufficient because the traffic there is low. Lowest power is indicated by blue colour (it is almost close to the permissible lows), however, the relief there is mountainous and there are no inhabited settlements, so such signal level is permissible.

When predicting field *E* intensity we use basic dependences for distribution of EMB – attenuation with direct visibility and behind a barrier. The purpose of predicting is to determine the average value of *E* which is due to the slow variations of the field (slow fading). Accordingly, it is necessary to know which areas are with direct visibility and which are not.

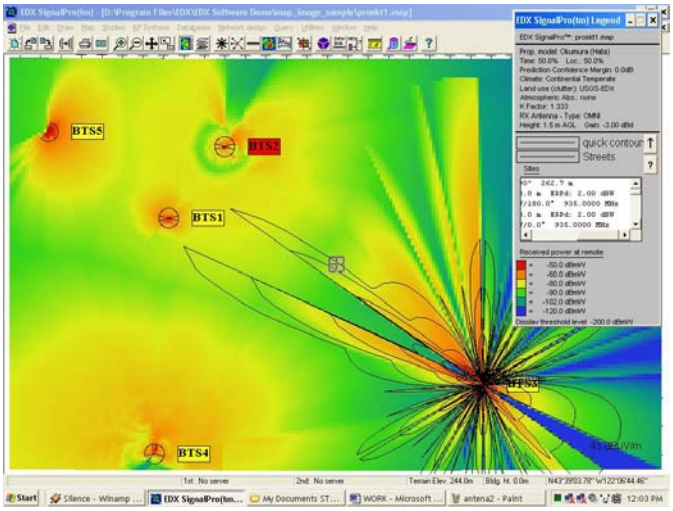

Fig.4. Level of signals in dBmW(Power gain at the antena of the mobile unit)

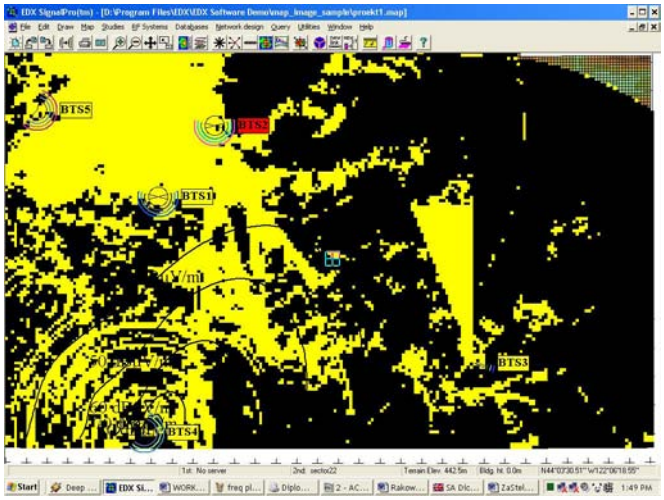

Fig.5. Line of sight zones and zones with signals reflected by the environment (yellow indicates line of sight; black – reflected signal)

Field intensity created by the transmitters is shown in Fig.6. Colour gradation is also used in there. The standard minimum value of intensity, which allows for quality connection, is *43 dBμV/m*.

Here the conclusions are similar with those in Fig. 4.Consequently, we draw the conclusion that the quality of connection across the investigated area is good and it is better for the densely populated areas and not so good for the sparsely populated and uninhabited areas (yet within the permissible limits). This is indicative of a correctly designed network whose parameters are selected comparatively well. The model development does not claim to be the perfect solution nevertheless it is helpful for the make-up of a network of adequate coverage.

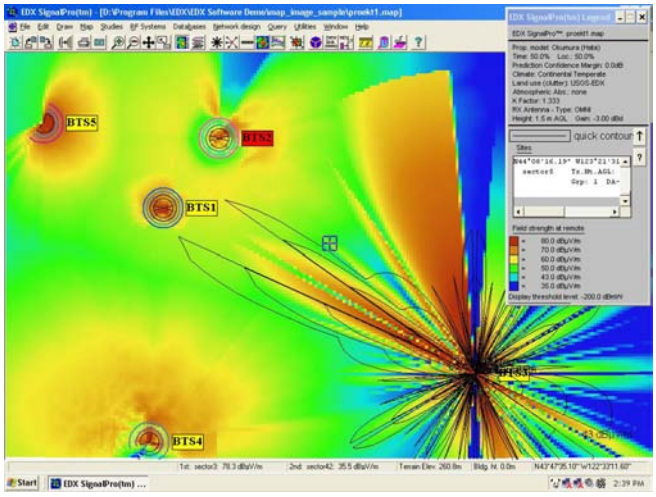

Fig. 6. Levels of field intensity in *dBμV* (minimum permissible level ***– 43dBmV/m*)**

IV. CONCLUSION

The aim of the paper is to build up a system of the steps needed to design a GSM network. Next comes the design of a model network by means of EDX-SignalPro" software. Further steps include the selection of appropriate digitalized map, investigation of traffic intensity, demographic distribution, utilization of land in the selected area etc. Based on these it is possible to select the number of BTSs and their location. After that all required network parameters are entered and results are visualized.

A GSM network design is a long and complex process, which involves a number of procedures, investigations and a sound knowledge of network standards. Soft products such "EDX-SignalPro" could be used effectively in various applications, which would considerably reduce the amount of time and funds that have been so far demanded by similar projects.

REFERENCES

[1] P.Pencheva, "Mobile networks", New Learning, Sofia, 2002.

[2] Moe Rahnema - "Overview of the GSM System and Protocol Architecture, IEEE Communications Magazine, April 1993

[3] Mikko Latineu, Jari Rantala, "Integration of Intelligent Network Servises into future GSM Networks", IEEE Communications Magazine, June 1995

[4] EDX, "Tools for Wireless Design", Software Product Catalog, 2003

Some Important Parameters of the SCP Technology

Veselin Demirev[1], Alexander Efremov[2]

Abstract – **Some important parameters of the SCP technology are defined and investigated in details. The first is the Shannon capacity of a SCP system, working in thermal noise, interference and combined environment. The second is the system Spatial Cross Correlation Function and its analytical presentation, leading to formulas for predicting the side lobe level, beam-width etc.**

Keywords – **Spatial correlation processing, Shannon capacity, SCCF**

I. INTRODUCTION

Description of a new radiocommunication technology, based on random phased antenna arrays approach and Spatial Correlation Processing (SCP) is given in [1]. Matrix presentations of the signals and the basic signal processing procedures, as well as computer simulations of the system spatial resolution properties are given in [2]. Some of the basic SCP system properties were investigated by means of the probability theory [3]. The goal of this report is to determine some new and important from communication point of view SCP parameters, as follows:

II. THE SHANNON CAPACITY OF THE SCP SYSTEMS

The SCP-GSO system analysis, given in [2], uses the standard thermal noise equations, typical for coherent demodulating schemes. The SCP pilot signal is random phase spread and as it was shown in [3], it has Gaussian probability distribution. In the ideal case of pure correlation with infinite period of time average, the product between the both independent Gaussian random processes (the thermal noise and the phase spread pilot) should vanish. In the real communication systems, because of the limited time average (in order of one bit period), this product can be assumed as equal to that of the coherent demodulation schemes. The detailed investigation of the SCP thermal noise properties, based on the probability theory of the cross-power density spectrum, will be done in a future report without any expected significant quantitative changes.

The standard formula for the Shannon capacity, expressed in bps/Hz is [4]:

$$C = \log_2(1 + \frac{P}{N_0 B_n}) \quad (1)$$

where P is the power of the received signal, N_0 is the noise spectral density and B_n is the receiver equivalent noise bandwidth at baseband.

For the case of SCP system in thermal noise limited environment, the equation (1) will have the form:

$$C = \log_2\left[1 + \frac{BBO_c}{G.F.K.T_o.B_n}\right] \quad (2)$$

where BBO_c is the cooperative output signal at baseband, G is the total receiver gain, F is the receiver noise figure, K is the Boltzman,s constant, T_0 is the standard temperature (290 deg. Kelvin).

For the case of SCP system in interference limited environment, the Eq. (1) will have the form:

$$C = \log_2\left[1 + \frac{BBO_c}{G.Tr(I.p^H)}\right] \quad (3)$$

where $Tr(I.p^H)$ is the power of the interference sources at the receiver input.

For the case of SCP system with only one interference source, the equation (1) will have the form:

$$C = \log_2\left[1 + \frac{1}{SCCF_{lin}}\right] \quad (4)$$

where $SCCF_{lin}$ is the Spatial Cross Correlation Function [1] of the SCP system, represented in linear form.

For the case of SCP system in mixed thermal noise and interference limited environment (which is the real case), the Eq. (1) will have the form:

$$C = \log_2\left[1 + \frac{BBO_c}{G.F.K.T_o.B_n + G.Tr(I.p^H)}\right] \quad (5)$$

III. ANALYTICAL PRESENTATION OF THE SCP SCCF PATTERN

The SCCF was introduced for the spatial interference analysis with one interference, as follows [1]:

$$SCCF\ (\phi,\theta)(dB) = 10\ \mathbf{lg}\left[\mathbf{BBO}_{\mathbf{inter}}.(\boldsymbol{\varphi},\boldsymbol{\theta})/\mathbf{BBO}_{\mathbf{c}}\right] \quad (6)$$

where the interference power at baseband is given with:

$$\mathbf{BBO}_{\mathbf{interferen\ ce}} = \mathbf{timeaver}\ G.(\mathbf{I}.\mathbf{p}) = G.\mathbf{Tr}(\mathbf{I}.\mathbf{p}^{\mathbf{H}}) \quad (7)$$

[1] Veselin Demirev is with the Faculty of Communications and Communication technologies, TU – Sofia, "Kl. Ohridsky" blvd. N8, 1756 – Sofia, Bulgaria, E-mail: demirev@homelan.bg

[2] Alexander Efremov is with the University of Chemical Technology and Metalurgy, "Kl. Ohridsky" blvd. N8, 1756 – Sofia, Bulgaria, E-mail: efremov_a@hotmail.com

In fact SCCF is the virtual antenna pattern of the SCP system at baseband. In [2] it was computer simulated for different tilt angles and real antenna diameters in Ku frequency band. It is important to derive an analytical presentation of the SCCF in order to predict some of the most important system parameters as beam-width, side-lobe level, etc.

The interference output signal, product of the multiplication process, is:

$$G(\mathrm{i}.\mathrm{p}) = \begin{vmatrix} i_1.p_1 & i_2.p_1 .... & i_n.p_1 .... & i_N.p_1 \\ i_1.p_2 & i_2.p_2 .... & i_n.p_2 .... & i_N.p_2 \\ ..... & ..... & ..... & ..... \\ i_1.p_n & i_2.p_n .... & i_n.p_n .... & i_N.p_n \\ ..... & ..... & ..... & ..... \\ i_1.p_N & i_2.p_N .... & i_n.p_n .... & i_N.p_N \end{vmatrix} = G \tag{8}$$

where i_n, p_n are the interference and the pilot signal at the output of the n^{-th} random antenna array element, G is the total receiver gain and the sum of the off-diagonal terms is zero. The real part of the n^{-th} diagonal term is:

$$\begin{aligned} &\mathrm{Re}(i_n.p_n) = \\ &= \pm 0{,}5.i_n.\cos\left[k.r_n.\sin\theta_c.\cos(\phi_c - \phi_n) - \right. \\ &\left. - k.r_n.\sin\theta_m.\cos(\phi_m - \phi_n)\right] \pm \\ &\pm 0{,}5.i_n(2\omega_{II}t + ...) \end{aligned} \tag{9}$$

After time-average procedure the total interference (Eq.7) is:

$$\begin{aligned} &BBO_{\text{int}\,erference} = \\ &= \pm 0{,}5G.i\sum_{n=1}^{N}\cos\, k.r_n\left[\sin\,\theta_c.\cos(\,\phi_c - \phi_n) - \right. \\ &\left. - \sin\,\theta_m.\cos(\,\phi_m - \phi_n)\right] \end{aligned} \tag{10}$$

The $SCCF_{linear}$ for this particular case is:

$$\begin{aligned} SCCF_{linear} &= \frac{BBO_{\text{int}\,erference}}{BBO_c} = \\ &= \frac{1}{N}\sum_{n=1}^{N}\cos k.r_n\left[\sin\theta_c.\cos(\phi_c - \phi_n) - \right. \\ &\left. \sin\theta_m.\cos(\phi_m - \phi_n)\right] \end{aligned} \tag{11}$$

Eq. (11) is equal to that of an antenna directivity pattern of a circular antenna array with uniform amplitude distribution, in-phase collimated in the direction, given with azimuth ϕ_c and zenith θ_c (the angular coordinates of the cooperative satellite).

It is well known that the analysis of such kind antenna aperture could be done in two ways, depending on the antenna diameter to wavelength ratio and the distance between the elements, as follows:

- Relatively small antenna electrical dimensions and inter-element spacing greater than the used wavelength. In this particular case, bearing in mind the random spacing, statistical approach can be used (introduced by Lo in [5]).
- High values of the electrical dimensions and small inter-element spacing (between half and one wavelength). This particular case, corresponding to the SCP technology, can be analysed with the well developed theory of the phased uniform excited circular apertures [6], as follows:

The directivity antenna pattern of a circular uniform phased aperture $F(\theta)$ is given by:

$$F(\theta) = \frac{2J_1(2\pi a.\sin\,\theta/\lambda)}{2\pi a.\sin\,\theta/\lambda} \tag{12}$$

where J_1 is the Bessel function of first order and a is antenna array radius. For this particular case the first side-lobe level is -17.6 db, the half power beam-width $2\Delta\theta_{0,5}$ and the maximum antenna gain G_o are given by:

$$2\Delta\theta_{0,5}(rad) = 1{,}02\,\lambda/2a \tag{13}$$

$$G_0 = \frac{4\pi^2 a^2}{\lambda^2} \tag{14}$$

The main principles of the proposed SCP technology are valid for all kind of random phase antenna arrays, but the Radial Line Slot Antenna (RLSA) array [1] was shown to be the most suitable for DVB-S applications. The RLSA feature is the lack of radiation slots in the middle of the aperture. It leads to non-uniformity in the aperture distribution, which influence over SCCF can be predicted by means of the Fourier transformation summing theorem [7], as follows:

$$\begin{aligned} &G_{linRLSA}(\theta) = \\ &= \frac{4\pi^2 a^2}{\lambda^2}F^{\,a}(\theta) - \frac{4\pi^2 b^2}{\lambda^2}F^{\,b}(\theta) = \\ &= \frac{4\pi^2}{\lambda^2}\left[a^2\,\frac{2J_1(2\pi a.\sin\,\theta/\lambda)}{2\pi a.\sin\,\theta/\lambda} - \right. \\ &\left. - b^2\,\frac{2J_1(2\pi b.\sin\,\theta/\lambda)}{2\pi b.\sin\,\theta/\lambda}\right] \end{aligned} \tag{15}$$

where $G_{linRLSA}(\theta)$ is the spatial gain pattern of the RLSA, a is its outer radius, b is the inner radius.

The spatial power gain patterns (in dB) of the outer and the inner circular apertures are given by:

$$G^{\,a}(\theta, dB) = 10\,\lg\left[\,\frac{2J_1(2\pi a.\sin\,\theta/\lambda)}{2\pi a.\sin\,\theta/\lambda}\,\right]^2 \tag{16}$$

$$G^{\,b}(\theta, dB) = 10\,\lg\left[\,\frac{2J_1(2\pi b.\sin\,\theta/\lambda)}{2\pi b.\sin\,\theta/\lambda}\,\right]^2 \tag{17}$$

The maximum gain of the RLSA for $\theta = 0$ will be:

$$G_{0\,RLSA} = \frac{4\pi^2(a^2 - b^2)}{\lambda^2} \tag{18}$$

In the end the SCCF of the RLSA will have the form:

$$SCCF\ (dB) = $$
$$= 10 \lg\left[\left[2J_1(2\pi a \sin\theta/\lambda)/2\pi a \sin\theta/\lambda\right]^2 - \right.$$
$$\left. - \frac{b^2}{a^2}\left[2J_1(2\pi b \sin\theta/\lambda)/2\pi b \sin\theta/\lambda\right]^2\right]\left[1-\frac{b^2}{a^2}\right]^{-1} \quad (19)$$

In Fig.1 the computed by Eqs.(16) and (17) spatial gain patterns of the outer and inner circular apertures are shown for comparison $(a = 28{,}5cm, b = 5cm, \lambda = 2{,}5cm,$ $\theta = -70^0\ to + 70^0, step\ 0{,}1^0)$

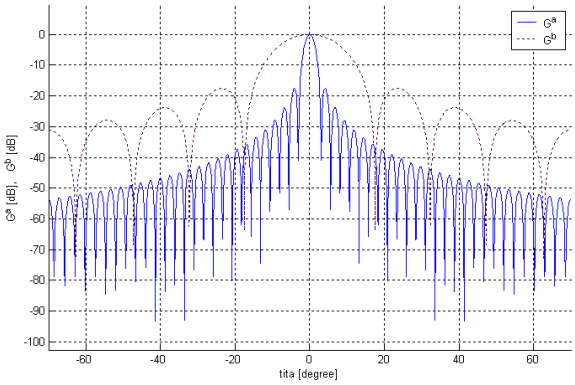

Fig.1. Spatial gain patterns of the outer and inner apertures

In Fig. 2 the computed with Eq.19 SCCF is shown. $(a = 28{,}5cm, b = 5cm, \lambda = 2{,}5cm,$ $\theta = -70^0\ to + 70^0, step\ 0{,}1^0)$:

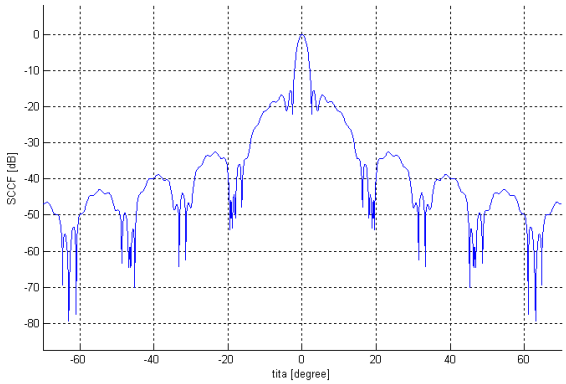

Fig.2. The computed SCCF

In Fig. 3 the computer simulated [2] SCCF is shown for comparison $(a = 28{,}5cm, b = 5cm, \lambda = 2{,}5cm,$ $\theta = -70^0\ to + 70^0, step\ 0{,}1^0)$.

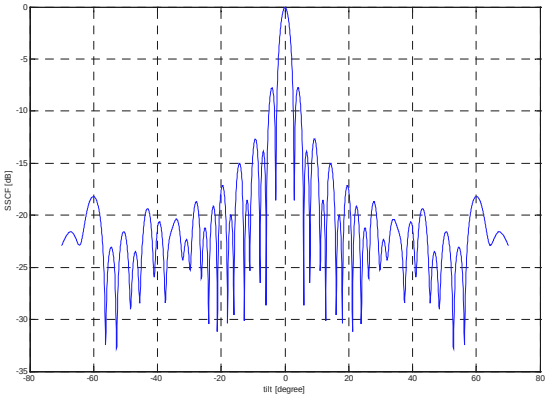

Fig.3. The computer simulated SCCF

IV. Conclusion

In this paper two important parameters of the SCP technology are defined and investigated in details. The first is the Shannon capacity of a SCP system, working in thermal noise, interference and combined environment. Equations for capacity calculations are derived. The second is the system Spatial Cross Correlation Function and its analytical presentation, leading to formulas for predicting the side lobe level, beam-width etc. Computer simulations, based on these formulas, are given too.

References

[1] V. Demirev, "SCP technology – the new challenge of broadband satellite communications", *ICEST'04 Conference Proceedings, pp. 159-162,* Bitola, Macedonia, 2004

[2] V. Demirev, A. Efremov, "SCP-CDMA GSO's system proposal", *ICEST'04 Conference Proceedings, pp.163-166*, Bitola, Macedonia, 2004

[3] V. Demirev, "The probability theory with application in SCP technology", *ICEST'04 Conference Proceedings, pp.167-168*, Bitola, Macedonia, 2004.

[4] S. Haykin, *Communication Systems*, John Wiley, 1994.

[5] Y. Lo, "A Mathematical Theory of Antenna Arrays with Randomly Spaced Elements", *IEEE trans. On Antennas and Propagation*, vol. AP-12, May, 1964.

[6] R. Hansen, *Microwave Scanning Antennas*, Academic Press, New York, London, 1966.

[7] W. Christiansen, J. Hogbom, *Radiotelescopes*, Cambridge University Press, 1969.

Application of SCP technology in Quasi-GEO satellite systems

Radoslav D. Markov[1] , Veselin B. Demirev[2]

Abstract – **In this paper a brief overview of the Quasi-GEO satellite systems is given; and the possible application of SCP technology in these systems. Afterwards is paid attention to the difficulties experienced, and the ways they are handled. Finally a model system analysis for a SCP system working on Quasi-GEO is given.**

Keywords – **SCP, Quasi-GEO, application**

I. INTRODUCTION

Geostationary systems provide fixed and mobile communications, as well as TV broadcasting services since 1964. They still suffer some problems as:

- The amount of the already existing systems limits the frequency and orbital resources in the most desired frequency bands, for example the Ku band
- The low elevation angles in the high latitude regions hamper the reception in urban areas and/or rough terrain. Mobile reception using horizontal antennas mounted over mobile platforms is just impossible.

II. QUASI-GEO SATELLITE SYSTEMS

An appropriate decision of the afore-mentioned problems is the use of satellite systems on high elliptic eccentricity polar orbits, known as Quasi-GEO. The active zone of the satellites is in the apogee, when the relative satellite -Earth velocity is low. Three systems of this type are being proposed – the American Virtual GEO system [1], [4], The Russian "Centaur", [2], [3] and the Japanese Quasi-Zenith Satellite System - QZSS [5], [6].

In fig.1 the satellite constellation configuration is displayed. The parameters of this orbit are:

Major axis – 20281 km, Apogee – 27300 km, Perigee – 525 km, Eccentricity – 0.66, Inclination – 63 degrees, Period – 8 h.

The advantages of the Quasi-GEO systems over standard GSO are obvious:

Quasi-GEO provides high elevation angles in high latitudes areas. In graph. 1 [3] the elevation angles for some of the largest cities in the world, both for Quasi-GEO and GSO are compared.

- Quasi-GEO allows frequency reuse of overcrowded GSO frequency bands, i.e. Ku band. In fig. 2 the active zones of GSO and Virtual GEO systems are shown. It is obvious that the minimum angle separation between satellites of both types is about 40 degrees. It allows simultaneous use of Ku band for both systems by the ground terminals with highly directed antennas (s.c. SDMA - Space Division Multiple Access).

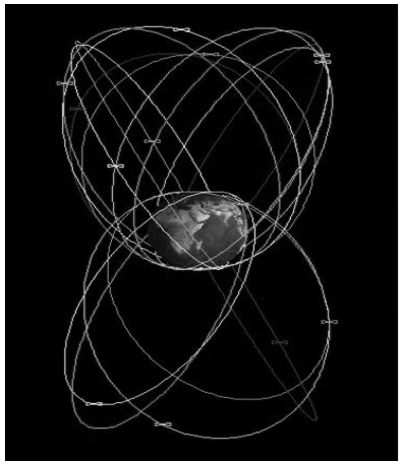

Fig. 1. The satellite constellation of Virtual GEO [4]

Graph. 1. Elevation angles for Quasi GEO and GSO

[1]Radoslav D. Markov is with the Faculty of Communications and Communication Technologies "Climent Ohridski" N8 1000 Sofia, Bulgaria,Email: rmarkov@tu-sofia.bg

[2]D-r Veselin B. Demirev is with the Faculty of Communications and Communication Technologies "Climent Ohridski" N8 1000 Sofia, Bulgaria,Email: demirev@homelan.bg

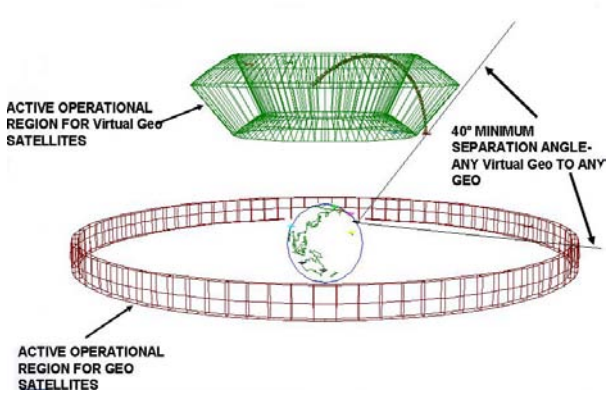

Fig.2. Comparison between Virtual GEO and GSO operational regions [4]

The application of the above-mentioned Quasi-GEO systems encounters several specific problems:

- It requires the use of high gain tracking antennas.
- The ground terminals need the exact angle coordinates of the active satellites. This requirement puts hard restrictions on the orbital Quasi-GEO satellites parameters.
- The need of soft hand-off between the satellites. When mechanical scanning tracking antennas are used, two antennas are needed at least.
- The relative movement between the Earth and the satellites leads to high Doppler shift of the information signals.

III. THE SCP TECHNOLOGY – AN APPROPRIATE DECISION FOR QUASI-GEO

In [8] a new radio technology was proposed – SCP, which stands for Spatial Correlation Processing. It allows the receiving of one or more radio signals, coming from one or several spatially distributed sources (satellites) and insures high gain of the antenna system. Its high spatial selectivity cancels the same frequency channel interference, coming from different space directions. The above stated objectives are achieved by means of additional pilot signal, transmitted in the band of information signals and available in the receiver by CDMA (Code Division Multiple Access) techniques. The SCP receiver terminal is equipped with antenna array with random phase aperture excitation. The phase shifts of the signals, coming from different antenna elements, are random at the antenna output regardless of the information source direction. These phase spread signals correlate with the recovered pilot signal, phase spread in the same manner. The result of the correlation process is the recovered information signal at base band. The signals, coming from other satellites, will propagate in different random environment. Their phase spreads will be different from these of the chosen pilot and will not correlate during the signal processing. This lack of correlation ensures the spatial and polarization selectivity of the SCP system.

The SCP technology allows virtual scanning of one or several antenna beams, with high gain and space selectivity. It is a unique technology and a revolutionary step in the development of the next generation satellite communications.

The application of the SCP technology in GSO, s requires specific approaches. In the case of fixed reception the antenna should be mounted vertically on the wall, looking to the chosen GSO satellite. In the case of mobile reception it should be mounted horizontally on the roof of the vehicle. In Quasi-GEO the antenna should be in horizontal position in both mobile and fixed reception.

Another advantage of the SCP technology is the ability for multi-beam reception, using several correlators, each one for the different satellite. The result is:

- Ability for soft hand-off between the satellites using single antenna aperture.
- Space diversity, which allows reception of the same information from several satellites, leading to increased reliability in urban and rough terrain areas.
- The collective systems in trains, aircrafts or ships allow the receiving of different TV programs from several satellites by means of a single antenna system.

Another advantage of SCP technology in Quasi-GEO is the lack of Doppler shift problems; being the same for the pilot signal and the information one in the process of correlation it is compensated.

To summarize the stated above we can say that while using fixed reception from GSO, s it is possible to use the conventional parabolic antennas, while for the Quasi-GEO systems that is inapplicable. The only reasonable solution for them is SCP.

IV. SYSTEM ANALYSIS OF SCP QUASI-GEO SATELLITE SYSTEM

The system analysis of SCP Quasi-GEO system could be made using the mathematical model, developed in [8] for SCP GSO's system. The specific approach here is that the link equation is defined for one array antenna element. Afterwards the received signal-to-noise ratio is multiplied by the number of the antenna array elements. The following assumptions are made:

- The antenna pattern of a single radiator is omnidirectional
- The gain for a single radiator is G_S =1,6 dBi
- The link equation is used in a simplified form [9]

The parameters for a Quasi-GEO system are as follows:

- EIRP = 56.4 dBW
- S = 42 000 km – the maximum distance to a Quasi-GEO
- f = 12 GHz (λ = 2.5 cm)
- Free space path loss; L = 206.5 dB
- R = 20 MB/s (information signal rate) and
- Rc = 1.23 MCh/s (pilot signal chip rate)
- Receiver noise figure F = 1 dB and antenna noise temperature T_A = 50 grad. K
- L_{add} = 5 dB – (additional losses)
- N = 4800 (number of elements in 80 cm antenna array) => N [dB] = 36.8
- L_{pol} = 3 dB – polarization losses

Calculated:

- Figure of merit per slot $G / T_S = G_S - 10 \lg T_S$ =1.6 - 20.88= - 19.28 dBi/grad. K
- Energy per bit over power noise density per antenna element:

$E_b / N_o(ips) = EIRP - L - L_{add} + G_S - 10\lg T_S + 228.6 - 10\lg R - L_{pol}$ = - 20.08 dB

- Carrier power per element: $C(ips) = EIRP - L - L_{add} + G_S$ = -153.5 dBW

The multiplying of the pilot and information signals of an element in the correlator and the following low-pass filtering is a process of a coherent demodulation. The result is N in-phase components at base band, which sum is the demodulated information signal. Bearing in mind the fact, that the signal-to-noise ration for the pilot signal is at about 20 dB higher than the one for the information signal, the total

(Eb/No)t=N(Eb/No)ips, (Eb/No)t [dB] = N [dB] + (Eb/No) [dB]ips = 16.72 dB

The total figure of merit for the system will be (G/T)[dB]=N[dB]+ (G/T)per slot[dBi/grad.K] = 36.8 –19.28 = 17.52 dBi/grad.K

REFERENCES

[1] "Elliptical satellite system, which emulates the characteristics of geosynchronous satellites" US Patent №5, 957,409, Sep. 28, 1999

[2] Тихонов О., ..."ИспольЬзование Эффекта относительной неподвижности спутников ..." 2001, Информационный Космический Центр "Северная Корона"

[3] http://www.spacecenter.ru/Kentavr_Major.htm

[4] http://www.virtualgeo.com/

[5] http://www.asbc.jp/business/serviceE.html

[6] http://www.gpsworld.com/gpsworld/article/article Detail.jsp ?id=61200&pageID=1

[7] Demirev V. "SCP Technology - the new challenge in broadband satellite communications" ICEST, 2004, Bitola, Macedonia, 2004.

[8] Demirev V. "GSO SCP-CDMA system proposal" ICEST, 2004, Bitola, Macedonia, 2004.

[9] Gordon G., W. Morgan "Principles of Communications Satellites" 1993, John Wiley & Sons.

Software Model of PRS Transmitter, Channel and Receiver

Stanyo Kolev[1], Dobri Dobrev[2], Alexander Aydemirski[3]

***Abstract* – We have made a software simulation of PRS system with first class, second grade transforming but the achieved results were not satisfying. And as We wanted to gain better results in detecting and correcting the errors, we have made another experiment using a system with third class, sixth grade transforming. The experiments and some graphical results are presented in this paper.**

Keywords – **PRS, PRS system**

I. INTRODUCTION

Partial Response Signaling finds many applications in the modern digital world. Manufacturers use it lately as a better way for transferring data in and out from hard disk drives, for example. As we got acquainted with the PRS signaling, we figured out that it can find its place in open air data transmission. So we have made a software model of such PRS system. Which is presented in this paper.

II. SOFTWARE MODEL OF PRS SYSTEM

The correlated signal is a signal with three or more levels. In order to achieve correlation between the symbols we need a suitable limitation of frequency band for the channel or a proper coding of the binary signal. In Figs. 1. and 2 are shown the two ways of forming the correlated signal.

Let the digital stream from the data source {a} is generated by binary sygnal with *n* symbols: {a} = {a_1, a_2, ... a_n}. As a rezult of the limitation of frequency band in the channel Fig.1. or the proper coding Fig.2, we can achieve a correlated signal {c} with many levels. The C_n symbol of this signal can be considered as correlated by all symbols of the binary signal {a} with the proper coefficients κ_1, κ_2, ... κ_n, as shown in Eq.1.

$$Cn = \kappa 1an + \kappa 2\ an\text{-}1 + ... + \kappa na1 \qquad (1)$$

According to the order and the values of the coefficients, we can distinguish several classes of correlated signals, which differ by number of levels, their shape and spectral density.

Data for forming of five classes of correlated signals is given in Table I.

[1]M.Sc. Stanyo Kolev Assoc.Prof. is with the Faculty of Radio Communications, Technical University of Sofia, 8, Kliment Ohridski St., Sofia 1000, Bulgaria, E-mail: s_kolev@market.bg
[2]Ph.D. Dobri Dobrev Assoc.Prof. is with the Faculty of Radio Communications, Technical University of Sofia, 8, Kliment Ohridski St., Sofia 1000, Bulgaria, E-mail: dobrev@tu-sofia.bg
[3]M.Sc. Alexander Aydemirski is with the Faculty of Radio Communications, Technical University of Sofia, 8, Kliment Ohridski St., Sofia 1000, Bulgaria, E-mail: aydemirsky@netbg.com

First we are going to made a model of PRS system with a logical processing, i.e. coding. In Fig.3. is shown a software model of PRS system from first class, second grade.

TABLE I
WEIGHT COEFFICIENTS

Class	Order	WEIGHT COEFFICIENTS									Number of levels
		K1	K2	K3	K4	.	.	.	.	Kn	
0	1	1									2
1	2	1	1								3
	3	1	1	1							4
	4	1	1	1	1						5
	n	1	1	1	1	1	.	.		1	n+1
2	3	1	2	1							5
	7	1	2	3	4	3	2	1			9
	n	1	2	3	.	.	.	3	2	1	n+2
3	3	2	1	-1							5
	7	-1	1	-2	3	-2	1	-1			7
4	3	1	0	-1							3
	7	1	2	1	0	-1	-2	-1			3
5	5	-1	0	2	0	-1					5
	9	1	0	-2	0	3	0	-2	0	1	7

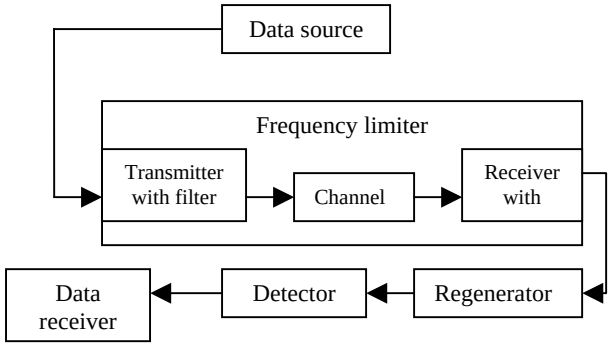

Fig. 1. Block diagram of PRS system with frequency limitation

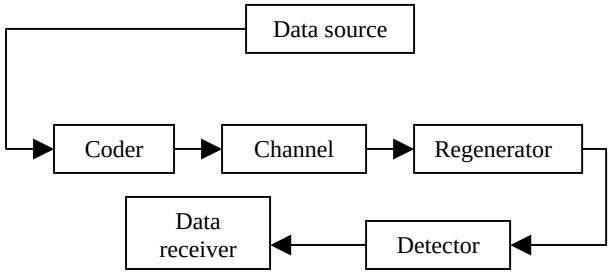

Fig. 2. Block diagram of PRS system with appropriate coding

The data source is made with the generator of odd NRZ row with normal distribution. The coder is made by next blocks: Memory1, Logical schemes – Logical Operator and Logical Operator1, as well as LO and LO1; Gain1 and recapitulator. The channel is made by recapitulator, which sums up the signal after the transmitter and the signal by the

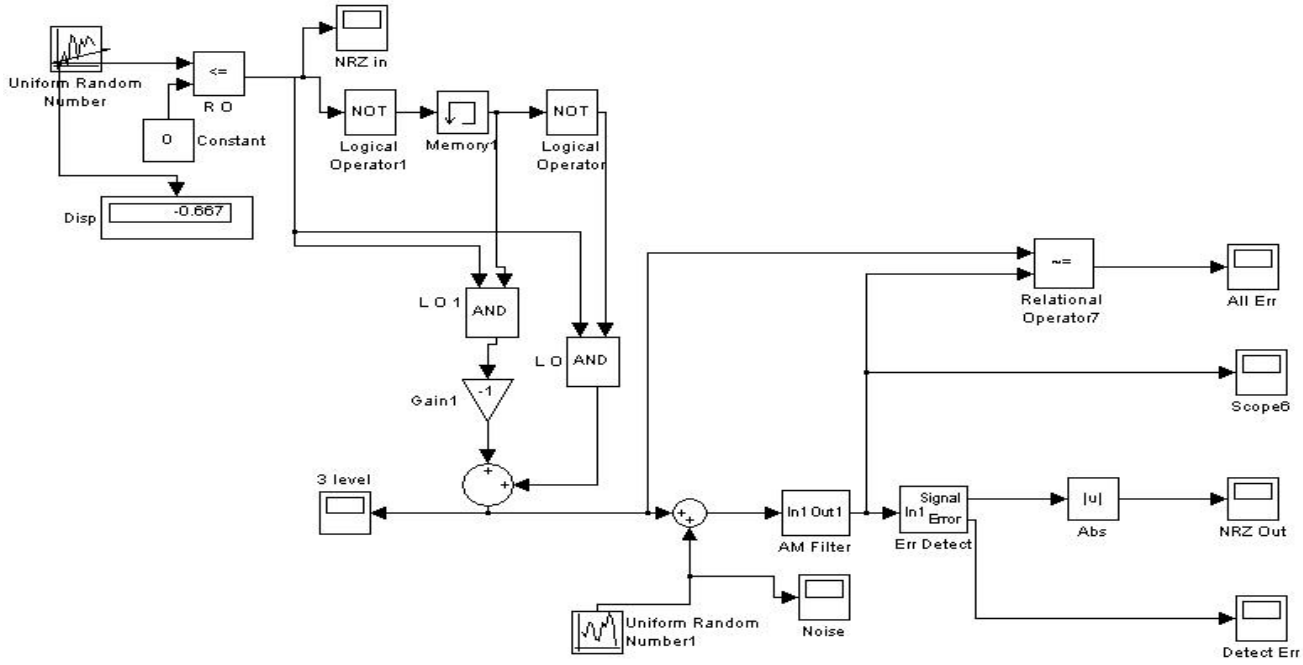

Fig. 3. Software model of PRS system I class II order

noise generator. The last imitates the presence of interference and different noises in the channel, which can have influence over the system – transmitter, channel, and receiver. The receiver is synthesized by an amplitude filter (AM filter) and error detector (Err Detect). The amplitude filter and the error detector are two separate systems. Their schemes are shown in Figs. 4 and 5.

We have to note that a modulator is not included in the transmitter, because the channel is made by error generator, whose signal recapitulates with the main signal. Transformation in binary NRZ signal needs only binary detector (Abs).

This code can find and correct only errors that take “1 as “-1” or the opposite, which rarely met in the real channel, due to the big distinction in levels. If we take in consideration that in coding the sequence “01” is forbidden, we can made a device to find these errors. This is what the “Err Detect” block does.

For modeling of this system, as well as taking the experimental results we used Matlab 6.5.

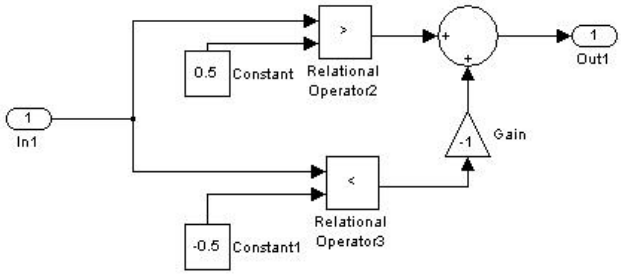

Fig. 4. Amplitude filter

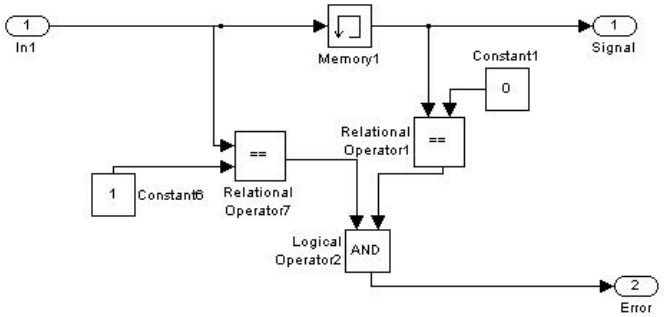

Fig. 5. Error Detector

In the scheme of the suggested model of PRS system we have put some functional blocks, which lead out graphical information for the signal in the most imporatnt points. After completing the fiftieth iteration we can observe the following progress of the signal.

The NRZ signal before the transmitter is shown in Fig. 6.

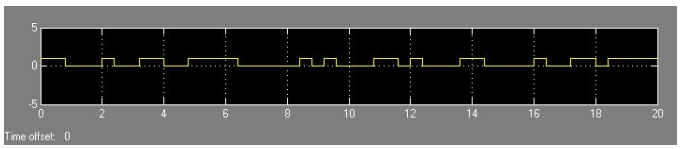

Fig. 6. NRZ in

In Fig. 7 we can see the signal after the transmitter and before the channel. As we can see the signal has three levels.

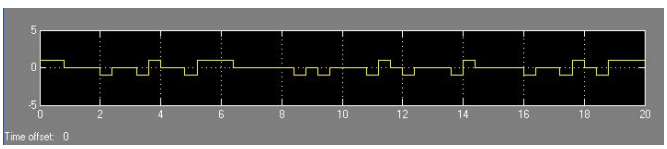

Fig. 7. Signal after the transmitter

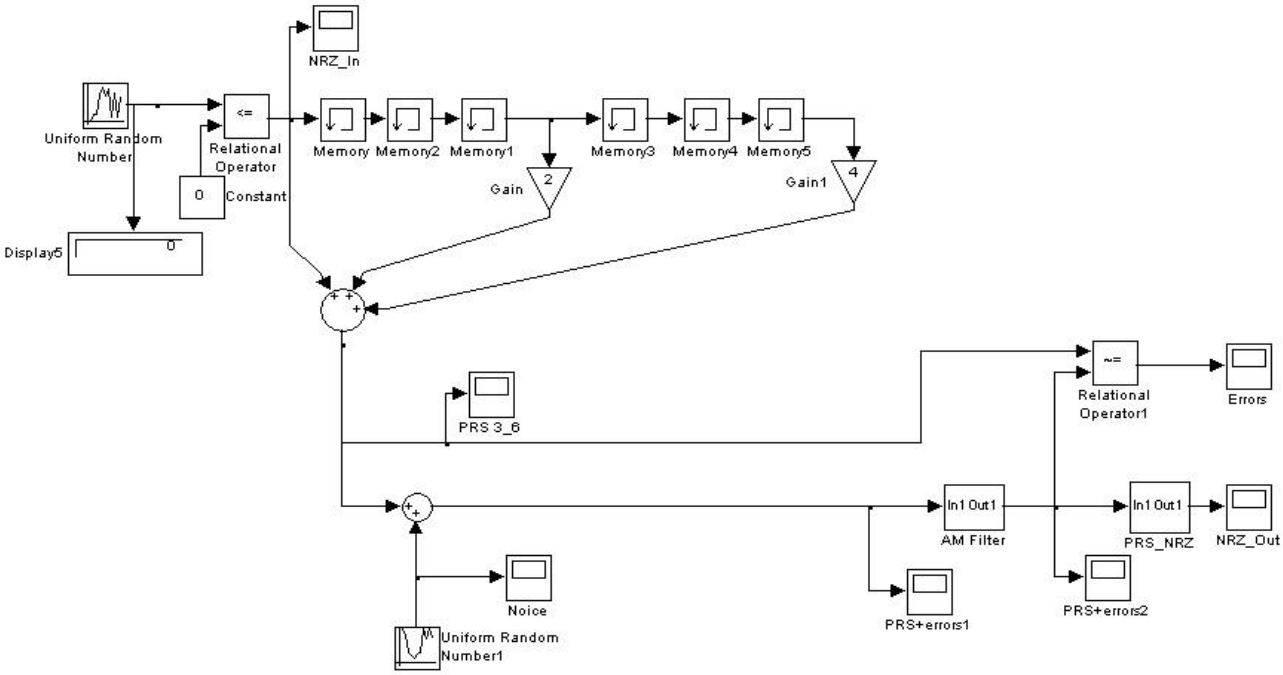

Fig. 12. Software model of PRS system III class VI order

The noise signal, recapitulated to the signal from the transmitter, in order to simulate real conditions in channel, can be seen in Fig. 8.

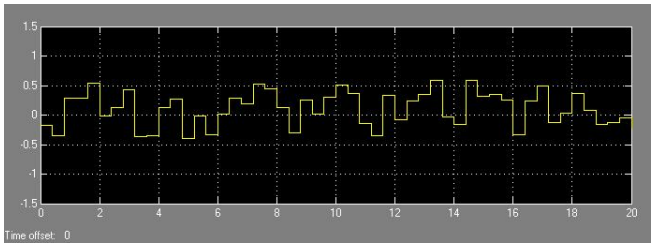

Fig. 8. Noise added in the channel

The signal of the errors is shown in Fig. 9.

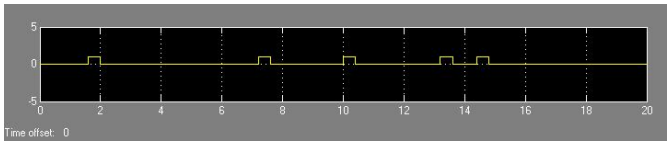

Fig. 9. Errors

The NRZ out signal can be seen in Fig. 10.

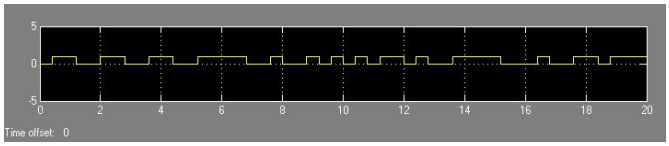

Fig. 10. NRZ out

The signal of the detected in the system errors is shown in Fig. 11.

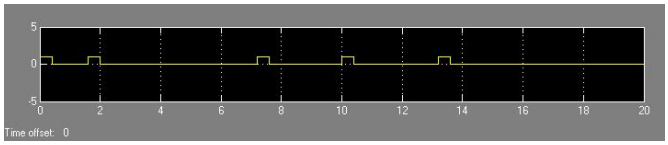

Fig. 11. Detected errors

In the "Scope All Err" Fig. 9. are shown all the errors added in the channel and in "Detect Err" are shown only detected errors, which are detected due to the forbidden combination. As we can see from 5 errors, the system has detected only 4, but they did not correct them. This is indicated with the level "1" in the exit "Detect Err".

If we compare Figs. 6 and 10, i.e. signals "NRZ in" and "NRZ out", we can see that if in level "1" only the errors are transmitted, the only undetected error is the error from the fifth "1" in "All Err".

In this experiment with PRS system, made up of transmitter, channel and receiver, we used first class, second grade transforming, and we couldn't achieve good results. The system doesn't detect and doesn't correct all the errors. At the expense of this the realization of the decoder is very simple and relevantly cheap.

In order to achieve good results from the experiment, we have searched a different resolution. We wanted to gain better results in detecting and correcting the errors, so we made another experiment using a system with third class, sixth grade transforming, which is shown in Fig. 12. The system uses eight grade amplitude manipulation and the Viterbi algorithm for detecting.

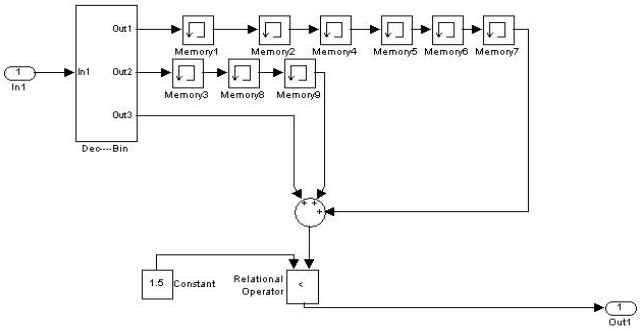

Fig. 13. PRS-to-NRZ

The next figures show the signal in particular points of the model. Their order is identical to that shown above.

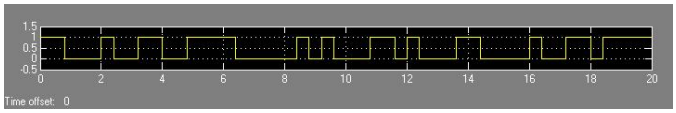

Fig. 14. NRZ in

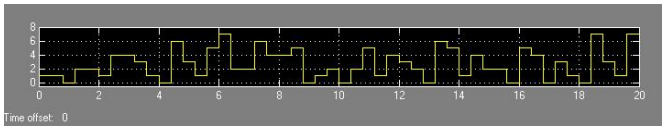

Fig. 15. Signal after the transmitter

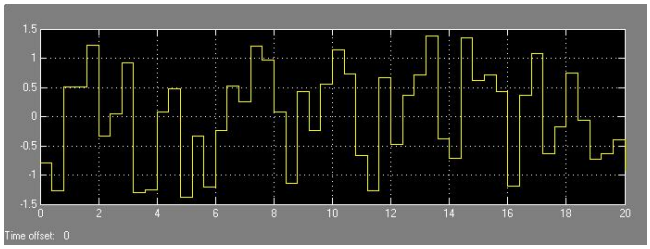

Fig. 16. Noise added in the channel

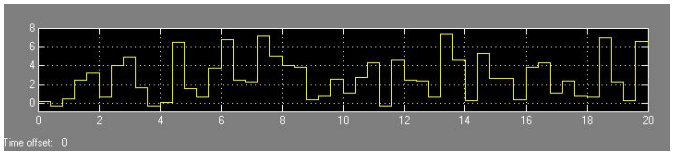

Fig. 17. PRS signal with the added noise

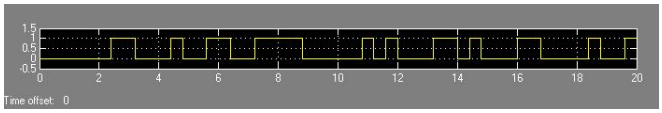

Fig. 18. NRZ out

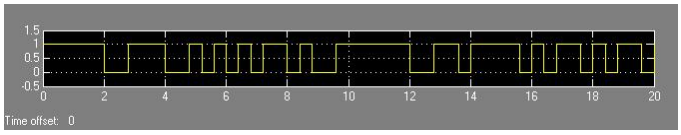

Fig. 19. Detected errors

In this simulation from 50 transmitted symbols, only 17 are received correctly. The others are errors. The decoder has detected and corrected these errors. The above figures show respectively: NRZ in signal, correlated signal with eight levels; the signal before the receiver with eight levels; NRZ out signal, at the exit of the detector. The latter signal is the same as the "in" signal, but delayed seven times.

From this simulation we can see, that the PRS system, that consists of a transmitter, a channel and a receiver, and which is third class sixth level is very resistant to noises. Unlike the system from first class, second grade, this system is relatively more complex. This leads to more expensive model. And yet this complexity and rising of the cost is right for the occasions, where the correct detection of the signal is needed.

III. Conclusion

In this paper the software model of PRS system, consisted of transmitter, channel and receiver, was presented. As the size of this paper is limited we have shown only two PRS systems. But we think that PRS signaling can and will find more and more applications in today's communications.

References

[1] Добрев Д. М., "Цифрови радиорелейни станции", Техника, 1987год.

[2] Kamilo Feher, "Digital Communications", 1981 by Prentis Hall

[3] Prabhu V. K., "ISI Performance of systems with Correlated Digital Signal", IEEE Transactions on communications, October 1973

[4] Георги Стоянов, "Теоретични основи на съобщителната техика", София, Техника 1987 год.

[5] A. Papoulis, Probability, Random Variables and Stochastic Processes, 3rd ed. New York: McGraw-Hill, 1991

[6] Mark C. Reed, "Iterative Receiver Techniques for Coded Multiple Access Communication Systems", University of South Australia, 1999

[7] Stefan Stanescu, Victor Soare, "Partial Response and Viterbi Detection Channel Simulator for Digital Magnetic", http://www.ici.ro/ici/revista/sic2000_3/art06.html

Session ITA:

INTERNET TECHNOLOGY AND APPLICATIONS

Integration of Object Oriented Web and Centura CMS

Ivan Petković[1], Milena Stanković[2], Milan Rajković[3], Petar Rajković[4]

Abstract – **Current Web content management systems have limited possibilities while designing frontend layout and user-interface in general. Because of their nature of being general purpose, not every thing that graphic designer has in his mind can be implemented via CMS. We offer a solution to the problem by integrating specially developed client side framework with the rest of the application.**

Keywords - **object oriented, client side, content management system**

I. INTRODUCTION

A content management system is, as the name says, a system used to manage the content of a web site. It typically consists of two elements: the content management application (also known as backend or BackOffice) and the content delivery application (or FrontEnd). First one allows the authors, to manage the creation, modification, and removal of content from a web site, while the other is focused on the content delivery to the users. Content management systems that are implemented using Web technologies, and where users interact with the system via Web, are known as Web content management systems.

We are witnesses of the enormous number of Web sites. Moreover, that number is growing exponentially. In order to attract users, Web sites must contain some unique features, they must be user-friendly and must have visual identity. In order to achieve visual identity, Web site's client side must be implemented differently than the concurrent's client side. Consequently, we can see various page layouts, Web site graphic designs and user interfaces. Implementing these features requires developing specially tailored code for each site.

On the other hand, content management systems, because of their nature as being general purpose, have mostly predefined format of displaying their content delivery application. That means several different Web sites powered by the same CMS look similar – which is just the opposite from the above-mentioned requirement – to have visual identity.

All authors are with the Faculty of Electrical Engineering, Aleksandra Medvedeva 14, 18000 Nis. Serbia nad Montenegro,
E-mail: {ivanp, mstankovic, mrajkovic, rajkovicp}@elfak.ni.ac.yu

In order to overcome this problem, we developed a framework for Web client development and a Web Content Management System (CMS) called *Centura*. Framework will be discussed in detail later, but it is important to mention that its main purpose is to enable easy development of advanced, visually unique Web clients (Web application's client side). It gives freedom in creating multimedia rich, user friendly and easy customizable Web sites. Since it has simple, butpowerful interface towards the server-side part of the application, it can be easily integrated. On the other hand, Centura is a general purpose, XML-powered CMS that can be used for managing web sites for small and medium sized organizations. We managed to integrate the above-mentioned framework and Centura, and the result was a content management system with the superior user interface and non-predefined FrontEnd display. Centura is still in development phase, but the first test version has already been used for managing the site of the laboratory [1].

The purpose of this paper is to describe the way Centura and the mentioned framework interact [2][3]. In section II we will discuss about the main parts of the Centura Content Management System, and afterwards, in section III, we will describe framework's architecture. Section IV will explain the points of integration between server part of the application and the framework, which resides on the client side. Section V will explain in more detail how the BackOffice section is implemented using framework's capabilities.

II. THE MAIN PARTS OF CENTURA

Centura is Web content management system developed using PHP as a server side technology, and a wide spectrum of client side technologies (HTML, CSS, DOM, JavaScript). It is a general purpose CMS which consists of a *front-end*, that is basically a Web site that can be accessed by all users, and a *back office* (figure 1), which is intended for the people who have permission to create and manage content. Although *Centura* is a Web application, its reach client interface reminds of desktop applications. As previously said, Centura consists of FrontEnd and BackOffice. Backoffice provides functionality for managing site content, users, workflow, settings and accounts.

Fig. 1 The BackOffice of Centura

The site content is hierarchically organized using the concept of *modules*, which are similar to folders in operating systems. Modules act as containers for other modules, binary files or items, but more importantly, they are used for setting the access permissions for users and groups. Basic access privileges are *read, write, delete, publish and admin*, but some special-purpose modules can have other predefined privileges, which are a combination of the basic ones.

An item is the key concept of *Centura*, because it represents a web page that will be displayed in the front-end. Items are XML structures that enable creating different types of web pages like *articles*, *courses*, and *polls*. They are created and edited using an online XML editor that is also a part of *Centura's* back-office.

The CMS supports advanced user management and access control. Users are organized into groups that all have administrators assigned to them. Users and groups can be later attached to modules by setting the corresponding access privileges (**Fig. 1**). The concept of the group administrator makes the user management completely distributed, where every group is controlled independently.

III. FRAMEWORK FOR WEB CLIENT

Purpose of the framework is rapid, quality and cost effective development of the Web application's client side. Its main features are:

- Object oriented approach
- Separation of content, control and presentation
- Elimination of redundancy
- Decreased development time and costs
- More flexible for team work
- Robustness
- Customizable
- Automated and visual development (using CASE tools)
- GUI components management and configuration
- Multilanguage support

Framework provides developers a more natural way of thinking. Instead of thinking on the level of HTML elements, they can think on the level of real world objects, like menus and page layouts. To be more specific, the framework recognizes several types of objects, including controllers, menu objects, layout objects, components, managers and other.

Framework is consisted of several subsystems, each assigned for distinct set of tasks. Following is the list of the subsystems:

- core, main subsystem that acts like the interface between the other subsystems and the rest of the application (e.g. server-side section)
- layout management subsystem, for manipulating, adding and removing page layouts. Every page layout (design) consists of one or more layout components
- navigation subsystem, whose primary purpose is to manage menu structures and the way how they are displayed
- windows management subsystem, which contains logic for creating, removing and managing windows in all other ways
- document management subsystem, with the main purpose to integrate all documents on the Web page into unique entity, therefore enabling interaction between them
- component management subsystem, for supporting and managing user interface components. Each component implements interface that provides customization, graphic and dictionary support (**Fig 3**)

As you can see on **Fig. 2**, Controller is the main component of the framework's core. Hence, all the communication between the external sources and the rest of the system is going through controller. This architecture provides minimal redundancy and optimal communication between framework and other systems.

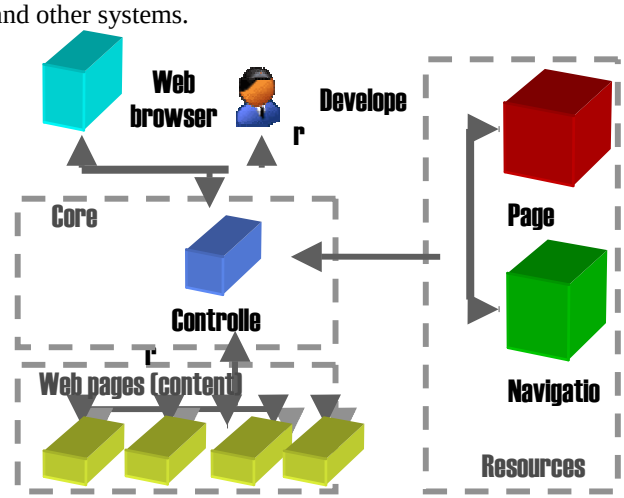

Fig. 2 Architecture of the Web site using the framework

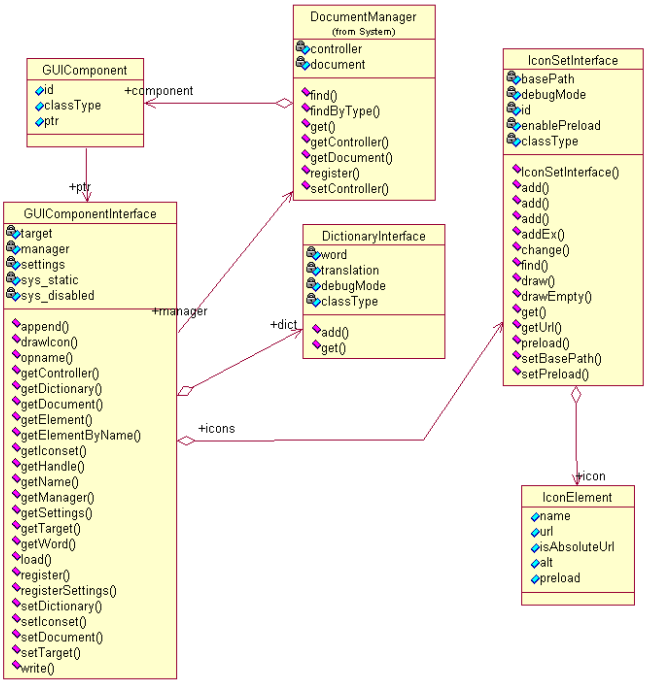

Fig 3 Framework's component class diagram

IV. Point of Integration

Since the framework was used for design and development of the entire client side of the BackOffice, we can sort its application into several categories:

- navigation development
- design and layout
- document manipulation
- management of components and managers

First three applications are described in the previous section. Last one represents extended functionality of the framework, as many components and managers were specially developed for the BackOffice purposes. Furthermore, framework's extendible architecture provides only solid basis for developing objects that are more advanced. As stated before, there are two types of objects used for extending framework's basic functionality – components and managers. Both components and managers are classes derived from *GUIComponent* base class. We can see from the class diagram shown on **Fig 3** that DocumentManager-class object knows about all registered components in the document. Important to say is that one Web page can contain multiple documents (stored in frames), and that framework defines only one DocumentManager-class object for each document on the page. Similar to Fascade design pattern [6], these managers possess logic how to manipulate components, and they act like an interface between controller object and the registered framework components. Document managers are connected with the Controller object, therefore creating the network of document managers with all the capabilities to interact with each other.

On the other hand, separation between dictionary object (DictionaryInterface), icon set object (IconSetInterface) and component (GUIComponentInterface) is crucial for the implementation of the concepts like customization, personalization and multilanguage support. In addition, these architecture represents the interface between client-side and server-side developers. Implementation files (definitions) of these classes are loaded in the beginning, but the setting object and dictionary object are defined by the server-side developers, who can, using this mechanism, change component's appearance or even add a new language.

V. BackOffice Design

Centura's BackOffice is quite different from the BackOffice sections of other Web CMS. Instead of having a standardized Web-based logic and layout, it possesses appearance and functionality of the desktop application. This provides much better "look and feel", a crucial factor when evaluating user-friendly environment.

As we can see on **Fig. 1**, BackOffice has Windows Explorer style layout. That means the screen area is divided into three main parts:

- Main menu and options area (on the top of the page)
- Navigation menu (on the left)
- Content (central part)

Navigation menu is implemented as a dropdown menu. Corresponding menu controller use dynamically created menu structure (*MenuDataInterface* derivate), and a class which implements dropdown menu (*MenuPresentationInterface* derivate).

Content area is loaded after a user selects a menu item (from the navigation menu). Framework supports seamless loading of the external pages into layout components, while the rest of the page stays intact. On contrary to the usual Web logic, rest of the page is not reloaded, which significantly decreases the download time. Loaded page is linked to the controller object, and therefore integrated into the system. Using this feature, several documents can interact with each other in a very simple and efficient way.

Seamless loading and multiple document manipulation happened to be extremely useful for purposes like selecting users, groups or items from the existing hierarchy. For this purpose, class named *ItemManager* has been designed and implemented. Menu structure is dynamically loaded only after the user requests the object of that class. On **Fig 3** we can see the *ItemManager* in action (in the opened window).

VI. Conclusion

Integration between the framework and the server side of the Centura CMS resulted in many significant improvements and benefits. Flexible and extendible architecture of the framework enables unlimited possibilities when designing Web site layout and user-friendly interface.

Our future work will be based on further integration of the framework and Centura CMS, in order to achieve even more flexible platform. That would provide advantages like online

design of the page or template layout and run-time customization and personalization of Web sites.

REFERENCES

[1] http://ciitlab.elfak.ni.ac.yu

[2] I. Petković, M. Stanković: *Object Oriented Web Client for Content Management Systems*, Proceedings of ICEST 2004, Bitola 16-19 June 2004, 289-292

[3] I. Petković: *Component Development of the Client Side of the Web Applications*; Proceedings of 6th International Conference on Telecommunications in Modern Satellite, Cable and Broadcasting Services, Telsiks 2003, October 2003.

[4] World Wide Web Consortium, *Document Object Model Level 3*, http:/ /www.w3.org/TR/2004/REC-DOM-Level-3-Val-20040127/

[5] I. Petković: *Component Development of the Client Side of the Web Applications*; Proceedings of 6th International Conference on Telecommunications in Modern Satellite, Cable and Broadcasting Services, Telsiks 2003, October 2003

[6] E. Gamma, R. Helm, R. Johnson, J. Vlissides: *Design Patterns*, Addison-Wesley, 1997

Multilingual Web Application Development on Unicode Database using Oracle XDK 10g

Daniela C. Nikolic[1], Jovanka D. Cekic[2], Milentije A. Maksimovic[3]

Abstract – **Data incorporated in XML are more self-describing and portable and can be easily shared, transformed, and transported across applications and platforms. In this paper we present a method for developing multilingual Web applications using Oracle XDK 10g - a standards-based set of components, tools and utilities – in order to provide automatic content delivering and update from Oracle10g database backend.**

Keywords – **multilingual web application, Oracle, Java, XML, XDK.**

I. INTRODUCTION

Development of the Internet has provided the companies around the world with the opportunity to optimize and expand their businesses. More than 90% of the world population is non-native English speaking. The challenge and the barrier towards a success on the global market is the development of applications with the support for different language and cultural requirements. A truly global Internet application needs to support data exchange in a wide range of character sets, and the user interface must present data in a format that matches the local convention of the user's language and country.

The Oracle 10g Database and Application server represent a fully internationalized platform for developing and deploying Internet applications with multilingual support. Oracle provides full support for Unicode 3.2 standard for storing, retrieving and updating data in different languages.

There are several approaches in the development of global Internet applications on Oracle 10g platform. [4] The solution presented in this paper is based on using one centralized database with a Unicode character set, and one instance of Oracle Application server. The application running on Oracle 10g AS is configured to support several locales simultaneously, so that each client can use different character set.

Oracle Application Server provides a possibility of developing applications using different programming languages and corresponding Web development environments. The HR application presented in this paper was developed using Java and XML technologies with XSLT extension function facility provided by Oracle XDK 10g and Oracle Application Server Containers for J2EE (OC4J).

II. XML AND DATABASE

XML is a markup language which can be run on any platform, operating system or environment and it is made in such a way to give designers mechanisms for better description of their content. XML does this by letting designers write their own document-type definitions – DTDs – which describe tags and attributes sets, and can be used for describing specific kinds of content. [1]

XML is fully internationalized for both European and Asian languages, with all conforming processors required to support the Unicode character set in both UTF-8 and UTF-16 encodings.

XML provides context for words, specifies document structure, and allows effective search capabilities. It is flexible, accessible and provides a universal format. [2]

Databases and XML offer complementary functionality for data storing. Database offers efficient retrieval, database administration, business intelligence, recovery tools and procedures, and blocking operations that compromise data integrity. XML offers easy information exchange, and interoperability between applications.

III. ORACLE XML SUPPORT

To help application developers in taking advantage of XML, Oracle Database 10g includes Oracle XML Developer's Kit (XDK). Oracle XDK 10g is a set of components, tools and utilities in Java, C, and C++ and available in Oracle Database 10g and Oracle Application Server 10g that ease the task of building and deploying XML-enabled applications.

Components of Oracle XDK are: XML Parsers, XSLT Processors, XSLT VM, XML Schema Processors, XML Java Beans, XML Class Generator, XML SQL Utility, XSQL Servlet, XML Pipeline Processor, and TransX Utility.

The overall XML infrastructure in Oracle database includes:

1. XMLType tables and views which provide the storage of XML data.
2. XML DB Repository which provides an XML document repository that is optimized for handling XML documents.
3. PL/SQL and SQL/XML functions which allow XML operations on SQL data and XML content.
4. Java and C XML programming which can be used to add functionality by building external procedures, such as creating

[1]Daniela C. Nikolic is with the University of Nis, Univerzitetski trg 2, 18000 Nis, Serbia and Montenegro, E-mail: eli@ni.ac.yu

[2]Jovanka D. Cekic is with the University of Nis, Univerzitetski trg 2, 18000 Nis, Serbia and Montenegro, E-mail: jovanka@ni.ac.yu

[3]Milentije A. Maksimovic is with the University of Nis, Univerzitetski trg 2, 18000 Nis, Serbia and Montenegro E-mail: maxa@ni.ac.yu

a Java Stored Procedure for SAX stream-based XML processing. [3]

The Oracle XDK provides the functionality to use standards-based interfaces to access, modify, transform, and validate XML documents.

IV. Designing XML Database for Web Applications

Before you start to design XML application using Oracle XML DB, you have to choose how to store XML data in a database, how to retrieve or generate XML, and how to create proper indexes for searching the content in the XML documents.

1. Storing XML data - There are different ways to store XML documents inside an Oracle XML database, and each of them offers different trade-offs in both performance and functionality. You can store XML documents in CLOB XMLTypes, XML Schema–based XMLTypes, relational tables, or external tables. In application presented in this paper CLOB XMLTypes are used, because this kind of storage best preserves the original format of XML documents and gives the maximum flexibility for XML schema evolution. Storing an intact XML document in a XML Type CLOB is a good strategy if the XML document contains static content that will only be retrieved as a whole or updated by replacing the entire document.

2. Loading XML data - Depending on the XML storage option chosen, you can use one of the associated data loading strategy in Oracle DB 10g: SQL*Loader, XML SQL Utility, TransX Utility, XSQL Servlet, HTTP / Web DAV, or FTP Interfaces. Upon insertion, XML documents are checked and only committed if well formed.

3. Generating and retrieving XML data - Oracle Database 10g provides the built-in support for XML, which greatly simplifies the retrieval of XML content and the conversion between relational datasets and XML-formatted data. You can generate XML from SQL data either with SQL XML functions or with PL/SQL package DBMS_XMLGEN.

4. Searching XML data – By storing XML data in Oracle DB 10g, you can create SQL indexes and enable users to efficiently search XML data. Oracle DB 10g provides two types of search on XML: the Xpath-based search provided along with the XML Type functions and the full text search using the Oracle DB component, Oracle Text. Oracle Text can provide both content and path indexes to search, but data retrievals need to be done by processing the whole document. [3]

V. System Architecture

XML is widely used in content management and Web publishing systems. One of the reasons is that data in XML format can easily be transformed by XSLT to various presentation formats, such as HTML, WML (Wireless Markup Language), SVG, or any other Web publishing format that clients request.

Application module presented in this paper represents human resource application that supports English and Serbian language, with XML data exchange.

Fig. 1 represents architecture of an Oracle 10g AS multilingual application and Oracle solution for XML document storage. It is mainly written in Java, using Java beans, and Java Server Pages (JSPs). It uses the Unicode capabilities available in Java, XML, JDBC, and the Oracle10g XML DB to support multilingual data and a multilingual user interface.

Clients access the Web application through a Web browser, passing chosen language as a parameter, which is then stored in the session data. The request is being redirected to the JSP page that instantiates a Java bean with business logic. The Bean accesses the database and extracts the XML data. Those data are transformed by XSLT JSP tag into the HTML UTF-8 encoded and than sent back to the client. An example is shown on the Fig. 2.

Database stores XML documents in XMLType column along with the appropriate encoding.

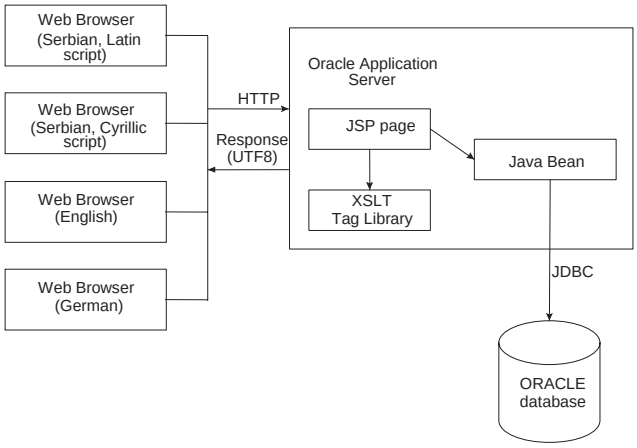

Fig. 1. System Architecture

VI. Multilingual Support

All the programming languages and technologies used for developing of this Web application have Unicode support.

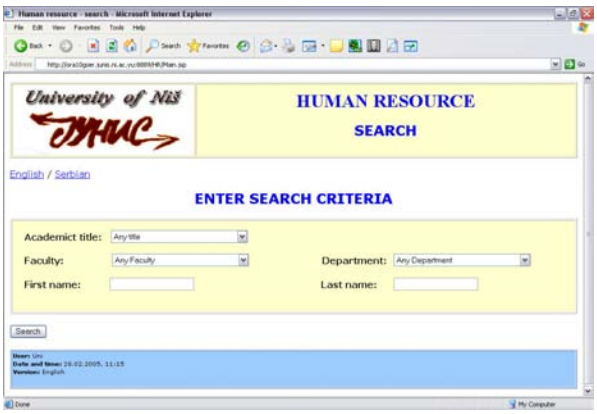

Fig. 2. Search page for HR application

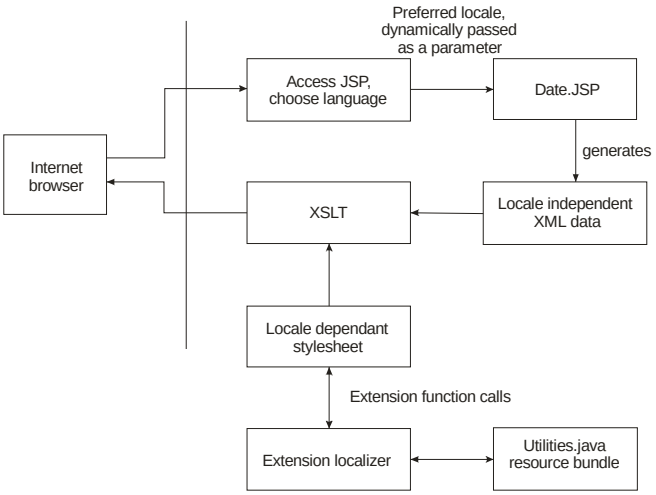

Fig. 3. Diagram of the data localization process

After the user selects a language, it is stored in the session parameters and used in data localization process, shown in Fig. 3. JSP first extracts locale-independent XML data from the database, and then forwards them to the XSLT transformation module. This module then transforms the data using locale-dependent XSL stylesheet (which also uses locale-dependent resource bundle with localized strings).

Multilingual support for the application is provided in the following way:

1. The localizer classes are used in this application to retrieve Locale-specific user interface prompts/resources. Every method accepts a valid ISO language code and returns the user interface prompt/resource string in that language. This application supports two Locales: English (en) and Serbian (sr). XSLT Stylesheet calls java function getInputProperty:

```
public static String getInputProperty(String s, String msg)
{
  Locale l    = new Locale(s);
  String lang = l.getLanguage();

  if (lang.equalsIgnoreCase("en") ||
lang.equalsIgnoreCase("sr"))  {

    // determine the session locale
    Locale        locale = new Locale(lang, "");
    // get the resource bundle for the locale
    ResourceBundle bundle =
ResourceBundle.getBundle("ApplicationMessages",
                                  locale);
    // return the translated message
    return bundle.getString(msg);
  }
  return "Error in Localizer";
}
```

2. Depending on the language function, corresponding file with all the prompts, messages and resources in that language is called. Example of English file:

```
bannertitle1=HUMAN RESOURSE
bannertitle2=SEARCH
...
```

For accessing Oracle 10g, database JDBC driver is used. This driver transparently converts the data stored in the database to and from Java strings. No special handling is necessary to access Unicode data stored in the database.

Search is implemented by doSearch method, which searches all property records for given criteria. If the given criteria is null or a string with 0 length, then that criteria is treated as a wildcard search. (All records will be selected for that field).

DBStatus object contains the result of the operation.

```
public DBStatus doSearch(String atitle, String faculty, String
department, String firstname, String lastname)
{
  String p_atitle;
  String p_faculty;
  String p_department;
  String p_firstname;
  String p_ lastname;

  //Do sanity check on the parameters passed
  if((atitle == null) || (atitle.length() == 0))
  {
    p_atitle = "%";
  }
  else
  {
    p_atitle = atitle.replaceAll("'", "") + "%";
  }
  ...
  DBStatus dbStatus = new DBStatus();
  if(conn == null)
  {
    dbStatus.flag = false;
    dbStatus.returnObject = "Database is not available";
    return dbStatus;
  }
  else
  {
    Statement stmt = null;
    ResultSet r = null;
    try
    {
      stmt = conn.createStatement();

      String query = "SELECT k.id, k.xml_data.getStringVal()
" + " FROM  kadrovi k" +
        " WHERE extractValue(k.xml_data,
'/PROPERTY/LOCATION/ATITLE/text()') LIKE '" + p_atitle
+ "' AND " + " extractValue(t.xml_data,
'/PROPERTY/LOCATION/FACULTY/text()') LIKE '" +
       p_faculty + "' AND " + "
extractValue(t.propertyxml,'/PROPERTY/LOCATION/DEPAR
TMENT/text()') LIKE '" + p_department + "' AND " + "
```

```
extractValue(t.propertyxml,'/PROPERTY/FIRSTNAME/text()')
>= '' + p_firstname + '' AND '' + ''
extractValue(t.propertyxml,'/PROPERTY/LASTNAME/text()')
>= '' + p_lastname;
      r = stmt.executeQuery(query);
      if(r == null)
      {
       dbStatus.returnObject = "Retrieved Null resultSet";
       dbStatus.flag = false;
      }
      else
      {
       Vector v = new Vector();
       XMLBean xb = new XMLBean();
       xb.setPropertySchema(requestURL);
       while(r.next())
       {
        Property p = xb.getPropertyObject(r.getString(2));
        p.propertyID = r.getString(1);
        v.add(p);
       }
       if(v.size() >= 1)
       {
        dbStatus.flag = true;
       }
       dbStatus.returnObject = v;
      }
     }
     catch(Exception e)
     {
      dbStatus.flag = false;
      dbStatus.ex = e;
      dbStatus.returnObject = "An error was generated while
searching property  records";
     }
     finally
     {
      try
      {
       stmt.close();
      }
       catch(SQLException sqe)
       {
       }
      }
      return dbStatus;
     }
```

VII. CONCLUSION

As XML becomes an integrated part of today's modern businesses, the need is critical for databases, application servers, and development tools that support the family of XML standards.

Because this support is entirely standards-based, businesses are assured that their application's interoperability will be maximized.

The Oracle XML Database (XML DB) refers to the collection of XML technologies built into the Oracle Database 10g, providing high-performance and in-built storage retrieval, and processing of XML. This in-built XML functionality is integrated with the Oracle-relational database server to bridge the gap between the relational table-row and XML hierarchical storage.

Oracle's programming interfaces – XML Developer's Kit (XDK) – provide a platform to efficiently build and deploy XML solutions.

REFERENCES

[1] N. Pitts: *XML In Record Time*^{TM}. Sybex Inc., 2000.

[2] D. S. Ray, E. J. Ray, *Mastering HTML and XHTML*, Sybex Inc., 2002.

[3] M. V. Scardina, B. Chang, J. Wang, Oracle Database 10g XML & SQL: Design, *Build & Manage XML Applications in Java, C, C++ & PL/SQL*, Berkeley, CA, McGraw-Hill/Osborne, 2004.

[4] T. M. Robertson, *Oracle Application Server 10g, Globalization Guide 10g (9.0.4)*, Oracle Corporation, 2003.

Using Semantic Web Technologies to Improve Web Searching of Human Resources

Goran S. Krstić

Abstract - **Today's web search engines do not rely or rely little on semantics. This paper considers potential possibilities of the Semantic Web, especially the field for improvement and advancement of the present web searching. In the end, it is given a possible scenario for searching human resources in the future semantic environment, which the Semantic Web should offer.**

Keywords - **Web searching, Semantic Web, Ontology, Human resources.**

I. INTRODUCTION

Efficient searching data on the Web mostly depends on the way they are organized and the mechanisms for representation the semantic contents within. The main problem about searching is not in search engines, but in the absence of meta data that would be built in web pages and would closer determine the meaning of those pages contents.

The Internet users still search the web due to keywords and hyperlinks in order to get to desired data. There is need for more efficient getting to searched information, but with spending less time. The Semantic Web should enable more efficient location of these data, when they become intelligible for both people and machines.

The central part in the Semantic Web vision occupies ontologies. The ontologies offer a possibility to work with heterogeneous representations of web resources and their interrelations. The ontologies enable for the web resources' contents and the information within to organize in predefined classes, which in the same time present certain knowledge from that domain [1].

The paper considers possibilities for improving searching the Web by using Semantic Web technologies. At the moment, there is a belief that the first to be created are the Semantic "isles", which would later be linked to the Semantic Web. In the end, it is given a scenario of a Semantic Web for searching human resources on the Web.

II. SEMANTIC WEB

The Semantic Web is a new layer in Internet which enables a semantic representation of the web pages contents [2].

A. Semantic Web Overview

The Semantic Web presents the extension of the existing Web, thus will contain many aspects of the latter, e.g. URI addressing model, protocols with small sets of commands, decentralization etc. The Semantic Web is still however, more a vision than reality [3].

The Semantic Web is based on the idea to create "machine intelligible" data that could be automated, integrated and used by different applications. By using the web language, e.g. RDF and OWL, it is possible to create semantic data models. These models are built on triples *resource-property-value.* A user can create his own classes and properties. Classes in Semantic Web languages are categories or types. Instances of those classes can be created and built up in web pages.

The Semantic Web is an attempt to make data readable to machines, the same way documents are readable to human. The Semantic web will, as well, enable software agents to perform certain actions and procedures automatically, which at present have to be performed manually, i.e. which existing applications cannot execute.

B. Semantic Web Technologies

W3C page on Semantic Web includes a diagram with semantic web architecture (www.w3.org/2000/talks/1206-xml2k-tbl/overview.html). According to this diagram, technologies are hierarchically ranged-from syntactic aspect to semantic meaning of data. The abridged presentation is given in Fig. 1:

Trust
Logic and Proof
Ontology
RDF Schema
RDF
XML Schema
XML

Fig. 1. The Semantic Web levels.

W3C is developing or has developed all the standards except the two at the top. Each level, as one can notice, is built based on the level below. The lowest level does not depend on any level above. Thus the levels can be developed independently. XML and XML Schema have become standards. RDF and OWL are recommendations. The other levels are developing.

Goran S. Krstić is with the Faculty of Economics, Trg kralja Aleksandra Ujedinitelja 11, 18000 Nis, Serbia and Montenegro, E-mail: gorca@ni.ac.yu

III. SEARCHING

Nowadays, the Internet searching is accomplished in the following manner: one inserts the terms being looked for, into the input box on a web page of a certain search location. The result comes out as an address list of the pages that satisfy the condition of searching. Most of the search locations offer also varieties of search aids. Yahoo was the first to define categories. They were not generated by using semantic web technologies, but they present the first usage of semantics on the Web. Many search locations offer additional terms for searching in keeping with a user's request.

No matter which search engine is used, the results that appear, in most cases are irrelevant hits, so that the user is forced to browse a large number of pages in order to get to the desired result.

A. Ttechniques for searching

Internet represents, so far, the greatest challenge for searching. Internet is the environment which is constantly developing and changing. It is inconsistent, and it contains documents of different types and structures. At the moment, there is no standard to index, catalogue, analyze or specify quality and performance of the search engines [3]. Some of the techniques for searching are the following:

Keywords. The most wide-spread approach for indexing on the web is searching resources due to the keywords list. When the user types one or more terms, the search engine tries to find them in its index. Addresses of the pages that contain inserted keywords, return as a result of searching.

It is considered that keywords, although they may be very useful, will not satisfy future growing needs for searching the Web.

Ontologies. Ontology is an explicit specification of the vocabulary for a certain domain; it includes definitions of classes, relations, properties, and limitations. Because of the great variety of data on the Web, the great number of ontologies is domain-directed or personalized in order to express individual or common interest [4]. Ontologies enable the web resource contents and information within, to organize in predefined classes.

The ideal case would be: when the computer itself could browse the contents of the documents, and according to the contents to classify it within a certain category. For example, let one category be "fiction". The computer browses a certain text and grasps that it is "fiction". Possible categories are specified by ontologies. Following that, terms used in queries should automatically map to the categories, provided in ontologies.

Alternatively, terms from ontologies may be presented to the user, who can choose one or more of them for a query. The categories contained in ontologies are presented to the user through corresponding interface, so he does not have to learn by heart all the categories and terms from the ontologies. The second approach is more realistic at the moment. The condition is that web pages be correctly marked, in accordance with ontologies.

Clustering. Search engines usually return a large number of results, which is hard to examine. It is desirable to group these results into adequate categories. Grouping the results into categories is called - *clustering*. One of the top search engines in clustering is Vivisimo (www.vivisimo.com). Vivisimo clusters short quotes from other search engines into *ad hoc* categories.

Ontologies can help in clustering because they enable explicit and clear classification of web resources in predefined categories. Clustering is a good way of presenting a large number of results to the user, and which will be worked on in the future.

B. The Possibilities of Semantic Web for searching improvement

In the present phase of web development is especially interesting the combining of free text searching with a possibility for using RDF meta data for searching [1, 4, 5].

The idea for Semantic Web is to add web pages marks that determine closer the meaning of those pages' contents. In a small domain certain ontology could be standardized, which would be later used by designers to describe the contents of the pages they create. Adding standard ontologies to web pages, enables above all, their better categorization. According to this, there is a need to enlarge the search engines' and agents' software, in order to extract these data. Documents marked in a standard way, using standard ontologies, can be classified better since the designer himself classifies a document into a certain category. In addition, the designer himself can determine the scale of classification, which would enable better ranging of the search results.

One of the advantages of machine readable meta data, as semantic marking, is that search engines can use it for performing additional semantic relations, i.e. they can perform inference.

Although there is a certain dose of doubt that the semantic searching will bring tremendously better results compared to traditional searching, using keywords, it could be expected that the semantic searching will improve the traditional one, offering:

- better categorization,
- possibilities for intelligent query extension and
- possibilities of inference.

In the future will be expected new methods, how the technologies developed for the Semantic Web can improve searching on the Web. One of the desired possibilities would be semantic analysis of the complete web pages' contents.

IV. A SCENARIO FOR SEARCHING HUMAN RESOURCES ON THE WEB

The scenario can be used as a demo or a vision. In both cases, the scenario can be viewed as a tool which helps technological innovations at different levels of a project development. Scenarios are useful for creating awareness on current technological limitations, as well as needs for their overcoming [6].

A. Scenario

The term ontology has roots in philosophy and implies a formal representation of concepts from a certain domain. Above all, they were introduced as ontologies on being. Thus it seems natural to use them for specifying human resources. In addition to this, man is a biological and social being, which implies many descriptions - ontologies. One of the possible scenarios is presented in Fig. 2.

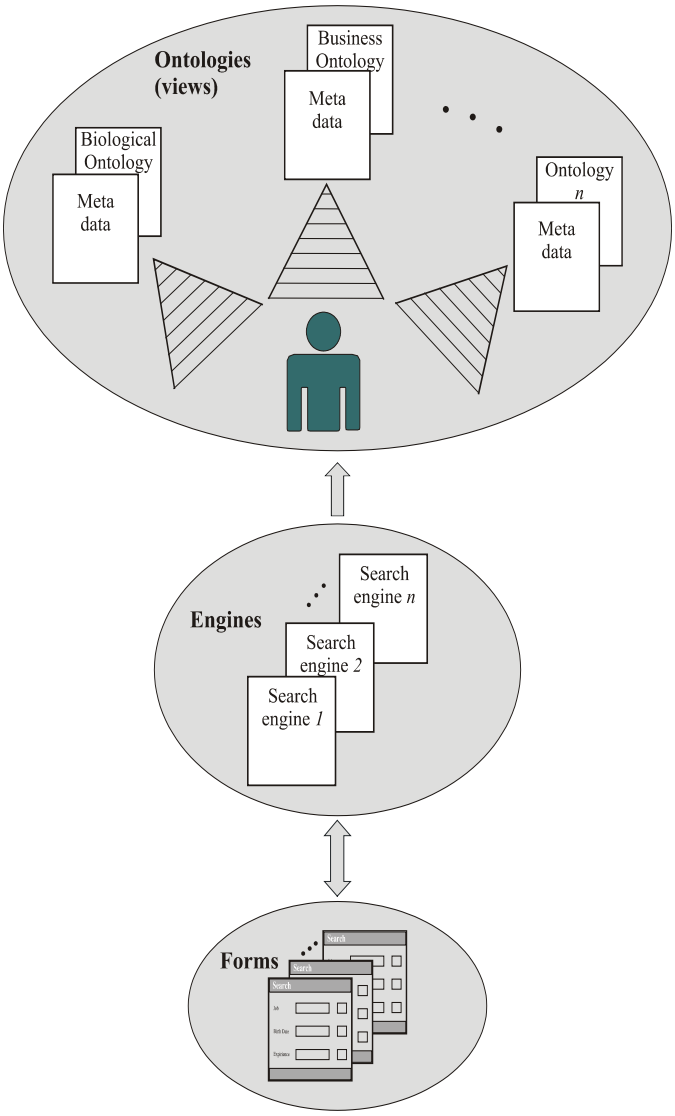

Fig. 2. A scenario for searching human resources.

Ontologies (biological, business, hobby etc.) represent various views of human being from various expects of observation. Using these ontologies, the web pages designers mark they web (home) pages. An example of embedding meta data into web pages is presented in Fig. 3. In the centralized environment, search engines cash out pages with meta data and then perform analyzing and indexing, in order to respond the user's queries. The system can be also distributed, where the role of searcher would take on specialized web agents. Meta data do not have to be known or visible to the user. They perform the searching by predefined forms, where each form corresponds on the structure of ontology.

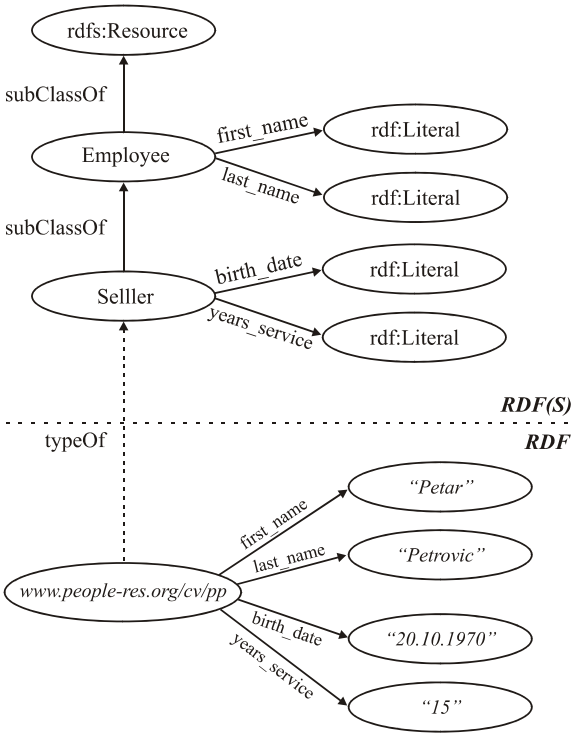

Fig. 3. Embedding meta data into web pages.

The *Employee* class has *first_name* and *last_name* properties. They are inherited in subclass *Seller*, which beside the mentioned has properties *birth_date* and *years_service*. It has to be emphasized that the approach here is to search employee categories before all, i.e. profile of employee is required, instead of person with a name, which exists anyway in the full text of a page, and it can be indexed in a classic manner. One part of RDF code which corresponds with the given example is:

```
...
xmlns=http://www.people-res.org/rdf/business#>
       <Seller rdf:about="http://www.people-
res.org/cv/pp.htm">
              <first_name>Petar</first_name>
              <last_name>Petrovic</last_name>
              <birth_date>20.10.1970</birth_date>
              <years_service>15</years_service>
              ...
       </Seller>
</rdf:RDF>
```

The user who does the searching does not have to know all the details, i.e. while searching he would be offered forms containing the list of classes (categories) and the properties from ontologies. While searching, at the same time user can use more then one ontology. In addition, the user can specify the coefficient of weight for each property, according to its significance for searching. As a result, one gets the matrix of weights:

$$W = \begin{bmatrix} w_{11} & w_{12} & \dots & w_{1n} \\ w_{21} & w_{22} & \dots & w_{2n} \\ \dots & \dots & \dots & \dots \\ w_{m1} & w_{m2} & \dots & w_{mn} \end{bmatrix}$$

Each row of the matrix presents weights of the properties from an ontology. Using weights, the user can emphasize how much is a certain property important for its searching (for example, from 1 to 10). The property not being requested from the user or not corresponding while being searched, automatically obtains the coefficient of 0 weights. The results are ranged according to the sum of matrix weights elements:

$$S = \sum w_{ij} \quad i = 1, m;\ j = 1, n$$

, so they range from the highest to the lowest.

During implementation of searching, it can be used the ontological indexing [1], i.e. the terms from ontologies are being indexed, similarly to indexing of keywords. Another method and more promising - is using some of the RDF query language. For example, RDF query language is SPARQL which is being developed by W3C.

The exposed scenario demands considerable verses of the web page designer in the ontology's contents. While users make queries trough offered forms, without need for knowing the ontologies themselves. Due to a relatively complex organization and a large number of possible ontologies, it should be expected that the role of ontology choice, and thus the domain of searching, undertake web services that would be specialized for certain domains of searching.

B. Approximate searching

The triples *object-attribute-value* can be observed as a separated case of the semantic nets [7]. In RDF we analogously have the triples *resource-property-value* (Fig. 4).

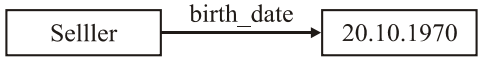

Fig. 4. An RDF triple.

A r*esource-property* relation is of the "*has"* type, and a *property-value* of the "*is"* type. This implies: Seller "has" birth_date and birth_date "is" 20.10.1970.

According to this, we can compare people. For this purpose, it can be used semantic nets metrics, where is applied the technique of conceptual distance. In this technique, the distance is calculated according to the number of arcs that are placed between the two concepts in the net. If the conceptual distance is small, the concepts are similar and vice versa (Fig. 5).

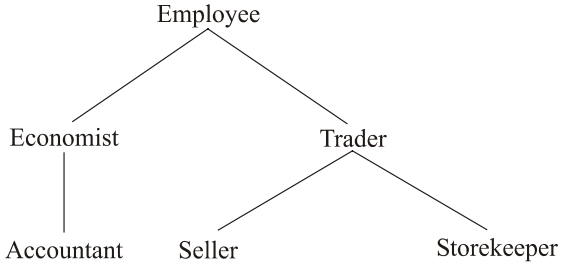

Fig. 5. A possible hierarchy of categories.

A person who is a seller is closer to a person who is a storekeeper, i.e. there is more similarity between them than with a person who works in the accountancy. The search software which is aware of this hierarchy, when there are not exact results, can retrieve approximate results. The user can specify the conceptual distance to which he wants to go, when there aren't exact hits.

V. CONCLUSION

The paper considers potential possibilities for applying the Semantic Web technologies for improving searching on the Web. The starting premises for realization of advanced semantic environment for retrieving human resources on the Web are given.

The Semantic Web is still more a vision than a real system. The result of implementation of presented scenario would be a distributed "database" of human resources. The advantage of this distributed database vs. centralized one is that every person would update the data on his Home page, without considering his geographic location. This would primarily contribute to search data more efficiently, providing approximate results when there are not exact hits. Further, it would provide more accurate data, better use of computer resources, and save cost of maintenance.

REFERENCES

[1] J. Davies, R. Weeks, "QuizRDF: Search Technology for the Semantic Web", *Proceedings of the 37th Hawaii International Conference on System Sciences*, 2004.

[2] T. *Berners*-Lee, J. Hendler, O. Lassila, "A new form of Web content that is meaningful to computers will unleash a revolution of new possibilities", *Scientific American*, May 2001.

[3] T. B. *Pasin*, *Explorer guide to the Semantic Web*, Manning, 2004.

[4] J. *Pokorny*, "Web Searching and Information Retrieval", *Computing in Science & Engineering*, July/August 2004.

[5] A. *Fernandes*, A. C. Moura, F. Porto, "An Ontology-Based Approach for Organizing, Sharing, and Queering Knowledge Objects on the Web", *Proceedings of the 14th International Workshop on Database and Expert Systems Applications (DEXA'03)*, 2003.

[6] M. *Visciola*, "Search Types and Context of Use in the Semantic Web", *Proceedings of the Fourth International Conference on Web Information Systems Engineering (WISE'03)*, 2003.

[7] Ž. Ristić, Z. Bošnjak, N. Balaban, *Ekspertni sistemi*, Savremena administracija, Beograd, 1993.

Internet Traffic Analysis System Based on Data Mining and OLAP

Jovanka D. Cekic[1], Saša B. Spasic[2]

Abstract – **The application of Data Mining and OLAP technologies in the Internet traffic analysis is described in this paper. It presents one of the solutions for the analysis of log files and data provided over SNMP protocol based on Open Source tools, whose low price facilitates its employment in small and medium-size enterprises.**

Keywords – **Internet traffic analysis, data mining, OLAP**

I. Introduction

Internet traffic data analysis is a very important part of Internet engineering and management, because traffic data measure very complex characteristics of network traffic. The vastness of the Internet network topology, together with complex statistical properties of Internet traffic data and very large databases, make the analysis very challenging. In this paper we present a method of analyzing log files of different applications and devices on the network, which can contain very heterogeneous data – IP addresses, timestamps, actions taken, response, etc, and can result in very large database.

The success of analysis itself depends mainly on ability to analyze the log database in detail. It is important to explore the raw data, because relying only on summaries only could be inadequate. Therefore, we have chosen data mining and OLAP techniques to perform a complex and necessary analysis.

Data mining, also known as "knowledge-discovery in databases (KDD)**",** has been defined as "The science of extracting useful information from large data sets or databases" [1]. It usually uses computational techniques from statistics and pattern recognition and is usually used in relation to analysis of data.

Online Analytical processing (OLAP) is an approach to quickly providing the answer to complex database queries, and is used in business reporting for sales, marketing, management reporting, data mining and similar areas. [2]

II. Data Mining Using OLAP

OLAP technology enables efficient use of large databases for online analysis, providing quick responses to complex analytical queries.

OLAP uses multidimensional data model and data aggregation techniques to organize and summarize large amounts of data, so it can be viewed and analyzed using online analysis and graphical tools. OLAP systems provide speed and flexibility to support real time analysis. [3]

The most efficient way of organizing an OLAP database is a multidimensional Cube that is sometimes called a database of subtotals.

Multidimensional cubes are created from data in the data warehouse fact and dimension tables. A fact table contains the measurements or facts of business processes and foreign keys for the dimension tables. [4] Dimension tables contain the context (i.e. characteristics) of the measurements. Each dimension table contains data for one dimension. The Dimension Attributes are the various columns in a dimension table. Dimension tables indicate how the aggregations of relational data can be analyzed. Dimension data are hierarchically organized. Multidimensional structures in which cubes are stored are specially designed for rapid query response, and they can contain data summarized, copied or directly read from the data warehouse [5].

Storing data in OLAP cubes, instead of in relational tables, provides more efficient way of retrieving data for reporting purposes. The key concept that provides faster data retrieval from the cubes is data aggregation. It is much easier to retrieve data that are already associated, than to perform a complex relational database search.

OLAP servers are categorized according to the way of data storage: Multidimensional OLAP (MOLAP), Relational OLAP (ROLAP), and Hybrid OLAP (HOLAP) [2].

In a MOLAP model cubes are stored in multidimensional database files. Data are stored on disk, in structures optimized for multidimensional access. The required schema contains a dimensional set of both base data and aggregations. Data access is very fast, and memory usage is very high.

In a ROLAP-model a multidimensional data cube is mapped to relational model, so that one cube is mapped to several relational tables. Special tables are created to hold the aggregation information.

HOLAP (Hybrid OLAP) combines these two models – multidimensional database files and relational tables.

III. Operations on the Cube

What gives the extra qualities to the analysis of the Cube, are operations on presented data. The user starts from one view of the data, choosing two dimensions for X and Y axis, and fact data for the table fields. The following operations are available:

1. Drill-down – a view of data more precisely grouped on the lower level of hierarchy.
2. Slice – segment selection on one dimension.
3. Dice – changing of chosen dimensions for the view

[1]Jovanka D. Cekic is with the University of Nis, Univerzitetski trg 2, 18000 Nis, Serbia and Montenegro, E-mail: jovanka@ni.ac.yu
[2]Sasa B. Spasic is with the "IRVAS" International, Nikole Pasica 32/4, 18000 Nis, Serbia and Montenegro E-mail: spaske@irvas.co.yu

IV. Architecture of an OLAP Based System

The Fig. 1. represents the architecture of a system based on OLAP. The transaction data repository contains data created by the application or the system that is being analyzed. These can, for example, be on-line sales data or, in this case, log files produced by the applications or devices in the computer network.

Data import procedure is a scheduled task (it is executed once per hour or day, or more often, depending on the data nature). It analyzes transactional data and writes them into the Cube, i.e. multidimensional database.

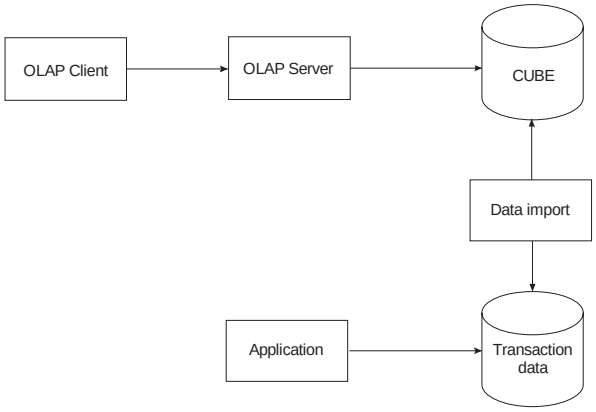

Fig 1. Typical OLAP system architecure

There is a large number of tools that can be used for implementing this kind of system. Microsoft offers a set of its own tools:

1. OLAP client – Excel pivot table
2. OLAP server – MS Analysis Server
3. Cube – MS Analysis Server
4. Transactional Data – MS SQL
5. Protocol between OLAP client and server - MS proprietary protocol using OLE DB provider for OLAP

Client and server can also be implemented using open source technologies:

1. OLAP client – Internet browser as a client, and Jpivot (jpivot.sf.net) as a Web application
2. OLAP Server – Mondrian [4]
3. Cube – any RDBMS can serve as a ROLAP repository (for example MySQL)
4. Transactional data – MySQL, log files etc.
5. Protocol – a custom protocol implemented using TCP/IP or XML/A

Also, there is a large number of very complex systems that implement data mining using OLAP, but their price as well as the price of their deployment (which often goes up to several hundreds thousand dollars) makes them unprofitable for application in the Internet traffic analysis.

The system presented on the Fig. 2 is based on ROLAP and open source technologies - Jpivot is used as an OLAP client and Mondrian as an OLAP server Therefore, it can be used for almost any type of analysis, because it provides a possibility of very fast data retrieval on one side and has a very low price on the other.

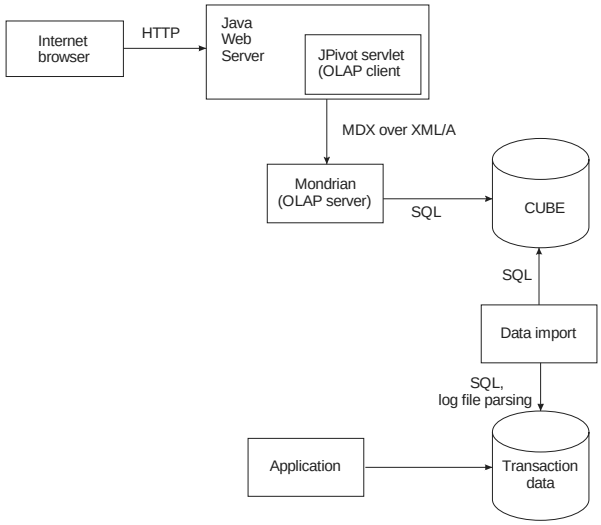

Fig 2. Applied OLAP system architecture

V. MDX – OLAP query language

MDX is an acronym for **M**ulti**d**imensional E**x**pressions. It is defined by Microsoft as "a syntax that supports the definition and manipulation of multidimensional objects and data" [3]. MDX is in many ways similar to SQL (Structured Query Language), but it is not an extension of the SQL. SQL cannot be used for so efficient an implementation of the features supplied by MDX.

Like SQL query, each MDX query requires a data request (the SELECT clause), a starting point (the FROM clause), and a filter (the WHERE clause). In that way specific portions of data can be easily extracted for analysis. MDX also contains a large set of functions for the data manipulation, as well as the ability to be extended with user-defined functions.

MDX also provides data definition language (DDL) syntax for managing data structures. It has commands for creating (and deleting) cubes, dimensions, measures, and their subordinate objects.

The purpose of Multidimensional Expressions (MDX) is to make data access easier and more intuitive by using multiple dimensions. MDX returns a subset of multidimensional data from cubes.

VI. XML/A – Web service for MDX queries

XML for Analysis, or XML/A [6], [7], formerly called Thin OLAP, is designed specifically for standardizing the protocol (communication between a client application and a data provider) over the HTTP. It implements the protocol by use of SOAP Web services. This standard has been supported by Microsoft, and the next releases of Microsoft Excel are expected to have a direct support for XML/A access to OLAP server. It supports the exchange of analytical data between clients and servers on any platform and with any language.

VII. ROLAP TOOLS

As we have chosen the ROLAP model and the open source tools for the Internet traffic analysis, the role of OLAP client component is taken over by Jpivot. Jpivot is a Java Web application, which runs on Java Servlet Container (for example Tomcat), and is by the way of working very similar to Excel pivot tables. Mondrian, which is also Java Web application, takes the role of an OLAP server, which provides XML/A Web service as a communication interface, and also a special protocol that runs over TCP/IP.

There are two more components missing for the completion of the system:

1. The component that creates and prepares ROLAP tables for the data, configuration files for Mondrian and Jpivot.

2. The component for incremental import of the analyzed data into the ROLAP tables.

VIII. DATA COLLECTING PROGRAM FOR ANALYSIS FROM SNMP AND LOG FILES

The system for analysis has to be applicable to arbitrary log files. Therefore, it is necessary to describe the contents of a log and the log files rotation strategy by means of an additional configuration file.

The part of the application related to data import part on the Fig. 2. contains two modules:

1. The first module analyses configuration files that contain the description of the repository with transactional data (log files, their position on disk and format, SNMP - Simple Network Management Protocol, data source, calculated data) and creates ROLAP mapping of the Cube. Additionally, this module creates a configuration for Mondrian and Jpivot based on configuration files.

2. The second module, which is executed periodically, analyzes log files, i.e. SNMP data sources and incrementally inserts data into the Cube.

IX. MODULE FOR ROLAP TABLES CREATION

Transactional data shown on the Fig. 1, which are monitored in a computer network, can be divided into two sets:

1. Log files with transactions
2. Traffic load on network-links

When a log file is the data source for the first module, for example a Web server log file, each data, except load (which is fact, or in Mondrian terminology measure column of fact table), is being declared a dimension. Dimension hierarchies are organized on that occasion, too:

1. Dates are grouped by month, and next on the higher level by year.

2. HTTP status codes can be grouped in the way described in HTTP specification [8] (1xx – informational, 2xx – success, 3xx – redirection, 4xx – client side errors and 5xx – server side errors).

3. URLs are grouped according to the configuration file.

4. IP address of the client grouped by arbitrary criteria (domain, country, geographic position etc).

In the configuration file, it is possible to define additional dimensions according to an arbitrary HTTP header or cookie. In that way it is possible to obtain the following data:

1. The data about browser, that are classified according to the browser type (Internet Explorer, Mozilla, etc.) on the higher, and according to the browser version on the lower level.

2. The data about users, which are classified by the application they are using (for example unregistered visitors, registered visitors, application administrators, etc).

3. The data about sessions, which are recognized on the basis of cookies, URLs or combined (that is very common with Java Web applications).

4. Hosts with virtual hosting can be classified according to different criteria.

If the data sources are SNMP queries, the first module recognizes the following data types as dimensions:

1. Octet String
2. Display String
3. Object Identifier
4. IP Address
5. Physical Address
6. Time Ticks

The following data types are recognized as a measure:

1. Integer
2. Counter
3. Gauge

Sometimes, the data for measure types represent dimensions, and they can be configured in that manner.
SNMP Sequences can be analyzed by treating their components separately, as a measure, dimension or a sequence, what is also defined in the configuration file.

The configuration file provides a possibility to define Calculated Members (with Mondrian) using a formula based on Measure data. Additionally, this module creates tables for storing data about the last import, provided by the module for update. That provides this module the possibility to operate incrementally.

X. MODULE FOR INCREMENTAL DATA UPDATE

In the case that data source is a log file, the module for incremental data update extracts a new part of the log, according to the existing data related to the last update and the strategy of log files rotation, and copies the data into the fact

table, updating in that way the dimension tables and inserting missing coordinates.

If the fact table contains calculated data, the module makes calculations based on the configured formulae, and stores the results in corresponding fact table columns. In case of SNMP data source the queries are sent by means of SNMP 2.x or 3.x protocol, and the further data processing is identical as with log files.

At the end of update the data about module progress are recorded, so that the next update would be incremental.

XI. Conclusion

ROLAP model has its limitations in comparison with MOLAP, because a model for generating indexes for relational tables cannot be efficiently used for indexing a database created in this manner. Also, a similar problem occurs when two dimensions are represented on a higher level of hierarchy – sometimes, in order to get a query results, it is necessary to analyze very large number of records from the fact table.

Mondrian has a caching mechanism that enables it to exceed these disadvantages, but it is not that efficient as with MOLAP.

The main advantage of this system is that OLAP Analysis offers more possibilities in comparison with common static analyses regarding data search (for example the impact of one separate component on the whole system or the web application parts efficiency), which may be incomplete in the classic analysis.

The low price of the software being used and open source components allows this solution to be used in smaller networks and enterprises where the internet traffic itself is of no primary importance. The components are, nevertheless, fast enough to make the analysis interactive.

References

[1] D. Hand, H. Mannila, P. Smyth: *Principles of Data Mining*. MIT Press, Cambridge, MA, 2001.

[2] E.F. Codd, S.B. Codd, C.T. Salley: “Providing OLAP (on-line analytical processing) to User-Analysts: An IT Mandate”, *Technical Report*, 1993 http://www.hyperion.com/products/whitepapers/

[3] Microsoft, *OLE DB Programmer's Reference*, Chapter 26, http://msdn.microsoft.com/library/default.asp?url=/library/en-us/oledb/htm/olapmdxgrammar.asp

[4] Julian Hyde, *How to design a Mondrian schema*, http://mondrian.sourceforge.net/schema.html

[5] Ming-Syan Chen, Jiawei Hah, Philip S. Yu: “Data Mining: An Overview from a Database Perspective”, *Ieee Trans. On Knowledge And Data Engineering*, 1997 http://cgi.di.uoa.gr/~pms510/Papers/han.pdf

[6] Robin Grosset, *The case for XML for Analysis*, http://www.xmla.org/download.asp?id=83

[7] Microsoft, Hyperion, *XML for Analysis Specification, Version 1.0*, http://www.xmla.org/download.asp?id=2

[8] World Wide Web Consortium, Hypertext Transfer Protocol - HTTP/1.1, 1999, http://www.ietf.org/rfc/rfc2616.txt

(5, 2) - Formal Languages

Violeta Manevska[1], Donco Dimovski[2]

Abstract – **The aim of this paper is to define a (5,2)-semigroup automata on free (5,2)-semigroup, with a special attention on (5,2)-formal languages recognizable by them.**

Keywords - **(5,2)-semigroup, (5,2)-semigroup automaton, (5,2)-language**

I. INTRODUCTION

Our goal in writing this talk is to examine a (5,2)-formal language and to proof some properties about them. In that means, we are given an example.

II. (5,2)-SEMIGROUPS AND (5,2)-SEMIGROUP AUTOMATA

Here we recall the necessary definitions and known results. From now on, let B be a nonemty set and let $(B,\cdot)$ be a semigroup, where $\cdot$ is a binary operation.

A semigroup automaton is a triple $(S,(B,\cdot),f)$, where S is a set, $(B,\cdot)$ is a semigroup, and $f: S\times B\to S$ is a map satisfying

$$f(f(s,x),y)=f(s,x\cdot y), \tag{1}$$

for every $s\in S$, $x,y\in B$.

The set S is called the set of **states** of $(S,(B,\cdot),f)$ and f is called the **transition function** of $(S,(B,\cdot),f)$.

A nonempty set B with the (5,2)-operation $\{\}: B^5\to B^2$ is called **a (5,2)-semigroup** iff the following equality

$$\{\{x_1^5\}x_6^8\}=\{x_1\{x_2^6\}x_7^8\}=\{x_1^2\{x_3^7\}x_8\}=\{x_1^3\{x_4^8\}\} \tag{2}$$

is an identity for every $x_1,x_2,x_3,x_4,x_5,x_6,x_7,x_8\in B$. It is denoted with the pair $(B,\{\})$.

Example 1: Let $B=\{a,b\}$. Then the (5,2)-semigroup $(B,\{\})$ is given by Table 1.

This example of (5,2)-semigroup is generated by an appropriate computer program.

A (5,2)-semigroup automaton is a triple $(S,(B,\{\}),f)$ where S is a set, $(B,\{\})$ is a (5,2)-semigroup, and $f: S\times B^4\to S\times B$ is a map satisfying

$$f(f(s,x_1^4),y_1^3)=f(s,\{x_1^4y_1\},y_2^3)=$$
$$=f(s,x_1,\{x_2^4y_1^2),y_3)=f(s,x_1^2,\{x_3^4y_1^3\}), \tag{3}$$

for every $s\in S$, $x_1,x_2,x_3,x_4,y_1,y_2,y_3\in B$.

TABLE 1
(5,2)-SEMIGROUP

{ }	
a a a a a	(a,a)
a a a a b	(a,a)
a a a b a	(a,a)
a a a b b	(a,a)
a a b a a	(a,a)
a a b a b	(a,a)
a a b b a	(a,a)
a a b b b	(a,a)
a b a a a	(a,b)
a b a a b	(a,b)
a b a b a	(a,b)
a b a b b	(a,b)
a b b a a	(a,b)
a b b a b	(a,b)
a b b b a	(a,b)
a b b b b	(a,b)
b a a a a	(b,a)
b a a a b	(b,a)
b a a b a	(b,a)
b a a b b	(b,a)
b a b a a	(b,a)
b a b a b	(b,a)
b a b b a	(b,a)
b a b b b	(b,a)
b b a a a	(b,b)
b b a a b	(b,b)
b b a b a	(b,b)
b b a b b	(b,b)
b b b a a	(b,b)
b b b a b	(b,b)
b b b b a	(b,b)
b b b b b	(b,b)

The set S is called the set of **states** of $(S,(B,\{\}),f)$ and f is called the **transition function** of $(S,(B,\{\}),f)$.

2.1⁰ Let $(S,(B,\cdot),\varphi)$ be a semigroup automaton. Then $(S,(B,\{\}),f)$ is a (5,2)-semigroup automaton with (5,2)-operation $\{\}: B^5\to B^2$ defined by

$$\{x_1^5\}=(x_1\cdot x_2\cdot x_3\cdot x_4,x_5)$$

and the transition function $f: S\times B^4\to S\times B$ defined by

$$f(s,x_1^4)=(\varphi(s,x_1\cdot x_2\cdot x_3\},x_4).$$ ■

[1]Violeta Manevska is with the University "St. Clement Ohridski"-Bitola, Faculty of Technical Sciences, Bitola, Ivo Lola Ribar b.b. 7000 Bitola, Macedonia,e-mail:violeta.manevska@uklo.edu.mk
[2]Donco Dimovski is with the Univesity "Sts. Cyril and Methodus"-Skopje, Faculty of Mathematics and Natural Sciences, Institute of Mathematics,e-mail: donco@iunona.pmf.ukim.edu.mk

2.2⁰. If $(S,(B,\{\}),f)$ is a (5,2)-semigroup automaton, then for every $c \in B$:

i) $(B^2,*_c)$ is a semigroup, where the operation $*_c$ is defined by $(x,y)*_c(u,v)=\{xycuv\}$ for every $(x,y),(u,v)\in B^2$;

(ii) $(S,(B^2,*_c),\psi)$ is a semigroup automaton, where the transition function $\psi: S\times B\times B^2 \to S\times B$ is defined by $\psi((s,a),(x,y))=f(s,a,x,y,c)$. ■

Example 2: Let $(B,\{\})$ be a (5,2)-semigroup given by Table 1 from Example 1 and $S=\{s_0,s_1,s_2\}$. A (5,2)-semigroup automaton $(S,(B,\{\}),f)$ is given by Table 2 and the graph in Fig. 1 .

This example of (5,2)-semigroup automaton is generated by computer.

TABLE 2
(5,2)-SEMIGROUP AUTOMATON

f	s_0	s_1	s_2
a a a a	(s_1,a)	(s_1,a)	(s_2,a)
a a a b	(s_1,a)	(s_1,a)	(s_2,a)
a a b a	(s_1,a)	(s_1,a)	(s_2,a)
a a b b	(s_1,a)	(s_1,a)	(s_2,a)
a b a a	(s_2,b)	(s_1,a)	(s_2,a)
a b a b	(s_2,b)	(s_1,a)	(s_2,a)
a b b a	(s_2,b)	(s_1,a)	(s_2,a)
a b b b	(s_2,b)	(s_1,a)	(s_2,a)
b a a a	(s_1,a)	(s_2,a)	(s_2,b)
b a a b	(s_1,a)	(s_2,a)	(s_2,b)
b a b a	(s_1,a)	(s_2,a)	(s_2,b)
b a b b	(s_1,a)	(s_2,a)	(s_2,b)
b b a a	(s_2,a)	(s_2,b)	(s_2,b)
b b a b	(s_2,a)	(s_2,b)	(s_2,b)
b b b a	(s_2,a)	(s_2,b)	(s_2,b)
b b b b	(s_2,a)	(s_2,b)	(s_2,b)

III. FREE (5,2)-SEMIGROUPS AND (5,2)-SEMIGROUP AUTOMATA ON THEM

Let B be a nonempty set. We define a sequence of sets $B_0, B_1, ..., B_p, B_{p+1}, ...$ by induction as follows:

$B_0 = B$.

Let B_p be defined, and let A_p be the subset of B_p of all the elements u_1^{2+3s}, $u_\alpha \in B_p, s \geq 1$. Define B_{p+1} to be $B_{p+1} = B_p \cup A_p \times \{1,2\}$.

Let $\overline{B} = \bigcup_{p\geq 0} B_p$. Then $u \in \overline{B}$ iff $u \in B$ or $u = (u_1^{2+3s}, i)$ for some $u_\alpha \in \overline{B}, s \geq 1, i \in \{1,2\}$.

Define a length for elements of $\overline{B}$, i.e. a map $|\ |: \overline{B} \to N$ (N is a set of positive integers) as follows:

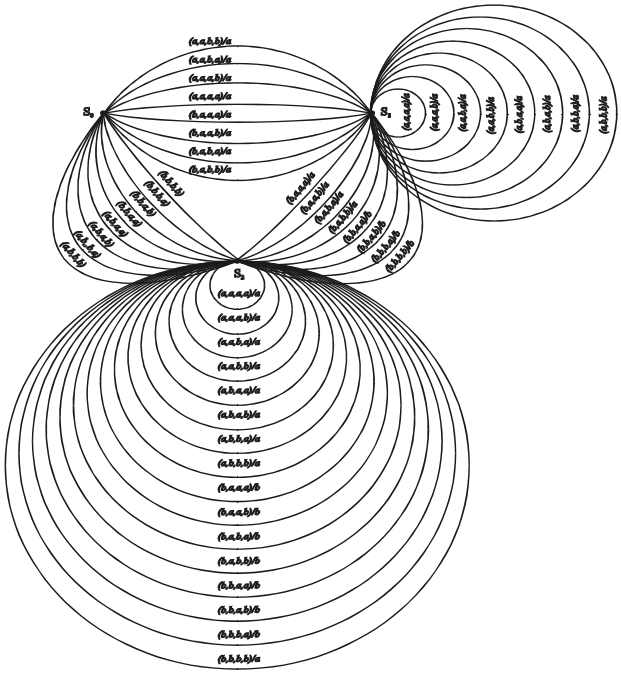

Fig. 1 (5,2)-semigroup automaton

1^0 If $u \in B$, then $|u| = 1$;

2^0 If $u = (u_1^{2+3s}, i)$, then $|u| = |u_1| + |u_2| + ... + |u_{2+3s}|$.

By induction on the length we are going to define a map $\varphi: \overline{B} \to \overline{B}$. For $b \in B$, let $\varphi(b) = b$. Let $u \in \overline{B}$ and suppose that for each $v \in \overline{B}$ with $|v| < |u|$, $\varphi(v) \in \overline{B}$ and

(1) If $\varphi(v) \neq v$, then $|\varphi(v)| < |v|$;

(2) $\varphi(\varphi(v)) = \varphi(v)$.

Let $u = (u_1^{2+3s}, i)$. Then, for each α, $\varphi(u_\alpha) = v_\alpha \in \overline{B}$ is defined, $|\varphi(u_\alpha)| \leq |u_\alpha|$ and $\varphi(\varphi(u_\alpha)) = \varphi(u_\alpha)$. Let $v = (v_1^{2+3s}, i)$.

(i) If for some α, $u_\alpha \neq v_\alpha$, then $|v_\alpha| < |u_\alpha|$, and so, $|v| < |u|$. In this case let $\varphi(u) = \varphi(v)$.

Because $|v| < |u|$, it follows that $\varphi(v)$ is defined, and moreover, (1) and (2) imply that

$|\varphi(u)| = |\varphi(v)| \leq |v| < |u|$, $\varphi(u) \neq u$ and

$\varphi(\varphi(u)) = \varphi(\varphi(v)) = \varphi(v) = \varphi(u)$.

(ii) Let $u_\alpha = v_\alpha$ for each α. Then $u = v$. Suppose that there is $j \in \{0,1,...,3s\}$ and $r \geq 1$, such that $u_{j+\nu} = (w_1^{3r+2}, i)$ for each $\nu \in \{1,2\}$ and let t be the smallest such j. In this case, let

$\varphi(u) = \varphi(u_1^t w_1^{3r+2} u_{t+4}^{3s+2}, i)$.

Because $\left|(u_1^t w_1^{3r+2} u_{t+4}^{3s+2}, i)\right| < |u|$ it follows that $\varphi(u)$ is well defined, and moreover, (1) and (2) imply that $\varphi(u) \neq u$, $|\varphi(u)| < |u|$ and $\varphi(\varphi(u)) = \varphi(u)$.

(iii) If $\varphi(u)$ can't be defined by (i) or (ii), let $\varphi(u) = u$. In this case, $\varphi(\varphi(u)) = \varphi(u) = u$ and $|\varphi(u)| = |u|$.

The above discusion and (i), (ii) and (iii) complete the inductive step, and so we have defined a map $\varphi : \overline{B} \to \overline{B}$. Moreover, we have proved the folloing:

Lemma: (a) For $b \in B$, $\varphi(b) = b$;

(b) For each $u \in \overline{B}$, $|\varphi(u)| \leq |u|$;

(c) For $u \in \overline{B}$, if $\varphi(u) \neq u$, then $|\varphi(u)| < |u|$;

(d) For each $u \in \overline{B}$, $\varphi(\varphi(u)) = \varphi(u)$. ■

Now, let $Q = \varphi(\overline{B})$. By Lemma (d),

$Q = \{u \mid u \in \overline{B}, \varphi(u) = u\}$.

Define a map $[\ ] : Q^5 \to Q^2$, by $[u_1^5] = (v_1^2)$

$\Leftrightarrow v_i = \varphi(u_1^5, i)$ for each $i \in \{1,2\}$.

Because $u_j \in Q$, it follows that $(u_1^5, i) \in \overline{B}$, and so $\varphi(u_1^5, i) \in Q$ for each $i \in \{1,2\}$. Hence $[\ ]$ is well defined.

Theorem: $(Q, [\ ])$ is a free (5,2)- semigroup with a basis B. ■

Let $(S, (B, \{\ \}), f)$ be a (5,2)-semigroup automaton.

Now, we define a sequence of maps

$\psi_0, \psi_1, ..., \psi_p, \psi_{p+1}, ...$ for a sequence of sets

$B_0, B_1, ..., B_p, B_{p+1}, ...$ by induction as follows:

$\psi_0 : B_0 \to B_0$ with $\psi_0(b) = b$, for each $b \in B_0$;

$\psi_1 : B_1 \to B_0$ with $\psi_1(b_1^n, i) = \{b_1^n\}_i$;

$\psi_2 : B_2 \to B_0$ with $\psi_2(u_1^n, i) = \{\psi_1(u_1)...\psi_1(u_n)\}_i$

$\vdots$

$\psi_p : B_p \to B_0$ with

$$\psi_p(u_1^n, i) = \{\psi_{p-1}(u_1)...\psi_{p-1}(u_n)\}_i$$

$\vdots$

Because $\overline{B} = \bigcup_{p \geq 0} B_p$, we define a map $\psi : \overline{B} \to B_0$ with $\psi(u) = \psi_p(u)$ for $u \in \overline{B}$ and $|u| \leq p$. Now we will prove that ψ is well defined. If

$u = (u_1^r (w_1^{2+3s}, i_1)(w_1^{2+3s}, i_2) u_{r+3}^{2+3t}, i)$,

$v = (u_1^r w_1^{2+3s} u_{r+3}^{2+3t}, i)$

and $\varphi(u) = \varphi(v)$, we have to prove that $\psi(u) = \psi(v)$. We have

$$\psi(u) = \psi_p(u) =$$

$$= \psi_p(u_1^r (w_1^{2+3s}, i_1)(w_1^{2+3s}, i_2) u_{r+3}^{2+3t}, i) =$$

$$= \{\psi_{p-1}(u_1)...\psi_{p-1}(u_r)\psi_{p-1}(w_1^{2+3s}, i_1)\psi_{p-1}(w_1^{2+3s}, i_2)$$
$$\psi_{p-1}(u_{r+3})...\psi_{p-1}(u_{2+3t})\}_i =$$

$$= \{\psi_{p-1}(u_1)...\psi_{p-1}(u_r)\{\psi_{p-2}(w_1)...\psi_{p-2}(w_{2+3s})\}_{i_1}...$$
$$\{\psi_{p-1}(w_1)...\psi_{p-2}(w_{2+3s})\}_{i_2} \psi_{p-1}(u_{r+3})...\psi_{p-1}(u_{2+3t})\}_i =$$

$$= \{\psi_{p-1}(u_1)...\psi_{p-1}(u_r)\psi_{p-1}(w_1)...\psi_{p-1}(w_{2+3s})$$
$$\psi_{p-1}(u_{r+3})...\psi_{p-1}(u_{2+3t})\}_i .$$

Also,

$$\psi(v) = \psi_p(v) = \psi_p(u_1^r w_1^{2+3s} u_{r+3}^{2+3t}, i) =$$
$$= \{\psi_{p-1}(u_1)...\psi_{p-1}(u_r)\psi_{p-1}(w_1)...\psi_{p-1}(w_{2+3s})$$
$$\psi_{p-1}(u_{r+3})...\psi_{p-1}(u_{2+3t})\}_i .$$

Hence $\psi(u) = \psi(v)$. On the other hand, $Q = \varphi(\overline{B})$, so it follows that the restriction of ψ on Q is well defined.

Now again, we define a sequence of maps

$\tau_0, \tau_1, ..., \tau_p, \tau_{p+1}, ...$ for a sequence of sets

$B_0, B_1, ..., B_p, B_{p+1}, ...$ by induction as follows:

$\tau_0 : S \times B_0^4 \to S \times B_0$ with $\tau_0(s, x_1^4) = f(s, x_1^4)$;

$\tau_1 : S \times B_1^4 \to S \times B_1$ with

$$\tau_1(s, (u_{11}^{1\alpha_1}, i_1), (u_{21}^{2\alpha_2}, i_2), (u_{31}^{3\alpha_2}, i_3), (u_{41}^{4\alpha_4}, i_4)) =$$
$$f(s, \psi_1(u_{11}^{1\alpha_1}, i_1), \psi_1(u_{21}^{2\alpha_2}, i_2), \psi_1(u_{31}^{3\alpha_3}, i_3), \psi_1(u_{41}^{4\alpha_4}, i_4))$$

$\tau_2 : S \times B_2^4 \to S \times B_2$ with

$$\tau_2(s, (u_{11}^{1\alpha_1}, i_1), (u_{21}^{2\alpha_2}, i_2), (u_{31}^{3\alpha_3}, i_3), (u_{41}^{4\alpha_4}, i_4)) =$$
$$f(s, \psi_2(\overline{u}_{11}^{1\alpha_1}, i_1), \psi_2(\overline{u}_{21}^{2\alpha_2}, i_2), \psi_2(\overline{u}_{31}^{3\alpha_3}, i_3), \psi_2(\overline{u}_{41}^{4\alpha_4}, i_4))$$

$\vdots$

$\tau_p : S \times B_p^4 \to S \times B_p$ with

$$\tau_p(s, (u_{11}^{1\alpha_1}, i_1), (u_{21}^{2\alpha_2}, i_2), (u_{31}^{3\alpha_3}, i_3), (u_{41}^{4\alpha_4}, i_4)) =$$
$$f(s, \psi_p(\overline{u}_{11}^{1\alpha_1}, i_1), \psi_p(\overline{u}_{21}^{2\alpha_2}, i_2), \psi_p(\overline{u}_{31}^{3\alpha_3}, i_3), \psi_p(\overline{u}_{41}^{4\alpha_4}, i_4))$$

$\vdots$

Now we define a map τ for the sequence of maps $\tau_0, \tau_1, ..., \tau_p, \tau_{p+1}, ...$ by $\tau : S \times \overline{B}^4 \to S \times \overline{B}$, so that $\tau|_{B_p} = \tau_p$ and

$$\tau(s, (u_{11}^{1\alpha_1}, i_1), (u_{21}^{2\alpha_2}, i_2), (u_{31}^{3\alpha_3}, i_3), (u_{41}^{4\alpha_4}, i_4)) =$$
$$\tau_p(s, (u_{11}^{1\alpha_1}, i_1), (u_{21}^{2\alpha_2}, i_2), (u_{31}^{3\alpha_3}, i_3), (u_{41}^{4\alpha_4}, i_4)) =$$
$$f(s, \psi_p(u_{11}^{1\alpha_1}, i_1), \psi_p(u_{21}^{2\alpha_2}, i_2), \psi_p(u_{31}^{3\alpha_3}, i_3), \psi_p(u_{41}^{4\alpha_4}, i_4)) =$$
$$f(s, \psi(u_{11}^{1\alpha_1}, i_1), \psi(u_{21}^{2\alpha_2}, i_2), \psi(u_{31}^{3\alpha_3}, i_3), \psi(u_{41}^{4\alpha_4}, i_4)).$$

Because ψ is well defined, it follows that τ is well defined. On the other hand, $Q=\varphi(\overline{B})$ so $\overline{\varphi}$ denotes the map $\overline{\varphi}: S\times Q^4 \to S\times Q$ defined by

$$\overline{\varphi}(s,(u_{11}^{1\alpha_1},i_1),(u_{21}^{2\alpha_2},i_2),(u_{31}^{3\alpha_3},i_3),(u_{41}^{4\alpha_4},i_4)) =$$
$$= \tau(s,(u_{11}^{1\alpha_1},i_1),(u_{21}^{2\alpha_2},i_2),(u_{31}^{3\alpha_3},i_3),(u_{41}^{4\alpha_4},i_4)) =$$
$$= f(s,\psi(u_{11}^{1\alpha_1},i_1),\psi(u_{21}^{2\alpha_2},i_2),\psi(u_{31}^{3\alpha_3},i_3),\psi(u_{41}^{4\alpha_4},i_4)).$$

Moreover, $(S,(Q,[\ ]),\overline{\varphi})$ is a (5,2)-semigroup automaton, where $(Q,[\ ])$ is a free (5,2)-semigroup with a basis B.

IV. RECOGNIZABLE (5,2)-LANGUAGES

Any subset $L^{(5,2)}$ of the universal language $Q^* = \bigcup_{p\geq 1} Q^p$, where Q is a free (5,2)-semigroup with a basis B, is called **a (5,2)-language (formal (5,2)-language)** on the alphabet B.

A (5,2)-language $L^{(5,2)} \subseteq Q^*$ is called **recognizable** if there exists:

(1) a (5,2)-semigroup automaton $(S,(B,\{\}),f)$, where the set S is finite;

(2) an initial state $s_0 \in S$;

(3) a subset $T \subseteq S$ such that

$$L^{(5,2)} = \{w \in Q^* \mid \overline{\varphi}(s_0,(w,1),(w,2)) \in T\},$$

where $(S,(Q,[\ ]),\overline{\varphi})$ is the (5,2)-semigroup automaton constructed above, for the (5,2)-semigroup automaton $(S,(B,\{\}),f)$.

We also say that the (5,2)-semigroup automaton $(S,(B,\{\}),f)$ **recognizes** $L^{(5,2)}$, or that $L^{(5,2)}$ **is recognized** by $(S,(B,\{\}),f)$.

Example 3: Let $(S,(B,\{\}),f)$ be a (5,2)-semigroup automaton given in Example 2. We construct the (5,2)-semigroup automaton $(S,(Q,[\ ]),\overline{\varphi})$ for the (5,2)-semigroup automaton $(S,(B,\{\}),f)$.

A (5,2)-language $L^{(5,2)}$, which is recognized by the (5,2)-semigroup automaton $(S,(Q,[\ ]),\overline{\varphi})$, with initial state s_0 and terminal state (s_1,a) is

$$L^{(5,2)} = \{w \in Q^* \mid w = w_1 w_2 ... w_q, \quad q \geq 5, \quad \text{where}$$

$$w_l = \begin{cases} (u_1^n,i),\ n\geq 5, u_\alpha \in Q \\ (a^*b^*)^* \end{cases},\ l \in \{1,2,...,q\},\ \text{and:}$$

a) If $i=1$, then:

a1) $(u_1^n,1)=a$, where

$$\psi_{p-1}(u_1)...\psi_{p-1}(u_n) = a(a\cup b)(a^t b^l a^h)^*,$$

a2) $(u_1^n,1)=b$, where

$$\psi_{p-1}(u_1)...\psi_{p-1}(u_n) = b(a\cup b)(a^t b^l a^h)^*$$

b) If $i=2$, then:

b1) $(u_1^n,2)=a$, where

$$\psi_{p-1}(u_1)...\psi_{p-1}(u_n) = (a\cup b)a(a^t b^l a^h)^*,$$

b2) $(u_1^n,2)=b$, where

$$\psi_{p-1}(u_1)...\psi_{p-1}(u_n) = (a\cup b)b(a^t b^l a^h)^*,$$

and $\psi_p(w_1)...\psi_p(w_q) = (a\cup b)a(a\cup b)^2(a^t b^l a^h)^*$, for $t+l+h=3k$, $t,l,h \in \{0,1,2,...\}$, $k\geq 1$, $q=3k+4$ }.

4.1⁰ Let $L^{(5,2)}$ be a (5,2)-language on the set B recognized by (5,2)-semigroup automaton $(S,(Q,[\ ]),\overline{\varphi})$. Let $(S,(Q,[\ ]),\overline{\varphi})$ be a (5,2)-semigroup automaton with initial state s_0 and a set of terminal states $T\times C \subseteq S\times B$. Then $x\widetilde{L}^{(2,1)}c \subseteq L^{(5,2)}$ for each $x\in Q$ and for any language $L^{(2,1)}$, which is recognized by the semigroup automaton $(S\times Q,(Q^2,*_c),\psi)$ with an initial state $s'_0=(s_0,x)$, a set of terminal states $T\times C$, where $\psi: S\times Q\times Q^2 \to S\times Q$ is a transition function defined by $\psi((s,x),y_1^2) = \overline{\varphi}(s,x,y_1^2,c)$ for $c\in Q^p$ and p is the least non-negative integer, such that $2+p \equiv 0 (\mathrm{mod}\, 3)$, and $\widetilde{L}^{(2,1)} = \{\widetilde{w} \mid w \in L^{(2,1)}\}$.

Proof: $L^{(5,2)}$ is a recognizable (5,2)-language on the set B by the (5,2)-semigroup automaton $(S,(Q[\ ]),\overline{\varphi})$ with an initial state s_0 and a set of terminal states $T\times C \subseteq S\times B^{n-t}$, so

$$L^{(5,2)} = \{w\in Q^* \mid w = w_1 w_2 ... w_{3q+4},\ q\geq 1 \text{ and}$$
$$\overline{\varphi}(s_0,(w_1^{3q+2},1),(w_1^{3q+2},2),\psi_{p-1}(w_{3q+3}),\psi_{p-1}(w_{3q+4})) =$$
$$\overline{\varphi}(s_0,\psi_{p-1}(w_1),(w_2^{3q+3},1),(w_2^{3q+3},2),\psi_{p-1}(w_{3q+4})) =$$
$$\overline{\varphi}(s_0,\psi_{p-1}(w_1),\psi_{p-1}(w_2),(w_3^{3q+4},1),(w_3^{3q+4},2)) \in T\times C\ \}.$$

By Proposition 2.2⁰, $(S\times Q,(Q^2,*_c),\psi)$ is a semigroup automaton. It recognizes a language $L^{(2,1)}$ with a set of initial states $s'_0=(s_0,x)$ and a set of terminal states $T\times C$, so it is of the form

$$L^{(2,1)} = \{w\in (Q^2)^* \mid \psi(s'_0,w) \in T\times C\}.$$

Let $w\in L^{(2,1)}$. It follows that $w\in (Q^2)^*$ and $\psi(s'_0,w)\in T\times C$. But $s'_0=(s_0,x)$, so

$$\overline{\varphi}(s_0,x,(\widetilde{w},1),(\widetilde{w},2),c) = \overline{\varphi}(s_0,x,w,c) =$$
$$= \psi((s_0,x),w) = \psi(s'_0,w) \in T\times C$$
.

Thus $x\tilde{w}c \in L^{(5,2)}$, i.e. $x\tilde{L}^{(2,1)}c \subseteq L^{(5,2)}$. ■

4.2⁰ Let $L^{(2,1)}$ be a recognizable language on the set B by a semigroup automaton $(S,(B,\|\ \|),\xi)$ with an initial state $s_0 \in S$ and a set of terminal states $T \subseteq S$, and $(S,(B,\{\}),f)$ be an (5,2)-semigroup automaton constructed by a semigroup automaton $(S,(B,\|\ \|),\xi)$. Let $f: S\times B^4 \to S\times B$ is a transition function defined by $f(s,x_1^4) = (\xi(s,\|x_1^3\|),x_4)$. Then $L^{(2,1)}a \subseteq L^{(5,2)}$, for each $a \in B$, where $L^{(5,2)}$ is a recognizable (5,2)-language on the set B by the (5,2)-semigroup automaton $(S,(Q,[\ ]),\overline{\varphi})$ with an initial state $s_0 \in S$ and a set of terminal states $T\times\{a\}$.

Proof: A language $L^{(2,1)}$ is recognizable by a semigroup automaton $(S,(B,\|\ \|),\xi)$ with initial state $s_0 \in S$ and a set of terminal states $T \subseteq S$, so

$$L^{(2,1)} = \{w \in B^* \mid \xi(s_0,w) \in T\}.$$

By Proposition 2.1⁰, $(S,(B,\{\}),f)$ is a (5,2)-semigroup automaton. We construct an (5,2)-semigroup automaton $(S,(Q,[\ ]),\overline{\varphi})$, where $Q = \varphi(\overline{B})$ and $\overline{\varphi}: S\times Q^4 \to S\times Q$ is a transition function defined by

$$\overline{\varphi}(s,(u_{11}^{1\alpha_1},i_1),(u_{21}^{2\alpha_2},i_2),(u_{31}^{3\alpha_3},i_3),(u_{41}^{4\alpha_4},i_4)) =$$
$$= f(s,\psi_p(u_{11}^{1\alpha_1},i_1),\psi_p(u_{21}^{2\alpha_2},i_2),\psi_p(u_{31}^{3\alpha_3},i_3),\psi_p(\overline{u}_{41}^{4\alpha_4},i_4)).$$

It follows that a recognizable (5,2)-language $L^{(5,2)}$ on the set B by (5,2)-semigroup automaton $(S,(Q,[\ ]),\overline{\varphi})$, with initial state $s_0 \in S$ and a set of terminal states $T\times\{a\}$ is of the form

$$L^{(5,2)} = \{w \in Q^* \mid w = w_1w_2\ldots w_{3q+4},\ q \geq 1 \text{ and}$$

$$\overline{\varphi}(s_0,(w_1^{3q+2},1),(w_1^{3q+2},2),\psi_{p-1}(w_{3q+3}),\psi_{p-1}(w_{3q+4})) =$$
$$= \overline{\varphi}(s_0,\psi_{p-1}(w_1),(w_2^{3q+3},1),(w_2^{3q+3},2),\psi_{p-1}(w_{3q+4})) =$$
$$= \overline{\varphi}(s_0,\psi_{p-1}(w_1),\psi_{p-1}(w_2),(w_3^{3q+4},1),(w_3^{3q+4},2)) \in T\times C\ \}.$$

Let $w \in L^{(2,1)}$, $|w| \geq 3q+3$ i.e. $w = w_1^{3q+3}$, $q \geq 1$ and $a \in B$. Then

$$\overline{\varphi}(s_0,(w_1^{3q+2},1),(w_1^{3q+2},2),\psi_{p-1}(w_{3q+3}),a) =$$
$$= \overline{\varphi}(s_0,(w,a)) = (\xi(s_0,w),a) \in T\times\{a\}.$$

Thus $wa \in L^{(5,2)}$, i.e $L^{(2,1)}a \subseteq L^{(5,2)}$. ■

V. CONCLUSION

The results was given in this paper, are of the scientific interest, because there was defined a (5,2)-languages as a consequence of the generalization of the semigroup automata in case (5,2). Also, here was given the conection between (2,1)-languages and (5,2)-languages.

REFERENCES

[1] D.Dimovski, "Free Vector Valued Semigroups", *Proc. Conf. "Algebra and Logic"*, Cetinje, (1986), 55-62

[2] Čupona G., Celakovski N., Markovski S., Dimovski D. "Vector Valued Groupoids, Semigroups and Groups", *Maced. Acad. Sci. and Arts*, Skopje (1988), pp. 3-73

[3] Trenčevski K., Dimovski D. "Complex Commutative Vector Valued Groups", *Maced. Acad. Sci. and Arts*, Skopje (1992)

[4] D.Dimovski, V.Manevska, "Vector Valued (*n*+*k*)-Formal Languages", *Proc. 10th Congress of Yugoslav Mathematicians*, Belgrade, (2001), 153-159

[5] V.Manevska, D.Dimovski, "Properties of the (3,2)-Languages Recognized by (3,2)-Semigroup Automata", *MMSC*, Borovets, (2002), 368-373

The Realization of the Distributed Computer Chess System

Vladan Vučković

Abstract - **This paper is concerned with the implementation of the asynchronous parallel search algorithm using distributed local network. The original solution is implemented and tested in author's chess application *Axon*. The standard approaches of parallelism use dual and quad server PC machine, which is expensive and rare compared with classical single processor PC machines. The author's solution introduces a new class of simple and efficient algorithm of the parallelisation, using standard single processor units connected via local 100Mb or 1Gbit networks. Compared with single processor search algorithms, the parallel algorithm significantly increases performance in test suites and practical play.**

Keywords - **Computer chess, search algorithms, parallel computing, local area networks.**

I. INTRODUCTION

The theory of computer chess is complex connecting many sub-domains like theory of games, decision trees, and theory of programming, operation research, and optimization. The nature of the computer chess could be explained very simply: namely, decision tree that is the base of machine chess-playing algorithm grows exponentially with factors depending of position, hash tables, number of pieces on the board…If we suppose that on the first level of the decision tree one has node with 30 exists, on the second level it will be 302=900 nodes, on the third 303 it will be 27000 etc. It is obvious that number of nodes, also with processing time depends exponentionaly of the level (depth) of the search tree. In theory, that effect is called combinational explosion. On the other hand, the quality of computer play strongly depends on depth of the decision tree so the effect of the exponential explosion limits the computer chess strength.

There are generally two approaches to overcome this problem: *Shannon-type-A* (full-width approach) and *Shannon-type-B* (selective search) **[1]**. The first one tries to solve the problem by using the simple pruning mechanisms based on Alfa-Beta technique with idea to decrease maximally the time needed to compute one single node.

This approach benefits maximally of the rapidly increasing speed of the modern CPU-s and also incorporates standard (cluster) parallelisation (IBM Deep Blue). The second approach (Type-B) is concentrate on heuristic pruning based on relatively extensive portion of knowledge, direct programmed into the evaluation or move generator function. This approach is very depended on the programmer skill and the quality of the implemented pruning, so the results could be very relative. On today's level of knowledge in this area, the best combination is to use near full-width approach in main searcher, and selective searcher in q-search procedure. The algorithms could be combined: Alpha-Beta, Null Move and PVS (NegaScout).

This paper has intention to investigate the other possibilities of computer chess strength increasing using parallelism if the other techniques are well implemented. The main pruning method is Alfa-Beta and it is implemented in author's *Axon* application with some technical improvements. The results of tests prove that the implementation of the pruning technique is able to cut the large parts of the tree improving the computer playing strength notably.

Vladan Vučković is with the Faculty of Electronic Engineering, University of Niš, 18000 Niš, Serbia and Montenegro, Email: vld@elfak.ni.ac.yu

II. STANDARD PARALLEL CHESS MACHINES

The standard research parallel chess machines are developed on several universities, as the stand alone applications or a part of some general parallel algorithm design:

- Chess on Massively Parallel Systems at University of Paderborn,
- Parallel Computing Works at CalTech,
- CilkChess Parallel Chess Program at MIT **[2]**,
- International Computer Chess Association.

The main characteristics of two leading parallel chess architectures will be presented in this section.

2.1 DEEP BLUE

Probably, the most important parallel chess machine was developed by the IBM Company, named *IBM Deep Blue* **[3]**. Deep Blue Computer is implemented as a 32-node IBM RS/6000 SP high-performance computer. Each node has a single micro channel card that contains 8 individual VLSI chess processors (specially designed IC's for chess computations). The total processing of the systems utilizes 256 chess processors and can evaluate 200,000,000 positions per second. The software was coded in C under the IBM AIX system. The system utilizes the MPI (message passing) method of parallalization that is standard for the IBM SP Parallel systems. This method can work well for this application since the data required for processing is relatively small and can be easily (and cheaply) replicated among the processors. Primarily communication between the processors is limited to delegate which processors examine which portions of the tree of possible moves (each level represents one player's move, so the root would have all the possible

moves one player could make, the next level would have the moves in response by the other player). Software determines a set of tactics/moves to explore and then determines likely outcomes and the goodness of them. Since chess is a complex game and the number of moves (and the moves that follow that, etc) is incredibly enormous, true brute force is not used. Highly unlikely moves are eliminated from further consideration (such as putting the king in checkmate). The original algorithm used is based on the alpha-beta algorithm. The system passes messages between all the processors and each processor works on a set of possible moves. Since each processor is examining a different set of moves, it is likely that parallel processing is applicable.

The following graph was compiled from information on the IBM website, but since the information was scattered, it should only be used as an approximation of true performance.

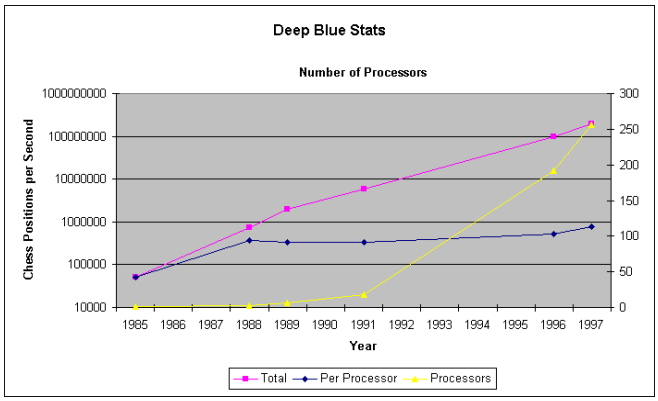

Fig. 1. The influence of parallelization to the CPP factor

The graph displays the number of chess positions per second that are computed. This is analogous to determining the goodness of a position and with some unlisted constant could be converted to operations per second metric. The line representing the positions per second per chess processor is calculated by dividing the total equally over the number of chess processors. This is just an average number, and may not be accurate. It is possible that one or more of the chess processors (but not all) are doing more work than others.

Obviously the number of calculations per second increases with time due to advances in chip technology and algorithm enhancements, but the overall enhancement of the system out performs Moore's law applied to one processor, leading to the conclusion that parallel computing was successful. It also appears that after 1988 there was a slight decrease in position per second, this is probably due to the overhead of parallel computation, but still allowed the overall performance of the machine to increase. Unfortunately data regarding the raw power of each processor running alone was not available to evaluate a true speedup performance. IBM estimates that for a single computer to analyze the same number of positions per second would need to run at about 1 Terahertz. IBM reports that the current Deep Blue system has a parallel efficiency of around 30%.

2.2 CILKCHESS

Cilkchess (developed on MIT university) is a complete rewrite of the previous chess program *(Socrates).* The parallel search algorithm uses a form of Jamboree-search to control parallel search overhead: at each node the first successor is searched serially. If it does not cause a cutoff, the remaining successors are searched in parallel. The transposition table is stored in 32 gigabytes of shared memory. Entries are not locked. (Although this goes against common parallel programming practice, it certainly is fast and seems to work well in practice.) In the late middle game, Cilkchess typically looks more than 15 ply (half moves) ahead and performs 5-11 million make-moves per second on a 256-processor SGI Origin 2000. The evaluation function is built for speed, uses only knowledge, which is known to work, few extensions, and null-move based forward pruning. In the latest version, the weights of the evaluation function are tuned using a temporal-coherence learning algorithm.

III. IMPLEMENTATION

The standard author's version of chess program *Axon* was modified, using relatively simply method of parallelization. The experimental parallel system use two PC computers, which are connected via local 100 Mb network The program was parallelized using *master-slave* methodology. Two identical programs use identical hardware are identical, but they compute different branches of the decision tree. Also, human operator has control only on the master machine where is possible to change position using standard Windows interface. In the phase of computing, master send small pack of date using distributed connection. The packet contains current position, flags, game history and list of moves for the processing on the slave unit. The key problem is how to split the total list of moves, to achieve optimal ballast of the processor strength in this multiprocessor environment. The presumption is that the speed (measured by the Axon Benchmark 4 hardware test) must be approximately equal. To demonstrate our solution assume that the current position given on the following diagram (Figure 2):

Fig. 2. AXON I Parallel version of program

The position is resumed from the grandmaster game - key move is winning Ng6!. When we analyze this position using *Axon Evaluation Tester* **[4]**, the following list of legal moves was generated:

0. H4H8 -> %.+.....a.r.p#it (<--)
1. H3E6 -> %..c.d.faq.np..t (<--)
2. H4F4 -> .s...d..a..np.it (1)
3. H4G5 -> .s.....a..np#it (2)
4. E5C4 -> .s.....a..np.i. (<--)
5. E5G4 -> .s.....a..n.#.. (1)
6. F2F4 -> .s.....a..n..it (<--)
7. A1C1 -> .s.....a...p.it (<--)
8. H3G2 -> .s.....a...p.it (1)
9. E1E3 -> .s.....a...p..t (<--)
10. H3F5 -> .s.....a....#.t (2)
11. E1E2 -> .s.....a.....t (1)
12. A1D1 -> .s.....a.....t (1)
13. E1C1 -> .s.....p.i. (2)
14. B2C3 -> .s.....p.i. (<--)
15. H3G4 -> .s.....#.t (3)
16. G3G4 -> .s.....#.t (<--)
17. G1F1 -> .s.....t (<--)
18. A3A4 -> .s.....t (<--)
19. G1H2 -> .s.....t (1)
20. G1G2 -> .s.....t (2)
21. A1A2 -> .s.....t (2)
22. A1B1 -> .s.....t (3)
23. F2F3 -> .s.....t (1)
24. G1H1 -> .s..... (3)
25. E1B1 -> .s..... (3)
26. B2C1 -> .s..... (1)
27. E1D1 -> .s..... (4)
28. E5D3 -> .s..... (2)
29. E1F1 -> .s..... (5)
30. E5F3 -> .s..... (3)
31. H3F1 -> .s..... (4)
32. H4H7 -> ..+..d..a...p#it (3)
33. H4F6 -> ...c.d.fa.rnp#it (4)
34. E5F7 -> ...c....a.rnp#i. (4)
35. E5C6 -> ...c....a.r.p#i. (5)
36. D4D5 -> ....md.fa..np#.t (<--)
37. H4E4 -> .....d.fa..np#it (5)
38. H4H5 -> .....d..a..np#.t (6)
39. H4H6 -> ....fa..np#it (7)
40. H4G4 -> ....f...np#it (8)
41. E5D7 -> ....a..n.#.. (6)
42. E1E4 -> ....a....#.t (6)
43. E5G6 -> ....#.. (7)

The list of moves is sorted and displayed together with their characteristically bits (weights.) *The basic rule for parallelization on two machines is to divide this list in two sub-lists*. The first sub-list contains move with **EVEN** indexes (0. H4H8, 2. H4F4, 4. E5C4 ...) and the second list incloses moves with **ODD** indexes (1. H3E6, 3. H4G5, 5. E5G4 …). After that, each sub-list is distributed to corresponding processor. In the phase of computing, each processor works on different set of moves, so the parallelization is achieved.

IV. Experiment and test results

To determine the factor of parallel efficiency of the new method, the experiment was carried out. The standard EPD test was used *(yazgac.epd).* Otherwise the EPD tests are commonly used as the benchmark tests for computer chess algorithms. They contents serious of test chess positions also with key moves.

The experiment consists of 3 phases. First, test will be performing on single processors on depth 7 each position. For the experiment, the PC with *AMD Sempron 2600+* processor/ 256 Mb Ram/ 50 Mb Hash will be used. After that, the same experiment will be performed on two machines working parallel, also with same hardware. The goal of the experiment will be to represent the acceleration of the best move searching on parallel machine compared to single-processor one. The experimental date could be systematized in the following table (Table 1). This table indicates that parallel system always found key moves faster (in less number of positions). The percentage of acceleration and the processor, which computes key move could not be, determine exactly, it is very dependent of the analyzed position. The theoretical reasons for these empiric conclusions are connected with the fact that the search tree is divided in two branches. Each sub-tree contains less elements then full tree, which is also dependent on position. For instance, in raw 30, total tree search on key move Re4 for the single processor holds 40308515 positions. The second (slave) processor, which found the right solution, processed only 28140075 nodes, that is 69.8% of full tree.

TABLE I
TABLE SHOWS NUMBER OF POSITIONS GENERATED WITH SINGLE AND DUAL SYSTEM ON DEPTH 7.

	Single		**Master**		**Slave**	
1	Bh7	728249	**Bh7**	717922	bxc3	596521
2	Rxg7	1466745	**Rxg7**	759523	Qd3	1512966
3	Rd4	1469002	Be7	1031013	**Rd4**	1525525
4	Nc5	1555512	Nxf6	10863177	Ng5	1564616
5	Bd6	1388059	**Bd6**	2597391	Rf1	1381623
6	Rc1	276446	Rf4	497102	**Rc1**	201065
7	Qd8	84001	Qd3	9823036	**Qd8**	56237

8	Qc7	10527566	**Qc7**	9189599	Bxf7	2148993
9	Qxg6	4963938	Qh3	5771366	**Qxg6**	3760483
10	Nh4	16605243	**Nh4**	15273693	Bg5	25709788
11	Ne5	3689251	Rh8	12246408	**Ne5**	2188589
12	O-O-O	37440614	**O-O-O**	32279825	Qa4	32454430
13	Qxh3	2050870	dxc4	19446143	**Qxh3**	1711382
14	Nxb8	1115403	**Nxb8**	1032344	Qd3	1335819
15	Bxg7	14547957	**Bxg7**	6283498	Bg5	10789489
16	a4	23997961	**a4**	22423349	h4	15604024
17	f5	2159123	**f5**	2076168	Nxd5	1212576
18	Qxg5	2690807	e5	12102548	**Qxg5**	2382803
19	Nc4	1466950	Nb5	3312836	**Nc4**	839488
20	Nc3	10621431	**Nc3**	7965793	Ra5	13809770
21	Kc3	346605	**Kc3**	196995	Kc2	177727
22	Bxe2	2965166	Rh2	2151353	**Bxe2**	1580737
23	h7	724166	**h7**	487909	Bc6	5719170
24	Rxh3	2243812	**Rxh3**	2138494	Rg3	7257178
25	c4	4190791	**c4**	2969132	h4	4569494
26	Rxd7	2520953	**Rxd7**	2032580	Bg3	25238813
27	Qxc6	14345697	Ne1	12422980	**Qxc6**	1243715
28	Kh2	7423320	**Kh2**	5258905	Qxa7	3803816
29	Rxf4	2872671	Qxf4	527141	**Rxf4**	2754258
30	Re4	40308515	Qh5	14897082	**Re4**	28140075
31	cxb5	4005703	**cxb5**	2622334	Rd1	3001105
32	Re1	8435525	**Re1**	5680953	Rd1	11814379
33	Qe2	2447903	**Qe2**	2128323	Rf3	2928657

V. CONCLUSION

The distributed computer chess system presented in this paper runs on two PCs with AMD Sempron 2600+ processors connected via 100Mb local area network. The software component is developed around the Axon I chess engine. The EPD test performed in this paper proves that parallel machine finds key moves faster in every case compared to single processor one. This conclusion may be generalized, so in practical testing or playing mode dual machine reacts more rapidly then the single one. In the future, the author intends to expand number of processors and to accommodate software for the efficient multi-processor work.

REFERENCIES

[1] Peter W. Fray *Chess Skill in Man and Machine*, texts and monographs in computer science, Springer-Verlag, 1977,1978, New York, USA

[2] Cilkchess at supertech.lcs.mit.edu/chess/

[3] Deep Blue at www.research.ibm.com/deepblue

[4] Vuckovic, Vladan "Decision Trees and Search Strategies in Chess Problem Solving Applications", *Proceedings of a Workshop on Computational Intelligence and Information Technologies*, pg. 141-159, February 27. 2001.

Some Approaches to Inheritance-Based Class Interface Extension

Ivan S. Veličković[1] and Marija D. Cvetković[2]

Abstract – **A brief discussion of inheritance-based class interface extension, its properties and applicability will be given in this paper. Two alternatives will be analysed: an approach based on multiple inheritance and approach based on nested classes. These approaches will be compared and possible application issues will be considered.**

Keywords – **Design Patterns, Inheritance, Nested Classes**

I. INTRODUCTION

The object-oriented approach is today's most exploited model for development of large software products. Simple reuse by means of inheritance and limitations over relations between entities (objects and classes) imposed by the encapsulation concept make this method suitable for simple and reliable integration and debugging of independent software components developed by different teams of developers. But a problem remains: following the rules imposed by object-oriented model doesn't necessarily lead to a good, reusable and decoupled solution. For this reason most modern software development techniques, faced with growing market and rising customer requirements, depend on reuse of well-known, well-tested and extendable but comprehensible object-oriented design solutions, known as Design Patterns [1].

In the development process of a complex application, user interactions (use cases) are usually grouped into separate and independent functional units (components, applications). These units operate over the same data and offer to a user another set of possible activities. From a developers point of view this means the implementation of a different interface for each independent unit. This burden of unit dependent interface methods, if placed in the same data implementation class, could make such a class difficult to maintain and modify. The solution is to separate universal, unit independent, methods of the data implementation class from, unit dependant methods. Different approaches could be used in order to achieve such goal. This problem is partially addressed by the *Bridge* design pattern [1]. *Bridge* offers a delegation-based solution for interface separation that is easy to extend, maintain and modify. Unfortunately, its application is difficult over data implementation classes (*Concrete Implementers*) that are, though inherited from the same base class, very different conceptually and architecturally. Another approach could be based on *Adapter* design pattern. Essentially, "adapting" one interface to another is what we are trying to achieve. On the other hand, introduction of a unit dependant interface can vary not just class external behaviour, but also its inner implementation. Probably the most intuitive choice could be the *Visitor* pattern. From a point of view, suggested solutions can be treated as an inheritance-based approaches to *Visitor* pattern realisation. Both approaches suggested in this paper offer a possible solution to this problem that cannot be elegantly solved by direct application of mentioned related design patterns.

This paper is organised as follows. Next section discusses a malicious behaviour of software reuse through inheritance. A method for encapsulation breach by means of friend class declaration of an inherited class is presented. Section III contains a brief description of proposed solutions. Finally the Section IV gives the application example of proposed methods.

Code samples are given in C++ language and UML diagrams follow Rational Unified notation.

II. INHERITANCE AND ENCAPSULATION DECAY

Inheritance, polymorphism and encapsulation are considered as base concepts of object-oriented programming. These concepts, if properly utilized, are means of safe software code reuse. The problem of good and safe object-oriented design relies on thin balance between these concepts. For the sake of simplicity lets consider the following example.

```
class CBaseClass
{
public:
     int GetPrivate() {return m_nPrivate;};
protected:
     int m_nProtected;
private:
     int m_nPrivate;
};

class CInheritedClass: public CBaseClass
{
friend class CUserClass; // encapsulation breach
...
};
class CUserClass
{
protected:
     CInheritedClass* pData;
...
};
```

Code Sample 1. An illustration of encapsulation breach with inheritance

By means of public inheritance access to all protected and public attributes of the parent class is given to all descendants. However, private members remain class-local, and can be

[1] Ivan S. Veličković is with Faculty of Electronics Engineering Aleksandra Medvedeva 14, 18000 Nis, Serbia and Montenegro, E-mail: ivanv@elfak.ni.ac.yu

[2] Marija D. Cvetković is with Faculty of Electronics Engineering Aleksandra Medvedeva 14, 18000 Nis, Serbia and Montenegro, E-mail: cveleglg@bankerinter.net

accessed only through public methods of the parent class, if such methods are available. In previous example such privileges are given to `CInheritedClass`. This means that by using this method of inheritance, children classes could gain less restrictive access to parent class implementation, which may result in encapsulation decay [2].

Notice a code line in the previous example that gives a friend privileges to `CUserClass`. This way the access to protected attributes of `CBaseClass` is given to a class that doesn't belong to the same family of classes. Should be mentioned that private members are still invisible to the friend-privileged class. This effect partially contradict well-known phrase that friendship is given, not inherited.

Another infamous inheritance topic is multiple inheritance. It is a method that can provide privileged access to a class implementation to another class that doesn't belong to the same family of classes. Because of its cumbersome behaviour this method of code reuse is often discouraged or forbidden by programming language syntax.

Regardless of the previous discussion proper use of mentioned techniques can represent a powerful tool.

III. SUGGESTED SOLUTIONS

Figure1 represents an UML class diagram of the multiple-inheritance-based solution. Abstract class *`CAbstractImp`* with pure virtual methods *`Operation1()`* and *`Operation2()`* defines unit (application or component) independent interface for implementation classes. Each inherited class implements this interface. On the other hand, unit specific interface is specified with abstract class *`CAppSpecificItfExt`*. Finally, unit specific concrete implementation is realized by means of multiple inheritance from unit specific interface definition class *`CAppSpecificItfExt`* and a corresponding unit independent concrete implementation class.

This solution can be realized in C++ through utilization of abstract classes and multiple inheritance, or in Java with interfaces and interface implementation. A problem arises if some additional *`CAppSpecificItfExt`* attributes and related methods need to be implemented. This would not be possible in Java and it is strongly discouraged in C++.

Figure 2 represents an UML class diagram of nested class based approach. The implementation class family is the same as in the previous discussion. Changes are made in unit specific interface extension classes. A pure virtual *`Bind()`* method is added to the interface of the abstract base class *`CAppSpecificItfExt`*. Purpose of this method is to enable *Visitor*-pattern-like biding between interface extension instance and corresponding implementation class instance. Implementation of the *`Bind()`* method, and a definition of a nested class inherited from the appropriate implementation class (classes with "X" prefixed names) are left to *`CAppSpecificItfExt`* child classes. Purpose of those nested classes is to provide a privileged reference (pointer) marked as `m_pItem`. Code Sample 2 describes this idea in detail. Additional implications are given through code comments.

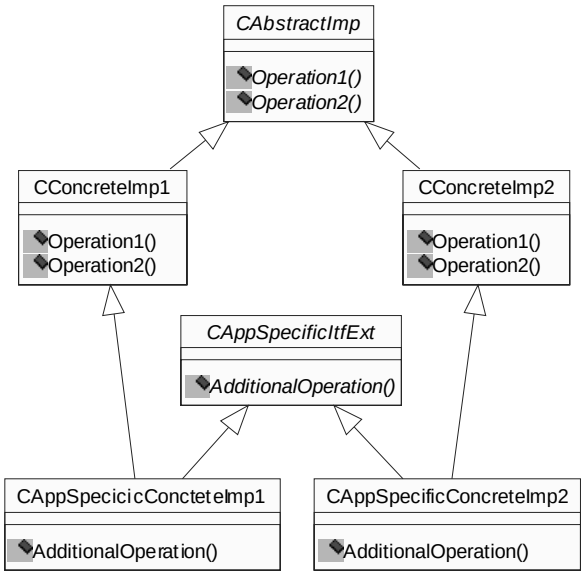

Figure 1. First solution based on multiple inheritance

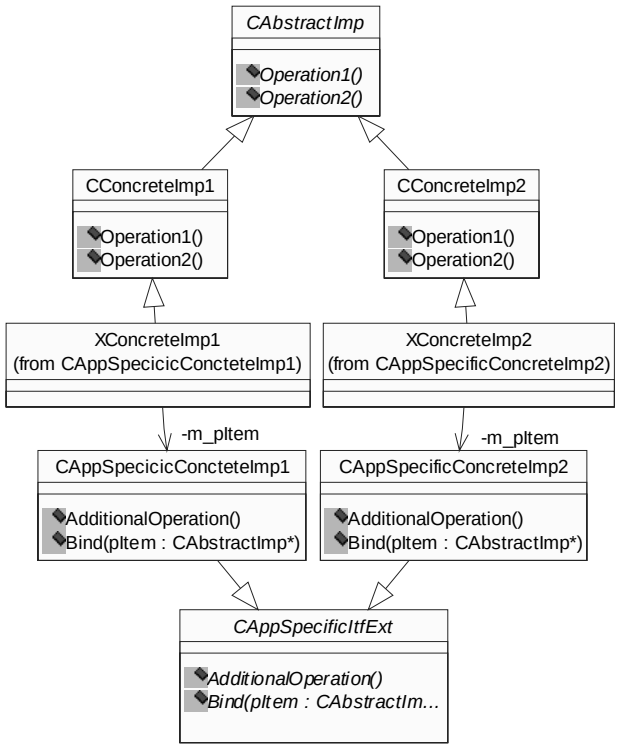

Figure 2. Second solution based on nested friend class definition

```
////////////////////////////////////////////////
class CAbstractImp
{
private:
    int m_nParentPrivate;
protected:
```

```
    int m_nParentProtected;
public:
    virtual enum eType GetType() = 0;
    // unit independent interface declaration
    virtual void Operation1() = 0;
    virtual void Operation2() = 0;
};

////////////////////////////////////////////////
class CConcreteImp1: public CAbstractImp
{
private:
    int m_nChildPrivate;
protected:
    int m_nChildProtected;
public:
    enum eType GetType() {
       return TYPE_CONCRETE_IMP_1;};
    // unit independent interface implementation
    virtual void Operation1();
    virtual void Operation2();
};

////////////////////////////////////////////////
class CAppSpecificItfExt
{
public:
    // unit dependant interface declaration
    virtual bool Bind(CAbstractImp* pItem) = 0;
    virtual void AditionalOperation() = 0;
};

////////////////////////////////////////////////
class CAppSpecificConcreteImp1: public
CAppSpecificItfExt
{
    class XConcreteImp1: public CConcreteImp1
    {
       friend class CAppSpecificConcreteImp1;
    } m_pItem;
    ...
public:
    bool Bind(CAbstractImp* pItem)
    {
       if(pItem->GetType() == TYPE_CONCRETE_IMP_1){
              m_pItem = (XConctreteImp*)pItem;
              return true;   // bind success
       }
       m_pItem = NULL;
       return false;         // bind failure
    }; // end method Bind()
    void AditionalOperation()
    {
       ...
       // somewhere in the code
       if(m_pItem){
              m_pItem->m_nParentProtected++;
              m_pItem->m_nChildProtected++;

              // following lines would not compile
              // m_pItem->m_nParentPrivate++;
              // m_pItem->m_nChildPrivate++;
       }
    }; // end method AditionalApplication
}; // end class CAppSpecificConcreteImp1
```

Code Sample 2. Code illustration of the second approach

Method described in Code Sample 1 is utilized by this approach to gain privileged access to protected members of implementation classes.

This approach can be implemented in C++ and Java without significant conceptual changes. Greatest disadvantage of this method is its complexity. Before manipulation over an instance of corresponding `CConcreteImp` an interface extension class instance should be bond with it. To reduce this drawback the *`CAppSpecificItfExt`* class can be used to maintain a *Flyweight*-pattern-like instance pool of interface extension objects [1]. Code Sample 3 illustrates this idea in detail. `UniversalBind()` static method is used to make binding process more transparent.

```
class CAppSpecificItfExt
{
    ...
private:
    static CAppSpecificItfExt*
       sm_arrPool[NUM_APP_SPECIFIC_IMPS];
public:
    static CAppSpecificItfExt*
       UniversalBind(CAbstractImp* pItem)
    {
       int index = (int)pItem->GetType();
       sm_arrPool[index]->Bind(pItem);
       return sm_arrPool[index];
    };

    static void CreatePool()
    {
       sm_arrPool[TYPE_CONCRETE_IMP_1] =
              new CAppSpecificConctreteImp1;

       sm_arrPool[TYPE_CONCRETE_IMP_1] =
              new CAppSpecificConctreteImp1;

    };
}
```

Code Sample 3. Flyweight-like implementation of unit specific interface object management.

Another possible simplification could be parameterisation of the *`CAppSpecificItfExt`* class. By passing appropriate X-prefixed class as a type parameter complete binding process would be placed into *`CAppSpecificItfExt`* class. This approach requires that global scope should be given to X-prefixed classes, which may lead to class count explosion and increased ambiguity.

IV. An Application Example

Both suggested solutions are tested with simulator of bipedal robot [3]. The simulator is constructed of several independent components: dynamics simulator, motion planer, 3D environment visualisator, 3D image interpreter and 3D environment and robot editor. Many of those are designed as independent applications and some of them communicate over network.

A coarse classification to editors and consumers can be adopted over these components. Editors provide user interface for creation and manipulation over relevant entities and consumers use these entities to perform required simulation tasks. Both type of components share the same entities definitions in form of concrete implementation classes. These definitions are centralized as independent library, which simplify debugging, and modification. Extensions of such definitions are component local. Editors are more user interface oriented. Their extensions can contain entity specific user interface objects like dialogs and property pages, and methods for user interaction events interpretation. On the other hand, consumer components are more simulation task oriented. Consumer components extensions are simulation specific and these extensions can contain simulation helper methods, methods for cross process/network boundary communication etc.

Nested classes approach appeared to be more appropriate for editor components. It is slower, more complex but more

intuitive in applications which require heterogeneous and massive interface extension. Also it is harder to maintain because some of its repetitive code segments are scattered over application specific interface extension classes.

Multiple inheritance approach appeared to be faster and easier to implement. No additional coding and binding is required, which makes it appropriate interface extension method for consumer components. However it suffers some limitation imposed by multiple inheritance.

As a result of immediate binding, both methods are sensitive to application independent classes modifications. This could be a great drawback in the early phases of application development, and great obstacle for further upgrades. However, because of great architectural differences no universal interface that would be used to separate class behaviour and its implementation can be defined.

V. CONCLUSION

This paper discussed two inheritance-based methods for class interface extension. Some of their advantages and drawbacks are exposed. Commented code examples are given to support this review. Both approaches are resulted from a practical problem proposed by a specific application request. Although application specific proposed solutions may help to overcome some general limitations imposed by object-oriented design process.

REFERENCES

[1] E. Gamma, R. Helm, R. Johnson, J. Vlissides, *Design Patterns – Elements of Reusable Object-Oriented Software*, Addison Wesley Longman, 1995.

[2] A. Snyder, "Encapsulation and inheritance in object-oriented languages", *Object-Oriented Programming Systems, Languages and Applications Conference Proceedings*, Portland, Oregon, 1986.

[3] G. S. Đorđević, N. Vukić, I. Veličković, I. Jovanović, M. Rašić, M. Vukobratović, "Visually Interactive Robot Simulator", *TELSIKS 2003 Conference Proce*edings, Niš, Serbia and Montenegro, 2003.

Session CSII:

CONTROL SYSTEMS II

Basic Communication Protocols in Vehicle Electronic Systems

Dragan S. Taranović[1], Jasna J. Radulović[2], Saša J. Jovanović[3], Andrija M. Savčić[4]

Abstract – **Today's vehicles are being equipped with a constantly increasing number of different electronic systems. Along with their need for extensive exchange of data and information in order to operate efficiently, the data quantities and speeds are also increasing continuously. In this paper, the analysis of some serial network protocols used in vehicles is presented.**

Keywords – **Vehicle networks, CAN, TTP.**

I. INTRODUCTION

Improvement in vehicle driving characteristics, driver and passenger comfort and reduction of vehicle exhaust emission is achieved through application of electronic control systems having a large number of sensors and actuators.

From the aspect of functionality, vehicles contain three parts, which can be independently controlled and which should exchange information based on appropriate standard procedure - protocol:

- control system for power unit, brakes and vehicle dynamics,
- system for signalization and diagnostics,
- system providing comfort and driver and passenger safety (air-conditioning, central lock-up, adjustment of seats and mirrors, lights, navigation, ...).

Classic system for data transfer and vehicle functions control has a star-like structure shown in Fig. 1., in which there is one main control unit (master), marked as MCU, and several local control units, LCU, sensors, S, and actuators, A, connected with the main control unit through local, serial or parallel connection. Processing of sensor signals and actuator commands can be realized in main microprocessor control unit or in appropriate local control system.

Star-like configuration of control system demands that main control system has a high speed processor in order to process all acquired information. Wire installation for connecting the sensors and actuators with control units is highly complicated and very long, and it makes the interaction between different systems harder, making the whole system susceptible to disturbances.

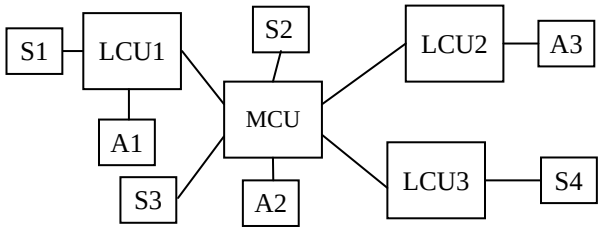

Fig. 1. Star-like configuration of control systems

A better quality of vehicle control is achieved by application of, usually, double-wire network to which all vehicle systems control units, "intelligent" sensors and "intelligent" actuators are attached on and communication is serial. Scheme of such a network is presented in Fig. 2. Main control unit need not to be present in this type of a network.

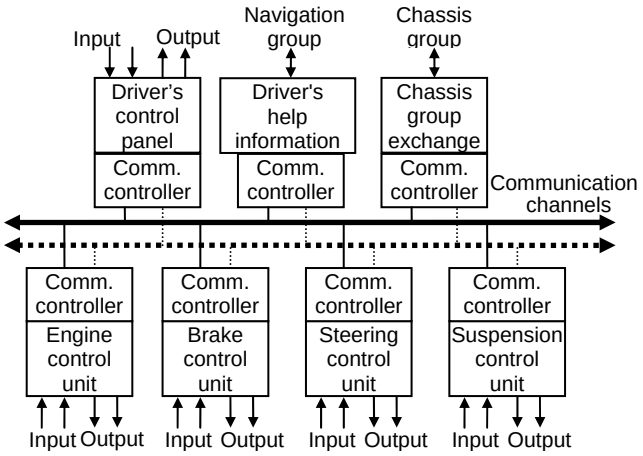

Fig. 2. Serial configuration of control systems

The vehicle, as a complex distributed electronic system, is composed of several network interconnected subsystems called “groups” (clusters) [2]. Each group realizes a separate function. Examples of groups are: electronic systems for drive unit control and vehicle dynamics control, electronic chassis systems (signaling and comfort), multimedial and electronic navigation systems, etc.

[1]Dragan Taranović is with the Faculty of Mechanical Engineering, Sestre Janjić 6, 34000 Kragujevac, Serbia and Montenegro, E-mail: tara@kg.ac.yu

[2]Jasna Radulović is with the Faculty of Mechanical Engineering, Sestre Janjić 6, 34000 Kragujevac, Serbia and Montenegro, E-mail: jasna@kg.ac.yu

[3]Saša Jovanović is with the Zastava Automobiles – R&D Department, Automobile Institute, Trg topolivca 4, 34000 Kragujevac, Serbia and Montenegro, E-mail: piter@ia.kg.ac.yu

[4]Andrija Savčić is with the Zastava Automobiles – R&D Department, Automobile Institute, Trg topolivca 4, 34000 Kragujevac, Serbia and Montenegro, E-mail: piter@ia.kg.ac.yu

II. VEHICLE NETWORKS

The vehicle usually has several networks with different hardware and software realizations, that is, they operate using different protocols [1]. Network and network protocols for automotive applications must have the following basic characteristics:

- high integrability composed with other components and systems of the vehicle as a whole, that is, probability of occurrence of random error should be negligible and should not affect the vehicle functioning,
- functional adjustment, that is, maximal waiting time for a transfer and to transfer information should be short enough in order not to interfere with control,
- configurability of the network, that is, the network can be easily broadened and modified,
- error resistance, that is, communication has to be reconstructed when error is debugged, while the existence of the spare channel is advisable and, sometimes, necessary,
- minimal number of interconnections, that is, every additional connection/connector increases the probability of error occurrence,
- dimensionally and functionally adjusted connectors,
- electro-magnetic compatibility, ,
- environment resistance – resistance against temperature, humidity, vibration, dust, fuel drops, oils, lubricants, etc,
- low price.

The vehicle network should provide a connection to other computer systems outside the vehicle (navigation, diagnostics, vehicle ecological parameters control...). That is why it must also satisfy general standards of computer equipment connections given by ISO7498 which defines the Open System Interconnection (OSI) with seven basic interconnection layers.

Three layers of network interconnection are enough for the use in vehicles: layer 1- physical layer, layer 2- data link layer and layer 7- application layer, although there are protocols defining all seven interconnection layers (SAEJ1939).

Application of networks in control systems of vehicle systems has induced a need for appropriate protocol for information exchange between network nodes. Several types of protocols has appeared because producers reacted differently and named the protocols as follows: Volkswagen - ABUS protocol, Renault & PSA - VAN protocol, Toyota - BEAN protocol, General motors - J1850VPW protocol, Ford - J1850PWM protocol...

Society of Automotive Engineers (SAE) has divided vehicle networks into three classes, depending on information transfer rate through network: A, B and C. Fast development of multimedia applications (Internet, digital TV), as well as, so called "control by wire", X-By-Wire (e.g. vehicle control system), demand higher data transfer rates, resulting in formation of yet not standardized class D. Basic characteristics and purpose of classes mentioned are given in Table I.

Protocols can be divided into event-triggered and time-triggered protocols, according to manner in which they produce information.

TABLE I

Network class	Transfer rate	Application
A	<10kb/s Small speeds	Driver and passenger comfort; mirror and seat adjustment, opening the trunk, central lock-up
B	10-125kb/s Medium speeds	Vehicle instruments, vehicle speed, exhaust emission data
C	125kb/s-1Mb/s High speeds	Real time control of engine functions, vehicle dynamics, braking system
D	>1Mb/s	Real time control of systems responsible for driver and passenger safety; multimedia applications

III. EVENT TRIGGERED PROTOCOL

Event triggered protocols operate on the principle of generating information from a network node when there has been a change in information sent by that node. This type of protocols is usually implemented by serial network.

Event triggered protocols are: CAN (Controller Area Network), LIN (Local Interconnection Network), Byteflight, etc.

Bosch, with it's CAN protocol, formed in 1985, and given the actual form in 1991, has become a leading manufacturer in the area of network protocols for automotive application. Bosch has made it's protocol opened for all users, making it accepted very soon and a basis for ISO11898 and SAE standards for vehicles and also for industry and other areas.

CAN network is made of nodes that have a structure shown in Fig. 3., according to the OSI interconnection model.

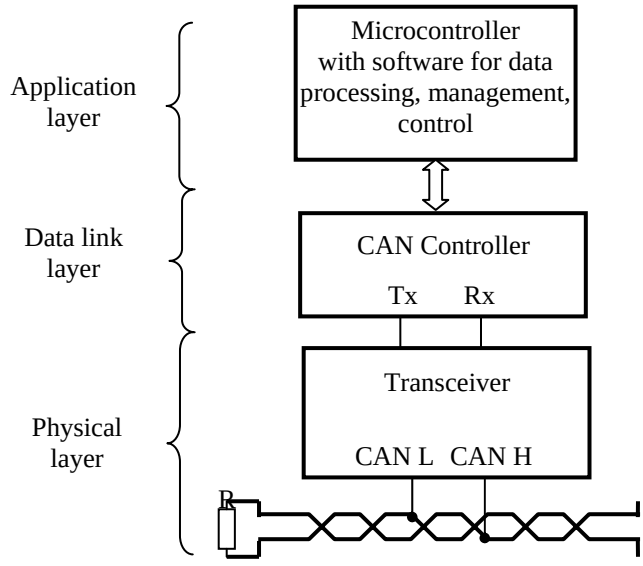

Fig. 3. Structure of CAN network node

The principle of operation of the network based on CAN protocol is based on the fact that only one network node sends the message at one moment and the message is received by all network nodes, including the one that sends it. The network should have the following features:

- Every message sent by a network has appropriate priority.
- Lower priority messages are guarantied to be sent after a certain time delay.
- The network should have flexibility in adding new nodes to the network.
- Synchronized receiving and transmission between all network nodes.
- Changeable format of data sent through the network.
- Several master nodes in the network.
- Error detection and signalization.
- Automatic repetition of inaccurate messages as soon as the network is available.
- Distinction between temporary and permanent errors in nodes and autonomous disconnection of inaccurate nodes.

Physical layer of CAN protocol consists of a line and a transceiver with appropriate connector.

The line as a medium is a double-wire cable with spanned conductors or with the shield. There are types of lines with only one conductor, where the mass is used as a second conductor. The line must be closed with characteristic resistance near to 120 Ω.

Transceiver is a part of the network node representing an electronic circuit which is directly connected to the line and which enables a two-way communication. It separates other electronic node parts from the line. If the line is long, it electrically separates the nodes from the line on which different disturbances can occur due to long length. Transceiver conducts a voltage processing of line data during the data receiving and sets the line in appropriate state during the data delivery. CAN communication go through the bits which can be dominant (logical 1) or recessive (logical 0).

Basic assumption for uninterrupted CAN protocol based network operation is that all network nodes are set to send and receive information at the same rate, that is, they must be synchronized.

Network message should have specific format and consist of segments. Basic message segments are shown in Fig. 5. The message begins with a dominant bit, representing the start of the message (SOF), then there are: the address or the identifier of a node emitting the message (IDENTIFIER), control part of a message (data length and type) (CONTROL), data, key for message accuracy checking and at the end (CRC), there is a confirmation on the message accuracy from all network nodes (ACK). The message is followed by a period of network inactivity in order to prepare the network for processing the next message (EOF).

Two basic CAN protocol types are defined in relation to identifier's length: Standard CAN protocol with the identifier 11 bits long, through CAN protocol 2.0A and Extended CAN protocol with the identifier 29 bits long, through CAN protocol 2.0B. Within the same network, nodes that support CAN 2.0B protocol can exchange information with nodes supporting CAN 2.0A protocol, while reverse exchange is not possible.

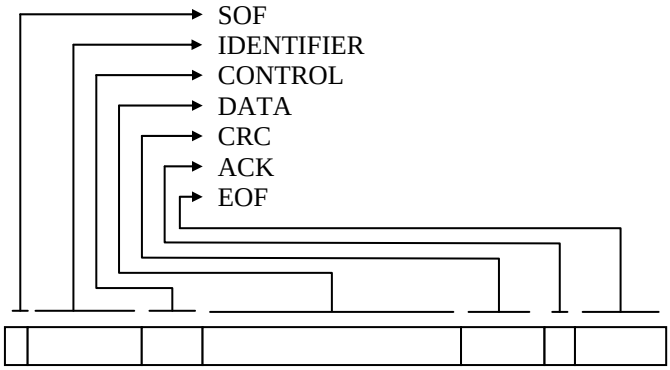

Fig. 4. Basic segments of CAN message

Message priority is determined by identifier, because every node has unique identifier. If two or more nodes start emitting the message at the moment when the line is available, a priority is given to the node which has a dominant bit at the difference in identifiers. Lower priority nodes stop emitting a message and transfer to receiving regime and the emitting of a new message waits until the line is available again.

The length of data in the message can vary between 0 to 8 bytes and it is defined by control bits sent before data.

Accuracy of received message is controlled by a sequence of 15+1 bits generated by a message sender and based on algorithm defined by standard, and it represents a segment of the message (CRC - Cyclic Redundancy Check).

Errors that occur during data transfer can have different shapes and origins, and they are detected by hardware and software processing of received signal. Basic hardware error detection is obtained by a node emitting a message, by comparison of the sent bit with the one read from the line. The next level in error detection is examination if there are 6 consecutive bits of the same type, because it is forbidden by a protocol. Error is also signalized in the case when there is an illegal bit at the end of constant length sequences (identifier, CRC, the end of the message...). Software error detection is obtained by checking of the message with the help of CRC sequence.

The line is available when at least 10 consecutive recessive bits are detected, 7 of which represent the end of the previous message and 3 or more represent a delay for next message preparation.

CAN protocol application layer is specific to every network node. At the application layer, network control units perform processing of data received by a network, as well as data received from the transducer locally connected to the control unit, and generate data necessary for sent by a network.

IV. TIME TRIGGERED PROTOCOL

Messages from TTP (Time Triggered Protocol) are sent in time intervals set in advance [6]. Total time by which all messages should occur is divided into intervals, sections, and at every node, a section is determined to which the message should be sent. All network nodes have access to the network and can read all other messages, including their own. Due to time definition of moment at which the message is sent, the

network must be timely synchronized, which is usually achieved by a special node that sends synchronization pulses to all nodes.

Time triggered protocols are: TTP/C, FlexRay®, etc. Their basic application is anticipated for systems critical from the aspect of safety, like "X-by-wire" systems, where the existing mechanical systems are substituted by mechatronic systems. Mechatronic systems have no reserve mechanical systems to take over the control in the case of electronic system failure, so it is necessary that electronic systems with their communication channels are made in such a way to be immune against any kind of error.

In order that time triggered protocol is able to function, it is necessary that each node should have separate TTP controller for protocol control, independent on the process that has been controlled at the node [6]. TTP controller has a message descriptor list (MEDL). Message description contains time position of the section to which the message is sent, the length of the message and serial number of the message sent, because messages with different contents can be sent to one section, but according to order set in advance. The scheme of network node access is shown in Fig. 6.

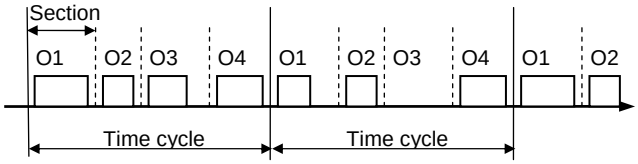

Fig. 5. Network node access at time triggered protocol

The message has a format set in advance, Fig. 7. The header contains information on sent data type, because there are two basic information types sent at DATA area: normal data used for sending information necessary for control and initialization data used for sending information on the state of TTP controller and network synchronization.

At time triggered protocol, the most dangerous error is so called "Bubbling idiot failure", which manifests through uncontrollable sending of messages from the node outside defined sections. The problem is solved by setting a node that monitors the network traffic (BUS Guardian) and occasionally can exclude the node from the network or perform the re-initialization of the network.

Determinancy of the time triggered protocol creates a great reliability in control systems, with even network loading, but it aggravates inclusion of new nodes into the network. Addition of new nodes requires a total reconfiguration of the entire network.

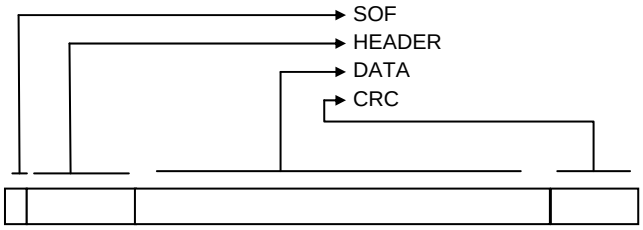

Fig. 6. Time triggered protocol message format

V. TIME TRIGGERED CAN PROTOCOL

Standard CAN protocol provide access to the line for all network nodes, but because of priority principle, some messages can be held back and, after a long enough time period, when they finally can be emitted, they became useless. Information loss is not desirable, especially in systems where "X-by-Wire" control is wanted. To avoid information loss, a time synchronization of network nodes and assignment of time interval when a node should emit it's message are proposed [5]. Time synchronization does not change a basic conception of CAN protocol and such a network is referred to as a Time Triggered CAN - TTCAN.

TTCAN divides time access to the network in such a way that, in certain time intervals, only some nodes - important for reliable control system functioning, have access to the line, while in other intervals, standard CAN protocol regimes are applied. In order to enable the system to function in this way, it is necessary for every node to have local clock which is occasionally synchronized with the network clock.

VI. CONCLUSIONS

Standard network protocols with serial communications enable great flexibility in introduction of new vehicle systems and in improvement of existing control units characteristics, but it is necessary to work on their development in order to enhance data transfer speed and reliability in data transfer, which are necessary for "drive-by-wire" principle.

ACKNOWLEDGEMENT

The paper is the result of the research within the project financed by the Ministry of science and environmental protection of the Republic of Serbia.

REFERENCES

[1] Rushby J.: "Bus architectures for safety-critical embedded systems", *EMSOFT 2001: Proceedings of the First Workshop on Embedded Software*, Volume 2211 of Lecture Notes in Computer Science, str.306-323, Lake Tahoe, SAD, Springer-Verlag, 2001

[2] Leen G., Heffernan D., Dunne A.: "Digital Networks in the Automotive Vehicle," *IEE Computer and Control Eng. J.*, p.p. 257-266, 1999

[3] Taranovic D., Grujovic A.: "Standardization of network protocols in vehicle electric interconnection", *Mobility & Vehicle Mechanics*, Volume 28, Kragujevac, 2002

[4] Robert Bosch Gmbh: *"CAN Specification Version 2.0"*, Stuttgart, 1991

[5] Hartwich F., Müller B., Führer T., Hugel R.: "CAN Network with Time-triggered Communication", *7nd International CAN Conference, CAN in Automation (CiA)*, 2000

[6] Scheidler C., Heiner G., Sasse R., Fuchs E., Kopetz H., Temple C.: "Time-Triggered Architecture (TTA)", *EMMSEC'97*, Florence, Italy, 1997

Ethernet Converting Module for Industrial Serial Interface

Stefan J. Ovcharov[1], Angel T. Stanchev[2], Nikolay T. Tuliev[3] and Peter I. Yakimov[4]

Abstract – **For controlling and monitoring the electrical power system, it is needed to be stored and computated the data for many electricity parameters measured in different points of the electrical system. In many cases it is needed the information for every parameter, to be sent to a monitoring and visualization main-system device, which is usually situated on a long distance from the basic measuring module.**

The results of this project will be used in designing an intelligent module for detecting the electricity quality with integrated Ethernet interface for network communication with main-system station.

Keywords – **Industrial interface, Ethernet, UDP, TCP/IP, PST08**

I. Introduction

For controlling the quality of the electricity, it is needed to be measured as many parameters as possible from different points of the network. The main goal of this project is to be designed technical equipment for transfer the measured values from the intelligent measuring modules to the main-station server through Ethernet. At the one side of the network is the intelligent device, which communication interface is type of industrial serial interface. At the other side of the network is a main station, which can be situated on a long distance. The interface for communication is based on Ethernet.

The integrated serial digital interface in PS intelligent modules gives the possibility for network connection between them and a Personal Computer. This connection is based on RS232 interface and the maximum devices, which can be connected to RS232 port of a PC is 10.

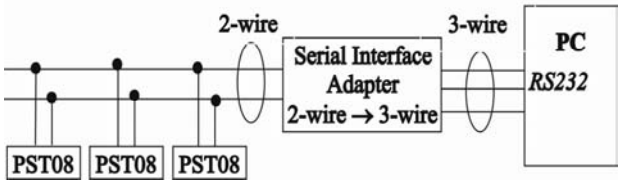

Fig. 1a. Network communication between PST08 and PC, based on the serial interface integrated in the intelligent sensors

[1]Stefan J. Ovcharov is with the Faculty of Electronic Engineering and Technologies, Dept. of Electronics, Technical University - Sofia, 1000 Sofia, Bulgaria, E-mail: sjo@tu-sofia.bg

[2]Angel T. Stanchev is with the Faculty of Electronic Engineering and Technologies, Dept. of Electronics, Technical University - Sofia, 1000 Sofia, Bulgaria, E-mail: astanchev@tu-sofia.bg

[3]Nikolay T. Tuliev is with the Faculty of Electronic Engineering and Technologies, Dept. of Electronics, Technical University - Sofia, 1000 Sofia, Bulgaria, E-mail: ntt@tu-sofia.bg

[4]Peter I. Yakimov is with the Faculty of Electronic Engineering and Technologies, Dept. of Electronics, Technical University - Sofia, 1000 Sofia, Bulgaria, E-mail: pij@tu-sofia.bg

The maximum speed of transfer is 9600 bps, and the physical connection is made through an adapter (Fig. 1a).

The Ethernet communication interface gives the possibility to connect many of the modules in network again by using interface adapter (Fig. 1b). This network permits transfers of data with 10Mbps.

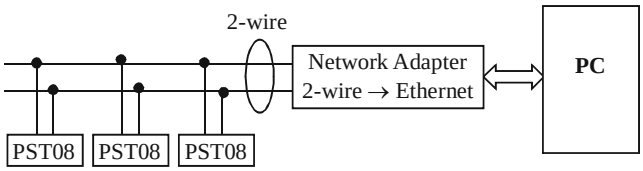

Fig.1b Ethernet network communication between PST08 and PC /2-wire serial interface converted to Ethernet/

II. Basic features of the Ethernet Converting Module

The 2-line serial interface has the following data transfer protocol: when the sensor receives command $02 (data from the measurement), the reply is:

TABLE I
Transmit data description

Byte Number	Content
0	Address
1	Command
2	40($28),
3, 4	$U1_{MS}$, $U1_{LS}$
5, 6	$U2_{MS}$, $U2_{LS}$
7, 8	$U3_{MS}$, $U2_{LS}$
9, 10	$I1_{MS}$, $I1_{LS}$
11, 12	$I2_{MS}$, $I2_{LS}$
13, 14	$I3_{MS}$, $I3_{LS}$
15, 16	P_{MS}, P_{LS}
17, 18	Q_{MS}, Q_{LS}
19, 20	Fст, Fмл
21 - 32	reserved
33, 34	φU2a, φU2b
35, 36	φU3a, φU3b
37, 38	φI1a, φI1b
39, 40	φI2a, φI2b
43, 44	CS1, CS2

The main disadvantages of the integrated digital serial interface in PST08 sensors refer to the impossibility of transferring data on a long distance. On the other side, this protocol is simple, but also non-standard. Besides that, the personal computers in now days don't have serial interface as integrated one and it is complicated to develop a network through RS232 interface, which is replaced by USB. Base on

these facts, it is decided to be used a new modern approach for network connection.

For realization of network connection between PST08 sensors and a PC, without making changes of the electrical circuit of the sensors, the only decision is to be used the digital serial interface integrated in the intelligent modules, but the data from it to be converted to another protocol suitable for transferring data faster and on a long distance. After this conclusion, it was decided to be designed an adapter module for converting the serial data into Ethernet packets. The Ethernet network is now very popular and it is not expensive to be made. The basic components needed for developing this kind of communication is an Ethernet controller, HUB or Switch and the physical connection – UTP/FTP cable and RJ45 plug and connector. After the investigation, it was made a conclusion that it is appropriate to be used RTL8019 integrated circuit produced by the Taiwan Company **Realtek**. This Ethernet controller is intended for 10Mb/s networks with 8-bit ISA interface. For controlling this IC it is needed an 8-bit data signal, address signals and IOW, IOR and Reset signals. IOW and IOR signals are for allowing writing and reading to/from the RTL8019 registers. For this purposes it is very convenient to be used an 8-bit microcontroller for realization of the physical and software interface between the serial data from the sensor and the Ethernet controller. For 8-bit microcontroller is chosen the PIC16F877 MCU produced by **Microchip**. This MCU has enough I/O pins for the purposes and its program FLASH memory and data EEPROM memory are enough for development. The main purpose of the microcontroller is to collect data from the serial interface, to store the information and after that to prepare Ethernet packets for sending through RTL8019.

For communication over IP protocol every device in the network has own MAC (6 Bytes) and IP (4 Bytes) address. When two devices want to communicate the sender has to note source and destination MAC and IP addresses.

For communication over Internet Protocol, the minimal service is UDP, adding only optional checksumming of data and multiplexing by port number. TCP (Transmission Control Protocol) is a connection-oriented transport service; it provides end-to-end reliability, resequencing, and flow control.

TCP enables two hosts to establish a connection and exchange streams of data, which are treated in bytes.The delivery of data in the proper order is guaranteed. TCP enables two hosts to establish a connection and exchange streams of data, which are treated in bytes. TCP can detect errors or lost data and can trigger retransmission until the data is received, complete and without errors. But in this case it is needed more resource from the MCU placed on the adapter module.

The adapter module connected with PST08 is similar to **gateway,** which makes possible communication between two devices with different standards and protocols. In this case, a command is sent from the main station in the network. Every adapter has an individual IP address, which corresponds to every intelligent sensor. It means that it is needed an adapter for every sensor. To be connected with a PC, the adapter modules have to be connected to a HUB or Switch. The adapter module recognizes the IP address sent from the main station and it sends a command to PST08 for data request. The sensor begins transmitting data to the adapter, where the PIC16F877 stores the data in its data EEPROM memory. The microcontroller prepares the packets for transmitting to the main station through Ethernet over UDP protocol (first tests are over UDP) or TCP. The software on a high level, installed on the PC, helps for collecting, storing and visualizing data in convenient for the user way. It is very important the transferred data to be protected against hacker attacks. All the commands and data have their own specific coding for transferring over UDP type of protocol. The Ethernet Converting Module can switch on its IP address by receiving command from the main station device. This command is transferred over ARP protocol.

III. ELECTRICAL CIRCUIT DESCRIPTION OF THE CONVERTER BOARD

From the designed electrical circuit shown in fig. 3 it can be found the following modules integrated in it:

- Serial interface communication;
- Microcontroller for communicating with Industrial Serial Interface of PST08 and driving the Ethernet controller;
- Ethernet controller for network communication over ARP, UDP and ICMP Internet Protocols.

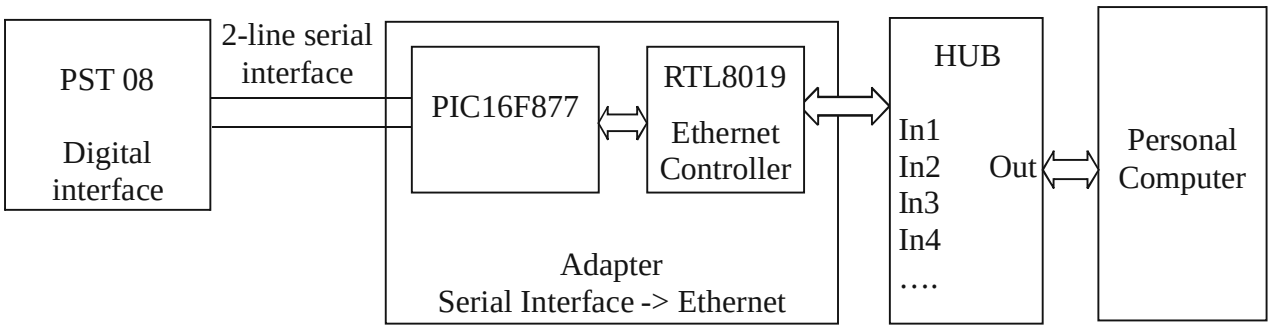

Fig. 2 Functional block diagram of the network system

1. Serial interface communication circuit is based on T1, T2 transistors and U3, U4 optocouplers. There are two lines from the side of microcontroller - Tx line – for transmitting data from the converter board to PST08; Rx line – for receiving data from PST08 to converter board.

The optocouplers in the electrical circuit shown in fig.4 are needed because of galvanic insulation between the receiving-transmitting lines of the adapter board and the PST08 Industrial Serial Interface (ISI). That is why it is used two 5V power supply lines, obtained from two different coils of a transformer. The connection of the converter board with ISI of PST08 is realized with CON2 connector. There are two lines named "+" and "–".

2. Microcontroller used in this circuit is PIC16F877-20I/PQ. The package is 44-pin QFP, and the integrated modules very useful for this project are 8Kwords (1 word is 14-bit) program memory, 368 bytes data RAM memory, 256 bytes EEPROM data memory and the hardware Universal Synchronous Asynchronous Receiver Transmitter (USART). The work of the microcontroller is organized as follows: 8-lines Port D of the microcontroller is connected to 8 data pins of RTL8019 Ethernet controller. For driving the RTL8019 IC it is needed also driving IOW, IOR and RESET signals and A0-A4 addressable lines. The EEPROM data memory is used for storing the basic MAC and IP addresses and the data coming from the PST08. The MAC address is unique for every adapter module, but the IP address can be changed through ARP protocol. In first place the PICMicro is waiting for a command from the main station over UDP, ICMP or ARP protocols. If the command is to change the IP address, the microcontroller takes the needed data which includes the new 4 bytes IP address, stores it in the EEPROM data memory, and resets. After reset the adapter module has new IP address. If the received packet is a command for asking data from PST08, the microcontroller stores the Ethernet packet in the RAM data memory takes the command from it and sends it through Tx line of the USART module. The ISI interface is so organized that if there is no connection between the converter board and the PST08, the byte transmitted by PICMicro Tx line is not received on Rx line. The microcontroller is making checking if every transmitted byte is received properly by the PST08. If it is not, the PICMicro is sending warning to the main station over UDP interface. If PST08 is received everything properly, the adapter module is waiting for coming data on Rx line of the PICMicro. One cycle of coming data is 44 bytes (table 1). All these bytes are stored in the EEPROM data memory. After all 44 bytes are received, the PICMicro prepares the UDP packet for transmitting the data to the main-station. In this case the data EEPROM memory is used for storing only 2x44 bytes data coming from PST08, which means that it stores only 2 measurement results. All of the statistics is made in the high level software installed on the main-station.

3. Ethernet controller RTL8019

The PICMicro is driving only the first 5 address lines, and the other are connected to GND and VCC as shown in fig. 3. For indication of network communication state it is used 2 LEDs – LED0 for indication of LINK presence; LED1 for Carrier Sense LED (LED_CRS = LED_TX + LED_RX). The physical connection for Ethernet communication is based on UTP/FTP cable with RJ-45 connector. In the electrical circuit in fig. 3 is shown the CON8 connector, which in this case is with integrated transformer. If the RJ-45 connector does not have integrated transformer it can be used external one. The interface is differential and it is needed TPTX+ and TPTX- lines for transmission and TPRX+ and TPRX- lines for receiving.

Another module in the electrical circuit is the "Prog" connector. This connector is used for In-Circuit Serial Programming Debugging of the PICMicro.

IV. RESULTS

After the tests made with the Ethernet communication between PST08 and main-station PC, it was found that this electrical circuit is enough for realizing an ARP, ICMP and non-standard UDP protocols. The connection is reliable and the transfer of data is fast enough for these purposes.

V. CONCLUSIONS

Ethernet communication is fast enough, it gives a possibility for collecting, storing and visualizing data on a PC screen situated on a long distance from the destination points, in this case the intelligent sensors. For reliable connection it is recommended to be used TCP, but the UDP is also convenient.

The electrical circuit shown in fig. 3 will be upgraded by using newer PICMicro with more EEPROM and RAM data memory. It can be used also another type of Ethernet controller which is specialized for Embedded Systems applications by SPI interface (For example this is the future product of Microchip – ENC28J60 – 10Mbits/s Ethernet controller). In this case it is not needed so many pins of the microcontroller.

REFERENCES

[1] Ovcharov St., N. Tuliev, A. Stanchev, Adapter module for Ethernet Network Communication over TCP/IP, Proceedings of the 13th International Scientific and Applied Science Conference "Electronics ET'2004", September 22-24, 2003, Sozopol, Bulgaria, book 2, pp. 60-65

[2] Ovcharov St., P. Yakimov, Instrumental interface for industrial network development, "Electrotechnics and electronics", Sofia, Bulgaria, in press (in Bulgarian)

[3] http://www.faqs.org/rfcs/rfc768.html – UDP

[4] http://www.faqs.org/rfcs/rfc791.html – IP

[5] http://www.microchip.com

[6] http://www.realtek.com.tw

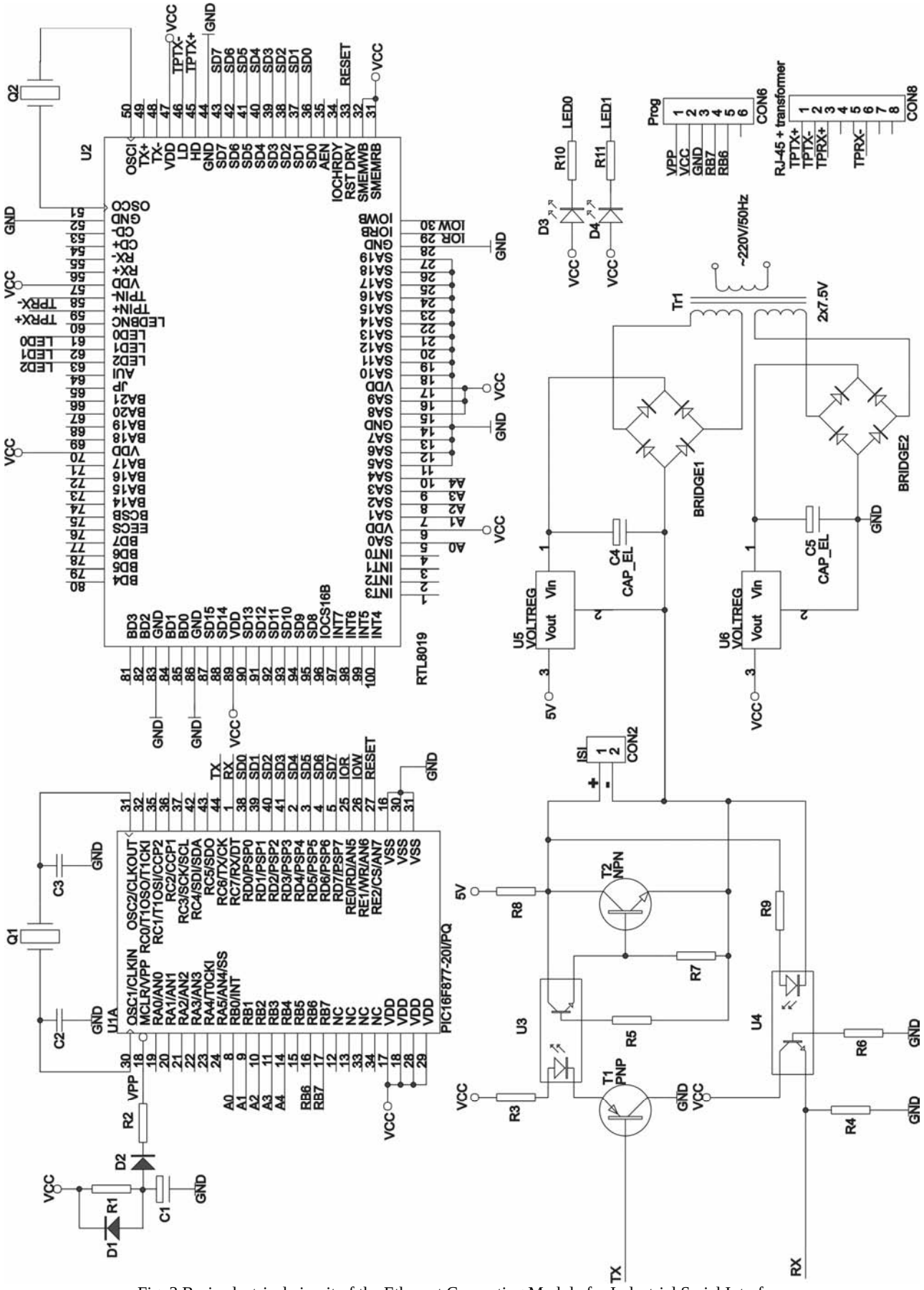

Fig. 3 Basic electrical circuit of the Ethernet Converting Module for Industrial Serial Interface

Automated Tracking of Marks on Moving Objects

Mladen Savov[1]

Abstract - **The problem of the automated tracking of marks, placed on moving objects, is discussed. Different techniques for localization of the marks are pointed out. Experiments with human body parts tracking have been carried out. The approach could be used for tracking of moving objects and evaluation of their kinetic characteristics.**

Keywords - **Tracking, Marks, Moving Objects, Human Motion**

I. INTRODUCTION

Object tracking in a sequence of images is an important task in the field of computer vision. Different techniques have been developed for estimation of the movement of vehicles, indoor and outdoor tracking of humans, analysis of motion in biomedicine, etc. Tracking results are mathematically analyzed and thus movement dynamics description is obtained.

The algorithms for objects' tracking are based on either optical flow or localization and tracking of features. *Optical flow* represents a displacement vector field in the image plane induced by the motion of objects, by the observer or both. Optical flow methods can be divided into three groups [2]: differential methods – they compute image velocity with spatio-temporal derivatives of the intensity; frequency methods – using information about the energy and the phase in the image spectrum; matching methods – calculating the displacements of tokens matched in small series of images. The goal of the *feature-based* tracking methods [4, 8] is to discriminate the moving features from the static ones and to calculate the point correspondences in a sequence of images. The correspondence techniques are based on tracking pixels and tokens – point, line or region.

The human motion analysis lies on the assumption that the body movement can be considered as a movement of articulated objects. The study of such motion is related to kinematics, which is concerned with the geometry of the object, its position, orientation and deformation. The *2D human tracking methods* are appearance-based (using texture, color, shape, etc.), or model-based (using preliminary information about the motion) [10]. A certain part of the methods use only one camera, but build 3D human body model [5]. They can be called *pseudo-3D methods*. Actual *3D methods* are used when two or more cameras, placed in different positions are working at the same time [6].

[1]Mladen Savov is with the Institute of Information Technologies – BAS, acad. G. Bontchev, bl.2, Sofia, Bulgaria, E-mail: ihaiha99@abv.bg.

In many cases the study of the movement of specific body parts such as face, hands, fingers, legs, etc. is needed. Human limbs can be modeled as a system of rigid objects connected with articulations with one or more degrees of freedom. In case of tracking, markers and constant background are often used. Many applications are developed in the area of security, motion estimation of physical exercises, etc. [7, 9].

II. ALGORITHMS FOR AUTOMATED TRACKING OF MARKS

In this study two methods for tracking, based on the localization of areas with specific light intensities, are investigated: localization of the marks in a region and with the assistance of a kinetic model.

According to the first method the moving marks in the *n*-th image are supposed to be located in a region near their centers of gravity in the previous image *n-1* from the sequence. The size of the search region (square or circle) is set according to the dimensions of the marks, their speed and computation time. The search is accomplished around predicted positions of the marks, calculated according to the equations:

$$\hat{x}_n = x_{n-1} + (x_{n-1} - x_{n-2}), \quad \hat{y}_n = y_{n-1} + (y_{n-1} - y_{n-2}), \tag{1}$$

where (x_{n-1}, y_{n-1}) and (x_{n-2}, y_{n-2}) are the coordinates of the corresponding mark in the previous two images. The coincidence of the light intensities of the pixels and the marks is determined by an admissible deviation for the components of the digital image – red, green and blue, expressed with three conditions related with the logical function "AND":

$$|R_n - R| < \theta \wedge |G_n - G| < \theta \wedge |B_n - B| < \theta, \tag{2}$$

where R_n, G_n and B_n are the color components of the current pixel, *R*, *G* and *B* determine the color of the mark and θ is a number between 0 and 255, which gives the maximal admissible deviation. The approach is appropriate for cases when the marks are clearly different from the other objects in the scene, no matter if the objects are moving or not. Problems can occur when two marks with identical light intensities get very close to one another or when one mark overlaps the other.

The description of the movement of connected objects can be based on certain kinetic model. The presence of such a model can facilitate the algorithm of tracking, as in that case the movement of the marks can be restricted to some determined trajectories – circles, for example. In case of marks placed on object's axes of rotation, such as human joints, the distance between marks placed on consecutive joints can be considered constant and the trajectory of one of them can be fixed on a circle centered at *(α, β)* in the previous and with radius *R* equal to the distance between them. To avoid some fluctuations, a certain thickness *r* at these circles is assumed. The condition for a pixel to be on the circle is:

$$(R-\frac{r}{2})^2 < (x-\alpha)^2 + (y-\beta)^2 < (R+\frac{r}{2})^2 \quad . \qquad (3)$$

Such motion model is idealized so its realization is restricted to the case when the camera is positioned perpendicularly to the examined object. Even in that particular case moving objects may not lie in the same plane, which will produce some offset from the position expected.

III. EXPERIMENTAL RESULTS

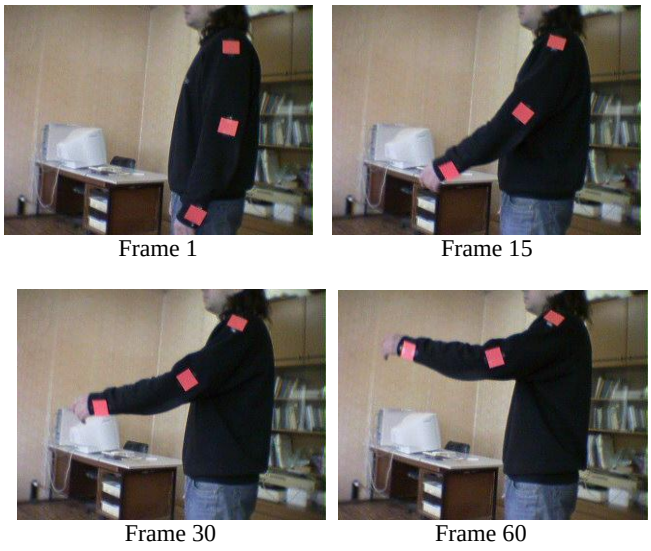

Frame 1 Frame 15

Frame 30 Frame 60

Fig. 1. Frames from the recorded sequence

In the experiments, a real indoor scene with a human arm movement has been investigated. Color rectangles have been pasted at the location of the three joints – shoulder, elbow and wrist, and used as marks. A movie in *AVI* file format, 25 frames per second, with consecutive positions of the arm has been recorded with a static Sony USB color camera and then has been divided in images in *BMP* file format, with resolution 640x480 and 24 bits per pixel. Using the described approaches, separated frames, containing the consecutive positions of the person's arm, have been processed (Fig. 1).

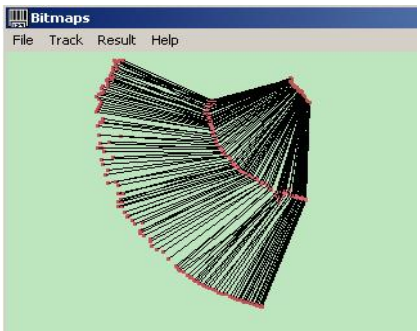

Fig. 2. Positions of the human arm in the image sequence

The best results have been obtained with the method of searching within region, using a square with size of 40 pixels and setting the admissible deviation for the color components to 10. In Fig. 2 the consecutive positions of the three marks are given, the marks in each frame being connected with lines, showing the current position of the arm. Tracking with the assistance of a kinetic model using a thickness of 20 pixels for the circles gives similar results.

IV. CONCLUSION

An automated tracking of colored marks on moving objects is realized with the help of different methods for localization of the positions of the marks in sequential images. The scene used in the experiments consists of a person with markers on his moving arm. Problems can occur if different marks get very close to one another or if one mark overlaps the other. A solution can be found using different colors for the marks or studying the trajectories and the velocities of movement of the marks. The developed algorithms are realized in a software program using Microsoft Visual C++. Possible applications can be found in the area of analysis of human motion when performing sport exercises (darts, boxing, cycling), biomedicine, gait recognition, security, etc.

ACKNOWLEDGEMENTS

This work is supported by the Institute of Information Technologies of BAS and by the Ministry of Education and Sciences under contract I-1302/2003.

REFERENCES

[1] D. Ballard, C. Brown, "Computer Vision". Prentice-Hall, Inc., New Jersey, USA, 1982.

[2] J. Barron, S. Beauchemin, D. Fleet, "On Optical Flow". 6th Int. Conf. on Artificial Intelligence and Information-Control Systems of Robots, pp.3-14, Slovakia, 1994.

[3] G. Baxes, "Digital Image Processing". John Wiley & Sons, Inc., New York, USA, 1994.

[4] M.-O. Berger, "Tracking rigid and no polyhedral objects in an image sequence". Proc. 8th Scandinavian Conference on Image Analysis, Vol.II, pp.945-952, Norway, 1993.

[5] C. Bregler, J. Malik, "Tracking People with Twists and Exponential Maps", Proc. IEEE Computer Vision and Pattern Recognition, pp. 8-15, 1998.

[6] D. Gavrila, L. Davis, "3-D model-based tracking of humans in action: a multi-view approach", Proc. CVPR, pp. 73-80, 1996.

[7] L. Goncalves, E. Bernardo, E. Ursella, P. Perona, Monocular Tracking of the Human Arm in 3D, ICCV Proceedings, pp. 764-770, 1995.

[8] J. Shi, and C. Tomashi, "Good Features to Track", Proc. CVPR, pp. 593-600, June 1994.

[9] J. Wang, S. Singh, "Video Analysis of Human Dynamics – a survey". Real-Time Imaging, Vol.5, pp.320-345, Oct. 2003.

[10] C. Wren, A. Azarbayejani, T. Darrell, A. Pentland, "Pfinder: Real-time tracking of the human body". IEEE transactions on pattern analysis and machine intelligence, 19 (7), pp. 780-785, 1997.

Research and Implementation of Direct Digital Synthesis (DDS) in Programmable Logic Devices

Goran D. Goranov[1]

Abstract – **The flexibility of the Direct Digital Synthesis (DDS) makes it suitable for synthesis of generators for application in many areas of the electronics. It is a common practice to use PLL for transistor converter control. This function could be implemented in analog or digital way. The alternative representation of the analog function is done by digital logic blocks, implemented by specialized integrated circuits or inside programmable logic devices. This paper presents the use of DDS as numerically controlled oscillator (NCO), implemented inside a Complex Programmable Logic Device (CPLD).**

Keywords – **Direct digital synthesis, PLL, phase ripple, programmable logic device.**

I. INTRODUCTION

The basic advantage of the digital synthesis is that the output frequency could be regulated fast and with high, a-priory stated accuracy of the value and the phase. This approach is spreading vastly in various fields of the digital electronics, and particularly in Digital Control Systems. With the development of new integrated circuits it becomes possible to implement the analog Phase-Locked Loop (PLL) function in alternative (digital) ways. The implementation of digital functional blocks inside an integrated circuit (programmable logic device) allows for operation at higher frequencies with smaller temperature error.

The union of algorithms and architectures for this purpose allows for the development of the necessary combinational and register structures, programmable generators, digital phase detectors, digital filters, etc. inside a single chip.

The goal of this research is to develop a possible application of DDS in control systems for transistor power converters. The application of DDS as Numerically Controlled Oscillator (NCO) is accompanied by the presence of a phase ripple (phase noise) [5] which must be compensated to certain extent.

II. DIGITAL PLL

The control of transistor power converter devices widely uses Phase- Locked Loop function, which adapts the control system to the characteristics of the converter according to given algorithm.

[1] Goran D. Goranov is with the department of Electronics, Technical University of Gabrovo, H.Dimitar str. 4., Bulgaria. E-mail: g_goranov@tugab.bg.

Fig.1 shows basic digital PLL, consisting of phase detector DPD, which converts the phase difference in a signal with certain duration, digital filter DLF, which converts the signal from the phase detector and digitally controlled oscillator DCO [1].

During the system operation the frequency fout of the output signal of the DCO aims to match the input frequency fin with certain accuracy. The change in the input frequency fin causes an increase or decrease of the phase difference between itself and the output fout, which leads to a tendency of frequency matching fin = fout.

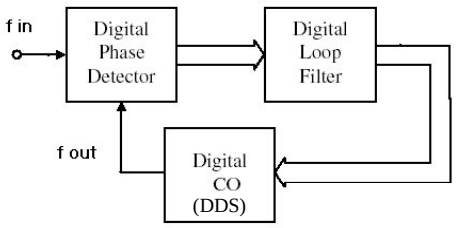

Fig.1. Digital PLL

It is essential that the output signal of the phase detector is processed. In this case the controlled oscillator DCO is based on DDS, thus it's necessary that the output signal of the detector is converted into a binary number.

It's possible to use filter- converter of time duration into digital code. The acquired code (word) N directly controls the oscillator, changing its frequency proportionally to the value of N – Fig.2. A requirement of the synthesis is that the clock frequency CLK is much greater than the frequency of the EVENT input – Fig.3 [2].

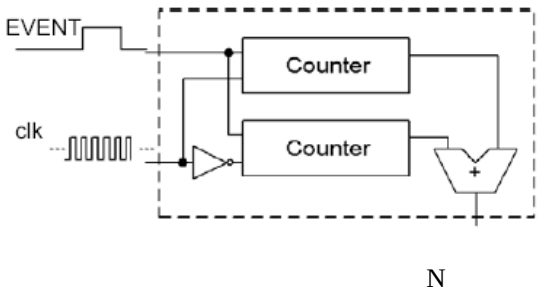

Fig. 2.Time-to-digital-code converter.

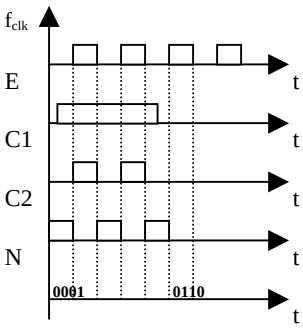

Fig. 3. Waveform of the time-to-digital-code converter.

III. PULSED-OUTPUT DDS

A simplified diagram of a DDS is shown in Fig. 4. The basic building blocks are Phase accumulator, P2A – phase-to-amplitude converter (a sine waveform, stored in memory), Digital-to-analog converter and low-pass filter [3], [4].

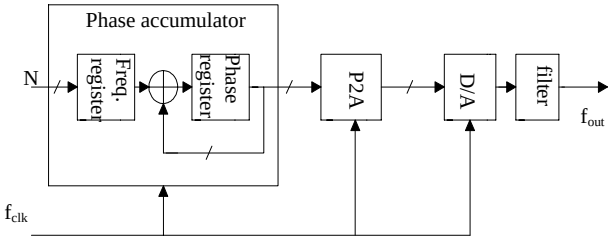

Fig.4. Block Diagram of a DDS.

DDS is normally carried out by specialized integrated circuits like the AD9830, manufactured by Analog Devices. Due to the fact that the transistor converters need only a pulse train only the phase accumulator can be used, which turns the DDS into so-called pulsed- output DDS.

The pulsed- output DDS is one of the application forms of DDS. It consists of only the phase accumulator, who's carry output (or the most- significant bit of the accumulator) is used as an output. The research and implementation of the DDS is carried out using PLD of the Xilinx Corporation, namely S10PC84 and the Xilinx Foundation software. An 8-bit accumulator is implemented (as shown in Fig.5), and the waveforms for its operation are shown in Fig. 6.

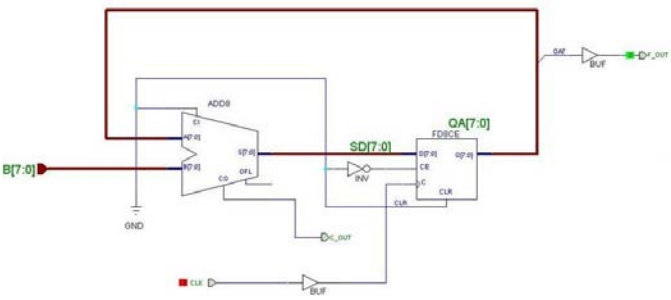

Fig.5. 8-bit wide phase accumulator.

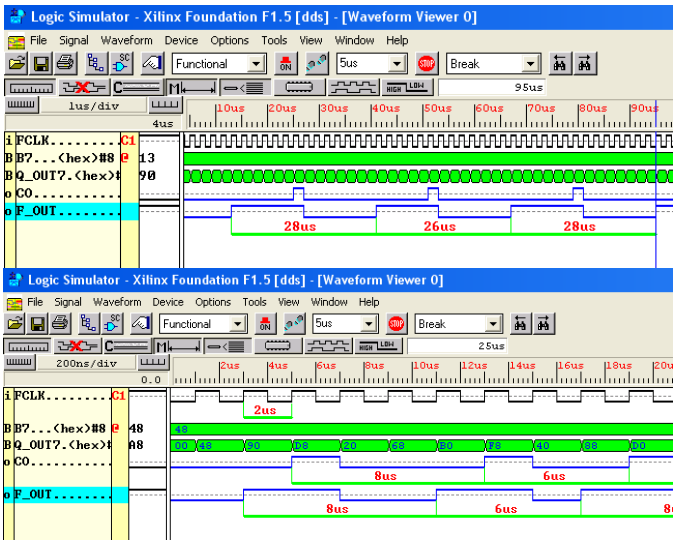

Fig.6. Waveforms of 8-bit wide phase accumulator operation.

The output frequency of the DDS is calculated from the equations:

$$f_{out} = \frac{N.f_{clk}}{2^k} \quad (1)$$

$$\frac{f_{out}}{f_{clk}} = \frac{N}{2^k} \quad (2)$$

Where the value of N determines the output frequency and k is the width of the adder and the register.

The frequency change step Δf is calculated according to:

$$\Delta f = \frac{f_{clk}}{2^k} \quad (3)$$

The maximal output frequency fout is fclk / 2, which will be acquired at 1/2N. The DDS operation is accompanied by a phase noise (phase jitter) of the output frequency with magnitude of 1/Tclk - Fig. 6. The presence of phase jitter is due to the fact that the accumulator can accomplish transitions only from integers, multiple to the clock period. Let us consider for example 4-bit wide phase accumulator (k=4) and an input word N=5. The ideal case should state that the accumulator must generate carry each 16/5 cycles, that is 3.2 clock periods, which is impossible. The real case introduces a phase jitter which will gradually decrease to zero and then increase to 1/Tclk. The first transition (Table. 1) must occur at 3.2 cycles, but it occurs after 4 cycles. The phase error is 4/5 of the period.

TABLE I.
N=5, k=4 (4-bit wide accumulator)

Accumulator output	Carry output
0000 (0)	1
0101 (5)	0
1010 (10)	0
1111 (15)	0
0100 (4)	1
1001 (9)	0
1110 (14)	0
0011 (3)	1
1000 (8)	0
1101 (13)	0
0010 (2)	1
0111 (7)	0
1100 (12)	0
0001 (1)	1
0110 (6)	0
1011 (11)	0
0000 (0)	1

After the second transition the error is 3/5 from the period and the ideal case shows that the transition must occur after 6.4 clock periods, but it actually occurs after 7 periods. The relation between N and the carry C determines the phase error:

$$\varepsilon = \frac{C}{N} \tag{4}$$

The phase jitter reduction is normally done by output frequency division, for example by 4, which decreases the phase noise by a factor of 4, as it is a function of the output frequency [5].

An alternative is to use reset of the flip-flops at the end of the cycle using the carry output of the adder – Fig. 7.

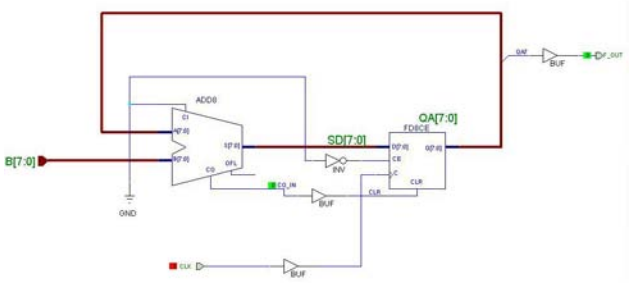

Fig.7. DDS with forced reset.

This approach changes the sensibility of the output frequency change. With the increase of the input word N the step with which the output frequency will rise will gradually increase. For example in Table 1 the first cycle begins with the value of 0 and ends with a remainder 4 after the carry, which happens on the fourth cycle i.e. after 4 Tclk periods. Forcing a reset actually causes the same cycle to be repeated each time by changing the value of the remainder, thus eliminating the phase noise, but also changing the step of the output frequency. Fig. 8 shows example waveforms of the clock frequency and output frequency of the DDS.

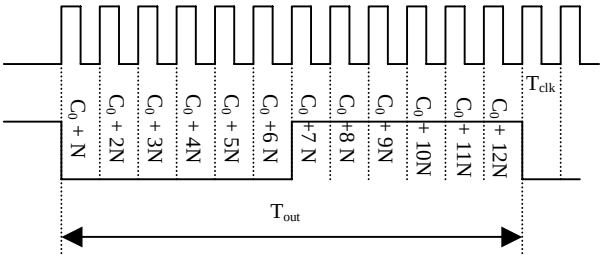

Fig.8. Output frequency and clock frequency

The value of the adder Sb depends on the count of the clock periods The count of the clock periods B is calculated according to:

$$B = \frac{T_{out}}{T_{clk}} = \left[\frac{2^k}{N}\right] \quad , \tag{5}$$

Where [x] is the round- down function, that returns the largest integer less than x. Thus, B is always an integer, and the adder value will be:

$$S_b = C_0 + B.N \tag{6}$$

Where C0 is the remainder value.

The overflow condition is $Sb \geq 2\kappa$, so:

$$C_0 + B.N \geq 2^k \tag{7}$$

$$B \geq \left[\frac{2^k - C_0}{N}\right] \tag{8}$$

It is obvious that B depends on the remainder value C0, and since after reset C0=0, we come to:

$$B \geq \left[\frac{2^k}{N}\right] \tag{9}$$

The number of clock pulses B is always an integer (1, 2, 3, …) which determines the non-uniform change in the frequency step and the varying duty-cycle. To achieve 50% duty-cycle the output frequency must be divided in two by a T-flip-flop. The waveforms from the simulation of the schematic, depicted in Fig. 7 show clearly the non-symmetrical output and the absence of phase jitter – Fig. 8.

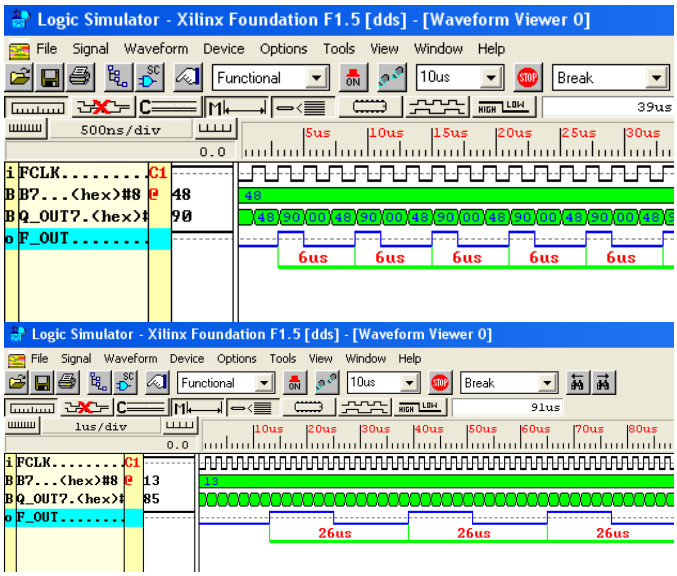

Fig.9. DDS with forced reminder zeroing..

The phase jitter elimination is on the price of the uniform output frequency change. In this case the change in output frequency is non- uniform and is given by the equation:

$$\Delta f = f_{clk} \frac{1}{B(B+1)} \qquad (10)$$

A small step is achieved with big values of the clock pulses B, i.e. smaller values of the input word N. The relation between Δf and N at different clock frequencies and the same phase accumulator architecture is shown on Fig. 9. It can be seen that a change in the output frequency for big N occurs only after serious increase in N, i.e. N being increased by more than 1. This effect follows directly from Eq. (9).

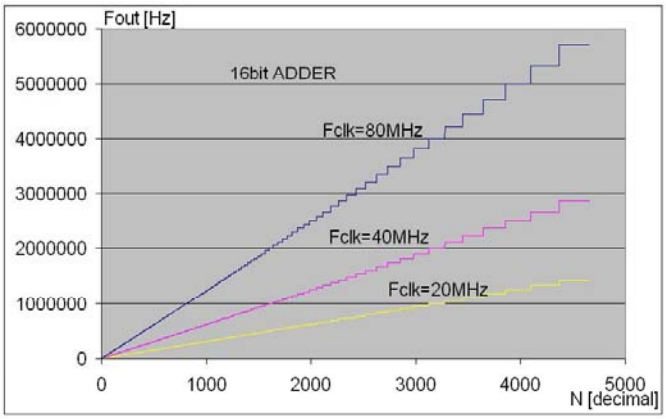

Fig.10. Relation between fout and N.

IV. Conclusion

The developed and analyzed digital DDS generator with forced reset of the remainder has relatively low and non-linear sensibility with respect to the input word N.

In this case the DDS is applicable after limiting the actual range of values of N up to 5% of the maximal value of N, which in turn depends on the width of the phase accumulator.

References

[1] *All Digital Phase-Locked Loop,©* P.E. Allen-2003.

[2] Thomas Olsson and Peter Nilsson, *A Digitally Controlled PLL for Digital SOCs***,** Dept. of Electroscience, Lund University. Box 118, SE-22100, Lund, Sweden. ISCAS 2003

[3] B. H. Hutchison, Jr., *Frequency Synthesis and Applications*, IEEE Press, New York, NY, USA, 1975.

[4] J. Tierney, C. Rader, and B. Gold *A Digital Frequency Synthesizer*, IEEE Trans. Audio and Electroacoust., Vol. AU-19, pp. 48-57, Mar. 1971

[5] Austin Lesea, *Frequency Synthesis*, XILINX Corporation, Xcell31-1Q99

Modeling and Optimization of an Electric Drive System with Dual-Zone Speed Regulation

Mikho R. Mikhov[1], Boyan G. Balev[2]

Abstract – **The performance of a DC electric drive system with dual-zone speed regulation has been discussed in this paper. Detailed investigation and analysis by means of modeling and computer simulation have been carried out for different loads at the respective transient and steady state regimes. The developed models and the results obtained can be used in optimization and final tuning of such types of speed control drive systems.**

Keywords – **Electric drive system, Dual-zone speed regulation.**

I. INTRODUCTION

By technological reasons dual-zone speed regulation is often required in industrial automation. Regulation is carried out at constant motor torque until a basic speed level is reached. After that, it is realized at constant power. The rated speed is most often regarded as basic speed value.

Usually one of the two fundamental principles of control are being employed in the electric drive systems with dual-zone speed regulation, namely:

a) independent control;

b) dependent control.

In the first case, up to a reference value of the input signal, the control is carried out through the armature voltage; above this value it is realized by the motor excitation current, at constant armature voltage.

By the second principle, for the entire range of speed regulation, control is done by the armature voltage, as the excitation current change is a function either of the back electromotive force (EMF) voltage, or of the armature voltage.

A distinctive feature of the dual-zone speed regulation is that the system structure changes along the process of regulation and the optimal coordination of zones creates the main control problem.

Mathematical modeling and computer simulation offer effective ways to investigate the electric drive systems in details, in various dynamic and static working regimes, especially when it is not possible or is inconvenient to carry out such tests in laboratory or industrial environments [4].

This paper discusses a DC electric drive system with dual-zone speed regulation, where control shift is a function of the motor back EMF voltage. Through modeling and computer simulation, operation in the transient and steady state regimes has been analyzed, at various loads and disturbances applied to the motor shaft. Some results from these investigations are reported.

[1]Mikho R. Mikhov is with the Faculty of Automatics, Technical University of Sofia, 8 Kliment Ohridski Str., 1797 Sofia, Bulgaria, E-mail: mikhov@tu-sofia.bg

[2]Boyan G. Balev is with Kontrax Ltd., 13 Tintiava Str., 1113 Sofia, Bulgaria, E-mail: bbalev@kontrax.bg

II. FEATURES OF THE ELECTRIC DRIVE SYSTEM

The electric drive system block diagram is shown in Fig. 1, where the following notations have been used: $G_{sc}(s)$ - transfer function of the speed controller; $G_{c_1c}(s)$ - transfer function of the armature current controller; K_{p_1} and τ_{p_1} - gain and delay of the armature voltage power converter; $R_{1\Sigma}$ - armature circuit resistance; $\tau_{1\Sigma}$ - armature circuit time-constant; K_{c_1f} and τ_{c_1f} - gain and time-constant of the armature current feedback; K_{sf} and τ_{sf} - gain and time-constant of the speed feedback; $G_{ec}(s)$ - transfer function of the back EMF voltage controller; $G_{c_2c}(s)$ - transfer function of the excitation current controller; K_{p_2} and τ_{p_2} - gain and delay of the excitation voltage power converter; $R_{2\Sigma}$ - excitation circuit resistance; $\tau_{2\Sigma}$ - excitation circuit time-constant; K_{c_2f} and τ_{c_2f} - gain and time-constant of the excitation current feedback; K_{ef} и τ_{ef} - gain and time-constant of the back EMF voltage feedback; K_{Φ} - coefficient of the magnetic flux curve gradient; c' и c'' - motor coefficients; V_{sr} - speed reference signal; V_{sf} - speed feedback signal; V_{c_1r} - armature current reference signal; V_{c_1f} - armature current feedback signal; V_1 - armature voltage; I_1 - armature current; T - motor torque; T_l - load torque applied to the motor shaft; J_{Σ} - total inertia referred to the motor shaft; ω - angular motor speed; V_{er} - back EMF voltage reference signal; V_{ef} - back EMF voltage feedback signal; V_{c_2r} - excitation current reference signal; V_{c_2f} - excitation current feedback signal; V_2 - excitation voltage; I_2 - excitation current; Φ - magnetic flux.

The electric drive system under consideration consists of two interrelated subsystems:

a) dual-loop subsystem for speed regulation, which includes an external speed loop and a subordinated armature current loop;

b) dual-loop subsystem for back EMF voltage regulation, including external back EMF voltage loop and subordinated excitation current loop.

Speed regulation until the value of $\omega \le \omega_{\text{rat}}$ is carried out at rated magnetic flux $(\Phi = \Phi_{\text{rat}})$, at the expense of the armature voltage change. At $\omega > \omega_{\text{rat}}$ the regulation is done

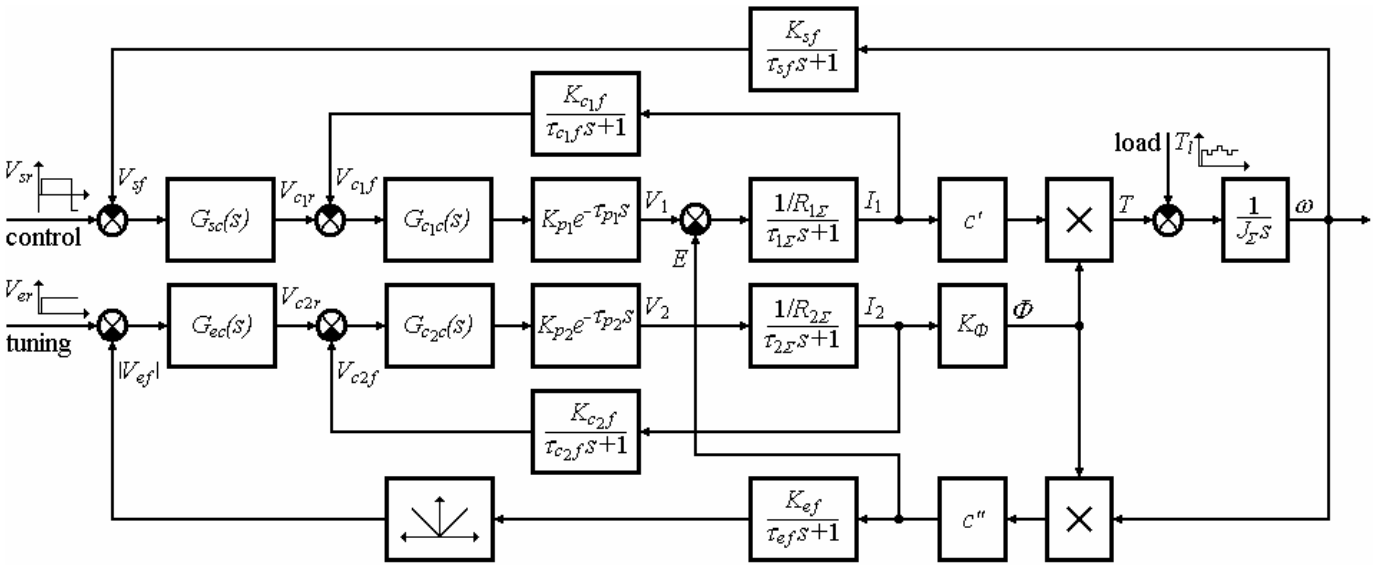

Fig. 1. Block diagram of the discussed electric drive

through the flux reduction $(\Phi < \Phi_{\text{rat}})$.

Within the entire range, speed is set up by the control signal V_{sr}, while through the tuning signal V_{er} a back EMF voltage, determining the basic speed is defined.

If the electric drive system should be of four-quadrant type with both current and speed reversion, the power converter for armature voltage is of reversive type, while the power converter for the excitation voltage is non-reversive. If speed direction changes, the feedback signal sign of V_{ef} changes, but the V_{er} signal remains with the same sign. For that reason, to avoid the V_{ef} sign influence, in four-quadrant drive systems an absolute value block is included.

III. Synthesis of Back EMF Voltage Sensor

In order to receive information about the back EMF voltage, a suitable sensor has been developed. The block diagram, illustratig the prosses of obtaining information about the back EMF voltage is shown in Fig. 2, where the used notations are as follows: $G_{vs}(s)$ - transfer function of the voltage sensor; $G_{cs}(s)$ - transfer function of the current sensor.

Evaluation of the back EMF voltage is carried out on the basis of a signal, proportional to the armature voltage and a signal about the armature current compensation, proportional to the voltage fall in R_a, i.e.:

$$V_{ef}(s) = V_v(s) - V_c(s). \tag{1}$$

Depending on both the voltage sensor and current sensor transfer functions, diverse back EMF voltage transfer functions $G_{es}(s)$ can be obtained.

Several versions have been explored to select the most appropriate pair. The one with the following transfer functions has been chosen:

$$G_{vs}(s) = \frac{K_{vs}}{\tau_a s + 1} \tag{2}$$

$$G_{cs}(s) = K_{cs} = K_{vs} R_a, \tag{3}$$

where τ_a is the electromagnetic time-constant of the respective armature circuit section.

After substitution of Eqs. (2) and (3) in Eq. (1), for the feedback signal V_{ef} the following expression is obtained:

$$V_{ef}(s) = \frac{K_{vs}}{\tau_a s + 1}\left[E(s) + I_1(s) R_a (\tau_a s + 1)\right] - \\ - K_{vs} R_a I_1(s). \tag{4}$$

From Eq. (4) the transfer function of the back EMF voltage sensor receives the following form:

$$G_{es}(s) = \frac{V_{ef}(s)}{E(s)} = \frac{K_{ef}}{\tau_{ef} s + 1}, \tag{5}$$

where the gain and the time-constant of the back EMF voltage feedback are defined respectively as:

$$K_{ef} = K_{vs} \tag{6}$$

and

$$\tau_{ef} = \tau_a. \tag{7}$$

Inserting a filter with a time-constant τ_{ef} into the feedback loop enhances the drive system noise protection.

In electric drive systems with single-zone speed regulation, the represented back EMF voltage sensor can be used for sensorless control, replacing the respective electromechanical speed sensor, fixed on the motor shaft.

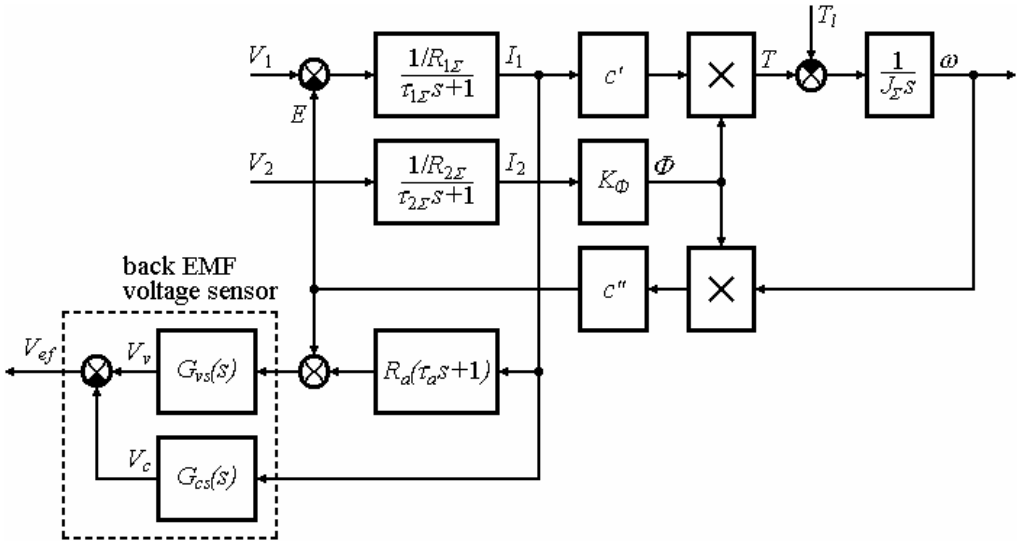

Fig. 2. Block diagram illustratig the prosses of obtaining information about the back EMF voltage

IV. Control Loops Optimization

The subsistems are of dual-loop type, with subordinated regulation. Control loops opitimization is carried out following the resepctive critera, providing for the necessary performnce [1], [3]. Controllers tuning is done sequentially, starting from the innermost loops.

The armature current loop optimization can be carried out taking into account or neglecting the internal feedback by the back EMF voltage. In the general case this depends on the ratio between the two big time-constants $\tau_{m\Sigma}$ and $\tau_{1\Sigma}$. The bigger summary electromechanical time-constant $\tau_{m\Sigma}$, the lower is the error from neglecting the back EMF voltage influence.

In the case of neglecting the internal feedback by the back EMF voltage, the transfer function of the armature current controller assumes the following form:

$$G_{c_1c}(s)=\frac{R_{1\Sigma}(\tau_{1\Sigma}s+1)}{2K_{p_1}K_{c_1f}\tau_{\mu c_1}s}, \tag{8}$$

where $\tau_{\mu c_1}=\tau_{p_1}+\tau_{c_1f}$ is the summary small time-constant of the loop, not subject to compensation.

Reading the back EMF voltage influence, the current controller transfer function is as follows:

$$G_{c_1c}(s)=\frac{\tau_{1\Sigma}\tau_{m\Sigma}s^2+\tau_{m\Sigma}s+1}{2K_{p_1}K_{c_1f}\tau_{\mu c_1}\tau_{m\Sigma}s^2/R_{1\Sigma}}. \tag{9}$$

One of the used versions for the first subsystem external loop optimization leads to the following transfer function of the speed controller:

$$G_{sc}(s)=\frac{4\tau_{m\Sigma}\tau_{\mu s}s^2+\tau_{m\Sigma}s}{8K_mK_{sf}R_{1\Sigma}\tau_{\mu s}^2s^2/K_{c_1f}}, \tag{10}$$

where: $\tau_{\mu s}=2\tau_{\mu c_1}$; $K_m=1/c'\Phi_{\text{nom}}$.

For the transfer function of the excitation currnent controller the following equation is obtained:

$$G_{c_2c}(s)=\frac{R_{2\Sigma}(\tau_{2\Sigma}s+1)}{2K_{p_2}K_{c_2f}\tau_{\mu c_2}s}, \tag{11}$$

where $\tau_{\mu c_2}=\tau_{p_2}+\tau_{c_2f}$ is the summary small time-constant of the respective loop, not subject to compensation.

After optimization of the back EMF voltage loop, an integral controller is achieved, with the following transfer function:

$$G_{ec}(s)=\frac{K_{ec}}{\left[2\tau_{\mu c_2}+\tau_a+\sqrt{(2\tau_{\mu c_2}+\tau_a)^2+\tau_a^2}\right]s}, \tag{12}$$

where $K_{ec}=K_{c_2f}/K_{ef}K_\Phi c''\omega$.

Using the MATLAB/SIMULINK software package a number of computer simulation models have been developed of systems with dual-zone speed regulation for various tunings of the control loops.

Detailed investigations have been carried out in the respective dynamic and static regimes at diverse loading, disturbances and work conditions.

V. Some Simulation Results

Fig. 3 shows some of the time-diagrams, obtained through inverstigations of the system in the first zone of speed regulation. The transient start process is shown, as well as operaton at steady state regime with rated load torque applied

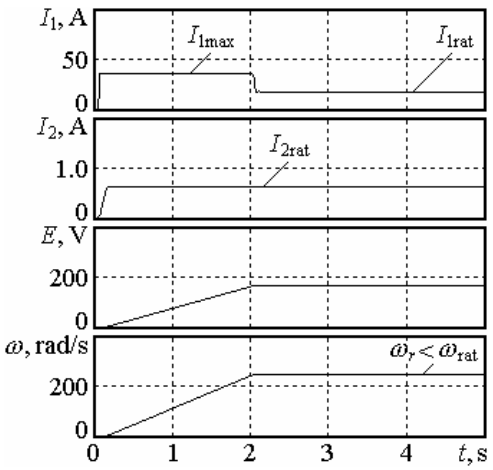

Fig. 3. Time-diagrams about the first zone of speed regulation

to the motor shaft. The set motor speed is $\omega_r < \omega_{rat}$ and the starting armature current is limited to the maximum admissible value of I_{1max}, which provides a maximum starting

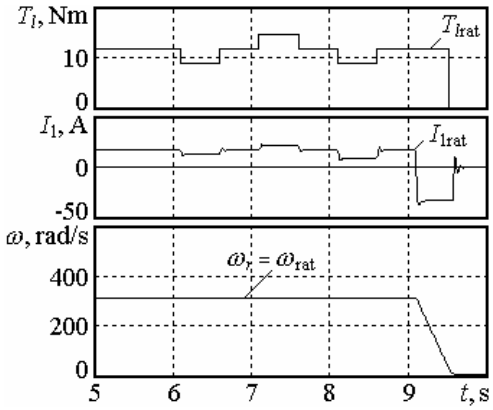

Fig. 4. Speed stabilization and braking regime

motor torque. The excitation current is of a consntant value of $I_2 = I_{2rat}$.

Fig. 4 represents speed stabilization in the presence of disturbances. The load torque is equal to the rated value T_{lrat}, while the disturbances applied sequentially are $\Delta T_l = -25\%$, $\Delta T_l = +25\%$ and $\Delta T_l = -25\%$, respectively. The braking regime is illustrated for initial motor speed of $\omega_r = \omega_{rat}$.

Fig. 5 shows torque/speed curves of the four-quadrant electric drive system, where ω_{max} is the upper bound of the speed regulation range and T_{max} is the maximum motor torque. At $\omega_r > \omega_{rat}$ excitation cuttent in steady state regime is $I_2 < I_{2rat}$, while the admissible armature current is automatically limited below the I_{1max} value.

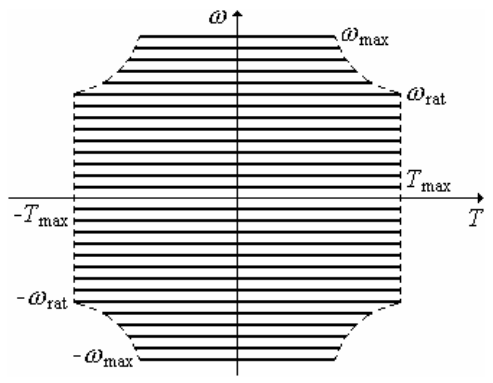

Fig. 5. Torque/speed curves of the four-quadrant drive system

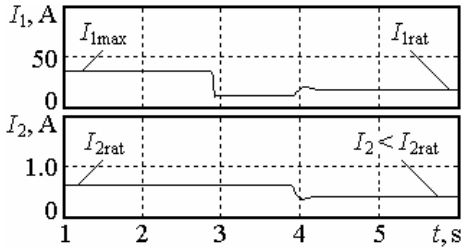

Fig. 6. Change of the motor currents in the zone with flux weakening

The change of the motor currents in the zone of speed regulation with flux weakening control is represented in Fig. 6.

VI. Conclusion

Computer simulation models of electric drive systems with dual-zone speed regulation have been developed, allowing investigations at various loads and disturbances applied to the motor shaft.

Optimization of the control loops by different criteria has been carried out, as well as analysis of the dynamic and static regimes for the respective versions of controllers tuning.

The rated parameters of the separately excited DC motor are as follows: $P_{rat} = 3.4$ kW, $V_{1rat} = 220$ V, $I_{1rat} = 17.6$ A, $\omega_{rat} = 314$ rad/s.

The simulation models and the results obtained from the respective investigations can be used as in optimization and tuning of drive systems of the class discussed above, so as illustration in the process of teaching about such types of electric drives.

References

[1] A. V. Basharin, V. A. Novikov, G. G. Sokolovskiy, *Control of electric drives*, Sankt Petergburg, Energoizdat, 1982 (in Russian).

[2] U. Keuchel, R. M. Stephan, *Microcomputer-based adaptive control applied to thyristor-driven dc motors*, London, Springer-Verlag, 1994.

[3] N. Mohan, *Electric drives – an integrative* approach, Minneapolis, MNPERE, 2003.

[4] C. Ong, *Dynamic simulation of electric machinery*, New Jersey, Prentice Hall, 1998.

[5] M. R. Mikhov, "Control of dual-motor drive systems", *ICMIT 2001 Conference Proceedings*, pp. 198-203, Yamaguchi, Japan, 2001.

The Probability Stability of Continuous Systems with Randomly Selected Parameters

Dragan Antic[1], Bojana M.Vidojkovic[2] and Biljana Vidojkovic[3]

***Abstract* – An approximate method for the probability stability estimation of systems whose parameters are random values is presented in this paper. This method can be applied to the continuous and discrete systems as well. In the paper the method is illustrated using the example of the second order electrical circuit. Electrical circuit is modeled using bond graphs wherewith obtaining the characteristic equation of the system is enabled. The characteristic equation of the system is essential for the calculation of the probability stability. The computation results are shown in table.**

***Keywords* – Probability stability, continuous systems, bond graph.**

I. INTRODUCTION

In many branches of industry the systems in which some parameters cannot be computed and measured precisely occur. It happens that the values of the parameters do not coincide with the nominal values because these parameters often depend on values having stochastic character. For that influence the properties of the system deviate from the desirable values. Those deviations can be very large and can make the normal work of the system impossible. That is why is necessary to estimate the influence of the stochastic values on the system properties. This estimation is very important for the system stability and quality working.

The basic methods for the probability stability estimation of the randomly selected parameters are given in [1-4]. These methods relate to the continuous systems. However, the method can be applied on discrete systems with the random parameters too, [5-7].

The calculation of the probability stability enables the determining of such parameter values for which the system has the largest probability stability. The advantage of this method is in its practical use. In this paper the presented method is illustrated on the electrical circuit whose parameters are random, exponentially distributed values. The presented method can be applied to the other probability distributions also.

The characteristic equation of the system is essential for the calculation of the probability stability. There are different methods for deriving characteristic equation. In this paper the causal bond graphs are used for obtaining the state space model and characteristic equation of the system, [8-10].

II. THE PROBABILITY STABILITY DETERMINING OF THE CONTINUOUS SYSTEMS

Let the transfer function of the continuous system is given by:

$$W(s)=\frac{s^n+b_{n-1}s^{n-1}+\cdots+b_1s+b_0}{s^n+a_{n-1}s^{n-1}+\cdots+a_1s+a_0} \tag{1}$$

The appropriate characteristic equation of this system is:

$$s^n+a_{n-1}s^{n-1}+\cdots+a_1s+a_0=0 \tag{2}$$

The coefficients of the characteristic equation are random variables with the probability density distributions $p_i(a_i)$. In the case when the system parameters are constant, system can be stable or non stable depending on parameter value. If the parameters of the system are random variables, the system can be stable with probability stability P. The main goal is to determinate that probability stability.

First the area stability of the system (1) must be obtained using some of the methods for the stability test, for example the Hurwitz criterion.

The system (1) is stable if all zeroes of the characteristic equation (2) are in the left half of the s –plane. The necessary and sufficient condition for the stability of system (1) is that all diagonal minors D_i of matrix D:

$$D=\begin{vmatrix} a_{n-1} & a_{n-3} & a_{n-5} & \cdots & 0 \\ a_n & a_{n-2} & a_{n-4} & \cdots & 0 \\ 0 & a_{n-1} & a_{n-3} & \cdots & 0 \\ 0 & a_n & a_{n-2} & \cdots & 0 \\ \vdots & \vdots & \vdots & \vdots & \vdots \\ 0 & 0 & 0 & \cdots & a_0 \end{vmatrix} \tag{3}$$

are greater than zero, i.e.:

$$D_1=a_{n-1}>0; \tag{4}$$

$$D_2=\begin{vmatrix} a_{n-1} & a_{n-3} \\ a_n & a_{n-2} \end{vmatrix}>0, \text{ etc}$$

[1]Prof.dr Dragan Antic, dipl.ing is with the Faculty of Electronic Engineering, Aleksandra Medvedeva 14, 18000 Nis, SCG, E-mail: dantic@elfak.ni.ac.yu

[2]Mr Bojana M. Vidojkovic, dipl ing is with the Faculty of Occupational Safety, Carnojevica 10a, 18000 Nis, SCG, E - mail: bojana@znrfak.znrfak.ni.ac.yu

[3]Mr Biljana Vidojkovic, dipl. ing. is with the Faculty of Science and Mathematics, Visegradska 33, 18000 Nis, SCG, E - mail: biljana@pmf.ni.ac.yu

The stability area of the continuous system (1) is obtained in the parametric space using the nonlinearities (4).

For the second order system $s^2 + a_1 s + a_0 = 0$ the stability area, S_2, is the first quadrant and it is defined by the next relations:

$$\begin{aligned} &a_1 > 0 \\ &a_1 \cdot a_0 > 0 \Rightarrow a_0 > 0 \end{aligned} \tag{5}$$

The stability area, S_3, for the third order continuous system $s^3 + a_2 s^2 + a_1 s + a_0 = 0$ is obtained from the next set of nonlinearities:

$$\begin{aligned} &a_2 > 0 \\ &a_1 \cdot a_2 - a_0 > 0 \Rightarrow a_1 > 0 \\ &a_0 \cdot (a_1 \cdot a_2 - a_0) > 0 \Rightarrow a_0 > 0 \end{aligned} \tag{6}$$

For the *n* – th order continuous system the area of stability is determinated using the relations (4), also. However, the calculation is far too complex. Particularly, the limits of the stability area are usually complex mathematical relations and is difficult to determinate the probability stability because it is necessary to integrate by the area of stability.

If the probability density distributions $p_i(a_i)$ are given and if parameters of the systems are independent variables, then the total density distribution is given by:

$$p(a_1, \ldots, a_n) = \prod_{i=1}^{n} p_i(a_i) \tag{7}$$

The probability stability of the system (1) is:

$$P = \int_{S_n} \cdots \int p(a_1, \ldots, a_n) da_1 \cdots da_n \tag{8}$$

For the calculation of probability stability the knowledge of the system characteristic equation is necessary. Further in the paper the derivation of the characteristic equation using bond graphs will be presented.

III. Obtaining the System Characteristic Equation using Bond Graphs

Bond graphs, introduced in 1961 by Paynter, are very actual nowadays as universal approach for modeling of different types of physical systems. The main advantage of this modeling technique is that it is based on the fundamental physical law – the law of the energy conservation. Bond graph consists of elements exchanging energy through the connection connected them. These connections are bonds. The bond is presented with the half arrow indicating the direction of the energy flow between connected bond graph elements. The transported power is the product of two variables, the effort and the flow. The effort (for example: voltage, force, pressure, etc.) and the flow (for example: current, velocity, volume flow rate, etc.) are generalization of similar phenomenon in physics.

The important advantage of bond graphs is the natural selection of the variables. The memory of the system is in I and C bond graph elements, so it is natural to connect state variables to these elements. This connection, for the effort storage, I element, is done by mathematical relation describing this element:

$$f(t) = \frac{1}{\alpha} \int e(\tau) \mathrm{d}\tau \tag{9}$$

It is obvious to select the state variable *x* as:

$$x = f \Rightarrow \dot{x} = \frac{1}{\alpha} e \tag{10}$$

or:

$$x = \alpha f \Rightarrow \dot{x} = e \tag{11}$$

The both selections are equal, but only one of them can be natural from the physical point of view. In both cases, the flow f is determinated by x and the effort e is obtained by system state and input.

For the flow storage, *C* element, the appropriate equation is:

$$e(t) = \frac{1}{\beta} \int f(\tau) \mathrm{d}\tau \tag{12}$$

with the next selection of the state:

$$x = e \Rightarrow \dot{x} = \frac{1}{\beta} f \tag{13}$$

or:

$$x = \beta e \Rightarrow \dot{x} = f \tag{14}$$

Hence, in this case the state variable is the effort *e*, while the flow *f* can be obtained from the system state and the input.

If we introduce the state equations in Eqs. (10) and (13) for all *I* and *C* elements, the system description in the state space is obtained as well as all flows of *C* elements and all efforts of *I* elements as functions of states and inputs. The flow of *I* element and the effort of *C* element are state variables and the outputs of these elements as well. Therefore, the calculations can be done considering that *I* elements are flow sources, and *C* elements are effort sources. Further, efforts and flows of other bond graph elements in bond graph can be obtained knowing their mathematical relations.

The application of bond graphs for system modeling and obtaining the characteristic equation will be illustrated on example of the second order electrical circuit. On Fig. 1 the second order electrical circuit is shown.

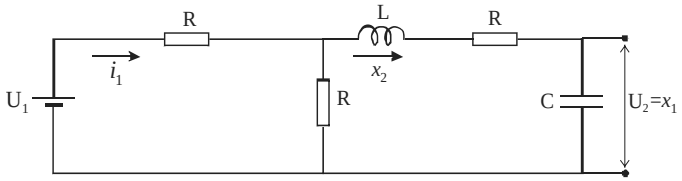

Fig.1. The second order electrical circuit

On Fig. 2 the causal bond graph model of given system is presented. This model is important for obtaining the state space equation.

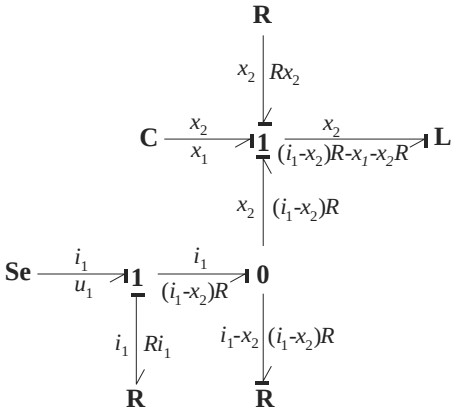

Fig.2. Causal bond graph model of the second order electrical circuit

In order to obtain the state space model, state variables are: effort on *C* element x_1 and flow through *L* element x_2. The state model is given by:

$$\begin{aligned}\dot{x}_1 &= \frac{1}{C}x_2 \\ \dot{x}_2 &= \frac{1}{L}\left((i_1 - x_2)R - x_1 - x_2 R\right)\end{aligned} \tag{15}$$

where current i_1 is:

$$i_1 = \frac{u_1 + Rx_2}{2R} \tag{16}$$

The state model becomes:

$$\begin{aligned}\dot{x}_1 &= \frac{1}{C}x_2 \\ \dot{x}_2 &= -\frac{1}{L}x_1 - \frac{3}{2}Rx_2 + \frac{1}{2L}u_1\end{aligned} \tag{17}$$

The state matrix is given by:

$$\mathbf{A} = \begin{bmatrix} 0 & \frac{1}{C} \\ \frac{-1}{L} & \frac{-3R}{2L} \end{bmatrix} \tag{18}$$

The characteristic equation of the system is obtained from the next relation easily:

$$\det(\mathrm{s}\mathbf{I} - \mathbf{A}) = 0 \tag{19}$$

where **I** is unit matrix of the second order and the characteristic equation is:

$$\mathrm{s}^2 + \frac{3R}{2L}\mathrm{s} + \frac{1}{LC} = 0 \tag{20}$$

IV. The Calculation Results

Comparing Eqs. (20) and (2) can be concluded that $a_1 = \frac{3R}{2L}$ and $a_0 = \frac{1}{LC}$. Assume that the resistance *R* and capacitance *C* change their values by the exponential law and the appropriate density distributions are $p_R = Ae^{-aR}$ and $p_C = Be^{-bC}$. The probability stability of the given electrical circuit due to the change of the parameter values should be determinate. Since a_1 and a_0 are the functions of the variables *R* and *C*, the transformation of this random variables must be done. Using the Jacobian:

$$J = \begin{vmatrix} \frac{\partial R}{\partial a_1} & \frac{\partial R}{\partial a_0} \\ \frac{\partial C}{\partial a_1} & \frac{\partial C}{\partial a_0} \end{vmatrix} \tag{21}$$

the next density distribution of the two – dimensional random variable is obtained:

$$p(a_1, a_0) = p(R, C) \cdot |J| \tag{22}$$

The probability stability of the system is obtained using Eq. (8) where S_2 is the first quadrant. The computation results are given in the next table. The resistance *R* does not influence on the computational results.

TABLE I
Computational Results

a	0.05	0.05	0.08	0.03	0.07	0.05
b	0.06	0.06	0.09	0.043	0.08	0.06
L $[H]$	1.5	1.1	0.6	0.2	0.2	0.1
P	0.329	0.424	0.776	0.883	0.981	0.997

V. Conclusion

Presented method enables the probability stability determining of the continuous systems with randomly selected parameters. This method can be used in practice which is demonstrated on the example of the second order electrical

circuit. Electrical circuit is modeled using bond graphs wherewith the obtaining the characteristic equation of the system is enabled. The results are given in table. Using this method is possibly to choose such values of parameters for which the system has the largest probability stability.

REFERENCES

[1] S. A. Ajsagaliev, G. S. Cerenskij, "Ocenka verojatnosti ustojcivosti linejnih sistem so slucajnimi parametrami", *Tehniceskaja kibernetika*, no 5, pp.119 – 202, 1981.

[2] A. M. Mihajlicenko, "K vyboru optimaljnogo metoda ocenki kacestva sistemy pri dejstvii parametriceskih vozmoscenij", Institut matematiki an USSR, Kiev, 1989.

[3] B. Dankovic, "The probability stability estimation of the systems with more random parameters", *Hipnef*, pp.300 – 307, 1988.

[4] B. Dankovic, M. Jevtic, "On the estimation of working capability of the automatic control system", *Hipnef*, Belgrade, Yugoslavia, pp.233 – 238, 1990.

[5] B. Dankovic, B. M. Vidojkovic, Z. Jovanovic, B. Vidojkovic, "The probability stability estimation of discrete systems with random parameters", *XXXVII International Scientific Conference on Information, Communication and Energy Systems and Technologies*, Nis, Yugoslavia, pp.257 – 260, 2002.

[6] Y.C.Schorling, T. Most, C. Bucher, "Stability analysis for imperfect systems with random loading", in *Proceedings of the 8th International Conference on Structural Safety and Reliability*, Newport Beach, USA, pp.1 – 9, 2001.

[7] Z. Jovanovic, B. Dankovic, "On the probability stability of discrete–time control systems", *FACTA UNIVERSITATIS (NIS)*, Vol.17, pp.11 – 20, April 2004.

[8] P. J. Gawthrop, L. Smith, *Metamodelling:* " Bond graphs and dynamic systems", London: Prentice Hall International, 1996.

[9] J. Thoma, "Introduction to bondgraphs and their applications", Oxford: Pergamon press, 1975.

[10] D. Antić, B. Vidojković, "Obtaining System Block Diagrams based on Bond Graph Models and Application of Bondsim Tools", *International Journal of Modelling & Simulation*, *21*(4), pp.257-262, 2001.

System Sensitivity and Identification Error Correlation for Discrete-time Dynamic Systems

B. Danković[1], D. Antic[2], M. Milojković[3]

Abstract- **This paper presents system sensitivity and identification error correlation for discrete-time dynamic systems. Parametric sensitivity of discrete-time dynamical systems is determined using simulation model. Using the same model and sum method, error of parametric identification is calculated. Finally, correlation between these two set of values is determined.**

Keywords- **Sensitivity, Identification, Correlation**

I. INTRODUCTION

It's well known fact that linear system's parameter sensitivity depends on system working frequency. For low frequencies, sensitivity is highest with respect to lowest parameter indexes. In case of high frequencies, sensitivity is highest with respect to highest parameter indexes.

On the other hand, it's well known that during inertial systems identification, it is easiest to estimate coefficients with lowest indexes. During estimation of coefficients with higher indexes, great error occur.

These two facts reveal existence of correlation between system sensitivity and identification error i.e. higher sensitivity implicates lower error and lower sensitivity implicates higher identification error.

In this paper, method for estimating correlation coefficient between process sensitivity and identification error is given. For sensitivity determining, system sensitivity model is used [1], [2]. For process identification, sum method is used. Identification error is calculated as difference between real system responce and responce from model obtained during system identification. For correlation coefficient between process sensitivity and identification error determining, known methods are used [2].

II. DETERMINING CORRELATION BETWEEN SYSTEM SENSITIVITY AND IDENTIFICATION ERROR

A. System Sensitivity

Parameter sensitivity is determined with sensitivity functions which are defined with [1]:

$$u_{a_i}(k) = \frac{\partial y(k, a_0, a_1, ..., a_n)}{\partial a_i}, i = 0,1,...,n \quad (1)$$

where y represents system output and $a_1,a_{2,...},a_n$ are system's parameters. Logarithm sensitivity functions can also be defined:

$$u_{l,a_i}(k) = \frac{\partial y(k, a_0, a_1, ..., a_n)}{\partial \ln(a_i)}, i = 0,1,...,n$$

Figure 1 shows a model for simultaneous measurement of sensitivity functions for linear n-th order discrete system which can be described with equation:

$$a_n \Delta^n y(k) + a_{n-1}\Delta^{n-1} y(k) + ... + a_1 \Delta y(k) + a_0 y(k) = x(k) \quad (2)$$

Sensitivity vector can be formed on the basis of measured sensitivities of single parameters:

$$\mathbf{u}_{Ma} = (u_{Ma_0} u_{Ma_1} ... u_{Ma_n}) \quad (3)$$

where:

$$\mathbf{u}_{Ma_i} = \max \left| u_{a_i}(k) \right|$$

B. Sum method

Consider discrete time dynamic system in form (2) with boundary conditions [4]:

$$y(0) = \Delta y(0) = ... = \Delta^{(n-1)} y(0) = 0$$

$$\Delta y(\infty) = ... = \Delta^{(n-1)} y(\infty) = 0$$

Using transformations elaborated in [5], we obtain equations for parameter estimation:

$$a_0 = \frac{x(\infty)}{y(\infty)}$$

$$a_1 = \frac{1}{y(\infty)} a_0 \sum_{k_1=0}^{N} [y(\infty) - y(k_1)] \Delta t$$

$$a_2 = \frac{1}{y(\infty)} *$$

$$* \{ a_1 \sum_{k_1=0}^{N} [y(\infty) - y(k_1)] \Delta t - a_0 \sum_{k_1=0}^{N} \sum_{k_2=k_1}^{N} [y(\infty) - y(k_2)] \Delta t^2 \}$$

...

$$a_m = \frac{1}{y(\infty)} \sum_{j=1}^{m} (-1)^{j+1} a_{m-j} S_j$$

where:

[1]Prof. dr Bratislav Dankovic is with the Faculty of Electronic Engineering, Aleksandra Medvedeva 14, 18000 Nis, Serbia and Montenegro, E-mail: dankovic@elfak.ni.ac.yu

[2]Prof. dr Dragan Antic is with the Faculty of Electronic Engineering, Aleksandra Medvedeva 14, 18000 Nis, Serbia and Montenegro, E-mail: dantic@elfak.ni.ac.yu

[3]Marko Milojkovic is with the Faculty of Electronic Engineering, Aleksandra Medvedeva 14, 18000 Nis, Serbia and Montenegro, E-mail: milojkovic@elfak.ni.ac.yu

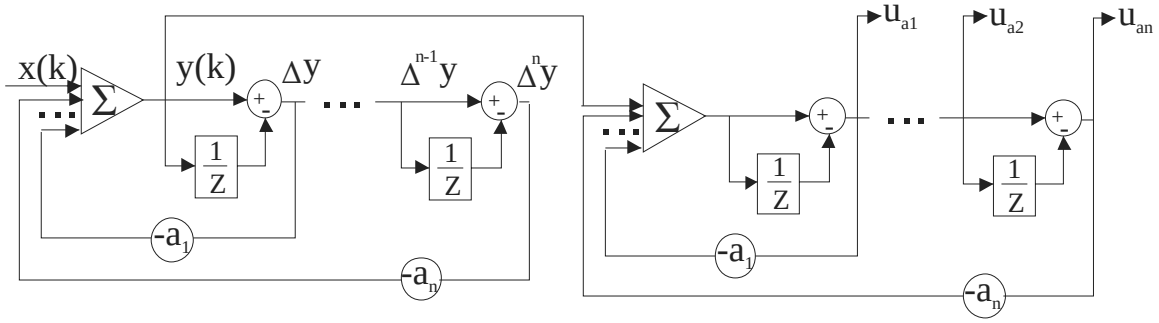

Fig. 1 Model for simultaneous measurement of sensitivity functions

$$S_j = \sum_{k_1=0}^{N} \sum_{k_2=k_1}^{N} \dots \sum_{k_j=k_{j-1}}^{N} [y(\infty) - y(k_1)]\Delta t^j; \quad m = 1,2,\dots,N;\ j = 1,2,\dots,m \tag{4}$$

where Δt represents discretisation period.

Equations (4) alowe identification of arbitrary order discrete systems, in form of linear diference equation based on measured responce values: $y_1,\dots,y_n$.

It's best to measure responce values in sampling moments. N should be large enough to satisfy:

$$y(N) > y(\infty)$$

Using equations above, vector of estimated parameter values can be found:

$$\hat{a} = (\hat{a}_1 \dots \hat{a}_n) \tag{5}$$

C. Correlation

Correlation between system sensitivity and identification error can be calculated using Persons correlation formula:

$$r = \frac{\sum_{i=0}^{n} (u_i - \bar{u})(\hat{a}_i - \bar{\hat{a}})}{\sqrt{\sum_{i=0}^{n} (u_i - \bar{u})^2} * \sqrt{\sum_{i=0}^{n} (\hat{a}_i - \bar{\hat{a}})^2}} \tag{6}$$

III. Experimental Determining of Correlation

Sensitivity functions are determined based on Fig.1 model for a fifth order system. These functions are measured in points u_{ai} $(i=1,\dots,n)$. Figures 2 and 3 show results for low and high frequency cases.

System coefficients are identified with sum method for fifth order system case. Starting system is:

$$0,0012\Delta^5 y + 0,0032\Delta^4 y - 0,114\Delta^3 y + \\ +0,955\Delta^2 y + 2,08y + y = x \tag{7}$$

Using equations (4), next system is obtained:

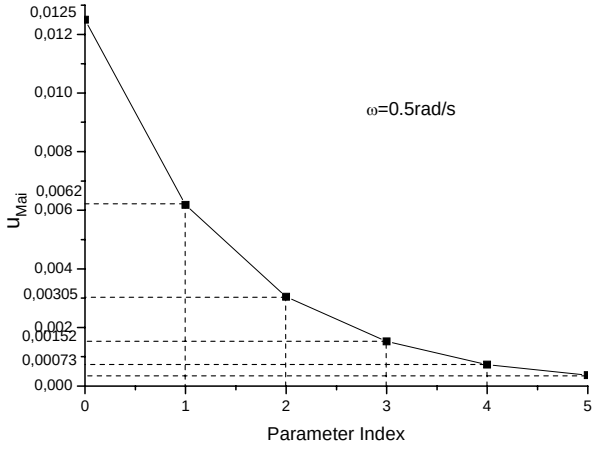

Fig. 2 U_{Mai} with respect to parameter index for low frequency case

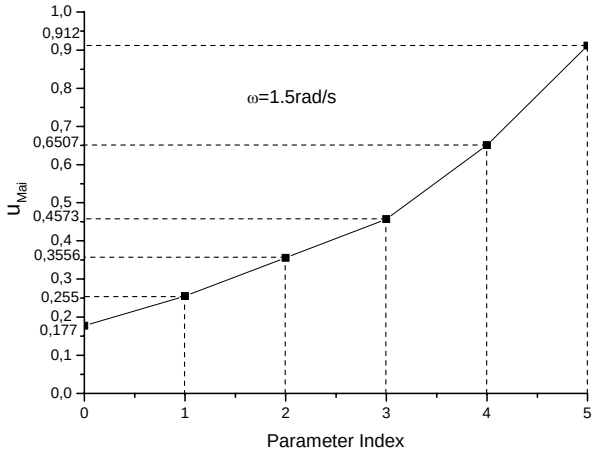

Fig. 3 U_{Mai} with respect to parameter index for high frequency case

$$-0,0123\Delta^5 y + 0,0127\Delta^4 y - 0,017\Delta^3 y + \\ +1,0098\Delta^2 y + 2,0397\Delta y + 1,004y = x \tag{8}$$

Fig. 4 shows error in percents of obtained system parameters (8) with respect to real parameters (7).

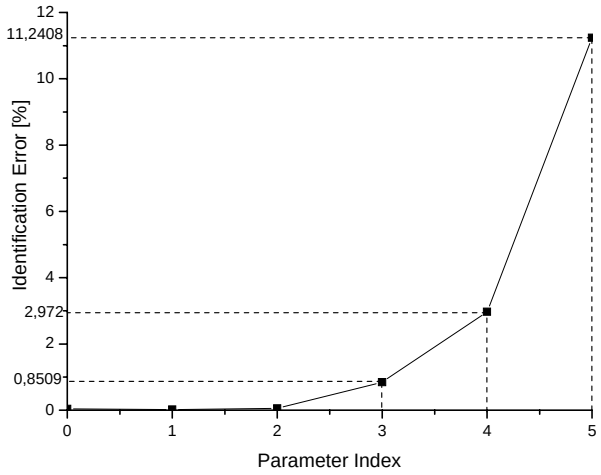

Fig. 4 Identification error with respect to parameter index for a low frequency case

System sensitivity and identification error correlation is calculated for the case of low frequency (figures 2 and 4). Using (6) and data logarithms, we obtain:

$$r = -0,98679$$

Obtained value shows high level of correlation between analyzed values. It means that parameters with respect to which the system is more sensitive, are easier to identify, and vice versa.

IV. CONCLUSION

Correlation between linear discrete system sensitivity and identification error is determined in this paper. Sensitivity model constructed using Δ operator is used for sensitivity functions determining. For low frequency, sensitivity is highest with respect to lowest parameter indexes. In case of high frequency, sensitivity is highest with respect to highest parameter indexes. Experimental results show high level of correlation between sensitivity and identification error.

REFERENCES

[1] Tomovic R, *Sensitivity Analisys of Dinamic Systems*, McGraw-Hill, New York, 1983.

[2] Gumovski R., *Sensitivity of the Control Systems (In Russian)*, Nauka, Moscow, 1993.

[3] Pintelon R., Schoukens J. , *System Identification*, IEEE Press, New York, 2001.

[4] Dankovic B., Antic D., Jovanovic Z., *Process Control-Process Identification*, Faculty of Electronic Engineering, Nis, 1996.

[5] Dankovic B., Stankovic M., "A Transformation which mapes Derivates into Differences", Publikacije Elektrotehnickog fakulteta, Beograd, 1985.

Poster Session PO1:

TELECOMMUNICATION SYSTEMS AND TECHNOLOGY

The First Results of Software Redesign of DKTS 30 Switching System to Support Extended Capacity

Milan Jovanović[1], Branko Kolašinović[1], Mirko Markov[1], Dimitar Komlenović[1]

Abstract – **The first results of work on the software redesign projects of the DKTS 30 switching system to support extended capacity were presented in this paper. The extended capacity switching system had been compared with the original DKTS 30 switching system, and some of the obtained results were given in this paper.**

Keywords – **switching system, software redesign, interprocessor communication.**

I. INTRODUCTION

The DKTS 30 public digital telephone exchange [1] is the newest product from the series of DKTS digital telephone switching systems. Although it has been successfully commercially exploited since 1999, it is still under development in order to:

- achieve better quality,
- provide new services and
- reduce the production price.

Like other modern telephone switching systems it is based on a large number of off-the-shelf microprocessors and microcontrollers, that frequently need to communicate with each other. That means that from this paper's point of view the DKTS 30 system represents distributed heterogeneous multicomputer that works in real time.

The simplified DKTS 30 system architecture was shown in Figure 1. The goal was to show only blocks taht are necesary to understand the presentation to follow. The system consists of central blocks and peripheral blocks. Central blocks are: administration (ADM), switching (KOM), synchronization (OSC), and UCP (*Universal Central Processor*). The UCP unit distributes the messages among the central and peripheral blocks. In order to increase the system reliability, the central blocks are duplicated. The central blocks are connected via a local Ethernet, which is doubled, too. All central blocks, except UCP units, are connected to both Ethernet networks.

The peripheral blocks are connected to UCP blocks via serial HDLC links. One pair of UCP units works in the load-sharing mode for a group of six peripheral units. Each of those six peripheral units is connected to to each of two UCP units by its own separate link. The peripheral blocks (PB) are subscriber blocks and interexchange trunks.

One of the main challenges facing DKTS 30 software engineering is the variety of microprocessors (Motorola 68360 and Intel family are present, processors from the PowerPC family are planned for future use), as well as the variety of operating systems that run on different parts of the DKTS 30 switching system (WinNT, Linux, pSOS, RTEMS).

[1] PUPIN TELECOM DKTS, Batajnički put 23, Belgrade, Serbia
E-mail: { milanj, brankok, mmarkov, dimitark}@ dkts.co.yu

The DKTS 30 software is based on object-oriented principles [2]. It was developed using UML notation [3] and standards for software projecting. The Rational Rose CASE tool and C++ language were used. The software is organized hierarchically with layers. Each layer provides a service to the higher layer, and simultaneously it is a client of the lower layer. Also, the software is organized as a collection of server objects that are distributed. Main software abstractions are modeled by these server objects. These servers are implemented as finite state machines (FSM). This is a common approach in design of embedded real-time systems [4]. Each FSM is designed according to the *Bridge* pattern [5], and consists of an interface and an implementation object. Interface and implementation objects may reside on different processors, and the only connection between them is their unique identifier of the object.

Software that runs on peripheral blocks is differently organized. In order to run faster, it is written on machine language and standard C language. It runs on an operating system originally developed by Iritel institute.

II. SOFTWARE REDESIGN PROJECT

The DKTS company has been slowly reorganized in order to become an organization based on projects. Using appropriate software tools: project plans are made, reports are written, sucessfulness of project realization is monitored, etc. A team is formed for each planned project. Members of one team can work on more differnet projects at the same time.

The maximal capacity of the original DKTS 30 switching system was 15872 subscribers. However, this number was shown to be insufficient with the uprising market demands. Therefore, the project of extending the capacity was undertaken. The project goal was to provide the maximum capacity of 174592 subscribers. The hardware changes were described in [6], while the planned software changes were described in details in [7]. This paper is dedicated to the first results of the software redesign project, so the planned and done hardware and software changes were described only to understand the presentation to follow.

This project includes: a redesign of the system image, a redesign of the interprocessor communication, more natural integration of the remote subscriber unit into the system, algorithms for distributed system supervision, appropriate changes in the system data base and the graphical user interface.

The project requirement was not only to trivially provide capabilities for a larger number of blocks in the system, but also to pay specific attention to the system performance. It was highly unlikely that the algorithms that were shown to be efficient with one traffic load would be efficient in the same way with much heavier traffic load.

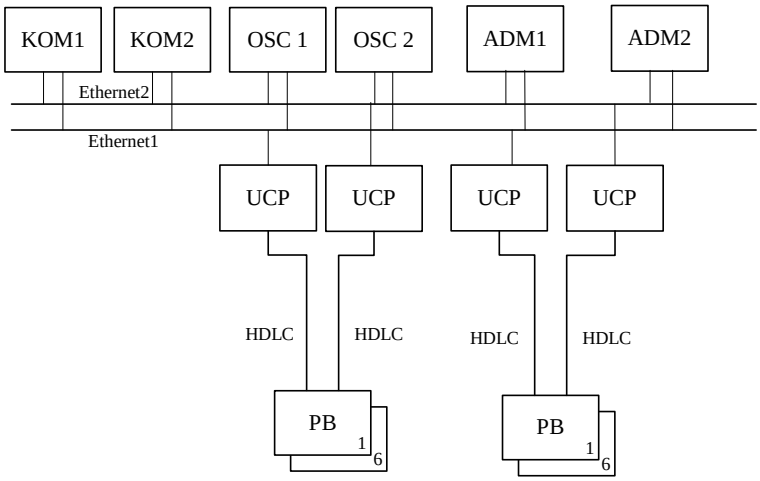

Figure 1. A simplified DKTS 30 system architecture

Concerning the software compatibility, it was decided that the new software has to be compatible with the original hardware, but not with the software of the original solution. That means that the new software can be executed on all DKTS 30 platforms, but that it can not be mixed with the old software.

The goal was to move beyond some obstacles that were present in previous software solutions due to required compatibility with the DKTS 20 system, which was put aside in the meanwhile. Special attention was payed to the intermediate period in order to make it possible to add new funcionalities to the software of the old system as well as to the software of the system with extended capacity.

Because of the decision to abandon compatibility with DKTS 20 peripheral blocks, it was convenient to undertake a redesign of the system software on peripheral blocks, which was shown to be a complex task contributing to the delay of the entire project.

Because of the large number of different processor types, different hardware platforms, various operating systems, situations in which it is necessary to perform potential error corrections in the field and in laboratory conditions, concurrently with adding new funcionality to the fisrt DKTS 30 system, a great attention was payed on developing methodologies for software testing.

As a result, a set of tests was designed. The set comprised different testing techniques: from the partial to the integral testing, with and without the use of call generator, etc. In the testing phase, the use of error information is increased. However, the great part of this code will be excluded from the final version in order to assure executable programs with the minimal time of execution. In addition to this, finite state machines whose only purpose is testing are designed. The FSM whose only task is to generate desired traffic is instantiated on every processor. This is an example of how interprocessor communication is tested.

III. APPLIED SOLUTIONS

From the software soultions realized in the project of extending capacity that concern this paper's topic, the most important ones are those that concern interprocessor communication. The base request of the redesign of the interprocessor communication was to decrease the number of messages needed in the operation of the switching system, as well as to additinaly incerease reliablity of the interprocessor communication. In order to fullfil these requirements, it was necessary to make some changes in a message header. The message header remained of the same length as it was. It contains the same fields as in the previous implementation: message type, source and destination internet address, message identification, destination object's identification. However, some changes were inevitable. First of all, the format of internet address had to be changed. Next, the way message type is marked was also changed. As a result of these changes, incompatibility with the previous software implementation became unavoidable. Among other things, with the new message caracterization, it became possible for clients in upper software layers to supress acknowledgement messages on the protocol layer when functional messages are used to acknowledge an application layer acknoledgement request.

In the aim of acchieving faster interprocessor communication, the SP protocol was abandoned. The SP protocol was used for communication between peripheral and UCP blocks via HDLC links [8]. The reason for the presence of this protocol in the previous implementation lay in requested compatibility with DKTS 20 peripheral blocks. Since the concept has been abandoned in the meanwhile, the NLC layer of the interprocessor communication protocol stack was eliminated. In adition to this, another historical role of the UCP board, which also existed due to requested compatibility with DKTS 20 peripheral blocks, became unnecessary in the new software environment. That was the NLB layer whose task was to perform message format conversion between DKTS 20 and DKTS 30, and vice verse.

The design of the first DKTS 30 switching system did not support communication between UCP boards belonging to one Ethernet with UCP boards that belong to another Ethernet. However, during the exploitation phase, the need for communication between peer boards was brought to attention. In addition to this, there was the need to put interprocessor communication under software supervision. Accordingly, it was decided to correct this defect by allowing software

routing from one Ethernet to another. Central blocks that have available network interfaces belonging to both Ethernets became potential routers. It was more than likely that this task would be committed to the OSC board, since the OSC board is the processor that is not overloaded with interprocessor communication responsibilities. The routing is now supported in system image. In addition to everything else, this routing may be used in the case of a failure of a network interface on boards with two network interfaces. For example, in previous software versions, the KOM board with an inactive network interface that belongs to the Ethernet A could not send a message to a UCP board connected to the Ethernet A.

A reduction of the number of messages passing through the system is acheived by the use of multicast techniques [10]. Instead of sending a large number of single messages to different destinations, it is now possible to send only one multicast message that is received by all procesors that are members of the specified multicast group. The great problem was the presence of several operatin system in the DKTS 30 switching system, each of which providing similar (but different) programming interface towards the multicast facilities. In addition to this problem, it was important to provide that all processors in the group receive a multicast message, but also to avoid duplicated messages, which may be the consequence of the use of alternative routes. Periodical updating of local image, sending information on block or network interface failure or activation, periodical checking of block states are cases in which it is evident that significant improvements in speed and efficiency are achieved.

IV. CONDITIONS OF THE ANALYSIS

There is a model of DKTS 30 switching system dedicated to extending capacity project in the research and development laboratory of DKTS. Although this model is rather modest comparing to the maximal capacity switching system, it has been shown to be adequate for phases of develpment and testing accomplished until now. All experiments to be described have been conducted on it. This model consists of 2 ADM units, 2 KOM boards, 2 OSC boards, 4 UCP boards, 4 and 4 clasical subscriber blocks, 2 interexchange trunks, and one extended subscriber block. There is a substantially better equipped model of DKTS 30 system also dedicated to extended capacity project in the DKTS testing department.

A call simulator *Anritsu* EF111A was used during the testing phase. The calls are established via 4 subscriber blocks, 3 of witch are connected to one pair of UCP boards, and the last one is connected to other pair of UCP boards. Due to limited number of available cables, only 24 dual telephone connections are formed, divided into 3 groups with 8 connections per each. To cover all cases of interest for testing, the first group consists of connections between subscribers that are connected to the same subscriber board, the second group consists of connections between subscribers that are connected to two subscriber boards that are on the same pair of UCP boards, and the third group consists of connections between subscribers that are connected to two subscriber boards that are connected to different pairs of UCP boards.

An asinchronous mode of establishing connections was chosen. The generated telephone traffic was controlled by call simulator parameters: duration of a call (path hold time) and the time between the end of one call and the beginning of the next call (release time)

V. RESULTS

Some results of accomplished comparison of the extended capacity *s*witching system (ECSS) and the original DKTS 30 switching system (OSS) were presented in this section.

The first experiment is related to software download to peripheral blocks: a clasical subscriber block (cSB), an extended subscriber block (eSB), a clasical interexchange trunk (cIT), and an interexchange trunk with SS7 signalization (sIT). The sizes of files to be downloaded are practically the same for both variants.

TABLE 1
SOFTWARE DONWLOAD TO PERIPHERAL BLOCKS

Peripheral unit	Number of units [512B]	OSS [s]	ECSS [s]
CSB	257	11	6
ESB	436	18	9
CIT	513	21	11
SIT	692	29	14

Table 1 shows that significant improvements were fulfilled. The software download to periperal blocks in the ECSS vatiant is even two times faster. The main reason for this improvement is abandonment of SP protocol that was used in communication between peripheral blocks and UCP blocks. The number of messages needed to download the sotware to peripheral blocks was significantly decreased in this way.

Besides, by a change of the download alghoritam, although it is still centralized, with the master administration in charge, additionaly was decreased the number of messages needed to download the software to peripheral blocks. The obtained improvement of software download to peripheral blocks enables significant decrease of startup time of the whole switching system during a cold start.

A new realization of switching system supervision also brings a significant improvement. A notification of all blocks in the system about a change in the system was given as an example (Table 2). One has to notice that functional answers to this notification messages are used to check a state of the blocks. Three variants are compared: original (centralized) solution (OS), original (centralized) solution with multicast to central blocks and unicast to peripheral blocks (MC), and distributed solution with multicast to central blocks where UCP boards have a role to notify and monitor peripheral blocks that are connected to them (DS). An average response time was given according to observing of the Ethernets and it is calculated from an appearance of the first message of one notification phase until the reception of the last response message of that phase. The number of messages on Ethernet is given for the maximal capacity original switching system, what means the system with 128 peripheral blocks. The

switching system model in the testing department was used for this experiment.

TABLE 2
NOTIFICATION AND POLLING OF BLOCKS

Verion	Number of messages on Ethernet	Average respnse time
OS	708	600 ms
MC	612	500 ms
DS	90	350 ms

The advantage of distributed solution compared to centralized solutions is clear. The benefit of using multicast has not to be neglected, although it is not as significant as it was expected, because of higher number of peripheral blocks compared to number of centralized blocks.

Encouraging results were also attained by testing the switching system by the call simulator (Table 3). During the testing of the original switching system each subscriber block was loaded with 2500 calls per hour (above that some problems are generated). The number of unseccesful calls of 500000 generated calls is about 1000, that means 0.2%. During the testing of extended capacity switching system each subscriber block was loaded with 6000 calls per hour. The number of unseccesful calls of 500000 generated calls is about 25, that means 0.005%.

TABLE 3
TESTING WITH CALL SIMULATOR

Version	Number of calls per subscriber block	Percent of unsecesful calls
OSS	2500	0.2%
ECSS	6000	0.005%

It was shown that discarding the compatibility with DKST 20 perihperal blocks, what means abandonment of SP protocol that was used in communication between peripheral and UCP blocks, as well as abandonment of conversion of messages on UCP boards, significantly increases throughput power of peripheral blocks, along with improved stability. According to paper [11], this means that it was reached almost the maximal traffic on peripheral blocks that KOM boards with current swithcing system architecture and organization can persist without saturation.

VI. CONCLUSION

A flexible base for the DKTS 30 switching system was provided by the software redesign project, although the main goal was to increase the capacity of the system. The first results of the work are encouraging, as was shown in this paper.

Significant improvements were fulfilled concerning software donwload on peripheral blocks. Even two times faster is download of software in the extended variant comparing with the original variant. The obtained improvement enables significant decrease of startup time of the switching system during a cold start.

A lot has been done to decrease the numer of messages that propagate through the system (SP protocol was abandoned, using of multicast, unnecessary response messages both on protocol and functional level were discarded). This, in the last instance, makes the response time to certain events significantly shorter. So, considerable improvement was fulfilled in the process of notification and polling of blocks in the swithcing system. The advantage of distributed solutions compared to centralized solution is clearly shown even for the original switching system with maximal capacity.

By abandonment of compatibility with DKTS 20 systems, the interprocessor communication with peripheral blocks was refined. Testing of the switching system by call simulator shows increased throughput power of peripheral blocks with new software, along with substantial improvement of work stability.

Because of not small complexity of the software redesign project in order to extend capcaity of digital public switching system DKTS 30, parallel work of the project members on different development projects which priority have been changed during the time, situations in which it is necessary to perform potential error corrections in the field and in laboratory conditions, concurrently with adding new funcionality to the first DKTS 30 system, there was no enough time to compare newly realized solutions with the original ones. As the project approaches its end, there will be more time to analysis and comparing of original DKTS 30 switching system with the switching system with extended capacity.

REFERENCES

[1] Jovanović M., Šuh T., *System DKTS 30 Main Characteristics, Telfor 1997*, Beograd, 1997.

[2] Booch G., *Object-Oriented Analysis and Design*, Second Edition, Benjamin-Cummings, 1994.

[3] *UML Semantics*, Rational Software Corporation, 1997.

[4] Selic B., Gullekson B., T.Ward P., *Real-Time Object-Oriented Modeiling*, Willey Professional Computing, 1994.

[5] Gamma E., Helm R., Johnson R., Vilsides J., *Design Patterns – Elements of Reusable Object-Oriented Software*, Addison-Wesley, 1994.

[6] Laketa S., Vidić P., Nikolić N., "Povećanje kapaciteta sistema DKTS", *Telfor 2003*, Beograd, 2003.

[7] Kolašinović B., Komlenović D., Jovanović M., "The Redesign of the Software of the DKTS 30 Switching System to Support Extended Capacity", *ICEST 2004*, Bitola, Makedonia, 2004.

[8] Jovanović M., Hiršl V., "Međuprocesorska komunikacija u telefonskoj centrali DKTS 30," *YU INFO 1999*, Kopaonik, 1999.

[9] Vujadinović D., Jovović Ž., "Funkcionalna konverzija poruka u sistemu DKTS20/30," *IT'98*, Žabljak, pp. 64-66, 1998.

[10] Deering S., "Host Extensions for IP Multicasting," *RFC 1112*, 1989.

[11] Markov M., Kolašinović B., Jovanović M., "Merenje opterećenja nekih resursa telefonske centrale DKTS 30 softverskom simulacijom poziva," *YUINFO 2002*, Kopaonik, 2002.

Alternative Architectures in the Network Management

Aleksandar Tsenov[1], Tashko Nikolov[2]

Abstract: **Network Management is needed to control and optimize the operation of the network and to respond to changing user requirements. Management includes the initialization, monitoring and modification of the network functions. In order to perform management, special functions are needed. To distinguish these functions from the normal network functions, this work includes the terms "management functions" and "primary functions".**

Management functions may be performed explicitly by human operators, but also automatically by dedicated soft- and hardware modules. In case human operators are responsible for network management, most management functions will be performed from a limited number of remote locations. In case management functions are performed automatically, it is possible to distribute the hard- and software modules that implement these functions over the various systems in the network.

This work explains how management functions can be designed together with primary functions. It also discuses, that it may not always be possible to design all management functions before the start of the operational phase. The alternative is: after the start of the operational phase the designer may decide to add the remaining management functions by developing new generation of network systems.

I. INTRODUCTION

Architectures for network management enable the designers to discuss management functions at a high level of abstraction and guide the design of management protocols and services. In this work it is assumed that architectures consist of: a set of architectural concepts; rules that tell how to use these concepts and models for designing a specific class of systems.

All current management architectures, notably the ISO, ITU-T and the IETF architectures, have been developed after the design of the network functions have been completed. Such approach indicates a specific conceptual view of the role of the management functions and invites to apply different architectural concepts for the design of management functions. This work proposes an alternative approach, in which no principle distinction is made between the management requirements and the requirements of primary functions. Both sets of requirements can be integrated into one set of requirements and elaborated in a single design process, which uses one architectural model.

To demonstrate that both kind of functions can be expressed in the architectural concepts and rules as used by the OSI – Reference model, tree models are developed – model of distributed management architecture, model of centralized management architecture and model of hybrid management architecture. A set of new definitions according to new architectures are also presented.

[1]Aleksandar Tsenov is with Telecom Department at Technical University of Sofia, "Kliment Ohridsky" Blvd 8, 1756 Sofia, Bulgaria, E-mail: akz@tu-sofia.bg

[2]Tashko Nikolov is with Telecom Department at Technical University of Sofia, "Kliment Ohridsky" Blvd 8, 1756 Sofia, Bulgaria, E-mail: tan@tu-sofia.bg

II. OSI MANAGEMENT, TMN MANAGEMENT AND INTERNET MANAGEMENT

The origin of OSI management can be found in ISO, most of the work is performed in collaboration with the ITU-T. The standards that results from this cooperation are published by both organizations without technical differences. Within the ITU-T, the OSI management recommendations are published as part of the X.700 series.

The first standard that describes OSI - management, is the *OSI Reference Model* [1]. This standard identifies OSI management as an important working area and provides initial definitions. The first outcome that presents the development of OSI management was the *OSI Management Framework* [2]. Later it was decided to produce an additional standard, which was called the *Systems Management Overview* [3]. These standards provide the basis for OSI management (Figure 1).

Title	ISO/IEC	ITU-T	Year
OSI Management Framework	7498/4	X.700	1989
OSI Systems management Overview	10040	X.701	1992

Fig. 1: The basis of OSI Management

The term TMN is introduced by the ITU-T as an abbreviation for Telecommunications Management Network. The concept of a TMN is defined by Recommendation M.30210 [4].

According to M.3010 "a TMN is conceptually a separate network that interfaces a telecommunications network at several different points". The relationship between TMN and the telecommunications network that is managed is shown on Figure 2.

According to this figure, the interface points between the TMN and the telecommunications network are formed by Transmission Systems and Exchanges. They are connected via Data communication network to one or more Operations systems. The Operations systems perform most of the management functions; these functions may be carried out by human operators but also automatically. It is possible that a single management function will be performed by multiple Operations systems. In this case the Data communication network is used to exchange information between the operations systems.

In the second half of the past decade the Internet grew to a size that management of the Internet could no longer be provided on an ad hoc basis: a structured and standardized approach to Internet management was required.

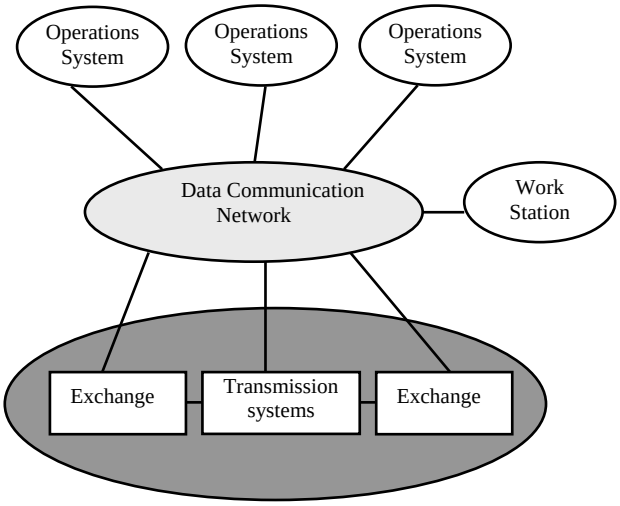

Fig. 2: General relationship of a TMN to a telecommunication network

SNMP (Simple Network Management Protocol)[5] is a further development of SGMP (Simple Gateway Management Protocol). SGMP was aimed at management of Intermediate Systems – Gateways. Because SGMP appeared to be a success, it was decided to extend its scope and include management of End System. To reflect this change, the protocol was renamed into SNMP.

It is important to say that no special standards have been defined for the Internet Management architecture; only protocols and MIBs have been standardized.

The main goal of the future enhancement of the Internet Management architecture are:

- All systems connected to the network should be manageable with SNMP;
- The cost of adding network management to existing systems should be minimal;
- It should be relatively easy to extend the management capabilities of existing systems;
- Network management must be robust.

III. An Alternative Management Architecture Models

The management architectures that where presented above can be characterized by the fact that they only consider management functions, and not the primary functions that should be managed. In this part of the work an alternative architecture will be presented that shows how primary functions should be extended with management functions. The view that management functions should be seen as extensions to the primary functions, implies that it should be possible to define both kind of functions in terms of a single set of architectural concepts and rules. Here we decided to use the concepts and rules of the OSI Reference model.

The main contribution of this work are the models that show how to apply these concepts and rules to explain the case that management is performed from one or more remote locations.

A service management architecture

In this section several models will be presented that show how existing services can be extended to include service management.

Figure 3 shows the part of the service design process. During the early design cycles the focus will be on the development of primary service functions. During the later design cycles the extension to include service management will be performed.

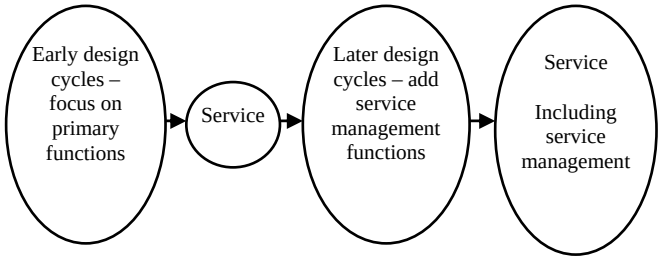

Fig. 3: Extending a service to include service management

Figure 4 shows the service model that guides the design of the primary functions. The model includes a service provider, a number of users and the SAPs (Service Access Points). Every SAP represents common parts of the communication between the user and the service provider. The *P* at each SAP indicates, that only the execution of Primary service is supported.

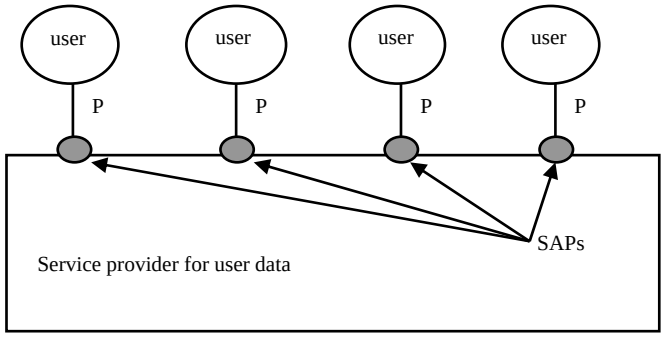

Fig. 4: Model of the design of primary functions

The addition of service management has consequences for the interaction between users and provider. This implies that the behaviour of the provider, as well the behavior of user ha-ve to be adapted. The models of this behavior should not be presented in this work.

IV. A Model for Distributed Service Management

The idea of the equal distribution of service management is to give all service users same set of service management fa-

cilities. A potential problem associated with this approach is, that interference between managing users can not be avoided. For reducing this problem, some restrictions upon a set of service management interactions should be set. One possible solution is shown on Figure 5.

In this model all SAPs support the same set of service management interactions (*M*). In fact the model is equal to the model that is shown on Fig. 4. – addition and equal distribution of service management does not modify the structure of the initial model.

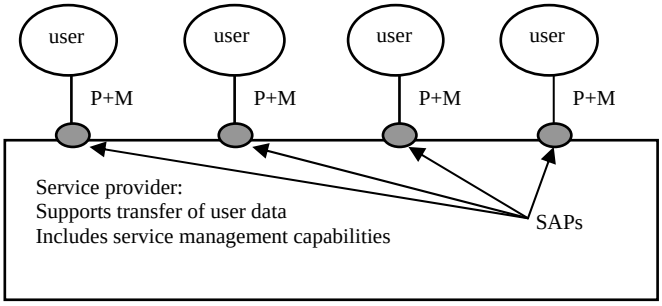

Fig. 5: Model of distributed service management

The result of service management addition is the change of user and provider behavior. This change must be reflected in the service definition as follows:

- Existing service primitives may be extended with special service management parameters;
- Special service management primitives may be defi-ned;
- The relationship between service primitives may be modified.

The extension of the service parameters may include parameters such as QoS negotiation, connection speed, needed recourse etc.

One example for new service primitive may be *ErrorReport* which primitive can include parameters such as *cause* for the error.

The relationship between the service primitives can be modified in order to add or to reject some functionality by examining any service.

It is important to note, that the changes of the service primitives and service parameters should not be intended for user data transport. This implies that these primitives:

- need not include address and user data parameters;
- need not be defined of a similar type of primitive at another SAP.

V. A Model for Centralized Service Management

The choice between distributed and centralized service management should be make by the designer and follows from the user requirements. The centralized approach is followed in case requirements exists that service management interactions should be confined to a single location. The purpose of such a requirement may be to prevent unauthorized service management access or to avoid the interference that may occur in case of multiple managing users. Centralized service management implies that all management interactions should be executed at one single SAP. This may be an existing SAP or a new service management SAP.

The model for centralized service management is presented in Figure 6.

One of the SAPs supports service management functions. This support is indicated with the letter M. The P+ in the square brackets indicates that this SAP may, but not need to support primary interactions.

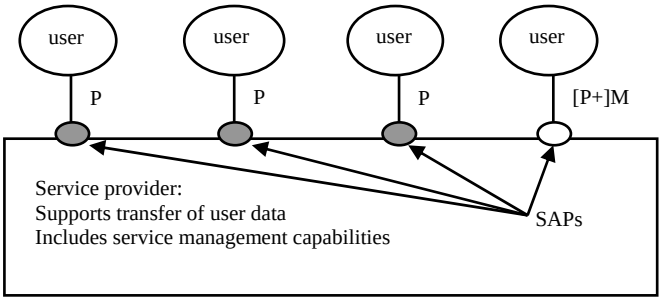

Fig. 6: Model of centralized service management

The impact on the service design definition in case of centralized service management is similar to the distributed service management discussed above. The main difference is the implementation of *Special service management SAP*. In this case the normal user SAPs leave unchanged and an additional SAP is proposed. Through this SAP the service manager may be connected to the provider. This might be an existing user which becomes ‘super user’ or an extra manager. In case of ‘super user’ the SAP may be divided in two parts - normal data SAP and special service management SAP (Figure 7).

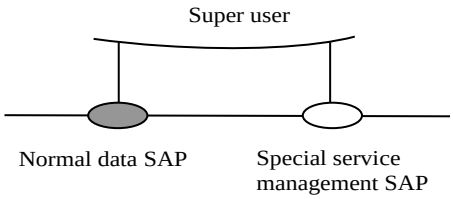

Fig. 7: Connecting the ‘Super user’ to the service provider

The second possibility is to connect a Service manager through special service management SAP. The service manager may not perform primary interactions and only management interactions.

VI. A Model for Hybrid Service Management

Distributed service management has, just as centralized service management, certain advantages and disadvantages:

- Distributed service management allows users to take immediate action in case they experience problems with

the service provider or in case they change their demand. Distributed service management it may be difficult to avoid interference in case different users want to initiate conflicting management actions. The potential weak point in this type of service management might be security;

- With centralized service management it is much easier to avoid conflicting management actions and to guarantee a high level of security. The problem in this case is, that user who experience problems should always contact the service manager. This might be impossible in some problem cases;

The idea behind hybrid service management is to combine the advantages ant avoid the disadvantages of both approaches, mentioned above. This can be accomplished by introducing different sets of service management interactions. In the hybrid service management approach all users get service management capabilities, but only one (or some) user gets more capabilities then other.

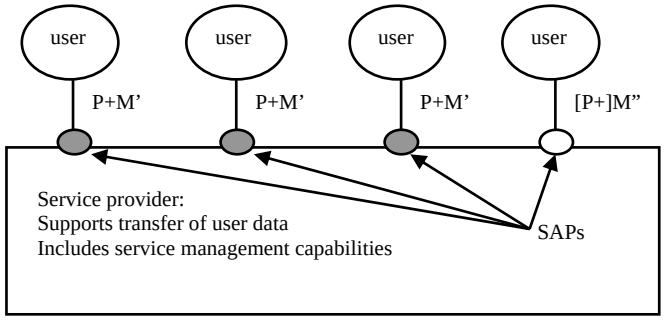

Fig. 8: Model of hybrid service management

As shown on Figure 8, the existence of two sets of service management interactions (M' and M") is suggested. It may be possible to define more than two sets – for example M'_1, M'_2 and so on. That means – different users may get different management interactions capabilities.

For example, in case of large public network, it may be advisable to define tree different sets:

- One set of service management interactions that may be only executed by a single central service manager. This manager may belong to the organization that owns the public network. The set of interaction may include operations on adding or removing users, adding or removing management services etc.;
- Another set of service management interactions that may only be executed by a small number of network users which become service managers. Each company that is connected to the public network may have their own service manager. The set of the service manager interactions will be smaller than the previous set and limited to the company. The service manager may for instance create or remove group addresses for use within the company.
- The set of service management interactions that may be executed at all remaining SAPs. This set may include for instance reachability tests.

The addition of hybrid service management involves the same changes to the service definitions as discussed in the previous section.

VII. CONCLUSIONS

In addition to service management concept other approaches may be performed. The authors propose the following concepts:

- protocol management concept;
- remote element management concept;

These concepts will be discussed by the authors in their future works.

It is important to say that every one of these concept should correspond to the specifics of the managed networks and of the managed services.

The service management concept involves implementation of new service primitives or service functions. These service primitives may carry primary service information that is encapsulated in an ordinary management operation command or vice versa. This may depend on the specific application or service to be applied.

In order to find the most secure architecture it is important to define the appropriate type of service management and, in case of centralized or hybrid management, the user who will be responsible to the functionality of the whole network. Which type of services will be allocated to the other user in the network is also decisive parameter of the network functionality.

All this concluding remarks give a wide area for further research and architecture design of networks with integrated primary functions and management functions.

REFERENCES

[1] ISO 7498: "Information Processing Systems – Open System Interconnection – Basic Reference Model", Geneva, 1984

[2] ISO 7498-4: "Information Processing Systems – Open System Interconnection – Basic Reference Model – Part 4: Management Framework", Geneva, 1989

[3] ISO 10040: "Information Processing Systems – Open System Interconnection – System Management Overview", Geneva, 1992

[4] CCITT "Recommendation M.3010, Principles for a Telecommunications Management Network", Geneva 1992

[5] RFC 1157: "Simple Network Management Protokol (SNMP)", Case J.D., Fedor M., Schoffstall M.L., Davin C., May 1990

[6] Atanasov Iv., "Critical Review on Advanced Service Creation Technologies", Electronic and Electrotechnics", ISSN 0861-4717, accepted paper, 2005

Coherent System of Synhronisation of Carrier Frequency Hopped Signals

Antonio Andonov[1]

Abstract:**The paper presents a method and a device of an accurate and independent (coherent) reproduction of the form of carrier frequency hopped signals in the transmitter and receiver. The base of that process is a coherent device of synchronization serviceable with random delay fluctuations.**

Key words: **carrier frequency hopped signals, coherent device**

I. INTRODUCTION

The coherent formation of signals transmitted is a way to increase the noise immunity of telecommunication systems. Nowadays, due to their features the coherent lines allow to reach the conditions of optimal receiving closely by satisfying the requirements for optimally simple technical implementation. The development of coherent carrier frequency hopped communication systems is grounded on the fact that they give a possibility to provide a great amplification with signal processing in the receiver. It is of a special significance for the mobile telecommunications because of the limited power resources. However, the requirements for the synchronization system have been considerably increased, especially for the system of delay monitoring. The purpose of this paper is to propose a device of accurate and independent (coherent) reproduction of the form of carrier frequency hopped signals in the transmitter and receiver.

Two patents of coherent systems of delay monitoring have been known. They belong to Motorola and have found application to radioconection with fast-movable objects (airforce planes), i.e. under conditions of rapid fluctuations of delay [2,3]. In the delay monitoring system (DMS) proposed in [2], the signal in transmitter, intended to be transmitted in the band of modulation frequencies, is summed with the narrow-band pilot signal with angular frequency ω_p. At the same time the summed output signal is mixed with the carrier frequency hopped signal of the synthesizer generating a signal of continuous phase $\omega(t)$. The structural circuit of the coherent DMS used in the examined narrow-band transmitting system is presented in Fig.1**.** The obtained signal entering the DMS input is of the kind of:

$$S_1(t) = \mathrm{Re}\left\{\exp j\left[\omega_p t + \varphi_1(t)\right]\right\} \quad (1)$$

where $\varphi_1(t)$ is the integral phase of the carrier frequency hopped signal received.

Antonio Vladimirov Andonov is witch the Higher School of Transport, Geo Milev Str.158, 1584 Sofia, Bulgaria

$$\varphi_1(t) = \int_0^T \omega(t')\,dt. \quad (2)$$

At the second input of the input mixer, reference signal $S_2(t)$ from the synthesizer frequency of carrier frequency hopped signals enters:

$$S_2(t) = \mathrm{Re}\left\{\exp\left[-j\varphi_2(t)\right]\right\} \quad (3)$$

where $\varphi_2(t)$ is the integral phase of the reference signal. The band filter (BF) separates the component corresponding to the frequency of pilot signal ω_p from the output signal. This component can be written in the kind of:

$$S_f(t) = \mathrm{Re}\left\{\exp j\left[\omega_p t + \varphi_1(t) - \varphi_2(t)\right]\right\} \quad (4)$$

Following the band filter, a circle for PPL (a phase-locked loop) is switched separating component S_f from the signal:

$$S_s(t) = K\left[\omega(t) - \varpi\right]\tau = K\left[\varphi_1(t) - \varphi_2(t)\right], \quad (5)$$

where K is the coefficient of the phase detector transmitting (PD); ϖ is the average angular frequency.

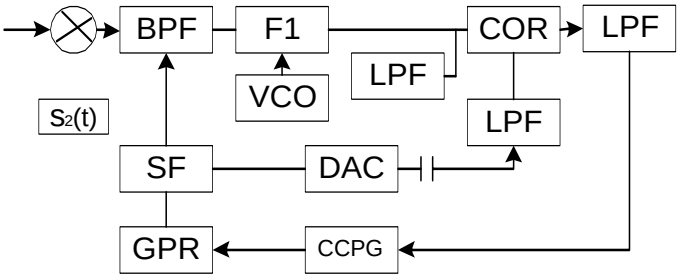

Fig1

The error signal formed is supplied to one of the correlator inputs made in the kind of multiplication and switched to a low pass filter (LPF) in series. At the other correlator input, a signal proportional to the reference frequency hopped signal is supplied. It is without a constant component, which is cut by a condenser. The second signal is:

$$S_s(t) = \omega(t) - \varpi \quad (6)$$

It should be underlined that to obtain the above ratio (5) it is necessary to provide a mode of operation in the linear section of the phase detector discrimination feature PD from the circle of PPL, which is satisfied for values $\tau << T$. Thus, at the corrector output signal

$$S_g(t) = c(t)\, f(t) = K\left[\omega(t) - \varpi\right]^2 \tau, \qquad (7)$$

is obtained, which after averaging in LPF has the kind of:

$$S_g(t) = K\overline{\left[\omega(T) - \varpi^2\right]^2}\tau \qquad (8)$$

The error signal obtained is used to final adjustment during the controllable clock pulse generator (CCPG) of DMS.

Another version of building a similar coherent delay monitoring system is described in [2]. The principal difference in comparison to the system examined in [1] consists in using a special device for phase synthesis (phase synthesizer) in the receiver in the part of a local generator-and-synthesizer carrying out the voltage to phase conversion. Thus the phase of the controllable signal for the phase synthesizer has to be equal to the value of the current synthesized frequency phase. The structure diagram of the DMS given is shown in Fig. 2. If the input signal in the receiver is presented with equation (1), then the signal at the output of the BPF (band pass filter) mixer intended to remove the frequency hopping will be described with equation (5).

In its general kind the phase of the received carrier frequency hopped signal can be written as:

$$\varphi_1(t) = \omega_0 \tau + \int_0^t \omega\left(t'\right) dt', \qquad (9)$$

where ω_0 is the central signal frequency.

$\omega\left(t'\right)$ is the amplitude of the random oscillation with a rectangular form, which determines the value of the carrier frequency hopped signal and which is allocated evenly between ω_p and $-\omega_p$.

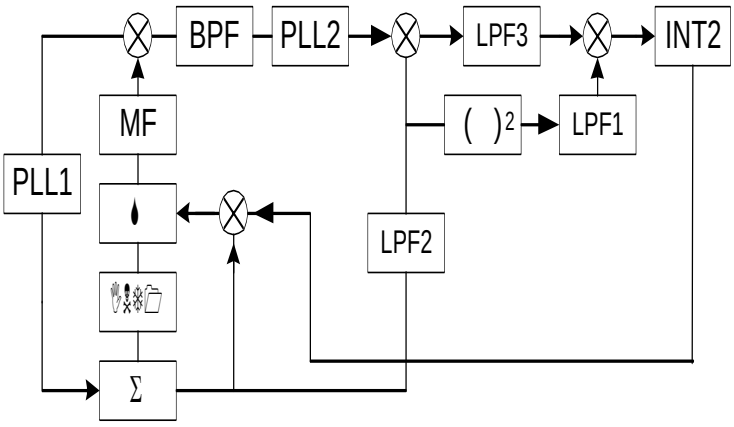

Fig.2

To accomplish the synchronization between the signal received and the reference signal in delay with a certain value to the phase, it is necessary to reduce the phase error to zero, i.e.:

$$\Delta\varphi = \varphi_2(t) - \varphi_1(t) \qquad (10)$$

For the case when $\tau << \tau_e$, an approximate equality has been accomplished:

$$\Delta\varphi \approx \tau \frac{d\varphi_1(t)}{dt}, \qquad (11)$$

or

$$\frac{d\varphi_1(t)}{dt} \approx \omega_0 + \omega(t). \qquad (12)$$

Hence, the assessment of the output signal phase can be presented in the kind of:

$$\hat{\varphi}(t) = \varphi_2(t) - \frac{\tau d\varphi_1(t)}{dt}. \qquad (13)$$

At that, the error of the assessment obtained can be evaluated by the expression:

$$\Delta\omega(t) = \omega(t+\tau) - \omega(t), \qquad (14)$$

with which $\left|\Delta\omega(t)\right| \le \left|\omega(t)\right|$.

The method proposed through the diagram in Fig.3 can be implemented in this way:

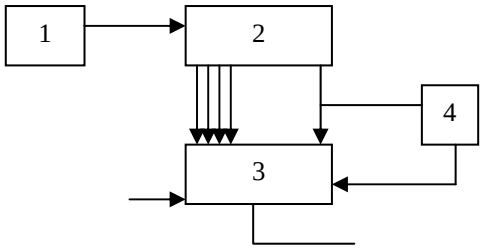

Fig.3

The signal determining the regularity of the phase change for the phase synthesizer (PS) is found at the first generator output and presents an integral of the sum of the phases of the central frequency received at the output of the circle for PPL1 (phase-locked loop 1) from the input radio signal and the signal entering from generator of pseudo random sequence (Gprs), which determines the value of $\omega(t)$. From the phase value, obtained in the removing device, the preliminary value of the evaluation of the phase error formed on the base of delay $\tau_з$ is deducted and the result obtained is used as a controlling effect for the PS. Thus PS forms a signal of the following kind:

$$S_2(t) = \mathrm{Re}\left[\exp j\left\{-\tau_з\omega(t) + \omega_0(t+\tau) + \int_0^{t+\tau}\omega\left(t'\right)dt'\right\}\right]. \qquad (15)$$

The synthesizer examined, which is called a direct synthesizer in [2], presents an addressed storage device (SD), where the values of $\exp jx$ are kept, and where x is a number supplied at the SD input. At that, the digital-to-analog

converter (DAC) operating according samples $\mathrm{Re}\{\exp jx\}$ is used at the SD output.

The signal at the mixer output is in the kind of:

$$S_m(t) = \mathrm{Re}\left\{\exp\left[(\tau - \tau_з) - \bar{\omega}(t)\right] - \tau_з \tau \dot{\omega}(t)\right\}. \quad (16)$$

Signal $S_m(t)$ passing through a band filter enters the input of the circle for PPL 2 (phase-locked loop 2). It divides the signal phase at the difference equal to the value of exponent argument $S_m(t)$. In the case examined, the circle for B PPL 2 in its structure and purpose is analogous to the circle for PPL 1 in DMS as described in [1]. . The signal at the output of the circle for PPL 2 is supplied to the input of the multiplier of the circuit for delay assessment, at the other end of which the value of $\omega(t)$ received by Gprs is averaged in PPL 1and LPF 1**.** The time constant of LPF 1 corresponds to the time constant of the BPF. In this way at the multiplication output the following signal is obtained:

$$S_D(t) = (\tau - \tau_з)\bar{\omega}^2(t). \quad (17)$$

The averaged value of $\bar{\omega}(t)$ is supplied to a squaring device and after averaging in LPF 2 with a time constant bigger than that of LPF 1, a signal of the following kind has been obtained:

$$S_d(t) = \bar{\omega}^2(t) \quad (18)$$

This signal is supplied as a divider to the input of a circuit for dividing. As a of dividend, a signal of the following kind is used:

$$\bar{S}_D(t) = (\tau - \tau_з)\overline{\bar{\omega}^2(t)}, \quad (19)$$

That is obtained from $S_д(t)$ by averaging in LPF 3. Thus a new evaluation of the delay is formed:

$$\tau'_з = \frac{S_д(t)}{S_d(t)} = \tau - \tau_з, \quad (20)$$

which at the integrator output is in the kind of:

$$\bar{\tau}'_з = \overline{\tau - \tau_з}. \quad (21)$$

The latter joins the multiplication where the next signal is formed for the frequency correction of the delay monitoring system DMS.

In comparison to the coherent system for monitoring described in [1], the circuit examined allows to remove the considerable phase distortions occurring at the moment of correlation. It is so because in that case the final adjustment is implemented not at the clock-pulse frequencies of the controllable clock-pulse generator CCPG, but directly in the generator phase on a signal copy, the phase synthesizer plays the part of which.

Another advantage of the given circuit stemming from its peculiarities is its capability to monitor Doppler's frequency displacement accurately. That is of a special significance in the carrier frequency hopped mobile radio telecommunications.

The disadvantages of these systems are the necessity of using a coherent synchronizing signal (pilot signal) and the possibility of operation only at minimal values of time delay, i.e. if the condition that the delay time is much less than the frequency element length of the carrier frequency hopped signal has been satisfied.

The purpose of the invention is to develop a method and a device for an accurate and independent (coherent) reproduction of the phase in the transmitter and receiver of carrier frequency hopped signals. On this basis, the task is to invent a coherent device of synchronization serviceable with random fluctuations of delays.

The problem has been solved developing a synthesizer frequency, which includes a source of standard (reference) signal, a generator of primary signals a switching circuit. The line of primary signals of an angular frequency corresponding to the reference signal is lead to the switching circuit output in a kind of a phase-displaced line. The switching system is synchronized with one of the primary signals and switching can be controlled by the choice of the number of primary signal cycles.

The advantage of the synthesizer frequency proposed is that the primary signals are generated at the same spectrum frequency as the reference signal source. As a sequence, if the switching circuit is synchronized with one of the primary signals, the chosen signal of the same frequency is obtained each time with the start of synthesis. That allows to control the synthesized signal phase and to reproduce it independently in the transmitter and receiver.

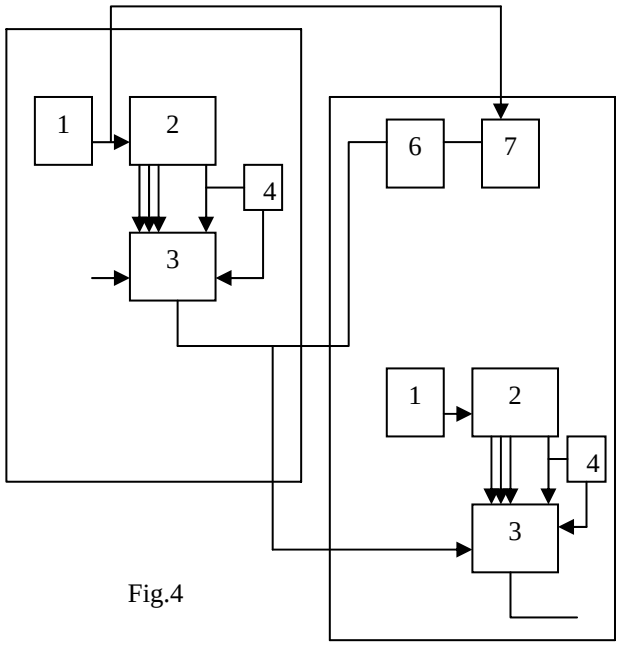

Fig.4

A sample of the proposed synthesizer frequency is shown in Fig. 1 presenting its block diagram. According to the invention the synthesizer frequency consists of a reference signal source, generator of primary simple signals made in the kind of a multi-pin delay line with N pins, a switching circuit, divider of frequencies synchronized with one of the generator simple signals and connected with the switching circuit pulse input.

The operation of the synthesizer is as follows: the signal of angular frequency ω_0 from the reference generator (1) is supplied to the input the generator of the signals (a multi-pin delay line with N pins). The switching circuit (3) is synchronized through the divider of frequencies (4) and switches at every k cycles of the primary signal. If the time interval between two switches is T_s , then the phase difference between the frequency synthesized and the reference signal increases with phase θ for time T_s . As $\theta = \frac{2\pi}{N}$, then the signal synthesized can be kept for an arbitrary part of time with a multiple use of N primary signals and the frequency of the signal synthesized ω_c will be $\omega_c = \omega_0 + \frac{k\theta}{T_s}$. Controlling the switching circuit (the choice of k), the output signal phase can be changed.

On the base of the synthesizer proposed, a device of carrier frequency hopped signals synchronization has been obtained.

It contains a transmitter that can be regulated (5), a receiver (8), a delay monitoring system (6), an extrapolator of the delay (7) and a reference signal source (), a generator of primary simple signals (2), a switching circuit (3), a divider of frequencies (4).

The advantage of the device proposed is that on the base of the delay assessment extrapolation, it determines the moment to start the synthesis of the desired signal in the correlator of receiver obtaining the same phase as that used in the transmitter.

A sample of the device of coherent synchronization according to the invention is shown in Fig. 4.

The operation of the device is as follows: In the standard delay monitoring circuit it is the delay current value is evaluated. For the delay compensation the extrapolator determines value $\tau^*(t)$ and hence the advance in time, i.e $\tau^*(t) = t - \tau(t)$ of transmitting in the transmitter, which is done by supplying the signal to the reference signals generator input (multi- pin delay line).

Let one of the n- number elements signals, which are due for those identically equal to zero out of the interval, is marked with $S_k[0,T]$. Then the signal transmitted can be described with the expression:

$$S(t) = \sum_{k=0}^{n} S_k(t - iT) \qquad (22)$$

With the presence of random time lag, the useful signal received is:

$$S(t,\tau(t)) = S(t - \tau(t)) = \sum_{t=0}^{n} S(t - iT - \tau(T)) \qquad (23)$$

Let present it in the kind of a know function of information discrete parameter $\theta(t)$ and random time lag $\tau(t)$, i.e.:

$$S(t,\theta,\tau) = S\left[t - \tau(t), \theta(t - \tau(t))\right] \qquad (24)$$

The discrete parameter takes constant values on tact interval $\theta(t) = \theta_i, \quad t \in [t_i, t_{i+1}]$. The values of the information parameter on the various tact intervals form a simple Markov's chain $\theta_i, i = 0,1,...,n$ with n states and a known matrix of the transition from the i-th into the j-th state $\Pi = \square_{i,j}$, and vector of the initial states $\square = \square_1$. The limits of the tact intervals are determined by a random time lag $\tau(t)$, i.e. $t_i = t_i(\tau)$. With the time lag realization specified, the limits of tact interval are:
$t_i = iT + \tau(t_i)$.

On tact interval t_i, t_{i+1}, signal $S(t,\theta,\tau)$ coincides with elementary signal $S_i(t - iT - \tau(t))$ if $\theta(t) = \theta_i$. Random time lag $\tau(t)$ corresponds to the signal lag caused by relative motion of the receiver and the transmitter and in the common case it can be examined a component of the diffusion Markov's process:

$$\lambda(t), \tau(t) = \lambda_1(t)$$

Process $\lambda(t)$ satisfies the system of stochastic differential equations:

$$\frac{\partial \lambda_i(t)}{\partial t} = f_i(t,\lambda) + n_i(t) \qquad (25)$$

Here $f_i(t,\lambda)$ are functions satisfying the condition of Lipshits [1] and $n_i(t)$ are a Gauss noises with intensity $b_{ij}(t,\lambda)$. The a priori probable features of process $\lambda(t)$ are determined by the equation of Kolmogorov-Foker-Plank [2]:

$$\frac{\partial W}{\partial t} = -\sum_{\alpha=1}^{n} \frac{\partial}{\partial \lambda}\left[a_\alpha(t,\alpha)W\right] + \frac{1}{2}\sum_{\alpha=1}^{n}\sum_{\gamma=1}^{n} \frac{\partial^2 b_{\alpha\gamma}(t,\alpha)W}{\partial \lambda_\alpha \lambda_\gamma} \equiv L[W] \qquad (26)$$

where $W = W(t,\lambda)$ is the a priori probable density of process $\lambda(t)$;

The observation on signal $S(t,\theta,\tau)$ is realized on the background of noise, i.e. it has kind of

$$\xi(t) = S(t,\theta,\tau) + n(t) \quad (27)$$

Where $n(t)$ is non- correlated with $\theta(\tau)$ and $\tau(t)$ is white noise of feature $\square\{n(t)\} = 0.$

With a certain realization of lag $\tau(t)$, the optimal (according to the criterion of the error probability minimum) assessment of the information discrete parameter constant in interval $[t_i, t_{i+1}]$ is determined with expression [1]:

$$\theta_i^* = \max^{-1}\{P(\theta_i = i)\} = \max_i^{-1}\{P[(i+1)T + \tau, i]\} \quad (28)$$

With random values of tact interval t_{i+1}, when posterior probabilities $P = (\theta_i = i)$ have to be compared, in the moments of time the conditional probability has to be examined with fixed τ, i.e.

$$P(\theta_i = i) = P[t_{i+1}(\tau), i/\tau] \quad (29)$$

The optimal assessment of the discrete parameter can be examined as a non-conditional discrete parameter posterior probability at the end of the interval under observation. The probability can be determined by the expression:

$$P[t_{i+1}(\tau), i/\tau] = P[i/\tau, \xi^{t_{i+1}(\tau)}] \quad (30)$$

made average with weight corresponding to posteriori probable density of random lag $P(t,\tau)$. Then in the i-th tact interval the algorithm of assessment of the information discrete parameters takes the kind of:

$$\theta_i^* = \max_i^{-1}\{P(\theta_i = i)\} = \max_i^{-1}\left\{\int P[t_{i+1}(\tau), i/\tau] P[t_{i+1}(\tau), \tau] d\tau\right\} \quad (31)$$

II. CONCLUSION

The paper presents an algorithm for optimal receiving signals with hop-like change of frequency with random lag. The direct examination on the random lag allows obtaining an algorithm involving a wide range of tasks. For example, such tasks are receiving signals for which the random lag occurs not only in moving away the limits of the time tact intervals but also in receiving under the conditions of changing lag.

The algorithm obtained (31) presents a summary of an algorithm for assessment of a constant parameter in a certain interval with the presence of indeterminacy at the moment of signal appearing.

REFERENCES

1. United States Patent № 4,454,604, Virtual Time Base Direct Synchronizer and Method Therefor, Invertor: Michael H. Myers, Scottsdale, Ariz, Jun.12,1984

2.United States Patent № 4,457,003, Time Reference Tracking Loop for Frequency Hopping, Invertor: Francis K. Reed, Scottsdale, Ariz, Jun.26,1984

Integrated Service Models on Alternative Management Architectures

Tashko Nikolov[1], Aleksandar Tsenov[2]

Abstract – **Network Management is needed to control and optimize the operation of the network and to respond to changing user requirements. Management includes the initialization, monitoring and modification of the network functions. All this functions are defined in the standards for the Telecommunications Management Networks – TMN.**
The Intelligent Network (IN) offers the most applicable architectural concept for effective and adaptive service creation and delivery.
One of the most important functions of the tele-communications networks for building an IN platform is the use of one-provider equipment. To avoid this disadvantage new ma-nagement principles for the IN are needed. TMN alone can not solve this problem.
This paper presents a modeling approach for integrated IN management protocol. The proposed solution includes a modification of the IN Application Protocol (INAP) implementing some typical for the Common Management Information Protocol (CMIP) functions. Particular models of many management service elements are developed using new Service Independent Blocks (SIB). The integration of the function in the IN management is based on the idea of Alternative Management Architectures creation, discussed in [1].

I. INTRODUCTION

Network management architectures provide designers with the ability to discuss management functions at a high level of abstraction and guide the design of management protocols and services. In this paper we assume that these architectures consist of: a set of architectural concepts; rules, describing how to use these concepts and models for designing specific class of systems [1].

All currently used management architectures, especially ISO, ITU-T and IETF architectures have been developed after the whole design of the network functions has been carried out. This is a demonstration of how important the management functions and leads to the idea of applying different architectural concepts for their design.

In this paper we propose a new method for the integration of the primary IN service functions with management service functions – basic service elements - is to be defined.

We also discus the principals of service creation, used in the Intelligent Networks [2] [3]. On this basis are developed models of some of the well known service elements (like ACSE – Association Control Service Element, CMISE – Commitment Management Service Element and ROSE – Remote Operation Service Element).

[1]Tashko Nikolov is with Telecom Department at Technical University of Sofia, "Kliment Ohridsky" Blvd 8, 1756 Sofia, Bulgaria, E-mail: tan@tu-sofia.bg
[2]Aleksandar Tsenov is with Telecom Department at Technical University of Sofia, "Kliment Ohridsky" Blvd 8, 1756 Sofia, Bulgaria, E-mail: akz@tu-sofia.bg

II. TMN MANAGEMENT

According to ITU-T, the term TMN is used as an abbreviation for Telecommunications Management Network. The concept of TMN is defined by Recommendation M.30210 as follows: "a TMN is conceptually a separate network that interfaces a telecommunications network at several different points" [4].

Fig.1 shows the relationship between TMN and the managed telecommunication network. As connection points between the TMN and the telecommunications network are used Transmission Systems and Exchanges. Together they are connected to one or more Operations systems via Data communication network. The Operations systems perform most of the management functions; these functions may be carried out by human operators or executed automatically. Multiple Operations systems can perform single management function. In this case the Data communication network is used to exchange information between the operations systems.

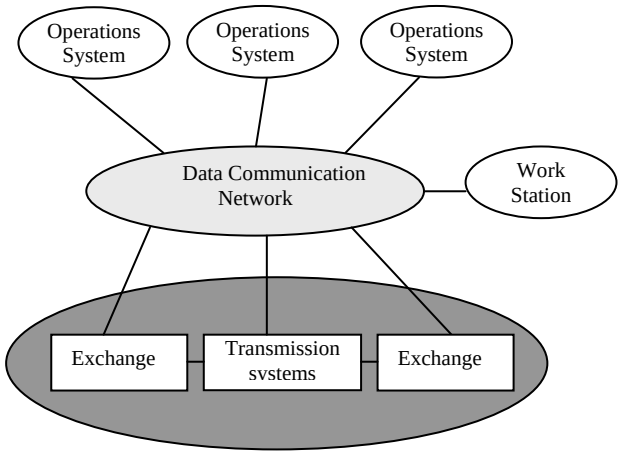

Fig. 1: General relationship of a TMN to a telecommunication network

III. SERVICE CREATION IN INTELLIGENT NETWORKS

The IN conceptual model interfaces the need of efficient creation of new services. From IN point of view, services are combination of features, composed of elementary building blocks called SIBs. The IN service scripts are linear decision trees as they are not allowed to contain loops. For this reason IN service scripts have less expressive power than programming language.

Special SIB called Basic Call Process (BCP) describes the call set up process. The points at which the call processing is interrupted and the service is triggered are called Points of Invitation (POIs). After finishing the processing of the service

logic the last SIB returns the control back to the BCP in the so called Point of Return (POR). To illustrate how SIBs may be combined to build service logic script, the call forwarding service is considered.

Call forwarding (CF) service is built on one core feature: *call forwarding* allows user to unconditionally redirect incoming calls to another number. This service has two optional features: *call logging* allows a record to be inserted each time a call is received by a particular telephone number; *customer profile management* allows the subscriber to manage the service profile in real time. When modeling service logic two cases have to be considered: service activation and service execution.

Figure 2 shows a simplified version of a service script for the activation of CF service. For the sake of simplicity, Figure 1 shows only SIBs flow with corresponding comments, but not SIB parameters. The activation of the CF service begins with subscriber, dialing a special number, provided by the network operator. This number provides access to the management functions of the subscriber profile. Service logic is activated in BCP Address Analyzed POI.

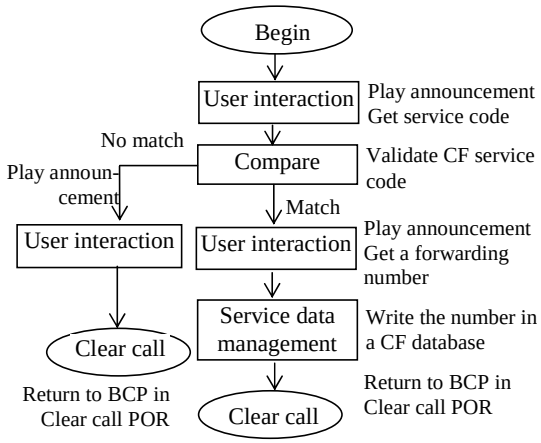

Fig. 2 Simplified service script for CF service activation

In essence, this service activation script performs the following actions:

- The user is asked for the service code and his input is received in the form of DTMF tones.
- The service code is verified against the CF service code.

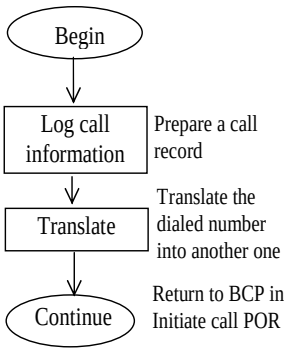

Fig. 3 Simplified service script for CF service execution

- If the received code is CF service code, the user is asked for a forwarding.
- The forwarding number is stored in the call forwarding database and the call is cleared.
- If the received code is not CF service code, the user is informed with an error message and the call is cleared.

Figure 3 shows a simplified version of a service script for CF service execution. The service logic is triggered in Address Collected POI.

IV. PROTOCOL INTEGRATION ASPECTS

The importance of integrated management systems development becomes apparent mostly because of the nonexistence of a unified management tool that could be used for different management applications – test equipment, protocol analyzers etc.

TMN provides functions like monitoring, control and coordination of the telecommunications resources. The core communication protocol in TMN is CMIP, which describes the syntax, the semantics and the time order of all message communications between the managing and the managed structures. CMIP uses ASN.1 (Abstract Syntax Notation One) data types and BER (Basic Encoding Rules) as well as GDMO (Guidelines for Definition of Managed Objects) for abstract description of the real resources in the managed networks.

The basic application protocol in the Internet Network is INAP. INAP as well as CMIP uses ASN.1 data types and BER. This allows the recognition of CMIP messages inside the IN – in form of communication primitives. The main reason why CMIP can not be used (without modification) in intelligent networks are the conceptual differences between IN and TMN.

The section below describes new models of an integrated protocol for intelligent networks management based on CMIP, example realization of new SIB's and enhancement of the Basic Call Process (BCP) in the Capability Set-1 (CS-1).

V. MODELS FOR INTEGRATED PROTOCOLS IN INTELIGENT NETWORKS MANAGEMENT

The model is developed, using the following method:

- New SIB's definition, according to Recommendation Q.1213;
- Model of interactions;
- Graphical representation of the developed service elements;

SIB "ACSE"

Definition: Control of network resources used by the connection between the managing structure (Manager) and the managed structure (agent) in order to perform the service element functions.

Operations: Receives Service Support Data and provides resource management. The result, returned after its execution is either positive (Success), or negative (Error). The element generates Call Instance Data or Error Cause respectively.

Graphical Representation (Figure 4)

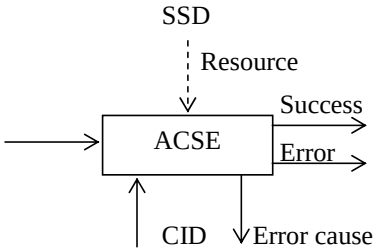

Fig. 4: Service Independent Block "ACSE"

SIB "ROSE"

Definition: This SIB is used to inform one managed structure about the operation of other managing structure.

Operations: This SIB performs the following operations:

- Acknowledgement;
- Operation result;
- Error notification;
- Operation reject.

Service Support Data: This service element uses the following service primitives:

RO-INVOKE . {request/indication}
RO-RESULT . {response/confirmation}
RO-ERROR . {request/indication}
RO-REJECT . {request/indication/response}

Graphical Representation (Figure 5)

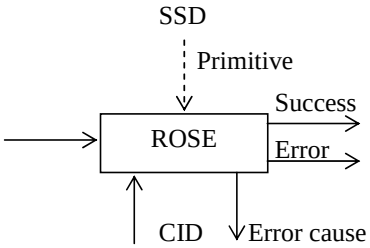

Fig. 5: Service Independent Block "ROSE"

SIB "CMISE"

Definition: This SIB is used for management.

Operations: This SIB performs the following operations using the corresponding primitives:

M-EVENT-REPORT . {request/indication} – reports an event – status change or error;

M-GET . {request/indication/response} – reads argument values;

M-CANCEL-GET . {request/indication/response} – stops reading;

M-SET . {request/indication/response} – sets argument value;

M-ACTION . {request/indication/response} – performs different actions over the managed object;

M-CREATE . {request/indication/response} – creates managed objects;

M-DELETE . {request/indication/response} – removes managed objects.

Graphical Representation (Figure 6)

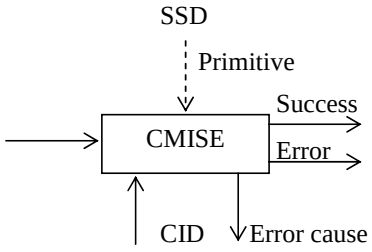

Fig. 6: Service Independent Block "CMISE"

Figure 7 and Figure 8 illustrate the distribution of the management functions when using ROSE SIB and of the CMISE SIB respectively.

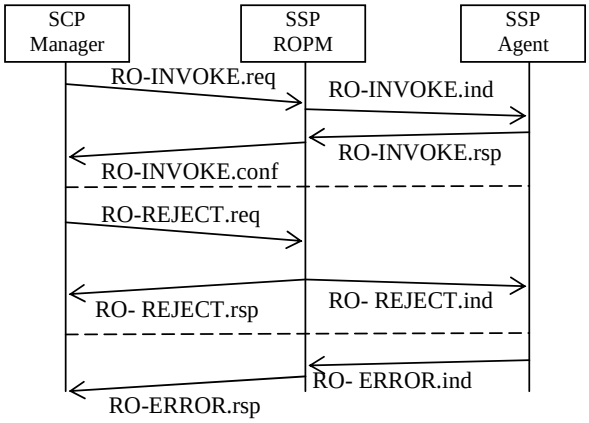

Fig. 7: Examples for the message interaction between IN – Functional blocks using Service Independent Block "ROSE"

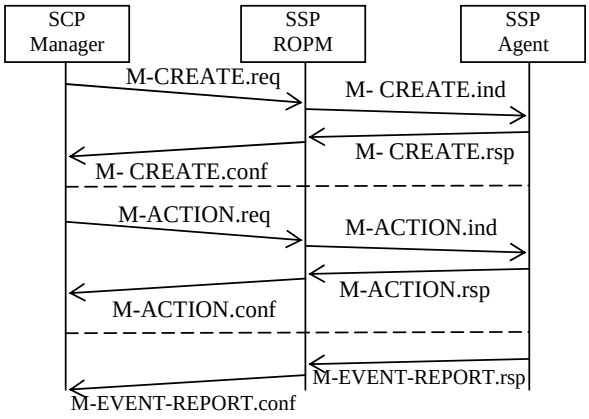

Fig. 8: Examples for the message interaction between IN – Functional blocks using Service Independent Block "CMISE"

One important SIB in the Intelligent network is the BCP (Basic Call Process) SIB – as introduced in part III. It is mandatory in all IN-services for establishing and releasing the connections in the Network. When integrated with management functions BCP starts the corresponding management service element. BCP contains two interface points called POI (Point of Initiation) and POR (Point of Return) – the first one indicates the request of IN service and

the second – the termination of a particular management function.

The graphical presentation of BCP is shown on Figure 9.

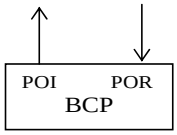

Fig. 9 Service Independent Block "BCP"

The proposed model for integration of the management service SIB ACSE with the primary functions of the Intelligent Networks is shown at Fig. 10.. Because of the limited space only this model will be presented. The other models are developed by implementing similar approach.

Upon receiving request for ACSE, through POI in BCP, a LOG - SIB is started, in order to collect initial data for the execution (when needed) of the new SIB's ROSE and CMISE. After that the ACSE is activated. ACSE has to check the available resources against those, needed for connection establishment. If enough resources are available, the Compare SIB is put in operation, which compares the initial data with the resources in order to negotiate the execution parameters of the requested service. When these parameters agree, the control is returned back to the BCP through the POR, carrying new data and again via the POI the management services ROSE and after that – CMISE are executed.

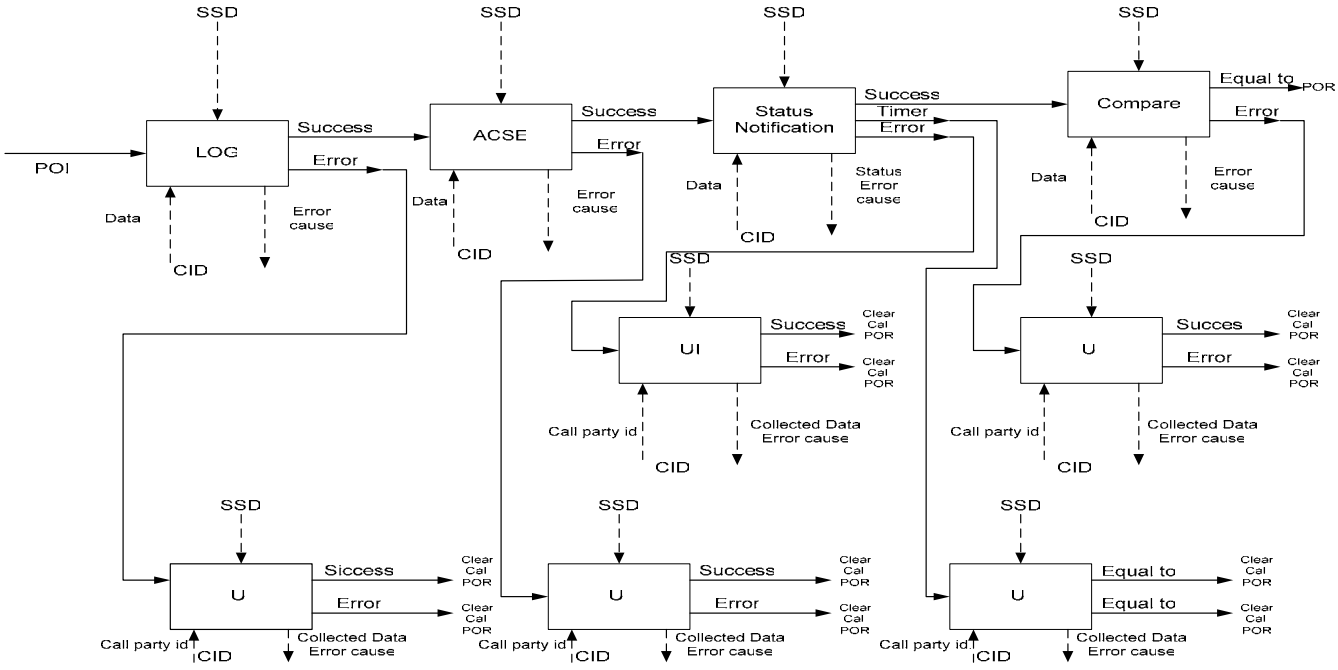

Fig. 10 Model of the management service ACSE

VI. Conclusions

The development of new integrated management functions in the application protocol INAP will bring out the necessity of new Service Independent Blocks – SIB's such as ACSE-SIB, CMISE-SIB and ROSE-SIB. These functions are defined as service elements in the management protocol CMIP in the TMN standards. This is the way to find how to integrate primary network functions (user services) with management functions in order to provide attractive services to the users.

These functions have to meet many different requirements resulting from the increasing user needs.

The models are not being validated because there are not enough suitable simulating tools, development of which is a subject of future work.

References

[1] Tsenov Al., T. Nikolov, "Alternative Architectures in the Network Management",

[2] Atanasov Iv., "Critical Review on Advanced Service Creation Technologies", Electronic and Electrotechnics", ISSN 0861-4717, accepted paper, 2005

[3] Johan Zuidweg, "Next Generation Intelligent Networks", Artech House, 2002

[4] ISO 10040: "Information Processing Systems – Open System Interconnection – System Management Overview", Geneva, 1992

[5] CCITT "Recommendation M.3010, Principles for a Telecommunications Management Network", Geneva 1992

[6] CCITT "Recommendation X.711, Commoninformation protocol Specification for CCITT Application", Geneva 1993

Implementing Intelligent Network Services with the Call Processing Language

Ivaylo Atanasov[1]

Abstract - **The increase of Internet telephony and the rise of the XML as a language standard have recently promoted proposals of XML-based scripting languages that can be used for telecommunications service creation. This paper shows how CPL and VoiceXML can be used to implement traditional intelligent network services.**

Keywords - **service creation, intelligent network, CPL, VoiceXML**

I. INTRODUCTION

The next generation networks (NGN) will provide voice, video, multimedia and data communications using packed-based transmission rather than switched connections. The NGN will converge fixed and mobile access using different technologies. In this heterogeneous environment service development platforms will provide open access to service building blocks. The idea behind service creation in NGN is to provide application programming interfaces (APIs) through which network capability features are accessible to third party application developers. An API is interface providing access to or programmability of software resources. Such as database applications or telecommunication protocol stacks. An API defines software resources in terms of objects and methods, data types and parameters that operate on these objects. Several industry efforts have emerged to develop such open APIs, including Parlay, JAIN and Open Service Access (OSA). Through APIs the service layer does not focus on individual resources, but accesses service capabilities residing in a core telecommunications network.

Several markup languages are proposed for call control, including SCML, XTML, CPL and VoiceXML. The most mature of these proposals are the Call Processing Language (CPL) and the Voice eXtensible Markup Language (VoiceXML). In this paper it is shown how services we are accustomed to use in the telephony network and in the future supported in the Internet can be implemented by CPL and VoiceXML.

II. INTELLIGENCE IN INTERNET

A large number of advanced telephony services are addressed in the standards for Intelligent Network (IN). Services are composed of features that are commonly used functions. A service feature is a specific aspect of a service and can be used in conjunction with other services/service feature as part of commercial offering.

1Ivaylo Atanasov is with the Faculty of Telecommunications, Technical University – Sofia, blvd "Kliment Ohridsky" 8, 1000 Sofia, Bulgaria, iia@tu-sofia.bg

The IN concept was invented for voice telephony networks and unfortunately it cannot be applied to the Internet in a straightforward way..

The architectural model of Internet telephony is rather different than that of traditional telephony network, where the intelligence is centralized In the Internet all signaling and media flow over an IP-based network and the intelligence is completely distributed. In addition, the Internet model transforms the location at which many services are performed. In general, end systems are assumed to be much more intelligent than traditional phones; so many service features which traditionally had resided within the network can be moved out to the edges and thus reducing the required network support. Other service features, such as those for numbering, routing, charging, access, and restriction, can be performed by specialized servers. Most of the services and service features of ITU-T IN can be provided by IETF standards for Internet telephony, e.g. SIP (the Session Initiation Protocol).

According to IETF definition of SIP, a SIP server can perform any of IN features that can be regarded as Internet equivalents. For example, a SIP proxy can query a DNS server for a particular IP address which resembles the way IN service logic translates freephone numbers. Number blocking services also have equivalent in the Internet. A SIP server can play a role of a firewall filtering traffic coming in from and going out to the Internet. A SIP server can modify or redirect SIP requests, but the definition does not specify how the SIP server is programmed to do this. That is why a CPL is developed that tells a SIP server what to do with a call.

Although there are many features of IN that can be recognized in the Internet, there are also a few IN features that simply do not make sense in the Internet. One of them is charging features. In the Internet there is traditionally no notion of charging for a connection. So services such as freephone or calling card calls simply do not make sense in the Internet.

III. CALL PROCESSING LANGUAGE

CPL is a language to describe and control Internet telephony services. It can be implemented on either network servers or user agents. It is meant to be independent of operating system or signaling protocol; it is anticipated that it will be used with both SIP and H.323. It is based on the XML, so parsing it is easy and many parsers for it are publicly available. The structure of the language maps closely to its behavior, so an editor can understand any valid script, even ones written by hand.

Implementations of CPL are expected to take place both in Internet telephony servers and in advanced clients; both can usefully process and direct users' calls, but a mechanism will be needed to transport scripts between clients and servers.

Each CPL script installed in a server has an owner, and is always associated with the address of his owner. A CPL script concerned with the owner of the script. A subaction is any action that can be reused within other actions. Top-level actions and subactions can contain the following elements:

- Switches, which compare an element of a SIP message against a set value and can make choices based on these comparisons. A switch in CPL can make a choice on the basis of originating or destination address, time and date, priority, or even free-form text strings in the subject or body of the SIP message.
- Location modifiers change the location to which the call must be routed. CPL allows location modifiers to specify anexplicit new address, or it can order the new address to be looked up in an internal or external database.
- Signaling actions specify what to do next with the SIP message after the possible modification. The options are to proxy the SIP message, to redirect it, or to reject it. Proxy means sending the message on to the destination or another SIP server and redirect means sending it back to the originator with a modified address.
- Non signaling actions are additional actions that are not related to the SIP message. There are two nonsignaling actions defined: sending an e-mail to a specified address, or writing information in a log file.

There are striking resemblances between CPL scripts and IN service scripts. Both specify how to process incoming and outgoing calls. Both are decision tree structures without loops.

CPL is non-expressively complete language; it can not be used to create arbitrary complex scripts, thereby limiting the resources a script needs for successful execution. For example, CPL has less expressive power than IN service features. IN service features that forward or screen calls can be translated directly into CPL constructs, but there are no CPL counterparts for the more complex IN service features for charging, call queuing, user interaction, and service data management. Table1 shows how IN service features can be translated to CPL.

Typically, CPL scripts execute within the context of a user agent. A user agent is an entity that exists in SIP and H.323 networks. User agents do not exist in present day IN networks; therefore, CPL scripts are not protocol agnostic.

CPL is only activated through call events; it cannot be activated through call unrelated events such as timer expiring or registration in a mobile IP network. CPL assumes that a database can be queried to provide location information of a registered user. CPL script can interact with a special voice-response server that provides user interaction functions, but it does not define how to handle with information that can be provided by a user interaction system.

CPL is targeted more at the end user, and is based on the philosophy that the end user uploads his call-processing scripts on a SIP server. CPL therefore does not allow any actions that can be considered internal to the service provider, such as charging or modifying data in a subscriber database.

CPL still offers a few important advantages that make it interesting for use in the IN environment. It is simple and transparent, and has a well-defined syntax and semantics. But most importantly, CPL has the potential to provide a uniform consists of top-level actions and subactions. The top-level actions describe what to do with incoming and outgoing calls call-processing language for SIP-based Internet telephony and IN.

IV. VOICE EXTENSIBLE MARKUP LANGUAGE

VoiceXML has been defined as a technology that allows a user to interact with the Internet through voice-recognition technology. Using VoiceXML, the user interacts with voice browser by listening to audio output that is either pre-recorded or computer-synthesized and submitting audio input through the user's natural speaking voice or through a keypad, such as a telephone. VoiceXML can also be described as a phone markup language that can be used for voice applications that provide phone access to content and information. VoiceXML is a high-level abstraction language and this means that developers with little training can use it. VoiceXML makes it easy to rapidly create new applications and shields developers from low level programming issues. VoiceXML also executes logic: main components of a VoiceXML-based speech service include tags, forms, rules that define the content and a speech browser for interpreting and presenting audio content.

The IN service features that support user interactions can be translated to VoiceXML dialogues.

V. IN SERVICE FEATURES

IN standards describe the services into two broad categories: services which IN vendor would actually wish to provide to customers; and service features which are lower-level building blocks used to construct the services.

This section summarizes in the Table 1 the characteristics of each service feature listed in Q.1211, in the context of the Internet telephony. The "location" column indicates the place at which the service feature is supported; "end" means that the service can be provided at an end system, "proxy" means at a proxy server, and "redirect" at a redirect server.

The "CPL equivalent" column presents CPL constructs that can be used in implementing the service feature. The CPL scripts are executed on SIP servers; thus only CPL constructs that implement IN service features provided by SIP proxy server and SIP redirect server are shown.

VI. CONCLUSION

In this paper XML-based technologies for NGN service creation are presented. The capabilities of CPL are presented for implementing of service features we are accustomed to use in telephony networks. CPL can be used as call-processing language for SIP-based telephony, but it has restricted expressive power. CPL is only activated through call events and does not define how to interact with servers that provide mobility management information (e.g. provide information for facilities nearest to the user location).

Hence, CPL does not support all services that can be based on underlying network capabilities. Conjugating CPL and Voice XML might be done in order to obtain user interaction that is supported by most of IN services.

TABLE 1 MAPPING IN SERVICE FEATURES TO CPL

Service feature	*Description of the service feature*	*Location*	*CPL equivalent*
Abbreviated Dialing (ABC)	Allows the definition of abbreviate dialing	End/Proxy/ Redirect	Location modifier
Attendant (ATT)	Allows virtual private network (VPN) to access an attendant position within the VPN	End/Proxy/ Redirect	Location modifier
Authentication (AUT)	Verifies that a user is allowed to exercise certain options.	End/Proxy	Address-switch followed by reject
Authorization code (AUTZ)	Allows a VPN user to override calling restrictions.	Proxy	Address-switch followed by reject
Automatic call back (ACB)	Allows the called user to automatically call back the last caller	End	-
Call distribution (CD)	Specifies the percentage of calls to be distributed among two or more destinations.	Proxy/Redirect	No direct equivalent
Call forwarding (CF)	Forwards incoming calls to another number	Proxy/Redirect	Location modifier followed by redirect
Call forwarding on busy/don't answer (CFC)	Forwards particular incoming calls if the called user is busy or does not answer within a specified number of rings.	Proxy/Redirect	Location modifier followed by proxy
Call gapping (GAP)	Restricts the number of calls that can be routed to a particular destination.	Proxy	Switch followed by reject
Call hold with announcement (CHA)	Allows subscribers to place a call on hold and transfer the call to another location.	End	-
Call limiter (LIM)	Specifies a maximum number of calls that can be simultaneously routed to a particular destination.	End	-
Call logging (LOG)	Creates a log record for each call received at a specified number.	All	Nonsignaling action log
Call queuing (QUE)	Queues calls meeting busy or no answer within a predetermined time. An announcement is given to the calling party.	End/Proxy	Proxy to queuing server
Call transfer (TRA)	Allows a user to place a call on hold and transfer the call to another location.	End	-
Call waiting (CW)	Notifies the called party, when on a call, that another party is trying to reach him.	End	-
Closed user group (CUG)	Allows a user to be a member of a set of VPN users who are normally authorized to make and receive calls only within the group.	End/Proxy	Address-switch followed by reject
Consultation calling (COC)	Allows the user to place a call on hold, in order to initiate a new call for consultation.	End	-
Customer profile management (CPM)	Allows users to manage their customer profiles in real time.	End/Proxy/ Redirect	Location modifier with lookup
Customized recorded announcement (CRA)	Allows a call to be completed to a (customized) terminating announcement instead of a subscriber line.	End	-
Customized ringing (CRG)	Allocates a distinctive ringing to a list of calling parties.	End	-
Destination user prompting (DUP)	Prompts called parties with a specific announcement.	End	-
Follow-me diversion (FMD)	Routes incoming calls to a new location.	End	-
Mass calling (MAS)	Allows the processing of huge numbers of incoming calls.	Proxy	No direct equivalent
Meet-me conference (MMC)	Reserves conference resources for making a multiparty call, indicating the date, time, and duration of the conference.	Other (e.g. using a conference bridge)	-

TABLE 1 MAPPING IN SERVICE FEATURES TO CPL (CONTINUETION)

Service feature	*Description of the service feature*	*Location*	*CPL equivalent*
Multiway calling (MWC)	Establishes multiple, simultaneous calls among parties.	End	-
Off net access (OFA)	Allows VPN users to access the VPN from any non-VPN exchange.	All	Address switch followed by reject
Off net calling (ONC)	Allows VPN users to call outside the VPN.	Proxy	Address switch followed by reject
One number (ONE)	Permits two or more terminating lines, also at different locations, to have a single telephone number.	Proxy/Redirect	Location modifier followed by proxy/Location modifier followed by redirect
Origin-dependant routing (ODR)	Enables users to accept or reject calls and, if they accept a call, route the call according to the calling party's geographical location.	Proxy/Redirect	Address-switch
Originating call screening (OCS)	Allows users to bar calls from certain areas.	End/Proxy	Address-switch followed by reject
Originating user prompter (OUP)	Allows users to provide an announcement requesting calling parties to enter a digit or series of digits.	All	Proxy calls to a VoiceXML server
Personal numbering (PN)	Supports a UPT number that uniquely identifies each UPT user and is used by calling parties to reach the UPT user.	Proxy/Redirect	Location modifier followed by proxy
Premium charging (PRMC)	Allows for the payback of part of the cost of a call to a value-added service provider.	-	-
Private numbering plane (PNP)	Allows subscribers to maintain a numbering plan within their private network that is separate from the public network.	End/Proxy/ Redirect	Location modifier followed by redirect/reject
Reverse charging (REVC)	Allows subscribers to be charged for the entire cost of calls they receive.	-	No direct equivalent
Split charging (SPLC)	Allows calling and called parties to share the cost of a call.	-	No direct equivalent
Terminating call screening (TCS)	Screens calls based on the terminating number called.	End/Proxy	Address-switch followed by reject
Time-dependent routing (TDR)	Enables users to accept or reject calls and, if they accept a call, route the call according to time and date.	Proxy/Redirect	Time-switch

REFERENCES

[1] Alan B. Johnston, SIP: Understanding the session Initiation Protocol, Artech House, 2004

[2] VoiceXML Forum, Voice eXtensible markup Language VoiceXML, 2000

[3] J. Lennox, X. Wu, CPL: A Language for User Control of Internet Telephony Services, RFC 3880, 2004

[4] Johan Zuidweg, Next Generation Intelligent Networks, Artech House, 2002

[5] Lennox, J., H. Schulzrinne, and La Porta T., Implementing Intelligent Network Services with the Session Initiation Protocol, CUCS-002-99, 1999

XML-Based Languages for Intelligent Service Creation

Evelina Pencheva[1], Ivaylo Atanasov[2]

Abstract - **CPL is a language that can be used to explain to SIP servers what to do with a call. VoiceXML is a language that is used to describe speech dialogues between the computer and the end user. In this paper we investigate how XML-based languages like CPL and VoiceXML can be used in creating value-added services in IP networks.**

Keywords - **service creation, intelligent network, CPL, VoiceXML**

I. INTRODUCTION

Intelligent Network (IN) was designed in the early 1990s for delivering value added services in circuit switched telephony networks. At that time the World Wide Web was still in its infancy and in many countries a single national operator still owned the network. Although there are many features of IN that can be recognized in the Internet, there is one important differrence. In IN these features are centrally controlled; in the Internet they are completely distributed through the network.

The IN and Internet protocol (IP) technologies are converging in a variety of ways including the use of IP for transmission of voice - voice over IP (VoIP) - for more cost effective transport of voice communications. In addition, efforts are underway to allow intelligence in public switched networks to interface and interact with intelligence in IP based networks, and doing so, provide greater overall intelligence.

An important effort to define capabilities for hybrid IN + IP networks involves the integration of IN with the Session Initiation Protocol (SIP). This integration will allow for more flexible service control options than could be afforded through either technology by itself.

The Call Processing Language (CPL) is a XML-based language to describe and control Internet telephony services. It is designed to be implementable on either network servers or user agents. It is meant to be simple, extensible, and independent of operating system or signaling protocol. It is suitable for running on a server where users may not be allowed to execute arbitrary programs, as it has no variables, loops, or ability to run external programs.

VoiceXML is a markup language that enables integration of voice services with data services using the familiar client-server paradigm. It separates user interaction code (in VoiceXML) from service logic. The language promotes service portability across implementation platforms and is easy to use for simple interactions, and yet provides language features to support complex dialogs.

[1]Evelina Pencheva is with the Faculty of Telecommunications, Technical University – Sofia, blvd "Kliment Ohridsky" 8, 1000 Sofia, Bulgaria, enp@tu-sofia.bg

[2]Ivaylo Atanasov is with the Faculty of Telecommunications, Technical University – Sofia, blvd "Kliment Ohridsky" 8, 1000 Sofia, Bulgaria, iia@tu-sofia.bg

In this paper we explore the capabilities of CPL and VoiceXML that help end users to define their call treatment. We consider an example of malicious call identification service and suggest service scripts in CPL and VoiceXML.

II. SERVICE CREATION IN INTELLIGENT NETWORKS

The IN provides great flexibility to service creation in general and also to the tailoring of services to suit the exact requirements of a particular user. Service creation in IN involves three basic components – SIBs, service features, and services. SIBs are the smallest building blocks that describe reusable network capability used to create service features. Some functions are commonly used for many services, for example, number translation services or mass calling services. These functions are called service features and are built of one or more SIBs. A service is built by combining one or more SIBs and features or services or both. To illustrate how SIBs can be combined to build service logic script, the malicious call identification service is considered.

The malicious call identification (MCI) service is built by combining the following core features: call logging (LOG) and originating call screening (OCS). LOG allows a record to be prepared each time a call is received by a special telephone number. OCS allows the served user to bar calls (call screening) from certain areas based on the district code of the area from which the call originates.

Malicious call identification service can incorporate one optional feature: customer profile management (CPM). CPM allows the subscriber to manage the service profile in real time, that is, changing answering places, control the announcements to be played, perform call distribution, change time-dependent routing, and so on.

Combining the optional feature CPM and the core feature OCS creates the remote control of malicious call identification service.

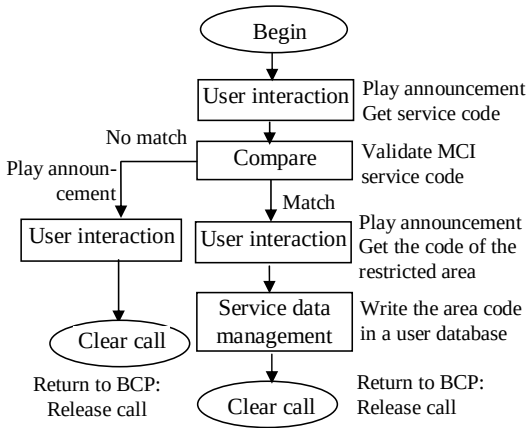

Figure 1 Service script for MCI service activation

When modeling service logic two cases have to be considered: service activation and service execution. Figure 1 shows a simplified version of a service script for the activation of MCI service. For the sake of simplicity, Figure 1 shows only SIBs flow with comments, but not SIB's parameters. When the subscriber wants to activate the MCI service, he has to dial a special number, provided by the network operator. This number accesses the management functions of the subscriber's profile.

In essence, this service activation logic performs the following steps:

- A message is played asking for the service code and user input is received in the form of DTMF tones.
- The service code is verified against the MCI service code.
- If the received code is MCI service code, a message is played to the user, asking for the district code of the restricted area and the user input is received.
- The restricted area code is stored in the user database and the call is cleared.
- If the received code is not MCI service code, an error message is played to the user and the call is cleared.

Basic call process (BCP) is a special SIB that describes the phases of call set up. At each of these phases it is possible to interrupt the call setup and to start execution of a service script. After finishing the processing of the service, the last SIB hands back control to the BCP.

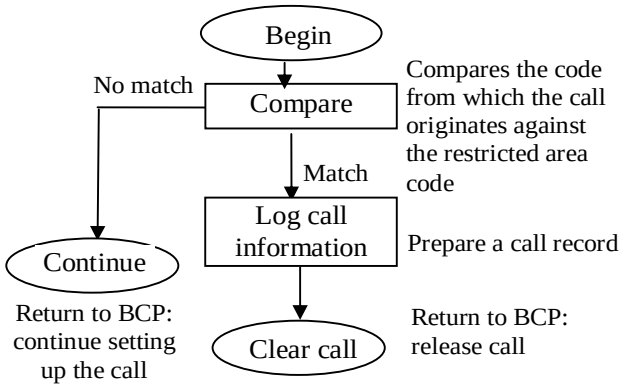

Figure 2 Service script for MCI service execution

Figure 2 shows a simplified version of a service logic for MCI service execution. The service proceeds in the following way.

- The district code from which the call originates is compared against the restricted area code.
- If the call originates from the restricted area, a record is prepared and the call is cleared.
- If the call originates from an area that is different than the restricted area the call setup continues.

III. XML-BASED LANGUAGES AND IN

The CPL can be used to describe and control Internet telephony services. It is not tied to any particular signaling architecture or protocol; it is anticipated that it will be used with both the SIP and H.323.

SIP is an application-layer Internet protocol for setting up multimedia conferences over the Internet. A SIP server can perform any of the IN features, such as those for numbering, routing, charging, access, and restriction. CPL provides tools for creating call-processing scripts that runs on SIP servers.

CPL is powerful enough to describe a large number of IN services and features, but it is limited in power so that it can run safely in Internet telephony servers. The intention is to make it impossible for users to do anything more complex (and dangerous) than describe Internet telephony services. Table 1 shows how some of the IN SIBs can be translated to CPL.

TABLE 1
MAPPING IN SIBS TO CPL

IN SIB	*CPL equivalent*
Algorithm	No direct equivalent: CPL is not a programming language
Charge	No direct equivalent
Compare	Switch
Distribute	Switch
Limit	Switch follow by reject
Log call information	Nonsignaling action (log)
Queue	No direct equivalent; could be implemented in CPL by proxying calls to a special queuing server
Screen	Switch follow by reject
Service data management	Location modifier with lookup (CPL does not allow to write in a database)
Status notification	Signaling action (proxy)
Translate	Location modifier
User interaction	No direct equivalent; could be implemented in CPL by proxying calls to a special voice response server with VoiceXML interpreter.
Verify	No direct equivalent.

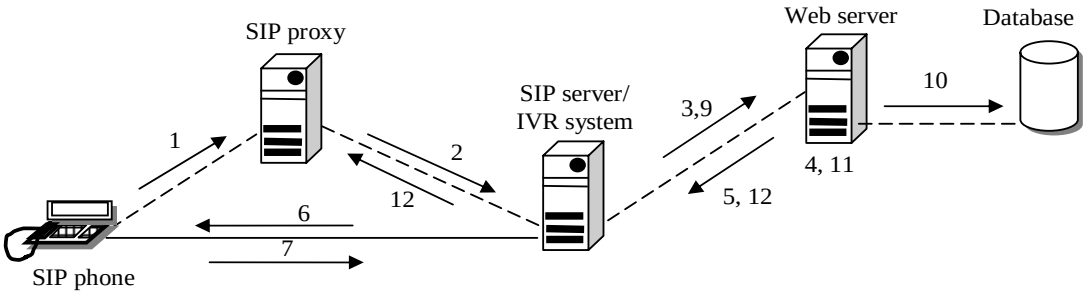

Figure 3 A scenario for MCI service activation

A voice service is viewed as a sequence of interaction dialogs between a user and an implementation platform. The dialogs are provided by document servers, which may be external to the implementation platform. Document servers maintain overall service logic, perform database and legacy system operations, and produce dialogs. A VoiceXML document specifies each interaction dialog to be conducted by a VoiceXML interpreter. User input affects dialog interpretation and is collected into requests submitted to a document server. The document server may reply with another VoiceXML document to continue the user's session with other dialogs. The user is prompted for input and then records it. The user input can be played back, and if the user approves it, is sent on to the server for storage using the HTTP[1] POST method. If the platform supports simultaneous recognition and recording, form and document scoped grammars can be active while the recording is in progress.

The JSpeech Markup Language (JSML) is a text format used by applications to annotate text input to speech synthesizers. JSML elements provide a speech synthesizer with detailed information on how to speak text and thus enable improvements in the quality, naturalness and understandability of synthesized speech output. JSML defines elements that describe the structure of a document, provide pronunciations of words and phrases, indicate phrasing, emphasis, pitch and speaking rate, and control other important speech characteristics. JSML can be used with conjunction of the VoiceXML.

IV. MCI SERVICE IMPLEMENTED BY CPL AND VOICEXML

The IN standards describing the interaction between service control function and service data function are defined in terms of INAP[2] information flows. In Internet telephony services, these interactions are replaced with HTTP requests to HTTP servers that hold the call screening data for a particular subscriber.

Let us consider MCI service provided over the Internet. Having the service the user can screen the call from a particular area. The steps for MCI activation, as shown in the Figure 3, are as follows:

1. The user dials a special number provided by service provider. The user agent (the software in the terminal) sends the *Invite* request to the SIP proxy.
2. The SIP proxy server looks at the address, determines that it belongs to SIP server with embedded Interactive Voice Relay (IVR) system and sends the *Invite* request on to SIP server/IVR system.
3. The SIP server/IVR system analyses the request and concludes that the user wants to activate a service. It determines the Web server that stores the service preparation script and sends a HTTP *GET* request to the Web server asking for service preparation script. The service preparation script can be a script written in PHP, Java, Perl or some other script language.
4. The service preparation script is executed and as result it creates a VoiceXML script that has to maintain the dialogue with the user in context of the service activation.
5. The Web server returns the HTTP reply with the VoiceXML script to the SIP server/IVR system.
6. The SIP server/IVR system starts interpreting the VoiceXML script and speaking to the user. The user is asked for the service he wants to activate.
7. The user inputs the MCI service code by DTMF tones.
8. The dialogue between the IVR system and the user continues for getting the restricted area code from which the user doesn't want to receive calls.
9. The SIP server/IVR system posts the information retrieved from the user to the Web server.
10. The Web server sends a SQL request to the Database for updating user data. The database acknowledges the update.
11. The Web server creates a CPL script for MCI service.
12. The CPL script is posted to the SIP proxy of the user.

Figure 4 shows an example of VoiceXML script that retrieves the user information needed for service activation. A subdialogue is used to get the service code and a form dialogue captures the restricted area code (359259). A subdialog is a mechanism for decomposing complex sequences of dialogs to better structuring, or to create reusable components. In the example, service activation may involve gathering several pieces of information, such as service code, the restricted area code, and others. A customer care service might be structured with several independent applications that could share this basic building block, thus it would be reasonable to construct it as a subdialog.

[1] Hyper Text Transfer Protocol
[2] Intelligent Network Application Protocol

```
<?xml version="1.0"?>
<vxml version="1.0">
  <form id="callcenter">
  <var name="service_code"/>
  <subdialog name="serviceinfo"
                src="srvc_info.vxml#basic">
  <filled>
    <assign name="service_code" expr="srvcinfo.code"/>
  </filled>
  </subdialog>
  <field name="area_code" type="digits">
     <prompt> What is the restricted area code?</prompt>
     <filled>
       <submit next="/cgi-bin/updatemci"/>
     </filled>
  </field>
 </form>
</vxml>

<?xml version="1.0"?>
<vxml version="1.0">
<form id="basic">
  <filled>
    <field name="code" type="digits">
     <prompt>
       What is the code of the service you want to activate?
     </prompt>
    </field>
    <return namelist="code"/>
  </filled>
</form>
</vxml>
```

Figure 4 A VoiceXML script for MCI service activation

Figure 5 shows an example of CPL script for the MCI service. If a call originates from area with 359259 code it is rejected and the information is logged. The SIP server should include information in the log, such as the time of the logged event information that triggered the call to be logged, and so forth.

```
<?xml version="1.0"?>
<cpl>
 <incoming>
  <address-switch field="origin" subfield="tel">
   <address subdomain-of="359259">
    <reject status="reject" reason="Not allowed to
          receive calls from 359259 subdomain"/>
     <log name=”rejectedcalls” comment=”origin”/>
   </address>
  </address-switch>
 </incoming>
</cpl>
```

Figure 5 A CPL script for MCI service

V. CONCLUSION

As the next generation network seemed to be IP-based SIP is seen as the future of call signaling and telephony. Many value-added services we are accustomed to use in the telephony networks can be implemented in IP networks with SIP.

Extremely complex telecom applications, as found in call centers, have become even more complex when integrating with e-mail and web applications for managing service profiles. For example, both call routing and e-mail routing to agents – based on various criteria such as queue length, call origin, time of day, customer ID – can be reduces to simple XML scripts when using SIP and CPL. CPL has restricted expressive power and can be used to describe decision structures for routing calls. As most of the services require user interaction CPL can be combined with VoiceXML to adapt the services to customer call-processing preferences.

SIP in conjunction of CPL and VoiveXML can implement any of IN features as those for numbering, routing, charging, access, and restriction.

REFERENCES

[1] Alan B. Johnston, SIP: Understanding the session Initiation Protocol, Artech House, 2004

[2] VoiceXML Forum, Voice eXtensible markup Language VoiceXML, 2000

[3] J. Lennox, X. Wu, CPL: A Language for User Control of Internet Telephony Services, RFC 3880, 2004

[4] Johan Zuidweg, Next Generation Intelligent Networks, Artech House, 2002

A Generic Call State Model for SIP Proxy

Hristo Froloshki[1], Evelina Pencheva[2]

Abstract – **Provisioning of value-added services in IP telephone networks requires a generic model of the behavior of SIP server. Definitions of states and transitions in call processing will enable service logic triggering. There are services that deal with outgoing calls and services that deal with incoming calls, so the model distinguishes between processing of the two types of calls. Different traffic cases are considered to synthesize common behavior.**

Keywords – **value-added services in IP telephony networks, behavior of a SIP proxy**

I. INTRODUCTION

Today the telecommunications business is almost entirely determined by the services offered and their price. In order to survive in the struggle for peace of the telecom market, network operators need not only the right technology, but the right tools to create value-added services in efficient way. In circuit switched networks services like freephone, premium rate and televoting are implemented centrally on an intelligent network (IN) platform. In the Internet the network intelligence is completely distributed. There is a need for protocols, models and tools for implementing intelligent services in distributed packet switched environment.

A perspective candidate for delivering IP telephony is Session Initiation Protocol (SIP). SIP is an application protocol, utilizing client/server architecture. The protocol is used for multimedia connections in Internet, and also offers status and availability capabilities. In [1] and [2] it is shown how services we are accustomed to use in telephony networks can be implemented in the Internet by the use of SIP signaling. Some of the services are implemented in the end system, while others reside the network nodes (SIP servers). For services implemented in the network it is necessary to describe in a generic way the behavior of SIP server in service provisioning.

The IN conceptual model introduces the concept of half call: basic call state model is defined for originating calls (O_BCSM) and for terminating calls (T_BCSM). Both O_BCSM and T_BCSM can trigger service logic. Following the proved IN concept the paper suggests a generic model of the behavior of a SIP server. This model enables and facilitates additional logical processing in call setup, management and release procedures.

[1]Hristo Froloshki is with the Faculty of Telecommunications, Technical University – Sofia, blvd "Kliment Ohridsky" 8, 1000 Sofia, Bulgaria, hef@tu-sofia.bg

[2]Evelina Pencheva is with the Faculty of Telecommunications, Technical University – Sofia, blvd "Kliment Ohridsky" 8, 1000 Sofia, Bulgaria, enp@tu-sofia.bg

II. IN BASIC CALL STATE MODELS

In the IN conceptual model the O_BCSM and T_BCSM implement the idea of half-call as state transition diagrams where the points in call (PICs) represent the states through which each call passes.

The transitions are caused by events. An event can have a detection point (DP) associate with it. DPs are the points at which the call processing can be suspended in order to hand over control to service logic. The separation between the originating and termination models allows the definition of different supplementary services, applicable to the corresponding party. An example for service, utilizing O_BCSM is freephone, where service logic needs to be activated to translate the number dialed to a local one. An example for service activated by T_BCSM is call forwarding on no answer. In this case service logic should be activated when a call is received and the subscriber hasn't answered it in a predefined time interval.

The idea of the half call concept is shown on Figure 1. The service switching function (SSF) supports both the O_BCSM and T_BCSM. Apart from this, the calling and the called party are not necessary connected to the same exchange or even to the same network. When the O_BCSM or T_BSCM encounters a DP this triggers the service control function (SCF).

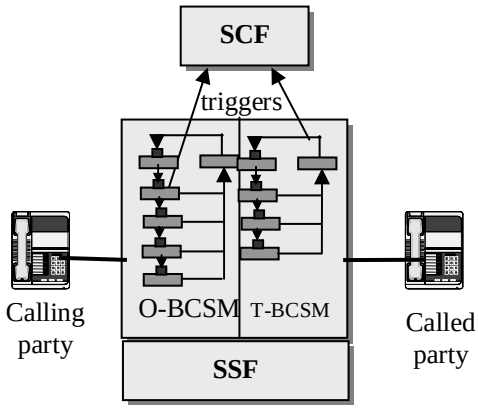

Figure 1 The O_BCSM and T_BCSM defined in the IN conceptual model

The SSF has a mechanism for handling DPs during call processing. There are different types of DPs that require specific actions to be taken. The trigger detection point (TDP) is set statically at the time of deployment of a service or when a user subscribes to it, while the event detection point (EDP) is set dynamically by service logic during the call. If the DP is armed as notification (TDP-N or EDP-N) the BCSM only informs the SCF and continues without waiting the response. If the DP is armed as request (TDP-R or EDP-R) the BCSM

suspends call processing, triggers the SCF and waits for instructions on how to proceed.

III. MODELLING APPROACH

The SIP proxy is modeled with a finite state machine, following the proven modeling approach used for description of SSF behavior in the IN conceptual model. Two groups of different call scenarios (Figure 2 a,b,c,d,e,f), including SIP, PSTN[1] and H.323 networks, are considered. The first group consists of scenarios where a call originates from the SIP network and terminates in the same or an external network. The second group of scenarios presents a call terminating in the SIP network. Every SIP phone runs a user agent, consisting of user agent client (UAC), responsible for establishing outgoing calls and user agent server (UAS), which accepts incoming calls.

A SIP proxy server is an essential part of the SIP network, for it provides functionality needed for establishing calls. It processes SIP requests and can perform user location, address translation, security screening or any other processing on the SIP requests.

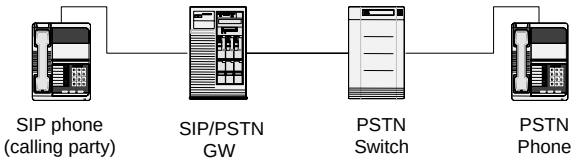

Figure 2 a SIP-to-PSTN scenario

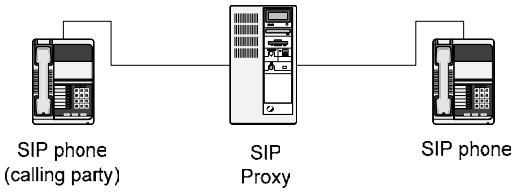

Figure 2 b SIP-to-SIP scenario

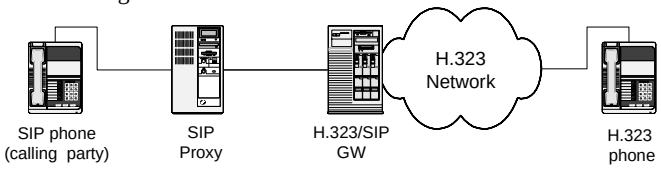

Figure 2 c SIP-to-H.323 scenario

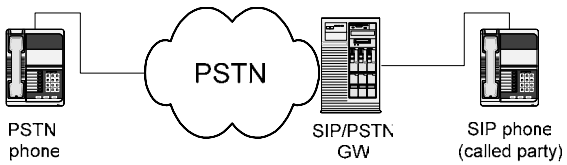

Figure 2 d PSTN-to-SIP scenario

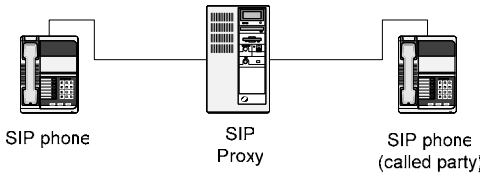

Figure 2 e SIP-to-SIP scenario

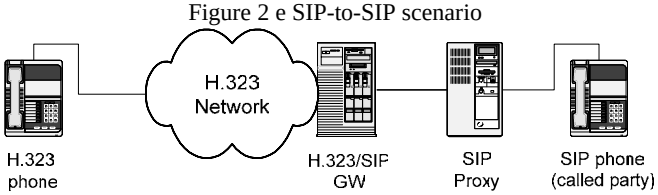

Figure 2 f H.323-to-SIP scenario

Actually, a SIP server can perform any of IN features, but the mechanism of control is different. In IN the SSF keeps tight control of the call state through BCSM. When the SCF interferes in the call processing the control is always returned to the SSF. In SIP there is no central entity that keeps tight control of call signalling. The request routed to a SIP proxy can be sent onward after processing or just transparently routed to another proxy. Nevertheless the behaviour of SIP proxy in call processing resembles the mechanism for service triggering in the BCSM. This server demonstrates similar behavior in the different scenarios and therefore the proposed state model is based on its states.

SIP signaling procedures for the above mentioned scenarios [3], [4] are considered. The communication between functional entities is broken down into elements and relations are found between the different traffic cases. The aim is to synthesize abstract generic models for SIP UAC and SIP UAS. Based on these models generic signaling flows between SIP UAC, SIP proxy and SIP UAS are developed. Having defined common signaling flows the behavior of SIP proxy is described by the use of a finite state machine.

Figure 3 shows a generic description of the behavior of a SIP UAC. The SDL[2] is used as a modeling tool.

In order to create a generic model of a SIP UAC common communication elements and signaling procedure parts are abstracted and put together. The model is described by the use of states and transitions. It starts with sending the *Invite* message to the called party. If authorization is not required, the transition to the next state is up to the type of the terminating network. The *Wait Progress* state is entered while checking the status of the called PSTN party. In the *Wait OK* state a positive response from the called party is anticipated. The *OK* message may be generated either by a SIP gateway, or by a SIP UAS. The *Alerting* state is where the calling party is notified that the *Invite* request has been received and alerting is taking place. The *RTP Session* state represents the active phase of the call. The *Authorizatio*n state is the point in session where the identity of the calling party is verified by proxy or registrar server.

The *Error Handling* state is used for processing of exceptions that might occur during call setup or release. Implementation details such as error identification codes, and their processing are not in the scope of this paper.

[1] Public Switched telephone Network

[2] Specification and Description Language

In the *Idle* state the UAS listens for incoming calls. After an *Invite* request is received, the server sends *Ringing* message, alerts the user (not shown on the figure) and sends *OK* response to the *Invite* request. The *Wait ACK* state is where final confirmation (*ACK*) for the establishing of media session is received.

The *RTP Session* state is where the actual conversation between parties takes place. Any party may terminate the communication by sending *BYE* message. An acknowledgment response for successful termination of the session is expected in *Wait OK* state.

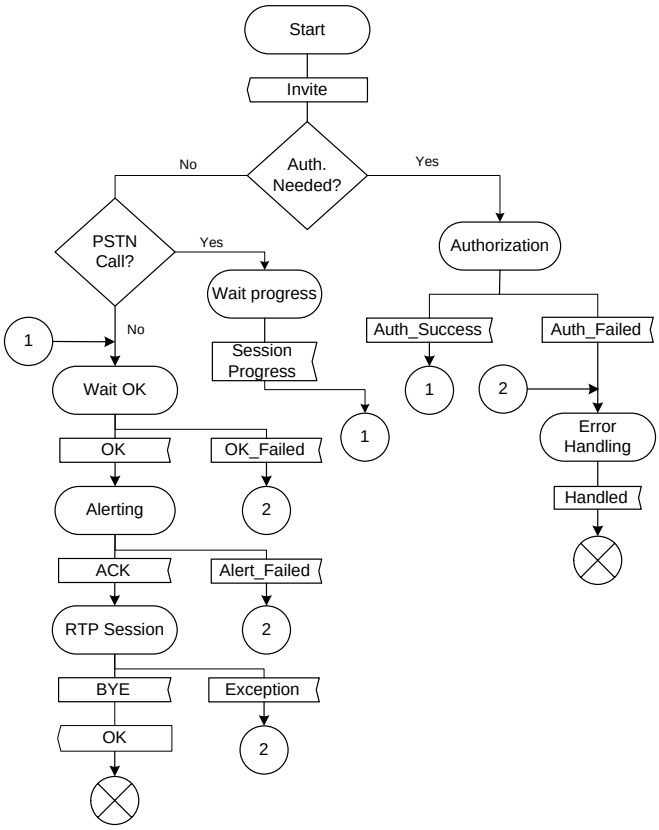

Figure 3 SDL description of a generic behavior of a SIP UAC

Figure 4 shows a generic description of the behavior of a SIP UAS.

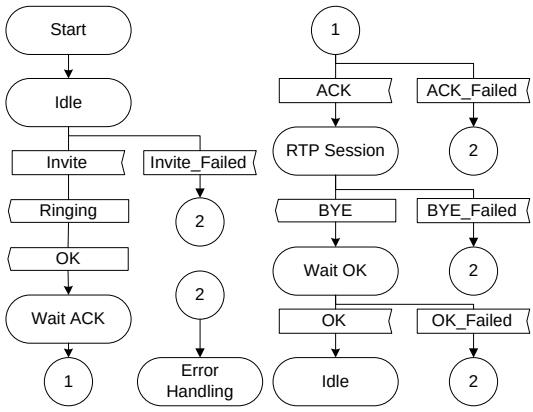

Figure 4 SDL description of a generic behavior of a SIP UAS

IV. SIP PROXY BEHAVIOUR MODEL

Based on the abstract models for SIP user agents generic signaling flows between user agents through SIP proxy servers are defined. The proposed message sequence in case of a stateful proxy is shown on Figure 5.

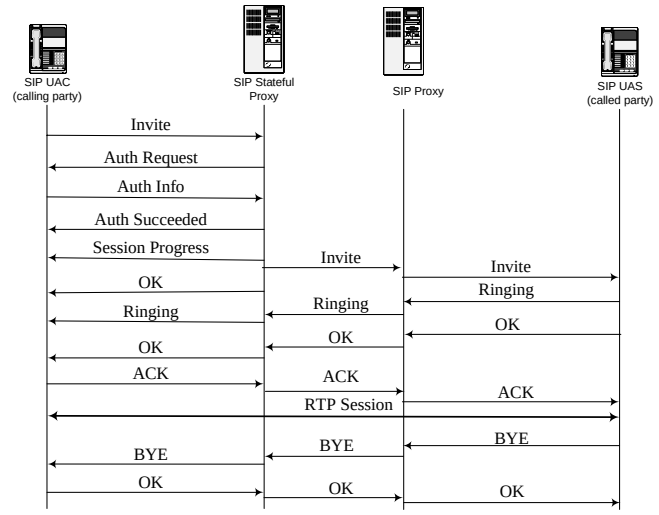

Figure 5 Generic signaling flows

The behavior of a SIP proxy can be described by states and transitions derived from the generic signaling flows. Following the half call concept in IN conceptual model two SIP proxy models are proposed: one for the SIP outgoing calls and one for the SIP incoming calls. There is a striking resemblance between the states and transitions in these models and the appropriate PICs and DPs in O_BSCM and T_BCSM.

Figure 6 presents the SIP proxy model handling outgoing calls. An *Invite* request is expected in the *O_Idle* state. The *Authorization* state performs identity verification procedures the aim is to acknowledge that the calling party is authorized to make a call. The *Address Analysis* state uses information received from the *Invite* message to identify destination address and additional parameters, needed for call setup. If the address information is complete, then the SIP proxy sends an *Invite* message to the called party. In case of SIP-PSTN call the *Session progress* message is sent to inform the calling party about the call progress and also the *OK* message acknowledges the establishment of an additional media channel. In the *Routing* state the receiving of a *Ringing* message indicates that the called party is alerted and then a *Ringing* message is sent to the calling party. An answer form the called party is expected in the *O_Alerting* state. The SIP proxy is informed when the called party answers with the *OK* message and it causes sending of the OK message to the calling party. The acknowledgment for established end-to-end session is received in the *O_Setup_Confirmation* state. In the *O_RTP session* state the actual data transfer takes place. Note that a SIP proxy server has no media capabilities, so the RTP stream passes transparently through the SIP proxy. The *O_Release* state is entered when a party ends the

communication. The acknowledgement for call released causes the transition back to the *O_Idle* state.

All exceptions during the normal SIP outgoing call processing are processed in the *O_Error_Handling* state.

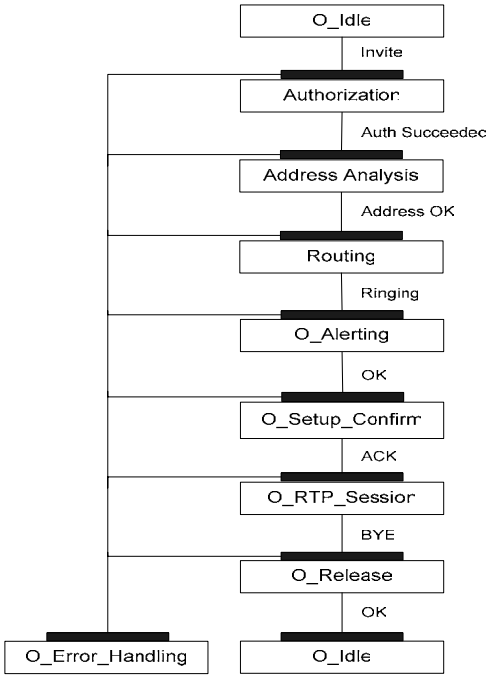

Figure 6 A generic stateful SIP proxy model handling outgoing calls

The generic behavior of SIP proxy server in case of SIP incoming call is shown in Figure 7.

The *Invite* request is received in the *T_Idle* state and this causes the transition to the *Present_call* state where the called party status is examined. If the called party is idle then a *Ringing* message is sent and the SIP proxy enters the *T_Alerting* state. The answer from the called party generates an *OK* message and a corresponding *OK* message is sent to the calling party. An acknowledgement for the established end-to-end connection is received in the *T_Setup_Confirmation* which causes the transition to *T_RTP_session* state. When a party hangs, the SIP server enters the *T_Release* state waiting for cancel acknowledgement.

All exceptions during the normal SIP incoming call processing are processed in the *T_Error_Handling* state.

The events causing transitions can have associate DPs. An event in an armed DP can trigger a service logic located on the same SIP server or on an external application server.

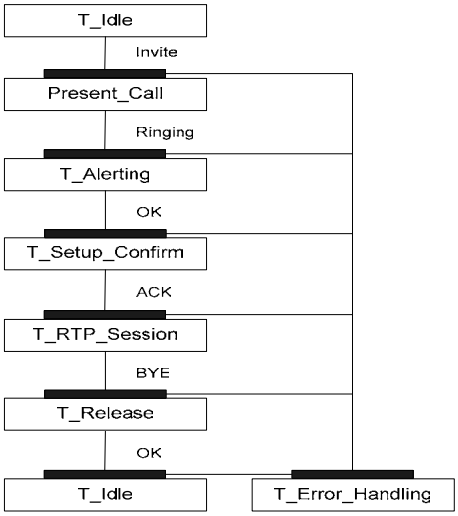

Figure 7 A generic SIP proxy model handling incoming

V. CONCLUSION

A generic model of a SIP proxy server is suggested. As it is in the IN conceptual model, the behavior of the SIP server is considered from two points of view: processing of outgoing calls and processing of incoming calls. The separation is required because there are services that deal with outgoing calls (for example originating call screening) and services that deal with incoming calls (blocking of malicious calls). The clear definition of the states and detection points enables service logic to interfere in the call processing.

REFERENCES

[1] Lennox I J., T Schulzrinne, F. La Porta, *Implementing Intelligent Network Services with the Session Initiation Protocol*, Tech-Report Number CUCS-002-99

[2] Pencheva E., V. Georgieva, *Modelling of Intelligence in Internet Telephone System*, ELECTRONICS'2004, Sozopol, Bulgaria Proceedings, book 3, pp 112-118.

[3] Alan B. Johnston, *Session Initiation Protocol*, Artech House Inc., 2004

[4] Rosenberg, J. et al., SIP: Session Initiation Ptorocol, RFC 3261, 2002

[5] Johan Zuidweg, *Next Generation Intelligent Networks*, Artech House Inc., 2002

Makes the Periodic Test the Systems Safety

Tashko A. Nikolov[1], Nikoleta H. Hristova[2]

Abstract - **The paper present the influence of several tests in the fault-tolerant control systems - absolute, relative and complete periodic tests, on the system reliability and safety. On the basis of some Markovian modelling techniques are offered generalised formula for obtaining the maximum safe period between system tests. On the one hand they avoid unnecessary over dimensioning and the resulting high manufacturing costs, while on the other hand it demonstrates a method of optimum distribution of the resource of the different tests in the fault-tolerant systems. Besides, it provides opportunities for additional comparative analysis of the different fail-safe and fault-tolerant structures.**

Keywords - **testing; failure detection; Markovian modelling**

I. INTRODUCTION

Stringent requirements on reliability and safety have been introduced for many technological processes in the fields of nuclear power, transport, space systems, chemical and other industries. These requirements affect the control systems as early in as design and development phase. They must take into account the growing requirements of the users, reflecting on their functionality and also they must be in line with the safety norms of the respective branch, national or international administrations. In many cases the safety requirements are determined in terms of the probability or mean time of a particular undesirable event occurrence.

The failure detection means in particular computer systems comprise three types of tests - *absolute, relative* and complete *periodic* ones [1, 8]. Let us assume that the failure detection facility in the three types of tests is *a*, *r* and *p*, respectively.

The absolute test has to detect failures for a period shorter than the system reaction time. The failure detection facility *a* of the absolute test is the probability of detecting the failure before the output of the result $(0 \le a \le 1)$.

The relative test consists of comparing two or more results from independent processing. The efficiency of the comparison r $(0 \le r \le 1)$ depends on the number of the compared information vectors N and on the dimensionality of these vectors n. If N=2, the probability of a wrong result obtaining is [8]:

$$(1-r) = (2^n - 1)/2^{2n} \tag{1}$$

where: *n* is the length (in bits) of the output vector

[1]Tashko Nikolov is with Telecom Department at Technical University of Sofia, "Kliment Ohridsky" Blvd 8, 1756 Sofia, Bulgaria, E-mail: tan@tu-sofia.bg

[2]Nikoleta Hristova is with Telecom Department at Technical University of Sofia, "Kliment Ohridsky" Blvd 8, 1756 Sofia, Bulgaria, E-mail: nhh@tu-sofia.bg

In case of N=3, i.e. triple modular redundancy system (TMR), the probability for obtaining of two or three equivalent results is: $3\{1\times(1/2^n)\times[(2^n-1)/2^n]\}$ and $1\times(1/2^n)\times(1/2^n)$ respectively.

The periodic test is a complete test of the system. It can be carried out both off-line (e.g. once a day, week or year) and on-line. In either case we can speak of a cycle of periodic test with duration T_{pt}. The failure detection facility *p* of the periodic test is the probability of failure detection at the complete testing (self testing) of the system $(0 \le p \le 1)$.

The purpose of the paper is to be established the requirements of the three types of test in order to be satisfied the safety criteria. The equations have to be valid for any kind of systems regardless of the number of redundant units and the used tests.

II. MODELLING TECHNIQUE

When the system reaction after occurrence of a failure is in accordance with an adopted criterion of after-failure behaviour, the failure is considered to be *safe* [3, 4, 10], otherwise it is considered to be *dangerous.* The dangerous failure rate is marked by λ_d, the safety failure rate is marked by λ_s. Obviously, $\lambda_s + \lambda_d = \lambda$

Since normally the cycle of the periodic test is longer than the system reaction time we believe that a dangerous failure of the system appears after a failure has not been detected by the absolute and relative tests

$$\lambda_d = (1-a)(1-r)\lambda \tag{2}$$

This, in a certain sense, is a worst-case assumption, because a new chance is given to the absolute and relative tests by the change of the information status [8].

Fig. 1 shows the model, described in [8]. From a dangerous state the system may be brought only into safety state with transition rate α. Consequently, an occurred dangerous failure can be detected only by the periodic test. Then for the restoration rate from a dangerous state we obtain:

$$\alpha = p / T_{pt} \tag{3}$$

The probability for staying in each state is [2, 6]:

$$P_1 = \frac{\alpha\mu}{\mu(\alpha + \lambda_d) + \alpha\lambda} \tag{4}$$

$$P_2 = \frac{\lambda_d \mu}{\mu(\alpha + \lambda_d) + \alpha\lambda} \tag{5}$$

$$P_3 = \frac{\alpha\lambda}{\mu(\alpha + \lambda_d) + \alpha\lambda} \tag{6}$$

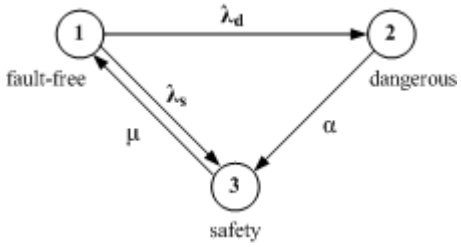

Fig. 1. Markovian graph of an element from the control system

In the model of safety control system the numbering of the states is rendered by an N numerical code, where N is the number of the modelling units. Each digit from this code can take one of the following values: 1, 2 or 3, which correspond to failure-free, dangerous and safety states of the element [6, 7, 2]. The transition rates in the graph can exist only between states whose codes differ in only one digit. That means the condition of ordinariness is being observed, e.g. in the time interval $(t, t+\Delta t)$ it is possible only one event to be realised.

The following Markovian graph (Fig. 2.) is obtained at a system consisting of two elements (e.g. 2-out-of-2 system) each described by a graph from Fig. 1.

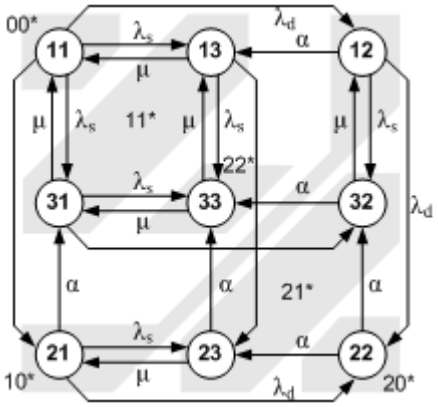

Fig. 2. Markovian graph of a 2-out-of-2 system

The probability for staying in any state is obtained by:

$$P_{a_s b_s c_s} = P_{a_s} \times P_{b_s} \times \ldots \times P_{k_s} \qquad (7)$$

where:

a, b,...,k are the numbers of the elements

s∈{1,2,3} are the numbers of the states: failure-free, danger and safety.

Reducing this graph according to [5], on the principle of number of failures occurred - number of failures detected, we obtain the so-called "impersonified" model. Here the numbering of the states is presented by a two-digit code, the first digit showing the number of failures that have occurred, the second showing how many have been detected [2]. The model is called "impersonified" because there is no information about the certain failed element. However, this is of no significance in the case when systems of static redundancy with identical reserved elements are investigated. All indicators of the "impersonified" graphs are marked by *.

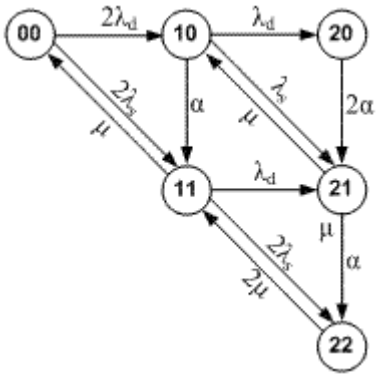

Fig. 3. "Impersonified" Markovian graph of a 2-out-of-2 system

$$\begin{aligned}
a^*_{00,10} &= \left[P_{11}(\lambda_d + \lambda_d)\right] / P_{11} = 2\lambda_d \\
a^*_{00,11} &= \left[P_{11}(\lambda_s + \lambda_s)\right] / P_{11} = 2\lambda_s \\
a^*_{11,00} &= \left[P_{13}(\mu + \mu)\right] / \left(P_{13} + P_{13}\right) = \mu \\
a^*_{22,11} &= \left[P_{22}(\mu + \mu)\right] / P_{22} = 2\mu
\end{aligned} \qquad (8)$$

The probabilities for staying in the separate states are:

$$\begin{aligned}
P^*_{00} &= P_{11} = P_{a_1} P_{b_1} = P_1^2 \\
P^*_{10} &= P_{12} + P_{21} = P_{a_1} P_{b_2} + P_{a_2} P_{b_1} = 2P_1P_2 \\
P^*_{11} &= P_{13} + P_{31} = P_{a_1} P_{b_3} + P_{a_3} P_{b_1} = 2P_1P_3 \\
P^*_{21} &= P_{23} + P_{32} = P_{a_2} P_{b_3} + P_{a_3} P_{b_2} = 2P_2P_3 \\
P^*_{22} &= P_{33} = P_{a_3} P_{b_3} = P_3^2
\end{aligned} \qquad (9)$$

When the system has at least one detected failure, it is in a safety state. Consequently, states 11, 21 and 22 are of the safety type. When unidentified failures emerge in both elements, there is no right result criterion and that is why state 20 is considered to be dangerous, while states 00 and 10 are considered as failure-free.

The graph of a multi-channel system (NMR system) is shown on Fig. 4.

In general, the formula for finding the probability for staying in each state is:

$$P^*_{ij} = \frac{n!}{(n-i)!(i-j)!\,j!}\left(P_1^{n-i} P_2^{i-j} P_3^{j}\right) \qquad (10)$$

where:

n - number of elements

i - number of occurred failures

j - number of detected failures

P_1 - probability for a failure-free state of separate element

P_2 - probability for a dangerous state of separate element

P_3 - probability for a safety state of separate element

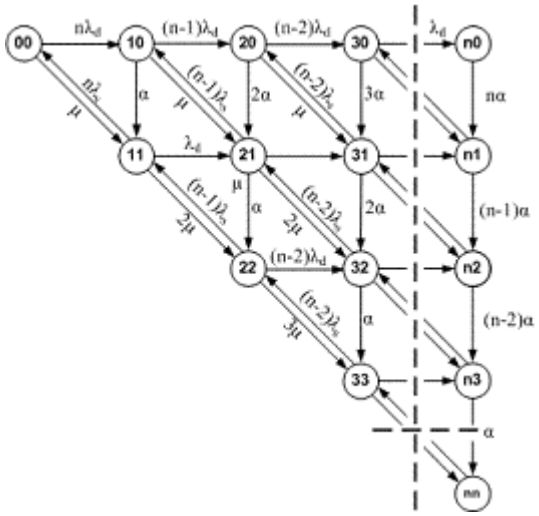

Fig. 4. "Impersonified" graph of NMR

III. MEAN TIME FOR DETECTION OF AN UNIDENTIFIED FAILURE

The problem of finding the admissible time for the existence of an unidentified failure comprises: *Designing a periodic test of such failure detection facility p and period T_{pt} satisfying the safety criteria, e.g. probability for dangerous failure of the system.*

The time required is the reciprocal value of the sum of the transition rates going out of the dangerous state of the system, e.g. the mean time for staying in a dangerous state [6, 5].

System 2-out-of-2 (NMR; N=2)

The dangerous state of the 2-out-of-2 System is 20, with probability $P_{20}^* = P_2^2$. Corresponding to Eq. (9) from Eq. (5) is obtained:

$$\alpha = \frac{\lambda_d \mu (1 - P_2)}{P_2(\lambda + \mu)} \tag{11}$$

$$T_d = 1/\alpha = \frac{P_2(\lambda + \mu)}{\lambda_d \mu (1 - P_2)} \tag{12}$$

where: T_d is the mean time for staying in a dangerous state.

The problem may be reduced to the evaluation of the mean time for staying in a dangerous state (T_d=1/α) as a function of probability for a dangerous failure of the individual element P_2, while in its turn P_2 may be presented as a function of the probability for dangerous failure of the system Q_d. That leads to obtaining implicitly the dependence $\alpha=f(Q_d)$ for various types of systems (e.g. N=1,2,3,...).

This makes possible:

1. Simplification of the problem for more complex systems (NMR, N>2).

2. Formulation of requirements both on the parameters of the periodic control and on the safety of the individual elements.

The analytical investigation of the dependencies for 2-out-of-2 is shown on Fig. 4., where Q_{dav} is the dangerous acceptable value.

System 2-out-of-3 (TMR)

We have a dangerous failure in TMR system when the difference between the number of the occurred failures and those that have been detected is larger or equal to two. Then the dangerous states are 20, 30 and 31. Consequently, for the probability of a dangerous failure we obtain:

$$Q_d = P_{20}^* + P_{30}^* + P_{31}^* \tag{13}$$

$$Q_d = 3P_1P_2^2 + P_2^3 + 3P_2^2P_3 \tag{14}$$

$$Q_d = P_2^2(3 - 2P_2) \tag{15}$$

$$2P_2^3 - 3P_2^2 + Q_d = 0 \tag{16}$$

The solution of Eq. (16) constitutes the formation of the criterion for safety for the individual elements of the general safety criterion for the system.

Three real roots are obtained in such a case, two of which are identical [10]. The results are graphically shown on Fig. 4.

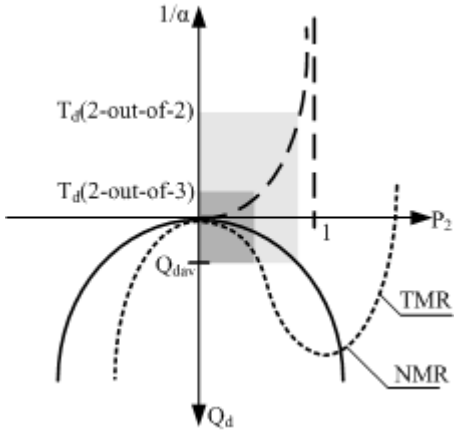

Fig. 4. Dependence between the mean time of staying in a dangerous state and the probability for dangerous failure by TMR

From Eq. (5) it is possible to be obtained certain dependence (Fig. 5.) between the three types of failure detection means – absolute test, relative test and complete periodic test. One may recognise easily that the absolute and relative tests are not present (e.g. $a=0$ and $r=0$), there is a determined value A for the time duration of the periodic complete test, by which the safety norm can be observed.

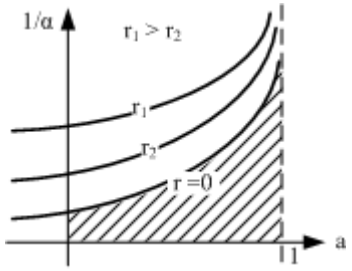

Fig. 5. Dependence between the time duration of the periodic test and the failure detection facility of the absolute and relative tests

$$1/\alpha_{(a=0)} = \frac{P_2(\lambda+\mu)}{(1-r)(1-P_2)\lambda\mu} \quad (17)$$

When $a = 0$ and $r = 0$ we obtain the following:

$$A = \frac{P_2(\lambda+\mu)}{(1-P_2)\lambda\mu} = \frac{P_2}{P_1(1-P_2)\lambda} \quad (18)$$

IV. EXAMPLES

Example 1.

A 2-out-of-2 system with the following indicators of the individual elements is given:

- Failure rate - $\lambda = 10^{-5}$ h^{-1}
- Repair rate - $\mu = 1$ h^{-1}
- Failure detection facility of the absolute test - $a = 0.5$
- Failure detection facility of the periodic test - $p = 0.95$
- Compared information vectors - $N = 2$
- Order of the compared vectors - n =8 bits
- Safety norm of the system - $Q_{dav} = 10^{-12}$

The maximum admissible time for detecting a hidden failure is required.

Procedure:

Step 1.: Calculation of the failure detection facility of the relative test from Eq. (1):

$$r = 1 - \frac{2^n - 1}{2^{2n}} = 1 - \frac{2^8 - 1}{2^{16}} = 0.9961$$

Step 2.: Calculation of the dangerous failure rate from Eq. (2):

$$\lambda_d = (1-a)(1-r)\lambda = 1.95 \times 10^{-8}, h^{-1}$$

Example 2.

A TMR system each element of which has the same parameters as in Example 1 is given. The maximum admissible time for the detection of a hidden failure is also required.

Procedure

Step 1: Calculation the failure detection facility of the absolute test from Eq. (3):

$$r = 1 - \frac{(2^n - 1)(3 \times 2^n - 2)}{2^{2n}} = 0.9884$$

Step 2: Calculation the dangerous failure rate from Eq. (8)

$$\lambda_d = (1-a)(1-r)\lambda = 5.28 \times 10^{-8}, h^{-1}$$

Step 3: Calculation the probability P_2 for a dangerous failure by each element depending on the safety criterion Eq. (16):

$$Q_d = (3 - 2P_2)P_2^2 = 10^{-12}$$

$$P_2 = 5.75 \times 10^{-7}$$

Step 4: Calculation the mean time T_d for staying in a dangerous state depending on Eq. (12):

$$T_d = 1/\alpha = \frac{P_2(\lambda+\mu)}{\lambda_d \mu(1-P_2)} = 9.9, h$$

Step 5.: Determination the maximum duration of the periodic system test from Eq. (3):

$$T_{pt} = p/\alpha = 0.95 \times 9.9 = 9.4, h$$

Table I. shows results about the maximum duration in dangerous state of the system for the two types of systems depending on the dimensionallity of the information vector. All other conditions are the same.

TABLE I

DEPENDENCE OF THE T_D ON THE DIMENSIONALLITY

***n*,bit**	**4**	**5**	**6**	**7**	**8**	**…**	**16**
T_d**(*N*=2),h**	3.33	6.66	13.3	25	51.3	…	13333
T_d**(*N*=3),h**	0.68	1.28	2.5	4.8	9.9	…	2555

V. CONCLUSION

On the basis of some Markovian modelling techniques are offered generalised formula for obtaining the maximum safe period between system tests. On the one hand they avoid unnecessary over dimensioning and the resulting high manufacturing costs, while on the other hand they avoid unnecessary over dimensioning and the resulting high manufacturing costs, while on the other hand it demonstrates a method of optimum distribution of the resource of the different tests in the fault-tolerant systems. Besides, it provides opportunities for additional comparative analysis of the different fail-safe and fault-tolerant structures. The dependencies shown in the paper between the value of the safety norm and the time parameters of the failure detection means could be applied in many practical cases. This dependence may be used not only for analysis of fault-tolerant computer systems (e.g. aeroplanes, nuclear power plants etc.)

REFERENCES

[1] Görke,W., *Fehlertolerante Rechensysteme*, Oldenburg Verlag München Wien, 1989

[2] Johnson,B.W., *Design and Analysis of Fault Tolerant Digital Systems*, Addison-Wesley Publishing, 1989.

[3] Redmil, F.J., *Dependability of critical computes systems*, Elsevier Applied Science, 1988 Part 1; 1989 Part 2.

[4] Bishop, P.G., *Dependability of critical computes systems*, Elsevier Applied Science, 1990 Part 3.

[5] Kochs, H.-D., *Zuverlässigkeit elektronischer Anlagen*, Springer, Berlin, 1984.

[6] Kuo W., Zuo M., *Optimal Reliability Modelling*, John Wiley&Sons, 2003.

[7] Nikolov,T., *Investigating the safety of control systems*, Dissertation, Technical University of Sofia, 1991.

[8] Echtle,K., B.Hinz, T.Nikolov, Hardware Fault Detection by Diverse Software, Hardware and Software Fault Tolerance in Parallel Computing Systems, ELLIS HORWOOD, London, 1992, pp.313-326

[9] Bronstein,I.N., K.A.Semendjajew, Taschenbuch der Mathematik, Verlag Harri Deutsch.

[10] Laprie, J.C., (ed.), Dependability: basic conceptsand terminology in English, French, German, Italian and Japenese, Wien, Springer, 1992

Considerations for DTMF Generation with Micro-Controller System

Petre Tzv. Petrov [1]

Abstract - **The micro-controller unit (MCU) is presents in many system connected to the telephone network . Sometimes MCU has free resources which could be used for additional functions. It is possible to use them for standard or user-defined single, Dual Tome Multi Frequency (DTMF) or multi-tone (MT) generation and recognition.**

Keyword - **DTMF generation, digital processor, micro-controller**

I. INTRODUCTION

The micro-controller (MCU – Micro Controller Unit) is present in many systems connected to the telephone network and some of its resources are free to be used for additional functions. Consequently it is possible to use them for analog signals (AS) generation and recognition and in particular for standard or user-defined single or Dual Tome Multi Frequency (DTMF) generation or for melody and other audio signal generation. Most of the general purpose MCUs such as Motorola 68HC11F1 [1] and Microchip PIC 18F876 [2] could be used successfully to generate audio signals. A lot of specialized integrated circuits designed to generated and recognize standard DTMF tones exists [e.g. 3, 4] and could be used but sometimes they are additional burden to the designer and the manufacturer of the system. In the privately owned communication systems an original one or multi-tone signaling system could be used.

The purpose of this paper is to apply and test the methods in the signal sampling and reconstruction described in [5, 6] in the field of DTMF generation and recognition by digital processor system and in particular by MCU-driven system.

DTMF generators are already implemented in some MCUs. For example in MC68HC05F32/F8 there are implemented DTMF/Melody Generators with signal sampling factor (SSF) N=Fd/Fs=28 and with 6-bit internal D/A converter [9] .

The value for N and n in these and many more cases are in relative good correspondence with the equations discussed in [5, 6] and given below:

$$n=\lg((N))+2=\lg(28)+2=6.81 \text{ bits} \quad (1)$$

and with the Eq. 2

$$N=\mathrm{LG}((1/\mathrm{EMAX}))=\mathrm{LOG}((1/0.00629))=7.32 \text{ BITS} \quad (2)$$

where logarithm in base 2 and Emax=0.629% for N=28.

In some cases using the MCU with build-in DTMF generator decoder is not possible and the only solution is to implement these functions on the general purpose processor already available in the project.

[1] Petre Tzvetanov Petrov is with "Microengineering"-Sofia, Bulgaria and expert-lecturer width OFPPT-Casablanca, Morocco.
Emails: ppetre@caramail.com and ptzvp@yahoo.fr.

II. DTMF TONES

The DTMF and call progress frequency list is given in Table I [3,4]. The solutions for DTMF generation discussed here are applicable for any the audio-tone and melody generation system and are interesting for different purposes (medical, security, voice synthesis, testing electronics equipment and communication channel etc).

TABLE I.
DTMF AND CALL PROGRESS TONES.

Description	Tone 1, [Hz]	Tone 2, [Hz]
Dial Tone	440	350
Busy	620	480
Ring-back	480	440
1	1209	697
2	1336	697
3	1477	697
4	1209	770
5	1366	770
6	1477	770
7	1209	852
8	1366	852
9	1477	852
0	1366	941
*	1209	941
#	1477	941
A	1633	697
B	1633	770
C	1633	852
D	1633	941

Although the sampling frequency Fd of approximately 8 KHz is used in some of the telephone connected equipment (Table II) this not a strict rule and the designer could take any sampling frequency Fd in order to solve the problem. But if the sampling frequency Fd is kept constant the amplitude error Emax is different for each frequency Fs of DTMF signals (Table II).

It is seen that DTMF tones are falling into two main groups: 1/ low group: 697, 770, 752 and 941 Hz and 2/ high group: 1209, 1336, 1477 and 1633 Hz. The "dead band" between the groups is 268Hz with central frequency of 1075Hz.

Note: 1/ With F=8kHz N=Fd/Fs>=4 for all frequencies and Eamax<=-3dB. 2/ Emax is a maximal amplitude error due to he possible sampling the SS/CS not in its maximum.

TABLE II
SAMPLING DTMF SIGNALS WITH FD=8KHZ

Low band (ΔF=244Hz)				High band (ΔF=424Hz)		
Fs, Hz	N	Emax		Fs, Hz	N	Emax
697	11.48	3.72%		1209	6.62	11.1%
770	10.39	4.53%		1336	5.86	11.4%
752	10.64	5.55%		1477	5.42	16.4%
941	8.50	6.75%		1633	4.9	19.9%

The following general rule (GR) for adding SS/CS was formulated: *1/ When k SS/CS signals with the same amplitude A are added the amplitude of the resulting signal could be up to k*A and the peak-to-peak amplitude of the same signal could be up to 2*k*A. or 2/. When k SS/CS are added the amplitude of the resulted signal cannot exceed the sum of the amplitudes of the signals in the sum.*

The major consequence of this GR is that the resolution and the accuracy of each signal component in the sum is reduced in comparison to the resolution and accuracy of the output signal. For example if an 8-bit DAC is used and only one SS/CS is generated it could have full 8-bits of accuracy and resolution (256 steps). If two tone are generated simultaneously each of them could have up to 7 bits (128 levels), if four tones are generated simultaneously they could have 6 bits (64 steps), etc and the Eq. 3 is applicable

$$Bs = \lg (Lv/k), [bit] \qquad (3)$$

where Bs are bits per signal component, Lv a levels in the staircase function of the converter (Lv = 2exp(n) or Lv = 256 for a n=8 bit converter) and k is the number of the tones in the sum (Table III). Also, the signal to noise ration (SNR) for each individual tone is reduced when the number of SS/CS k is increased and the number of bits n is kept constant.

In some case in order to keep the reconstructed SS/CS fully symmetrical (to zero the direct current (DC) offset) *the number of the signal levels is reduced by one* (for example 255 levels or steps are used instead of 256 for an 8-bit DAC with middle level at 127th step or 127 (+127, -127) steps and not at 127.5 (+127.5, -127.5) or at 128 (+127,-128) steps. The table below (SIN16_6) is an example with codes for SS generation with SSF N=16, n=6 bit and 64 levels from 64. The middle level is Lmiddle=31.5, the minimal level is Lmin= 0, the maximal level is Lmax=63, the resolution in phase is LSBph=360/16=22.5 deg., the asymmetry (the difference between the positive and the negative amplitude) is 1*LSB and the angle of the first sample is φ0=0deg.

```
SIN16_6   FCB  31, 44, 54, 61, 63, 61, 54, 44
          FCB  31, 19, 09, 02, 00, 02, 09, 19
```

Some amplitude optimization (or exemption of the GR given above) could de done during the DTMF generation. This is possible because the frequencies of the DTMF tones are known and the phase relations between the two tones are controllable and the duration of the tones are also known. Consequently the maximum peak to peak value of the sum of two fully defined SS/CS could be less that the sum of the two peak-to-peak value and this is predictable.

Another consideration is the minimum amplitude value of the sum of two or more SS/CS. It is possible that the sum of two signals to become too small (comparable to the value of one least significant bit (LSB)). It is suggested that the smallest AS amplitude to be at least 10*LSB (or to have at least 3 bits of value) in order to be reconstructed with good THD, IMD and SNR and relative weight of one LSB to be less than 10%. The full scale (FS) range of the converter is not always possible to use in order to avoid the under-voltage and over-voltage which are leading to he irreversible lost of information.

TABLE III
NUMBER OF SIGNALS K AND THEIRS PEAK-TO PEAK AMPLITUDE WHICH COULD BE GENERATED WITH AN 8-BIT DAC.

k, Nb of signals	Parameter per signal			
	n, bits	Lv, Levels per signal	SNR, dB	Nmax, (Fd/Fs)
1	8	256	49.92	64
2 **	7**	128**	43.9**	32**
4	6	64	37.88	16
8	5	32	31.86	8
16	4	16	25.84	4
32	3	8	19.82	2
64	2	4	13.8	2*
128	1	2	7.78	2*

Notes: *- conditional value; ** - for DTMF

Two approaches for DTMF and multiple tone generation are evaluated:

1. Using one sampling frequency Fd=constant for generating all tones (for example with N=Fd/Fs>=4) and different SSF N=Fd/Fs for each tone in the sum.
2. Using one SSF N=Fd/Fs for all frequencies, and different sampling frequency for each SS/CS in the DTMF (sampling frequency Fd=variable).

The second approach was retained because only one sine table is needed for all tones and only one evaluation of the spectrum of the produced SS/CS approximation is needed. The disadvantage is that multiple sampling frequencies Fd should be generated. Usually this is not a difficulty for most of the MCUs where several timers are available or could be added at low cost and a powerful interrupt system exists.

In order to produce a DTMF or any dual-tone AS two main methods are used:

1. Generating two individual AS and summing them.
2. Digitally summing the samples of the two AS and using one DAC to produce the analog function.

The first approach is considered better because each output signal could be controlled individually, but the second approach is simpler and cheaper.

The SNR for each individual SS/CS in the sum could be theoretically calculated according to the Eq. 4

$$SNR=6.02*n+1.76, [dB] \qquad (4)$$

Where n is the number of bits used to represent the peak to peak amplitude of the tone.

III. CHOOSING THE SAMPLING FREQUENCY FD AND NUMBER OF BITS PER TONE N

According to the Nyquist criteria and the sampling theorem of Whittikar-Shannon-Kotelnikov the sampling frequency Fd should be at least two times higher than the synthesized tone Fs (or Fd>=2*Fs). We will abandon this criteria and the theorem because they have the followings weak points and are unpractical:

1. They do not cover the cases when the AS could be constructed with SSF N=Fd/Fs<2.
2. They do not give the possibility to calculate the minimum number of bits n into the digital word used to represent the analog signal.
3. They do not evaluate the errors and the quality of the produced signal (amplitude errors, DC error, THD, IMD, SNR, etc.)

Since the needs of the nowadays DTMS standards are largely satisfied with SSF N>8 and n>= 6 bit we will use the approach defined in [5, 6] and based on the Eq 5 and Eq. 6 for the maximal amplitude error Emax, SSF N=Fd/Fs and the recommended minimum of the converters bits n(dac):

$$Emax = 1-\sin(90-180/N)), [-] \quad (5)$$

For N= 2 to 48 the approximate Eq. 6 is applicable.

$$n(dac)>=lg(N)+D, bits \quad (6)$$

For any value of N>=2 Eq. 7 is applicable

$$n(dac)>=lg(1/Emax)+D, bits \quad (7)$$

where lg is in base 2, and D is a constant from 0 to 4, depending on the application. If we are using the formula above we could calculate the maximum recommended SSF Nmax when the number of bits n are known and vice versa. Using higher SSF than the calculated Nmax for the selected number of bits n is possible but not always useful due to the rounding errors. Table IV is giving sampling frequencies for DTMF generation with N=8 and 16. Musical notes also could be generated (Table V).

TABLE IV
SAMPLING FREQUENCIES FOR DTMF FREQUENCIES WITH N=FD/FS=8 AND N=FD/FS=16

Tone, Hz	Fd (N=8), Hz	Fd(N=16) , Hz
697	5576	11152
770	6160	12320
752	6816	13632
941	7528	15056
1209	9672	19344
1336	10688	21376
1477	11816	23632
1633	13064	26128
n, bits	>=5	>=6

TABLE V
SAMPLING FREQUENCIES FOR THE MUSICAL NOTES FROM OCTAVE 4 WITH N=FD/FS=8 AND N=FD/FS=16

Note	Tone, Hz	Fd (N=8), Hz	Fd(N=16) , Hz
C	261.63	2093.04	4182.08
C#	277.18	22.17.44	4434.88
D	293.66	2349.28	4698.56
D#	311.13	2489.04	4978.0
E	329.63	2637.04	5274.08
F	349.23	2793.84	5587.68
F#	369.99	2959.92	5919.84
G	392.00	3136	6272
G#	415.30	3322.4	6644.8
A	440.00	3520	7040
A#	466.16	3729.28	7458.56
B	493.88	3951.04	7902.08
n, bits		>=5	>=6

IV. MAIN PROBLEMS TO BE SOLVED

The following questions should be solved in order to generate successfully AS with digital processor system:

1. Choosing the method for signal reconstruction. Usually the choice is between the pulse width modulation (PWM) and direct signal synthesis with DAC.
2. The followings methods for samples calculation are possible 1/ to calculate the samples of the complex AS and using one DAC or 2/ simultaneously to generate with two DACs two separate AS and summing them in an analog system or 3/ to generate two separate samples from two different AS and summing them digitally in one DAC.
3. Choosing the size of the tables. If the same SSF (e.g. N=16) for generating all DTMF signals is used, only one sine table is needed with N entries
4. Choosing the length of the digital word n which if necessarily but usually multiple of 8 bits. It depends on the SSF, the errors and the signal to noise ratio (SNR).
5. Choosing the method of the amplitude correction, in any. For example in some systems it is necessarily to amplify additionally the higher frequency signal. This could be done either by multiplying the amplitude of the higher frequency samples or by reducing the amplitude of the low frequency samples or both of them in the same time. The multiplication and the division could be done with shifting, adding and subtracting. The correction of the amplitude depends on the parameters of the communication channel and the SSF N. If the same SSF is used for all generated SS/CS the same maximal amplitude error Emax is maintained and the amplitude correction could be avoided. In all cases the signals should be kept in the allowed range.
6. Choosing the type of the analog filters after the DAC. In most of the cases it is obligatory to use first or maximum a second order passive low pas filter in order to keep the production cost low. In order to keep the filter as simple as possible it is necessarily to use the maximum SSF N

(preferably N>8 for a SS) and the maximum number of bits according to the Eq. 5 or Eq. 6 and preferably n>=5 bits. In most of the cases N>=16 and n>=6 bits are giving excellent results for DTMF.

7. Switching On/Switching Off problem during AS generation should be resolved. In order to minimize the THD the synthesis of each tone should be started from amplitude zero and with minimal slew rare (SR) and should be ended in zero (when is possible) and whole number of periods of each signal should be generated. Normally the switching ON process is generating more harmonics than the switching OFF.
8. An alternative approach with digital signal processor (DSP) was evaluated and was considered as inappropriate either because the addition of a DSP is not possible in many cases or DSP cannot be used at the moment to solve the tasks implemented in a MCU.

V. CONCLUSIONS

The methods described in [5, 6] were applied for a MCU-based system for single or multiple tone (sine wave) generation and results where obtained. Solutions for MCUs Motorola 68HC11F1 and Microchip PIC16F876 were developed but the paper is applicable of any system based on a digital processor.

It is considered that *any real signal extend in an finite frequency range due to its finite slew rate (SR), finite peak to peak amplitude (App) and finite power (Ps). Real signals are generated and transmitted in the components with finite frequency characteristics.* It is wrong to imagine signals with infinite SR and "ideal angles" as the "ideal square wave signal" and to apply to them the Furrier transform which is a good solution only for signals with finite SR. If this application is done an impossible to correct error will be generated due to the different nature of the "ideal" signal and the Fourier transform.

In most of the cases increasing the SSF N and the corresponding increasing of the number of bits n in the digital word is the perfect solution in order to enhance the quality of the signal generation and processing. For example choosing a higher value for the SSF N will lead to simpler filter after the reconstructing DAC and to less THD and IMD.

The AS (even a simple one as a SS/CS) is containing an infinite quality of information which could be only partially represent in a digital form. In order to represent the AS as accurate as possible in the digital form the highest possible values for N and n should be chosen.

The THD of the reconstructed SS/CS and the IMD of the sum of two or more SS/CS are directly related to the chosen SSF N and number of the bits n. Two approached were tested:

1/ fixing N and changing n; 2/ fixing n and changing N.

Is was found that there is a practical optimal set of values for N and n. Consequently for a fixed value of N in most of the cases there is no practical use to enlarge n more than the values given with Eq. 5 or Eq. 6. The reverse is also true.

In general when the AS is sampled two parameters are changed: 1/ the time is changed from analog to discrete
2/ the amplitude is changed from analog to discreet.
In order to analyze the situation the approach "One change at a time" was used. The amplitude should be changed to discrete and time is kept analogous and vise versa.

One more problem with the accuracy of SS/CS signal reconstruction is that the signals parameters are changing with changes of the signal amplitude. For example the amplitude value of SS at +90 degree is coded with maximal accuracy and the value of +270 degree with minimal relative accuracy, which is a source of additional signal distortion and could be investigated.

REFERENCES

[1] Motorola, MC68HC11F1 Programming Reference Manual, Rev. 2, 1993, USA.

[2]. Microchip Technology Inc., PIC16F87X 28/40pin, 8-bit CMOS FLASH Microcontrollers Data Sheet, DS30292B, 1999, USA

[3]. Motorola, MC145740 Dual Tone Multiple frequency Line Interface, Data Sheet, 2000, USA

[4] Motorola, MC145446A Single-Chip 300-Baud Modem with DTMF Transceiver, Data Sheet, 1996, USA

[5]. Petrov P. Tzv., Sampling factor and amplitude errors during the sinusoidal and cosinusoidal signal conversion, ICEST-2004, June 16-19, Bitola, Macedonia.

[6]. Petrov P. Tzv., Method and examples of calculating the sampling frequency when the maximum rate of change and amplitude of the signal are known. ICEST-2004, June 16-19, Bitola, Macedonia.

HFC Networks – Status and Perspectives

Oleg Borisov Panagiev[1]

Abstract - **In the Hybrid fiber/coaxial (HFC) network, a number of 500-2000 subscribers in CATV network may cause serious collisions during the request phase. This paper discus status and perspectives HFC networks – structures, spectrum, communication medium and applications. HFC used M-ary quadrature amplitude modulation for the transmission of a compressed digital video signal (MPEG) along with the common amplitude modulation with a partial suppression of the vestigial sideband (AM-VSB).**

Keywords - **Cable television (CATV), HFC, fiber node, MPEG-2**

I. INTRODUCTION

Cable television (CATV) networks are engineered primarily to deliver a specific service using specific technologies. The technical analysis of cable therefore focuses on the basic capabilities of the cable medium.

The first systems have been built from two essential components: coaxial cable and broadband amplifiers. The television signals that are delivered over a traditional cable network are not fundamentally different from the signals delivered over the air, but a cable system can often deliver better quality signals and more channels, and there are technological reasons why this is so.

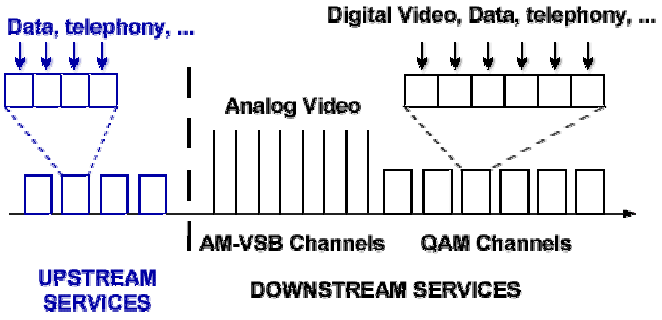

Fig.1. Spectrum HFC

Each TV channel is modulated in a 8 MHz channel between the frequencies of 47 MHz and 860 MHz (the range used varies among cable service providers). A television 'tunes' to the desired frequency and demodulates the original TV signal from the carrier wave. This is identical to lower frequency broadcasts like FM radio (frequency spectrum - 87 MHz to 108 MHz - is sandwiched in the range used for TV broadcasts) - Fig.1.

[1]O. B. Panagiev is a system engineer at the Technical University of Sofia, e-mail: olcomol@yahoo.com

When designing the system for cable television with the aim of minimal nonlinear distortions, it is necessary to optimize the number of the transmitted programs (channels) and the number of the amplifiers connected in series from the Head End to any point of CPN. It is know that, with the increase of the number of programs, the level in the exit of every amplifier has to decrease.

Cable systems are not limited to the bandwidth that is designated by the CENELEC for broadcast television; a cable can carry as many channels as the infrastructure will permit, which in modern systems can be a hundred channels or more.

The transmission, or encoding, of analog television signals is done in the same manner as it is for broadcast television, receiving these signals is straightforward.

There are TV that is not built specifically to receive cable will require an external receiver because a wider range of frequencies is used on cable systems, and sometimes because a television receiver cannot properly discriminate between adjacent channels. This external receiver (a *set-top box*) re-transmits a selected channel to one that the television can receive. Modern televisions, however, can often tune cable channels directly.

II. THE CABLE TOPOLOGY

The coaxial cable and broadband amplifier technologies define the essential capabilities of cable networks. But we also need to understand how real cable systems are actually built out of these and other components such as optical fiber, since this introduces both technological and economic constraints on using cable to support other communication applications.

We begin by identifying four basic components of a cable network: the *head end*, the *trunk network*, the *distribution network*, and *drops*. Cable networks are topologically organized as a tree, with the head end at the base of the tree, and the trunk, distribution, and drop parts of the network forming successively smaller branches (Fig.2).

The features for the CATV – coaxial network:

- the network consists mainly of passive components;
- the amplifiers are capable of relaying signals in both directions;
- the network topology is tree-shaped, branching out from the head-end, reflecting the usage of the network (i.e., analog broadcast services);
- the set-top box simply acts as a tuner or channel selector for the TV, but may include some analog access control mechanism for pay-TV channels;
- the network is effectively a shared media system which is contention-free at present (only one transmitter, the head end), but will not be contention-free in the future (with interactive digital services and data services) unless a media access control protocol is used.

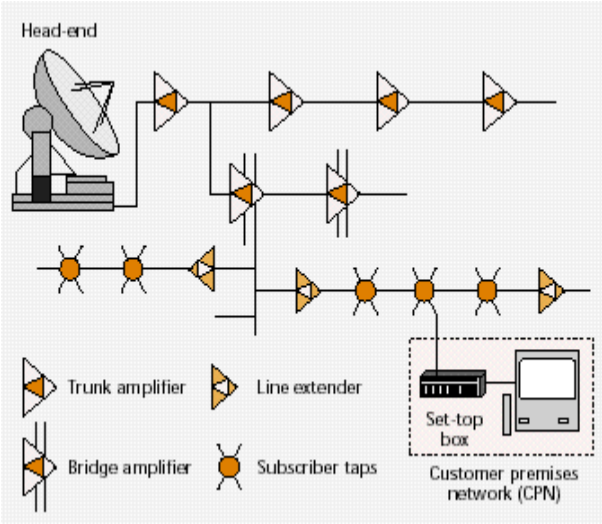

Fig.2. CATV – coaxial network

III. HYBRID FIBER/COAXIAL SYSTEMS (HFC)

The modern cable systems use both coaxial and fiber optic cables for transmission - *hybrid fiber/coaxial* (HFC) systems.

Optical fiber has several advantages over coaxial cable. Foremost are that fiber has the potential of carrying far more bandwidth, is much more immune to noise, and attenuates signals much less. Furthermore, fiber cable itself is not significantly more expensive than coaxial cable.

The connections and end points of broadband fiber optic networks are far more expensive than they are with coaxial. Optical sources and receivers that send and receive electrical signals on a fiber network cost hundreds or thousands of euros. Making connections on a fiber network requires relatively expensive splicing operations. The result is that while fiber can be more cost-effective for long-haul point-to-point communication, coaxial is less expensive where there are many branches and connections in a network.

Hybrid fiber/coaxial systems (Fig.3) use fiber in just this way. The trunk parts of the network, where there are long distances of cable with few branches, are replaced with fiber, and the distribution network within a neighborhood remains as an ordinary coaxial system.

Fiber trunks have the advantage of eliminating long chains of broadband amplifiers that add noise and the potential for failures on the cable system; over these lengths, fiber requires no amplification. The only amplifiers that remain between the head end and subscribers are those in the distribution network, so that the entire path to a subscriber may have at most four to ten amplifiers. But a hybrid fiber/coaxial system is not typically a digital transmission system; the fiber portions are generally carrying analog signals that are simply re-transmitted onto the coaxial at fiber nodes. Since the fiber itself is inexpensive relative to its supporting infrastructure (sheaths, splices, and transmitters and receivers), adding more strands of fiber does not dramatically drive up the cost of a trunk system. As a result, hybrid fiber/coaxial systems are typically built with individual fibers connecting each coaxial distribution network to the head end.

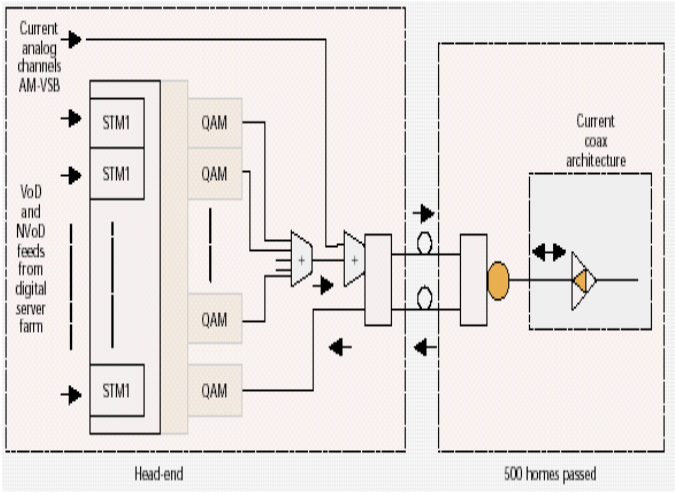

Fig.3. Hybrid fiber/coaxial network.

Because hybrid fiber/coaxial networks are be less expensive to build, can carry more bandwidth, and are more reliable than traditional all-coaxial networks, they are the preferred architecture for building new or upgrading existing cable television networks regardless of future strategies.

For digital transmission there are currently many modulation and coding schemes in use. One of the reasons for the differences in CATV networks around the world is the lack of standardization in the CATV community, especially compared with the telecom sector. Such bodies as are currently addressing the issue of standardization:

- CENELEC (Comité Européen de Normalisation Electrotechnique) and European Telecommunications Standards Institute (ETSI);
- IEEE 802.14 Working Group (WG) and ATM Forum Residential Broadband WG (North America based, but with worldwide participation);
- Digital Video Broadcasting (DVB) and Digital Audio Video Council (DAVIC).

The digital SDH carrier (Fig.3) is being used solely for telephony while the current coaxial/analog architecture is being used for digital data! In many cases this is due to the lack of an integrated carrier such as asynchronous transfer mode (ATM). Since ATM equipment is now widely available, the maturing HFCs can take digital feeds from the head-end directly to the SDH carrier with conversion at the street box. The *server farm* of digital video servers would require careful management to perform such functions as load balancing and fail safety, to provide the best utilization of the resources available and a reliable service. The quadrature amplitude modulation (QAM) functions would probably be realized as a bank of modems that would also require (at the very least) monitoring to preempt any faults or detect the presence of particularly errorprone channels. If ingress (or other noise) is a problem, the management actions here might involve signaling/interaction with other components such as amplitude modulation vestigial sideband (AM-VSB) transceivers in order to select less noisy channels. This means that the AM-VSB transceivers must be capable of being managed dynamically and in real time. This dynamic channel selection

may also apply to the cable modem at the customer premises network (CPN), so there is a need for this device to be manageable also.

In the future, the fiber node and street box may support fiber to the curb (FTTC) or fiber to the home (FTTH), so the importance of this device in terms of management will increase. Also, the equipment at these points may become more complex (especially the street box) if ATM is used to deliver to the set-top box or cable modem. In these cases, more sophisticated management facilities will be necessary.

IV. Two-Way Transmission

Our description of CATV systems so far depicts a network that distributes signals only from the head end to subscribers, and cannot transmit signals back to the head end.

For the most part this is accurate, as the engineering of these systems reflects the fact that they are used to carry television service to subscribers and not the other way. But it is possible to carry two-way signals on a cable system, and in fact many cable systems are either built with some two-way capability or designed so that this can be added to the system later on. The coaxial cable medium is not itself directional, and sending signals on it in one direction does not preclude also sending signals in the other direction. This is true generally for any wire line medium; telephone networks in fact carry voice signals in two directions simultaneously over the same circuit, and it is possible to separate these two signals at the ends of the line.

In practice the noise on upstream channels comes mostly from external sources of noise (such as noise generated from radio transmitters, electric motors, computers) that leak into the system through imperfections in the network and home wiring. Such noise is called *ingress*, and it is difficult to characterize exactly because it depends on the nature of particular sources. Different parts of the cable spectrum can have very different upstream noise characteristics simply because the sources of noise change at different frequencies. A hybrid fiber/coaxial architecture can provide some relief to the noise funneling problem. Because neighborhood distribution networks are connected individually to the head end by fiber trunks, the sources of combined upstream noise can be limited to one neighborhood, and can be reduced as neighborhood nodes are made to serve a smaller number of subscribers. If we expect that the total upstream noise rise in proportion to the number of subscribers, then splitting a 5000-subscriber into ten 500-subscriber nodes might improve the upstream signal-to-noise ratio by 10 dB.

V. HFC Application

The applications that we can easily list for cable are for the most part existing applications that would be carried on a new medium. This is conceptually similar to recent efforts use the Internet to carry voice communication (so called Internet telephony) and fax communication. It is also just what cable television systems did in their original role as distributors of broadcast television. But some important communication applications we use today grew out of existing services: fax transmissions now account for a significant amount of telephone traffic, and the tremendously popular World- Wide Web application is only a recent use of much older Internet technology. Voice and fax communication, for example, are two applications that are supported by standard telephone service. Internet service (specifically the IP transport that is provided by the network) supports the applications of electronic mail, remote login. In the case of telephone service, the network technology was engineered around one application but other applications were able to adapt to what the service provided.

Several entertainment applications for cable fall into the category of *playback* applications that involve delivering a data stream, usually for video or audio, over time to a device that plays it to users. Implementations often use data compression schemes, such as the MPEG standards for audio and video that can dramatically reduce the data rate required for transmission.

The Table I below summarize the technical demands that these communication applications would place on CATV systems.

TABLE I

Application:	Network Traffic:	Other Issues:
Broadcast Video	2×10^6 b/s downstream (compressed) variable but limited rates.	Providers need security mechanisms for pay-per-view applications.
Video-on-Demand	3×10^6 b/s downstream (compressed), variable but limited rate. Small (10^3 b/s) upstream rate.	Providers need security mechanisms for pay-per-view applications.
Advanced Television	10^7 b/s downstream (compressed).	Similar to television applications.
Digital Audio	10^6 b/s downstream.	Playback demands similar to video delivery.
Telephony	6×10^5 b/s two-way (uncompressed) fixed rate.	Packetization delay may be a problem. Users demand privacy. Standards demand very high reliability.
Video Conferencing	10^5 b/s two-way (compressed), highly variable data rates.	Latency is a problem for interactivity. Privacy is important to users.
Computer Networks	10^5 to 10^8 b/s or more, two-way traffic. May be very bursty.	Traffic characteristics and future needs depend on what applications will be used.
Electronic Games	Depends on application.	Interactive multi-player games demand low-latency two-way communication.
Telemetry	10^3 b/s, very bursty.	Security is important to prevent fraudulent use. Reliability may be essential for some applications.

VI. Conclusion

Although cable networks have been engineered primarily to deliver a broadcast television service, modern hybrid fiber/coaxial networks have the potential to provide a powerful communication medium that could support a variety of applications. Because cable networks are built to transmit high-bandwidth signals, they can support aggregate data rates on the order of several gigabits per second. The transmission characteristics on cable are not symmetric—communication upstream is inherently more difficult than downstream—but the largest bias against upstream traffic is simply the small bandwidth allocation that is typically given to upstream communication when cable networks are built. Cable networks share a coaxial transmission medium among multiple users, and while this on one hand gives cable the

flexibility to dynamically use resources as needed, it on the other hand requires technical means of allocating resources. Furthermore, the shared medium can create privacy, security, and reliability problems that cable communication systems may need to address. The sorts of applications we envision being supported by cable systems have diverse communication needs, some taking advantage of the high data rates that cable can support, some demanding high reliability from the network, and so on. One vision of how these applications might be supported on cable networks would devote specific services to specific applications, but it is equally conceivable that many of these applications might be integrated into a single service. The Internet, or something like it, may in the future become a common platform for supporting many applications. This may blur our distinction between services and applications, but regardless of this the technical demands of applications must ultimately be satisfied by the underlying network technology.

REFERENCES

[1] O.B. Panagiev, “Some Capabilities of the Optical Technologies in the Cable Television Systems”.,IX NSASC "Electronics'2000, Sozopol 20-22 sept. 2000

[2] IEEE Commun. Mag., vol. 35, no. 6, June 1997.

[3] M. Laubach, “Using ATM over Hybrid Fiber-Coax Networks,” presented at SPIE Eastern Conf., Philadelphia, PA, Oct. 23, 1995.

[4] IEEE Commun. Mag., vol. 36, no. 3, Mar. 1998.

[5] C. Eldering, H. Nageen, and G.Floyd “CATV Return Path Characterization for Reliable Communications.” *IEEE Communications* 33, no. 8 (August 1995): 62-69.

[6] D. Estrin, “Data Communications via Cable Television Networks: Technology and Policy Considerations.” Master’s thesis, Massachusetts Institute of Technology, 1982.

[7] D. Feldmeier “A CATV-Based High-Speed Packet-Switching Network Design.” Master’s thesis, Massachusetts Institute of Technology, 1986.

[8] P. Fockens, “The 43 Mbit/s Digital 16-VSB Modem for Cable TV.” *Communications Technology*, May 1994.

[9] H. Fowler, and W. Leland “Local Area Network Traffic Characteristics, with Implications for Broadband Network Congestion Management.” *IEEE Journal on Selected Areas in Communications* 9, no. 7 (September 1991).

[10] D. Lindstrom, “Sniffing A Cable Modem Network: Possible or Myth?”, SANS Institute, 2002

[11] http://www.cablemodem.com

[12] http://rpcp.mit.edu

Review of SCP-RPSC Technology

Veselin B. Demirev[1]

Abstract – **The theory of SCP technology in transmit mode (SCP-RPSC) is considered in the report. The specific properties of the system are widely discussed. Equations for evaluating the system performances are derived too.**

Keywords **– SCP technology, SCP RPSC, S-DVB, Spatial cross correlation function**

I. INTRODUCTION

A new principle to realize the receiving satellite ground systems antennas was proposed in [1, 2, 3]. The name of the new radio technology is Spatial Correlation Processing (SCP). The idea to use the same principle in transmit mode [4] was born during the SCP project research. The transmitting antennas, as well as the receiving random phase antenna arrays in SCP technology are pure passive, without any active or nonreciprocal elements. The specific SCP processing is situated in the receiver. According to the basic electromagnetic antenna lows the replacement of the passive transmitting antenna with passive random phase antenna array in the transmitter, and vice versa in the receiver should not change the system working principles and system parameters.

The transmitted by the random phase antenna array signals have specific phase spread. It can be considered as random spatial coding. That is why the term SCP-RPSC (Random Phase Spread Coding) will be used instead SCP, transmit in the text below. The signals and the propagation matrix components in the SCP-RPSC case will be denoted with "t".

II. THE MAIN SCP-RPSC FEATURES

The main features of the SCP technology in receive mode are listed in [1].

The proposed SCP-RPSC system will have the following additional features:

- Providing full duplex interactive system with one simple and cheap transmit-receive antenna.
- The transmitted random poly-phase spread signals will not cause significant harmful interference to the conventional satellites, using the same frequency channels. The interference will be similar to that, caused by the sidelobes of a phased antenna array with random inter elements spacing.
- The transmitted random poly-phase spread signals are uniformly radiated in the space above the antenna. Several satellites, equipped with the same SCP receivers and providing space diversity, receive them. The knowledge of the receiving satellites positions for the transmitting equipment is not necessary (as it is for a conventional satellite earth station).
- The transmitted random poly-phase spread signals have low detection probability for the conventional microwave receivers (due to the low spectral power flux density, similar to CDMA case), leading to low active jamming probability.
- The SCP-RPSC approach could be a breakthrough technology, leading to unpredictable increase of the frequency reuse factor in satellite and terrestrial wideband networks. Close situated subscriber terminals could communicate with terrestrial or satellite base stations, using the same frequency channel without interference. The isolation between the terminals will be provided by their specific random phase spread coding, due to their specific random design.
- The practical SCP principles implementations in transmit and receive mode will drastically change the existing paradigm in the satellite communication business in general. Many of the existing problems of the proposed LEO, MEO and GSO satellite systems, dealing with frequency and orbital resource sharing, beam pointing, beam shadowing, etc., will be solved successfully.

III. BACKGROUND OF THE SCP-RPSC TECHNOLOGY

A block scheme of a SCP-RPSC satellite system is shown in Fig.1, where:

- (1) is a transmitter of SCP signals (modulated information signals and CDMA-spread pilot signals).
- (2) is a Random Phase Antenna Array (RPAA) or Radial Line Slot Antenna (RLSA) in some particular cases .
- (3) is a conventional microwave receiving antenna.
- (4) is a conventional one channel receiver with IF output.
- (5) is a SCP Pilot recovery unit.
- (6) is a SCP Signal recovery unit (correlator).
- (7) is a baseband signal processing equipment.

Following the block-scheme, shown in Fig. 1, the RPAA transports the transmitted signals $c_{c,t}; c_{p,t}$ from the antenna input (connected to the SCP transmitter) to the RPAA elements. Let the transfer functions between the input and the

[1] Veselin B. Demirev is with the Faculty of Communications and Communication technologies, TU – Sofia, "Kl. Ohridsky" blvd. N8, 1756 – Sofia, Bulgaria, E-mail: demirev@homelan.bg

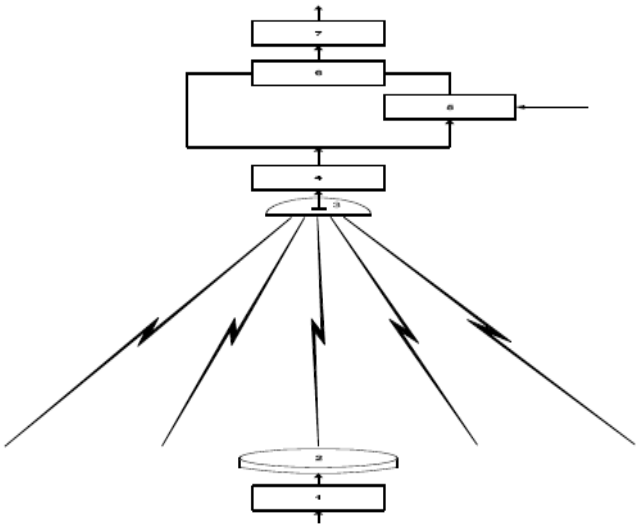

Fig. 1. Block scheme of a SCP-RPSC satellite system

outputs (the RPAA elements) be represented by the column vector a_t:

$$\mathbf{a}_t = \begin{vmatrix} a_{t1} \\ a_{t2} \\ a_{t3} \\ \cdots\cdots \\ a_{tn} \\ \cdots\cdots \\ a_{tN} \end{vmatrix} \tag{1}$$

Where $a_{t,n=L_{t,an}}.e^{j\gamma n}$, $L_{t,an}$ is the gain of a single RPAA element in transmit mode (propagation losses are included), $\gamma_n = 2r_n / \lambda_g + \Delta\gamma_n$, where the first term is the phase shift due to RPAA and the second – the phase shift due only to the inner elements and to the element inclination in the case of circular polarization of the receiving antenna (3).

Due to the finite transfer function that exists between the input and output ports of a RPAA, the signals appearing at its elements will be those at the input modified by the transfer function a_t. The signal vectors $c_{c,t}; c_{p,t}$, combining all transmitted signals appearing at the outputs of the RPAA elements, are:

$$\mathbf{c_{c,t}} = \left| a_{t1}c_{c,t} \quad a_{t2}c_{c,t} \quad a_{t3}c_{c,t} \ldots \right.$$
$$\left. \ldots a_{t,n}c_{c,t} \ldots. \quad a_{t,N}c_{c,t} \right| = \mathrm{a}_t\, c_{c,t} \tag{2}$$

$$\mathbf{c_{p,t}} = \left| a_{t1}c_{p,t} \quad a_{t2}c_{p,t} \quad a_{t3}c_{p,t} \ldots. \right.$$
$$\left. a_{t,n}c_{p,t} \ldots. \quad a_{t,N}c_{p,t} \right| = \mathrm{a}_t\, c_{p,t} \tag{3}$$

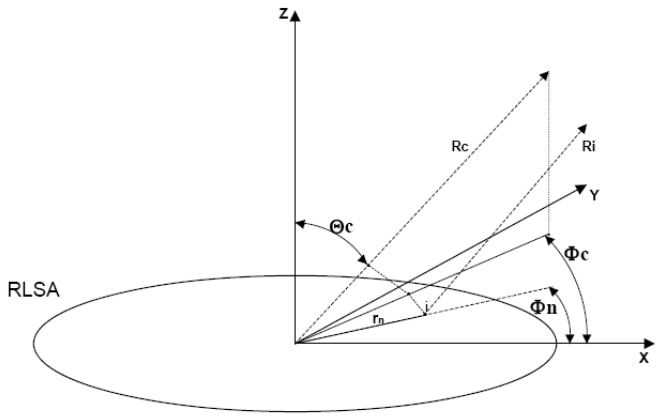

Fig. 2. The coordinate system, centred at a terminal

The receiving satellite (base station) is located at angular coordinates ϕ_c, θ_c and distance R_c to the cooperative signal source (subscriber terminal) (Fig.2). Each element of the transmitting RPAA can be considered as separate signal source, received by a conventional antenna (3). Thus the antenna (3) output will carry signals from all antenna elements. Let $s_{t,n}$ be the transfer function between n^{-th} RPAA element and antenna (3). Then:

$$s_{t,n} = L_{t,n} e^{-j\psi_n} \tag{4}$$

Where $L_{t,n}$ are the free space propagation losses, $\psi_n = kr_n \sin\theta_c \cos(\phi_c - \phi_n)$ is the phase of the signal, received by antenna (3) and transmitted by n^{-th} RPAA element relative to its centre [5], circular antenna aperture is considered, $k = 2\pi / \lambda$ - free space phase constant, r_n, ϕ_n - the coordinates of the n^{-th} element. In this case:

$$\mathbf{s}_t = \begin{vmatrix} s_{t1} \\ s_{t2} \\ \cdots\cdots \\ s_{t,n} \\ \cdots\cdots \\ s_{t,N} \end{vmatrix} \tag{5}$$

Where s_t is called a column matrix or vector, representing the space transfer function between the terminal RPAA and the antenna (3).

In analogy the transfer functions for information and pilot signals are:

$$\mathbf{s}_{\mathbf{c},t} = \begin{vmatrix} s_{c,t1} \\ s_{c,t2} \\ \cdots\cdots \\ s_{c,t,n} \\ \cdots\cdots \\ s_{c,t,N} \end{vmatrix} \qquad \mathbf{s}_{\mathbf{p},t} = \begin{vmatrix} s_{p,t1} \\ s_{p,t2} \\ \cdots\cdots \\ s_{p,t,n} \\ \cdots\cdots \\ s_{p,t,N} \end{vmatrix} \tag{6}$$

The signal transmitted by the n^{-th} RPAA element, at the input of the receiving antenna (3) is:

$$x_{t,n} = s_{t,n} a_{t,n} c_t \tag{7}$$

And that for the cooperative and for the pilot signals are:

$$\begin{aligned} &x_{c,t,n} = s_{c,t,n} a_{t,n} c_{c,t}; x_{p,t,n} = \\ &= s_{p,t,n} a_{t,n} c_{p,t} \end{aligned} \tag{8}$$

Therefore the signal vector, combining the signals from all RPAA elements, at the input of the receiving antenna (3) is:

$$\begin{aligned} &\mathrm{x}_t = \left| \; x_{t1} \quad x_{t2} \ldots . x_{t,n} \ldots . x_{t,N} \; \right| = \\ &= \left| \; s_{t1} a_{t1} c_t \quad s_{t2} a_{t2} c_t \ldots . s_{t,n} a_{t,n} \right. \\ &\left. c_t \ldots . s_{t,N} a_{t,N} c_t \; \right| \end{aligned} \tag{9}$$

In analogy the signal vectors, combining the cooperative and pilot signals from all RPAA elements at the antenna (3) input are:

$$\mathbf{x}_{\mathbf{c},t} = \mathbf{s}_t \mathbf{a}_t c_c; \mathbf{x}_{\mathbf{p},t} = \mathbf{s}_{\mathbf{p}} \mathbf{a}_t c_p \tag{10}$$

The signal vector, representing the output of antenna (3) is:

$$\mathbf{i}_{\mathbf{t}} = G_A \mathbf{x}_{\mathbf{t}} \tag{11}$$

Where G_A is the gain of the antenna (3). In analogy the vectors of cooperative and pilot signals are:

$$\mathbf{i}_{\mathbf{c,t}} = G_A \mathbf{x}_{\mathbf{c,t}}; \mathbf{p}_{\mathbf{t}} = G_A \mathbf{x}_{\mathbf{p,t}} \tag{12}$$

The received by the receiving antenna (3) signals are amplified in Low Noise Amplifier (LNA), downconverted, amplified and correlated in the Correlator unit. Consider for simplicity the process without math description of CDMA pilot spreading and dispreading, which in principle will not change the investigated interference environment and thermal noise properties.

The total receiver gain G, product of the above-mentioned actions, will be:

$$G = G_{LNA} G_{DC1} G_{IFA1} G_{DC2} G_{IFA2} \tag{13}$$

Where G_{LNA} is the gain of the LNA, G_{DC1} is the gain of the first down converter, G_{IFA1} is the gain of the first Intermediate Frequency Amplifier (IFA), G_{DC2} is the gain of the second down converter and G_{IFA2} is the gain of the second IFA.

The signal vector, representing the receiving signal at the correlator input, will be:

$$\mathbf{i}_{\mathbf{t,IF}} = G \mathbf{i}_{\mathbf{t}} \tag{14}$$

In analogy the signal vectors, representing the cooperative and pilot signals at correlator input, will be:

$$\mathbf{i}_{\mathbf{c,t,IF}} = G \mathbf{i}_{\mathbf{c,t}}; \mathbf{p}_{\mathbf{t,IF}} = G \mathbf{p}_{\mathbf{t}} \tag{15}$$

The multiplier output signal, product of the multiplication process, will be:

$$\begin{aligned} &(\mathbf{i}_{c,t,IF} \mathbf{p}_{t,IF}) = G(\mathrm{i}_{c,t} \mathrm{p}_t) = \\ &= G \begin{vmatrix} i_{c,t1} p_{t1} & i_{c,t2} p_{t1} \ldots . & i_{c,t,n} p_{t1} \ldots . & i_{c,t,N} p_{t1} \\ i_{c,t1} p_{t2} & i_{c,t2} p_{t2} \ldots . & i_{c,t,n} p_{t2} \ldots . & i_{c,t,N} p_{t2} \\ \ldots\ldots & \ldots\ldots & \ldots\ldots & \ldots\ldots \\ i_{c,t1} p_{t,n} & i_{c,t2} p_{t,n} \ldots . & i_{c,t,n} p_{t,n} \ldots . & i_{c,t,N} p_{t,n} \\ \ldots\ldots & \ldots\ldots & \ldots\ldots & \ldots\ldots \\ i_{c,t,1} p_{t,N} & i_{c,t,2} p_{t,N} \ldots . & i_{c,t,n} p_{t,n} \ldots . & i_{c,t,N} p_{t,N} \end{vmatrix} \end{aligned} \tag{16}$$

Where the $j-k$ off-diagonal term consists of:

$$\begin{aligned} &(i_{c,t,j} p_{t,k}) =_{-}^{+} i_{c,t} e^{j\left[\omega_{II} t - k r_j \sin\theta_c \cos(\phi_c - \phi_j) + k_g r_j\right]} \\ &e^{j\left[\omega_{II} t - k r_k \sin\theta_c \cos(\phi_c - \phi_k) + k_g r_k\right]} \end{aligned} \tag{17}$$

In Eq. (17) $i_{c,t}$ is the amplitude of the information signal per RPAA element (BPSK modulation and uniform amplitudes of the antenna elements are considered), the same for the pilot is chosen to be 1(the pilot signal is considered as noise free because of the used high CDMA Processing Gain).

By means of

$$\cos A \cos B = 0{,}5\cos(A-B) + 0{,}5\cos(A+B),$$

Eq. (17) can be represented in real form as:

$$\begin{aligned}&\mathrm{Re}(i_{c,t,j}\,p_{t,k}) =^{+}_{-} 0{,}5 i_{c,t}\\&\cos\left[-kr_j \sin\theta_c \cos(\phi_c-\phi_j)+k_g(\,r_j-r_k\,)+\right.\\&+kr_k \sin\theta_c \cos(\phi_c-\phi_k)\left.\right]\pm\\&\pm 0{,}5 i_{c,t}(2\omega_{II}t+.....)\end{aligned} \tag{18}$$

The second term of Eq. (18) is with double second IF and after Low Pass Filtering (LPF-typical for the correlation process) it cancels. The first part is a sample function of a random phase process, given by the matrix (16).

A basic SCP technology requirement (in order to obtain smooth omnidirectional cooperative pattern) is the sum of the off-diagonal matrix terms to be zero. This requirement is fulfilled when the signals phase probability density function is uniform in the interval 0 – 360 degrees, the channel is real with Additive White Gaussian Noise (AWGN) and the correlation process is digital. For this reason only the cases of pure diagonal matrices are considered in the text below.

The real part of the n^{-th} diagonal term of matrix (16) consists of:

$$\begin{aligned}&\mathrm{Re}(i_{c,t,n}\,p_{t,n}) =\\&=\pm i_{c,t}\cos^2\left[\omega_{II}t-kr_n\sin\theta_c\cos(\phi_c-\phi_n)+k_g r_n\right]\end{aligned} \tag{19}$$

Eq. (19) can be presented as follows:

$$\begin{aligned}&\mathrm{Re}(\,i_{c,t,n}\,p_{t,n}) =\\&=^{+}_{-} 0{,}5 i_{c,t}\,^{+}_{-}\,0{,}5 i_{c,t}\cos(2\omega_{II}t+.....)\end{aligned} \tag{20}$$

The second term of (20) vanishes after LPF. The first term represents the demodulated information signal per RPAA element at baseband. The total baseband output signal will be N times more, equal to the trace of the matrix (16) (the N diagonal elements of (16) are in phase):

$$BBO_{\,c,t} =^{+}_{-} 0{,}5 G i_{\,c,t} N \tag{21}$$

The physical explanation of the process, described above, is that the phase shifts for the pilot and information signals per RPAA element are equal (they use the same frequency and have the same propagation path and environment). During the process of coherent demodulation (correlation) the double frequency term of (20) vanishes after LPF, while the difference part is with zero phase. It means that all diagonal elements of the autocorrelation matrix (16) are with zero phases too (or they are in phase).

The formal mathematical way to describe the above mentioned correlation process and the result (21) in matrix form is:

$$\mathrm{BBO}_{\,c,t} = \mathrm{timeaver}\;\; G(\mathrm{i}_{\,c,t}\,\mathrm{p}_{\,t}) = G\,\mathrm{Tr}(\mathrm{i}_{\,c,t}\,\mathrm{p}_{\,t}^{\,\mathrm{H}}) \tag{22}$$

Where p_t^H is the Hermitian (transpose and conjugate) matrix of p_t.

In order to evaluate the space interference rejection pattern (similar to the antenna pattern in classical antennas) between the cooperative terminal and a interference terminal, located in the same place, it is necessary to correlate the pilot signal, coming from the cooperative terminal, with the information signal from the interference terminal. The last should be shifted at small angles in azimuth and elevation step by step. In analogy with (22), we can determine the interference signals:

$$\mathrm{BBO}_{t,\mathrm{interference}} = \mathrm{timeaver}\,G(i_t\,\mathrm{p}_t) = G\,\mathrm{Tr}(i_t\,\mathrm{p}_t^{\,\mathrm{H}}) \tag{23}$$

The Spatial Cross - Correlation Function, transmit (SCCF,t) can be introduced for the spatial interference analysis, as follows:

$$\begin{aligned}&SCCF_t(\phi,\theta)(dB) =\\&=10\lg\left[\mathrm{BBO}_{t,\mathrm{inter.}}(\varphi,\theta)/\mathrm{BBO}_{c,t}\right]\end{aligned} \tag{24}$$

IV. Conclusion

In this paper the application of SCP technology in transmit mode is proposed. The particular features of the proposed system are defined. The matrix presentations of the signals at different system points are given. The Spatial Cross – Correlation Function in transmit mode is derived too.

References

[1] V. Demirev, "SCP technology – the new challenge in broadband satellite communications", *ICEST,04 Conference Proceedings, pp.159-162*, Bitola, Macedonia, 2004.

[2] V. Demirev, A. Efremov, "SCP-CDMA GSO,s system proposal", *ICEST,04 Conference Proceedings, pp.163-166*, Bitola, Macedonia, 2004.

[3] V. Demirev, "The Probability Theory with Application in SCP Technology", *ICEST,04 Conference Proceedings, pp.167-168*, Bitola, Macedonia, 2004 .

[4] V. Demirev, "Radiocommunication method and system with poly-phase spreading", *Bulgarian Patent Office applicant report*, N 106819/ 13.06.02.

[5] R. Mailloux, *Phased Array Antenna Handbook*, Artech Hause, 1994.

Poster Session PO2:

SIGNAL PROCESSING AND NEURAL NETWORK

Investigation of Back Propagation Algorithm Implementation in Analog Neural Networks

Aleksandar B. Bekiarski[1] and Liliana E. Docheva[2]

Abstract—**Intriguing point of analog neural network implementation is the influence of network parameters over analog neural network behaviour. While such a simulation ignores the parallelism issues inherent in neural networks, it nevertheless provides us to investigate an analog neural network behaviour in relation to network parameters variation. In this paper, an investigation of an analog neural network by means of Matlab simulation is made.**

Keywords— **Neural network, Analogue methods, Analogue models**

I. INTRODUCTION

A popular method for study of neural networks is network simulation using computers. It is appropriate approach from a theoretical and illustrative standpoint, but their applicability to practical implementations of analogue neural network is doubtful. The analysis of the circuits assumed that all the components were ideal. In this paper a simulation using Matlab is presented, but in equations take part the parameters of real components. The variation of some of them reflects to learning and recognition properties of the neural network. In such a way an influence of parameter variation to the learning and recognition properties of the neural network can be examine.

II. ANALOG NEURAL CELL MATHEMATICAL MODEL

In last years many researchers investigated different an analog neural network implementation. In [6] neural network implementation by means of analog amplifiers is presented. Equation 1 depicts activation function of an implemented on this way neuron.

$$\mathrm{h}_\mathrm{k}^1 = \frac{g_{mk}}{W_0 / L_0 U_c} \sum_j W_j / L_j U_{W_{kj}} u_{zj} \qquad (1)$$

Equation \ref{u} depicts neuron output voltage.

$$y_k^l = g(h_k^l) = \frac{1}{\beta_{OR} U_{OR}} \alpha_{FC} I_\beta \tanh\left(\frac{h_k^l}{2\beta_{is} U_{is} U_t} \right) \qquad (2)$$

where W/L are the MOS resistive circuit multiplier width/length ratios, U_C controls the total transconductance g_{mk}, α_{FC} is the emitter-collector current gain, I_B is the bias current, β is MOSFET tranconductance parameter, U_{OR}, U_{IS} are control voltage and U_t is thermal voltage.

A Matlab model, which includes parameters of real components is made on basis of these equations.

Assuming:

$$\frac{\alpha_{FC} I_\beta}{\beta_{OR} U_{OR}} = A \qquad (3)$$

and

$$\frac{g_{mk} W_j / L}{2.W_0 / L_0 \beta_{IS} U_{IS} U_t U_c} = B \qquad (4)$$

the equation 2 simplifies to:

$$y_k^l = A^L \tanh\left(B^L \sum_j U_{wkj} u_{yi}^{\,l-1} \right) \qquad (5)$$

The parameter variation leads to A and B variation.

$$\frac{(\alpha_{FC} + \Delta\alpha_{FC})(I_B + \Delta I_B)}{(\beta_{OR} + \Delta\beta_{OR}) U_{OR}} = A + \Delta A \qquad (6)$$

$$\frac{(g_{mk} + \Delta g_{mk}) W_j / L_j}{2.W_0 / L_0 .(\beta_{is} + \Delta\beta_{is}) U_{is} (U_t + \Delta U_t) U_c} = B + \Delta B \qquad (7)$$

Then from equations 6 and 7 the output neuron voltage cell be written as

$$y_k^L = (A + A^L) \tanh((B + B^L) . \sum U_{W_{kj}} . u_{y_i}^{l-1}) \qquad (8)$$

III. MATLAB SIMULATION RESULTS

In the discussed paper a two-layer neural network with four neurons in the input layer, three neurons in the hidden layer and one neuron in the output layer is presented

Simulation was performed with neural network showed to igure 1. On this way it is showen that most appropriate results are obtained at A=1. Figure 2 shows that at η =0.1 and A=1 the characteristic has least steepness of all.

[1]Aleksanser Bekiarski is with the Faculty of Communications and Communications Technologies, Technical University, Kliment Ohridski 8, 1000 Sofia, Bulgaria, E-mail: aabbv@tu-sofia.bg

[2]Aleksanser Bekiarski is with the Faculty of Communications and Communications Technologies, Technical University, Kliment Ohridski 8, 1000 Sofia, Bulgaria, E-mail: aabbv@tu-sofia.bg

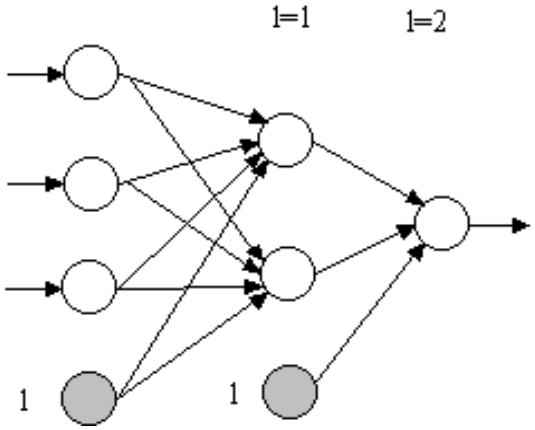

Fig. 1. A two-layer neural network

The learning patterns are:

$$x_1 = \begin{bmatrix} -1 \\ -1 \\ -1 \end{bmatrix} \quad x_2 = \begin{bmatrix} 0 \\ -1 \\ -1 \end{bmatrix} \quad x_3 = \begin{bmatrix} 1 \\ 1 \\ 0 \end{bmatrix}$$

$$x_4 = \begin{bmatrix} -1 \\ -1 \\ 0 \end{bmatrix} \quad x_5 = \begin{bmatrix} 0 \\ 1 \\ 1 \end{bmatrix} \quad x_6 = \begin{bmatrix} 1 \\ 1 \\ -1 \end{bmatrix}$$

$$x_7 = \begin{bmatrix} -1 \\ 0 \\ 0 \end{bmatrix} \quad x_8 = \begin{bmatrix} 0 \\ 0 \\ -1 \end{bmatrix} \quad x_9 = \begin{bmatrix} 1 \\ -1 \\ 0 \end{bmatrix}$$

$$x_{10} = \begin{bmatrix} -1 \\ 0 \\ 1 \end{bmatrix} \quad x_{11} = \begin{bmatrix} 1 \\ 0 \\ 1 \end{bmatrix} \quad x_{12} = \begin{bmatrix} 0 \\ -1 \\ 1 \end{bmatrix}$$

$$x_{13} = \begin{bmatrix} -1 \\ 1 \\ -1 \end{bmatrix}$$

d_1=-1, d_2=0, d_3=1, d_4=-1, d_5=0, d_6=1, d_7=-1, d_8=0, d_9=1, d_{10}=-1, d_{11}=1, d_{12}=0, d_{13}=-1

The recognition patterns are:

$$x_1 = \begin{bmatrix} 1 \\ 0 \\ -1 \end{bmatrix} \quad x_2 = \begin{bmatrix} 0 \\ 0 \\ 1 \end{bmatrix} \quad x_3 = \begin{bmatrix} -1 \\ 1 \\ 1 \end{bmatrix}$$

$$x_4 = \begin{bmatrix} 0 \\ 0 \\ 0 \end{bmatrix} \quad x_5 = \begin{bmatrix} 1 \\ -1 \\ -1 \end{bmatrix} \quad x_6 = \begin{bmatrix} -1 \\ -1 \\ 1 \end{bmatrix}$$

$$x_7 = \begin{bmatrix} 0 \\ -1 \\ 0 \end{bmatrix} \quad x_8 = \begin{bmatrix} 1 \\ 1 \\ 1 \end{bmatrix} \quad x_9 = \begin{bmatrix} 0 \\ 1 \\ 0 \end{bmatrix}$$

$$x_{10} = \begin{bmatrix} 1 \\ 0 \\ 0 \end{bmatrix} \quad x_{11} = \begin{bmatrix} -1 \\ 0 \\ -1 \end{bmatrix} \quad x_{12} = \begin{bmatrix} 1 \\ -1 \\ 1 \end{bmatrix}$$

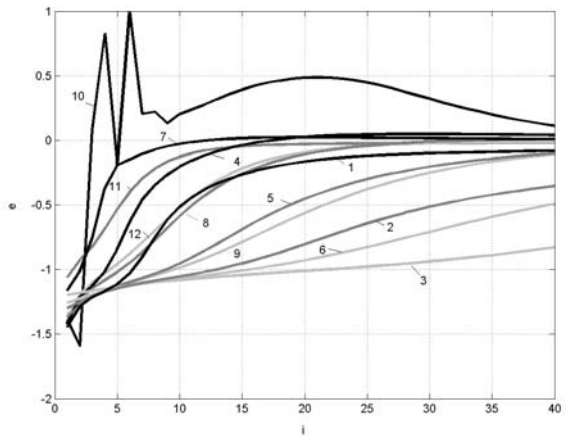

Fig. 2. Variation of A and B reflects to recognition capability of neural network.

TABLE I
NOTATION OF FIGURE 2

A	B	notation
1	0.77	1
1	0.4	2
1	o.26	3
1.25	0.77	4
1.25	0.4	5
1.25	0.26	6
1.66	0.77	7
1.66	0.4	8
1.66	0.26	9
2.5	0.77	10
2.5	0.4	11
2.5	0.26	12

With η increasing the characteristic steepness increasing too. When A increase, learning rate decrease. A_t=2.5 the neural network is capable only for value η=0.1. Figures 3, 4, 5 depict these dependences. The values of the parameters of a neuron are: I_B=50mA, U_{OR}=5V, α_{FC}=0.5, β_{is}=1mA/V^2, U_t=26mV, g_{mk}=1mA/V, U_{IS}=5V, W_j/L_j=1, U_C=5V, W_0/L_0=1, 2 or 3, β_{OR}=2,3,4 or 5mA/V^2. For β_{OR}=2mA/V^2, the value of A is A=2.5, for β_{OR}=3mA/V^2, the value of A is A=1.66, β_{OR}=4mA/V^2, A=1.25 and for β_{OR}=5mA/V^2, the value of A is A=1. Respectivly for W_0/L_0=1, the value of B is B=0.77, for W_0/L_0=2, the value of B is B=0.4, and for W_0/L_0=3, the value of B is B=0.26.

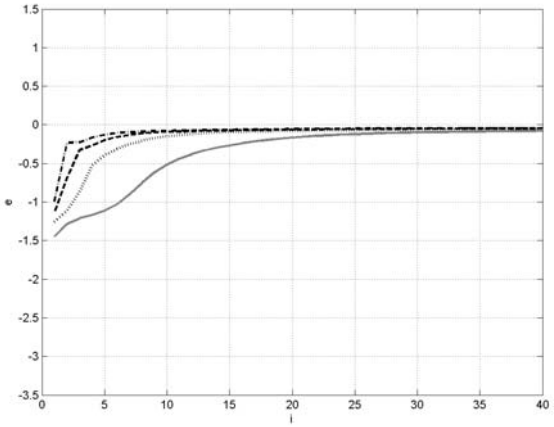

Fig. 3. Influence of η to recognition capability of neural network, A=1, B=0.77.

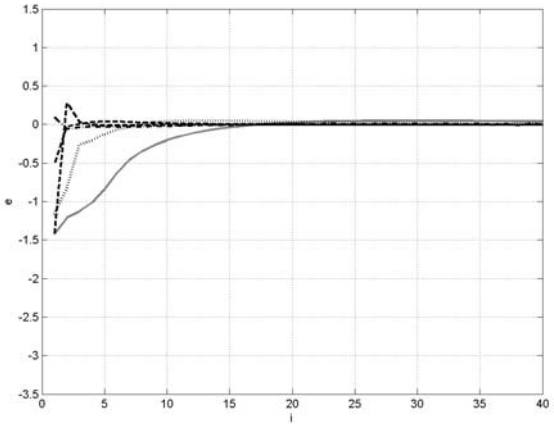

Fig. 4. Influence of to recognition capability of neural network, A=1.25, B=0.77.

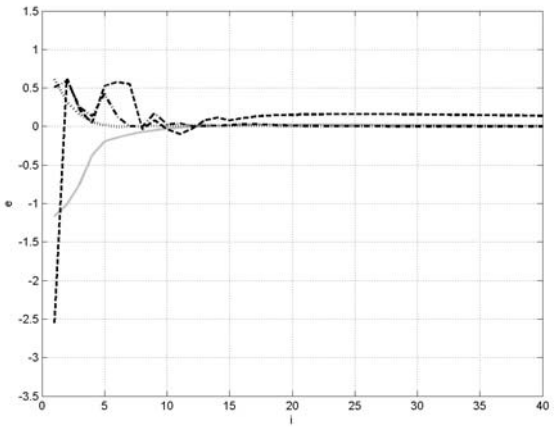

Fig. 5. Influence of η to recognition capability of neural network, A=1.66, B=0.77.

TABLE II
FIGURE 3,4,5 - NOTATION VALUE OF B IS B=1

A	η	notation	Figure N:
1	0.5	- -	3
1	0.4	-.-	3
1	0.3	. .	3
1	0.2	gray	3
1.25	0.5	- -	4
1.25	0.4	-.-	4
1.25	0.3	. .	4
1.25	0.2	gray	4
1.66	0.5	- -	5
1.66	0.4	-.-	5
1.66	0.3	. .	5
1.66	0.2	gray	5

IV. CONCLUSION

In this paper a computer simulation using Matlab is presented. In neural network equations take part the parameters of real components. The variation of some of them reflects to learning and recognition properties of the neural network. In such a way an influence of parameter variation to the learning and recognition properties of the neural network can be examine. The simulation results shows that neural network has adequate behaviour for values for A=1 and for B=0.77.

REFERENCES

[1] A. Bekiarsky, L. Docheva, "Neural Network design through analog methods"*Communication, electronic computer systems*, Vol. 1,pp 112-117.Sofia 2000

[2] Al. Bekiarski, L. Docheva. "Les modeles analogiques de reseaux de neurons" *Techniques et Technologies Fondamentales de la Nouvelle Economie*, Albena ,Bulgaria, 2002.

[3] A. Bekiarski, L. Docheva, I. Dochev. "Analysis of precision of neural network designed with analog methods". *International Scientific Conference, ICEST* Nish, Yugoslavia, 2002.

[4] Liliana Docheva , Aleksander Bekiarsky, Ivo Dochev. "Computer-based Neural network in education". *15th EAEEIE Conference* Sofia, Bulgaria, 2004.

[5] Docheva L., A. Bekiarsky, "Neural Networks modeling through analog equivalent scheme", *Energy and information systems and technologies*, Vol. 2, pp 471-475. Bitola 2001. Albena ,Bulgaria, 2002.

[6] T. Lehman. Hardware Learning in Analogue VLSI Neural Networks. Denmark.1994.

[7] Draghici S,"Neural Network in analog hardware-design and implementation issues", International Journal of Neural Systems, vol.10,N:1,pp.19 42,2000.

[8] Seon M., V. Asari "A parallel architecture for real-time segmentation of image with comlex background environment", 10th NASA Symposium on VLSI Design 2002, pp.8.2.1-8.2.7,2002.

[9] Shih-Chii Liu "A Normalizing aVLSI Network with Controllable Winner- Take-All Properties", Analog Integrated Circuits and Signal Processing, 31,Kluwer Academic Publishers. 47 _ U53, 2002

[10] Shih-Chii Liu "A Neuromorphic aVLSI Model of Global Motion Processing in the Fly", IEEE Transactions on Circuits and Systems UII: Analog and digital signal processing, vol. 47, N:. 12, pp. 1458-1467, December, 2000.

[11] Boegerhausen M. , P. Suter, Shih-Chii Liu "Modeling Short-Term Synaptic Depression in Silicon", Neural Computation 15, pp. 331 _ U348. 2002 Massachusetts Institute of Technology

[12] Shih-Chii Liu, J. Kramer, G. Indiveri et al. "Orientation Selective a VLSI Spiking neurons", Neural Networks 14, pp. 629-643, 2001.

[13] Pasio A, M. Laiho, A. Kananen, K. Halonen, J. Poikonen "A Mixed-Mode Polinominal Tipe Cellular Nonlinear Network for analising Brain Electrical Activity in Epilepsy", International Journal of Cyrcuit Teory and Aplications, vol. 30, pp.165-180, 2002.

[14] Schreiter J., U. Ramacher "Analog Implementation for networks of integrate-and-_re neurons with adaptive local connectivity". NNSP 2002. 2002.

[15] Koosh V. "Analog Computation and learning in VLSI", California, 2001

[16] Nazeih M. Botros, M. Abdul-Aziz "Hardwer Implementation of an arti_- cial Neural Network", IEEE International Conference on Neural Networks, Vol.3, pp. 1252-1257, 1993

[17] Ramacher U., J. Beichter, N. Bruls, E. Sicheneder, "Architecture and VLSI design of a VLSI neural signal processor", IEEE International Symposium on Circuits and Systems, Vol.3, pp. 1975-1978, 1993

[18] Roska T., L. Chua "The CNN Universal Machine: An analogic Array, Computer" IEEE Transactions on circuits and systems II Analog and Digital signal processing, vol. 40, N: 3,pp.163-173, 1993.

[19] Jayadeva, S. C. Dutta Roy, A. Chaudhary "Compact analogue Neural Network: a new paradigm for neural based combinatorial optimization", IEE Proceedings - Circuits Devices Systems, Vol.146,N:3, June, pp. 111-116, 1999

[20] Johnson D., J. Marsland, W. Ecclecton "Neural Network Implementation using a single MOST per synapse", IEEE Transactions on Neural Networks, Vol.6, July, pp. 1008-1011, 1995

[21] Leong P., M. Jabri "A Low Power Trainable Analogue Neural Network Classifaer chip", IEEE 1993 Custom Integrated Circuits Conference, pp. 4.5.1-4.5.4, 1993

[22] Jabri M., P. Leong, Burr J., B. Flower, K. Lai, S. Pickard, E. Tinker, R. Coggins ,"An analogue neural network using MCM technology ", Artifical Neural Networks and Expert Systems,1993.Proceedings, First New Zealand International Conference, pp. 122-125, 1993

[23] Cichoski A., J. Ramirez-Angulo, R. Unbehauen ,"Architectures for analog VLSI implementation of neural networks for solving linear constraints", ISCAS'92. IEEE International Symposium on Circuits and Systems, pp. 1529-1532, 1992.

[24] Wang Yiwen, "A Modular Analog CMOS LSI for Feedforward Neural Networks with On-Chip BEP Learning", IEEE International Symposium on Circuits and Systems, Vol.4, pp. 2744-2747, 1993

[25] Han II-Song, "Modular Neural Network Hardware Implementation of Analog-Digital Mixed Operation", IEEE International Conference on Neural Networks, Vol.2, pp. 707-710, 1993

[26] Wang Yiwen, "Analog CMOS Implementations of Backward Error Propagation", IEEE International Conference on Neural Networks, Vol.2, pp. 701-706, 1993

[27] Chen L., Wedlake, M, Deliyannides, G., Kwok,H.L. "Hibrid architecture for analogue Neural network and its circuit implementation", IEE Proceed-ings - Circuits, Devices and Systems, Vol.143 Issue:2 , April 1996 pp. 123-128, 1996

[28] Hernandez M.,R. Ascencio, C. Galicia "An arti_cal neural network on a complex programmable logic device as a virtual sensor"

[29] Lim D., G. Moschytz, "A programable modular Cellular Neural Network Cell", CNNA'94 International Workshop on Cellular Neural Networks and their applications, Rome, Italy, December 18-21, 1994, pp. 79-84,1994.

[30] Coggins R., M. Jabri, B. Flower, S. Pickard "Low Power Intracadiac Electrogram Classi_cation using Analogue VLSI", IEEE Transactions on Neural Networks, Vol.4,N:3, May, pp. 376-382, 1994

[31] Meijer, P. "Neural Network Applications in Device and Subcircuit Modelling for Circuit Simulation". Philips Electronics N.V. Eindhoven, The Netherlands,2003.

[32] Moerland P., E. Fiesler "Hardware Friendly Learning Algorithms for Neural Networks an Overview", Proceedings of the Fifth International Conference on Microelectronics for Neural Networks and Fuzzy Systems MicroNeuro' 96, 1996.

Predictive Neural Network Model for CELP Coding

Sn.Pleshkova-Bekjarska[1]

Abstract - **Linear prediction technique is widely used in speech coding methods and systems. The speech signal can be represented by a few parameters that possess the important feature of the linear process. Linear prediction coding (LPC) is in the base of different modifications of CELP standards of speech coding. It is the goal of this article to represent this part of CELP coder as a predictive neural network model and to investigate the theoretical and practical advances of this representation.**

Keywords - **speech, speech coding, speech prediction, neural networks, predictive neural networks.**

I. INTRODUCTION

Linear prediction coding (LPC) is the essential part of CELP method [1].The implementation of LPC analysis in the standard CELP coders is based on the traditional LPC algorithms [2] for calculating the linear prediction coefficients using the correlation between speech samples in a short time sequence – frame in which it is possible to consider the speech signal as a stationary. These algorithms are well investigated and optimized for hardware or software applications [3]. But it is interesting and useful to consider the possibilities of Neural Network Model implementation as linear prediction part of the CELP coders. Such a possibility is based on the wide range of Neural Network applications and the ability of these networks to solve many of engineering tasks. It is necessary to analyzing the characteristics and effectiveness of different types of Neural Networks in sense of speech linear prediction. Such a study is shown in [4] for a single two layers perceptron. Now the goal of this article is to extend this study for other Neural Networks types such as Predictive Neural Networks.

II. PREDICTIVE NEURAL NETWORK MODEL OF LPC

The proposed Predictive Neural Network Model can be based on the structures of Multiple Adaptive Linear Neural Networks. These structures allow determination of the coefficients of prediction for all frame speech samples in comparison of a single two layers perceptron. The block structure of this proposed network is shown in Fig. 1.

First it is necessary to use a tapped delay line (TDL) to have all N frame speech samples p_k as the inputs of adaptive neural network $pd_1(k),..., pd_N(k)$. The input speech signal is entered from left, and passed through $N-1$ delay stages D.

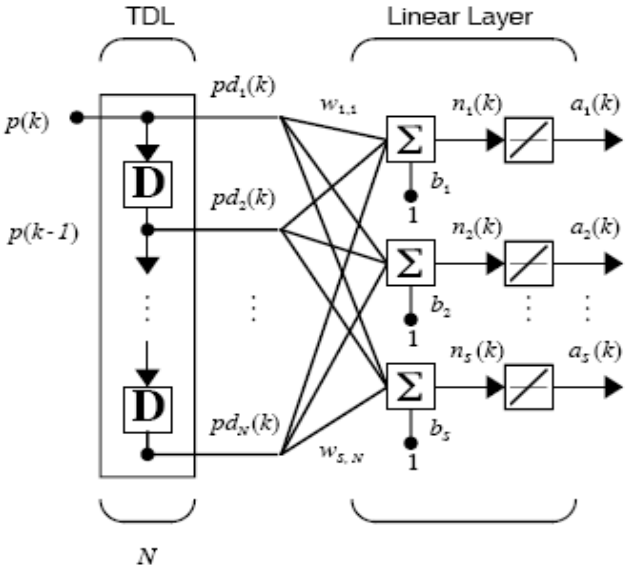

Fig.1. Neural networks structure.

The output of the taped delay line (TDL) is a N – dimensional vector, made up of the input speech signal at the current time, the previous input signal, etc. The weights of Linear Layer $w_{1,1},...,w_{S,N}$ represent the coefficients of linear prediction coding using in CELP method. The weights are sum up in blocks $\sum$ together with bias $b_1,...,b_S = 1$. The outputs of blocks $\sum$ are $n_1(k),...,n_S(k)$. The transfer functions are choose linear. The outputs $a_1(k) - a_S(k)$ of neural network are the predicted speech samples if the network is trained to give these samples with a defined minimal error:

$$a_j(k) = \sum_{i=1}^{N} w_{j,i}\, a(k-i+1) + b_j, \qquad (1)$$

where

$a_j(k)$ is the j-th output of network for $j = 1,...,S$;

N – number of past speech samples $pd_2(k),..., pd_N(k)$ plus current speech sample $pd_1(k)$;

[1]Sn.Pleshkova is with the Faculty of Communications and Communications Technologies, Technical University, Kliment Ohridski 8, 1000 Sofia, Bulgaria, E-mail: snegpl@tu-sofia.bg.

$w_{j,i}$ - weight from $i-th$ input to $j-th$ neuron for $i=1,...,N$ and $j=1,...,S$;

b_j - bias of $j-th$ neuron for $j=1,...,S$.

The advantage of this proposition is that the calculated weights $w_{j,i}$ after training of neural network are related with all N speech samples p_k in each frame.

If it is necessary to satisfy the CELP standard in which there are ten coefficients of linear prediction, then the number of the weights in each sum must be N=10 and must correspond to past speech samples according to $a_j(k)$. In the traditional linear prediction methods it is widely used the so called L2 criterion:

$$L_2 = \sum_n \left\{ \sum_n a(i)s(n-i) \right\}^2, \tag{2}$$

where

$\{a(i)\}$ is the unknown coefficient, only $a(0)=1$;

$\{s(n)\}$ - the n- th speech signal sample.

The solution of equation (2) is easily derived from a matrix equation. Neural-like stochastic gradient method also works well. On the other hand there is a so called L1 criterion defined by:

$$L_1 = \sum_n \sum_i a(i)s(n-i), \tag{3}$$

As this expression cannot be differentiated, another approach be devised. It is possible to define an objective function to be minimized:

$$L_1 = \sum_n y(n). \tag{4}$$

Under the linear constraints:

$$-y(n) \le \sum_i a(i)s(n-i) \le y(n), \tag{5}$$

where:

$$a(0)=1,\ a(i)=b(i)-\alpha,\ b(i)\ge 0,$$
$$\alpha \ge 0,\ y(n)\ge 0.$$

This approach is comprehensive and give an unique solution, but highly complexity in computation, which is a serious disadvantage.

III. Neural Network Aproach

For the neural network defined in Fig.1 it is possible to describe the outputs of the hidden layer $\{H_j(n)\}$ and the output layer $\{O_j(n)\}$ respectively as follow:

$$H_j(n) = f\left(\sum_{i=0}^{P-1} W_{ij} I_i(n) \right),$$

$$O(n) = f\left(\sum_{i=0}^{Q-1} V_j H_j(n) \right), \tag{6}$$

where $W_{i,j}$ and V_j are the coupling coefficient between the input layer and hidden layer, and between the hidden layer and output layer respectively. The function $f(.)$ represents a certain linear or not linear function. The L1 criterion for network learning can be formulated by:

$$E = \sum_{n=0}^{N-1} |e(n)| =$$

$$E = \sum_{n=0}^{N-1} |d(n) - O(n)|. \tag{7}$$

The above expression can be rewrite as:

$$E = \sum_{n=0}^{N-1} \mathrm{sgn}[e(n)]e(n),$$

$$\mathrm{sgn}[e(n)] = \begin{cases} 1 & if \quad e(n) \rangle 0 \\ -1 & if \quad e(n) \end{cases} \langle 0 \tag{8}$$

It is possible to assuming that the error never become zero, so the partial derivatives with regard to each coupling coefficient can be obtained:

$$\frac{\partial E}{\partial V_j} = -\sum_{n=0}^{N-1} \mathrm{sgn}[e(n)] f'\left(\sum_{m=0}^{Q-1} V_m H_m(n) \right) H_j(n)$$

$$\frac{\partial E}{\partial W_{ij}} = -\sum_{n=0}^{N-1} \mathrm{sgn}[e(n)] f'\left(\sum_{l=0}^{P-1} W_{ij} I_l(n) \right)$$

$$f'\left(\sum_{m=0}^{Q-1} V_m H_m(n) \right) V_j I_i(n), \tag{9}$$

where $f'(x)$ means $df(x)/dx$.

The gradient in (9) might change suddenly from a present value to the following value, since the surface of E is not continuous. However, if the coupling coefficients are updated descending along this gradient, it is supposed to reach the optimal solution whereby the L1 criterion is minimized. It is proposed in this article to try to achieve the convergence toward the improved value by taking the incremental changes ΔV_j and $\Delta W_{i,j}$, that is:

$$\Delta V_j = -\eta_1 \frac{\partial E}{\partial V_j} \approx -\eta_1 \frac{\partial e(n)}{\partial V_j}$$
$$\Delta W_{ij} = -\eta_2 \frac{\partial E}{\partial W_{ij}} \approx -\eta_2 \frac{\partial e(n)}{\partial W_{ij}}, \qquad (10)$$

where η_1 and η_2 are the additional variables that define the convergence rate.

The proposed approach is very similar to the back propagation (BP) algorithm, but the different problem occurs in the decision of the learning coefficients η_1 and η_2. The gradient of L1 criterion has always certain value as its own nature, which is shown in Fig.2. In this figure (a) represent L2 surface, (b) – more complex L2 surface, (c) – L2 surface and (d) – more complex L2 surface.

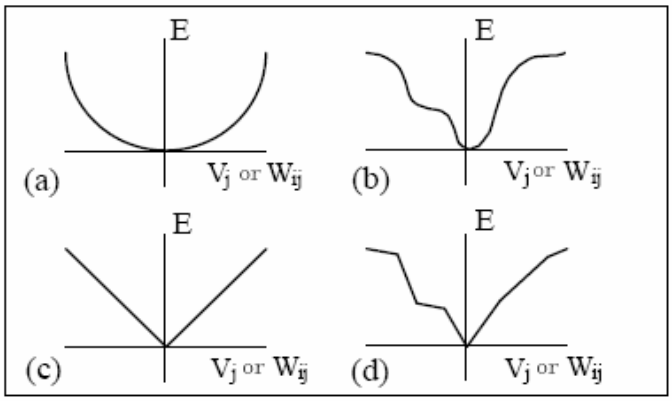

Fig.2a,b. A practical simulation in Matlab.

Therefore, the incremental learning rule in equation (10) sometimes results an unstable solution. In order to avoid such a situation, the learning coefficients must be set small enough with the convergence.

IV. MATLAB SIMULATION

The block schema from Fig.1 represent the structure of the proposed perceptual neural network. It is possible to present this network in Matlab notations for a practical simulation.This representation is shown in Fig.3.

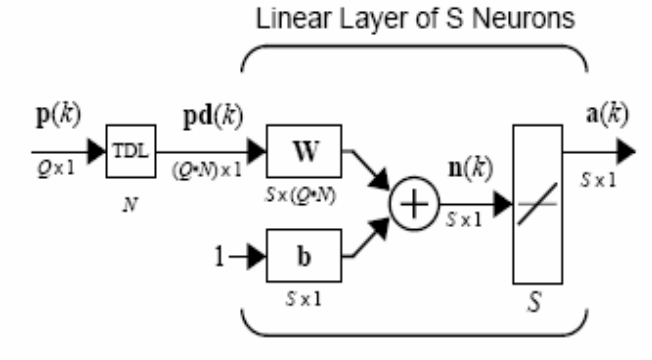

Fig.3. Block schema of practical simulation

The results of a practical simulation for a given real speech signal of vowel /a/ with 256 samples are present. Fig. 4(a) and Fig. 4(b) show L2 residuals difference and L1 residuals difference respectively with the proposed perceptual neural network.

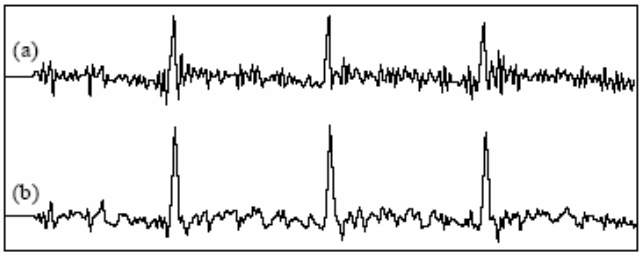

Fig.4 a,b. The results of practical simulation.

V. CONCLUSION

It is shown that the L1 learning criterion give a more realistic predicted speech signal, because the excitation signal perceived with the proposed neural network corresponding much more to the pitch frequency of the real speech signal. It is possible to use these results in practical implementation in a CELP coder.

REFERENCE

[1] Atal B.S., Schroeder M.R. “Stochastic coding of Speech at Very Low Bit Rates”, Proceedings of ICC, pp. 1610-1630,1984.

[2] Draft GSM 06.20, version 0.3, Half - rate Speech Transcoding, European Telecommunications Standard Institute (ETSI), 1995.

[3] Atal, B.S.,Schroeder, M.R. “Code excited linear prediction (CELP): High quality at very low Bit Rates“, Proc. ICASSP, vol3, pp937-940, 1985.

[4] Pleshkova Sn., Momchedjikov M. “Neural Network Modeling of Speech Coding Prediction”, Proceedings of Papers ICEST 2004, vol.1, pp 95-97,Bitola, Macedonia, 2004

Results from Sampling, Reconstruction and Synthesis of Analog Signals with Microprocessor System

Petre Tzv. Petrov[1]

Abstract: **There is a description of results from experiments with an analog input and output ports for a microprocessor-based system. The analog signal is sampled, converted into digital codes reconstructed and stored into the memory if necessarily. New ideas, theorems and rules for evaluation of the sampling and reconstruction process are proposed.**

Keywords: **sampling and reconstruction of analog signals**

I. INTRODUCTION

The conversion of analog signal (AS) into digital codes is one of the most important tasks during the data acquisition, measurement and digital signal processing. That is the reason to attempt to analyze and evaluate the errors during the analog to digital (A to D) conversions. Because the direct current (DC), the sinusoidal (SS), co-sinusoidal (CS) and multi-tone signals (MTS) are the basic test signals for the analog channels the results are given for them.

The paper resumes the results from sampling and reconstruction of AS with microprocessor system based on Motorola 6809 microprocessor unit (MPU) with additional hardware for possible synchronization of A to D conversions with the sampled AS. The approach described in [1] was developed and tested.

II. THE MICROPROCESSOR SYSTEM

The system based on the Motorola 6809 microprocessor is running at 1MHz+-0.01%. It is supported by the followings resources and was used as a principal controlling hardware: 4KB static RAM for the user program and data; 4KB EPROM with monitor program and constants; RS232C interface based on 6850; Motorola 6840 programmable timer module (PTM); six seven segments indicators; keyboard with 25 keys; expansion connectors for input output expansion boards and a power supply module for +-5V and +-12V. The block diagram of the system is shown on the Fig 1.

III. THE ANALOG PORTS

An additional board (called analog input and output port) was developed with an 8-bit analog to digital converter (ADC) and 8-bit digital to analog converter (DAC).

[1]Petre Tzvetanov Petrov is with "Microengineering"-Sofia, Bulgaria and expert-lecturer with OFPPT-Casablanca, Morocco, Emails: ppetre@caramail.com and ptzvp@yahoo.fr.

The board is intended to convert synchronously or asynchronously (to a particular level crossing or point in the time) an AS into digital codes and digital codes into analog staircase function (step function). It is with one input for the AS and a possibility to test the analog port with on board reference voltage. The sample and hold circuit (SH) could be switched on and off in order to evaluate the influence of the SH to the accuracy and the maximal input frequency to be converted. The clock of the ADC is produced from the system clock E or by appropriate external TTL clock source.

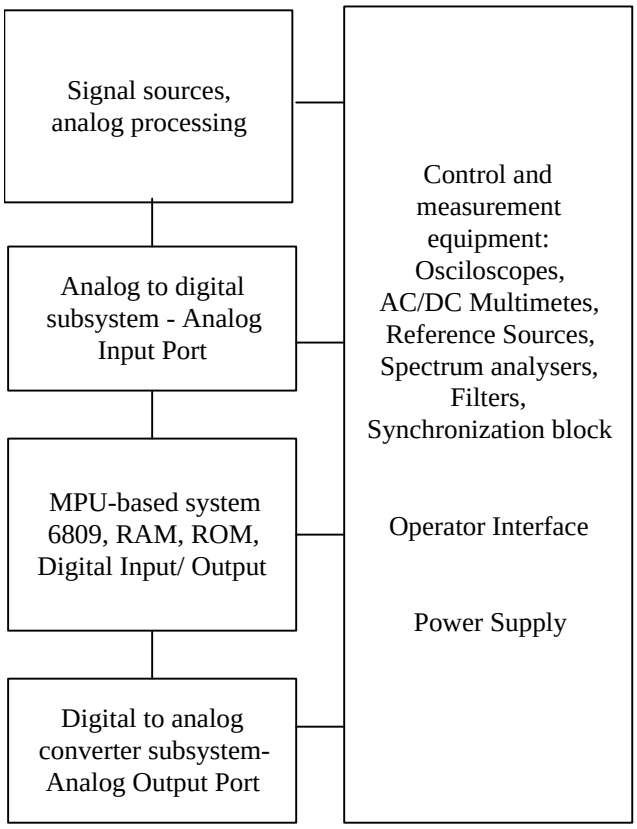

Fig. 1. Block diagram of Motorola 6809 MPU-based system with analog input/output ports for AS sampling and reconstruction.

The input analog port is build around the 8-bit ADC0801, a SH LF398 and source of reference voltage with TL431(A) normally adjusted to 5.120V. Under these conditions we have:

- reference voltage Vref=5.120V;
- minimum analog input voltage Vamin=0.00V;
- full scale analog input voltage Vfs=5.100V;
- one least significant bit (LSB) =Vref/2exp(8)=20mV.

A second analog port was tested with Analog Device AD570. ADC0801 and AD570 are not pin to pin compatible

but they have similar characteristics. AD570 has internal clock and internal reference voltage source.

The analog output port is build around the 8-bit DAC0808, operational amplifier LF356, 8-bit digital register 74HC273 and several resistors. DAC0808 is using the same source of reference voltage as ADC0801 or external voltage reference. In the first case the ADC and DAC has the same full-scale voltage Vfsadc and the same weight for the LSB (e.g. Vfsadc=Vfsdac=5.100V and LSB=20mV).

IV. Assembler Programs

The following programs in Assembler were developed:

1/ Converting the AS into digital codes with ADC and reconstructing it immediately with DAC. An example of such a program giving the maximum conversion speed of approximately 11KHz with name ADCDAC.ASM is given below. Since the time of the execution time is fixed and Fd = 1/Td =const the frequency of the sampled signal Fs should be changed in order to evaluate the influence of the different sampling factor N=Fd/Fs. The synchronization with a particular level of the sampled AS is not provided.

```
* Name: ADCDAC.ASM (Motorola 6809 @ 1 MHz)
* Td =  91 us,  Fd =  10.989KHz,  Tadc = 64 us
                ORG     $200
ADC             EQU     $2000   ; ADC
DAC             EQU     $3000   ; DAC
* Sampling period Td = (5+72+14)us = 91 us
* Put SH in Hold Mode and START of the ADC
ADCDAC          STA     ADC     ; 5us;
* Wait (5*ACCA+2)us = 72 us; ACCA=14
                LDA     #14     ; 2 us
LOOP            DECA            ; 2 us
                BNE     LOOP    ; 3us
* Read ADC and put SH in Sample Mode
                LDA     ADC     ; 5 us ;
                STA     DAC     ; 5 us ; Write to DAC
                JMP     ADCDAC ; 4 us; Loop again.
```

2/ Converting the AS with fixed number of bits n and variable SSF N (sampling frequency Fd).

3/ Converting the AS with variable number of bits n and fixed SSF N (sampling frequency Fd).

4/ Starting the analog conversion with programmable delay from the zero crossing of the signal in order to evaluate the influence of the ground noise and the amplitude of the samples to the quality of the reconstructed signal.

V. The Signal Sampling Factor

The term “signal sampling factor” (SSF) or encoding factor N is defined in [1] and is given by the Eq. 1:

$$N=Fd/Fs=Fd/Fmax>0 \quad (1)$$

where Fd is the sampling (encoding) frequency; Fmax is the maximal signal frequency to be converted (in case of band wide or multi-tone AS) and Fs is the frequency of sinusoidal signal (SS) or co-sinusoidal signal (CS) to be converted.

VI. The Factor of the Sample and Hold

In order to evaluate the role of the sample and hold circuit (SH) a parameter called “sample and hold factor” (SHF) Nsh was introduced and is defined by the Eq. 2

$$Nsh=Tadc/Tapsh \quad (2)$$

Where Tadc is the time of analog to digital conversion or the aperture time of the used A to D converter and Tap is the aperture time of the SH. In order to enlarged the band of the frequency converted with one ADC, normally we are in need of SH circuit with Nsh>>1.

VII. Basic Sampling Theorems

The equipment was intended primarily to test the new sampling theorem, discussed in [1] to evaluate the influence of the number of the converters bits n , the total harmonic distortion (THD) and intermodulation distortions (IMD).

The method of sampling and direct reconstruction of the AS was used and the analog “original” and its digital “copy” were compared. The signals before ADC and after the DAC were compared and processed. Several parameters (SSF, SHF), theorems and assumptions were formulated and are given below. They are applicable for a SSF N=Fd/Fs>=2. In some cases the reconstruction of the SS/CS is still possible with N<2 but we will not examine this case here.

Theorem 1: The maximum amplitude error Emax during the conversion of SS A=Am*sin(2*π*Fs*t) is given by the formula Emax = 1-sin(90-(180/N)), where N=Fd/Fs>=2 is the SSF and under the condition that the conversion error Econv is zero (Econv=0, the number of the converters bits n=∞).

Theorem 2: If the maximal amplitude error Emax for a SS A=Am*sin(2*π*Fs*t) is given, the SSF N=Fd/Fs>=2 could be calculated with the formula N= 180/(90-arcsin(1-Emax)) and under the condition that the conversion error Econv is zero (Econv=0, the number of the converters bits n=∞).

Theorem 3: The maximum amplitude error Emax during the CS A=Am*cos(2*π*Fs*t) conversion is given by the formula Emax=1-cos(180/N), where N=Fd/Fs>=2 is the SSF and under condition that the conversion error Econv is zero (Econv=0, the number of the converters bits n=∞).

Theorem 4: If the maximal amplitude error Emax for a CS A=Am*cos(2*π*Fs*t) is given, the SSF N=Fd/Fs>=2 could be calculated with the formula N=180/arccos(1-Eamax) and under the condition that the conversion error Econv is zero (Econv=0, the number of the converters bits n=∞).

The theorems 1, 2, 3 and 4 are giving the possibility to calculate the SSF N when the maximum amplitude error Eamax is known and vice versa. Once the SSF N is calculated it is easy to calculate the sampling frequency Fd using the formula given in [1] Fd = N*Fmax = N*Fs

Theorem 5: For a direct reconstruction of a sum of k SS and/or CS signals plus a direct current (DC) component at least N=3*k+1 samples are needed.

The Theorem 5 is based on the assumption that each of the signal components has at least thee independent parameters to

reconstruct : amplitude (Ak), frequency (Fk) and phase (φk) and one sample is needed to reconstruct the DC component. Assumption that the phases are zero (φk=0) and that the DC component is also zero (DC=0) does not reduce the number of the parameters to reconstruct.

A relation between the number of bits n in the digital word and the number of the frequency components k coded in the word was formulated and the following theorems are offered.

Theorem 6: The number of the SS and/or CS components k in a complex AS cannot exceed 2exp(n), where n is the number of bits n used to code this signal (k<= 2exp(n)).

Theorem 7: Every AS with limited slew rate (SR<∞) and limited peak to peak amplitude App (App<∞) could be approximated as a finite sum of SS and/or CS signals and a DC signal. Every SS and/or CS component in the sum has three basic parameters: amplitude, frequency and phase.

Definition: The simplest band wide signal (BWS) could be represented as a sum of a SS or CS and a direct current (DC) component and given with the formulas S=Asin(ωt+φ)+B or C=Acos(ωt+φ)+B. It has four basic parameters: amplitude A, frequency ω=2πFs or Fs, phase φ and a DC component B. Since four parameters should be transferred into digital form at least two bit will be needed to code them. In the paper for the signal frequency is used the abbreviation Fs.

Theorem 8: In order to reconstruct the simplest band wide signal given with the definition above at least four samples per period are needed or N=Fd/Fs>=4.

Theorem 9: In order to minimize the DC offset with direct signal reconstruction the SSF should be N=Fd/Fs = 4*p, where p is a positive integer number p=1, 2, 3…. Only the case with constant sampling intervals are concerned (Fd=const).

Table 1 is a resume of the amplitude and phase steps and resolutions during the A to D conversions of AS with an ideal converter. The phase resolution is important when the signal is containing more than one signal component with the same frequency but with a different phase (e.g. when a two or three phase 50/60Hz signals are summed and only one signal is produced and sampled).

VIII. LSB IN AMPLITUDE AND LSB IN PHASE

A parameter called "least significant bit in amplitude" (LSBa) defined with the formula LSBa=Vfs/(2exp(n)-1 or with the formula LSBa=Vref/2exp(n) is used in the sampling theory. Now, we could introduce the parameter "LSB in phase" with the Eq. 3

$$LSBph=360deg./N=360deg*Fs/Fd \quad (3)$$

Also parameters "Resolution in amplitude" (Ra) and "resolution in phase" (Rph) could be introduced with the corresponding Eq. 4 and Eq. 5

$$Ra=+-0.5*LSBa \quad (4)$$

$$Rph=+-0.5*LSBph=+-180deg/N \quad (5)$$

TABLE 1.
STEP AND RESOLUTION IN AMPLITUDE AND PHASE DURING THE ANALOG TO DIGITAL CONVERSION WITH AND AN IDEAL ADC

Parameter	Step (LSB) and resolution (R)
Amplitude (a)	LSBa=Vref/2exp(n) Ra=+-0.5*LSBa
Phase (ph)	LSBph=360/N Rph=+-0.5*LSBf=+-180/N

IX. CALCULATING THE NUMBER OF BITS

The discussed MPU equipment is offering the following possibilities:

1/ to transfer all of the bits between the ADC and DAC.

2 /to put some of the bits from the ADC in low state before writing them into the DAC.

3/ to put some of the bits from the ADC in high state before writing them into the DAC.

4/to delay the samples between the ADC and the DAC.

5/to generate AS from digital samples stored into memory.

The Eq. 6 for the minimum number of bits n is suggested in order the converter to be considered as an "ideal"

$$n>=lg(1/Emax)+D, [bit] \quad (6)$$

where lg is a logarithm in base 2 and D is a constant. In most of the cases D is chosen between 0 and 4 additional bits and depends on the application. The Eq. 6 is valid if Emax is equal to one step in the transfer characteristic of the converter.

In fact Eg 7 could be used as a quantity of information Qa which could be transferred from the analog to digital form of the signal.

$$Qa = lg (1/Emax) \quad (7)$$

X. CONCLUSIONS

Results were obtained and some of them are stated below:

1/ Theorem 1 to 4 are developed for evaluating the maximum amplitude error Eamax when sampling a SS or CS. The theorem 1 to 4 are valid for an ideal converter with infinity number of bits n (n=∞), e.g. in the case when the converters error could be neglected.

2/ It is found that SSF N=Fd/Fs=4 is guaranteeing a maximum difference between the amplitude of the "original" SS or CS and corresponding maximal digital code less than –29.3% or –3dB and this is valid for n=∞.

3/ The SSF N=Fd/Fs=2 and the frequency Fd=2*Fs (Nyquist frequency) is not very interesting. Nevertheless this is the frequency when the amplitude error Emax is changing from 0% to 100% when the phase of the SS/CS is changing from 0 do 90 deg. At this frequency the ADC is working as a "phase modulator", which normally is not his primary function. The frequency 2*Fs could be called "the frequency of full phase (or 90 deg.) to amplitude modulation".

4/ The usefulness of the new terms SSF and SHF was proven. The term SSF is giving a good idea about the error during the sampling process and about the methods of the signal reconstruction.

5/ The term SHF or Nsh is defining the ratio of enlarging the band of the AS to be converted into digital codes with one ADC with or without sample and hold circuit in from of it.
6/ The relations between the signal SSF N=Fd/Fs and the minimum number of bits n in the digital word was proven.
7/ It is suggested that the term " quantization noise" widely used in the publications is replaced with the term "error conversion function" during the SS/CS conversion or "conversion rounding function" because this error function is completely defined and determined by the characteristics of the signal and the transfer characteristics of the converter.

The method of sampling and direct signal reconstruction is described in [1]. Several practical circuits with ADC0801/2/3/4/5 and 6809 are published in [2]. The theorem of C.E. Shannon (1948) may be found in many sources, e.g.[3]. More information about the integrated circuit in the system is available from theirs manufacturers National Semiconductor Corp., Texas Instruments Inc., Analog Devices Inc. and Motorola Inc. in theirs respective catalogs [4, 5, 6, 7].

The equipment was used to evaluate the maximum amplitude, phase, frequency and function error between the "original" AS which was sampled under different conditions with different SSF N=Fd/Fs, amplitude, phase, spectrum with and without sample and hold and compared with the "digital copy". Table II is containing some of the obtained results.

TABLE II
MAXIMAL AMPLITUDE ERROR EMAX, MINIMAL NUMBER OF BITS N AND SIGNAL TO NOISE RATIO SNR FOR N FROM 2 TO 16.

N	Emax [%]	n(adc), [bit]	SNR , [dB]
2	100	0+2	1.76+12.04
3	50	1+2	7.78+12.04
4	29.3	1.77+2	12.4+12.04
5	19.1	2.39+2	16.14+12.04
6	13.4	2.9+2	19.22+12.04
7	9.9	3.33+2	21.84+12.04
8	7.61	3.72+2	24.13+12.04
9	6.09	4.05+2	26.15+12.04
10	4.89	4.32+2	27.96+12.04
11	4.05	4.63+2	29.61+12.04
12	3.40	4.86+2	31.11+12.04
13	2.91	5.1+2	32.49+12.04
14	2.51	5.32+2	33.77+12.04
15	2.18	5.52+2	34.97+12.04
16	1.92	5.7+2	36.08+12.04

It was proven t han the maximal amplitude errors during the sampling of a SS/CS depends on the SSF N=Fd/Fs. Table III is illustrating the maximal amplitude error E for the first sampled period of a SS/CS for SSF N from 2 to 16. It is clearly seen than the amplitude errors of two adjacent values (one pair and the other impair) could be quite different. Moreover for the positive and the negative period error (Epmax and Enmax) are equal for N pair and could be not equal for N impair. Concerning the direct current (DC) offset or the DC difference between the AS and the staircase approximation is minimal or zeroed when the N=4*k (k=1, 2, 3...)

TABLE III.
MAXIMAL AMPLITUDE ERRORS DURING THE FIRST PERIOD OF SS/CS, [%] FOR SAMPLING FACTOR N=FD/FS 2 TO 16

N	Amplitude errors E during the first period of SS/CS conversion with n=∞, [%]			
	Maximal	Positive and negative		Peak to peak
	Emax	Epmax	Enmax	Eppmax
2	100	100	100	100
3	50	50	0	25*
4	29.3	29.3	29.3	29.3
5	19.1	19.1	0	9.55*
6	13.4	13.4	13.4	13.4
7	9.9	9.9	0	4.95*
8	7.61	7.61	7.61	7.61
9	6.03	6.03	0	3.02*
10	4.89	4.89	4.89	4.89
11	4.05	4.05	0	2.02*
12	3.40	3.40	3.40	3.40
13	2.91	2.91	0	1.46*
14	2.51	2.51	2.51	2.51
15	2.19	2.19	0	1.09*
16	1.92	1.92	1.92	1.92

Note: (*) – With N= odd value Epp is never equal to zero. When En=0, Ep=Emax and vice versa.

REFERENCES

[1] Petre Tzv. Petrov, Method and equipment for sampling and direct reconstruction of AS s. Technical University-Sofia. 2003. Bulgaria. Brochure 32p.

[2] Petre Tzv. Petrov. More than 111 electronic circuits. Sofia. Tehnika. 2001. Bulgaria.

[3] C.E. Shannon. A mathematical Theory of Communication. The Bell System Technical Journal. Vol. 27, pp. 379-423, 623-656, July, October, 1948.

[4] Motorola Inc., 6809 Programming Manual, 1989. USA.

[5] National Semiconductor Corp., Data Conversion/Acquisition Data Book., 1984. USA.

[6] National Semiconductor Corp. National Analog and Interface Products Data Book. 1999. USA.

[7] Analog Devices Corp. Integrated Circuits. Volume I. 1984. USA..

Chaos Detection in Colpitts Oscillator

Igor Đurović, Vesna Rubežić, Miloš Daković[1]

Abstract – **Detection of chaotic state in nonlinear chaotic Colpitts oscillator has been studied. A new approach, based on concentration measure of the time-frequency representation, is proposed for estimation of the current circuit state and applied to Colpitts oscillator.**

Keywords – **chaos detection, nonlinear oscillator, time-frequency representations**

I. INTRODUCTION

Nonlinear systems (electrical, mechanical, biomedical, economical) that under the specific conditions exhibit chaotic behavior, attracted wide interest of researches in the last several decades [1]-[4]. One of important topics in this area is detection of the current system state. There are several techniques for chaos detection: Lyapunov exponents, Kolmogorov entropy, Poincare sections [5]. Lyapunov exponents are the most commonly used quantitative measure of chaos. Since Lyapunov exponents are calculation demanding, they are unusuable in the systems that in short interval, by varying one or several parameters, undergo different states. The other methods are applied in such cases.

In this paper, chaos detection in nonlinear oscillatory circuits, based on a time-frequency representation, is considered. Proposed detector estimates system state using a concentration measure of time-frequency representation. Detector has no information about oscilattor's structure and parameters. In this paper, detection is applied in case of the Colpitts oscillator, a simple circuit that is usually used in communications.

After the introduction, Colpitts oscillator is described in short in Section II. Proposed detector is studied in details and simulation results are shown in Section III. Finally, the conclusions and future research topics are given.

II. COLPITTS OSCILLATOR

Colpitts oscillator that we consider is shown in Fig. 1a. The circuit consist of a single bipolar junction transistor Q which is biased in its active region by appropriate choice of V_{EE}, R_{EE} and V_{CC}. The feedback network consists of an inductor L with series resistence R_L, and a capacitive divider composed of C_1 and C_2. If we suppose, as in [1], that bipolar transistor works in directly active region and cutoff, we can model transistor as a two-segment piecewise linear voltage controlled nonlinear resistor (Fig. 1b).

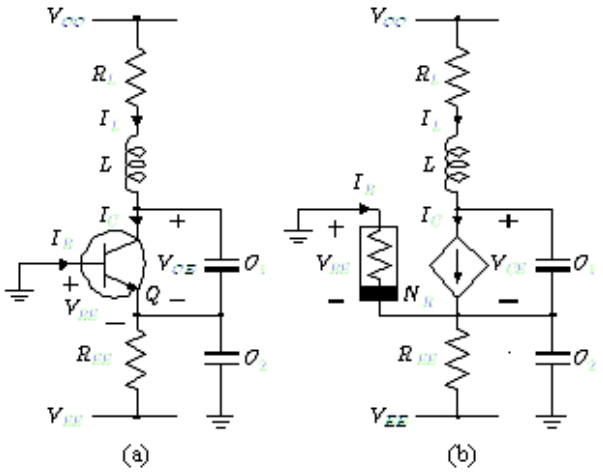

Fig. 1. (a) Colpitts oscillator with bipolar transistor. (b) Its equivalent circuit.

Thus, circuit can be described by system of three state equations:

$$C_1 \frac{dv_{CE}}{dt} = i_L - I_C \quad C_2 \frac{dv_{BE}}{dt} = -\frac{V_{EE} + v_{BE}}{R_{EE}} - i_L - I_B$$

$$L \frac{di_L}{dt} = V_{CC} - v_{CE} + v_{BE} - i_L$$

where N_R is characteristic of nonlinear resistor, given as:

$$I_B = \begin{cases} 0 & if \quad v_{BE} \le V_{TH} \\ \dfrac{v_{BE} - V_{TH}}{R_{ON}} & if \quad v_{BE} > V_{TH} \end{cases}$$

$$I_C = \beta_F I_B$$

V_{TH} is voltage threshold, R_{ON} is on-resistance for small signals and β_F is direct current gain.

This oscillator, with the suitable choice of parameters, exhibits chaotic behavior and can be exploited as a transmitter in chaotic-carrier communication systems [6].

Note that dynamic of the chaotic Colpitts oscillator linear conjugates to that of the asymmetric Chua's oscillator [7].

III. PROPOSED DETECTOR

We consider behavior of Colpitts oscillator with parameters as in [1]: $C_1 = 54\text{nF}$, $C_2 = 54\text{nF}$, $L = 98.5\mu\text{H}$,

[1]Authors are with the Faculty of Electronic Engineering, Cetinjski put bb, 81000 Podgorica, Serbia and Montenegro, E-mail: [igordj, vesnar, milos]@cg.ac.yu,

$R_{EE} = 400\Omega$, $V_{EE} = -5\text{V}$, $V_{CC} = 5\text{V}$, $\beta_F = 255$, $R_{ON} = 100\Omega$, $V_{TH} = 0.75\text{V}$. Resistor R_L is linearly varied in the range from 67Ω to 5Ω. R_L is bifurcation parameter and route to chaos is period-doubling [2]. Time varying of parameter R_L causes change of the system state. Consequently, spectral content of the signal is changed and time-frequency representation is suggested as a natural tool for analysis. The short-time Fourier transformation (STFT) is applied in development of our detector, as the simplest and the most commonly used time-frequency representation [8]:

$$STFT(t, f) = \int_{-\infty}^{\infty} x(t+\tau) w(\tau) e^{-j2\pi f\tau} d\tau \qquad (2)$$

where $x(t)$ is the signal of the interest, (here, it is voltage or current), while $w(t)$ is window function.

Logarithm of the STFT magnitude of signal $v_{BE}(t)$ is considered and shown in Fig. 3a. In interval from 67Ω to 57Ω, oscillator exhibits periodic motion with the main frequency close to 88kHz. In the time-frequency plane the DC component, main frequency and components corresponding to main frequency multipliers can be seen. Logarithm of the STFT magnitude for $R_L = 59\Omega$ ($t = 2\text{ms}$) is shown in Fig 3b. Decrease resistance R_L causes period-doubling bifurcations. Periodic attractor with twice period occurs in the phase space. In the time-frequency plane, a subharmonic (which magnitude is lower than the one of the main harmonic) and its multipliers can be seen (Fig. 3c). After several period-doubling bifurcations system gets into chaos (Fig. 2b). In the time-frequency plane, between DC component and the main harmonic, there are many components of the same order of magnitude as dominant components. Logarithm of the STFT magnitude for $R_L = 48\Omega$ ($t = 5\text{ms}$) is shown in Fig. 3e. After that, chaos occurs, again. Finally, for $R_L = 9\Omega$, oscillator returns to periodic regime.

Note that similar results are obtained for signals $v_{CE}(t)$ and $i_L(t)$.

From previous consideration, we conclude that oscillator state can be estimated based on a concentration measure of signal's time-frequency representation between DC component and the main harmonic component. Thus, we create a concentration measure of the STFT as:

$$m(t) = \int_{0}^{f_m(t)} u_{\Omega(t)}(t; f)\, df \qquad (3)$$

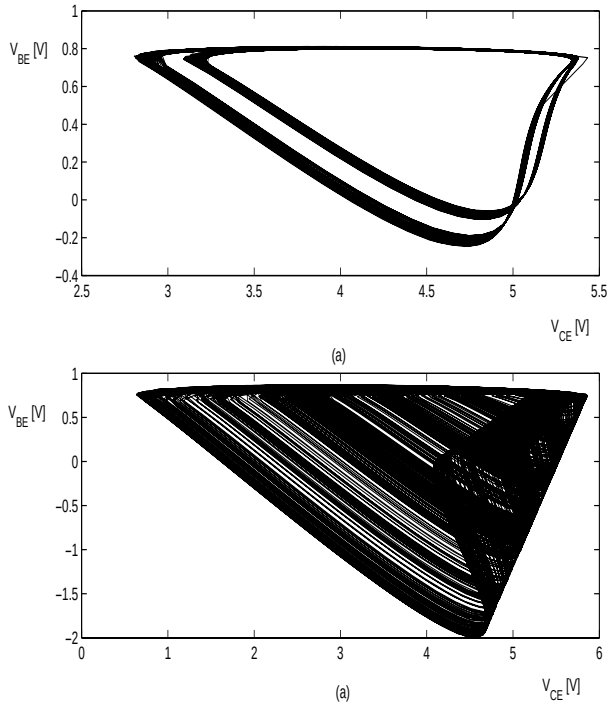

Fig. 2. (a) Period 2 attractor ($R_L = 57\Omega$). (b) Chaotic attractor $R_L = 35\Omega$.

where $\Omega(t)$ is threshold, $f_m(t)$ is frequency of the main spectral component. Function $u_{T(t)}(t; f)$ is given as:

$$u_{T(t)}(t; f) = \begin{cases} 1 & |STFT(t, f)| \geq \Omega(t) \\ 0 & \text{elsewhere.} \end{cases}$$

Procedure can be summarized in several steps.

I step - Calculation of the STFT using Eq. (2).

II step – Determination of the main spectral component $f_m(t)$ as a position of maximum in the STFT, excluding region around DC component:

$$f_m(t) = \arg\max_{f > \varphi} |STFT(t, f)| \qquad (4)$$

where φ is region of DC component (its width is several frequency samples).

III step – Threshold $\Omega(t)$ selection so that the STFT samples with magnitude higher than $\Omega(t)$ contain almost all signal's energy. Energy that remains outside of this region is very small:

$$(1-\varepsilon) \int_{0}^{\infty} |STFT(t, f)|^2 \, df = \int_{0}^{\infty} |STFT(t, f)|^2 \, u_{\Omega(t)}(t; f) df. \qquad (5)$$

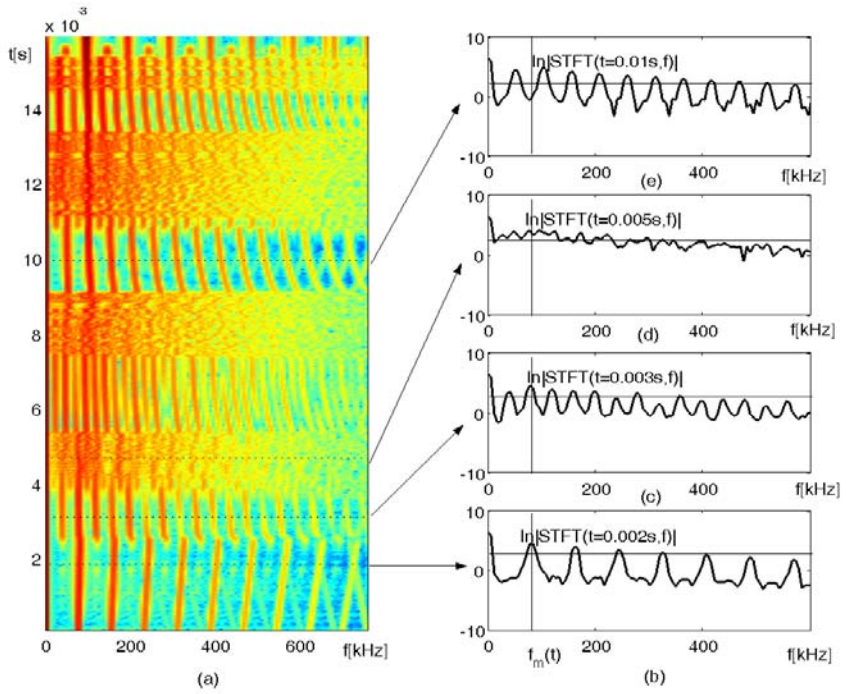

Fig. 3. (a) STFT. (b) Logarithm of the STFT for t=2ms - period 1 orbit. (c) Logarithm of the STFT for t=3ms - period 2 orbit. (d) Logarithm of the STFT for t=5ms - chaos. (e) Logarithm of the STFT for t=10ms - periodic window.

Note that our algorithm works well for relatively wide range of parameters ε. To determine threshold $\Omega(t)$, the magnitudes of the STFT samples, in considered instant, are sorted in descending order. Threshold is selected as a position where the rest of sorted sequence has energy smaller or equal to:

$$\varepsilon \int_0^{\infty} |STFT(t, f)|^2 \, df \, .$$

In Fig. 3 the threshold is shown as a solid horizontal line.

IV step – Detector response calculation according to relation (3). To avoid possible noise influence and other errors, detector response $m(t)$ is averaged within a small interval around considered instant:

$$m'(t) = \frac{1}{p} \int_{t-p/2}^{t+p/2} m(\tau) d\tau \, . \qquad (6)$$

V step – Determination of current state based on $m'(t)$:

$$\begin{aligned} m'(t) &\geq C(t) \quad \text{chaotic regime} \\ m'(t) &< C(t) \quad \text{periodic regime} \end{aligned} \qquad (7)$$

where $C(t)$ is detection threshold. In chaotic regime, it is expected that the STFT in entire region $[0, f_m(t)]$ is above the threshold. Thus, the expected value of $m'(t)$ in chaotic regime is close to $f_m(t)$. However, in periodic regime values of the STFT between the DC and the main spectral component are small. We assume that width of signal's components is known and determined by the used window function. Numerical calculation using Hanning window results with three nonzero frequency samples for frequency of sinusoidal component on frequency grid. Then, the expected value of $m'(t)$ in periodic regime, for the Hanning window of the width T, is $5/T$ (5 frequency samples, 3 of the main component and 2 of DC component, since one is in negative frequency region). Threshold is selected as the arithmetic mean of the expected values of detector response in periodic and chaotic regimes:

$$C(t) = \frac{f_m(t) + \frac{5}{T}}{2} \qquad (8)$$

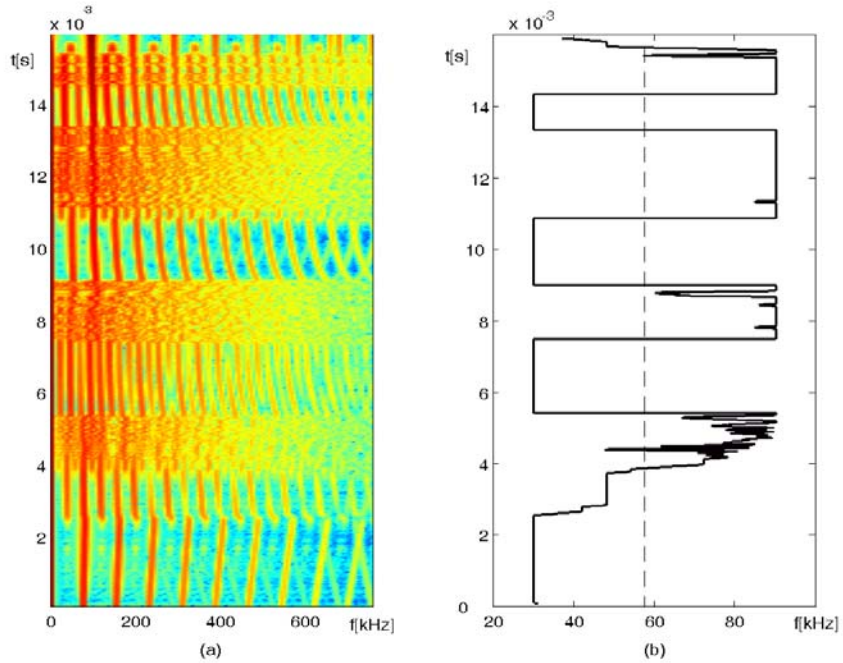

Fig. 4. (a) Time-frequency representation. (b) Thick line - detector response; dash line - threshold.

IV. Simulation Results

In this section, the proposed detector is considered in the case of period-doubling route to chaos. Parameters of the Colpitts oscillator are the same as in previous section. We set $\varepsilon = 0.016$. Illustration of the time-frequency representation is repeated in Fig. 4a. Detector response is shown in Fig. 4b. Threshold is marked with dashed horizontal line. Regions where the detector response is above the threshold corresponding to chaos behavior. Our results are according to theory. Periodic windows are, also, correctly detected.

V. Conclusion

A simple chaotic state detector is presented. Using of the concentrating measure of the STFT samples enabled tracking and estimation time-varying behavior of the nonlinear oscillators. Colpitts oscillator is numerical analyzed, since it is well known in theory. Proposed estimator is tested on the other chaotic oscillators and obtained results are satisfactory.

In future work we will extend proposed detector to distinguish between various attractors.

References

[1] M. P. Kennedy, "Chaos in the Colpitts oscillator," *IEEE Trans. Circuits Syst. I*, vol. 41, no. 11, pp. 771-774, Nov. 1994.

[2] M. P. Kennedy, "Three steps to chaos-Part II: A Chua's circuit primer," *IEEE Trans. Circuits Syst.*, vol. 40, no. 10, pp. 657-674, Oct. 1993.

[3] W. A. Brock, D. A. Hsieh and B. LeBaron, Nonlinear dynamics, chaos, and instability: statistical theory and economic evidence. MIT Press, Cambridge, MA, 1991.

[4] D. Mackey and L. Glass, "Oscillation and chaos in physiological control systems," *Science* vol. 197, pp. 287-289, July 1977.

[5] J. C. Sprott, *Chaos and Time-Series Analysis*. New York: Oxford University Press, 2003.

[6] A. V. Oppenheim, G. W. Wornell, S. H. Isabelle and K. M. Cuomo, "Signal processing in the context of chaotic signals," *Proc. IEEE ICASSP*, vol. 4, pp. 117-120, 1992.

[7] M. P. Kennedy, "On the relationship between the chaotic Colpitts oscillator and Chua's oscillator," *IEEE Trans. Circuits Syst. I*, vol. 42, no. 6, pp. 376-379, June. 1995.

[8] L. Cohen, "Time-frequency distributions-a review," *Proc. IEEE*, vol. 77, no. 7, pp. 941-981, July 1989.

An Inductive Method and Database in Energy Management

Geo V. Kunev[1]

Abstract – **Most of human activities are related to consumption of energy. The sources of energy are electric current, gas, oil, etc. The consumers of energy can be industry, house heating, etc. The main goal of Energy management is to achieve the balance between sources and energy consumers, providing the desired quality and minimum of charges. An application of inductive approach in form of classifying algorithm and developing of appropriate database for estimation of buildings thermo-isolation with use of infrared thermography is given.**

Keywords – **Infrared thermography, Energy management**

I. Introduction

The tasks of Energy management can be supported in different wais – from home energy budget calculations, through the computer based office systems, to using the most advanced methods of applied mathematics, and - in this case – using of inductive approach in form of Databases and Data mining techniques [4] to made statistical estimations and decisions on buildings thermo isolation quality.

II. An Unified Classification Method

Today's approach in searching complex estimations, based on databases, is Data mining, or KDD. It uses most sophisticated statistical and other methods for machine learning and estimating of different cases and factors. The used method is some unification of different statistical methods for classification, accenting on the same calculating formulas and procedures [1]. It combines the most frequently used statistical approaches – the Bayes probability, and geometry interpretation (Fig.1).

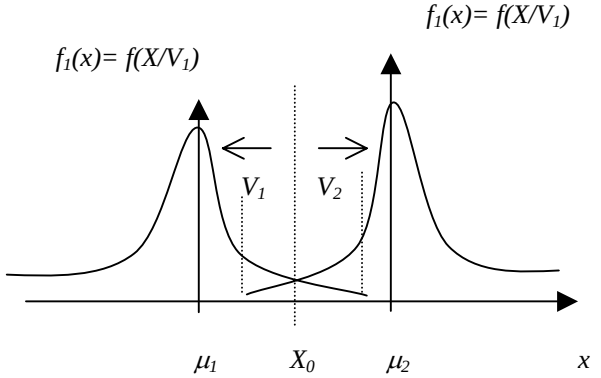

Fig. 1. Two classes classification

In the simplest case, we have two classes V_1 and V_2 and we need to find the boundary line and value X_0 , which divides the classes. We can use estimation:

$$X \in V_1, \text{ if } X<X_0 = \frac{\mu_1 + \mu_2}{2}; \quad X \in V_2, \text{ if } X>X_0 \qquad (1)$$

In the Bayes interpretation, the classification can be done, knowing aposteriori probabilities:

$$X \in V_1, \text{ if } P_i f(X/V_i) > P_j f(X/V_j); \ (i,j_{i\neq j}=1,2) \qquad (2)$$

where P_i и P_j – are apriory probabilities for V_1 и V_2. classes' appearance.

Except some cases [5]: (3)

$$X \in V_1, \text{ if } \frac{X^2}{2}\left(\frac{1}{\sigma_2^2}-\frac{1}{\sigma_1^2}\right)+X\left(\frac{\mu_1}{\sigma_1^2}-\frac{\mu_2}{\sigma_2^2}\right)+\left(\frac{\mu_2^2}{2\sigma_2^2}-\frac{\mu_1^2}{2\sigma_1^2}\right)>\ln\frac{P_2}{P_1}$$

If $\sigma_1=\sigma_2=\sigma$, *.and* $P_1=P_2$, we have a minimax strategy.

III. Infrared Thermography

To estimate the thermo isolation quality of buildings, we use the modern infrared thermography technology [2]. This way, we can directly view the outer walls thermo-conditions, and make digital comparison with the example image (Fig.2).

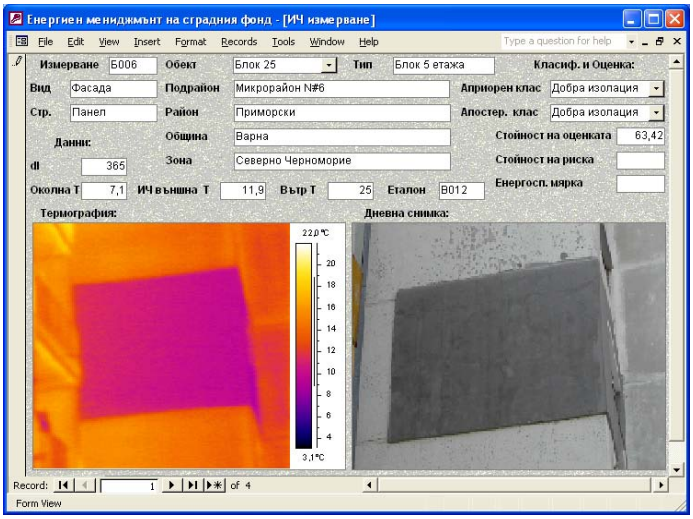

Fig. 2. Using infrared thermography

[1]Geo Kunev is with the Faculty of Computer Sciences, TU Varna, Studentska 1, 9000 Varna, Bulgaria, E-mail: geo_qnew@hotmail.com

The images are of two types – IR (infrared), and daylight (Fig.2). The estimating procedure is based on:
1. Digital distance to the example image,
2. Average outer walls temperature,
3. Ambient temperature,
4. Average inner walls temperature

The inductive method was verified in the form of MatLab programs, experimenting with two and more a priory classes and different number of classification factors. The most effective variant is described here (in brief):

```
l12=load('12'); l22=load('22');
mean_1=mean(l12); mean_2=mean(l22);
cov_1=cov(l12); cov_2=cov(l22);
s1=size(l12); s2=size(l22);
cov_pretegl=(cov_1.*s1(1)+cov_2.*s2(1))./(s1(1)+s2(1));
A=inv(cov_pretegl)*(mean_1-mean_2)'
B=1/2.*(mean_1+mean_2)*A
lt1=load('12tst');
lt2=lt1*A-B;
lt3=(lt1*A-B)*[1 1];
for i=1:size(lt2);
  if(lt3(i,1)>0) lt3(i,2)=1;
  else lt3(i,2)=2;
  end
end
lt3
```

IV. Developing Databases

The task of inductive estimating needs many data, to provide the process of training the system. So, a database was developed to hold data and images (Fig.3). Except the above mentioned data, we need some more data:
1. Types of buildings,
2. Types of construction,
3. Areas,
4. Zones,
5. Other.

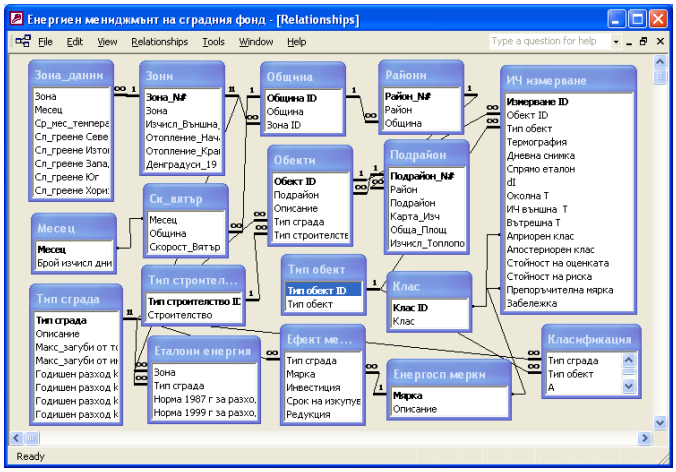

Fig. 3. Energy management database

The same database is used to support the estimation of common buildings heat consumption of the city of Varna [3], and to advance the appropriate strategy (Fig.4.)

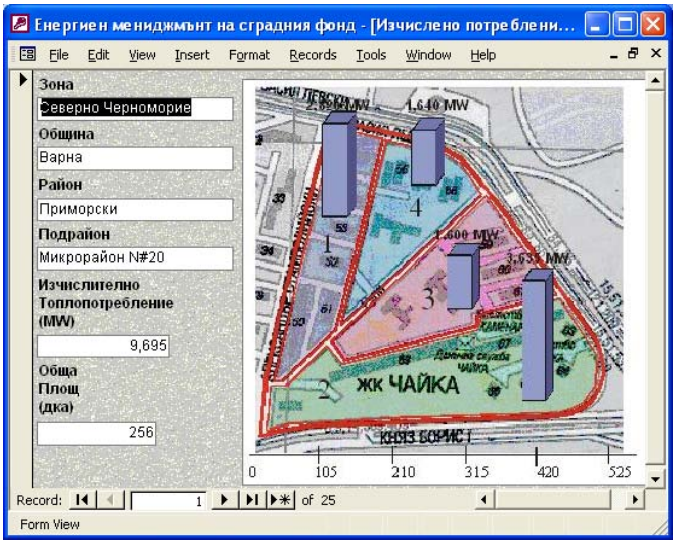

Fig. 4. Heat consumption estimation of Varna city

The used method and the developed database prototype demonstrate the power of combining the latest IT technology in form of databases and data mining techniques with classical thermo-analysis tools, as Ashrae [6].

V. Conclusion

Usage of unified inductive method for estimation offers relatively easy way to estimate the thermo isolation of buildings, but we need first to have data to provide the system training. The developing of inductive databases [4], enabling both data and knowledge support, is a way to achieve better effectiveness.

Acknowledgement

Thanks to the help and co-operation of prof. A.Nedev's team from Technical University of Varna, Bulgaria, and prof. W.Wild's team from Rostock University, Germany.

References

[1] A.Nedev, G.Kunev, G.Varbanov, D.Ilieva, Relation Conditions Between Geometric and Stohastic Approaches nn Image Recognition Problem Solving, Telecom 2003, Varna, Bulgaria

[2] Kunev G., Nedev A, Wild W. Application of Infrared Thermography Technical Diagnostics: Holistic Approach, Telecom 2002, p.689-696, Varna, Bulgaria

[3] Bulgaria District Heating II Project (BG-PE-6402)

[4] G. Kunev, V. Antonova, P. Vladimirova, System Modeling via Databases, ICEST2004, Bitola, Makedonia, 2004

[5] Tenekedjiev, K., Karakatsanis, N., Bekiaris, A. Fictitious Covariance Matrices, ACDM'2000, Plymouth, UK, 2000

[6] ASHRAE Handbook of Fundamentals, 1997

Fonts Recognition by Using Typographic Features of Connected Components

Milen Dimitrov[1] and Antoaneta Popova[2]

Abstract: **Many different methods and systems of printed text recognition (OCR) are developed till now. These methods can be divided in two types. The mono/ single-font methods recognize characters from one, preliminary defined font only. Although first developed these methods give better results than the second type multi-fonts text recognition methods. The purpose of the multi-fonts text recognition is to recognize symbols with random/ unspecified shape, slope and size. Unfortunately the final results of these systems are not enough good. The presented paper describes a method for preliminary optical font recognition (a-priori OFR system) for giving this information on the next step to the recognition system. The purpose is to increase the multi-font text recognition accuracy. As recognition features are used text line typographic attributes extracted from the connected components and their bounding rectangles.**

A two layers neural network with back propagation is used as a classifier. The experiments with a font set of different typeface, weight, slope and size were carried out and described.

Keywords: **Optical font recognition, typographic features, text recognition**

I. INTRODUCTION

The hard-copy/paper based documents volume continues to increase with high speed although the soft copy/electronic documents usage, which is opposite to the expectation. The main reason is the human comfortable feeling when he reads and acquires of the paper documents.

From other side the soft copy/electronic documents have serious advantages in their storage, retrieval, restoration and updating. As results, the paper documents converting into their electronic versions, named print documents recognition (OCR) becomes very popular in the last 10-15 years. Analogical to the popularity of the newspapers, magazines, even after the radio discovery, the paper documents, which exist from hundred years, will continue to play an important role in our live.

The text recognition systems can be divided into three groups [2]:

- mono-font – Algorithms for a text processing only with a single font. Today the mono-font OCR systems reach a very high accuracy– more than 99%.
- multi-font – These systems work with a set of fonts, and often correspond to defined practical requirements.
- omni-font – These systems are independent on the font.

The entering of a great number new fonts in the computer industry makes very difficult the database supporting of base models for the multi-font OCR systems. This is the reason the omni-font OCR systems to be preferable. Unfortunately these systems give not so good results. The applying of a-priory algorithm for the optical font recognition (OFR) can increase significantly the accuracy. These methods are named a-priori.

A-posteriori methods for OFR are performed over a text with a known content (after OCR for instance). They are used for concrete font identification, as example for a completely electronic restoration of the original document.

The purpose of this paper is to research, develop and test an algorithm and a program model for the a-priory fonts' identification.

In a paragraph II is presented a brief analysis of some existing researches on the topic. A paragraph III describes the main definitions used in the developed algorithm. A paragraph IV presents the applied method and a paragraph V- the obtained results. At the end a paragraph VI contents the results analysis and describes the possible improvements.

II. EXISTING APPROACHES ANALYSIS

On the background of the huge number OCR publications the researches connected to the Optical Font Recognition (OFR) are discourage number. Ones of the most popular researches were published by Zramdini and Ingold [1], [3], [6]. They present a depth research of a completely font recognition system without the preliminary content knowledge (ApOFIS). The system extracts 8 careful chosen global typographic text features, which are passed to a Bayesian classifier. A created base fonts' model in advance is used with a priory known 280 fonts. In a literature [1] are presented and analyzed the efficiency of the features, as well as the text line length influence, and in [6] is done an evaluation of the recognition accuracy dependency on the input images quality decreasing.

A similar approach is used in [4]. The typographic features are extracted from a normalized image 9x9, and basically emphases on the edge symbols lines (serif). But this approach depends on the used languages, because of taking in account the specific symbols as g/g, a/a. As a classifier a back propagation neural network (BPNN) is applied.

Opposite to the methods using features, in [2] is shown an algorithm with a comparison to etalons by a nearest neighbor classifier, using single-side tangential distance.

[1] Milen Dimitrov is a Project Manager in Komero Technologies Int.- Sofia, Bulgaria
[2] Antoaneta Popova is an Associate Professor in the Technical University- Sofia, Bulgaria

In [7] an interesting algorithm is suggested for a dominated text determination with small key words (stop-words) vocabulary applying.

III. Definitions

The font is described with the following properties [5], [3]:

- family (typeface) - a descriptive name
- size - describing in typographic points (pt)
- weight - normal, light, bold
- slope - roman, italic

The typeface fonts are divided into 2 groups – serif (with small lines on the symbols' edges) and sanserif (without such lines).

A big variety of typeface fonts exist. While some of them are easy distinguished even by a beginner, others are very similar and difficult for identification even by an expert. But for the text recognition (OCR) improvement is more important to determine a correct size, weight and slope in the stage of OFR and it is not so important to find the exact typeface.

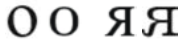

Figure 1. Example for easy and difficult distinguished symbols from two font typefaces (Times New Roman и Journal)

Although a single document contents a dominated font, the font is not a property on the document level. Theoretically the font is a property on a symbol level, but in practice it is a feature of the word as a part of the text line. Furthermore could be considered, that in one text line (sentence) exists only one typeface and font size, but the fonts are different mainly in the slope and/or weight.

The typographic structure of a single text line is defined as:

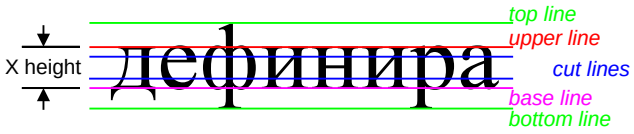

Figure 2. Typographic structure of a text line

The dominated symbols in the line are the small letters (lower case). In consequence of the fact that they can have or not ascenders or descenders the text line consists by three vertical zones (Figure 2): upper, central and bottom. Four dividing lines form these zones: top, upper, base and bottom lines. The height of the central zone is named X-height.

The experiments in the present paper are done on the text line/row, which can contain one or more words.

IV. Used Method Description

The main stages in the suggested method of the fonts' recognition are:

- Typography determination – detection of typographic zones and dividing lines
- Features extraction
- Learning
- Classification

A. Typographic line analysis

Most often the typographic zones founding is performed on the base of the vertical image profile [1], [3], [8]. However many times, the correct local maximum detection is impossible because of a lightly or noisy profile distribution.

Figure 3. Profile with an impossible correct detection of lines

In this paper are suggested the applying of the connected components approach. Because of this first the connected components (CC) in the binary images are detected: using 4 or 8 connected neighborhood. The coordinates of the bounding rectangles are defined too.

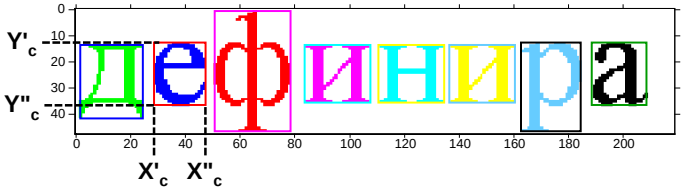

Figure 4. Connected components and the bounding rectangles

The distribution (histogram) determination of the Y coordinates for the bounding rectangles is the next step. This distribution appears as a profile P_y^V similar to the image profile. Two profiles are calculated - for the upper and the bottom zones. The upper and bottom edges $Y_c^{'}/Y_c^{"}$ of the bounding rectangles are used:

$$P_y^{VU} = \sum_{x=1}^{W} Y_c^{'},\ P_y^{VD} = \sum_{x=1}^{W} Y_c^{"},\ \ P_y^V = P_y^{VU} + P_y^{VD} \qquad (1)$$

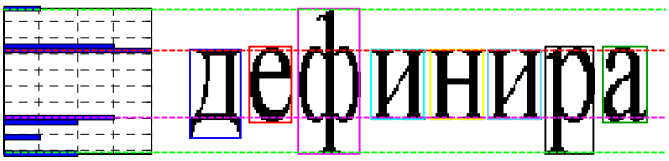

Figure 5. Profile of the symbol bounding rectangles

The text lines are analyzed on base of the found profile. All local maximums are detected in the profile - y is a local maximum if:

$$P_{y-1}^V < P_y^V \ and \ P_{y+1}^V < P_y^V \qquad (2)$$

During the local maximums detection the profile values less than a defined minimum value are not used.

The lines defining X-height appear global maximums corresponding in P_{VU} and P_{VB}:

Upper line - $L_u = \arg\max_y P_y^{VU}$

Base line - $L_b = \arg\max_y P_y^{VD}$

X-height is determined by:

$$H_X = L_b - L_u \quad (3)$$

If this line distance H_X is more than the threshold $H_{X\min}$ the given text line is accepted for an analyzing and opposite if is less than the threshold the text line is rejected:

$$H_X > H_{X\min} \quad (4)$$

The threshold is determined on the base of the supposed minimal font's size S_{min}:

$$H_{X\min} = 0.5\frac{S_{\min}}{72.27}R \quad (5)$$

Typically S_{min} = 8 pt. R is e the scanning resolution. In the below researches are applied *R=300 dpi*.

The rest local maximums are used for a founding the others dividing lines:

Top line - L_t - within the borders of $y = 0 \div L_u - 1$

Bottom line - L_d - within the borders of $y = L_b + 1 \div H$

B. Features extraction

One of the main text line features is the X-height determined by (3).

Typically the upper and bottom zones' heights are approximately 40-60% of the X-height. Because of this if the corresponding local maximum is outside of this zone are assumed that this dividing line and its corresponded zone do not exist.

The goal of the next step is to decrease the influence of the non-character components (".", "," and etc.) and the small objects (noise appears during the scanning). The components are filtered referring to the criteria:

a) The area A_c of the connected components to be bigger than a given threshold T_p:

$$A_c = \sum_x^{W_c}\sum_y^{H_c} B_{xy}^c > T_P \quad T_P = 0.2H_X^2, \quad (6)$$

where B_{xy}^c are pixels of the connected component/object *c*.

b) The components' sizes W_c and H_c to be in the defined boundaries:

$$\begin{aligned} T_{W\max} \ge W_c \ge T_{W\min} \quad W_c = X_c^{''} - X_c^{'} + 1 \\ T_{H\max} \ge H_c \ge T_{H\min} \quad H_c = Y_c^{''} - Y_c^{'} + 1 \end{aligned} \quad (7)$$

The concrete thresholds depend on the possible symbols in the script, and for the Latin and Cyrillic they are in the ranges:

$$\begin{aligned} T_{W\max} = 1.8 \div 2.0H_X \quad T_{W\min} = 0.05 \div 0.15H_X \\ T_{H\max} = 1.8 \div 2.2H_X \quad T_{H\min} = 0.7 \div 0.8H_X \end{aligned} \quad (8)$$

If the rejected connected components exceed 40% the text line is eliminated from the analyzing. The normalized connected components area is the percentage content of black/object elements in one connected component:

$$A_c^{'} = \frac{A_c}{W_c H_c} \quad (9)$$

The averaged value of this area A_v is used as a next feature, playing an important role in the font weight determination:

$$A_v = \sum_{c=1}^{C} A_c^{'}, \quad (10)$$

where C is the connected components' number after their filtration.

The next feature is the averaged value of the components bounding rectangles widths:

$$W_v = \sum_{c=1}^{C} W_c \,. \quad (11)$$

As a next feature is used the transition width between the background-object-background R_k on the cutting lines (black runs). Two cutting lines instead one central are used with a purpose to avoid the strokes in the symbol's center (e, g, к, ж and etc.):

$$L_T^{'} = L_u + 0.25H_X \quad L_T^{''} = L_b - 0.25H_X \quad (12)$$

The average value of the transitions' widths R_v (not bigger than given threshold) for the both lines is the next selected feature:

$$R_v = \frac{1}{K_{L_T}}\sum_k^{K_{L_T}} R_k \;\; for \;\; R_k < 0.4W_v \quad (13)$$

where K_{L_T} is the number of all transitions for both cut lines.

On the base of the horizontal profile P_x^H and its first derivative $P_x^{H'}$:

$$P_x^H = \sum_y^H B_{xy} \quad P_x^{H'} = P_{x+1}^H - P_x^H \quad x = 1 \div W - 1 \quad (14)$$

The profile density P_v is calculated:

$$P_v = \frac{1}{W_S}\sum_x^{W-1} P_x^{H'} \; if \; P_x^H > 0, \quad (15)$$

where W_S is the total width of CC, excluding overlaying.

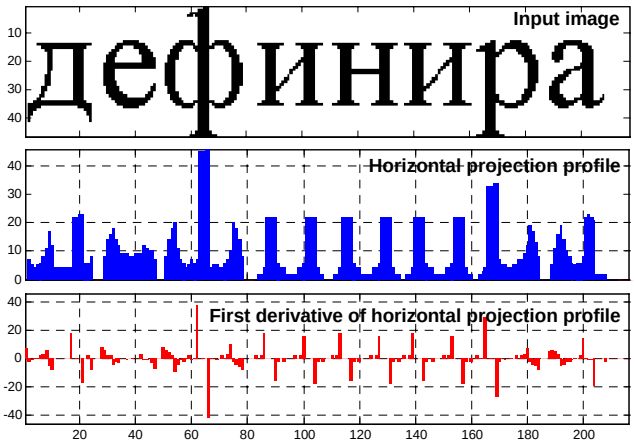

Figure 6. Horizontal profile and its first derivative

Only the parts of the profile, where the connected components (CC) are projected, are taken into account. The

purpose is to avoid the empty spaces between letters and words. For a better distinguish between serif and sanserif typeface fonts the contour elements (CE) of the connected components are used. CE is determined by applying of 8 masks in the 3x3 pixels region (white – background, colored – object, gray – value does not matter):

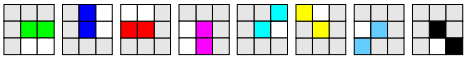

Figure 7. Contour elements masks

For a influence decreasing of the text content only CE are used, which are positioned in the upper and bottom edge of CC:

$$B_{xy} \ for\ y \in \left[Y_c^{'}, Y_c^{'} + 0.2H_c\right] \cup \left[Y_c^{''}, Y_c^{''} - 0.2H_c\right] \quad (16)$$

For each mask m is obtained a CC number e_c^m, which is normalized with the CC area:

$$E_c^m = e_c^m / A_c .$$

An average value is used as a final feature:

$$E_v^m = \frac{1}{C}\sum_{c=1}^{C} E_c^m,\ m = 1 \div M = 8 \quad (17)$$

C. Neural Network classification

A completely connected back propagation neural network is applied with 14 inputs, 700 neurons in the hidden layer and 144 in the output layer. Each output neuron corresponds to a given font and its target value is binary (0/1).

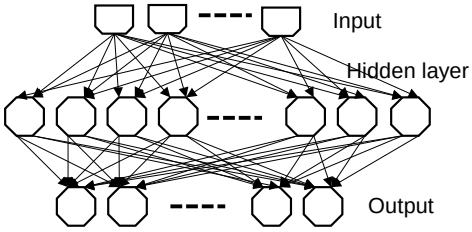

Figure 8. A back propagation neural network classifier structure

V. Experimental Results

A set of 12 typeface fonts is used, 3 sizes (10, 12, 14 pt) and 4 combinations of weight/slope (Normal, Italic, Bold, BoldItalic) - total 138 fonts (AGRevueCyr doesn't have Bold and BoldItalic). Automatically were generated 50 text lines for each font (total 7200 images of text lines). The width of text lines is arbitrary (from 2 to 9 words/15 to 60 characters).

The neural network was learned with all 7200 input images entered on the occasionally order with 1000 epochs/iterations.

The classification is tested with 10 text lines for each font (1380). The test images are obtained with scanning of real documents (hard copies).

The achieved classification rates is given in the below table.

TABLE1.
THE FONTS CLASSIFICATION RATE EXPERIMENTAL RESULTS

Size	10 pt				12 pt				14 pt			
Typeface	N	B	I	BI	N	B	I	BI	N	B	I	BI
AGRevueCyr	98.63	-	97.77	-	99.80	-	99.54	-	99.94	-	99.84	-
Arial	96.24	96.99	95.98	96.07	97.62	97.91	96.89	97.33	98.57	98.92	96.84	97.27
Balkan	97.89	98.01	95.68	96.93	98.92	98.73	97.60	97.89	98.57	98.92	97.74	98.37
CourierNew	97.70	97.96	97.08	97.45	98.77	98.92	97.58	97.76	98.99	98.87	97.71	97.66
Hebar	97.30	97.69	97.46	97.80	98.65	99.09	97.86	97.59	99.00	99.24	97.99	97.90
Kudriashov	97.50	98.45	97.23	97.99	98.49	98.68	96.14	97.33	98.14	98.52	96.90	96.85
Lazurski	97.81	97.90	98.02	97.97	97.68	97.98	96.30	97.62	97.88	98.04	97.55	97.86
LozenCondensed	96.48	96.69	95.00	95.99	96.23	96.64	95.07	97.41	98.28	98.67	98.06	98.22
Maritsa	97.13	97.52	97.09	97.63	98.48	98.92	97.69	97.68	98.83	98.48	95.78	97.73
Peterburg	96.43	97.26	96.31	96.08	97.77	97.93	96.53	97.12	98.27	98.74	97.00	97.28
Times New Roman	96.24	96.99	95.98	96.07	97.62	97.91	96.89	97.33	98.57	98.92	96.84	97.27

VI. Conclusion

In this paper we have presented a font identification model, which uses the Neural Network classifier, capable to perform a-priori OFR. The training of the system was carried out using dominated lowercase letters, and including also uppercase letters and digits of the considered fonts. The recognition rate for characters reaches 95.75- 100%. The work has proved that the suggested 14 topographic features are suitable for the font identification. The parameters like size, slope and weight are recognized with very high accuracy. The font's family parameter remains with no so high classification rate. The font families which are differ from others (like AGRevueCyr) are easy for recognition.

Some improvements can be done in future: determination of the discrimination possibilities of the features; evaluation of the text line length influence (number of symbols); taking in account the text lines with dominated capital letters. The next step will be to implement "OFR+OCR" module aimed at document characterization or classification.

References

[1] A. Zramdini, R. Ingold, "Optical Font Recognition Using Typographical Features", *IEEE Trans. On PAMI*, Vol. 20, N:8, 1998.

[2] S. La Manna, A. M. Colla, A. Sperduti, "Optical Font Recognition for Multi-Font OCR and Document Processing".

[3] A. Zramdini, R. Ingold, "Optical Font Recognition from Projection Profiles", *Electronic Publishing*, Vol. 6, 1993.

[4] M. C. Jung. Y. C.Shin, S. N. Srihari, "Multi-font Classification using Typographical Attributes". http://www.math.unipd.it

[5] S. Ozturk, B. Sankur, "Font Clustering and Cluster Identification in Document Images".

[6] A. Zramdini, R. Ingold. "A Study of Document Image Degradation Effects on Font Recognition", 3-th Int. Conf. of Document Analysis and Recognition, Montreal, Canada, ICDAR 1995.

[7] T. K. Ho. "Fast Identification of Stop Words for Font Learning and Keyword Spotting", Bell Laboratories.

[8] D. Dordevic, L. Josifovski, D. Mihajlov. "Character Shape Preclassification in Mixed Script OCR for Macedonian Language", 18-th Int. Conf. Information Technology Interfaces ITI, Pula, Croatia, 1996.

Calculation of the Sampling Losses for Nonuniformly Sampled Data

Rossen G. Miletiev[1], Slavcho Lishkov[2]

Abstract - **A new definition of the optimum nonuniform sampling sequence is proposed. This definition is based on the spectrum analysis of nonuniformly sampled data according to Koh-Wicks-Sarkar spectrum estimation equation. Also simulation results are represented to calculate the sampling losses in comparison with the uniform sampling scheme.**

Keywords - **spectrum analysis, nonuniformly sampled data**

I. INTRODUCTION

Nonuniformly sampled data occurs in several applications such as geophysics [1], Laser Doppler Anemometry (LDA) [2], oscilloscopes [3] and radar or sonar signal processing [4]-[5]. Such type of data is used by the system designers to avoid aliasing in the signal spectrum or due to the technical problems, it is sometimes impossible to perform regular sampling.

Several methods for spectrum analysis of the nonuniformly sampled data is proposed, such as Lomb periodogram [6], Koh-Wicks-Sarkar equation [5], Dirichlet transformation [7], SECOEX method [8], non-uniform DFT [9] and some approximation methods [10]-[11]. But only few publications examine closely the problem with the optimum sampling sequences based on these spectrum estimation methods. These publications study the effect of the sampling scheme on the estimation performance and define the optimum sampling sequence for the alias frequency suppression to obtain low-aliasing spectrum estimation methods.

This paper studies the sampling losses of the nonuniformly sampled data depending on the sampling scheme and defines an equation for the optimal sampling sequence.

II. MATHEMATICAL BACKGROUND

Lets a continuous complex signal *x(t)* is sampled at time instants, $t=t_k$, $k=0,1,..,N$-1. The frequency response $E(j\omega)$ at frequency ω of the sequence is estimated by the equation [5]:

$$E(j\omega)=\frac{\sum_{k=0}^{N-1}x(t_k)\cos\omega(t_k-\tau)}{\sqrt{\sum_{k=0}^{N-1}\cos^2\omega(t_k-\tau)}}+j\frac{\sum_{k=0}^{N-1}x(t_k)\sin\omega(t_k-\tau)}{\sqrt{\sum_{k=0}^{N-1}\sin^2\omega(t_k-\tau)}} \quad (1)$$

where τ is a free parameter, defined as:

$$\tan(2\omega\tau)=\frac{\sum_{k=0}^{N-1}\sin 2\omega t_k}{\sum_{k=0}^{N-1}\cos 2\omega t_k} \quad (2)$$

The equation (2) can be written in the following way:

$$\sum_{k=0}^{N-1}\sin 2\omega(t_k-\tau)=0\cdot \quad (3)$$

If we note the expression $\mu=\sum_{k=0}^{N-1}\cos 2\omega(t_k-\tau)$ and substitute the equation (3) in this expression, then the following equations can be written:

$$\sum_{k=0}^{N-1}\sin^2\omega(t_k-\tau)=\frac{1}{2}(N-\mu) \quad (4)$$

$$\sum_{k=0}^{N-1}\cos^2\omega(t_k-\tau)=\frac{1}{2}(N+\mu) \quad (5)$$

$$\sum_{k=0}^{N-1}\sin\omega(2t_k-\tau)=\mu\sin\omega\tau \quad (6)$$

$$\sum_{k=0}^{N-1}\cos\omega(2t_k-\tau)=\mu\cos\omega\tau \quad (7)$$

In this case we define the optimal sampling sequence as the time sampling sequence, which sets the spectrum peaks of the input signal to its maximum value.

If the signal contains the frequency component ω_0, then the optimal sampling sequence satisfies the following equation:

$$|E(\omega_0)|^2=\max \quad (8)$$

So, if we perform the input complex signal *x(t)* as a sum of two signals $x(t)=x_1(t)+jx_2(t)=\cos\omega_0 t+j\sin\omega_0 t$, then the frequency response of the input signal is a sum of the partial frequency responses:

$$E(\omega_0)=E_1(\omega_0)+jE_2(\omega_0) \quad (9)$$

Each partial frequency response can be estimated by the equation (1). So if we substitute the equations (4) – (7) in the partial frequency responses $E_1(\omega_0)$ and $E_2(\omega_0)$, then the final expressions can be written as:

$$E_1(\omega_0)=\frac{1}{\sqrt{2}}\sqrt{N+\mu}\cos\omega_0\tau-j\frac{1}{\sqrt{2}}\sqrt{N-\mu}\sin\omega_0\tau \quad (10)$$

$$E_2(\omega_0)=\frac{1}{\sqrt{2}}\sqrt{N+\mu}\sin\omega_0\tau+j\frac{1}{\sqrt{2}}\sqrt{N-\mu}\cos\omega_0\tau\cdot \quad (11)$$

Therefore, the frequency response of the input signal can be estimated by equations (9) - (11):

$$E(\omega_0)=\frac{1}{\sqrt{2}}\cos\omega_0\tau\left(\sqrt{N+\mu}-\sqrt{N-\mu}\right)+ j\frac{1}{\sqrt{2}}\sin\omega_0\tau\left(\sqrt{N+\mu}-\sqrt{N-\mu}\right) \quad (12)$$

The power spectrum can be estimated by the equation (12):

$$|X(\omega_0)|^2=N+\sqrt{N^2-\mu^2} \quad (13)$$

[1]Rossen Miletiev is with the Technical University of Sofia, 8 Kl. Ohridski Blvd, 1000 Sofia, Bulgaria, E-mail: miletiev@yahoo.com

[2]Slavcho Lishkov is with the Technical University of Sofia, 8 Kl. Ohridski Blvd, 1000 Sofia, Bulgaria

So, the optimal sampling scheme satisfies the equation:

$$\mu = 0 . \tag{14}$$

So, the optimal sampling scheme is up to the following requirements according to equations (3) and (14):

$$\begin{cases} \sum_{k=0}^{N-1} \cos 2\omega_0 t_k = 0 \\ \sum_{k=0}^{N-1} \sin 2\omega_0 t_k = 0 \end{cases} \tag{15}$$

The uniform sampling sequence defines the time samples according to the equation $t_k=kT$, which modifies the equation (15) to the following term:

$$\begin{cases} \sum_{k=0}^{N-1} \cos 2\omega_0 t_k = \dfrac{\sin N\omega_0 T}{\sin \omega_0 T} \cos(N-1)\omega_0 T \\ \sum_{k=0}^{N-1} \sin 2\omega_0 t_k = \dfrac{\sin N\omega_0 T}{\sin \omega_0 T} \sin(N-1)\omega_0 T \end{cases}, \tag{16}$$

$$\text{where } \omega_0 = 2\pi k f_0 = 2\pi k \, f_s / N .$$

Therefore, the uniform sampling scheme is optimal according to equation (15), because it satisfies the both trigonometric sums for the frequencies, defined by the Fourier transform.

The nonuniform sampling case is difficult to be analyzed because the equation (15) can not be solved in the general case. By reason of this circumstance, we will analyze the sampling losses, which are generated by the deviation of the used sampling sequence from the optimal one.

To analyze the sampling losses, we assume the sampling scheme, shown at Fig.1.

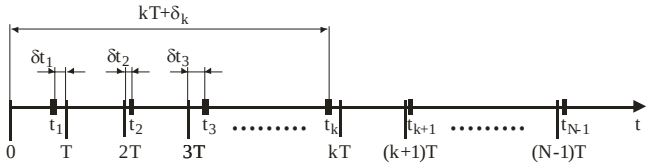

Fig.1. Sampling diagram

The sampling losses are evaluated by the equation:

$$\varepsilon = \frac{|X(\omega_0)|^2}{|X(\omega_0)|^2_{\max}} = \frac{1+\sqrt{1-\left(\dfrac{\mu}{N}\right)^2}}{2} \tag{17}$$

Therefore, the sampling losses vary from 0dB to 3dB according to parameter value μ/N (Fig.2).

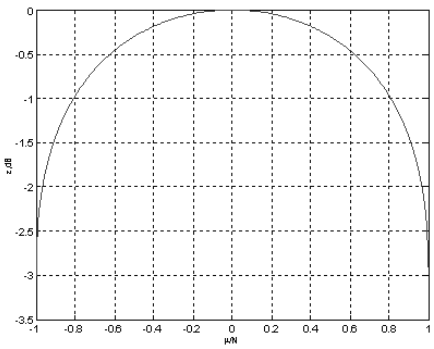

Fig.2. Sampling losses vs. parameter μ/N

The shown figure displays that the sampling losses can be neglected if the parameter value μ/N is smaller than 0,3. In this case the losses are smaller than 0,1dB, which defines such types of sampling schemes as quasi-optimal ones.

When the parameter value μ/N exceeds this limit, the losses increased very fast and they are equal to 1dB when the analyzed parameter is set to 0,8.

III. Simulation Results

The influence of the sampling sequence over the sampling losses is calculated by simulation using MATLAB routine. We implement three times per 100 independent generation of sampling instants δ_k, which are uniformly distributed in the following intervals:

- $\delta_k \le 1/2 T$
- $\delta_k \le 1/4 T$
- $\delta_k \le 1/8 T$.

Then we calculate the sampling losses in these three simulations according to equation (17) using equations (4)-(7) below and above Nyquist limit for each case.

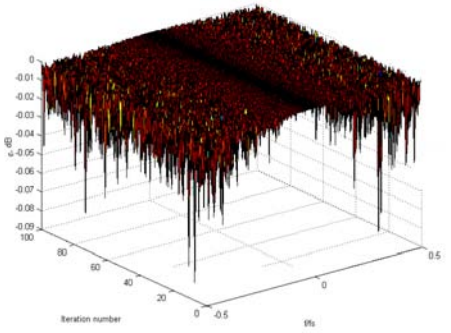

(a)

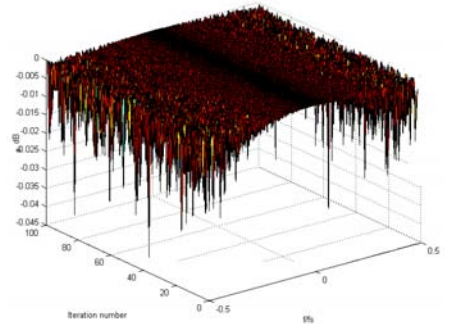

(b)

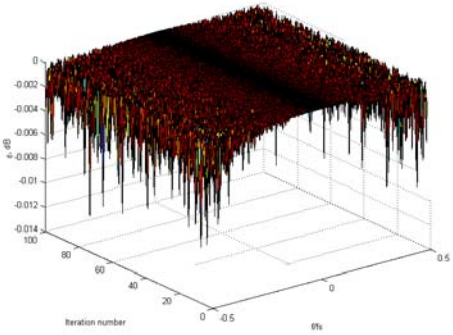

(c)

Fig.3. Sampling losses below Nyquist limit

The simulation results below Nyquist frequency in these three cases are shown at Fig.3a-c respectively. The simulation results show that the maximum sampling losses are reduced from 0,1dB to 0,01dB while the sampling instants δ_k are decreased from $^1/_2$T (Fig.3a) to $^1/_8$T (Fig.3c).

The simulation results are totally different when we calculate the sampling losses above Nyquist limit. In this case the simulation results are represented at Fig.4a-c for the chosen sampling instants intervals.

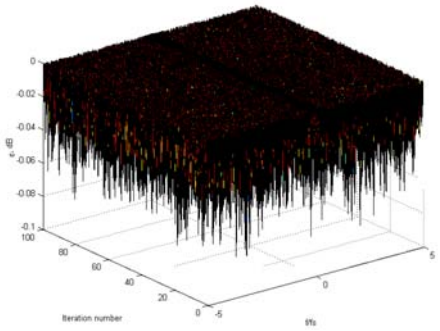

(a)

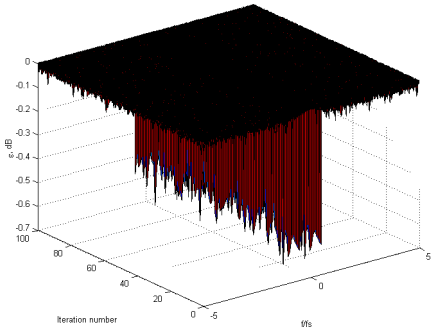

(b)

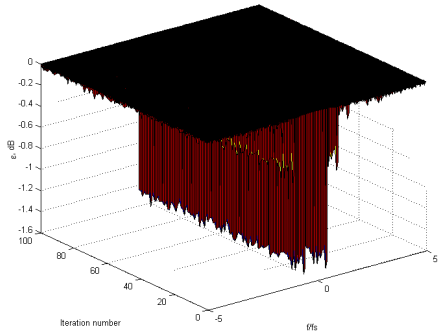

(c)

Fig.4. Sampling losses above Nyquist limit

The shown figures display that the sampling losses remain unchanged when the analyzed frequencies differ from the values $f = {kf_s}/{2} = {k}/{2T}, k = \pm1,\pm2,....,\pm\infty$.

When the chosen frequencies are much closed to these values, the sampling losses increased very quickly from 0,1dB to 1,6dB while the sampling instants δ_k are decreased from $^1/_2T$ (a) to $^1/_8T$ (c).

The represented results show that the sampling losses remain below 0,1dB while the sampling intervals satisfy the equation $\delta_k \le {}^1/_2T$. These losses are nearly independent from the chosen sampling intervals.

IV. Conclusion

This paper studies the sampling losses of the nonuniformly sampled data depending on the sampling scheme and defines an equation for the optimal sampling sequence.

The sampling losses are calculated according to the sampling interval choice and an optimal nonuniform sampling scheme equation is defined. The simulation results show that the sampling losses are very small and they are nearly independent from the chosen sampling scheme while the sampling intervals do not exceed $^1/_2T$ limit.

Therefore, this sampling scheme is recommended due to its low sampling losses and low aliasing frequency response at very wide frequency range.

References

[1] P. Yuou, E. Baert and M. F. Loutre, “Spectral analysis of climate data,” *Surv. Geophys.*, vol. 17, pp. 619–663, 1996.

[2] C. Tropea, “Laser doppler anemometry: Recent developments and future challenges,” *Meas. Sci. Technol.*, vol. 6, pp. 605–619, 1995.

[3] Y. Rolain, J. Schoukens, and G. Vandersteen, “Signal reconstruction for non-equidistant finite length sample sets: A “KIS” approach,” *IEEE Trans. Instrum. Meas.*, vol. 47, pp. 1046–1052, 1998.

[4] R.Pribic, “Radar irregular sampling,” *ICASSP 2004*, vol.3, pp.933-936, 2004.

[5] J. Koh, T. Sarkar and M. Wicks, ‘Spectral analysis of nonuniformly sampled data using a least square method for application in multiple PRF system,” *Proceedings of IEEE International Conference on Phased Array Systems and Technology 2000*, pp. 141 -144

[6] N. Lomb, “Least square frequency analysis unequally sampled data,” *Aerophysics and space science*, vol.39, pp.447-462, May, 1975

[7] M. Tuszynski and A. Wojtkiewicz, “Application of the Dirichlet transform in analysis of nonuniformly sampled signals,” 1992 IEEE International Conference on Acoustics, Speech, and Signal Processing ICASSP-92, May 23-26, 1992, San Francisco, USA, Vol. 5, pp.25-28

[8] W. Chen, G. Zhou and G. Giannakis, “Velocity and acceleration estimation of doppler weather radar/lidar signals in coloured noise,” *IEEE International Radar Conference*, 1995, pp.2052-2055

[9] Qing Huo Liu and Nhu Nguyen, “An accurate algorithm for nonuniform fast Fourier transform (*NUFFT*’s),” *IEEE Microwave and guided wave letters*, Vol.8, No.1, 1998, pp.18-20

[10] D. Bland, T. Laakso and A. Tarczynski, “Analysis of algorithms for nonuniform-time discrete Fourier transform,” *IEEE International Symposium on Circuits and Systems* ISCAS '96, Vol. 2 , 12-15 May 1996, pp: 453 -456

[11] D. Bland, T. Laakso and A. Tarczynski, “Spectrum estimation of non-uniformly sampled signals,” *Proceedings of the IEEE International Symposium on Industrial Electronics*, ISIE '96, Vol.1, 17-20 Jun 1996, pp. 196 -200

Fingerprints Compression with IDP

Roumen Kountchev [1], Vladimir Todorov [2], Roumiana Kountcheva[2]

Abstract - **In this paper new algorithm for compression of grayscale fingerprint images is presented. The algorithm is based on the Inverse Difference Pyramid Decomposition, followed by lossless compression of the obtained data. For the lossless compression is used adaptive run-length coding. The results of the compression are compared with those, obtained with software, based on the wavelet decomposition.**

Keywords **– Image coding, grayscale fingerprints compression**.

I. INTRODUCTION

The problem of effective fingerprint images compression is an object of many research and application works [1,2,3,6,8,9]. The method Wavelet Scalar Quantization (WSQ) has been adopted by the Federal Bureau of Investigations (FBI) as its standard for fingerprint compression [1]. It involves three steps: a Discrete Wavelet Transform (DWT), adaptive scalar quantization of the wavelet coefficients and a two-pass Huffman coding. The still image compression standard JPEG2000 [4] ensures even better results for fingerprints compression.

The aim of this paper is the presentation of new efficient algorithm for lossless and visually lossless compression of grayscale fingerprint images. It is based on the Inverse Difference Pyramid (IDP) [5] method for image decomposition with Walsh-Hadamard Transform. The data, obtained in result, is processed with new adaptive run-length data coding and entropy coding. In Section II are presented the main steps of the algorithm, in Section III are given the results, compared with those, obtained with the FBI free software for fingerprints compression [6] and with methods based on the JPEG2000 standard [7] and are pointed some of the main advantages of the presented method, compared with the known ones**.** Section IV presents the main applications of the method and its future development.

II. ALGORITHM FOR IMAGE COMPRESSION

The algorithm is developed on the basis of the two-level Inverse Difference Pyramid (IDP) method for image decomposition [5]. In correspondence with this decomposition each image block [B(8)] with size 8 x 8 pixels is described with the relation:

$$[B(8)] = [\tilde{B}_0(8)] + [E_0(8)]. \quad (1)$$

[1]Roumen Kountchev is with the FCTT, Radiocom. Dept., Technical University of Sofia, Bul. Kl. Ohridsky 8, Sofia, Bulgaria, E-mail: rkountch@tu-sofia.bg

[2]Vladimir Todorov and Roumiana Kountcheva are with T&K Engineering, Mladost 3, P.O.Box 12, Sofia 1712, Bulgaria, E-mails: todorov_vl@yahoo.com. kountcheva_r@yahoo.com

Here $[\tilde{B}_0(8)]$ and $[E_0(8)]$ are matrices with size 8x8 elements each, which represent the first and the second component of the IDP decomposition for levels p = 0,1 respectively. The first one, $[\tilde{B}_0(8)]$ is approximation of the block [B(8)], and the second one $[E_0(8)]$ is a difference matrix, representing the approximation error.

The compression algorithm is described with the following steps:

1. The image matrix is divided in blocks [B(8)], with total number m×n.

2. The component $[\tilde{B}_0(8)]$ for the level p = 0 is calculated, using the two-dimensional inverse Walsh-Hadamard Transform [4].

$$[\tilde{B}_0(8)] = (1/64)[H_0(8)]^{-1}[\tilde{S}_0(8)][H_0(8)]^{-1}, \quad (2)$$

where $[H_0(8)]$ is Walsh-Hadamard matrix with size 8x8 elements,

$$\tilde{s}_0(u,v) = m_0(u,v)s_0(u,v), \quad (3)$$

is a coefficient with frequency (u,v) in the transform $[\tilde{S}_0(8)]$ of the component $[\tilde{B}_0(8)]$, and

$$m_0(u,v) = \begin{cases} 1 \text{ if } (u,v) \in V_0; \\ 0 - \text{in other cases,} \end{cases} \text{ for u,v=0,1, ... ,7} \quad (4)$$

is the element (u,v) of the binary matrix-mask $[M_0(8)]$ with size 8×8. This mask defines the area of the retained coefficients V_0 in the transform $[\tilde{S}_0(8)]$.

In relation (3) $s_0(u,v)$ are the elements of the transform matrix $[S_0(8)]$. It is defined with the direct two-dimensional Walsh-Hadamard Transform of the block [B(8)] in accordance with:

$$[S_0(8)] = [H_0(8)][B(8)][H_0(8)] \quad (5)$$

In particular, if $m_0(u,v)=1$ and for u,v = 0,1 the total number of the retained coefficients in the area V_0 is 4.

3. The component $[E_0(8)]$ is defined for the level p = 1 in accordance with the relation:

$$[E_0(8)] = [B(8)] - [\tilde{B}_0(8)] \quad (6)$$

4. The difference matrix $[E_0(8)]$ is divided in four sub-matrices for the level p = 1

$$[E_0(8)] = \begin{bmatrix} [E_0^1(4)] & [E_0^2(4)] \\ [E_0^3(4)] & [E_0^4(4)] \end{bmatrix}, \quad (7)$$

where each is defined as follows:

$$[E_0^k(4)] = (1/16)[H_1(4)]^{-1}[S_1^k(4)][H_1(4)]^{-1} \text{ for } k = 1,..,4 \quad (8)$$

Here $[H_1(4)]$ is a Walsh-Hadamard Matrix with size 4x4 elements, and

$$[S_1^k(4)] = [H_1(4)][E_0^k(4)][H_1(4)] = \begin{bmatrix} s_1^k(0,0) & s_1^k(1,0) & s_1^k(2,0) & s_1^k(3,0) \\ s_1^k(0,1) & s_1^k(1,1) & s_1^k(2,1) & s_1^k(3,1) \\ s_1^k(0,2) & s_1^k(1,2) & s_1^k(2,2) & s_1^k(3,2) \\ s_1^k(0,3) & s_1^k(1,3) & s_1^k(2,3) & s_1^k(3,3) \end{bmatrix} \quad (9)$$

is the transform of the sub-matrix $[E_0^{k_1}(4)]$ with size 4x4 elements, and $s_1^k(u,v)$

5. The coefficients $s_p(u,v)$ are defined for the corresponding IDP level p of each block, [B(8)], in correspondence with Table 1.

TABLE 1.
DEFINITION OF COEFFICIENTS

Level	Type of coefficients $s_p(u,v)$	Total number of coefficients Σ_p
p = 0	$s_0(u,v)$ for u,v = 0,1	$\Sigma_0 = \sum_{u=0}^{7}\sum_{v=0}^{7} m_0(u,v) = 4$
p = 1	$s_1^k(u,v)$ for u,v = 0,1,2,3 and k = 1, 2, 3, 4	$\Sigma_1 = 4\times16 = 64$

6. The coefficients $s_p(u,v)$ are arranged from the two-level IDP blocks in corresponding sub-bands.

- for p = 0 the corresponding sub-band with spatial frequency (u,v) is described with a matrix with size m×n:

$$[S_0(u,v)] = \begin{bmatrix} s_0^1(u,v) & s_0^2(u,v) & .. & s_0^m(u,v) \\ s_0^{m+1}(u,v) & s_0^{m+1}(u,v) & .. & s_0^{2m}(u,v) \\ .. & .. & .. & .. \\ s_0^{m(n-1)}(u,v) & s_0^{m(n-2)}(u,v) & .. & s_0^{mn}(u,v) \end{bmatrix} \quad (10)$$

u, v = 0,1;

- for p = 1 the corresponding sub-band with spatial frequency (u,v) is described with a matrix with size m×n:

$$[S_1(u,v)] = \begin{bmatrix} [S_1^1(u,v)] & [S_1^2(u,v)] \\ [S_1^3(u,v)] & [S_1^4(u,v)] \end{bmatrix}, \; u,v = 0,1,2,3, \quad (11)$$

where:

$$[S_1^k(u,v)] = \begin{bmatrix} s_0^{k,1}(u,v) & s_0^{k,2}(u,v) & ... & ... & s_0^{k,m/2}(u,v) \\ s_0^{k,\frac{m}{2}+1}(u,v) & s_0^{k_1,\frac{m}{2}+2}(u,v) & ... & ... & s_0^{k,m}(u,v) \\ ... & ... & ... & ... & ... \\ ... & ... & ... & ... & ... \\ s_0^{k,\frac{m}{2}(\frac{n}{2}-1)}(u,v) & s_0^{k,\frac{m}{2}(\frac{n}{2}-2)}(u,v) & ... & ... & s_0^{k,\frac{mn}{4}}(u,v) \end{bmatrix} \quad (12)$$

is a sub-matrix with size (m/2)×(n/2) and number k = 1, .., 4.

7. Each sub-band (u,v) is processed using a "meander" scan in horizontal direction (Figure 1) correspondingly for levels p = 0,1 and the obtained coefficients α_I are arranged in one-dimensional massif $\{\alpha_I\}$ for i =1,2,..,(68×m×n).

8. The numbers from the massif $\{\alpha_I\}$ are processed with adaptive RLE:

- The histogram $h(\alpha_I)$ of the numbers α_I is calculated;
- The "free" intervals in the histogram are calculated, where $h(\alpha_I) = 0$ for i = s, s+1, . . , k;
- The most frequent lengths $L_0(i)$ of sequential zero values in the massif $\{\alpha_I\}$ are represented with codes, which are defined with the values of i in the "free" intervals;
- The lengths L(i) of the series of zeros, whose values are outside the "free" intervals of the histogram $h(\alpha_I)$, are coded in accordance with the usually used for the RLE way, with code words containing the zero value and the number of its consecutive appearances;

9. The sequence $\{\beta_I\}$, prepared after adaptive RLE of the one-dimensional massif $\{\alpha_I\}$, obtained in step 8 is coded with entropy coding [3]. The compressed sequence obtained in result is $\{\chi_I\}$.

10. Each sub-band (u,v) from levels p = 0,1 obtained at the end of step 6 is processed sequentially following "meander" scan in vertical direction. After that are preformed steps 8 and 9 and at the end of step 10 the corresponding compressed data is arranged in the sequence $\{\delta_I\}$.

11. The final combination of compressed data $\{\nu\}$ representing the processed image is selected in result of the comparison of the lengths of the two sequences $D\{\delta_I\}$ and $D\{\chi_I\}$. In case, that $D\{\delta_I\} \geq D\{\chi_I\}$ is accepted that $\{\nu\} \equiv \{\chi_I\}$, else - $\{\nu\} \equiv \{\delta_I\}$. The selected sub-band scan direction is notified with a special flag bit in the compressed data header.

The decompression is performed applying over $\{\chi_I\}$ the already described operations in inverse order.

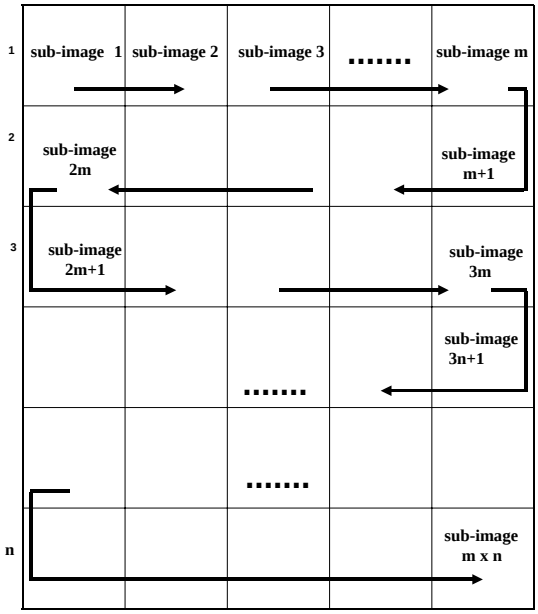

Figure.1. "Meander" scan of the sub-image blocks (horizontal direction).

III. RESULTS

The method efficiency was evaluated using the free FBI software for fingerprints compression (lossy compression) and Algovision LuraTech [7] (lossless compression). All IDP results are obtained with TKView, implementing the IDP method.

For the research were used several hundred grayscale fingerprints images with size 288x353 pixels. Example test images are shown in Figure 2.

Figure 2.a,b. Test images.

The fingerprint images have some peculiarities, which are important for their processing and compression. One of them is that their histograms differ from those of the natural pictures very much. This is shown in Figure 3. The main energy of the fingerprint histogram is concentrated in relatively small number of values, while for usual natural image this arrangement is more uniform. This helps to increase the run-length coding efficiency because there are "free" areas in the histogram. Another peculiarity is that the orientation of the lines in the image has higher correlation with some of the two-dimensional Walsh-Hadamard functions and the number of meaning and non-meaning coefficients varies depending on the direction of the sub-blocks' meander scan (in horizontal or vertical direction). In result, the compression ratio is higher when the proper direction was chosen. In order to increase the compression ratio, the scan was performed twice, and the better result was selected.

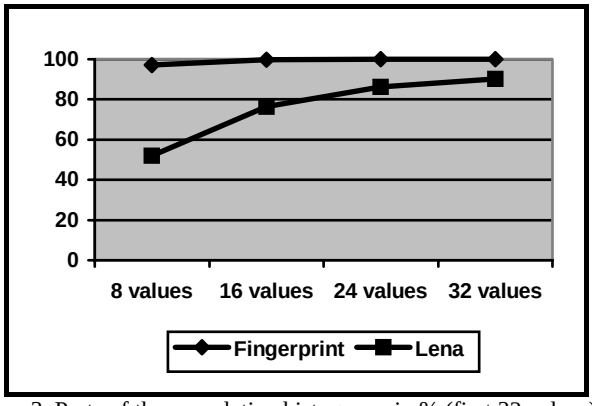

Figure 3. Parts of the cumulative histograms in % (first 32 values) for test image "Lena" and test fingerprint image from Fig.2.a.

Comparison with the FBI standard. The comparison results for visually lossless compression are presented in Figure 4.a,b.:

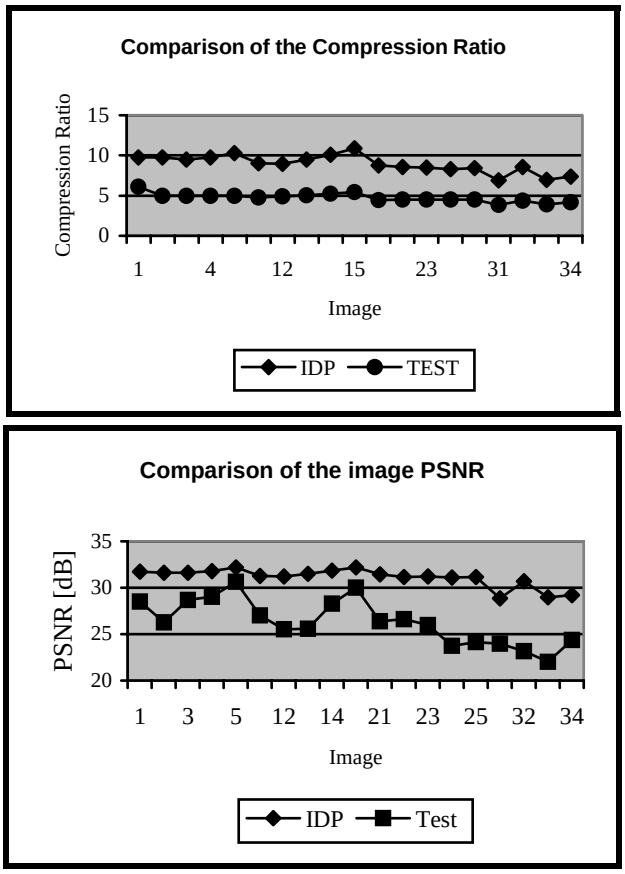

Figure 4.a,b. Comparison results for IDP and FBI standard.

The results in Figure 4 show that the compression ratio obtained with the IDP method is much higher than that with the FBI free software and together with this the quality of the restored IDP images is better (PSNR is higher).

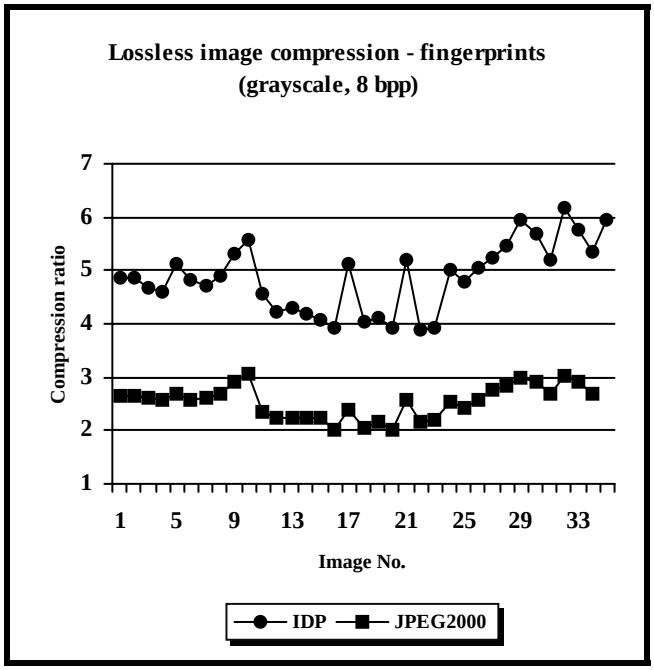

Figure 5. Graphic presentation of the compression results with IDP and JPEG2000

Comparison with Algovision LuraTech (JPEG2000). The results are shown in Table 1 and Figure 5.

TABLE 2.
LOSSLESS COMPRESSION RESULTS

No.	Image	IDP PSNR=∞	JPEG2000 PSNR=∞
1	01gs	4,88	2,64
2	02gs	4,88	2,65
3	03gs	4,66	2,63
4	04gs	4,59	2,59
5	05gs	5,11	2,70
6	11gs	4,84	2,58
7	12gs	4,70	2,61
8	13gs	4,89	2,69
9	14gs	5,33	2.93
10	15gs	5,56	3,08
11	21gs	4,56	2,34
12	22gs	4,22	2,25
13	23gs	4,29	2,23
14	24gs	4,19	2,24
15	25gs	4,07	2,24
16	31gs	3,91	2,02
17	32gs	5,13	2,40
18	33gs	4,03	2,06
19	34gs	4,11	2,17
20	35gs	3,94	2,01
21	41gs	5,21	2,56
22	42gs	3,89	2,18
23	43gs	3,94	2,19
24	44gs	5,03	2,54
25	45gs	4,80	2,43
26	51gs	5,04	2,57
27	52gs	5,25	2,75
28	53gs	5,48	2,82
29	54gs	5,96	2,99
30	55gs	5,67	2,91
31	61gs	5,21	2,70
32	62gs	6,16	3,03
33	63gs	5,75	2,92
34	64gs	5,35	2,67
35	65gs	5,95	2,97

For the comparison IDP-JPEG2000 was used *Algovision LuraTech* [7], based on the wavelet decomposition. The software offers the option "JPEG2000, lossless compression". The obtained results show that the image quality in both cases is the same, but the compression ratio for IDP is higher.

The results of the investigation show that the IDP compression has certain advantages compared with the FBI standard and with the JPEG2000, as follows:

- The IDP method is more efficient for fingerprint images compression, due to the peculiarities in their coefficients' histograms.
- The results, concerning the image quality and the compression ratio, obtained with the IDP-based TKView are more consistent than those, obtained with the other test programs.
- The computational complexity of the IDP method (respectively - of TKView) is smaller than that of the other methods and corresponding test programs. This results from the fact that the IDP compression uses 2D Walsh-Hadamard transform, which is easier to implement than the wavelet transforms.

The same algorithm is implemented for color images as well. In this case the RGB image is presented as Y, Cr, Cb one and after that each component is processed independently. This approach is interesting for color fingerprint images.

IV. CONCLUSION

The comparison of the obtained results was made for lossless compression (JPEG2000) or for compression with very high quality (FBI test software) of the restored images. This approach was preferred because the image quality is of great importance for the selected class of images (fingerprints). As it is known, the fingerprints databases are increasing very quickly recently and the importance of their efficient compression grows as well.

The further development of the method will continue in following directions:

- Increasing the efficiency of the lossless coding of the coefficients values with arithmetic coding;
- Increasing the method efficiency with adaptive selection of the participating coefficients, retaining the restored image quality;
- Developing new algorithms for lossless compression of color fingerprint images.

REFERENCES

[1] J. Bradley, C. Brislawn, T. Hopper, The FBI Wavelet Scalar Quantization Standard for Grayscale Fingerprint Image Compression, Proceedings of Visual Information Processing II, SPIE Vol. 1961, April 1993, pp. 293–304.

[2] B. Sherlock, D. Monro. Optimized Wavelets for Fingerprint Compression, Proc. of IC on ASSP'1996.

[3] S. Kasaei, M. Deriche, B. Boashash. A Novel Fingerprint Image Compression Technique Using Wavelets Packets and Pyramid Lattice Vector Quantization. IEEE Transactions on Image Processing, Vol. 11, No. 12, Dec. 2002, pp. 1365-1378.

[4] D. Salomon. Data compression. Springer-Verlag, 2004.

[5] R. Kountchev. Image Compression with Recursive IDP Algorithm. ICEST'2003, 16-18 Oct. 2003, Sofia, Bulgaria, pp. 273-276.

[6] Software Package for Finger Prints Compression Version 0.1. Washington University, Dept. of Mathematics, 1993.

[7] www.algovision-luratech.com

[8] ftp://ftp.c3.lanl.gov/pub/WSQ/documents

[9] ftp://ftp.c3.lanl.gov/pub/WSQ/WWWdemo

Comparative Analysis of Genetic and Evolutionary Approaches in the Study of Multilayer Models of the Artificial Neural Networks

Hristo I. Toshev[1] and Chavdar D. Korsemov[2]

Abstract - **The paper makes comparative analysis of artificial neural networks and of evolutionary computation.Multilayer models are introduced with some of their main features from a genetic or evolutionary viewpoint. For the purpose of the study mathematic formalism is applied by penalty functions, based on an apriori set number of the next generations.**

Keywords - **genetic approaches, evolutionary computation, artificial neural networks, multilayer models.**

I. INTRODUCTION

Multilayer models are introduced with some of their basic properties from the genetic and evolutionary points of view. Examples of such models are the generalized evolutionary artificial neural network design model (GEANNDM) and the artificial neural network design model (ANNDM). The chosen ANN models (including the design-, the optimization- and the learning- phases) are animated starting from an evolutionary computation (EC) background, including genetic synthesis. A mathematical formalism is presented for the task of multilayer model investigation by means of penalty functions based on a predefined number of a series of generations.

II. THE ANN MODELS METHODOLOGY

About The Physical Nature Of The ANN Application Tasks

Any specific task has its own concrete physical nature. Therefore the common aspects of the different *categories* or *clusters* from the ANN-application tasks loose from their distinctness. The categorization and the clusterization of the ANN-application tasks may serve as a true prerequisite for the *identification of the common properties of the tasks*. This will guarantee the enhancement and the acceleration of the ANN-design process.

About The Initial Setting of the Possible ANN Architecture

The *initial* setting of the ANN architecture is independent of the ANN parameter optimization and the following training. Therefore it may be done independently of the other sequences in the ANN-design process. The authors present a deductive tree per any of the two ANN architecture types (feedforward and recurrent) in Fig. 1 and Fig. 2. The affirmative branches follow [1] and the most outstanding feature of the affirmative architecture is chosen by the authors for the corresponding fork condition.

1°. If the condition for *linear separability* is valid then the initial architecture is a *single-layer perceptron* else go to 2°.

2°. If the condition for an *approximate optimum* is valid then the initial architecture is a *multilayer perceptron* (*stochastic approximation* is actual) else go to 3°.

3°. If the task is a *multivariable interpolation* then the initial architecture is with *radial basis functions* (*statistical approximation* is actual) else the algorithm ***stops***.

Fig. 1. Feedforward ANN Architecture Initial Setting Algorithm

1°. If the *speed is not critical* to the model performance then the initial architecture is a *Hopfield network* else go to 2°.

2°. If the condition for *pattern stability* is valid then the initital architectture is an *ART* else go to 3°.

3°. If the *dimensions of the input and of the output are equal* then the initial architecture is a *Willshaw - von der Malsburg map* else go to 4°.

4°. If the condition for *data compression* is valid then the initial architecture is a *Cohonen map* else the algorithm ***stops***.

Fig. 2. Recurrent ANN Architecture Initial Setting Algorithm

About The Retraining of the ANN And About Its Upgrade

Based on the genetic and evolutionary approaches the authors offer a *step-by-step optimization* instead of the *element-by-element optimization* (as it is the case with the usual ANN-design process). They consider this aspect as one of the most significant in the ANNDM model. The optimization versions may be defined in different and

[1] Hristo I. Toshev is with the Institute of Information Technologies, Bulgarian Academy of Sciences, Acad. G. Bonchev str., bl. 29A, 1113 Sofia, Bulgaria, E-mail: toshev@iinf.bas.bg

[2] Chavdar D. Korsemov is with the Institute of Information Technologies, Bulgarian Academy of Sciences, Acad. G. Bonchev str., bl. 29A, 1113 Sofia, Bulgaria, E-mail: korsemov@iinf.bas.bg

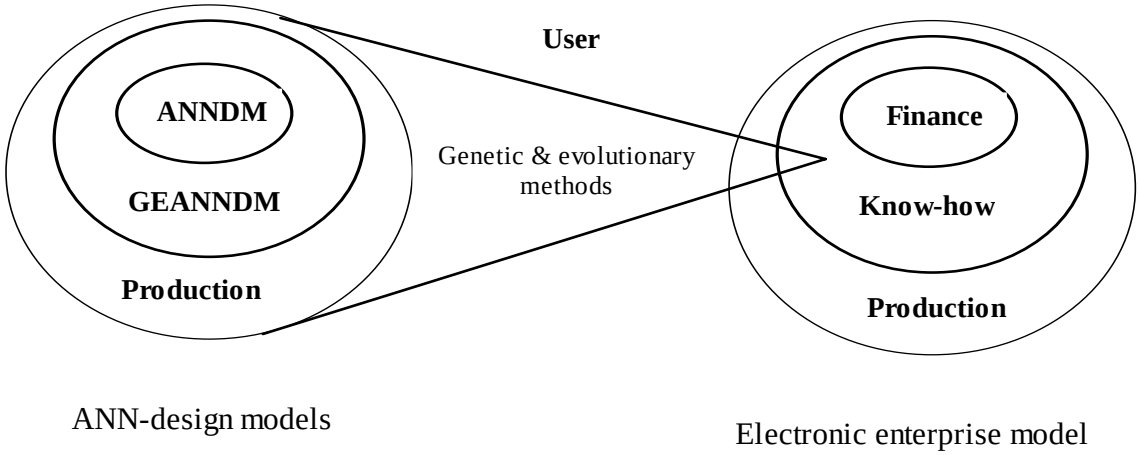

Fig. 3. Interrelations Between Different Multilayer Models

complementary ways which include the simple parameter variations as a private case; these versions are seen to be based on the already mentioned approaches which are not only more powerful but they also include the immediate participation of the designer in the man-machine dialog.

In fact the alternative approach is designed for the effective application of genetic and evolutionary methods. This means that the *fixed* values are replaced by *possible* values. Besides it is possible to output the mathematical formulation of the actual constraints, of the possible crossovers, of the number and of the composition of the generations of the solution elements (i. e. of the admissible given number of done iterations) and also of any possible statistical information. In this sense the authors consider the ANNDM model as a synthesis of a software for mathematical modeling (e. g. MatLab) and of a software for ANN modeling and study (e. g. NeuralWorks Explorer, NeuralWorks Professional II, [2]) *plus additional properties*.

It is clear that this approach lowers the obstacles mainly in the stages of identification of the ANN-application task and also of identification of the training paradigm (supervised, unsupervised or hybrid). The psychological comfort is strongly increased in the form of a proximity and a friendliness for the designer and the apparent reduction of the possible design expenses is already a reality. Also it is quite possible to determine the data representation, the architecture and the training algorithm as a consequence of the identified application task and of the training paradigm respectively.

III. The Multilayer Models as a Convenient Basis for Applications of Genetic and Evolutionary Methods

The Relations Between The Multilayer Models

Analogical to the presented GEANNDM model is the model of an enterprise for electronic ware shown in Fig. 3. The usual approach may deny the analogy between the two models. Anyway the authors state that both triple-layer models are isomorphic to a number of features the first one being the number of the layers of course (the most evident difference being the transform of the "user-designer" couple into the enterprise working staff). In fact the GEANNDM model is just one of the many possible links of the whole know-how enterprise layer.

Corollary 1. The multilayer model approach makes possible the investigation not only of separate models, but also of relationships between different multilayer models.

Genetic And Evolutionary Approaches To Multilayer Models

The multilayer model search space is denoted with S and $F \subseteq S$ denotes the *feasible* search subspaces. Every such model has its peculiarities or *constraints* which are set by the physical nature of the concrete task. Applied to the two presented models this means that the constraints are defined by the up-to-date development of the science and also by the actual *possibilities* like the investments, production base, qualifications and skill of the working staff. Another feature of the serial manufacture is the *continuity* in the new production models concerning different aggregates and systems of the older models (from the point of view of the genetic and the evolutionary approaches it means that all these possibilities define in a complementary way such properties like the penalties in the evolutionary methods and also the crossovers and the mutations in the new generations for the genetic methods).

Corollary 2 (**for serial manufactures**). Most important are the different generations of serial models (from the genetic point of view) and the *constraints of the design and of the serial production* (from the evolutionary point of view).

Mathematical Formulation Of The Multilayer Models And The Constraints

The authors present the following approach. Let us choose in a random manner two neighbouring layers, the one is relatively peripheral and the other is the relative core. From the point of view of the possible optimizations the default numbering is a basis to accept that the relatively peripheral layer is identified with the whole search space S and that the relative core represents the feasible subspaces F of the solutions. In turn this is a convenient basis for application of the developed evolutionary approaches, namely the penalty

functions (the constraints). The constraints may be set in a bidirectional manner as inward or outward constraints concerning the final layer in this micro-bilayer submodel. Therefore it is an option to define the multilayer model in any of the two possible manners with respect to the penalties.

Corollary 3. The multilayer models are a natural basis for application of the evolutionary methods, namely the penalties (the constraints) defined in any of the two layers in the micro-bilayer submodels and oriented to the other layer in them.

It is possible that the default numbering might insert some inconvenience and especially in the case when the physical nature of the layer which is the relative core becomes very important for some aspect of the multilayer model. Then it is possible to make a *version* of the basic model with the *inverse numbering* of at least two neighbouring layers after which the investigation may proceed in the usual way.

Corollary 4. The constraints and the penalties may be introduced by default numberings or by inverse numberings of (versions of) the basic multilayer model. The reason for the inverse numbering usually lies in the physical nature of the relative core which induces *outward* constraints. *It is the physical nature of every layer which makes it unique in the whole multilayer model.*

The Penalty Functions In The Multilayer Models

The authors introduce the mathematical description of the multilayer model such that the penalty functions may be classified in three types: 1) *inside* any concrete layer, 2) *between* any two layers in a single multilayer model, 3) *between any two multilayer models*:

$$\mathrm{eval}\left(\overline{X}\right)=f\left(\overline{X}\right)+\sum_{l=1}^{L}a_l\left[\lambda(t)\sum_{j=1}^{m}f_j^{2}\left(\overline{X}\right)\right]^{l} \qquad (1)$$

where:

$\mathrm{eval}\left(\overline{X}\right)$ — feasible and unfeasible solutions if $\overline{X}\in F$ is the optimal solution of the general non-linear programming model with continuous variables;

$f\left(\overline{X}\right)$ — goal function for optimization;

$\lambda(t)$ — updated every generation t in the following way [5]:

$$\lambda(t+1)=\begin{cases}(1/\beta_1)\cdot\lambda(t), & \text{if } \overline{B}(i)\in F \text{ for all } t-k+1\le i\le t\\ \beta_2\cdot\lambda(t), & \text{if } \overline{B}(i)\in S-F \text{ for all } t-k+1\le i\le t\\ \lambda(t), & \text{else}\end{cases}$$

$f_j\left(\overline{X}\right)$ — constraint violation measure for the *j*-th constraint such that [6]:

$$f_j\left(\overline{X}\right)=\begin{cases}\max\left\{0,g_j\left(\overline{X}\right)\right\}, & \text{if } 1\le j\le q\\ \left|h_j\left(\overline{X}\right)\right|, & \text{if } q+1\le j\le m\end{cases}$$

Here $g_j\left(\overline{X}\right)\le 0,\ j=1,...,q$ and $h_j\left(\overline{X}\right)=0,\ j=q+1,...,m$ is a set of additional constraints $m\ge 0$ the intersection of which with the search space S defines the feasible set F.

l — indicator of the constraint type with upper bound $L=\{2|3\}$:

$$l=\begin{cases}1: \text{inside a given layer (the lowest constraint level);}\\ 2: \text{between two layers inside a given multilayer model (the moddle constraint level);}\\ 3: \text{between two multilayer mod els (the highest const - raint level).}\end{cases}$$

a_l — coefficient array reflecting the weights of the different constraint levels in the formula. It is adjusted heuristically.

IV. CONCLUSIONS

Hierarchical structures of a pyramidal type interpreted with multilayer models are introduced with their advantages and limitations. Hierarchical systems are complemented in a natural way but not overlapped by structures without hierarchies. Both types of organizations arrange and represent *in different ways* objects from a *common* domain. The multilayer models provide the most relevant description of the ensemble of features of the ANN learning process.

REFERENCES

[1] S. Haykin. *Neural networks*. Englewood Cliffs, Macmillan Publishing Co., 1994.

[2] D. Williams and J. B. Gomm. The introduction of neural network projects in a degree of electrical and electronic engineering. 12th Int. Conf. on Systems for Automation of Engineering and Research SAER'98, Proc. 19-20 September 1998, Varna - St. Konstantin resort, Bulgaria, pp. 102-106, 1998

[3] J. C. Bean and A. B. Hadj-Alouane. A dual genetic algorithm for bounded integer programs. Department of Industrial and Operations Engineering, The University of Michigan, TR 92-53, 1992.

[4] Zb. Michalewicz. The significance of the evaluation function in evolutionary algorithms. *Evolutionary algorithms*, L. D. Davis, K. De Jong, M. D. Vose, L. D. Whitley (eds.), Springer, 1999, pp. 151-166, 1999

[5] E. Falkenauer. Applying genetic algorithms to real-world problems. *Evolutionary algorithms*, L. D. Davis, K. De Jong, M. D. Vose, L. D. Whitley (eds.), Springer, 1999, pp. 65-88, 1999

[6] S. Koynov, Ch. Korsemov and H. Toshev. The design of the artificial neural networks as a basis for their generalized evolutionary model. 15th Int. Conf. on Syst. for Automation of Engineering and Research SAER'2001, Proc. 21-23 September 2001, Varna - St. Konstantin resort, Bulgaria, pp. 185-190, 2001

[7] S. Koynov, Ch. Korsemov and H. Toshev. The artificial-neural-networks-design generalized evolutionary model. 15th Int.

Conf. on Syst. for Automation of Engineering and Research SAER'2001, Proc. 21-23 September 2001, Varna - St. Konstantin resort, Bulgaria, pp. 191-195, 2001

[8] A. Jain. Artificial Neural Networks: A Tutorial. IEEE Computer, 1996, March, pp. 31-44, 1996

[9] D. B. Fogel, E. C. Wasson and E. M. Boughton. Evolving Neural Networks for Detecting Breast Cancer. Cancer Letters, v. 96, 1995, pp.49-53, 1995

[10] V. Ilchev "Transformation of Lineary Separable Sets in Hough Spase", *Comptes rendus de l' Academie Bulgare des Sciences*, Tome 56, 2003, № 1, pp. 31-36, 2003..

[11] L. Docheva, A. Bekiarski, "Analogue Neural Network Comparative Simulation by Means f MATLAB and PSPICE Software Produkts" , Proceedings of the XXXVIII International Scientific Conference on Information, Communication and Energy Systems and Technologies ICEST 2003, Sofia, pp.270-272, 2003.

[12] M. Bonilla, I. Baruch, J. M. Flores, M. M. Goire, B. Nenkova "Model Reference Adaptive Neural Control of a Variable Structure System", - In: *Cybernetics and Information Technologies*, V. 3, No. 2, pp. 3-14. 2003

[13] I. Baruch., J.M.Flores and B. Nenkova, "Adaptive Control Schemes Based on Recurrent Trainable Neural Networks", *Cybernetics and Information Technologies*, Vol. 4, No. 1, Sofia, pp. 89-102, 2004.

A Genetic Algorithm for a Traveling Salesman Problem

Milena N. Karova[1] Vassil J. Smarkov[2] Stoyan P. Penev[3]

Abstract - **This paper introduces a flexible method for finding a solution to the traveling salesman problem using a genetic algorithm. The traveling salesman problem comes up in different situations in out world. It is a special kind of optimization problem. There had been many attempts to address this problem using classical methods, such as integer programming and graph theory algorithms with different success The solution, which this paper offers, includes a genetic algorithm implementation in order to give a maximal approximation of the problem, modifying a generated solution with genetic operators.**

Keywords: **genetic algorithm, TSP, traveling salesman problem, constraints, optimization, approximation, selection, genetic operator, crossover**

I. INTRODUCTION

The genetic algorithms are an optimization technique based on natural evolution. They include the survival of the fittest idea info a search algorithm which provides a method of searching which does not need to explore every possible solution in the feasible region to obtain a good result. Genetic algorithms are based on the natural process of evolution. In natureq the fittest individuals are most likely to survive and mate; therefore the next generation should be fitter and healthier because they were bred from healthy parents. This same idea is applied to a problem by first 'guessing' solutions and then combining the fittest solution to create a new generation of solutions which should be better than the previous generation. We also include a random mutation element to account for the occasional mishap in nature.

The genetic algorithm process consists of the following steps:

1. Encoding
2. Evaluation
3. Crossover
4. Mutation
5. Decoding

A suitable encoding is found for the solution to our problem so that each possible solution has unique encoding and the encoding is some form of a string. The initial population is then selected, usually at random though alternative techniques using heuristics have also been proposed. The fitness of each individual in the population is then computed that is, how well

the individual fits the problem and whether it is near the optimum compared to the other individuals in the population.

[1]Milena N. Karova is with the department of Computer Science, Studentska 1, Technical University Varna Email: mkarova@ieee.bg

[2]Vassil J. Smarkov is with the department of Computer Science, Studentska 1, Technical University Varna Email: smarkov@ieee.bg

[3]Stoyan Penev is student, department of Computer Science, Technical University Varna Email penev@engineer.bg

This fitness is used to find the individual's probability of crossover. If an individual has a high probability (which indicates that it is significantly closer the optimum than the rest of its generation) then it is more likely to be chosen to crossover. Crossover is where the two individuals are recombined to create new individuals which are copied into the new generation. Next mutation occurs. Some individuals are chosen randomly to be mutated and then a mutation point is randomly chosen. The character in the corresponding position of the string is changed. Once this is done, a new generation has been formed and the process is repeated until some stopping criteria have been reached. At this point the individual who is closest to the optimum is decoded and the process is complete.

II. CONSTRAINTS

The genetic algorithms are used for solving complex problems such as NP-hard problems. They can be used in teaching different machines such as robots and simple evolving programs. They can also be used in creating pictures and music.

One of the great advantages of the genetic algorithm is the hing level of parallelism because of whish the programs are very easy to apply. Once created, a genetic algorithm with small changes can be adjusted to solve a completely different problem. The choice of coding technique and calculation of fitness function can be very complicated and difficult.

The main advantage of the genetic algorithms is that they can found a feasible solution for a very short time.

Two of the main problems that occur was choosing proper methods of crossover and mutation. We have implemented two types of crossover – cycle crossover and a custom one. The user can choose which one to use in the calculation. Let us take a closer look at the Cycle crossover.

First of all it fits perfectly to the way our tour is represented in the chromosome. For example if our tour is

Tour = 1234

This means that we go from city 1 to city 2 to city 3 to city 4.Unlike other methods of crossover here we do not pick a crossover point at all. We choose the first gene from one of the parent chromosome. If our parents are

parent1 = 12345678

parent2 = 85213647

say we pick 1 from parent 1,

child = 1*******

We must pick every element from one of the parents and place it in the position it was previously in. Since the first position is occupied by 1, the number 8 from parent2 cannot go there. So we must now pick the 8 from parent1.

child = 1*******8

This forces us to put the 7 in position 7 and 4 in position 4, as in parent1.

child = 1**4**78

Since the same set of position is occupied by 1,4,7,8 in parent1 and parent2, we finish by filling in the blank positions with the elements of those positions in v2. Thus

child 1 = 15243678

and we get child2 from the complement of child1

This type of crossover ensures that each new created chromosome is legal. A chromosome is legal if it is constructed according to the requirements of the salesman problem. In this crossover, notice that it is possible for us, to end up with the offspring being the same as the parents. This is not a problem since it will usually occur if parents have high fitness, in which case, it could still be a good chance.

If we want to solve this problem or other like not getting trapped in a local optimum we could use mutation. Due to the randomness of the process we will occasionally have chromosomes near a local optimum but none near the global optimum. Therefore the chromosomes near the local optimum will be chosen to crossover because they will have the better fitness and there will be very little chance of hiding the global optimum. So mutation is a completely random way of getting to possible solutions that would otherwise not be found.

Mutation is performed after crossover. The mutation index (MutInd) must decide weather to perform mutation on this child chromosome or not. We then choose a point to mutate and switch that point. For instance, in our example we had

child = 12345678

If we choose the mutation point to be gene three and 7, the child would become

child = 12745638

We simply switched the places of genes 3 and 7.Another mutation that takes place is inverting a sub tour in our child chromosome. Let us have the chromosome

child = 12345678

And choose the same mutation points 3 and 7.The sub tour between these tow point is switched in reverse order

child = 12765438

After the mutation process the program makes a strict verification of the chromosome. If it is not legal then the chromosome is ignored.

The idea of the traveling salesman problem is to find a tour of a given number of cities, visiting each city once and returning to the starting city where the length of this tour is minimized.

The product finds a solution to the traveling salesman problem. For this purpose we use cities, chromosomes and populations. Each city is represented by an object of class TCity. The declaration is:

```
TCity=class( TObject )
    Name:String;
    x,y: Integer;
  end;
```

Each city is situated on coordinates (x, y) on the map. In the working process a defined number of cities are being created. Then the program solves the traveling salesman problem for these cities. The combination of cities is stores into an object collection citylist.t consists of objects of class TCity.

A tour or a chromosome represents a succession of indexes of cities. An index of object city in the collection citylist is the same as the index of the city. A tour contains variable of type TChromosome.

TChromosome=array[0 .. 32] of Integer;

This is an array of 32 elements, each one has an integer value. Let M is a variable of type TChromosome:

Var M:TChromosome;

Then the tour starts from city with index M[1], continues to city with index M[2]. The maximum number of cities is 32, which is the length of the array.

III. POPULATION

Population is a combination of chromosomes. In our program to present the population we use array of 1002 chromosomes. The thousand and first chromosome stores the worst tour. The name of the array is population.

Population: array [0 1001] of TChromosome;

For each chromosome we calculate the length that is coded into it, actually this is the fitness of the tour. It is stored in the next array:

popFitness: array[0 .. 1001] of Real;

Now we know that the tour with index I has a fitness popFitness[i].

The maximum number of towns is 32. The current number is stored in the variable townCount. In the same, way the

number of populations – popCount. In the process of mutation, we use the coefficient MutInd.

IV. Basic Functions

In this product were used sixteen basic functions and procedures in order to create a completely working program.

2.1 DrawCity
2.2 ShowCities
2.3 DrawChromosome
2.4 GenerateTownSet
2.5 CreateTown
2.6 GetClick
2.7 Mutate
2.8 CleaUp
2.9 SaveToText
2.10.Sort
2.11.Image1MouseMove
2.12.seTownCountChange
2.13.TownKeyPress
2.14 CreatePopulation
2.15 TestCrossOver
2.16 CrossOver

V. Interface

The interface [Fig.1] is Windows Forms oriented, showing the current result at the moment they are calculated. In this order one of the stop criteria is that the user can terminate the calculations if he found a feasible solution

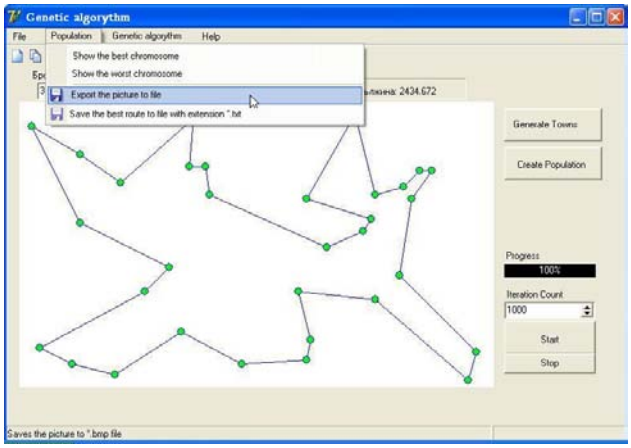

Fig. 1. Program Interface

The options screen [Fig.2] allows us to change the parameters of the genetic algorithm. We can change the mutation, inversion, and transposition coefficients.

VI. Conclusion

Genetic algorithms appear to find good solutions for the traveling salesman problem, however it depends very much on the way the problem is encoded and which crossover and mutation methods are used. It seems that the methods that use

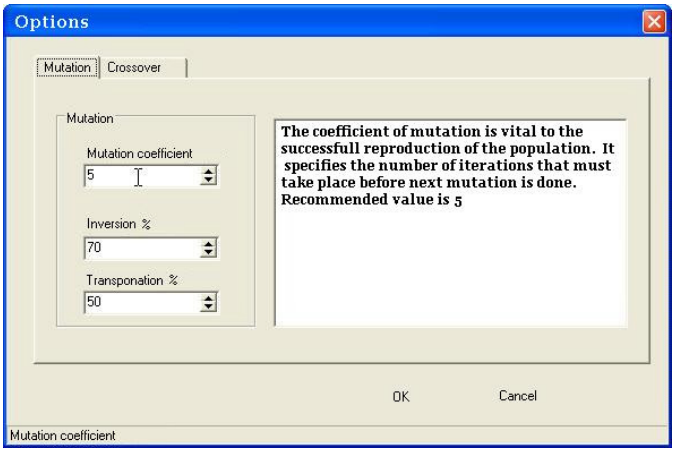

Fig. 2. Options Screen

heuristic information or encode the edges of the tour perform the best and give good indications for future work in this area.

Overall, it seems that genetic algorithms have proved suitable for solving the traveling salesman problem. As yet, genetic algorithms have not found a better solution to the traveling salesman problem that is already known, but many of the already known best solutions have been found by some genetic algorithm methods also.

It seems that the biggest problem with the genetic algorithm devised for the traveling salesman problem is that it is difficult to maintain structure from the parent chromosomes and still end up with a legal tour in the child chromosomes. Perhaps a better crossover or mutation routine that retains structure from the parent chromosomes would give a better solution that we have already found for some traveling salesman problems.

References

[1] Goldberg D. L., "Genetic Algorithms in Search, Optimization, and Machine Learning", Addison-Wesley, 1989

[2] Goldberg D, "Web Courses", http://www.engr.uiuc.edu/OCEE, 2000.

[3] Mitchell M., "An Introduction to Genetic Algorithms", Massachusetts Institute of Technology, 1996.

[4] Paechter B., Rankin R., Cumming A., "Timetabling the Classes of an Entire University with an Evolutionary Algorithm", Napier University, Edinburgh, Scotland.

[5] Michalewicz Z., Janikow C., "Handling constraints in genetic algorithms" *In Proceeding of the 4th International Conference in Gas*. Morgan Kauffman, 1991

[6] Michalewicz Z, Genetic Algorithms+ Data Structures = Evolution Programs, Springer Verlag, 1992.

[7] Holland, John H., "Adaption in Natural and artificial systems", the Mit Press, 1992

[8] Spears, W. M. and DeJong K., "An analysis of multi-point crossover", *Foundations of Genetic Algorithms*, pages 301-315, Morgan Kaufmann, 1999.

[9] Syswerda, G., "Uniform crossover in genetic algorithms", *Procedings of the Third International Conference on Genetic Algorithms*, pages 2-9, 1995

Poster Session PO3:

COMPUTER SYSTEM AND INTERNET TECHNOLOGY

Models and Program System Development for Safety Exploitation in Maritime Transport

Geo Kunev[1], Valentina Antonova[2], Petar Antonov[3]

Abstract – **Fast acceptance of principles of Quality Assurance in the transport industry is a base for developing of Intelligent Systems for Quality Assurance – IQMS (Intelligent Quality Management System) – as a tool for preventing of problems. The availability of such system (certified according to series of standards ISO 9000) is becoming more and more in a prerequisite for participation in international trade, including transportation process. Development of IQMS in maritime transport industry will give a possibility for preventive control and constantly improving of transport activity organization.**

Keywords – **IQSM, Database, Software**

I. INTRODUCTION

The technological progress in transport industry, in particular – maritime transport industry – do not follow automatically to the decreasing of fault and accidents level. The statistical data show that 80% of accidents in the shipping are caused by human factor. In the result, the society set requirements to the maritime industry for transparency and safety for humans, environment, and material resources. In shipping this bring to the acceptance of the chapter IX to the SOLAS convention (Ch.IX "Management for the Safe Operation of Ships), which is compulsory for ship owners, managers and their ships - International Safety Management (ISM) Code [1].

II. THE IQMS NEED IN MARITIME TRANSPORT

Many of accepted quality management conceptions have been used for safety management, in order to create a system for preventing accidents, collisions and environment pollution.

A Safety Management System in a Maritime Ttransport Oorganization, operating ships, should ensure:
- confidence to clients and the society that the safety and environment protection requirements are kept,
- systematical planning and performing of transport activities and services according to the documented rules,
- evidences (objective), that the relevant methods for the safety and environment protection requirements are applied,
- launching of effective corrective actions, to prevent appearances or reiteration of appeared problems,
- readiness to actions along the whole transport-logistic chain on raised accident situations, to restrain and minimize of accident consequences.

III. A MODEL

Rendering an account of the fact, that the requirements of ISM Code are in practice adaptation of the Standard ISO 9902 requirements in the shipping area [2], and they have more restricted range, it is recommended to create a united for safety and quality management system (SQMS), that suits the both standards requirements. The span, functional requirements and objectives of such system in the frame of transport logistic are shown in Fig.1,

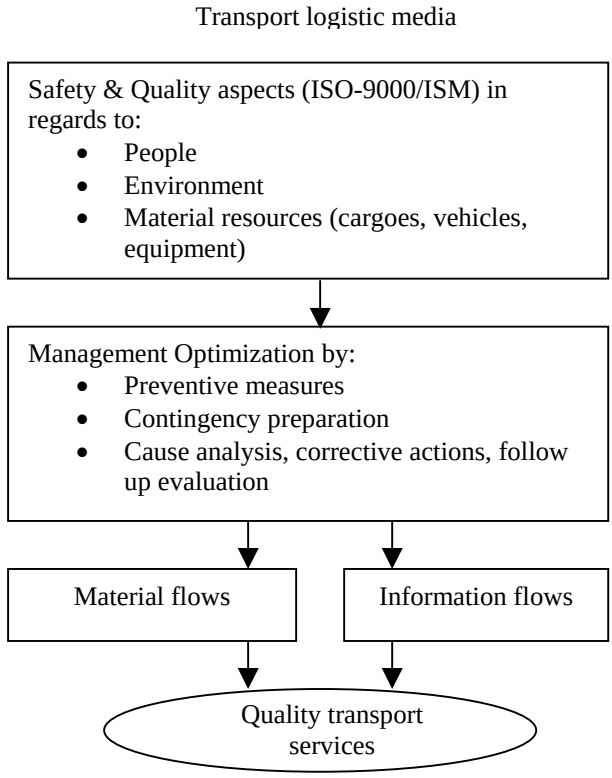

Fig. 1. IQMS for Maritime Transport

[1]Geo Kunev is with the Faculty of Computer Sciences, TU Varna, Studentska 1, 9000 Varna, Bulgaria, E-mail: geo_qnew@hotmail.com
[2]Valentina Antonova is with the Faculty of Computer Sciences, TU Varna, Studentska 1, 9000 Varna, Bulgaria, E-mail: valy@ieee.bg
[3]Petar Antonov is with the Faculty of Computer Sciences, TU Varna, Studentska 1, 9000 Varna, Bulgaria, E-mail: antonovp@ms.ieee.bg

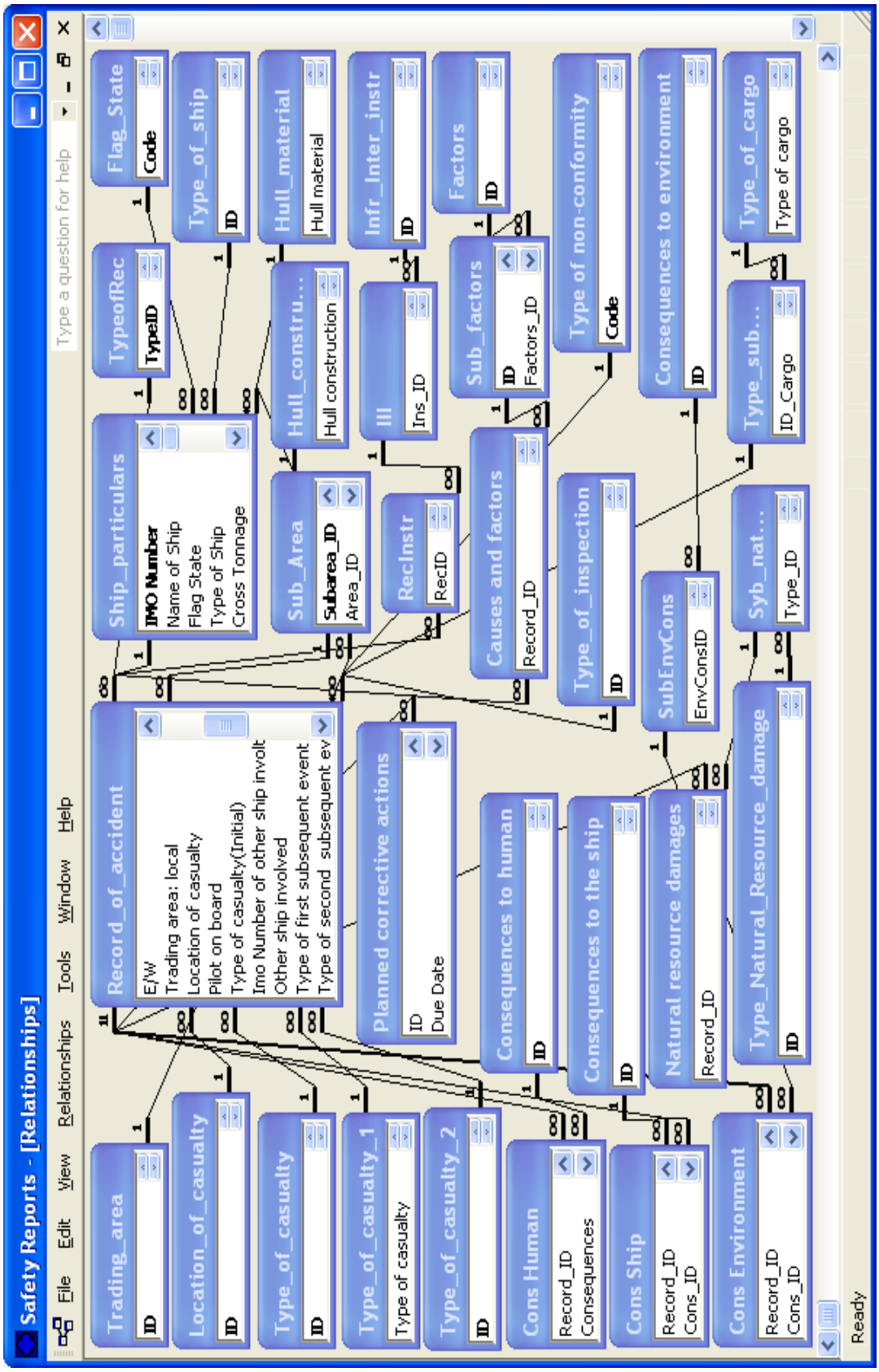

Fig. 2. Database prototype

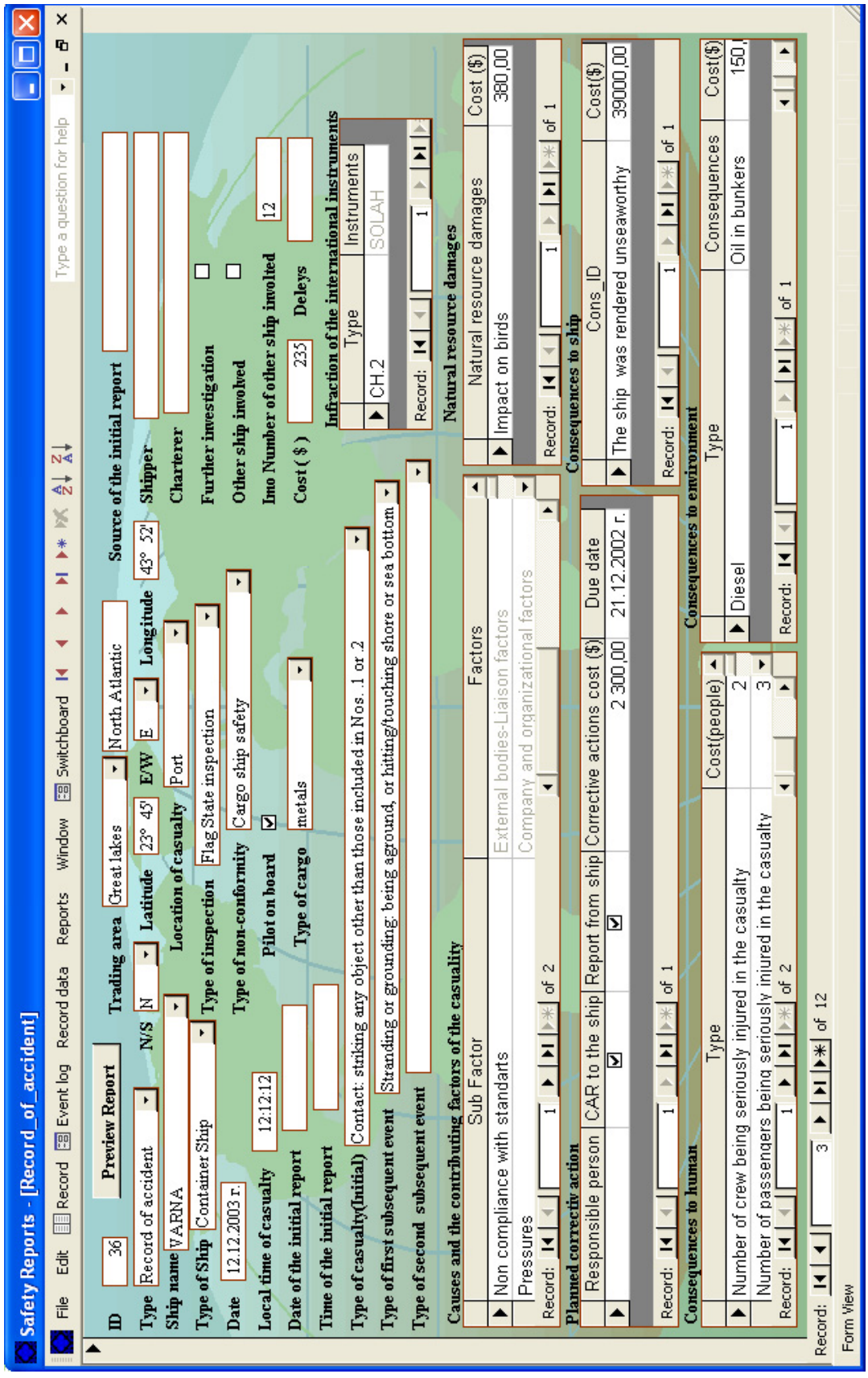

Fig. 3. Report subsystem

IV. Analysis & Prototyping

Document and data analysis include:
- ISO-9002 and ISM standards
- Quality control standard documents
- Available accident data from BMF - Varna
- Theoretic and software solutions [3]
- Possible software environments

Based on standards, the information about maritime events (accidents) include data objects:
- trading areas
- trading sub-areas
- types of ships
- types of cargo
- flag states
- hull construction
- hull material
- consequences to human
- consequences to ship
- consequences to environment
- natural resources damages
- types of natural resources damages
- causes and factors
- types of causes and factors
- types of records
- planned corrective actions
- types of casualty
- location of casualty
- type of inspection
- type of non-conformity
- ship particulars

A prototype of the system has been designed and realized, including:
- Database for storage of all standard documents and operative data: Areas, Ships, Types of Events (Accidents), Types of Records, Types of Reporting documents, etc.
- Report generating subsystem,
- Data analysis subsystem.

The database Safety Reports is a relational database, allowing to hold and manipulate all data, described above. Except the scheme (Fig.2) with tables and relationships, it include queries and end-user interface in form of menus, screen-forms and reports.

The Report generating subsystem (Fig.3) is a tool, allowing to search and display single or multiple accidents data based on single or multiple search arguments. In this version, it has being realized, using the MS Access functionality, called search by form. It allows to search data on:
- areas and sub-areas
- types of ships
- ship name
- types of accidents
- types of casualty (initial)
- types of first consequent event
- types of second consequent event
- consequences to human
- consequences to ship
- consequences to environment
- natural resources damages
- planned corrective actions
- pilot on board
- etc.

The data-analysis subsystem allows calculating and visualizing some statistical analysis on raw data, which is important for IQMS decision – makers – the maritime administration officers.

It offers:
- summarizing,
- averaging,
- finding trends
- finding max and min values

on most of available numeric data in the database.

It is possible to add extra functionality in form of Data Mining subsystem; which allows applying the more advanced mathematical methods for searching patterns and regularities in raw data.

The prototype database has been realized on Windows XP, MS Access XP environments in order to be used as local IQMS system. It is possible to migrate the system to advance distributed or Internet – accessible databases as Oracle, or MS SQL Server.

V. Conclusion

The developed IQMS system is a useful instrument in maritime management routine. It offers adequate support for most of data storage and data processing today needs in quality management in maritime transportation.

The system is functional and, according to the needs and resources of the end clients – Quality and Safety Control Sections in Maritime Transport, it is possible to migrate the system to more powerful environments, like MS SQL Server, Oracle.

Acknowledgement

The main documents and raw data in this work are available thanks to the help of Bulgarian Maritime Fleet.

References

[1] International Safety Management Code

[2] ISO 9002 for Maritime Transport

[3] G. Kunev, V. Antonova, P. Vladimirova, System Modeling via Databases, ICEST2004, Bitola, Macedonia, 2004

Material Characteristics Representation: Requirements, Definition and Implementation

Marija D. Cvetković[1], Jean-Dominique Lenard[2], Ljubica V. Mudri[3], Milena Stanković[4]

Abstract – **This paper describes the problem of reusability of materials in computer simulation and visualization in architecture. Architectural and functional requirements for software implementation are discussed, along with the description of the software tool for creating, storing and manipulating material description files.**

Keywords – **Material Characteristics, Material Explorer, Xmat**

I. INTRODUCTION

In the early phases of the architectural design a "project of building" is imprecise and incomplete [1], because it is just a sketch and details are not yet defined. On the other hand, validation of the technical qualities of buildings by experts with sophisticated techniques is preformed in the detailed design phase. These quantitative mathematical methods use precise and complete data that are available only at the end of the design.

For the question of luminous ambiences, at the beginning of the design (sketch phase), the architects' approach is rather intuitive. Towards the end of the design, when everything is well defined, it is possible to perform simulations to verify if the ambience in a given project is close enough to architectural intentions and if norms and recommendations are respected. However, in that phase it is too late to advise on possible modifications of the buildings morphology. On the contrary, materials (their surface appearance) may generally be changed at any stage of the design.

To bring the resulting ambience closer to intentions, architects may use several different computer programs to help them in the process of design and representation of ambiences of architectural project. These programs allow them to simulate imaginary buildings, and to verify their intentions, preferences and respect of norms. On the other hand, programs follow strictly defined geometrical and physical laws, which give quantitative accuracy to the project.

For modeling and simulation in architecture there is a great number of different computer programs available on the market, such as AutoCAD, ArchiCAD, 3Dstudio Max, Radiance, etc. All these programs offer similar possibilities for modeling different geometrical primitives, but their capability to simulate luminous ambiance of the building is different. Definition of luminous ambiance involves description of artificial light sources (luminaries characteristics and position), natural light sources (sun, sky), building position and environment, and description of materials used for building interior and exterior.

Although every architectural project has its original structure and shape, the number of available materials is limited to the number of existing materials. So it is not unusual to use materials, which are already used in some other projects.

In this paper we consider the reusability problem of materials in computer simulation and visualization, and offer software tool for creating, storing and manipulating with material description files. The paper is organized as follows. In next section, architects concept of material description is faced with computer simulation approach. Sections III and IV describe architectural and functional requirements, which software should follow. The last section contains the description of software implementation and application.

II. MATERIAL REUSABILITY

According to previous discusion it is recomendable to have reusable material descriptions. From architect point of view this would enable easy search and use of materials in project. Also, using of “existing“ materials, gives certanity to architect's choice of appropriate materials. On the other hand, from the programmers point of view, this reusability, means the definition of a universal format for storing description of material characteristics, which should be easy to search using different criteria.

It should be taken into consideration that existing formats, enable precise and accurate definition of materials in terms such as: color component values (red, green, blue); reflection and transmission coeficients; specular, diffuse and ambient component; pattern or texture used etc. Architects use more qualitative and subjective descriptions of ambient and materials, such as: calm, dark, dynamic [2]. During the design many architects look for these keywords to symbolize an ambiance they wish to create. This adds one more requirement for material file format: it should include description of both physical (optical, thermal, etc.) and subjective characteristics of materials. This indicate an important requirement for such format - it should be easily extendable.

The final aim is to enable architect to search through large number of materials, to examine their characteristics, and to use some of them for further work in various simulation

[1] Marija D. Cvetković is with the Faculty of Electronic Engineering, Aleksandra Medvedeva 14, 18000 Nis, Serbia and Montenegro, E-mail: cveleglg@bankerinter.net
[2] Jean-Dominique Lenard is with De Luminae Lab, Paris, FranceE-mail: jdlenard@club-internet.fr
[3] Ljubica V. Mudri is with Paris-Belleville School of Architecture, Paris, France, E-mail: lmudri@club-internet.fr
[4] Milena Stanković is with the Faculty of Electronic Engineering, Aleksandra Medvedeva 14, 18000 Nis, Serbia and Montenegro, E-mail: mstankovic@elfak.ni.ac.yu

programs. It is also desirable to have some images which represent material examples.

III. ARCHITECTURAL REQUIREMENTS

Previous section gives us guidelines that should be followed in definition of a format for storing material characteristics. Main attributes of this format are enumerated in next list:

- It should be easy to semantically search files in this format, using different searching criteria.
- Appending of new characteristics to existing material description files should be easy and it should not violate the logical structure of a file, which means that format should be extendable.
- Format should be easy to interpret and preview to a user.
- It is desirable do define a format that is program independent, and that is easily converted to other textual formats. This would enable material reusability in different simulating programs.

Following this requests we defined Xmat file format. This format, as described in [3], is based on XML. It inherits all XML advantages described in [4], which offers additional advantages to this format: legibility, logical structure, and possibility of semantic validation of files contents through concept of XMLSchemas. Appropriate XMLSchema, which contains description of all possible entities in Xmat documents, is also defined in [3]. Every material definition in Xmat format contains physical, quantitative and descriptive, qualitative information about material. Section of Xmat document that contains physical data is based on Radiance material definition.

Radiance is open-source, Unix based, software for accurate lighting simulation and visualization based on ray-tracing algorithm [5]. Its input files are composed of textual description of geometric primitives and materials they are made of. These files can be entered manually or imported from other simulation programs such as AutoCAD, 3DStudio etc. The imported files contain only description of geometric primitives, and appropriate materials are assigned to them afterwards.

The main reason why we selected Radiance is its format for material definition. While other programs use parameters like specular, ambient and diffuse components for defining material characteristics, radiance use more intuitive concept of *material types.* Each material type in Radiance, describe one kind of material behaviour [6]. For example: a *plastic* surface has a color associated with diffusely reflected radiation, but the specular component is uncolored; for *metal* surfaces the specular component is modified by the material color [7]. This description of materials is analogous to their real behavior. To define different *plastic* materials, user simply varies basic material parameters: red, green, and blue color components, reflection secularity fraction and material roughness.

Code samples 1. and 2. give material description in Radiance and Xmat format.

```
void metal gold
0
0
5 0.6 0.8 0.4 0.7 0
```

Code sample 1.

Example of material description in Xmat format includes some additional information: architect and project name.

```
<Material>
 <Metal>
    <ModifierName>void</ModifierName>
    <Identifier>gold</Identifier>
    <Color>
       <Red>0.6</Red>
       <Green>0.8</Green>
       <Blue>0.4</Blue>
    </Color>
    <Specularity>0.7</Specularity>
    <Roughness>0</Roughness>
 </Metal>
 <Architect>Clément Vergely</Architect>
 <Project>Wurth Foundation</Project>
</Material>
```

Code sample 2.

Material definitions in Xmat format are stored in a *material base*. Each base entity, stored in Xmat file, contains one material description. Special textual files are defined for material base search and manipulation..

IV. FUNCTIONAL REQUIREMENTS

All requests previously described can be organized in a few basic features that should be implemented in the software. In Figure 1. these features are represented in a form of Use Cases, following Rational Rose unified notation. From the sake of simplicity, some rather complex features are represented as one use case. All features should be implemented respecting to architectural requirements defined in Section III.

Use Case diagram contains only one actor – *User*, who represents user of the software.

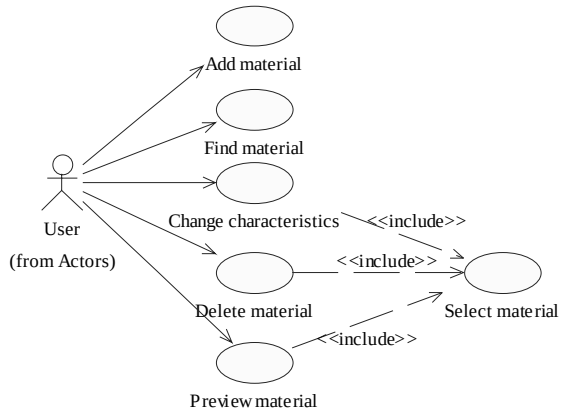

Figure 1. Use Case diagram

Each use case in the diagram represents one specific feature:

Add material use case enables user to add a new material to Material base. A material could be added from different sources: it can be imported from some existing Radiance file, or it can be added from a scratch. Initial material file is analysed and stored in Xmat file, which is then appended to the material base.

- Material base can contain great number of materials, and program should provide some kind of mechanism for searching through it. Feature *Find material* should enable user to find material in material base, based on different criteria.
- *Change material* – once material is stored in base it can be changed in few different ways: existing characteristics can change their values, or some new characteristics can be added to material. Characteristics for each material can be, as described earlier, different: radiance material definition, optical, thermal, subjective etc.
- *Delete material* – possibility to delete selected material from Material Base
- When user select material it is important to *preview material* characteristics. Characteristics can be in text and/or image format.
- Feature *Select material* is simple use case included from other more complex use cases. Its functionality is to enable material selection for further actions.

V. Material Explorer

Following all defined requirements software tool Material Explorer is created. Material Explorer was developed in QtDesigner, in Linux operating system.

Material Explorer main window is shown on Figure 2. Main widow can be divided on two areas: area for setting search filters, and area for preview of material characteristics.

To find material(s) with certain characteristics user should define query for searching. Query is easily defined using filters drop down boxes. Every filter contains one characteristic and a corresponding value. For example, if user sets a filter to have characteristic ”Project” and value ”Project1” that means that he wants to find all materials in material base which were used in project “Project1”. Up to four filters can be set, and relations between them can be *and* or *or*, which provides definition of complex filters. Final query value is previewed in the bottom of the window.

List of available characteristics and their values is composed from database contents, e.g. list of characteristics contains all characteristics that exist in material base. When user choose come characteristic in drop down box, corresponding value drop down box is filled with all possible values for that characteristic.

Each time filters contents are changed material list, in left part of the main window, is updated. Material list contains all materials from material base, which have values equal to filter values.

When a material in the list is selected its data, from Xmat file, and image, if exists, are previewed in the right bottom part of a window. Selected material can be changed or deleted.

Toolbar contains all features defined in previous sections. User interface for these features is simple and descriptive, so even the non-professional users can use Material Explorer.

The common applications of Material Explorer are described as follows. In the process of the design an architect develops a project in AutoCAD or some other simulation program. Defined scene can be imported to Radiance. Imported objects, as mentioned in Section III, do not contain appropriate material definitions, and the architect should manually define materials, and assign them to the objects. Further Radiance simulation is beyond this discussion. The material definitions, since described using Radiance syntax, contain only material optical characteristics, and they are not appropriate for storing and searching for further projects.

To preserve materials used in some project, the best way is to store them in some kind of base or library, and to attach them some additional data, which would simplify their future use. Utilization of Material Explorer is a good mean for this task. Materials defined in Radiance can be easily attached to Xmat material base. Afterwards user can add some additional data for each material file, such as: architect name, project name, material manufacturers name, material type (brick, concrete, wood), some qualitative expressions that describe material behaviour or architects subjective impressions. For architects, the character of some space is determined by its luminous ambiance. Since the objects made of different materials compose the ambiance, subjective impressions of the ambiance are closely linked to those materials. *Change material* feature would also enable adaptation of an existing material for some new purposes.

On the other side, engineer or any other expert who gives advice to an architect, could use Material Explorer to define some technical characteristics of materials, such as thermal characteristics, material weight and durability, fire resistance etc. In the process of consulting or design an engineer can search the material base in order to find most appropriate material for some purpose. His approach is rather quantitative and based on the physical principles.

All these additional data are used in Material Explorer as keywords, which enable user easy and semantic search of the material base. Search criterion can be complex, due to existence of four filters. User can also attach an image to the material, which would simplify selection of an appropriate material for some purpose.

True benefits of this software, in the process of material selection and manipulation, become visible when material base contains hundreds of materials collected from different projects.

VI. Conclusion

This paper describes dual nature of architectural project, represented through disparity of objective and subjective approach. It focuses on problem of materials reusability in computer simulation and visualization in architecture. In addition software tool for creating, storing and manipulating with material description files, has been realized. This will

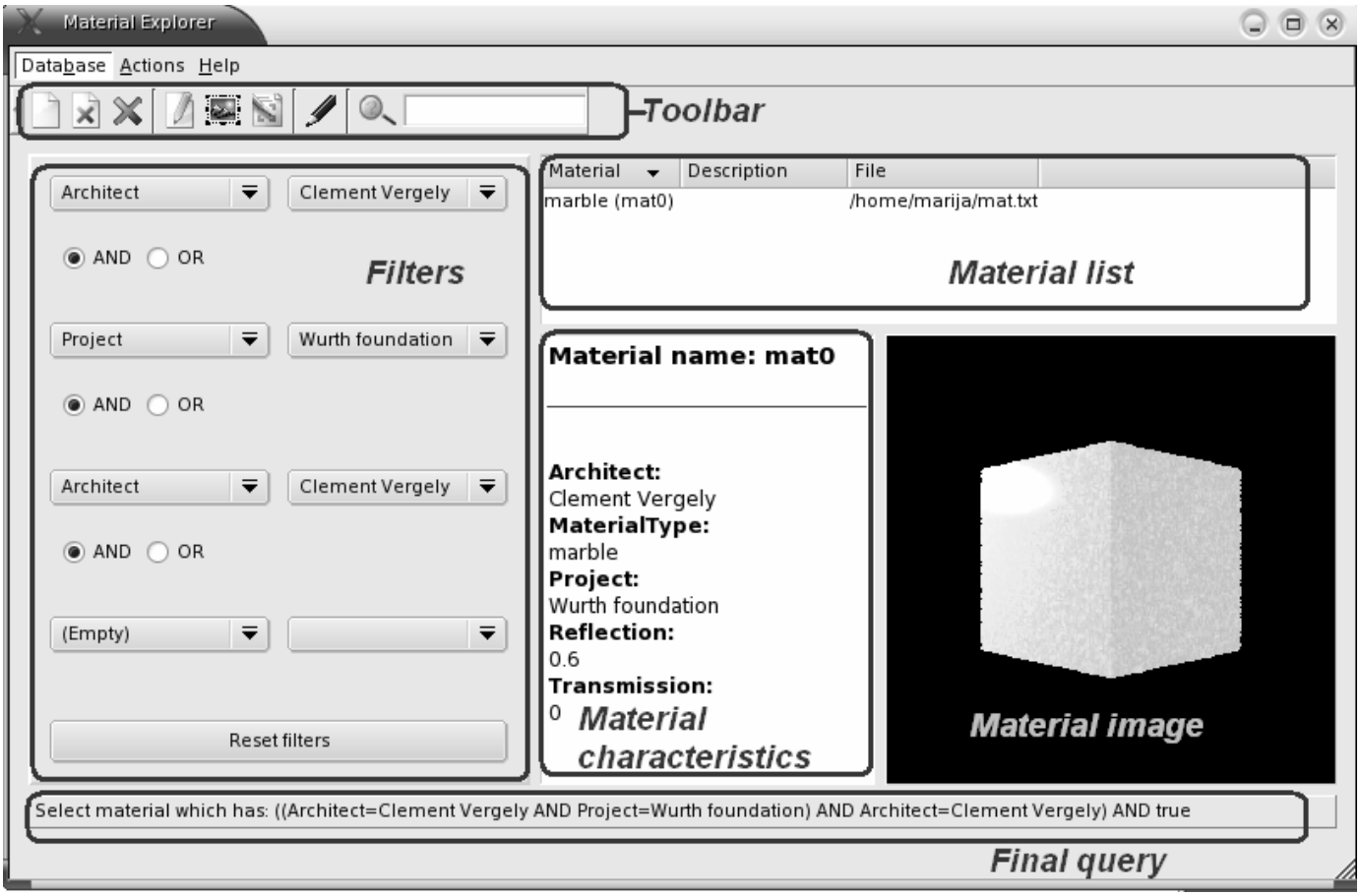

Figure 2 – Material Explorer main window

help designers to manipulate, preview, choose through a larger number of materials (several thousands) using both technical (physical) and architectural (qualitative) characteristics.

The final goal is to regroup a very large number of materials and their characteristics for various technical areas (thermal, acoustics, cost, sustainability, visual aspect, etc.). This will make these materials ready for simulation in all these areas; hence improve the speed of validation of buildings behavior.

REFERENCES

[1] L. MUDRI, "Interaction between Qualitative and Quantitative Approaches in the Teaching of Architectural Design", *Florence International Conference for Teachers of Architecture*, Florence, September 1995.

[2] L. Mudri, J.D. Lenard, M. Cvetković, "Objective data from Radiance and subjective intentions from architects", *Radiance Workshop*, Fribourg, Switzerland, 2004.

[3] M. Cvetković, J.D. Lenard, M. Stanković, "XML reprezenatcija karakteristika materijala za potrebe računarske simulacije u arhitekturi", *ETRAN 2005 Conference Proceedings*, Budva, 2005.

[4] *Extensible Markup Language (XML) 1.0 (Second Edition)*, W3C Recommendation, October 2000.

[5] G.Ward, "The RADIANCE Lighting Simulation and Rendering System", *Computer Graphics*, July 1994.

[6] G. Ward, *Behavior of Materials in RADIANCE*, Lawrence Berkeley Laboratory

[7] G. L. Ward, R. Shakespeare, *Rendering with Radiance*, Morgan Kaufmann Publishers, 1998.

Modelling and Monitoring NFRs in Autonomic Systems: AS-TROM Approach

O. Ormandjieva

Abstract – **This paper is the first report on the ongoing research targeting the rigorous development of autonomic (self-managing) systems with built-in continuous monitoring of their non-functional requirements for quality through self-diagnosis, followed by planning. The research is focusing on Autonomic Systems - a significant and new strategic and holistic approach to the design of computer-based systems. Autonomic elements have complex life cycles, continually sensing and responding to the environment in which they are functioning. Therefore, the autonomic system can be classified as a real-time reactive system. The autonomic system requires solid formal foundations for system development and functioning. The Timed Reactive Object Model (TROM) formalism for real-time reactive systems, created at Concordia University, is being extended to model autonomic systems whose architecture, system configuration, and continuous self-monitoring of their quality are to be specified within a single formal framework.**

Keywords – **Autonomic Systems, Formal Methods, Software System Quality, Non-Functional Requirements (NFRs).**

I. INTRODUCTION

Software systems are characterized both by their functionality (what the system does) and by their non-functionality (how the system behave with respect to some observable attributes like reliability, reusability, maintainability, etc.) Both aspects are relevant to software development. However, non-functional issues have received little attention compared to functional ones. The non-functionality is addressed by just a few approaches, often semi-formal or informal and limited in scope. The increasing trend toward developing complex software systems has highlighted the need to build software non-functional requirements (NFRs) into the software system. To model and validate these non-functional requirements new techniques have to be developed in addition to existing formal methods and tools.

This paper is focusing on Autonomic Systems - a significant and new strategic and holistic approach to the design of computer-based systems. This is a new and challenging area in Software Engineering discipline emerged in 2001 from the needs of the industry [6, 7] that has created interests in different research groups worldwide.

The main characteristic of autonomic computing is self-management, i.e., continually monitoring of its own use and quality in the face of changing configurations and external conditions based on automatic problem-determination algorithms. One of the most important aspects of self-management is to perform self-diagnosis to check the system's quality status. Building self-monitoring system requires specifying what to monitor. In our approach, a set of non-functional requirements of quality expressed as constraints on the functional requirements, forms the set of rules for monitoring.

The automation of system self-management requires solid formal foundations for system development, including integration of the NFRs into the development process. The Timed Reactive Object Model (TROM) formalism created at Concordia University [10, 11] has the required expressiveness power for specifying autonomic elements. One of the first objective of this research is to extend TROM formalism to include the specification of the autonomic system architecture, configuration, NFRs and self-monitoring rules within a single formal framework AS-TROM.

The paper is organized as follows: Section 2 describes the AS-TROM formalism. Section 3 introduces the NFRs in Software Engineering. The related work is surveyed in Section 4. Our approach is explained in Section 5. The conclusions and the future work directions are outlined in Section 6.

II. FORMALISM

The TROMLAB development environment is an integrated facility based on the TROM formalism [10] for modeling, analyzing, and developing real-time reactive systems. The process model in TROMLAB supports the iterative development approach, which provides the following benefits:

- Reduces risks by exposing them early in the development process.
- Gives importance to the architecture of the system's configuration.
- Designs modules for large-scale software reuses.

The TROM formalism is a three-tier formal model [10]. As a layered model, each upper tier communicates only with its immediate lower tier. The independence between the tiers makes the modularity, reuse, encapsulation, and hierarchical decomposition possible. The three-tier structure describes the system configuration, reactive classes, and relative Abstract Data Types. The upper-most tier is the subsystem configuration specification. It specifies the object definition, their collaboration, and the port links, which regulate the communication tunnels between objects. The middle tier is the TROM class, which is a Generic Reactive Class and is included in the subsystem. TROM class is a hierarchical finite state machine augmented with ports, attributes, logical assertions on the attributes, and time constraints. The lowest tier is the Larch Shared Language (LSL) trait that represents Abstract Data Type used in the TROM classes.

The AS-TROM formalism is extending the TROM formalism through adding one more tier (see Fig. 1) to include the specification of the autonomic system architecture, system

configuration, and self-monitoring within a single formal framework. AS-TROM is expressive enough for developing autonomic elements.

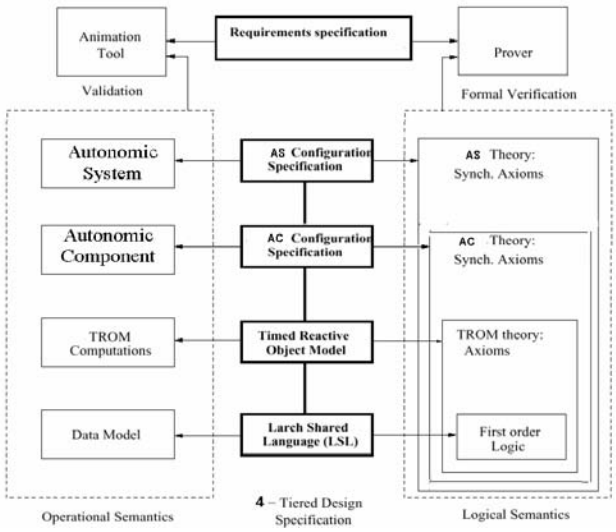

Fig. 1. AS-TROM: four-tier formal model

The design of the autonomic system is specified through formally modeling the autonomic components and their relations, and the timing requirements constraining system's behavior to ensure safety and liveness properties of the system. The formal model of the autonomic system design has to be validated by simulating its behavior and reasoning on the results from the simulation. System verification takes place at the next stage. The AS-TROM model of the system has to be mechanically translated to a set of PVS [9] theories consisting of axioms describing the timed behavior of the system. Time critical properties such as safety and liveness, are to be included as lemmas in PVS theories and verified formally similarly to the current TROM process (see Fig 2).

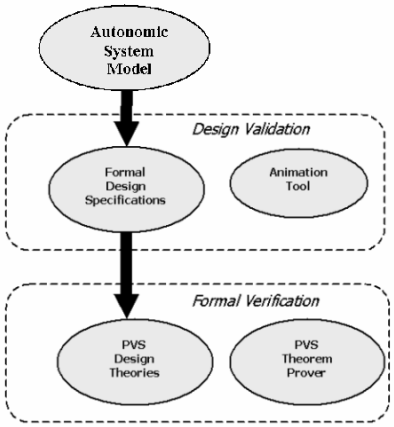

Fig. 2. AS-TROM: Specification, Validation and Verification Methodology

III. NFRs

Once a software system has been deployed, it is straightforward to observe whether or not a certain functional requirement has been met, as the areas of success or failure are rigidly defined. The same is not true for NFRs of quality as these refer to measurable quantities, which usually tend to be strongly interdependent and are among the most expensive and difficult to deal with [1, 2]. According to the software engineering standard IEEE Std.830-1998 [12], NFR is defined as "a software requirement that describes not what the software will do, but how the software will do it, for example, software performance requirements, software design constraints, software external interface requirements and software quality attributes". NFRs had been neglected by the requirements engineering practice and research. Usually NFRs are expressed in a natural language, suffering from ambiguities and potential conflicts. As a consequence, NFRs are difficult to validate and verify; therefore, they are usually evaluated subjectively. The above, and the importance of the NFRs for developing high quality complex systems have motivated the second objective of this work, namely, to develop the hierarchical model of quality NFRs and integrate its specification within the AS-TROM formalism through mapping to system's functional requirements specification.

IV. Related Work

The most widespread approach for dealing with non-functional requirements is the NFR framework [1]. A very important aspect of non-functional requirements decomposition using the NFR Framework is that, as far as NFR softgoal are refined into more detailed ones, it is possible to identify interactions between non-functional requirements. These interactions include positive and negative contributions and have a critical impact on the decision process for achieving other non-functional requirements.

The Unified Process for developing OO systems provides a relatively minimal level of support for expressing NFRs [2]. Extension mechanisms of the UML standard [8] have been used to capture the non-functional requirements expressed in NoFun [4, 5], a language created to provide a basis for establishing quality models in a formal way. The work targets the complete set of quality requirements as described in the ISO/IEC 9126 International Standard. The authors propose the separation of FRs and NFRs where each class is associated with an NFR element, expressed in OCL [5].

Paper [3] discusses a sequence of systematic steps towards an early consideration of specifying and separating requirements. This makes it possible to identify and resolve conflicts earlier in the development cycle and promotes traceability of broadly scoped requirements throughout system development, maintenance and evolution. The approach is presented within four categories of activities: FRs identification and specification, NFRs identification and specification, composing requirements and analysis/design activities. Formalism for the FRs is provided through specifying their pre and post conditions formally using first order predicate logic.

Our work builds upon the existing methods but differs from them in important ways: i) this research proposal takes

advantage of the formal representation of components in AS-TROM formalism, and the autonomy of components in agent-oriented paradigm; ii) formalization of both FRs and NFRs within the same formal framework AS-TROM so that the NFRs can be validated and verified automatically.

V. APPROACH

Autonomic systems automatically monitor and seek opportunities to improve their own quality characteristics such as reliability, availability and performance. The corresponding NFRs have to be specified formally and mapped to autonomic elements' behaviour so that the achievement of the above NFRs can be monitored automatically. Behavioural changes due to the environment and/or system evolution have to be detected automatically, and the self-diagnosis of the system quality against changes must be modelled, followed by the planning of self-healing reaction when the system's behaviour fails to meet the NFRs requirements. The changed configuration may be verified while the system is running without affecting the system integrity. We are currently working on the development of a new AS-TROM formal language powerful enough to describe the structure and the behaviour of the autonomic systems, as well as the non-functional properties constraining the behaviour of the system. The development process formalization would allow for formal validation and verification of FRs and their conformance to the corresponding, guarantying the high quality of the final product and allowing for continuous quality control on the evolving software structures.

The automation of system self-management requires solid formal foundations for system development, validation and verification, including integration of the NFRs into the system formal specification. In this research, each NFRs is regarded as a mathematical theory whose set of axioms is defined by the required scale type of the measurement, and the empirical observations on the attribute to measure. NFRs in this context are regarded as abstractions of algorithms for their quantification, without imposing restrictions on the measurement mechanism other than the axioms specified in the theory. TROM formalism allows for theory inclusion, therefore, the NFRs constraining an autonomic element are to be included in the theory of the corresponding element's specification, thus formalizing the mapping of non-functional requirements to the specification of the components' behavior. Formally expressed NFRs within the same AS-TROM language are formalized as theorems and should be provable from the autonomic elements' behavioral specification automatically.

An important step in achieving successful NFRs monitoring is to achieve the right balance of system quality attributes. The quality model is a rigorous hierarchical decomposition of NFRs for quality from their general statements to algorithms for their evaluation (measurements). This involves identifying the conflicts among several desired quality attributes, and working out a satisfactory balance of attributes satisfaction. The quality model for autonomic systems chosen for our work is the one developed for real-time reactive systems, and based on the TROM formalism as described in [11]. The TROM quality model differs from the existing quality models for reactive systems: i) the measurements are theoretically validated, and ii) are based on the formal specification of the system in TROM. Therefore, it allows the assessement of quality of design solutions at early in the development process.

The solid formal bases for the measurements specified within the same formal framework allow for automation of the evolving automatic system's self-monitoring mechanism. The research achievements in modelling of two of the most important autonomic systems quality requirements, namely, reliability and performance, are described below.

Reliability. The reliability assessment model based on TROM formalism and its empirical validation has been reported in [13, 14, 15, 16, 17, 18]. The reliability model based on Markov chains of the system's expected change is constructed from the system configuration specification. This model serves as the basis of the evolution engine that calculates the reliability prediction factors, and will be used for formalizing the autonomic systems' early reliability assessment. The reliability requirements for autonomic elements and systems have to be specified formally and mapped to system behaviour so that the achievement of the reliability can be monitored automatically.

Performance. The current research work includes performance formalization within the same framework and their crosscutting with autonomic system's behaviour. Some of the results have been published in [19, 20].

Novelty. To the best knowledge of the authors, there is no similar approach reported in the literature on formal specification of non-functional requirements and the system functional model within the same formal framework, for autonomic systems.

VI. DISCUSSION AND NEXT STEPS

This paper is a preliminary report on the ongoing research which main objective is the rigorous approach to developing and evolving autonomic systems whose architecture, system configuration, and continuous self-monitoring of their quality are to be specified within a single formal framework.

The research is focusing on Autonomic Systems - a significant and new strategic and holistic approach to the design of computer-based systems. Autonomic systems will need a mechanism to acquire and represent high-level specifications of NFRs and map them onto lower-level actions. We must develop and analyze algorithms and negotiation protocols for conflicting NFRs, and determine what bidding or negotiation algorithms are most effective.

Safety and Liveness. One of the most challenging tasks in autonomic software system self-monitoring is to assure the conformance to the safety and liveness properties, especially as these systems are to be used in sensitive and often life-critical environments such as medical systems, air traffic control, and space applications. In AS-TROM these properties will be expressed as invariants on the system's behavior, that is, it should be possible to derive those properties from the postcondition of each the system function leading to a change of state. The formalization of the safety and liveness

properties would allow for their automatic monitoring after each state change of the system.

Mechanical Support. The AS-TROM process formalization would allow for formal validation and verification of FRs and their conformance to the corresponding NFRs, guarantying the high quality of the final product and allowing for continuous quality control on the evolving software structures. The tool chosen for verification purposes is PVS [9], a verification assistant that provides mechanized support for formal specification and verification and is based on classical, typed higher-order logic. A mechanism for mapping AS-TROM specifications to PVS theories has to be developed as part of this research work.

Long term objectives. The basic issue for autonomic systems will be to combine the processing of environment and machines to create a more effective overall computation. The interaction between the environment and the autonomic systems will be framed by the predictability and trustability issues, which depend on the unexpected system behavior. The long term work in this direction shall be contributing to building up of a shared ground for environment–computer interaction.

REFERENCES

[1] L. Chung, B. A. Nixon, E. Yu and J. Mylopoulos, "Non-Functional Requirements in Software Engineering". *Kluwer Academic Publishing*. 2000.

[2] R. R. Yong. "The Requirements Engineering Handbook". *Artech House Publishers*. 2004.

[3] M. Kassab, C. Constantinides, O. Ormandjieva. "Specifying an

Separating Concerns From Requirements to Design: A Case Study". *Accepted at ACIT-SE 2005*.

[4] Franch X., Botella P. "Putting non-functional requirements into software architecture". *In Proceedings of the Ninth International Workshop on Software Specification and Design*, pp. 60– 67, 1998**.**

[5] Pere Botella, Xavier Burgues, Xavier Franch, Mario Huerta, Guadalupe Salazar. "Modelling Non-Functional Requirements", 2001.

[6] P. Horn. "Autonomic Computing: IBM's Perspective on the State of Information Technology". *IBM Manifesto*, October 2001, http://researchweb.watson.ibm.com/autonomic/manifesto

[7] J.O. Kephart, D. M. Chess. "The Vision of Autonomic Computing". *IEEE Computer*, January 2003, pp.41-50.

[8] M. Fowler. "UML Distilled 3/e: A Brief Guide to the Standard Object Modeling Language". *Addison-Wesley Pearson Education, Inc*. 2004.

[9] PVS: http://pvs.csl.sri.com/

[10] V.S. Alagar, R. Achuthan, D. Muthiayen, "TROMLAB: A Software Development Environment for Real-Time Reactive Systems", *Technical Report, (first version 1996, revised 1998)*, Concordia University, Montreal, Canada.

[11] O. Ormandjieva. "Deriving New Measurement for Real Time Reactive Systems". *Ph.D. Thesis*, Computer Science & Software Engineering Department, Concordia University, 2002.

[12] IEEE Std.830-1998. "Software Requirements Document".

[13] V.S. Alagar, O. Ormandjieva. "Reliability Assessment of E-Commerce Applications". *In Proceedings of 1st International Conference on E-Business and Telecommunication Networks (ICETE 2004)*, pp.30-37.

[14] V.S. Alagar, O. Ormandjieva, M. Zheng. "Two-tier Agent Architecture for Trusted Communication in Ad-Hoc Mobile Networks (Extended Abstract)". In *Proceedings of the Winter International Symposium on Information and Communication Technologies 2004 (WISICT04)*, pp.392-397.

[15] V.S. Alagar, M. Haydar, O. Ormandjieva, M. Zheng. "A Rigorous Approach for Constructing Self-Evolving Real-Time Reactive Systems". *Journal of Information and Software Technology, (2003*), pp. 743-761.

[16] V.S. Alagar, O. Ormandjieva, M. Zheng. "Incremental Testing for Self-Evolving Timed Systems". In *Proceedings of the Third International Conference on Quality Software (QSIC 2003)*, p.12-19.

[17] V.S. Alagar, O. Ormandjieva,M. Zheng. "Managing Complexity in Real-Time Reactive Systems". In *Proceedings of the Sixth IEEE International Conference on Engineering of Complex Computer Systems (ICECCS2000)*, Tokyo, Japan, 2000.

[18] V.S. Alagar, Ormandjieva. "Reliability Assessment of Web Applications". *In Proceedings of the 26th Annual International Computer Software and Applications Conference (COMPSAC 2002)*, pp.405-414.

[19] V.S. Alagar, O. Ormandjieva, Shi Hui Liu. "Scenario-Based Performance Modelling and Validation in Real-Time Reactive Systems". *In Proceedings of Software Measurement European Forum 2004 (SMEF2004)*.

[20] V.S. Alagar, Shi Hui Liu, O. Ormandjieva, Jian Shen. "Performance Assessment in Real-Time Reactive Systems". *In Proceedings of the 7th IASTED International Conference on Software Engineering and Applications (IASTED - SEA 2003)*, pp.397-206.

Application of Bezier Curves in Knitting Industry CAD/CAM Systems

Elena I. Zaharieva-Stoyanova[1]

Abstract - **This paper treats the problems realted to the curves usage for presentation of knitting objects patterns. The possibilities of Bezier curves application are investigated. Two functions drawing Bezier curves are represented. Their application for a graphics representation of knitting products' patterns is given, too. The paper shows the possibilities of theirs usage in CAD/CAM systems in knitting industry automation. The examples of functionality are given. Bezier curves may be used to form necklines and sleeves as cuts of knitting products. This method gives us a good precision using three or four control points.**

Keywords - **Bezier curves, computer graphics, CAD/CAM systems, knitting industry**.

I. Introduction

Computer Aided Design is one of the most important applications of Computer Graphics. CAD/CAM systems development is closely related to a usage of computer graphics software algorithms. To realize the CAD/CAM systems software the developer has to use mathematical methods and algorithms for screen representation of designed objects. The kind of these objects determines the proper methods and algorithms applied in the particular CAD/CAM system.[4]

Knitting products and knitting structures are designed in CAD/CAM systems for knitting industry automation. Because this paper does not treat the problems related to knitting structures representation, these kinds of methods will be not discussed.

Usually, as designed objects the patterns of knitting products are represented with straight-line polygons. [4],[5] This manner of pattern representation is used because of following reasons:

- It is possible for the knitting products size to have a little tolerance in limits of ±1 cm.
- It is easer to process straight-lines than curves.
- Knitting machines are not so precise in material production. This precision depends on a knitting machine performance called fine or gauche. The performance is related to the number of needles per inch or cm. It determines a loop size and a thread thickness, too.

Because of these reasons the patterns of knitting products are described as straight-lines poligons without curves. If there is curve section, the workers form it additionally by cutting material.

Cutting material to form products is not a good solution for modern knitting production. More over, modern knitting machines are precise and they have great abilities to knit products by Fully Fashion (FF) method. It imposes usage of curves in graphics representation of knitting products in CAD/CAM systems.

This paper treats the problems related to Bezier curve application in knitting object pattern design. Functions drawing Bezier curves are created. These functions will be used for a graphics representation of knitting products' patterns. The paper shows the possibilities of their usage in CAD/CAM systems in knitting industry automation.

II. Bezier Curves

A Bezier curve in its most common form is a simple cubic equation that can be used in any number of useful ways. Originally it was developed by Pierre Bezier for CAD/CAM operations. [1],[2],[3]

Bezier curves are defined using m control points, known as knots. Two of these are the end points of the curve, while the others effectively define the gradient at the end points. These points control the shape of the curve. The curve is actually a blend of the knots. This is a recurring theme of approximation curves; defining a curve as a blend of the values of several control points. [2],[10]

A Bezier curve is represented in parametric form as:

$$x = p_x(t)$$
$$y = p_y(t) \tag{1}$$

Let (x0,y0), (x1,y1), ...(xm,ym) be control points. The Bézier parametric curve function is of the form:

$$p_x(t) = \sum_{i=0}^{m} C_m^i t^i (1-t)^{m-i} x_i$$
$$p_y(t) = \sum_{i=0}^{m} C_m^i t^i (1-t)^{m-i} y_i \tag{2}$$

A parameter t value varies from 0 to 1.

The value of the coefficient Cm is:

$$C_m^i = \frac{m!}{i!(m-i)!} \tag{3}$$

Using the vector form the formula (1) is represented as:

[1]Elena I. Zaharieva-Stoyanova is with the Department Computer Systems and Technologies, Technical University of Gabrovo, 4 H. Dimitar, 5300 Gabrovo, Bulgaria, E-mail: zaharieva@tugab.bg.

$$P(t) = \begin{bmatrix} p_x(t) \\ p_y(t) \end{bmatrix} \tag{4}$$

Than, Bezier curve given as formula (2) is represented as:

$$P(t) = \sum_{i=0}^{m} C_m^i t^i (1-t)^{m-i} P_i \tag{5}$$

For better graphics interpretation let us transform this formula as:

$$P(t) = (1-t)^m P_o + \sum_{i=1}^{m-1} C_m^i t^i (1-t)^{m-i} P_i + t^m P_m \tag{6}$$

For computer presentation the equation (6) is better than (5) because there is division by zero if i=0, or i=m. Moreover, the function n! for n=0 is not defined.

The examples for graphics representation of Bezier curves are given on fig. 1.

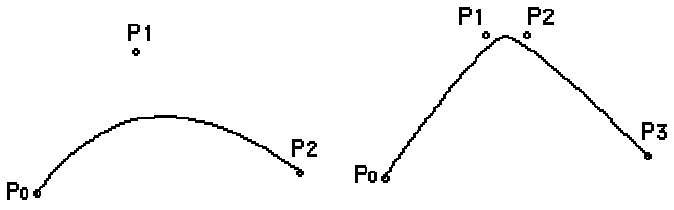

Fig.1. Examples of Bezier curves

III. Bezier Curves Generation Functions

Using formula (6) let us present the equation for three control points. The value of P(t) is determined by the following equation:

$$P(t) = (1-t)^2 P_o + 2(1-t)tP_1 + t^2 P_2 \tag{7}$$

Using four control points, the equation (6) is represented as:

$$P(t) = (1-t)^3 P_o + 3(1-t)^2 tP_1 + 3(1-t)t^2 P_2 + t^3 P_2 \tag{8}$$

Using Visual C++ 6.0 and Microsoft Foundation Class Library the function drawing Bezier curves are created. The following functions Bezier2 and Bezier3 draw Bezier curves with three and four control points, respectively.

The function drawing a Bezier curve using three control point is:

```
void Bezier2(CDC *pDC, CPoint P0, CPoint P1, CPoint P2)
{
   double t, dt, x, y;
   pDC->MoveTo(P0);

  dt=0.1;
  t=0;
  while (t<=1)
  {
        x=(1-t)*(1-t)*P0.x+2*(1-t)*t*P1.x+t*t*P2.x;
        y=(1-t)*(1-t)*P0.y+2*(1-t)*t*P1.y+t*t*P2.y;
        pDC->LineTo(CPoint((long)x,(long)y));
        t+=dt;
   }
}
```

The function drawing a Bezier curve using four control point is:

```
void Bezier3(CDC *pDC, CPoint P0, CPoint P1, CPoint P2,
CPoint P3)
 {
    double t, dt, x, y;

     pDC->MoveTo(P0);

    dt=0.1;
    t=0;
    while (t<=1)
     {
        x=pow((1-t),3)*P0.x+3*pow((1-t,2))*t*P1.x
+3*t*t*(1-t) *P2.x+t*t*t*P3.x;
        y=pow((1-t),3)*P0.y+3*pow((1-t),2)*t*P1.y
+3*t*t*(1-t) *P2.y+t*t*t*P3.y;

        pDC->LineTo(CPoint((long)x,(long)y));
        t+=dt;
        }
 }
```

The parameters P0, P1, P2, P3 represent control points. CPoint is a class describing a point with x, y -coordinates. The parameter pDC is a pointer to Device Context (DC) corresponding to the monitor as an output device.

To find a current position of x,y the function Bezier2 uses the equation (7), and function Bezier3 uses the equation (8). The value of the t-parameter varies from 0 to 1 with a step dt=0.1. Because these functions are used for graphics representation of knitting object patterns the precision related with dt value is enough.

IV. Application of Bezier Curves Generation Functions

Using the fact that the seizes of knitting products allow a little tolerance, the most CAD/CAM systems in knitting industry do not use the curves for graphics representation of knitting patterns. [7],[8],[9],[11]

In most cases the presentation of these objects as straight-line polygons is allowed but using the curves give us better

precision. Forming sleeves and necklines requires curves usage as graphics objects.

The example for the Bezier2 function usage is shown on fig. 2. The drowning of neckline and sleeve is an application of this function. The positions of the control points are given, too.

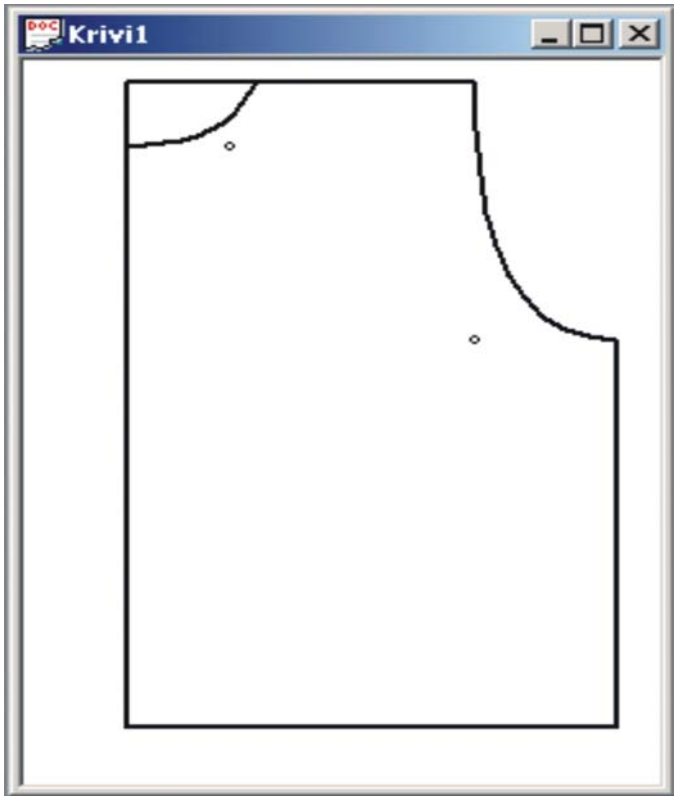

Fig. 2. Knitting pattern using Bezier2 function

Figure 3 present the forming of a neckline by using Bezier3 function. In comparison to previous example the neckline is formed more precisely but the difference is not great. It means that the usage of four control points has the approximate precision as the usage of three control points.

Figure 4 is an example of drawing a sleeve by using of Bezier3 function.

As it is shown by the examples the Bezier curves may be used to form necklines and sleeves in pattern of knitting products. The curve has a good precision. Is not necessary to use more than four control points. The main problem is the estimation of control points' positions. An interactive method is recommended to find the proper x,y-coordinates of control proints.

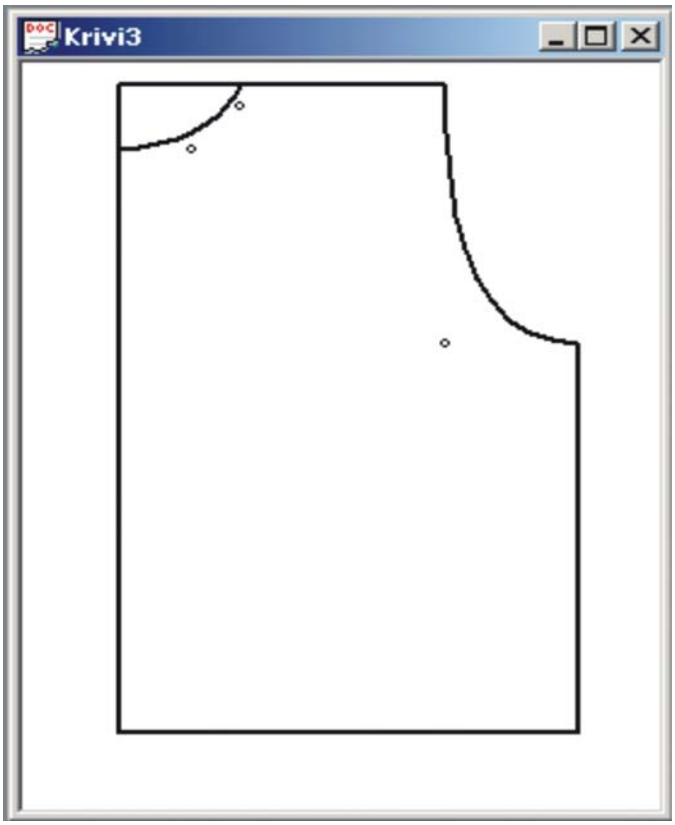

Fig. 3. Knitting pattern using Bezier2 and Bezier3 functions

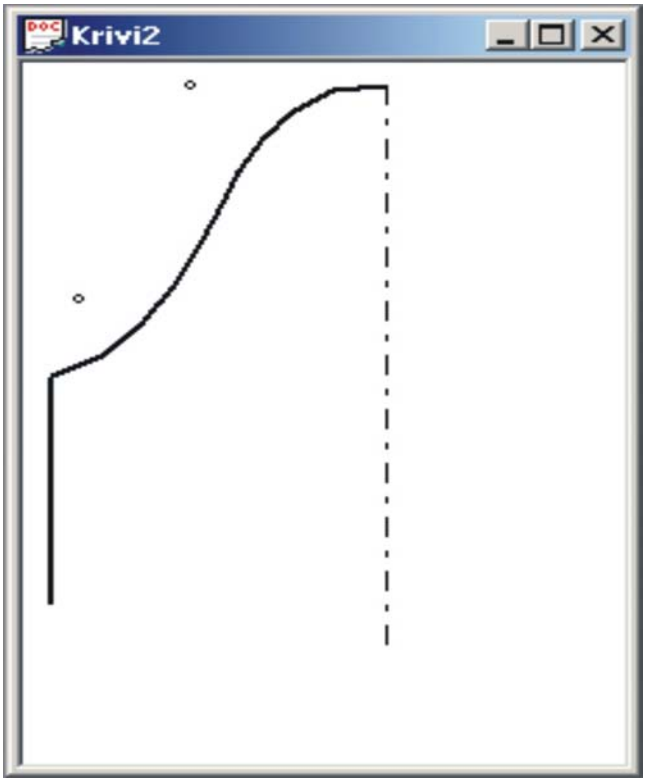

Fig. 4. Knitting pattern using Bezier3 function

V. CONCLUSION

For a graphics presentation of knitting objects patterns in CAD/CAM systems straight-lines polygons are used usually. To show these patterns more precisely, it is necessary to apply curves as polygons' sections. This paper treats the problems related to the curves usage for presentation of knitting objects patterns. The possibilities of Bezier curves application are investigated.

This paper presents two functions for drawing Bezier curves and their application for a graphics representation of knitting products' patterns. The paper shows the possibilities of theirs usage in CAD/CAM systems in knitting industry automation. The examples of functions application are given.

Bezier curves may be used to form necklines and sleeves in pattern of knitting products. This method gives us a good precision using three or four control points. To estimate the proper x,y-coordinates of control points an interactive method is recommended.

The presented functions have an application in CAD/CAM systems in knitting industry. The Bezier curves may be used successfully in automation of the other branches of textile industry as tailoring, embroidery.

REFERENCES

[1] Brourke P., Bézier curves, December 1996.

[2] Pavlidis T., Algorithms for Graphics and Image Processing, Bell laboratories, Computer Science Press, 1982.

[3] Лукипудис Е., Компютърна графика и геометрично моделиране, София, Техника, 1996.

[4] Zaharieva-Stoyanova E., J. Angelova, CAD system structure for design of weft knitted garments, Scientific Conference EMF'2004, 20-21 Sept. 2004, Sv.sv. Konstantin &Elena, pp.173-178.

[5] Zaharieva-Stoyanova, E., "Application of Image Processing methods in CAD/CAM Systems for Knitting Industry Automation", 1st IEEE International Symposium "Intelligent Systems", Sep. 2002, Varna, Bulgaria, pp. 55-58.

[6] Zaharieva-Stoyanova E., N.Siniagina, Image Coding in CAD/CAM systems for Knitting ingustry, Automatica&Informatics 5-6/2001, pp 51-54

[7] Sirix 110/210, Instructions, Part I, II, Reutlingen, 2001

[8] DeSignaKnit, Demo, www.knitcraf.com

[9] Stitch&MotifMaker, www.softwareknitting.com

[10] www.moshplant.com

[11] www.knitwares.ca.

Code-Based Graph Representations And Software Reengineering

Violeta T. Bojikova[1], Mariana Ts. Stoeva[2]

Abstract - **The purpose of this work is to summarize the role of software reengineering in software maintenance process and to show the place of the software clustering process in the software-reengineering model. The code-based graph representation is one of the open problems, because the results of clustering process depend on this representation. In this paper we discuss and present our observations about the code-based graph representation problem.**

Keywords – **software reengineering, software-clustering algorithms, software representation**

I. INTRODUCTION

Companies often have legacy systems, which have to be maintained. Since the 1950's over 100 billion LOC have been written. Legacy software is a valuable asset, which cannot be easy discarded or redeveloped. Something has to be done to help keep the cost of maintenance down. When legacy software has a high business value and low changeability the reengineering is the recommended variant to its development (figure 1). Chikofsky and Cross define software reengineering as "the examination and alteration of a subject system to reconstitute it in a new form and subsequent implementation of that form". This definition is technology oriented while Arnold's definition is goal-oriented: Software reengineering is defined by Arnold as "any activity that:

- improves one's understanding of software, or,
- prepares or improves the software itself, usually for increased maintainability, reusability, or evolve ability".

Although the two definitions do not necessarily correspond, both the above authors provide good introductions to software reengineering.

In figure 1 we try to summarize the characteristics of software reengineering activity: role, processes, goals, actual status, main problems and their solutions and show the place of the software clustering process in the software-reengineering model.

As we see in figure 1, code-based graph representation algorithms and tools (Code Analysis tools) are needed to help software maintainers.

II. THE GRAPHS IN THE SOFTWARE REENGINEERING AREA

Large software systems tend to have a rich and complex structure. Designers typically present the structure of software systems as one or more directed graphs. For example, a directed graph can be used to describe the modules, classes, functions, operators of a system and their static interrelationships using nodes and directed edges, respectively. Graphs are commonly used not only for system's visualization [10], but also as input for automatic clustering algorithms [1,2,3,10], the goal of witch is to extract the high level structure of the program under study. The problem of code-based graph representation is one of the open problems in software clustering area, because the results of clustering process depend on this representation.

In Bunch (software clustering tool) [1,2,3] are used module dependency graphs (MDGs). MDG is directed graph that represents the software modules (e.g., classes, files, packages) as nodes, and the relations (e.g., function invocation, variable usage, class inheritance) between modules as directed edges (figure 3). The MDG of the clustered software systems in [1,2,3] are recovered automatically from its source code using tools such as CIA [8] (for C), Acacia [7] (for C and C++) or Star [9] for Turing [4]. However, even the MDGs of small systems can be complex. Then appropriate abstractions of their structure are needed to make them more understandable and, thus, easier to maintain [1,2,3]. Once the MDG is created, Bunch's clustering algorithms can be used to create the partitioned MDG.

A number of software clustering algorithms is developed to separate the graph's nodes (i.e., modules) into clusters (i.e., subsystems). Decomposing source code components and relations into subsystem clusters is an active area of research. Numerous clustering approaches have been proposed in the reverse engineering literature, each one using a different algorithm to identify subsystems than producing an architectural view.

The software reengineering literature shows that the problem of automatically creating abstract views of software structure is very computationally expensive (NPhard), so a hope for finding a general solution to the software is unlikely.

[1] Violeta Bojikova is with the Department of Computer Science Varna Technical University, Bulgaria, e-mail: vbojikova2000@yahoo.com

[2] Mariana Stoeva is with the Department of Computer Science Varna Technical University, Bulgaria e-mail: mariana_stoeva@abv.bg

Figure 1: Software Reengeneering: Role, Characteristics and problems

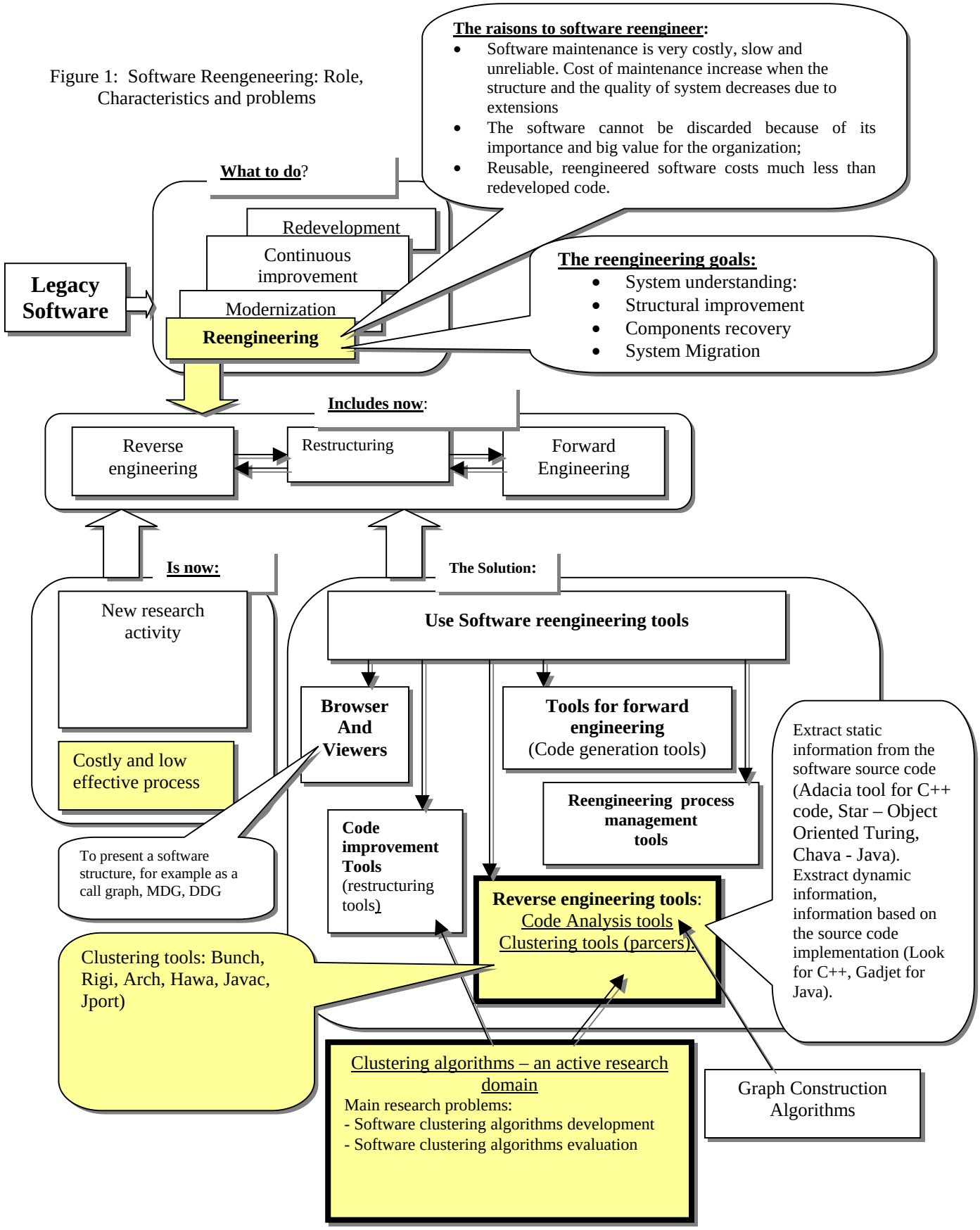

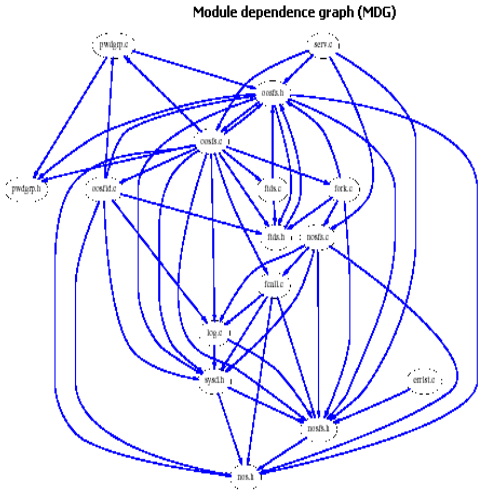

figure 3.

In [6] are used call graphs (CG) [6] as input of automatic clustering algorithms. Call graphs and control flow graphs (CFG) are commonly used in the fields of program slicing (figure 2) and regressing testing [5]. The observation is that determining the call graph for a procedural program is fairly simple. However, this is not the case for programs written in object-oriented languages, due to polymorphism. A number of algorithms for the static construction of an object-oriented program's calls graph have been presented in the literature in recent years. In [6] for example, are presented three such algorithms on the automatic clustering of a Java program. The problem is that object-oriented programs have an inherently richer structure than those written in procedural languages, and so even medium sized programs produce large graphs. Because software clustering is a NP-hard problem, existing clustering tools are not able to process large graphs with weighted arcs and nodes, at the same time.

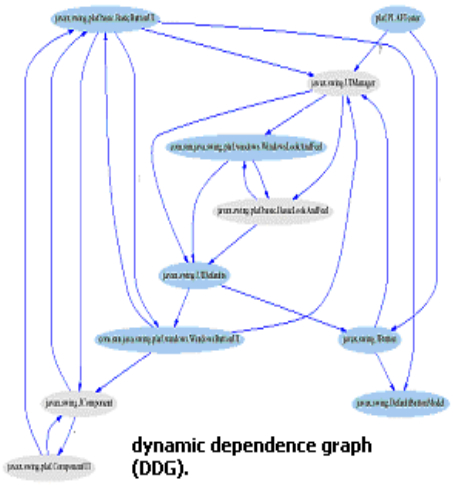

figure 3.

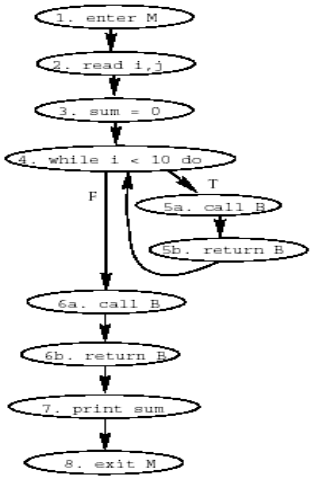

Control-flow graph — procedure M

```
   procedure M
1  begin M
2     read i,j
3     sum = 0
4     while i < 10 do
5        call B
      endwhile
6     call B
7     print sum
8  end M
```

figure 2.
Procedure M and the resulting CFG

Understanding the dynamic structure of a system is helpful during software maintenance. The observation is that a number of algorithms for the static construction of an object's oriented call graph have been developed in the software reengineering literature in the recent years. The problem is that the source representation algorithms and tools must help software engineers extract also the dynamic structure of object oriented programs. Dynamic analysis is an open problem in software clustering. Our observation is that static analysis, using a tool such as Chava [11] reveals part of the complete design. It not reveals the relationships between the classes at runtime. Dynamic analysis can be used to complement static source code analysis, which may not provide all of the software information.

In [12] Juan Gargiulo and S. Mancoridis develop a tool, called Gadget, which try to extract the dynamic information of an Object Oriented Java program. A DDG (dynamic dependence graph) is created (figure 4), where nodes represent classes or objects and edges represent relations (i.e. method invocation) between two objects or between a static

class and an object. The problem is that Gadget presents only the dynamic (running) relations and does not show the static relations such as inheritance relations.

III. CONCLUSION

Software supports many business, government, and social institutions. As the processes of these institutions change, so must change the software that supports them. Changing software systems that support complex processes can be quite difficult, as these systems can be large (e.g., thousands or even millions of lines of code) and dynamic. There is a need to develop sound software reengineering methods and tools to help software engineers understand and maintain large and complex systems so that they can modify the functionality or repair the known faults of these systems.

In this paper we try to summarize the characteristics of software reengineering activity: role, processes, goals, actual status, main problems and their solutions and to show the place of the software clustering process (figure 1) in the software-reengineering model.

In this paper we underline that the oriented graphs are commonly used in much software reengineering activities: automatic-clustering algorithms, in the fields of program slicing and regressing testing.

The observation is that a number of algorithms for the static construction of an object's oriented graph have been developed in the software reengineering literature in the recent years. But these clustering tools are not able to process large graphs with weighted arcs and nodes, at the same time. The problem is that even medium object-oriented programs produce such graphs because of polymorphism.

Dynamic analysis is an open problem in software reengineering. The source representation algorithms and tools must help software engineers extract also the dynamic structure of object oriented programs but there isn't enough experience in this field.

REFERENCES

[1]. Mitchell, Mancoridis, Traverso, " Search Based Reverse Engineering", In the ACM Proceedings of the 2002 International Conference on Software Engineering and Knowledge Engineering (SEKE'02), Ischia, Italy, July, 2002. pp. 431-438

[2]. Spiros Mancoridis, Brian Mitchell, C. Rorres, Y. Chen, and E. R. Gansner, Using Automatic Clustering to Produce High-Level System Organizations of Source Code, IEEE Proceedings of the 1998 International Workshop on Program Understanding (IWPC'98)

[3]. Spiros Mancoridis, Brian Mitchell, Y. Chen, and E. R. Gansner, Bunch: A Clustering Tool for the Recovery and Maintenance of Software System Structures, IEEE Proceedings of the 1999 International Conference on Software Maintenance (ICSM'99)

[4]. Mary Jean Harrold, Cregg Rothermel, "A Coherent Family of Code-Based Graph Representations for Object-Oriented Software", Dep. Of Computer and Information Science, Ohao State University

[5]. Sinha, S., Harrold, M. J., and Rothermel, G. 2000. Interprocedural control dependence. Technical Report GIT-CC-00-17 (June), College of Computing, Georgia Institute of Technology.

[6]. Derek Rayside, Steve Reuss, Erik Hedges, and Kostas Kontogiannis. The effect of call graph construction algorithms for object-oriented programs on automatic clustering. In Margaret-Anne Storey, Anneliese von Mayrhauser, and Harald Gall, editors, IWPC'00, pages 191–200, Limerick, Ireland, June 2000.

[7]. Y. Chen, E. R. Gansner, and E. Koutsofios. A C++ Data Model Supporting Reachability Analysis and Dead Code Detection. In Proceedings of the European Conference on Software Engineer-ing/ Foundations of Software Engineering, 1997

[8]. B. Krishnamurthy. Practical Reusable Unix Software. John Wiley & Sons, Inc., New York, 1995.

[9]. S. Mancoridis, R. C. Holt, and M. W. Godfrey. A Program Understanding Environment based on the "Star" Approach to Tool Integration. In Proceedings of the Twenty Second ACM Computer Science Conference, pages 60–65, March 1994.

[10]. В.Т.Божикова, М.Н.Карова "Създаване, визуализация и операции на програмни структури", Proceedings of the Int'l Scientific Conference on Energy and Information Systems and Technologies, Vol.3., Bitola, pp. 813-819, June 7-8, 2001

[11]. Jeffrey Korn etc. "Chava: Reverse engineering and Tracking of Java Applets"

[12]. Spiros Mancoridis and Juan Gargiulo, "Gadget: A Tool for Extracting the Dynamic Structure of Java Programs", ACM/IEEE Proceedings of the 2001 International Conference on Software Engineering and Knowledge Engineering (SEKE'01)

Poster Session PO4:

ELECTRONICS

Approaches to Improve of Network Driver for Industrial Purposes

Stanimir D. Mollov[1]

Abstract – **The paper presents the approaches to improve of network driver for industrial purposes. The transmission of the messages over the industrial network has been discussed. An analysis of the serial asynchronous interface has been done. Due to the analyses it is decided to apply the variant of realized an additional special signal, which enables output buffer of the network driver. Possibilities for existing conflict situations have been analyzed. The variants for their overcoming are offered.**

Keywords – **network driver, output buffer, serial interface**

I. INTRODUCTION

The driver for the local array network for industrial purposes realizes all sending and receiving functions, protected times, repeating when an error occurs. Besides its own work area in the operating memory, the driver supports and state's word. The driver communicates with the software through that word by setting and cleaning flags. It is consist of: initializing part, receiver and transmitter.

The driver for the local array network has the following entry points shown on fig.1.

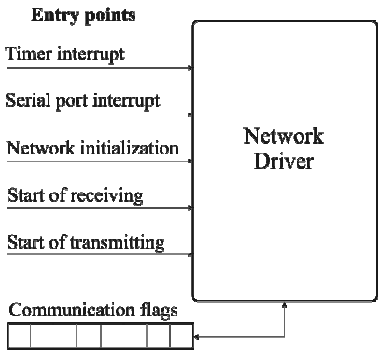

Fig. 1 Entry points of the network driver

Interrupt from system timer – the control is given here in case of interrupt from system timer. This entry point only modifies the counters of the protected times and checks whether the protected time is past.

Interrupt from serial port – this is the interrupt from serial port, which submits request when a symbol is received from the network and when a transmission of a symbol is finished.

[1]Stanimir D. Mollov is with the Faculty of Electronic Engineering, and Technologies, TU – Sofia, 1797, Sofia, Bulgaria, E-mail: smollov@abv.bg

Network initialization – this entry point is being called for initial initialization of the serial port. The receiver and the transmitter are set in inactive state.

Start of receiving – this entry point sets the address of the input buffer and its maximum length. The driver does the necessary changes in the state's word. By this way the driver sets the receiver in active mode. After that the receiver starts to watch the line and to receive the messages for this station. After a message is receiver the receiver marks that by setting the appropriate flags in the state's word and goes into end of receiving mode.

Start of transmission – this entry point is activated only in case of inactive transmitter (the transmission of the last message is finished). Here the address of the output buffer, the length of the message and the recipient are writing. The driver makes the necessary changes in the state's word and sets the transmitter in active mode. From here on the transmitter checks whether the line is busy and when it is not used starts the transmission of the message. After the transmitting had finished it mark by setting the appropriate flags in the state's word and goes into inactive mode**.**

II. TRANSMITTING THE MESSAGES VIA THE INDUSTRIAL NETWORK

The network driver processes each received symbol. In the receiving mode it watches the line and receives the messages, which are destined for this station. In the transmission mode the driver check whether the line is busy and when is not used starts the transmission of the message.

Due to the high noise level in the communication environment, it is necessary the transferred data to be blocked in comparatively short blocks.

After the sender send the data block via industrial network, the receiver acknowledges its receipt. Positive receipt (ACK) means that the transmission had finished successfully. Negative receipt (NAK) means that the sender must resend this block, because of a block receive error.

All actions in the local area network have own protected times. If the station transmitter had not received the acknowledgment at a fixed time interval, it repeats the transmission of the current data block. If the acknowledgment from the receiving station was positive, but it had not received, due to the noises in the network, the transmitting station has to repeat the same message. The receiver will find out that the block transmission sequence is broken thanks to the block identifier. The transmission interruption is done by sending a BREAK signal. That is recognized like error in the format of transmission data by all station including sender.

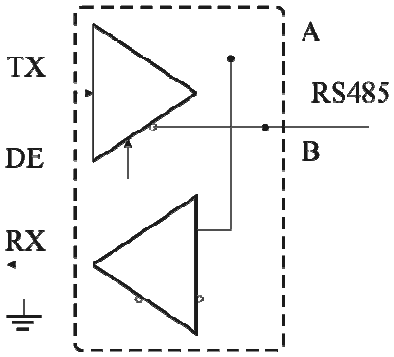

Fig. 2 Output buffer of the network driver

A conflict situation is possible to appear when more than one station from local area network starts transmission at the same time. Each sender listens to the line (receives its own transmission) and compares the sent and the received information. In case of a difference (someone transmits over the line too) the sender interrupts the transmission and sends a BREAK signal to inform the others users for the conflict situation. After that each station continues to receive, but does not start transmission before a certain time, that depends on user's address in the network.

III. Interface for Data Transmission

For bi-directional data transmission usually are used two types of interfaces: half-duplex and full-duplex. The full-duplex interfaces used separated communication lines (fig.3), while half-duplex interfaces used common communication line (fig.4) as for the transmission as well as for the receiving.

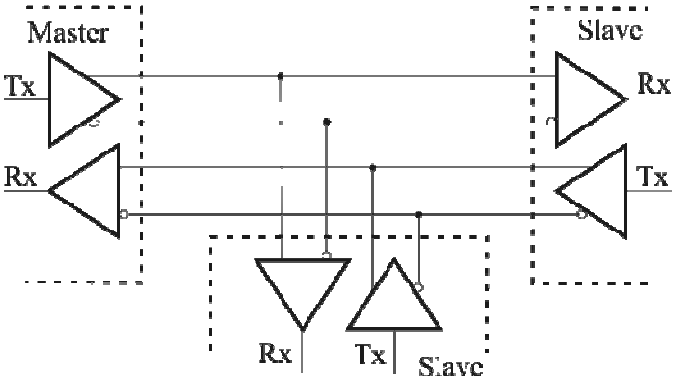

Fig.3 Full –duplex interface

Normally RS485 network uses "half-duplex" interface. All device transmitters and receivers in this network are connected to the same bus. Due to this, it is necessary certain precautions to be taken to avoid the activation of more than one transmitter at the same time. For this purpose a special signal must be created, which enables output driver of transmitter, when some data is transmitting. The correctly determining the position and duration of time interval, during which an output driver on RS485 transmitter is enabled, increases the reliability of information.

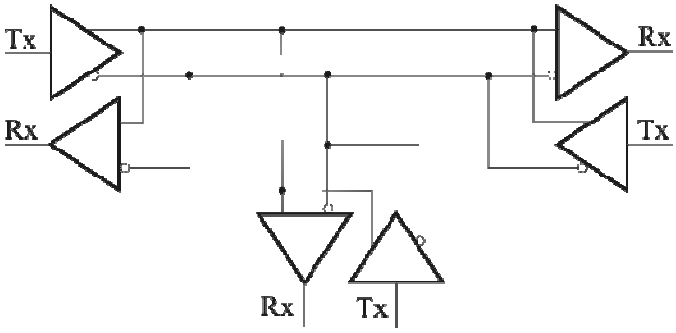

Fig. 4 Half-duplex interface

IV. Serial Asynchronous Interface

The serial communication is a suitable way for connection between controllers or between controllers and other smart devices. It offers a physical interface with a minimum number of lines. Usually the connection between controllers over the industrial network is based on serial communication asynchronous interface. The asynchronous transmission do not supports the clock frequency between transmitter and receiver. Because of this the number of communication line is decreased. Normally the correspondents are clocked by own clock generators. The synchronization between them is accomplished from additional bits, included into the transmitting information.

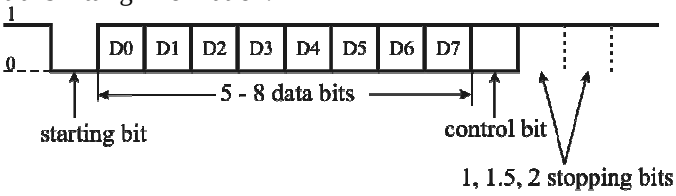

Fig.5 Serial asynchronous standard

The serial asynchronous standard is shown on fig.5. When the line is not active, its state is logical 1. In the beginning the starting bit is sent with active level is logical 0. Immediately follow the data bits. The data byte is transmitted with the least significant bit in front. After that the control bit (parity/no parity) and the 1-2 stopping bits are transmitted.

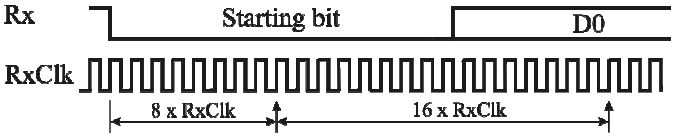

Fig.6 Synchronization between transmitter and receiver

The transmitter and receiver are functionally independent, but use the same data format and baud rate. The baud rate generator fig.7 produces a clock either x16 or x64 of the bit shift rate.

After the first falling edge on Rx line the receiver waiting 8 clocks cycles RxClk and checks the input signal level. If it is logical 1 the next receiving is interrupted. If it is logical 0 the receiver accepts that the starting bit is arrived. After that the

remaining bits are receiving at time interval equal to 16 clock cycles of RxClk. By this way all bits are sampled in the middle of its transmission time interval. The changes of the transmission speed may reflect over correctly reception.

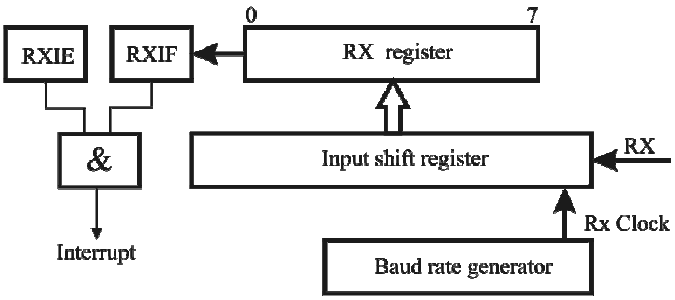

Fig. 7 Asynchronous receiver

The asynchronous receiver block diagram is shown on fig.7. The heart of the receiver is an input shift register. The RX register obtains its data from the shift register. Once the shift register transfers the data to the RX register, the flag bit RXIF is setting. The interrupt can be enabled/disabled by setting/clearing enable bit RXIE. The flag RXIF will reset only when the data is reading from RX register.

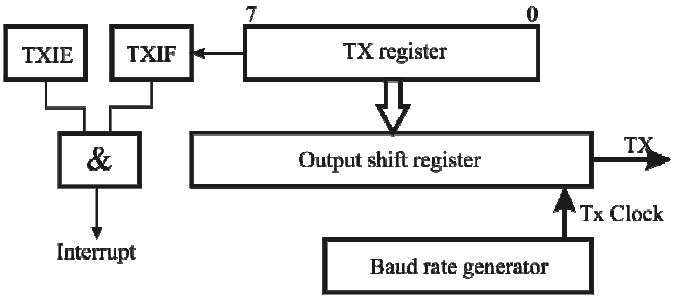

Fig.8 Asynchronous transmitter

The asynchronous transmitter block diagram is shown on fig.8. The shift register obtains its data from the TX register. The TX register is software loading with data. Once the TX register transfers the data to the shift register, the TX register is emptying and flag bit TXIF is setting. The interrupt can be enabled/disabled by setting/clearing enable bit TXIE. The flag TXIF will reset only when new data is loading into the TXREG register.

V. Network Driver

A. Transmission Mode

In the transmission mode the network driver checks whether the line is busy or not. If the line is free the driver enable own output buffer (fig.2) and start the transmission of the message. The activating of the output buffer must occur before transmitting starting bit of the first byte of the message. The deactivating of the output buffer must occur after transmitting stopping bit of the last byte of the message. A conflict situation may occur when the transmitter remaining in active state when the answer of the previous message is transmitted via network. In this case the transmitters of two stations are enabled at same time. The transmitter of the first station holds the line in logical 1 (last stopping bit of the message). The transmitter of the second station tries to hold the line in logical 0 (first starting bit of the answer). To get out of this conflict it is necessary to decrease the time for deactivating the output buffer after transmitting the last stopping bit of the message.

Two variant may be used to deactivate output buffer after last stopping bit:

- via interrupt;
- via polling the interrupt flag or another special bits; controlled by output shift register.

To use the first variant it is necessary the interrupt from the transmitter to be enabled. This performs by setting the TXIE bit. When the output shift register is loading from the TX register, the flag bit TXIF is setting and the micro-controller enters into interrupt mode. The deactivating of the output buffer should occur with time delay after setting TXIF. That time interval is equal to the time for physical transmitting of the contents of the output shift register.

It is possible to use interrupt from the receiver if the station listens and compare for a right transmission. After transferring the last byte of the message from TX register into the output shift register the interrupt from receiver is enabling. This interrupt deactivates output driver of the transmitter.

The advantage of using interrupt is that the processor time is used effectively for other tasks. The disadvantage of using interrupt is the necessity of time for storing and restoring the contents of the processor registers when the interrupt is generated.

A special bit, which shows the status of the output shift register, may be used to deactivate of the output buffer. A good example is an asynchronous transmitter embedded in microcontrollers PIC produced by Microchip (fig.9). While TXIF indicated the status of the TXREG register, another bit TRMT shows the status of the TSR register. Status bit TRMT is a read only bit, which sets when the TSR register becomes empty. No interrupt logic is tied to this bit, so it has to be permanently polling to determine if the TSR register is empty. When the TMRT bit is setting, a time delay equal to the time for one bit transmitting must be generated. After this delay the output buffer must be disabled.

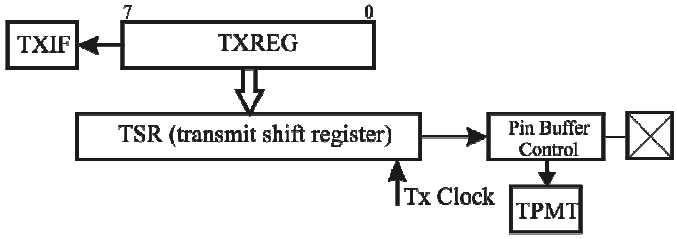

Fig.10 USART transmitter block diagram

B. Receiving Mode

After receiving of the last byte of the message the network driver analyze it. The analysis is accomplished on the base of

checksum attached to the end of the message. The station transmitter calculates and attaches the checksum at the end of message. The station receiver also calculates such checksum from incoming bytes of the message. At the end station receiver compares the received and calculated checksum and creates the answer to station transmitter. If these two values are equal the answer is positive else the answer is negative and the transmitter station must repeat the message.

The time for generating the answer of the receiving message may be rather short. In this case it is possible the station receiver to reply before the output buffer of the station transmitter is not disabled (fig.11).

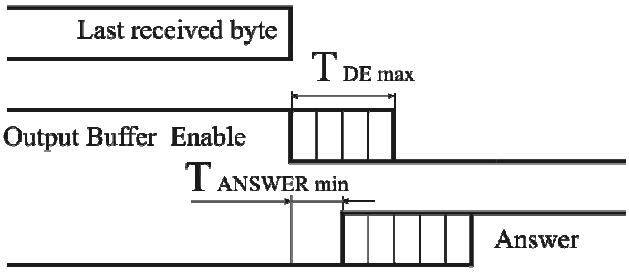

Fig.11 A possibilities for a conflict situation

$T_{DE\ max}$ – maximum time interval for deactivating of the output buffer of the transmitter after the last byte

$T_{ANSWER\ min}$ – minimum time interval for transmitting the answer after receiving the last byte of the message

To avoid from this conflict situation it is necessary the following condition must be keep:

$$\frac{T_{DE\max}}{T_{ANSWER\min}} < \frac{1}{2} T_{Bit}$$

,where T_{Bit} is the time for transmitting a bit. T_{Bit} depends of the used transmission speed.

If this condition is broken the right transmission is not guaranteed.

There are several solutions to avoid from situations:

- using a software delay (all other interrupts may be enable);
- using a timer interrupt;
- using an interrupt from transmitter.

The last one solution is shown on fig .12. The station receiver sends two preliminary symbols before answer. When the preliminary symbol is transmitted the output buffer is not enabled. After loading the preliminary byte into the output shift register the interrupt is generating.

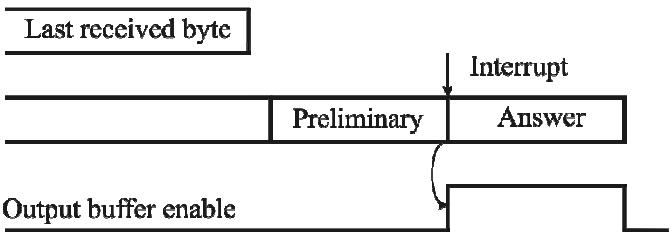

Fig. 12 Interrupt from transmitter

The interrupt loading the answer into TX register and activates the output buffer. In this case a total time delay is equal to time for transmitting the preliminary symbol.

C. Input Buffer

To increase the effectiveness of data exchange speed the input buffer of the network driver is realized as shown in fig.13. After receiving the current message the network driver change the current input buffer address (If been IBUF1 then IBUF2 is a new input buffer and vice versa). So, a new message is allowed to arrive before the previous message is transferred input buffer to input message queue.

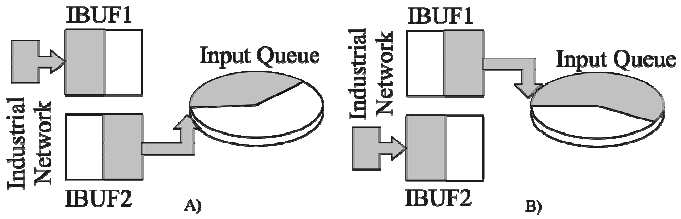

Fig. 13 Input buffer organizing

VI. CONCLUSION

In this paper the approaches for improve of network driver for industrial purposes are discussed. The transmission of the messages over the industrial network is discussed. An analysis of the serial asynchronous interface has been done.

Possibilities for existing conflict situations have been analyzed. The variants for their overcoming are offered.

The article describes also another variant of the enable signal ending, using a special bit which is dependent of the used micro-controller.

In the paper the condition to avoid from conflict situations is present. If this condition is broken the right transmission is not guaranteed.

REFERENCES

[1] Dimitrov, E., G. Mihov, I. Tashev, M. Mitev, *Local array network for industrial controller*, Proceedings of the Int. Scientific Conference ENERGY AND INFORMATION SYSTEM AND TEHNOLOGIES, . vol. 3 pp. 608-613, June 7-8, 2001, Bitola, Macedonia.

[2] Herbert, F. *Implementing Network Protocols and Drivers – with STREAM.* Embedded Systems Programming, April, 1997, p.28.

[3] Herhandez, E., Chidester, and A. George, "*Adaptive Sampling for Network Menagement"*, Journal of Network and System Management, Journal Publications from the HCS Research Lab, 1999.

[4] DS41124C – PIC16C745/765 Datasheet, Microchip Technology Inc., 1999

Extending the Possibilities of the PSpice Simulation in the Power Electronics Using Postprocessing in the Graphical Analyzer Probe

Elissaveta D. Gadjeva[1], Georgi Tz. Kunov[2] , Mario E. Ivanov[3]

Abstract – **The possibilities for advanced simulation of power electronic circuits are investigated using the PSpice program and the incorporated functions of the graphical analyzer Probe. The proposed investigations are applied to the basic power electronic circuits: thyristor rectifiers (single phase, three-phase one-wave, three-phase full-bridge rectifiers), bridge resonant inverter as well as current fed inverter. Similarly, the extended possibilities can be applied to another power electronic circuits.**

Keywords – **Power electronics, Computer modeling, PSpice simulation, Power converters, Parametric analysis.**

I. INTRODUCTION

The general-purpose *PSpice*-like simulators are widely used for the analysis of variety electrical and electronic circuits [1,6,7]. The time-domain analysis is often applied due to the specific characteristics of the electromagnetic processes which take place in the power electronics. The analysis results are highlighted with the voltage and current waveforms of the building elements in the time domain. These dependencies, however, can not describe some important circuit characteristics such as the regulation abilities, the load characteristics, as well as the circuit stability as a function, for instance, of the load variation [2,3,4,5].

The parametric analysis is widely used for a detailed investigating of electronic circuit of different kinds. It is applied to construct the regulation characteristics of the thyristor rectifiers.

The *Append* function allows the obtaining of family of curves and gives the possibility to compare the regulation characteristics of different rectifiers.

The load and regulation characteristics in power electronics are analyzed using generalized parameters such as quality factor *Q* (for the resonant inverters) and load coefficient *B*=1/(*fRC*) for the current fed inverters. The parametric analysis allows the load resistance calculation depending on the introduced generalized parameter.

The usage of macro-definitions in the graphical analyzer *Probe* allows to extend significantly the possibilities for constructing of generalized parameters. Based on macros, using the incorporated analog functions in *Probe*, a number of characteristics can be calculated: **RMS**, mean values, powers, time intervals and another quantities, which characterize the power electronic circuit.

II. DETERMINATION OF RECTIFIER REGULATION CHARACTERISTICS

A. Single phase rectifier (*Fig. 1*)

In order to construct the regulation characteristics, the on-time delay with respect to the start value of the corresponding positive half-wave, is defined as a parameter.

The following parameter values are used for the sources:

– Vac is a sinusoidal voltage source of **VSIN** type [magnitude V=50V, frequency F=50Hz, time delay TD=0, initial phase PHASE=0]

– Ig1, Ig2 are pulse current sources of **IPULSE** type [I1=0, I2=0.5A, TD={TDvar}, TR=TF=1μs, PW=500μs, PER=20ms]

The on-time delay TD with respect to the start value of the corresponding positive half-wave, is defined as a parameter TDvar.

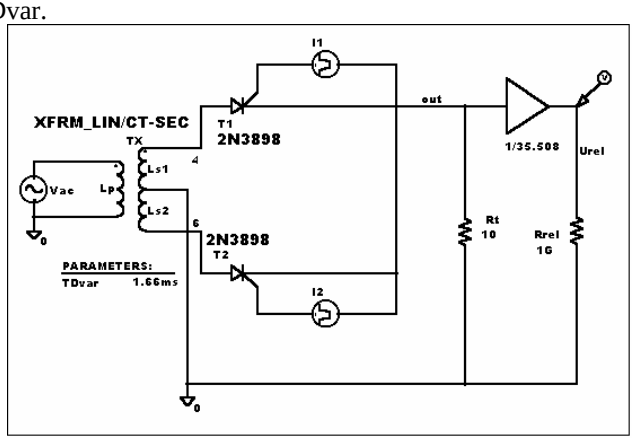

Fig. 1. Single phase rectifier

TD={TDvar} for the thyristor T1 and TD={TDvar + 10ms} for the thyristor T2. A linear variation is defined for TDvar from 0ms to 10ms by an increment of 0.5ms.

The **GAIN** block is introduced in order to obtain the output voltage in normalized form: GAIN=1/Vout(TDvar=0).

[1]Elissaveta D. Gadjeva is with the Faculty of Electronic Engineering, Technical University of Sofia, Kliment Ohridski Str. No 8, 1000 Sofia, Bulgaria, E-mail: egadjeva@tu-sofia.bg

[2]Georgi Tz. Kunov is with the Faculty of Electronic Engineering, Technical University of Sofia, Kliment Ohridski Str. No 8, 1000 Sofia, Bulgaria, E-mail: gkunov@tu-sofia.bg

[3]Mario E. Ivanov is with the Faculty of Electronic Engineering, Technical University of Sofia, Kliment Ohridski Str. No 8, 1000 Sofia, Bulgaria, E-mail: mario@tu-sofia.bg

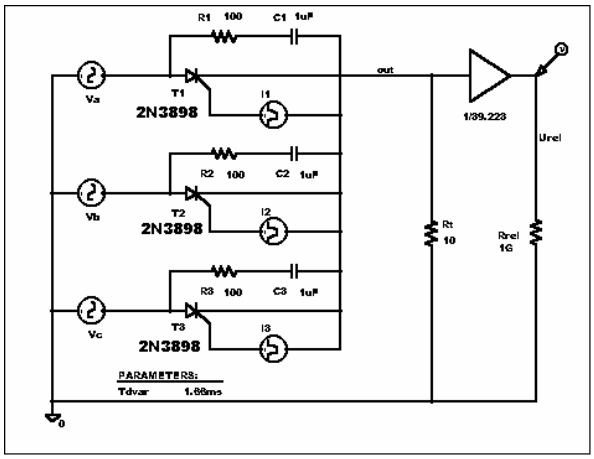

Fig. 2. Three-phase one-wave rectifier

B. Three-phase one-wave rectifier (*Fig. 2*)

The following parameter values are used for the sources:
– Vac1, Vac2 and Vac3 have identical parameters with the source used in Fig. 1. The only difference is in the phase. The values PHASE1=0, PHASE2=-120^{o} and PHASE3=120^{o} define the three-phase system of voltages.
– Ig1, Ig2, Ig3 have identical basic parameters with the sources used in Fig. 1. The difference is in the delay TD. It defines the beginning and the interval of regulation.

TD={TDvar+1.66ms} for the current Ig1, TD ={TDvar+ 8.33ms} for Ig2 and TD={TDvar+15ms} for Ig3. A linear variation is defined for TDvar from 0 ms to 8.5ms by an increment of 0.5ms.

C. Three-phase full-bridge rectifier (*Fig. 3*)

The differences in the source values with respect to those used in Fig. 1 and Fig. 2, are in the duration of the on-time pulses PW=3.5ms and in the time delays TDvar, as shown in Table 1. A linear variation is defined for TDvar from 0 ms to 7.5ms by an increment of 0.5ms.

TABLE I
TIME-DELAY VALUES

Ig1	Ig2	Ig3	Ig4	Ig5	Ig6
1.66ms	5.0ms	8.33ms	11.66ms	15ms	18.33ms

A linear variation is defined for TDvar from 0 ms to 8.5ms by an increment of 0.5ms.

D. PSpice simulation of rectifier regulation characteristics

As a result of the simulation, the regulation characteristics are obtained as a dependence of the normalized mean value of the rectified voltage regulation characteristics with respect to the on-time angle (represented by TDvar). This characteristic is shown in Fig. 6. The value of the rectified voltage in the normalized form are obtained at the output of the block **GAIN**. The gain is defined in the form:

$$GAIN = \frac{1}{V_{avg,out}\Big|_{TD=0}}$$

where $V_{avg,out}\Big|_{TD=0}$ is average value of the rectified voltage for *TD*=0.

The calculation of the average normalized value of the rectified voltage *Uoutrel* is obtained using the postprocessing in the graphical analyzer *Probe*. It is defined using the following macrodefinition in the *Trace/Macros* menu:

Uoutrel = Max(Avg(V(Uout))).

The family of regulation characteristics is obtained following the next procedure:
1. Plot/Axis Settings/X_Axis/Performance Analysis
2. Trace/Add…/Macros/Uoutrel.

Using the *File/Append* option, it is possible to visualize on the same screen and compare the regulation characteristics of the rectifier circuits in Fig 1, Fig. 2 and Fig. 3. The corresponding result is shown in Fig. 4.

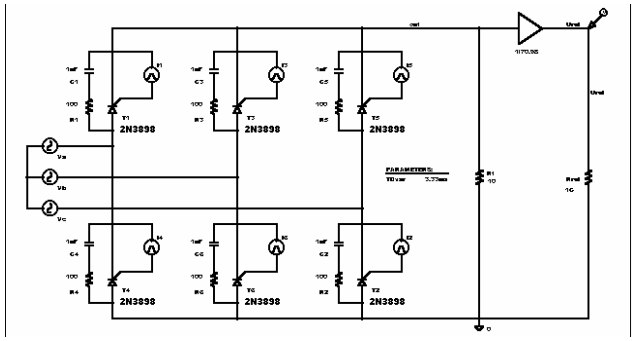

Fig. 3. Three-phase full-bridge rectifier

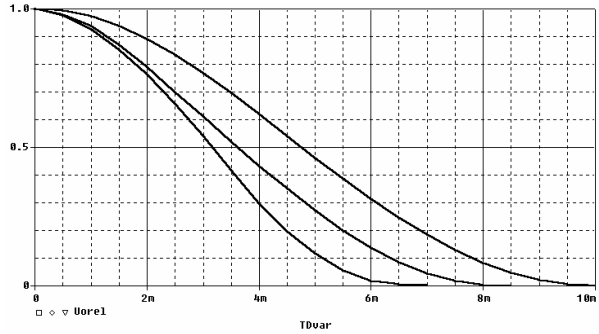

Fig. 4. Regulation characteristics

III. DETERMINATION OF TIME INTERVALS

The *PSpice* simulator allows the investigation of time intervals depending on parameters. As an example, the on-state time interval is obtained depending on the quality factor *Q* fir the full-bridge resonant inverter shown in Fig. 5. Ig1, Ig2, Ig3 and Ig4 are pulse current sources of IPULSE type with the following parameters: I1=0, I2=0.5A, TR=TF=1μs, PW=50μs, PER=200μs.

TD=0μs for Ig1 and Ig2 and TD=100μs for Ig1 and Ig2.

The circuit parameters are: Lvar = 200μH; Cvar = 2μF. Hence

Rvar = {SQRT(2*Lvar/Cvar)/Q}. (1)

The quality factor *Q* of the series resonant circuit is defined as a global parameter with a linear variation from 1.0 to 2.0 by

an increment of 0.1. The load resistor value Rt is automatically calculated from (1).

The waveforms of the voltage across one of the thyristors, the current through the load, as well as the voltage across the load, are shown in Fig. 6.

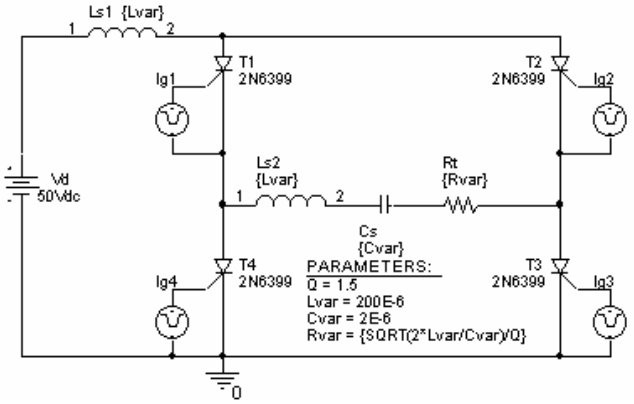

Fig. 5. Bridge resonant inverter

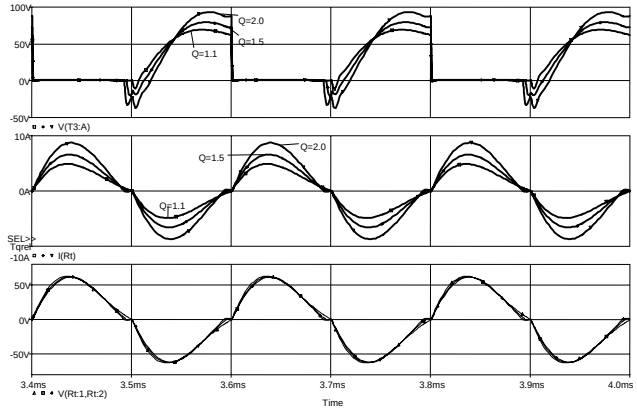

Fig. 6. The basic waveforms of tne resonant inverter

It is seen that the increasing of *Q* leads to increasing of the thyristor voltage and current. The turn-on time T_t decreases and the turn-off time T_q increases. The load voltage does not change its value significantly.

The normalized values $T_{q\,rel}(Q)$ and $T_{t\,rel}(Q)$ of the corresponding parameters T_q and T_t with respect to the commutation period PER, as well as the load power $P_r(Q)$ are shown in Fig. 7.

The following macro-definitions are constructed for this purpose:

PER=200E-6
NUM=20
Tqrel = (XatNthYp(V(T3:A),0.1, NUM)-
XatNthYn(V(T3:A),-0.1, NUM))/PER
Ttrel = (XatNthYn(V(T3:A),-10, NUM-1)-
XatNthYn(V(T3:A),10, NUM-1))/PER
Pr = Max(RMS(I(Rt)))*Max(RMS(V(Rt:1,Rt:2)))

The *Probe* function **XatNthYp(1,Y_value,n_occur)** is used to obtain the argument **X** when the function **1** reaches the **Y_value** for the **(n_occur)**-th time in the positive direction. Similarly, the function **XatNthYn(1, Y_value,n_occur)** is used for the negative direction. The **RMS** function is used for the load power calculation.

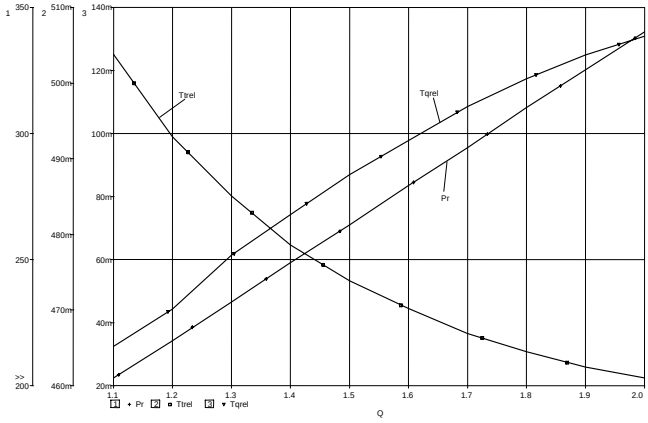

Fig. 7. The normalized values Tqrel Ttrel and the load power

IV. DETERMINATION OF THE LOAD CURVES

The bridge current fed inverter (Fig. 8) is used as an example, where the circuit elements are calculated for a given load coefficient *B*, defines as a parameter.

The current fed inverter circuit is simulated for the frequency F = 1kHz, corresponding to PER=1ms, and the time-delay of the pulse sources Ig2 and Ig4 is TD=0.5ms. The load coefficient *B* is defined as a global parameter.

$$B = \frac{1}{F.R_{var}\ C_{var}} \qquad (2)$$

It is changed using value list:

The circuit parameters are: Cvar = 10μF; F = 1kHz. Hence

Rvar = {1/(F*Cvar*B)}. (3)

The normalized values of the load voltage *Urtrel*, the DC fed current from the source *Idrel*, as well as the turn-off time *Tqrel* are shown in Fig.9 depending on the load coefficient.

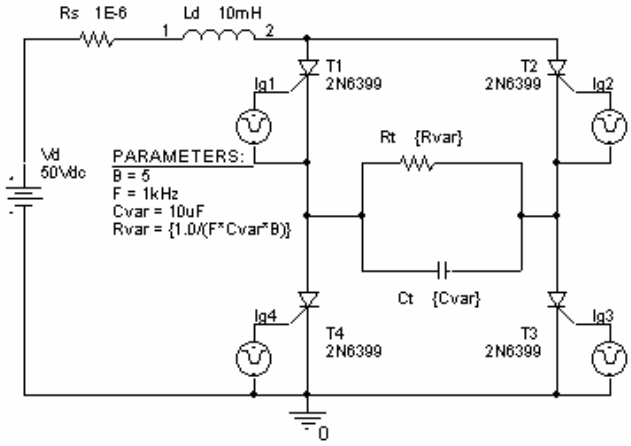

Fig. 8. Bridge current fed inverter

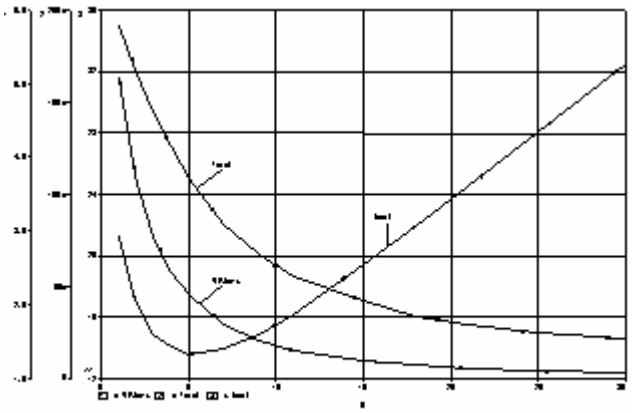

Fig. 9. Load characteristics of the current fed inverter

The following macro-definitions are constructed for this purpose:

PER=1E-3
NUM=20
Vd=50V
Cvar=10uF
Tqrel = (XatNthYp(V(T3:A),0.1, NUM)-
XatNthYn(V(T3:A),-0.1, NUM))/PER
VRtrel = Max(RMS(V(Rt:1,Rt:2)))/Vd
Idrel = Max(I(Rs))*PER/(Vd*Cvar)

The *Probe* functions **XatNthYp** and **XatNthYn** are used for the *Tqrel* calculation, and the **RMS** function is used to the *VRtrel* determination.

V. CONCLUSION

An approach is proposed to computer-aided investigation of power electronic circuits using the *PSpice* simulator and the extended possibilities for postprocessing using the graphical analyzer *Probe*. Based on macromodel approach, the families of regulation characteristics are constructed for rectifier circuits. The dependence of the turn-on time and turn-off time of the thyristors for resonant inverters is obtained, as well as the load characteristics of the current fed inverters. The proposed approach can be extended to another power electronic circuit types.

REFERENCES

[1] R. Ramshaw and D. Schuurman, “PSpice Simulation of Power Electronics Circuits”, Chapman & Hall, 1997.

[2] N. Mohan, T. Undeland, W. Robbins, “Power Electronics: Converters, Applications and Design”, John Wiley & Sons, Inc., 1989.

[3] N. Nachev. G. Malleev, “Power Electronics”, Technika, Sofia, 1979 (in Bulgarian)

[4] S. Tabakov, “Power Electronic Circuits and Devices”, Technika, 1987 (in Bulgarian).

[5] Bobcheva M., S. Tabakov, P. Goranov, Converter Devices, Tekhnika, Sofia, 2002. (In Bulgarian).

[6] G. Kunov, G. Staichev, E. Gadjeva, “Spice Modeling and Optimization of a Frequency-Controlled Inverter/Double Current Rectifier System", 3-th Intern. Workshop “Compatibility in Power Electronics” CPE’2003, Gdansk, pp.289-292.

[7] OrCAD PSpice and Basics, Cicuit Analysis Software, OrCAD Inc., USA, 1998.

Computer Modeling of Characteristics of Heavy Current Radio-Frequency Argon Discharge

Iliycho P. Iliev[1], Snezhana G. Gocheva-Ilieva[2], Hristo I. Semerdzhiev[3]

***Abstract* — Two theoretical experimental models, describing electric field and gas temperature of RF argon discharges are presented. Numerical simulations show a way to prevent the thermal overheating of the discharge by the variation of current density and electric field at a constant electric power. An increase of almost 100^0C of the maximum argon gas temperature with the 10-15% increase of the measureless electric power is also obtained.**

***Keywords* — RF (radio-frequency) discharge, electric field, gas temperature, overheating.**

I. Introduction

A subject of numerical study is the electrical field and the temperature profile of the neutral gas in RF capacity argon discharge. This type of discharge continues to be topical and is a subject of analytical and numerical studies. The RF discharges have a number of advantages: higher volumetric density of the electrical power, better ionizing stability. The externally fixed electrodes make the gas discharge device more reliable and with a bigger operating time. The RF discharge finds great use in a number of gas discharge devices: gas lasers and metal vapor lasers, in order to produce thin layers (thin films), in the semi-conductor industry (etching), for light sources and displays. They are used in analytical chemistry for spectral analysis of the solid materials.

Electric and temperature fields are the main characteristics of the gas discharge. They determine gas kinetic, electrical, thermal and optical characteristics of the discharge and are a subject of active studies. The values of these quantities depend on a huge amount of factors: geometric design, type and pressure of the inert gas, voltage and electricity in the discharge, type and quality of the materials, conditions for cooling the device. Numerical modeling often only allows evaluation of the huge amount of factors and as a result defines the most optimal characteristics and conditions for the use of the gas discharge device.

There is a large number of mathematical models, which allow the determination of the characteristics of the gas discharge device, including the electric field and the temperature profile. Detailed description of the existing models is given in [1-4] and the quoted literature there. In recent times there has been active work to create mixed (hybrid) models, which combine the advantages of the existing.

II. Modeling of the Electric Field

One of the hybrid models for determining the electric field is developed in [3]. This model is entirely theoretical and is based on two famous models - the fluid and the Monte-Carlo models. The purely theoretical models have some disadvantages: connected with the long calculation time, they calculate simple geometric lines and simple boundary conditions. Despite of the huge amount of examined equations they aren't precise enough. They are hard to use for calculating complicated optimizing problems.

The model we suggested is also hybrid – theoretical-experimental. A modified fluid model is used in the base by using experimental data: distribution of the charged particles inside the volume of the discharge, speed and ionized sections and constants. With this model a number of equations calculating the well known characteristics of the discharge are excluded. It is possible, that the electric field can be defined more precisely in complicated geometric design and allow the multidimensional optimizing problems in order to find the effective values of the electric field while solving specific engineering problems (see also [5]).

A. Description of the model

We will consider the heave-current discharge (γ discharge) inside an argon medium with a current of 30 *Torr*, a charging frequency of 13,56 *MHz* and electric power 200*W*. With this type of discharge the density of the current is considerable (up to 400 mA/cm^2). The physical law for the constant density of the current is broken and by increasing the voltage the current grows. A secondary electric emission from the electrons rises (γ processes). This type of discharge can be compared with the constant-current abnormal glow discharge. With these conditions the parameters of the plasma are defined in a time, considerably smaller than the half-period of the charging frequency. This means the conductivity current exceeds the displacement current and the conductivity of the plasma is coming close to that of the constant-current glow discharge: $\sigma = en_e v_d$, $\vec{j} = \sigma \vec{E}$. Here e is the electron charge, μ_e is the electron mobility, v_d is the drift velocity, $\vec{j}$ is the current density and $\vec{E}$ is the electric field distribution.

[1] Ilycho P. Iliev is with the Technical University of Plovdiv, 25 Tzanko Dusstabanov street, 4000 Plovdiv, Bulgaria

[2] Snezhana G. Gocheva-Ilieva is with the University of Plovdiv, 24 Tzar Assen street, 4000 Plovdiv, Bulgaria, E-mail: snow@pu.acad.bg

[3] Hristo I. Semerdzhiev is with the University of Plovdiv, 24 Tzar Assen street, 4000 Plovdiv, Bulgaria

As an example we will consider the geometric design of the discharge device, consisting of two inserted cylindrical tubes, the external made by quartz and the internal by Al_2O_3, and supplied with two external symmetric longitudinal electrodes (see Fig. 1). This kind of geometry is typical for some metal vapor lasers [6].

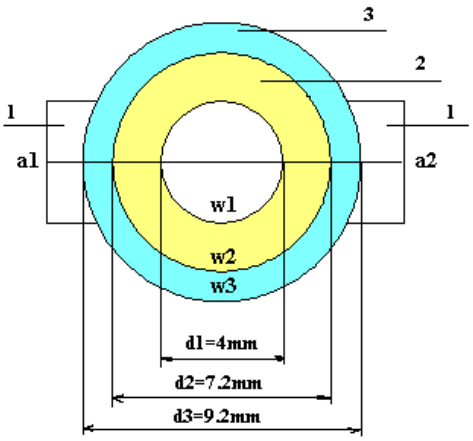

Fig. 1. Example of the cross-section of a discharge device: 1- external electrodes; 2- Al_2O_3 tube; 3- qwartzous tube

In order to obtain the scalar potential distribution in the cross section of the volume discharge we solve two-dimensional quasistationary Poisson equation

$$\frac{\partial^2 U}{\partial x^2}+\frac{\partial^2 U}{\partial y^2}=-\frac{e}{\varepsilon_0}\left(n_i(x,y)-n_e(x,y)\right) \qquad (1)$$

under the following mixed boundary value conditions:

$$\varphi_L=0,\ \varphi_R=U_a, \qquad (2)$$

$$\varphi_\Gamma=0, \qquad (3)$$

$$\varepsilon_i E_{in}=\varepsilon_j E_{jn}, \qquad (4)$$

where ε_0 is the dielectric constant, $n_i(x,y)$ and $n_e(x,y)$ are the ion and electron concentrations, respectively. The boundary conditions (2) describe that at the left electrode the applied voltage is zero, and at the right electrode is U_a. The zero condition (3) represent the often grounded metal body of the discharge tube, i.e. zero potential (Dirichlet condition). The condition (4) take into account the electric field transfer trough the boundaries of the two dielectrics (Newmann condition), where E_{in} and E_{jn} denote the normal components of the electric field on the boundaries of the materials with dielectric constants ε_i, ε_j.

Fig.2 shows a typical experimental particle distribution in γ discharge [1]. Similar distributions are calculated in [3].

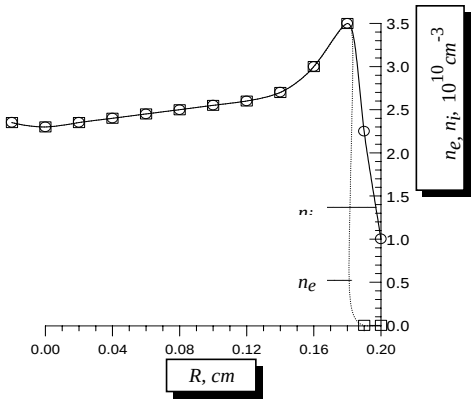

Fig. 2. Distribution of the charged particles n_e, n_i on the line $a1$-$a2$.

In order to determine the electric field we apply the following algorithm: (a) Begin to give the voltage U_a at the right (charged) electrode and typical distributions of the charged particles (for our example see Fig.2); (b) Find the potential U by solving the problem (1-4); (3) Calculate the electric field from $\vec{E}=-\mathrm{grad}U$; (d) Find the current density by means of the formula $j=en_e v_d E$ with $v_d=f(E/p)$ for the argon [7]; (e) Calculate the volume average density of the electric power $\langle jE\rangle$ and the total power $P=\langle jE\rangle V$, where V is the volume of the discharge; (f) If the resulting power P differs to the initial power P_0, than change the data for $n_i(x,y)$ and $n_e(x,y)$ and repeat the calculations until $P=P_0$ is reached.

B. Numerical results and discussion

The model was carried out for an initial power P_0=200W and different electrode voltage U_a, applied to the charged electrode. The solution of the elliptic problem (1)-(4) was obtained by means of a finite difference scheme of accuracy order $O(h^2)$, with step $h\to 0$ and the successive over-relaxation method (SOR method).Fig. 3 shows the scalar potential distributions and electric field intensity E on the central line $a1$-$a2$ (see Fig.1) at U_a =200V. Fig. 4 illustrates the electric field distributions at U_a =200V and 400V, respectively. These numerical results are in good qualitative agreements with simple one-dimensional analytical models [1] and discharges, operating at similar conditions [8]. The availability of higher values of the electric field E at the electrode region can be explained by the noncompensate electron charges in this region.

The model allows to evaluate the variation of current density j and electric field E at the maintenance of a constant electric power P_0. Their values are of great importance for the outcome characteristics of the discharge device (for instant for the metal vapor laser devices it means the outcome laser power). The constant electric power P_0 provides a constant maximum temperature of the argon discharge, which prevent its thermal overheating.

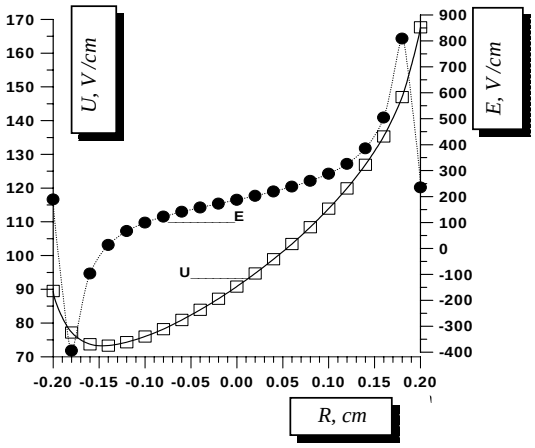

Fig. 3. Distributions of the potential U and electric field E on the central line $a1$-$a2$ at U_a =200V.

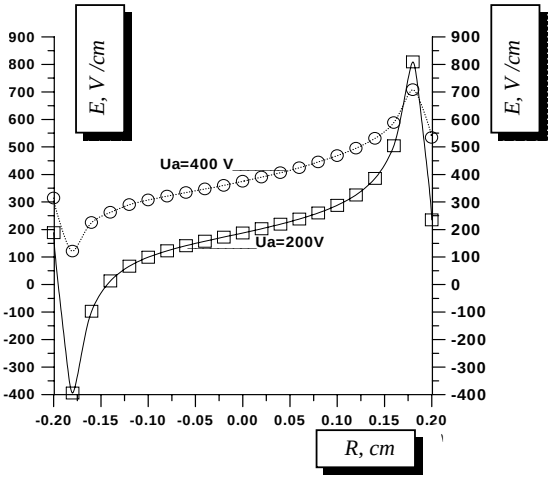

Fig. 4. Electric field distributions at U_a =200V and 400V on the line $a1$-$a2$ at a constant electric power P_0 = 200W.

III. Modeling of the Gas Temperature Profile

The overheating of the argon gas medium could considerably influence the discharge parameters and even to make device unusable. For this reason, the gas temperature T_g is a subject of permanent interest [4]. In [4] a complex theoretical hybrid method, including Monte-Carlo model, fluid method and heat conductivity equation for direct current argon discharge is developed.

In our considerations for heavy current argon discharge a theoretical experimental approach is applied. It is based on the solution of two-dimensional steady state heat conductivity equation and the results from the previous section, under the same assumptions. In addition the known experimental data for the heat conductivity coefficient, kinematical viscosity coefficient, the volume extension coefficients of the materials and gases are used.

A. Description of the mathematical model

Only a brief description of the model will be presented here. More detailed similar model was developed in [9-10]. In order to find the temperature of the neutral argon gas T_g in the cross section of the discharge it is necessary to solve the two-dimensional steady state heat conductivity equation

$$\mathrm{div}\,(\lambda_g\,\mathrm{grad}T_g) + q_v = 0, \tag{5}$$

where λ_g is the conductivity coefficient of the argon gas, q_v is an internal temperature source. The Eq. 5 was solved with the mixed boundary value conditions of the third and fourth kind in cylindrical configuration [11]

$$Q = \alpha F_{w3}(T_{w3} - T_f) + F_{w3}\varepsilon c[(T_{w3}/100)^4 - (T_f/100)^4], \tag{6}$$

$$q_l = 2\pi\lambda_1(T_{w1} - T_{w2}) / \ln(d_2 - d_1), \tag{7}$$

$$q_l = 2\pi\lambda_2(T_{w2} - T_{w3}) / \ln(d_3 - d_2), \tag{8}$$

where Q is the total heat flux, T_{w1}, T_{w2} and T_{w3} are the temperatures of the three surfaces $w1$, $w2$ and $w3$, respectively (see Fig.1), T_f is the surroundings temperature, λ_1 and λ_2 are the thermal conductivities of the internal and external mediums, α is the heat transfer coefficient, ε is integral emisivity of the material, c = 5,67 $W/(m^2K^4)$ is the black body radiation coefficient, F_{w3} is the outside surface area, $q_l = Q/l$ is the linear density of the heat flux and l is the length of the discharge tube. Eq. 6 shows the heat exchange through the surroundings and the outer surface of the body. The first term at the right hand side represents the Newton-Rihmann's law of convective heat exchange and the second term represents the Stefan-Boltzmann law of radiation heat exchange. The Eqs. 7-8 give the heat transfer condition trough the two contacting surfaces of the composite wall in cylindrical configuration.

The function q_v is found by using the results from the previous section and the formula $q_v(x,y) = j(x,y)E(x,y)$. The heat transfer coefficient α is calculated by means of the Nusselt criteria $Nu = \alpha H / \lambda$ [11]. For a free convection the Grashof criteria is given by $Gr = g\beta H^3\Delta T / \upsilon^2$, where g is the gravitational acceleration, β is the coefficient of cubical heat expansion of the gas, $\Delta T = T_{w3} - T_f$ is the temperature difference of the wall and the fluid and ν is its kinetic viscosity. For the horizontal tubes at natural air convection the following dependence holds Nu = 0,46 $Gr^{0,25}$ [11].

In the calculations we use T_f = 300K, $H = d_3$ = 9,2mm, β_{air} =3,41.$10^{-3}K^{-1}$, λ_{air} = 0,0251$W(mK)$, υ_{air} = 15,7.$10^{-6}m^2/s$ [7].

B. Numerical results and discussion

For numerical solving of the Eqs. 5-8 we applied finite difference method. The conditions (7)-(8) were radially transferred to the external boundary (see [9-10]).

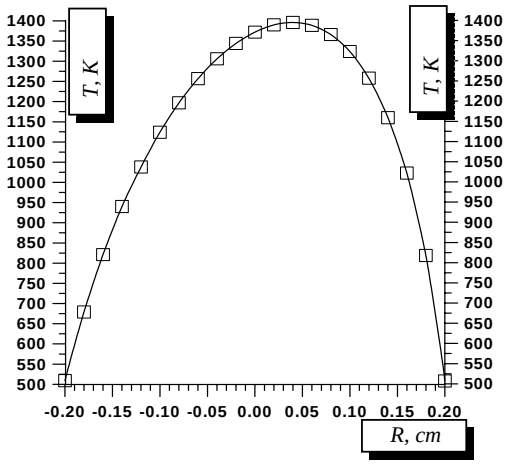

Fig. 5. The temperature distribution T_g on the line $a1$-$a2$.

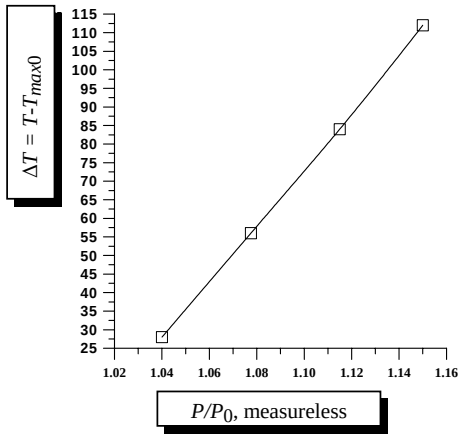

Fig. 6. Absolute increase of the maximum temperature $\Delta T = T - T_{max0}$ with respect of a of the electric power P/P_0.

Fig. 5 illustrates the obtained gas temperature distribution T_g in the cross section of the discharge on the line $a1$-$a2$. The maximum temperature is not in the center and is a little shifted to the direction of the charged electrode. The latest fact is due to the asymmetrical power volume density distribution q_v, as well to the electric field E (see Fig.4).

The numerical determination of the temperature profile could be used for improving the engineering design and operational capacities of the discharge devices. In Fig. 6 the maximum argon gas temperature as a function of the electric power is drawn. It is shown an increase of the electric power with 10-15% involving the increase of the argon gas temperature by at almost 100^0C. It means, that a such increase of the power can cause bad operational parameters of the discharge and its physical destroy.

IV. Conclusion

The presented models can be also applied to other gas discharge devices, operating at the similar types of gas discharge. By numerical simulations the temperature profile can be optimized by different engineering solutions, including the cooling conditions, such as natural and constrained cooling, external metal fins, etc. The aim is to establish some optimal correlation between the electric power and the gas temperature in order to prevent the discharge overheating and to improve the outcome characteristics of the discharge.

Acknowledgement

This work was supported by the Scientific Fund of Plovdiv University "Paisii Hilendarski", Bulgaria.

References

[1] Yu.P. Raizer, M.N. Shneider and N.A. Yatsenko, *Radio-Frequency Capacitive Discharges*, N.Y.: CRC Press, 1995.

[2] C.G. Lister, "Low-Pressure Gas Discharge Modeling", *J. Phys.*, 25, pp. 1649-1680, 1992.

[3] A. Bogaerts, M. Yan, R. Gijbels and W.J. Goedheer, "Modeling of α and γ Ionization of Argon in an Analytical Capacitively Coupled Radio-Frequency Glow Discharge", *J.Appl. Phys.*, vol..86, pp. 2990-3004, 1999.

[4] A. Bogaerts, R. Gijbels and V.V. Serikov, "Calculation of Gas Heating in Direct Current Argon Glow Discharges", *J.Appl. Phys.*, vol. 87, no 12, pp. 8334-8344, 2000.

[5] S. Zhang and X. Hu, "New Microwave Diagnostic Theory for Measurement of Electron Density in Atmospheric Plasmas", *Chin. Phys. Lett.*, vol. 22, no 1, pp.168-170, 2005.

[6] N. Reich, J. Mentel and J. Mizeraczyk, "CW radio-frequency excited white-light He-Cd^+ laser," *IEEE J. of Quantum Electron.*, vol. 31, no. 11, pp.1902-1909, 1995.

[7] *Physical Quantities*, Handbook, Moscow: Energotomizdat, 1991.

[8] Talaat, M.E. "A Two-Electron Group Model Theory for Radio-Frequency Ionization of Noble Gases with Turbulent Flow", *IEEE Transaction on Plasma Science*, 19, pp. 176-188, 1991.

[9] I.P. Iliev, "Gas Temperature Distribution in Radio-Frequency He-Cd Laser", *Elektrotechnica & Elektronica*, vol. 5-6, pp. 9-13, 2002.

[10] I.P. Iliev, "Intensification of Cooling in the Cross-section of Radio-Frequency Helium-Cadmium Laser", *Elektrotechnica & Elektronica*, vol. 7-9, pp. 48-51, 2002.

[11] M.O. Peshev, S.G. Batov and D.Z. Uzunov, *Heat Technology*, Sofia, Technika, 1978.

Analysis of Magnetron Discharge Regions in Vacuum Chamber under Test

Raina Tzeneva[1], Peter Dineff[2]

Abstract - **A cold cathode magnetron ionization principle is employed to measure the pressure within the vacuum interrupter by using existing interrupter elements as principal parts of an ionization gauge and by immersing the vacuum apparatus in a magnetic field. The role of a metallic vapor-condensing shield of tubular configuration as a collector of the positive ion current is studied. The magnetron discharge of *G. Phillips* (1898) is used, and the magnetic field is oriented along the direction of the electrodes of a vacuum interrupter. Using appropriate modeling of the electric and magnetic field, the characteristic plasma toroidal regions in the space of the vacuum apparatus are determined.**

Keywords – **Magnetron ionization, Magnetron pressure measurement method, Metallic vapor-condensing shield, Vacuum circuit interrupter.**

I. INTRODUCTION

Nowadays, the best principle of indirectly measuring the pressure inside a vacuum envelope is that of the magnetron. A cold cathode magnetron ionization principle is employed to measure the pressure within the vacuum interrupter by using existing interrupter elements as principal parts of an ionization gauge and by immersing the vacuum circuit apparatus in a magnetic field, Fig. 1 [2, 3, 5, 6, and 8].

Measuring the pressure in factory made *vacuum circuit interrupters* (*VCI*) has always been a great problem for the manufacturers of vacuum switchgear during its shelf life, which is longer than ten or twenty years. The *VCI* cannot maintain the pressure inside itself during all that time, and customers want to be sure that the pressure in the vacuum envelope will not be increased considerably for this period. That is why there is a need of a technique that will permit detecting any residual pressure alterations in *VCI*, [6, 7].

The *VCI* comprises an evacuated and sealed envelope, a pair of separable contacts or electrodes within that envelope, which can move from an engaged position to a spaced-apart position in order to define an arcing gap therebetween, and a *metallic vapor-condensing shield* (*MVCS*) of tubular configuration surrounding the gap and electrically isolated from at least one of the electrodes by an evacuated space surrounding that electrode [3, 6, 7].

There are two possible cases of a diode ionizing gauge for measuring the pressure inside the *VCI*-vacuum envelope with the participation of *MVCS* as a cathode, Fig. 1:

♦ *MVCS* as the cathode of a cold cathode ionizing gauge performs the role of a collector for measuring the ion current, and the two contacts of *VCI* are closed and have the same potential, i. e. together they form the anode of the ionizing gauge, Fig. 1a;

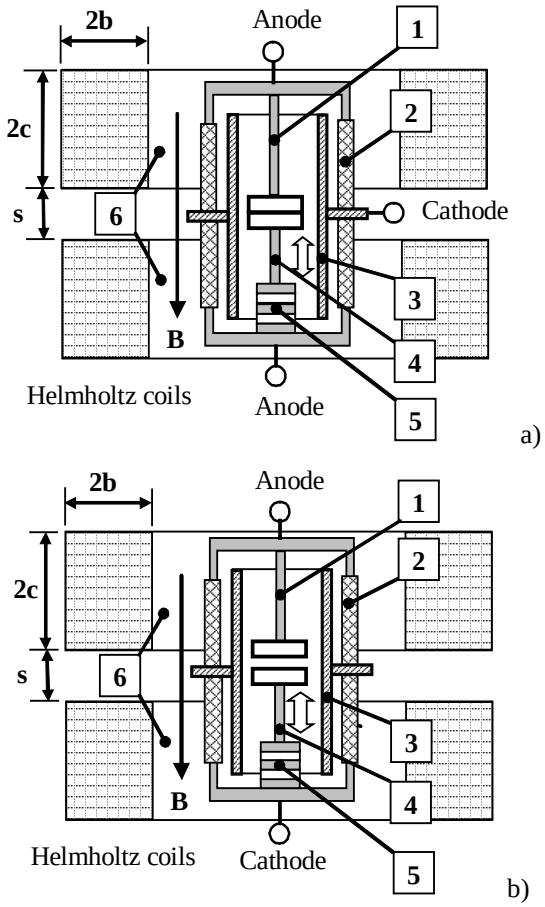

Fig. 1. Sectional view of the vacuum interrupter employed as a diode ionization gauge for indirect pressure measurement within the vacuum sealed envelope when an exterior electrical connection to the metallic vapor-condensing shield (*MVCS*) is either available (a) – closed electrodes and negative potential at *MVCS*; or unavailable (b) – opened electrodes and floating potential at *MVCS*.

1 – fixed electrode; **2** – insulating cylinder; **3** - metallic vapor-condensing shield; **4** – movable electrode; **5** – sylphon; **6** – *Helmholtz* coils.

[1]Raina T. Tzeneva is with the Department of Electrical Apparatuses, Faculty of Electrical Engineering, Technical University of Sofia, 8 Kliment Ohridski Blvd., 1000 Sofia, Bulgaria, E-mail: tzeneva@tu-sofia.bg.

[2]Peter Dineff is with the Department of Electrical Apparatuses, Faculty of Electrical Engineering, Technical University of Sofia, 8Kliment Ohridsk iBlvd., 1000 Sofia, Bulgaria, E-mail: dineff_pd@abv.bg.

♦ *MVCS* participates indirectly in the measurement, staying at floating potential, Fig. 1b; this case is characteristic for many of the modern *VCI*, *MVCSs* of which have not any tap outside the *VCI* vacuum sealed envelope.

In both cases the *VCI* vacuum envelope is immersed in a constant magnetic field oriented along the axis of the electrodes, which corresponds to the well-know circuit of *G. Phillips* (1898) for the ignition of a magnetron discharge, Fig. 2 [4].

Measuring the pressure in the sealed envelope with the help of the *VCI* contact system transforms *VCI* into a magnetron-type diode ionization gauge.

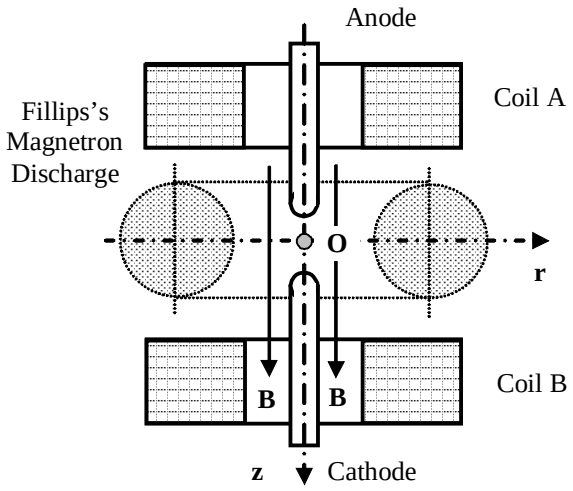

Fig. 2. Spatial arrangement of the *Fillips*'s magnetron ionizing discharge.

The possibility of placing the evacuated *VCI* envelope fully in a relatively uniform magnetic field created by two *Helmholtz* coils, coaxially situated, allows investigating the conditions provided by the electrodes and *MVCS* for the ignition and the burning of the magnetron discharge.

THE TASK of the present work consist in revealing the participation of the electrodes and metallic vapor-condensing shield in the occurrence and maintenance of a cold cathode magnetron discharge in the space between the electrodes as well as between the electrodes and the metallic vapor-condensing shield of the ionizing gauge inside the evacuated *VCI* envelope.

II. General formulation of investigations

The vacuum circuit interrupter is immersed in the magnetic field of two *Helmholz* coils, coaxially situated above each other, the magnetic flux density **B** of which is oriented along the axis of the vacuum device, Fig. 1.

The metallic vapor-condensing shield has a rotationally symmetric shape and is placed in such a way in the space inside the interrupter that creates a labyrinth transition from the space before the insulating cylinders to that inside *MVCS* that it ensures the necessary protection of the insulating cylinders from metal vapors and metallization, Fig. 1.

The so selected technical solution provides a relatively uniform magnetic field in the space of the vacuum sealed envelope and similar conditions for the manifestation of the cathode magnetron ionization principle in the three characteristic regions of burning of the magnetron discharge depending on gauge construction, Fig. 3:

♦ the higher region of discharge between the flange of the fixed contact and the upper part of *MVCS*, or in the region of the higher labyrinth sealing, Figs. 3 and 4;

♦ the central region of discharge between the touching contacts and *MVCS*, Fig. 3, or in the region between the open contacts and between them and the central part of *MVCS*, Fig. 4;

♦ the lower region of discharge between the flange of the movable contact, sylphon and lower part of *MVCS*, or in the region of the lower labyrinth sealing, Figs. 3 and 4.

Lucek and *Pearce*, [3], were the first to find out that modifying the flange design in order to create the labyrinth transition leads to instability of the magnetron discharge and of the cathode current measured.

Our investigations, [7], performed on modern designs of vacuum interrupters indicated that in this case it is most appropriate to use the circuit of inverse magnetron ionizing discharge where *MVCS* is the cathode, as it is shown in Fig. 1a.

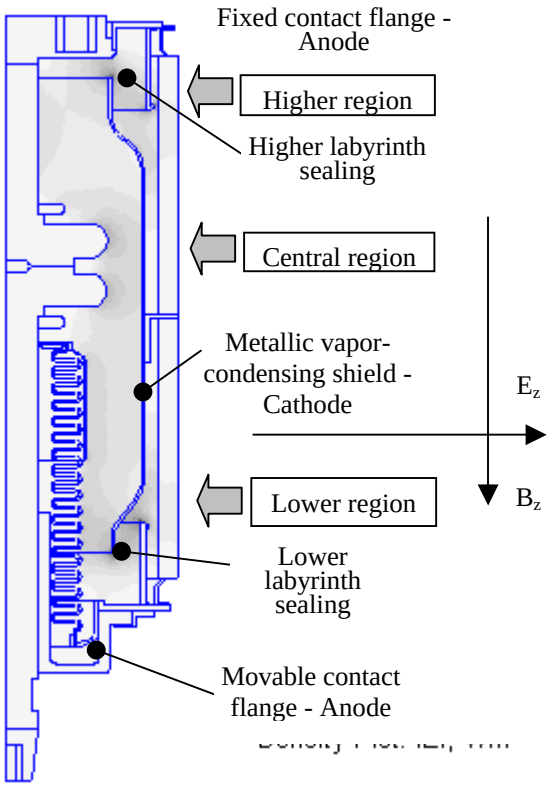

Fig. 3. Picture of the distribution of electric field intensity value |E| in the space of the *VCI* closed contact system – anode, and *MVCS* - cathode.

III. RESULTS AND DISCUSSION

The role of *MVCS in* the two main case of measuring is investigated: ♦ the measurement circuit or the first model according to Fig. 3 and ♦ the measurement circuit or the second model according to Fig. 4.

Using modern software products based on the numerical method of boundary elements, two distributions of the electric field intensity |**E**| have been obtained, each of them corresponding to the selected variant of the pressure measurement by measuring the positive ion currents, Figs. 3 or 4. The relatively uniform magnetic field makes visible the regions of burning of the magnetron ionizing discharge that form the total positive ion current.

It is known that the height of the cycloid h_e, along which the free electron drifts in a plane transversal to the direction of magnetic field ***B***, and gains energy $e.V_i$, sufficient for an α- or electron impact ionization, is defined as follows:

$$h_e\, E_r \geq e\, V_i \quad \text{or} \tag{1}$$

$$h_e\, E_r = 2\, \mu_0{}^2\, \frac{m_e}{e}\, \frac{E_r{}^2}{B_z{}^2} \geq e\, V_i\,, \tag{2}$$

where $\mu_0 = 4\,\pi\,10^{-7}$ H/m is the magnetic constant; $m_e = 9.11 \times 10^{-31}$ kg – the electron mass; $e = 1.602 \times 10^{-19}$ C – the electron charge; E_r – the radial component of the of electric field intensity; B_z – the axial component of the magnetic field; V_i – the first ionization potential.

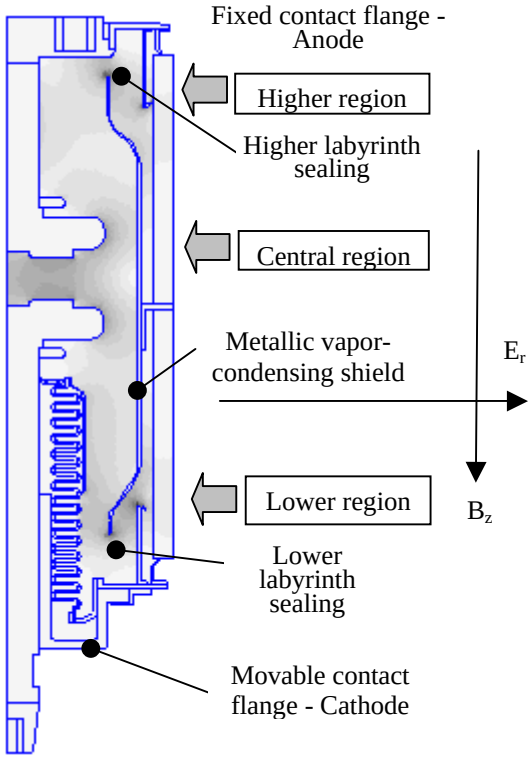

Fig. 4. Picture of the distribution of electric field intensity value |E| in the space of *VCI* at open contact system and *MVCS* under the action of a floating potential.

The first ionization potential for oxygen is $V_i\,(O_2) = 13.618$ V, and for nitrogen - $V_i\,(N_2) = 14.534$ V, which allows calculating the critical ratios of the magnetron ionization for oxygen and nitrogen, respectively:

$$\text{for oxygen: } \left(\frac{E_r}{B_z}\right)_{cr} \geq 1102 \text{ , kV/(T m)} \tag{3}$$

$$\text{for nitrogen: } \left(\frac{E_r}{B_z}\right)_{cr} \geq 1138 \text{ , kV/(T m)} \tag{4}$$

This permits to determine the conditions of magnetron ionizing discharge in different regions depending on the magnetic field created, the *Helmholtz* coils having the following geometrical parameters, Fig. 1: 2 R_2 = 375 mm; 2 R_1 = 255 mm; 2 b = 60 mm; 2 c = 60 mm; s = 9, 19, 29, 39, 49, 59, or 69 mm. The number of turns in each of the two coils is 150.

The seven models of the magnetic field (s = var) allow determining the values of its axial component B_z for various distances *s* between coils. Maximal magnetic flux density B_z in the lower region does not depend on the distance between coils, s ∈ [9…69] mm: B_z = 0.0086 T.

Maximal magnetic flux density B_z in the central region diminishes with increasing distance *s* - s/B_z, mm/T: 9/0.0117; 19/0.0114; 29/0.0110; 39/0.0107; 49/0.0103; 59/0.0099; 69/0.0096.

Maximal magnetic flux density B_z in the higher region demonstrates analogous behavior, but is of values lower than those in the central region of the interrupter - s/B_z, mm/T: 9/0.0113; 19/0.0111; 29/0.0108; 39/0.0105; 49/0.0102; 59/0.0098; 69/0.0096.

The magnetic field is most homogeneous in the space of the interrupter investigated at *s* = 69 mm.

Calculated critical values of intensity $(E_r)_{cr}$ of the electric field – at $h_e\, E_r = e\, V_i$, for *s* = 69 mm, for oxygen and nitrogen, respectively, are shown in Table 1 for the different regions of magnetron ionizing discharge.

TABLE 1

REGION OF MAGNETRON IONIZING DISCHARGE	OXYGEN	NITROGEN
	E_R, kV/m	E_R, kV/m
MODEL OF MEASURING (CLOSED ELECTRODE, AVALABLE SHIELD)		
Higher discharge region	10.58	10.92
Central discharge region	10.58	10.92
Lower discharge region	9.48	9.79
MODEL OF MEASURING (OPENED ELECTRODE, UNAVALABLE SHIELD)		
Higher discharge region	10.58	10.92
Central discharge region	10.58	10.92
Lower discharge region	9.48	9.79

Data in Table 1 allow making the following conclusions: *first*, the two regions of the vacuum interrupter – the higher and central ones – have same critical values of intensity E_r, irrespective of the measurement circuit; *second*, it is possible to determine the space of burning of magnetron ionizing discharge in the three regions of *VCI*, irrespective of the measurement circuit for critical intensity E_r; *third*, the lower

region of magnetron ionizing discharge has a critical ignition voltage which is considerably lower.

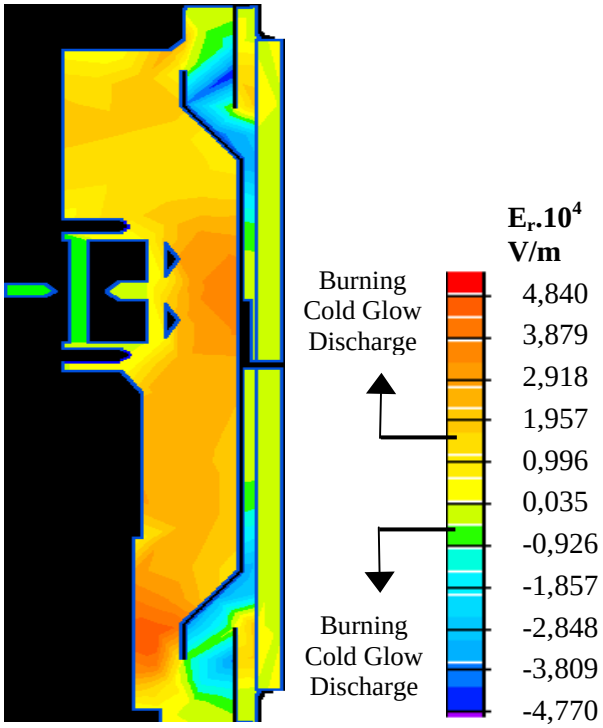

Fig. 5. Spaces of magnetron ionizing discharge in the higher (a), central (b), and lower (c) regions of the evacuated envelope at closed contact system of *VCI* and *MVCS* – cathode.

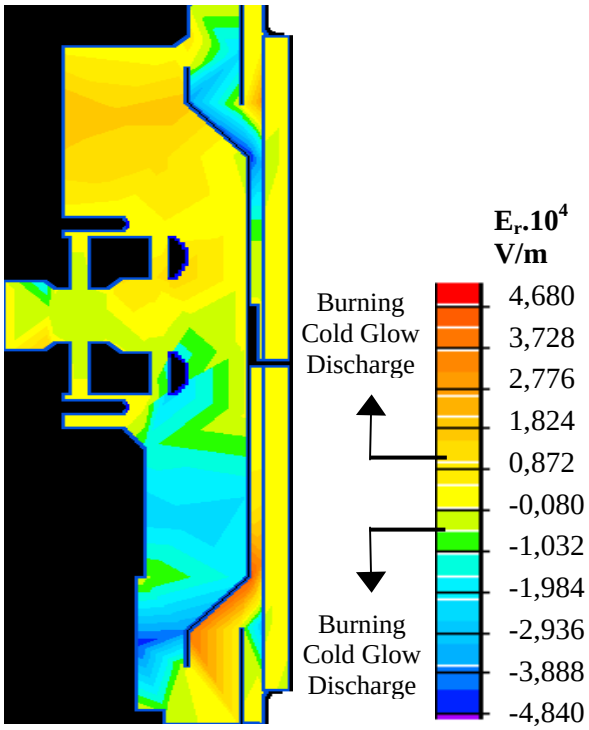

Fig. 6. Spaces of magnetron ionizing discharge in the higher (a), central (b), and lower (c) regions of the evacuated envelope.

The presented distribution of radial component E_r of the electric field in a cross-section symmetrical to the axis of the vacuum interrupter permits – by using the software product *Photo Shop 6* – determining the volume of the space of intensive ionization and burning of magnetron ionizing discharge: it is 85 % of the whole volume (Fig. 5) and 35 % of the whole volume (Fig. 6), respectively.

To our regret, the method of measurement with a closed contact system remains inapplicable to modern vacuum interrupters because most often the metallic vapor-condensing shield or *MVCS* has not any tap outside the vacuum envelope. Accordingly, it becomes mandatory to use the second method, i. e. that of measuring with an open contact system. However, it provides a considerably smaller magnetron ionizing volume, which also means lower sensibility.

IV. Conclusion

The magnetron ionizing method of indirect pressure measurement by focused action of the magnetic field in the central region of *VCI*, patented by *Watrous* (1971), does not provide any real advantages as the lower region is characterized by a more strongly expressed ionization. In that case of measurement, the almost equivalent higher region of magnetron air ionization, i. e. that of oxygen and nitrogen should not be ignored as well [4, 7].

The modeling investigation performed has shown that this pressure measurement can be realized locally in the same way in the region of each of the two labyrinth transitions of the vacuum interrupter.

The simultaneous use of all three characteristic regions of magnetron ionizing discharge (with the participation of *MVCS*) in measuring the pressure by means of the discharge current increases strongly the sensitivity of the magnetron method of pressure measurement.

The movable contact region, together with that of the lower labyrinth transition, or the lower region of the vacuum interrupter remains the most active region of magnetron air ionization, irrespective of the method of measurement.

References

[1] G. L. Saksaganski, *Electro-Physical Vacuum Pumps*, Moscow, Energoatomizdat, 1988 (in Russian).

[2] J. D. Cobine and J. M. Lafferty, Vacuum Device Gas Measurement Apparatus and Method, US-Patent Appl. No 3,495,165, Patented Feb. 10, 1970.

[3] P. Dineff, *Electrotechnology. Introduction to Electrotechnology*, Technical University, Sofia, Bulgaria, 2000 (in Bulgarian)

[4] P. A. Redhead. Ionization Vacuum Gauges, US-Patent Appl. No 3,051,868. Patented Aug. 28, 1962.

[5] W. W. Watrous, Method and Apparatus for Measuring Pressure in Vacuum Interrupters, US-Patent No 3,575,656, Patented Apr. 20, 1971.

[6] Zhao Zjyu et al., "Study on Internal Pressure Measurements in Vacuum Interrupters", *Proceedings of XIX ISDEIV*, pp. 775-778, China, 2000.

[7] R. Tzeneva, P. Dineff, "Most Possible Zones for Discharge Initiation in a Vacuum Circuit Interrupter under Test", *XXXIX International Conference on Information, Communication and Energy Systems and Technologies ICEST'2004 Proceedings of Papers*, v. 2, pp. 537-540, Bitola, Macedonia, 16 – 19 June, 2004.

Remote System for Monitoring, Diagnostics and Control of Switch Mode Power Supplies for Distance Learning

M. Popov[1], M. Bobcheva[2], G. Kunov[3]

***Abstract*: In the present paper a remote system for monitoring, diagnostics and control of switch mode power supplies is discussed. The main system components (programmable forward converter power supply, programmable load, 10-channel digital multi-meter, 2 channel digital oscilloscope, and a personal computer) communicate over National Instruments LabView environment. Synthesized is a soft control panel for local and remote programming.**

***Keywords:* Distance learning, Programmable power supply, LabView, Forward converter.**

I. INTRODUCTION

A main part of the education process in all engineering schools is reserved for laboratory exercises and experiments. This approach not only demonstrates the main concepts of the study but also practically proves the basic theories. On the other hand equipping and maintaining laboratories is extremely expensive in our days. The laboratory assistants are required to install the equipment, to present the experiment, to train the students and finally to generate reports. Having in mind that the labs are accessible only at equipment and lab assistant presence, this activity appears to be time consuming as well.

Things might look a way better if the main lab experiments were accessible from home 24 hours a day, 7 days a week or accessible during professor's lecture for demonstrations, theory proves and details explanations. How about if a high tech company research group gives access to its extremely expensive equipment out of regular business ours?

All theses ideas can be made true by building a flexible programmable system for remote monitoring and control of industrial equipment. Internet is giving a great chance for remote access and data exchange. Fig.1 shows a similar system. The lab experiment together with equipment is located on the left hand side. It receives commands and returns data to the system controller.

[1] Technical University of Sofia, Faculty of Electronic Engineering and Technologies, Department of Power Electronics, Sofia 1797, Bulgaria, e-mail: mariannp@abv.bg

[2] Technical University of Sofia, Faculty of Electronic Engineering and Technologies, Department of Power Electronics, Sofia 1797, Bulgaria,

[3] Technical University of Sofia, Faculty of Electronic Engineering and Technologies, Department of Power Electronics, Sofia 1797, Bulgaria, e-mail: gkunov@tu-sofia.bg

The controller is equipped with WEB server which is publishing the results over the internet. These results are visible to N- number of remote stations. Something more! At certain conditions, the control over the system can be passed over to any remote station. In this way the remote user can exercise 100% control over the system. Of course some restrictions apply. The main is that the system can have only one controller at a time no matter remote or local.

Fig.1

A small but fully functional system for remote control, monitoring and analysis of a programmable power supply performance was built up and put into service for the purpose of this paper. A focus was given to student remote education in real conditions.

II. RESEARCHED OBJECT

A programmable power supply based on a transformer forward converter has been researched and analyzed as shown on fig. 2

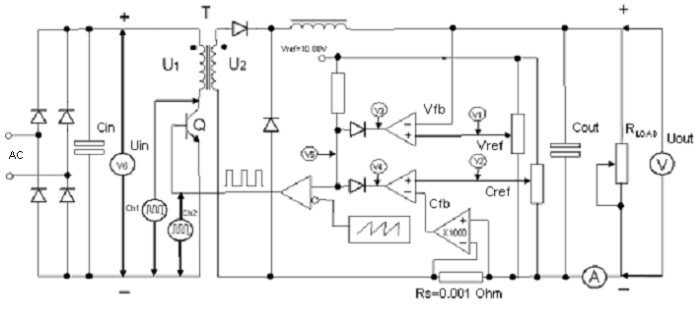

Fig. 2

The power supply operates in constant voltage as well as in constant current mode. The voltage and current references **V1** and **V2** are generated by digital potentiometers. The voltage and current error amplifier outputs **V3** and **V4** are compared

between each other so active is the lower one **V5**. This approach benefits automatic mode crossover based on the power supply setup and the load. Significant points of interest are the actual signal levels of **V1** through **V6** as well as **A** and **V** readings on the DMM as designated on fig. 2 The other useful information is gathered by Ch1 and Ch2 waveforms representing **Uds** and **Ugs** across the power switch**.**

III. CONTROL AND MEASUREMENT SYSTEM

A. System overview

This is an open system built up of programmable instruments interfaced by GPIB cables and probes for scanning and measurement of signals that are of significant importance for the automated analysis and remote control of the whole system. For detail see fig.3 The system controller is equipped with GPIB-PCI card which serves as a system bus. All requirements for building up a GPIB network are taken care of as follows:

- max. cable length between two devices is less or equal to 2m.
- total cable length is less than 15m.
- all devices are powered up

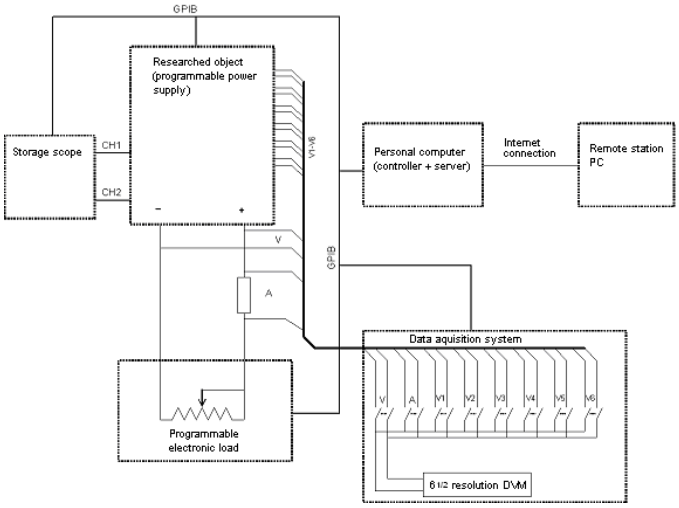

Fig. 3

B. System main components

Object under research:

-100W programmable power supply capable of delivering 10V and 10A at the output.

Peripheral instruments:

- Electronic programmable load compatible with the power supply under test.
- 10 Channel data acquisition system with 6 ½ digit resolution DVM.
- 60 MHz, 2 channel storage oscilloscope.
- System controller + web server – personal computer.
- One or more remote stations - personal computers.

C. Control and programming environment.

The control of the system is based on National Instruments LabView industrial programming environment. It benefits a graphical programming mode which gives full visualization of the algorithms as well as an enormous set of ready made routines, subroutines, modules and instrument drivers. All these features significantly reduce the development time and cost.

Installed is a program pack NI 1.70 for communication between LabView and the GPIB interface. In addition this pack supports RS 232 connectivity which is a great plus for older instruments. Both interfaces are controlled by SCPI commands that allow mixed systems. Also included is a server module which features remote control of the system over the internet. For proper remote control a minimum system requirements are needed for the remote stations. LabView basic is a must as wall as an internet browser and access. No instrument drivers are needed.

D. Soft panel

The whole system control is given to a virtual screen (fig.4). This screen is hosted by the controller and is visible to all remote stations. There is no difference in the functionality between controller and remote station.

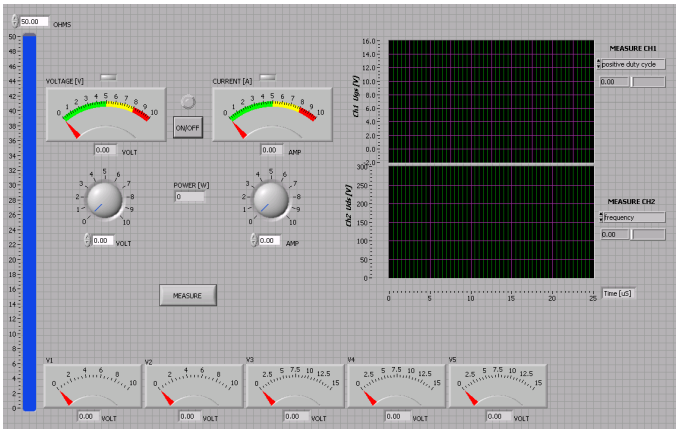

Fig. 4

The main Volt and Ammeter visualize the reading of A and V meters on fig.2

Below, the analog readings are digitalized as well. The rectangular LEDs above the main Volt and Ammeter indicate the actual mode as follows:

Voltage mode - green

Current mode - amber

Note: See fig. 5, 6, 7 and 8 for details

In between the main meters a virtual **ON/OFF** button is located. This button has two functions:

1. Activates Vref and Cref from the digital pots on fig.2
2. Activates Load reference.

Vref and Cref are adjusted by rotating the round knobs **VOLT** and **AMP.** A digital set is also available under the knobs. In between is located the watt meter which reading is refreshed

90 times a second. The analog-digital meters V1 through V5 indicate DC voltage in the corresponding points from fig.2 Due to relatively slow data transfer rates, these meters do not operate in dynamic mode. Readings are taken in constant mode by depressing **MEASURE** button. The same button activates Ch1 and Ch2 oscillogramme loading. This process requires scope setup data notification prior each measurement. Once notified the scope takes some time to apply the settings and to establish steady waveforms good for capture and transfer over the GPIB . This may take up to 20 sec. Because 8 line data bus is used, the transfer time is negligible compared to scope setup time. The main scope setup parameters are:

- amplitude
- time base
- coupling (DC)
- trigger level
- trigger source
- trigger slope ect.

The software features automated analysis of the results. A drop down menu is available right next to the oscillogram screens. Varieties of parameters are selectable. In result the desired parameter is calculated and displayed in proper measure units at the end of each test. The user can select between: frequency, period, rise time, fall time, max. value, min. value, RMS, duty cycle, pick to pick, overshoot ect. See fig. 5

Different modes of operation are set by adjusting the following references:

Voltage-(Vref)
Current-(Cref)
Load-(Rload).

The load is electronic and programmable, configured for constant resistance operation. This mode is accessed indirectly. The main programmable parameters are voltage and current.

Constant resistive mode is obtained by regulating either the current or voltage in order to fulfill the requirement for constant resistance. Due to the fact that the system under test (power supply and load) has two independent regulators they always operate in different modes. If the power supply is operating in constant voltage mode, then the load will operate in constant current mode and vice versa. In this way both, current and voltage are regulated in such a way, that R=U/I=const These modes are established fully automatically and depend on

Voltage-(Vref)
Current-(Cref)
Load-(Rload).

The value of the load resistor is defined by the slider position located on the left hand side of the display (fig.2)
It varies between 0 and 50 Ohm and can be set digitally either.

IV RESULTS

All results have been visualized in the research process. The main modes of operation have been analyzed, starting from no load and ending to full load.

Fig. 5 indicates the analysis at the following conditions:

Vref=1V
Cref= 10A
Rload= 50 Ohm

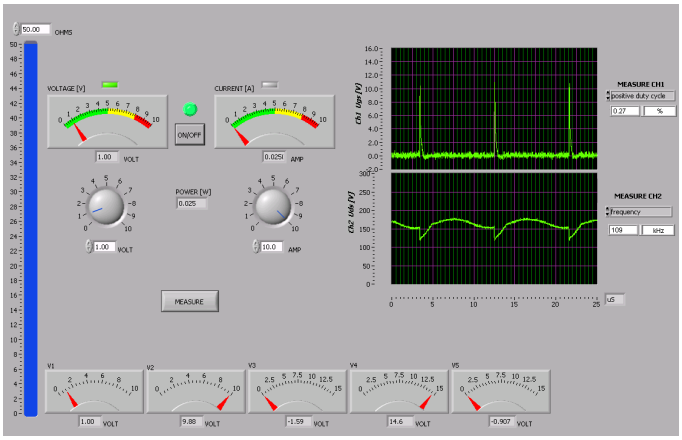

Fig. 5

These conditions put the unit under test in constant voltage mode of operation. **VOLTAGE** LED indicates that. Independently of current high reference, due to the high resistance of the load, the output current is negligible (0.025A). In accordance the output power is also minimal (0.025W) as well as the duty cycle of the power switch **Q.**

When the load is dramatically reduced the results on fig.6 are observed at the following conditions:

Vref=10V
Cref= 10A
Rload= 0.1 Ohm

Because the output current reaches its max. value 10A, then the unit under test goes into constant current mode of operation. Due to the very low load value, the voltage drop across it is insignificant 1.09V The resulting output power increases up to 10.87W and respectively the duty cycle goes up to 2,82%

Fig.7 shows full power generation (Pout=94.61W) under the following conditions:

Vref=10V
Cref= 10A
Rload= 1.05 Ohm

The unit under test is operating in constant voltage mode with duty cycle of 39.2%

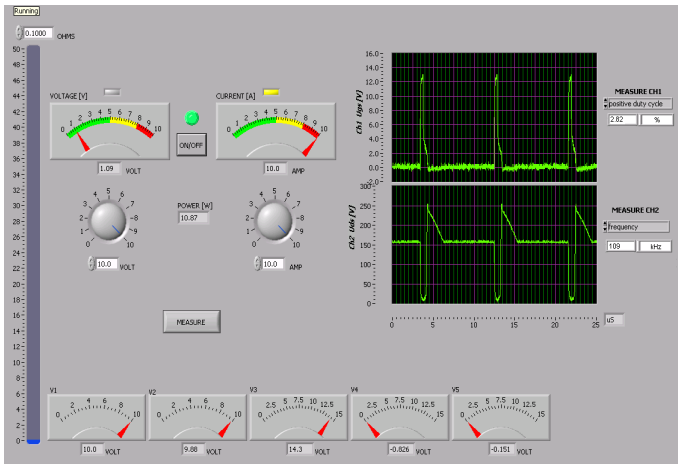

Fig. 6

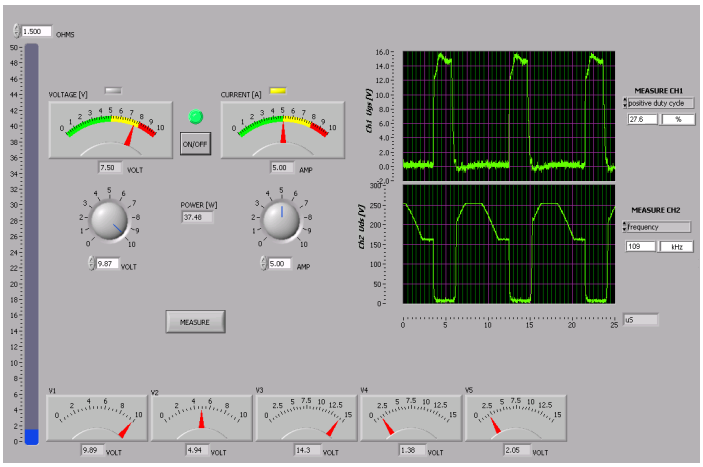

Fig. 8

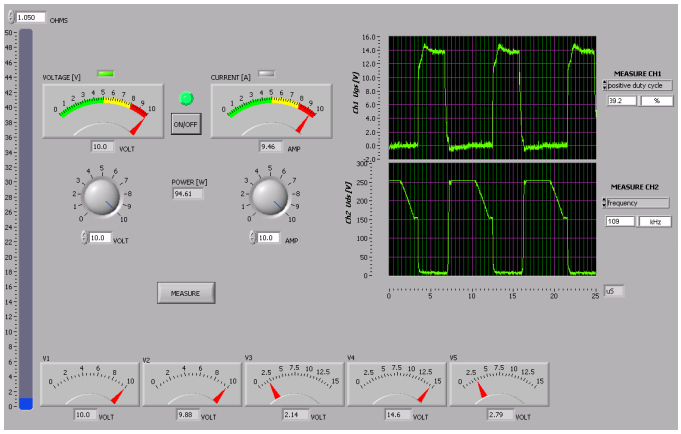

Fig. 7

The last experiment (fig. 8) represents intermediate load under the following conditions:

Vref=9.87V
Cref= 5A
Rload= 1.5 Ohm

These conditions put the unit under test in constant current mode of operation while the output power decreases to 37.48W as well as the duty cycle to 27.6%.

IV. Conclusions

The results obtained under the current research are valuable and accurate enough for laboratory experiments headed towards student distance learning. The data generated is good for report creation and further analysis. Because the programming environment LabView operates in graphical mode, a quick and easy way is offered for further improvement and upgrade of the current version. In near future a couple of new modules will be added featuring automated plot drawing, results e-mailing and printing.

References

[1] Switch mode Power Supply Handbook (McGraw-Hill Handbooks) by Keith Billings
[2] Fundamentals of Power Electronics (Second Edition) by Robert W. Erickson
[3] LabView analysis Concepts April 2003 Part number 370192B-01
[4] GPIB software and hardware tutorial - National instruments developer zone
[5] SCPI Consortium Handbook- September 2002

Home Automation Based on 1-Wire Interface

Marin Marinov[1], Ivan Topalov[2], Todor Djamiykov[3]

Abstract – **In this paper we are presenting a way for automating home processes using a wired network. The network is made using Dallas Semiconductors 1-Wire interface and devices. The control is achieved through a personal computer and a web browser. The automation includes heating and cooling, lighting control, etc.**

Keywords – **1-Wire interface, Home automation, Sensor networks.**

I. Introduction

The concept of an intelligent house, where devices could be controlled remotely, and would be automated for both comfort and energy efficiency is very appealing. The interface to the devices could be either wireless or wired. In case of a wireless solution there will be a need either of batteries or either of power lines. Our solution is positioned between both strategies. It is a wired one, but uses the power lines also for data transfers. This leads to a total of two wires needed for each sensor or controlling device. In some cases the number of needed wires can be reduced even to one.

1-Wire protocol requires a master device. We have chosen to use Dallas Semiconductors Kit – TINI. It uses DS80C400 microcontroller which is a 1-Wire and Ethernet ready microcontroller.

All the control of the master and 1-Wire devices is achieved through a personal computer and the use of a Web Browser. The use of this program suggests a real easy and user friendly interface.

II. 1-Wire Protocol

The 1-Wire net is a low-cost bus based on a PC or microcontroller communicating digitally over twisted-pair cable with 1-Wire components. The network is defined with an open-drain master/slave multidrop architecture that uses a resistor pull-up to a nominal 5 V supply at the master. A 1-Wire net-based system consists of three main elements: 1) a bus master with controlling software; 2) wiring and associated connectors; and 3) 1-Wire devices. The 1-Wire protocol uses conventional CMOS/TTL logic levels with operation specified over a supply voltage range of 2,8 V to 6 V.

The 1-Wire net allows tight control because no node is allowed to speak unless requested by the master, and no communication is allowed between slaves, except through the master. Both master and slaves are configured as transceivers permitting bit sequential data to flow in either direction, but only one direction at a time. Technically speaking, data transfers are half-duplex and bit sequential over a single pair of wires, data and return, from which the slaves "steal" power by use of an internal diode and capacitor. Data is read and written least significant bit first. Data on the 1-Wire net is transferred with respect to time slots. For example, to write a logic one to a 1-Wire device, the master pulls the bus low and holds it for 15 microseconds or less. To write a logic zero, the master pulls the bus low and holds it for at least 60 microseconds to provide timing margin for worse case conditions (Fig. 1).

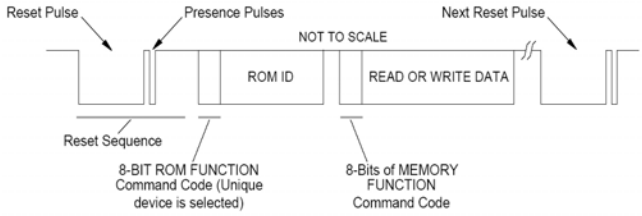

Fig. 1. A typical 1-Wire communication sequence.

A system clock is not required, as each 1-Wire part is self clocked by its own internal oscillator that is synchronized to the falling edge of the master. Power for chip operation is derived from the bus during idle communication periods when the DATA line is at 5V by including a half wave rectifier onboard each slave.

Within each 1-Wire slave is stored a lasered ROM section with its own guaranteed unique, 64-bit serial number that acts as its globally unique address.

The entire collection of 1-Wire devices plus the host form a type of miniature local area network, or MicroLAN; they all communicate over the single common wire. The most significant byte in the ROM code of each device contains a Cyclic Redundancy Check (CRC) value based on the previous 7 bytes of data for that part. When the host system begins communication with a device, the 8-byte ROM is read, LSB first. If the CRC that is calculated by the host agrees with the CRC contained in byte 7 of ROM data, the communication can be considered valid. If this is not the case, an error has occurred and the ROM code should be read again.

The length of the maximum wiring depends on the type of wires used. When using Category 5 twisted pair, controlling

[1]Marin Marinov, Faculty of Electronics, Technical University of Sofia, 8 Kliment Ohridski Blvd., Sofia 1756, Bulgaria, E-mail: mbm@tu-sofia.bg
[2]Ivan Topalov, Faculty of Electronics, Technical University of Sofia, 8 Kliment Ohridski Blvd., Sofia 1756, Bulgaria E-mail: vantop@hotmail.com
[3]Todor Djamiykov, Faculty of Electronics, Technical University of Sofia, 8 Kliment Ohridski Blvd., Sofia 1756, Bulgaria. E-mail: tsd@tu-sofia.bg

slew rates and substituting an active pull-up, reliable communication over 300m of cable with more than 500 assorted 1-Wire devices was demonstrated. Without slew rate control and active pull-up, the limit is about 100 meters with 150 1-Wire devices.

II. Block Diagram

As we know how the 1-Wire protocol works we are ready to present the structure of the whole system. Of course it consists of a master node and slave nodes. All the computation is done in the master node, while the slave nodes represent different sensors and executing devices.

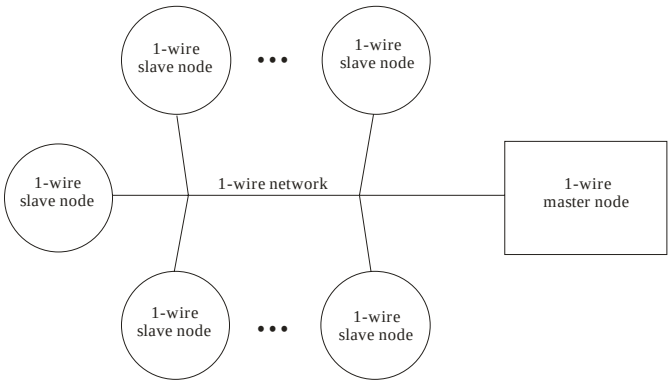

Fig. 2. Block diagram of an automation system

As it is shown on Fig. 2 there is an unlimited number of 1-Wire nodes connected to the network. The 1-Wire network shown on the figure consists only of one wire is it is the real situation. We are not counting the ground, because in some cases the central heating or water pipes can be used for ground wire.

The principle of operation is as the following: The master node asks each sensor slave node constantly for its status. When the master node determines that a given sensor has passed over a predefined limit it tells another slave 1-Wire node to react according to an algorithm defined by the user. A simple example is controlling the temperature in a room. The user sets 20ºC the temperature. Then the master node checks the temperature sensor in the observed room, and in case it sees deviation from the setup temperature it reacts. If the temperature is below the threshold and it is a heating season, the node tells the execution slave node, in our case a relay, to open the heating electro-magnetic valve. When the temperature reaches the threshold, master node tells the execution slave node to shut the valve.

III. Sensor and Actuator Slave Nodes

Dallas Semiconductors offers a variety of 1-Wire devices. The simple of all these devises is the temperature sensor. The biggest advantage of this sensor is that the measured value is ready for calculations – it is coming out of the sensor straight in a two complement value. We have stopped our attention at the use if DS18B20. The core functionality of it is its direct-to-digital temperature sensor. The resolution of the temperature sensor is user-configurable to 9, 10, 11, or 12 bits, corresponding to increments of 0.5ºC, 0.25ºC, 0.125ºC, and 0.0625ºC, respectively. The default resolution at power-up is 12-bit. The DS18B20 powers-up in a low-power idle state; to initiate a temperature measurement and A-to-D conversion, the master must issue an appropriate command. Following the conversion, the resulting thermal data is stored in the 2-byte temperature register in the scratchpad memory and the DS18B20 returns to its idle state.

One of the biggest advantages of this sensor is its size. It is fitted in a TO-92 and has three pins, one pin is common – ground, one is data IO – DQ pin, and a third pin for power, in case the user wants to use a separate power source. Fig. 3. illustrates TO-92 case for DS18B20.

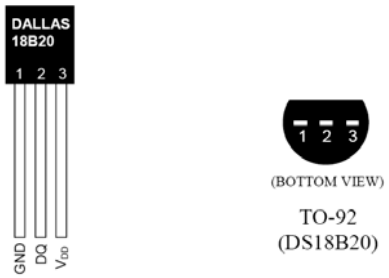

Fig. 3. TO-92 case of DS18B20

The usage of this sensor is very simple. Just plug it to the wires and it is ready for use. The only important thing is the user to know which sensor in which room is placed. The rest is achieved through software and 1-Wire protocol.

The practical use of the temperature sensor is very popular because of its function to monitor a predefined temperature. In both occasions – heating and cooling, the control of the room temperature is achieved through measuring the temperature in the particular room. For better performance we use several temperature sensors in one room and then average the temperature reading from all sensors. Thus we achieve better control, because the temperature close to the source of heat or cold is different from the one in the other corner of the room. Also the temperature close to outer walls and windows is different. We also use a temperature sensor placed on top of the source of heat or cold to observe and control the device itself. This is used like a precaution safety backup switch in case of failure in the device producing heat or cold.

All the information from the temperature sensors goes to the master 1-Wire device. It reads the temperature and reacts accordingly the predefined algorithm.

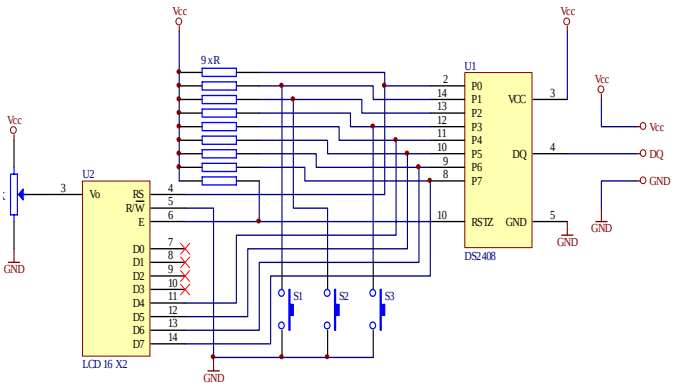

Fig. 4. Display and buttons module

The temperature thresholds are stored in the 1-Wire master device and are entered through a personal computer and a web browser.

In case the user wants to set the temperature without using a computer, and this setup to be done in each room, he can use a separate module, placed in each room for setting the temperature. In this module there are several buttons and a LCD display. All the data entered through this module and displayed on the LCD are communicated again through 1-Wire protocol. In other words, this is a monitoring and control module connected to the 1-Wire master device. There are no control functions in this module, it is only an interface for the user. The main part of this module, as shown on fig. 4., is the 1-Wire 8-channel addressable switch.

The DS2408 is an 8-channel, programmable I/O 1-Wire chip. PIO outputs are configured as open-drain and provide an on resistance of 100 Ω max. A robust PIO channel-access communication protocol ensures that PIO output-setting changes occur error-free. A data-valid strobe output can be used to latch PIO logic states into external circuitry such as a D/A converter (DAC) or microcontroller data bus.

DS2408 operation is controlled over the single-conductor 1-Wire bus. Device communication follows the standard Dallas Semiconductor 1-Wire protocol. Each DS2408 has its own unalterable and unique 64-bit ROM registration number that is factory lasered into the chip. The registration number guarantees unique identification and is used to address the device in a multidrop 1-Wire net environment. Multiple DS2408 devices can reside on a common 1-Wire bus and can operate independently of each other. The DS2408 also supports 1-Wire conditional search capability based on PIO conditions or power-on-reset activity; the conditions to cause participation in the conditional search are programmable. The DS2408 has an optional V_{CC} supply connection. When an external supply is absent, device power is supplied parasitically from the 1-Wire bus. When an external supply is present, PIO states are maintained in the absence of the 1-Wire bus power source. The RSTZ signal is configurable to serve as either a hard-wired reset for the PIO output or as a strobe for external circuitry to indicate that a PIO write or PIO read has completed.

Devices described up to now were for sensing and setting the temperature thresholds. We need also devices for controlling the heating or cooling devices. The simplest way is to put a relay which is controlled over 1-Wire interface.

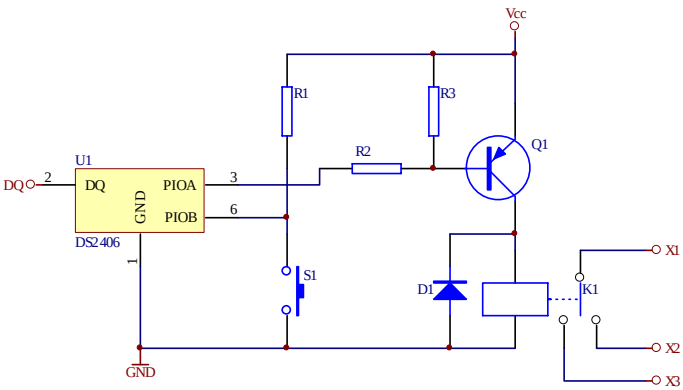

Fig. 5. 1-Wire relay and button

The schematic for this solution is shown on Fig. 5.

It is a simple solution based on DS2406 – dual addressable switch plus 1kbit memory. The DS2406 offers a simple way to remotely control a pair of open drain transistors and to monitor the logic level at each transistor's output via the 1-Wire bus for closed loop control. Each DS2406 has its own 64-bit ROM registration number that is factory lasered into the chip to provide a guaranteed unique identity for absolute traceability.

The device's 1024 bits of EPROM can be used as electronic label to store information such as switch function, physical location, and installation date. Communication with the DS2406 follows the standard Dallas Semiconductor 1-Wire protocol and can be accomplished with minimal hardware such as a single port pin of a microcontroller.

Multiple DS2406 devices can reside on a common 1-Wire network and be operated independently of each other. Individual devices will respond to a Conditional Search command if they qualify for certain user-specified conditions, which include the state of the output transistor, the static logic level or a voltage transition at the transistor's output.

In our case, one of the PIO pins is used for controlling the relay and the other is for reading the status of a button. The button might be used for manual control of given process or device. Except controlling heating and cooling devices, it can be used also for controlling lights in the home.

Such board can be fitted also in the wall lights switch. And by pressing the button it will turn on and off the lights in the room and also gives the opportunity all the lights in the home to be controlled by one single place.

When there is no need for a button the solution shown on Fig. 6. can be used. It uses DS2405 instead DS2406 as on Fig. 5.

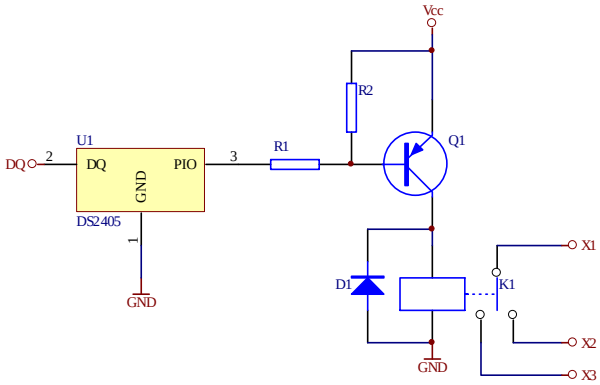

Fig. 6. Single 1-Wire relay

The DS2405 Addressable Switch is an open drain N-channel transistor that can be turned on or off by matching the 64-bit factory-lasered registration number within each part. If the relay is replaced with an LED we receive a remote 1-Wire indicator. Fig. 7 shows the proposed solution for 1-Wire indicator.

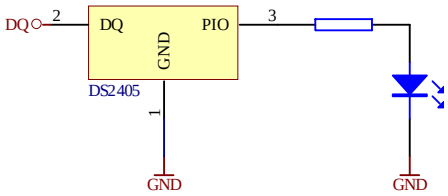

Fig. 7. 1-Wire LED indicator

All these intelligent slave nodes are connected to the 1-Wire master device. The master node in our case is doing all the computation and storing of data. It can be a simple microcontroller, a personal computer or a high performance microcontroller.

IV. 1-WIRE MASTER NODE

Our solution for the master 1-Wire node is based on a high performance microcontroller from Dallas Semiconductor DS80C400. The DS80C400 network microcontroller offers the highest integration available in an 8051 device. Peripherals include a 10/100 Ethernet MAC, three serial ports, a CAN 2.0B controller, 1-Wire® Master, and 64 I/O pins.

To enable access to the network, a full application-accessible TCP IPv4/6 network stack and OS are provided in ROM. The network stack supports up to 32 simultaneous TCP connections and can transfer up to 5 Mbps through the Ethernet MAC. Its maximum system-clock frequency of 75 MHz results in a minimum instruction cycle time of 54ns. Access to large program or data memory areas is simplified with a 24-bit addressing scheme that supports up to 16MB of contiguous memory.

To accelerate data transfers between the microcontroller and memory, the DS80C400 provides four data pointers, each of which can be configured to automatically increment or decrement upon execution of certain data pointer-related instructions. The DS80C400's hardware math accelerator further increases the speed of 32-bit and 16-bit multiply and divide operations as well as high-speed shift, normalization, and accumulate functions.

DS80C400 is the core of the evaluation module DSTINIm400. In addition to the DS80C400, the DSTINIm400 includes a real-time clock, 1MB flash, 1MB static RAM, and support for an external Ethernet PHY for connecting to a wide variety of networks. The circuit board is designed as a module to be plugged into a 144-pin SODIMM connector. For evaluation, the DSTINIm400 can be inserted into the DSTINIs400 socket board (for future use, both boards are referred to as a TINI module). The combination of the two boards allows full evaluation of the features of the DS80C400 using an Ethernet network.

As described before, TINI provides all the necessary to run a smooth 1-Wire network. It has memory to store the firmware, 1-Wire outputs for the network, and Ethernet connectivity for personal computer operation. The operation is simple. All devices, sensors, buttons, and relays are 1-Wire devices and all are connected to the TINI. TINI from its side is doing all the computation, monitors the sensors and controls the relays. Besides this, TINI is serving a web server, which server is the door to a user interface. TINI is connected to an Ethernet Local Area Network (LAN) where the HTTP server is accessible. A personal computer is also connected to the LAN and accesses the web server through a Web Browser. The purpose of this solution is to give even to non technical people the ability to use and setup the home automation system. This is the main reason to use a web browser.

The options that can be set up through the web browser are a lot. First and important option is to designate a name for each slave node. This means to give a name to the unique 64-bit ROM registration number in each 1-Wire device. The name should be also unique and should hint the type of node – sensor or execution device, and the room in which it is placed. After the names are setup comes the time to define the function for each execution device that should do. If it is a heating device, the user makes a relation with the sensors placed in the same room and sets the temperatures for thresholds.

So, we have a heating occasion, the execution device when turned on turns the power on for the heating device. The TINI checks the temperature in the room in regular intervals predefined by the user. When the temperature goes over the threshold for the room it turns off the heating system. But the algorithm continues to work and continues to measure the temperature.

The web browser is the interface for the user to setup the algorithms. All the settings are stored in the TINI module, which means that the personal computer can be turned off, while the home automation system can continue to work. There is also a battery on the TINI module which can keep the data in case of power failures. Another option is to use the real time clock on the TINI. This gives the option to set up some devices to turn on and off at particular time.

In some occasions the setup of the temperatures for the rooms can be done through the use of the 1-Wire IO module with LCD display and buttons. This module is placed in each room and is accessible for the user.

V. CONCLUSION

With the help of the variety of 1-Wire devices a cheap and easy to design and implement home automation system can be achieved. The control and monitoring includes individual room heating and cooling, lights, open door checking, etc. The master device is a module based on DS80C400. The module is doing all the computation and is accessed via a web browser on a personal computer. The web browser reveals the potential and simplicity for use.

REFERENCES

[1] Awtrey, D., Transmitting Data and Power over the 1-Wire Bus," Sensors: 48-51, Feb. 1997.
[2] Awtrey, D., The 1-Wire Weather Station, Sensors: 34-40, June 1998.
[3] Dallas Semiconductor. MicroLAN Design Guide, Sep. 2003.
[4] Hill, J., R. Szewczyk, A. Woo, S. Hollar, D. Culler, and K. Pister. System architecture directions for networked sensors. In Proceedings of the 9th International Conference on

Architectural Support for Programming Languages and Operating Systems ASPLOS-IX, pages 93–104, Cambridge MA, USA, November 2000.

[5] Howarth, D.: Performing Data Acquisition over the Internet. Sensors Magazine, January 1998.

[6] Yamasaki, H. K. Takahashi.: Advanced intelligent sensing system using sensor fusion. Proceedings of the 1992 International Conference on Industrial and Electronic Instrumentation and Automation. Vol. 1, 1993.

A Study of Lead-Free Surface Mount Technologies

R. Pranchov[1], Z. Georgiewa[2], M. Palabikian, N. Serafimov

Abstract – **The paper describes problems concerning the application of lead–free solder inks for SMT (surface mounting technology), as well as lead–free solder alloys for conventional PCB (printed circuit board) technology. Comparative technological and design tests of test SMT printed circuit boards with different final plating have been carried out. Destructive tests for peeling and shearing strength determining, combined with thermal cycles have been implemented also.**

Keywords – **Lead–free solder alloys, test printed circuit board, peeling strength, shearing strength.**

I. Introduction

Abandoning lead as an essential material in electronic manufacturing is an inevitable process. Proof is the EU directive RoHS which requires the restriction of dangerous substances from electronic and electrical equipment. In accordance with the latter lead should be eliminated from electronic products put on the market after July 1, 2006. It is therefore essential for the electronic products manufacturers to be informed about the possible choice of lead–free solder alloys, used for soldering, printed circuit board and electronic components pin plating. They should possess similar features in comparison with the most commonly used nowadays tin–lead (SnPb) solder alloys. Literature study shows, that possibilities for lead–free solder alloy choice is not very wide. Most serious pretenders for substituting tin-lead alloys are tin and copper, as well as tin, copper and silver alloys [1,2].

Subject of a comparative investigation of this paper are tin, copper and silver alloys, as well as tin–lead alloy. The aim is to examine solder stability and reliability in cases of SMT and conventional technology.

II. Experiments

Lead–free solder inks for SMT are being prepared from the most common Sn–Ag–Cu alloys: Sn96,5-Ag3,0-Cu0,5; Sn95,5-Ag3,8-Cu0,7; Sn95,5-Ag4,0-Cu0,5. Evaluation of solder inks is being carried out in accordance with the following criteria: availability, price, printing, melting, temperature ageing, and reliability characteristics of solders [3]. Examined solder inks show very good similar printing characteristics Fig.1.

[1]R. Pranchov, M. Palabikian and N. Serafimov are with the Communication Faculty of Technical University of Sofia.

[2]Z. Georgiewa is with Electron Consortium AD, Sofia, e-mail **zgeorgiewa@mail.bg**

Melting temperatures of the three inks lie between 218°C and 220 °C (219,77 °C, 218,8 °C and 220,23 °C, appropriately). These values are very close to each other, but Sn95,5–Ag3,8–Cu0,7 solder ink has the lowest melting temperature [4].

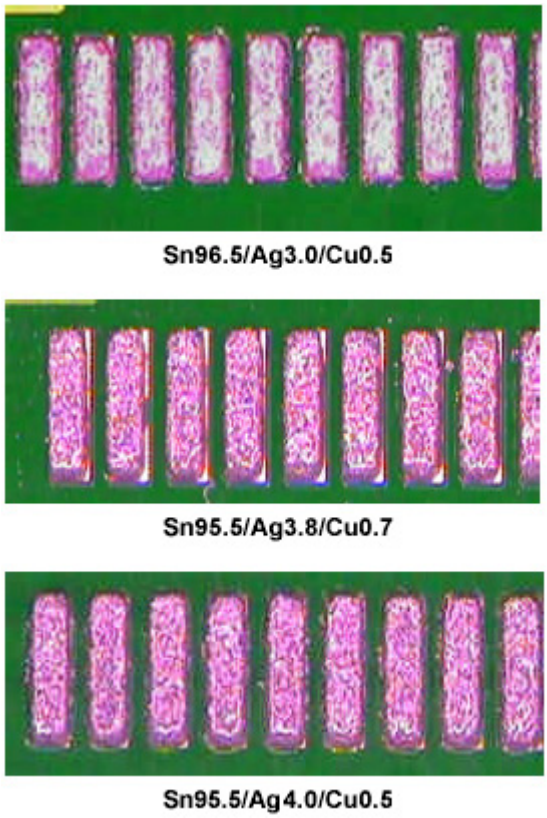

Fig. 1

For experimental needs a test SMT printed circuit board has been implemented. Fig. 2 shows its topology. Pads for mounting the most common footprints are provided: FLAT – 1206, 0805 and 0603; MELF; SOT 23 and SOT 89; SO; PLCC and TOFP. Hence all commonly used standard surface mounting devices are being used in our experiment – resistors, capacitors, transistors and integrated circuits. Printed circuit boards are produced in accordance with the conventional subtractive technology. Some of the PCBs are with final tin-lead plating, the rest – with a gold one. Although gold final plating is more often being used, the percent of Sn–Pb plated PCBs is relative high in the transition period and it is possible to combine Sn–Pb plated PCBs with lead–free soldering materials.

A lead–free solder ink type TCS552 – 1 with the following ingredients: Sn 95,5; Ag 3,8; Cu 0,7 and melting temperature 217 °C has been chosen for our experimental purposes. Soldering is being carried out in a four – zone REFLOW oven with infrared heating and air convection. For comparison, another test PCB has been mounted with a lead solder ink type R256 (Sn 62; Pb 36; Ag 2) with a melting temperature 183 °C.

For pads mechanical strength and reliability evaluation a destructive test method has been used, wherein strength for peeling the pad from the test board has been measured. The test boards have been passed through temperature cycles with a given duration.

III. Experimental Results

TABLE 1

PCB#	Technological characteristics	Melting temperature, °C	Solder outer appearance	Defects
01	SnPb plating SnPbAg ink	225	Proportional, smooth, shining solders; excellent pad wetting.	Not observed
02	SnPb plating SnAgCu ink	242	Incomplete ink melting, rough mat solders; unburned flux traces round pads outlines	Cold solders
03	SnPb plating SnAgCu ink	245	Incomplete ink melting, rough mat solders; unburned flux traces round pads outlines	Cold solders
04, 05	SnPb plating SnAgCu ink	250	Complete ink melting; good pad wetting; smooth shining solders	Not observed
06	Au plating SnAgCu ink	250	Complete ink melting; good pad wetting	Areas without ink are not observed
07, 08, 09	Au plating SnAgCu ink	250	Complete ink melting; good pad wetting; smooth shining solders	Not observed

Seven PCBs with different final plating and different soldering temperatures have been examined. The overall results are given in Table 1.

Pads mechanical properties have been examined by means of destructive peeling strength measurement. There are three possible cases - pad destruction, solder peeling from pad, pad peeling from PCB. Tests have been done after applied

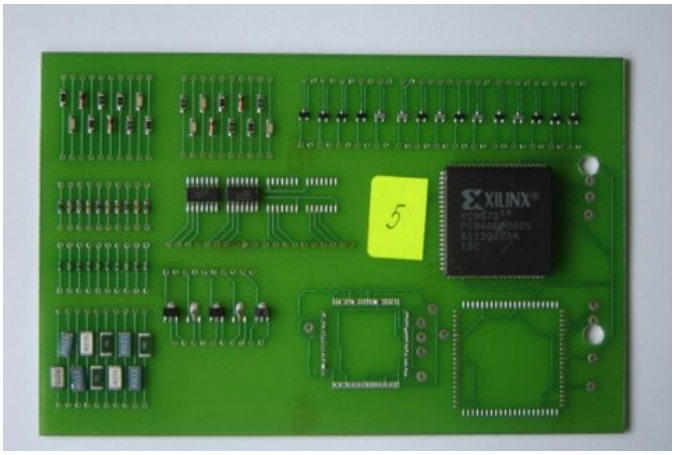

Fig. 2

temperature cycles with the following parameters: +85 °C (25 min), ambient temperature equalization (5 min), -25 °C (25 min), ambient temperature equalization (5 min). Peeling strength measurements have been done at regular cycle intervals - 0, 5 and 10 by means of a four - channel measuring bridge type MK from "HOTTINGER - BALDWIN - MESSTECHNIK", with the following parameters: matching range ± 26000; 1 scale count = 1 μm/m for a typical strain gauge; carrier frequency 180 Hz; precision 0,1 %. Each measurement comprises 10 pads per test cycle. Corresponding results (peeling strength mean value) are shown in Fig. 3. Series 1 (blue) data are the results (mean value) from a tin-lead solder alloy (SLT 60) strength test, whereas Series 2 (red) - these (mean value) from a lead-free alloy. Peeling strength of lead-free alloy solders is about 20% higher than tin-lead alloy solders strength. More important, no pad destruction was observed, at all.

IV. Conclusion

Comparative examinations of lead-free (TCS 552-1 type) and tin-lead (R256 type) solder inks, as well as lead-free and tin-lead solder alloys reveal very good technological and mechanical properties of the examined lead-free solder ink and alloy. Lead-free solder alloys are technologically compatible with golden plated PCBs.

Products proposed from the solder producer are appropriate for substituting the lead solders and inks for conventional and surface mount printed circuits. The only requirement for using lead-free materials is the higher temperature of the REFLOW process and of the solder iron used.

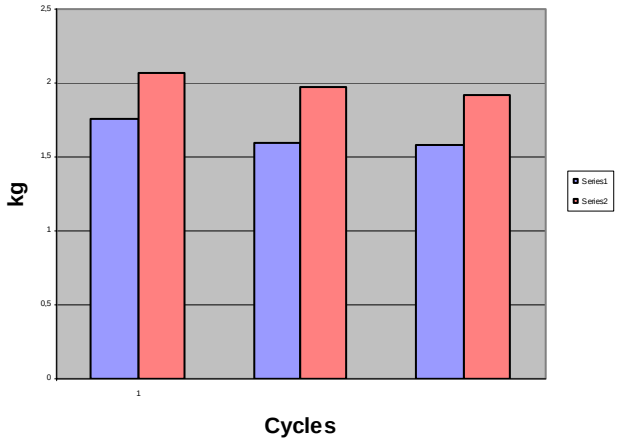

Fig. 3

REFERENCES

[1] Seelig K. and D. Sukarski. A comparison of Tin - Silver - Copper Lead - Free Solder Alloys. AIM, 1998.

[2] Seelig K. A Comparison of Leading Lead - Free Alloys. AIM, Vol. 1, 1998.

[3] Lead - Free Solder Paste Evaluation. Lead - Free Report 1, Kester, http://www.kester.com.

[4] Lead - Free Solutions. Kester, http://www.kester.com.

Noises in Photodetectors

Ivan S. Kolev[1], Tsanko V. Karadzhov[2] Elena N. Petkova[3]

Abstract – **Noises in photodetectors (internal and external) cause a change in the form of the output signal.**

Keywords – **Noise, Photodetector, PIN Photodiode, Noise Equivalent Power.**

I. INTRODUCTION

A. Background noise

Is generated by the thermal radiation of the earth, sun, planets, moon, aurora borealis, sky, stars, earth atmosphere, vehicles, industrial sites, light sources, radiation factors of cosmic origin.

The background noise generates a noise current, which is superposed to the dark current of the photodetector – Id.

B. Thermal noise

Is caused by the chaotic thermal movement of electrons along semiconductors. It depends on temperature. Thermal noise has an even spectrum within time t. It is reduced by cooling the photodetector.

C. Shot noise

The light flux (the flux of photons) entering the photodetector input fluctuates within time thus resulting in the fluctuation of the output current signal.

The higher the level of the desired signal, the higher the shot noise. Shot noise has an even spectrum within a wide frequency range.

D. Additional noise

Is caused by the unequal structure in the volume, as well as on the semiconductor crystal surface.

E. Noises of 1/f spectral density

Are within the range of the sound frequencies**.**

Noises depend on the direct current operating point, as well as on the signal frequency.

[1]Ivan S. Kolev. Department of Electronics, Technical University – Gabrovo, Street "Hadji Dimiter" No. 4, 5300 Gabrovo, Bulgaria, phone: +359 66 801064.

[2]Tsanko V. Karadzhov. Department of Electronics, Technical University – Gabrovo, Street "Hadji Dimiter" No. 4, 5300 Gabrovo, Bulgaria, phone: +359 66 801064, e-mail: karadjov_st@abv.bg

[3]Elena N. Petkova. Department of Electronics, Technical University – Gabrovo, Street "Hadji Dimiter" No. 4, 5300 Gabrovo, Bulgaria, phone: +359 66 801064.

Noise calculations are part of the frequency analysis. The root-mean-square total in the output unit is calculated by means of the PSPICE product [10].

Today there are two quick-acting photodetectors – PIN photodiodes and avalanche photodiodes.

II. PHOTODIODES AND PIN PHOTODIODES

Usually shot noise I_{Ndr} is normalized towards the frequency band.

$$\frac{I_{Ndr}}{\sqrt{\Delta f}} = \sqrt{2qI_D} = 17.9\sqrt{I_D} \qquad (1)$$

where: q – electron charge;
I_D – dark current.

If I_{Ndr} is entered in phemtoamperes $/\sqrt{Hz}$, then I_D is obtained in nanoamperes ($1fA=10^{-15}A$).

Flicker effect – photodiode noise at low frequencies.

The cut-off frequency of the Flicker effect f_{fl} does not exceed 20 Hz.

The dark current I_D consists of two components:

- leakage current
- PN-junction current

The shot noise is generated only by the PN-junction. The leakage current generates only a low thermal noise and a noise causing the Flicker effect.

If the photodiode frequency band is of $f_1 \div f_2$ ($f_2 > f_1$)

$$I_N(f_1 \div f_2) = I_{N0}\sqrt{(f_2 - f_1) + f_{fl}\ln\left(\frac{f_2}{f_1}\right)} \qquad (2)$$

where: I_{N0} – noise current, standardized/normalized towards the width of the frequency band, and it is expressed by formula (1),

f_2 – upper cut-off frequency – 3 dB level
f_1 – lower cut-off frequency – 3 dB level

When the voltage in the PN-junction is 0, there is a thermal noise only in the differential resistance of the PN-junction.

$$I_{Ntherm} = \sqrt{4kT / R_{diff\,0}} = \frac{4}{\sqrt{R_{diff\,0}}} \qquad (3)$$

where: K – Boltzmann's constant
T – absolute temperature
R_{diff0} – photodiode differential resistance at zero voltage.

R_{diff} is in GΩ, I_{Nth} – fA/√Hz

The differential resistance at zero voltage is difficult to measure; however, it can be calculated by the expression:

$$R_{diff\,0} = \left(\frac{kT}{q}\right) I_0^{-1} \tag{4}$$

$$\frac{kT}{q} \approx 0.025V = 25mV \tag{5}$$

I_0 – reverse saturation current
kT/q – thermal potential

$$I_{Ntherm} = \sqrt{4qI_0}\,25.3\sqrt{I_0} \tag{6}$$

where: I_{Nth} – fa/√Hz
I_0 – nA

At zero voltage there isn't any noise due to the flicker effect. Therefore, this mode is preferred for the operation of the photodiode at low noises. There isn't any flicker noise in the $f_2 \div f_1$ frequency band.

III. TYPICAL PARAMETERS

A. Signal/noise ratio

The ratio between the photocurrent obtained upon illuminating the photodiode and the noise current in the absence of a desired signal (dark current) is

$$\frac{S}{N} = \frac{I_{ph}}{I_N} = \frac{\Phi S_\Phi}{I_N} \tag{7}$$

$$\frac{S}{N} = \frac{EeS_\Phi}{I_N} \tag{8}$$

Φ – light flux, lm
S_Φ – integral current sensitivity, mA(μA)/lm
Ee – illumination, lx

B. Noise Equivalent Power (NEP)

$$NEP = \frac{I_N / \sqrt{\Delta f}}{S_\Phi} \tag{9}$$

$$NEP = EeA_\Phi \frac{U_N}{U_S}; \frac{W}{\sqrt{Hz}} \tag{10}$$

Ee – illumination, W/m^2
A – area – m^2
NEP is proportional to $1/S_\Phi$
U_N – root-mean-square value of the noise voltage
U_S – root-mean-square value of the signal voltage
A_{ph} – area of the photodiode

The S/N ratio increases with a square root of the A_{ph} area of the photodiode, the signal increases linearly with the area, and the noise changes with a square root of the area.

$$\frac{S}{N} = \frac{A_\Phi}{\sqrt{A_\Phi}} = \sqrt{A_\Phi} \tag{11}$$

C. Susceptibility

$$D = \frac{1}{NEP}\frac{U_S}{EeA_\Phi U_N} \tag{12}$$

A D* parameter, referred as the "detecting" ability of the photodetector, has been used. Within it, the signal/noise ratio is standardized towards the square root of the area and illumination.

$$D^* = D\sqrt{A_\Phi} \tag{13}$$

$$D^* = \frac{S/N}{Ee\sqrt{A_\Phi}} = \frac{S_\Phi . \sqrt{A_\Phi \Delta f}}{I_N}; cm\sqrt{Hz}W^{-1} \tag{14}$$

$$D^* = S_\lambda \sqrt{A_\Phi \Delta f}\, I_N \tag{15}$$

$$D^* = \sqrt{A_\Phi / NEP} \tag{16}$$

$$I_N = \sqrt{I_N^2} \tag{17}$$

$$D^* \equiv \lambda, f_M, \Delta f\ ,\ NEP \equiv \lambda, f_M, \Delta f \tag{18}$$

λ – wavelength
f_M – modulation frequency
I_N – root-mean-square value of the noise.

D.Noise Power

$$P_N \sim I_N^2 \sim \Delta f \tag{19}$$

Noise power is proportional to $\sqrt{A_\Phi}$

The D* quantity is inversely proportional to the threshold power of the photodiode when the latter has an area of $1cm^2$ and a frequency of 1 Hz.

If $\sqrt{A_\Phi}$ and $\sqrt{\Delta f}$ are set single values, then the $\frac{I_N}{S_\Phi}$ ratio is an illumination power where the signal/noise ratio is equal to one.

Two photodetectors have to be compared according to $\frac{I_N}{\sqrt{\Delta f}}$ rather than to I_N. The following components are included in the noise current of the photodetector:

Thermal noise (Johnson or Naiquist noise). They are determined by the thermal movement of the carriers.
root-mean-square value of the noise current
I_{ph} - photocurrent

$$I_{Ntr}^2 = 4KT.\Delta f.R \tag{20}$$

E. Shot noise

Statistical nature of passing of the carriers through the p^+-i junction and fluctuations of the generation-recombination processes.

$$I_{Nth}^2 \approx 2q(I_{ph} + I_D)\Delta f \quad (21)$$

F. I_N noise of 1/f spectrum

Deviation of the structure from the physical ideal form – surface recombinations and leakage; insignificant when f>10 kHz .

G. Background noise

I_{Nfon} – from the fluctuations of the radiation of the objects around the photodetector at T_{fon} temperature.

H. Photon noise

I_{Nfot} – statistical fluctuations of the photons fallen onto the photodetector. It is of quantum discrete nature.

These noises, excluding $I_{Nтехн}$, have an even spectrum of white (flat) noise. The photon statistics (the photon noise) responds to Poisson distribution where the root-mean-square deviation from $N_Φ$ is equal to $\sqrt{N_Φ}$.

$N_Φ$ – density of the photons flow

The minimal value of the noise equivalent power when the flow is 1 photon per second

$$P_{equN} / \sqrt{\Delta f} = E_φ = h\nu \quad (22)$$

where: h – Plank's constant
ν – frequency of fluctuations
$E_φ$ – photon energy

$$E_\varphi = \frac{1.23}{\lambda} = 4.1.10^{-15} V \quad (23)$$

λ - μm, $E_φ$ – eV, ν – Hz

$$N_Φ = 5.10^{15} \lambda . P_{rad}\text{, } N_Φ\text{, } C^{-1}cm^{-2} \quad (24)$$

P_{rad} – density of the radiation power

При λ=0.5 μm и Δf=1 Hz $P_{еквmin}=10^{-19}$W

Such a power can be fixed by an "ideal" photodetector in heterodyne reception.

The shot noise affects the sensitivity threshold of the photodetector.

The minimum limit light flux is:

$$\Phi_{\lim} = \frac{\sqrt{2q(I_D + I_{ph})\Delta f}}{S_\lambda} \quad (25)$$

$S_λ$ – monochromatic sensitivity

In order to reduce the sensitivity threshold (increase the dynamic range), it is necessary to decrease the dark current I_D. However, I_D is a temperature function, therefore the photodetector should be cooled.

Signal/noise ratio of a photodiode with an amplifier.

$\frac{S}{N}$ = the power of the signal to the power of the shot noise + the power of the amplifier noise (26)

S – power of the signal

N – power of the signal + power of the amplifier noise

The shot noise has two components:

$$- I_{NS}^2 = \frac{2q\left[2P_{OIIT}.q.\eta_Q\right]\Delta f}{h.E_Φ} \quad (27)$$

P_{opt} – optical power

$η_Q$ – quantum efficiency

The quantum efficiency is equal to the number of the added electrons to the number of the falling photons.

- from the photodetector dark current

$$I_{Nd}^2 = 2q.I_d.\Delta f \quad (28)$$

The noise of the amplifier is expressed by the John's noise over the photodiode load resistor at efficient temperature $T_{ef.}$

$$I_{NA}^2 = 4K.T_{eф} / R_L \quad (29)$$

$$\frac{S}{N} = \frac{2\left[P_{opt}q.\eta_Q / h.E_Φ\right]^2}{\left[2q.I_D + 4q\left(P_{opt}q.\eta_Q / h.E_Φ\right) + 4KT_{eff} / R_L\right]\Delta f} \quad (30)$$

The equivalent noise power

$$NEP = 4KT_{eff}.\Delta f^2\left(2\pi C\right); \Delta f = \left(2\pi.R_L C\right)^{-1} \quad (31)$$

C – equivalent capacity

With photodiodes where C=1pF, the optimal input resistance at a frequency of 100 MHz is 10^3 Ω, and the power of the amplifier noise is 5.10^{-15}W.

If S/N=1 , the minimum optical power where the desired signal of the photodiode can be differentiated from the noise is:

$$P_{\min} = \left(\frac{h.E_Φ}{q\eta_Q}\right) B\left[2nKT_{eff}.C\right]^{\frac{1}{2}} \quad (32)$$

the thermal noise is:

$$I_{Nth}^2 = \left(\frac{4KT}{R}\right)\ln_2 B \quad (33)$$

B – transmission speed

I_{n2} – Personik integral [9]

For example, with PIN photodiodes

NEP=$3.3.10^{-14}$W/√Hz

I. Detection threshold, specific susceptibility

$$D^* = 3.1.10^{12}\frac{cm\sqrt{Hz}}{W} \quad (34)$$

J. Types of sensitivity in photodiodes

- integral current sensitivity

$$S_I = \frac{\Delta I_{ph}}{\Delta\Phi(\Delta E)}; \frac{\mu A, mA}{lm(lx)} \text{ or A/W} \quad (35)$$

- spectral (monochromatic) sensitivity – modification of the photocurrent per unit of radiant flux of the falling monochromatic radiation

$$S_\lambda = \frac{\Delta I_{ph}}{\Delta P(\Phi)}; A/W \quad (36)$$

- volt integral sensitivity – the ratio between the photosignal voltage and the power of the radiation flux with a set spectral composition causing a change in the photocurrent

$$S_U = \frac{\Delta U}{\Delta P(\Phi)}; V/W$$

IV. AVALANCHE PHOTODIODES

Noises are mainly shot noises. The root-mean-square value of the noise is:

$$I_N^2 = 2q.I.\Delta f.M^X \quad (37)$$

I – current through the avalanche photodiode

M – coefficient of avalanche multiplication

X – a number from 2 to 3

In the equivalent circuit of the avalanche diode a generator of noise I_N is included – fig. 1

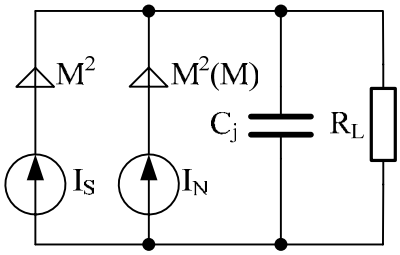

Fig. 1

With avalanche photodiodes, the signal/noise ratio depends on M. The derivative of

$$\frac{d\left(\frac{S}{N}\right)}{dM} = 0 \quad (38)$$

has to be identified.

The minimum is at M=(50÷60)

Noise current in avalanche photodiodes

$$I_{dr}^2 = 2q\left(I_{DN} + M^2 F.I_{DM}\right)\ln_2 B \quad (49)$$

I_{DN} – non-multiplying component of the current I_D

I_{DM} – multiplying component of the current I_D

For example, with avalanche photodiodes, NEP=2.10^{-14}W/√Hz

V. NOISES IN CHARGE COUPLED DEVICES

The noise from the dark current is known as a white or shot noise [1]. It is proportional to the thermally generated electrons, i.e. to the dark current.

$$\overline{\Delta n^2} = \sqrt{\frac{1}{q.f_T} J_g.l.w.m} \quad (40)$$

J_g – current density

F_T – clock frequency

l, m, w – number of elements in a cell.

With these devices, the NEE parameter, Noise Equivalent Exposure, is defined. For example, NEE=$0.2.10^{-3}$μJ/cm^2

V. NOISES IN PYROELECTRICELEMENTS

The noise response– (μV) in the time function (min) (band filter 0.5÷5 Hz) of the pyroelectric element RPY 100 of Philips is given in fig. 2. The voltage, peak to peak, of the same pyroelectric element is (20÷45) μV

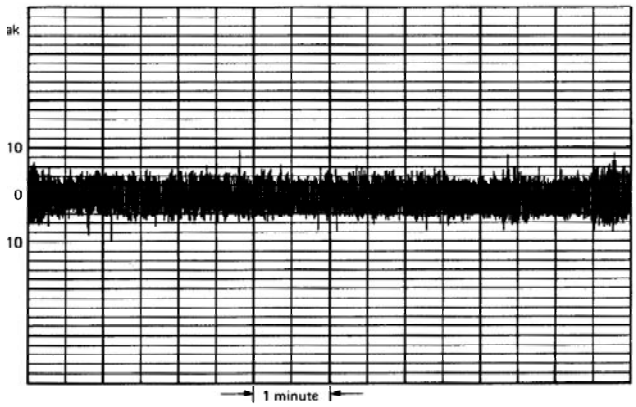

Fig. 2

VI. CONCLUSIONS

The consideration of noises in photodetectors and the reduction of their influence on their operation improve the parameters and function of the optoelectronic devices using photodetectors.

REFERENCES

[1] Atanasov, A. S. CCD – Application. Sofia, Technics, 1988.

[2] Velchev, N. B. Fundament of optoelectronics. Plovdiv, University's Publication, Plovdiv, 2002.

[3] Fiber optical communication. Devices, Circuits and Systems, Radio and Communication, 1982.

[4] Kolev, I. S. Optoelectronics. Gabrovo, Technical University, University Publication. "V. Aprilov", 2004.

[5] Kolev, I. S. Infrared optoelectronics. Gabrovo, Technical University, University Publication. "V. Aprilov", 2004..

[6] Nosov, U. R. Optoelectronics. M. Radio and Communication, 1989.

[7] Application of optoelectronic devices. M. Radio and Communication, 1981.

[8] Takov, T. B. и V. S. Minchev. Semiconductor Sensors. Sofia, Technics, 1986.

[9] Optical communication Technics. Photodetectors. Moskva, Mir, 1988.

[10] Shoikova, E. and other. Analysis and design with PSPICE. Technical University - Sofia, 2000.

General Analysis of Resonant Inverters with Reverse Diodes, Operating at Various Modes

Nikola P. Gradinarov[1], Nikolay L. Hinov[2], Tzvetan L. Marinov[2]

Abstract – **In this paper is obtained a general analysis of resonant inverters with reverse diodes (RIRD), operating at various modes.**

This work will show the possibility that the results from the analysis of RIRD at under resonance mode and continuous current can be spread out and used for the over resonance mode and continuous current.

This generalization is useful even at methodical point of view when introducing with the RIRD operation, and to perform comparative analysis of the qualities of the power circuit at the both modes.

Keywords – **Resonant inverters with reverse diodes, Analysis, Under resonance mode, Over resonance mode.**

I. INTRODUCTION

The analysis of resonant inverters with reverse diodes RIRD when the current is ahead of the inverter voltage (under resonance mode) is presented at [1, 2, 6, 7, 8]. In [2, 8] are obtained the expressions of the inverter current and the voltage across the commutating capacitor and with their assistance the required for the design the RIRD at this mode quantities are worked out.

The analysis of RIRD when the current is behind of the inverter voltage (over resonance mode) is presented at [3, 4, 5, 7]. There are also the expressions of the inverter current and the voltage across the commutating capacitor, which express the required quantities to design the RIRD, operating in this mode.

With the assumption that the active and the reactive components are quite ideal a same equivalent circuit is valid. The inverter current at the examined cases is described by one ant the same common expression.

At methodical point of view it is much comfortable to use the analysis in established operation at under resonance mode, as at the first part of the semi wave the energy flow is form the power supply to the load, but at the second part the flow is backwards, which is just opposite for the over resonance mode.

This work will show the possibility that the results from the analysis of RIRD at under resonance mode and continuous current can be spread out and used for the over resonance mode and continuous current.

[1] Nikola P. Gradinarov is with the Faculty of Electronic Engineering, TU-Sofia, Ohridski 8, 1000, Sofia, Bulgaria,
E-mail: n_gradinarov@tu-sofia.bg

[2] Nikolay L. Hinov is with the Faculty of Electronic Engineering, TU-Sofia, Ohridski 8, 1000, Sofia, Bulgaria,
E-mail: hinov@tu-sofia.bg

[3] Tzvetan L. Marinov is with the Faculty of Electronic Engineering, TU-Sofia, Ohridski 8, 1000, Sofia, Bulgaria,
E-mail: tz_marinov@tu-sofia.bg

II. BASIC EQUATIONS

The schematic of the RIRD is shown at fig.1a, but at fig.1b the corresponding equivalent circuit. It is valid for the both examined modes, as the different initial conditions are affected by the corresponding polarities of their energy sources.

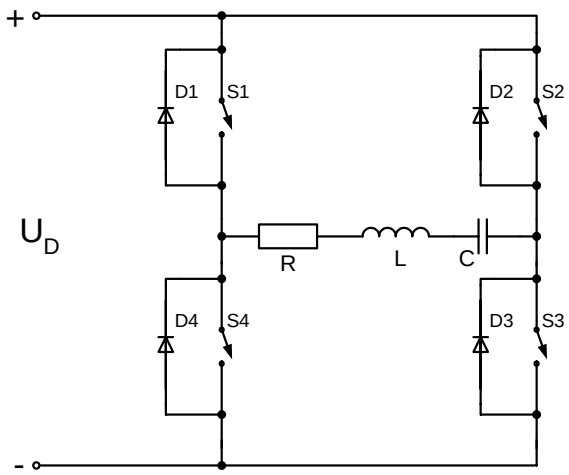

Fig.1a

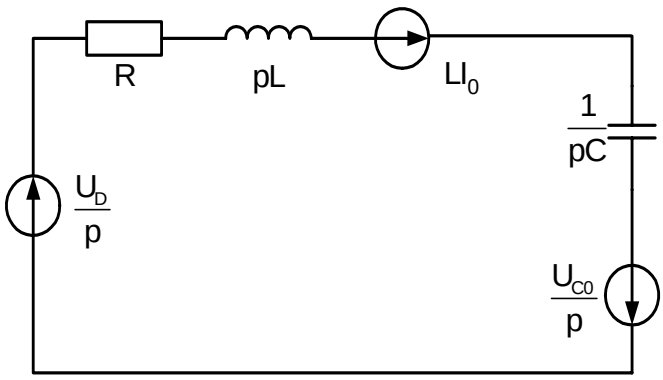

Fig.1b

The waveforms of the inverter voltage and the inverter current for the both cases are shown at fig.2 and fig.3. The analysis of the processes in established regime, operating at under resonance mode [1, 2] and the obtained by this analysis expressions for the inverter current and the voltage across the commutating capacitor follow:

$$i(\vartheta) = \frac{2k_{od}U_d}{\omega_0 L}\Upsilon e^{-\delta\frac{\vartheta}{\omega}}\sin\frac{\pi}{\lambda}(\vartheta+\psi), \qquad (1)$$

$$u_C(\vartheta) = U_d - 2k_{od}U_d \Xi e^{-\delta\frac{\vartheta}{\omega}} \sin\frac{\pi}{\lambda}(\vartheta+\varphi), \qquad (2)$$

where $\theta=\omega t$, ω - control (gate) frequency, $R=R_{(1)}$ is the equivalent load resistance, L and C are the equivalent commutating inductance and capacitance, U_d is the power supply DC voltage, $\omega_0 = \sqrt{\frac{1}{LC} - \delta^2}$ is the natural frequency of the serial resonant circuit, $\delta = \frac{R}{2L}$ is its attenuation coefficient, $\nu = \frac{\omega}{\omega_0}$ is frequency coefficient, $\lambda = \frac{\pi\omega}{\omega_0}$ - normalized to the control frequency angle of conduction of the controllable switches, $\Upsilon = \sqrt{\left(1 - a\frac{\delta}{\omega_0}\right)^2 + a^2}$, $\Xi = \sqrt{1 + \left(\frac{\delta}{\omega_0} - a - a\left(\frac{\delta}{\omega_0}\right)^2\right)^2}$, h and a are:

$$h = \frac{\frac{1}{\pi}\ln\left(\frac{k}{k-1}\right)\sin\frac{\pi}{\nu} + \cos\frac{\pi}{\nu} + \left(\frac{k-1}{k}\right)^{\frac{1}{\nu}}}{\left(\frac{k-1}{k}\right)^{\frac{1}{\nu}}\left(\frac{1}{\pi}\ln\left(\frac{k}{k-1}\right)\sin\frac{\pi}{\nu} - \cos\frac{\pi}{\nu}\right) - 1},$$

$$a = \frac{\sin\frac{\pi}{\nu}}{\frac{1}{\pi}\ln\left(\frac{k}{k-1}\right)\sin\frac{\pi}{\nu} - \cos\frac{\pi}{\nu} - \left(\frac{k}{k-1}\right)^{\frac{1}{\nu}}}.$$

The hesitation coefficient k has the appearance $k = \frac{1}{1 - e^{-\frac{\delta\pi}{\omega_0}}}$ and $k_{od} = \frac{1}{1 - h.\left(\frac{k-1}{k}\right)^{\frac{1}{\nu}}}$ is quantity which characterizes the serial RLC circuit, and it is called hesitation coefficient of the RIRD, operating at under resonance mode, but $\psi = \frac{\lambda}{\pi}\text{arctg}\frac{a}{1 - a\frac{\delta}{\omega_0}}$, $\varphi' = \frac{\lambda}{\pi}\text{arctg}\frac{1}{\frac{\delta}{\omega_0} - a - a\left(\frac{\delta}{\omega_0}\right)^2}$.

The average current, consumed from the DC power source is I_d is expressed by:

$$I_d = -\frac{4k_{od}\delta U_d}{\omega_0 R\pi F}\Upsilon\Delta, \text{ where} \qquad (3)$$

$$\Delta = e^{-\frac{\delta\pi}{\omega}}\sin\left(\frac{\pi}{\lambda}(\pi+\psi)+\alpha\right) - \sin\left(\frac{\pi}{\lambda}\psi + \alpha\right),$$

$$F = \sqrt{\left(\frac{\delta}{\omega}\right)^2 + \left(\frac{\pi}{\lambda}\right)^2} \text{ and } \alpha = \text{arctg}\left(\frac{\pi}{\lambda}/\frac{\delta}{\omega}\right).$$

The expressions for the average current through the switch I_{av} and I_{dav} through the diodes follow:

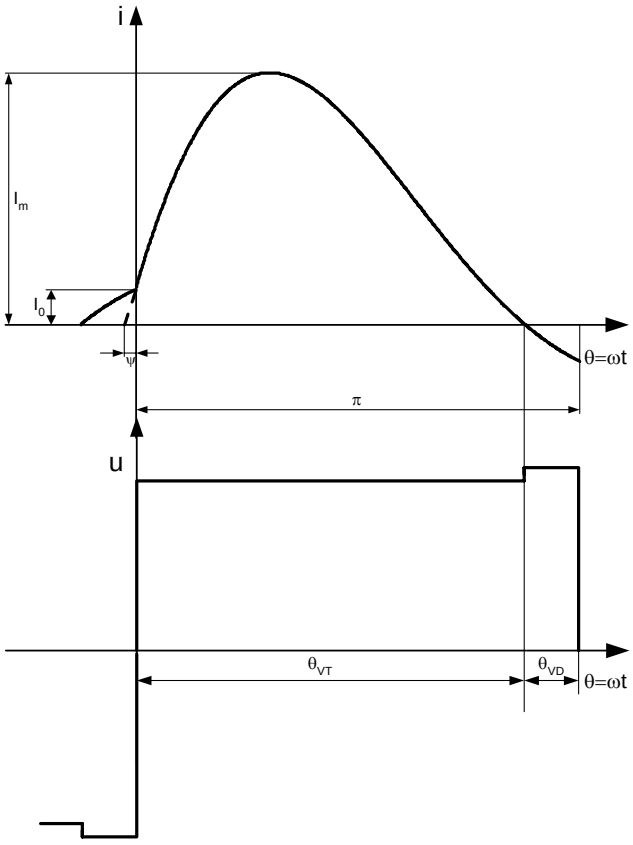

Fig.2

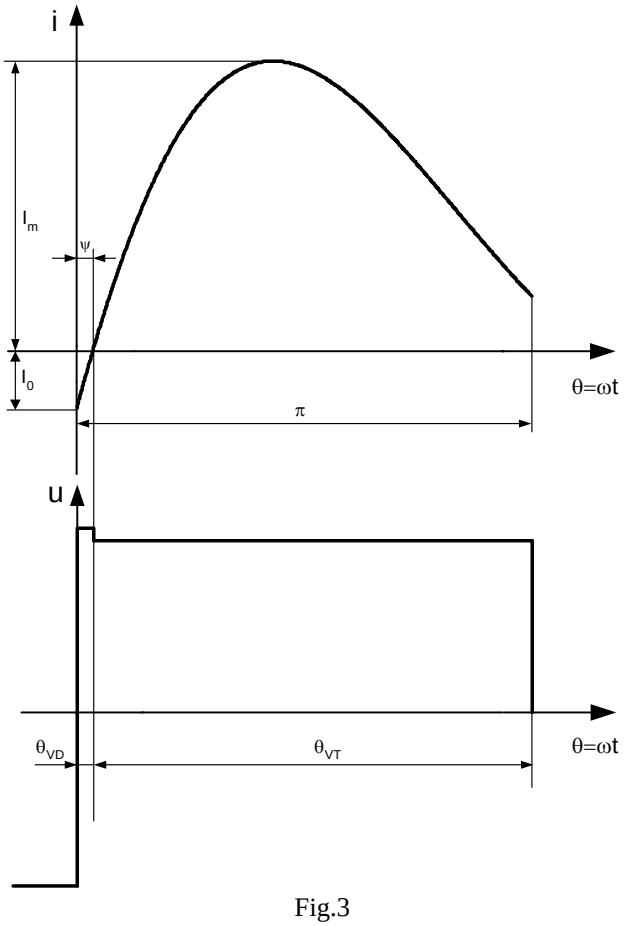

Fig.3

$$I_{av} = \frac{k_{od} U_d}{\omega_0 L \pi F} \Upsilon \left(e^{-\frac{\delta}{\omega}(\lambda - \psi)} \sin\alpha + \sin(\frac{\pi}{\lambda}\psi + \alpha) \right), \quad (4)$$

The average current through the diodes I_{dav} is determined by the expression:

$$I_{dav} = I_{av} - \frac{I_d}{2}. \quad (5)$$

For determination of the RMS value of the load voltage U it is used the equation for the balance of the active power at the input and the output, which has the following appearance at various type of load:

$$P_d = U_d I_d = UI = \frac{U^2}{R} \text{ - active load,} \quad (6)$$

$$P_d = U_d I_d = UI\cos\varphi_T = \frac{U^2}{R}\cos^2\varphi_T \text{ - active-inductive load,}$$

$$P_d = U_d I_d = UI\cos\gamma = \frac{U^2}{R_{(1)}}\cos^2\gamma \text{ - parallel compensated load,}$$

where I is the RMS value of the inverter current, $R_{(1)}$ is the resistance at the first harmonic of the inverter current when parallel compensated load, φ_T is the power factor of the active-inductive load, but γ is angle of displacement of the parallel compensated load circuit.

Finally the RMS value of the load voltage is:

$$U = \sqrt{U_d R I_d} \text{ - when active load,}$$

$$U = \frac{1}{\cos\varphi_T}\sqrt{U_d R I_d} \text{ - when active-inductive load,} \quad (7)$$

$$U = \frac{1}{\cos\gamma}\sqrt{U_d R I_d} \text{ - when parallel compensated load,}$$

where the quantity $I_d R$ is substituted with the determined by expression (3), which is function of the coefficient k and ν.

The rest of the quantities, required for the design are presented in [2].

The expressions for the inverter current and the voltage across commutating capacitor when RIRD operates at over resonance mode are determined in [3, 4, 5] and they are:

$$i(\theta) = \frac{2K_{odn} U_d}{\omega_0 L_k} \Upsilon_n e^{-\delta\frac{\theta}{\omega}} \sin\frac{\pi}{\lambda}(\theta - \psi_n), \quad (8)$$

$$u_C(\theta) = U_d - 2K_{odn} U_d \Xi_n e^{-\delta\frac{\theta}{\omega}} \sin\frac{\pi}{\lambda}(\theta + \varphi_n), \quad (9)$$

where $\Upsilon_n = \sqrt{\left(1 + a_n \frac{\delta}{\omega_0}\right)^2 + a_n^2}$,

$\Xi_n = \sqrt{1 + \left(\frac{\delta}{\omega_0} + a_n + a_n\left(\frac{\delta}{\omega_0}\right)^2\right)^2}$ and

$K_{odn} = \frac{1}{1 - h_n e^{\frac{-\delta\pi}{\omega}}} = \frac{1}{1 - h_n\left(\frac{k-1}{k}\right)^{\frac{1}{\nu}}}$ is quantity characterizing the serial RLC circuit, and it is called hesitation coefficient of RIRD, operating at over resonance mode, but h_n and a_n are :

$$h_n = \frac{\frac{1}{\pi}\ln\left(\frac{k}{k-1}\right)\sin\frac{\pi}{\nu} + \cos\frac{\pi}{\nu} + \left(\frac{k-1}{k}\right)^{\frac{1}{\nu}}}{\left(\frac{k-1}{k}\right)^{\frac{1}{\nu}}\left(\frac{1}{\pi}\ln\left(\frac{k}{k-1}\right)\sin\frac{\pi}{\nu} - \cos\frac{\pi}{\nu}\right) - 1},$$

$$a_n = \frac{\sin\frac{\pi}{\nu}}{\left(\frac{k}{k-1}\right)^{\frac{1}{\nu}} + \cos\frac{\pi}{\nu} - \frac{1}{\pi}\ln\left(\frac{k}{k-1}\right)\sin\frac{\pi}{\nu}}, \text{ but}$$

$$\psi_n = \frac{\lambda}{\pi}\operatorname{arctg}\frac{a_n}{1 + a_n\frac{\delta}{\omega_0}} \quad \text{and} \quad \varphi_n = \frac{\lambda}{\pi}\operatorname{arctg}\frac{1}{\frac{\delta}{\omega_0} + a_n + a_n\left(\frac{\delta}{\omega_0}\right)^2}$$

are the initial phase displacements of the inverter current and the voltage across the total commutating capacitor.

The consumed from the DC power supply current and the average values through the switches and the reverse diodes as function of the general parameters of the introduced in the analysis equivalent circuit of the AC circuit – the coefficients k and ν are:

$$I_d = -\frac{2K_{odn} U_d \Upsilon_n}{\pi\omega_0 L_k F}\Delta_n, \text{ where} \quad (10)$$

$$\Delta_n = e^{-\frac{\delta\pi}{\omega}}\sin\left(\alpha + \frac{\pi}{\lambda}(\pi - \psi_n)\right) - \sin\left(\alpha - \frac{\pi}{\lambda}\psi_n\right),$$

$$I_{av} = \frac{-K_{odn} U_d \Upsilon_n}{\pi\omega_0 L_k F}\left(e^{-\frac{\delta}{\omega}\pi}\sin\left(\alpha + \frac{\pi}{\lambda}(\pi - \psi_n)\right) - e^{-\frac{\delta}{\omega}\psi_n}\sin\alpha\right) \quad (11)$$

$$I_{dav} = I_{av} - \frac{I_d}{2}. \quad (12)$$

The RMS value of the load voltage is determined by the same expressions (7) just the same as at under resonance mode.

From the comparison of the expressions, which describe the currents and the voltages at the both modes it is seen that the generalized hesitation coefficients k_{od} and k_{odn} are quite equal, and the initial phase angles of the inverter current and the voltage across the equivalent commutating capacitor have equal magnitudes and different signs, which

express the different phase displacement between the inverter current and inverter voltage at the both modes. The same is valid for the coefficient “a”, which expresses the initial conditions of the inverter current related to the inverter voltage in both cases.

Then from expression (1) for the inverter current and the voltage across the commutating capacitor (2) at under frequency mode when substitute “Ψ”, “φ” and “a” respectively by “-Ψ”, “-φ” and “-a” the corresponding expressions at over resonance mode are obtained (8) and (9).

This gives us a reason to use the results from analysis of RIRD at under resonance mode as equal results to the analysis at over resonance mode. For this purpose it is required for all the expressions, describing the operation of RIRD and under resonance mode the frequency coefficient “ν” to be greater than unity, when over resonance mode is present.

To determine the average values of the currents through the switches and the diodes, could be used their expressions at under resonance mode (4) and (5), if the integral boundaries are substituted in accordance with fig.3.

III. CONCLUSION

This general look over the processes in the RIRD for the both modes and continuous current, allows the well known and spread results for under resonance mode to be used to evaluate the inverter behavior when the load or the gate frequency varies and of course for its design.

This generalization is useful even at methodical point of view when introducing with the RIRD operation, and to perform comparative analysis of the qualities of the power circuit at the both modes.

REFERENCES

[1] Gradinarov N., N. Hinov “Analysis and design of resonant inverter with reverse diodes”, Proceeding at fifth national scientific-practical conference with international participation “Electronics ‘96”. Symposium of scientific works, book 3, pp.185-190, 27-29 September, 1996, Sozopol.

[2] Gradinarov N., N. Hinov, “Analysis of resonant inverter with reverse diodes operating at complex load”. Symposium of scientific proceedings at sixth national scientific-practical conference with international participation “Electronic engineering – ET’97” 24-27 September 1997, Sozopol, pp.74-79.

[3] Gradinarov N., N. Hinov, “Analysis of serial resonant RLC inverters with reverse diodes, operating at over resonant frequency mode”, Proceedings of The seventh international conference “ELECTRONICS ‘98”, pp.177-182, 23-25 September, 1998, Sozopol.

[4] Hinov N., “Design of resonant inverters with reverse diodes, operating at over resonant frequency mode – part I”, Symposium of scientific proceedings of the National conference with international participation “Electonics’2002”, 17 - 18 October 2002, Sofia, 2002, pp.78-84.

[5] Hinov N., “Design of resonant inverters with reverse diodes, operating at over resonant frequency mode – part II”, Symposium of scientific proceedings of the National conference with international participation “Electonics’2002”, 17 - 18 October 2002, Sofia, 2002, pp.85-90.

[6] Bobtcheva M., N. Gradinarov and Co. Power electronics. TU-Sofia, 2001.

[7] Mohan N., Undeland T. E., Robbins W. Power electronics - Converters, Applications and Design. Second edition, John Wiley&Sons Inc, New York, 1995.

[8] Gradinarov N. P., “Research elaboration and development of resonant inverters with technical application” Doctorate Thesis. Technical University – Sofia, 2002.

Poster Session PO5:

EDUCATION QUALITY AND REMOTE ECOLOGICAL MONITORING

Studying on Digital Filters in MATLAB Environment

Veska M. Georgieva[1], Slavcho D. Lishkov[2], Dimiter C. Dimitrov[3] and Vanja D. Ivanova[4]

Abstract – **Digital filters are modeled as discrete-time linear systems. They can be used for many tasks: to separate signals and noise added during different processes, to separate signals into their constituent frequencies, to demodulate signals, to restore signals that have be degraded by some process, known or unknown . With help of the computer simulation it's made a trial in the paper to illustrate their basic characteristics and possibilities. It can be used by deeper studying the type of digital filters, their characteristics and their properties. The computer simulation is realized in MATLAB environment. The paper can be used in engineering education in studying on these systems.**

Keywords – **Digital filters, linear-time systems, noise separation, signal restoration, signal demodulation, computer simulation.**

I. INTRODUCTION

The digital filtration account for influence to the spectrum of the processing signals by definite computing algorithm. Choosing the best filter structure depends on the task the filter will perform. Some structures are more suited to or may be more computationally efficient for particular tasks. For example, often it is not possible to build recursive (IIR) filters to run at very high speeds and instead, we can use a nonrecursive (FIR) filter. FIR filters are always stable and have well-behaved round off noise characteristics.

The goal of filter design is to perform frequency dependent alteration of a data sequence. A very precise specification could ask to achieve the performance goals with the minimum filter order, or it could call for an arbitrary magnitude shape, or it might require an FIR filter. Filter design methods differ primarily in how performance is specified. There are 3 forms of realization: direct, cascade and parallel. In the practice often can be used cascade and removal cascade form [1]. The goal of the synthesis is to obtain a transfer characteristic and the respectively realization. This characteristic can be obtained by analogue low-pass filter prototype or by bilinear z -transform. The transfer characteristic can be achieved by polynomial approximation. Dependency from the type of the polynomial approximation, practically applications have following low- pass filter prototypes: Butterworth, Chebyshev Type I, Chebyshev Type II, and elliptic filters.

It's described in the paper a laboratory exercises for the undergraduate course on Signals and Systems of students from faculty of communications and from faculty of computer systems. The students can synthesize digital filters and analyze different filter responses such a magnitude response, phase response, impulse response and pole-zero plots on the base of definite filter coefficients. The filter they design is then computed using the default filter design method and filter order. They can investigate the change of the signal by filtration in time and frequency domain, too.

The computer simulation can be realized in the program environment of MATLAB with using the system for visual modelling SIMULINK and FDA TOOL.

II. PROBLEM FORMULATION

The problem on studying on digital filters can be presented with following features:

-There 4 type of filters: low-pass, high-pass, band-pass and rejector. They are described by the transfer characteristics, respectively by their coefficients. For the IIR filters is given in Eq.1[1].

$$H(z)=\frac{Y(z)}{X(z)}=\frac{a_0+a_1z^{-1}+...+a_Mz^{-M}}{1-[b_1z^{-1}+...+b_Nz^{-N}]}=$$

$$=\frac{\sum_{m=0}^{M}a_mz^{-m}}{1-\sum_{m=1}^{N}b_mz^{-m}} \quad (1)$$

The complex frequency coefficient can be obtained in Eq.2 from Eq.1 by the substitution $z=e^{jwT}$.

$$H(j\omega)=\frac{a_0+a_1e^{-j\omega T}+...+a_Me^{-j\omega T}}{1-[b_1e^{-j\omega T}+...+b_Ne^{-j\omega T}]}=$$

$$=\frac{\sum_{m=0}^{M}a_me^{-j\omega T}}{1-\sum_{m+1}^{N}b_me^{-j\omega T}} \quad (2)$$

The magnitude and phase responses are given in Eq.3 and Eq.4.

$$|H(j\omega)|=\sqrt{\frac{A^2+B^2}{C^2+D^2}} \quad (3)$$

$$\varphi(\omega)=arctg\frac{B}{A}-arctg\frac{D}{C} \quad (4)$$

[1]Veska M. Georgieva is with the Faculty of Communication, TU-Sofia, Kl.Ohridsky str.8, Sofia, Bulgaria, E-mail: vesg@tu-sofia.bg
[2]Slavcho D. Lishkov is with the Faculty of Communication, TU-Sofia, Kl.Ohridsky str.8, Sofia, Bulgaria.
[3]Dimiter C. Dimitrov is with the Faculty of Communication, TU-Sofia, Kl.Ohridsky str.8, Sofia, Bulgaria, E-mail: dcd@tu-sofia.bg
[4]Vanja D. Ivanova is with the Faculty of Communication, TU-Sofia, Kl.Ohridsky str.8, Sofia, Bulgaria.

where A and C are the real part of $H(j\omega)$, B and D are the imaginer part. The impulse response $h(n)$ can be obtained by Eq.5.

$$Y(n) = \sum_{m=-\infty}^{n} X(m)h(n-m) = \sum_{m=0}^{\infty} h(m)X(n-m) \tag{5}$$

By fulfillment of condition $h(n) = 0$ for $n < 0$, the recursive filter is causal. It is stable by the condition, given in Eq.6 [3].

$$\sum_{n=-\infty}^{\infty} |h(n)| < \infty \tag{6}$$

So on base of computer simulation we can formulate following problems:

1. To synthesize digital filters in the 4 types by the polynomial approximation of Butterworth, Chebyshev Type I, Chebyshev Type II, and elliptic filters.
2. To choose the best filter design method and filter order.
3. To analyze a magnitude response, phase response, impulse response and pole-zero plots of the synthesized digital filters.
4. To investigate the change of different signals by filtration in time and frequency domain, too.

By the simulation we need to see the going processes. The characteristics can be given in graphical mode.

III. EXPERIMENTAL PART

The formulated problems are solved by computer simulation in MATLAB, version 6.5 with using the Filter Design & Analysis (FDA) TOOL and SIMULINK TOOLBOX. FDA TOOL is a powerful user interface for designing and analyzing filters. It enables the students to quickly design digital FIR or IIR filters by setting filter performance specifications, by importing filters from MATLAB workspace, or by directly specifying filter coefficients [2]. FDA TOOL also provides tools for analyzing filters, such as magnitude and phase and impulse response plots and pole-zero plots. It can be shown the best form of realization. The students can change only one or some parameters. In this case FDA TOOL can design the filter with the determinate parameters and compatibility optimized characteristics. It can be choose the filter transform, the type of the filter and the frequency, too. There are the following options:

- Type of the filter by ‚Response Type'
- IIR or FIR filters and the method of approximation by 'Design Method'
- Filter order
- Frequency specifications
- Magnitude specifications
- Form structure and coefficients by 'Filter Coefficients'
- Filter transform by 'Frequency Transformations'

On the other side, models can be created by the students without experience in using of the other programming tools. It's may be a great priority, because visual presentation of the fulfillment simulation can be realized. So the students can create a model to filtration of different signals. It's possible to simulate the process and to investigate the change of the signals by the intuitive easy graphical interface of SIMULINK.

The running time can be set in constant or variable step. The students can observe a running process by the block 'Scope', which is included in the model, too. They can analyze the signal spectrum by the block PSD. The realized model of filtration is given on Fig. 1.

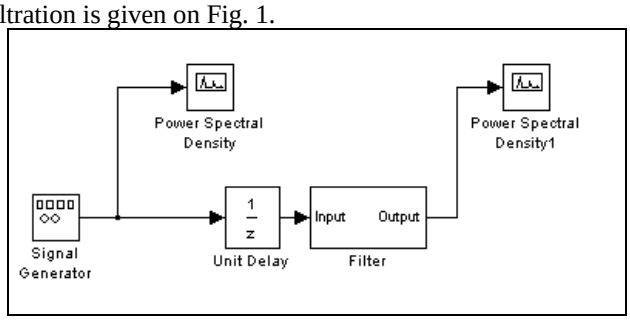

Fig.1. A model of filtration in SIMULINK

The Magnitude response, Phase response, Impulse response and Pole/Zero Plot for low-pass filter with f_s =8000 Hz, f_p =1600 Hz, f_c =2000 Hz, $A_{\min}$ =40 dB, $A_{\max}$ =1 dB by polynomial approximation of Butterworth, Direct Form II, order 17, stable is given on Fig.2.

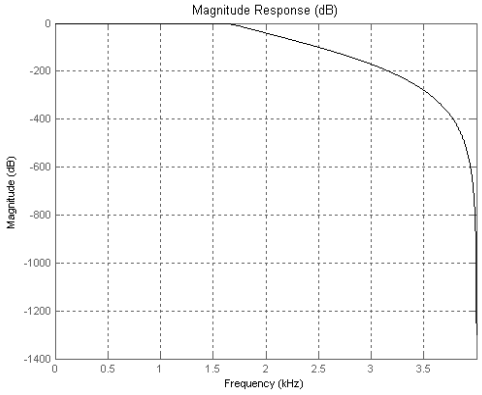

Fig.2a. Magnitude response

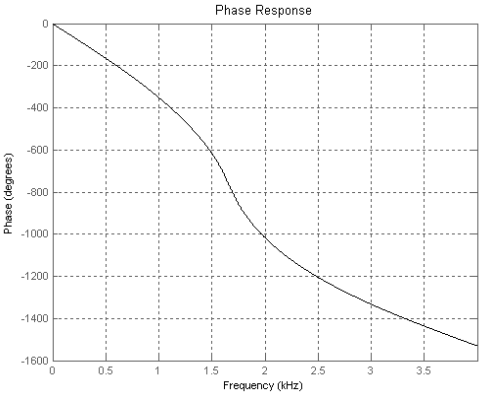

Fig.2b. Phase response

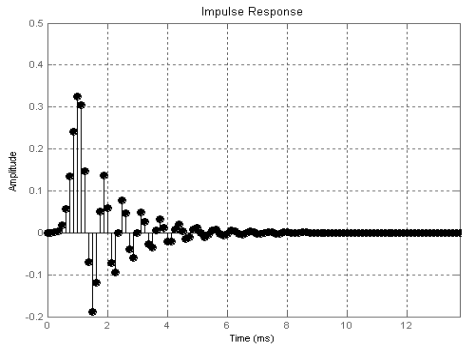

Fig.2c. Impulse response

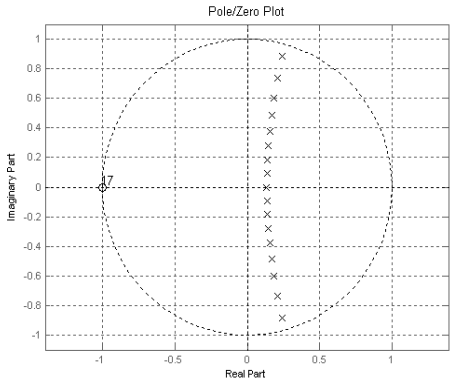

Fig.2d. Pole/Zero Plot

On Fig.3 we can see the change of the signal form and its spectrum by the same filter.

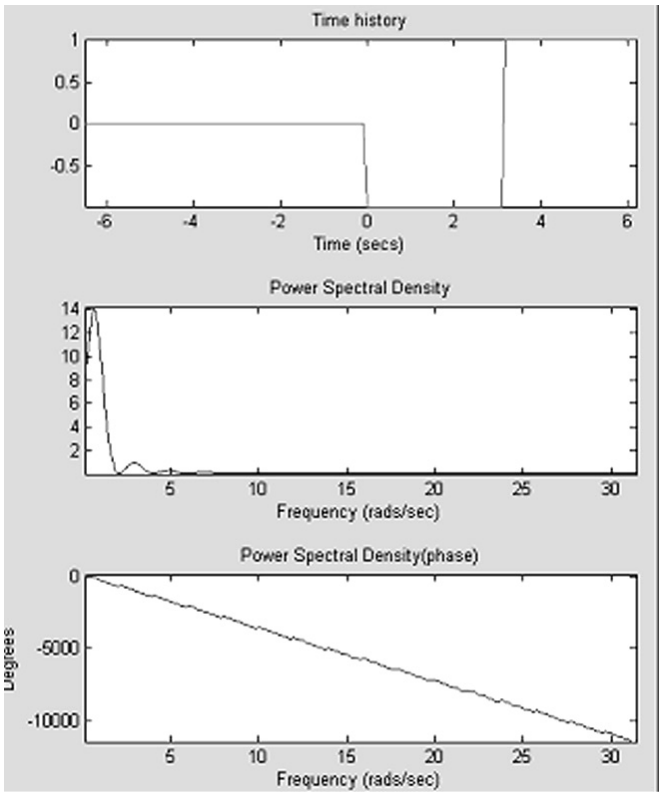

Fig.3a. Input signal

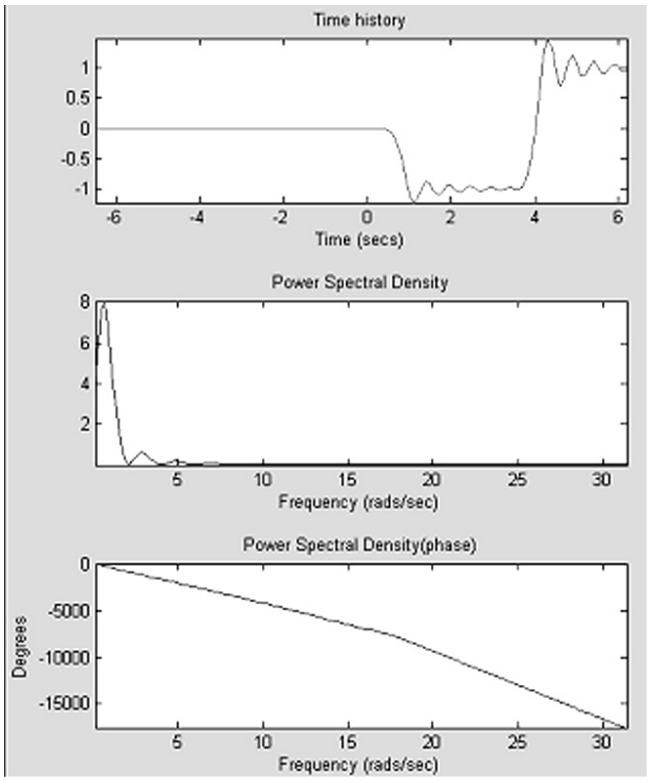

Fig.3b. Output signal

IV. CONCLUSION

The studying of digital filters is one of the very important problems in the theory of the signals. It's made a trial in the paper to present the possibility of the computer simulation in MATLAB environment to get deeper insight on the syntheses of digital filters and analyzes of different filter responses such a magnitude response, phase response, impulse response and pole-zero plots on the base of definite filter coefficients. The filter they design is then computed using the default filter design method and filter order. By help of simulation they can investigate the influence of the filtration on the signal form and its spectrum. The method can be developed and the described exercise can be used for web based distance education.

REFERENCES

[1] Иванов Р., "Цифрова обработка на едномерни сигнали", Габрово, Almamater International,1999

[2] MATLAB 6.5, User's Guide, www.mathwork.com

[3] Фердинандов Е. "Сигнали и системи", "Сиела", София, 1999.

Spectrum Signal Analysis in MATLAB Environment

Veska M. Georgieva[1], Slavcho D. Lishkov[2], Dimiter C. Dimitrov[3]

Abstract – **The spectrum signal analysis is very important in communication. Its basic application is the signal processing, such as filtration, detection and identifying of the different signals on the noise background, bandwidth limitation in the channel. With help of the computer simulation it's made a trial in the paper to illustrate this process by different signals. It can be used by deeper studying the type of spectral characteristics and their properties. The computer simulation is realized in MATLAB environment. The paper can be used in engineering education in studying this process.**

Keywords – **Communication, signal processing, spectrum analyses, detection and identifying of signals,, computer simulation.**

I. INTRODUCTION

The signal analysis in the time domain is not always sufficient. In many practical cases is necessary the complex signal analyses. This includes obligatory analyses in the frequency domain. The goal of spectral estimation is to describe the distribution (over frequency) of the power contained in a signal, based on a finite set of data. The various methods of spectrum estimation available in the signal processing can be categorized as follows: nonparametric methods, parametric methods, subspace methods. Nonparametric methods are those, in which the estimate of the PSD (Power Spectral Density) is made directly from the signal itself [1]. Parametric methods can yield higher resolutions than nonparametric methods in cases, when the signal length is short. These methods use a different approach to spectral estimation; instead of trying to estimate the PSD directly from the data, they model the data as the output of a linear system driven by white noise, and then attempt to estimate the parameters of that linear system. The most commonly used linear system model is the all-pole model, a filter with all of its zeroes at the origin in the z-plane. The output of such a filter for white noise input is an autoregressive (AR) process. For this reason, these methods are sometimes referred to as AR methods of spectral estimation [1].

Subspace methods, also known as high-resolution methods or super-resolution methods, generate frequency component estimates for a signal based on an eigenanalysis or eigendecomposition of the correlation matrix [1].

The most popular are the nonparametric methods. Their priorities over the others are: good computing efficiency (based on FFT) and the spectra estimation is proportional to the power of the input signal harmonic components. The failings are: the frequency resolution is dependent from the size of the segment and not from the type of the input signal; there is 'dilute' of the spectral maximums and this method can be used to not numerous input discrete. But they can be successful used by many signals.

At the university level, the material studied becomes more abstract and more mathematical. The students need to become a deeper insight of the practical application of the most popular methods. It's described in the paper a laboratory exercises for the undergraduate course on Signals and Systems of students from faculty of communications and from faculty of computer systems.

The computer simulation can be realized in the program environment of MATLAB with using the system for visual modelling SIMULINK. In this case, the spectrum analysis is based on the nonparametric methods.

II. PROBLEM FORMULATION

The problem on spectrum signal analysis can be presented with following features:

- There 2 type of signals: analogue and discrete (periodic and aperiodic) signals. The signals can have different forms such as rectangular, triangular, saw-tooth, exponential, Gaussian, arbitrarily. Their parameters can be determinate by the students.

- Let $S(t)$ is an aperiodic analogue signal, it has the following CFT, given in Eq.1 [3]:

$$G(\omega) = \int_{-\infty}^{\infty} S(t) e^{-j\omega t} dt \qquad (1)$$

where $G(\omega)$ is the Fourier Spectral Density. In general case, it's a complex function, described with Eq.2[3].

$$G(\omega) = \mathrm{Re}[G(\omega)] + j\,\mathrm{Im}[G(\omega)] = |G(\omega)| e^{j\varphi(\omega)} \qquad (2)$$

where $|G(\omega)|$ is the Amplitude Fourier Spectrum, $\varphi(\omega)$ is Phase Fourier Spectrum and $|G(\omega)|^2$ is the Power spectrum of the signal $S(t)$.

In case of the discrete signal $S(n\Delta t)$, DFT must be used, given in Eq.3 [3].

[1]Veska M. Georgieva is with the Faculty of Communication, TU-Sofia, Kl.Ohridsky str.8, Sofia, Bulgaria, E-mail: vesg@tu-sofia.bg
[2]Slavcho D. Lishkov is with the Faculty of Communication, TU-Sofia, Kl.Ohridsky str.8, Sofia, Bulgaria.
[3]Dimiter C. Dimitrov is with the Faculty of Communication, TU-Sofia, Kl.Ohridsky str.8, Sofia, Bulgaria, E-mail: dcd@tu-sofia.bg

$$G[k]=\sum_{n}^{N-1} S[n]e^{\frac{j2\pi nk}{N}}, k\in[-N/2, N/2-1] \quad (3)$$

and $|G(k)|^2$ is the discrete Power Spectrum.

So on base of computer simulation we can formulate following problems:

1. To create a model, which can be used by generating of different signals and estimating its spectrum
2. To analyze the properties of the spectrum functions by the definite signals
3. To investigate the influence of the signal form on the spectrum

By the simulation we need to see the going processes. The characteristics can be given in graphical mode.

III. EXPERIMENTAL PART

The formulated problems are solved by computer simulation in MATLAB, version 6.5 environment with using the SIMULINK TOOLBOX.

This can provide direct access to the basic possibilities of the program environment. On the other side, models can be created by the students without experience in using of the other programming tools. It's may be a great priority, because visual presentation of the fulfillment simulation can be realized. SIMULINK possesses an intuitive easy graphical interface. This method gives better results, it's precisely and we can see the computed functions direct in graphical mode. For a model creating are used direct the existing in SIMULINK blocks for PSD [2].

To generate the analogue signals with different forms such as rectangular, triangular, saw-tooth, exponential and Gaussian, the students can use the following blocks: 'Ramp', 'Step', 'Repeating Sequence', 'Fcn', 'MATLAB Function', 'Product', 'Pulse Generator'. By giving parts of the periodic triangular, saw-tooth and sinusoidal signals, can be separated only parts of them, for example for one half of period. This can be made by multiplication with suitable tuning of "Pulse Generator" on amplitude.

The exponential and Gaussian signals can be generated in 2 ways: First as detached program, this can be m-file, kept in MATLAB work environment. It can by used by control of the block 'MATLAB Function'. The priority in this case is that the time intervals for the signal changes can be given beforehand. The second way is by description of the signal in block 'Fcn'. The signal is not limited in this case and can be made by block "Ramp". The second way is better of two reasons:

- 'Fcn' works rusher than 'MATLAB Function'
- Signal parameters can be changed easier with the goal to investigate their influence to the spectrum

The running time can be set in constant or variable step. The students can observe a running process by the block 'Scope', which is included in the model, too.

An example for a simulated model is given in Fig.1. It's generated a following signal, given in Eq.4 :

$$S(t)=\begin{cases}\frac{2a}{T}t+a, -T/2\le t\le 0\\ -\frac{2a}{T}t+a, 0\le t\le T/2\end{cases} \quad (4)$$

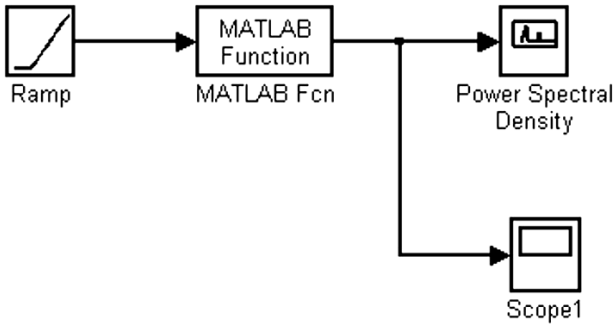

Fig.1. Signal generating model

In Fig.2 we can see the signal in the time and frequency domain, too.

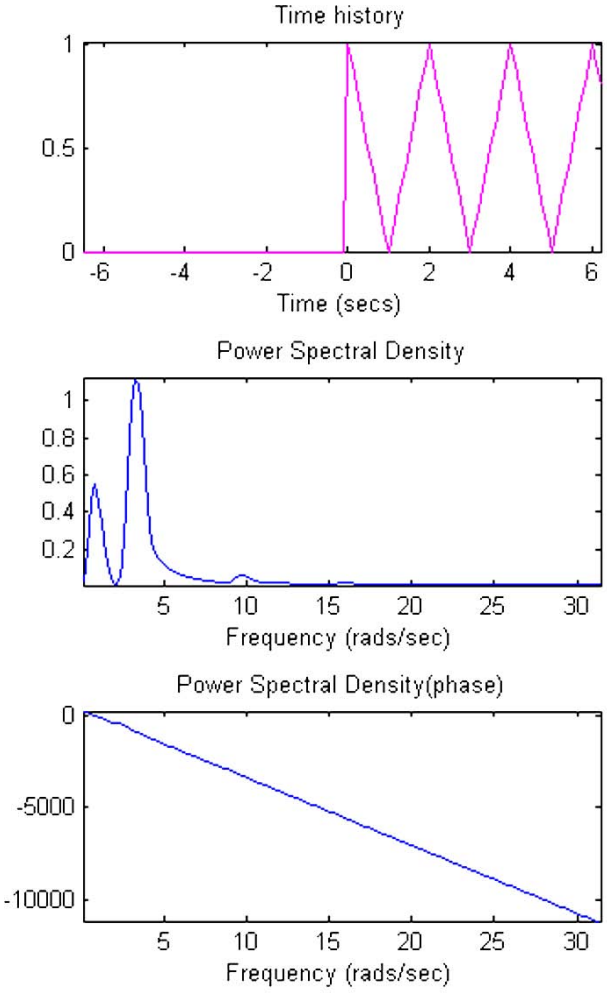

Fig.2. Generated signal

By using of blocks 'Derivative' and 'Integrator' it's made possible to investigate their influence to the spectrum of the signal, given in Fig. 3 and Fig.4

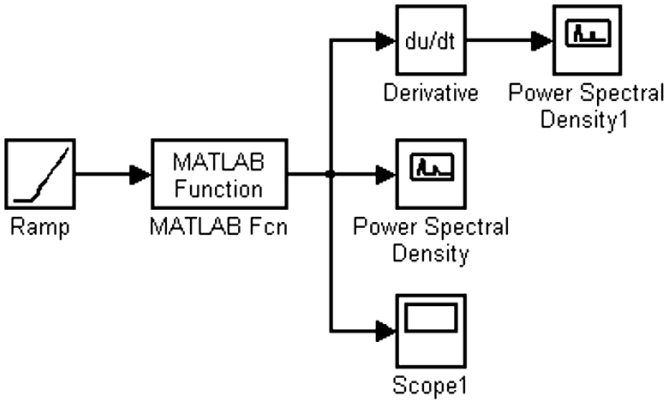

Fig.3. Model for spectrum analysis of integrated signal

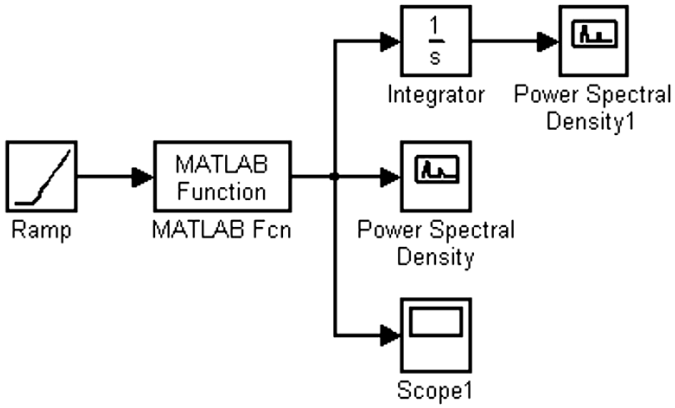

Fig.4. Model for spectrum analysis of derivative signal

IV. Conclusion

The spectrum signal analysis is one of the very important problems in the theory of the signals. It's made a trial in the paper to present the possibility of the computer simulation in MATLAB environment to get deeper insight on studying the spectral functions, their properties in case of analogue and discrete signals. The students can create models to generate different signals and to change their parameters. They can also generate models to compute the spectral functions. So with the help of simulation they can investigate the influence of the signal parameters on the PSD. The method can be developed and the described exercise can be used for web based distance education.

References

[1] Ingle Vinay K. & Proakis John G., Digital Signal Processing Using MATLAB, Brooks/Cole Publishing Company, 2000

[2] MATLAB 6.5, User's Guide, www.mathwork.com

[3] Фердинандов Е. "Сигнали и системи", "Сиела", София, 1999

Correlation Signal Analysis in MATLAB Environment

Veska M. Georgieva[1], Dimiter C. Dimitrov[2], Slavcho D. Lishkov[3]

Abstract – **The correlation signal analysis is applicable by detection and identifying of the different signals on the noise background as well as by the accident processes. This is one of the very important problems in the theory of the signals. It's made a trial in the paper to present the possibility of the computer simulation in MATLAB environment by deeper studying the type of correlation functions, their properties and relation with the power spectral density in case of analogue and digital signals. The paper can be used in engineering education in studying this process.**

Keywords – **Correlation functions, detection and identifying of signals, accident processes, power spectral density, computer simulation.**

I. INTRODUCTION

At the university level, the material studied becomes more abstract and more mathematical. It's described in the paper a laboratory exercises for the course on Signals and Systems of students from faculty of communications and from faculty of computer systems.

The correlation signal analysis can present the change of the signals in time domain without their spectrum. On the base of theory of correlation signal analysis, with help of computer simulation, the students get deeper insight of the auto correlation and cross correlation. They can investigate their properties and their relation with power spectral density of the signals.

The computer simulation can be realized in the program environment of MATLAB with using the system for visual modelling SIMULINK. A model can be created, which generate the analysed signals and functions. There are 2 methods to create a model in SIMULINK. First it's can be used mathematical formulae for creating building blocks, which computed the correlation functions and second by direct using of blocks for auto correlation and cross correlation. By generation in case of analogue signals can be used functions from SIMULINK, as well as functions from files in MATLAB [1]. A program can be made in case of digital signals, so the signals can be choose from the user.

II. PROBLEM FORMULATION

The problem on the correlation signal analysis can be presented with following features:

- There are 2 types of signal - analogue and digital (periodic and aperiodic). The analogue signals can have different forms such as rectangular, triangular, saw-tooth, exponential, Gaussian. Their parameters can be determinate by the students. Digital signals and their parameters can be determinate totally from the students.

- Two types of correlation functions can be investigated – auto correlation and cross correlation. Their mathematical description is given in Eq.1, respectively in Eq.2 [3].

$$\Psi(\tau) = \lim_{T\to 0} \frac{1}{T} \int_{-\frac{T}{2}}^{\frac{T}{2}} S(t)S(t-\tau)dt \qquad (1)$$

$$\Psi_{12}(\tau) = \lim_{T\to 0} \frac{1}{T} \int_{-\frac{1}{T}}^{\frac{1}{T}} S_1(t)S_2(t-\tau)dt \qquad (2)$$

where $S(t), S_1(t), S_2(t)$ are the represented signals and τ is a time delay.

- Following properties of the correlations function can be investigated – even, periodic, max value, one to one correspondence to signals.

- The relation of the functions with the power spectral density can be investigated. Its mathematical description is given in Eq.3 and in Eq.4 [3].

$$\Psi(\tau) = \frac{1}{2\pi} \int \left| S(j\omega) \right|^2 e^{j\omega\tau} d\omega \qquad (3)$$

$$\left|S(j\omega)\right|^2 = \int_{-\infty}^{\infty} \Psi(\tau) e^{-j\omega\tau} d\tau \qquad (4)$$

where $\left|S(j\omega)^2\right|$ is the power spectral density of the analyzed signal.

So on base of computer simulation we can formulate following problems:

1. To create a model of the generated signals and correlation functions.
2. To analyze the properties of the correlation functions by the definite signals.
3. To investigate the influence of the spectrum band width on the correlations function.
4. To analyze the influence of the amplitude spectral density of the different signals on the correlation functions.

By the simulation we need to see the going processes. The characteristics can be given in digital and graphical mode.

[1]Veska M. Georgieva is with the Faculty of Communication, TU-Sofia, Kl.Ohridsky str.8, Sofia, Bulgaria, E-mail: vesg@tu-sofia.bg
[2]Dimiter C. Dimitrov is with the Faculty of Communication, TU-Sofia, Kl.Ohridsky str.8, Sofia, Bulgaria, E-mail: dcd@tu-sofia.bg
[3]Slavcho D. Lishkov is with the Faculty of Communication, TU-Sofia, Kl.Ohridsky str.8, Sofia, Bulgaria.

III. EXPERIMENTAL PART

The formulated problems are solved by computer simulation in MATLAB, version 6.5 environment with using the SIMULINK TOOLBOX.

For a model creating are used direct the existing in SIMULINK blocks for auto correlation and cross correlation [2]. This method gives better results, it's precisely and we can see the computed functions direct in graphical mode, too.

To generate the analogue signals with different forms such as rectangular, triangular, saw-tooth, exponential and Gaussian, the students can use the following blocks: 'Ramp', 'Step', 'Repeating Sequence', 'Fcn', 'MATLAB Function', 'Product', 'Pulse Generator'. The using blocks can be connected in the model informative and by the control, too. The type of the connection is dependent on the block and on the logic of his work. The exchanging data can be described in scalar, vectors and matrices. The running time can be set in constant or variable step. The students can observe a running process by the block 'Scope', which is included in the model, too. An example for a simulated model is given in Fig.1. It's generated a signal with Gaussian form and also computed its correlation function.

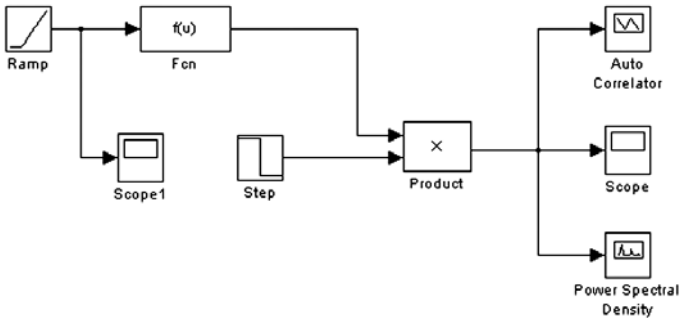

Fig.1 Model for autocorrelation with Gaussian signal

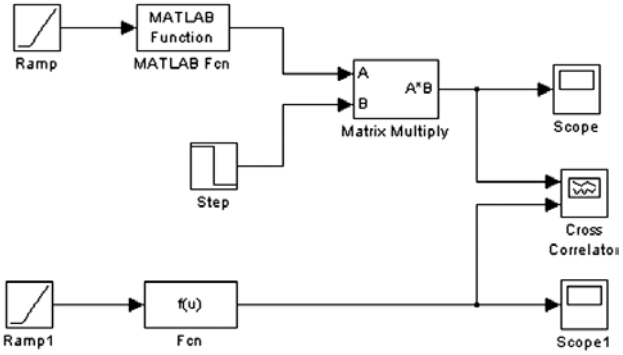

Fig.2 Model for cross correlation with Gaussian and exponential signal

The other example for a model of computing a cross correlation of signals with Gaussian and exponential form is given in Fig.2.

Fig.3 presents in graphical mode the signal and its power spectral density. The investigated signal has a Gaussian form with amplitude 3V and continue time 3 s.

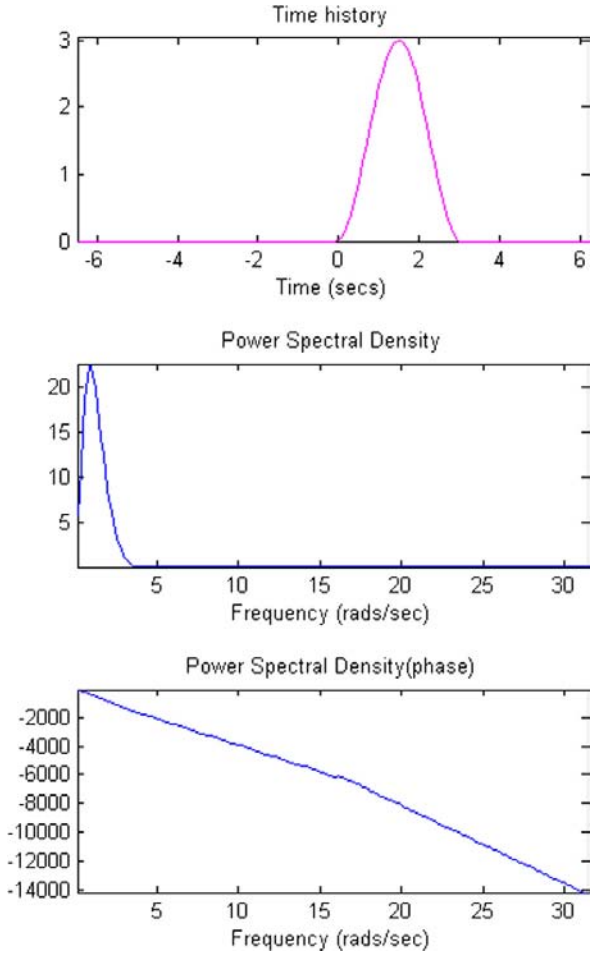

Fig.3. Power Spectral Density of the Gaussian signal

The exactly program is used for generation of digital signals and computing of the auto correlation and cross correlation. Its algorithm make possible to be choose the signal (as combination of "0" and "1"), its length (8, 16, 32 bits) and the type of correlation, too.

IV. CONCLUSION

The correlation signal analysis is one of the very important problems in the theory of the signals. It's made a trial in the paper to present the possibility of the computer simulation in MATLAB environment to get deeper insight on studying the type of correlation functions, their properties and relation with the power spectral density in case of analogue and digital signals. The students can create models to generate different signals and to change their parameters. They can also generate models to compute the correlation functions. So with the help of simulation they can investigate the influence of the signal parameters on the correlation and observe the running processes.

REFERENCES

[1] Ingle Vinay K. & Proakis John G., Digital Signal Processing Using MATLAB, Brooks/Cole Publishing Company, 2000

[2] MATLAB 6.5, User's Guide, www.mathwork.com

[3] Димитров Д., Каменов Ц., Костадинова В., "Ръководство за лабораторни упражнения по сигнали и системи", "Нови знания", София, 2001

An Optimization of the Weeks' Distribution of the Subjects' Horariums.

Mariya I. Eremieva[1]

Abstract – **The article discusses the optimum distribution of the subjects' horariums during each of the term weeks of the university. The paper suggests an algorithm for defining the schedule of dividing the horariums of each school subject by the weeks of the term. In order to create the schedule, it is necessary to have the following information: the school programs, the number and the different kind of the streams for each course as well as the limit of the possible weekly horarium.**

Keywords - **time table, exact methods, distribution, weeks' horariums of the study subjects.**

I. INTRODUCTION.

In the beginning of the XXI century there are two fundamental trends that emerge clearly in the educational sphere:

1) The importance of the education continuously increases and becomes a dominating factor in the modern civilization. The system of traditional education is being replaced by the technologies of the innovated education witch apart from being orientated towards modern material and information resources, are also directed towards the creation of abilities in the students to prognosticate and reorganize the development of the future.

2) The competition and the rivalry present in the global world are more and more taking place in the national educational programs as well. There is a new competition among the educational institutions to attract students by offering them higher quality educational services and better perspectives for realization.

II. OPTIMISATION OF THE STUDY PROCESS ORGANIZATION.

These two trends define the new challenge facing the development of the world's higher education. One of these trends is the introduction of degrees into the education. The approved, during the 29 session of the General conference of UNESCO in November 1997, International classification of the standards of the education, (ISCED) initiated multi-degree structure of the whole educational system [1].

In ISCED, the term education is interpreted as to include all intentional and systematic activities, which are supposed to cover the needs of knowledge. In some countries these needs are described as cultural activities and education. According to ISCED the education must be interpreted as organized and continuous communication, intended to bring knowledge. In ISCED, an elaborate interpretation is made of the main categories in this definition:

1. The communication is a connection between two or more persons, involved in exchanging information (messages, ideas, knowledge, strategies and so on). The communication can be verbal and non-verbal, direct (face to face) or non-direct (remote). It can use large variety of channels and media.
2. Studying is every improvement in the behavior, information, knowledge, understanding, and way of thinking or skills.
3. The organized communication means that it is planned according to a sequence with explicit and implicit aims. It includes security agency (person or organization) which provides education and the methods of educating, through which .the communication is realized
4. Continuous category means, that education has elements of infinity and continuity. There are no conditions for minimum duration, but this minimum is defined in operative documents. Under the conditions of mass education the scientific organization and the optimization of planning of the school process are of great importance. The main principles of planning are:

- Connection between theory and practice. The studied subjects must have the opportunity to be practiced.
- Harmonizing of the volume of the study information with the study time of the students.
- Taking into account the time order inter and inner subject connections.

Therefore, by these principles, decisions are taken about the developing of the structure-logical scheme (SLS) for every school subject. SLC shows the objectives of the subject and its connection to previous and next subjects in the school plan of the defined subject.

To form an optimal organization it is needed to be paid careful attention to the planning of the school process, which is connected with the creation a timetable of the school subjects. The quality of the timetable shows the level of the organization of the school process. Very important part of creating the timetable is the school plan. There are two kinds of school plans:

1. For every school year each subject gets a horarium, needed for its through study, which must be multiplied by the number of the school weeks in the term.
2. The horarium, needed for studying each subject is defined by required volume of the information in it.

Therefore, there are two ways of creating a timetable of the subjects. The first is by using "typical week", the timetable is created for the first, or for both: the first and the second week, from the term and after this, it is repeated for all the rest. In

[1] Mariya I. Eremieva is with the Naval Academy , 9000 Varna, Bulgaria, E-mail: eremievam@abv.bg

TABLE 1
INPUT DATA FOR THE SCHEDULE

subject	code of the spec.	Courses number	Kind of the class	continuance	Halls' code	Teachers' code	Kind of halls	Number of the week
Math. analysis	1	1	1	2	2501	-	Hall	1
Math. analysis	1	1	2	2	2501	-	Hall	1
Math. analysis	1	1	3	2	-	2507	classroom	1
Informat - DB	1	1	1	2	2505	-	Hall	1
Informat - DB	1	1	2	2		2506	laboratory	1
Sum data	1	1		10	6	4		1

the second way before creating a timetable, it is necessary to create a special document "schedule of dividing the horariums for subject" for the weeks of the term. It is necessary to keep the sequence of the classes according to the school plan for the subject and for the different studied subjects for the specified specialty. The advantage of the first way is the short technical work for creating the timetable for "typical" week and its duplication. Its disadvantages are:

1. the different subjects according to their defined time study , which is multiplied to the number of the weeks, are in inequality positions;
2. the defined for the "first" week sequence of lecturer and practice classes is not optimal for the remaining weeks of the term;
3. the connection among the classes of one subject and among the different subjects is damaged..

The second way – creating a time table for every week – escapes from these disadvantages, but it is a very continued process and it is needed high qualified work of plan-making specialists.

In the military academies taking into account the specificity of education, which is in accordance with the inclusion of study and outside study classes, requirements are formed, to which each time-table of the subjects should accord.

III. AN ALGORITHM FOR THE DISTRIBUTION THE HORAROUM.

This paper suggests an algorithm for defining the schedule of dividing the horariums for each school subject by the weeks of the term. For creating the schedule it is necessary to have the following information: the school programs, suggested by the different departments, the distribution of courses and specialties, the number and the different kinds of streams for every course, the limit of the possible weekly horarium. For every school subject is known the horariums, kind of subjects, the sequence of their realization, the needed halls and suggested teachers. There is separate schedule created for each course and specialty.

Whether this schedule is with high quality is determined by analyzing the number of the characteristics of the school subjects: number of classes, exercises, total summary of the classes.The schedule is in TABLE 1. Following this information it is estimated:

1. the distribution of the week horarium of the subjects for the different kinds of classes: lections, laboratories, exercises;
2. the connection between the subjects of the specified specialty;;
3. whether the weeks' horarium is regular or irregular for all the term.
4. whether the total summary of the classes for every specialty is in the previous defined limits – 30..40; These limits are defined by the academic council .for each university.

It is suggested to be assigned link codes between the subjects for improving the quality of the created schedules. If the studied material on one subject is a base for other subject, the first receives a priority **1**, and the second – **2**..

Till now in the most universities, specialists –plan – makers create the schedules. In this paper is suggested an algorithm, based only on "exact" methods for distributing the horarium for each subject of the term.

On Fig. 1 is shown the algorithm of creating the weeks' horariums. Because of the specificity of education in the military academies the start or the end of the term is at different time for each course and specialties. In the variable "***brw***" is used the maximum number of school weeks, which includes the period since the first date of the term till the last date of the term for all study units. If ***i*** –is the number of the course, ***j*** – the number of the speciality and ***k*** – the number of the school weeks of the term, then the count of the school days for all weeks for all courses and specialities is written and stored in the three-dimensional matrix ***Week[i,j,k].*** The two-dimensional matrix ***Studydays[i,j]*** shows the total count of school days for the term for each course and specialty. From this total count are deduced the interruptions during the term, needed to get the real value only of the study days. In ***Hor[I,j,l]*** is entered the horarium for each subject for ***i*** course and ***j*** specialty. With Eq. 1 is decided the horarium for the "**k**" week of the term.

$$horweek[ijkl] = \frac{hor[ijl].week[ijk]}{studydays[ij]}., \qquad (1)$$

In two variables ***cjalo*** and ***ost***, (Eq. 2 and Eq. 3) are stored the fractional and the whole part for each subject's horarium.

$$cjalo = \text{int}\,eger(horweek[ijkl]), \quad (2)$$

$$ost = horweek[ijkl] - cjalo. \quad (3)$$

If the rest is less than 1, for this week, there is a week's horarium for this subject, which is equal to the variable ***cjalo***. If the rest is bigger than 1, these actions are taking place:

$$\begin{aligned} horws &= horws + cjalo, \\ osts &= osts + ost, \end{aligned} \quad (4)$$

In the ***horws*** *(Eq. 4)* are summed the weeks' horariums for each subject. Here is the difference between ***limbeg*** (the start possible value of the week's horarium for each course and speciality) and the equaled week's horarium -***horws***. When ***horws*** is between ***limbeg*** and ***limend***, the process of distribution for the week is finished.

With the suggested algorithm for defining the weeks' horarium for the subjects is achieved regular distribution of the total horarium for the subjects for the weeks, and this algorithm escapes from the possibility for overloading some subject or for non – distributed classes.

IV. CONCLUSIONS

1. Creating the SLC of the preparation of the future specialists on the base of SLS of all studied subjects allows the school process contents to be optimized.
2. Coordinating the quantity of the studied information with the available time of the students gives the opportunity to be defined the optimal time, needed for studying each subject.
3. Realizing .the principle of sequence and the connection between the school subjects finishes with the creating of a program and an optimal time table of the classes during the term
4. Defining the main principles of planning allows the defining of an optimal weekly horarium for every subject according to the school plan.
5. For defining the weeks' horariums of the subjects are used only "***exact***" methods.

REFERENCES

[1] International Standard Classification of Education ISCED1997.UNESCO. November 1997.

[2] Основы научной организации труда в ВВУЗАХ, Москва, 1984

[3] Использование ЭБМ в организации и планировании учебного процеса, "Высшая школа" Москва,1982

.

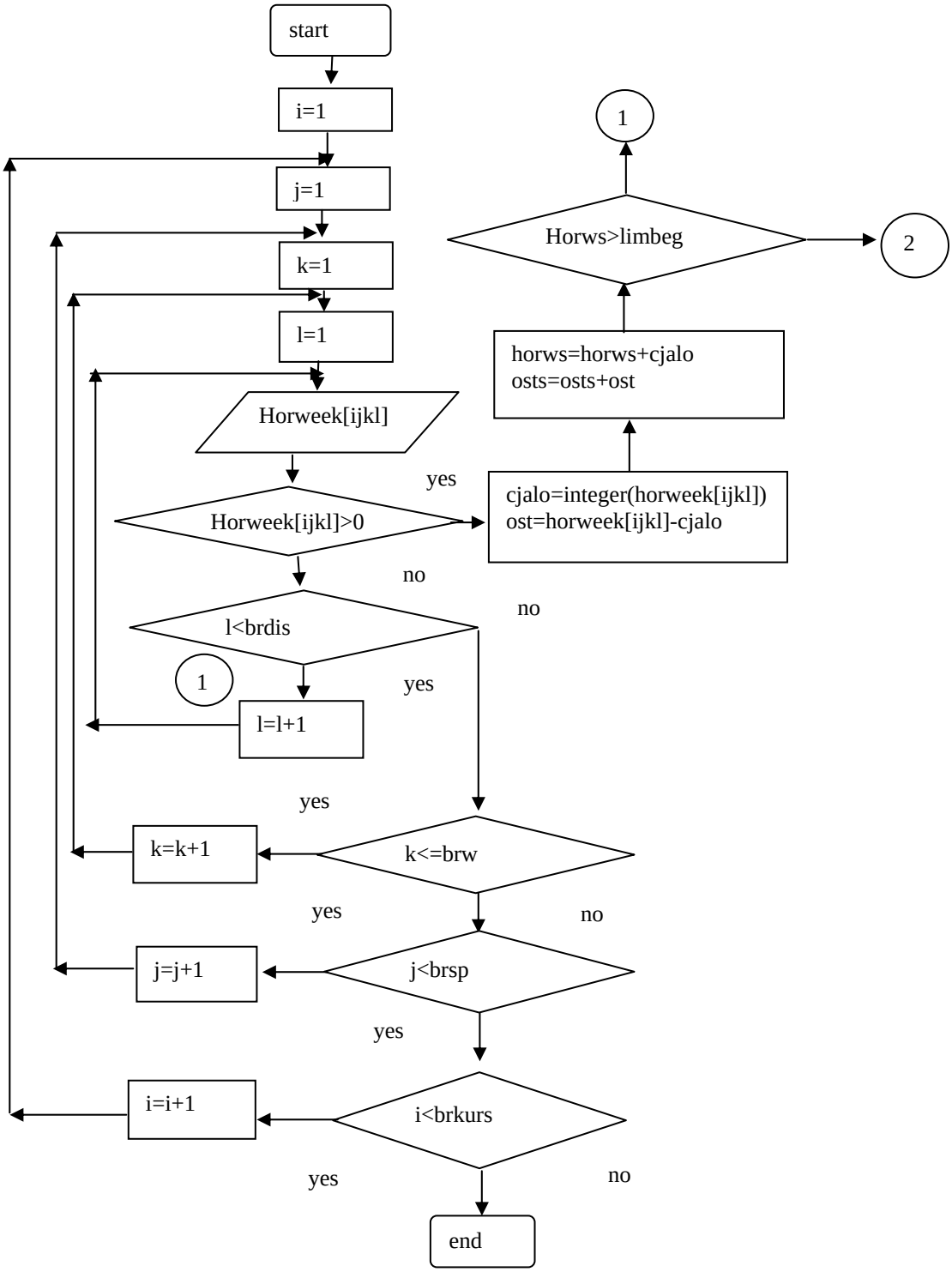

Fig. 1 An algorithm for defining the weeks' horariums for the all subjects

Mobile Learning and Testing with Java-enabled Phones

Rosen S. Ivanov[1], Mihail B. Momchedjikov[2]

Abstract – **The widespread use of mobile phones among students suppose possibility to develop mobile learning tools. The paper presents an approach to integrating mobile phones into traditional learning and testing process, which combines the advantages and benefits of both. The main problems, corresponding to mobile testing tools for Java-enabled phones development and methods for their solution is described.**

Keywords – **Mobile learning, M-learning, Java midlets.**

I. INTRODUCTION

The term "mobile learning" (m-learning) refers to the use of mobile and handheld devices (mobile phones, smartphones and PDAs) in learning process. Mobile phones are much more reasonably priced than desktops, and therefore represent a less expensive method of accessing the Internet services like the m-learning portals.

Mobile phones are becoming very popular within the communities of university students. Nearly 100% of students have a mobile phone [1] (Italy - 94%, Finland and Sweden - 92% , UK, France and Spain - 82%). The widespread use of mobile phones among students supposes possibility to use this technology to improve the motivation of and communication with students.

Mobile learning is an additional channel to communicate with students and to deliver learning and testing content. The main advantages and benefits of the m-learning are [2]:

- can be used anywhere and anytime;
- can be used of these students who do not take all the courses for the academic year;
- increases motivation to self-learning;
- can be used of peoples with disabilities.

When the m-learning tools are developed the focus will be pedagogical - technologies, standards and specifications in mobile communications used to the creation of the mobile learning tools will contribute to successful learning for the students. The rules for the creation of successful learning tools for distance education are well known by now and must be applied to the new mobile learning tools. E-learning technology is the state of art for distance learning in Europe [5-8]. M-learning is the next generation of learning.

[1] R. Ivanov is with the Department of Computer Systems and Technologies, TU of Gabrovo, Bulgaria, E-mail: rs-soft@ieee.org.

[2] M. Monchedgikov is with the Department of Padio-engineering, TU of Sofia, Bulgaria.

In traditional learning scenarios, for example blackboard or a projector is used for the presentation of the learning material. This scenarios offer many advantages - if there are questions or unclear points each student can immediately ask the teacher and receive an answer. Vice versa, a teacher can test knowledge by asking a questions. Using up-to-date mobile phones with integrated Java Virtual Machine (JVM), high speed mobile data communication (including streaming) and multimedia processing (audio, video) capabilities, mentioned above learning scenarios can be simulated and enhanced [3].

To use mobile phones as a learning tools they need to support application-development technologies such as:

- Wireless Application Protocol (WAP) which allows data communication between WAP-enabled mobile phones and Internet services;
- Java 2 Micro Edition (J2ME) which is a general platform for programming embedded devices;
- Microsoft .NET framework which includes C# language as an alternative to Java;
- NTT DoCoMo i-mode.

Using WAP we can develop Wireless Markup Language (WML) applications. WML is a tag-based document language. The main disadvantages of the WML-based applications are: limited memory size of WAP browser, limited type of objects that can be displayed (text and images), cannot integrate programming logic in WML code, increased number of request to application server etc.

The real mobile applications are written in C++, C# or Java. The mobile device could download Over-The-Air and run such applications. The advantages of J2ME applications (midlets) are as follows:

- lower price of Java-enabled mobile phones in comparison with PDAs and smartphones with operating systems like Symbian and Microsoft Mobile 2003;
- Java applications are platform-independent;
- allows development of the fully Java-based client-server applications;
- Java security model provides a very restricted environment in which to run untrusted midlets;
- Java Development Kit 1.2 allows development of the signed midlets.

II. M-LEARNING SYSTEM ARCHITECTURE

We use fully Java-based client-server communication model architecture shown in Fig.1.

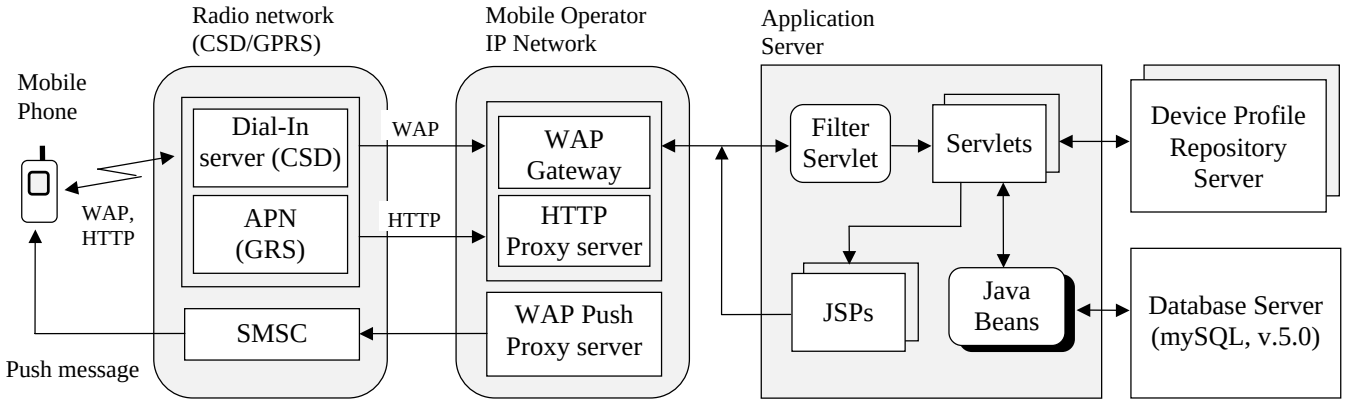

Fig. 1. M-learning system architecture

Three layer architecture is used:

- Layer 1 - Client;
- Layer 2 - Application server;
- Layer 3 - Database server.

The mobile terminal (client) should support WAP and J2ME technologies. Tomcat Servlet Engine is used as a WEB application server. Tomcat is an open source project available from the Apache Software Foundation [9] that supports Servlets v.2.2, Java Server Pages (JSP) v.1.1 and Java Beans technologies. The open source database mySQL [10] is deployed as the server database.

The client-server communication flow is as follows:

- A client asking for particular service submits a request (WAP if WML browser generates request or HTTP if Java midlet generates request) to the application server;
- The client's request is retransmitted to the WAP Gateway or HTTP Proxy Server via Dial-In server if CSD bearer (9.6kbps data rate) is used or Access Point Name (APN) if GSPS bearer (52kbps data rate) is used;
- The WAP Gateway transforms WAP request into an HTTP request and sends it to the Application Server;
- The application server replies to the request by returning an answer: WML code if request is from WML browser and eXtensible Markup Language (XMS) if request is from m-learning Java tool;
- The answer is transmitted to the WAP Gateway or HTTP proxy server;
- WAP Gateway or HTTP Proxy sends back the content of answer to the client.

A. M-learning midlet downloading

M-learning midlet can be downloaded and stored permanently into Flash File System (FFS) of the mobile terminal if following conditions are fulfilled:

- mobile phone supports J2ME technology, Mobile Information Device Profile (MIDP) v.1.0 or 2.0;
- the client was registered to the m-learning system as an user;
- Java Application Management System (ASM) could be able to download through OTA application with size of 45KB;
- The memory for Record management System (RMS) must be at least 25KB.

The registration to the m-learning service is realized from an HTML form. The user must enter your name, family and personal number. If the registration is successful the user receives an identification number (user ID) that holds information for tests which user could download.

When application server receives a blind request from mobile terminal it returns a WML deck with registration form as shown in Fig. 2.

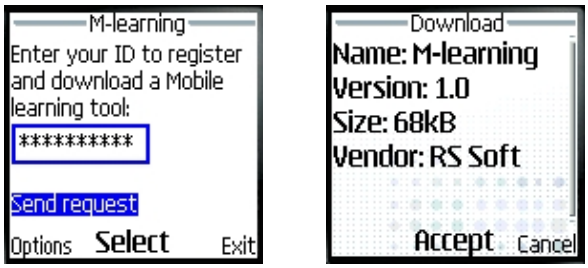

Fig. 2. Registration to the m-learning service

The application server checks entered user identification number (user ID) and prepare an answer:

- Error message if user ID is not valid, request was sent from mobile phone emulator, mobile phone cannot support Java technology or cannot download Java archive with required size;
- Java Archive Descriptor (JAD) file.

The content of JAD file is generated dynamically, because different versions of m-learning application are used:

- MIDP 1.0 version with application-specific XML parser;
- MIDP 1.0 version with Enhydra's XML-RPC package;
- MIDP 2.0 version with Enhydra's XML-RPC package;

When WAP browser receives JAD file Java AMS is started. Java AMS tries to download content of Java archive file (JAR) into download buffer in SRAM. After successful

downloading application is stored into the FFS. The URL to JAR file is described in JAD file as shown in Fig. 3.

```
HTTP/1.1 200 OK
Content-Type: text/vnd.sun.j2me.app-descriptor
Content-Length: 394
Date: Fri, 25 Feb 2005 06:53:05 GMT
Server: Apache Coyote/1.0

MIDlet-1: M-learning, ,mlearning.Mlearning
MIDlet-Jar-Size:45326
MIDlet-Jar-URL:
http://rs.tugab.bg/mlearning/jars/MIDP1A.jar
...
User-ID: GH56KLN809
Mobile-ID: SGHC100G
```

Fig. 3. Content of JAD file (Samsung C100)

B. Mobile phone profile recognition

Mobile phones have different range of input and output capabilities, network connectivity, Java MIPD and Connected Limited Device Configuration (CLDC) versions etc. The User Agent Profile (UAProf) extends WAP 2.0 to enable Application server to recognize hardware and software properties of the mobile terminal. UAProf is an XML format document which is published on a Public Repository Server (see Fig. 1). If mobile phone supports UAProf specification the field "Profile" in HTTP request header holds URI to this document. In opposite application server analyzes field "Accept" to determine a part of phone properties.

We use Apache XSTL (eXtensible Stylesheet Language Transformations) processor to parse UAProf XML document to plain ASCII text. The required information (Phone Vendor and Model, Number of soft keys, Screen size, Bits per pixel, Java platform, Java packages, Browser version, Security support, WAP version, HTML version, XHTML version, Cc/pp accept, Maximum WML deck size, Push accept, Push message size, Player version, RTSP method capable etc.) is stored in UAProf database.

C. Client-server message format

Every MIDP compatible device must support HTTP. For maximum compatibility HTTP should be used as the transport protocol between client and server. J2ME platform does not offer standardized mechanisms for message format. In proposed application an XML-based message format is implemented. XML is used as an industry standard format. XML allows realizing any data exchange between the client and server. The main advantage of XML is that it is standardized and thus highly portable.

The MIDP environment does not provide integrated support for XML parsing and generating. We use two versions of XML message formatting:

- XML-RPC package from Enhydra [11];
- Application-specific XML parser and generator.

XML-RPC is an extremely lightweight messaging protocol enabling the execution of remote procedure over the network through HTTP. The client places an XML message through HTTP POST method that the application server parses. This results in a local procedure that returns the response also in the form of the XML message. XML-RPC enables data types to be specified and transmitted as parameters in platform-neutral approach. At the server side we use XML-RPC support from Apache Software Foundation [12], which can be applied together with the Tomcat Servlet Engine.

One of disadvantages of XML-based packages is their size. XML-RPC package from Enhydra occupies 24KB of program memory. It is important to take this into account when developing applications for mobile phones, since some of them limit size of downloaded Java application. In these cases we use application-specific XML parser and generator that occupy only 12KB of memory. In this case, at the server side Document Object Model (DOM) parser is used.

The content of XML message depends on type of request or answer. For example, when a new test must be downloaded following parameter are sent to server: User-ID; Mobile-ID; Password; Language; Subject; Test type (self test or exam); difficulty level and Checksum. The content of the generated test contains following parameters: Test-ID; Number of questions; Type, Time and Body for each question and Checksum.

Four types of questions are supported:

- type 1 - one-choice question;
- type 2 - multi-choice question;
- type 3 - missing word(s);
- type 4 - error correction.

The "Body" parameter contains question's data and tags that control visualization of the information. M-learning midlet micro-browser analyzes tags and displays information according to tag's names:

- <t> Text </t>;
- <a> Text - answer;
- <m> Text </m> or <m/> - missing word(s);
- URI - URI to image file;
- <A> URI </A> - URI to audio file;
- <v> URI </v> - URI to video file.

III. EXPERIMENTS

When midlet is started the main menu of application has been displayed as shown in Fig. 4.

Fig. 4. Menu of the application (Nokia 6230)

The combination of low-level MIDP User Interface (UI) Application Programming Interface (API) and high-level UI API is used to control information drawn on the screen. The high-level UI API is portable across all MIDP-enabled phones and low-level UI API gives complete access to the screen and the input events. The main menu includes following items:

- Tests - allows new test downloading, start, continue or delete the test;
- Statistics - information for student's grades;
- Calendar - includes information such as the dates of exams, calendar of classes and news;
- Config - allows setting of the password, language, difficulty level and time interval in seconds after that next question is displayed;
- Teachers - allows searching for selected teacher and sending a message (E-mail or SMS) to him;
- Help - includes useful information for test downloading and navigation in menu.

The process of the new test downloading is shown in Fig. 5.

Fig. 5. New test downloading (Nokia 6230)

Different types of questions are shown in Fig. 6.

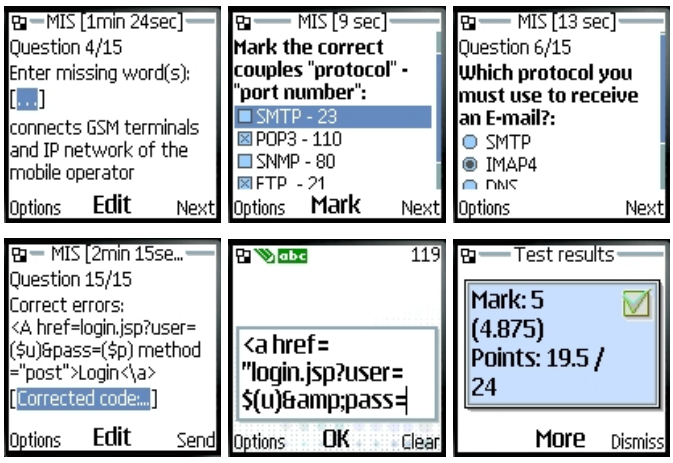

Fig. 6. Types of questions and final result (Nokia 6230)

In Fig. 7 teacher searching procedure is shown.

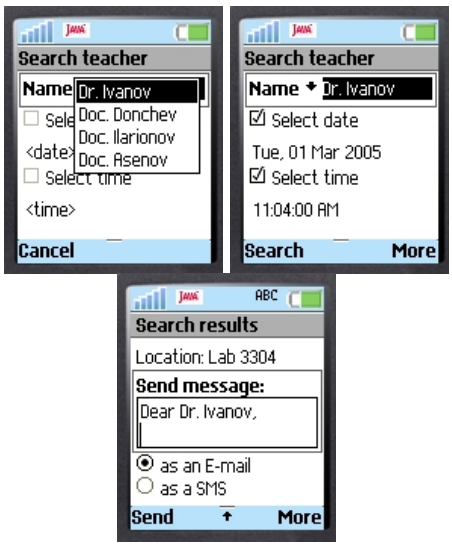

Fig. 7. Teacher searching (Sony Ericsson Z500)

IV. Conclusion

The challenge for universities now is to develop didactic tools for mobile devices and to integrate them into their learning strategies. For this reason it is important to develop mobile learning tools which complement the traditional process of learning. Despite the limited possibilities of Java-enabled mobile phones, it is possible to design learning tools like interactive tests.

Mobile learning allows students freely to decide on when to study during a day or a week. The WAP 2.0 and MIDP 2.0 Push technologies (see Fig. 1) could be a way of giving important information to the students (via SMS Center), such as their grades, responses to their assignments etc.

The small size, weight and multimedia capabilities of the mobile phones make them particularly effective for users with disabilities: customize screen colors, text size and fonts; generate vibrating or visual alerts; realize multi-modal interface. Text-To-Speech (TTS) technology can assist users who have visual impairments and find it difficult to read the screen. Voice-To-Command technology can aids users who may find it difficult to type or use the keyboard.

References

[1] J. Attewel, C. Savill-Smith, "Mobile learning and social inclusion: focusing on Learners and Learning", A book of papers "Learning with mobile devices: Research and Development", pp.3-11, ISBN 1-85338-833-5, 2004.

[2] M. Perry at al., "Dealing with Mobility: Understanding Access Anytime, Anywhere", ACM Transactions on Computer-Human Interaction, Vol.8, No.4, pp.323-347, Dec. 2001.

[3] M. Mayorga-Toledano, A. Fernandez-Morales, "Learning tools for Java0-enabled phones: an application for actual studies", A book of papers "Learning with mobile devices: Research and Development", pp.95-98, ISBN 1-85338-833-5, 2004.

[4] M-learning project, http://www.m-learning.org

[5] Project "Leonardo Da Vinci", http://europa.eu.int/comm/education/programmes/leonardo/leonardo_en.html

[6] Project "ISOPIA's m-Learning", http://www.isopia.com/main.html

[7] Project m-learning ResultsMART, http://www.learningcitizen.net/mlearning/mlearning.shtml

[8] Project "Aictc's m-Learning", http://www.aictc.com/moblieComputing/mLearning.htm

[9] Web site of the Jakarta Tomcat project, http://jakarta.apache.org/tomcat/index.html

[10] Web site of the MySQL open source database project, http://www.mysql.com

[11] Web site of the Enhydra KXML-RPC project, http://kxmlrpc.enhydra.org

[12] Web site of the XML-RPC project of the Apache Software Foundation, http://ws.apache.org/xmlrpc

Application of the Internet Technologies in the Non-Standard Test Control in Estimation of Students' Knowledge

Mariya I. Eremieva[1]

Abstract – **The article discusses the use of a form for the completion of the test. The data are sent to the server, where a function can estimate them and the examinee can receive back his/her results and estimation. The no standard test is designed in Java Script.**

Keywords – **form, test-control, no standard test, estimation, Java Script.**

I. INTRODUCTION

The changes in the economic and social life define the priorities of our time: knowledge, information and communications. The most important is the quality estimation of students' knowledge.

II. THE THEORY AND METHODOLOGY OF THE TESTS.

The didactic test logic switches on in the common contests of the information security on the educational process and can be applied like a special application and development of technology of receiving feed back information for the teacher about the following basic aspects:

1. Receiving individual information of the level of knowledge according the educational goals, fixed in the educational program on the relevant subject.
2. Get a notion about the general level of knowledge in the different groups.
3. Get a notion about the general level of knowledge of regional and national level.
4. Determination of the gaps and the strong components in the valid program of education, based on the test.
5. The didactic tests are developed on one scientific base, many scientist of different countries have been working on their development. The next stage in the development of the test method is related to improving his scientific bases. Many methods of quality assessment of the tests are worked out (trustworthiness and validity). K.Pierson publishes the first researches in this area.

Very important contribution in the development of the theory and methodology of the tests make also Ch.Spearman, who unite and develop further the psychological theory of the theory with the theory of the physic measures, which reveal the trustworthiness of the test. T.Kelly creates the first standardized test of initial school degree. The term test has many meanings - it means examination, try-out, control, it's a method for examining and verifying the knowledge in different areas – in particular for verification of the intellectual abilities. In the broad sense the test is a scientific method of making study of determinate qualities of the personality, which can be put into practice when the definite conditions are observed, and under definite goal which is scientifically well founded. The creation of the test should satisfy already established scientific requirements and the results of the test making are analyzed and can be compared with preliminarily created norms, generally valid criteria of assessment. The didactic test is an instrument for measuring the results of the educational activity over definite educational content, which can be assimilated in the conditions of the organized educational process. Every didactic test consist of an organized succession of questions and tasks. With them can be verified the level and the degree of execution of the requirements of the educational program on the respective educational discipline in relation to the knowledge and the abilities of the students. According to the purposes, character and aspects of the used test's tasks their number can vary – from 5,10 to 50,100 and even more. Independent of the content and typology of the questions and tasks in the didactic test all of them have the same inner structure. Every question is built by the combination of the following three components:

Introductory part consists information about the tested persons and it is the base for the formulation of the real question. Here are included the exit information, explanations, directions and indications necessary for the problems.

Formulation of the problem based on the previous information. It is a concrete task, requirement, which has to be done by the tested persons. The ways of posing the question can be different;

The answer needs of independently finding of the searched result or selection among the proposed alternatives.

Every test should consist of the following qualities:

1. Objectivity – independence of leading the test and the results of it by the author.
2. Trustworthiness – shows the precision of the procedure of leading the test like a measure cause every measure is accompanied with mistakes and the testing is measure.
3. Validity – shows the degree of it's correspondence about the achieving or un achieving on determined for measure educational purposes.

[1]Mariya I. Eremieva is with the Naval Academy , 9000 Varna, Bulgaria, E-mail: eremievam@abv.bg

4. Comparison – the results of one didactic test, received by different educated people can be compared one by one.

5. Economy – it is mainly concerned with the possibilities of one already ready test to be applied within investigations with mass character and a large number of students to be tested, and finally conclusions on national level can be made. On this way the test's material can be used many times.

6. Balance – it refers to the representativeness of the selectioned tested problems for covering the determined for measure educational contents and purposes. The most elementary form for achieving the balance is the Tyler's two – dimensional matrix with the dimensions level of assimilation and educational content.

7. Specificity – determines the degree which is necessary to solve the tested problems and the specific knowledge which are acquired after the educate has passed the educational course.

The didactic tests are classificated in 14 groups in [3] from G.Bijkov. The most known are:

1. The standardized and no standardized tests. The standardized test is based on already existing theory and the no standardized test is created by the educators for immediately applying within one educational institution.

2. General tests for achievements. The number of true solved problems reports the achievements of tested persons or the made mistakes for preliminarily determine time.

3. Diagnostic tests – they show the type of difficulties which the educated meets and why is it difficult to him – because he doesn't know the concrete fact material or he can't put on practice the learned.

4. Preliminarily tests – they are made to determine the incoming level of the educatedл

5. Processual, forming tests – they are offered after the complete study of a part of the educational content. On the basis of the results the lapses in the knowledge of the educated are verified and in consequence are filled in.

6. Final tests- this are tests, which are made at the end of one determinate date of the education – when one determinate cycle of lections is finished.

7. Normative and criterial didactic tests – they try to find an answer of the question. If the objectives of the respective normative documents are reached for each subject.

8. Adaptive and computering tests – the construction of these tests is very difficult and durable investigation process, which is based on the new theories of tests with probable and information-theoretical character.

Nowadays when the computer technologies are becoming more and more popular is a fact that these tests satisfy best the general qualities of the didactic tests. They are actually in the distance education. By them the educated gets a notion about his degree of the educated disciplines, about the lapses, which he has, commit at the time of his preparation. The general defect was the lack of back connection with the educated.

III. CREATING THE COMPUTERING TEST

By the computer tests the presenting of questions, their answering and verification is made by the using of a computer' program (test program). Priority of such tests is the great economy of time and resources, but their preparation acquires knowledge about these so-called authors languages for creating a computer educating programs. A part of the difficulties are avoided since with the bringing in the Internet technology and the mass creation of WEB pages. The using of JAVASCRIPT gives opportunity to rely with the educated, the consumer. JAVASCRIPT works in the WEB browser if it is conformable to it. This means that the last one can be used for problems, which aren't related with the server like the HTML forms and the CGI scripts. JAVASCRIPT is pure marked text, which is added to the WEB pages and gives opportunity to contact the consumer with forms. Forms' data – the answers of the questions are resented to the educated where a function for assessment of the test has been made. The proposed test is developed like a structural test. Every question has only one correct answer wit which agree all the experts. Controversial problems and the using of "tricks" and "devices" in the defining of the questions are not appropriate for the assessment.

To avoid the possible learning by heart of the questions and the answers by the educated, the proposed test is develop in 5 possibly variants and for each of them the consequence is different. Every educated person operates with determined structural information and every question has 4 possible answers and only one is correct. The answers are presented in the form with "radio" buttons and that assuree the indication of only one possible answer.

After the test finishes the button "assessment" should be pressed to submit the control of the function, which evaluates the result of the educated. The button "delete" clears the form and the button "send" sends it to the teacher. On figure 1 is shown the mean screen of the test, on figure 2 – the process of the test solving and on figure 3 can be seen the result.

IV. CONCLUSIONS

1. The test operates with data base which allows her actualization from unprofessionalists in the area of programming.
2. He posses a new "Random code" for mixing the questions and answers which makes difficulties for their knowing by minimum.
3. The assessment is by an algorithm which is conformable with the new tendencies for assessment (the halves at the ending estimation are eliminated).
4. Universality of the product is achieved and the last is designed for Windows XP, but there aren't any problems to work in irrelevant versions (Windows 98).
5. Impartiallyassessment of the educated is achi-eved

REFERENCES

[1] Todd Stauffer “Absolute beginner’s guide to creating WEB Pages, Edition Soft Press LTD 2003

[2] G. Bijkov “Reforming pedagogics”,Edition . , Education 1994.

[3] G. Bijkov “Theory and methods of diagnostician tests”. Education.

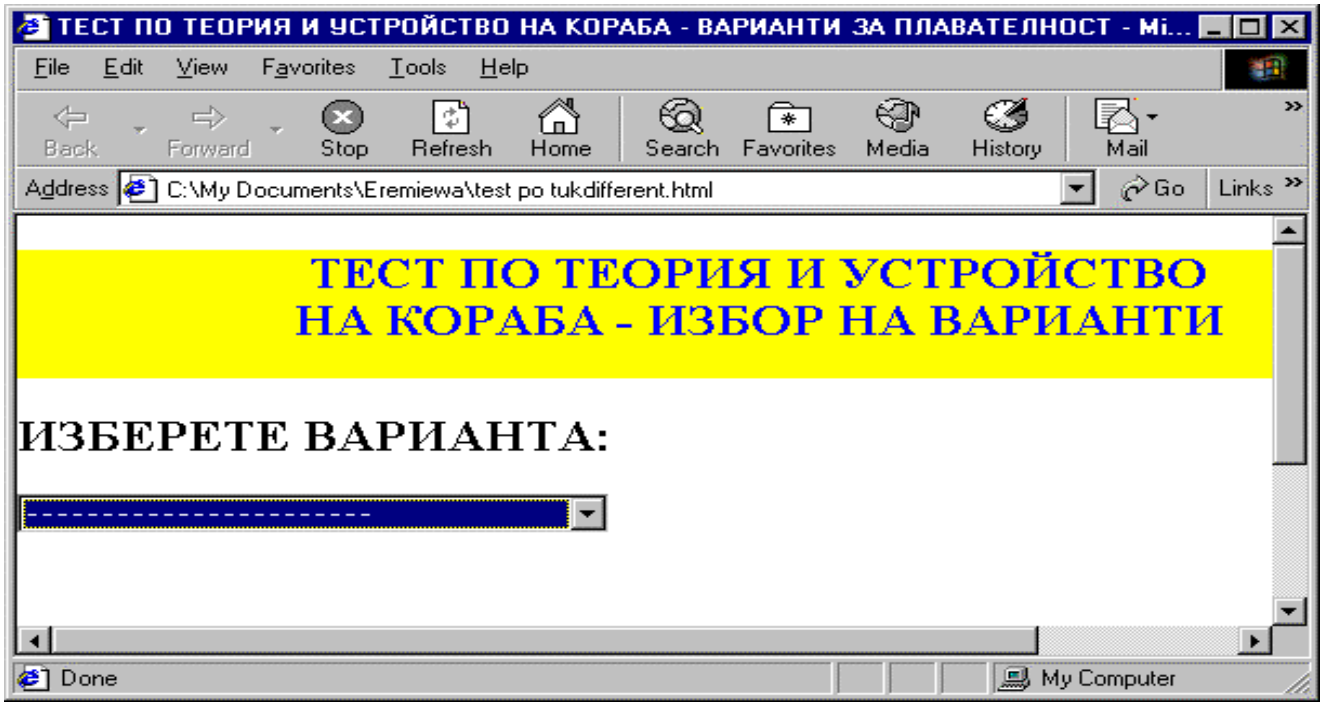

Fig. 1 Main screen

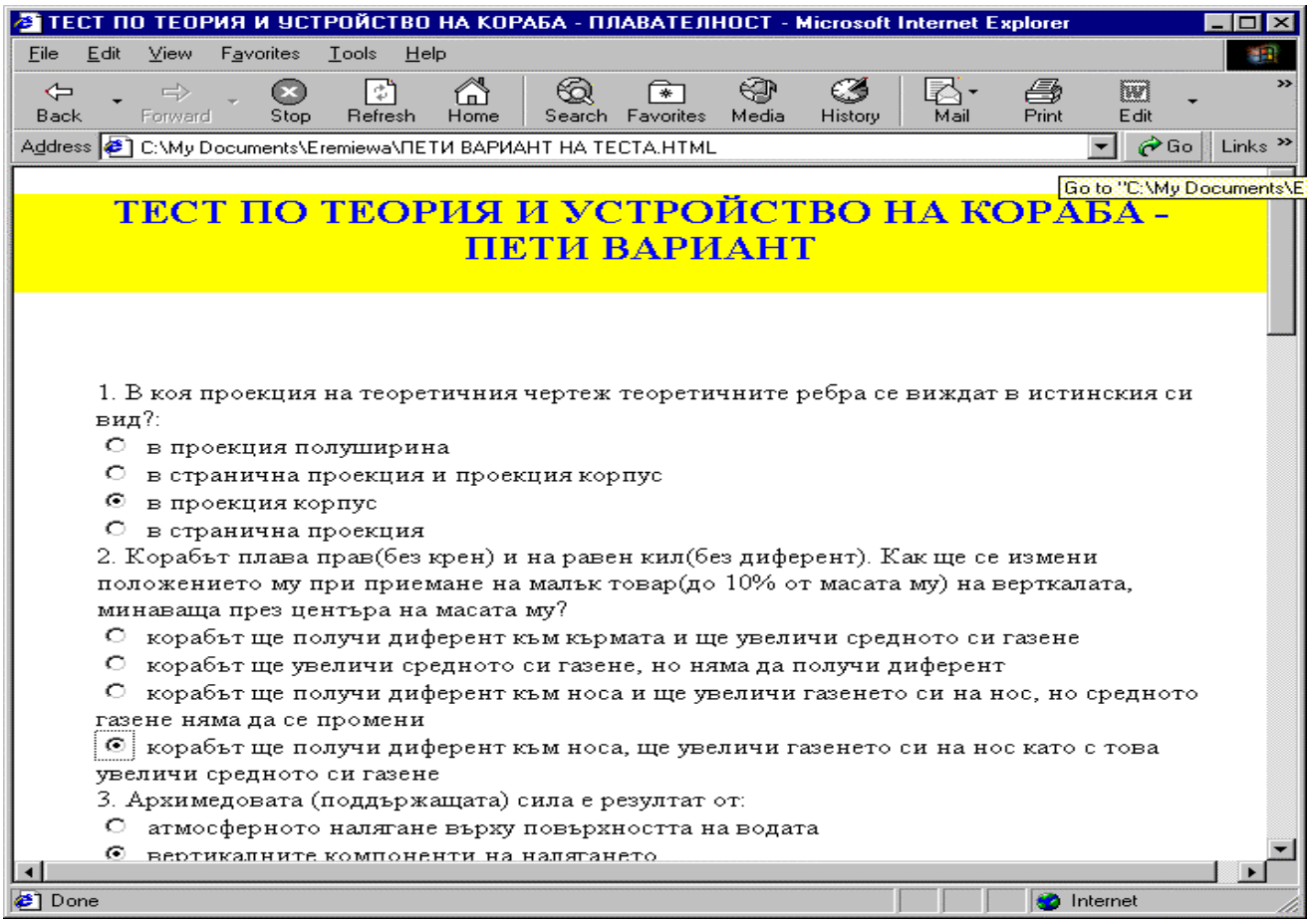

Fig. 2 Decision of the test

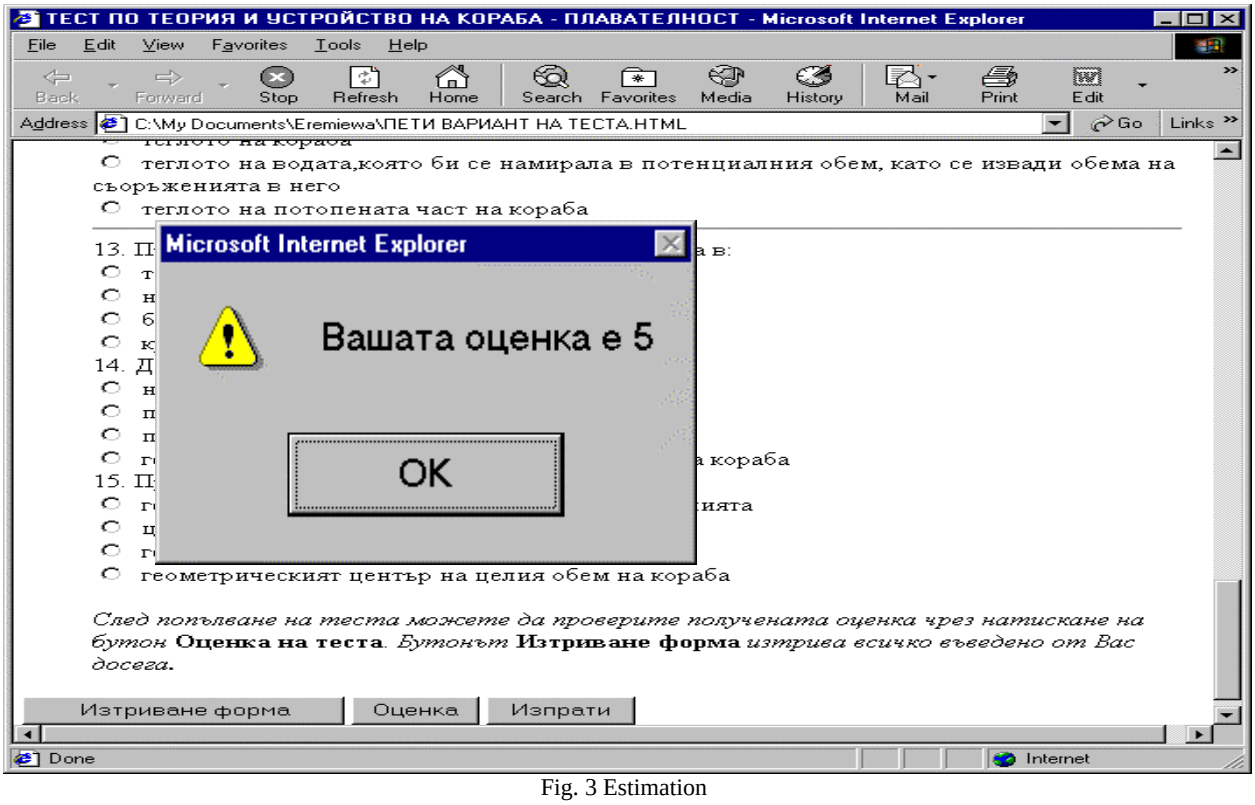

Fig. 3 Estimation

Lidar Registration of Orographic Internal Gravity Waves in the Atmosphere

Georgi Kolarov[1], Ivan Grigorov[2]

Abstract - **Local dynamics of low and medium layers in the troposphere causes diffusion on pollutants emitted from ground-based sources, typical for larger cities. Internal gravity waves (IGW) of orographic origin are a continuously operating means of action of dynamic processes in the atmosphere above Sofia city. In this paper, the results of analysis made on the periodic structure of IGW, registered through remote lidar measurements are presented.**

Keywords **– Gravity waves, Lidar, Dynamic of the atmosphere**

I. INTRODUCTION

Internal gravity waves in the atmosphere are sometimes visually observed by the cyclic shape of the clouds. They are part of the common dynamic of the atmosphere and transmit wave momentum and energy from one place to another. Most waves are of small dimensions and act on a local scale, but they do play a role in the diffusion of gaseous and aerosol pollutants in the boundary layer of the atmosphere.

IGW of orographic origin arise as a result of dragging the ground air flow when overcoming a mountainous obstacle [1]. For registration of the IGW, terrestrial or airborne installations are used. Relatively new and highly effective means of remote studying of IGW are radars and lidars [2]. The object of our research was to register IGW of orographic origin at altitudes up to 10 km, using high spatial resolution (30m) in the area above Sofia city both at day- and night-time.

II. EXPERIMENTS

Lidar experiments were held on the territory of the Institute of Electronics at BAS, Sofia city. The city is situated in a field surrounded to the north by Stara Planina Mountain, to the south by Vitosha Mountain, to the east by Plana Mountain, and to the west the plain is open, as it can be observed on the satellite photograph (fig. 1). The orographic situation around Sofia fosters formation of IGW in the atmosphere. Vitosha Mountain is located 6 km southwards from the city center, the ridge reaching a height of more than 1500 m above the plain (peak Cherni Vrah – 2390 m), and having longitudinal dimensions of about 15 km. Its proximity and significant dimensions and height often result in IGW when winds are coming from the south, southwest and southeast.

[1]Georgi Kolarov is with the Institute of Electronics, Bulgarian Academy of Sciences, 72, Tsarigradsko Shosse blvd., 1784-Sofia, Bulgaria, E-mail: kolarov@ie.bas.bg

[2]Ivan Grigorov is with the Institute of Electronics, Bulgarian Academy of Sciences, 72, Tsarigradsko Shosse blvd., 1784-Sofia, Bulgaria, E-mail: ivangr@ie.bas.bg

Orographic waves have been observed in the area of Sofia by the fluctuations of the atmospheric pressure [3]. The authors note that in 90% of the measuring time waves were observed, with the largest amplitude resultant from a wind coming from Vitosha and a wave period between 5 and 30 minutes in most cases.

The lidar appliances, employed for the experiments conducted in the current study was supplied with a CuBr laser (λ=510 nm) with pulse duration 10 ns and pulse repetition 13 kHz [4]. We sounded vertically upwards, and photon counts from photo detector were registered by Photon Counting Board LD_P 03_01, allowing registration of the backscattered lidar signal in altitude with spatial resolution of 30m, in 1024 strobes and cumulating time of 60s. The sounding height was 1km to 10km. The studies were conducted in 14 days in the months October 2004 – February 2005, when the sky was cloudless. The total duration of lidar profile records for this period is 48 hours, as in 39 hours or 77% of the total sounding time, presence of waves was registered. The duration of one experiment for atmosphere sounding was 1.5 hours. In two days, the records from consecutive soundings were combined into longer series, respectively 6 and 9 hours continuously. The wind speed and direction and air temperature were measured with meteorological mast. In most experiments the wind speed is below 0.5 m/s and its direction is unstable.

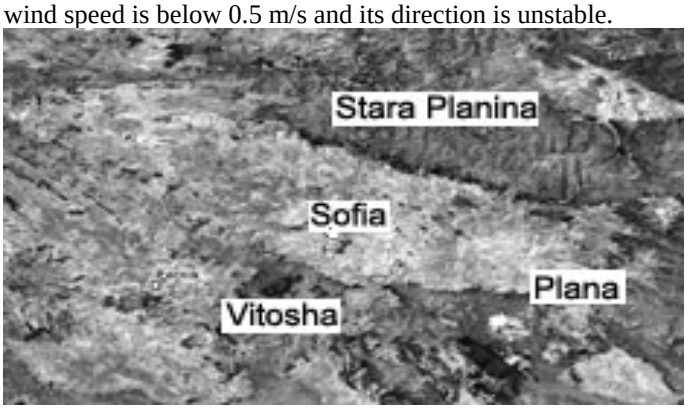

Fig.1. Map of the region of Sofia city

The lidar parameters determined registration of discrete temporal series (realizations) of 90 numerical values each, distant by time intervals of Δt=1 min. Each realization represents the time distribution of a lidar backscatter from an atmospheric layer of 30 m thickness, located at a certain height. Each lidar signal record contained 360 realizations. After filtering, the spectra of these realizations were constructed using Fourrier transformation and the respective

IGW periods were determined. Often in one spectrogram 2 or 3 significant spectral lines were observed, which shows that the waves registered represent superposition of waves with different wavelengths.

III. Results and Comments

Typical spectrograms, obtained in the analysis of temporal series of lidar data are shown on fig. 2 and fig. 3, on which summarized results from the experiments carried out on 1.12.2004 and 11.01.2005 respectively, are presented.

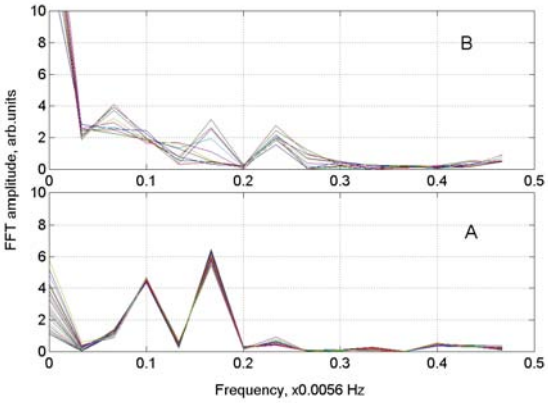

Fig.2. Spectrograms of the temporal series from a lidar sounding held on 01.Dec. 2004. For heights lower than the mountain ridge, well stressed periodic processes can be observed (A), which fade out at higher altitudes (B).

The spectrograms on fig. 2 represent the results of a lidar sounding with 1.5h duration between 15:50h and 18:20h LT. Fig. 2A presents the spectrograms of realizations of 30 sequential height intervals each of 30 m thickness, situated within a height range of 1000m-2000m above the lidar. For these heights it is typical that they are lower or of comparable height with this of the Vitosha Mountain, which causes the appearance of orographic IGW due to southern wind streams. Thus for these heights wave periods of 29 and 18 minutes respectively are registered. In contrast to these spectra, the spectrograms from higher altitudes show absence of a wave process. Fig. 2B shows the results from analysis of temporal series for 10 sequential layers of the same thickness for heights of 2500-2800m above the lidar. For these altitudes and above, until the end of the sounding range of the lidar, no cyclic processes exhibiting regularity are observed.

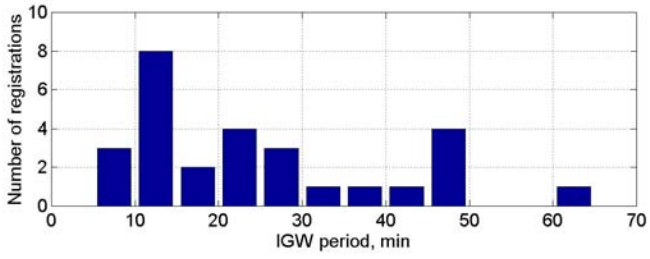

Fig.4. Histogram of registered IGW periods

The spectrograms of fig.3 are a summary of 4 consecutive lidar soundings from 11.01.2005, with a total duration of 6 h. Three spectral lines are significant for the respective heights of 1000m –2000m and they have periods of 50 min , 36 min, and 26 min respectively. From the spectrograms for heights of above 2km it is obvious that no noteworthy wave processes are observed (fig. 3b).

Fig. 4 represents the histogram of distribution of the periods of registered orographic IGW from all lidar soundings. Most often, waves with periods between 10 and 20 minuites are observed. The three local maximums for intervals 5-15min, 20-30min, and 45-50min correspond to the most frequently observed wave superpositions.

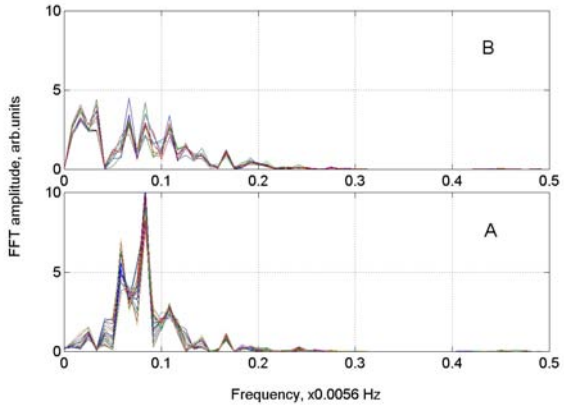

Fig.3. Spectrograms of the temporal series from a lidar sounding held on 11.Jan.2005. Superposition of 3 waves can be observed (A), which fade out at higher altitudes (B).

IV. Conclusion

The lidar system at our disposal allowed remote and simultaneous in many atmospheric layers observation of periodic structures, that represent a manifestation of internal gravity waves in the atmosphere. The lidar soundings in the area of Sofia city during the fall and winter period, with a total duration of 48 hours, confirmed the presence of such waves in 77% of the total number of experiments. At altitudes of about 2-2.5 km, fading to insignificant amplitude values was observed in the temporal series, which testified to the decomposition of the periodic structures studied. Such behaviour is characteristic for waves of orographic origin. Orographic IGW appear and depend on the wind structure and are part of the dynamics of lower and ground atmospheric layers. They are undoubtedly one of the mechanisms for distribution of gaseous and aerosol pollutants around Sofia.

References

[1] M. J. Miller, “Subgrid-scale orographic drag”, *Meteo-rogical Training Course Lecture Series*, ECMWF, 2004.

[2] C. Staquet and J.Sommeria, “Internal Gravity Waves From Instabilities to Turbulence”, *Annu. Rev. Fluid Mech*., no.34**,** pp. 559-93, 2002.

[3] И. П. Чунчузов, А.И. Отрезов, П. П. Фирстов, “Экспериментальное исследование внутренних гравитационных волн в горной местности”, *Физика атмосферы и океана*, vol. 27, no.4 , pp.362-368, 1991.

[4] G. V. Kolarov, I. V. Grigorov, Or. I. Vankov, “Lidar observation of gravity waves in the throposphere and low stratosphere above Sofia”, *Proc. of 19-th ILRC*, pp. 63-64, Annapolis, Maryland, USA, July,1998.

Process Model and Collaborative Mechanisms for Agile Energy and Ecology Management in Industry

Milorad B. Tošić[1], Miomir S. Stanković[2], Valentina M. Milićević[3]

Abstract – **In this paper, we present the process model of activities relevant for achieving energy and ecology efficiency goals in industry. Being highly complex, multidisciplinary, and heterogeneous, such a process requires intensive use of information technologies in order to be efficiently and effectively executed in dynamic business environments. Next, we propose a set of selected collaborative information system's mechanisms that may be applied in the supporting information technology infrastructure.**

Keywords Ð **Collaborative information systems, energy efficiency, ecology efficiency, agile methodology**

I. INTRODUCTION

Advancements in the Information Technology (IT) are rapidly becoming leading force in human society development. As a consequence, the mutual impact is more and more evident where IT not only changes the way humans live and work (including businesses, social life, government, entertainment, etc.) but it also suffers tremendous pressure to deliver human-oriented value that is actually needed [10].

When the businesses slowed down, the cost cutting became imperative, and energy cost and energy performance suddenly attracted more interest again from the management. Although energy and ecology (EE) efficiency and energy conservation are common terms now days, successful implementation of an EE management program in a real industrial environment is still high risk venture for a team assigned to do that. The complexity arises from the need to tie together people, procedures and technologies in order to achieve consistent and sustainable performance improvement.

In this paper we identify process model for EE management in industry. Our motivating factor in this work is to provide the supporting information technologies (IT) infrastructure. We envision the Energy and Ecology Efficiency Management System (e3MS) as the intelligent information system, collecting information, processing and presenting it in a structured way and cooperate with users and other systems in problem solving, discovery, access, retrieval and manipulation of a wide variety of multimedia data and knowledge.

The problem understanding and acceptance level of EE efficiency aspects within an enterprise is called *motivation factor*. The motivation factor of the authority structures, informal groups and other influential actors in the company, is identified as the crucial success factor for EE efficiency management.

The collaborative IT mechanisms promise high levels of the EE efficiency motivation factor by effective interaction, information exchange and knowledge sharing between all relevant actors within the enterprise, independent of their function, education degree and physical location.

Agile development combines creative teamwork with an intense focus on effectiveness and maneuverability [6]. Particularly, the agile development methodologies bring-in high value when applied vertically [4], including strategic level [5]. Adoption of the agile methodologies for initiation and management of the EE efficiency process, which is a very complex activity spanning whole organization, may deliver significant benefits, such as: 1) reduced risks in implementing EE efficiency projects; 2) significantly reduced overhead costs; and 3) improved project success rate. To the best of our knowledge, the agile methodology, in spite of the significant practical results in several other application domains, has not jet been applied to the EE efficiency management in industry.

In this paper, we propose mechanisms of collaborative information systems as component of the supporting IT infrastructure for adoption of agile methodologies in the EE management application domain. In Section 2 we give brief introduction into collaborative information systems, agile methodologies, and EE management. In Section 3 we present a process model, based on agile methodologies, for strategic EE management in industry. Section 4 describes mechanisms of the collaborative information systems with respect to the developed model. In Section 5 we discuss presented results in the context of related work. Finally, Section 6 concludes the paper and indicates further research directions.

II. BACKGROUND

Collaborative systems have gained considerable attention in recent years as they provide many advantages such as effective customer-supplier relations, knowledge sharing, improved problem solving capabilities and increased

[1] Milorad B. Tošić is with the Faculty of Electronic Engineering, Aleksandra Medvedeva 14, 18000 Niš, Serbia and Montenegro, E-mail: mbtosic@yahoo.com

[2] Miomir Stanković is with the Faculty of Occupational Safety, Čarnojevića 10a, 18000 Niš, Serbia and Montenegro, E-mail: cesiru@ptt.yu

[3] Valentina M. Milićević is with the Faculty of Electronic Engineering, Aleksandra Medvedeva 14, 18000 Niš, Serbia and Montenegro, E-mail: valentina@elfak.ni.ac.yu

efficiency of product development [3]. More and more organizations realize that in order to effectively manage innovation, knowledge generation and sharing are of the crucial importance. There is a continuing pressure to generate new knowledge through collaborative means and manage these actions in a way that will provide innovative and productive actions for the organizations, as the main driving factor of the organizational competitiveness.

To be effective, the collaborative groupware must support actual work practices as the participants construct them, rather than simply officially sanctioned and well documented practices. The groupware provides the technological capabilities to communicate across time and place. The type of groupware adopted in any organization is important and can provide many of the advantages depending on the level the best practices are adopted.

Agile development combines creative teamwork with an intense focus on effectiveness and maneuverability [6]. Agile models are more effective than traditional models because they are just barely good enough, they do not have to be perfect and present a practice-based methodology for effective modeling and documentation of software-based systems. Agile modeling approach can be applied to requirements, analysis, architecture, and design [1]. An important aspect of agile methodology is that it is not a complete development process. Agile methodology's focus is on effective modeling and documentation. For example, in the software development domain, it doesn't include programming activities, although it will tell you to prove your models with code. It doesn't include testing activities, although it will tell you to consider testability as you model. It doesn't cover project management, system deployment, system operations, system support, or a myriad of other issues [6].

One of the most useful lessons that a *EE management practitioner* can learn from working with the people, is the range and breadth of issues that they didn't know, didn't understand or were not confident about, which in turn hindered them to implement EE management programs. These issues ranged from simple technical details about some calculation, to missing the whole concept or context for energy management. Energy management has of course strong technical component, but *if the focus is on technical aspects only, the results will be limited*. *EE management needs to focus on people* because technical expertise and sophisticated equipment will fail to produce results unless people are committed and receptive to the changes recommended for performance improvement. Working with people of diverse background unified by a common goal, always presents a challenge to find the most effective way to help them understand and implement EE management system procedures and techniques.

Energy management can be defined as: Controlling energy flows, in a systematic manner, and according to a plan prepared in advance, with the objective of achieving company's goals at the lowest possible energy cost. It is a continuous process that integrates the entire sequence of events, starting with a commitment to energy conservation from end-user to top management, and proceeding to improved operation and maintenance procedures, quality control, financing and construction of energy conservation equipment, monitoring and follow-up.

Energy auditing is study of a facility, that has to determine one or all of the following: a) to determine how and where energy is being used or converted from one form to another, i.e. to establish a base line energy consumption; b) to identify opportunities to reduce energy usage, and define energy conservation measures; c) to evaluate the economics and technical practicability of implementing these measures, and recommend feasible energy efficiency improvement projects; d) to formulate prioritized recommendations for implementing improvement projects with the aim to cut the energy costs. In practice, energy audit of an industrial plant is often reduced only to checking the efficiency of the main utilities, like boilers, chillers or air compressors. It is obvious that such most simplified form of energy audit can yield only partial results, and cannot bring full benefits of a comprehensive energy management program.

Energy efficiency improvement projects are key practical solution to the problems of energy wastage, identified during an energy audit, and presented with full technical and financial evaluation.

III. Process Model for Strategic Energy and Ecology Management in Industry

The process model comprises several different significant management aspects of the energy and ecology management in industry. In such a case, agile methodology is very promising approach to achieve high efficiency of the resources invested in the project. The methodology favorites iterative steps integrating information technologies, knowledge management, EE efficiency technologies, as well as business process management and project management knowledge body. Following the methodology, work at the project is focused on the particular practical problems that are selected with respect to solutions with the greatest potential to deliver strategic value.

Model of the EE management process in industry is given in Fig. 1 in a form of the State/Activity Model UML diagram. The process starts with the strategic decision for continuous improvement of EE efficiency in the enterprise. After the decision is made, the collaborative process starts to continuously accumulate information about EE efficiency, where all players from the enterprise relevant to EE efficiency are involved. Using the growing body of collective knowledge and information, strategic decision makers can get first insight, begin learning about, and achieve common ground agreement regarding the current state in order to be able to make informed decisions. They exercise the accumulated knowledge by setting EE efficiency goals according to the existing business strategy. At the operation management level, the analysis and reporting activity is initiated, while activity for identification of the set of possible corrective actions is initiated in parallel at the strategy level. Then, decision makers assign priorities to the set of possible

corrective actions. Using the collected knowledge, decision makers are able to select a single, most promising action from the set of actions. Note that the same candidate action may be assigned different levels of priority in different iterations of the management process. Then, the request for proposals is issued regarding the selected action, and one or more project proposals are collected. If detailed project proposal exists and proposal is validated, the project implementation is launched and the process iteratively continues back to the collaborative process of gathering information. If the proposal is not validated, then we validate project through prototype implementation. In the case project proposal doesn't exist, the identified candidate solutions are inserted into the set of possible corrective actions, while the process iteratively goes back to analysis and reporting.

IV. COLLABORATION MECHANISMS

As is shown in Fig. 1, collaboration among actors in the system is of the crucial importance. Actors collaborating within the system are diverse, including human actors, such as strategic decision makers, managers, knowledge workers, engineers, etc., as well as software actors such as knowledge artifacts, processes, information, agents, etc. Collaboration facilitates the core process activities, such as decision-making, knowledge accumulation and usage, dissemination of the information to all relevant stakeholders, etc. As such, we identify collaboration as one of the most important success factors. Hence, we believe that investment in the IT support for the collaboration may significantly contribute to the enterprise strategic competitive advantage by improving process scalability, integration and flexibility, while delivering financially measurable benefits.

In the following, we propose several mechanisms of the collaborative information systems that may be effectively used in the supporting IT infrastructure for EE management in industry. For each of the proposed mechanisms, we briefly present features that are of the highest relevance for the EE management domain, only. Comprehensive discussion of the mechanisms is out of the scope of the paper.

- ***Work Group (WG)***: The work group is a first class object in the EE management system. In other words, the WG may engage in interaction with other first class objects in the system, such as users, actors, roles, processes, data, etc. Any user may create a WG. The creator has full access to the WG's resources, such as information artifacts, processes, and interactions with other members of the WG. Being a first class object, implies that the WG may be the creator of some other WG. We identify the following roles relevant to WG mechanism: *a) System Administrator* – administers the group from the aspect of a Provider, providing IT resources for the group. For example, the System Administrator may set storage and processing time limits for every group (or for the group of groups); *b) Content Administrator* – administers the content that is accumulated within the group boundaries. She has no author rights on the content. Instead, she has the right to do content administration (for example, statistics, content

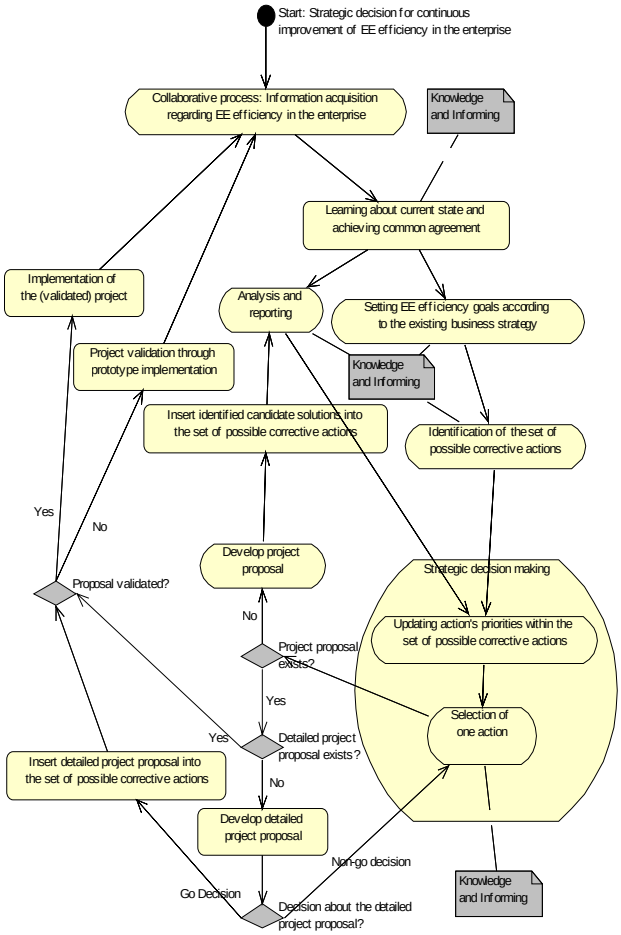

Fig. 1. Process model for EE management in industry

mining, fault-tolerance, back-up, etc.); *c) Workgroup Administrator* – is member of the WG that has privileges to organize activities within the group (for example, configuration of resource usage, WG's workflow, etc.); *d) Workgroup Member* – is any user participating in the WG. It is important to note that same user (or actor) may concurrently act in different roles within same or different WGs.

- ***Multi view****:* The Multi view mechanism is intended to support heterogeneous interactions between humans and the system. Namely, different users naturally assume different system's usage patterns, according to the user's knowledge, understanding, communication, and learning potential. It may include: *a)* Interface for accessing system resources; *b)* Multilanguage support; *c)* Interface for being aware of other system's elements.

- ***Indicators****:* We may identify the following types of indicators: *a) Activity Indicators* – number of active users, number of passive users, periodical review of the group's activity, level of interaction intensity, etc. The indicators may be assigned to a user, group or to any other system's element.

b) Social Indicators - for example, number of users interested in sharing the same system element; *c) LD ("likes-dislikes") Indicator* – an actor in the system may like/dislike some other system's element (other user or group, resource, time of the day, etc.).

- ***Forms:*** Forms are collaboratively developed, usually within a WG. These forms are then used to structure communication with actors outside the WG (questionnaires, surveys, reports, etc.). Also, the forms are used for knowledge and information acquisition.

- ***Reports:*** Collaborative, multi-user development of diverse reports. The forms may be used as report's templates.

V. Discussion And Related Work

In [7], the author is primarely concerned with user interaction aspect of software and Web site development. He is impressed with the Usage-Centered Design/Agile models when it comes to collaboration, but identifies the need for further techniques, including goal-oriented modeling, to achieve true user-centered design. In spite of different application domain, we have independently identified the same need. In this paper, we proposed the user-centered design process for EE efficiency management in industry and proposed supporting collaboration mechanisms. The agile methodology, based on collaboration and goal-oriented modeling, is the prime candidate for organizations and systems leanning towards Service Orinented Architecture (SOA)[8]. In fact, the SOA is target platform for implementation of the proposed methodology. Similar methodology, called Innovation Pipeline[5], is applied at the strategy level in the product development domain. The innovation pipeline methodology is based on two-stage pipeline process model while our methodology supports iterative process. Descriptive presentation of «stages» in the innovation pipeline fully supports formally modeled process as we propose in this paper.

In this paper, the State/Activity Model UML diagram is used for model specification of the EE management process in industry. For future research, we plan to integrate the goal-oriented requirements language (GRL) and the scenario-oriented notation Use Case Maps (UCM) [9] for process modeling purpose. GRL is designed to support goal-oriented and agent-oriented modeling and reasoning, providing guidance to the design process. UCM allows the behavioral aspects of the designed system to be visualized at varying levels of abstraction. The two notations complement each other enableing technical solutions to be described and evaluated with respect to corresponding contributions to the objectives of different stakeholders, while guiding the design towards viable solutions.

VI. Conclusion

In this paper, we developed process model facilitating application of agile methodologies to the strategic level of the EE management in industry. Also, we identified basic mechanisms of the collaborative EE management system.

References

[1] http://agilemodeling.com/

[2] Bodin, L.D., Gordon, L.A. Loeb, M.P., "Evaluating security investments using the analytic hierarchy process", *Communication of the ACM*, Vol.48, No.2, 2005, pp.78-83.

[3] Engelbart, D., "Toward High-Performance Organizations: A Strategic Role for Groupware", *Bootstrap Institute*, June 1992 (AUGMENT,132811,), http://bootstrap.org/augdocs/augment-132811.htm

[4] Fischer, G., Giaccardi, E., Ye, Y., Sutcliffe, A. G., & Mehandjiev, N., "Meta-Design: A Manifesto for End-User Development," *Communications of the ACM*, 47(9), 2004, pp. 33-37.

[5] Henderson, A., "The innovation pipeline: design collaborations between research and development", *Interactions*, Vol. 12, Issue 1 January + February 2005, pp.24-29, ACM Press.

[6] Highsmith, J., Cockburn, A., "Agile Software Development: The Business of Innovation", *IEEE Computer*, Sept. 2001.

[7] Hudson, W., "A tale of two tutorials: a cognitive approach to interactive system design and interaction design meets agility", *Interactions*, Vol. 12, Issue 1 January + February 2005, pp.49-51, ACM Press.

[8] Huhns, M., Singh, M., "Service-Oriented Computing: Key Concepts and Principles," *IEEE Internet Computing*, vol. 9, no. 1, 2005, pp. 75-81.

[9] Liua, L., Yu, E., "Designing information systems in social context: a goal and scenario modelling approach," *Information Systems* 29 (2004), pp. 187–203.

[10] Tosic, M., "Meta-Architecture for Intelligent Information Systems", *Workshop on Designing for Reflective Practitioners: Sharing and Assessing Progress by Diverse Communities*, CHI2004.

AUTOR INDEX